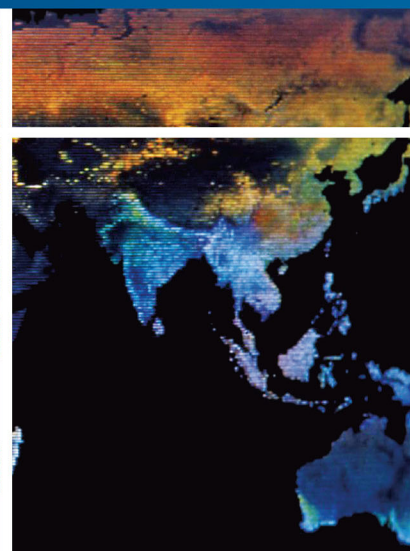
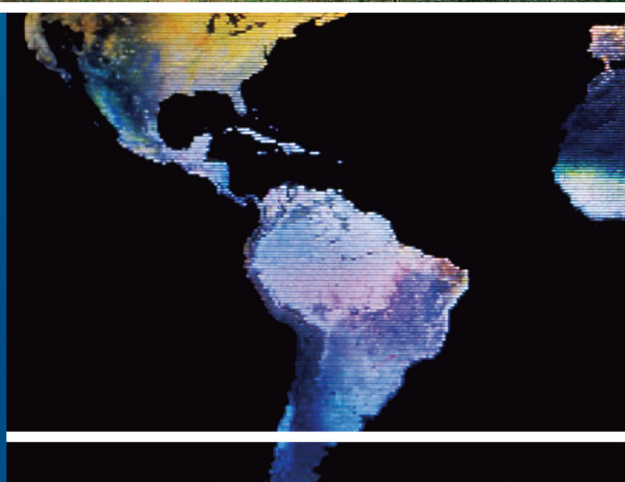
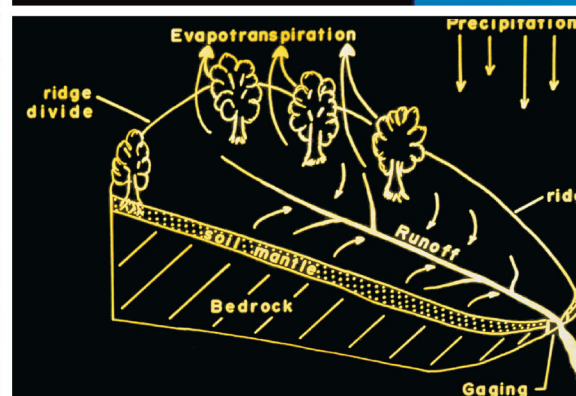


PHYSICAL HYDROLOGY

Third Edition



S. Lawrence Dingman



PHYSICAL HYDROLOGY

Third Edition

S. Lawrence Dingman

University of New Hampshire



Long Grove, Illinois

For information about this book, contact:

Waveland Press, Inc.
4180 IL Route 83, Suite 101
Long Grove, IL 60047-9580
(847) 634-0081
info@waveland.com
www.waveland.com

Cover photo credits (from top to bottom): Delta River, Alaska, photo by author. Meteorological station, photo by author. Earth surface composite, courtesy of NASA. Watershed water-balance drawing, courtesy of R. S. Pierce, US Forest Service.

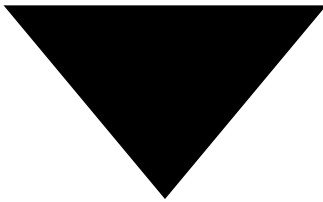
Copyright © 2015 by S. Lawrence Dingman

10-digit ISBN 1-4786-1118-9
13-digit ISBN 978-1-4786-1118-9

All rights reserved. No part of this book may be reproduced, stored in a retrieval system, or transmitted in any form or by any means without permission in writing from the publisher.

Printed in the United States of America

7 6 5 4 3 2 1



Contents

Preface ix

Part I: Introduction 1

1 Hydrology: Basic Concepts and Challenges 3
1.1 Definition and Scope of Hydrology 3
1.2 Approach and Scope of This Book 3
1.3 Physical Quantities and Laws 7
1.4 Dimensions and Units 7
1.4.1 Dimensions 7
1.4.2 Units 8
1.4.3 Dimensional Properties of Equations 8
1.5 Properties of Water 9
1.5.1 Freezing and Melting Temperatures 10
1.5.2 Density 10
1.5.3 Surface Tension 10
1.5.4 Viscosity and Turbulence 11
1.5.5 Latent Heats 12
1.5.6 Specific Heat (Heat Capacity) 12
1.5.7 Solvent Power 12
1.6 Hydrologic Systems and the Conservation Equations 13
1.6.1 Hydrologic Systems 13
1.6.2 The Conservation Equations 14
1.7 The Watershed 15
1.7.1 Definition 15
1.7.2 Delineation 15
1.8 The Regional Water Balance 17
1.8.1 The Water-Balance Equation 18
1.8.2 Evaluation of Water-Balance Components 19
1.8.3 Summary 23

1.9 Special Characteristics of Hydrologic Variables 23
1.9.1 Spatial Variability 23
1.9.2 Temporal Variability 24
1.10 Hydrologic Storage 27
1.10.1 Definition 27
1.10.2 Storage Effects 27
1.10.3 Residence Time 28
1.11 Uncertainty in Hydrology 28
1.11.1 Causes of Uncertainty 28
1.11.2 Treatment of Random Uncertainty in Computations 29
1.12 Application of Basic Concepts to Modeling Watershed Functioning 36
1.13 The Future of Hydrology 39
▼ EXERCISES 41 ▼ NOTES 45
2 The Global Context: Climate, Hydrology, and the Critical Zone 47
2.0 Introduction 47
2.1 Basic Aspects of Global Climate 47
2.1.1 Laws of Radiant Energy Exchange 47
2.1.2 The Atmosphere 49
2.1.3 Global Energy Budget 51
2.1.4 Latitudinal Energy Transfer 54
2.1.5 The General Circulation and the Distribution of Pressure and Temperature 55
2.1.6 Large-Scale Internal Climatic Variability and Teleconnections 59
2.2 The Global Hydrologic Cycle 63
2.2.1 Stocks and Fluxes 63
2.2.2 Distribution of Precipitation 67
2.2.3 Distribution of Evapotranspiration 71
2.2.4 Distribution of Runoff 74
2.2.5 Continental Water Balances 77

2.2.6 Rivers, Lakes, and Reservoirs	77
2.2.7 Material Transport by Rivers	79
2.2.8 Climate Change and the Hydrologic Cycle	84
2.3 Hydrology and the Critical Zone	100
2.3.1 Hydrology, Soils, and Climate	100
2.3.2 Hydrology, Vegetation, and Climate	104
▼ EXERCISES	107
▼ NOTES	108

Part II: Surface-Atmosphere Water and Energy Exchange 109

3 Principles and Processes 111

3.0 Introduction	111
3.1 Pressure-Temperature-Density Relations	111
3.2 Water Vapor	112
3.2.1 Vapor Pressure	113
3.2.2 Absolute Humidity	113
3.2.3 Specific Humidity	113
3.2.4 Relative Humidity	113
3.2.5 Dew Point	114
3.2.6 Precipitable Water	114
3.3 The Evaporation Process	114
3.3.1 Vapor Exchange	114
3.3.2 Latent Heat	115
3.4 The Precipitation Process	116
3.4.1 Cooling	117
3.4.2 Condensation	117
3.4.3 Droplet Growth	118
3.4.4 Importation of Water Vapor	119
3.5 Turbulent Exchange of Momentum, Mass, and Energy	119
3.5.1 Turbulence	120
3.5.2 Vertical Distribution of Wind Velocity	122
3.5.3 Turbulent Diffusion	122
3.5.4 Eddy Correlation	129
▼ EXERCISES	132
▼ NOTES	132

4 Precipitation 133

4.1 Meteorology	133
4.1.1 Fronts and Extra-Tropical Cyclones	134
4.1.2 The Intertropical Convergence Zone	136
4.1.3 Tropical Cyclones	137
4.1.4 Convective Precipitation	141
4.1.5 Orographic Precipitation	141
4.1.6 Occult Precipitation and Dew	146

2.2.7 Material Transport by Rivers	79
2.2.8 Climate Change and the Hydrologic Cycle	84
2.3 Hydrology and the Critical Zone	100
2.3.1 Hydrology, Soils, and Climate	100
2.3.2 Hydrology, Vegetation, and Climate	104
▼ EXERCISES	107
▼ NOTES	108
4.1.7 Moisture Sources and Precipitation Recycling	146
4.1.8 Determining Precipitation Type	147
4.2 Measurement	148
4.2.1 Point Measurement	148
4.2.2 Radar Measurement	159
4.2.3 Satellite Measurement	161
4.3 Areal Estimation from Point Measurements	162
4.3.1 Direct Weighted Averages	162
4.3.2 Spatial Interpolation (Surface Fitting)	166
4.3.3 Comparison of Methods and Summary	171
4.3.4 Precipitation-Gauge Networks	172
4.3.5 Uncertainty Analysis of Gauge Networks	172
4.4 Precipitation Climatology	181
4.4.1 Long-Term Average Precipitation	181
4.4.2 Variability of Precipitation	182
4.4.3 Extreme Rainfalls	185
4.4.4 Anthropogenic Effects on Precipitation Climatology	198
▼ EXERCISES	200
▼ NOTES	202
5 Snow and Snowmelt 203	
5.1 Hydrologic Importance of Snow	203
5.2 Material Characteristics of Snow	205
5.2.1 Snow Properties	205
5.2.2 Snowpack Metamorphism	208
5.3 Measurement of Snow and Snowmelt	209
5.3.1 Precipitation	210
5.3.2 Snowfall	213
5.3.3 Snowpack and Snow Cover	213
5.3.4 Snowmelt, Ablation, and Water Output	218
5.4 Distribution of Snow	218
5.4.1 Effects of Elevation and Aspect	219
5.4.2 Effects of Vegetation	219
5.5 Snowmelt Processes	221
5.5.1 The Snowpack Energy Balance	223
5.5.2 Energy-Exchange Processes	226
5.5.3 Relative Importance of Energy-Balance Terms	234
5.6 Snowmelt Runoff Generation	239
5.6.1 Flow in the Unsaturated Zone	240
5.6.2 Flow in the Basal Saturated Zone	244
5.7 Snowmelt Modeling	244
5.7.1 Importance of Modeling	244
5.7.2 Approaches to Snowmelt Modeling	245
5.7.3 Evaluation of Snowmelt Models	246
5.7.4 Summary	250
▼ EXERCISES	251
▼ NOTES	252

6 Evapotranspiration 253

- 6.1 Evaporation and Heat-Exchange Processes 254
 6.1.1. Vapor-Pressure Relations 254
 6.1.2 Evaporation as a Diffusive Process 254
 6.1.3 Latent-Heat Exchange 255
 6.1.4 Sensible-Heat Exchange 255
 6.1.5 The Bowen Ratio, the Psychrometric Constant, and the Evaporative Fraction 256
 6.1.6 The Energy Balance 256
 6.2 Classification of Evapotranspiration Processes 257
 6.3 Free-Water and Lake Evaporation 257
 6.3.1 Eddy Correlation 258
 6.3.2 Mass Transfer 258
 6.3.3 Energy Balance 260
 6.3.4 Penman or Combination Method 263
 6.3.5 Pan Evaporation 267
 6.3.6 Water-Balance Approach 270
 6.3.7 Summary and Example Calculations 271
 6.4 Bare-Soil Evaporation 274
 6.5 Transpiration 275
 6.5.1 The Transpiration Process 275
 6.5.2 Measurement of Transpiration 277
 6.5.3 Modeling Transpiration 278
 6.6 Interception and Interception Loss 283
 6.6.1 Definitions 285
 6.6.2 Field Measurement of Interception 286
 6.6.3 Modeling 286
 6.6.4 Evaporation of Intercepted Water 290
 6.6.5 Hydrologic Importance of Interception Loss 290
 6.7 Potential and Reference-Crop Evapotranspiration 292
 6.7.1 Conceptual Definition 292
 6.7.2 Operational Definitions 293
 6.7.3 Direct Measurement: Lysimeters, Pans, and Atmometers 295
 6.7.4 Comparison of PET/RET Estimation Methods 296
 6.8 Actual Evapotranspiration 298
 6.8.1 Potential-Evapotranspiration Approaches 298
 6.8.2 Water-Balance Approaches 304
 6.8.3 Turbulent-Exchange and Energy-Balance Approaches 306
 6.8.4 Methods Based on Water Quality 307
 ▼ EXERCISES 307 ▼ NOTES 309

**Part III:
Water Movement on the Land 311****7 Principles of Subsurface Flow 313**

- 7.1 Material Properties of Porous Media 313
 7.1.1 Distribution of Particle Sizes and Pores 313
 7.1.2 Particle Density 315
 7.1.3 Bulk Density 315
 7.1.4 Porosity 315
 7.2 Water Storage 320
 7.2.1 Volumetric Water Content 320
 7.2.2 Saturation 323
 7.3 Basic Principles of Saturated Subsurface Flow 323
 7.3.1 Darcy's Law 323
 7.3.2 Limitations of Darcy's Law 324
 7.3.3 Permeability and Hydraulic Conductivity 324
 7.3.4 General Saturated-Flow Equation 325
 7.4 Basic Principles of Unsaturated Subsurface Flow 328
 7.4.1 Surface Tension and Capillarity 328
 7.4.2 Darcy's Law for Unsaturated Flow 330
 7.4.3 Soil-Water Pressure 330
 7.4.4 Unsaturated Hydraulic Conductivity 333
 7.4.5 Analytic Approximation of $\psi(\theta)$ and $K_h(\theta)$ Relations 334
 7.4.6 $\psi(\theta)$ and $K_h(\theta)$ Relations and Soil Texture 335
 7.4.7 General Unsaturated-Flow Equation 339
 ▼ EXERCISES 342 ▼ NOTES 343

8 Infiltration and Water Movement in Soils 345

- 8.1 Water Conditions in Soils 345
 8.1.1 Field Capacity 345
 8.1.2 Permanent Wilting Point 347
 8.1.3 Soil-Water Status 348
 8.1.4 Hydrologic Soil Horizons 350
 8.1.5 Equilibrium Soil-Water Profiles 352
 8.1.6 Relation between Hydrologic and Pedologic Horizons 353
 8.2 The Infiltration Process 355
 8.2.1 Definitions 355
 8.2.2 General Features 356
 8.2.3 Factors Affecting Infiltration Rate 357

8.3 Measurement of Infiltration	359	9.5 Evaluation of Ground-Water Balance Components	422
8.3.1 Ring Infiltrometers	359	9.5.1 Recharge from Infiltration, R_I	422
8.3.2 Tension (Disc) Infiltrometers	360	9.5.2 Recharge from Surface Water, R_{SW}	430
8.3.3 Sprinkler-Plot Studies	360	9.5.3 Ground-Water Contribution to Streamflow, Q_{GW}	431
8.3.4 Observation of Soil-Water Changes	361	9.5.4 Capillary Rise, CR	436
8.3.5 Preferential Flow	361	9.5.5 Deep Seepage, G_{in} and G_{out}	438
8.4 Quantitative Modeling of Infiltration at a Point	361	9.6 Impacts of Ground-Water Development on Areal Hydrology	441
8.4.1 Idealized Conditions	361	9.6.1 Hydraulics of Ground-Water Development	441
8.4.2 Solutions to the Richards Equation	361	9.6.2 Effects of Ground-Water Extraction	446
8.4.3 The Green-and-Ampt Model	366	9.6.3 "Safe Yield"	450
8.4.4 Comparison of Green-and-Ampt and Philip Models	375	▼ EXERCISES 451	▼ NOTES 453
8.5 Infiltration Over Areas	375		
8.5.1 Spatial and Temporal Variability of Infiltration	375		
8.5.2 Modeling Infiltration Over Areas	375		
8.6 Redistribution of Soil Water	381	10 Runoff Generation and Streamflow 455	
8.6.1. Redistribution without Evapotranspiration	381	10.1 The Watershed and the Stream Network	455
8.6.2. Redistribution with Evapotranspiration	383	10.1.1 The Watershed	455
8.7 Summary	384	10.1.2 The Stream Network	456
▼ EXERCISES 386	▼ NOTE 387	10.1.3 Drainage Density	458
9 Ground Water in the Hydrologic Cycle 389		10.1.4 Relations between Network Properties and Stream Response	458
9.1 Aquifers and Aquitards	390	10.2 General Characteristics of Stream Response	459
9.1.1 Definitions	390	10.2.1 Basic Features	459
9.1.2 Unconfined and Confined Aquifers	390	10.2.2 Heuristic Hydrograph Separation	462
9.1.3 Storage Properties of Aquifers	392	10.2.3 Event-Flow Volume	465
9.1.4 Transmission Properties of Aquifers	395	10.2.4 Quantitative Description of Response Hydrographs	469
9.1.5 Aquifer Response Time and Residence Time	396	10.2.5 Effects of Input and Basin Characteristics on the Hydrograph: Exploration via a Simple Model	471
9.2 Regional Ground-Water Flow	397	10.3 Identification of Runoff Sources	477
9.2.1 Equation for Steady Ground-Water Flow	397	10.4 Event-Flow-Generation Processes	478
9.2.2 General Features of Regional Ground-Water Flow	397	10.4.1 Channel Precipitation	479
9.2.3 Effects of Topography	399	10.4.2 Overland Flow	480
9.2.4 Effects of Geology	400	10.4.3 Subsurface Flow	487
9.2.5 Synthesis: Effects of Topography, Geology, and Climate	404	10.4.4 Overview of Hillslope Processes	499
9.3 Ground-Water-Surface-Water Relations	408	10.5 Channel Processes	503
9.3.1 Ground Water and Streams	408	10.5.1 Hydraulic Relations	503
9.3.2 Ground Water and Lakes and Wetlands	414	10.5.2 Simple Streamflow Routing	505
9.3.3 Ground Water and the Ocean	416	10.6 Rainfall-Runoff Modeling	505
9.4 Ground Water in the Regional Water Balance	416	10.6.1 Runoff Processes and Rainfall-Runoff Models	506
		10.6.2 The Watershed as an Impulse-Response System	510
		10.6.3 Inputs to Rainfall-Runoff Models	510
		10.6.4 Rainfall-Runoff Models	514
		▼ EXERCISES 529	▼ NOTES 529

Appendix A: Measurement Precision, Significant Figures, and Unit and Equation Conversion 531

- A.1 Measurement Precision and Significant Figures 531
- A.2 Unit Conversion 532
- A.3 Conversion of Dimensionally Inhomogeneous Equations 537

Appendix B: Water as a Substance 539

- B.1 Structure of Water 539
- B.2 Properties of Water 544

Appendix C: Statistical Concepts Useful in Hydrology 549

- C.1 Random Variables, Populations, and Samples 549
- C.2 Probability 549
- C.3 Probability Distributions 550
- C.4 The Normal Distribution 555
- C.5 Time Series, Exceedence Probability, and Return Period 556
- C.6 Covariance, Correlation, and Autocorrelation 556
- C.7 Data Analysis: Hypothesis Tests 559
- C.8 Data Analysis: Display and Preliminary Assessment 560
- C.9 Data Analysis: Identifying Candidate Probability Distributions 562
- C.10 Data Analysis: Estimating Parameters of Probability Distributions 565
- C.11 Data Analysis: Sampling Error 566

▼ NOTE 570

Appendix D: Estimation of Daily Clear-Sky Incident Solar Radiation 571

- D.1 Extraterrestrial Solar Radiation 571
- D.2 Clear-Sky Radiation on a Horizontal Surface 575
- D.3 Radiation on a Sloping Surface 577

Appendix E: Stream-Gauging Methods for Short-Term Studies 579

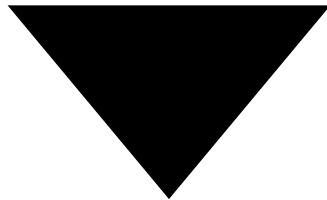
- E.1 Selection of Measurement Location 580
- E.2 Volumetric Gauging 580
- E.3 Velocity-Area Method 580
- E.4 Dilution Gauging 585
- E.5 Gauging with Portable Weirs and Flumes 586
- E.6 Stage Measurement 589

Appendix F: Hydrologic Simulation Modeling 595

- F.1 What Is a Simulation Model? 595
- F.2 Purposes of Simulation Models 596
- F.3 Types of Simulation Models 597
- F.4 The Modeling Process 600
- F.5 Model Evaluation 602
- F.6 Final Words of Caution 604

Appendix G: Development of Scientific Hydrology 607

- References 611
- Index 635



Preface

The goal of *Physical Hydrology* is to develop an understanding of the conceptual basis of the science of hydrology and to introduce the quantitative relations that implement that understanding in addressing scientific and water-resources-management questions. Previous editions apparently fulfilled a need for a comprehensive text in hydrology for upper-level undergraduates and graduate students, and I have been pleased with its reception by colleagues and students.

At the time of the first edition (1992), hydrology was still in the process of establishing itself as a distinct discipline with vital insights to fundamental and practical environmental problems (Eagleson et al. 1991), and the book was intended as a contribution to that process. By the time of the second edition (2002), much progress had been made in that regard, and my primary goals in revising *Physical Hydrology* were to incorporate significant advances in hydrologic science, to provide an explicit connection of that science to hydrologic modeling, and to make more complete and useful the treatment of the relation between scientific hydrology and water-resources management.

Hydrology is now well established as a distinct geoscience and, in the decade-plus since the second edition, there has been what seems to be exponential progress in the field. Much of this progress (which has been published in many dozens of different journals) is due to improvements in the ability to observe hydrologic variables and to assimilate and analyze large areally distributed data sets. But there has also been significant conceptual progress in understanding the ways in which the physics of micro-level processes relate (or don't relate) to the larger scales dictated by hydrologic questions and data availabil-

ity; in understanding the connections among hydrology, climate, ecosystems, soils, and geology; in understanding the nature and limitations of simulation models; and in developing new statistical techniques appropriate to the quantity and quality of hydrologic data.

It has been a daunting challenge to incorporate this progress in the third edition, and one that can be, at best, only partially met. In this attempt I have, in addition to making essential updates, made major changes in the organization and scope of the book: Former chapters 1–9 and portions of some appendices have been substantially reorganized into 10 chapters within three major sections, plus seven appendices, as described below.

Part I: Introduction

Chapter 1: Hydrology: Basic Concepts and Challenges

This chapter is a greatly expanded and much more substantive introduction to hydrologic science that now includes dimensions and units, properties of water, characteristics of hydrologic variables (including nonstationarity), and uncertainty in hydrology, as well as hydrologic systems and conservation equations. The chapter concludes with an application of many of the basic concepts in a case study exploring the prediction of watershed runoff.

Chapter 2: The Global Context: Climate, Hydrology, and the Critical Zone

As in the previous edition, chapter 2 provides an overview of the global aspects of the hydrologic cycle

and its interactions with climate, soils, and major biomes. In addition to describing the basic features of global water and energy balances, this chapter incorporates many of the advances in these areas, particularly the role of teleconnections. It includes a detailed survey of the observational evidence for recent changes in hydroclimate and an analytical exploration of the impact of climate change on runoff.

Part II: Surface-Atmosphere Water and Energy Exchange

Chapter 3: Principles and Processes

This chapter provides the basic physical concepts for understanding precipitation, snowmelt, and evapotranspiration, which are covered in the following three chapters. It introduces relevant gas laws and the characterization of atmospheric water vapor, and describes the processes of precipitation formation and evaporation. The detailed treatment of turbulent diffusion in the lower atmosphere, which was formerly in an appendix, is now incorporated here.

Chapter 4: Precipitation

The scope of this chapter is essentially the same as in the second edition, with updated treatments of the meteorology, measurement, areal estimation, and climatology of precipitation.

Chapter 5: Snow and Snowmelt

This chapter also retains the scope of the previous editions, covering the hydrologic importance, material characteristics, measurement, and distribution of snow, as well as the physics and modeling of snowmelt.

Chapter 6: Evapotranspiration

This chapter now occupies a more logical place in the sequence of topics, while retaining the basic treatment of the second edition. After reviewing the basic physics and classification of evaporative processes, it develops the basic approaches to estimating evaporation from water surfaces, bare soil, plants (interception and transpiration), and land surfaces, including the concepts of potential and reference-crop evapotranspiration.

Part III: Water Movement on the Land

Chapter 7: Principles of Subsurface Flow

This chapter provides the essential physics for understanding infiltration, ground-water flow, and runoff generation covered in the following chapters. It introduces the material properties of porous media and provides a more unified development of Darcy's law and the general equations of saturated and unsaturated subsurface flow than in the second edition. Capillarity is now discussed here as a basis for understanding water movement in the unsaturated zone. The moisture-characteristic and conductivity-characteristic curves, their analytic approximations, and their relations to soil texture are presented here in more detail than in the previous edition.

Chapter 8: Infiltration and Water Movement in Soils

This chapter retains the treatment of the second edition, including water conditions in soils, qualitative and expanded quantitative descriptions of the infiltration process, the measurement of infiltration, infiltration over areas (now including scaling approaches), and redistribution of soil moisture.

Chapter 9: Ground Water in the Hydrologic Cycle

As in the second edition, this chapter focuses on basic relations of regional ground-water flow to topography, geology, and climate and the connections between ground water and surface water in lakes, streams, and the ocean. The ground-water balance and approaches to estimating its components remain a central focus, and the discussion of base-flow separation has been expanded to include the base-flow index. As before, the chapter concludes with an introductory treatment of well hydraulics as a basis for understanding the effects of ground-water development on regional hydrology and the concept of "safe yield."

Chapter 10: Runoff Generation and Streamflow

The contents of this chapter are essentially the same as in the second edition, but they have been reorganized to provide a more logical treatment. The chapter begins with a description of the watershed and its stream network and introduces the basic features of streamflow hydrographs and the geologic, topographic, meteorologic, and antecedent conditions that affect their shape. There is an expanded and updated discussion of chemical and isotopic end-member analysis for identification of runoff sources. The effects of channel processes on runoff characteristics are introduced. As in the second edition, the chapter concludes with an overview of conceptual rainfall-runoff models, including unit hydrographs and an updated treatment of the curve-number approach.

Appendices

Appendix A: Measurement Precision, Significant Figures, and Unit and Equation Conversion is as in the second edition, except that the discussion of dimensions has been moved to chapter 1. This appendix now includes a table that can be used to make virtually any unit conversion that may arise in hydrology.

Appendix B: Water as a Substance is also similar to that in the second edition, but the introduction to some of water's unusual properties is also now incorporated in chapter 1. The appendix now includes an introduction to stable water isotopes and their use in hydrologic analysis.

Appendix C: Statistical Concepts Useful in Hydrology covers essentially the same material as in the second edition, except that (1) there is an expanded discussion of regional frequency analysis and (2) the discussion of model evaluation has been moved to appendix F. The tables and boxes for this appendix are included on the disk accompanying the text.

Appendix D: Estimation of Daily Clear-Sky Incident Solar Radiation is a revised and streamlined version of appendix E of the second edition. Material in the former appendix D (Water and Energy in the Atmosphere) is now incorporated in chapter 3.

Appendix E: Stream-Gauging Methods for Short-Term Studies is essentially the same as appendix F of the second edition.

Appendix F: Hydrologic Simulation Modeling is a revised version of material that was covered in chapter

2 of the second edition. It now concludes with an expanded presentation of quantitative criteria used for model calibration and validation (formerly treated in appendix C).

Appendix G: Development of Scientific Hydrology is an extensively revised overview of the history of scientific hydrology that concluded chapter 1 of the second edition.

Other New Features

- Each chapter is accompanied by a number of exercises. These have been revised to emphasize analyses using material and data obtained from the World Wide Web and exploration of the local hydrologic environment.
- The disk accompanying the text has been revised, and in addition to providing Excel programs (including incident solar radiation, snowmelt, evapotranspiration, and infiltration) to use in conjunction with the exercises, it includes some longer explorations of lake water balances and the use of simulation modeling in exploring watershed hydrologic processes.
- SI units are now used exclusively.
- In keeping with the goal of providing an entrée to the literature of the field, this edition continues the practice of supporting its discussion with extensive reference citations, in the style of a journal article rather than that of most textbooks. In this revision, over 400 new reference citations have been added, and they now total over 1,100.
- Chapter 10 of the second edition of *Physical Hydrology* provided much valuable material on water-resources management. Although an extensive discussion of this topic was not included in the third edition, most of the second edition chapter 10 has been made available as an additional resource for students and instructors on the CD that accompanies the text.
- The detailed discussions of the way various hydrologic processes are simulated in the BROOK model have been dropped. Though the space previously devoted to describing the BROOK model as a window on simulation modeling had a justifiable purpose, omitting it seemed wise because (1) the model was not in widespread use and (2) there are many available models, and each instructor likely has her/his own preference that she/he may wish to use in conjunction with the text.

Acknowledgments

Don Rosso, my editor at Waveland Press, first suggested that I undertake a third edition and has guided the process from the beginning. Extensive discussions with Richard H. Cuenca of Oregon State University and J. Matthew Davis of the University of New Hampshire, as well as the comments of three anonymous reviewers of the complete text, had a major influence on shaping the book's re-organization.

My thanks go again to all those who helped with reviews of all or parts of previous editions: J. M. Harbor, R. L. A. Adams, W. A. Bothner, C. V. Evans, S. E. Frolking, F. R. Hall, R. C. Harriss, S. L. Hartley, E. Linder, D. S. L. Lawrence, M. A. Person, G. A. Zielinski, Marc Parlange, David Huntley, Benjamin S. Levy, Guido D. Salvucci, Kaye L. Brubaker, Michael E. Campana, David L. Brown, Richard Kattleman, Richard H. Hawkins, James Buttle, David Tarboton,

Richard Vogel, W. Breck Bowden, James R. Wallis, Barry Keim, Mark Person, and C. Anthony Federer.

Diane Evans of Waveland Press has worked tirelessly to identify incorrect cross-references, missing literature citations, inconsistent symbols, and other editorial errors. I've corrected those, but am responsible for any that remain.

I am eternally grateful to Francis R. Hall, who was my mentor at UNH and did much to educate me about the science of hydrology and guide me through some of the pitfalls of academia. And, as with previous editions, I could not have completed this work without the love, support, and editorial assistance of my wife, Dr. Jane Van Zandt.

S. Lawrence Dingman
Eastham, Massachusetts



Part I

Introduction



Hydrology

Basic Concepts and Challenges

1.1 Definition and Scope of Hydrology

Hydrology is the geoscience that describes and predicts the occurrence and circulation of the earth's fresh water. The principal focus of hydrology includes:

- the distribution and movement of water substance on and under the earth's land surfaces, including its exchanges with the atmosphere;
- its physical and chemical interactions with earth materials; and
- the biological processes and human activities that affect its movement, distribution, and quality.

The circulation of water on land occurs in the context of the **global hydrologic cycle**, which includes the spatial and temporal variations of water substance in the oceanic and atmospheric as well as the terrestrial compartments of the global water system (figure 1.1). Thus, the study of the global hydrologic cycle is included in the scope of hydrology (Eagleson et al. 1991). The hydrologic cycle is a central component of the earth's climate system at all scales, from local to global (Peixoto and Oort 1992).

Figure 1.2 shows the major storage components and flows of the global hydrologic cycle, and figure 1.3 (on p. 5) shows the storages and flows of energy

and water that constitute the **land phase** of the cycle. Figure 1.4 (on p. 6) gives a quantitative sense of the range of time and space scales in the domain of hydrologic science.

Figure 1.5 (on p. 6) shows the position of hydrologic science in the spectrum from basic sciences to water-resource management. Hydrology is an inherently interdisciplinary geoscience, built upon the basic sciences of mathematics, physics, chemistry, and biology, and upon its sister geosciences. Much of the motivation for answering hydrologic questions has and will continue to come from the practical need to manage water resources and water-related hazards. Thus, hydrologic science is the basis for hydrologic engineering and, along with economics and related social sciences, for water-resources management.

1.2 Approach and Scope of This Book

This text has three principal themes:

1. The basic physical concepts underlying the science of hydrology and the major conceptual and practical challenges facing it (chapters 1, 3, and 7).
2. The global scope of hydrologic science, including its relation to global climate, soils, and vegetation (chapter 2).

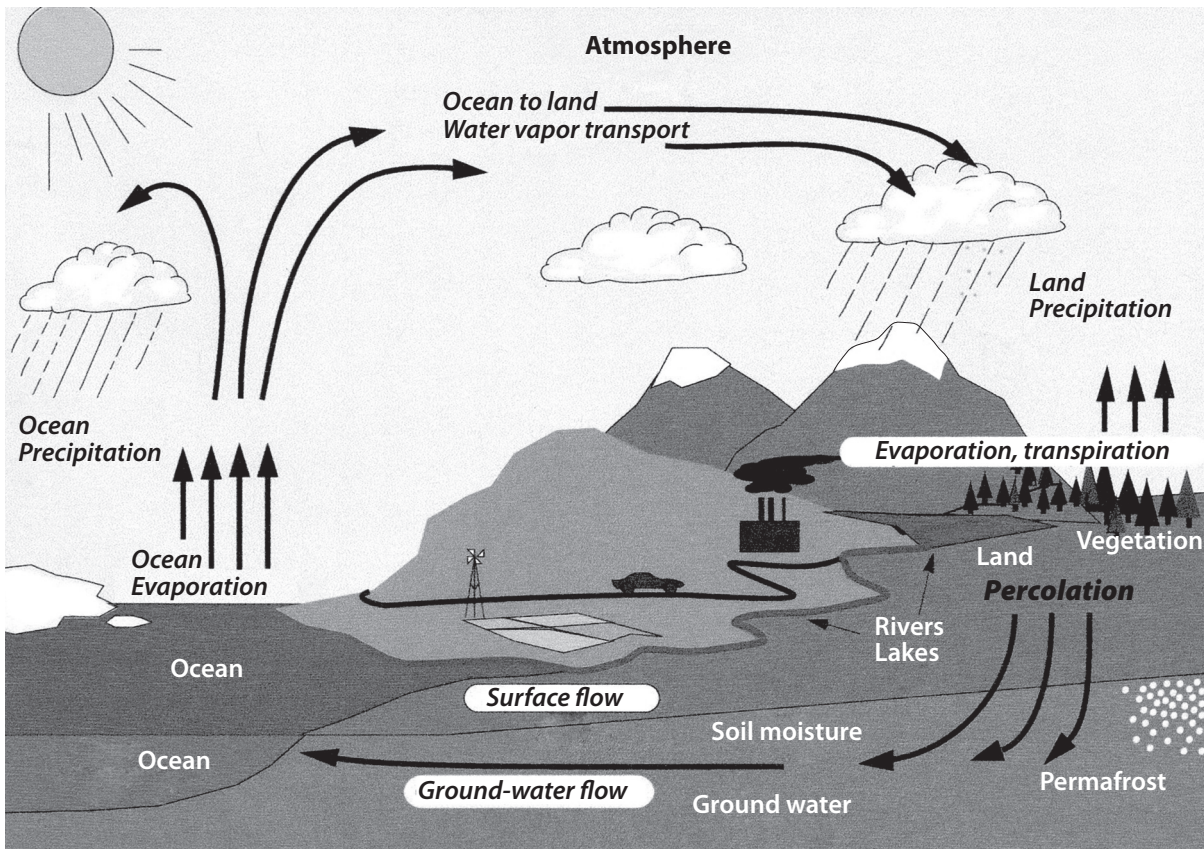


Figure 1.1 Pictorial representation of the global hydrological cycle [Trenberth et al. (2007). Estimates of the global water budget and its annual cycle using observational and model data. *Journal of Hydrometeorology* 8:758–769, reproduced with permission of American Meteorological Society].

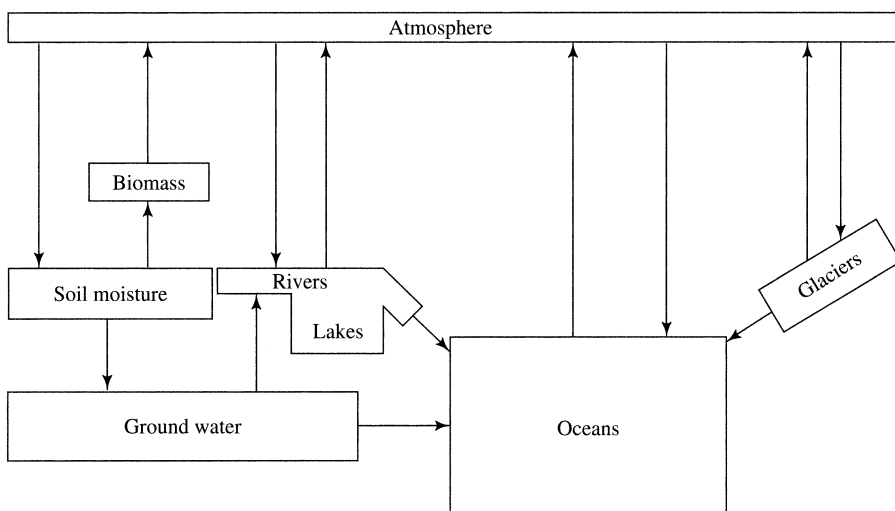


Figure 1.2 The principal storages (boxes) and pathways (arrows) of water in the global hydrologic cycle.

3. The land phase of the hydrologic cycle (chapters 4–6 and 8–10, which proceed more or less sequentially through the processes shown in figure 1.3).

A series of appendices supplement the main themes, including: (A) dimensions, units, and numerical precision; (B) properties of water; (C) statistical concepts; (D) computation of clear-sky solar radiation; (E) stream-gauging methods; (F) hydrologic modeling; and (G) the history of hydrology.

The treatments in chapters 3–10 draw on your knowledge of basic science (mostly physics, but also chemistry, geology, and biology) and mathematics to develop a sound intuitive and quantitative sense of the way in which water moves through the land phase of the hydrologic cycle. In doing this we focus on (1) relatively simple but conceptually sound quantitative

representations of physical hydrologic processes and (2) approaches to the measurement of the quantities and rates of flow of water and energy involved in those processes. Chapter 3 introduces the basic physical principles underlying the processes of precipitation formation, snowmelt, and evapotranspiration, which are covered in chapters 4–6. Chapter 7 introduces the basic physical principles underlying the movement of water in the subsurface, which are the foundation for understanding soil-water, ground-water, and runoff processes discussed in chapters 8–10.

The material covered in this text constitutes the foundation of physical hydrology; the advances in the science that come in the next decades—in understanding watershed response to rain and snowmelt, in forecasting the hydrologic effects of land-use and

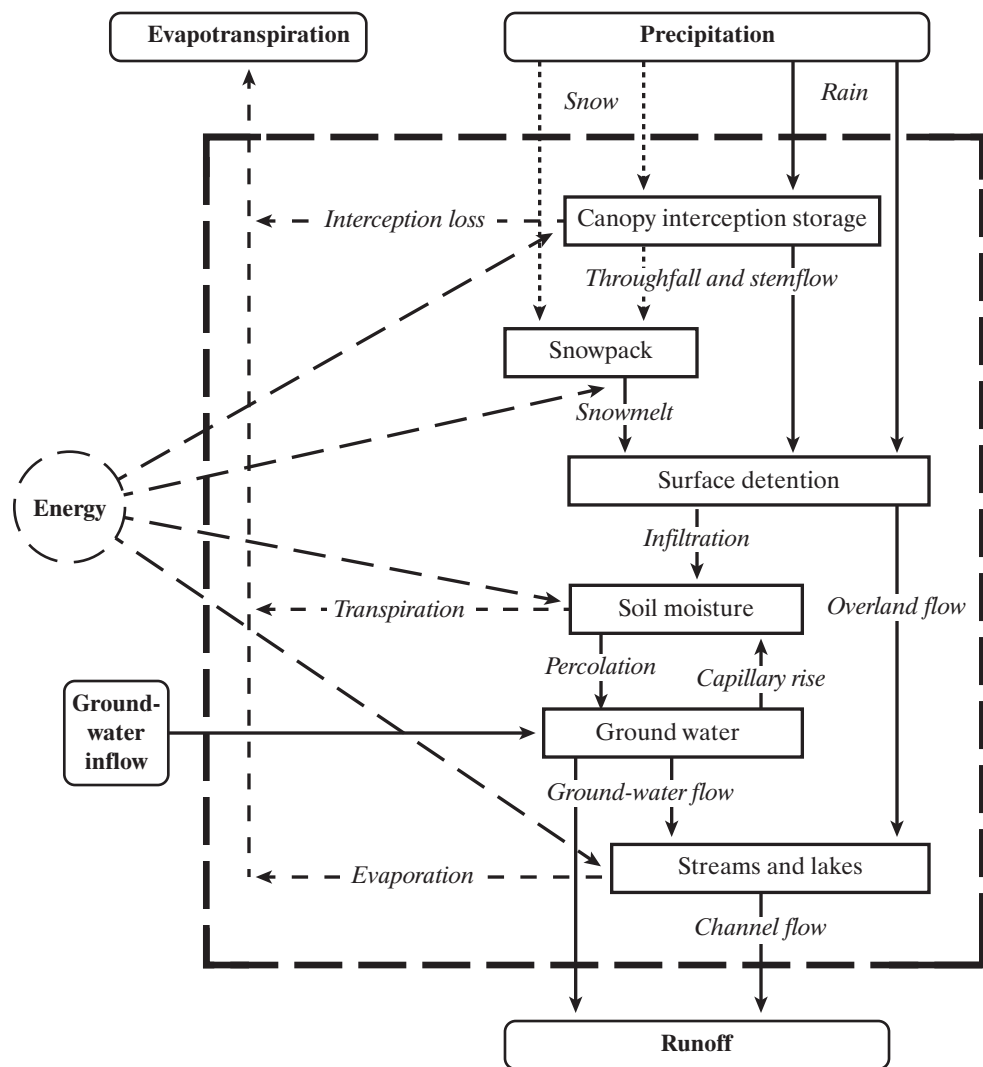


Figure 1.3 The principal storages (boxes) and pathways (arrows) of water in the land phase of the hydrologic cycle. The heavy dashed line represents the boundary of a watershed or other region.

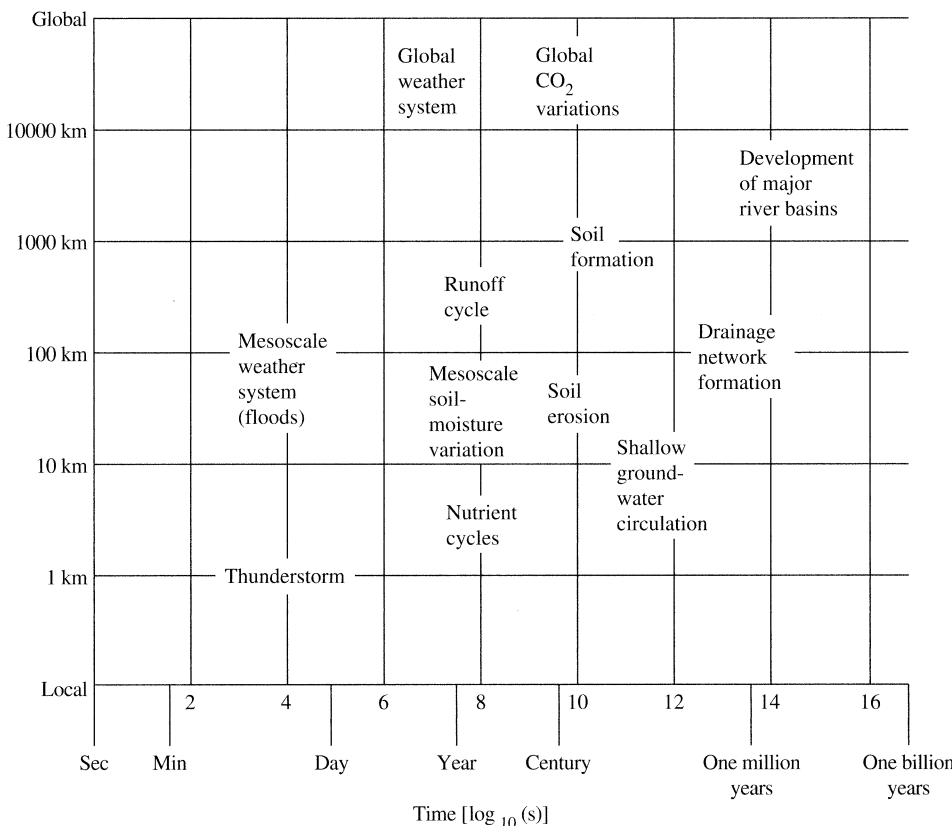


Figure 1.4 Range of space and time scales of hydrologic processes (Eagleson et al., *Opportunities in the Hydrologic Sciences* © 1991 by the US National Academy of Sciences. Reprinted with permission of the National Academy Press).

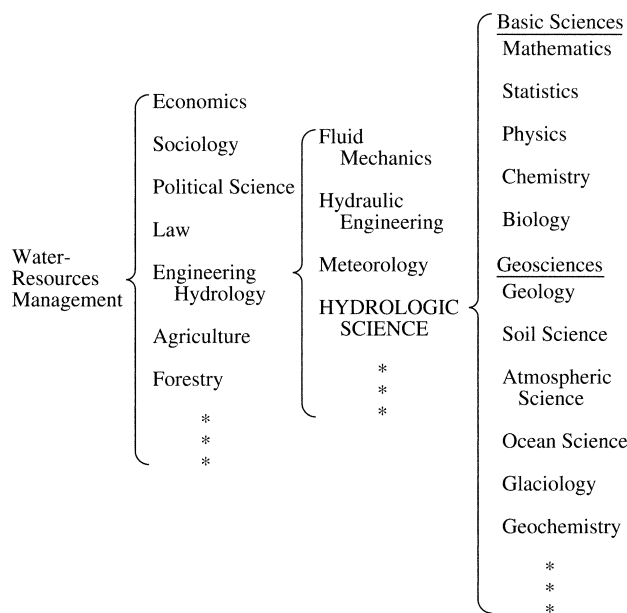


Figure 1.5 Hydrologic science in the hierarchy from basic sciences to water-resources management [adapted from Eagleson et al. (1991)].

climatic change over a range of spatial scales, in understanding and predicting water chemistry, and in other areas—will be built upon this foundation.

1.3 Physical Quantities and Laws

Hydrology is a quantitative geophysical science and, although it is not a fundamental science in the sense that physics and chemistry are, its basic concepts are founded on physical laws. Hydrological relationships are usually expressed most usefully and concisely as mathematical relations among hydrologic quantities, and familiarity with mathematics at least through calculus is required to understand and express hydrological concepts. In many practical and scientific problems, the essential mathematical relations involve statistical concepts, which are often somewhat theoretical and abstract; the basic statistical concepts frequently applied in hydrology are summarized in appendix C.

In this chapter we distill concepts from physics, statistics, and mathematics that are so frequently applied in hydrology that they can be considered basic hydrological concepts. In doing this, we will encounter a number of basic challenges that hydrologists face in pursuing their science. These problems arise because of the scale and complexity of hydrologic processes, difficulties of measurement (important quantities like evapotranspiration and ground-water flow are largely unobservable), and temporal changes (past and future) in boundary conditions.

The basic quantitative relations of physical hydrology are derived from fundamental laws of classical physics, particularly those listed in table 1.1. Derivations of hydrologic relations begin with a statement of the appropriate fundamental law(s) in mathematical form, with boundary and initial conditions appropriate to the situation under study, and are carried out by using mathematical operations (algebra and calculus). This is the approach that we will usually follow in the discussions of hydrologic processes in this text.

1.4 Dimensions and Units

1.4.1 Dimensions

Quantities determined by *measuring* take on a value corresponding to a point on the real number scale that is the ratio of the magnitude of the quantity to the magnitude of a standard unit of measure-

Table 1.1 Summary of Basic Laws of Classical Physics Most Often Applied in Hydrologic Analyses.

Conservation of Mass

Mass is neither created nor destroyed.

Newton's Laws of Motion

1. The momentum of a body remains constant unless a net force acts upon the body (= conservation of momentum).
2. The rate of change of momentum of a body is proportional to the net force acting on the body, and is in the same direction as the net force (force equals mass times acceleration).
3. For every net force acting on a body, there is a corresponding force of the same magnitude exerted by the body in the opposite direction.

Laws of Thermodynamics

1. Energy is neither created nor destroyed (= conservation of energy).
2. No process is possible in which the sole result is the absorption of heat and its complete conversion into work.

Fick's First Law of Diffusion

A diffusing substance moves from where its concentration is larger to where its concentration is smaller at a rate that is proportional to the spatial gradient of concentration.

ment;¹ their dimensional quality is expressed in terms of the fundamental physical **dimensions** force [F] or mass [M], length [L], time [T], and temperature [Θ].

The fundamental dimensional character of measured quantities can be expressed as $[M^a L^b T^c \Theta^d]$ or $[F^e L^f T^g \Theta^h]$, where the exponents a, b, \dots, h are integers or ratios of integers.

The choice of whether to use force or mass is a matter of convenience. Dimensions expressed in one system are converted to the other system via Newton's second law of motion:

$$[F] = [M L T^{-2}]; \quad (1.1a)$$

$$[M] = [F L^{-1} T^2]. \quad (1.1b)$$

The dimensions of energy are $[F L]$ or $[M L^2 T^{-2}]$.² Some physical relations will be clearer if we use [E] to designate the dimensions of energy; thus we define

$$[E] \equiv [M L^2 T^{-2}] = [F L]. \quad (1.2)$$

Quantities obtained by *counting*, or as the ratio of measurable quantities with identical dimensions, are **dimensionless**; their dimensional character is denoted as [1].

Quantities obtained as logarithmic, exponential, and trigonometric functions are also dimensionless.³

Table A.2 gives the dimensional character of quantities commonly encountered in hydrology. Those with dimensions involving length only are classed as **geometric** (angle is included here also), those involving length and time or time only are **kinematic**, those involving mass or force are **dynamic**, and those involving temperature are **thermal** (latent heat is included here also).

1.4.2 Units

Units are the arbitrary standards in which the magnitudes of quantities are expressed. When we give the units of a quantity, we are expressing the ratio of its magnitude to the magnitude of an arbitrary standard with the same fundamental dimension (except, as noted, in the common temperature scales, where an additive term is also involved).

The **Système International** (SI) is the international standard for all branches of science; it will be used throughout this text.

Hydrologists also encounter the **centimeter-gram-second (cgs) system**, which was an earlier version of the SI system. The **British, or common, system** is still the official measurement system of the United States, and so appears in reports of government agencies such as the US National Weather Service (NWS) and the US Geological Survey (USGS).

Largely because of the United States' retention of the British system, hydrologists commonly find it necessary to convert from one set of units to another; rules for doing this are given in appendix A.

It's important to observe unit conversion rules carefully to avoid egregious and embarrassing mistakes!

1.4.3 Dimensional Properties of Equations

The two most important rules to incorporate into your thinking are:

1. An equation that completely and correctly describes a physical relation has the same dimensions on both sides of the equal sign, i.e., it is **dimensionally homogeneous**.
2. In equations, the dimensions and units of quantities are subject to the same mathematical operations as the numerical magnitudes.

A corollary of this latter rule is that only quantities with identical dimensional quality can be added or subtracted.

While there are no exceptions to the requirement of dimensional homogeneity, there are some important qualifications:

- Dimensional homogeneity is a *necessary* but not a *sufficient* requirement for correctly and completely describing a physical relation.
- Equations that are not dimensionally homogeneous can be very useful approximations of physical relationships.

This latter situation arises because the magnitudes of hydrologic quantities are commonly determined by the complex interaction of many factors, and it is often virtually impossible to formulate the physically correct equation or to measure all the relevant independent variables. Thus, hydrologists are often forced to develop and rely on relatively simple **empirical equations** (i.e., equations based on observed relations between measured quantities) that may be dimensionally inhomogeneous. Often, such equations are developed via the statistical process of **regression analysis**. Finally, it is important to recognize that

Equations can be dimensionally homogeneous but not unitarily homogeneous. (However, all unitarily homogeneous equations are of course dimensionally homogeneous.)

This situation can arise because each system of units includes "superfluous" units, such as miles (= 5,280 ft), kilometers (= 1,000 m), acres (= 43,560 ft²), hectares (= 10⁴ m²), liters (= 10⁻³ m³), etc.

As noted, dimensionally and/or unitarily inhomogeneous empirical equations are frequently encountered in hydrology. Because of this:

- The practicing hydrologist should check every equation for dimensional and unitary homogeneity.
- The units of each variable in an inhomogeneous equation MUST be specified.
- If you want to change the units used in an inhomogeneous equation, at least one of the coefficients or constants must change.

The above rules are crucial because

If you use an inhomogeneous equation with units other than those for which it was given, you will get the wrong answer.

Surprisingly, it is not uncommon in the earth sciences and engineering literature to encounter inhomogeneous equations for which units are not specified—so *caveat calculator!*

In practice, there are often situations in which we want to use an inhomogeneous equation with quantities measured in units different from those used in developing it. The steps for determining the new numerical values when an inhomogeneous equation is to be used with new units are detailed in appendix A.

1.5 Properties of Water

Forces acting on water cause it to move through the hydrologic cycle, and the physical properties of water determine the qualitative and quantitative relations between those forces and the resulting motion. These physical properties are in turn determined by its atomic and molecular structures. Thus, although the detailed study of these structures and properties is outside the traditional scope of hydrology, it is important for the student of hydrology to have some understanding of them.

The physical properties of water are highly anomalous. As explained in more detail in appendix B,

Most of the unusual properties of water are due to its being made up of polar molecules that form **hydrogen bonds** between adjacent water molecules and between water molecules and earth materials.

Here we briefly describe the properties of water most important to its behavior in the hydrologic cycle. These are summarized in table 1.2 and described in more detail in appendix B.

Table 1.2 Summary of Properties of Liquid Water (see appendix B for more details).

Property	Uniqueness	Value at Surface	Importance
Melting and boiling points	Anomalously high for molecular weight.	Melting: 0°C Boiling: 100°C	Permits liquid water, as well as vapor and ice, to exist on earth's surface.
Density (ρ_w)	Maximum at 3.98°C, not at freezing point. Expands on freezing.	999.73 kg/m ³ (10°C)	Controls velocities of water flows. Lake and rivers freeze from top down; causes stratification in lakes.
Surface tension (σ)	Higher than most liquids.	0.074201 N/m (10°C)	Controls cloud droplet formation and raindrop growth; controls water absorption and retention in soils.
Viscosity (μ)	Lower than most common liquids.	0.001307 N · s/m ² (10°C)	Controls flow rates in porous media; low value results in turbulence in most surface flows.
Latent heat of vaporization (λ_v)	One of the highest known.	2.471 MJ/kg (10°C)	Controls land-atmosphere heat transfer and atmospheric circulation and precipitation.
Latent heat of fusion (λ_f)	Higher than most common liquids.	3,340 J/kg (0°C)	Controls formation and melting of ice and snow.
Specific heat (heat capacity) (c_w)	Highest of any liquid except ammonia.	4,191 J/kg · K (10°C)	Moderates air and water temperatures; determines heat transfer by oceans.
Solvent capacity	Excellent solvent for ionic salts and polar molecules.		Solution initiates erosion and transports erosion products; plant nutrients and CO ₂ delivered in solution.

1.5.1 Freezing and Melting Temperatures

The hydrogen bonds that attract one water molecule to another can only be loosened (as in melting) or broken (as in evaporation) when the vibratory energy of the molecules is large—that is, when the temperature is high. Because of its anomalously high melting (273.16 K) and boiling temperatures (373.16 K), water is one of the very few substances that exists in all three physical states—solid, liquid, and gas—at earth-surface temperatures (figure 1.6). The Kelvin temperature unit and the Celsius temperature scale are defined by the freezing and melting temperatures of water.

1.5.2 Density

Mass density, ρ_w , is the mass per unit volume [$M\ L^{-3}$] of water, while **weight density** (or **specific weight**), γ_w , is the weight per unit volume [$F\ L^{-3}$]. These are related by Newton's second law (i.e., force equals mass times acceleration):

$$\gamma_w = \rho_w \cdot g, \quad (1.3)$$

where g is the acceleration due to gravity [$L\ T^{-2}$] ($g = 9.81\ m/s^2$ at the earth's surface). Liquid water flows in response to spatial gradients of gravitational force and pressure (i.e., weight per unit area), so either ρ_w or γ_w appears in most equations describing the movement of liquid water.

The change in density of water with temperature is highly unusual (figure 1.7): liquid water at the freezing point is approximately 10% denser than ice and, as liquid water is warmed from 0°C, its density initially increases. This anomalous increase continues until density reaches a maximum of 1,000 kg/m³ at 3.98°C; above this point the density decreases with temperature, as in most other substances.

In the SI system of units, the kilogram (kg) is defined as the mass of 1 m³ of pure water at its temperature of maximum density, and the newton (N) is the force required to impart an acceleration of 1 m/s² to a mass of 1 kg (i.e., 1 N = 1 kg · m/s²). Note that the kilogram is commonly used as a unit of force as well as of mass: 1 kg of force (kg) is the weight of a mass of 1 kg at the earth's surface. Thus, from equation (1.3), 1 kg_f = 9.81 N.

The anomalous density behavior of water is environmentally significant. Because ice is less dense than liquid water, rivers and lakes freeze from the surface downward rather than from the bottom up. And, in lakes where temperatures reach 3.98°C, the density maximum controls the vertical distribution of temperature and causes an annual or semiannual overturn of water that has a major influence on biological and physical processes. However, except in modeling lake behavior,

The variation of water density with temperature is small enough relative to measurement uncertainties that it can be neglected in most hydrological calculations.

1.5.3 Surface Tension

Molecules in the surface of liquid water are subjected to a net inward force due to hydrogen bonding with the molecules below the surface (figure 1.8). **Surface tension** is equal to the magnitude of that force divided by the distance over which it acts; thus its dimensions are [F L⁻¹]. Surface tension can also be viewed as the work required to overcome that inward pull and increase the surface area of a liquid by a unit amount ([F L]/[L²] = [F L⁻¹]).

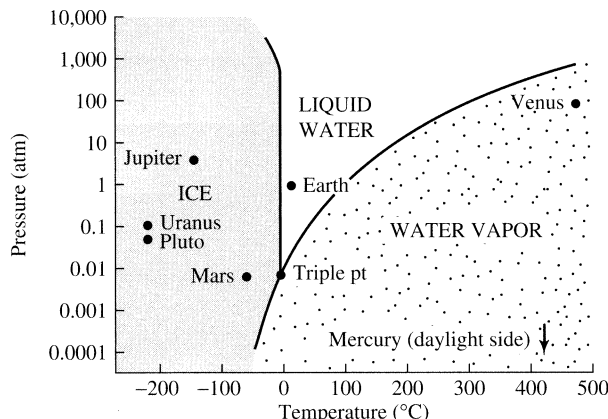
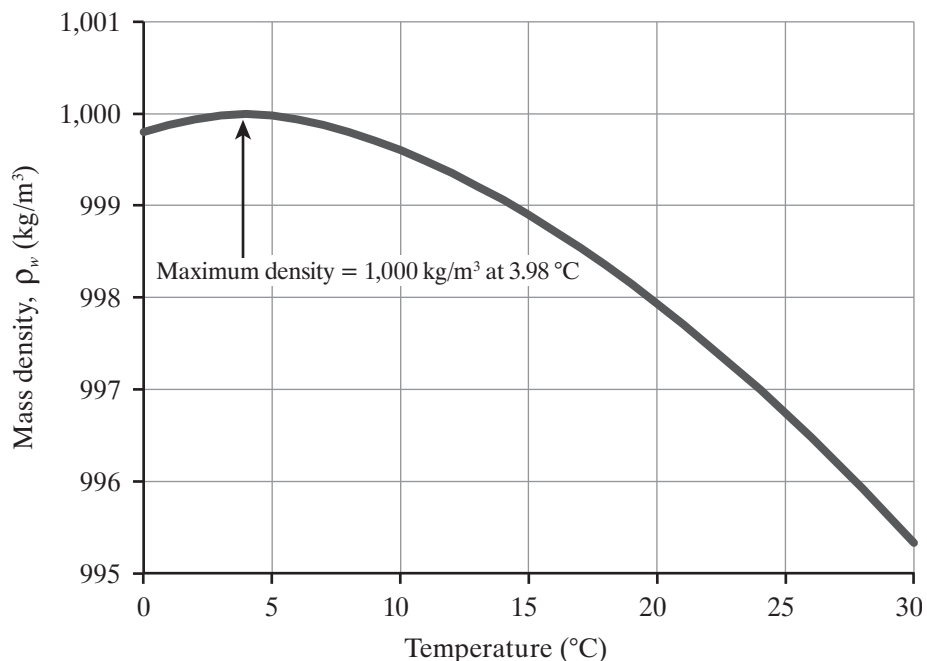


Figure 1.6 Surface temperatures and pressures of the planets plotted on the phase diagram for water (Eagleson et al., *Opportunities in the Hydrologic Sciences* © 1991 by the US National Academy of Sciences. Reprinted with permission of the National Academy Press).

Figure 1.7 Variation of density with temperature for pure water. It is highly unusual that the maximum density occurs at 3.98°C rather than at the freezing point (0°C), as it does for most liquids. It is also unusual that the solid form, ice, has a lower density (917 kg/m³) than the liquid at the freezing point.

These anomalies have major impacts on the temperature structure of lakes, the behavior of rivers during freezing and thawing, the weathering of rocks, and other phenomena.



Surface tension significantly influences fluid motion where a water surface is present and where the flow scale is less than a few millimeters—i.e., in soils that are partially saturated or in which there is an interface between water and an immiscible liquid (e.g., hydrocarbons). As described in section 7.4.1, surface tension produces the phenomenon of **capillarity**, which affects soil-water distribution by pulling water into dry soils and holding soil water against the pull of gravity.

As might be expected from its strong intermolecular forces, water has a surface tension higher than most other liquids. Surface tension decreases rapidly as temperature increases, and this effect can be important when considering the movement of water in soils (see chapter 7). Dissolved substances can also increase or decrease surface tension, and certain organic compounds have a major effect on its value.

The relative importance of surface-tension force relative to gravitational force in water flows is quantitatively reflected in the dimensionless **Bond number**, *Bo*, given by

$$Bo \equiv \frac{\gamma_w \cdot L^2}{\sigma}, \quad (1.4)$$

where σ is surface tension, γ_w is weight density, and L is a characteristic length of the flow (e.g., soil-pore diameter or flow depth). In flows with $Bo < 1$, surface-tension forces exceed gravitational forces.

1.5.4 Viscosity and Turbulence

Flows of liquid water occur in response to gradients in gravity and/or pressure forces. **Viscosity** is the internal intermolecular friction that resists mo-

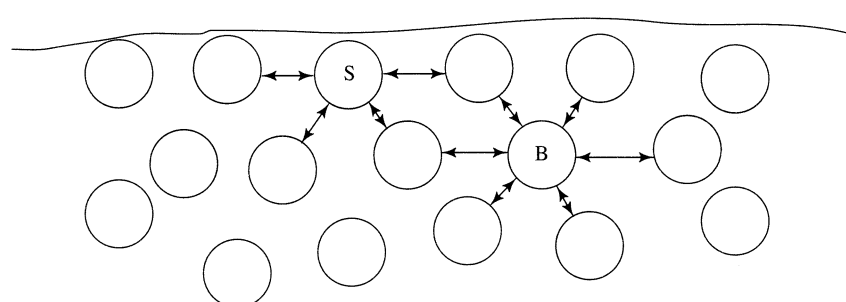


Figure 1.8 Intermolecular forces acting on typical surface (S) and nonsurface (B) molecules.

tion of a fluid. An important concomitant of viscosity is the **no-slip condition**: the flow velocity at a stationary boundary is always zero, so that any flow near a boundary experiences a velocity gradient perpendicular to the boundary. At small spatial scales (centimeter scale or less) and low flow velocities (less than a few cm/s), viscous resistance controls the gradient and the rate of flow.

However—and somewhat surprisingly—the viscosity of water is low compared to other fluids because of the rapidity with which the intermolecular hydrogen bonds break and reform (about once every 10^{-12} s). Thus, as flow scales and velocities increase, inertial effects soon dominate the effects of viscosity, so that formerly straight or smoothly curving flow paths become increasingly chaotic due to eddies. This phenomenon, called **turbulence**, produces a resistance to flow that depends on the flow scale and velocity, and is typically orders of magnitude larger than that due to viscosity. Hence, the physical relations describing subsurface flow in soil pores, where viscosity usually dominates, and in surface flows, where turbulence dominates, are very different.

The relative importance of turbulent and viscous resistance in a flow is quantitatively reflected in the dimensionless **Reynolds number**, Re :

$$Re \equiv \frac{U \cdot L \cdot \rho_w}{\mu} \quad (1.5)$$

where ρ_w is mass density, μ is dynamic viscosity, and U is average velocity. In subsurface flows, L is the soil-pore diameter and flows with $Re < 1$ are dominated by viscous resistance; in open-channel flows, L is the flow depth and flows with $Re < 500$ are dominated by viscous resistance.

1.5.5 Latent Heats

Latent heat is energy that is released or absorbed when a given mass of substance undergoes a change of phase. Its dimensions are energy per mass, [$E M^{-1}$], or [$L^2 T^{-2}$]. The term “latent” is used because no temperature change is associated with the gain or loss of heat. The large amounts of energy required to break hydrogen bonds during melting and vaporization, and which are released by the formation of bonds during freezing and condensation, make water’s latent heats very large relative to other substances.

The **latent heat of fusion** is the quantity of heat energy that is added or released when a unit mass of substance melts or freezes. For water, this is a signifi-

cant quantity, 3.34 KJ/kg. Latent heat of fusion plays an important role in the dynamics of freezing and thawing of water bodies and of water in the soil: Once the temperature is raised or lowered to $0^\circ C$, this heat must be conducted to or from the melting/freezing site in order to sustain the melting or freezing process.

The **latent heat of vaporization** is the quantity of heat energy that is added or released when a unit mass of substance vaporizes or condenses. Vaporization involves the complete breakage of hydrogen bonds, and water has one of the largest latent heats of vaporization of any substance. The latent heat of vaporization decreases with temperature. At $10^\circ C$ its value is 2.471 MJ/kg, more than six times the latent heat of fusion and more than five times the amount of energy it takes to warm water from the melting point to the boiling point.

As discussed in chapters 2 and 3, water’s enormous latent heat of vaporization plays an important role in global heat transport (1) as a source of energy that drives the precipitation-forming process and (2) as a mechanism for transferring large amounts of heat from the earth’s surface into the atmosphere.

1.5.6 Specific Heat (Heat Capacity)

Specific heat (or **heat capacity**), c_w , is the property that relates a temperature change of a substance to a change in its heat-energy content. It is defined as the amount of heat energy absorbed or released per unit mass per unit change in temperature. Thus its dimensions are [$E M^{-1} \Theta^{-1}$] = [$L^2 T^{-2} \Theta^{-1}$]. The thermal capacity of water at $10^\circ C$ is very high (4.191 KJ/kg K) and decreases slowly as temperature increases.

The temperature of a substance reflects the vibratory energy of its molecules. The heat capacity of water is very high relative to that of most other substances because, when heat energy is added to it, much of the energy is used to break hydrogen bonds rather than to increase the rate of molecular vibrations. This high specific heat has a profound influence on organisms and the global environment: It makes it possible for warm-blooded organisms to regulate their temperatures, and makes the oceans and other bodies of water moderators of the rates and magnitudes of ambient temperature changes.

1.5.7 Solvent Power

Because of the unique polar structure of water molecules and the existence of hydrogen bonds, almost every substance is soluble in water to some degree.

Ionic salts, such as sodium chloride, readily form ions that are maintained in solution because the positive and negative ends of the water molecules attach to the oppositely charged ions. Each ion is thus surrounded by a cloud of water molecules that prevents the ions from recombining. Other substances, particularly polar organic compounds such as sugars, alcohols, and amino acids, are soluble because the molecules form hydrogen bonds with the water molecules.

The importance of the solvent power of water to biogeochemical processes cannot be overstated. The first steps in the process of erosion involve the dissolution and aqueous alteration of minerals, and a significant portion of all the material transported by rivers from land to oceans is carried in solution (chapter 2). Virtually all life processes take place in water and depend on the delivery of nutrients and the removal of wastes in solution. In plants, the carbon dioxide necessary for photosynthesis enters in dissolved form (chapter 6); in animals the transport and exchange of oxygen and carbon dioxide essential for metabolism take place in solution.

1.6 Hydrologic Systems and the Conservation Equations

1.6.1 Hydrologic Systems

Several basic hydrologic concepts are related to the simple model of a **system** (as shown in figure 1.9).

- A system consists of one or more **control volumes** that can receive, store, and discharge a conservative substance.
- A **conservative substance** is one that cannot be created or destroyed within the system. These are **mass** ($[M]$ or $[F L^{-1} T^2]$), **momentum** ($[M L T^{-1}]$ or $[F T]$), and **energy** ($[M L^2 T^{-2}]$ or $[F L]$).

In most hydrologic analyses it is reasonable to assume that the mass density (mass per unit volume $[M L^{-3}]$) of water is effectively constant; in these cases volume $[L^3]$ (i.e., mass/mass density, $[M]/[M L^{-3}]$) may be treated as a conservative quantity.

A control volume can be any conceptually defined region of space, and can be defined to include

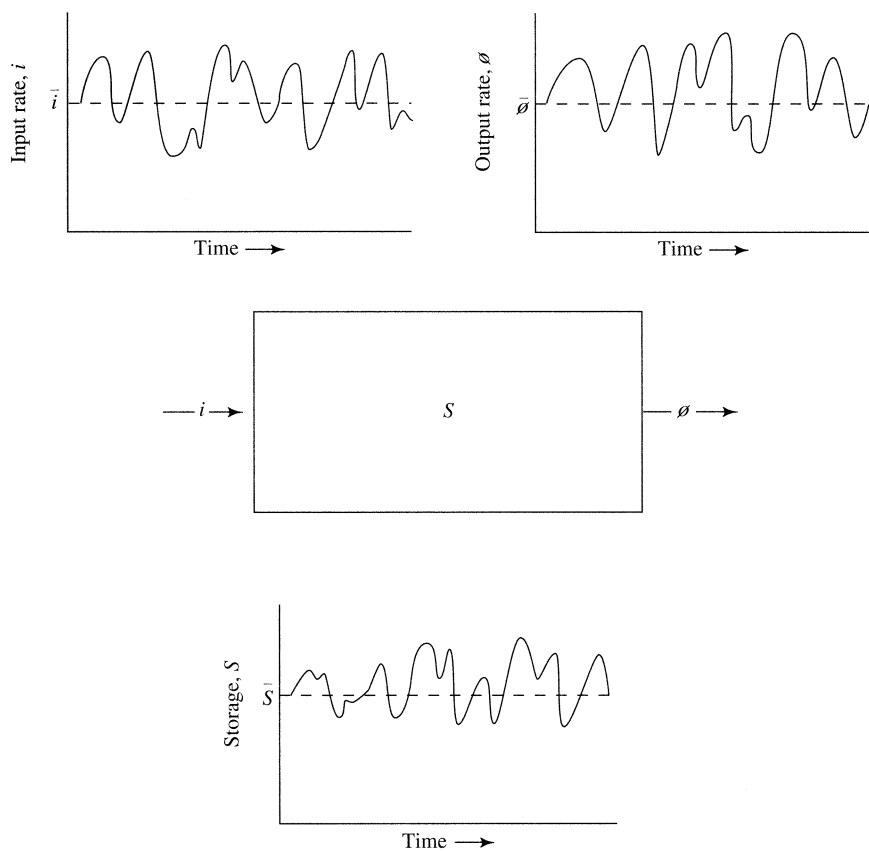


Figure 1.9 Conceptual diagram of a system.

regions that are not physically contiguous (e.g., the world's glaciers). Horton (1931, p. 192) characterized the range of scales of hydrologic control volumes:

Any natural exposed surface may be considered as a [control volume] on which the hydrologic cycle operates. This includes, for example, an isolated tree, even a single leaf or twig of a growing plant, the roof of a building, the drainage basin of a river-system or any of its tributaries, an undrained glacial depression, a swamp, a glacier, a polar ice-cap, a group of sand dunes, a desert playa, a lake, an ocean, or the earth as a whole.

The storages in figures 1.2 and 1.3 are systems linked by flows. The outer dashed line in figure 1.3 indicates that any group of linked systems can be aggregated into a larger system; the smaller systems could then be called **subsystems**.

1.6.2 The Conservation Equations

The basic conservation equation can be stated in words as:

The amount of a conservative quantity entering a control volume during a defined time period, minus the amount of the quantity leaving the volume during the time period, equals the change in the amount of the quantity stored in the volume during the time period.⁴

Thus the basic conservation equation is a generalization of (1) the conservation of mass, (2) Newton's first law of motion (when applied to momentum), and (3) the first law of thermodynamics (when applied to energy) (table 1.1). In condensed form, we can state the general conservation equation as

$$\text{Amount In} - \text{Amount Out} = \text{Change In Storage}, \quad (1.6)$$

but we must remember that the equation is true *only*: (1) for conservative substances; (2) for a defined control volume; and (3) for a defined time period.

If we designate the amount of a conservative quantity entering a region in a time period, Δt , by I , the amount leaving during that period by \mathcal{O} , and the change in storage over that period as ΔS , we can write equation (1.6) as

$$I - \mathcal{O} = \Delta S. \quad (1.7)$$

Another useful form of the basic conservation equation can then be derived by dividing each of the terms in equation (1.7) by Δt :

$$\frac{I}{\Delta t} - \frac{\mathcal{O}}{\Delta t} = \frac{\Delta S}{\Delta t}. \quad (1.8)$$

If we now define the average rates of inflow, μ_I , and outflow, $\mu_{\mathcal{O}}$, for the period Δt as follows:

$$\mu_I \equiv \frac{I}{\Delta t}, \quad (1.9)$$

$$\mu_{\mathcal{O}} \equiv \frac{\mathcal{O}}{\Delta t}, \quad (1.10)$$

we can write equation (1.8) as

$$\mu_I - \mu_{\mathcal{O}} = \frac{\Delta S}{\Delta t}. \quad (1.11)$$

Equation (1.11) states that the average rate of inflow minus the average rate of outflow equals the average rate of change of storage.

Another version of the conservation equation can be developed by defining the instantaneous rates of inflow, i , and outflow, \mathcal{o} , as

$$i \equiv \lim_{\Delta t \rightarrow 0} \frac{I}{\Delta t}, \quad (1.12)$$

$$\mathcal{o} \equiv \lim_{\Delta t \rightarrow 0} \frac{\mathcal{O}}{\Delta t}. \quad (1.13)$$

Substituting these into equation (1.8) allows us to write

$$i - \mathcal{o} = \frac{dS}{dt}. \quad (1.14)$$

Equation (1.14) states that the instantaneous rate of input minus the instantaneous rate of output equals the instantaneous rate of change of storage.

All three forms of the conservation equation, equations (1.7), (1.11), and (1.14), are applied in various contexts throughout this text. They are called **water-balance equations** when applied to the mass of water moving through various portions of the hydrologic cycle; control volumes in these applications range in size from infinitesimal to global and time intervals range from infinitesimal to annual or longer (figure 1.4). A special application of these equations, the regional water balance, is discussed in section 1.8, and an application of them to develop a model of watershed functioning is presented in

section 1.12. As indicated in figure 1.3, energy fluxes are directly involved in evaporation and snowmelt, and the application of the conservation equation in the form of **energy-balance equations** is essential to the understanding of those processes developed in chapters 5 and 6. Consideration of the conservation of momentum is important in the analysis of fluid flow, and this principle is applied in the discussion of turbulent exchange of heat and water vapor between the surface and the atmosphere in chapter 3.

1.7 The Watershed

1.7.1 Definition

Hydrologists commonly apply the conservation equation in the form of a water-balance equation to a geographical region in order to establish the basic hydrologic characteristics of the region. Most commonly, the region is a *watershed*:

A **watershed** (also called **drainage basin**, **river basin**, or **catchment**) is the area that topographically appears to contribute all the water that passes through a specified cross section of a stream (the **outlet**) (figure 1.10). The surface trace of the boundary that delimits a watershed is called a **divide**. The horizontal projection of the area of a watershed is called the **drainage area** of the stream at (or above) the outlet.

The watershed concept is of fundamental importance because it can usually be assumed that at least most of the water passing through the stream cross section at the watershed outlet originates as precipitation on the watershed, and the characteristics of the watershed control the paths and rates of movement of water as it moves over or under the surface to the stream network. To the extent this is true,

Watershed geology, soils, topography, and land use determine the magnitude, timing, and quality of streamflow and ground-water outflow.

Thus, the watershed can be viewed as a natural landscape unit, integrated by water flowing through the

land phase of the hydrologic cycle and, as William Morris Davis (1899, p. 495) stated,

“One may fairly extend the ‘river’ all over its [watershed] and up to its very divides. Ordinarily treated, the river is like the veins of a leaf; broadly viewed, it is like the entire leaf.”

Although political boundaries do not generally follow watershed boundaries, water-resource and land-use planning agencies recognize that effective management of water quality and quantity requires a watershed perspective. At the same time, it must be recognized that there are places in which topographically defined watershed divides do not coincide with the boundaries of ground-water flow systems; this is especially likely to occur in arid regions where topography is subdued and underlain by highly porous materials (e.g., Saudi Arabia, portions of the US Great Plains). This is discussed further in section 1.8.2.3.

1.7.2 Delineation

Watershed delineation begins with selection of the watershed outlet: the location of the stream cross section that defines the watershed. This location is determined by the purpose of the analysis. For quantitative studies of water budgets or stream response, the outlet is usually a stream-gauging station where streamflow is continuously monitored. For geomorphic analyses of landscapes and stream networks, the outlets are usually at stream junctions or where a stream enters a lake or an ocean. For various water-resource analyses the outlet may be at a hydroelectric plant, a reservoir, a waste-discharge site, or a location where flood damage is of concern. As indicated in figure 1.10, upstream watersheds are nested within, and are part of, downstream watersheds.

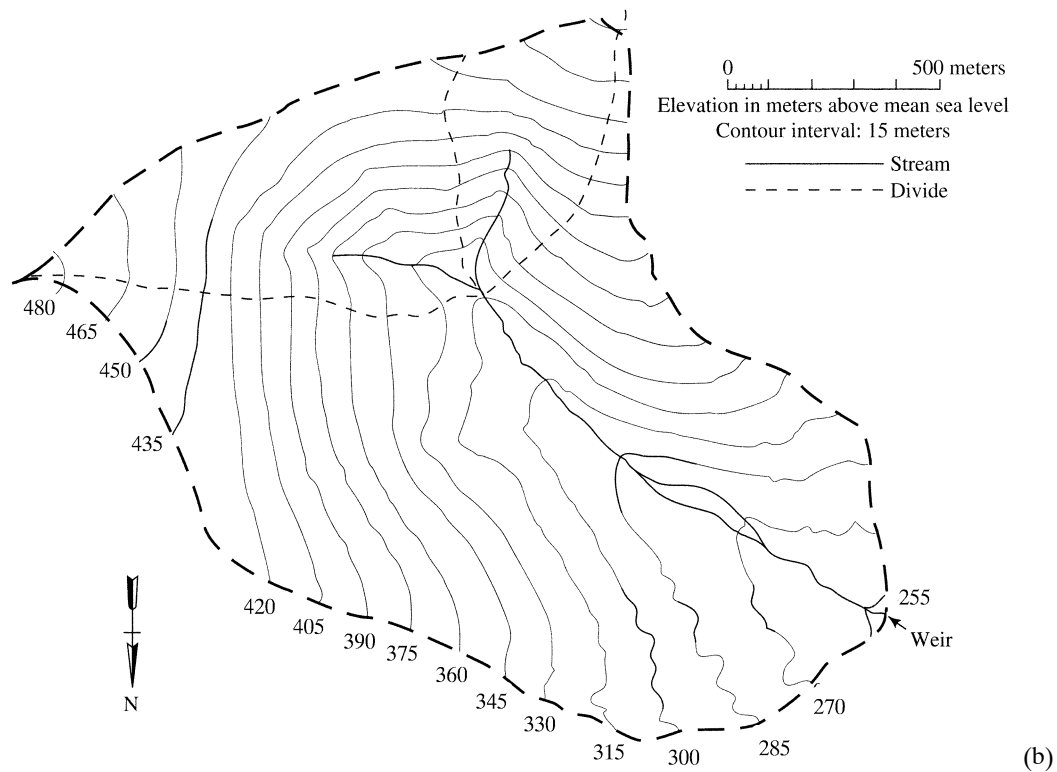
1.7.2.1 Manual Delineation

Although largely superseded by digital methods (see section 1.7.2.2), understanding the process of manual delineation provides valuable insight into the watershed concept. Furthermore, digital watershed delineations often contain errors, so it is essential to check them.

Manual watershed delineation requires a topographic map (or stereoscopically viewed aerial photographs). To trace the divide, start at the location of the chosen watershed outlet, then draw a line away from the left or right stream bank, *maintaining the line*



(a)



(b)

Figure 1.10 (a) Oblique aerial photograph of Glenn Creek Watershed, Fox, Alaska, looking southeast. Discharge-measurement weir is visible near center of photograph. (b) Glenn Creek Watershed and tributary watersheds delineated on a topographic map.

perpendicular to the contour lines. Frequent visual inspection of the contour pattern is required as the divide is traced out to assure that an imaginary drop of water falling streamward of the divide would, if the ground surface were imagined to be impermeable, flow downslope and eventually enter the stream network upstream of the outlet. Continue the line until its trend is generally opposite to the direction in which it began, and is generally above the headwaters of the stream network. Then return to the starting point and trace the divide from the other bank, eventually connecting with the first line.

Note that a divide can never cross a stream, though there are rare cases where a divide cuts through a wetland (or, even more rarely, a lake) that has two outlets draining into separate stream systems. The lowest point in a drainage basin is always the basin outlet, i.e., the starting point for the delineation. The highest point is usually, but not necessarily, on the divide.

1.7.2.2 Digital Delineation

In recent years there has been a rapid development of readily accessible and generally reliable digital tools for watershed delineation. These are based on **digital elevation models (DEMs)**, which are computer data files that give land-surface elevations at grid points. The DEM elevations are based on radar reflections collected by satellite. The original data usually contain many errors due to false readings from vegetation, areas of radar shadowing by topography, lack of reflections from water surfaces, and other effects. Thus elaborate techniques are required for removing spurious depressions and rises, filling in areas subject to shadowing, and incorporating previously digitized stream networks (Tarboton et al. 1991; Martz and Garbrecht 1992; Tarboton 1997; Verdin and Verdin 1999; Lehner et al. 2008; Pan et al. 2012). However, different techniques may provide widely differing results, as found by Khan et al. (2013) for the Upper Indus River Watershed in Pakistan.

Currently, there are two web-based services that provide automated watershed delineation. In the United States, the USGS provides the StreamStats (<http://water.usgs.gov/osw/streamstats>) application that not only delineates watersheds for user-selected basin outlets, but also provides data on a large number of watershed characteristics and measured or estimated streamflow statistics. Globally, a team of scientists connected with the World Wildlife Fund has developed the HydroSHEDS database (<http://hydrosheds.cr.usgs.gov>)

describing the earth's topography, drainage networks, and watersheds at three resolutions: 90, 500, and 1,000 m. Figure 1.11 shows the HydroSHEDS map of the major watersheds of Africa.

The automated approach to watershed delineation allows the concomitant rapid extraction of much hydrologically useful information on watershed characteristics (such as the distribution of elevation and land-surface slope) that could previously be obtained only by very tedious manual methods.

1.8 The Regional Water Balance

The regional water balance is the application of the conservation of mass equation to the water flowing through a watershed or any land area, such as a state or continent.

The upper surface of the control volume for application of the conservation equation is the surface area of the watershed (or other land area); the sides of the volume extend vertically downward from the divide some indefinite distance assumed to reach below the level of significant ground-water movement.

In virtually all regional hydrologic analyses, it is reasonable to assume a constant density of water because its density changes little with temperature, and any variation is much smaller than the uncertainties in the measured quantities. Thus we can treat volume [L^3] rather than mass as a conservative quantity. For comparative analyses of hydrologic climate it is useful to divide the volumes of water by the surface area of the region, so that the quantities have the dimension [L] ($= [L^3]/[L^2]$).

Computation of the regional water balance is a basic application of hydrologic concepts because

Evaluation of the regional water balance provides the most basic characterization of a region's hydrology and potential water resources.

In this section we will first develop a conceptual regional water balance, from which we can define some useful terms and show the importance of climate in determining regional water resources, following which we consider some of the observational challenges intrinsic to hydrology.

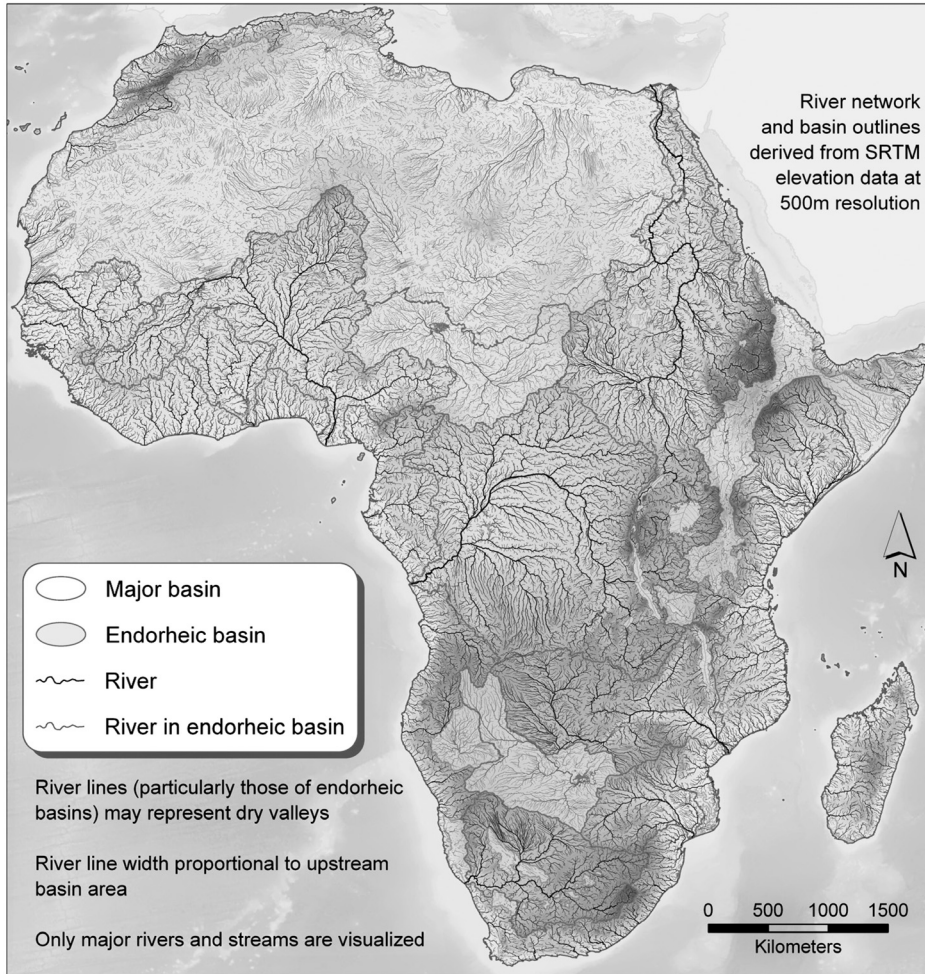


Figure 1.11
HydroSHEDS map of major African watersheds and rivers [Lehner et al. (2008). New global hydrography derived from spaceborne elevation data. *Eos* 89(10):93–104, with permission of the American Geophysical Union].

1.8.1 The Water-Balance Equation

Consider the watershed shown in figure 1.12. For any time period of length Δt we can write the water-balance equation as

$$P + GW_{in} - (Q + ET + GW_{out}) = \Delta S, \quad (1.15)$$

where P is precipitation (liquid and solid), GW_{in} is ground-water inflow (liquid), Q is stream outflow (liquid), GW_{out} is ground-water outflow (liquid), and ΔS is the change in all forms of storage (liquid and solid) over the time period. ET is **evapotranspiration**, the total of all water that leaves a region as vapor via direct evaporation from surface-water bodies, snow, and ice, plus **transpiration** (water evaporated after passing through the vascular systems of plants; the process is described in section 6.5). All the quantities in (1.15) are total amounts for the period Δt . If we

average the water-balance quantities over a reasonably long time period (say, many years), we can write the water balance as

$$\mu_P + \mu_{GW_{in}} - [\mu_Q + \mu_{ET} + \mu_{GW_{out}}] = \mu_{\Delta S}, \quad (1.16)$$

where μ denotes the long-term average of the subscript quantity. To be representative of the hydrologic climate of a region, the time period used for averaging should be “many” years long, so that the annual climatic cycle and, hopefully, the major interannual variability is averaged out. Thus ideally Δt would be decades long—on the order of the 30-yr period used to compute climatic normal values in the United States. However, as one considers periods of many decades and longer, the possibility of significant trends due to climate or land-use changes increases and the validity of long-term averages becomes uncertain. This prob-

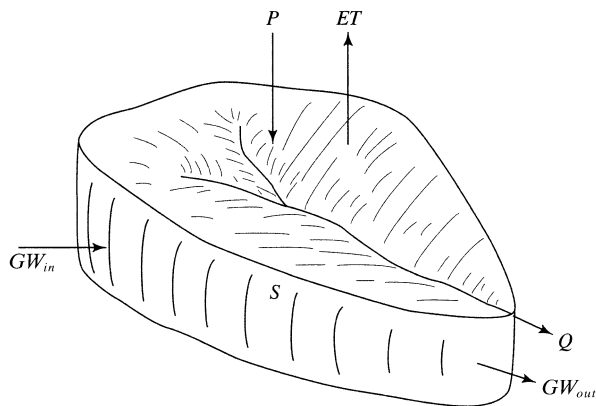


Figure 1.12 Schematic three-dimensional diagram of a watershed, showing the components of the regional water balance: P = precipitation, ET = evapotranspiration, Q = stream outflow, GW_{in} = ground-water inflow, GW_{out} = ground-water outflow.

lem of *nonstationarity* is one of the major challenges to hydrology; it is discussed further in section 1.9.2.3.

Unless there are obvious reasons for thinking otherwise (e.g., melting of glaciers, construction of large reservoirs, large-scale water transfers in or out, extensive pumping and export of ground water), it is commonly assumed that water storage is not significantly increasing or decreasing over time, so that $\mu_{\Delta S} \approx 0$. And, because watersheds are topographically defined and ground-water flow is driven by gravity (section 8.2), we can often also assume that ground water and watershed divides coincide so that GW_{in} is negligible. With these assumptions, we can write (1.16) as

$$\mu_Q + \mu_{GWout} = \mu_P - \mu_{ET}. \quad (1.17)$$

Note that the units of the quantities in (1.16) and (1.17) are *rates*; i.e., their dimensions are $[L T^{-1}]$ or $[L^3 T^{-1}]$.

We now introduce an important definition:

The sum of streamflow and ground-water outflow is called **runoff (RO)**,⁵ i.e.,

$$RO = Q + GW_{out}.$$

Therefore,

$$\mu_{RO} = \mu_P - \mu_{ET}. \quad (1.18)$$

Runoff is the rate at which liquid water leaves the region, and

The average runoff represents the maximum rate at which nature makes water available for human use and management, i.e., it is the **potential water resource** in a region.

However, as we will explore later in this chapter,

The temporal variability of runoff must be evaluated in assessing the *actual* regional water-resource availability.

As we will see in chapter 6, evapotranspiration is determined largely by meteorologic variables, so both precipitation and evapotranspiration can be considered to be externally imposed climatic “boundary conditions.” Thus, from equation (1.18),

Runoff is a residual or difference between two climatically determined quantities.

One obvious implication of these results is that natural and anthropogenic climate changes will have impacts on water resources—a phenomenon that has recurred frequently in human history.

1.8.2 Evaluation of Water-Balance Components

Evaluation of the regional water balances obviously involves measurement of its components. In this section we introduce the major challenges involved in measuring the terms in equation (1.16) and in justifying the assumptions leading to equation (1.18). These challenges are some of the central focuses of current hydrologic research; they are discussed in more detail in later chapters addressing individual water-balance components.

Note that all components of the water balance are subject to interannual variability and perhaps cycles and trends as well as seasonal variability, so evaluation of the long-term average value of each component (even at a single measurement station) involves careful application of statistical principles, some of which are presented in appendix C. And, as in any discipline, every hydrologic measurement is subject to some uncertainty; the evaluation of this uncertainty is discussed in section 1.11.

1.8.2.1 Streamflow

In most humid regions, at least, streamflow is usually by far the major component of runoff. If the region of interest is a watershed, streamflow can be measured at a single point—a **gauging station** at the watershed outlet. Continuous monitoring at gauging stations is expensive because it requires elaborate on-site instrumentation and continued calibration (see appendix E), but it can usually be done relatively precisely. If the water balance is to be computed for a region other than a watershed (e.g., country or continent), spatial as well as temporal averages of measurements at several gauging stations must be computed. This presents a statistical challenge because of the typically uneven distribution of gauging stations, the nested nature of watersheds, the effects of scale, and other complications that increase uncertainty.

Despite the importance of streamflow data, maintenance of a comprehensive global river monitoring network faces numerous technological, economic, and institutional obstacles. Because of this, the number of gauging stations and access to river discharge information has been declining since the 1980s, especially in developing nations (Vörösmarty et al. 1999; International Association of Hydrological Sciences 2001). Even in developed countries, the streamflow-measuring network is frequently informationally sparse (Mishra and Coulibaly 2009). As a result, there has been intensive interest in developing satellite-based methods for measuring streamflow (Bjerkie et al. 2003, 2005; Bjerkie 2007; Smith and Pavelsky 2008; Durand et al. 2014). However, remote-sensing techniques are considerably less precise than on-site measurements.

1.8.2.2 Precipitation

The measurement of precipitation at a point is conceptually simple but, as examined in chapter 4,

subject to many sources of error. The error is compounded when snow is involved (chapter 5). Computation of areal average values requires consideration of the density and distribution of individual gauges (most gauges are located at relatively low elevations in populated areas), the degree to which observations at nearby gauges are duplicative, and other factors.

Milly and Dunne (2002) examined sources of error in precipitation measurements as part of a global study of water balances in large watersheds (average area = 51,000 km²). They considered three additive sources of error: (1) poor distribution of gauges, (2) errors in measurements at individual gauges (section 4.2.1.2.7), and (3) failure to sample high elevations, where precipitation usually increases due to *orographic effects* (section 4.1.5). In watersheds with the highest precipitation errors, the main error source was failure to sample high elevations. Overall, however, the three error sources varied in importance. Figure 1.13 shows that there is only a very general decrease in error with gauge density, and that densities at least on the order of 100 gauges/10⁶ km² are required to achieve errors in the range of 10% in assessing water balances in large watersheds. Although this density seems sparse (it is equivalent to one gauge in an area 100 km on a side), such densities are found only in a very small fraction of the global land area (Milly and Dunne 2002).

1.8.2.3 Ground-Water Inflow and Outflow

Regional ground-water inflow and outflow rates are not directly measurable. The best information one can hope for is monitoring of water-level elevations in strategically located wells along with detailed knowledge of the regional geology and in-situ measurement of the hydraulic conductivity of important geologic formations. If enough information and resources are avail-

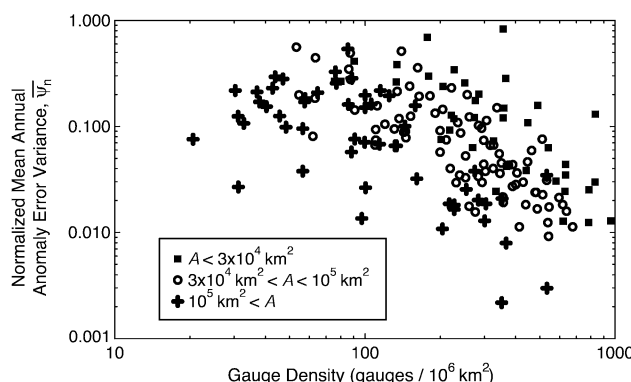


Figure 1.13 Scatter plot of relative error in watershed average precipitation as a function of gauge density. Errors are smaller for larger watersheds [Milly and Dunne (2002)]. Macroscale water fluxes: 1. Quantifying errors in the estimation of basin mean precipitation. *Water Resources Research* 38(10), with permission of the American Geophysical Union].

able, the magnitudes of the ground-water terms can be assessed by developing a ground-water model of the region. This information is seldom available, so the usual practice is to use existing geologic and topographic information to infer, at least qualitatively, the magnitudes of the ground-water terms. Very commonly, this information is not available, and these components are simply assumed to have negligible magnitude.

However, as explained in section 9.2, there are many topographic and geologic situations in which upstream watersheds contribute water to regional ground-water systems that ultimately appears in the streams draining downstream watersheds, and recent research suggests that ground-water flows are often significant components of the regional water balance. Schaller and Fan (2009) found that μ_Q/μ_{RO} for 1,555 watersheds in the United States ranged from 0.03 to 8.9, with half the watersheds being importers of ground water ($\mu_Q/\mu_{RO} > 1$) and half being exporters ($\mu_Q/\mu_{RO} < 1$). They concluded that the distribution of importing and exporting watersheds is well correlated with climatic trends, with higher values of μ_Q/μ_{RO} associated with more arid regions, and that climate may be used as a first-order predictor of μ_Q/μ_{RO} . Other influencing factors were (1) geology; (2) watershed size (larger watersheds tend to collect the ground-water flows of tributaries and have μ_Q/μ_{RO} closer to 1; and (3) relative position or elevation of a watershed, i.e., headwaters versus coastal zones. This is discussed further in section 9.5.5.2.3.

1.8.2.4 Storage

The net change in watershed storage over a period of observation is the difference between the amount of water stored as ground water and in rivers, lakes, soil, vegetation, and snow and ice at the end of the measurement period and the amount stored at the beginning of the period. If S_t represents the watershed storage at the end of year t and $\Delta S_t \equiv S_t - S_{t-1}$ is the change in storage over year t , then the average change in storage over a T -yr period, $\mu_{\Delta S}$, is

$$\mu_{\Delta S} = \frac{\sum_{t=0}^T \Delta S_t}{T} = \frac{S_T - S_0}{T}. \quad (1.19)$$

Until very recently, the only way of directly observing storage changes was to combine periodic representative observations of all storage components distributed over the region of interest. Such observations—particularly of ground water, which is usually the largest storage reservoir—are virtually never avail-

able. Lacking these, hydrologists attempt to minimize the value of $\mu_{\Delta S}$ by (1) using long measurement periods (large T) and (2) selecting the time of beginning and end of the measurement period such that storage values are likely to be nearly equal (small ΔS_t). In the United States, the USGS attempts to minimize the values of ΔS_t , and hence $S_T - S_0$, by beginning the **water year** on 1 October, on the assumption that by this time transpiration will have largely ceased and soil moisture and ground-water storage will have been recharged to near their maximum levels. However, other water-year spans may be more appropriate for specific regions—for example, in northern areas the time of disappearance of the annual snowpack in the spring may be a time when watershed storage is likely to be full.

A new tool for directly observing regional storage changes became available in 2002, when the Gravity Recovery and Climate Experiment (GRACE) satellite mission was launched. The GRACE mission consists of two satellites at an altitude of ~450 km in an identical polar orbit. Mass redistribution on earth is measured by precisely monitoring the distance between the two satellites and tracking their positions via global-positioning-system satellites (Tapley et al. 2004). The GRACE signal reflects changes in vertically integrated stored water, including snowpacks, glaciers, surface water, soil moisture, and ground water at all depths. The system can measure mass changes equivalent to ~1 cm of water at the land surface over a distance of a few hundred kilometers or more, and the measurements can be used to assess total water-storage changes in regions over many hundreds to thousands of kilometers. At these scales, many studies have shown that GRACE-derived stored-water observations compare well with ground-based measurements and hydrological models (figure 1.14), and indicate that GRACE can be used to monitor hydrological systems and improve hydrological modeling (Lettenmaier and Famiglietti 2006; Güntner 2008; Ramillien et al. 2008; Longuevergne et al. 2010).

However, if the spatial scale of interest is less than a few hundred kilometers, or if the time period for averaging includes periods before 2002, GRACE data cannot be used. Thus, hydrologists often face a near-total absence of observations of storage changes and must revert to the older strategy—which usually amounts to simply assuming that $\mu_{\Delta S}$ is negligible.

1.8.2.5 Evapotranspiration

Like ground water, regional evapotranspiration rates are not directly measurable. Unlike ground wa-

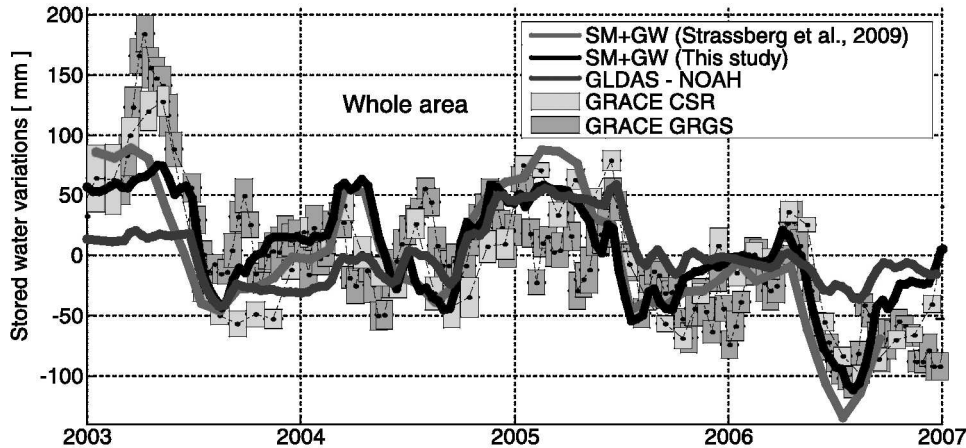


Figure 1.14 Comparison between GRACE-derived stored-water variations for the High Plains aquifer (United States) with storage estimates derived from ground-based measurements. GRACE estimates are shown as rectangles (height reflects uncertainty) using two different methodologies. Continuous curves are ground-based estimates using three different methodologies [Longuevergne et al. (2010). GRACE hydrological estimates for small basins: Evaluating processing approaches on the High Plains Aquifer, USA. *Water Resources Research* 46, with permission of the American Geophysical Union].

ter, however, evapotranspiration rate is virtually always a significant, and very often the major, component of the water balance. Thus, one of the major challenges to hydrologic science is the determination of regional evapotranspiration.

As discussed in detail in chapter 6, local evapotranspiration rate, et , is determined by solar radiation input, K ; net infrared radiation input, L ; air temperature, T_a ; relative humidity, RH ; wind speed, u_a ; soil-water content, θ ; vegetation height, z_{veg} ; and leaf area, LAI :

$$et = f_{et}(K, L, T_a, RH, u_a, \theta, z_{veg}, LAI). \quad (1.20)$$

Thus computation of regional evapotranspiration rate requires representative regional information about a large number of meteorological, soil, and vegetation variables and a functional model for f_{ET} . However, even in an intensely instrumented research watershed, Kampf and Burges (2010) found that various forms of f_{ET} gave et estimates that varied by 18%.

Since one cannot expect to have reliable measurements of all the dependent variables in (1.20) over an extensive area, other strategies must be used to estimate et . Various approaches to this problem are described in section 6.8. However, because the direct computation of average regional evapotranspiration is so intractable, it is often estimated from the

regional water balance via equation (1.17), usually with the additional assumption that GW_{out} is negligible, i.e., as

$$\mu_{ET} = \mu_P - \mu_Q. \quad (1.21)$$

Equation (1.21) is probably the most common application of hydrologic analysis. For example, in a global analysis of the effects of vegetation density and type on evapotranspiration, Peel et al. (2010) used (1.21) to compute evapotranspiration for 861 globally distributed watersheds with ostensibly good measurements of μ_P and μ_Q . Interestingly, equation (1.21) gave negative values of μ_{ET} for 114 (13%) of the watersheds. The possible reasons for this physically impossible result illustrate the kinds of measurement challenges that hydrologists face: (1) underestimation bias in the watershed average precipitation estimate; (2) unknown error in the streamflow observations; (3) unknown anthropogenic interwatershed water transfers; or (4) existence of significant unknown subsurface flows (GW_{in} or GW_{out}). Peel et al. (2010) judged that the first of these was the most likely cause of error in this case. Note that the results of Schaller and Fan (2009) also indicate that the assumption of negligible ground-water inflows and outflows may often introduce errors into estimates of evapotranspiration made via equation (1.21).

1.8.3 Summary

The regional water balance is a concise statement of a region's hydrologic climate and available water resources. However, the above discussions make clear that evaluating the terms in the water-balance equation presents major conceptual and measurement challenges. Much of the rest of this text focuses on methods for dealing with these challenges. In particular, the next two sections of this chapter introduce some of the conceptual issues that confront the characterization of quantities that vary spatially and through time.

In addition to these scientific and technical issues, it is important to note that the information available for hydrologic studies is subject to social and political influences because

Measurements of critical water-balance quantities are carried out by governments, and require continued commitments of resources.

1.9 Special Characteristics of Hydrologic Variables

Statistical techniques were developed to make inferences about the properties of a target **population** from the properties of **samples** drawn from that population. In classical statistics, inferences are based on the assumptions that (1) every element of the sample is equally representative of the population, (2) every element of the sample has an equal chance of being selected, and (3) the confidence in inferences can be increased by increasing the sample size.

Because hydrologic variables are distributed in either space or time or both, one or more of these assumptions is often not satisfied. The sample values of spatially distributed quantities are influenced by geologic, topographic, vegetational, climatic, and cultural factors that produce regional trends, redundancies, discontinuities, and sampling gaps. Sample values distributed in time are subject to temporal trends, seasonal and other cycles, and unavoidable sampling limitations (i.e., one cannot go back in time to sample). The following subsections introduce some of the approaches that hydrologists use to deal with the challenges of spatially and temporally distributed variables. More detailed discussion of statistical concepts is given in appendix C, and in Helsel and Hirsch (1992).

1.9.1 Spatial Variability

Precipitation, soil moisture, evapotranspiration, ground-water levels, and the properties of topography, snowpack, soil, and vegetation that influence hydrologic processes vary spatially over the geographic regions that constitute control volumes for hydrologic analyses. Descriptions of spatial variability are based on measurements made at discrete points (e.g., precipitation gauges). These measurements, which may be expressed as time averages, constitute spatial samples.

Traditional statistical methods, such as those described in appendix C, can be used to compute spatial averages and measures of spatial variability from the point values. However, spatially distributed quantities usually have two characteristics that can cause conventional statistical measures to be misleading: (1) measurement points are unevenly distributed over the region and (2) values measured at "nearby" points are likely to be similar and, to some extent, redundant. The point values are therefore almost always an unrepresentative sample of the true field, and commonly large portions of the area have no information.

Because of this, and because of the importance of accurately quantifying variables such as precipitation, special techniques have been developed for characterizing and accounting for spatial variability. The essence of the most widely used of these techniques is to examine the measured point values to identify a mathematical model that relates the average difference $\Delta p(d)$ in values observed at two points a distance d apart. Such a model can be represented as

$$\Delta p(d) \equiv E[p(x_i, y_i) - p(x_j, y_j)] = f_d(d) \quad (1.22)$$

where $p(x_i, y_i)$ and $p(x_j, y_j)$ are the observations at map coordinates (x_i, y_i) and (x_j, y_j) , $E[\dots]$ indicates the average of the expression in brackets, d is the distance between the two points, and $f_d(d)$ is the mathematical model. Once a suitable model is identified, it can be used with the observed values to estimate values of p at grid points throughout the region of interest. These observed and estimated values can then be contoured, and the contours integrated to determine the regional average. Details of these techniques are discussed in the context of rainfall analysis in section 4.3; however, they apply to other spatially distributed quantities as well.

Increasingly, statistical concepts are being developed to facilitate combining ground-level measurements of precipitation with satellite or radar observa-

tions to enhance information about areal distribution (e.g., Anagnostou et al. 2010; AghaKouchak et al. 2011; Lin and Wang 2011; Xie and Xiong 2011).

1.9.2 Temporal Variability

1.9.2.1 Time Series

As noted, the inputs, storages, and outputs in figures 1.1, 1.2, and 1.8 are all time-distributed variables. Thus, the concept of time variability is inherent to the concept of the hydrologic system, and we have seen how time averaging is applied to develop alternative forms of the conservation equations. Descriptions and comparisons of time-distributed variables in terms of their average value, variability, and other characteristics are made by applying the statistical methods described in appendix C to data samples called *time series*:

A **time series** is a time-ordered sequence of discrete values of a variable separated by a constant time interval Δt .

Time series are conventionally treated as representative samples of the long-term behavior of the variable (but see the discussion in section 1.9.2.3).

For all time-series analyses, the time interval, Δt , must be selected and the total time period of interest divided into intervals of length Δt . Usually $\Delta t = 1$ yr for water-balance or flood analysis, but for other purposes Δt might be 1 day or 1 month. Some hydrologic time-series variables are inherently **discrete**—for example, the number of days with more than 25 mm rain in each year at a particular location. However, variables like precipitation, evapotranspiration, and streamflow are **continuous** time traces that take on values at every instant in time.

For statistical analysis, one must convert a continuous trace into discrete form. To do this, first specify the time interval, then, depending on the purpose of the analysis, select a single value of the variable of interest associated with each interval. Figure 1.15 and table 1.3 show typical values used to discretize time-series samples for various types of analyses, and figure 1.16 shows three time series developed from the continuous measurements at a streamflow-gauging station. In all three cases, $\Delta t = 1$ yr, but different dis-

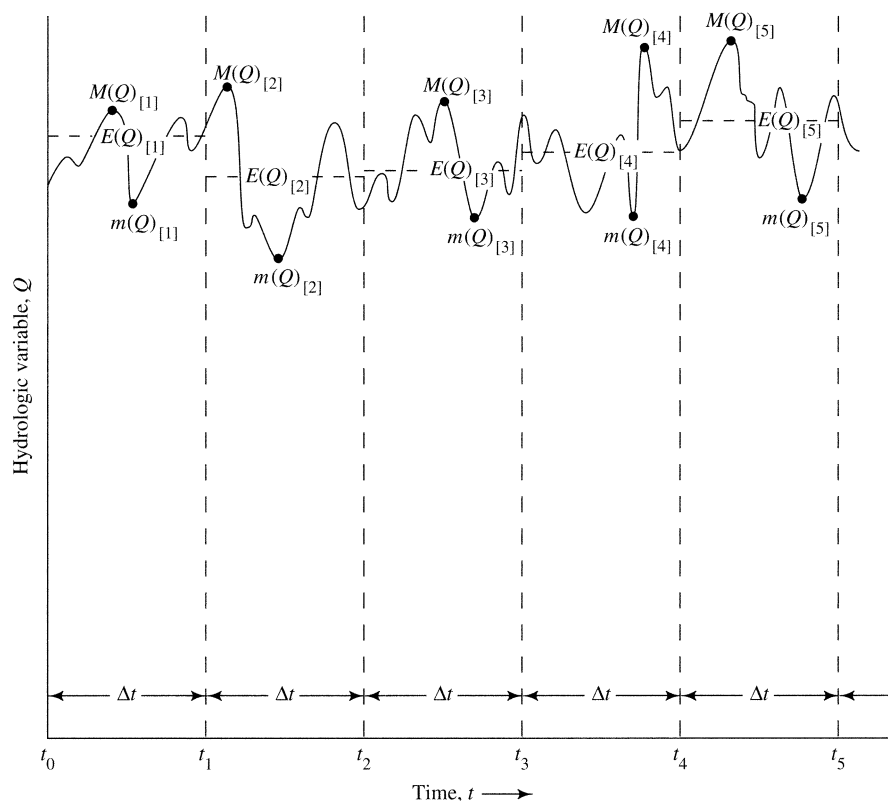


Figure 1.15 Schemes for converting a continuous time trace into a discrete time series. For each Δt , one may select the average [$E(Q)$], maximum [$M(Q)$], or minimum [$m(Q)$].

Table 1.3 Examples of Time Series Discretization for Various Analyses.

Variable	Purpose of Analysis	Value Used for Discretization
precipitation, evapotranspiration	water balance	annual total or average
streamflow	flood	annual instantaneous maximum
streamflow	water balance	annual total or average
streamflow	drought, low flow	annual minimums of overlapping consecutive day (d) averages; $d = 1, 7, \dots, 180$
storage	water balance	value at beginning or end of year

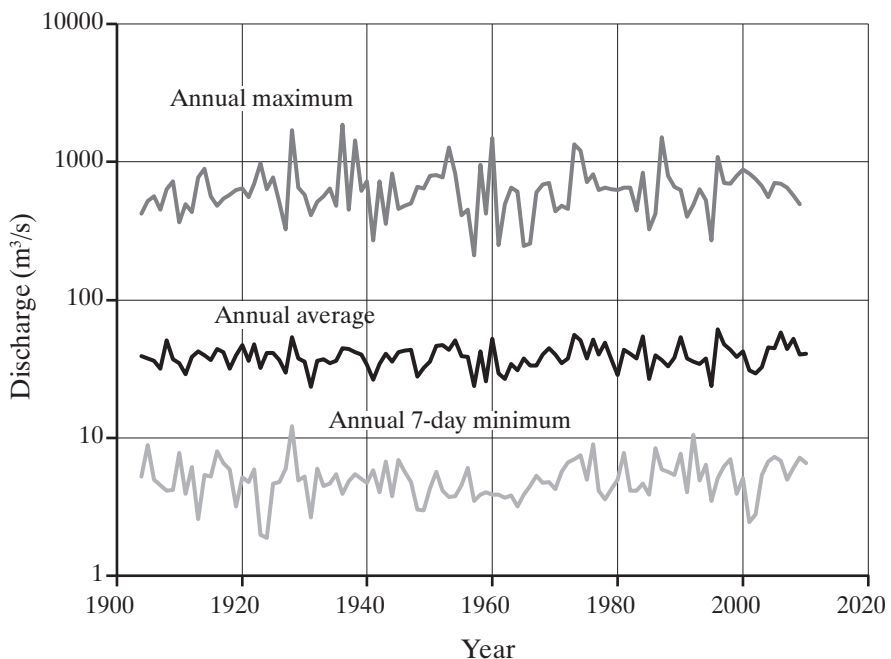


Figure 1.16 Traces of the annual maximum daily streamflow, annual average daily streamflow, and annual minimum 7-day average streamflow for the Pemigewasset River, New Hampshire.

charge values are selected for different analyses. It is important to note that time series developed from a single continuous time trace by choosing different discretizing schemes and/or different Δt values will in general have very different statistical characteristics.

1.9.2.2 Temporal Variability of Streamflow

As noted in section 1.8.1, the long-term average streamflow rate, μ_Q , is highly significant because it represents the rate at which water is potentially available for human use and management (assuming negligible ground-water outflow). However, due to the seasonal and interannual variability of precipitation, snowmelt, and evapotranspiration, streamflow is highly variable over time: even in humid regions unregulated streamflow at a given location typically varies over three or more orders of magnitude. Be-

cause of this large time variability, we cannot rely on the average flow to be available most of the time, and

The rate at which water is *actually* available for use is best measured as the streamflow rate that is available a large percentage—say 95%—of the time.

One conceptually simple but highly informative way to summarize the variability of a time series is a cumulative frequency graph called a *duration curve*:

A **duration curve** is a graph showing the fraction (percent) of time that the magnitude of a given variable is exceeded.

Duration curves are commonly used to depict the temporal variability of streamflow; such curves are called **flow-duration curves (FDCs)**. Figure 1.17 shows the FDC for the Pemigewasset River at Plymouth, New Hampshire, the same streamflow record analyzed in figure 1.16. To illustrate the significance of time variability, note that the average streamflow rate for the years plotted in figure 1.16 was $39.2 \text{ m}^3/\text{s}$. The minimum and maximum daily average flows were 1.27 and $1,620 \text{ m}^3/\text{s}$, respectively, so the ratio of maximum to minimum was $1,270!$ The rate that was exceeded 95% of the time was $5.38 \text{ m}^3/\text{s}$, so the “available water resource” for this watershed is only about 14% of the average flow. Looked at another way, the streamflow equaled or exceeded the average only about 27.5% of the time. These values are typical of medium-sized humid watersheds; table 1.4

summarizes the general effects of watershed properties on natural streamflow variability.

The most widely used strategies for increasing water availability are (1) to decrease streamflow variability by building reservoirs (section 1.10.2) and (2) to extract water from natural ground-water storage reservoirs (chapter 9). One may also attempt to increase it by increasing μ_P through “rain making” (section 4.4.4.2), or by modifying vegetation to reduce μ_{ET} (section 6.6.5.2). However, all interferences in the natural hydrologic cycle usually have significant environmental, social, economic, and legal consequences.

1.9.2.3 Nonstationarity

Implicit in the usual computation of regional water balances and many other hydrological analyses is the assumption that there are no significant

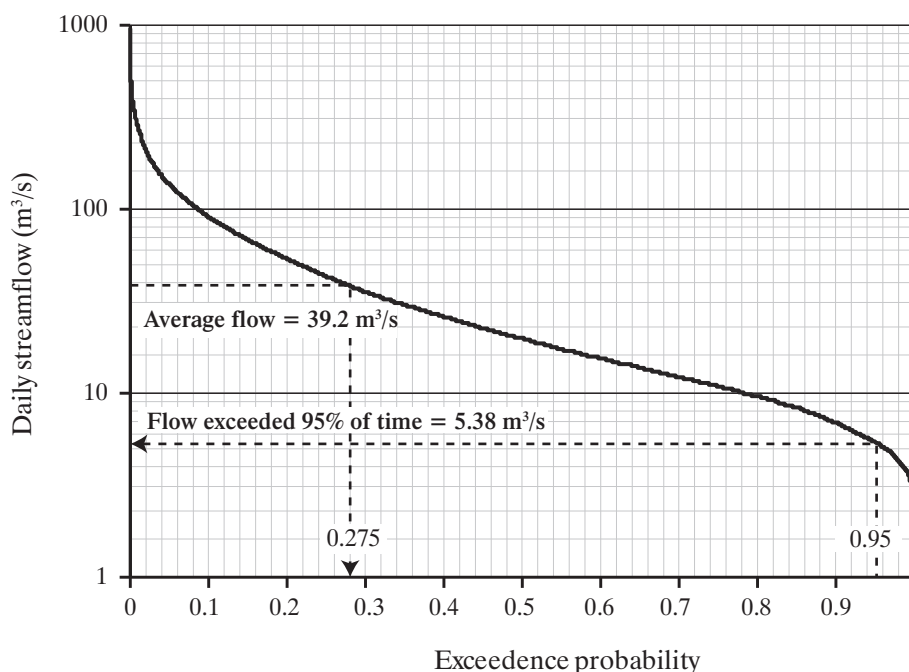


Figure 1.17 Flow-duration curve for the Pemigewasset River, New Hampshire. Note that the average flow, $39.2 \text{ m}^3/\text{s}$, is exceeded only 27.5% of the time. The flow that is available 95% of the time is $5.38 \text{ m}^3/\text{s}$, so the “available water resource” for this watershed is only about 14% of the average flow.

Table 1.4 General Effects of Watershed Properties on Relative Time Variability of Natural Streamflow.

Property	Effect
Size	• Larger watersheds tend to have lower variability (storage effect).
Geology	• Watersheds underlain by porous formations (sand, limestone) tend to have lower variability. • Watersheds underlain by crystalline rock and/or clay tend to have higher variability.
Climate	• Watersheds in humid regions tend to have lower variability. • Watersheds in regions of highly seasonal precipitation or snowmelt or in arid regions tend to have higher variability.

long-term trends or cycles, i.e., that hydrologic time series are **stationary**.

Stationarity is the assumption that a time series is a representative sample of long-term (i.e., future) behavior.

If stationarity can be assumed, most traditional statistical concepts can be applied to time series, including the idea that increasing sample size (i.e., length of observation period) increases confidence in statistical inferences. Clearly, this idea is questionable if the underlying system is changing over time.

As pointed out by Milly et al. (2008), the stationarity assumption has long been compromised by human disturbances (e.g., water infrastructure, channel modifications, drainage works, land-cover and land-use changes) as well as natural climate changes and low-frequency internal variability (the *teleconnections* discussed in section 2.1.6). Traditionally, water-resource planners have considered natural change and variability to be sufficiently small to allow stationarity-based design, and have made adjustments for significant known human disturbances.

However, substantial anthropogenic change of the earth's climate is altering the means and extremes of precipitation, evapotranspiration, and rates of discharge of rivers (see section 2.2.8), and the relation between precipitation and streamflow (Zhang et al. 2011). Because of this, Milly et al. (2008, p. 573) assert that "stationarity is dead and should no longer serve as a central, default assumption in water-resource risk assessment and planning." Development of a replacement for the concept is a daunting conceptual and practical problem for hydrologists. The solution will have to combine historical and paleohydrologic measurements with projections of improved climate and hydrologic models (e.g., Gilroy and McCuen 2012). Milly et al. (2008, p. 574) emphasize that

"In a nonstationary world, continuity of observations is critical."

Statistical tests described in section C.8.5 can help detect nonstationarity in time series of climatic and hydrologic data.

1.10 Hydrologic Storage

1.10.1 Definition

In the global hydrologic cycle a given molecule of water is always in one of the storage components of figure 1.2, and in the land phase of the cycle a given molecule is always in one of the components of figure 1.3. Thus, although the term "storage" often connotes a static situation, water is always moving through any control volume and

Water in the hydrologic cycle is always in motion
AND always in storage, and any hydrologic
control volume represents storage.

1.10.2 Storage Effects

In many hydrologic reservoirs, such as lakes, segments of rivers, ground-water bodies, and watersheds, the outflow rate increases as the amount of storage increases.⁶ For these situations, we can model the relation between outflow rate, ϕ , and storage volume, S , as

$$\phi = f_o(S). \quad (1.23)$$

In some cases, the nature of the **outflow function** $f_o(S)$ can be developed from the basic physics of the situation. In most hydrologic control volumes, such as natural watersheds, equation (1.23) is merely a conceptual model. In the model of watershed functioning described in section 1.12, observations of ϕ and $d\phi/dt$ are used to deduce the form of $f_o(S)$.

The simplest version of equation (1.23) describes a **linear reservoir**:

$$\phi = k_R \cdot S, \quad (1.24)$$

where k_R is a positive constant. Although no natural reservoir is strictly linear, equation (1.24) is often a useful approximation of hydrologic reservoirs (section 10.2.5). Furthermore, k_R has a simple physical interpretation in a linear reservoir: Since ϕ and S have the dimensions of $[L^3 T^{-1}]$ and $[L^3]$, respectively, the dimensions of k_R are $[T^{-1}]$ and, as will be shown in section 1.10.3, $1/k_R$ is a significant reservoir time constant.

Where equation (1.23) applies, storage has two effects on outflow time series:

1. Storage decreases the *relative variability* of the outflows relative to the inflows. Standard statistical

measures such as the coefficient of variation (ratio of standard deviation to mean; section C.3.5) or simple ratios determined from FDCs, such as Q_{95}/μ_Q , can be used to quantitatively characterize relative variability.

- Storage increases the *persistence* of the outflows relative to the inflows, i.e., the tendency for high values to be followed by high values, and low values by low values.

As explained in section C.6.2, persistence can be characterized by the *autocorrelation coefficient* of a time series.

As noted earlier, equation (1.23) applies to most watersheds, and table 1.4 lists some watershed characteristics associated with varying degrees of outflow variability. And, of course, water-supply reservoirs are built to increase the available water resource by decreasing outflow variability.

1.10.3 Residence Time

The **residence time** of a reservoir is the average length of time that a “parcel” of water spends in the reservoir.

Residence time (also called **transit time** or **turn-over time**) is a universal relative measure of reservoir storage (Bolin and Rodhe 1973). For a reservoir in steady state (which can usually be assumed for natural hydrologic reservoirs), the average rates of inflow and outflow are equal, and

Residence time, T_R , can be calculated by dividing the average reservoir storage, μ_S ([M] or [L^3]), by the average rate of inflow, μ_I , or outflow, μ_θ ([$M T^{-1}$] or [$L^3 T^{-1}$]).

That is,

$$T_R = \frac{\mu_S}{\mu_I} = \frac{\mu_S}{\mu_\theta}. \quad (1.25)$$

For many hydrologic reservoirs, such as lakes, values of μ_S and μ_I or μ_θ can be readily determined, and computation of residence time is straightforward. For others, such as watersheds and ground-water bodies, it may be difficult to determine the value of μ_S with precision; in these cases, we can usually speak of residence times in relative terms—for

example, under similar climatic regimes, streams receiving water from ground-water reservoirs with large residence times (i.e., with large volumes of storage per unit watershed area) will tend to have less variable and more persistent streamflow than those receiving water from reservoirs with shorter residence times (table 1.4).

For a linear reservoir, equation (1.24) applies to the average values, i.e.,

$$\mu_\theta = k_R \cdot \mu_S \quad (1.26)$$

and we see from (1.25) that the reservoir constant k_R equals the inverse of the residence time:

$$k_R = \frac{1}{T_R}. \quad (1.27)$$

We can quantify the variability and persistence effects of storage (section 1.10.2) as functions of residence time for a linear reservoir, as shown in figure 1.18. Note that the effects are substantial, even for small values of μ_S/μ_θ .

1.11 Uncertainty in Hydrology

1.11.1 Causes of Uncertainty

Hydrology is a highly uncertain science due to natural variability and to lack of knowledge (Montanari et al. 2009). Some of the specific causes of this uncertainty are:

- Many hydrologic processes are inherently random (weather processes, subsurface flow paths).
- Hydrologic processes in a given region may be affected by processes occurring in distant regions and/or at earlier times.
- Although the physics of many important processes are known at the “microscopic” scale, we do not completely understand the dynamics of these processes at the watershed and larger scales at which they are observed and modeled.
- We cannot observe in detail, and thus cannot mathematically represent, the geometry of hydrologic control volumes (soils, aquifers, river beds, watersheds), as well as most of the initial and boundary conditions.
- Hydrologists typically work under conditions of data scarcity.

As discussed in detail in appendix F, computer models simulating the functioning of the hydrologic

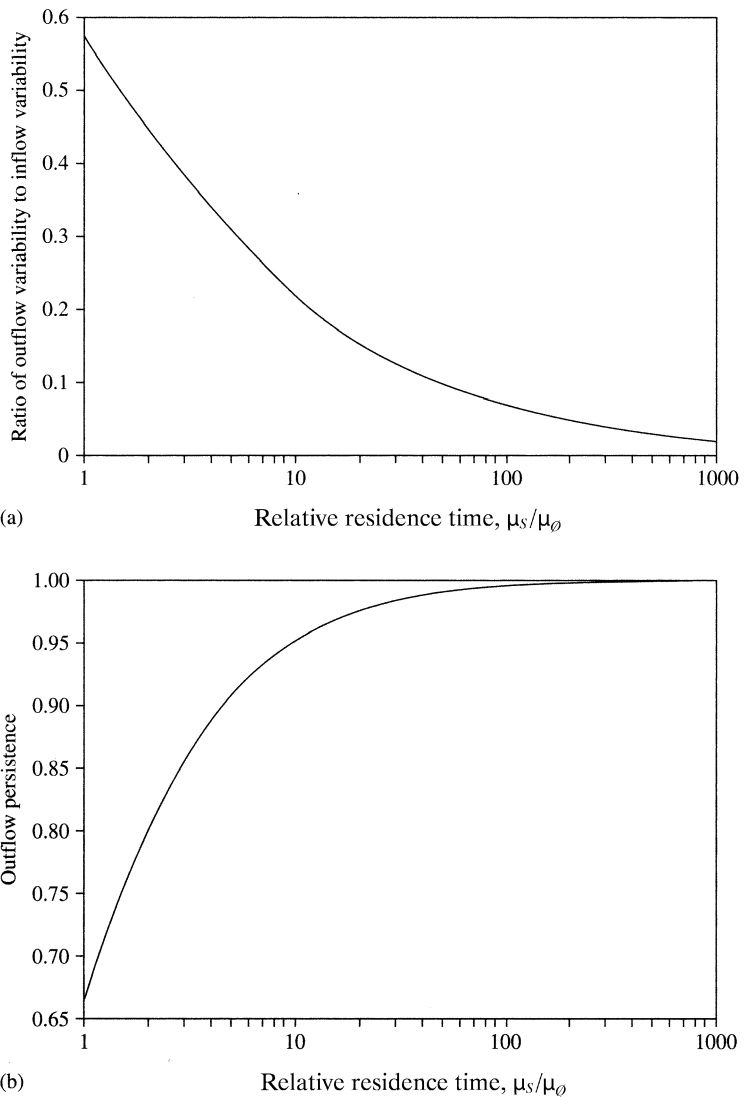


Figure 1.18 (a) Ratio of relative variability of outflows to relative variability of inflows as a function of relative residence time μ_s/μ_ϕ for a linear reservoir [equation (1.24)]. (b) Persistence of outflows (expressed as the autocorrelation coefficient) as a function of relative residence time for a linear reservoir when inflows have no persistence.

cycle are widely used as tools in scientific investigations, as means of making real-time forecasts of natural hazards, and for assessing longer-term effects of climate change or proposed water-resource infrastructure. In all applications, quantifying the uncertainty of the model output response is extremely important, and uncertainty assessment is receiving increasing attention in hydrologic research (Montanari et al. 2009). In the remainder of this section, we discuss a more limited but equally important aspect of uncertainty: the assessment of uncertainty in measured quantities and its propagation in computations.

1.11.2 Treatment of Random Uncertainty in Computations

Every measurement, no matter how precisely and carefully made, is made with some degree of uncertainty about the difference between the result of the measurement and the “true” value of the measured quantity. Consequently, any computation made with measured quantities is also subject to uncertainty. Thus,

Understanding uncertainty and how it propagates through computations is an essential aspect of science.

1.11.2.1 Systematic and Random Error

The result of a measurement of a quantity x is expressed as

$$x_{\text{meas}} = x \pm \delta x, \quad (1.28)$$

where x_{meas} is the measured value and x is the “true” value. The difference, δx , is the **error**: the upper and lower bound of the range⁷ in which the observer is “reasonably confident” that the true value lies.

Measurement errors are of two types: *systematic* and *random*.

Systematic error, or bias, is due to inherent tendencies for instrumentation or methods of observation to consistently record values that are on average higher or lower than the “true” values.

These biases are often difficult to detect, but can be quite serious in hydrology. For example, virtually all methods for measuring precipitation at a point significantly undermeasure the true value (see section 4.2.1). In fact, Adam and Lettenmaier (2003) estimated that global precipitation is undermeasured by about 12%. Detecting systematic errors is often difficult and requires careful analysis of the particular methodology involved and comparison with other methods, so there are no general approaches to accounting for them.

Thus, although one must always be aware that systematic errors may be present, the discussion here deals only with random errors:

Random error results from unpredictable fluctuations in values obtained in a given measurement situation that are equally likely to be greater than or less than the true value. The likelihood of random error is inversely reflected in the **precision** of a given measurement.

1.11.2.2 Absolute and Relative Error

In equation (1.28), δx is called the **absolute error**.

In hydrology, uncertainty is often expressed as a relative value, ε , where

$$\varepsilon \equiv \frac{\delta x}{x_{\text{meas}}}. \quad (1.29)$$

ε is called the **relative error**.

It is virtually never possible to know with 100% assurance the range in which the true value lies, so the confidence in a given measurement is usually specified as:

$$\text{“I am } 100 \cdot p \% \text{ sure that } x_{\text{meas}} - \delta x \leq x \leq x_{\text{meas}} + \delta x” \quad (1.30)$$

or

$$\text{“I am } 100 \cdot p \% \text{ sure that } x_{\text{meas}} - \varepsilon \cdot x_{\text{meas}} \leq x \leq x_{\text{meas}} + \varepsilon \cdot x_{\text{meas}}” \quad (1.31)$$

where $0 \leq p < 1$. Obviously the values of p and δx or ε are related:

δx and ε increase as p increases for a given measurement situation.

Appendix A presents the concepts of precision and significant figures, and these concepts must be kept in mind when stating uncertainties. As noted there, most hydrological measurements are made with no more than 3-significant-figure precision, and

Uncertainty δx cannot be stated with a greater *absolute* precision than the measured value.

For example, if discharge is reported as $32.5 \text{ m}^3/\text{s}$ with a relative precision $\varepsilon = 10\%$, the uncertainty δx must be given as $3.2 \text{ m}^3/\text{s}$, not $3.25 \text{ m}^3/\text{s}$.

1.11.2.3 Statistical Characterization of Random Error

The central theory of random errors is called the **Gaussian theory of errors**. It is based on the assumptions that (1) the underlying processes generating the observed values are unchanged during the measurements; (2) we are at least conceptually able to make a large number N of repeated measurements of a quantity x using the same methodology; and (3) each measurement is subject to a number of sources of potentially compensating positive and negative

random error. Five elements of the Gaussian theory of errors are central to the analysis of random errors:

1. The best estimate of the true value of x is given by

$$x = x_{\text{meas}} = \mu_x, \quad (1.32)$$

where μ_x is the arithmetic mean of the observations,

$$\mu_x \equiv \frac{1}{N} \cdot \sum_{i=1}^N x_i. \quad (1.33)$$

2. If a histogram plotting the number of times a given value x_i is measured versus the difference between that value and μ_x , the histogram will follow the **normal distribution** (figure 1.19).

The normal distribution is described in detail in appendix C; it is the familiar “bell-shaped curve” in which the probability of measuring a particular value of x_i decreases symmetrically and asymptotically toward zero as $|x_i - \mu_x|$ increases.

3. The basic characterization of absolute uncertainty is quantified as the **error standard deviation**, σ_x , which is calculated from the observations as

$$\sigma_x \equiv \left[\frac{1}{N-1} \cdot \sum_{i=1}^N (x_i - \mu_x)^2 \right]^{1/2}. \quad (1.34)$$

4. It is a property of the normal distribution that $\sim 68\%$ of the values are within $\pm 1 \cdot \sigma_x$ of μ_x ; thus a smaller value of σ_x reflects a more precise set of measurements.
5. The properties of the normal distribution allow us to relate any value of p with a particular multiple of the standard deviation, $k(p) \cdot \sigma_x$; this relation is shown in figure 1.20 (on p. 33).

Because about 68% of the measured values are within $\pm \sigma_x$ of μ_x , we can now define $\delta x = \sigma_x$ for $p = 0.68$ and write (1.29) as

$$\begin{aligned} &\text{“I am 68% sure that} \\ &x_{\text{meas}} - \sigma_x \leq x \leq x_{\text{meas}} + \sigma_x \end{aligned} \quad (1.35a)$$

Similarly, if we express a measurement precision with 95% confidence, $p = 0.95$, $k(p) = 1.96$, $\delta x = 1.96 \cdot \sigma_x$, and the statement becomes

$$\begin{aligned} &\text{“I am 95% sure that} \\ &x_{\text{meas}} - 1.96 \cdot \sigma_x \leq x \leq x_{\text{meas}} + 1.96 \cdot \sigma_x \end{aligned} \quad (1.35b)$$

In summary, the Gaussian theory of errors allows us to relate all the quantities involved in specifying random uncertainty:

If we have information about p (the confidence statement) and δx (the absolute precision) or ε (the relative precision), we can calculate σ_x for the particular measurement as

$$\sigma_x = \frac{\delta x}{k(p)} = \frac{\varepsilon \cdot x_{\text{meas}}}{k(p)}. \quad (1.36)$$

As we will see in the following section, the value of σ_x is required for determining how errors propagate through computations involving measured values. Box 1.1 (on pp. 34–36) describes how σ_x is determined in various situations encountered in hydrologic measurements.

1.11.2.4 Error Propagation

As noted,

Uncertainty in measured values
produces uncertainty in calculated
quantities derived from measured values.

Computation of these derived uncertainties is called **error propagation**. Here we give two general formulas for assessing the uncertainty of a quantity y that is any function of m measured variables x_1, x_2, \dots, x_m , i.e., where

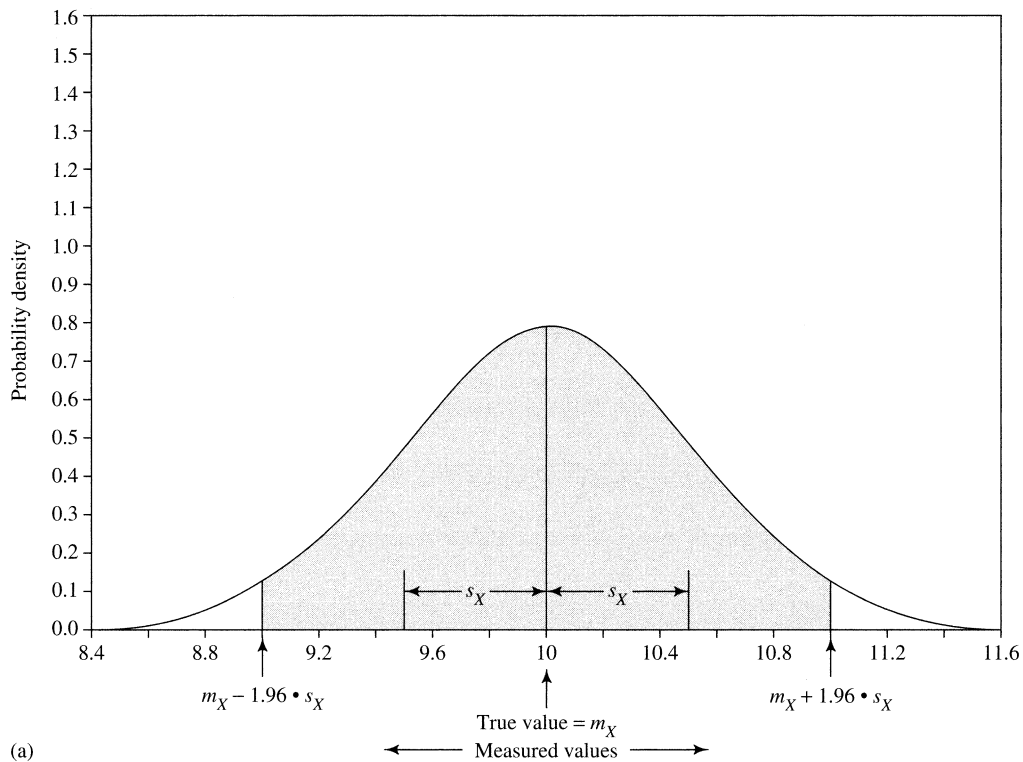
$$y = f(x_1, x_2, \dots, x_m). \quad (1.37)$$

1. If the errors in all the measured variables are *random, independent* (i.e., errors in any variable x_i are not correlated with errors in any other variable x_j), and *normally distributed* (as we have been assuming in the formulas in section 1.11.2.3), it can be shown from the definition of the standard deviation that

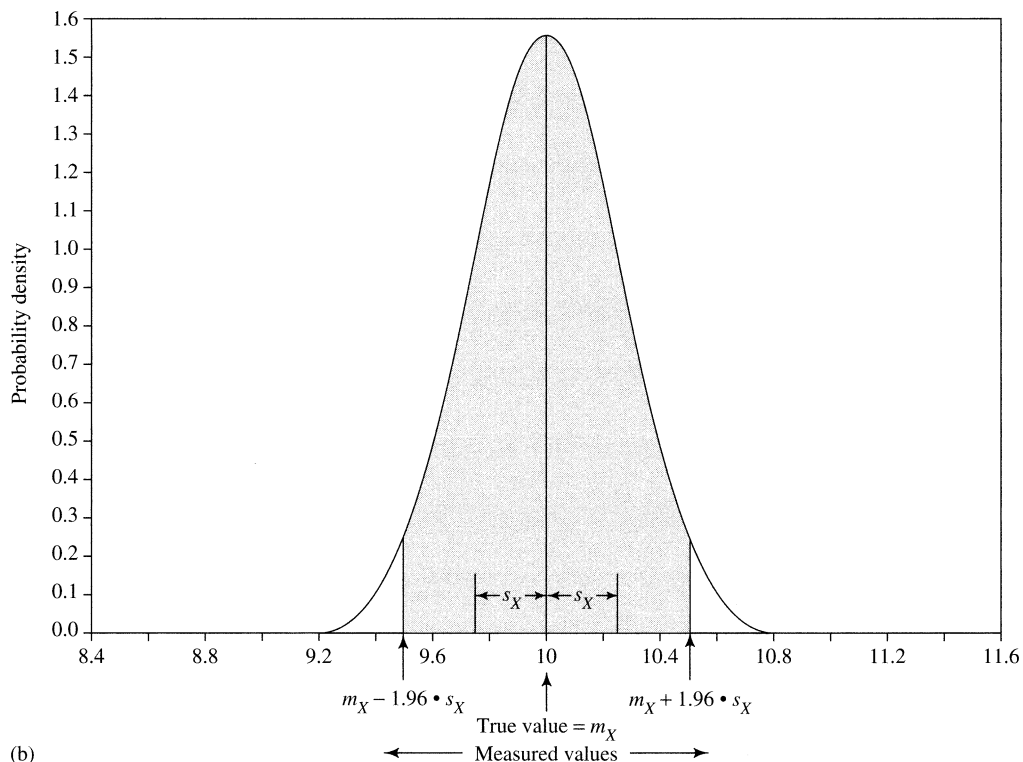
$$\begin{aligned} \sigma_y &= \left[\left(\frac{\partial y}{\partial x_1} \cdot \sigma_{x1} \right)^2 + \left(\frac{\partial y}{\partial x_2} \cdot \sigma_{x2} \right)^2 + \right. \\ &\quad \left. \dots + \left(\frac{\partial y}{\partial x_m} \cdot \sigma_{xm} \right)^2 \right]^{1/2}. \end{aligned} \quad (1.38)$$

2. Even if errors in some of the variables are not independent and normally distributed, we can specify an upper bound for σ_y as

$$\sigma_y \leq \left| \frac{\partial y}{\partial x_1} \right| \cdot \sigma_{x1} + \left| \frac{\partial y}{\partial x_2} \right| \cdot \sigma_{x2} + \dots + \left| \frac{\partial y}{\partial x_m} \right| \cdot \sigma_{xm}. \quad (1.39)$$



(a)



(b)

Figure 1.19 Probability distribution of potential measurement errors of a quantity X , shown as having a true value $X = 10$. Such errors are usually assumed to be symmetrical about the true value and to follow the normal distribution (see appendix C). (a) Example of a case where one is 95% sure that the true value is within 10% of the measured value, so that $s_X = 0.1 \cdot X/1.96 \approx 0.5$. (b) Example of a case where one is 95% sure the true value is within 5% of the measured value, so that $s_X = 0.05 \cdot X/1.96 \approx 0.25$. In both cases the shaded area = 0.95 (the probability p).

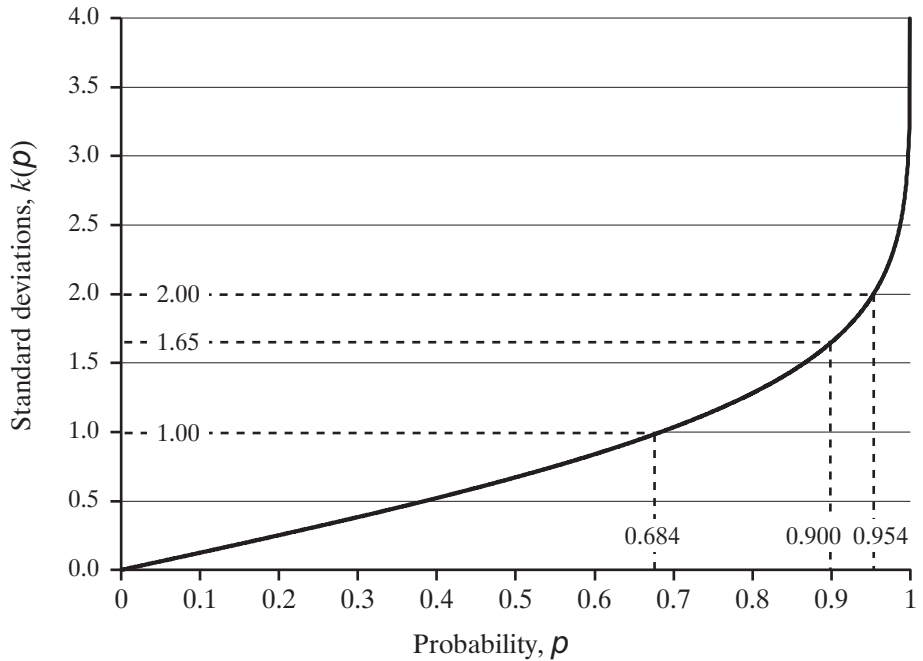


Figure 1.20 Relation between the probability, p , that a given measured value is within $k(p)$ standard deviations of the true value, as given by the normal distribution.

Taylor (1997) gives derivations of these formulas. Equation (1.39) is useful for specifying the maximum error even when one is not sure that all the measurement errors are uncorrelated and normally distributed. Table 1.5 lists formulas derived from (1.38) and (1.39) for computing the error standard deviation for specific types of quantitative relations commonly encountered in hydrology.

As noted above, equation (1.21) is often applied to estimate regional evapotranspiration. In this case the assumption of independent measurement errors is warranted, so we can use equation (1.38) to give the uncertainty in the result as

$$\sigma_{\mu ET} = \left[\sigma_{\mu P}^2 + \sigma_{\mu Q}^2 \right]^{1/2}. \quad (1.40)$$

Table 1.5 Computation of Uncertainty for Specific Quantitative Relations.

Relation	Variables Independent and Random Equation (1.38)	General Upper Bound Equation (1.39)
Sums and differences $y = x_1 \pm x_2 \pm \dots \pm x_m$	$\sigma_y = \left(\sigma_{x1}^2 + \sigma_{x2}^2 + \dots + \sigma_{xm}^2 \right)^{1/2}$	$\sigma_y \leq \sigma_{x1} + \sigma_{x2} + \dots + \sigma_{xm}$
Products and quotients $y = \frac{x_1 \cdot x_2 \cdot \dots \cdot x_j}{x_{j+1} \cdot x_{j+2} \cdot \dots \cdot x_m}$	$\frac{\sigma_y}{y} = \left[\left(\frac{\sigma_{x1}}{x_1} \right)^2 + \left(\frac{\sigma_{x2}}{x_2} \right)^2 + \dots + \left(\frac{\sigma_{xm}}{x_m} \right)^2 \right]^{1/2}$	$\frac{\sigma_y}{y} \leq \frac{\sigma_{x1}}{x_1} + \frac{\sigma_{x2}}{x_2} + \dots + \frac{\sigma_{xm}}{x_m}$
Power functions $y = a \cdot x^b$	$\sigma_y = a \cdot b \cdot x^{b-1} \cdot \sigma_x; \quad \frac{\sigma_y}{y} = b \cdot \frac{\sigma_x}{x}$	
Exponential functions $y = a \cdot \exp(b \cdot x)$	$\sigma_y = a \cdot b \cdot \exp(b \cdot x) \cdot \sigma_x; \quad \frac{\sigma_y}{y} = b \cdot \frac{\sigma_x}{x}$	
Logarithmic functions $y = a \cdot \ln(b \cdot x)$	$\sigma_y = \left \frac{a}{x} \right \cdot \sigma_x; \quad \frac{\sigma_y}{y} = \frac{\sigma_x}{ x \cdot \ln(b \cdot x)}$	

Box 1.1 Determination of Measurement Uncertainty

1B1.1 Single Measurement

The theory of random errors is developed by imagining a very large number of repeated identical measurements of a given quantity. Such a situation is rarely possible in hydrology, particularly for field measurements, where we typically have a single measurement of a given quantity at a given place and time. However, the theory can be applied to a single measurement, provided we have information about the uncertainty of such measurements generally. Ideally, such information should be based on systematic studies of measurement precision. In many cases, especially for field observations involving several steps, such studies have been used to develop “generally accepted” values for a given measurement type. For example, for individual stream-discharge (volume rate of streamflow) measurements, the USGS (Sauer and Meyer 1992) uses $p = 0.68$ and rates the precision of its measurements as

Quality	$\varepsilon\%$ ($p = 0.68$)
“Excellent”	2
“Good”	5
“Fair”	8
“Poor”	> 8

Thus for a “good” discharge measurement, where discharge $x_{meas} = 32.5 \text{ m}^3/\text{s}$, $\delta x = \varepsilon \cdot x_{meas} = 0.05 \cdot 32.5 = 1.6 \text{ m}^3/\text{s}$, and one would state

“I am 68% sure that discharge is between
 $30.9 \text{ m}^3/\text{s}$ and $34.1 \text{ m}^3/\text{s}$.”

When needed for the error-propagation computations described in section 1.11.2.4, the error standard deviation can then be calculated from equation (1.36) as

$$\sigma_x = \frac{1.6 \text{ m}^3/\text{s}}{\sqrt{1}} = 1.6 \text{ m}^3/\text{s}.$$

1B1.2 Repeated Measurements

In some situations, as in laboratory experiments, one may actually make repeated measurements of a particular quantity. In this case, the best estimate of the true value is again the mean μ_x as in equation (1.33). However, the error standard deviation of this quantity is given by the **standard error of the mean**, $\sigma_{\mu x}$, which is calculated from statistical theory (section C.11.2.1) as

$$\sigma_{\mu x} = \frac{\sigma_x}{\sqrt{N}}. \quad (1B1.1)$$

Thus we would now state the confidence in our result as

“I am 68% sure that $\mu_x - \sigma_{\mu x} \leq \mu_x \leq \mu_x + \sigma_{\mu x}$.” (1B1.2)

1B1.3 Time-Series Values at a Single Location

1B1.3.1 General Case

Hydrologists often use average annual values of precipitation and other quantities to characterize the hydrologic climate at a particular location. The average annual value is calculated as the mean μ_x of the time series of annual values x_t for the T years of record:

$$\mu_x \equiv \frac{1}{T} \cdot \sum_{t=1}^T x_t. \quad (1B1.3)$$

If the measured values are **independent**—i.e., if there is no reason to suspect that there is a systematic relation between successive values of x_t , such as a trend or cycle—we can again use the standard error of the mean to characterize the error standard deviation [equation (1B1.1)]:

$$\sigma_{\mu x} = \frac{\sigma_x}{\sqrt{T}}. \quad (1B1.4)$$

If a significant time trend is identified (see box C.9 on the disk), the effective sample size T_{eff} for calculating the standard error is smaller than T ; so the uncertainty is larger than given by (1B1.4). The value of T_{eff} can be calculated using the methods described in section C.11.4.

1B1.3.2 Average Annual Streamflow

The USGS measures and reports average streamflow for each year at some 25,000 stream gauges. It reports the uncertainty of annual average streamflow using a scheme similar to that described above for individual streamflow measurements (Risley and Gannett 2006). However, for average annual streamflow the confidence level $p = 0.95$ and relative errors are reported as

Quality	$\varepsilon\%$ ($p = 0.95$)
“Excellent”	5
“Good”	10
“Fair”	15
“Poor”	> 15

Thus, if the average annual streamflow for a given year is $\mu_Q = 17.2 \text{ m}^3/\text{s}$ at a gauge rated “good,” the uncertainty is $\delta \mu_Q = \varepsilon \cdot \mu_Q = 0.10 \cdot 17.2 = 1.7 \text{ m}^3/\text{s}$, and one would state

“I am 95% sure that the annual discharge is between $15.5 \text{ m}^3/\text{s}$ and $18.9 \text{ m}^3/\text{s}$.”

The error standard deviation for average annual streamflow is then given by equation (1.36):

$$\sigma_{\mu Q} = \frac{1.7}{\sqrt{1.96}} = 0.9 \text{ m}^3/\text{s} \text{ (rounded)}.$$

1B1.3.3 Long-Term Average Streamflow

The 7-yr average streamflow at a given gauge, μ_{QT} , is calculated as

$$\mu_{QT} = \frac{1}{T} \cdot \sum_{t=1}^T \mu_{Qt}, \quad (1B1.5)$$

where μ_{Qt} are the average annual streamflows for years $t = 1, 2, \dots, T$. The error standard deviation for each year, $\sigma_{\mu Qt}$, is found as described in section 1B1.3.2; i.e.,

$$\sigma_{\mu Qt} = \frac{\varepsilon \cdot \mu_{Qt}}{1.96}. \quad (1B1.6)$$

Assuming stationarity, the error standard deviation of the T -yr average streamflow is found from (1.38), (1B1.5), and (1B1.6) as

$$\begin{aligned} \sigma_{\mu QT} &= \left[\left(\frac{1}{T} \cdot \frac{\varepsilon \cdot \mu_{Q1}}{1.96} \right)^2 + \left(\frac{1}{T} \cdot \frac{\varepsilon \cdot \mu_{Q2}}{1.96} \right)^2 + \right. \\ &\quad \left. \dots + \left(\frac{1}{T} \cdot \frac{\varepsilon \cdot \mu_{QT}}{1.96} \right)^2 \right]^{1/2} \quad (1B1.7) \\ &= \left(\frac{1}{T} \cdot \frac{\varepsilon}{1.96} \right) \cdot \left(\sum_{t=1}^T \mu_{Qt}^2 \right)^{1/2}. \end{aligned}$$

1B1.4 Values Measured Over an Area

Quantities such as precipitation, snow depth, soil moisture, or vegetation properties are distributed over areas, such as a drainage basin. Areal averages of such quantities are typically calculated from time series of measurements at several points within the area. Computations of the areal average and its uncertainty are complicated by the distribution of sampling points, the correlation between measurements at different points, and any spatial and temporal trends. There is no simple general approach to such computations, even in the absence of systematic errors (which can be large).

One reasonably straightforward approach to assessing random uncertainty that is applicable in areas within which there are no regional trends has been developed in the context of precipitation by Rodriguez-Iturbe and Mejia (1974). In this approach, annual precipitation is determined at N gauges for each of T years. The average is calculated at each gauge, and the average of the averages is taken as the areal average μ_{Ax} . The areal standard deviation σ_{Ax} is similarly calculated over all the gauges. The overall error standard deviation σ_x is then found by multiplying σ_{Ax} by (1) a factor $F_1(T)$ that depends on the number of years of record and the strength of any time trends and (2) a factor $F_2(N)$ that depends on the number of gauges and the pattern of spatial correlation of the gauges:

$$\sigma_x = F_1(T) \cdot F_2(N) \cdot \sigma_{Ax}, \quad (1B1.8)$$

where $F_1(T) \leq 1$ and $F_2(N) \leq 1$. More details on this approach are given in section 4.3.5.

1B1.5 Quantities Determined by Counting

Hydrologists are often concerned with the average number of events, such as floods, droughts, or days with rainfall, that occur in a given time period (such as a year). Such values are determined by examining streamflow or weather records, and counting the number of event occurrences, n_t , in the T time periods of record. The average μ_n is found as

$$\mu_n = \frac{1}{T} \cdot \sum_{t=1}^T n_t. \quad (1B1.9)$$

In this case there is no measurement error, but there is uncertainty as to how well the average calculated for the period of record represents the true average. From the statistical theory, this uncertainty is given by the error standard deviation σ_n where

$$\sigma_n = \mu_n^{1/2} \quad (1B1.10)$$

1B1.6 Example

A study of precipitation measured at 29 gauges over a period of 30 yr in a region of eastern Nebraska and northern Kansas gave the average precipitation $\mu_p = 619$ mm/yr, with a measurement uncertainty $\sigma_{\mu p} = 23.4$ mm/yr. Measurements on the Big Nemaha River at Falls City, Nebraska, which drains the region, give average streamflow for the same period $\mu_{QT} = 157$ mm/yr, and are rated "good." Assuming no ground-water inflows or outflows, we want to calculate (a) the average annual evapotranspiration, μ_{ET} , (b) its uncertainty, σ_{ET} , and (c) the 95% confidence limits for μ_{ET} .

- a. Using equation (1.21),

$$\mu_{ET} = 619 - 157 = 462 \text{ mm/yr.}$$

- b. Referring to section 1B1.3.3, the "good" rating for streamflow measurements corresponds to $\varepsilon = 0.1$, so $\sigma_{\mu Qt} = 0.1 \cdot \mu_{Qt}/1.96$. Using equation (1B1.7) with the measured μ_{Qt} values for each year, we find $\sigma_{\mu Qt} = 1.5$ mm/yr. Applying equation (1.40):

$$\begin{aligned} \sigma_{\mu ET} &= \left[\sigma_{\mu p^2} + \sigma_{\mu Q^2} \right]^{1/2} \\ &= \left[23.4^2 + 1.5^2 \right]^{1/2} \\ &= 23.4 \rightarrow 23 \text{ mm/yr.} \end{aligned}$$

- c. Thus, the 95% confidence limit = $1.96 \cdot 23 = 46$ mm/yr and

"I am 95% sure that the average annual evapotranspiration is between 416 and 508 mm/yr."

For this example, the absolute and relative errors are

Component	Amount (mm/yr)	Absolute Error	Relative Error
		Standard Deviation (mm/yr)	Standard Deviation (%)
Precipitation	619	23	3.7
Streamflow	157	1	0.6
Evapotranspiration	462	23	5.0

Obviously in this case virtually all the uncertainty in the evapotranspiration estimate is due to the uncertainty in the precipitation value—a common occurrence in water-balance computations.

Note that the absolute uncertainty in μ_{ET} is larger than that in μ_P or μ_Q , and that the magnitudes of the errors are related as the sides of a triangle (figure 1.21). Note also that equation (1.40) assumes no **model error**, i.e., that equation (1.21) is correct, and there is no ground-water inflow or outflow.

1.12 Application of Basic Concepts to Modeling Watershed Functioning

To demonstrate the significance and power of the basic concepts introduced in this chapter, we conclude by describing the conceptually simple but useful predictive model of watershed functioning developed by Kirchner (2009). This model was applied to two research watersheds in Wales (figure 1.22) where streamflow was continuously monitored and there were well-distributed observations of precipitation and of meteorological data that allow computation of evapotranspiration. Kirchner's approach is particularly valuable for examination here because it makes straightforward use of basic systems concepts (section 1.6), water-balance relations (section 1.8.1), and simple storage relations (section 1.10) to develop a predictive watershed model (appendix F).

In these watersheds, ground-water inflows and outflows appear to be negligible, and equations (1.14) and (1.15) can be combined as

$$\frac{dS}{dt} = p - et - q, \quad (1.41)$$

where S is watershed storage volume, t is time, p is instantaneous watershed precipitation rate, et is instantaneous watershed evapotranspiration rate, and q is instantaneous streamflow rate at the watershed outlet.

As discussed in section 1.8.2.4, it is not usually possible to measure watershed storage. However, if at least most of the precipitation infiltrates into the unsaturated zone and then into the ground-water reservoir (which appears true for these watersheds) before entering the stream network, the physics of subsurface flow justifies the assumption that the streamflow rate is a single-valued function of storage only, i.e., that $dq/dS > 0$ for all q and S . As noted by Kirchner (2009), watersheds are large and complex, so we cannot use fundamental physics to determine the form of this function *a priori*. Instead, we make use of equation (1.23) and write it as

$$q = f_{W1}(S), \quad (1.42)$$

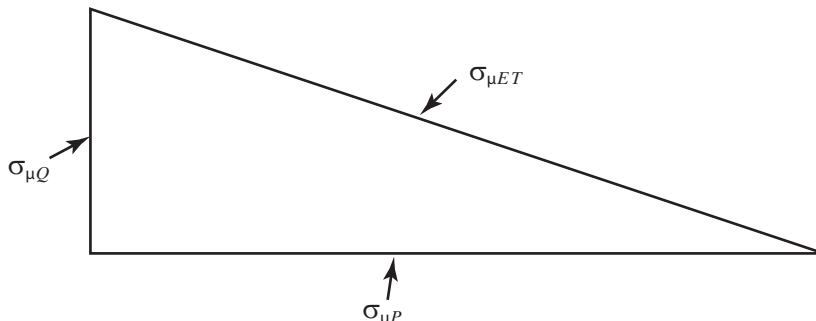
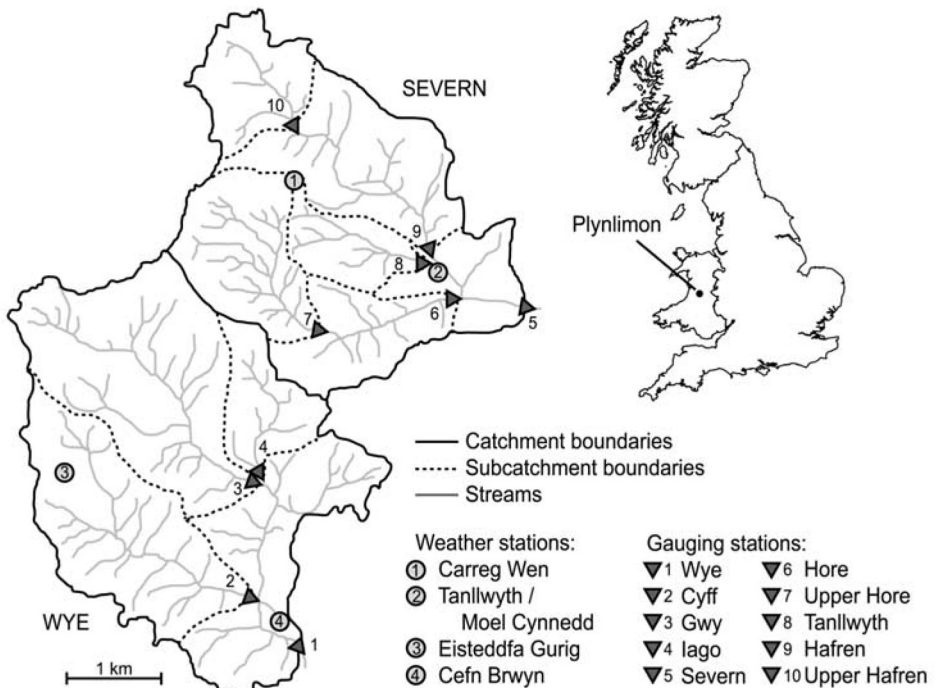


Figure 1.21 Geometric representation of error magnitude of evapotranspiration estimate calculated via equation (1.21), $\sigma_{\mu ET}$, relative to measurement errors in precipitation, $\sigma_{\mu P}$, and streamflow, $\sigma_{\mu Q}$, as given by equation (1.40).

Figure 1.22 Location map for the headwater catchments of the Severn and Wye Rivers at Plynlimon, Wales, studied by Kirchner (2009). Locations of automatic weather stations (circles) and gauging stations (triangles) are shown [Kirchner (2009)]. Catchments as simple dynamical systems: Catchment characterization, rainfall-runoff modeling, and doing hydrology backward. *Water Resources Research* 45, with permission of the American Geophysical Union].



where f_{W1} is the **watershed storage function**. If the assumptions about f_{W1} are true, we can invert (1.42) to give

$$S = f_{W1}^{-1}(q). \quad (1.43)$$

Thus, the measured discharge provides an implicit measure of the volume of water stored in the watershed.

To derive information about the nature of the storage-discharge relation, we can use the chain rule for derivatives and (1.41) to relate the rate of change of streamflow to the rate of change of storage:

$$\frac{dq}{dt} = \frac{dq}{dS} \cdot \frac{dS}{dt} = \frac{dq}{dS} \cdot (p - et - q). \quad (1.44)$$

The term dq/dS represents the sensitivity of discharge to changes in storage, which normally would be expressed in terms of S . However, because of our assumptions about f_{W1} , dq/dS can also be expressed as a function f_{W2} of q :

$$\frac{dq}{dS} = f_{W2}(q). \quad (1.45)$$

Combining (1.44) and (1.45) we see that

$$f_{W2}(q) = \frac{dq}{dS} = \frac{dq/dt}{dS/dt} = \frac{dq/dt}{p - et - q}, \quad (1.46)$$

which implies that dq/dS can be determined from instantaneous measurements of precipitation, evapotranspiration, discharge, and the rate of change of discharge. And, because discharge can be measured more reliably than precipitation or evapotranspiration at the watershed scale, f_{W2} can be most accurately evaluated at times when precipitation and evapotranspiration fluxes are small compared to discharge. Under these conditions,

$$f_{W2}(q) = \frac{dq}{dS} \approx -\frac{dq/dt}{q}. \quad (1.47)$$

Because evapotranspiration is negligible at night, Kirchner (2009) used (1.47) to determine f_{W2} from simultaneous values of q and dq/dt for rainless nighttime periods. There are several detailed steps to this determination, but Kirchner concluded that the relationship was well approximated by a simple power law:

$$-\frac{dq}{dt} = a \cdot q^b, \quad (1.48)$$

as shown in figure 1.23. (The minus sign reflects the fact that discharge decreases during rainless periods.) Then, from (1.47) and (1.48),

$$f_{W2}(q) = \frac{dq}{dS} = a \cdot q^{b-1}. \quad (1.49)$$

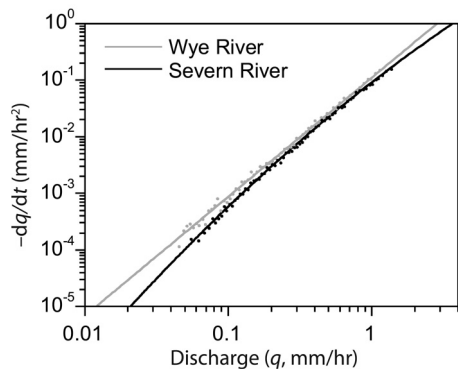


Figure 1.23 Plot of $\ln(|dq/dt|)$ versus $\ln(q)$ for the Wye and Severn Rivers. Note logarithmic axis scales. Both relationships approximate a straight line as given by equation (1.48) [Kirchner (2009)]. Catchments as simple dynamical systems: Catchment characterization, rainfall-runoff modeling, and doing hydrology backward. *Water Resources Research* 45, with permission of the American Geophysical Union].

Equation (1.48) can be integrated to give the relation between discharge and storage:

$$q = [a \cdot (2 - b) \cdot (S - S_0)]^{1/(2-b)}, \quad (1.50)$$

where S_0 is a constant of integration. The behavior of this relation, as well as the physical interpretation of S_0 , depends on whether $b < 2$, $b = 2$, or $b > 2$ (see paragraphs 32–37 of Kirchner 2009). Whichever the case, (1.50) allows specification of the storage-discharge relation.

More important for hydrologic predictions, one can use (1.46) along with (1.47) to write an equation giving streamflow as a function of precipitation and evapotranspiration:

$$dq = a \cdot q^{b-1} \cdot (p - et - q) \cdot dt. \quad (1.51a)$$

Kirchner (2009) discusses mathematical aspects of using (1.51a) for practical streamflow predictions. To illustrate the basic idea, we can write (1.51a) in finite-difference form as

$$q_{t+1} = a \cdot q_t^{b-1} \cdot (p_t - et_t - q_t) \cdot \Delta t + q_t, \quad (1.51b)$$

where the subscripts indicate successive time periods and $t + 1 = t + \Delta t$. Then, once a and b have been determined from analysis of past streamflow records (as described in figure 1.23) and an initial discharge q_0 is specified, future values of q_t can be predicted from successive values of p_t and et_t .

Figure 1.24 shows that Kirchner's model gave very good streamflow predictions, confirming the

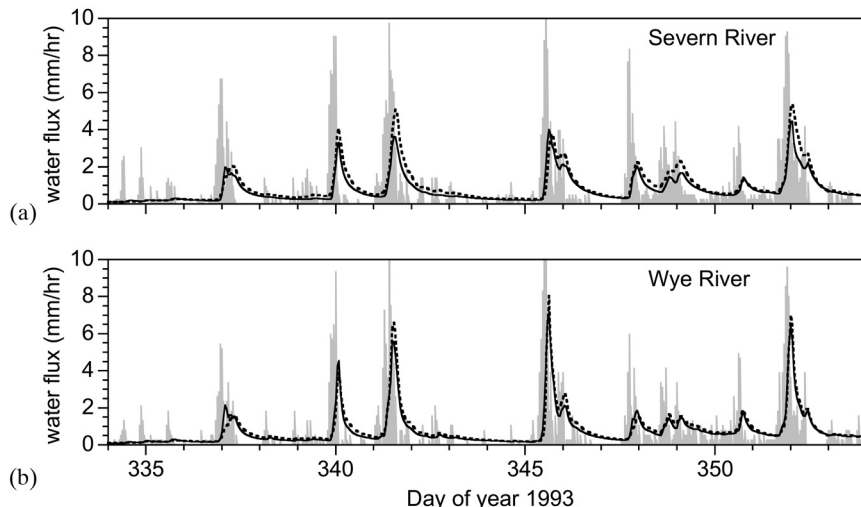


Figure 1.24 Predicted hourly discharge (dotted black curves) using the approach of Kirchner (2009) [equation (1.51b)], compared with measured discharge (solid black curves) and hourly rainfall (gray) for the (a) Severn and (b) Wye Rivers during 20-day periods in December 1993. Predicted discharge is generally similar to observed discharge [Kirchner (2009)]. Catchments as simple dynamical systems: Catchment characterization, rainfall-runoff modeling, and doing hydrology backward. *Water Resources Research* 45, with permission of the American Geophysical Union].

applicability of the basic hydrologic concepts discussed earlier. Note, though, that the basic storage relations [equations (1.47) and (1.48)] are based on analyses of measured streamflow values. Therefore, their validity

1. is proportional to the precision of discharge measurements (section 1.11.2) and
2. could be altered by changes in climate and/or land use (nonstationarity).

1.13 The Future of Hydrology

Subsequent chapters of this text focus on the physics of individual hydrologic processes. These principles are essential components of hydrologic science. However, as we have seen in this chapter, there are intrinsic challenges to hydrology that impede the extrapolation of the basic physics processes operating instantaneously at a “point” (i.e., a small, relatively homogeneous region of the earth’s surface) to an understanding of the hydrology of a finite area over a finite time.

In addition to these intrinsic problems, it has become apparent in recent decades that there are new extrinsic challenges facing the science and practice of hydrology. Human population and development have been increasing dramatically for the last 150 years, to the point where human impact on the earth’s surface now rivals natural geologic and biologic forces (Sanderson et al. 2002), and the anthropogenic effect on climate is all but certain (Intergovernmental Panel on Climate Change 2007; Gillett et al. 2012). The major hydrologic impacts include declining snow cover, de-

creases in ground-water storage due to pumping, major alteration of river flow regimes from dams, and the effects of land-use changes on water quality, ground-water recharge, evapotranspiration, and streamflow.

Wagener et al. (2010, p. 1) argue that these nearly ubiquitous and increasing anthropogenic modifications of the hydrologic cycle require a “paradigm shift” in hydrology to focus on “predictions of system behavior that are beyond the range of previously observed variability or that result from significant alterations of physical . . . system characteristics to become the new norm.” Hydrologists must be able not only to understand how individual hydrologic processes function, but also to synthesize and integrate the behavior of hydrologic systems, including the effects of changing (i.e., nonstationary) climate, soils, topography, vegetation, and land use. The key elements of the changes in the science and practice of hydrology envisioned by Wagener et al. (2010) are summarized in table 1.6 on the following page.

Thus, although the basic physical principles described in this text are powerful tools, the degree of knowledge that can be obtained with them is bounded. Hydrologists must be as aware of these limitations as they are of the tools themselves. Thus, we have tried to point out the assumptions behind each conceptual approach and the difficulties in applying it, because

It ain't so much the things we don't know
that gets us in trouble.
It's the things we know that ain't so.⁸

Table 1.6 Key Elements of a Paradigm Shift in Hydrologic Science.

Current	Future
Humans are external to the hydrologic system.	Humans are intrinsic to the hydrologic system, both as agents of change and as beneficiaries of ecosystem services.
Assumption of stationarity: past is a guide to the future.	Nonstationary world: past is no longer a sufficient guide to the future, expected variability could be outside the range of observed variability.
Predicting response, assuming fixed system characteristics: boundary value problem with prescribed fixed topography, soils, vegetation, climate.	Both system and response evolve: no longer a boundary value problem, boundary conditions and interfaces themselves evolve and are coupled. Becomes a complex adaptive system.
Learning from studying individual places (often pristine experimental catchments) to extrapolate or upscale to other places.	Comparative hydrology: learning from individual places embedded along gradients (e.g., changing climate, human imprint) and across spatial scales.
Hydrologists as analysts of individual processes or features at small scales (akin to a microscope) or as synthesists of whole system behavior at large scales (akin to a telescope).	Hydrologists as both analysts <i>and</i> synthesists (akin to the <i>macroscope</i>) studying the coupled system across a range of time and space scales.
Observations to characterize input-output behavior in individual (mostly) pristine places.	Observations to track the evolution of both structure and response in coupled systems and subsystems.
Observe and analyze pristine places and extrapolate to make predictions of human impacts.	Observe and analyze real places where humans live and interact with the hydrologic system at range of scales.
Model predictions derive credibility by reproducing historical observations.	Model predictions derive credibility via more in-depth diagnostic evaluation of model consistency with underlying system and testing of behavior outside of observed range.
Observation, prediction (modeling) and management are separate exercises (without feedbacks!).	Real-time learning: observations (sensing, including participatory human sensing), modeling and management are interactive exercises with feedbacks and updating.
Strong separation between engineering and science approaches to hydrology education.	Integration of qualitative and quantitative aspects into a holistic teaching of hydrology.
Focus on teaching established solutions to current problems.	Focus on teaching of evolving skill sets with a strong scientific basis that can be adapted to solving new problems and to understanding new phenomena.

Source: Wagener et al. (2010). The future of hydrology: An evolving science for a changing world. *Water Resources Research* 46, with permission of the American Geophysical Union.

▼ EXERCISES

1. Using the rules presented in appendix A and table A.2, convert the measured values in the left-hand column of the table below to their equivalents in other units given in the same row.

Convert	to	to	to
Weight density of water 1.00 g/cm ³	kg _f /m ³	lb/ft ³	N/m ³
Atmospheric pressure 14.7 lb/ft ²	dyne/cm ²	N/m ²	kPa
Dynamic viscosity of water 1.80×10^{-2} dyne · s/cm ²	N · s/m ²	lb · s/ft ²	Pa · s
Velocity 14 cm/s	ft/s	m/d	mi/hr
Discharge 653 ft ³ /s	m ³ /s	gal/min	gal/d
Rainfall-runoff conversion 1.00 in rain on 1.00 mi ²	ft ³	gal	m ³
Rainfall-runoff conversion 1.00 in rain on 1.00 mi ² for 1.00 hr	ft ³ /s	L/s	m ³ /s
Water-balance conversion 1.00 in rain on 1.00 mi ² in 1.00 yr	ft ³ /s	L/s	m ³ /s
Area 1.00 mi ²	m ²	km ²	ha
Temperature 12°F	°C	K	
Temperature 63.2°F	°C	K	
Temperature 14.7°C	°F	K	
Temperature 20°C	°F	K	
Temperature difference of 9.6 F°	C°	K	
Temperature difference of 12.9 C°	F°	K	
Heat capacity of water 1.00 cal/g · °C	J/kg · K	BTU/lb _m · °F	

2. The following equations are taken from the hydrologic literature. The units in which the equation quantities were originally measured are given as the “old” units. In this exercise, we want to convert the equations to use with a “new” set of units, using the steps below. “[1]” designates a dimensionless quantity. Conversion factors can be found in table A.2.
- Check each equation for dimensional and unitary homogeneity.
 - For equations that are not homogeneous, change the appropriate constants so that the equation is correct when using the new units as described in section A.3.
 - The modified equation should be in exactly the same form as the original, with only the appropriate constant values changed. The constants should have the same number of significant figures as in the original.
 - Check your results by substituting values as described in section A.3.

i. $I = 0.00042 \cdot H + 0.00026 \cdot H \cdot P$

Symbol	Definition	Old Units	New Units
I	interception	mm	in
H	height of grass	mm	in
P	precipitation	mm	in

ii. $B = 0.00061 \cdot p \cdot \frac{(T_s - T_a)}{(e_s - e_a)}$

Symbol	Definition	Old Units	New Units
B	Bowen ratio	[1]	[1]
p	atmospheric pressure	mm	in Hg
T_s	surface temperature	°C	°F
T_a	air temperature	°C	°F
e_s	surface vapor pressure	mb	in Hg
e_a	air vapor pressure	mb	in Hg

iii. $R_n = 0.83 \cdot K_{in} - 54$

Symbol	Definition	Old Units	New Units
R_n	net radiation	cal/cm ² · d	W/m ²
K_{in}	incident solar radiation	cal/cm · d	W/m ²

iv. $E = \frac{3.64}{T_a} \cdot \frac{u_a}{\left[\ln\left(\frac{z_m}{z_0}\right) \right]^2} \cdot (e_a^* - e_a)$

Symbol	Definition	Old Units	New Units
E	evaporation rate	cm/d	mm/d
T_a	air temperature	K	°C
u_a	wind speed	km/d	m/s
z_m	measurement height	cm	m
z_0	roughness height	cm	m
e_a^*	saturation vapor pressure	mb	kPa
e_a	actual vapor pressure	mb	kPa

v. $Q = w \cdot H \cdot K_h \cdot \frac{\Delta h}{\Delta x}$

Symbol	Definition	Old Units	New Units
Q	ground-water flow rate	m ³ /d	ft ³ /s
w	width of aquifer	m	ft
H	saturated thickness	m	ft
K_h	hydraulic conductivity	m/d	ft/s
Δh	change in water-table elevation	m	ft
Δx	distance between elevation measurements	m	ft

vi. $Q = 0.278 \cdot C \cdot I \cdot A$

Symbol	Definition	Old Units	New Units
Q	flood peak discharge	m^3/s	ft^3/s
C	runoff coefficient	[1]	[1]
I	rainfall rate	mm/hr	in/hr
A	drainage area	km^2	mi^2

vii. $T_c = \frac{L^{1.15}}{7,700 \cdot H^{0.38}}$

Symbol	Definition	Old Units	New Units
T_c	time of concentration	hr	hr
L	length of drainage basin	ft	km
H	drainage basin relief	ft	km

viii. $Q = \frac{484 \cdot A \cdot R}{0.5 \cdot D + 0.6 \cdot T_c}$

Symbol	Definition	Old Units	New Units
Q	flood peak discharge	ft^3/s	m^3/s
A	drainage area	mi^2	km^2
R	volume of runoff per unit area	in	mm
D	storm duration	hr	hr
T_c	time of concentration	hr	hr

ix. $Q_{ef} = (0.085 + 0.734 \cdot q_o) \cdot P$

Symbol	Definition	Old Units	New Units
Q_{ef}	volume of event flow per unit area	in	mm
q_o	antecedent discharge	ft^3/s	L/s
P	total storm rainfall	in	mm

x. $C = 95 \cdot Q^{0.7}$

Symbol	Definition	Old Units	New Units
C	concentration of suspended sediment	mg/L	mg/L
Q	discharge	ft^3/s	m^3/s

- Show that the Bond number [equation (1.4)] and the Reynolds number [equation (1.5)] are dimensionless.
- Compare the Bond numbers and Reynolds numbers for the following flows and write a brief statement comparing the relative importance of surface tension and viscosity in each.

Flow	$U (\text{m}/\text{s})$	$L (\text{m})$	$\rho (\text{kg}/\text{m}^3)$	$\sigma (\text{N}/\text{m})$	$\mu (\text{N} \cdot \text{s}/\text{m}^2)$
Infiltration into soil	0.005	0.002	1,000	0.0756	0.00179
Hillslope runoff	0.1	0.02	1,000	0.0756	0.00179
Small stream	1	1	1,000	0.0756	0.00179

4. Obtain a topographic map of a nearby area, select a stream having tributaries, and manually delineate its watershed above its mouth. (This will be a lot easier if the watershed is entirely on one map.)
 - a. What are the highest and lowest elevations in the watershed?
 - b. What is the approximate watershed area? Determine this using a planimeter, grid or dot counting, or a computer-based technique.
 - c. What information is available about the geology, soils, and land cover in the watershed?
5. Obtain a topographic map of a nearby area that includes a small lake. Locate the lake outlet and manually delineate the lake's watershed. (This will be a lot easier if the watershed is entirely on one map.)
 - a. What are the highest and lowest elevations in the watershed?
 - b. What is the approximate watershed area? Determine this using a planimeter, grid or dot counting, or a computer-based technique.
 - c. What proportion of the watershed is occupied by the lake?
 - d. What information is available about the geology, soils, and land cover in the watershed?
6. Section 1.7.2.2 describes the USGS StreamStats (<http://water.usgs.gov/osw/streamstats>) application that delineates watersheds for user-selected basin outlets and provides data on watershed characteristics and streamflow statistics.
 - a. Access this program and select a state for which the application is “fully implemented.”
 - b. Under “Interactive map,” click on “General information” and review the list of basin characteristics provided.
 - c. Return to the previous page and click on “Interactive map.” Set the map scale at 1:24,000.
 - d. Use the “Navigation” tool to locate the outlet of a watershed (e.g., where a stream enters a larger stream or a lake).
 - e. Using the “Watershed delineation from a point” tool (\bullet_+), click on the outlet and wait until the application delineates the watershed.
 - f. Click on the “Basin characteristics” tool (to the right of the delineation tool) to get information on watershed area, etc.
7. The table below gives the drainage area, average precipitation (determined from measurements at meteorological stations), and average streamflow (measured near the mouths) of four large rivers.

Watershed	Area, A (km2)	Average Precipitation, P (mm/yr)	Relative Error, ε_P (%)	Average Streamflow, Q (m3/s)	Relative Error, ε_Q (%)
Connecticut River, USA	20,370	1,100	10	386	5
Yukon River, Canada & USA	932,400	570	20	5,100	10
Euphrates River, Iraq	261,100	300	10	911	10
Mekong River, Thailand	663,000	1,460	15	13,200	5

- a. Using equation (1.21) and assuming no ground-water inputs or outputs, use this information to compute the estimated long-term average evapotranspiration, ET , for each watershed.
- b. How well do your calculated ET values conform to those shown for the same watersheds on figure 2.27?
- c. Use the information in the table, equations (1.36) and (1.40), and example 1B1.6 to compute the 95% absolute and relative uncertainties in your ET estimates.
8. A lake with a drainage area of A_D [L 2] has a surface area of A_L [L 2] and an average depth of z_L [L]. The long-term average rates of precipitation and evapotranspiration for the land

portion of the drainage basin are p_D and e_D , respectively [L T^{-1}]. For the lake itself, the average rate of precipitation and evaporation are p_L and e_L , respectively [L T^{-1}]. Average rate of stream outflow from the lake is Q [$\text{L}^3 \text{T}^{-1}$]. There is no ground-water inflow or outflow to the basin.

- a. Using these symbols, and assuming that all quantities are in a consistent system of units (no unit conversions required):
 - i. Write the water-balance equation for the drainage basin.
 - ii. Write the water-balance equation for the lake.
 - iii. Write the expression for the residence time of the lake.
- b. Below are data for Lake Winnipesaukee, New Hampshire's largest lake:
Drainage basin: $A_D = 940 \text{ km}^2$; $p_D = 1,240 \text{ mm/yr}$; $e_D = 500 \text{ mm/yr}$
Lake: $A_L = 180 \text{ km}^2$; $p_L = 952 \text{ mm/yr}$; $Q = 15.1 \text{ m}^3/\text{s}$; $z_L = 18 \text{ m}$
 - i. Use the equations you derived in 8a to estimate average lake evaporation, e_L . Does the answer differ if you use the drainage-basin equation (8.a.i) or the lake equation (8.a.ii)?
 - ii. Compare the estimate(s) of e_L with the given value of e_D . What are possible explanations for the differences?
 - iii. Calculate the residence time for the lake.
 - iv. Compare the magnitudes of the inflows to the lake from drainage-basin runoff and precipitation. What are the water-quality implications of these numbers?
 - v. Compare the magnitudes of the outflows to the lake via streamflow and evaporation.

Note: The file LWinnBal.doc on the disk accompanying this text contains more detailed background on how the various water-balance estimates were determined. Reviewing this information will be instructive in showing students how hydrologic analyses are carried out using typically available data.

9. Table C.2 (which can be found on the disk accompanying the text) shows average annual streamflow for the Diamond River at Wentworth, New Hampshire, for 1971–2000 as measured by the USGS. Assuming the measurements are rated “good,” use the approach described in sections 1B1.3.2 and 1B1.3.3 of box 1.1 to calculate the 95% confidence intervals for long-term streamflow.
10. Write out the detailed steps leading from equation (1.44) to equation (1.51b).

▼ NOTES

- ¹ The Celsius and Fahrenheit temperature scales are *interval*, rather than *ratio*, scales and hence require designation of an arbitrary zero point as well as a unit of measurement.
- ² This latter formula can be readily remembered by recalling Einstein's famous formula $E = mc^2$, where E is the amount of energy in a quantity of mass, m , and c is the velocity of light.
- ³ The arguments of exponential and trigonometric functions should be dimensionless, though one sometimes encounters empirical relations in which this rule is violated.
- ⁴ This is stated colloquially as “Baldy's Law”: “Some of it plus the rest of it equals all of it.” We do not know who Baldy is or was.
- ⁵ Note that hydrologists also use the term “runoff” to denote overland flow, which is discussed in chapter 10.
- ⁶ Note that there are many hydrologic reservoirs for which this relation does *not* hold, e.g., a melting snowpack, the global atmosphere, the global ocean.
- ⁷ δx is always stated as a positive value and the error range is assumed symmetrical, except that the lower bound cannot be < 0 for quantities that are always positive.
- ⁸ This quote has been attributed to at least three American humorists: Artemus Ward (pseudonym of Charles Farrar Browne), Mark Twain, and Will Rogers.



2

The Global Context Climate, Hydrology, and the Critical Zone

2.0 Introduction

The global hydrologic cycle links the hydrosphere, the atmosphere, the biosphere, the cryosphere, and the lithosphere; transferring water substance, dissolved and particulate matter, and energy among them (figure 1.1).

Although the global cycle is one of the two main focuses of the science of hydrology, most hydrologic analyses, whether for scientific understanding or for analyzing water resource management problems, are done at spatial scales much smaller than global, and processes at these smaller scales are the focus of most of this book. However, increasingly sophisticated satellite observations, more powerful earth-systems modeling, and improved scientific communication are opening new avenues of research at the global scale and revealing linkages and feedbacks among local hydrologic processes and the larger-scale dynamics of earth's climate, soils, and vegetation.

To provide the essential global context for hydrologic science, this chapter summarizes the major features of the earth's climate and hydrologic cycle and describes these linkages, particularly the global

distributions of soils (the pedosphere, the surface of the lithosphere) and vegetation (the biosphere). The pedosphere and the biosphere form the surface of the land that mediates land-atmosphere exchanges of water and energy; together these constitute the **Critical Zone**.

2.1 Basic Aspects of Global Climate

2.1.1 Laws of Radiant Energy Exchange

The energy that determines the earth's climate and drives the hydrologic cycle arrives in the form of electromagnetic radiation from the sun, so we begin with a review of the laws of radiant-energy exchange.

All matter at a temperature above absolute zero radiates energy in the form of electromagnetic waves that travel at the speed of light. The rate at which this energy is emitted is given by the

Stefan-Boltzmann law:

$$F_{EM} = \varepsilon \cdot \sigma \cdot T^4, \quad (2.1)$$

where F_{EM} is the rate of energy emission per unit surface area per unit time (flux) [$\text{E L}^{-2} \text{T}^{-1}$], T is the absolute temperature of the surface, σ is a universal

constant called the **Stefan–Boltzmann constant** [$E L^{-2} T^{-4}$] ($\sigma = 4.90 \times 10^{-9} \text{ MJ/m}^2 \cdot \text{K}^4 \cdot d = 5.67 \times 10^{-8} \text{ W/m}^2 \cdot \text{K}^4$), and ϵ is a dimensionless quantity called the **emissivity** of the surface.

The value of ϵ ranges from 0 to 1, depending on the material and texture of the surface. A surface with $\epsilon = 1$ is called a **blackbody**; most earth materials have emissivities near 1 (table 2.1).

The wavelength, $\lambda[\text{L}]$, and frequency, $f[\text{T}^{-1}]$, of electromagnetic radiation are inversely related as

$$\lambda \cdot f = c \quad (2.2)$$

where c is the speed of light [$L \text{ T}^{-1}$] ($c = 2.998 \times 10^8 \text{ m/s}$). The spectrum of electromagnetic radiation extends over 21 orders of magnitude (figure 2.1).

According to Planck's law, the wavelength of the energy emitted by a radiating surface decreases as its temperature increases, and the wavelength at which the maximum radiant energy flux occurs, λ_{max} , is inversely related to the absolute temperature T via **Wien's displacement law**:

$$\lambda_{max} = \frac{2,897}{T}, \quad (2.3)$$

where λ_{max} is in μm .

Table 2.1 Emissivities of Various Forms of Water and Various Earth Materials.

Material	Emissivity, ϵ
Dense clouds	0.99
Liquid water	0.95
Ice	0.97
Snow, dirty	0.97
Snow, fresh	0.99
Sand, dry	0.95
Sand, wet	0.98
Peat, dry	0.97
Peat, wet	0.98
Light sandstone	0.98
Limestone	0.92
Gravel	0.92
Grassy vegetation	0.97–0.98
Corn, beans	0.94
Cotton, tobacco	0.96
Sugar cane	0.99
Cactus	0.98
Deciduous forest	0.95
Coniferous forest	0.97

Source: Lee (1980), Brutsaert (1992), Gray and Prowse (1992).

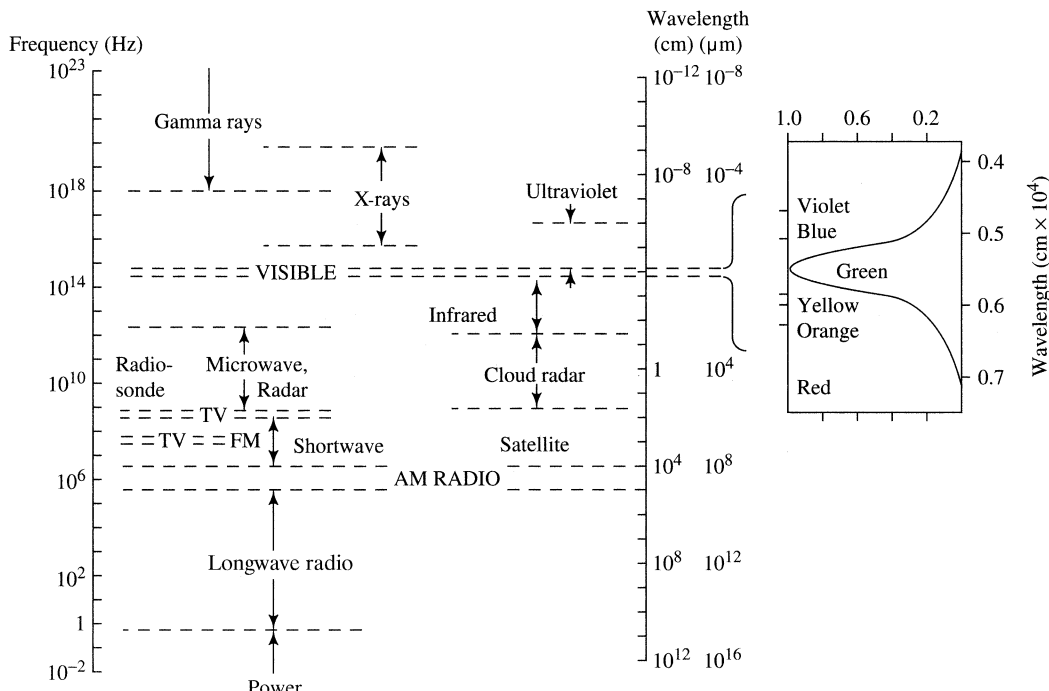


Figure 2.1 The electromagnetic spectrum [Miller et al. (1983)].

Electromagnetic energy is transmitted through a vacuum undiminished, but when it strikes matter some of it may be reflected and/or absorbed. The following terms are used to describe the interactions of matter and radiant energy *at a given wavelength*:

- **Absorptivity**, α_λ , is the fraction of the incident energy at wavelength λ that is absorbed by a surface; this energy raises the temperature of the matter and/or causes a phase change (melting or evaporation).
- **Reflectivity**, ρ_λ , is the fraction of the incident energy at wavelength λ that is reflected by the surface; this energy does not affect the matter and continues traveling undiminished in a new direction.
- **Transmissivity**, τ_λ , is the fraction of the incident energy at wavelength λ that is transmitted through the matter; this energy does not affect the matter and continues traveling undiminished in the original direction.

The values of α_λ , ρ_λ , and τ_λ must each be between 0 and 1, and, for a given surface and wavelength, must always sum to 1:

$$\alpha_\lambda + \rho_\lambda + \tau_\lambda = 1. \quad (2.4)$$

The values of α_λ , ρ_λ , and τ_λ vary with the type of the matter and the wavelength.

The emissivity ε in equation (2.1) is an integrated value over all emitted wavelengths. According to **Kirchoff's law**,

$$\varepsilon_\lambda = \alpha_\lambda, \quad (2.5)$$

where ε_λ is the emissivity at a given wavelength. For many earth-surface materials, the transmissivity $\tau_\lambda = 0$, so that from (2.4) and (2.5) reflectivity is related to emissivity as

$$\rho_\lambda = 1 - \varepsilon_\lambda. \quad (2.6)$$

2.1.2 The Atmosphere

2.1.2.1 Composition

The atmosphere is a mixture of gases, principally nitrogen (N_2 , 78%) and oxygen (O_2 , 21%), in which liquid and solid particles are suspended. The proportions of the major constituents, and many of the minor ones, are effectively constant over the time and space scales typically used in hydrologic analysis (table 2.2). However, the concentrations of components of particular hydrologic significance—water vapor, liquid water and ice in clouds, dusts, and smoke particles, and various gaseous and particulate pollutants—are highly variable in space and time. Also of hydrologic significance are the well-mixed minor constitu-

Table 2.2 Composition of the Atmosphere.

Permanent Constituents	Volume (%)	Variable Constituents	Volume (%)
Nitrogen (N_2)	78.084	Water vapor (H_2O)	< 4
Oxygen (O_2)	20.946	Water (liquid and solid)	< 1
Argon (Ar)	0.934	Carbon dioxide (CO_2)	0.0400 ^a
Neon (Ne)	0.001818	Methane (CH_4)	0.00019 ^b
Helium (He)	0.000524	Sulfur dioxide (SO_2)	< 0.0001
Krypton (Kr)	0.000114	Nitrous oxide (N_2O)	0.0000328 ^c
Hydrogen (H_2)	0.00005	Carbon monoxide (CO)	0.00002
Xenon (Xe)	0.0000087	Dusts (soot, soil, salts)	< 0.00001
Radon (Rn)	6×10 ⁻¹⁸	Ozone (O_3)	< 0.000007 ^d
		Nitrogen dioxide (NO_2)	< 0.000002 ^e
		Ammonia (NH_4)	Trace

^a Global average is 0.0345%: concentration is increasing about 0.001 volume % per year (Ramanathan 1988) due to burning of fossil fuels, cement manufacture, and deforestation (Rosenberg 1987).

^b Concentration is increasing about 0.00002 volume % per year (Ramanathan 1988) due to increased rice paddy cultivation, domestic animals, and other causes (Rosenberg 1987).

^c Concentration is increasing about 0.000001 volume % per year (Ramanathan 1988) due to increased fertilizer use and burning of fossil fuels (Rosenberg 1987).

^d Concentration in the stratospheric ozone layer appears to be decreasing (Callis and Natarajan 1986) due to chemical reactions involving chlorinated fluorocarbon compounds used as refrigerants and propellents. Concentrations in the troposphere are increasing (Ramanathan 1988) due to industrial activity and automobile use.

^e Concentrations in the stratosphere are increasing about 0.000003 volume % per year (Callis and Natarajan 1986).

ents called “greenhouse gases,” chiefly carbon dioxide (CO_2), methane (CH_4), nitrous oxide (N_2O), chlorofluorocarbons (CFCs), and ozone (O_3). Although present in very small proportions, these gases, along with water vapor, strongly affect the energy budget of the atmosphere (as discussed in more detail in section 2.1.3). Greenhouse gases are produced naturally and by human activities, especially the burning of fossil fuels and the practices of agriculture, deforestation, and manufacturing. Their concentrations are increasing over time, with measurable effects on global temperature and hydrologic processes.

2.1.2.2 Vertical Structure and Dynamics

The earth’s atmosphere extends from the surface to a height of about 700 km. This gaseous envelope is characterized by the typical vertical distributions of pressure and temperature shown in figure 2.2. The pattern of vertical temperature gradients delineates three distinct layers—the troposphere, stratosphere, and mesosphere—between which there is little mixing. Vertical temperature and pressure gradients vary with latitude, season, and local weather patterns: the boundary between the troposphere and the stratosphere is higher (15 to 16 km) near the equator and lower (5–6 km) over the poles, and is higher in summer than in winter at a given location. Virtually all the processes that directly influence climate, weather, and hydrologic activity take place in the troposphere.

Winds are produced by horizontal gradients of atmospheric pressure, and exchanges of water vapor and latent and sensible heat between the surface and the atmosphere are controlled by turbulence created by surface friction acting on winds in the lowest layer of the troposphere, called the **mixed layer**. Above this, the ground-induced turbulence gradually decreases and the wind dynamics are increasingly controlled solely by horizontal pressure gradients and, at moderate to high latitudes, the Coriolis force. The entire layer in which winds are affected by the frictional resistance of the surface is called the **planetary boundary layer**. The thickness of this layer varies in space and time from a few tens of meters to one or two kilometers depending on the topography and roughness of the surface, the wind velocity, and the rate of heating or cooling of the surface (Peixoto and Oort 1992; Seidel et al. 2012).

The vertical temperature gradient in the troposphere is called the **lapse rate**; its average value is $-6.5^\circ\text{C}/\text{km}$. However, the local near-surface gradient is highly variable and may even temporarily reverse direction; this phenomenon is called an **inversion**. The local lapse rate has a strong influence on the buoyancy of vertically moving “parcels” of air and hence on the vertical transport of water vapor and heat. Approaches to quantifying the dynamics of the turbulent exchange of water vapor and energy in the mixed layer are presented in section 3.5.

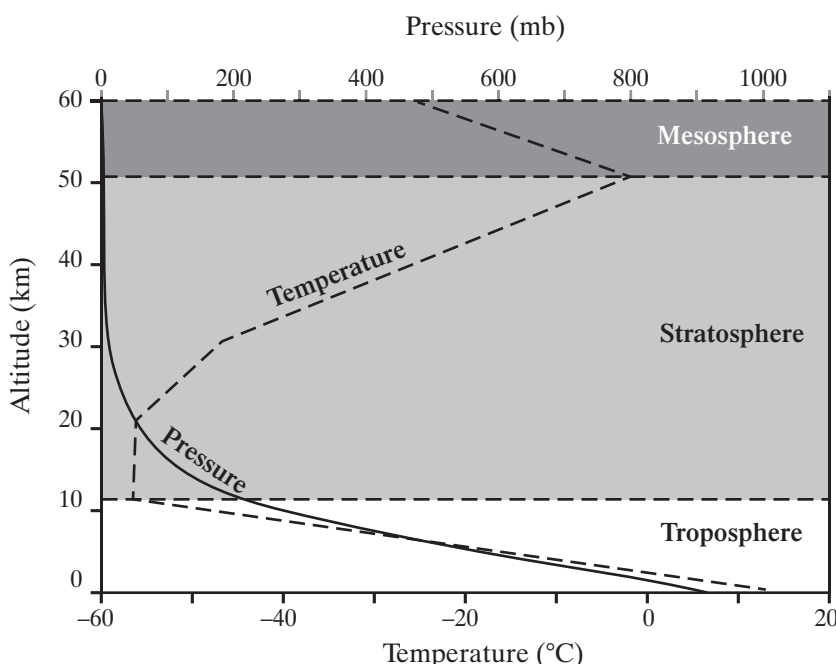


Figure 2.2 Atmospheric “spheres” and the average vertical distribution of temperature and pressure. The maximum height of the planetary boundary layer is about 2 km.

2.1.3 Global Energy Budget

Solar input constitutes virtually all the energy entering the earth-atmosphere system; contributions from radioactive decay in the earth's interior and from anthropogenic sources are comparatively negligible. In this section we trace out the fate of solar energy in the earth-atmosphere system prior to its ultimate reflection or re-radiation back to space and establish the overall energy budgets of the atmosphere, the surface, and the earth-atmosphere system (figure 2.3; table 2.3). All these energy values are estimates of globally and seasonally integrated averages of values that are highly variable in time and space, and which are subject to considerable uncertainty (Trenberth et al. 2011; see also Church et al. 2011). To make the relative importance of the various processes more apparent, table 2.3 also shows energy-flux values normalized so that the energy input from the sun = 100 units.

2.1.3.1 Solar (Shortwave) Radiation

The sun's energy arrives at the outer edge of the atmosphere at an average rate of 1.74×10^{17} W. This quantity divided by the area of the planar projection of the earth, 1.28×10^{14} m², is called the **solar constant**, S ; thus $S = 1,364$ W/m².

Dividing S by 4 gives the average energy flux over the spherical surface at the top of the atmosphere, called the **extraterrestrial solar irradiance or insolation**; $I = 341$ W/m².

This solar energy flux fluctuates by about 0.1% over the 11-year sunspot cycle (Duffy et al. 2009), but has shown no significant longer-term trends, at least over recent decades (Hinkleman et al. 2009).

Curve (a) in figure 2.4 on p. 53 is the spectrum of solar radiation at the top of the atmosphere. The spectrum extends from the **near-ultraviolet** (wavelengths from 0.2 to 0.4 μm) to the **near-infrared** (0.7 to 3 μm), with a pronounced peak in the **visible range** (0.4 to 0.7 μm). Radiation in the 0.2 to 3 μm range is **shortwave radiation**.

The sun's radiant energy is subject to absorption and reflection (scattering) by gases and other constituents as it travels through the atmosphere. Some of the gases in the earth's atmosphere are strong absorbers of energy in particular portions of the solar spectrum. In particular, oxygen (O₂) and ozone (O₃) in the lower stratosphere shield terrestrial biota from much of the energy in the ultraviolet range, which is damaging to most forms of life. Water vapor also absorbs a significant portion of the sun's energy in the "near-infrared" range.

On average, 78 W/m² of incoming shortwave radiation energy are absorbed by the atmosphere, including clouds. Another 79 W/m² are reflected in the atmosphere, principally by clouds, and scattered by atmospheric gases and particles ultimately to outer space. Thus, after absorption and reflection, 184 W/m² of energy reach the surface. Virtually all the energy arriving at the earth's surface is at wavelengths less than 4 μm, and most of it is in the visible

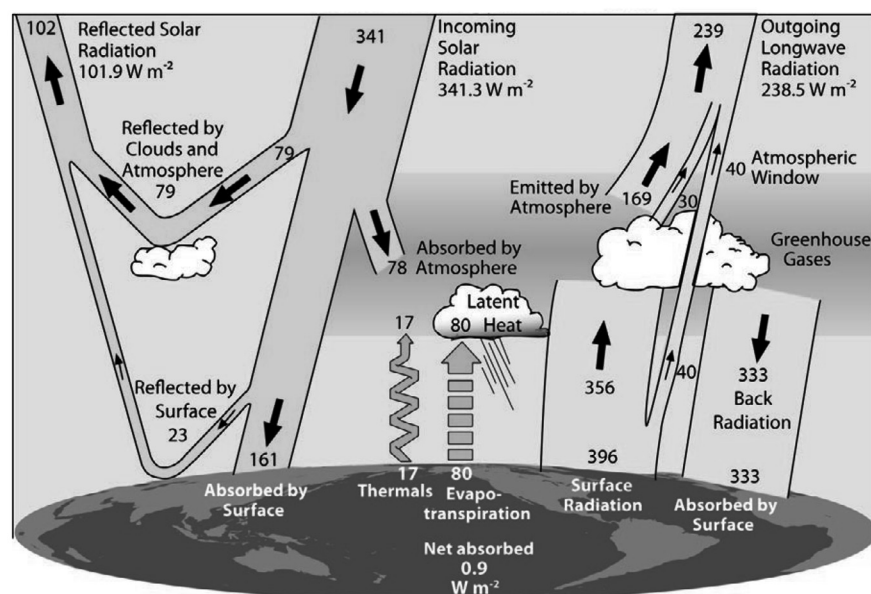


Figure 2.3 Average global energy balance of the earth-atmosphere system [Trenberth et al. (2009). Earth's global energy budget. *Bulletin of the American Meteorological Society* 90:311–323, reproduced with permission of American Meteorological Society].

Table 2.3 Average Global Energy Balance of the Earth-Atmosphere System, the Atmosphere, and the Earth's Surface (see figure 2.4).

	Normalized Units	W/m ²	Estimated Uncertainty (%)
Surface			
<i>Inputs</i>			
Solar radiation (SW)	54	184	5
Atmospheric emission (LW)	97 151	333	10
<i>Outputs</i>			
Reflected solar radiation (SW)	7	23	10
Terrestrial emission (LW)	116	396	10
Latent heat	23	80	10
Sensible heat	5 151	17	5
Atmosphere			
<i>Inputs</i>			
Solar radiation (SW)	100	341	3
Surface reflected solar radiation (SW)	7	23	10
Terrestrial emission (LW)	116	396	10
Latent heat	23	80	10
Sensible heat	5 251	17	5
<i>Outputs</i>			
Solar radiation to surface (SW)	54	184	5
Cloud reflected solar radiation (SW)	23	79	10
Surface reflected solar radiation (SW)	7	23	10
Downward emission (LW)	97	333	10
Upward emission (LW)	70 251	239	3
Earth-Atmosphere System			
<i>Inputs</i>			
Solar radiation (SW)	100	341	3
<i>Outputs</i>			
Reflected solar radiation (SW)	30	102	3
Upward emission (LW)	70 100	239	3

LW = longwave

SW = shortwave

Source: Trenberth et al. (2009).

range [0.4 to 0.7 μm; curve (b) of figure 2.4]. This is **incident solar radiation**.

The fraction of incident solar radiation that is reflected by a surface (i.e., the total reflectivity of energy in the visible range, $0.4 \leq \lambda \leq 0.7 \mu\text{m}$) is the **albedo**, α , of the surface; i.e.,

$$\alpha \equiv \frac{\int_{0.4}^{0.7} \rho_\lambda \cdot d\lambda}{0.4} \quad (2.7)$$

Albedos of common earth materials are listed in table 2.4 on p. 54; the average albedo of the surface is $(23 \text{ W/m}^2)/(184 \text{ W/m}^2) \approx 0.125$. A total of 102 W/m² of solar irradiance are ultimately reflected from the atmosphere, clouds, and the surface back to outer space; thus the global reflectivity, or **planetary albedo**, equals $(102 \text{ W/m}^2)/(341 \text{ W/m}^2) = 0.30$.

After atmospheric absorption and reflection and surface reflection, 161 W/m² of insolation are absorbed to heat the land and water at the earth's surface and cause evaporation and melting. This warming is balanced by net upward transport of latent and sensible heat and terrestrial radiation.

2.1.3.2 Terrestrial (Longwave) Radiation and the Greenhouse Effect

The solar radiation absorbed at the surface warms the land and oceans and provides latent heat for evaporation and melting. Some of this energy, a net of 28 units, is transferred to the atmosphere by the turbulent-transfer processes described in chapter 3: 80 W/m² associated with evaporation (*latent heat*) and 17 W/m² as direct heating (*sensible heat*).

The net energy exchanges at the surface result in an average earth-surface temperature of about 289 K (16°C). Following the Stefan–Boltzmann law [equation (2.1)], this temperature produces an upward **terrestrial radiation** flux of about 396 W/m². Following the Wien law [equation (2.3)], this energy is in the infrared range, with wavelengths between 4 and 60 μm and a peak near 10 μm [curve (c) of figure 2.4]. Terrestrial radiation is also called **longwave radiation** or **thermal radiation**.

Naturally occurring and human-introduced gases and clouds strongly absorb specific wavelengths of the longwave radiation emitted by the surface (upper portion of figure 2.4). Of the 396 W/m² of this energy emitted by the surface, 40 W/m² are transmitted through the atmosphere directly to outer space and 356 W/m² are absorbed in the atmosphere by clouds and gases. The longwave radiation resulting from this heating produces a 199 W/m² of upward flux to

outer space and 333 W/m^2 of downward flux to warm the surface.

The absorption and downward re-radiation of longwave radiation in the atmosphere is called the **greenhouse effect**, which controls the temperature of the earth's surface and atmosphere.

The greenhouse effect raises the average surface temperature about 34°C from its value in the absence of terrestrial radiation-absorbing components, -18°C , to its current value of 16°C .

The most important contributors to the greenhouse effect are water vapor (which accounts for 50% of the absorption); clouds (25%) and carbon dioxide (CO_2) (19%); with ozone (O_3), nitrous oxide (N_2O), methane (CH_4), aerosols, chlorinated fluorocarbons (CFCs), and aerosols accounting for about 7% (Schmidt et al. 2010). Curve (d) of figure 2.4 is the spectrum of earth's emission to outer space after absorption in the atmosphere.

The term “greenhouse gases” (GHGs) refers to the *noncondensing* gases: CO_2 , N_2O , CH_4 , O_3 , and CFCs. Note that

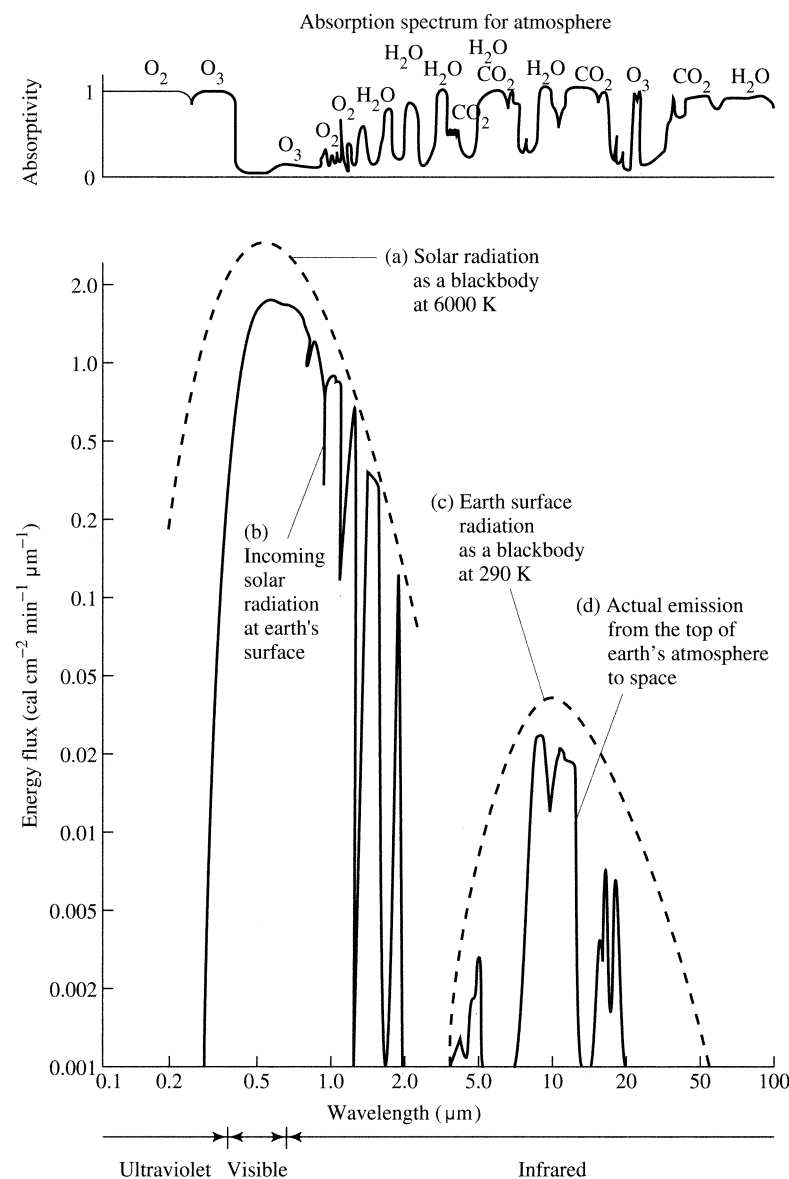


Figure 2.4 Spectra of energy (a) emitted by a blackbody at $6,000 \text{ K}$; (b) received at the earth's surface (global average); (c) emitted by a blackbody at 290 K ; and (d) emitted to space by the earth-atmosphere system (global average). Upper graph shows absorption spectrum for principal absorbing gases in the atmosphere [adapted from Barry and Chorley (1982); Miller et al. (1983)].

Although only 25% of the greenhouse effect is directly due to GHGs, the warming induced by increasing GHGs allows the air to hold more water vapor and clouds, creating a positive feedback that produces the remaining 75% of the effect (Lacis et al. 2010).

Table 2.4 Visible-Range Reflectance (Albedo) of Various Forms of Water and Various Earth Materials.

Surface	Conditions	Albedo, α
Clouds	Low overcast: 100 m thick	0.40
	200 m thick	0.50
	500 m thick	0.70
Liquid water	Smooth: solar angle 60°	0.05
	30°	0.10
	20°	0.15
	10°	0.35
	5°	0.60
	Wavy: solar angle 60°	0.10
Solid water	Fresh snow: low density	0.85
	high density	0.65
	Old snow: clean	0.55
	dirty	0.45
	Glacier ice: clean	0.35
	dirty	0.25
Sand	Dry, light: high sun	0.35
	low sun	0.60
	Gray: wet	0.10
	dry	0.20
	White: wet	0.25
	dry	0.35
Soil	Organic: dark	0.10
	Clay	0.20
	Sandy: light	0.30
Grass	Typical fields	0.20
	Dead: wet	0.20
	dry	0.30
Tundra, heather		0.15
Crops	Cereals, tobacco	0.25
	Cotton, potato, tomato	0.20
	Sugar cane	0.15
Trees	Rain forest	0.15
	Eucalyptus	0.20
	Red pine forest	0.10
	Mixed hardwoods in leaf	0.18

Source: Lee (1980).

Anthropogenic emissions are rapidly increasing the concentrations of GHGs (figure 2.5). It is virtually certain that most if not all of these increases are caused by human activities—particularly the burning of fossil fuels and the clearing of forests—and these activities show every sign of continuing, and perhaps accelerating, for at least the next several decades.

CO₂ concentration is currently about 400 ppm—about 60% larger than the preindustrial value of 250 ppm—and is projected to reach 500 ppm or higher by 2050, higher than the earth has experienced in the last million or so years. The concentrations of methane and chlorofluorocarbons are increasing at even faster relative rates than is CO₂ and are many times more effective (per molecule) than CO₂ at absorbing longwave radiation.

Thus, it is virtually certain that the increase in global surface temperatures since about 1850 (figure 2.6) has been caused by human-generated increases in GHG concentrations (Karl and Trenberth 2003; Intergovernmental Panel on Climate Change 2007; Hansen et al. 2008; Lean and Rind 2008; Chapman and Davis 2010; Hansen et al. 2010). The increase in direct radiative forcing due to anthropogenic GHGs is 2.74 W/m² (Montzka 2010); this has caused a surface-temperature increase of about 1°C.

2.1.4 Latitudinal Energy Transfer

As we have just seen, the major determinant of global climate is the overall energy budget of the earth, especially the balance between insolation and terrestrial radiation, which establishes the global average surface temperature. The first-order spatial and temporal variabilities of climate are determined by the spherical shape of the earth (figure 2.7 on p. 56), its elliptical orbit around the sun, and the 23.5° tilt of its axis of rotation (figure 2.8 on p. 57), which produce the seasonal and latitudinal variations in insolation shown in figure 2.9 (on p. 56).

As a result of these planetary characteristics, the net radiation balance (i.e., the difference between solar radiation received and the terrestrial radiation emitted) is positive for latitudes below about 35°, and negative poleward of that. Because average total energy inputs and outputs must be in balance at all latitudes, there is a net poleward transfer of energy from the regions of surplus to those of deficit; the magnitude of this transfer is indicated by the RT curve in figure 2.10(a) on p. 58. Most of the transfer occurs via the general circulation of the atmosphere (AT curve; section 2.1.5), with oceanic transport

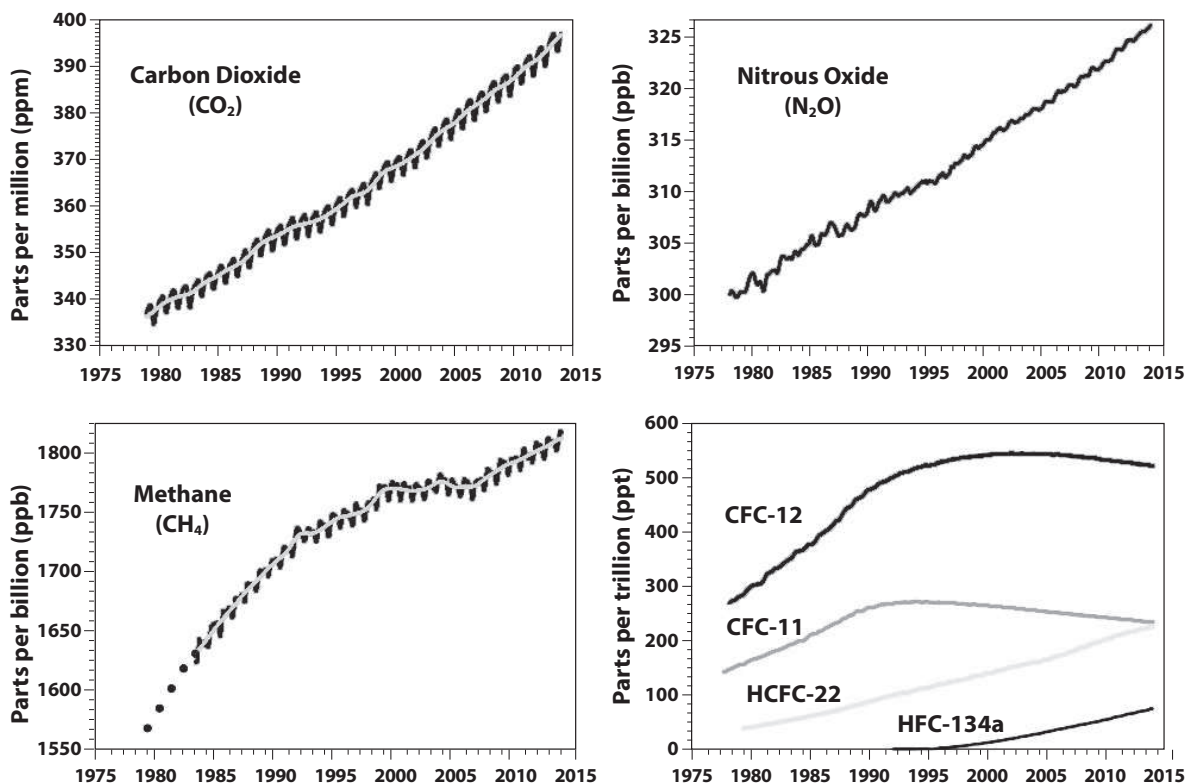


Figure 2.5 Global average concentrations of greenhouse gases (CO_2 , N_2O , CH_4) and four species of CFCs, 1978–2010 [Butler and Montzka (2014)].

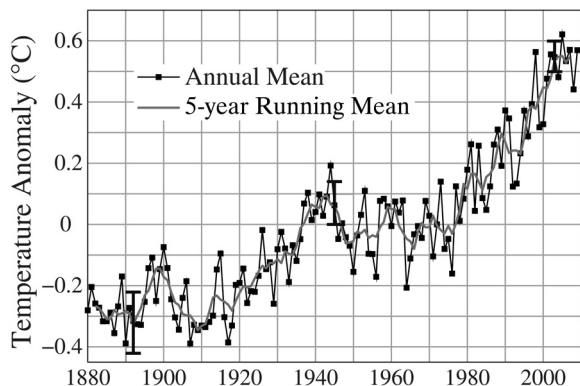


Figure 2.6 Average global surface temperature anomalies, 1880–2010. Zero value is 1951–1980 average. Two-standard-deviation-error bars are shown at 1892, 1944, and 2003 [Hansen et al. (2010)]. Global surface temperature change. *Reviews of Geophysics* 48, with permission of the American Geophysical Union].

(OT curve) of greater magnitude only in the tropics. Figure 2.10(b) shows the portions of atmospheric transport due to sensible heat (DSE curve), latent heat (LE curve), and kinetic energy (KE curve).

2.1.5 The General Circulation and the Distribution of Pressure and Temperature

The unequal latitudinal distribution of radiation and the requirement for the conservation of angular momentum on the rotating earth give rise to a system of three circulation cells in the latitude bands from $0\text{--}30^\circ$, $30\text{--}60^\circ$, and $60\text{--}90^\circ$ in each hemisphere, along with the jet streams and characteristic prevailing surface-wind directions (figure 2.11 on p. 58). This system is called the **general circulation** of the atmosphere. The cell nearest the equator is responsible for most of the poleward atmospheric energy transfer between latitudes 0° and 30° , but mechanisms other than the general circulation dominate the atmospheric transfer at higher latitudes: Winds

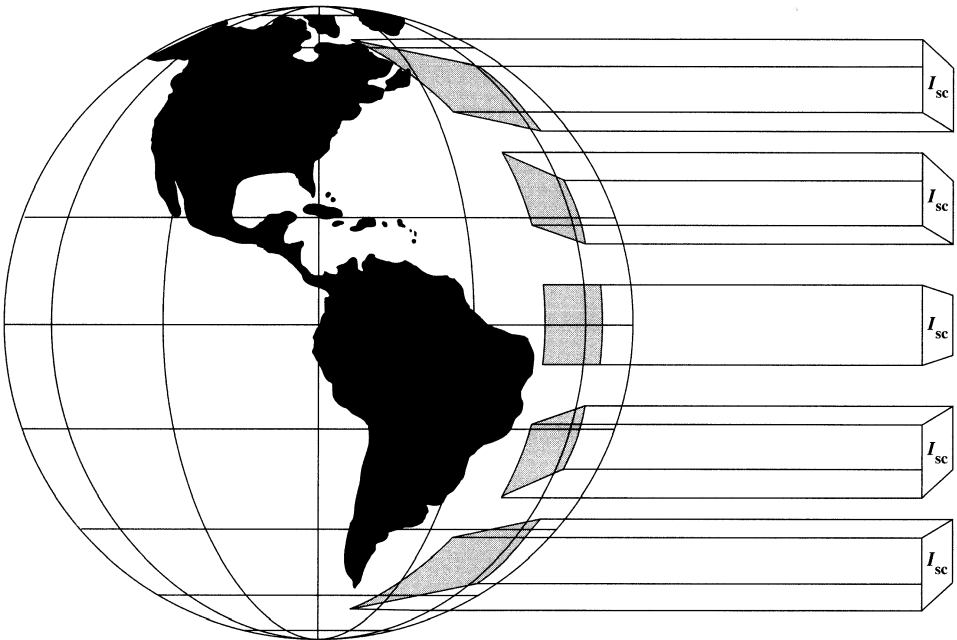


Figure 2.7 Latitudinal variation of solar-radiation angle of incidence and intensity, I_{sc} ($\text{J E L}^{-2} \text{T}^{-1}$). At higher latitudes a given energy flux is spread over a larger area [Day and Sternes (1970)].

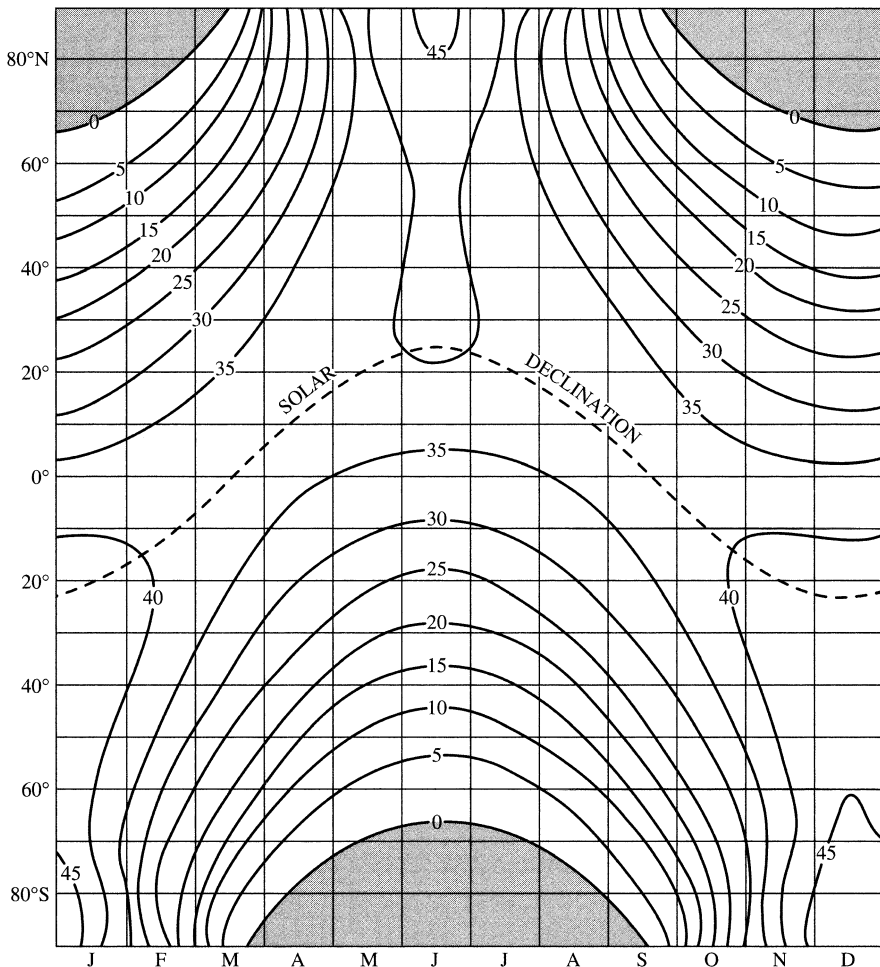


Figure 2.9 Daily total receipt of solar radiation (MJ/m^2) at the top of the atmosphere as a function of latitude and time of year [Peixoto and Oort (1992). *Physics of Climate*. New York: American Institute of Physics. With kind permission of Springer Science+Business Media].

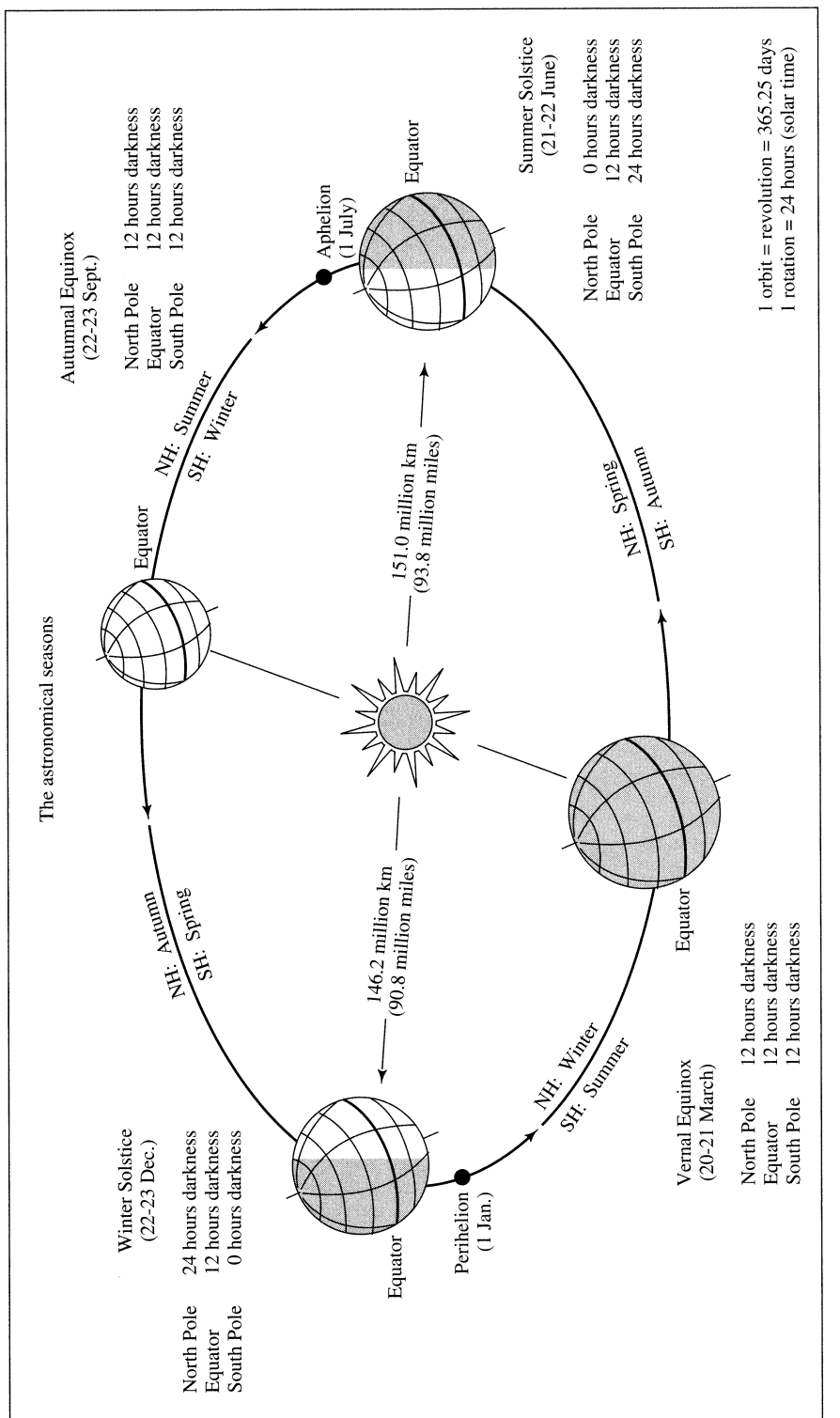


Figure 2.8 Revolution of the earth around the sun, showing that the occurrence of summer and winter in the Northern and Southern Hemispheres is determined by the 23.5° tilt of the rotational axis toward or away from the sun [J. E. Oliver and J. J. Hidore (1984). *Climatology: An Introduction*, p. 30. © 1990. Reprinted by permission of Pearson Education, Inc., Upper Saddle River, NJ].

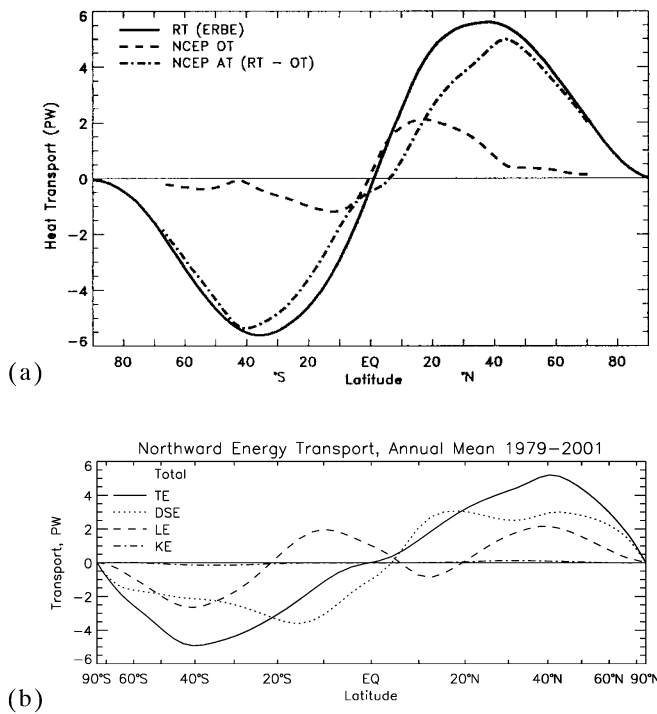


Figure 2.10 (a) Global latitudinal heat transport. Solid line is the total transport required to balance the top of atmosphere radiation budget; dashed line is estimate of ocean-heat transport, dot-dashed line is estimated atmospheric transport [Trenberth and Caron (2001)]. Estimates of meridional atmosphere and ocean heat transports. *Journal of Climate* 14:3433–3443, reproduced with permission of American Meteorological Society]. (b) Annual and zonal mean northward atmospheric energy transport for 1979–2001. TE = total; DSE = “dry static energy” (sensible heat); LE = latent heat; KE = kinetic energy of wind [Trenberth and Stepaniak (2003)]. Covariability of components of poleward atmospheric energy transports on seasonal and interannual time scales. *Journal of Climate* 16:3691–3705, reproduced with permission of American Meteorological Society].

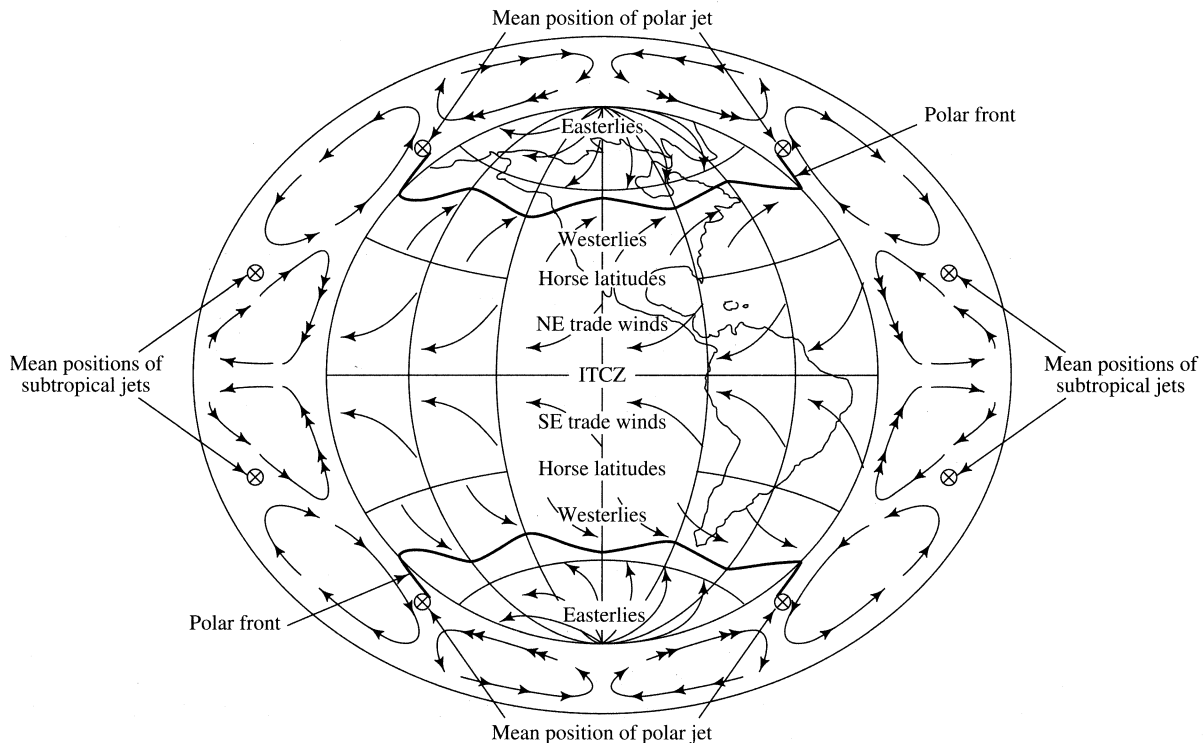


Figure 2.11 The general circulation of the atmosphere. Double-headed arrows in cross section indicate that the wind has a component from the east [Miller et al. (1984)].

circulating in large-scale horizontal eddies—both the quasi-stationary zones of high and low pressure discussed below and the moving cyclonic storms that dominate weather systems in the midlatitudes—are the major agents of transport above latitude 30° (Barry and Chorley 1982).

Figure 2.11 shows that the general circulation results in regions of rising air near the equator and near latitude 60°, and descending air near latitude 30° and the poles. The zones of ascent are characterized by relatively low atmospheric pressures at the surface, and those of descent by high pressures. However, because of the distribution of continents and oceans, the zones of high and low pressure actually occur as cells rather than continuous belts (figure 2.12 on the following page).

Horizontal pressure gradients are the basic driving force for winds; these pressure forces along with forces induced by the motion itself (centrifugal forces, the Coriolis effect due to the earth's rotation, and friction) produce surface winds that move approximately parallel to isobars, but with a tendency to spiral inward toward low-pressure centers and outward from high-pressure centers. In the Northern Hemisphere, the sense of circulation is clockwise around highs (**anticyclonic circulation**) and counter-

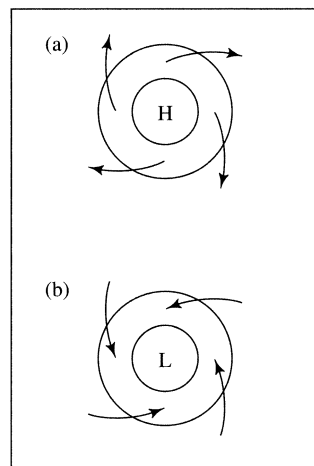


Figure 2.13 Arrows show general directions of surface winds in (a) anticyclonic circulation (around high-pressure cells) and (b) cyclonic circulation (around low-pressure cells) in the Northern Hemisphere. Solid lines are **isobars**: lines of equal atmospheric pressure. Circulations in the Southern Hemisphere are reversed (i.e., circulation around cyclones is clockwise).

clockwise around lows (**cyclonic circulation**) (figure 2.13); the circulations are in the opposite sense in the Southern Hemisphere.

The subtropical high-pressure zone exists as cells over the Pacific and Atlantic Oceans; these cells are especially well defined in the summer, and occur farther to the north in the summer than in the winter. Since winds circulate clockwise around these highs, the coastal areas of southwestern North America and Europe are subject to dry, cool northerly winds in the summer. Conversely, the southeastern United States, Hawaii, the Philippines, and Southeast Asia are subject to warm, moist winds from the tropics and have warm, humid summers with frequent rain. The subpolar low-pressure zone occurs as cells over the northern Pacific and Atlantic, which are especially evident in winter. These cells, called the Aleutian Low (Pacific) and Icelandic Low (Atlantic), are “centers of action,” where major midlatitude cyclonic storms develop their greatest intensities.

Figure 2.14 on p. 61 shows the global distribution of mean temperature in January and July. This distribution is clearly strongly related to the average receipt of solar radiation and hence to latitude, but it is modified by the distribution of the continents and oceans. Because of water's very high heat capacity, the annual temperature range of the oceans is much less than that of the continents. This is reflected in the equatorward dip of the isotherms over the ocean in summer (oceans cooler than land), and the poleward dip in winter (oceans warmer than land).

The very cold winter temperatures in the centers of the North American and Asiatic landmasses are due to radiational cooling and distance from the relatively warm oceans; these low temperatures produce cells of high density and high pressure. The situation is reversed in summer, when extensive solar radiational heating occurs, and these continents are then sites of generally low pressure. Note particularly the summertime trough of low pressure over southern Asia; winds associated with this trough carry the monsoon rains on which the agricultural economy of this vast and populous region depends.

2.1.6 Large-Scale Internal Climatic Variability and Teleconnections

Beginning in the late 1960s, oceanographic and atmospheric measurements, global observations via satellite, and careful study of historical records have established that the present state of the earth's cli-

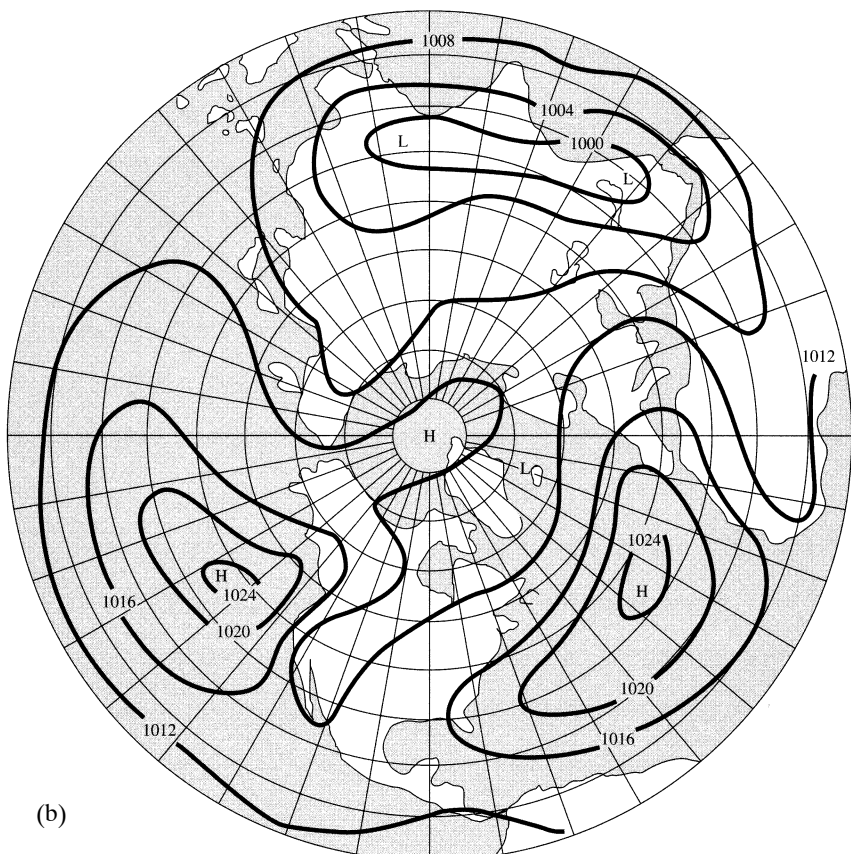
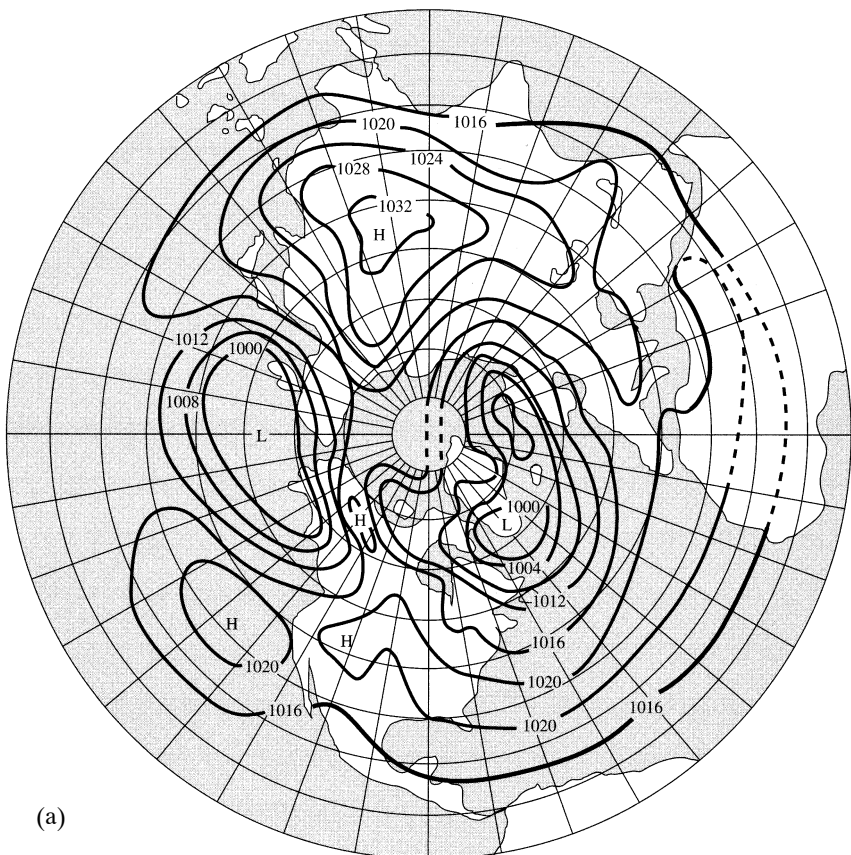


Figure 2.12 Normal sea-level pressures (mb) in the Northern Hemisphere in (a) January and (b) July [Miller et al. (1984)].

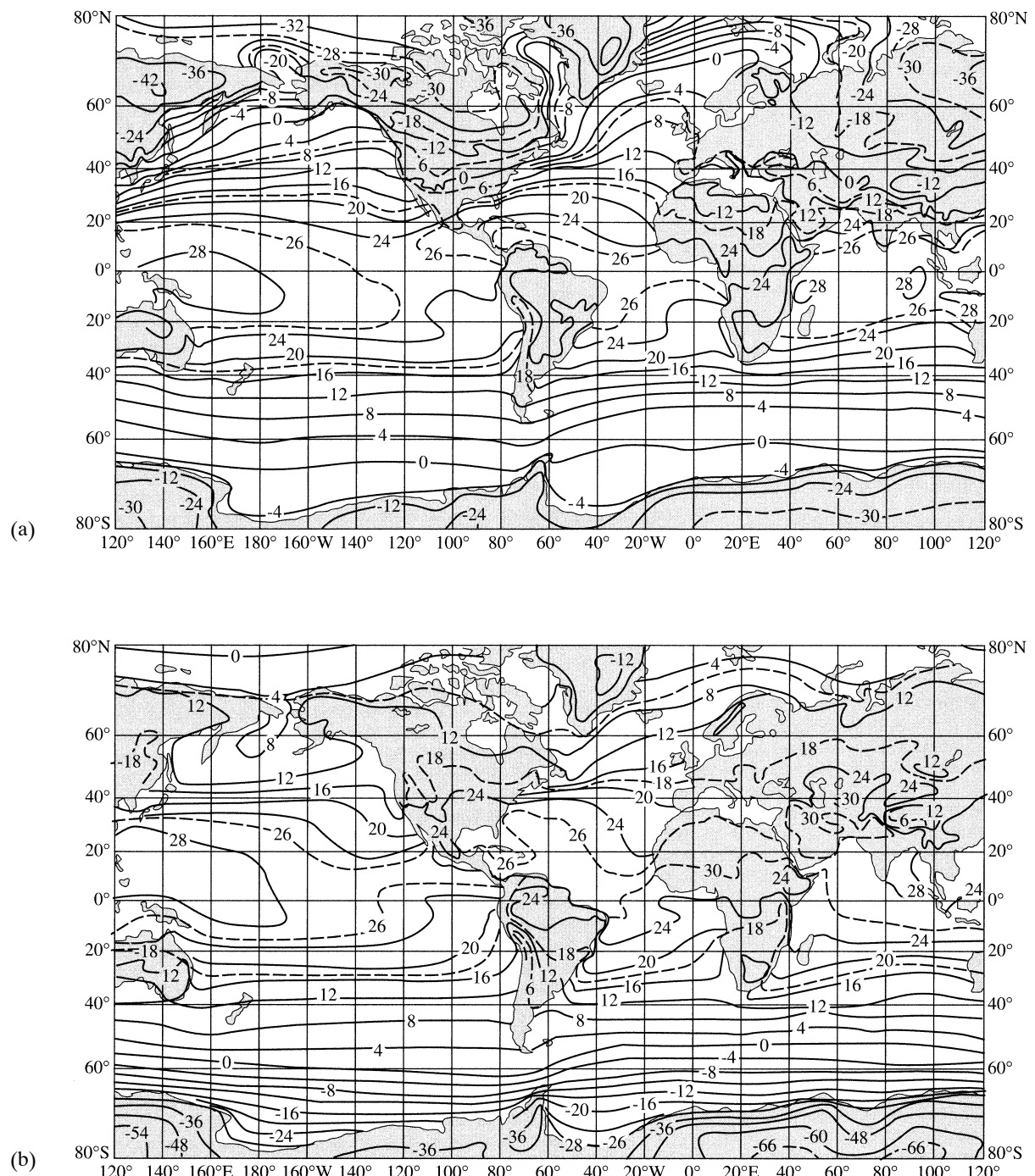


Figure 2.14 Distribution of mean temperature ($^{\circ}\text{C}$) in (a) January and (b) July [Peixoto and Oort (1992). *Physics of Climate*. New York: American Institute of Physics. With kind permission of Springer Science+Business Media].

mate is characterized not only by the mean features of the global circulation discussed above, but by persistent, inherent large-scale oscillations that produce interannual to interdecadal variability in that circulation. These in turn produce characteristic quasi-regular fluctuations in temperature, precipitation, and hydrologic phenomena in particular regions, which are called **teleconnections**. Here we describe the four most persistent and prominent of these, El Niño and the Southern Oscillation, North Atlantic Oscillation, the Pacific–North America Oscillation, and the North Pacific Oscillation.

2.1.6.1 El Niño and the Southern Oscillation (ENSO)

The best known system of teleconnections, and the only one that is truly global in extent, is called the **El Niño–Southern Oscillation (ENSO)**, a quasi-cyclic, wave-like phenomenon with a period of three to seven years that has persisted for at least the last 450 years (Rasmusson 1985; Enfield 1989). This phenomenon consists of an oscillation between a warm phase (“El Niño”), during which abnormally high sea-surface temperatures (SSTs) occur off the coast of Peru¹ accompanied by low atmospheric pressure over the eastern Pacific and high pressure in the western Pacific, and a cold phase (“La Niña”) with low SST in the eastern Pacific and the opposite pressure anomalies. There is considerable evidence that ENSO is an inherently oscillatory phenomenon that requires no outside forcing.

The typical ENSO warm episode begins in the late spring to fall of year 1 with abnormally strong westerly winds in the equatorial Indian Ocean, low pressures in eastern Australia, and warming SSTs in the South Pacific. As winter progresses, a tongue of abnormally warm water forms off the coast of Peru; this intensifies and builds westward along the equator during the spring and summer of year 2. The peak of the warm phase usually occurs between July and December of year 2, with abnormally high SSTs extending westward to the international date line. These are accompanied by abnormal westerly winds and strong convergence along the equator, high pressures and lowered sea levels in the western Pacific and Indonesia, and low pressures and elevated sea levels in the eastern Pacific. A pool of abnormally cold water and enhanced westerly winds also occur near latitude 45° in the North Pacific. The decline of the warm phase typically begins in January to April of year 3, when the equatorial pool of high SSTs begins to shrink, and most of the SST, wind, and pres-

sure anomalies dissipate by the end of the summer of year 4.

The end of an ENSO warm phase begins when the eastward waves of warm water are reflected off South America and, in a complicated process that involves poleward circulation of the reflected westward-moving surface water and atmospheric processes, the SST returns to its original levels and the easterly trade wind flow is reestablished (Enfield 1989). Continued cooling of SSTs in the eastern Pacific leads to the cold phase of ENSO (La Niña).

The atmospheric pressure fluctuations associated with the changes in SSTs shift the jet stream in the eastern North Pacific and North America to the south (warm phase) or north (cold phase). These shifts can steer unusual weather systems into low- and midlatitude regions around the world. The result is unusually warm or cold winters in particular regions, drought in normally productive agricultural areas, and torrential rains in normally arid regions (Rasmusson 1985). Some of the teleconnections associated with ENSO episodes are indicated in figures 2.15 and 2.16 on pp. 64 and 65; the most consistent are the severe droughts in Australia and northern South America and heavy rainfall in Ecuador and northern Peru. In other places the effects can vary from episode to episode depending on the state of the atmosphere. For example, the 1976–1977 event was associated with drought along the West Coast of the United States, while that of 1982–1983 produced increased storminess (Enfield 1989). The severe drought in the north-central United States in the summer of 1988 was a consequence of the 1986–1987 ENSO event (Trenberth et al. 1988). The strong 1997–1998 event produced warm and dry conditions from India to northern Australia (leading to extensive forest fires in Indonesia); dry conditions in the eastern Amazon region; a wet winter with considerable flooding along the West, Gulf, and South Atlantic Coasts of the United States; and a warm winter in the northeastern United States. A number of studies have found relationships between streamflows and ENSO cycles (e.g., Dracup and Kahya 1994; Eltahir 1996; Amarasekera et al. 1997; Piechota et al. 1997). Since ENSO anomaly patterns persist for several months, useful long-range hydrological forecasts can be made for the regions shown in figures 2.15 and 2.16 (Halpert and Ropelewski 1992).

Because ENSO is such a large-scale process involving the ocean and atmosphere, it likely influences, and is influenced by, warming due to anthropogenic

greenhouse-gas production (Sun and Bryan 2010). Current information on ENSO is given at <http://www.elnino.noaa.gov>.

2.1.6.2 North Atlantic Oscillation (NAO)

Two of the most prominent, persistent features of atmospheric pressure in the Northern Hemisphere are the Icelandic Low (figure 2.12a) and the Azores High (figure 2.12b). Wallace and Gutzler (1981) showed that there is a strong correlation between the strengths of these two features: An abnormally intense/weak Icelandic Low tends to occur with an abnormally intense/weak Azores High. This is the dominant mode of atmospheric-pressure variability in the North Atlantic region (Hurrell 1995), and is called the **North Atlantic Oscillation (NAO)**.

The strength of the NAO is characterized by the **NAO index**, which is defined as the difference between normalized monthly sea-level-pressure anomalies at weather stations in the Azores and Iceland, and characterizes the steepness of a north-south atmospheric pressure gradient across the North Atlantic Ocean (figures 2.17 and 2.18 on p. 66). In its positive mode, the gradient is steep and the jet stream and weather systems moving across eastern North America and the North Atlantic tend to parallel latitude lines (**zonal flow**). The negative phase of the NAO index corresponds to a weaker north-south pressure gradient, and the jet stream and weather systems tend to encounter “blocking” that induces a meandering path with a longitudinal component (**meridional flow**).

When the NAO shifts between its modes of variability, the North Atlantic Ocean experiences changes in wind speed and direction that affect heat and moisture transport to the surrounding continents and seas (Hurrell 1995). As documented by Visbeck et al. (2000), significant associations have been observed between the NAO and winter temperatures in Europe, Asia, and North America; the advance and retreat of glaciers in Europe; and the extent of Arctic sea ice. Bradbury et al. (2002) reported associations between the NAO and weather phenomena in New England and documented strong correlations between winter streamflows and the NAO index.

2.1.6.3 Pacific–North America Oscillation (PNA)

The Pacific–North America Oscillation (PNA), like the NAO, is reflected in a negative correlation of sea-level pressures, in this case between a region extending through western Canada and far eastern Siberia and a large portion of the central and north-

central Pacific (figure 2.17). In its positive phase, pressure is above normal over the ocean and below normal over land. The PNA pattern affects the character of mid-tropospheric airflow across North America (Wallace and Gutzler 1981), and is a good indicator of the mean location of the polar front during the winter (Leathers et al. 1991). The positive phase is associated with above-average temperatures over western Canada and below-average temperatures over southeastern and south-central United States. It is also associated with above-normal precipitation in northwestern United States and below-average precipitation in the Midwest. As might be expected, the PNA is influenced by ENSO, such that its positive phase tends to occur with El Niño and its negative phase with La Niña. A source for current information on PNA and the NAO can be found at <http://www.cpc.ncep.noaa.gov/products/precip/cwlink/pna/nao.shtml>.

2.1.6.4 North Pacific Oscillation (NPO)

The North Pacific Oscillation (NPO) is an oscillation in sea-level pressures between a land area in eastern Siberia and a portion of the central Pacific Ocean west of the international date line and between latitudes 20° and 40° (west of the area most affected by the PNA). Linkin and Nigam (2008) concluded that the NPO is more strongly linked to marginal sea-ice variability in the Arctic than are other Pacific modes (ENSO, PNA). They also showed that NPO is correlated with meridional movements of the Asian–Pacific jet stream and Pacific storm tracks and, although somewhat weaker than PNA or ENSO, has more influence on Arctic sea ice and North American winter hydroclimate, especially Alaskan, Pacific Northwest, Canadian, and US winter air temperatures and Pacific Northwest, western Mexico, and south-central Great Plains winter precipitation.

2.2 The Global Hydrologic Cycle

2.2.1 Stocks and Fluxes

Figure 2.19 on p. 67 is a snapshot of the global hydrologic cycle in action. This “cycle” is actually a complex web of continual flows, or **fluxes**, of water among the major **stocks** of water. As described in chapter 3, the sun provides the latent-heat energy for evaporation and is the ultimate source of the kinetic energy of turbulence that mixes water vapor in the atmosphere to drive the cycle against the pull of gravity.

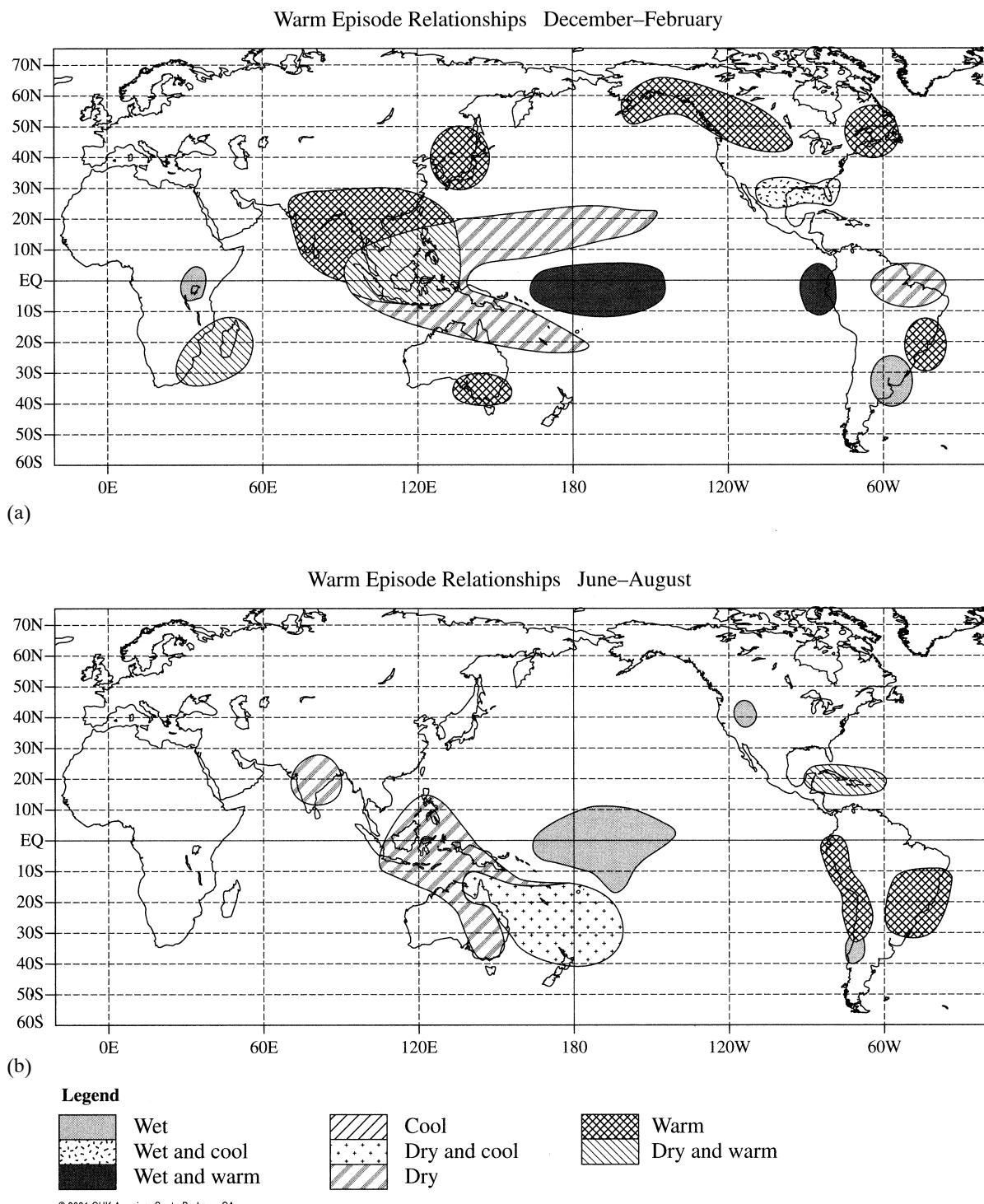


Figure 2.15 Typical climatic anomalies associated with the warm (El Niño) phase of ENSO. (a) Winter (December–February). (b) Summer (June–August) [US National Oceanic and Atmospheric Administration Climate Prediction Center (<http://www.cpc.ncep.noaa.gov>)].

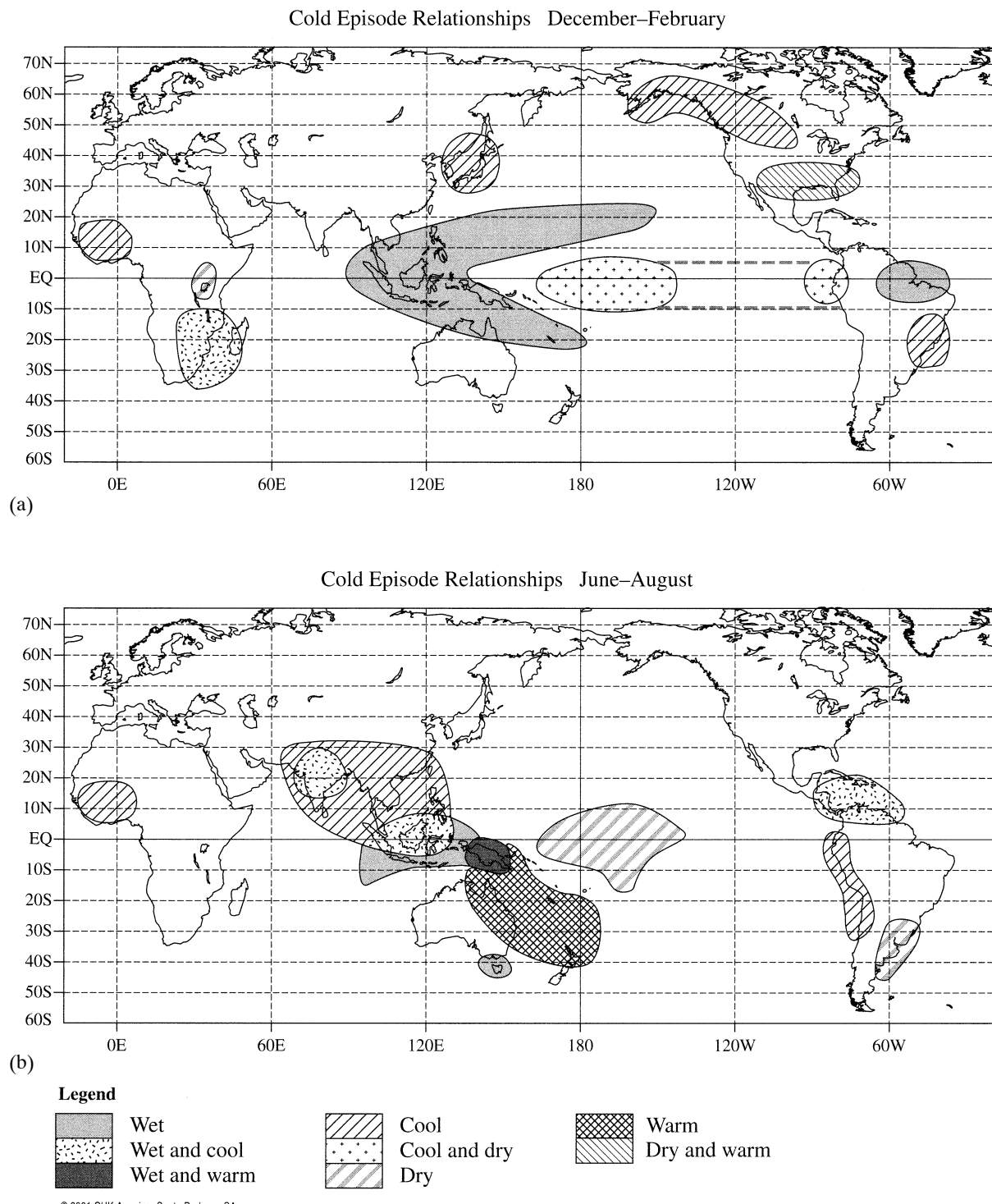


Figure 2.16 Typical climatic anomalies associated with the cold (La Niña) phase of ENSO. (a) Winter (December–February). (b) Summer (June–August) [US National Oceanic and Atmospheric Administration Climate Prediction Center (<http://www.cpc.ncep.noaa.gov>)].

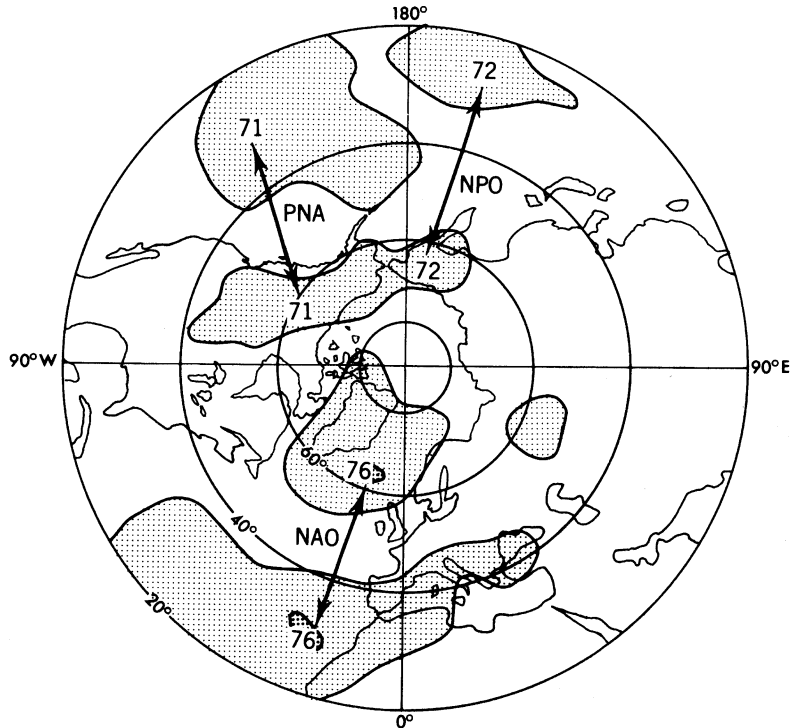


Figure 2.17 Spatial distributions of strongest negative correlations (percent) of sea-level pressure associated with Pacific–North America Oscillation, North Atlantic Oscillation, and North Pacific Oscillation [Peixoto and Oort (1992). *Physics of Climate*. New York: American Institute of Physics. With kind permission of Springer Science+Business Media].

North Atlantic Oscillation

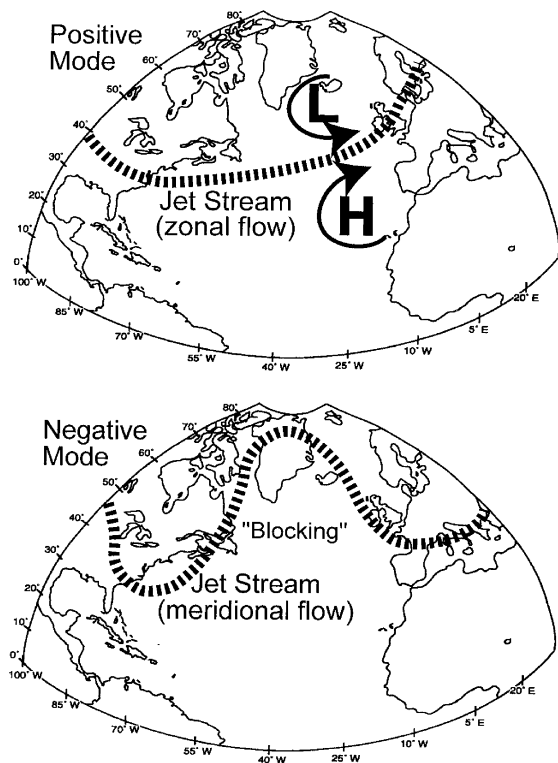


Figure 2.18 Circulations associated with the positive and negative phases of the North Atlantic Oscillation. In its positive mode, the pressure gradient between the Icelandic Low and the Azores High is steep and the jet stream and weather systems tend to move parallel to latitude lines. In its negative phase there is a weaker north-south pressure gradient, and the jet stream and weather systems tend to encounter “blocking” that induces a meandering path [Bradbury et al. (2002). New England drought and relations with large scale atmospheric circulation patterns. *Journal of the American Water Resources Association* 38:1287–1299, courtesy of the American Water Resources Association].

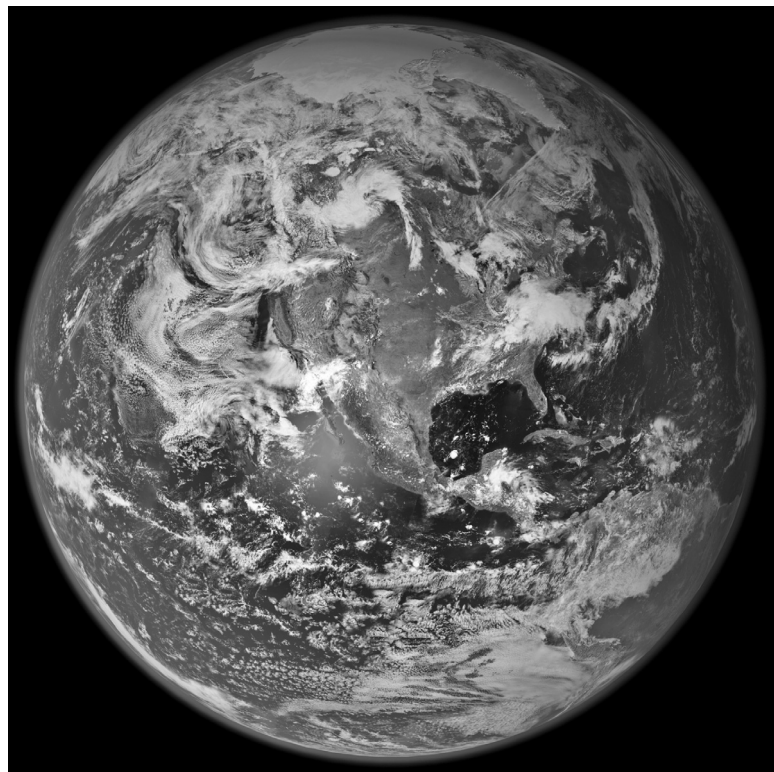


Figure 2.19 The global hydrologic cycle in action (courtesy of US National Aeronautics and Space Agency).

Figure 2.20 and tables 2.5 (on p. 68) and 2.6 (on p. 69) show the average quantities of water in the major global stocks and fluxes based on recent satellite and ground observations and model analyses by Trenberth et al. (2007): Almost 97% of the water on earth is in the oceans (figure 2.21 on p. 69); of the fresh water, about 63% is in solid form in glaciers,² 36% is ground water; and only about 0.5% is in surface-water bodies. As with the global energy balance, there are significant uncertainties in estimation of the stocks and flows in the global hydrologic cycle (Trenberth et al. 2011).

The major features of the global cycle are:

1. The oceans lose more water by evaporation than they gain by precipitation;
2. Oceans receive about 77% of the global precipitation and contribute 85% of the global evapotranspiration;
3. Land surfaces receive more water as precipitation than they lose by evapotranspiration;
4. In the continental part of the cycle, the precipitated water is recycled by evapotranspiration a number of times before returning to the oceans as river and ground-water runoff; and
5. The excess of water on the land returns to the oceans as runoff, balancing the deficit in the ocean-atmosphere exchange.

All living things participate in the global hydrologic cycle; your role is quantified in box 2.1 on p. 69.

2.2.2 Distribution of Precipitation

Regions characterized by rising air tend to have relatively high average precipitation, and those characterized by descending air tend to have low precipitation. Thus the general circulation (figure 2.11) produces belts of relatively high precipitation near the equator and 60° latitude, and relatively low precipitation near 30°, where most of the world's great deserts occur (figure 2.22 on p. 70). The equatorial belt of high precipitation is especially pronounced because warm easterly winds from both hemispheres carrying large amounts of moisture evaporated from tropical oceans converge in the **intertropical convergence zone (ITCZ)**. The peaks of precipitation coincident with the midlatitude zone of rising air are produced mainly by extratropical cyclonic storms that tend to develop along the polar front.

Because precipitation rates are influenced by topography, air temperatures, frontal activity, and

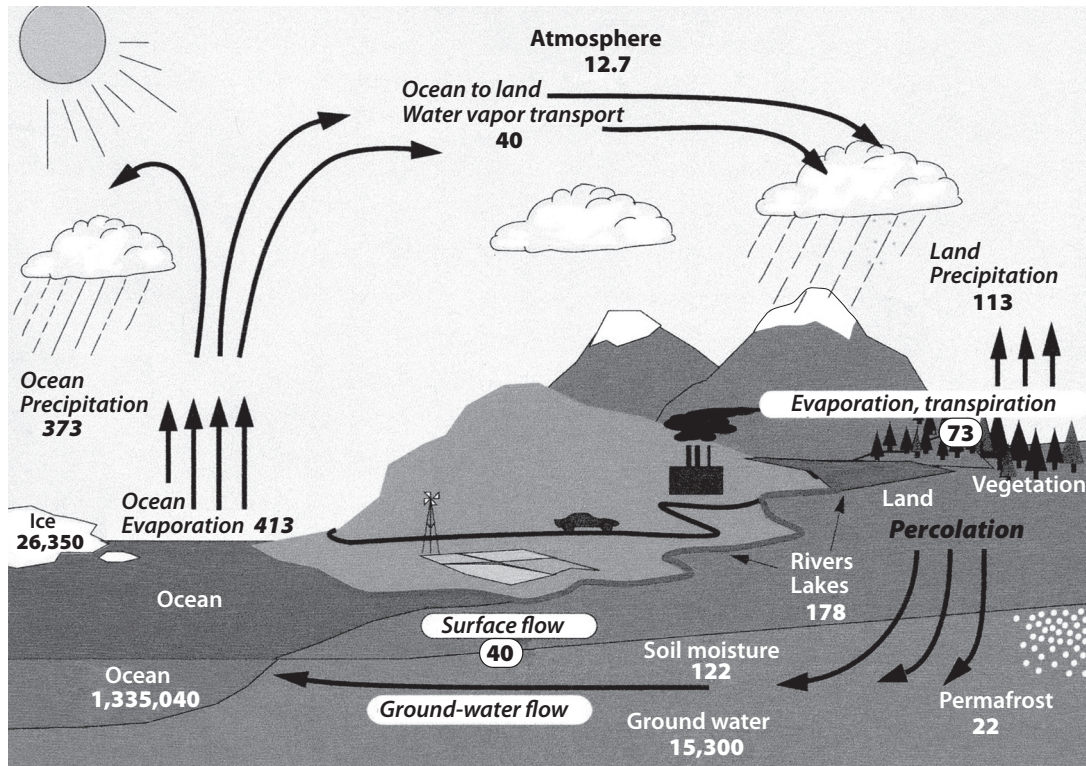


Figure 2.20 The global hydrologic cycle. The volume (10^3 km^3) of water found in each main type of global reservoir is shown; the rates ($10^3 \text{ km}/\text{yr}$) of flow through the system for annual fluxes are italicized [Trenberth et al. (2007)]. Estimates of the global water budget and its annual cycle using observational and model data. *Journal of Hydrometeorology* 8:758–769, reproduced with permission of American Meteorological Society].

Table 2.5 Major Global Water Stocks.

Global Stock	Area (km^2)	Volume (km^3)	Percent of Total Water ⁵
Oceans	361,300,000 ¹	1,335,040,000 ²	96.95
Ground water	134,800,000 ¹	15,300,000 ²	1.11
Soil moisture	82,000,000 ¹	122,000 ²	0.0089
Glaciers and permanent snow	16,227,500 ¹	26,350,000 ²	1.91
Antarctica	13,980,000 ¹	21,600,000 ¹	
Greenland	1,802,400 ¹	2,340,000 ¹	
Arctic islands	226,100 ¹	83,500 ¹	
Mountains	224,000 ¹	40,600 ¹	
Permafrost	14,600,000 ³	23,100 ⁴	0.0017
Rivers and lakes	150,858,700 ¹	178,000 ²	0.013
Fresh lakes	1,236,400 ¹	91,000 ¹	
Salt lakes	822,300 ¹	85,400 ¹	
Rivers	148,800,000 ¹	2,120 ¹	
Marshes	2,682,600 ¹	11,470 ¹	
Biologic water	510,000,000 ¹	1,120 ¹	0.00008
Atmosphere	510,000,000 ¹	12,700 ²	0.00092
Total	510,000,000 ¹	1,377,387,000 ⁵	

¹ Data from Shiklomanov and Sokolov (1983).

² Updated values from Trenberth et al. (2007).

³ Center of range (12,210,000 to 16,980,000 km^2) given by Zhang et al. (2000).

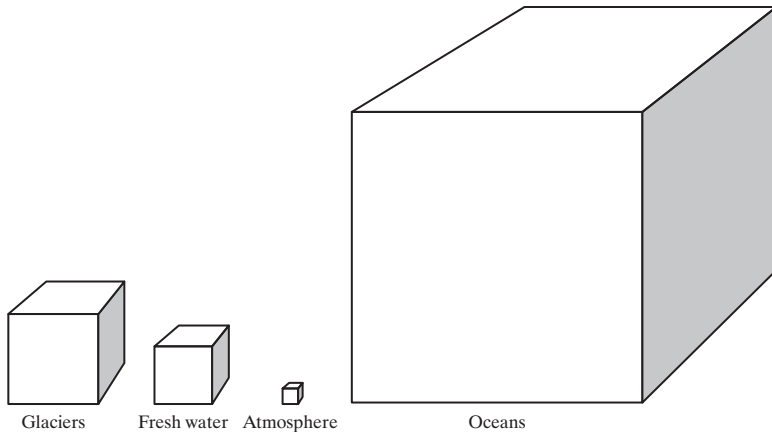
⁴ Center of range (10,800 to 35,460 km^3) given by Zhang et al. (2000).

⁵ Based on Trenberth et al. (2007) estimates.

Table 2.6 Stocks and Annual Fluxes for Major Compartments of the Global Hydrologic Cycle.

Stock	Volume (10⁶ km³)	Sources	Input Flux (10³ km³/yr)	Sinks	Output Flux (10³ km³/yr)
Oceans	1,335	Precipitation	373	Evaporation	413
		Runoff	40		
Atmosphere	0.0127	Land evapotranspiration	73	Land precipitation	113
		Ocean evaporation	413	Ocean precipitation	373
Land	42.1	Land precipitation	113	Land evapotranspiration	73
Total	1,377			Runoff	40

Source: Data from Trenberth et al. (2002).

**Figure 2.21** Relative volumes of water in oceans, glaciers, fresh water, and atmosphere.

Box 2.1 Your Role in the Global Hydrologic Cycle

Western culture tends to view human beings as separate from nature. While we may recognize that we are connected in an ecological sense to the rest of the world—that we depend upon it to supply the food, clothing, and shelter that are essential for our existence—we think of the environment as being “out there.” In fact, each of us is part of the great biogeochemical cycles that have moved matter and energy through the global ecosystem for billions of years. None of the atoms that currently constitute your body was part of you at birth; each atom has a finite residence time within you before it leaves to continue its ceaseless cycling.

Table 2B1.1 shows the amounts of water in typical humans and the rates of intake of water from various sources. For adults, the average rate of output (via breathing, perspiration, urine, and feces) is essentially equal to the average rate of input. As we have done for other reservoirs, we can calculate the average residence time of water in the typical human male and female using equation (1.25). If you perform this computation

with the data in the table, you will see that the residence time of water in both sexes is about 14 days. Thus, on the average, the water in your body is completely replaced every two weeks. The hydrologic cycle is flowing through you, as well as through the rivers, aquifers, glaciers, oceans, and atmosphere of the world.

Table 2B1.1 Human Water Content and Uptake.

	Man	Woman
Percentage of weight as water	60	50
Weight of water (kg)	42	25
Average intake (kg/d)	3.00	2.10
in milk	0.30	0.20
in water	0.15	0.10
in other fluids	1.50	1.10
free water in food	0.70	0.45
from oxidation of food	0.35	0.25

Source: Harte (1985).

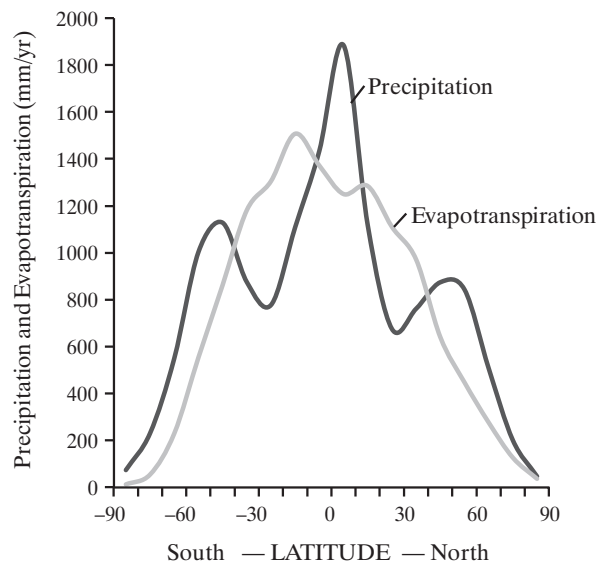


Figure 2.22 Latitudinal distribution of average rates of precipitation and evapotranspiration [data from Peixoto and Oort (1992)].

wind directions in relation to moisture sources, global precipitation patterns (figure 2.23) show significant deviations from the general latitudinal distribution depicted in figure 2.22. The major causes of these deviations are mountain ranges, such as the Rocky–Andean Mountain chain, the Alps, and the

Himalayas. These ranges induce high rates of precipitation in their immediate vicinity and typically produce “rain-shadow” zones of reduced precipitation over large areas leeward of the prevailing winds. Note, for example, the dry zone in the Great Plains of North America extending from latitude 20° to above latitude 60°, and the effects of the Himalayas in blocking moisture-laden winds from reaching the interior of Asia.

Recent research has documented the importance of **atmospheric rivers** (ARs) to the distribution of precipitation in the midlatitudes (Ralph and Dettinger 2011). ARs are narrow corridors of concentrated water-vapor transport in the lower atmosphere extending across long stretches of the ocean (figure 2.24). They are quantitatively defined as having (1) vertically integrated water-vapor concentrations equivalent to 2 or more cm of liquid water; (2) wind speeds of greater than 12.5 m/s in the lowest 2 km; and (3) a long (several thousand km) and narrow (less than 400–500 km wide) shape. Where ARs encounter mountainous coasts, such as the Pacific Coast of North America, they can cause extreme precipitation and flooding, and make important contributions to the annual rain and snowfall. Understanding the behavior of ARs may shed light on how changing climate patterns influence extreme precipitation and floods.

The seasonal distribution of precipitation, including its occurrence in the form of rain or snow, has important hydrologic and climatic implications

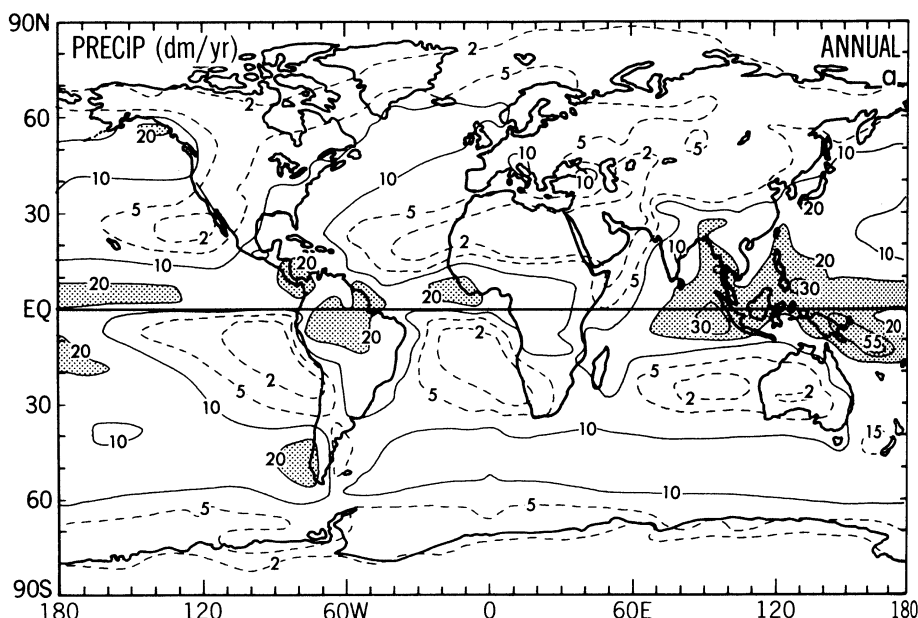


Figure 2.23 Global average annual precipitation rate (dm/yr) [Peixoto and Oort (1992). *Physics of Climate*. New York: American Institute of Physics. With kind permission of Springer Science+Business Media].

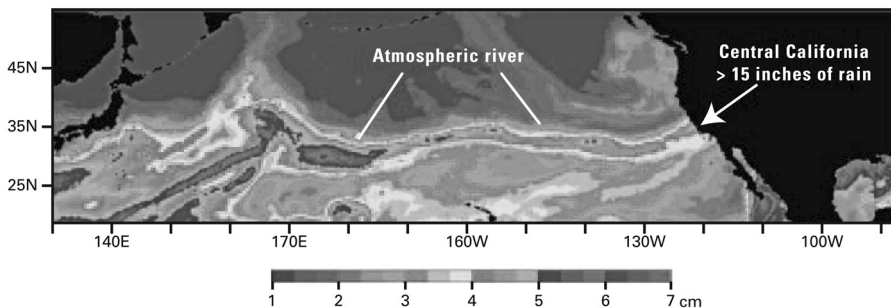


Figure 2.24 A Special Sensor Microwave Imager satellite image of an atmospheric river impacting California on October 13–14, 2009. The scale (in cm) shows the amount of water vapor present throughout the air column if all the water vapor were condensed into one layer of liquid (*precipitable water content*) [Ralph and Dettinger (2011). Storms, floods, and the science of atmospheric rivers. *Eos* 92(32):265–266, with permission of the American Geophysical Union].

and, as discussed later in this chapter, significant impacts on soil formation and vegetation. Figure 2.25 shows the global distribution of seven general precipitation regimes. The reversal of circulation associated with the development of winter high pressure and summer low pressure over the huge land mass of Asia interacts with the topography and the migration of the ITCZ to produce a particularly strong seasonality of precipitation in much of Asia and Africa; this is the **monsoon**.

Figure 2.26 on p. 73 shows the global distribution and duration of seasonal snow cover. Much of the Northern Hemisphere land surface above 40° latitude has a seasonal snow cover of significant duration; in the Southern Hemisphere snow occurs only in mountainous areas and Antarctica. The principal hydrologic effect of snow is to shape the seasonal distribution of runoff by delaying the release of precipitated water. In many places—notably much of western North America—runoff from snowmelt provides most of the water used for domestic supply and irrigation.

In addition to direct impacts on water resources, the extent, duration, and depth of seasonal snow cover play a major role in providing feedbacks between climate and hydrology. Snow helps to maintain colder temperatures by reflecting much of the incoming solar energy (see table 2.4) and, in melting, by absorbing energy that would otherwise contribute to warming the near-surface environment. The surface cooling induced by snow has profound effects on surface and air temperatures, global circu-

lation patterns and storm tracks, and precipitation (Berry 1981; Dey and Kumar 1983; Dickson 1984; Walsh 1984; Barnett et al. 1988; Leathers and Robinson 1993; Groisman et al. 1994). Snow also acts as an insulating blanket that helps to retain heat in the soil, which is important hydrologically as well as biologically: If the soil is prevented from freezing, its ability to accept infiltrating meltwater is generally enhanced (Dingman 1975). The insulating effect of snow is also important in maintaining perennially frozen ground (permafrost), which is a major hydrologic feature in much of the Northern Hemisphere (section 2.3.1). The extent, duration, and depth of seasonal snow cover are very sensitive to climate change (section 2.2.8), and due to the feedback effects noted above, any changes in its extent and duration will induce further changes in global climate and hydrology.

2.2.3 Distribution of Evapotranspiration

Evapotranspiration includes all processes involving the phase change from liquid or solid to water vapor. Globally, its principal components are evaporation from the oceans and transpiration by land vegetation. The overall pattern of latitudinally averaged evapotranspiration (figure 2.22) is similar to that of the radiation balance and temperature, reflecting the importance of the availability of energy to supply the latent heat that accompanies the phase change. The maximum occurs in the Southern Hemisphere tropics, reflecting the large area of the Pacific Ocean in these latitudes.

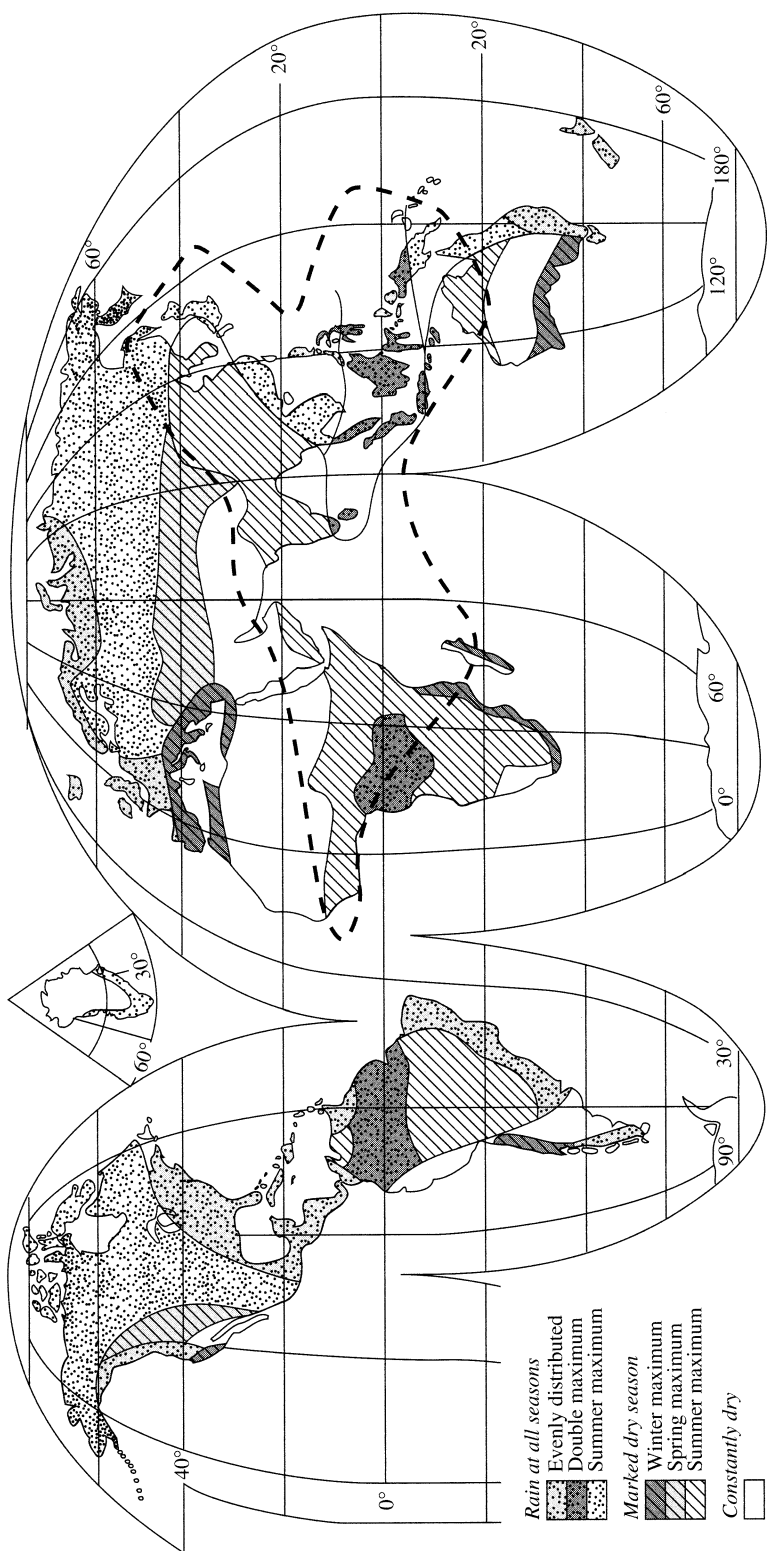


Figure 2.25 Generalized map of seasonal precipitation regimes. Heavy dashed line encloses the monsoon region of Asia and Africa [J. E. Oliver and J. J. Hidore (1984). *Climatology: An Introduction*, p. 100. © 1990. Reprinted by permission of Pearson Education, Inc., Upper Saddle River, NJ].

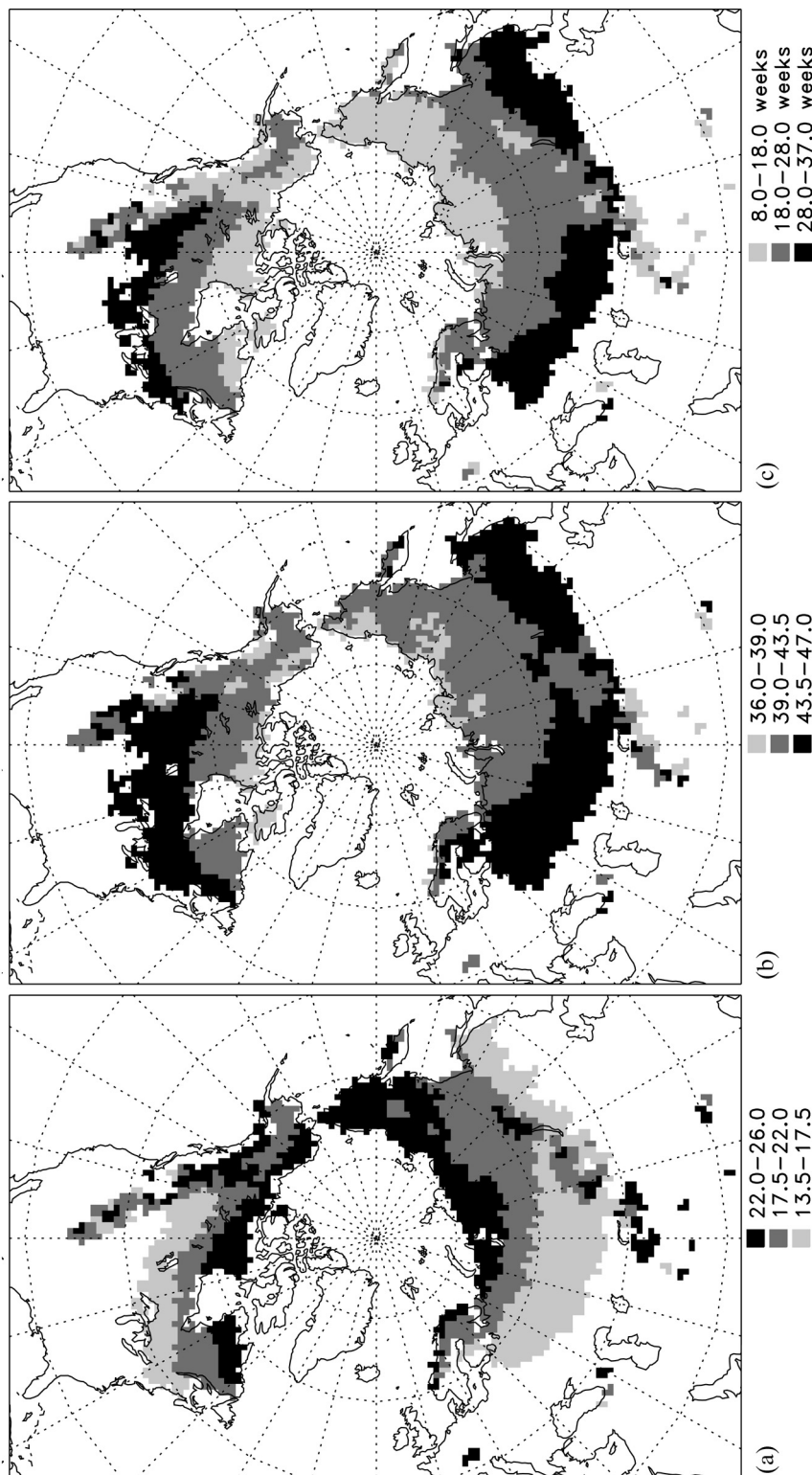


Figure 2.26 Global distribution of snow cover (scale numbers are weeks of the year). (a) Average week of year in which last seasonal snow cover occurs. (b) Average week of year in which first seasonal snow cover occurs. (c) Average annual duration of snow cover. [Reproduced from Dye (2002). Variability and trends in the annual snow-cover cycle in Northern Hemisphere land areas, 1972–2000. *Hydrological Processes* 16:3065–3077, with permission of Wiley].

Figure 2.27 shows the global distribution of oceanic evaporation and continental evapotranspiration. As expected, there is a general correlation between mean annual temperature and mean annual evapotranspiration (compare figure 2.14). In the oceans, the basic latitudinal patterns are distorted largely by the effects of surface currents (e.g., note the effect of the warm Gulf Stream off northern Europe and the cold currents flowing equatorward off western South America and North America). The highest continental values are in the tropical rain forests of South America, Africa, and southeast Asia, while the lowest are in the Sahara Desert, Antarctica, arctic North America, and central Asia.

On land surfaces, the climatic evaporative demand, which is chiefly a function of solar radiation, humidity, and wind, is called the **potential evapotranspiration**; more specific definitions and ways of calculating this quantity are discussed in chapter 6. Thus, actual evapotranspiration on land may be either **energy-limited**, where potential evapotranspiration is less than the precipitation (humid regions); or **water-limited**, where potential evapotranspiration exceeds precipitation (arid regions). As shown in figure 2.28, well over half the global land area is water-limited.

2.2.4 Distribution of Runoff

Figure 2.29 shows the global distribution of annual runoff, i.e., the difference between precipitation and evapotranspiration for the continents. This map shows a close correspondence with annual precipitation (figure 2.23) and with areas of energy-limited and water-limited evapotranspiration (figure 2.28). The highest average runoff rates, near 3,000 mm/yr, occur on the east coast of the Bay of Bengal, while the Amazon Basin of northern South America is the largest region with runoff exceeding 1,000 mm/yr.

Figure 2.30 on p. 76 shows seasonal runoff regimes, which are determined by: (1) the season in which the most runoff occurs (spring, summer, winter, fall) and (2) the degree to which runoff is concentrated in that season (more than 80%, 50 to 80%, and less than 50%). In most areas that have a seasonal snow cover or are glacierized, the maximum runoff occurs in the melt season: summer in arctic, subarctic, and alpine regions, and spring at lower latitudes. A summer maximum also occurs in regions with monsoonal climates, such as India and southeast Asia, and other areas with summer precipitation maximums (figure 2.25). Fall and winter runoff maxima are also directly related to concurrent rain-

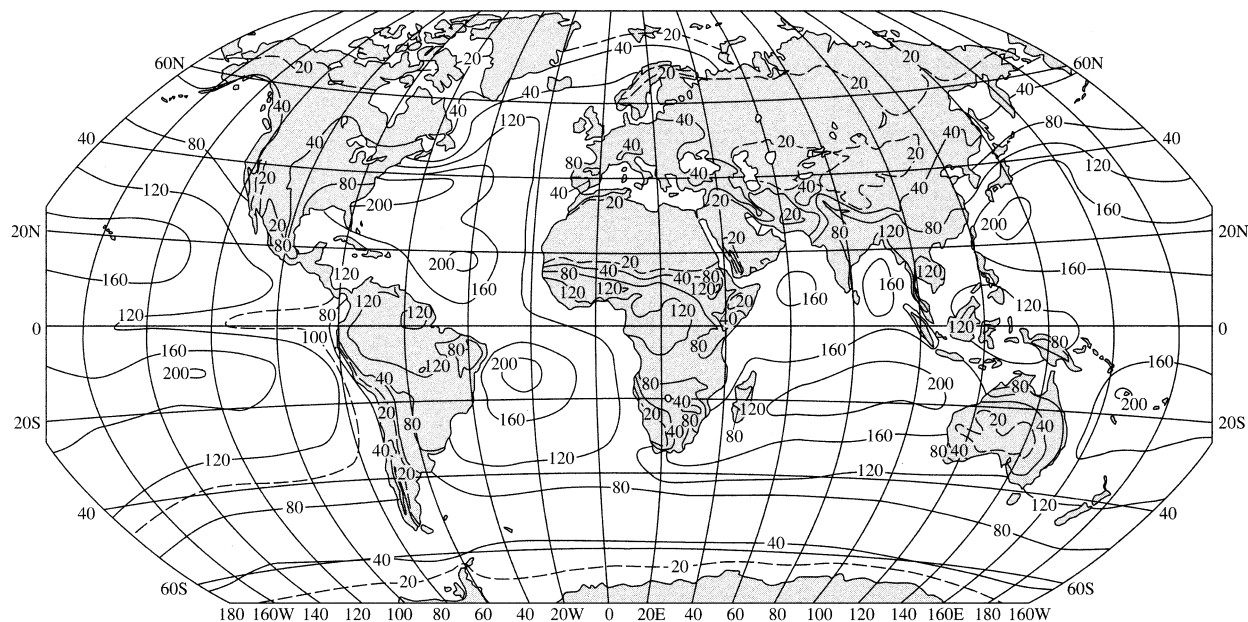


Figure 2.27 Global distribution of average oceanic evaporation and continental evapotranspiration (cm/yr) [Peixoto and Oort (1992). *Physics of Climate*. New York: American Institute of Physics. With kind permission of Springer Science+Business Media].

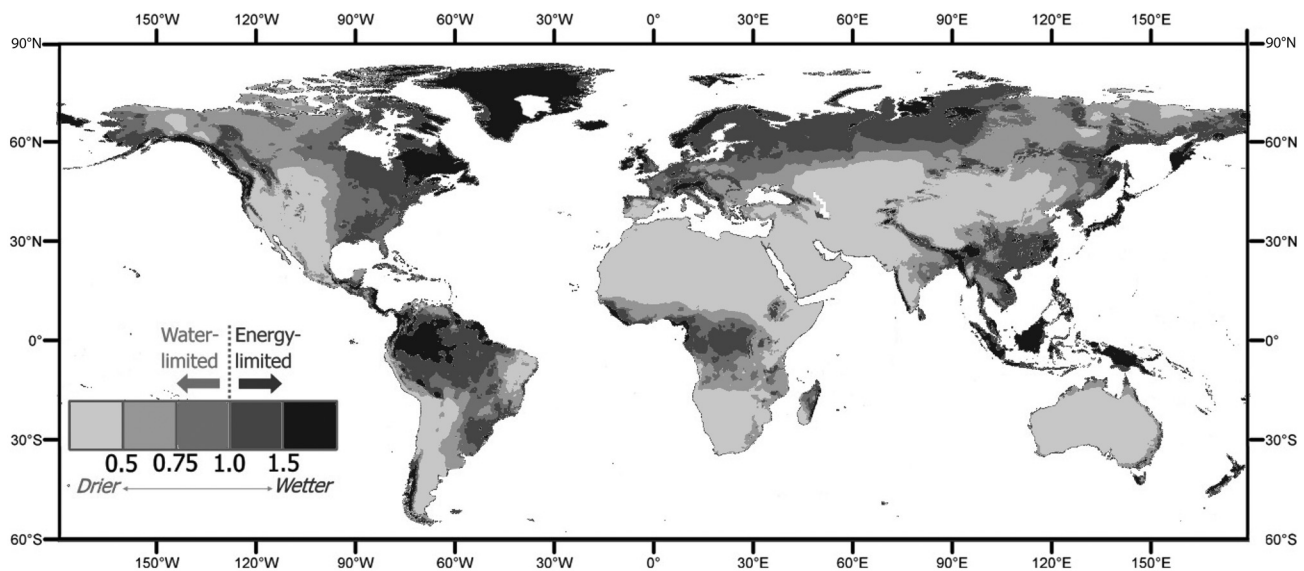


Figure 2.28 Global distribution of the ratio of average annual precipitation to evapotranspiration, P/ET . In energy-limited areas, $P/ET < 1$; in water-limited areas, $P/ET > 1$ [McVicar et al. (2012). Global review and synthesis of trends in observed terrestrial near-surface wind speeds: Implications for evaporation. *Journal of Hydrology* 416–417:182–205, with permission of Elsevier].

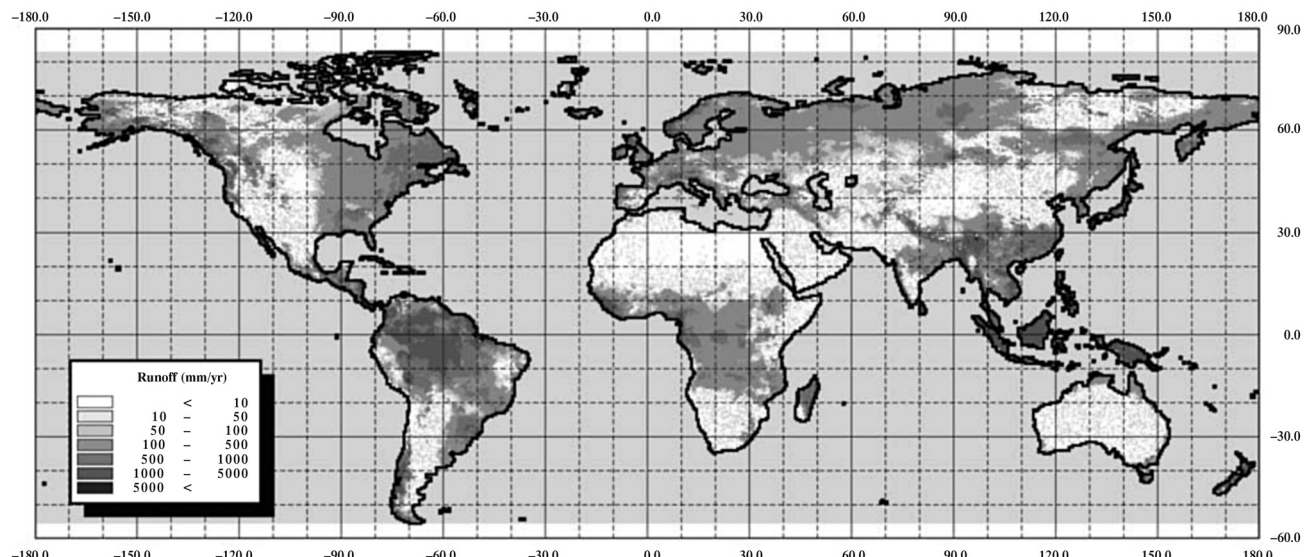


Figure 2.29 Global distribution of average annual runoff [Fekete et al. (2002)]. High-resolution fields of global runoff combining observed river discharge and simulated water balances. *Global Biogeochemical Cycles* 16(3), with permission of the American Geophysical Union].

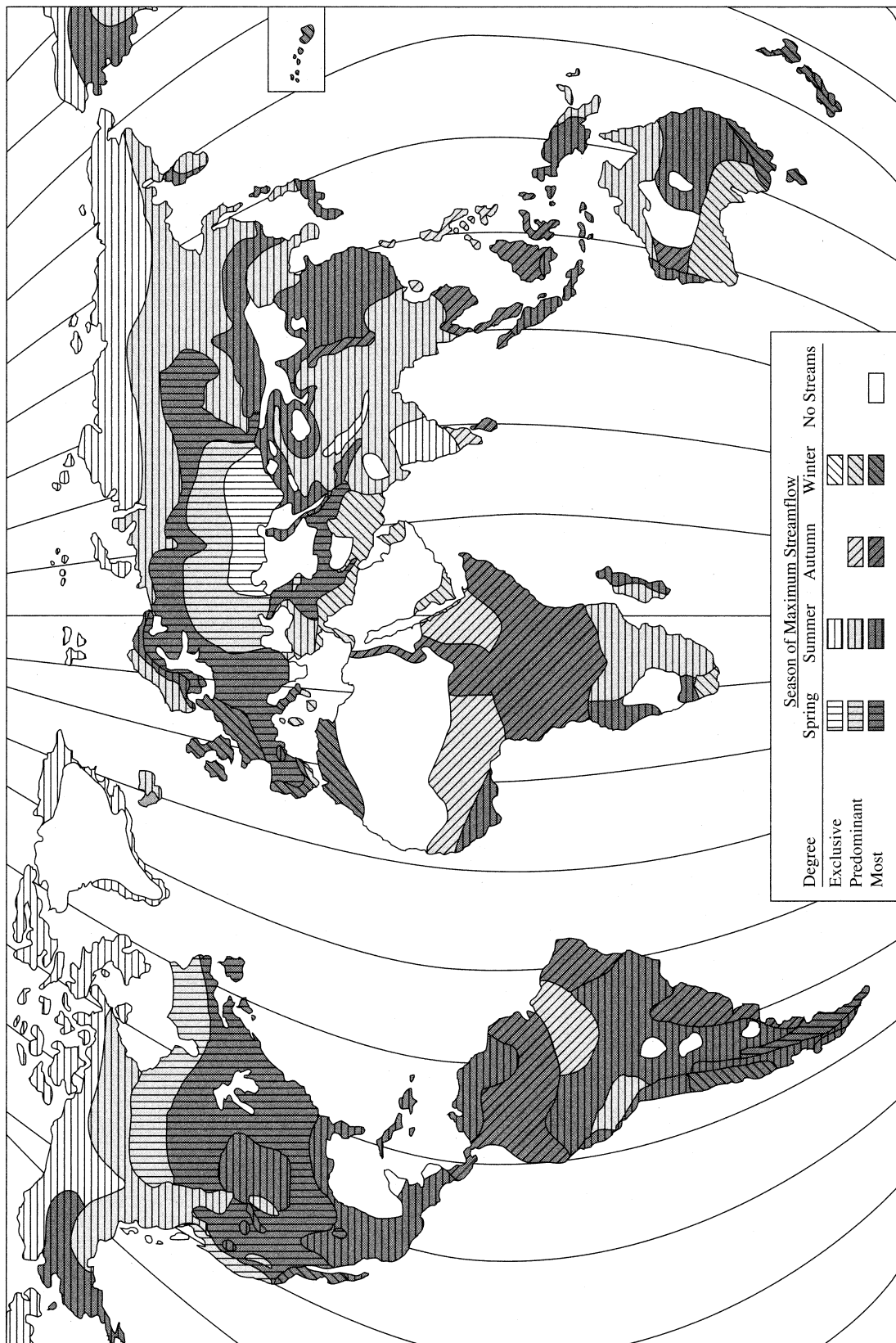


Figure 2.30 Seasonal runoff regimes [adapted from L'vovich (1974). *World Water Resources and Their Future*. Trans. by R. L. Nace, with permission of the American Geophysical Union].

fall maxima. More recent discussions of the seasonality of global runoff are given by Kuhl and Miller (1992), Dettinger and Diaz (2000), and Luk'yanovich (2011).

Note that the seasonal pattern of runoff is commonly quite different from that of precipitation, due to the seasonality of evapotranspiration and the storage of precipitation as snow. In northeastern United States, for example, precipitation is equally distributed through the year, but 25% of the annual runoff typically occurs during one spring month and only 10% in the three months of summer. The effect of snowmelt in concentrating the period of runoff becomes more pronounced the longer the annual snow cover persists; in northern Alaska one-half of the annual runoff occurs in a three- to 10-day period (Dingman et al. 1980).

2.2.5 Continental Water Balances

Recall from section 1.8.1 that the average runoff rate represents the maximum available water resources of a region. As shown in table 2.7, this quantity varies greatly among the continents (and, of course, within each continent). South America is by far the wettest continent in terms of both precipitation and runoff per unit area, Antarctica is the driest in terms of precipitation, and Australia has by far the lowest runoff per unit area.

2.2.6 Rivers, Lakes, and Reservoirs

Rivers are the major routes by which “surplus” water on the continents returns to the oceans as runoff (table 2.6); the rate of direct runoff to the oceans as ground water is estimated to be about 5% of total river flow (Gleick 1993, p. 136).

The amount of water present in rivers at any time is a very small fraction of global fresh water (ta-

ble 2.5), and the natural residence time of water in rivers is about 15 days. Table 2.8 shows the average discharges and drainage areas of the 16 largest rivers in the world (ranked by discharge); figure 2.31 shows their locations. Together, these rivers drain 22.9% of the world’s land area and contribute 32.8% of the total runoff to the oceans; the Amazon River alone delivers 16% of the total runoff. (Note that only rivers draining directly to the ocean are included in table 2.8; there are tributaries of the Amazon that have larger discharges than many of the rivers listed.)

Most natural and artificial lakes are through-flowing, receiving surface and ground-water runoff and discharging to rivers; some in arid areas are drainage termini and lose water only by evaporation. The main hydrologic functions of natural and man-made lakes are: (1) to provide storage that reduces the time variability of flow in the rivers that drain them (figure 1.18); (2) to increase the travel time of runoff, inducing loss of sediment load and other water-quality changes (Vörösmarty et al. 1997); and (3) to increase evaporation by providing large permanently wet surfaces. Fresh-water lakes hold about two years’ worth of global runoff, cover about 2.4% of the earth’s unglacierized land surface (Lehner and Döll 2004), and contribute about 3% of the total land evapotranspiration (L’vovich 1974). Table 2.9 on p. 79 lists the world’s 25 largest natural lakes (ranked by average volume), and figure 2.31 shows their locations. For more information on lakes around the world, the International Lake Environment Committee Foundation provides a World Lake Database (<http://www.ilec.or.jp/en/>).

Vörösmarty et al. (1997) have analyzed the effects of dams on global fresh water. The construction of reservoirs (figure 2.32 on p. 80) has increased the volume of fresh surface-water storage by about sev-

Table 2.7 Continental Water Balances.

Continent	Area (10^6 km^2)	Precipitation		Evapotranspiration		Runoff	
		(km^3/yr)	(mm/yr)	(km^3/yr)	(mm/yr)	(km^3/yr)	(mm/yr)
Europe	10.1	6,660	659	3,878	384	2,772	275
Asia	44.4	29,970	675	16,739	377	13,091	298
Africa	30.0	20,250	675	15,750	525	4,517	150
Australasia	8.2	5,404	659	4,141	505	1,320	154
North America	22.4	14,963	668	9,072	405	5,892	263
South America	17.9	27,298	1,525	15,573	870	11,715	655

Source: Data from Fekete et al. (2002) and B. Fekete (pers. comm. 2013).

Table 2.8 The World's 16 Largest Rivers in Terms of Average Discharge to Ocean.

River	Drainage Area		Discharge			Percent of Global Runoff
	10^3 km^2	Percent of Land Area	m^3/s	km^3/yr	mm/yr	
1. Amazon	5,854	3.93	210,000	6,642	1,135	16.61
2. Congo	3,699	2.48	41,400	1,308	354	3.27
3. Orinoco	1,039	0.70	35,800	1,129	1,087	2.82
4. Changjiang	1,794	1.20	29,900	944	526	2.36
5. Brahmaputra	583	0.39	19,900	628	1,077	1.57
6. Mississippi	3,203	2.15	19,300	610	190	1.53
7. Yenisey	2,582	1.73	19,000	599	232	1.50
8. Paraná/La Plata	2,661	1.79	18,000	568	213	1.42
9. Lena	2,418	1.62	16,800	531	220	1.33
10. Mekong	774	0.52	16,600	525	678	1.31
11. Tocantins	769	0.52	16,200	511	664	1.28
12. Ob	2,570	1.73	13,100	412	160	1.03
13. Ganges	956	0.64	12,800	404	423	1.01
14. Irrawaddy	406	0.27	12,500	393	968	0.98
15. St. Lawrence	1,267	0.85	11,500	363	287	0.91
16. Amur	2,903	1.95	11,200	354	122	0.89

Source: Dai and Trenberth (2002).

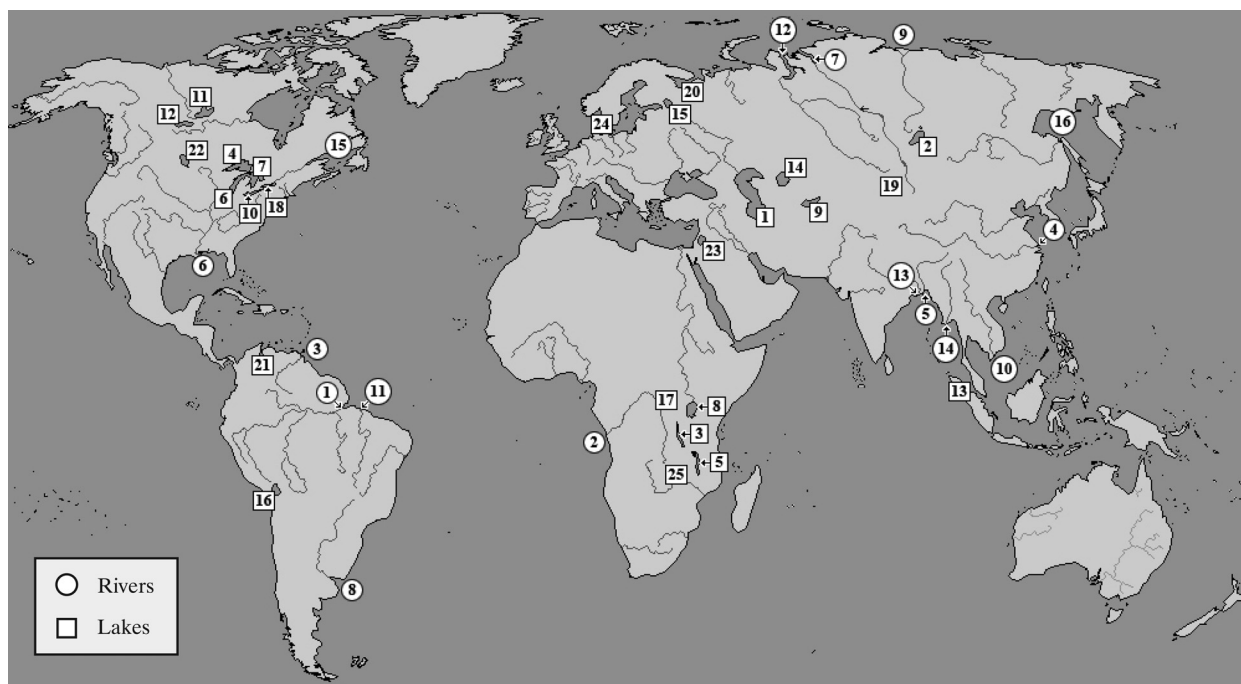


Figure 2.31 Locations of the world's 16 largest rivers (refer to table 2.8). Locations of the world's 25 largest lakes (refer to table 2.9).

Table 2.9 The World's 25 Largest Lakes in Terms of Average Volume.

Rank	Lake	Average Volume (km ³)	Average Surface Area (km ²)	Maximum Depth (m)
1	Caspian Sea ^a	78,200	375,000	1,000
2	Lake Baikal	23,000	31,500	1,700
3	Lake Tanganyika	18,900	33,000	1,450
4	Lake Superior	12,000	82,500	360
5	Lake Nyasa	7,000	26,000	706
6	Lake Michigan	4,750	57,500	275
7	Lake Huron	3,550	59,700	227
8	Lake Victoria	2,700	66,000	1,450
9	Lake Issyk-kul	1,730	6,200	702
10	Lake Ontario	1,700	19,000	250
11	Great Bear Lake	1,600	31,000	300
12	Great Slave Lake	1,500	28,000	400
13	Lake Toba	1,260	1,100	450
14	Aral Sea ^{a,b}	1,020	64,100	68
15	Lake Ladoga	908	18,000	230
16	Lake Titicaca	760	8,100	270
17	Lake Kivu	569	2,400	630
18	Lake Erie	520	25,700	64
19	Lake Chovsgol Nuur	480	2,620	260
20	Lake Onega	295	9,650	127
21	Lake Maracaibo ^a	280	13,650	145
22	Lake Winnipeg	250	24,500	25
23	Dead Sea ^a	188	970	395
24	Lake Vanem	165	5,600	95
25	Lake Kariba	160	5,400	78

^a Saline water.^b Aral Sea volume, area, and depth have dropped markedly from these numbers due to extraction of most of the water from major inflowing streams for use in irrigation.

Source: Data from Gleick (1993).

enfold, and some 42% of global runoff is now intercepted by man-made reservoirs. Globally, these reservoirs increase the average residence time of water in rivers by one or two months. This impoundment-induced aging leads to significant changes in several biophysical processes including water balance, flow regime, re-oxygenation of surface waters, and trapping of particulate sediments.

2.2.7 Material Transport by Rivers

In addition to their role in the global water cycle, rivers are the means by which the products of continental weathering are carried to the oceans. Thus they are a crucial link in the **tectonic cycle** in which rock material is formed deep in the earth's crust, raised to the surface by tectonic processes, eroded and

transported to the oceans, and ultimately reincorporated into the lower crust and upper mantle (Howell and Murray 1986). The natural materials transported by rivers are also parts of the biogeochemical cycles involving carbon, oxygen, nitrogen, hydrogen, phosphorus, silicon, sulfur, and many other minerals that are essential for the maintenance of lake and ocean ecosystems (Deevey 1970). Rivers also transport pollutants and, in places such as the Gulf of Mexico, have delivered excessive amounts of nutrients resulting in serious degradation of marine ecosystems.

Rivers transport material as individual ions or molecules in solution (**dissolved load**), or as solid particles (**particulate load**). The **concentration** of a dissolved or particulate material constituent x is its mass (or weight) per unit volume of water ($[M\ L^{-3}]$

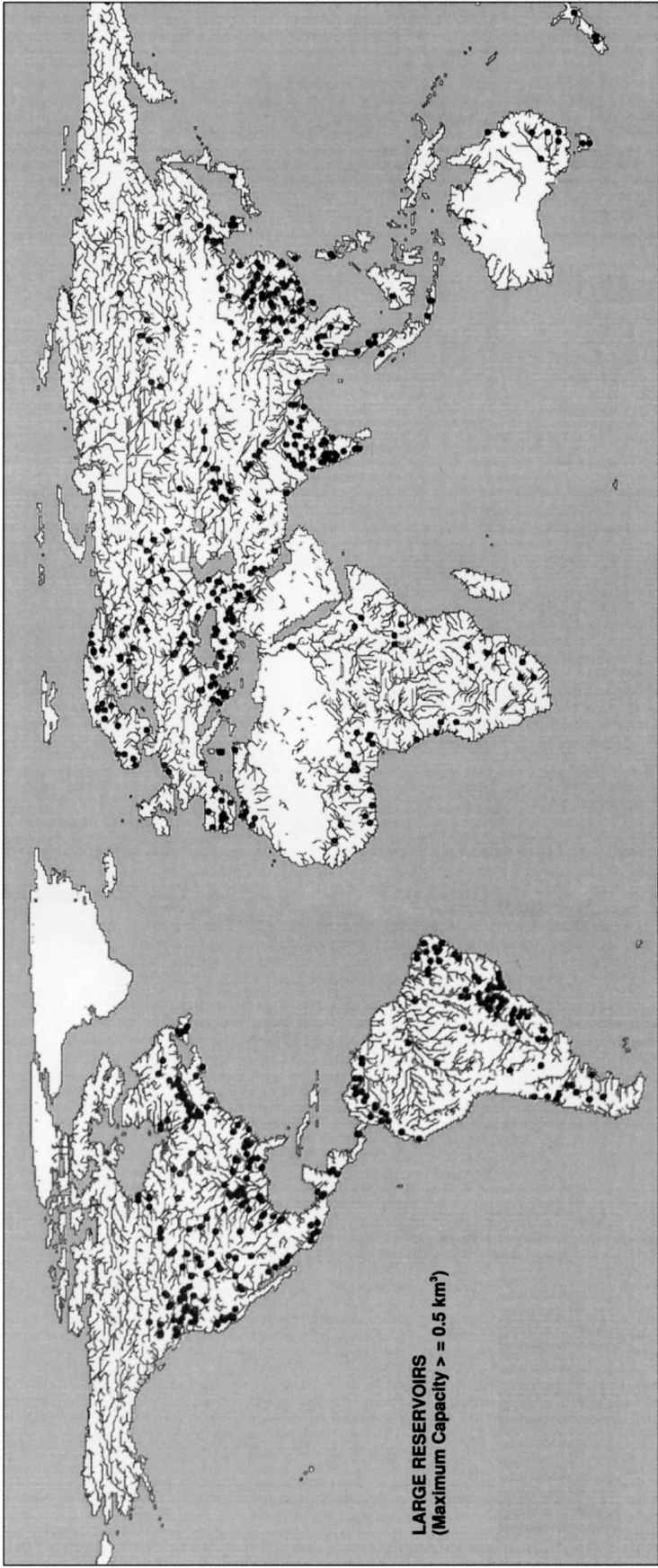


Figure 2.32 Locations of human-made reservoirs with volumes $> 0.5 \text{ km}^3$ [Vörösmarty et al. (1997). The storage and aging of continental runoff in large reservoir systems of the world. *Ambio* 26(4):210–219. © Royal Swedish Academy of Sciences].

or $[F L^{-3}]$), C_x ; the constituent **load**, L_x , is the rate of discharge of the material constituent ($[M T^{-1}]$ or $[F T^{-1}]$). The relation between the two quantities is

$$L_x = C_x \cdot Q, \quad (2.8)$$

where Q is the water discharge $[L^3 T^{-1}]$. The load per unit drainage area ($[M T^{-1} L^{-2}]$ or $[F T^{-1} L^{-2}]$) is called **sediment yield**.

In this section, we review current estimates of the global rates of material transport to the oceans and some of the global relations between material transport and climate, geology, topography, and vegetation. In viewing these data, it must be recognized that they are highly uncertain, especially for particulates, because (1) the sampling network is very sparse in many regions (and nonexistent in some); (2) even at a given location and time it is difficult to collect a representative sample; (3) sediment concentrations are strong functions of streamflow and hence are highly variable in time; and (4) variables that affect sediment load (such as land-use conditions and reservoir construction) commonly change over time (Meybeck et al. 2003; Syvitski 2003; Walling and Fang 2003).

2.2.7.1 Dissolved Material

Table 2.10 lists the estimated mean composition of the river waters of the world. However, composition varies widely in different regions, largely due to variations in rock type and climate (Berner and Berner 1987). Gibbs (1970) showed that rivers draining areas with high annual precipitation and runoff tend to have low total dissolved concentrations and compositions similar to that of precipitation (i.e., they are relatively rich in sodium $[Na]$ and chlorine $[Cl]$) and largely independent of rock type. In climates with moderate precipitation and runoff, concentrations are at moderate levels and composition is dominated by rock type and tends to be high in calcium (Ca) and bicarbonate (HCO_3). As one moves toward drier climates, water chemistry becomes increasingly controlled by fractional crystallization due to evaporation: Concentra-

tions increase, and the composition shifts from $Ca-HCO_3$ toward $Na-Cl$. The ultimate end-member in this progression is sea water (figure 2.33).

Walling and Webb (1987) examined data for some 500 rivers worldwide, and found average dissolved-sediment yields ranging from less than $1 T/km^2 \cdot yr$ to $750 T/km^2 \cdot yr$; the average was about $40 T/km^2 \cdot yr$. Figure 2.34 shows the global variation of total dissolved load for major river basins (data are sparse for other areas), and table 2.11 on p. 83 shows loads for the continents and selected rivers. The high loads in southern Asia reflect the high discharges in those regions (see figure 2.29), while those in central

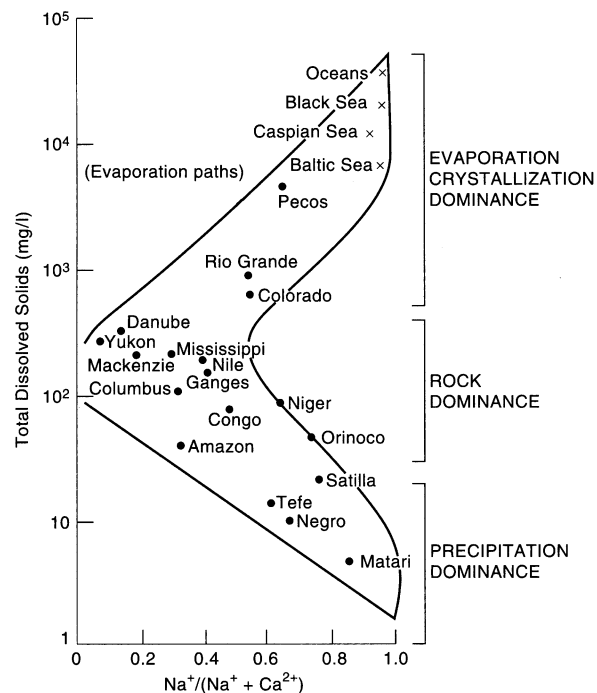


Figure 2.33 Variation of the concentration ratio $Na/(Na + Ca)$ as a function of total dissolved solids showing major processes controlling the chemistry of world rivers [adapted from Berner and Berner (1987)].

Table 2.10 Average Dissolved-Solids Composition of Global River Runoff.

	Ca	Mg	Na	K	Cl	SO_4	HCO_3	SiO_2	Total Dissolved Solids
Actual (mg/L)	14.7	3.7	7.2	1.4	8.3	11.5	53.0	10.4	110.1
Natural (mg/L)	13.4	3.4	5.2	1.3	5.8	6.6	52.0	10.4	99.6
% due to pollution	9	8	28	7	30	43	2	0	10.5

Source: Berner and Berner (1987).

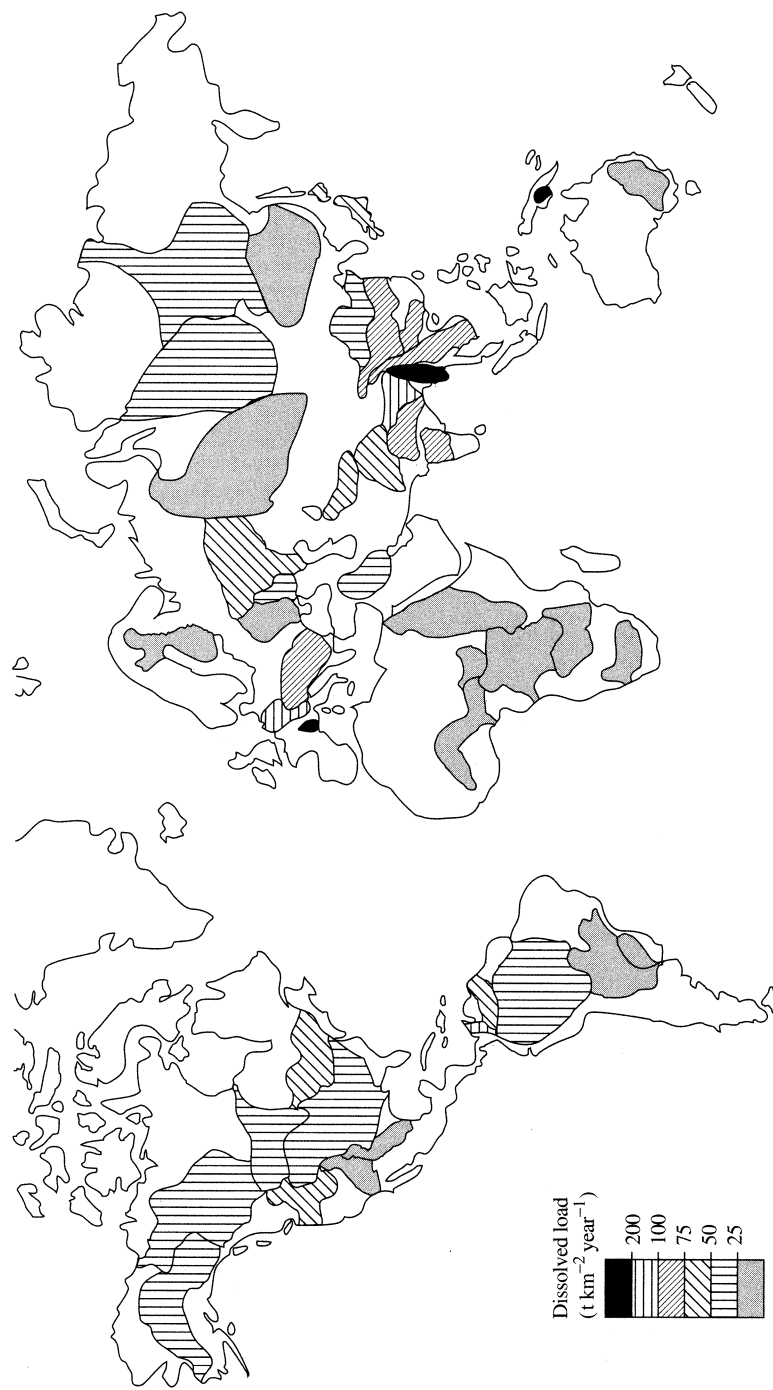


Figure 2.34 Dissolved sediment yields in major river basins of the world [Walling and Webb (1987). Material transport by the world's rivers: Evolving perspectives. In IAHS Publ. No. 164, courtesy of International Association of Hydrological Sciences].

Table 2.11 Sediment Loads, Yields, and Erosion Rates by Continent and Major Rivers.

River	Area (10 ³ km ²)	Discharge (km ³ /yr)	Particulate Load (10 ⁶ T/yr)	Dissolved Load (10 ³ T/day)	Particulate Yield (T/km ² /yr)	Dissolved Yield (T/yr km ²)	Total Yield (T/km ² yr)	Physical Erosion Rate (mm/10 ³ yr)	Total Erosion Rate (mm/10 ³ yr)	% Particulate
Africa										
Congo	18,288	4,517.0	973	551	53	7	60	21.3	24.1	88
Niger	3,699	1,308.0	48	101	13	10	23	5.2	9.2	57
Nile	2,240	193.0	58	38	26	6	32	10.4	12.8	81
Orange	3,830	1.2	245	33	64	3	67	25.6	26.8	96
Zambezi	940	0.4	117	4	124	2	126	49.6	50.4	98
Asia										
Ganges ^a	32,518	13,091.0	7,930	4,360	244	36	280	97.5	111.9	87
Huang Ho	1,539	1,032.0	985	414	640	93	733	256.0	293.2	87
Inclis	890	628.0	1,191	60	1,338	25	1,363	535.2	545.2	98
Irrawaddy	1,143	104.0	313	216	274	69	343	109.6	137.2	80
Lena	406	393.0	252	249	620	212	832	248.0	332.8	75
Mekong	2,418	531.0	19	153	8	23	31	3.2	12.4	26
Ob	774	525.0	143	162	185	76	261	74.0	104.4	71
Yenesei	2,570	412.0	13	126	5	18	23	2.0	9.2	22
"Australia" ^b	2,582	599.0	13	164	5	23	28	2.0	11.2	18
Murray ^c	4,476	1,320.0	205	803	46	38	84	18.3	33.5	55
Danube	1,030	0.7	26	22	25	8	33	10.0	13.2	76
Europe										
Dnieper	788	2,772.0	841	1,164	88	42	130	35.2	52.0	68
Rhône	510	166.0	84	145	107	67	174	42.8	69.6	61
Volga	99	1.7	2	30	4	22	26	1.6	10.4	15
Columbia	1,460	1.9	57	153	580	566	1,146	232.0	458.4	51
Mackenzie	724	252.0	12	58	17	29	46	6.8	18.4	37
Mississippi	1,723	290.0	88	121	51	26	77	20.4	30.8	66
St. Lawrence	3,203	610.0	394	389	123	44	167	49.2	66.8	74
Yukon	1,267	363.0	5	2,110	4	608	612	1.6	244.8	1
S. America										
Amazon	17,732	11,715.0	3,138	2,077	136	31	167	54.5	66.9	81
Magdalena	5,854	6,642.0	1,188	795	203	50	253	81.2	101.2	80
Orinoco	252	231.0	195	55	773	77	850	309.2	340.0	91
Paraná	1,039	1,129.0	213	85	205	30	235	82.0	94.0	87
Antarctica										
Total	41,324.0	16,034.0	10						61.4	

^aIncludes Brahmaputra.^bIncludes New Zealand and large Pacific Islands.^cIncludes Darling River.

Source: Compiled from Knighton (1998), Ludwig and Probst (1998), Vörösmarty et al. (2000), Dai and Trenberth (2002), and Fekete et al. (2002).

Europe are due to widespread soluble rocks, especially limestones. The very high loads of the Irrawaddy River in Southeast Asia and on New Guinea are produced by a combination of readily weathered rocks, high rates of weathering due to high temperatures and precipitation, and high discharges. The presence of crystalline rocks with low solubilities in much of Africa and Australia gives rise to generally low dissolved loads on those continents.

2.2.7.2 Particulate Material

The natural rate of erosion of particulate material is determined by climate, rock type, topography, tectonic activity, and vegetation. Wilkinson (2005) calculated that the current rate of movement of earth materials by humans (principally through agriculture, mining, forest clearing, and construction) is now more than 10 times the natural geologic rate of 7.2×10^9 T/yr (about 0.02 mm/yr). Thus these activities have greatly increased global sediment transport in historic times and, along with the effects of lakes and reservoirs acting as sediment traps (also greatly increased by humans; see Vörösmarty et al. 1997 and Graf 1999), strongly affect the global patterns of particulate-sediment yield.

Milliman and Syvitski (1992) found that contemporary particulate-sediment yields range from 1.2 to 36,000 T/km² · yr and are positively related to drainage area, maximum watershed elevation, and runoff (figure 2.35). The highest yields are in areas with seasonal-rainfall climates (compare figure 2.25) coupled with active mountain building (India) or highly erodible soils (China); high yields are also associated with mountain belts in Alaska, the Andes, and the western Mediterranean region, and in Taiwan, the Philippines, and New Zealand, where human activity also plays a significant role in sediment production. The areas of lowest yields (outside of deserts) are in northern North America and Eurasia, equatorial Africa, and eastern Australia, where low relief is coupled with resistant rocks and/or extensive vegetative cover.

2.2.7.3 Total Material Transport to Oceans

Table 2.11 shows estimates of dissolved and particulate-sediment loads and yields for the continents; the total load of dissolved plus particulate material to the oceans is about 17.4×10^9 T/yr. When allowance is made for the amount of sediment being trapped in reservoirs, the total rate of sediment transport is between 19.0×10^9 and 20.0×10^9 T/yr, of which about 80% is particulate and 20% is dissolved (Walling and Webb 1987). Assuming an average rock density of

2,500 kg/m³, this total sediment yield represents the removal of 7.8×10^9 m³/yr, or about 0.06 mm/yr worldwide. This is about twice the average erosion rate through geologic history (Wilkinson 2005).

Oceania and the Pacific Islands have the highest particulate and total yields due to their steep terrain and high precipitation. Europe has the highest dissolved yield and is the only continent in which dissolved load exceeds particulate load. Africa has the lowest particulate, dissolved, and total sediment yields due to its generally low relief, widespread resistant rocks, and extensive desert areas.

2.2.8 Climate Change and the Hydrologic Cycle

2.2.8.1 Overview

The atmospheric concentration of CO₂ (abbreviated as [CO₂]) before the industrial age was about 250 ppmv. The present concentration is about 400 ppmv, and figure 2.6 shows that global average temperature has increased by about 1°C since 1880 (Hansen et al. 2010). [CO₂] is expected to reach close to 1,000 ppmv by the end of the century if stringent efforts to reduce emissions are not implemented, and current climate models predict that this will increase global average temperature by 5 to 10°C. Figure 2.36 on p. 86 shows the global temperature forecast to 2030, accounting for the effects of solar variability, ENSO, volcanic activity, and anthropogenic causes (chiefly GHG emissions) using a model that was highly successful in reproducing temperature changes from 1980 to 2010. This model indicates that the **climate feedback factor** for CO₂ is about 0.5 to 1°C/(W/m²). However, recent studies of [CO₂] through geological history indicate that the last time [CO₂] = 1,000 ppmv was 30 million years ago, when the average global temperature was about 16°C higher than today (~31°C). These reconstructions of the earth's actual climatic history suggest that the long-term feedback factor, which could include releases of methane from marine sediments and changes in vegetation and geological weathering rates, is closer to 2°C/(W/m²). Thus, as noted by Kiehl (2011, p. 159),

If the world reaches such concentrations of atmospheric CO₂, positive feedback processes can amplify global warming beyond current modeling estimates. The human species and global ecosystems will be placed in a climatic state never before experienced in their evolutionary history and at an unprecedented rate.

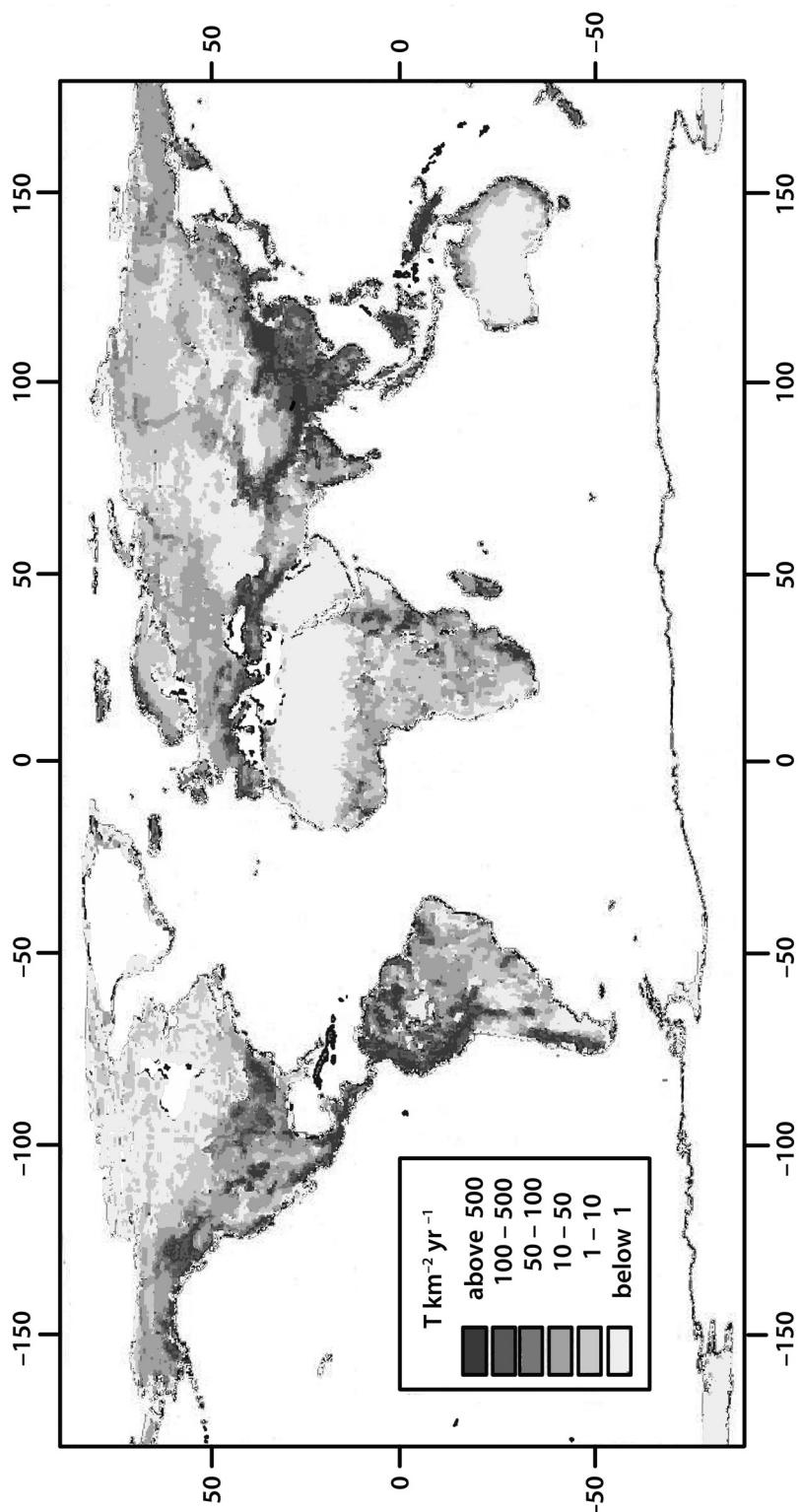


Figure 2.35 Global distribution of particulate-sediment yields. The highest rates are in the mountainous areas of Central and South America, the Alps and Caucasus, the Himalayas, and in central China. The lowest are in regions of low precipitation in the North American Arctic, and the deserts of north Africa and Australia [Ludwig and Probst (1998). River sediment discharge to the oceans: Present-day controls and global budgets. *American Journal of Science* 298:265–295, used with permission of American Journal of Science].

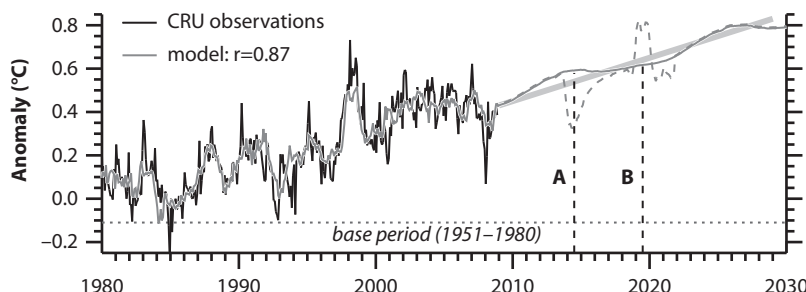


Figure 2.36 Observed global mean monthly temperatures (up to 2008) and forecast temperatures to 2030 incorporating effects of ENSO, volcanism, solar irradiance, and anthropogenic effects [Lean and Rind (2009)]. How will Earth's surface temperature change in future decades? *Geophysical Research Letters* 36, with permission of the American Geophysical Union].

The global hydrologic cycle is a major part of the earth's climate system, and will change in response to natural or anthropogenic climate changes. Much of the recent warming of the earth's surface is reflected in a rise in ocean temperatures (Murphy et al. 2009; Johnson et al. 2010), which causes an increase in evaporation. Both climate models and observations indicate that total atmospheric water vapor increases by about 7%/°C due to warmer air being able to hold more water vapor (Wentz et al. 2007), as dictated by the **Clausius–Clapeyron (C-C) relation** (box 2.2). Because warmer oceans and land surfaces will increase evaporation rates, and a warmer atmosphere can hold more water vapor, it is widely predicted that increasing temperature will cause an increase in global precipitation rates and an intensification of the hydrologic cycle. Satellite observations over the last two decades generally confirm this prediction; they indicate that global evaporation, total atmospheric water (more than 99% of which is in vapor form), total precipitation, and the intensities of the heaviest rainfall events have increased at about the rate predicted by the C-C relation (Allen and Ingram 2002; Wentz et al. 2007; Min et al. 2011; Durack et al. 2012). Theory also suggests that, because

more rainfall is concentrated in larger storms, less will occur in smaller events and dry periods and droughts will last longer.

As shown in figure 2.37, current climate models do reasonably well at forecasting global precipitation, but recent precipitation changes have not simply followed global temperature. This is because precipitation changes are dominated by natural solar and volcanic forcing, which varies on short timescales, whereas the temperature response is dominated by steadily increasing anthropogenic GHG forcing.

Thus, past and future global warming will be accompanied by changes in the timing, amounts, and distributions of precipitation, evapotranspiration, snow, soil moisture, streamflow, and other factors; these in turn will force major adjustments in the magnitudes, timing, and locations of floods, droughts, water demands, supplies, and water quality. While complete examination of the likely hydrologic and water-resources impacts of these climate changes would require a separate book-length treatment, the next section provides a review of recent observed hydrologic changes and forecasts. Following this, section 2.2.8.3 explores the sensitivity of runoff to climate changes.

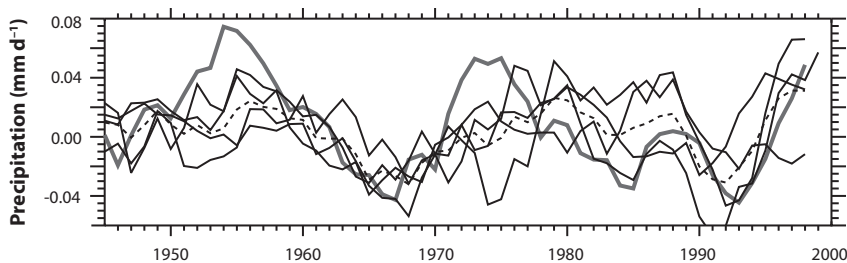
Box 2.2 Water-Vapor Capacity of the Atmosphere

The water-holding capacity of the air is given by the **saturation vapor pressure**, denoted e^* . The value of e^* depends on temperature, and its rate of change with temperature is given by the Clausius–Clapeyron equation, which is derived from thermodynamic principles (see, e.g., Peixoto and Oort 1992). In integrated form, the e^* versus temperature relationship is closely approximated as

$$e^* = 611 \cdot \exp\left(\frac{17.27 \cdot T}{T + 237.3}\right), \quad (2B2.1)$$

where e^* is in pascals ($= N/m^2$) and T is temperature in °C. Thus e^* increases approximately exponentially with temperature (figure 3.3); at earth-surface temperatures, this rate is about 6.5%/°C to 7%/°C.

Figure 2.37 Variability of global mean precipitation, 1945–2000. Darkest line shows measured values, other solid lines are model estimates. The dashed line is an average of the models [Allen and Ingram (2002). Constraints on future changes in climate and the hydrologic cycle. *Nature* 419:224–232. Reprinted by permission from Macmillan Publishers Ltd.].



2.2.8.2 Evidence for Recent Climate-Related Hydrologic Changes

Huntington (2006) reviewed recent evidence for the intensification of the global hydrologic cycle that is predicted to accompany global warming; his results are summarized below and in table 2.12. Additional reports of recent climate-related hydrologic changes are noted in box 2.3.

Huntington (2006) reported evidence that global land precipitation increased by about 2% over the twentieth century, but with significant regional variations: Land precipitation increased by 7 to 12% between 30 and 85°N and by 2% between 0 and 55°S, but with substantial decreases in some regions. In the United States, spring, summer, and fall precipitation increased during the twentieth century, but there was little change in Canada.

Increases in snow-water equivalent averaging about 4 to 5% per decade were reported in North America and Russia. There was variability in the extent of seasonal snow cover in fall and winter, but there were widespread decreases in spring snow-cover extent across Russia, China, and the Swiss Alps, and the extent of spring snow cover decreased rapidly after 1980 in North America. The ratio of snow to total precipitation decreased in March in New England in the United States and in Canada south of 55°N latitude.

A number of hydrologic and phenological studies cited by Huntington (2006) showed that the length of the growing season has increased substantially, suggesting that evapotranspiration has increased, at least in humid regions. Evapotranspiration increases of about 1 mm/yr have also been inferred from hydrologic budget analyses of four major US river basins from 1950 to 2000. Other studies found increases in lower troposphere water vapor (precipitable water content) in the last half of the twentieth century. Al-

though cloudiness increased before the 1980s, the trend reversed during the late 1980s to the early 1990s, so the long-term trend remains uncertain. The diurnal temperature range, which is inversely related

Table 2.12 Summary of Trends in Land-Area Hydroclimatic Variables.

Variable	Twentieth Century	Latter Half of the Twentieth Century
Precipitation	Increasing (R, G)	
Runoff	Increasing (R, G)	Increasing (R, G)
Tropospheric water vapor		Increasing (R)
Cloudiness		No change
Tropical storm frequency and intensity		No change
Floods	No change	Increasing (R, G)
Droughts		Increasing (R)
Soil moisture		Increasing (R)
Seasonal glacier mass balance		Increasing (G)
Pan evaporation		Decreasing (R)
Actual evapotranspiration		Increasing (R)
Growing-season length ^a	Increasing (R)	Increasing (R)
Growing-season length ^b		Increasing (R)

R = regional

G = global

^aBased on records of temperature or agricultural killing frost.

^bBased on satellite-derived “onset of greenness” normalized difference vegetation index.

Source: Huntington (2006).

Box 2.3 A Sampling of Reports of Recent Large-Scale Changes in the Hydrologic Cycle^a

Cloud Cover, Humidity, and Wind Speed

- Atmospheric water content (precipitable water) has increased globally since about 1988 (Wentz et al. 2007).
- Atmospheric water vapor has increased at a rate of 0.27 mm per decade from 1988 to 2006; the increase is largest in the tropics and Northern Hemisphere and relatively small in the Southern Hemisphere (Mears et al. 2010).
- Water vapor over the oceans increased by 2.4% from 1988–2006 (Wentz et al. 2007).
- Wind speeds over the global ocean have increased by 5 to 10% over the last 20 years (Young et al. 2011).
- Cloud cover increased over wide areas of the globe since 1900 (Henderson-Sellers 1992; Karl et al. 1993; Dai et al. 1997).

Precipitation

- Global precipitation increased by 2.8% from 1988–2006 (Wentz et al. 2007).
- Global land precipitation has increased by about 30 mm/yr since 1900 (Levinson et al. 2010).
- Precipitation in the Arctic has generally increased in the last century, especially in winter (Hinzman et al. 2005).
- The number of land-falling tropical cyclones in the United States has increased since 1994, and the number of heavy rainfall events associated with those storms was more than double the long-term (1895–2008) average (Kunkel et al. 2010).
- From 1970 to 2004 the number of category 4 and 5 hurricanes has increased globally; this increase is directly linked to increasing sea-surface temperatures (Hoyos et al. 2005).
- In the midlatitudes, there is a widespread increase in the frequency of very heavy precipitation during the past 50 to 100 years (Groisman et al. 2005).
- Precipitation increased in southern Canada by 13%, in northern Canada by 20%, and in the United States by 4% during the last 100 years; greatest increases were in eastern Canada and adjacent regions of the United States (Groisman and Easterling 1994).
- Decadal to multidecadal variability of global precipitation increased since 1900 (Tsonis 1996).
- Proportion of precipitation occurring in extreme one-day events increased in the United States in the last 30 to 80 years (Karl et al. 1995).
- Fall precipitation increased in central United States between 1948 and 1988 (Lettenmaier et al. 1994).

- The 2010 drought in the Amazon rain forest was unique in timing and intensity since record keeping began (1903). Since the mid-1970s, the length of the dry season and the number of “dry” and “very dry” events have increased (Marengo et al. 2011).

Snow

- Snowpack reductions in the northern US Rocky Mountains in the last 50 years are almost unprecedented compared to the previous 800 years, and are due to springtime warming caused by positive reinforcement of anthropogenic warming by decadal variability (Pederson et al. 2011).
- The average annual duration of Northern Hemisphere snow cover has decreased by 15 to 18 days since the early 1970s (Dye 2002).
- A rapid reduction in arctic snow-cover duration (due primarily to an early disappearance of snow cover in spring) occurred in the 1980s and has continued (Dirksen et al. 2010).
- Snow-covered areas have declined in all latitude bands in the Northern Hemisphere since 1973 (Pielke et al. 2004).
- Spring snow-cover extent in the Northern Hemisphere declined steadily and decreased by about 8% from the 1970s to 2000s (Robinson 2010).
- Areal snow cover in the Northern Hemisphere declined 10% in the past 20 years (Groisman et al. 1994).
- Northern Hemisphere snow-cover extent decreased by 2.5 to 5% between 1978 and 1999 (Comiso and Parkinson 2004).

Evapotranspiration

- Pan evaporation in the United States and former Soviet Union has declined since 1950 (Peterson et al. 1995).
- Pan evaporation in China decreased by 5.4 mm/yr² from 1960 to 1991 due to decreasing wind speed and insolation offsetting increased temperature, then increased by 7.9 mm/yr² from 1992 to 2007 as the temperature effect became dominant (Liu et al. 2011).
- Global atmospheric evaporative demand has declined over the last 50 years, largely due to a 0.7 m/s decline in wind speed (McVicar et al. 2012).
- Global evaporation increased by 2.6% from 1988–2006 (Wentz et al. 2007).

Streamflow

- Streamflow remained steady or increased over the last decade (2000–2009) in all continents and ocean catch-

ments, except Africa and the Mediterranean/Black Sea drainage, when compared to the long-term mean (Fekete et al. 2010).

- Annual streamflow increased by 15.5% over northern Canada from 1964–2007, consistent with other parts of the Arctic (Déry et al. 2009).
- Shrinking glaciers and snowpacks are reducing discharge in rivers that drain the central Rocky Mountain region (Wolfe et al. 2011).
- Mean annual discharge from the six largest rivers of the Eurasian Arctic increased about 12% from 1936 to 2009 (Shiklomanov 2010).
- Mean annual discharge from the four largest rivers of the North American Arctic increased about 10% from 1970 to 2009 (Shiklomanov 2010).
- Winter–spring streamflow strongly increased at over 50% of US gauging stations from 1948 to 1988, with strongest trends in north-central region (Lettenmaier et al. 1994).
- Streamflow has increased, especially in fall and winter, during past 50 years in most of conterminous United States (Lins and Michaels 1994).
- Runoff has increased in the United States between 1900 and 2008, and precipitation has accounted for almost all of the runoff variability during that period (McCabe and Wolock 2011).

Lakes

- The number and size of lakes on permafrost areas in Siberia have decreased by 11% and 6% respectively between 1973 and 1998, almost certainly due to permafrost melting (Smith et al. 2005).
- Surface water of large lakes around the world warmed by 0.045 to 0.10°C/yr from 1985 to 2009, with far greater warming in the mid- and high latitudes of the Northern Hemisphere than in low latitudes and the Southern Hemisphere (Schneider and Hook 2010).

Glaciers and Permafrost

- Most arctic glaciers experienced net loss of water since 1940, contributing 0.13 mm/yr to sea-level rise (Dowdeswell et al. 1998).

^aSee also Loaiciga et al. (1996), Huntington (2006), Arndt (2010), Lubchenco and Karl (2012).

• Permafrost warmed by up to 4°C in Alaska since 1976 (Osterkamp 2007).

- Over the last 18 years, the rate of loss of ice from the earth's glaciers accelerated at the following rates: Greenland—21.9 Gt/yr², Antarctica—14.5 Gt/yr², mountain glaciers and ice caps—12.6 Gt/yr² (Rignot et al. 2011).
- The average balances for arctic glaciers have been generally negative over the past 40 years (Hinzman et al. 2005).
- There was an abrupt, large increase in the extent of permafrost degradation in northern Alaska since 1982 associated with record warm temperatures during 1989–1998, mainly in massive ice wedges that had been stable for thousands of years (Jorgenson et al. 2006).
- The rate of mass loss from four glaciers in the Canadian arctic islands was 5 to 7 times faster in 2005–2009 than in 1963–2004 (Sharp et al. 2011).
- Permafrost temperatures increased 0.5 to 2°C during the last several decades in Alaska, northwest Canada, Siberia, and northern Europe (Romanovsky et al. 2010).
- Alpine glacier mass balances were generally negative for the eighteenth consecutive year. Decadal mean annual mass balance was –198 mm in the 1980s, –382 mm in the 1990s, and –624 mm for 2000–2008 (Pelto 2010).
- The portion of the Greenland ice sheet experiencing summer melting expanded by 17% from 1992 to 2002 (Comiso and Parkinson 2004).

Growing Season and Plant Growth

- Plant growth in northern high latitudes increased from 1981 to 1991 (Myneni et al. 1997).
- Growing season has increased by 10 to 20 days in the last few decades, largely due to earlier beginning (Linderholm 2006).

to cloudiness, decreased over most land areas in the latter half of the twentieth century.

Streamflow is a particularly meaningful indicator of climate change because (1) it areally and temporally integrates precipitation and evapotranspiration and (2) it amplifies changes in precipitation: Karl and

Riebsame (1989) concluded that a given relative change in precipitation is amplified to a one- to sixfold change in relative streamflow (see discussion in section 2.2.8.3). However, streamflow is also directly affected by anthropogenic changes due to water imports and exports, reservoir construction, irrigation, etc.

Sources cited by Huntington (2006) indicated an increase in continental runoff generally during the twentieth century, from individual major rivers globally and from many smaller rivers in the Northern Hemisphere. This is consistent with the study of Labat et al. (2004), who found a 4% increase in global runoff for each 1°C temperature increase between 1875 and 1994 (figure 2.38). However, regional variations were significant: runoff increased in North America, Asia, and South America; decreased in Africa; and showed no trend in Europe. In contrast, Pečáková et al. (2003) found no significant trends in the streamflows of large rivers from all continents (except Antarctica) over the nineteenth and twentieth centuries, but identified cycles averaging 14 and 28 years, and a 20- to 22-year cycle in some regions. These cycles may be related to teleconnections (section 2.1.6), and may appear to be trends when shorter time periods are examined.

An important question is to what extent observed and forecast temperature changes affect the

frequency and intensity of extreme weather events such as hurricanes, floods, and droughts. Huntington (2006) cited several regional studies that report increases in intense precipitation events, but found no definitive evidence of change in the intensity of tropical storms. However, Kunkel et al. (2010) reported that the number of land-falling tropical cyclones in the United States has increased since 1994, and the number of heavy rainfall events associated with those storms was more than double the long-term (1895–2008) average. A few studies found an increase in the frequency of extreme floods, but others did not detect trends in flooding in the United States, Canada, Scandinavia, or central Europe.

A global analysis by Dai et al. (2004) found that, since the 1970s, the fraction of land surface characterized as “very dry” more than doubled, while “very wet” areas declined slightly; another study (Robock et al. 2000) found increases in areas of both severe drought and moisture surplus. Huntington (2006) reported considerable evidence for lengthen-

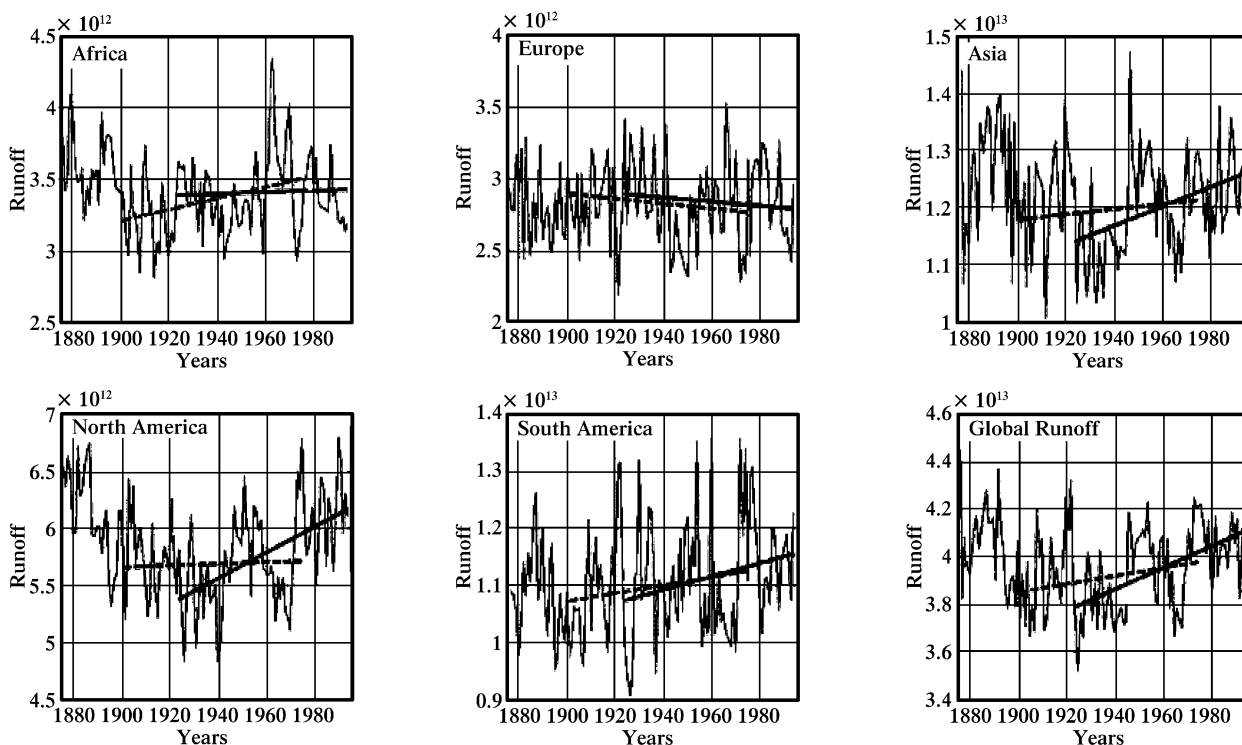


Figure 2.38 Mean annual runoff (in L/s) for five continents and linear trends for 1900–1970 and 1925–1994 intervals. Except for the African and European continents, mean annual runoff increases more rapidly during the second period, coincident with a rapid global warming [Labat et al. (2004). Evidence for global runoff increase related to climate warming. *Advances in Water Resources* 27:631–642, with permission of Elsevier].

ing of the growing season throughout the Northern Hemisphere which, along with increasing temperatures, would be expected to be associated with increased evapotranspiration and decreased growing-season soil moisture. Robock et al. (2000) reported increases in summer soil moisture in recent decades at almost all sites having long-term records; they attributed this to increases in precipitation and cloud cover that more than compensated for increased evapotranspiration. Temperature increases over the last century appear to have increased the frequency of ENSO events, and these regionally variable changes in dryness and wetness are attributed to both ENSO-induced decreases in precipitation and warming-induced increases in evaporation.

Huntington's (2006) review found that subpolar and mountain glaciers throughout the world are losing mass in response to warming. One study found that many such glaciers are experiencing higher winter snowfall that is more than compensated by increased summer ablation, which is further evidence for a recent intensification of the hydrologic cycle. There is consistent evidence of later freeze-up and earlier break-up in rivers and lakes in the Northern Hemisphere from 1846 to 1995; over this period freeze-up dates averaged 5.8 days per 100 years later, and break-up dates averaged 6.5 days per 100 years earlier. A few longer time series reveal reduced ice cover beginning as early as the sixteenth century, with increasing rates of change after about 1850. Earlier spring snowmelt runoff was reported in Siberia and western United States and Canada, earlier river and lake ice-out in New England, and a longer frost-free season in the United States between 1948 and 1999.

Huntington (2006) concluded that the widespread increases in precipitation, evapotranspiration, water vapor, and runoff noted above suggest that the theoretically expected intensification of the water cycle has occurred during at least the last half of the twentieth century, and more recent studies (box 2.3) suggest that this trend is continuing. Observations of ocean salinity showing a 3% decrease in precipitation minus evaporation in subtropical oceans (a relative increase in evaporation) and 7% (Northern Hemisphere) and 16% (Southern Hemisphere) increases in high-latitude oceans (a relative increase in precipitation) reinforce this conclusion (Helm et al. 2010).

2.2.8.3 Runoff Sensitivity to Climate Change

Because runoff spatially and temporally integrates hydrologic inputs and outputs, and because

long-term average runoff represents the available water resource of a region (section 1.8.1), the sensitivity of runoff to climate change is a critical concern. Here we explore this question using simple analytical relations among long-term average water- and energy-balance quantities (expressed as water fluxes [L T^{-1}]). To make the notation less cumbersome here we use simpler symbols to represent the water-balance components introduced in section 1.8: $P \equiv \mu_P$, $ET \equiv \mu_{ET}$, $RO \equiv \mu_{RO}$.

These relations begin with an expression relating evapotranspiration, ET , to precipitation, P , and potential evapotranspiration, PET , which expresses the evaporative demand of the climate (section 2.2.3):

$$ET = f_B(P, PET). \quad (2.9)$$

The function f_B is a “Budyko-type equation,” named for the Russian climatologist M. I. Budyko, who explored such relations (Budyko 1958, 1974). Although many versions of f_B have been proposed, Yang et al. (2008) used physical, dimensional, and mathematical reasoning to show that the appropriate form of a simple relation between ET and climate is

$$ET = \frac{PET \cdot P}{(P^w + PET^w)^{1/w}}, \quad w > 0, \quad (2.10)$$

where w is a parameter that depends on watershed characteristics. Because of interrelations among these characteristics, it is difficult to specify a physically based relation for w . However, Yang et al. (2007) established empirical relations for nonhumid regions of China, indicating that w (1) increases with the ratio of soil hydraulic conductivity to rainfall rate and the ratio of soil-water storage capacity to potential evapotranspiration and (2) decreases with average watershed slope.

Figure 2.39 shows the relation between ET/P and PET/P as given by equation (2.10). The ratio PET/P is called the **aridity index**; actual evapotranspiration is **energy-limited** in humid regions ($PET/P < 1$) and **water-limited** in arid regions ($PET/P > 1$). Curves with low values of w characterize regions with relatively small storage (e.g., rocky, steeply sloping watersheds where rainfall is quickly converted to runoff), while those with high w values represent relatively flat watersheds with high subsurface storage.

From section 1.8, average precipitation, P , evapotranspiration, ET , and runoff, RO , are related as

$$RO = P - ET, \quad (2.11)$$

where we assume no long-term storage changes or ground-water inputs. Combining (2.10) and (2.11) gives a relation between runoff and climate:

$$RO = P \cdot \left[1 - \frac{PET}{\left(P^w + PET^w \right)^{1/w}} \right]. \quad (2.12)$$

We can now use equation (2.12) to explore how RO responds to climate changes, i.e., changes in PET and P . Taking derivatives of (2.12) yields

$$\frac{\partial RO}{\partial P} = 1 - \frac{1}{\left[1 + \left(\frac{P}{PET} \right)^w \right]^{1+1/w}} \quad (2.13)$$

and

$$\frac{\partial RO}{\partial PET} = -\frac{1}{\left[1 + \left(\frac{PET}{P} \right)^w \right]^{1+1/w}}. \quad (2.14)$$

Note that (2.13) and (2.14) assume that precipitation and potential evapotranspiration are independent. We have seen in section 2.2.3 and box 2.2 that both P and PET are positively related to temperature at the global scale, but the relations vary regionally, even in sign, so it is reasonable as a first approximation to assume independence at the watershed scale. [See Yang et al. (2008) for further discussion.]

Equations (2.13) and (2.14) are graphed in figure 2.40. Figure 2.40a shows that, in humid regions ($PET/P < 1$), most of a change in precipitation is reflected in a change in runoff ($\partial RO/\partial P > 0.5$), with lit-

tle effect due to watershed characteristics. In arid regions ($PET/P > 1$), the effect of a precipitation change on runoff varies strongly with watershed type, being small in watersheds with large storage (large w) and much greater where storage is small. Figure 2.40b shows that watershed type has a much greater effect on $\partial RO/\partial PET$ in humid regions than in arid regions.

The sensitivity of runoff to changes in climate is usually expressed as **climate elasticity**, defined as the ratio of the relative change in runoff, dRO/RO , to the relative change in the climatic parameters. Thus the elasticity of runoff to precipitation, $\varepsilon(RO, P)$, is

$$\varepsilon(RO, P) \equiv \frac{dRO/RO}{dP/P} = \frac{dRO \cdot P}{dP \cdot RO}. \quad (2.15)$$

This expression is evaluated in box 2.4 on p. 94 and graphed in figure 2.41 on p. 95. Note that all values of $\varepsilon(RO, P)$ are greater than 1, indicating that a 1% increase in precipitation produces a greater than 1% increase in runoff. Elasticity increases with w and decreases with increasing precipitation.

As noted in box 2.4, it is more meaningful to relate fractional changes in runoff to absolute, rather than relative, increments of temperature, so that we express the temperature elasticity of runoff as

$$\varepsilon(RO, T) \equiv \frac{dRO/RO}{dT} = \frac{dRO}{RO \cdot dT}. \quad (2.16)$$

Using an expression relating PET to temperature [equation (2B4.2); figure 2.42 on p. 96], the expression for this is derived in box 2.4 and plotted in figure 2.43 on p. 97. As expected, $\varepsilon(RO, T)$ values are negative; they are also much smaller than $\varepsilon(RO, P)$ values.

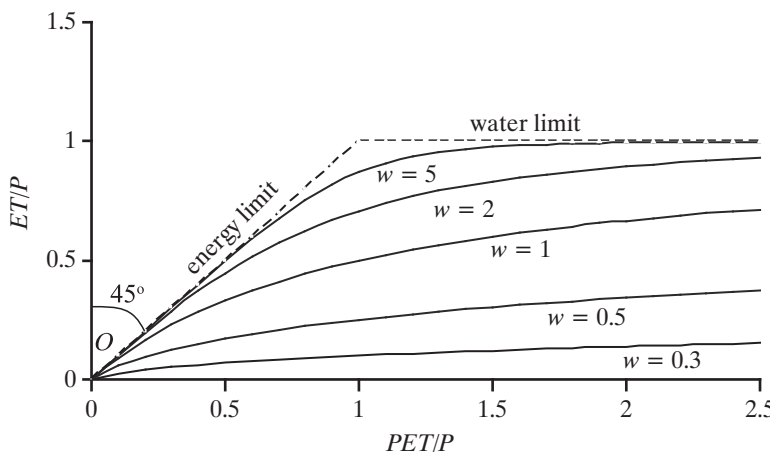


Figure 2.39 The relation between ET/P and PET/P as given by equation (2.10). The ratio PET/P (horizontal axis) is the aridity index; The parameter w characterizes regional water storage [Yang et al. (2008)]. New analytical derivation of the mean annual water-energy balance equation. *Water Resources Research* 44, with permission of the American Geophysical Union].

Some example calculations of elasticity/sensitivity using the above relations are given in box 2.4.

The climate elasticity of runoff has also been investigated using more elaborate hydrologic models and empirically by examination of streamflow and climatic data. The conclusions of these studies are generally consistent with those determined via equation (2.12). For example, Karl and Riebsame (1989) examined the sensitivity of streamflow in the United

States to changes in temperature and precipitation using historical data and concluded that 1 to 2°C temperature changes typically have little effect on streamflow, whereas a given relative change in precipitation produces a one- to sixfold change in streamflow. Sankarasubramanian et al. (2001) found empirical values of $\epsilon(RO,P)$ ranging from 1 to 3.5 in the United States, with highest values in semiarid regions, and Sankarasubramanian and Vogel (2003)

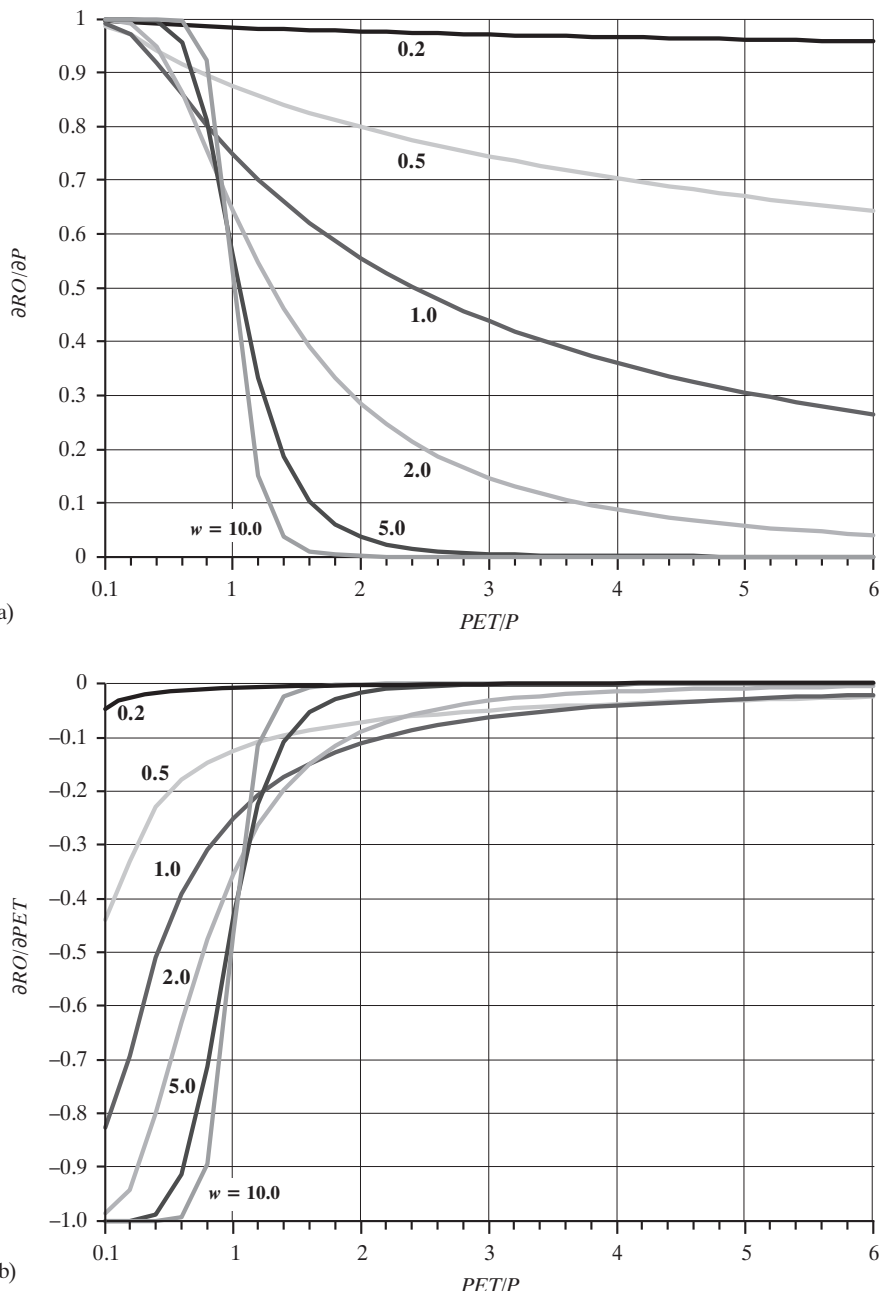


Figure 2.40 (a) $\partial RO / \partial P$ as a function of aridity index, PET/P [equation (2.13)]. (b) $\partial RO / \partial PET$ as a function of inverse of aridity index [equation (2.14)].

Box 2.4 Derivation of Runoff Elasticity to Changes in Precipitation and Temperature

Precipitation Elasticity

From (2.12) and (2.13) we can write the elasticity of runoff to precipitation, $\epsilon(RO, P)$ as

$$\epsilon(RO, P) \equiv \frac{dRO/RO}{dP/P} = \frac{1 - \frac{1}{\left[1 + \left(\frac{P}{PET}\right)^w\right]^{1+w}}}{1 - \frac{PET}{\left(P^w + PET^w\right)^{1/w}}} \quad (2B4.1)$$

Temperature Elasticity

Given the strong dependence of potential evapotranspiration on temperature, a number of formulas have been used for estimating monthly average potential evapotranspiration from monthly average temperature alone (see section 6.7.2.1). For estimating annual PET from average annual air temperature, Gardner (2009) used

$$PET = 1.2 \times 10^{10} \cdot \exp(-4,620/\bar{T}), \quad (2B4.2)$$

where PET is in mm/yr and \bar{T} is mean annual air temperature (K). Although this relationship is approximate, we use it to explore the essential aspects of hydrologic response to climate change.

The change of runoff with temperature is found as

$$\frac{\partial RO}{\partial T} = \frac{\partial RO}{\partial PET} \cdot \frac{\partial PET}{\partial T}. \quad (2B4.3)$$

From (2B4.2),

$$\frac{\partial PET}{\partial T} = \frac{5.54 \times 10^{13} \cdot \exp(-4,620/\bar{T})}{\bar{T}^2}. \quad (2B4.4)$$

Substituting (2.12) and (2B4.4) into (2B4.3) then gives

$$\frac{\partial RO}{\partial T} = -\frac{5.54 \times 10^{13} \cdot \exp(-4,620/\bar{T})}{\left[1 + \left(\frac{PET}{P}\right)^w\right]^{1+w} \cdot \bar{T}^2}. \quad (2B4.5)$$

Equation (2B4.5) could be used to calculate the elasticity of runoff to temperature, $\epsilon(RO, T)$, as

$$\epsilon(RO, T) \equiv \frac{\partial RO/RO}{\partial T/T}. \quad (2B4.6)$$

However, because T is a large number, it is more meaningful to relate a fractional change in runoff to an actual temperature increment, dT , rather than to a relative change $\partial T/T$. This relation is found by multiplying (2B4.5) by dT and dividing by (2.12):

$$\frac{\partial RO}{RO} = -\frac{5.54 \times 10^{13} \cdot \exp(-4,620/\bar{T})}{\bar{T}^2 \cdot P \cdot \left[1 + \left(\frac{PET}{P}\right)^w\right]^{1+w} \cdot \left[1 - \frac{PET}{\left(P^w + PET^w\right)^{1/w}}\right]} \cdot dT, \quad (2B4.7)$$

where PET is given by (2B4.2).

Example Calculations

Here we use the above relationships to compare the changes in average runoff resulting from a 7% increase in average precipitation and a 1°C increase in average temperature in watersheds with $w = 0.5$ and $w = 2$ in two regions:

Region	Annual P (mm)	Annual T (°C)
Humid temperate	1,000	10
Arid subtropical	200	20

Referring to the figures indicated, we find:

Table 2B4.1 Humid Temperate Region.

w	Figure	$\epsilon(RO, P)$	Figure	$\partial RO/RO \cdot dT$
0.5	2.41a	1.17	2.43a	-0.010
2	2.41c	2.19	2.43c	-0.069

Table 2B4.2 Arid Subtropical Region.

w	Figure	$\epsilon(RO, P)$	Figure	$\partial RO/RO \cdot dT$
0.5	2.41a	1.32	2.43a	-0.017
2	2.41c	2.98	2.43c	-0.106

Multiplying the above values by the increases in P and T gives the following values of dR/RO :

Table 2B4.3 Humid Temperate Region.

w	Due to $dP/P = 0.07$	Due to $dT = 1^\circ C$
0.5	0.082	-0.010
2	0.153	-0.069

Table 2B4.4 Arid Subtropical Region.

w	Due to $dP/P = 0.07$	Due to $dT = 1^\circ C$
0.5	0.092	-0.017
2	0.209	-0.106

Thus the runoff responses are considerably larger (in absolute value) in the arid subtropical watersheds, and for a given climate, are considerably larger in watersheds with more storage.

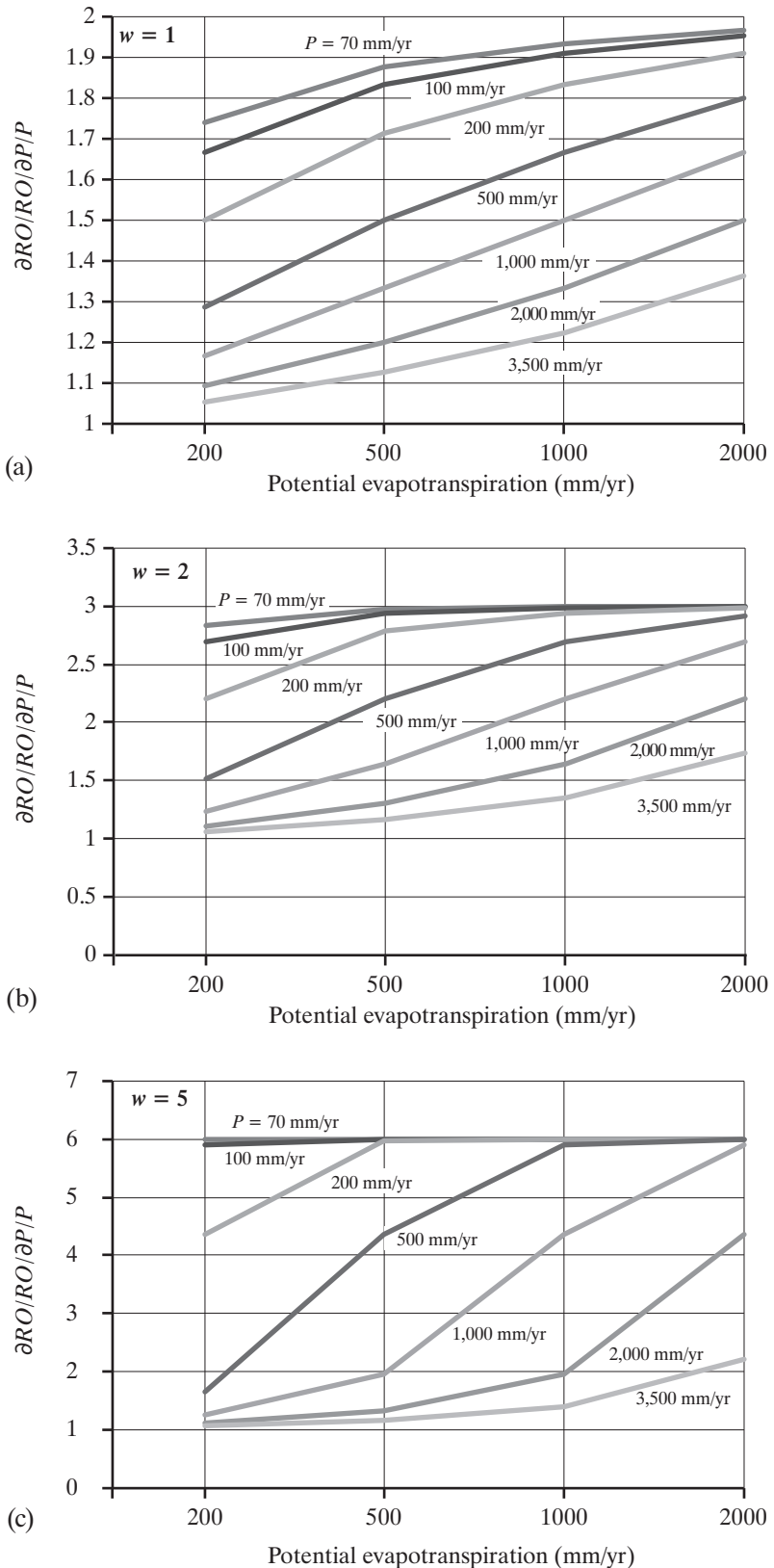


Figure 2.41 Elasticity of runoff to precipitation, $\varepsilon(RO,P)$, as a function of potential evapotranspiration, PET , and precipitation, P [equation (2B4.1)]. (a) $w = 1$; (b) $w = 2$; (c) $w = 5$.

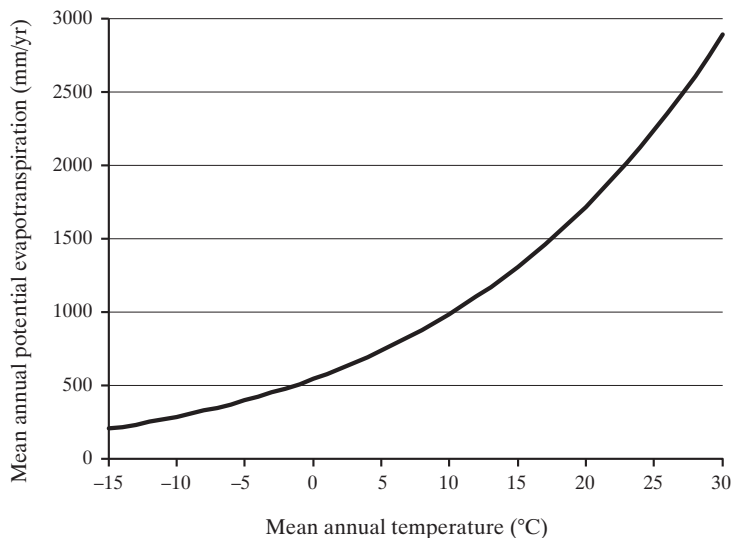


Figure 2.42 Generalized relation of average annual potential evapotranspiration as a function of mean annual temperature as postulated by Gardner (2009) [equation (2B4.2)].

showed that $\epsilon(RO,P)$ values depend on the aridity index and soil-water storage. Yang and Yang (2011) found $\epsilon(RO,P)$ ranging from 1.6 to 3.9 and $\epsilon(RO,F)$ ranging from -0.02 to $-0.11^{\circ}\text{C}^{-1}$ in two large Chinese watersheds. McCabe and Wolock (2011) reported that runoff has increased in the United States during the past century and that precipitation has accounted for almost all of the runoff variability, while temperature effects have been small, even though temperatures have increased significantly. Tang and Lettenmaier (2012) found that $\epsilon(RO,P)$ ranges from 1 to 3 and $\epsilon(RO,F)$ from 0.02 to $0.06^{\circ}\text{C}^{-1}$ in major global watersheds.

The general conclusions from all of these studies are:

1. $\epsilon(RO,P) > 1$ everywhere and typically ranges from 1 to 3 or more;
2. $\epsilon(RO,P)$ increases with mean annual evapotranspiration and temperature and decreases with mean annual precipitation;
3. For a given climate, $\epsilon(RO,P)$ increases with watershed storage (w);
4. In humid regions ($PET/P < 1$), a change in precipitation (dP) mostly transforms into runoff ($dRO > dET$).
5. In arid regions ($PET/P > 1$), a change in precipitation (dP) mostly transforms into evapotranspiration ($dRO < dET$).
6. $\epsilon(RO,F)$ typically ranges from -0.02 to $-0.10^{\circ}\text{C}^{-1}$; and

7. The effects of global warming-induced precipitation changes on runoff will be greater than the effects of increased evapotranspiration due to temperature increase.

The above conclusions appear to be well founded theoretically and supported by observation. However, predicting the magnitude, and even the direction, of local and regional hydrologic change due to climate and land-use change is challenging because many factors are involved in addition to the direct responses to changes in precipitation and temperatures. For example, experiments indicate that higher CO_2 concentrations tend to reduce water use by plants (Lemon 1983), and this could offset increases in evapotranspiration from land surfaces due to the temperature effect. Thus, one plausible scenario is that evaporation from the oceans will increase, while land evapotranspiration will change little, or perhaps even decrease. Further uncertainty exists because of the difficulty in predicting the hydrologic effects of changes in length of growing season, area of plant cover, plant species, wind speed, and cloudiness, and because there is considerable feedback between land evapotranspiration and global temperature and precipitation (Shukla and Mintz 1982; Loaiciga et al. 1996).

2.2.8.4 Moisture Recycling

A major aspect of this feedback is the recycling of continental precipitation and evapotranspiration. To study these phenomena globally, van der Ent et al. (2010) split the total precipitation at a given point

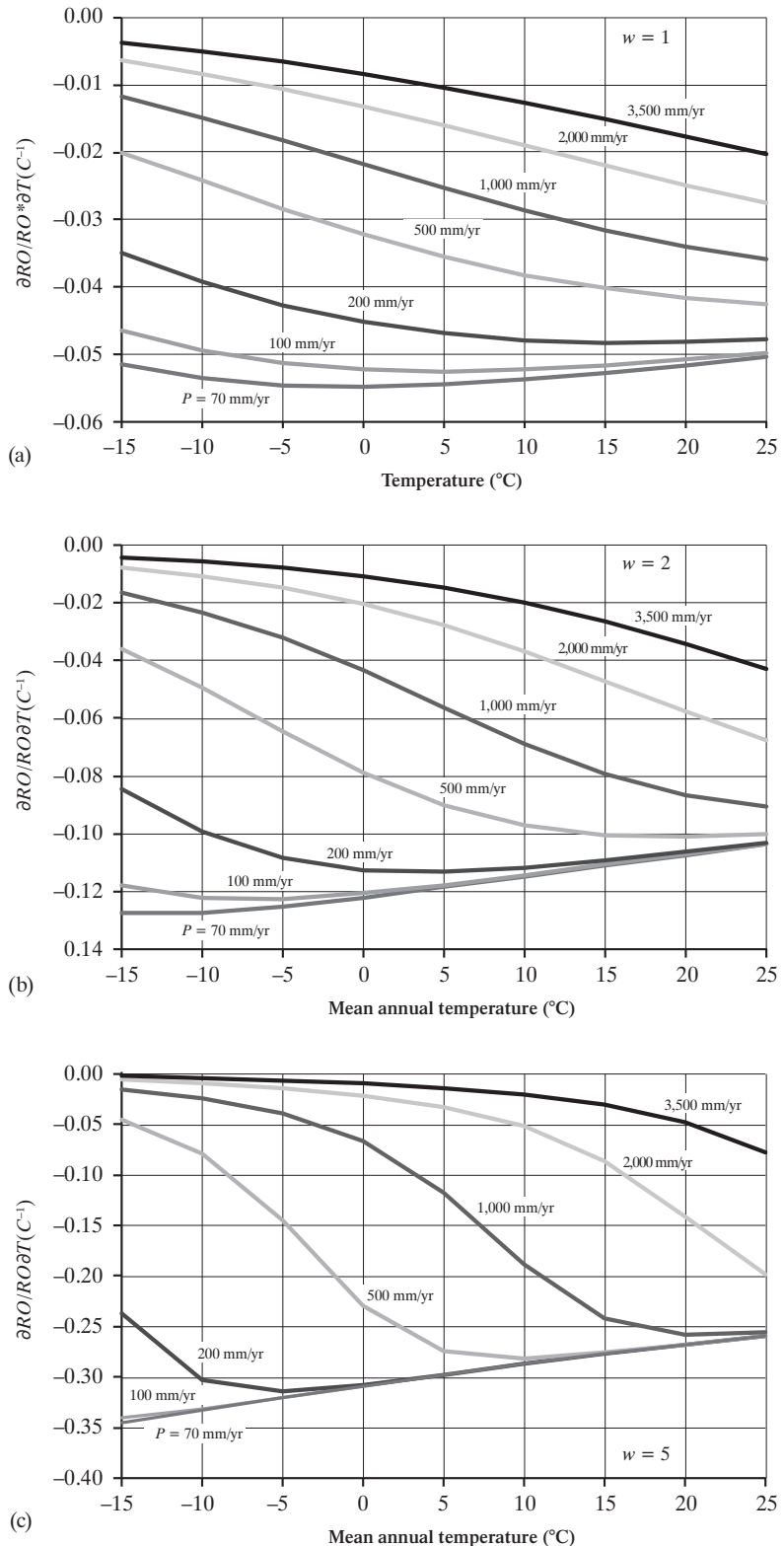


Figure 2.43 Relative change in average annual runoff ($\partial RO/RO$) per unit change in average annual temperature (dT) as a function of annual average temperature (T) as calculated in box 2.4. (a) $w = 1$; (b) $w = 2$; (c) $w = 5$.

$P(x,y)$ into two portions: one that has continental origin (i.e., most recently evaporated from any continental area), $P_C(x,y)$, and one that has an oceanic origin (i.e., most recently evaporated from the ocean), $P_O(x,y)$, and defined the local **precipitation-recycling ratio**, $R_P(x,y)$ as

$$R_P(x,y) \equiv \frac{P_C(x,y)}{P(x,y)} = \frac{P_C(x,y)}{P_C(x,y) + P_O(x,y)}. \quad (2.17)$$

$R_P(x,y)$ shows the dependence of precipitation at a given location (x,y) on upwind continental evapotranspiration to sustain precipitation. The local **evapotranspiration-recycling ratio**, $R_{ET}(x,y)$, was similarly defined as

$$R_{ET}(x,y) \equiv \frac{ET_C(x,y)}{ET(x,y)} = \frac{ET_C(x,y)}{ET_C(x,y) + ET_O(x,y)}, \quad (2.18)$$

where $ET_C(x,y)$ is terrestrial evapotranspiration that returns as continental precipitation, and $ET_O(x,y)$ is terrestrial evapotranspiration that precipitates on an ocean. Thus $R_{ET}(x,y)$ indicates the importance of evaporation at a certain location in sustaining downwind precipitation. Globally, the long-term average ET_C equals the average P_C .

Applying water-balance concepts (section 1.8) to the atmosphere, van der Ent et al. (2010) determined the global distribution of $R_P(x,y)$ (figure 2.44) and $R_{ET}(x,y)$ (figure 2.45). Oceanic sources are dominant in North America, though in the West about 60% of the evaporation returns to the continent downwind.

South America shows three distinct moisture-recycling patterns: Evapotranspiration from the Guianas and the Amazon region becomes precipitation to the south in the Río de la Plata basin; there is local recycling east of the Andes; and there is very little moisture recycling in Patagonia. East Africa gets most of its precipitation from the Indian Ocean and, along with central Africa, contributes moisture to West Africa, which gets much of its precipitation from continental sources. Between Europe and Asia, the main moisture flux is westerly, as reflected in the eastward increase of $R_P(x,y)$; 40 to 70% of the evaporation from Europe returns to a continental area. Much of the precipitation in western and northern China, Mongolia, and Siberia is of continental origin. Local moisture recycling [high values of both $R_P(x,y)$ and $R_{ET}(x,y)$] is very important in the Tibetan plateau. Although most precipitation in the south of India, Southeast Asia, and Oceania is of oceanic origin, values of R_P near 30% indicate that continental precipitation is important there. In the northern part of Australia, Indonesia, and Papua New Guinea, which are very wet areas, $R_{ET}(x,y)$ is about 40%.

Table 2.13 summarizes the recycling ratios for the continents and gives the continental and global precipitation multipliers, $M_P(x,y)$, defined as

$$M_P(x,y) \equiv \frac{P(x,y)}{P_O(x,y)} = \frac{1}{1 - R_P(x,y)}. \quad (2.19)$$

$M_P(x,y)$ is the amplification of precipitation due to continental evaporation. When integrated over a

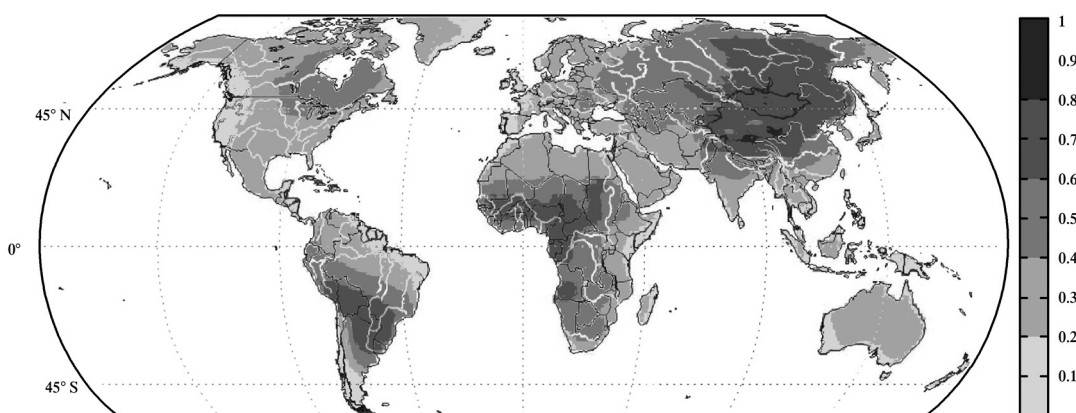


Figure 2.44 Average continental precipitation recycling ratio (1999–2008) [van der Ent et al. (2010). Origin and fate of atmospheric moisture over continents. *Water Resources Research* 46, with permission of the American Geophysical Union].

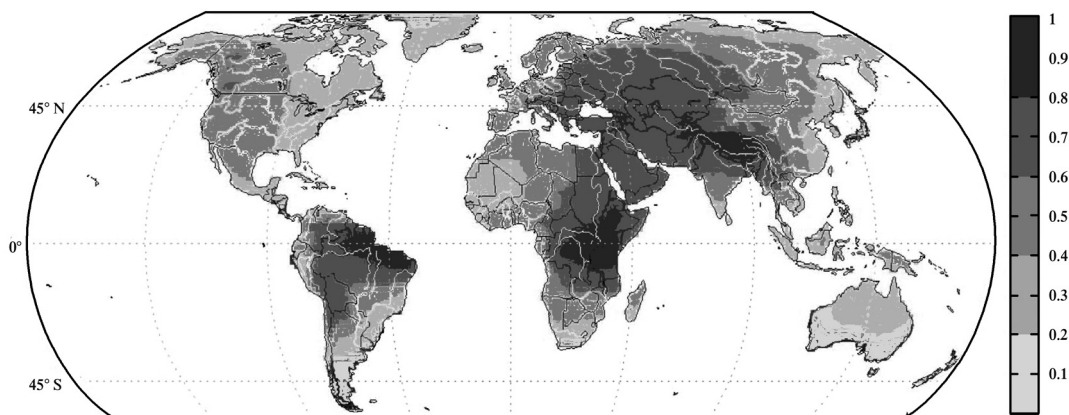


Figure 2.45 Average continental evapotranspiration recycling ratio (1999–2008) [van der Ent et al. (2010). Origin and fate of atmospheric moisture over continents. *Water Resources Research* 46, with permission of the American Geophysical Union].

year and all continental areas the multiplier is also the average number of times a water particle has sequentially fallen on the continent. As noted by van der Ent et al. (2010), recycled moisture multiplies precipitation by a factor 1.67 globally, and by much more in some regions: $M_P(x,y) = 3$ in the Río de la Plata basin in South America and is as high as 10 in western China.

Clearly, the feedbacks of moisture recycling play an important role in the global climate. Thus large-scale land-use changes currently taking place could interact with changes due to global warming, perhaps reinforcing them in some areas and weakening them in others. Clearly there is much to learn about the global hydrologic cycle and its complex feedbacks with human activities, and there are many potentially fruitful avenues of study. As noted by Eagleson (1986),

Because of humanity's sheer numbers and its increasing capacity to affect large regions, the hydrologic cycle is being altered on a global scale with consequences for the human life support system that are often counterintuitive. There is a growing need to assess comprehensively our agricultural, urban, and industrial activities, and to generate a body of knowledge on which to base plans for the future. It seems safe to say that these actions must come ultimately from global-scale numerical models of the interactive physical, chemical, and biological systems of the earth. Of central importance among these systems is the global hydrologic cycle, and its representation in these models presents many analytical and observational challenges for hydrologists.

A major challenge for hydrologists is to establish the linkage between local-scale and global-scale processes, and this is the subject of much current re-

Table 2.13 Annual Average Moisture Recycling by Continent (1999–2008).

Region	Precipitation Recycling Ratio, R_P (%)	Evapotranspiration Recycling Ratio, R_{ET} (%)	Precipitation Amplification Factor, M_P
North America	27	35	1.37
South America	36	59	1.56
Africa	45	55	1.82
Europe	22	27	1.28
Asia	34	52	1.52
Oceania	18	27	1.22
All continents	40	57	1.67

Source: van der Ent (2010).

search. The final section of this chapter introduces some of the broad interconnections between soils and vegetation and hydrology. Subsequent chapters develop more detailed relations between soil and vegetation processes that control the land phase of the hydrologic cycle.

2.3 Hydrology and the Critical Zone

The Critical Zone (CZ) is “the heterogeneous, near surface environment in which complex interactions involving rock, soil, water, air and living organisms regulate the natural habitat and determine availability of life sustaining resources” (US National Research Council 2001).

The CZ extends from the top of the vegetation to the bottom of the aquifer (figure 2.46) and includes the near-surface biosphere and atmosphere, the pedosphere (the region in which soil-forming processes

operate), and the surface and near-surface portions of the hydrosphere and lithosphere. Water movement is the principal agent in transporting mass and energy through the CZ. Because of the importance of these exchange processes to natural processes and to human life, there is increasing interest in focusing on the CZ as an integrating, although heterogeneous, framework for scientific study (Wilding and Lin 2006; Lin 2010).

Most of the following chapters of this book focus on the detailed processes of water movement and storage in the CZ. In the remainder of this chapter we introduce the broad relations between climate, hydrology, and the major CZ components, soils (the pedosphere), and vegetation (the biosphere).

2.3.1 Hydrology, Soils, and Climate

2.3.1.1 Soils and Hydrology

The conditions at the soil surface are a major determinant of hydrologic response to rain or snowmelt, as they determine whether water input moves downslope to streams quickly over the surface, or infiltrates to become subsurface runoff, water used in

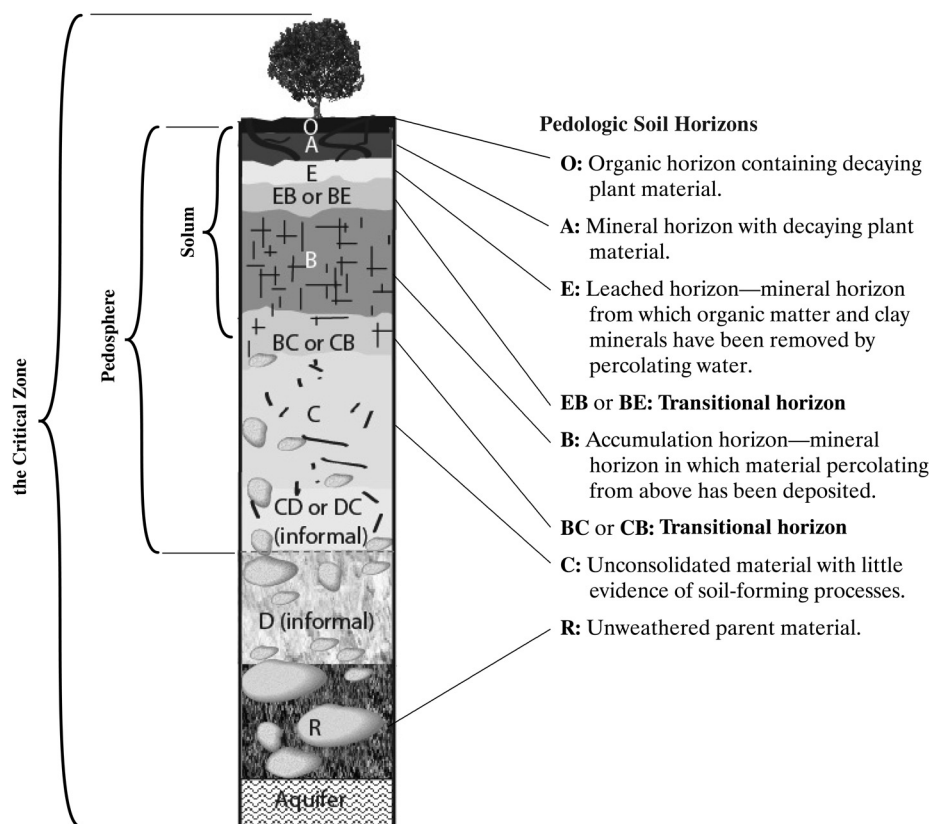


Figure 2.46
Components of the Critical Zone (CZ). The CZ extends from the top of the vegetation to the bottom of the aquifer and includes the near-surface biosphere and atmosphere, the pedosphere (the region in which soil-forming processes operate), and the surface and near-surface portions of the hydrosphere and lithosphere [adapted from Lin (2010)].

plant transpiration, or ground-water recharge. In addition, soil-moisture content of soils influences energy and moisture exchanges with the atmosphere (Dirmeyer 2011).

Quantitative relations describing how soil properties affect the infiltration, storage, and flow of water are the subject of chapters 7, 8, and 9; the relation of soil moisture to evapotranspiration is discussed in chapter 6. Here we introduce the major properties of soils that influence water movement through the land phase of the hydrologic cycle:

1. *Propensity for infiltration of water*, determined by the size and abundance of surface pores, which is a function of the type of geologic material present, biotic activity (presence of root holes and animal burrows), whether temperatures are above or below freezing (discussed further below), and slope (steeper slopes are more likely to shed surface water as surface runoff).
2. *Ability to transmit or retain infiltrated water*, determined by pore size (large pores more readily conduct water; smaller pores have a stronger tendency to retain water due to surface tension) and orientation (which influences whether water is transmitted vertically or parallel to the slope).
3. *Depth to the water table or to an impermeable surface*, which determines distance over which soil pores are available to store infiltrated water.

The seasonal or continuous occurrence of soil temperatures below 0°C is a climatic factor with important hydrologic implications, because water in the solid state is essentially immobile. However, the depth and extent of seasonal freezing are highly dependent on the severity of winter temperatures and on local surface conditions, especially vegetative cover and snow depth (snow is an effective insulator that can maintain above-freezing soil temperatures). **Permafrost** is the condition in which soils and/or their underlying parent materials remain at temperatures below 0°C continuously for more than two years, with only a thin surface layer thawing in the summer. Permafrost is almost always a barrier to the movement of water (Williams and van Everdingen 1973), so its presence controls the percolation of infiltrated water and the movement of ground water and thereby exerts a major influence on the hydrologic cycle (Dingman 1973).

2.3.1.2 Soil Formation and Classification

Soils are the central component of the CZ, and constitute a geomembrane across which water and

solutes, energy, gases, solids, and organisms are exchanged with the atmosphere, biosphere, hydrosphere, and lithosphere to create a life-sustaining environment (Lin 2010). Soil formation is essentially a hydrologic phenomenon, because soils are formed by the physical and chemical alteration of geologic materials associated with the downward percolation of water. The nature of the soil at any location is determined by

1. *Climate*: especially temperature and the amount and timing of liquid water availability;
2. *Parent material*: the physical and chemical nature of the geologic materials on which soil-forming processes operate;
3. *Biota*: the types of microorganisms and vegetation present, which mediate many chemical processes and affect the physical structure of soil;
4. *Topography*: particularly landscape position (ridge, slope, or valley); slope angle, which affects drainage; and slope aspect (direction), which affects microclimate; and
5. *Time*: over which soil-forming processes have been operating, determined by geologic history and disturbance by humans.

The operation of soil-forming processes over time produces the characteristic **soil horizons** shown in figure 2.46. A widely accepted taxonomy defines 12 **soil orders**, based largely on the degree of development of these horizons; the major features characterizing the soils in each order are given in table 2.14.

2.3.1.3 Global Distribution of Soil Orders

With the passage of time the influence of climate on soil type increases, reducing the influences of parent material and topography. Thus we would expect a reasonably strong relation between climate and soil type on a global scale. This is confirmed by table 2.14 and figure 2.47 (on p. 103), which shows the worldwide distribution of soil orders; this map can be compared with figures 2.14 and 2.23.

The occurrence of Entisols and some Inceptisols is determined primarily by recent geologic history and topography rather than climate, so soils of these orders are found in many regions. Note, however, that Inceptisols are widespread in the Arctic and subarctic, where soil-forming processes proceed only slowly. Inceptisols are also found on recent alluvial and colluvial deposits like those of the Mississippi and Amazon valleys and the Himalayas.

Table 2.14 Principal Characteristics of the 12 Soil Orders.

Order	General Features	Climate	Vegetation	Relief	Parent Material	Time	% Coverage of Global Land ^a
Alfisols	Thin O, thin A, thin to moderate E; B horizon (25–75 cm)	Tropical to temperate	Deciduous forest, grassland, prairie	Moderately well to moderately poorly drained	Varies	200 to 1,000 yr or longer	13.2
Andisols	Thick A, thin B, unaltered C	All except very cold	Variable	Variable, often on steep slopes	Volcanic ash, pumice, cinders, lava	< 100 yr	0.8
Aridisols	Surface crusts or pavements, little to no O	Cold and warm deserts	Desert plants	Flat terraces to steep slopes	Varies	10^4 to 10^6 yr	18.8
Entisols	Little development of soil horizons	All	Thin, often bare ground	Flat alluvium to steep slopes	Recent deposits, resistant rocks, disturbed material	Mostly recently exposed or deposited material	8.3
Gelisols	Thick O, permafrost < 2 m below surface; cryoturbation	Continuously below 0°C	Lichens, moss, tundra plants	Any; more common on north-facing slopes	Any	10^4 to 10^6 yr	17.8 ^b
Histosols	Thick O of slightly decayed plant material	> 80% of growing season has > 40 mm of rain	Bog, swamp, marsh plants	Flat	Lacustrine deposits	< 10 ⁴ yr	0.9
Inceptisols	Little development of soil horizons	All except arid	Usually forest; also grassland or prairie	Mostly steep slopes	Mostly recent glacial or fluvial deposits	< 10 ⁴ yr	8.9
Mollisols	O 45–75 cm of decomposed plants, granular A, blocky B	Warm to cold, precipitation > 200–800 mm/yr	Mostly prairie or grassland	Flat to gently rolling plains	Varies; often on glacial deposits	Varies	8.6
Oxisols	Thin O, intensely leached A (> 30 cm); highly permeable	Mostly wet tropical	Savannah to tropical rain forest	Level highlands or river terraces	Highly weathered sediments	5×10^4 to 10^5 or more yr	8.5
Spodosols	Well-developed O, A, E, and B	Mostly cool, humid; mid- to high latitude	Conifer and deciduous forest, heaths	Variable	Glacial till, other coarse-grained deposits	< 10 ⁴ yr	4.3
Ultisols	Thin O, well-developed B	Temperate to tropical; subhumid to humid	Mostly forest; some savannah	Variable	Siliceous igneous or sedimentary rocks	$\approx 10^4$ yr	5.6
Vertisols	Minimal horizon development; disturbed by shrink-swell processes	Variable, but with distinct wet/dry seasons	Mostly grassland and savannah; some forest	Gentle slopes	Variable, feldspar-rich or calcareous	< 10 ³ yr	1.8

^aValues from Donahue et al. (1983) except as noted.^bFrom Zhang et al. (2000).Source: Department of Soil Science, College of Agricultural and Life Sciences, University of Wisconsin-Madison (<http://www.soils.wisc.edu>).

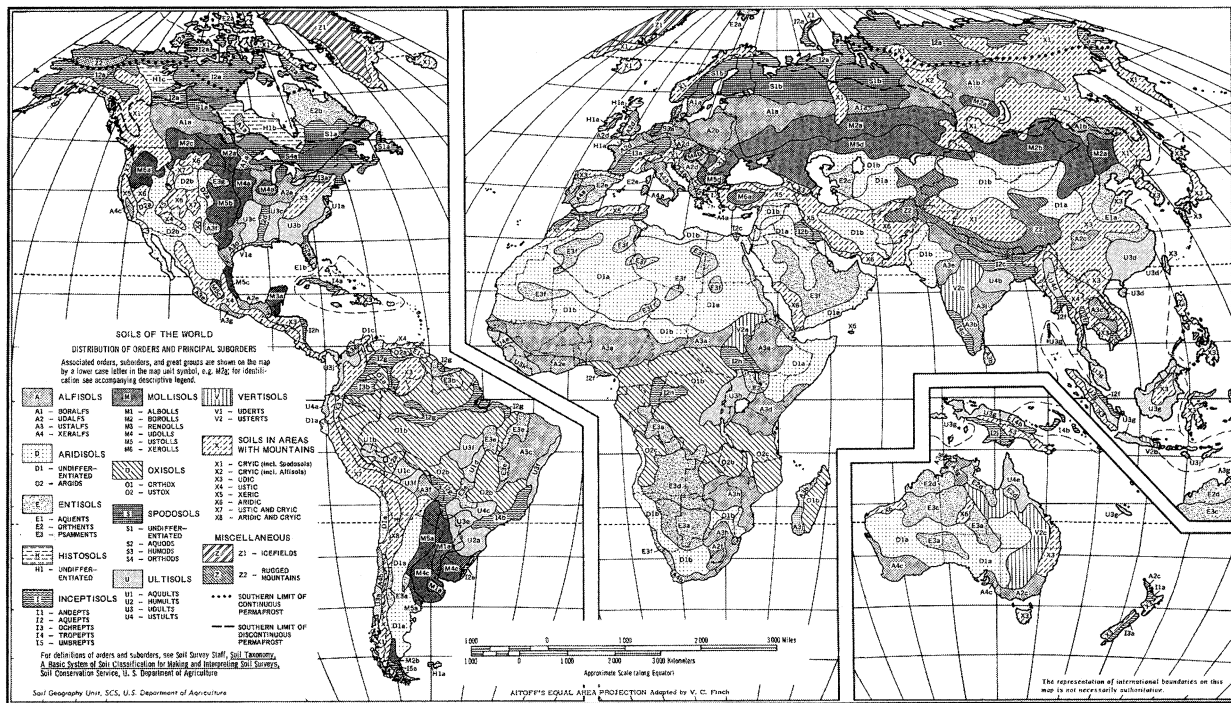


Figure 2.47 Global distribution of soil orders (map prepared by US Department of Agriculture). A larger-scale, color map can be viewed at http://www.nrcs.usda.gov/wps/portal/nrcs/detail/soils/use/?cid=nrcs142p2_054013.

The development of soils of the remaining orders is determined mostly by climatic factors, particularly annual temperature, annual precipitation, and seasonal distribution of precipitation. Brief descriptions of the distributions of these soils and their relation to climate are given below. Note that hydrologically significant seasonal freezing of soil occurs in many winters over much of the Northern Hemisphere land areas above 40° latitude (figure 2.47).

Alfisols are naturally fertile soils that occur in large regions to the north of the Mollisols in the Northern Hemisphere, as well as in several regions between about 35°N and S. These areas have sub-humid to humid climates, and typically support grassland, savanna, or hardwood forests.

Andisols form on recent volcanic deposits on which soil horizons are not highly developed. They are generally highly permeable.

Aridisols occur in desert regions, which are concentrated near 30° latitude. However, in South America the zone of Aridisols extends southward from 30° in the rain shadow of the Andes, and in

In Asia these soils are found near 40° in the shadow of the Himalayas.

Gelisols occur where permafrost is present within 2 m of the surface. Figure 2.47 delineates areas in which this condition is spatially continuous and those in which it is discontinuous; in the latter areas, permafrost is typically present under north-facing slopes and absent under south-facing slopes. Permafrost depths range from 60 to 90 m at the southern edge of the continuous-permafrost zone up to 1,000 m in northern Alaska and arctic Canada (Brown and Péwé 1973; Zhang et al. 2000).

Histosols are concentrated where more than 80% of the growing season (defined as months with average temperature $> 10^{\circ}\text{C}$) has > 40 mm of precipitation (Lottes and Ziegler 1994). The largest zones of Histosols are north of latitude 50°N (Canada, British Isles).

Mollisols, which include some of the naturally most productive, and hence most widely cultivated, soils, occur in climates ranging from temperate to cool and semiarid to humid. They are

concentrated in the grassland belts north of the Aridisols belts of the Northern Hemisphere, and are also found near 30°S in central South America.

Oxisols are excessively weathered soils confined to the tropical and subtropical rain forests on either side of the equator, where intense leaching has been occurring for long periods of geologic history.

Spodosols develop in well-drained sites in cool, wet climates under hardwood and conifer forests. They are widespread in the northeastern United States and southeastern Canada and in a large belt north of 60° latitude in Scandinavia and the former Soviet Union.

Ultisols are largely confined to within 20° of the equator, where climates are humid and subtropical or tropical and soil-forming processes are intense. There are also large areas of these soils in southeastern United States and southeastern China.

Vertisols form where geologic material weathers to clay minerals that swell when wet and shrink when dry, and their distribution is determined in part by the nature of the parent material. However, these soils are most commonly associated with climates that experience a pronounced alternation of wet and dry seasons.

Global maps of soil depth and soil moisture storage capacity can be viewed at <http://www.fao.org/nr/land/soils/en/>.

2.3.2 Hydrology, Vegetation, and Climate

2.3.2.1 Vegetation and Hydrology

Several aspects of vegetative structure directly affect hydrologic response. The main impact is on the water and energy balances of the land surface: Plant transpiration accounts for over 90% of water-vapor and latent-heat transfer from land globally, and exceeds runoff in most regions. Quantitative relations describing how plant properties affect the partitioning of the water and energy at the surface are presented in chapters 3, 5, and 6. Here we introduce the major properties of plants that influence the land phase of the hydrologic cycle:

1. *Fraction of ground shaded by leaves*, which is a function of plant type and spacing, determines the extent of the transpiring surface and the degree to which rain and snow are intercepted and retained to promptly evaporate.
2. *Plant height*, which is a function of plant type, determines the roughness of the surface, and

hence the efficacy of air turbulence in the exchange of water vapor and heat between the land and the atmosphere.

3. *Water conductance of leaves*, which is species dependent, exerts a strong control on the rate of transpiration.
4. *Areal extent of plant root systems and associated biota*, which have a major effect on surface porosity, and hence on the propensity for rain and snowmelt to infiltrate.
5. *Depth of root systems*, which is a determinant of the size of the soil-storage reservoir from which water is available for transpiration.

2.3.2.2 Biomes

Biomes (also called **ecoregions**) are major regions of broadly similar natural vegetation. Although there are many schemes for defining biomes, it is widely recognized that the distribution of major plant communities is controlled by climate. Whittaker (1975) identified six major structural types of land vegetation, which are based on the characteristics that most directly affect hydrologic response: plant height, leaf type, and plant spacing:

1. **Forest**—dominated by tall trees, generally closely spaced;
2. **Woodland**—dominated by small trees, generally widely spaced and with well-developed undergrowth;
3. **Shrubland**—dominated by shrubs, with total plant coverage exceeding 50% of the land area;
4. **Grassland**—two main types: tropical (savannas) or temperate;
5. **Scrubland**—dominated by shrubs, with plant coverage between 10 and 50%; and
6. **Desert**—with plant coverage below 10%.

In Whittaker's (1975) scheme, the occurrence of these structural types in various climatic zones produces 21 major terrestrial biomes (table 2.15) that are simply related to mean annual temperature and mean annual precipitation (figure 2.48). Note that vertical biome boundaries closely parallel lines of equal aridity index. The global distribution of Whittaker's biomes is shown in figure 2.49 on p. 106.

A more elaborate update of Whittaker's scheme utilizing somewhat different biome definitions has been developed by Olson et al. (2001); Milly and Shmakin (2002) and Bonan et al. (2002) relate numerical values of the hydrologically important

Table 2.15 Biome Types Identified by Whittaker (1975).^a

	Structural Types					
	Forest	Woodland	Shrubland	Grassland	Scrubland	Desert
Climatic Gradient	Tropical rain forest	Elfin woods	Temperate shrublands	Savanna	Warm semidesert scrublands	True deserts
	Tropical seasonal forests	Tropical broadleaf woodlands	Alpine shrublands	Temperate grasslands	Cool semideserts	Arctic-alpine deserts
	Temperate rain forests	Thornwoods	Tundra	Alpine grasslands	Arctic-alpine semideserts	
	Temperate deciduous forests	Temperate woodlands				
	Temperate evergreen forests					
	Taiga					

^aSee figure 2.48 for climatic ranges and figure 2.49 for global distribution.

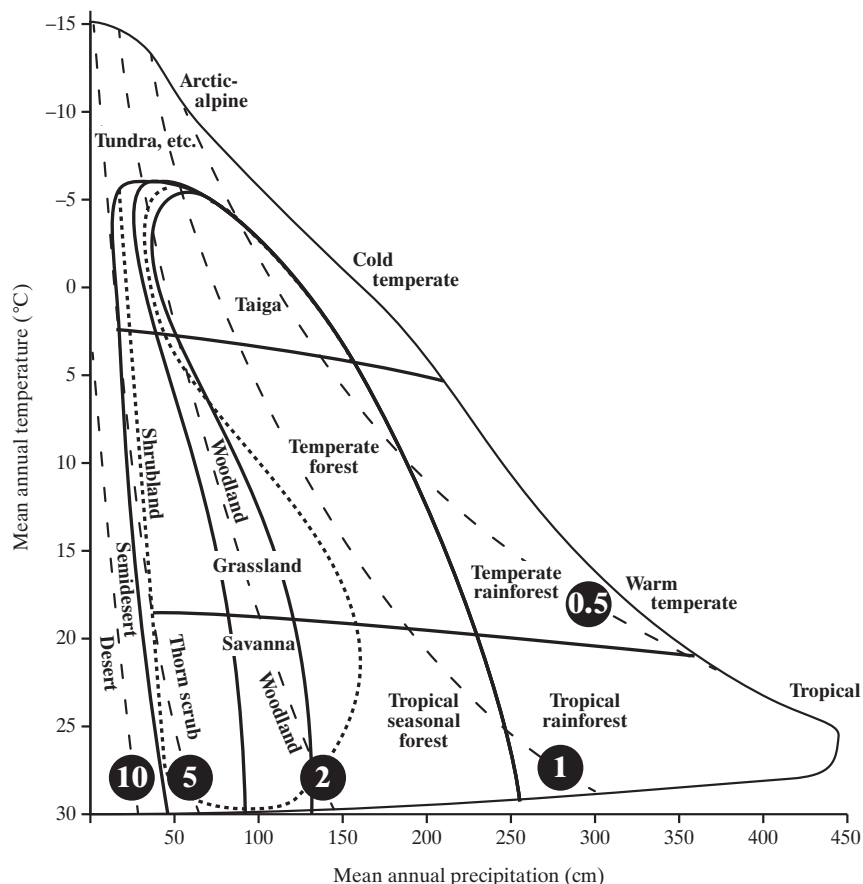


Figure 2.48 Relation of world biome types to mean annual temperature and mean annual precipitation. The aridity index (PET/P) is shown with long-dashed lines and circled numbers. For climates within the short-dash lines (maritime versus continental climates), soil types and fire history can shift the balance between woodland, shrubland, and grassland [adapted from Whittaker (1975)].



Figure 2.49 Global distribution of biome types identified by Whittaker (1975). Some biome types are combined for simplification (see table 2.15).

vegetation properties discussed in section 2.3.2.1 to biomes (see also table 6.4).

The exact mechanisms by which climate affects vegetation type are the object of current research. Ealeson (1982, 2004) has developed a theory in which climate, soil, and vegetative type evolve synergistically: In drier climates, where the availability of water is limiting, the character of the vegetative cover adjusts to maximize soil moisture; in moist climates where available radiant energy is limiting, there is an ecological pressure toward maximization of biomass

productivity. Studies using hydrometeorologic models suggest that vegetation type may be determined by the balance between precipitation and evapotranspiration, along with thermal controls on growth (Woodward 1987). In North America, Currie and Paquin (1987) found a high correlation between the numbers of tree species and average annual evapotranspiration in North America, and Wilf et al. (1998) documented a close relation between average leaf area and mean annual precipitation across a range of climates.

▼ EXERCISES

- Given the following representative temperatures:

	Average Earth Surface	Snow	Typical Cloud	Sun
Temperature (°C)	15	0	-20	6,000

- Calculate the rate of electromagnetic energy emission for each surface in W/m^2 , assuming all surfaces are blackbodies.
- Calculate the wavelength of maximum radiation in μm and determine the portion of the spectrum in which it occurs (figure 2.1).
- Consult the following websites and summarize information about the current and historical status of
 - ENSO and the relations between ENSO status and precipitation and temperature anomalies in the United States:
<http://www.pmel.noaa.gov/tao/elnino/1997.html>
<http://www.esrl.noaa.gov/psd/enso/mei/>
<http://www.cpc.ncep.noaa.gov/products/predictions/threats2/enso/elnino/index.shtml>
 - North Atlantic Oscillation (NAO) and the relations between NAO status and precipitation and temperature anomalies in the United States:
 NAO: <http://www.cpc.ncep.noaa.gov/data/teledoc/nao.shtml>
 - Pacific–North America Oscillation (PNA) and the relations between PNA status and precipitation and temperature anomalies in the United States:
 PNA <http://www.cpc.ncep.noaa.gov/data/teledoc/pna.shtml>
- Calculate the residence times for the global oceanic, atmospheric, and terrestrial reservoirs using the values in figure 2.20.
- Use the precipitation and runoff values in table 2.7 to estimate average annual evapotranspiration for each continent.
 - Do those estimates equal the estimates of evapotranspiration in the table?
 - If not, what might account for the differences?

5. The table below gives average precipitation, streamflow, and temperature for four large rivers.

Watershed	Area, A (km 2)	Average Precipitation, P (mm/yr)	Average Streamflow, Q (m 3 /s)	Average Temperature, T (°C)
Connecticut River, USA	20,370	1,100	386	10
Yukon River, Canada & USA	932,400	570	5,100	-5
Euphrates River, Iraq	261,100	300	911	17
Mekong River, Thailand	663,000	1,460	13,200	28

- a. For each watershed, estimate average potential evapotranspiration (PET) via equation (2B4.2) and determine whether each watershed is water-limited or energy-limited (section 2.2.8.3).
- b. Determine the value of the storage parameter w in equation (2.12) for each watershed. To do this, program a spreadsheet to solve equation (2.12) with trial values of w , using your answers from exercise 1.7 to give Q in mm/yr. Find the applicable value for each watershed by entering trial values of w until the quantity $\left|(\hat{R}O - RO)/RO\right| < 0.01$, where $\hat{R}O$ is the runoff estimated via equation (2.12).
6. For the region in which you live, or a specific watershed, obtain information from the US Geological Survey, US National Weather Service, and/or other appropriate federal or state sources to estimate the long-term average precipitation (P), runoff (RO), and temperature (T). Estimate the regional potential evapotranspiration PET using T in equation (2B4.2), or from other sources as given by your instructor. Then determine a best-fit value of the storage parameter w in the Budyko equation [equation (2.12)] by programming the equation in a spreadsheet and adjusting the value of w until the calculated value of RO most closely approximates the regional value.
7. Using the values determined in exercise 2.3 and/or 2.4,
- estimate the elasticity of runoff to precipitation via equation (2B4.1);
 - estimate the relative change in runoff due to a temperature increase of 1°C via equation (2B4.7).
8. For the region in which you live, obtain information from the US Natural Resources Conservation Service (formerly Soil Conservation Service) and/or other appropriate federal or state agencies to determine the dominant types of soils.
- Which of the 12 soil orders in table 2.14 do the dominant local soils belong to?
 - What are the main hydrologically relevant properties of the dominant local soils?
9. What type of natural vegetation dominates the region in which you live (see table 2.15)? Is this consistent with the average precipitation and temperature ranges shown in figure 2.48?
10. Using data from figure 2.20 and table 2B1.1,
- What fraction of the global annual runoff passes through your body in a year?
 - In a typical lifetime of 70 years, what fraction of the earth's fresh water passes through your body?
 - Assuming you use 100 gal/d of water for various purposes, what fraction of the global annual runoff do you use in a year?
 - What fraction of the earth's fresh water do you use in a lifetime?

▼ NOTES

¹ The term "El Niño" refers to the Christ child, and was given by Peruvian fishermen (whose catches were adversely affected by the phenomenon) because the unusual warming usually becomes pronounced around Christmas.

² The total volume of glacier ice was about twice its present value as recently as 18,000 years ago, when the last glaciation was at its peak; this produced a corresponding lowering of sea level.



Part II

Surface-Atmosphere Water and Energy Exchange

3



Principles and Processes

3.0 Introduction

Exchanges of water and energy between the surface and the atmosphere are central processes of the hydrologic cycle. Water is exchanged via precipitation and evaporation; energy exchanges occur via three modes: (1) electromagnetic radiation, (2) **sensible heat** (heat flows driven by temperature gradients), and (3) **latent heat** (heat flows accompanying vapor-liquid phase changes).

The laws of radiant-energy exchange and the composition and structure of the atmosphere were introduced in section 2.1. This chapter describes the basic physics of precipitation formation, evaporation, and sensible- and latent-heat exchanges between the surface and the atmosphere. We begin by describing the basic equations of state for atmospheric gases and introducing several quantities used to characterize atmospheric water-vapor content.

3.1 Pressure-Temperature-Density Relations

Air is a mixture of compressible gases (table 2.2), and the pressure at any altitude is determined by the weight of the overlying atmosphere. The rate

of change of pressure, p , with altitude z (figure 2.2) is given by the **hydrostatic relation**:

$$\frac{dp}{dz} = -\rho \cdot g, \quad (3.1)$$

where ρ is mass density and g is gravitational acceleration.

The pressure, absolute temperature, T , and density of a gas are related via the **ideal gas law**. Thus, for dry air (subscript da):

$$R_{da} = \frac{p}{T \cdot \rho_{da}}, \quad (3.2)$$

where R_{da} is the **gas constant** [$L^2 T^{-2} \Theta^{-1}$] = [$E M^{-1} \Theta^{-1}$], which depends on the molecular weight of the gas. For dry air, $R_{da} = 287 \text{ J/kg} \cdot \text{K}$ (table 3.1), and equation (3.2) relates the density of dry air at normal sea-level pressure ($p = 101.3 \text{ kPa}$) to absolute temperature as

$$\rho_{da} = \frac{352}{T}, \quad (3.3)$$

where ρ_{da} is in kg/m^3 (table 3.2). Similarly for water vapor (subscript v),

$$R_v = \frac{e}{T \cdot \rho_v}, \quad (3.4)$$

Table 3.1 Near-Surface Values of Physical Properties of Air.**Dry Air**

Molecular weight, M_{da}	= 28.966 g/mol
Density, ρ_{da}	= 1.292 kg/m ³
Gas constant, R_{da}	= 287.04 J/kg · K
Specific heat at constant pressure, c_p	= 1,005 J/kg · K

Water Vapor

Molecular weight, M_{H_2O}	= 18.016 g/mol
Gas constant, R_v	= 461.5 J/kg · K
Specific heat at constant pressure, c_p	= 1,846 J/kg · K

Source: List (1971).

where e is the **vapor pressure** (section 3.2.1) and $R_v = 461 \text{ J/kg} \cdot \text{K}$. The gas constants are related as

$$\frac{R_{da}}{R_v} = \frac{M_{H_2O}}{M_{da}} = \frac{18.0}{28.9} = 0.622, \quad (3.5)$$

where M_{H_2O} is the molecular weight of water and M_{da} is the effective molecular weight of dry air.

By virtue of their molecular motion and collisions, each constituent of a mixture of gases exerts a pressure, called a **partial pressure**, which is proportional to its concentration. The sum of the partial pressures of the gases in the atmosphere equals the total atmospheric pressure. The partial pressure of water vapor is called the **vapor pressure**, and is designated e [F L⁻²]. Treating air (subscript a) as a mixture of dry air and water vapor, **Dalton's law** gives the total pressure p as the sum of the partial pressures of the constituents:

$$p = p_{da} + e. \quad (3.6)$$

Combining (3.2), (3.4), (3.5), and (3.6),

$$\rho_a = \frac{p}{R_{da} \cdot T} \cdot \left(1 - 0.378 \cdot \frac{e}{p}\right). \quad (3.7)$$

Thus we see that moist air is *less dense* than dry air. However, the typical surface air pressure is $p \approx 10^5 \text{ Pa}$ while vapor pressures seldom exceed $7 \times 10^3 \text{ Pa}$, so the effect of water vapor on density can generally be neglected.

Because air has a low heat conductivity, a “parcel” of air that moves vertically does not immediately exchange heat with surrounding air and initially retains its original temperature; this is called an **adiabatic process**. However, the parcel becomes subject to the pressure of its new position: If it moves to a *higher* elevation, its pressure *decreases* and therefore its density and temperature also decrease to satisfy equation (3.7); this temperature decrease without loss of heat is **adiabatic cooling**. If it moves to a lower elevation, the converse happens and there is **adiabatic warming**. Under these conditions, it can be shown from the first law of thermodynamics, the ideal gas law, and the hydrostatic equation that the rate of change of temperature with elevation for dry air, Γ_{da} , is

$$\Gamma_{da} \equiv -\frac{dT}{dz} = \frac{g}{c_{pd}}, \quad (3.8)$$

where c_{pd} is the heat capacity of dry air at constant pressure. Γ_{da} is called the **dry adiabatic lapse rate**; the value of $c_{pd} = 1,005 \text{ J/kg} \cdot \text{K}$, so $\Gamma_{da} = 9.75 \times 10^{-3} \text{ K/m} = 9.75 \text{ K/km}$. Note that the lapse rate is defined as the *negative* of the vertical rate of change of temperature.

As shown in figure 2.2, the average near-surface rate of decrease of temperature with altitude is about $6.5 \text{ }^{\circ}\text{C}/\text{km}$, somewhat less steep than Γ_{da} . This is because the water vapor in ascending air parcels often cools to the point of condensation, liberating latent heat that raises the temperature. However, Γ_{da} is the rate at which a parcel of dry air cools/warms when it moves upward/downward in a turbulent eddy or when forced over a barrier, as long as any contained vapor does not condense.

3.2 Water Vapor

Water in vapor form consists of separate H₂O molecules mixed among the molecules of the other gases of the air. The amount of water vapor in the atmosphere is highly variable in time and space, and is of critical importance to the earth's energy balance (chapter 2), the formation of clouds and precipita-

Table 3.2 Density of Air, ρ_{da} , at Sea Level as a Function of Temperature, T [$p = 101.3 \text{ kPa}$].

$T (\text{ }^{\circ}\text{C})$	-20	-15	-10	-5	0	5	10	15	20	25	30
$\rho_{da} (\text{kg/m}^3)$	1.39	1.36	1.34	1.31	1.29	1.26	1.24	1.22	1.20	1.18	1.16

tion (section 3.4), and the dynamics of evapotranspiration (chapter 6). Depending on the context, the amount of water vapor may be quantified in the various ways described below.

3.2.1 Vapor Pressure

As noted, vapor pressure is the partial pressure of water vapor. The maximum vapor pressure that is thermodynamically stable is called the **saturation vapor pressure**, designated e^* . The saturation vapor pressure is a function only of temperature, T (figure 3.1); its value can be calculated as

Horizontal Liquid Surface ($T \geq 0^\circ\text{C}$):

$$e^* = 611 \cdot \exp\left(\frac{17.27 \cdot T}{T + 237.3}\right); \quad (3.9a)$$

Ice ($T \leq 0^\circ\text{C}$):

$$e^* = 611 \cdot \exp\left(\frac{21.87 \cdot T}{T + 265.5}\right), \quad (3.9b)$$

where e^* is in Pa and T is in $^\circ\text{C}$. Note that equations (3.9a) and (3.9b) are empirical relations that are sufficiently accurate for hydrologic computations.¹ The true relation between e^* and T is a complex formula called the Clausius–Clapeyron equation (box 2.2).

Under most natural conditions, e^* given by (3.9a) represents the maximum amount of water vapor that the atmosphere can hold at temperature T , and at that point the addition of more water vapor or

the lowering of the temperature usually results in **condensation** via the formation of liquid droplets or ice crystals (clouds or fog; see section 3.4).

3.2.2 Absolute Humidity

The **absolute humidity** (also called the **vapor density**), ρ_v , is the mass of water vapor per unit volume of air.

The ideal gas law [equation (3.4)] relates absolute humidity to vapor pressure:

$$\rho_v = \frac{e}{R_v \cdot T}. \quad (3.10)$$

3.2.3 Specific Humidity

Specific humidity (also called **mixing ratio**), q , is the concentration of water vapor expressed as the mass of water vapor per unit mass of dry air. Thus

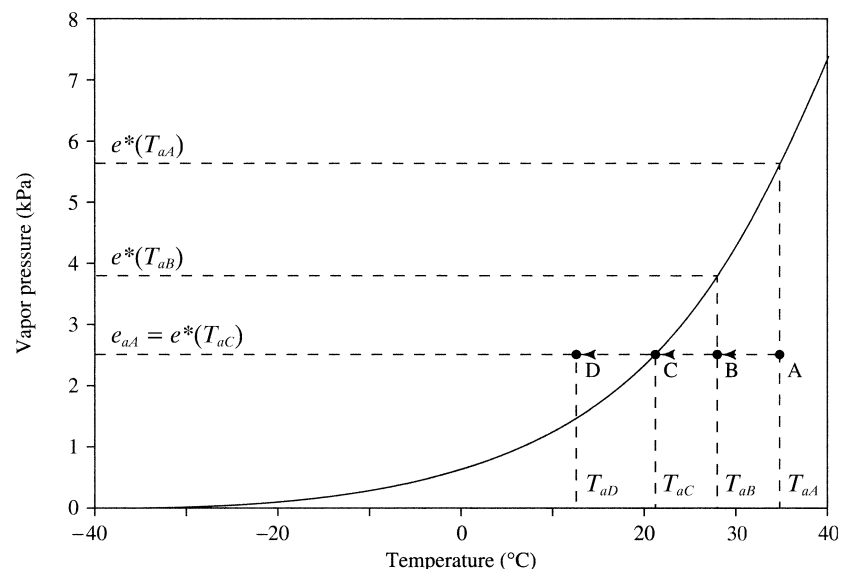
$$q = \frac{\rho_v}{\rho_{da}} = \frac{0.622 \cdot e}{p}. \quad (3.11)$$

3.2.4 Relative Humidity

The most familiar measure of the amount of water vapor in the atmosphere is the **relative humidity**, RH , which is the ratio (commonly expressed as a percent) of its actual vapor pressure, e , to the saturation vapor pressure at the prevailing temperature, e^* :

$$RH \equiv \frac{e}{e^*}. \quad (3.12)$$

Figure 3.1 The curve is the relation between saturation vapor pressure, $e^*(T_a)$, and air temperature, T_a , as given by equation (3.9a). The arrows trace the state of a parcel of air that initially has vapor pressure $e^*(T_{aA})$, temperature T_{aA} , and relative humidity $RH_A = e_{aA}/e^*(T_{aC})$ (point A). When the air is cooled to T_{aB} , its relative humidity has increased to $RH_B = e_{aB}/e^*(T_{aC})$; when it is cooled to T_{aC} , its relative humidity has increased to $RH_C = e_{aC}/e^*(T_{aC}) = 1$. T_{aC} is the dew point for this parcel of air. If cooled to T_{aD} without condensation, the parcel is supersaturated (point D).



In figure 3.1, point A represents the temperature and vapor pressure of an unsaturated “parcel” of air. If this parcel is now cooled (for example, by being forced to rise to a higher elevation), its state moves leftward, as indicated by the arrows. In this process, its vapor pressure does not change, but its relative humidity increases (point B). With further cooling to point C, the parcel has reached its saturation vapor pressure and its relative humidity is therefore 100%. As noted, cooling to this point usually results in condensation.

3.2.5 Dew Point

The temperature to which a parcel with a given vapor pressure has to be cooled in order to reach saturation (point C in figure 3.1) is called the **dew point**, T_{dp} .

The dew point is a direct measure of the amount of water vapor in the air, and it can be calculated from equation (3.9a) as

$$T_{dp} = \frac{\ln(e) - 6.415}{0.0999 - 0.00421 \cdot \ln(e)}. \quad (3.13)$$

where T_{dp} is in °C and e is in Pa.

As noted above, under most natural conditions the cooling of air to its dew point induces condensation. However, it is possible to cool a parcel of air below its dew point without causing condensation. Under these conditions the air is **supersaturated**, and its state is represented by a point above the curve in figure 3.1 (e.g., point D). Although supersaturation in clouds rarely exceeds 1% (Barry and Chorley 1987), it may have an important influence on precipitation formation (section 3.4).

3.2.6 Precipitable Water

Precipitable water, W , is the amount of water vapor in a column of the atmosphere of unit area extending from the surface to the top of the atmosphere, i.e.,

$$W \equiv \frac{1}{\rho_w} \cdot \int_0^{Z_A} \rho_v(z) \cdot dz, \quad (3.14)$$

where ρ_w is the mass density of liquid water, z is elevation, and Z_A is the height of the atmosphere (troposphere). Note that the dimensions of W are [L], and it represents the depth of water that would result from the complete condensation and precipitation of all the water vapor above a particular location at a particular time.

The average annual precipitable water content varies globally from about 2.5 mm in polar regions to

over 50 mm in the tropics (Peixoto and Oort 1992). Yang and Koike (2005) derived a semi-empirical formula for estimating precipitable water as a function of near-surface air temperature, T_a , and relative humidity, $RH(\%)$:

$$W = 0.0493 \cdot \left(\frac{RH}{T_a} \right) \cdot \exp \left(26.23 - \frac{5,416}{T_a} \right), \quad (3.15)$$

where W is in mm.

3.3 The Evaporation Process

3.3.1 Vapor Exchange

The process of evaporation is physically the same for cloud droplets, open-water surfaces, plant tissues (**transpiration**), soil pores, and water in its frozen state. In figure 3.2, initially dry air with a temperature of T_a lies above a horizontal water surface with a temperature of T_s . The molecules at the surface are attracted to those in the body of the liquid by hydrogen bonds, but some of the surface molecules have sufficient energy to sever the bonds and enter the thin layer of air just above the surface. The number of molecules with this “escape energy” increases as T_s increases. The water molecules entering the surface layer move in random motion, and as these molecules accumulate in the layer, some will re-enter the liquid. The rate at which they re-enter is proportional to the concentration of molecules in the layer. An equilibrium is soon reached, at which the rates of escape and re-entry are equal and the vapor pressure in the layer immediately above the surface is equal to the saturation vapor pressure, e_s^* , at the temperature of the surface, T_s . The relation between e_s^* and T_s is given by equation (3.9a).

Molecules moving into the air above the surface layer are subject to dispersion away from the surface by turbulent eddies. Under given wind and temperature conditions their concentration at a reference level reaches a steady-state vapor pressure, e_a .

The rate of evaporation E is the net rate at which molecules move from the saturated surface layer into the air above, and that rate is proportional to the difference between the vapor pressure of the surface layer and the vapor pressure of the overlying air:

$$E \propto (e_s^* - e_a). \quad (3.16)$$

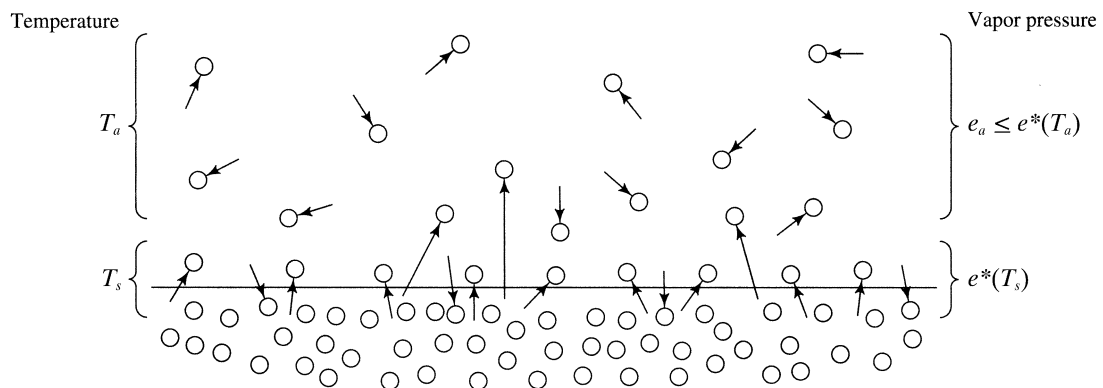


Figure 3.2 Schematic diagram of flux of water molecules over a water surface. The vapor pressure at the surface is equal to the saturation vapor pressure, e_s^* , at the temperature of the surface, T_s ; the vapor pressure of the overlying air is e_a . The evaporation rate is proportional to $(e_s^* - e_a)$; if $e_a > e_s^*$, condensation occurs.

The proportionality factor depends on the reference height and on the factors controlling the diffusion of water vapor in the air, principally the wind velocity and the nature of the surface, as described in detail in section 3.5. Equation (3.16) is the basis for the *mass-transfer approach* for estimating evapotranspiration (sections 3.5.3.4 and 6.3.2).

Equation (3.16) is straightforward, but note that

Depending on the temperature of the surface and the temperature and humidity of the air, the difference between the two vapor pressures can be positive, zero, or negative, and

1. if $e_s^* > e_a$, evaporation is occurring;
 2. if $e_s^* < e_a$, water is condensing on the surface; and
 3. if $e_s^* = e_a$, neither condensation or evaporation is occurring.
-

Note also that the value of e_a can be less than or equal to the saturation vapor pressure at the air temperature, e_s^* (i.e., relative humidity can be less than or equal to 100%), and

Evaporation will occur even if the relative humidity equals 100%, as long as $e_s^* > e_a$.

When humidity is 100% ($e_a = e_s^*$), the evaporating water will normally condense in the overlying air to form a fog or mist.

For most situations of hydrologic interest, the evaporating surface is essentially horizontal, so that the number of water molecules just below the surface is the same as in the surface. However, in tiny spherical cloud droplets, there are more molecules in the surface than in the next layer below. Because of this, the intermolecular hydrogen-bond forces acting on the surface molecules are weaker than for a horizontal surface. Thus the vapor pressure at the surface of a very small droplet is higher than given by equation (3.9a) for a horizontal surface, and there is a correspondingly greater tendency for the molecules to evaporate.

Evaporation occurs in exactly the same way whether the underlying surface is liquid water or ice (snow). The only difference between the two situations is that the saturation vapor pressure for an ice surface at a given temperature is slightly lower [equation (3.9b)] (figure 3.3). This has important implications for the formation of precipitation (section 3.4.3).

3.3.2 Latent Heat

The **latent heat of vaporization**, λ_v , is the quantity of heat energy that must be absorbed to break the hydrogen bonds when evaporation takes place; this same quantity is released when the bonds are re-formed upon condensation. Thus

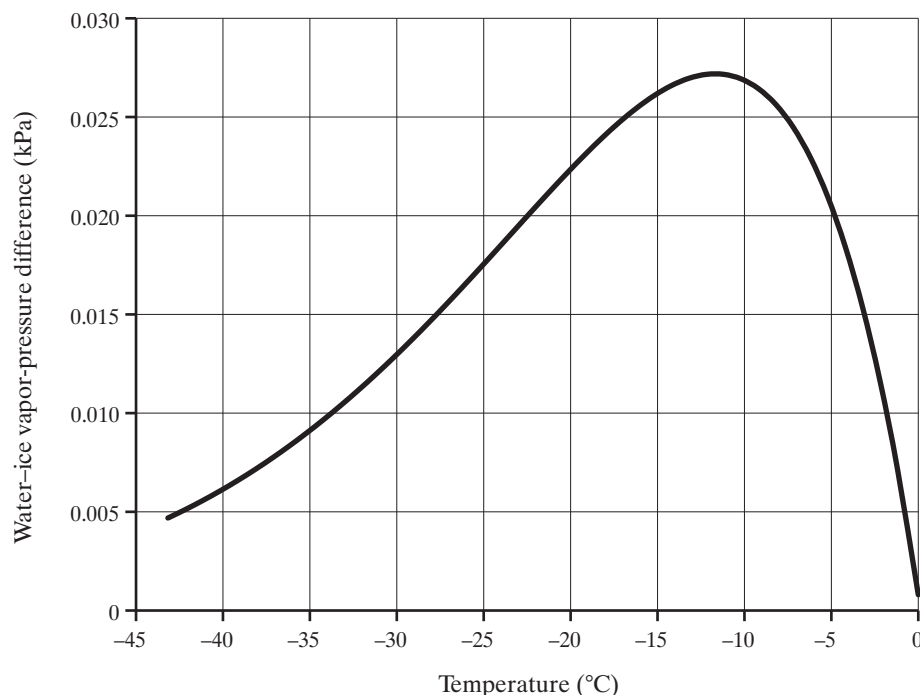


Figure 3.3 Difference between saturation vapor pressure over liquid water [equation (3.9a)] and ice [equation (3.9b)] at temperatures below 0°C.

- Evaporation is always accompanied by a transfer of heat out of the evaporating surface; i.e., the surface cools.
- Condensation in the atmosphere is always accompanied by a transfer of heat into the air; i.e., the air warms.
- Condensation on the surface is always accompanied by transfer of heat to the surface; i.e., the surface warms.

This process is called **latent-heat exchange**.

Because of this coupling, the rates of latent-heat and mass (water) transfer are directly proportional. When the underlying surface is liquid water,

$$\lambda E = \lambda_v \cdot \rho_w \cdot E, \quad (3.17)$$

where λE is the rate of latent-heat transfer per unit area per unit time [$E L^{-2} T^{-1}$], E is the rate of evaporation or condensation [$L T^{-1}$], ρ_w is the density of water [$M L^{-3}$], and λ_v is the latent heat of vaporization [$E M^{-1}$]. The latent heat decreases slightly with the temperature of the evaporating surface, T_s , approximately as

$$\lambda_v = 2,501 - 0.00236 \cdot T_s, \quad (3.18)$$

where λ_v is in MJ/kg and T_s is in °C (Shuttleworth 1992).

If the underlying surface is snow or ice, energy is required to disrupt the molecular structure of ice as well as to sever hydrogen bonds with neighboring molecules; this phenomenon is called **sublimation**. Thus in this case latent-heat transfer involves the latent heat of fusion, λ_f , as well as the latent heat of vaporization:

$$\lambda E = (\lambda_v + \lambda_f) \cdot \rho_w \cdot E, \quad (3.19)$$

where $\lambda_f = 0.334 \text{ MJ/kg}$. λ_f is not a function of temperature, because melting takes place at 0°C at atmospheric pressure. The sum $\lambda_v + \lambda_f$ is the **latent heat of sublimation**.

3.4 The Precipitation Process

In order to produce hydrologically significant rates of precipitation, a sequence of four processes must occur: (1) cooling to the dew point; (2) condensation; (3) droplet growth; and (4) importation of water vapor. An introductory examination of these processes will help the hydrologist understand regional and seasonal patterns of inputs to the hydrologic cycle, the potential effects of local and global climate perturbations on those patterns, the ways in which atmospheric pollutants may affect precipitation (e.g., acid rain), and attempts to manage precipi-

tation as a water-resource-management strategy (e.g., cloud seeding).

3.4.1 Cooling

To begin the formation of precipitation, air containing water vapor must be cooled to its dew point. A parcel of air can lose heat by: (1) radiation to cooler surroundings; (2) mixing with a cooler body of air; (3) conduction to a cool surface (e.g., cool ocean water or snow); (4) adiabatic cooling by horizontal movement to a region of lower pressure; and (5) adiabatic cooling by vertical uplift. Cooling by the first four of these processes may produce fog or drizzle, but

Only vertical uplift can cause rates of cooling high enough to produce significant precipitation.

Figure 3.4 shows how the temperature and specific volume (inverse of density) of a parcel of air change adiabatically as it is vertically displaced: If no condensation occurs (figure 3.4a), its temperature will decrease at the dry adiabatic lapse rate, $\Gamma_{da} \approx 1^\circ\text{C}/100 \text{ m}$. If condensation occurs (figure 3.4b), its temperature will decrease at a lower rate due to the liberation of latent heat. This **saturated adiabatic lapse rate**, Γ_s , varies with temperature, initial vapor pressure, and elevation, but is typically about one-half the dry rate: $\Gamma_s \approx 0.5^\circ\text{C}/100 \text{ m}$. The average lapse rate in the troposphere, about $0.65^\circ\text{C}/100 \text{ m}$ (figure 2.2), is a weighted average of the dry and saturated lapse rates.

The meteorological situations that can produce significant rates of uplift and adiabatic cooling are discussed in chapter 4; uplift rates range from about 1 m/s along frontal surfaces to as much as 30 m/s in thunderstorm cells.

3.4.2 Condensation

When air above the freezing point is cooled to the dew point, liquid water is thermodynamically stable and randomly colliding water-vapor molecules tend to form tiny droplets. However, as described in section 3.3.1, a small spherical droplet has a high tendency to evaporate because the ratio of the number of molecules in the surface layer to the number just below the surface is high, producing a high vapor pressure. As the droplet diameter increases, this ratio decreases, so that there are relatively more hydrogen bonds holding the molecules in the outer layer, decreasing the vapor pressure. Thus very small

cloud droplets are unstable, and some 10^8 molecules must collect to form a stable droplet of about 10^{-4} mm diameter. The chance of this happening by random collision is effectively zero, and

In order for condensation to occur when the dew point is reached, water-molecule-attracting particles larger than 10^{-4} mm must be present to provide substrates. These particles are called **cloud condensation nuclei (CCN)**.

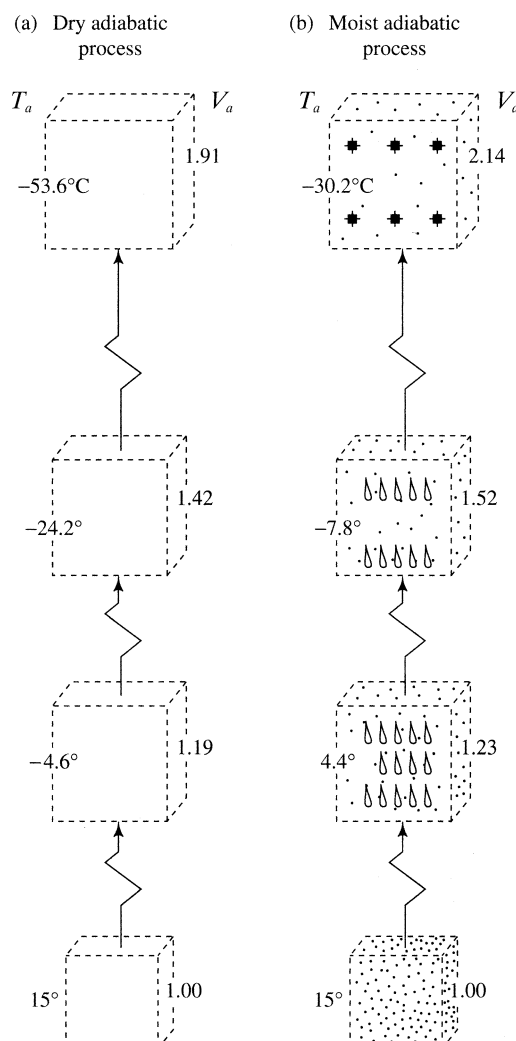


Figure 3.4 Adiabatic expansion and cooling during uplift of (a) air in which no condensation occurs and (b) air saturated at 15°C . T_a is air temperature and V_a is relative volume ($= 1/\rho_a$) [adapted from Miller et al. (1983)].

Air usually contains hundreds of CCN per cubic centimeter. The major natural sources of CCN are meteoric dust, windblown clay and silt, volcanic material, smoke from forest fires, and sea salt.² It is estimated that the natural concentrations of CCN are 50 to 100 per cubic centimeter (cm^{-3}) over the oceans, and about 400 to 500 cm^{-3} or more over the continents (Wallace and Hobbs 1977). Human activities produce CCN (chiefly combustion products, including the sulfur and nitrogen compounds that produce acid precipitation) in concentrations of 3,500 cm^{-3} or more. Radke and Hobbs (1976) estimated that the global anthropogenic production rate of CCN may be comparable to the natural production rate. In some industrial areas most CCN are anthropogenic and concentrations can reach 30,000 cm^{-3} (Miller et al. 1983).

Condensation releases latent heat that was removed from the surface when the water evaporated, and the evaporation/condensation process is an important mechanism of energy exchange between the surface and the atmosphere. Furthermore, the liberation of latent heat in condensation produces a positive feedback that tends to sustain the precipitation process by warming the surrounding air, reducing its density, and increasing its tendency to rise, cool, and produce more condensation.

3.4.3 Droplet Growth

The preceding discussion shows that condensation to form clouds occurs when: (1) water vapor is present; (2) there is a sufficient degree of uplift to bring about cooling to the dew point; and (3) sufficient CCN are present. This condensation forms cloud droplets with diameters in the range 0.001 to 0.2 mm (figure 3.5); droplets of this size range have fall velocities less than 0.7 m/s. Thus,

In order for precipitation to fall from clouds to earth, some droplets must grow to a size such that their fall velocity exceeds the rate of uplift (usually greater than 1 m/s) and such that they can survive evaporation as they fall.

There are two processes by which cloud droplets can grow several orders of magnitude to form raindrops of 0.4 to 4 mm diameter, or snowflakes of even larger size:

1. **Droplet collision** occurs at temperatures above 0°C because condensation on CCN produces cloud-water droplets of varying sizes.

The larger droplets have larger fall velocities than the smaller ones and, because of this velocity dif-

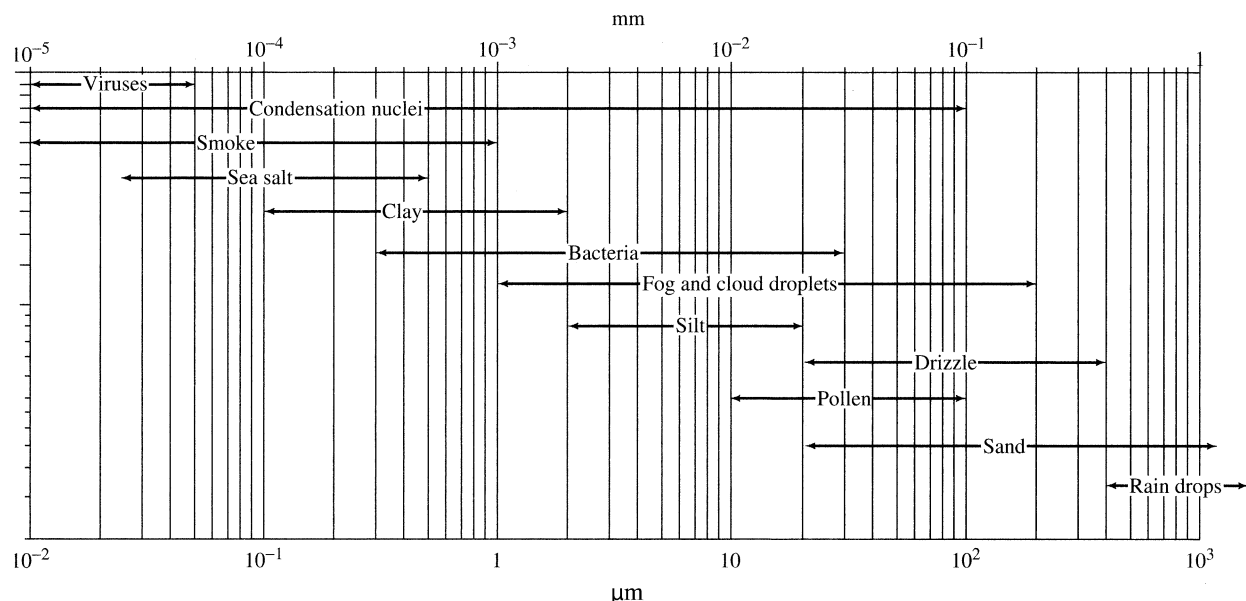


Figure 3.5 Size ranges of nongaseous atmospheric constituents (logarithmic scale) [data from Miller et al. (1983)].

ferential, collisions occur between falling droplets of different sizes. Many of these collisions result in the coalescence of the two droplets and hence the gradual growth of the larger ones. Ultimately these become large enough to fall out of the cloud.

2. Ice-crystal growth

occurs in clouds at temperatures below 0°C.

Typically, there are relatively few CCN present that are effective seeds for direct condensation as ice crystals, such as clay minerals. Thus at below-freezing temperatures, condensation as super-cooled liquid water on other types of CCN initially dominates. In the resulting mixture of ice crystals and water droplets, the saturation vapor pressure of an ice surface at a given temperature is somewhat less than the saturation vapor pressure of a liquid-water surface at that temperature (figure 3.3). This differential causes H₂O molecules to evaporate from the liquid particles and condense as ice on the ice crystals. The ice crystals thus tend to grow at the expense of the liquid droplets, and eventually acquire a size and fall velocity that allows them to fall through the cloud as snowflakes. Further growth by collision may also occur as the flakes fall. If the temperature below the cloud is above 0°C, the snowflakes will melt and reach the earth as raindrops; otherwise they will fall as snow.

3.4.4 Importation of Water Vapor

The concentration of liquid water and/or ice in most clouds is in the range of 0.1 to 1 g/m³ (Gilman 1964). The following computation will show that even if all the water in a very thick cloud at a given time were to fall as rain, the total depth of precipitation would be relatively small:

Consider a 10,000-m thick cumulonimbus (i.e., thunderhead) cloud, such that the total cloud volume above each 1 m² of ground surface is 10,000 m³. If the concentration of water substance in the cloud is 1 g/m³, the total volume of cloud water above each 1 m² is 10,000 cm³. If all this water fell as precipitation, its depth would be 1 cm. This value—a moderate rainfall—represents a near maximum for the amount of precipitation produced by all the water initially present in a cloud at a given time.

Thus, since most rain-producing clouds are much less than 10,000 m in thickness and have water concentrations less than 1 g/m³, a final requirement for the production of significant amounts of precipitation is that

A continual supply of water vapor must be imported into the cloud by converging winds to replace that which falls out (figure 3.6).

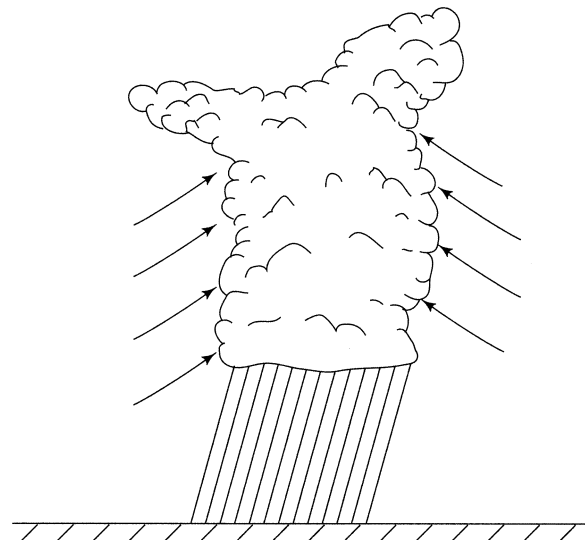


Figure 3.6 In order to produce significant amounts of precipitation, vapor-bearing winds must provide a continual supply of water to precipitation-producing clouds.

3.5 Turbulent Exchange of Momentum, Mass, and Energy

The large-scale vertical structure of the atmosphere was described in section 2.1.2.2. The planetary boundary layer is the region in which the atmosphere is affected by the surface; its thickness ranges from a few tens of meters to one or two kilometers, depending on the general topography, the nature of the surface, the wind velocity, surface and air temperatures, solar radiation, and other factors.

The dynamic structure of the lowest part of the planetary boundary layer is shown in figure 3.7. This is the **mixed layer** (or **Prandtl layer**), which is strongly affected by turbulent eddies caused by

1. **forced convection** due to surface-frictional effects on winds, and/or
2. **free, or thermal, convection** due to heating by the surface.

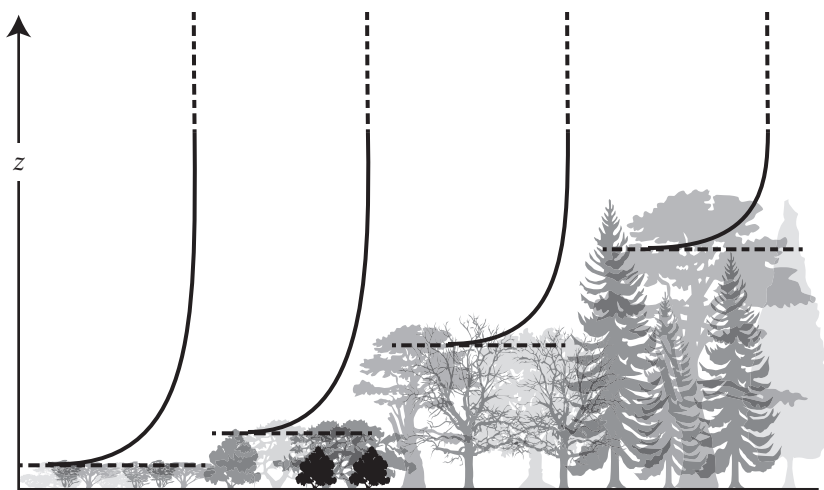


Figure 3.7 Schematic diagram of velocity profiles in the lowest portion of the planetary boundary layer for surfaces of varying roughness (not to scale). z is elevation. This is the layer in which the surface directly affects atmospheric dynamics that control surface-atmosphere exchanges of heat and water vapor. It consists of the **interfacial sublayer**, which extends from the surface to the horizontal dashed lines, where the wind velocity is zero. Above this is the turbulent **mixed layer** in which velocity increases upward (solid curves show the velocity profile).

Turbulence is characterized by chaotic eddies with strong vertical components that mix the air (figures 3.8 and 3.9), transferring water vapor and latent and sensible heat between the surface and the atmosphere in a process called **turbulent diffusion**. This section describes how turbulent-diffusion processes are quantified, which is an essential basis for understanding and modeling snowmelt (chapter 5) and evapotranspiration (chapter 6).

3.5.1 Turbulence

We first consider turbulence generated only by surface-frictional forces acting on a steady horizontal wind (forced convection) when the effects of density differences on vertical motion are negligible. Later we consider how buoyancy effects may enhance or suppress frictionally generated turbulence (section 3.5.3.7).

If the surface is very smooth, there is an extremely thin ($< 1 \text{ mm}$) layer in which the air's viscosity creates a frictional drag. More commonly this layer is absent and the surface friction is due to the roughness of vegetation or water waves. In either case the friction produces a surface at which the wind velocity is zero (horizontal dashed lines in figure 3.7); this is called the **virtual surface**. Below the virtual surface height is the **interfacial sublayer** (Brutsaert 1992), in which surface roughness elements suppress turbulence. Above the viscous layer or the roughness features, the gradient of upward-increasing vertical velocity induces a layer of pronounced turbulence that defines the mixed layer,

which is typically some tens of meters thick. Vertical fluxes of heat and water vapor are essentially constant throughout this layer.

Consider a land surface across which a steady wind is blowing. Because of turbulent eddies, the instantaneous horizontal wind velocity, $u(z)$, at any level z above the virtual surface fluctuates in time. We can describe this situation by separating the instantaneous velocity into a time-averaged component, $\bar{u}(z)$, and a deviation from that average caused by the eddies, $u'(z)$, so that at any instant

$$u(z) = \bar{u}(z) + u'(z), \quad (3.20)$$

where $u'(z)$ may be positive or negative and the overbar denotes time-averaging. By definition the time-averaged value of the fluctuations equals zero, so

$$\bar{u}'(z) = 0, \quad (3.21)$$

and

$$\overline{\bar{u}(z) + u'(z)} = \overline{\bar{u}(z)} + \overline{u'(z)} = \overline{\bar{u}(z)}. \quad (3.22)$$

At any level, the wind speed $\bar{u}(z)$ is the velocity averaged over a time period appropriate for defining the “prevailing conditions” for the analysis (typically one hour to one day). To simplify the notation, we will henceforth use the symbol $u(z)$ rather than $\bar{u}(z)$ to denote this time average.

Turbulent eddies have a pronounced vertical component, so turbulence is also reflected in a time-varying *vertical* air velocity at a given level, designated $v(z)$. This component can be similarly sep-

rated into a time-averaged component, $\overline{v(z)}$, and an instantaneous deviation from that average, $v'(z)$:

$$v(z) = \overline{v(z)} + v'(z). \quad (3.23)$$

However, there is no net vertical air movement, so the time average of both components is zero, i.e.,

$$\overline{v(z)} = 0 \quad (3.24)$$

and

$$\overline{v'(z)} = 0. \quad (3.25)$$

Because the average wind speed $u(z)$ increases upward in the mixed layer, a parcel of air moving upward [i.e., with $v'(z) > 0$] at a given instant has a lower horizontal velocity than the average at the new level. This momentarily reduces the horizontal velocity at that level, so that $u'(z) < 0$. Conversely, a parcel moving downward [$v'(z) < 0$] tends to increase the velocity at the lower level [$u'(z) > 0$]. Thus the instantaneous vertical and horizontal velocity fluctuations at a given level have the opposite sign, are negatively correlated, and operate to reduce the vertical velocity gradient. The observed vertical gradient

Figure 3.8 Conceptual diagram of the process of momentum transfer by turbulent diffusion. Friction caused by surface roughness reduces average wind velocities (straight arrows) near the surface and produces turbulent eddies (circular arrows), resulting in a net downward transfer of momentum. The vertical component of the eddies transports heat and water vapor upward or downward depending on the directions of temperature and vapor-pressure gradients.

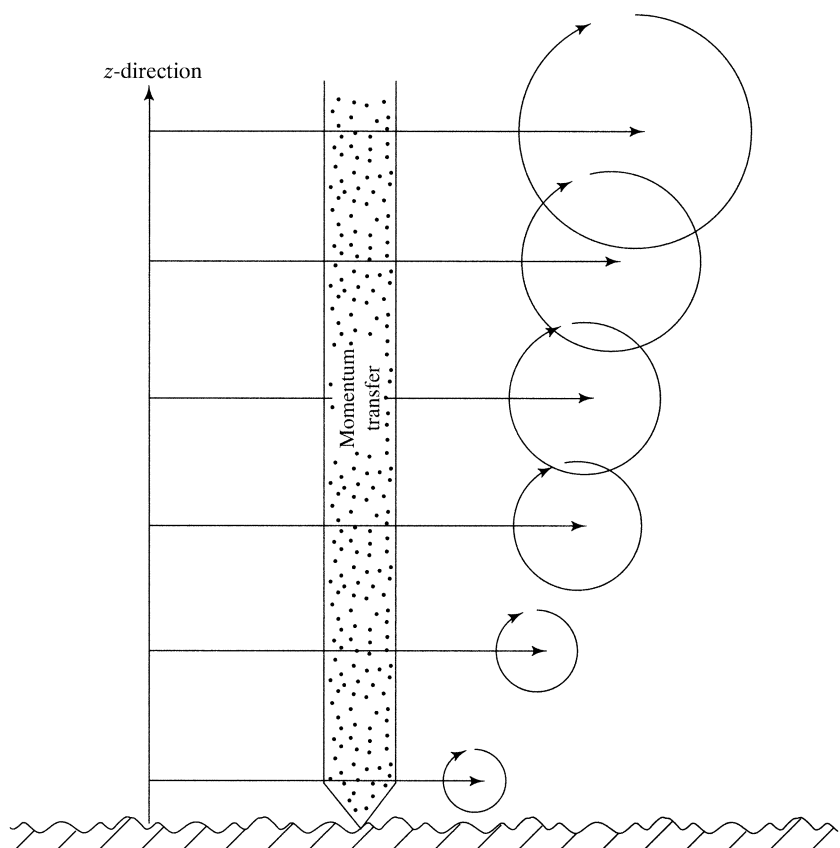
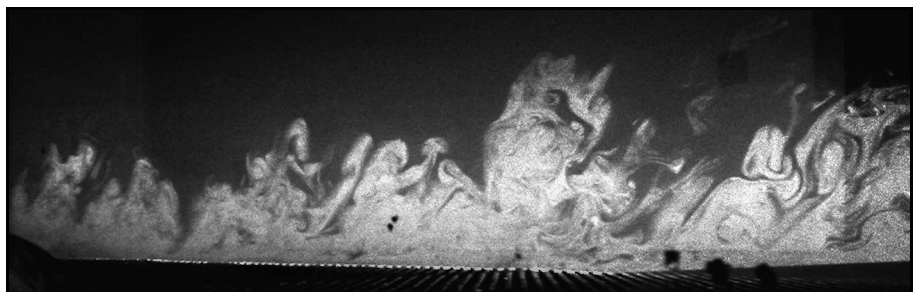


Figure 3.9 Turbulence generated by boundary friction in laboratory flows of air in wind tunnels. Flow is from left to right. Turbulence is made visible by injecting oil droplets into the flow (image courtesy of Fernando Porté-Agel).



of average velocity $du(z)/dz$ is the result of this turbulent mixing of momentum.

The intensity of turbulence is proportional to the magnitude of the velocity fluctuations, and the negative correlation between the horizontal and vertical fluctuations allows us to characterize that intensity by a quantity called the **friction velocity**, u_* , defined as

$$u_* \equiv \left(-\overline{u' \cdot v'} \right)^{1/2}, \quad (3.26)$$

where the minus sign is required because simultaneous values of u' and v' have opposite signs.³ For forced convection within the mixed layer,

The friction velocity is a constant for a steady wind blowing over a given surface,

i.e., u_* is not a function of z . As will be shown in the following discussion, the friction velocity can be evaluated from measurements of the vertical velocity distribution and is a critical parameter in characterizing the exchanges of water vapor and energy between the surface and the atmosphere.

3.5.2 Vertical Distribution of Wind Velocity

Theoretical considerations and measurements in the mixed layer show that for a steady wind blowing over a given surface,

The vertical distribution of horizontal wind velocity near the surface can be well represented by a logarithmic relation:

$$u(z) = \frac{1}{\kappa} \cdot u_* \cdot \ln \left(\frac{z - z_d}{z_0} \right), \quad (3.27)$$

$$z_d + z_0 \leq z < z_{ml},$$

where $u(z)$ is the appropriately time-averaged velocity at height z above the ground surface, u_* is the friction velocity, κ is a dimensionless constant, the height z_d is called the **zero-plane displacement height**, z_0 is the **roughness height**, and z_{ml} is the height of the top of the mixed layer.

Figure 3.10 shows the general form of the velocity distribution described by equation (3.27). The relation was formulated and experimentally verified in the early twentieth century by Ludwig Prandtl and

his student Theodore von Kármán, and is known as the **Prandtl–von Kármán universal velocity distribution**. It is universal because it describes turbulent flows over boundaries in any situation, including water flow in rivers and air flow over airplane wings. Experiments show that $\kappa = 0.4$ in most situations, and that z_d and z_0 can be taken to be proportional to the average height of the roughness elements on the surface. Table 3.3 gives typical z_0 values for various surfaces, and we will usually estimate z_d and z_0 for vegetated surfaces as

$$z_d = 0.7 \cdot z_{veg} \quad (3.28)$$

and

$$z_0 = 0.1 \cdot z_{veg}, \quad (3.29)$$

where z_{veg} is the average vegetation height. Note from (3.27) that $u(z) = 0$ at $z = z_d + z_0$, which is the virtual surface. Using (3.28) and (3.29), this level is at $z = 0.8 \cdot z_{veg}$.

Elaborate instrumentation to record the rapid fluctuations of horizontal and vertical velocity is required to determine u_* via equation (3.26). Fortunately, we can also evaluate u_* in a given situation from measurements of average wind velocity using equation (3.27): If we measure velocity at a single height, designated z_m , where $z_m > z_d + z_0$, then

$$u_* = \frac{\kappa \cdot u(z_m)}{\ln \left(\frac{z_m - z_d}{z_0} \right)}. \quad (3.30a)$$

Alternatively, if we measure velocity at two heights, denoted z_2 and z_1 , where $z_2 > z_1 > z_d + z_0$, then

$$u_* = \frac{\kappa \cdot [u(z_2) - u(z_1)]}{\ln \left(\frac{z_2 - z_d}{z_1 - z_d} \right)}. \quad (3.30b)$$

Figure 3.11 on p. 124 shows the velocity profiles when a given velocity is measured at a fixed height above two different vegetation heights, as in the example of box 3.1, also on p. 124.

3.5.3 Turbulent Diffusion

3.5.3.1 Diffusion

Diffusion is the process by which constituents of a fluid, such as its momentum, heat content, or a dissolved or suspended constituent, are transferred from one position to another within the fluid. Such transfers occur whenever there are differences in

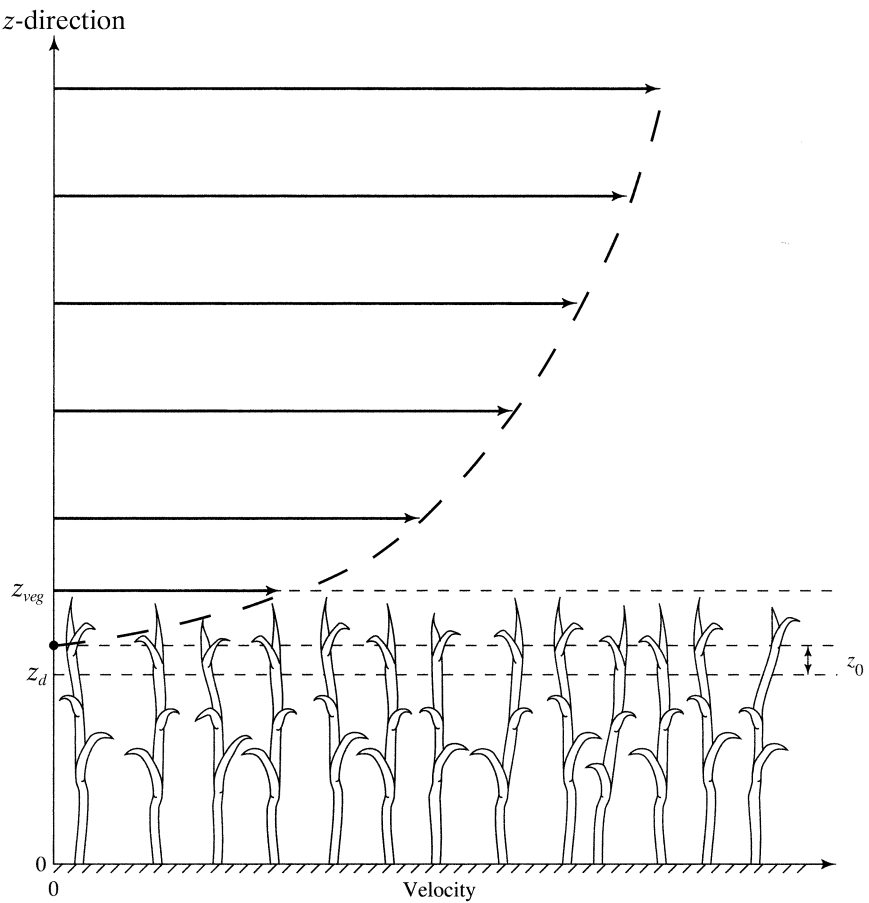


Figure 3.10 Vertical distribution of wind velocity over a vegetative surface of height z_{veg} . The long-dashed curve follows the logarithmic relation of equation (3.27). The zero-plane displacement, z_d , is about $0.7 \cdot z_{veg}$ and the roughness height, z_0 , is about $0.1 \cdot z_{veg}$. Note that equation (3.27) gives $u(z) = 0$ when $z = z_0 + z_d$.

concentrations of the constituent in different parts of the fluid. According to **Fick's law**,

The rate of transfer of a constituent S in the z -direction is directly proportional to the gradient of concentration of S in the z -direction:

$$F_S = -D_S(z) \cdot \frac{d\chi_S(z)}{dz}, \quad (3.31)$$

where F_S is the rate of transfer of S in direction z per unit area per unit time (called the **flux** of S), χ_S is the volumetric concentration of S , and D_S is called the **diffusivity** of S in the fluid (figure 3.12 on p. 125).

The minus sign in equation (3.31) indicates that S always moves from regions where its concentration is higher to regions where its concentration is lower. In the present context, z represents elevation above a

Table 3.3 Typical Values of Roughness Height, z_0 , for Various Surfaces (see also table 6.4).

Surface	z_0 (m)
Large water surfaces	0.0001–0.0005
Snow	0.0001–0.0005
Mud flats	0.0001–0.0005
Short grass	0.008–0.02
Long grass, prairie	0.02–0.06
Short agricultural crops	0.05–0.10
Tall agricultural crops	0.10–0.20
Prairie with scattered bushes and trees	0.20–0.40
Continuous bushland	0.20–0.40
Mature pine forest	0.80–1.5
Bushland in rugged terrain	1.0–2.0
Tropical forest	1.5–2.5
Alpine terrain with scattered tree stands	3.0–4.0

Source: Brutsaert (1992).

surface (ground, snow, or water). In general χ_S and D_S are functions of z , but the flux F_S does not vary with z at a given place and time.

3.5.3.2 Diffusivity

Note from equation (3.31) that diffusivity always has dimensions $[L^2 T^{-1}]$, while the dimensions of the

other quantities depend on the nature of the property S : either mass [M], momentum $[M L T^{-1}]$, or energy $[M L^2 T^{-2}] = [F L] = [E]$. The magnitude of the diffusivity depends on (1) the nature of the property S , (2) the properties of the medium, and (3) the physical mechanism by which the property is transferred. In

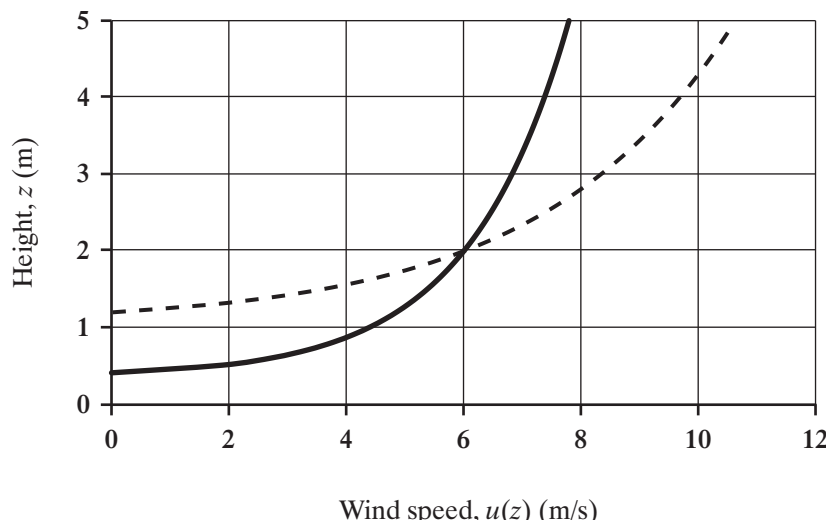


Figure 3.11 Wind-velocity profiles for the example of box 3.1. In both curves a velocity of 6 m/s is measured at a height of 2 m. Curve 1 (solid) is for a vegetation height of 0.5 m, curve 2 (dashed) is for a vegetation height of 1.5 m.

Box 3.1 Example Calculations of Wind Profiles

Suppose an anemometer is set up at a height of 2 m above the ground in a corn field. Use equation (3.27) to calculate the velocity profiles up to a height of 5 m above the ground when the anemometer measures a velocity of 6.0 m/s when (a) the corn is at a height of 0.5 m and (b) the corn is at a height of 1.5 m. Plot both profiles on the same graph.

- a. When $z_{veg} = 0.5$ m, equations (3.28) and (3.29) give the zero-plane displacement height, z_d , and the roughness height, z_0 , as

$$z_d = 0.7 \times 0.5 \text{ m} = 0.35 \text{ m};$$

$$z_0 = 0.1 \times 0.5 \text{ m} = 0.05 \text{ m}.$$

Then, with $\kappa = 0.4$, equation (3.27) becomes

$$u(z) = 2.5 \cdot u_* \cdot \ln\left(\frac{z - 0.35}{0.05}\right).$$

Using equation (3.30a), the friction velocity when $u(2 \text{ m}) = 6 \text{ m/s}$ is thus

$$u_* = \frac{6 \text{ m/s}}{2.5 \cdot \ln\left(\frac{2 - 0.35}{0.05}\right)} = 0.69 \text{ m/s.}$$

This value is then used in equation (3.27) to generate the vertical wind profile (figure 3.11).

- b. When $z_{veg} = 1.5$ m, the zero-plane displacement height, z_d , and the roughness height, z_0 , are
 $z_d = 0.7 \times 1.5 \text{ m} = 1.05 \text{ m};$
 $z_0 = 0.1 \times 1.5 \text{ m} = 0.15 \text{ m}.$

Then equation (3.27) becomes

$$u(z) = 2.5 \cdot u_* \cdot \ln\left(\frac{z - 1.05}{0.15}\right).$$

The friction velocity when $u(2 \text{ m}) = 6 \text{ m/s}$ is thus

$$u_* = \frac{6 \text{ m/s}}{2.5 \cdot \ln\left(\frac{2 - 1.05}{0.15}\right)} = 1.30 \text{ m/s.}$$

This value is then used in equation (3.27) to generate the vertical wind profile when the corn is higher (figure 3.11).

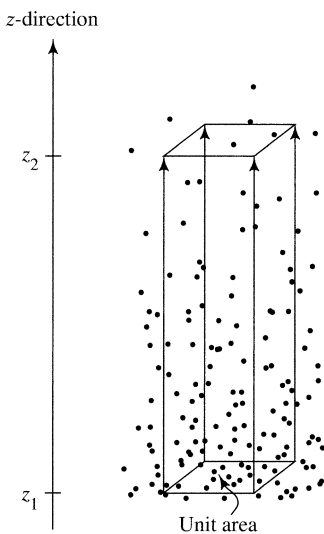


Figure 3.12 Conceptual diagram of the general diffusion process. Concentration of dots indicates concentration of quantity S . The rate of movement of S from z_1 to z_2 is proportional to the diffusivity.

the mixed layer of the atmosphere, momentum, mass (water vapor and other constituents, such as pollutants), and energy (latent and sensible heat) are exchanged between the surface and the air and diffused vertically by turbulent eddies, so $D_S(z)$ is the **turbulent diffusivity** for the various properties.

When buoyancy effects are negligible it is usually assumed that the diffusivities of momentum [$D_M(z)$], water vapor [$D_V(z)$], and sensible heat [$D_H(z)$] have the same value at a given time and place, i.e.,

$$D_S(z) = D_M(z) = D_V(z) = D_H(z). \quad (3.32)$$

Thus we can use Fick's law and the Prandtl–von Kármán relation to develop relations for the diffusivity of momentum, and then take advantage of (3.32) to derive useful practical approaches for calculating the vertical transfer of water vapor and latent and sensible heat under conditions of forced convection. These relations are developed in sections 3.5.3.3 to 3.5.3.6. Section 3.5.3.7 describes criteria and modifications to account for thermally induced buoyancy effects.

3.5.3.3 Diffusion of Momentum

Momentum equals mass times velocity, so the concentration of momentum (momentum per unit volume) at any level z equals the mass density of the

air times the velocity, $\rho_a \cdot u(z)$. Thus, for momentum, equation (3.31) becomes

$$F_M = -D_M(z) \cdot \frac{d[\rho_a \cdot u(z)]}{dz}, \quad (3.33)$$

where F_M is the momentum flux and $D_M(z)$ is the diffusivity of momentum in turbulent air. In the lowest levels of the atmosphere ρ_a can be considered constant at the prevailing air temperature [equation (3.3)], so equation (3.33) can be simplified to

$$F_M = -D_M(z) \cdot \rho_a \cdot \frac{du(z)}{dz}. \quad (3.34)$$

As noted, velocity always increases with height because frictional drag slows air movement near the ground, so $du(z)/dz$ is always positive. Thus F_M is always negative, reflecting the transfer of momentum downward from where velocities are higher to where they are lower via turbulent eddies (figure 3.8).

Note that momentum flux F_M has the dimensions $[M L^{-1} T^{-2}] = [F L^{-2}]$, i.e., a force per unit area, and physically represents the horizontal frictional force that causes the vertical gradient of wind velocity. Thus the momentum flux F_M is equal to the frictional force per unit area, or **shear stress**, τ_0 , exerted by the surface on the wind and by the wind on the surface. (It is this shear stress that produces waves on water surfaces.) It can be shown that momentum flux and shear stress are related to friction velocity as

$$F_M = \tau_0 = -\rho_a \cdot u_*^2. \quad (3.35)$$

From the Prandtl–von Kármán law [equation (3.27)],

$$\frac{du(z)}{dz} = \frac{u_*}{\kappa \cdot (z - z_d)}, \quad (3.36)$$

showing that the velocity gradient decreases with height. From equations (3.34)–(3.36), we see that

$$D_M(z) = \frac{u_*^2}{du(z)/dz}, \quad (3.37)$$

and combining (3.36) and (3.37) gives

$$D_M(z) = \kappa \cdot u_* \cdot (z - z_d), \quad (3.38)$$

showing that diffusivity increases linearly with height.

As we see in the example of box 3.1, u_* , and hence $D_M(z)$, can be determined from measurements of wind velocity. We will use equation (3.38) in the following sections to derive expressions for comput-

ing the magnitudes of the vertical transfer of water vapor (evaporation/condensation) and latent and sensible heat.

3.5.3.4 Diffusion of Water Vapor

The absolute humidity ρ_v is the concentration (mass/volume) of water vapor in air (section 3.2.2), so the equation for the vertical flux of water vapor, F_V [M L⁻² T⁻¹], is

$$F_V = -D_V(z) \cdot \frac{d\rho_v(z)}{dz}, \quad (3.39)$$

where $D_V(z)$ is the diffusivity of water vapor in turbulent air. Note that (3.39) represents evaporation as a positive flux: If humidity decreases upward, $d\rho_v(z)/dz < 0$, $F_V > 0$, and evaporation is occurring; if humidity increases upward, $d\rho_v(z)/dz > 0$, $F_V < 0$, and the flux is downward (condensation is occurring).

It is more common to write (3.39) in terms of vapor pressure, e ; this can be done using (3.4) to give

$$F_V = -D_V(z) \cdot \frac{0.622 \cdot \rho_a}{p} \cdot \frac{de(z)}{dz}. \quad (3.40a)$$

Dividing by the density of water, ρ_w , gives an expression for evaporation/condensation, E , in the units of depth per unit time [L T⁻¹]:

$$E = -D_V(z) \cdot \frac{0.622 \cdot \rho_a}{p \cdot \rho_w} \cdot \frac{de(z)}{dz}. \quad (3.40b)$$

A practical relation for computing evaporation/condensation from measurements of wind speed and vapor pressure can be developed by noting (3.37) and dividing the right-hand side of (3.40b) by D_M while multiplying it by $u_*^2/[du(z)/dz]$:

$$\begin{aligned} E &= -\frac{0.622 \cdot \rho_a}{p \cdot \rho_w} \cdot \frac{D_V(z)}{D_M(z)} \cdot \frac{u_*^2}{du(z)/dz} \cdot \frac{de(z)}{dz}, \\ E &= -\frac{0.622 \cdot \rho_a}{p \cdot \rho_w} \cdot \frac{D_V(z)}{D_M(z)} \cdot u_*^2 \cdot \frac{de(z)}{du(z)}. \end{aligned} \quad (3.41)$$

This relation can then be written in finite-difference form via the approximations

$$de(z) \approx e(z_2) - e(z_1) \quad (3.42)$$

and

$$du(z) \approx u(z_2) - u(z_1). \quad (3.43)$$

Finally, from equation (3.30b),

$$u_*^2 = \frac{\kappa^2 \cdot [u(z_2) - u(z_1)]^2}{\left[\ln\left(\frac{z_2 - z_d}{z_1 - z_d}\right) \right]^2}, \quad (3.44)$$

and combining (3.41)–(3.44) gives

$$E = -\frac{0.622 \cdot \rho_a}{p \cdot \rho_w} \cdot \frac{D_V(z)}{D_M(z)} \cdot \frac{\kappa^2 \cdot [u(z_2) - u(z_1)] \cdot [e(z_2) - e(z_1)]}{\left[\ln\left(\frac{z_2 - z_d}{z_1 - z_d}\right) \right]^2}. \quad (3.45a)$$

If we assume that the surface velocity $u_s \equiv u(z_d + z_0) = 0$ and that e_s is the vapor pressure at the evaporating surface, we can write (3.45a) as

$$E = -\frac{0.622 \cdot \rho_a}{p \cdot \rho_w} \cdot \frac{D_V(z)}{D_M(z)} \cdot \frac{\kappa^2 \cdot u(z_m) \cdot [e(z_m) - e(z_s)]}{\left[\ln\left(\frac{z_m - z_d}{z_0}\right) \right]^2}. \quad (3.45b)$$

Equation (3.45) is widely used as the basis for the **mass-transfer approach** to calculating evapotranspiration. As noted, it is commonly assumed that $D_V(z) = D_M(z)$ and that the zero-plane displacement z_d and the roughness height z_0 are the same for water-vapor exchange and momentum when buoyancy effects are negligible. With these assumptions, we can define a **water-vapor-transfer coefficient** K_E with dimensions [L² F⁻¹],

$$K_E \equiv \frac{0.622 \cdot \kappa^2 \cdot \rho_a}{\rho_w \cdot p \cdot \left[\ln\left(\frac{z_m - z_d}{z_0}\right) \right]^2}. \quad (3.46a)$$

Noting that $\kappa = 0.4$ and that typical near-surface values for ρ_a , ρ_w , and p can often be assumed (tables 3.1 and 3.2), we can write

$$K_E \equiv \frac{1.2693 \times 10^{-6}}{\left[\ln\left(\frac{z_m - z_d}{z_0}\right) \right]^2} \text{ kPa}^{-1}. \quad (3.46b)$$

With (3.46) we can write (3.45b) in its most simplified form as:

$$E = K_E \cdot u(z_m) \cdot [e(z_s) - e(z_m)]. \quad (3.47)$$

Note that the minus sign from (3.45) is dropped because the signs of $e(z_s)$ and $e(z_m)$ are reversed.

Equation (3.47) emphasizes that, for a given surface,

Evaporation/condensation rate is essentially proportional to the product of surface/air vapor-pressure difference and wind speed.

Equations of this form are discussed further in section 6.3.2.

3.5.3.5 Diffusion of Latent Heat

As discussed in section 3.3.2, a transfer of latent heat always accompanies a transfer of water vapor [equations (3.17) and (3.19)]. Thus the diffusion equation for latent-heat flux, $F_{\lambda E}$, follows directly from equation (3.39),

$$F_{\lambda E} = -D_V(z) \cdot \lambda \cdot \frac{dp_v(z)}{dz}, \quad (3.48)$$

where λ is the appropriate latent heat. Thus, transfer relations for latent-heat flux λE are formulated simply by multiplying the relations for evaporation/condensation [equation (3.45)] by $\rho_w \cdot \lambda$ to give

$$\lambda E = -\frac{0.622 \cdot \rho_a \cdot \lambda}{p} \cdot \frac{D_V(z)}{D_M(z)} \cdot \frac{\kappa^2 \cdot [u(z_2) - u(z_1)] \cdot [e(z_2) - e(z_1)]}{\left[\ln\left(\frac{z_2 - z_d}{z_1 - z_d}\right) \right]^2}. \quad (3.49a)$$

or

$$\lambda E = -\frac{0.622 \cdot \rho_a \cdot \lambda}{p} \cdot \frac{D_V(z)}{D_M(z)} \cdot \frac{\kappa^2 \cdot u(z_m) \cdot [e(z_m) - e(z_s)]}{\left[\ln\left(\frac{z_m - z_d}{z_0}\right) \right]^2}. \quad (3.49b)$$

As in (3.47), we can define a latent-heat-transfer coefficient $K_{\lambda E}$ as

$$K_{\lambda E} \equiv K_E \cdot \lambda \cdot \rho_w = \frac{0.622 \cdot \rho_a \cdot \lambda \cdot \kappa^2}{p \cdot \left[\ln\left(\frac{z_m - z_d}{z_0}\right) \right]^2}, \quad (3.50)$$

and write (3.49) as

$$\lambda E = K_{\lambda E} \cdot u(z_m) \cdot [e(z_s) - e(z_m)]. \quad (3.51)$$

Near sea level and near 0°C,

$$K_{\lambda E} = \frac{3.1745 \times 10^{-3}}{\left[\ln\left(\frac{z_m - z_d}{z_0}\right) \right]^2} \text{ MJ/m}^3 \cdot \text{kPa}. \quad (3.52)$$

3.5.3.6 Diffusion of Sensible Heat

The diffusion equation for vertical sensible-heat flux, F_H , is

$$F_H = -D_H(z) \cdot \frac{d[\rho_a \cdot c_p \cdot T(z)]}{dz}, \quad (3.53a)$$

where $D_H(z)$ is the diffusivity of heat in turbulent air, c_p is the specific heat of air at constant pressure [$\text{E M}^{-1} \Theta^{-1}$], and T is the absolute temperature. Because ρ_a and c_p are effectively constant in near-surface conditions (table 3.1) and $dT(z)/dz = dT(z)/dz$, this can be simplified to

$$F_H = -D_H(z) \cdot \rho_a \cdot c_p \cdot \frac{dT(z)}{dz}. \quad (3.53b)$$

Following the same reasoning used to derive the relations for evaporation/condensation, we find that the upward sensible-heat flux H is given by

$$H = -\rho_a \cdot c_p \cdot \frac{D_H(z)}{D_M(z)} \cdot \frac{\kappa^2 \cdot [u(z_2) - u(z_1)] \cdot [T(z_2) - T(z_1)]}{\left[\ln\left(\frac{z_2 - z_d}{z_1 - z_d}\right) \right]^2}, \quad (3.54a)$$

or

$$H = -\rho_a \cdot c_p \cdot \frac{D_H(z)}{D_M(z)} \cdot \frac{\kappa^2 \cdot u(z_m) \cdot [T(z_m) - T(z_s)]}{\left[\ln\left(\frac{z_m - z_d}{z_0}\right) \right]^2}. \quad (3.54b)$$

As with water-vapor and latent-heat exchange, it is commonly assumed that $D_H = D_M$ for forced convection and that the zero-plane displacement z_d and the roughness height z_0 are the same for sensible-heat exchange and momentum. Thus, analogously to water-vapor exchange, we can define a **sensible-heat-exchange coefficient**, K_H [$\text{E L}^{-3} \Theta^{-1}$], as

$$K_H \equiv \frac{\kappa^2 \cdot \rho_a \cdot c_p}{\left[\ln\left(\frac{z_m - z_d}{z_0}\right) \right]^2}, \quad (3.55)$$

and write the sensible-heat-exchange relation as

$$H = K_H \cdot u(z) \cdot [T(z_s) - T(z_m)], \quad (3.56)$$

where $T(z_s)$ is surface temperature. Using the typical near-surface values $\rho_a = 1.292 \text{ kg/m}^3$ and $c_p = 1.005 \times 10^{-3} \text{ MJ/kg} \cdot \text{K}$,

$$K_H \equiv \frac{2.0775 \times 10^{-4}}{\left[\ln\left(\frac{z_m - z_d}{z_0}\right) \right]^2} \text{ MJ/m}^3 \cdot \text{K}. \quad (3.57)$$

Equation (3.56) emphasizes that

Sensible heat-exchange rate is essentially proportional to the product of temperature gradient and wind speed.

3.5.3.7 Effects of Atmospheric Stability

As noted, the average value of the lapse rate in the troposphere is 6.5°C/km . However, the local near-surface lapse rate (often called the **environmental lapse rate**), Γ , is highly variable in space and time and may even temporarily reverse direction; this latter phenomenon is called an **inversion**.

When a parcel of air moves vertically in a turbulent eddy with vertical velocity v , it warms (if descending), or cools (if ascending) at the dry adiabatic lapse rate, Γ_{da} (assuming no condensation occurs). Peixoto and Oort (1992) show that the buoyancy-induced vertical acceleration, dv/dz , of an air parcel displaced vertically a small distance δz is given by

$$\frac{dv}{dz} = \frac{g \cdot \delta z \cdot (\Gamma - \Gamma_{da})}{T}, \quad (3.58)$$

where g is gravitational acceleration and T is average temperature. Thus the relative magnitudes of Γ and Γ_{da} determine the near-surface stability conditions (figure 3.13):

- $\Gamma < \Gamma_{da}$: **Stable** conditions ($dv/dz < 0$) exist if the ambient lapse rate is less steep than the dry adiabatic rate, because an elevated ($\delta z > 0$)/lowered ($\delta z < 0$) parcel will be cooler/warmer and denser/less dense than the surrounding air (figure 3.13a), and hence will tend to return to its original elevation. Thus $D_V/D_M < 1$ and $D_H/D_M < 1$, and the actual rates of turbulent exchange are less than given by the equations derived in sections 3.5.3.4–3.5.3.6.

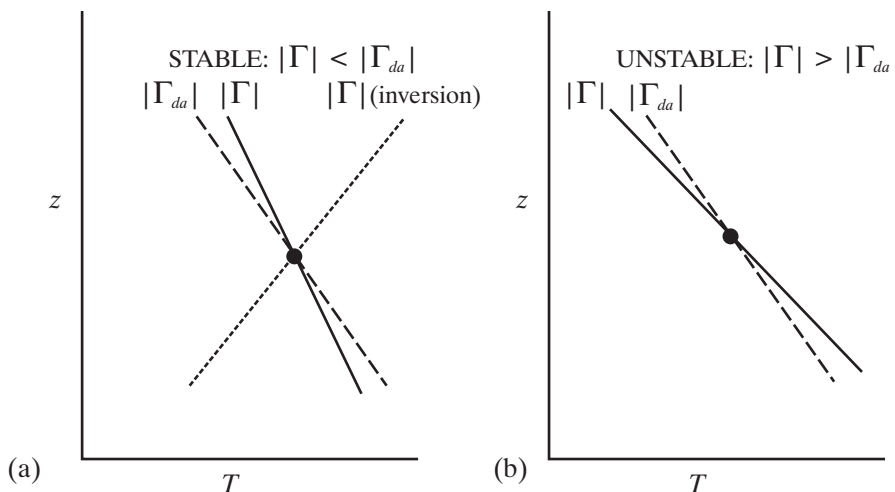


Figure 3.13 The dot indicates the height of an air parcel at an initial time. If the parcel is displaced upward or downward, it cools or warms at the dry adiabatic lapse rate Γ_{da} (long-dashed line). (a) *Stable* conditions exist if the ambient lapse rate (solid line) is less steep than the dry adiabatic rate ($|\Gamma| < |\Gamma_{da}|$); an inversion (short-dashed line) exists when temperature increases with height. (b) *Unstable* conditions exist if the ambient lapse rate is steeper than the dry adiabatic lapse rate ($|\Gamma| > |\Gamma_{da}|$).

Stable conditions typically occur when warm air overlies a cold water surface or a snowpack or when there is a temperature inversion.

- $\Gamma = \Gamma_{da}$: **Neutral** conditions ($dv/dz = 0$) exist when the ambient lapse rate is equal to the dry adiabatic lapse rate, because an elevated/lowered parcel will have the same temperature and density as the surrounding air, and there will be no buoyancy effects. Under neutral conditions, the diffusivities of water vapor and sensible heat can be assumed to be identical to the diffusivity of momentum [equation (3.32)] because the same turbulent eddies are responsible for the transport of all three quantities, as assumed in deriving the relations in sections 3.5.3.4–3.5.3.6.
- $\Gamma > \Gamma_{da}$: **Unstable** conditions ($dv/dz > 0$) exist if the ambient lapse rate is steeper than the dry adiabatic lapse rate, because an elevated/lowered parcel will be warmer/cooler and hence less dense/denser than the surrounding air (figure 3.13b) and hence will continue to rise/descend. Thus buoyancy effects enhance vertical transport, which can produce significant upward transport of water vapor and/or sensible heat but little downward transport of momentum. Thus $D_V/D_M > 1$ and $D_H/D_M > 1$, and the actual rate of turbulent exchange is greater than given by the equations derived in sections 3.5.3.4–3.5.3.6. Unstable conditions typically occur when wind speed is low and the surface is strongly heated by the sun (see discussion of convective rainfall in section 4.1.4), or over an artificially heated water surface.

Practical approaches to accounting for stability effects in near-surface turbulent diffusion are discussed in box 3.2 and summarized in table 3.4, both on p. 130. Brutsaert (1992) presents a more detailed discussion of stability effects.

3.5.4 Eddy Correlation

From equations (3.26) and (3.35), the downward flux of momentum is related to the time average of the simultaneous turbulent fluctuations in horizontal and vertical velocity at a given level as

$$F_M = \rho_a \cdot (-\overline{u' \cdot v'}). \quad (3.59)$$

Using analogous notation, we can express the instantaneous value of specific humidity, q , at any level as sums of a time-averaged value (denoted by

the overbar) and an instantaneous fluctuation from the average (denoted by the prime):

$$q = \bar{q} + q' \quad (3.60)$$

where $\bar{q}' = 0$.

Figure 3.16 shows a situation in which the average specific humidity decreases upward. When a parcel of air moves upward a small distance δz , it undergoes a vertical velocity fluctuation v' . At the new level, the mean humidity is q' lower than at the original level. The average upward flux of water vapor, F_V , equals the average value of simultaneous fluctuations of humidity and vertical velocity:

$$F_V = \rho_a \cdot (\overline{q' \cdot v'}). \quad (3.61)$$

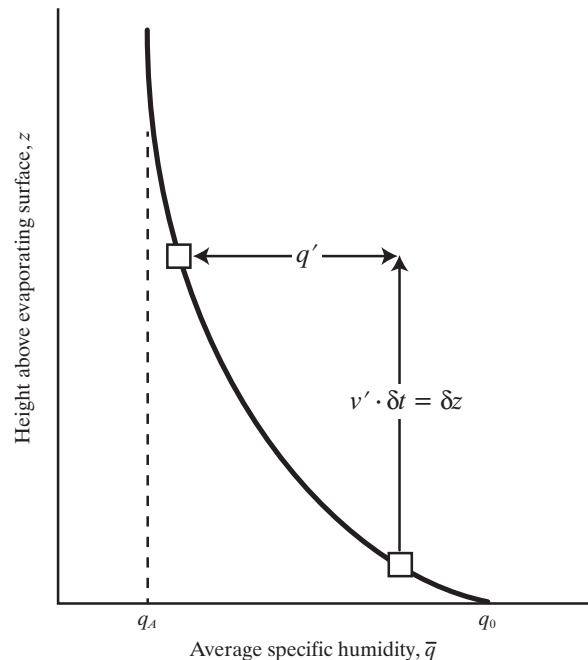


Figure 3.16 An atmosphere with a free-air humidity of q_A overlies a surface with a humidity q_0 , with $q_A < q_0$. When wind blows across the surface, turbulent eddies transport air and water vapor vertically. When a parcel of air (box) moves upward a small distance δz , it undergoes a vertical velocity fluctuation v' during a time interval $\delta t = \delta z/v'$. At the new level, the mean humidity \bar{q} is q' lower than at the original level. The converse happens in downward-moving eddies. The curve represents the equilibrium conditions, in which net vertical transport is given by equation (3.61) [adapted from Brutsaert (1992)].

Box 3.2 Effects of Atmospheric Stability on Turbulent Exchanges

Richardson Number

The stability state of the atmosphere is characterized by the dimensionless **Richardson number**, Ri , which is the ratio of the rate of destruction of turbulent kinetic energy by buoyancy forces to the rate of production of that energy by surface roughness acting on the horizontal wind flow. Its fundamental physical definition is

$$Ri \equiv \frac{g \cdot [d\bar{F}(z)/dz]}{\bar{F} \cdot [du(z)/dz]^2}, \quad (3B2.1)$$

where g is gravitational acceleration, z is elevation, \bar{F} is absolute temperature,^a u is wind velocity, and \bar{F} is average near-surface temperature. For calculating the stability state from typical near-surface measurements, the **bulk Richardson number**, Ri_B , is used:

$$Ri_B \equiv \frac{g \cdot z_m \cdot [\bar{T}_a(z_m) - \bar{T}_s]}{0.5 \cdot [\bar{T}_a(z_m) + \bar{T}_s] \cdot u^2(z_m)}, \quad (3B2.2)$$

where z_m is measurement height, \bar{T}_a is air temperature, and \bar{T}_s is surface temperature. Figure 3.14 shows Ri_B as a function of 2 m wind speed and air temperature for a surface at $\bar{T}_s = 273.26$ K (e.g., a melting snow surface). Note that the major effects of nonneutrality occur at low wind speeds.

Stability Correction Factors

Turbulent-exchange rates can be adjusted for stability effects by multiplying the values of E , LE , and H calculated via the equations derived in sections 3.5.3.4–3.5.3.6 by a **stability-correction factor**, C_{stab} . The factors given here were developed by Andreadis et al. (2009).

Unstable Conditions ($Ri_B < 0$):

$$C_{stab} = (1 - 16 \cdot Ri_B)^{1/2}, \quad (3B2.3)$$

Stable Conditions ($Ri_B > 0$):

Compute

$$Ri_u = \frac{1}{\ln\left(\frac{z_m}{z_0}\right) + 5}; \quad (3B2.4)$$

then for $0 < Ri_B \leq Ri_u$

$$C_{stab} = \left(1 - \frac{Ri_B}{0.2}\right)^2, \quad (3B2.5a)$$

and for $Ri_B > Ri_u$

$$C_{stab} = \left(1 - \frac{Ri_u}{0.2}\right)^2. \quad (3B2.5b)$$

Figure 3.15 shows the correction factors calculated by equations (3B2.4) and (3B2.5) for $z_m = 2$ m and $z_0 = 0.0015$ m for the same conditions as figure 3.14. Table 3.4 summarizes stability conditions, criteria, and correction factors.

Note that corrections for unstable conditions have often been approached empirically. For example, the water-vapor transfer coefficient K_E [equation (3.46)] and the sensible-heat-transfer coefficient K_H [equation (3.55)] can be estimated as functions of the difference between surface and air temperatures (e.g., Dingman et al. 1968; Rasmussen et al. 1995).

Note

^a Strictly speaking, **potential temperature**, rather than actual temperature, should be used (see Peixoto and Oort 1992, p. 47). However, for near-surface conditions, the two are essentially identical.

Table 3.4 Summary of Stability Conditions, Criteria, and Correction Factors for Near-Surface Transport of Water Vapor and Latent and Sensible Heat.

Ambient Lapse Rate (Absolute Value)	Stability Condition	Richardson Number, Ri_B	Turbulence	$D_V/D_M, D_H/D_M$	Correction Factor, C_{stab}
> Adiabatic	Unstable	< 0	Enhanced	> 1	Equation (3B2.3)
= Adiabatic	Neutral	0	Normal	1	1
< Adiabatic	Stable	> 0	Suppressed	< 1	Equations (3B2.4) and (3B2.5)

The evaporation rate E [L T^{-1}] is then

$$E = \frac{\rho_a}{\rho_w} \cdot (q' \cdot v'). \quad (3.62)$$

The same reasoning can be used for temperature, leading to the analogous expression for upward sensible-heat flux, F_H :

$$H = F_H = \rho_a \cdot c_p \cdot (\overline{T'_a \cdot v'}). \quad (3.63)$$

[Strictly speaking, equation (3.63) should use the *potential* temperature rather than the measured tem-

perature but, as noted in box 3.2, we can generally use the measured temperature with negligible error.]

Equations (3.59)–(3.63) are the basis for the **eddy-correlation method** of measuring sensible- and latent-heat transfer and evaporation. The method has the advantage over the turbulent-diffusion approach in avoiding the need to invoke somewhat heuristic characterization of the surface roughness [equations (3.28) and (3.29)] and corrections for stability. However, it requires the use of very sensitive instruments capable of measuring very rapid fluctuations of velocity, humidity, and temperature (on the

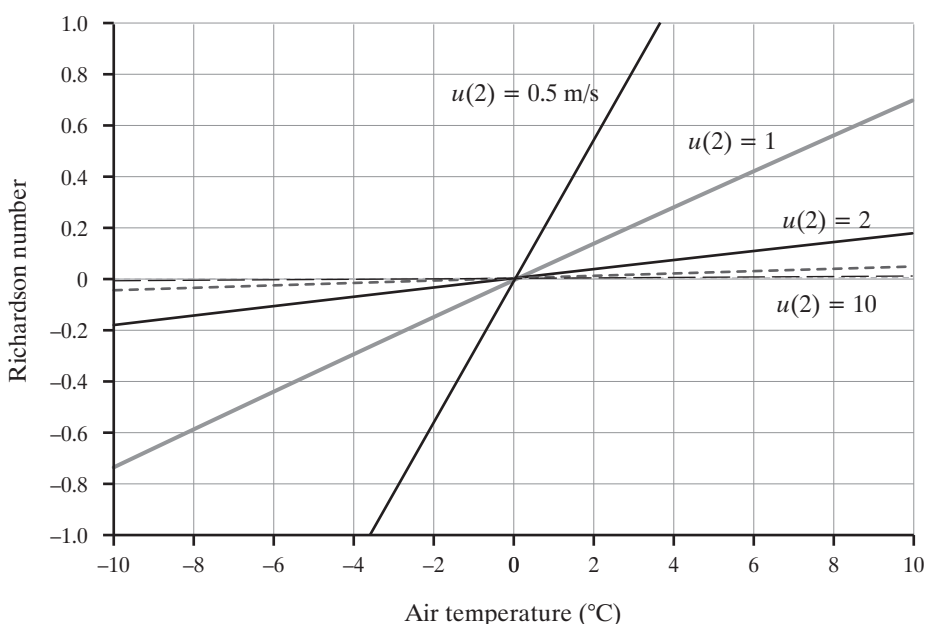


Figure 3.14 Bulk Richardson number Ri_B as a function of 2 m wind speed and air temperature for a surface at $F_s = 273.26 \text{ K}$ (e.g., a melting snow surface) [equation (3B2.2)]. Note that the major effects of nonneutrality occur at low wind speeds.

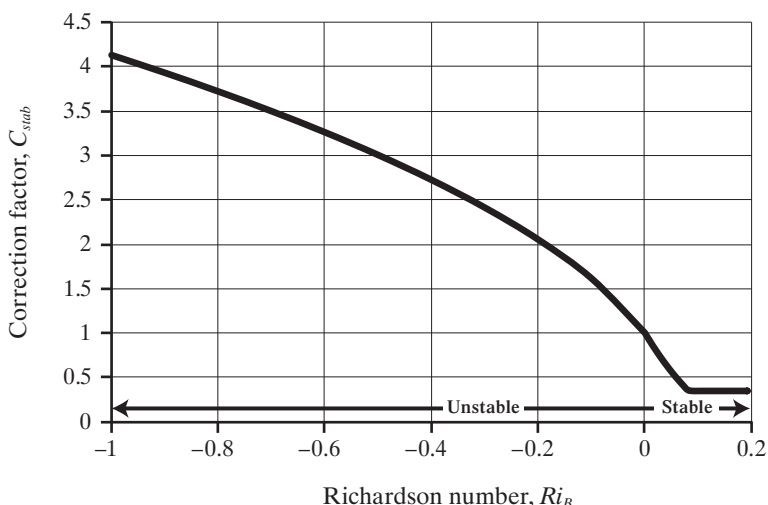


Figure 3.15 Stability-correction factors C_{stab} calculated by equations (3B2.4) and (3B2.5) for $z_m = 2 \text{ m}$ and $z_0 = 0.0015 \text{ m}$ for the same conditions as figure 3.14.

order of 10 per second), and thus is used only in special research situations.

▼ EXERCISES

- Given the following air temperatures (T_a) and relative humidities (RH):

Case:	A	B	C	D
T_a (°C)	22	3	-7	29
RH (%)	53	74	100	22

- Compute the vapor pressure, e , in kPa.
 - Compute the absolute humidity, ρ_v , in kg/m³.
 - Compute the dew point, T_{dp} , in °C.
- The following table gives measurements of air temperature (T_a), relative humidity (RH), and water-surface temperature (T_s) on different days for a lake. For each day, determine whether evaporation or condensation is occurring.
- | Day: | 1 | 2 | 3 | 4 | 5 |
|------------|----|-----|----|-----|----|
| T_a (°C) | 2 | 22 | 5 | 8 | 12 |
| RH (%) | 55 | 100 | 76 | 100 | 83 |
| T_s (°C) | 4 | 26 | 2 | 2 | 17 |
- From examination of figure 3.3, at what temperatures would you expect the growth of ice crystals in supercooled clouds to be most rapid? Explain your reasoning.
 - Assuming the average lapse rate of 6.5°C/km (section 3.1) and the average surface temperature of about 17°C, at what elevation does this temperature typically occur?
 - Suppose 2 cm of rain fell from a nimbostratus cloud (typical dense, rain-producing cloud layer) that remains about 700 m thick during the storm. Assuming a cloud water content of 0.5 g/m³, how much more rain fell than was in the cloud at any time?
 - Suppose an anemometer is set up at a height of 2 m above the ground in a corn field. Use equation (3.27) to calculate the velocity profiles up to a height of 5 m above the ground when the anemometer measures a velocity of 4 m/s and

- the corn is at a height of 0.5 m;
- the corn is at a height of 1.5 m.

Plot both profiles on the same graph (arithmetic axes), with z on the vertical axis (m) and $u(z)$ on the horizontal axis (m/s).

- Using values of constants given in the text; a measurement height of $z_m = 2$ m; values of $z_d = 0$ m and $z_0 = 10^{-5}$ m (typical of a water surface); and the assumption that $D_V = D_M$:

 - Use equation (3.46) to calculate a typical value of K_E in 1/kPa for use in equation (3.47).
 - Use equations (3.47) and (3.50) to calculate evaporation (or condensation) rate in mm/d and the latent-heat-transfer rate in MJ/m² · d for the following days. Be sure to check units!

Day:	1	2	3	4	5
$u(2 \text{ m})$ (m/s)	2.4	1.6	3.2	0.5	5.0
$T(2 \text{ m})$ (°C)	5.2	12.2	19.3	0.7	9.9
$RH(2 \text{ m})$ (%)	100	86	68	40	100
T_s (°C)	7.0	8.0	15.6	5.5	9.9

- Using values of constants given in the text, and the same assumptions as in exercise 3.6, use equation (3.54) to calculate a typical value of K_H for equation (3.55) in MJ/m³ · °C.
- Use equation (3.55) to calculate the sensible-heat-transfer rate in MJ/m² · d for the cases in exercise 3.6. Be sure to check units!

▼ NOTES

¹ Equation (3.9a) gives e^* values within 0.1% of the true value for $T = 0$ to 35°C. The 237.3 in the denominator is correct; it is not a misprint for 273.2, the adjustment from °C to K.

² Water molecules are especially attracted to certain types of particles, which are called **hygroscopic nuclei**. Condensation may occur on these nuclei even at relative humidities as low as 76%. Sea salt is the most common of the hygroscopic nuclei, but it is usually present only in low concentrations (Miller et al. 1983).

³ Note that although $\bar{u}' = \bar{v}' = 0$, the average of their product $\overline{|u' \cdot v'|} > 0$.



4

Precipitation

Precipitation is all forms of water that reach the surface from the atmosphere; it includes rain, snow, hail, dew, and frost. All water enters the land phase of the hydrologic cycle as precipitation. Thus in order to assess, predict, and forecast hydrological responses, hydrologists need to understand how the amount, rate, duration, and quality of precipitation are distributed in space and time:

The accuracy of forecasts of hydrologic response can be no better than the accuracy of precipitation assessments (Fekete et al. 2004).

Global patterns of precipitation were outlined in section 2.2.2, and the physics of precipitation formation was described in section 3.4. This chapter begins with an overview of the meteorology of precipitation. Following this we focus on methods of measuring precipitation at a point and of estimating precipitation over a region. Estimates of regional precipitation are critical inputs to water-balance and other types of models used in water-resource management, and sound interpretation of the predictions of such models requires an assessment of the uncertainty associated with their output, which in turn depends in large measure on the uncertainty of the input values, as

discussed in section 1.11. The uncertainty associated with a value of regional precipitation consists, in turn, of two parts: (1) errors in point measurements and (2) uncertainty in converting point-measurement data into estimates of regional precipitation. Thus a central goal of this chapter is to develop an understanding of these errors and uncertainties.

The remainder of the chapter discusses the climatology of precipitation, including methods of characterizing seasonality and extreme values, which determine corresponding aspects of hydrologic response, especially floods. The chapter concludes with a brief assessment of inadvertent and intentional human influences on precipitation and their implications for hydrologic analyses.

4.1 Meteorology

Section 3.4 describes the sequence of processes required to produce precipitation: (1) cooling of air to the dew-point temperature; (2) condensation on nuclei to form cloud droplets or ice crystals; (3) growth of droplets or crystals into raindrops or snowflakes; and (4) importation of water vapor to sustain the process. Although air may cool by radiation, mixing, conduction, or horizontal movement from high to low pressure regions, only adiabatic cooling

due to vertical uplift is rapid enough to produce hydrologically significant precipitation. This section begins with a survey of the meteorological situations in which significant rates of adiabatic cooling occur, and the characteristic spatial and temporal precipitation patterns associated with each situation. Following this, the phenomena of occult precipitation (fog drip), which is a significant component of annual water input in some places, and dewfall, which is a frequent and widespread form of precipitation, are discussed. We then survey the proximal and distal sources of the water that falls as precipitation, which are critical determinants of major feedbacks that determine hydrologic responses to changes in climate and land use. The section concludes with a discussion of the rain-snow transition, which is an important consideration in hydrologic modeling.

4.1.1 Fronts and Extra-Tropical Cyclones

An **air mass** is a subcontinental-scale body of air within which temperature, humidity, and lapse rate are essentially uniform at a given elevation. Air circulating for several days over extensive surfaces takes on the characteristics of that surface, and can be identified as one of six air-mass types (table 4.1). The characteristics of a given air mass are modified as it moves (see, for example, Barry and Chorley 1987),

but it typically maintains its general identity for many days. **Fronts** are boundaries between contrasting air masses; these are regions about 100 to 200 km wide in which horizontal temperature and pressure gradients are relatively large.

Figure 4.1 describes the process of **cyclogenesis** at fronts. While few actual cyclones follow this sequence exactly, it provides a framework for understanding the major precipitation-producing processes in the midlatitudes. The **isobars** (lines of equal atmospheric pressure) at fronts are subparallel, and the front is a low-pressure trough typically with relatively cold, denser air to the north and warm, less dense air to the south (figure 4.1a). Because the circulations of the abutting air masses are clockwise, wind blows in opposite directions on either side of the front to create a zone of wind shear. Often, the eddies generated in this zone trigger instabilities in the boundary that appear as waves when viewed in plan. Outside the tropics, where Coriolis force is significant, these waves typically develop into **extratropical cyclones**. Much of the precipitation between approximately 30° and 60°N and S latitudes is associated with extratropical cyclones. These storms are also the principal agents of poleward energy transfer in the midlatitudes.

Cyclonic storms form when the frontal wave develops further, such that the counterclockwise circu-

Table 4.1 Characteristics and Origins of Major Air-Mass Types in the Northern Hemisphere.

Air-Mass Type	Characteristics	Source Regions	
		Winter	Summer
Continental arctic (cA)	Very cold, moist	Arctic Ocean/Greenland	
Continental polar (cP)	Cold, dry	Eastern Europe Northern Asia Canada/northern United States	Northern Siberia Northern Canada
Continental tropical (cT)	Warm, dry	North Africa Arabia/Himalayas Mexico/California	North Africa Arabia/central Asia Mexico/southwest United States
Maritime arctic (mA)	Very cold, moist		Arctic Ocean/Greenland
Maritime polar (mP)	Cold, moist	Northern Pacific Ocean Western North Atlantic Ocean	Northern Pacific Ocean Central North Atlantic Ocean
Maritime tropical (mT)	Warm, moist	Central Atlantic Ocean Gulf of Mexico Central Pacific Ocean Bay of Bengal India Arabian Sea	Central Atlantic Ocean Gulf of Mexico Central Pacific Ocean

Source: Barry and Chorley (1987).

lation around the wave apex intensifies (figure 4.1c). To the west of the apex, cold air displaces the warm air to create a **cold front**, and the warmer air rises along the frontal surface. East of the apex the warm air displaces cold air at the surface to create a **warm front**, and the warmer air rises along the frontal surface here also. Cloud formation, often leading to precipitation, commonly occurs along one or both frontal surfaces (figure 4.2a) and at the apex, where the air converging at the center of the counterclockwise circulation must also rise. Typically, cold fronts

have relatively steep slopes, about 1 in 30 to 40, while warm fronts have slopes of 1 in 60 to 120; thus precipitation is usually more intense and areally more concentrated at cold fronts than at warm fronts. Note that the isobars now form a quasi-circular pattern around a low-pressure center at the apex (figure 4.1c); typically the diameter of a fully developed cyclonic circulation is on the order of 1,500 km.

Cold fronts usually move faster than warm fronts, so the evolution of an extratropical cyclone typically follows a sequence something like the one shown in

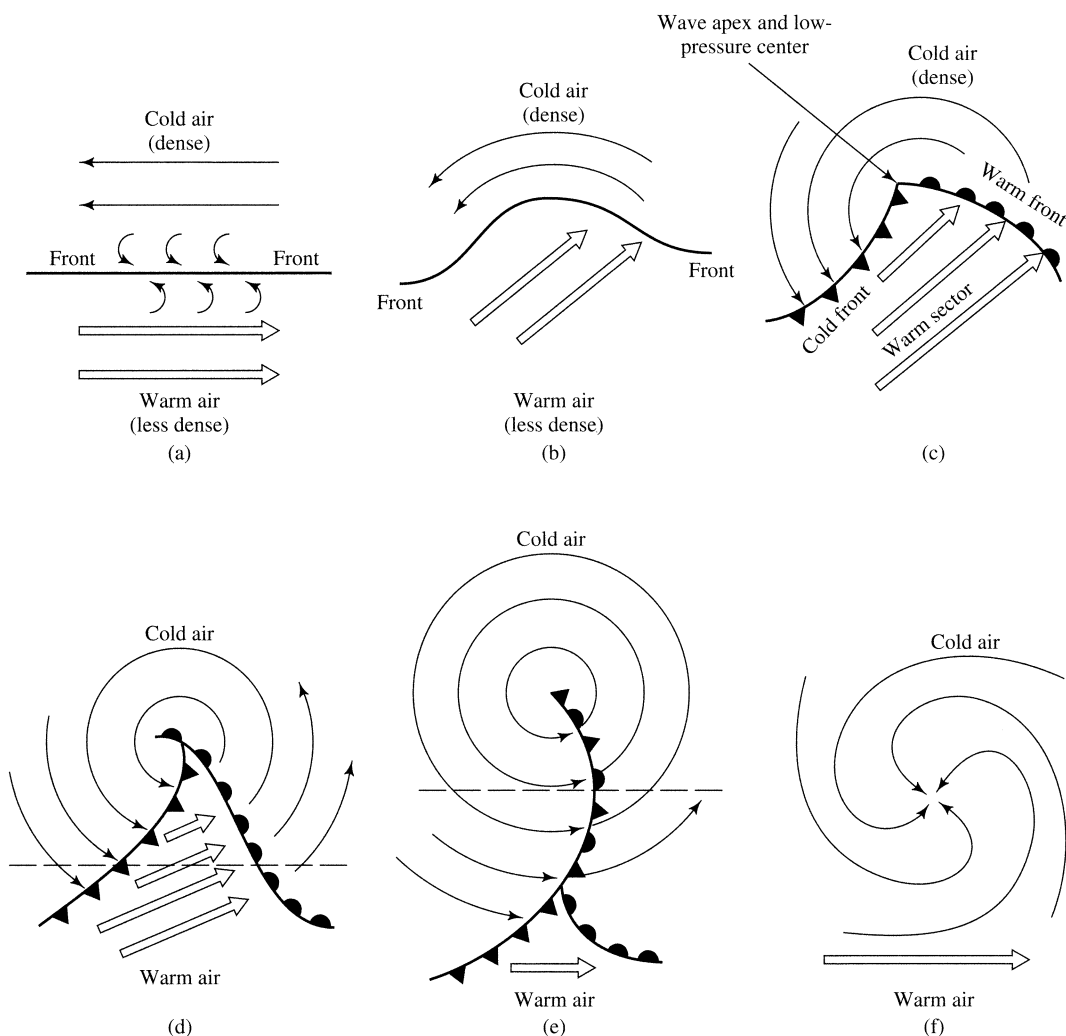


Figure 4.1 Typical sequence of development of extratropical cyclones (map view). Arrows indicate wind flow. (a) Stationary front between two air masses, showing eddies due to wind shear. (b) Initial wave development from eddy. (c) Intermediate stage with distinct cold and warm front and warm sector between. (d) Late stage with occlusion beginning. Dashed line is location of cross section in figure 4.2a. (e) Front largely occluded. Dashed line is location of cross section in figure 4.2b. (f) Final stage, with front dissipated [Miller et al. (1984)].

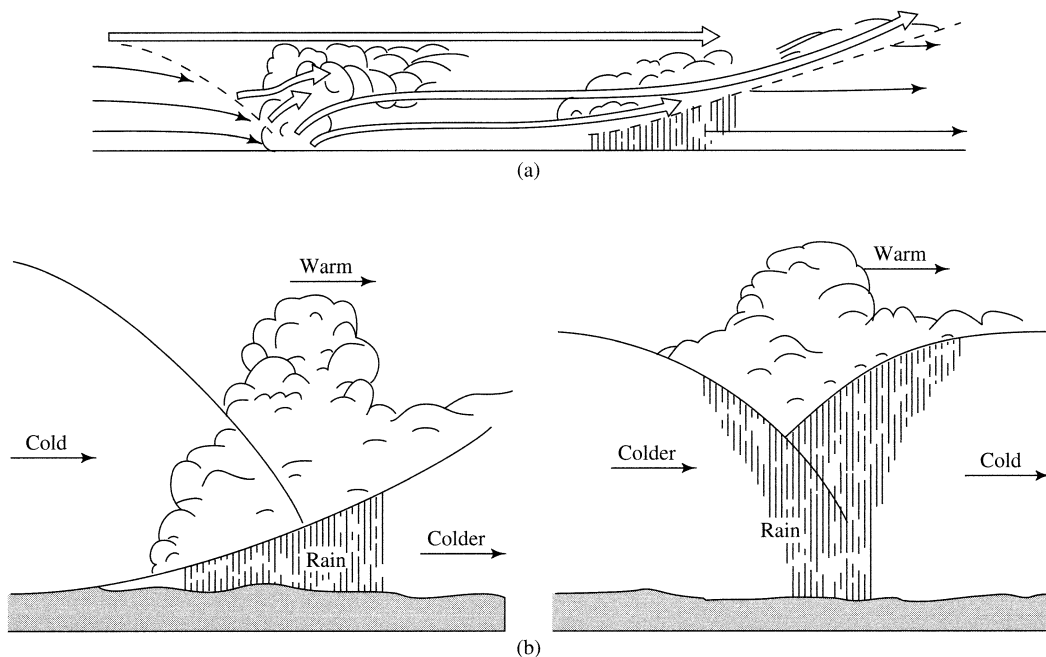


Figure 4.2 Cross-sectional view of extratropical cyclone development. Arrows indicate wind flow. (a) Section through warm sector along dashed line of figure 4.1(d). (b) Sections for two types of occluded fronts along dashed line of figure 4.1e [Miller et al. (1984)].

figures 4.1c and 4.1d. Where the cold front overtakes the warm front there is colder air everywhere at the surface with warm air above, and the front is said to be **occluded** (figure 4.1e). Although the air-mass contrast at the surface is now weaker, it is still present aloft (figure 4.2b) and the rising of the warm air over the cold may continue to generate precipitation—in fact, the maximum rainfall intensity usually occurs during the early stages of occlusion (Miller et al. 1983).

Ultimately, several processes combine to bring the rain production to a halt: the temperature difference between the air masses decreases due to adiabatic cooling of the rising warm air and warming of descending cold air, the pressure contrast that initiated the convergence is reduced, and the inflow of moisture is reduced (figure 4.1f).

Evolution to the stage shown in figure 4.1c usually takes 12 to 24 hr, and the process is typically completed in another two or three days (Miller et al. 1983). Because the development takes place in the zone of westerly winds, the low-pressure center at the apex of the cyclonic circulation moves generally eastward, at a speed of about 1,000 km/day, as the cyclone evolves.

Figure 4.3 is a weather map showing a typical extratropical cyclonic storm over North America, generating precipitation over an area of some $500,000 \text{ km}^2$. Precipitation associated with extratropical cyclones thus covers wide areas, and persists for tens of hours to days at a given location. Because rates of uplift are relatively low, precipitation intensities are generally low to moderate. As noted above, precipitation at cold fronts usually covers a smaller area and is more intense than warm-front precipitation, and on occasion rates of uplift at cold fronts are similar to that produced by thermal convection (see below), producing bands of intense thunderstorms.

On a given winter day there are usually about 10 cyclonic storms in various stages of development throughout the midlatitudes. The net result of these storms, in addition to the production of precipitation, is the climatically critical equatorward transfer of colder air and the poleward transfer of warmer air and latent heat of condensation (figure 2.10).

4.1.2 The Intertropical Convergence Zone

The equatorward air flow in the low-latitude cells (or Hadley cells) of the general circulation (fig-

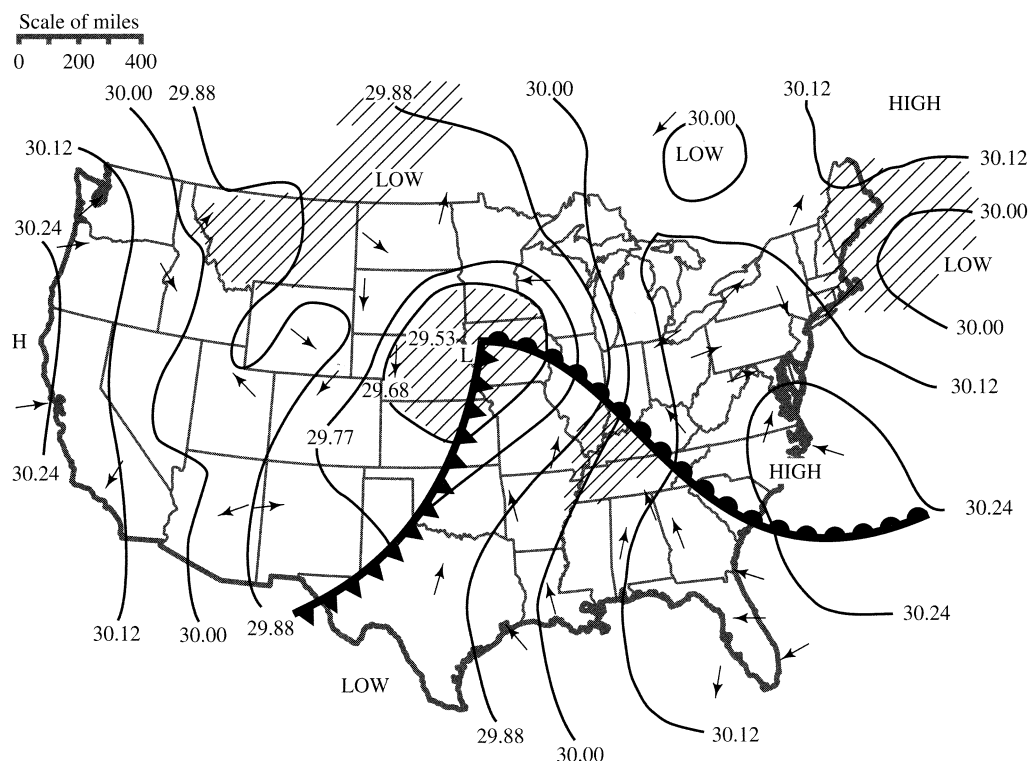


Figure 4.3 Weather map showing a cyclonic storm over the United States on 22 April 1970. Solid lines are isobars (pressure is measured in inches of mercury [in Hg]; multiply by 3.384 to convert to kPa). Shaded area is region of precipitation. Arrows show wind direction.

ure 2.11) creates a zone of convergence that circles the globe in tropical regions, called the intertropical convergence zone (ITCZ). The ITCZ migrates seasonally and is spatially discontinuous and intermittent (Barry and Chorley 1987), but it is persistent enough to create the equatorial band of high average precipitation that is apparent in figures 2.22 and 2.23.

4.1.3 Tropical Cyclones

Tropical cyclones are cyclonic storms that form over the North and South Pacific and the North Atlantic oceans between 5° and 20° latitude. They have the potential to develop into extremely intense storms, which are called **hurricanes** (North America), **typhoons** (eastern Asia), **cyclones** (Indian Ocean), and **baguios** (China Sea).

Tropical-cyclone formation is not associated with fronts. It begins with a small low-pressure disturbance in a maritime tropical air mass. Sea-surface temperatures of at least 27°C (Miller et al. 1983) are required to induce high rates of evaporation into the

converging and rising air; the cooling of this air then triggers condensation, and the accompanying release of latent heat further fuels the uplift. If conditions are right, the circulation will intensify until winds near the center reach speeds as high as 65 m/s. A fully developed hurricane (by convention, a tropical storm becomes a hurricane when its winds exceed 33 m/s) has the structure shown in figures 4.4 and 4.5 (on p. 139).

Because they form in the belt of easterly winds, the initial movement of hurricanes is usually westward; however, they often move poleward into the zone of westerly winds and may be swept well into the midlatitudes (figure 4.6 on p. 139). Because of the reduction in evaporation, their intensity lessens when they move over colder water or, especially, land. However, they can persist for thousands of kilometers over land, moving at speeds of about 5 to 7 m/s and delivering very high rates of rainfall, as well as destructive winds, over hundreds of thousands of square kilometers.

Figures 4.7 and 4.8 on p. 140 show the global frequency and seasonality of tropical cyclones. The concentration of storms in the summer/early fall reflects the necessity of high sea-surface temperatures in triggering hurricane development.

Most of the highest riverine floods of medium-to large-size drainage basins along the eastern seaboard of the United States have been caused by hurricanes. Notable examples (among many) include the infamous "'38 Hurricane" (21 September 1938), which dumped between 7 and 15 cm of rain in 24 hr

on most of New England (Brooks 1940) and caused massive flooding; Hurricane Agnes, which spent almost a week over the Middle Atlantic states in June 1972 and produced exceptionally serious flooding in the Carolinas, near record floods in Virginia, and record-breaking floods in central Pennsylvania and western New York (Hopkins 1973); and Hurricane Irene, which produced widespread devastating floods throughout Vermont in August 2011. Interestingly, the '38 Hurricane had other lasting hydrologic effects: So many trees were destroyed by its winds

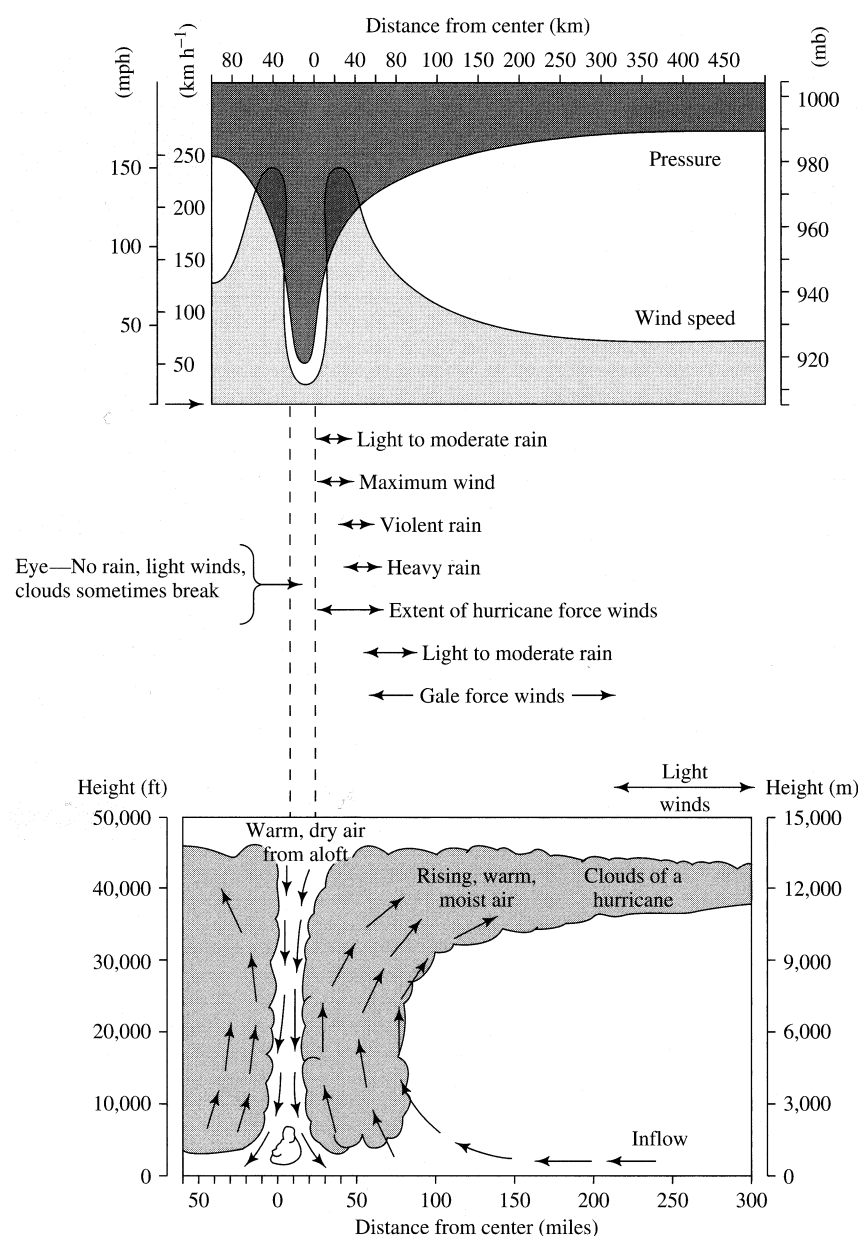


Figure 4.4 Vertical section of a fully developed hurricane showing patterns of wind, pressure, and rain [Miller et al. (1984)].

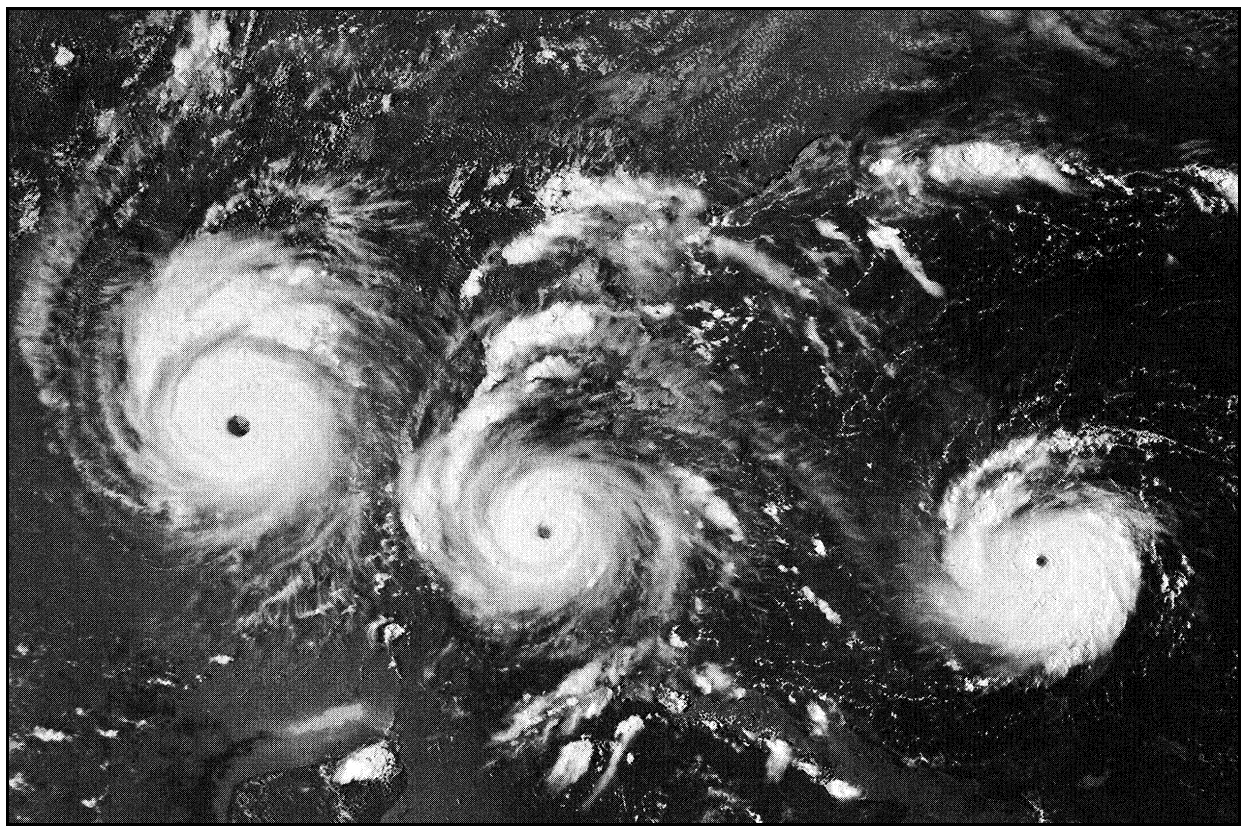


Figure 4.5 Successive satellite images of Hurricane Andrew moving across the southeastern United States, 24–26 August 1992.

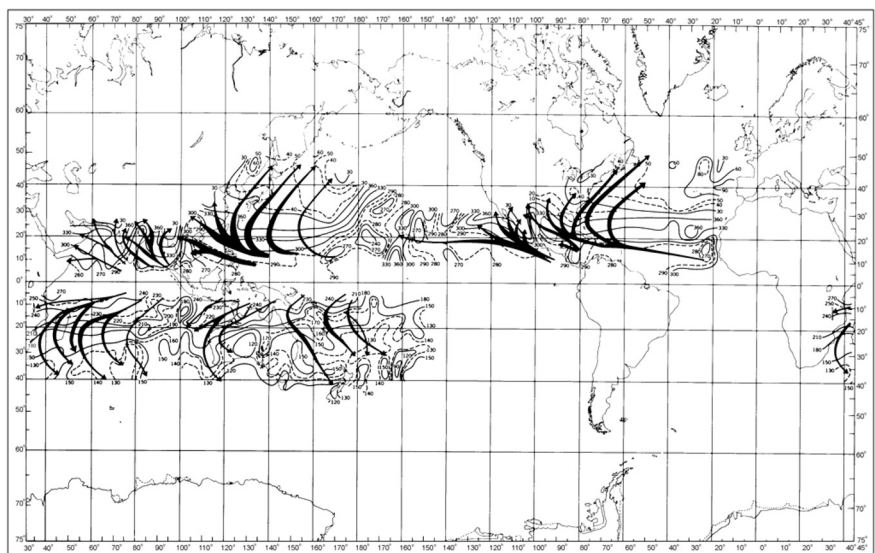


Figure 4.6 Arrows show global tropical cyclone tracks; width of arrow is proportional to storm frequency. Isolines show the direction toward which storms moved [US National Imagery and Mapping Agency (2002)].

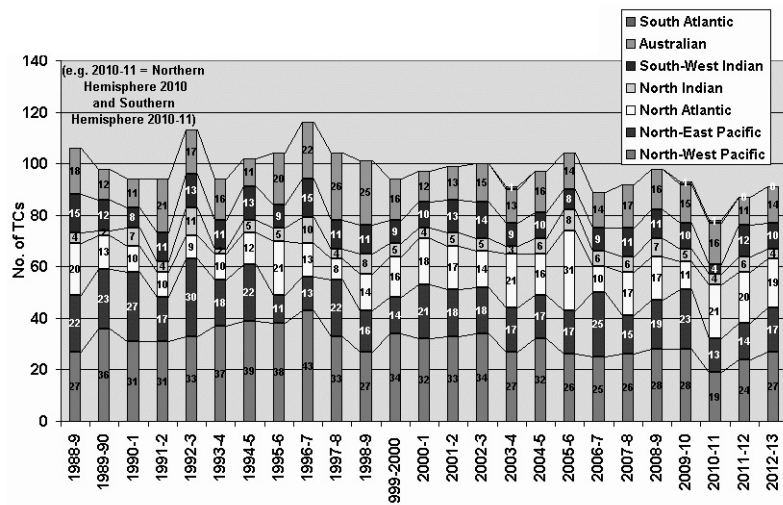


Figure 4.7 Global tropical cyclone activity by ocean basin, 1988–2013 [United Kingdom Meteorological Office (<http://www.metoffice.gov.uk/weather/tropicalcyclone>)].

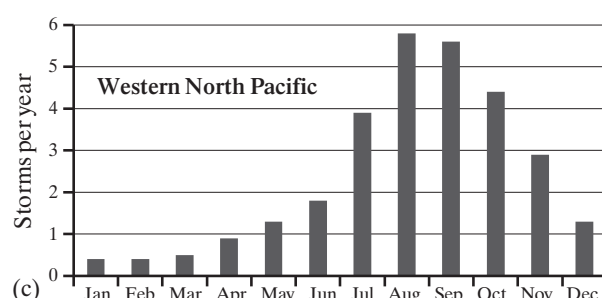
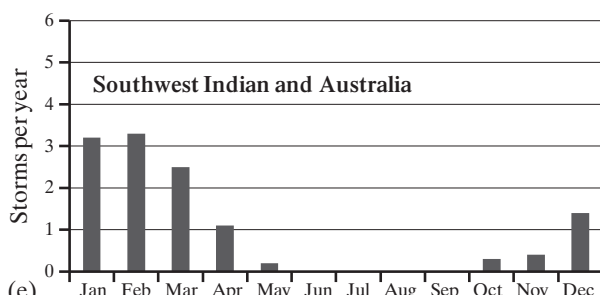
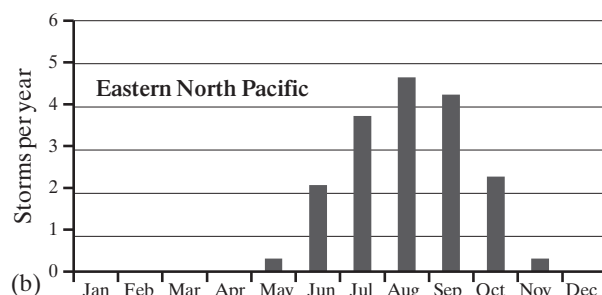
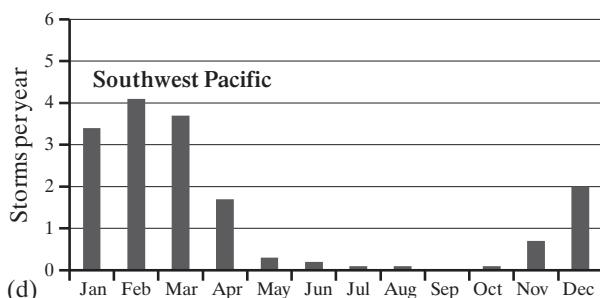
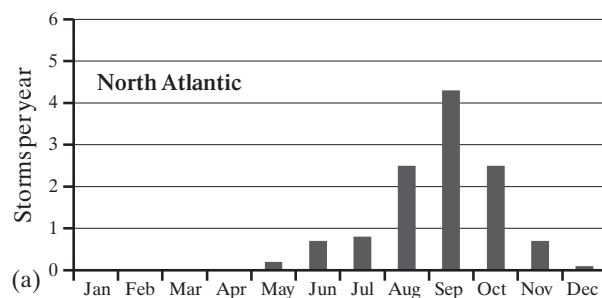


Figure 4.8 Seasonality of tropical cyclones in (a) North Atlantic Ocean, (b) eastern North Pacific Ocean, (c) western North Pacific Ocean, (d) southwest Pacific Ocean, (e) southwest Indian Ocean and Australia (US National Imagery and Mapping Agency 2002).

that evapotranspiration was reduced in central New England, causing a significant increase in the annual flow of rivers draining the region in the following three years (Patric 1974). Barlow (2011) showed that tropical cyclones are major contributors to extreme rainfall events in northeastern North America, and Knight and Davis (2009) found that the contribution of tropical cyclone precipitation to extreme rainfalls in the southeastern United States has been increasing 5 to 10% per decade due to increases in precipitation per storm and frequency of storms.

4.1.4 Convective Precipitation

Convective precipitation occurs when surface heating creates atmospheric instability that accelerates vertical uplift (section 3.5.3.7). The process is diagrammed in figure 4.9: During a summer day when intense solar radiation heats the ground surface, the air in contact with the surface is warmed from temperature T_0 to T_1 . The rising air cools initially at the dry adiabatic rate Γ_{da} , which is steeper than the ambient lapse rate Γ . If the air is relatively dry it will continue to rise and cool at the rate Γ_{da} until its temperature equals the ambient temperature. At this point, the atmosphere is stable: further rising would make the parcel colder and denser than the surrounding air, so convection ceases at this level. However, if the parcel contains enough moisture so that its dew point is reached during uplift, unstable condi-

tions persist and cooling continues at the saturated adiabatic rate Γ_{sat} . In this case, the parcel's temperature remains higher than ambient, and uplift and condensation continue, forming clouds and often leading to significant precipitation. Figure 4.10 shows cumulus clouds formed due to thermal convection over Cuba.

Thermal-convection cells usually cover areas of a few square kilometers. Rates of uplift due to thermal convection can be very high, reaching 10 to 30 m/s (Barry and Chorley 1982), compared with about 1 m/s along a typical frontal surface. Thus these cells produce very intense rain, often accompanied by lightning, thunder, and hail, covering small areas and lasting less than an hour. However, the frictional drag caused by the falling rain acts as negative feedback to eventually reduce the uplift velocity.

Figure 4.11 shows the average number of days with thunderstorms for the 48 contiguous United States; most of these storms occur in summer and are due to thermal convection.

4.1.5 Orographic Precipitation

In most regions of the world, long-term mean precipitation increases with elevation due to **orographic uplift**. This occurs because horizontally moving air encounters a topographic barrier and acquires a vertical component of motion as it flows over that barrier. The rate and degree of cooling are

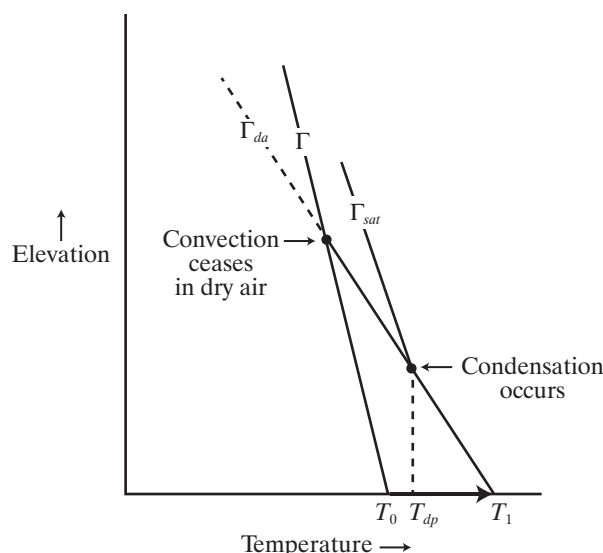


Figure 4.9 Formation of convective rainfall due to solar heating of ground.

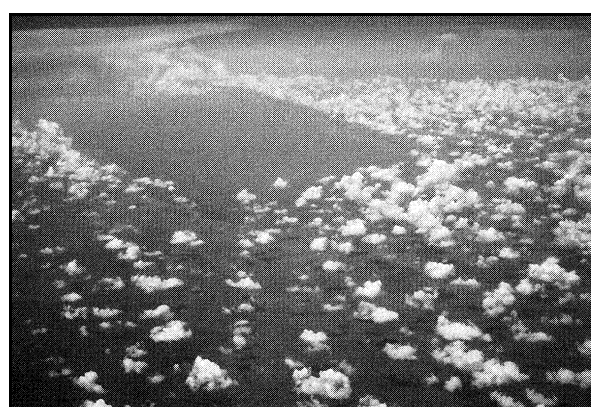


Figure 4.10 Fair-weather cumulus clouds formed by thermal convection over Cuba. Note that the clouds are present only over the land—the heat capacity of the sea prevents it from heating sufficiently to cause convection (photo by author).

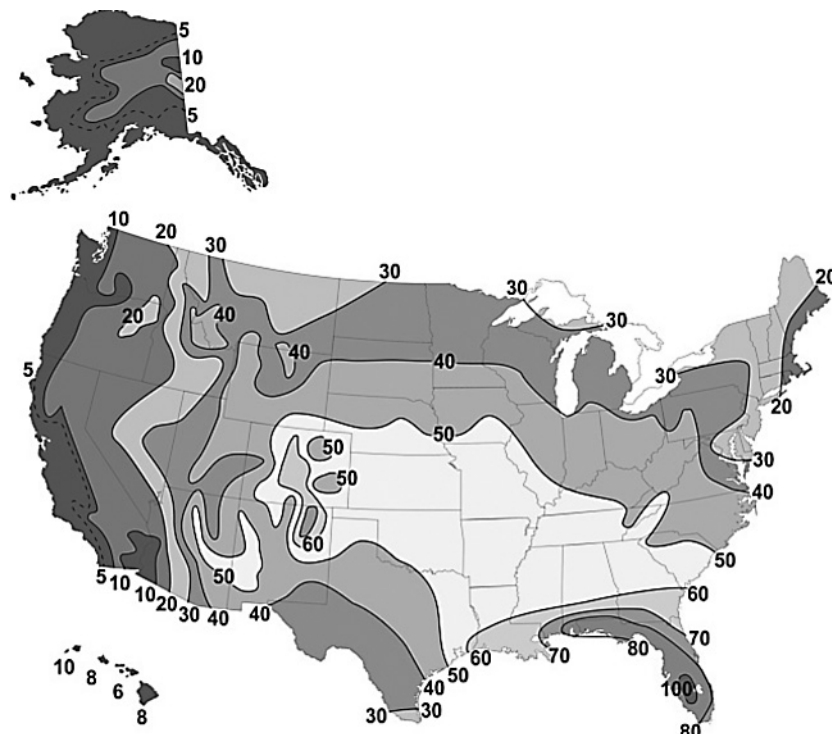


Figure 4.11 Mean annual number of thunderstorm days in the United States [US National Weather Service (http://www.srh.weather.gov/jetstream/tstorms/tstorms_intro.htm)].

determined by the wind speed, the wind direction relative to the barrier, the steepness and height of the barrier, and the temperature and humidity conditions that control convective stability.

Although the orographic effect is widespread, the rates of increase of precipitation with elevation vary widely from region to region (figure 4.12), and may even reverse at the highest elevations, especially in tropical regions (Barry and Chorley 1982). Within a region of orographic effect, the precipitation-elevation relation varies as a function of the aspect and inclination of individual slope facets and their relation to local topographic barriers. Barros and Lettenmaier (1994) reported orographic enhancement of precipitation by factors of 150 to 185% for hills up to a few hundred meters relief, and more than 300% when relief exceeds 1 to 2 km. However, orographic effects can be produced by topographic rises of only a few meters (Barry and Chorley 1982); figure 4.13 shows cumulus clouds induced by relatively small hills in the southern Great Plains of the United States.

Clouds and precipitation form on the windward slope of the topographic barrier, and peak precipitation often occurs windward of the crest. The downward air movement on the lee side causes adiabatic warming, which tends to dissipate the clouds and

thus turn off the precipitation-producing process, producing a **rain shadow**. A classic orographic situation exists in the central West Coast of North America (figure 4.14 on p. 144), where a series of mountain ranges are nearly perpendicular to persistent, moist westerly winds from the Pacific Ocean, and there is a close relation between long-term average precipitation and topography over a distance of 850 km. The reduced precipitation east of the Fraser Valley occurs because the air has lost most of its moisture by this point, but a subdued orographic effect persists.

In many, if not most, situations, orographic effects are the result of convective, frontal, or cyclonic mechanisms interacting with topography rather than a separate precipitation-generating mechanism. Even in the classic situation shown in figure 4.14, much of the precipitation comes from extratropical cyclones. The orographic effect is due to: (1) an increase in the duration of precipitation at higher elevations, and/or (2) higher intensities at higher elevations when precipitation is occurring at all elevations. The effect of increased duration is shown in figure 4.15 on p. 145 for an intensely gauged region in New England. Hendrick et al. (1978) also reported a threefold increase in hours of winter precipitation between 400 m and 1,200 m elevation in northern Vermont, but found

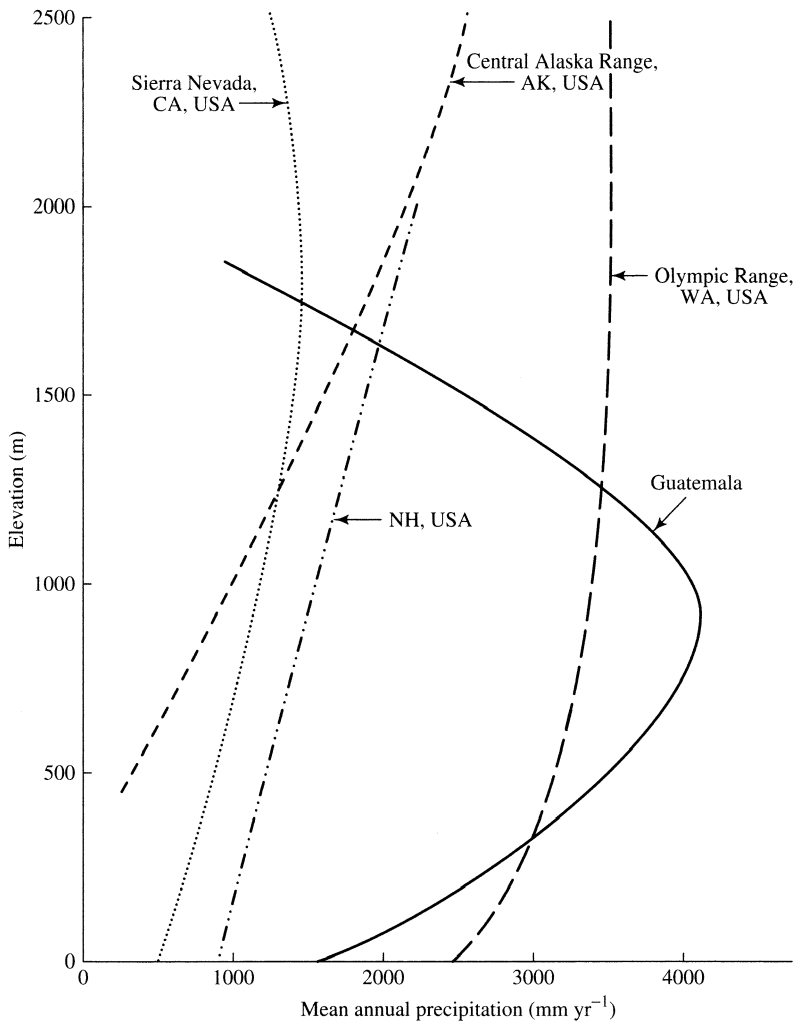


Figure 4.12 Relations between mean annual precipitation and elevation in several regions of North America [data from Barry and Chorley (1982) and Dingman et al. (1971, 1981)].



Figure 4.13 Cumulus clouds induced by uplift over small hills in the southern Great Plains of the United States (photo by author).

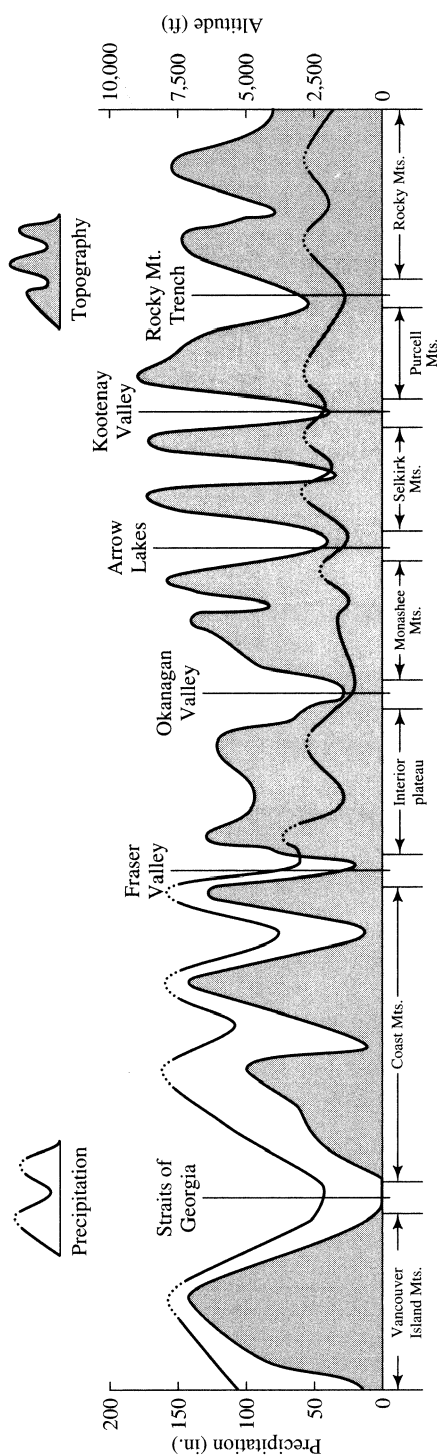


Figure 4.14 Relation between mean annual precipitation and topography across southern British Columbia, Canada [adapted from Bruce and Clark (1966)].

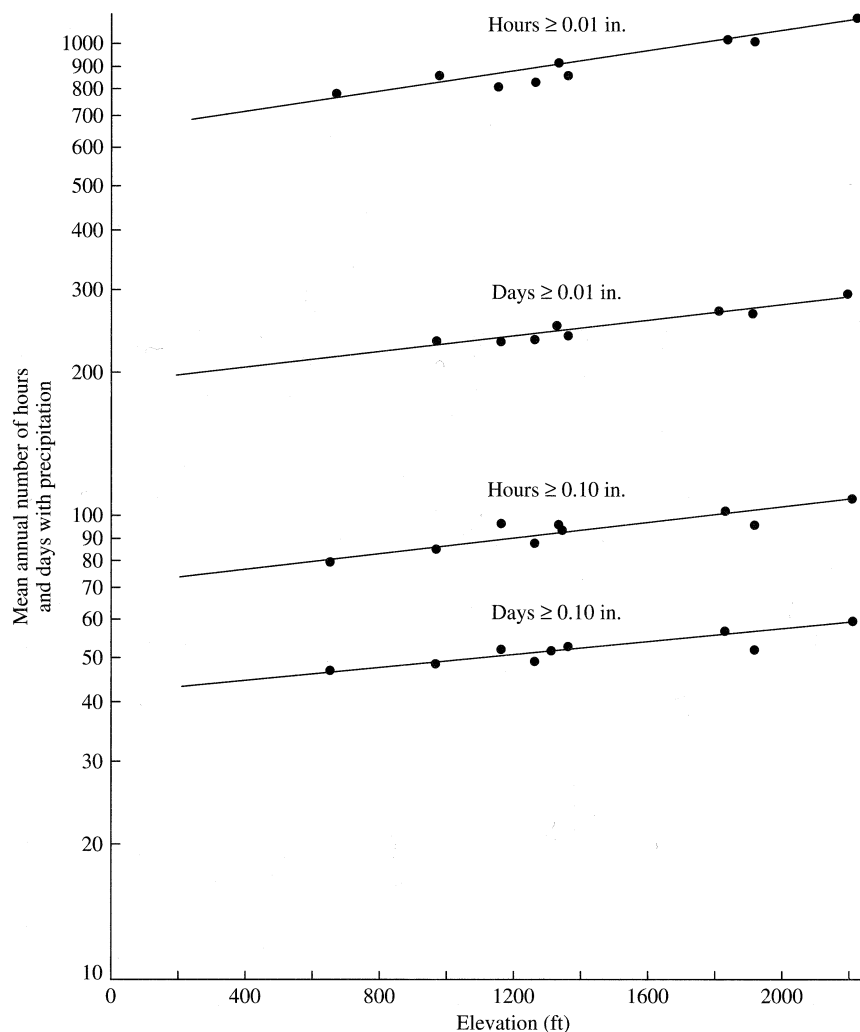


Figure 4.15 Number of days and hours with precipitation as a function of elevation in the Sleepers River watershed, Vermont [Engman and Hershfield (1969)].

that 75% of the difference in precipitation at the two elevations was due to the increase in intensity.

Because topography is permanent, orographic effects are reflected in long-term average precipitation values, and some of the highest average precipitation rates globally are due to orographic effects (see section 4.4.3.1). A well-known example occurs in conjunction with the monsoon over the Indian subcontinent: In summer, a northward shift in the position of the ITCZ and accompanying changes in circulation patterns induce moist southerly winds from the Bay of Bengal. These winds converge and rise over the Khasi Hills in Assam, India (north of Bangladesh), producing persistent heavy rains and giving the city of Cherrapunji (elevation 1,402 m) the highest measured average annual rainfall in the world: 11,872 mm/yr, more than half of which oc-

curs in June, July, and August (see table 4.9). Another extreme orographic situation is Mt. Waialeale in Kauai, Hawaii (1,570 m), where the average precipitation is 11,684 mm/yr.

Orographic effects can also produce extreme rainfall events. Smith et al. (2011) showed that some of the largest rainfall totals ever recorded for storms of less than 6-hr duration were produced by orographically enhanced convective thunderstorms in the central Appalachian region of the United States (section 4.4.3.1). They found that the frequency of catastrophic flooding in that region is controlled by the effect of complex terrain in altering thunderstorm dynamics.

In regions with significant relief and otherwise similar climate, the orographic effect commonly accounts for much of the spatial variation of precipita-

tion. For example, Dingman et al. (1988) found that elevation accounted for 78% of the spatial variation in long-term mean precipitation in New Hampshire and Vermont. Thus, one can often exploit the effect in estimating the average precipitation over a region, as in the hypsometric method discussed later in this chapter. The orographic effect can also carry over into many hydrological relations: Dingman (1981) showed that average streamflows, dry-season streamflows, and floods were all significantly related to elevation in central New England.

One of the most widely used approaches to generating maps of average annual precipitation from rain-gauge data, called PRISM (Parameter-Elevation Independent Regressions on Slopes Model) (Daly et al. 1994) (<http://prism.nacse.org>) is based largely on incorporation of orographic effects.

4.1.6 Occult Precipitation and Dew

Occult precipitation is precipitation that is “combed out” of clouds that encounter trees or other vegetation, and which is therefore not captured by normally sited precipitation gauges. **Fog drip** occurs when clouds move through forests, cloud droplets are deposited on vegetative surfaces, and the water drips to the ground. **Rime** is formed when super-cooled clouds encounter exposed objects, such as trees, that provide nucleation sites for ice-crystal formation and the buildup of ice, much of which eventually falls to the ground in solid or liquid form.

Several studies have shown that occult precipitation is hydrologically important in many high-elevation areas and in certain other environments. For example, fog drip amounts to about 450 mm/yr (20% of annual precipitation) at elevations above 1,200 m in northern New England (Lovett et al. 1982); about 880 mm/yr (about 30% of the annual precipitation) in a Douglas fir forest in Oregon (Harr 1982); and is the sole source of water in “cloud forests” on the rainless coast of Peru (Lull 1964). Rime contributes 38 to 50 mm/yr to water input in the Cascade Mountains in Washington (Berndt and Fowler 1969) and 20 to 30 mm/yr in the mountains of New Mexico (Gary 1972).

Dew forms under conditions of radiant cooling when the temperature of a surface (e.g., soil or a leaf) falls below the dew point and vapor condenses on the surface. The amount of dewfall is determined by how much and for how long the temperature is below the dew point, the humidity, the air circulation, and the properties of the surface (Monteith 1957).

The ratio of potential condensation to potential evaporation is roughly 1:7 in humid climates and 1:14 in arid climates, so dew generally does not contribute significantly to long-term precipitation. However, in semiarid and arid regions, dewfall can equal or exceed all other forms of precipitation for extended periods, e.g., totals of 50 to 100 mm/yr were reported in the Negev Desert of Israel (Zangvil 1996), and in humid regions it may be the biggest component over short periods. For example, Xiao et al. (2009) found that dew contributed up to 6.9% of the annual precipitation and over 20% of the precipitation of some months to crops and grass in northern Germany. In spite of its generally small contribution to precipitation totals, it appears that dew contributes significantly to the efficiency of water use by plants in humid as well as arid regions (Ben-Asher et al. 2010).

4.1.7 Moisture Sources and Precipitation Recycling

The global precipitation recycling ratio was defined in section 2.2.8.4 as the fraction of land precipitation that originates as continental evapotranspiration; this value averages 40% (table 2.13). As shown in figure 2.45, more than half the precipitation in central South America, western Africa, and a large part of Asia, including most of China, originates as land evapotranspiration. This ratio is important in assessing feedbacks that could affect hydrologic response to climate and the potential for direct human modification of climate through land-use changes.

The **local recycling ratio** is the ratio of precipitation in a particular region that originates as evapotranspiration from that region. Table 4.2 summarizes some estimates of local recycling ratios. Two environmentally sensitive regions have been found to have particularly high values of local recycling: the Amazon basin, and the Sahel region of sub-Saharan Africa. In the Amazon, Lee and Boyce (2010) estimated that the transpiration of flowering plants increases recycling of precipitation up to ~300 mm/yr (20% of total precipitation), increases the wet-season duration, and decreases atmospheric stability that promotes precipitation; it is feared that the destruction of the rain forest will significantly affect at least the regional hydrologic cycle (Lean and Warriow 1989). The Sahel, at the southern edge of the western Sahara, is a region of strong climatic fluctuation where there are concerns that local recycling pro-

Table 4.2 Estimates of Annual Precipitation Recycling Ratio.

Region	Recycling Ratio (%)	Source
Amazon	25	Brubaker et al. (1993)
Amazon	25	Eltahir and Bras (1994)
Amazon	35	Eltahir and Bras (1994)
Mississippi basin	10	Benton et al. (1950)
Mississippi basin	24	Brubaker et al. (1993)
Sahel	35	Brubaker et al. (1993)
Sahel	>90	Savenije (1995)

duces positive feedbacks that will amplify the desertification due to intensive land use (Savenije 1995).

Local precipitation recycling is at least seasonally important in other regions, and in some places is enhanced by land-use modifications. Evaporation from large lakes, such as the Laurentian Great Lakes, gives rise to localized regions of high precipitation on their downwind shores, especially in late fall and early winter. Similar effects have been found from large reservoirs: Degu et al. (2011) examined precipitation gradients near 92 large reservoirs in North America and found enhancements of humidity, convective instability, and precipitation in regions of Mediterranean (i.e., with highly seasonal precipitation) and semiarid climates. In central Alaska, moisture evapotranspired from extensive wetlands during summer may contribute a significant proportion of that season's precipitation. A similar effect, but due to irrigation, occurs in the US Great Plains: DeAngelis et al. (2010) found a correlation between high evapotranspiration over the heavily irrigated area above the Ogallala aquifer and warm-season rain up to 1,000 km downwind, producing precipitation increases of 15 to 30%.

4.1.8 Determining Precipitation Type

Weather observations usually report only the total liquid-water equivalent of precipitation without specifying whether it fell as rain, sleet, or snow. Obviously the type of precipitation is critical hydrologic information, because rain immediately recharges soil water and/or moves quickly to streams, whereas snow may be stored for extended time periods before melting.

Outside the tropics, most precipitation originates as snow in supercooled clouds (section 3.4), and the type of precipitation reaching the surface is determined by the height of the 0°C surface: Rain

occurs if that surface is high enough to allow complete melting, sleet occurs if there is partial melting, and snow if no melting. In a study in the Cascade Mountains in the United States, Maurer and Mass (2006) showed that observations of freezing height by vertically oriented radar did provide reliable partitioning (see also Bocchieri 1980). Because such observations are not widely available, the partitioning decision has usually been based on local surface air temperature, which is typically reported at precipitation-gauge sites. However, surface lapse rates are highly variable in space and time, so a fixed air-temperature criterion is likely to be unreliable.

Clearly a sound and practical basis for determining precipitation type would be extremely valuable; for example, Rutter et al. (2009) found that accurate partitioning of rain/snow had a major influence on the success of snowmelt models. Ding et al. (2014) reviewed published partitioning algorithms based solely on air temperature; they found that they varied considerably and generally had success rates of well under 50% when applied to new conditions when air temperatures were in the range 0–4°C. Using over 400,000 observations from a 29-yr period at over 700 stations in China, they formulated an alternative algorithm based on station elevation, daily average humidity, and daily average **wet-bulb temperature** (box 4.1). Wet-bulb temperature is the temperature that a parcel of air would reach if it were cooled to saturation by the evaporation of water, with all the latent heat of evaporation supplied by the parcel. Thus it approximates the temperature of precipitation more closely than does air temperature. Wet-bulb temperature can be calculated as a function of air temperature, humidity, and atmospheric pressure (equation 4B1.1).

As shown in figure 4.16 on p. 149, Ding et al. (2014) found that the rain/sleet and sleet/snow boundaries shifted toward higher wet-bulb temperatures as station elevation increased, and that the probability of sleet increased strongly as relative humidity increased. Their algorithm incorporates these effects, and had success rates between 53 and 66% when air temperatures were in the range 0–4°C, which is considerably better than approaches based on air temperature alone. Since the method is based on a very large data base and diverse conditions, it appears to be the most reliable practical approach for partitioning. However, it has not been tested outside China, and significant uncertainty remains about precipitation type at temperatures near 0°C.

Box 4.1 Rain/Snow Partitioning of Precipitation

As noted in the text, precipitation is almost always recorded as a depth of liquid water for a given time period, without specification as to whether it fell as rain, sleet, or snow. The type is critical for hydrologic analysis and modeling, so some algorithm must be used to determine it. The method developed by Ding et al. (2014), which is based on station elevation, wet-bulb temperature, and humidity, was far more successful in partitioning than algorithms based on air temperature alone and is described here. Their procedure approximates the effects of elevation and humidity on precipitation type that are shown in figure 4.16.

Step 1: Basic Data

Determine station elevation, z (m), and the daily average air temperature, T_a ($^{\circ}$ C), and relative humidity, RH (fraction), for the day of the precipitation event.

Step 2: Calculate Wet-Bulb Temperature

Wet-bulb temperature, T_{wb} ($^{\circ}$ C), is calculated as

$$T_{wb} = T_a - \frac{e^*(T_a) \cdot (1 - RH)}{\Delta(T_a) + 0.000643 \cdot p(z)}, \quad (4B1.1)$$

where $e^*(T_a)$ is saturation vapor pressure (kPa), given by

$$e^*(T_a) = 0.611 \cdot \exp\left(\frac{17.3 \cdot T_a}{T_a + 237.3}\right); \quad (4B1.2)$$

$\Delta(T_a)$ is the slope of the e^*-T_a relation (kPa/ $^{\circ}$ C), given by

$$\Delta(T_a) = \left[\frac{2,508.3}{(T_a + 237.3)^2} \right] \cdot \exp\left(\frac{17.3 \cdot T_a}{T_a + 237.3}\right); \quad (4B1.3)$$

and $p(z)$ is atmospheric pressure (kPa), given by

$$p(z) = 101.3 \cdot \exp(-0.00013 \cdot z). \quad (4B1.4)$$

Step 3: Calculate Parameter T_0

The parameter T_0 is empirically related to RH and z :

$$T_0 = -5.87 - 1.042 \times 10^{-4} \cdot z + 8.85 \times 10^{-8} \cdot z^2 + 16.06 \cdot RH - 9.614 \cdot RH^2. \quad (4B1.5)$$

Step 4: Calculate Threshold Temperatures

The snow/sleet threshold, T_{min} , is found as

$$T_{min} = \begin{cases} T_0 + 11.756 - 23.1 \cdot RH + 10.289 \cdot RH^2 & \text{if } RH > 0.78 \\ T_0 & \text{if } RH \leq 0.78 \end{cases}. \quad (4B1.6)$$

The sleet/rain threshold, T_{max} , is found as

$$T_{max} = \begin{cases} 2 \cdot T_0 - T_{min} & \text{if } RH > 0.78 \\ T_0 & \text{if } RH \leq 0.78 \end{cases}. \quad (4B1.7)$$

Note that if $RH \leq 0.78$, $T_{max} = T_{min}$; i.e., sleet does not occur.

Step 5: Determine Precipitation Type

$$\text{type} = \begin{cases} \text{snow if } T_{wb} \leq T_{min}; \\ \text{sleet if } T_{min} < T_{wb} < T_{max}; \\ \text{rain if } T_{max} \leq T_{wb}. \end{cases}$$

4.2 Measurement

Precipitation is the input to the land phase of the hydrologic cycle, so its accurate measurement is the essential foundation for quantitative hydrologic analyses, such as real-time flood forecasting or calibration and validation of hydrologic models (MacMillan et al. 2011). Unfortunately, there are often many reasons for concern about the accuracy of precipitation measurements, and these must be understood and accounted for in scientific and applied hydrologic analyses.

Observations of precipitation are made as point measurements at traditional rain-gauge stations (section 4.2.1) and over areas via radar (section 4.2.2)

and satellite (section 4.2.3). Estimations of precipitation over an area, such as a drainage basin, can be developed from point measurements, which is the focus of section 4.3, or by combining point measurements with radar and/or satellite observations.

4.2.1 Point Measurement

4.2.1.1 Types of Precipitation Gauges

Conceptually, the measurement of precipitation at a point is straightforward: A **rain gauge** or **precipitation gauge** may be as simple as a vessel open to the air in which the collected water substance is periodically measured or continuously recorded. The volume collected is divided by the area of the opening and recorded as the depth of precipitation.¹

Basic aspects of storage and recording gauges are described here; details of construction and operation are given by Shaw (1988), Nystuen et al. (1996), Strangeways (2007), World Meteorological Organization (WMO 2008), and Habib et al. (2010). The National Oceanic and Atmospheric Administration also provides information on their website: <http://www.ncdc.noaa.gov/crn/instrdoc.html>.

Nonrecording **storage gauges** may be simple straight-sided cylinders in which precipitation depth is periodically measured by a dipstick. However, they commonly contain a funnel that magnifies the depth of liquid precipitation (typically tenfold) for increased

precision. Accumulated water volume may also be measured by weighing or by decanting to a calibrated vessel. Nonrecording gauges are typically used to determine several hourly to daily precipitation totals.

Conventional recording gauges also collect precipitation in a vessel that must be periodically emptied, with the accumulated amounts tracked in various ways:

- **Weighing gauges** collect precipitation in a vessel on a scale and continuously record the accumulated weight. Older versions record the weight as a continuous trace on a chart on a rotating drum or

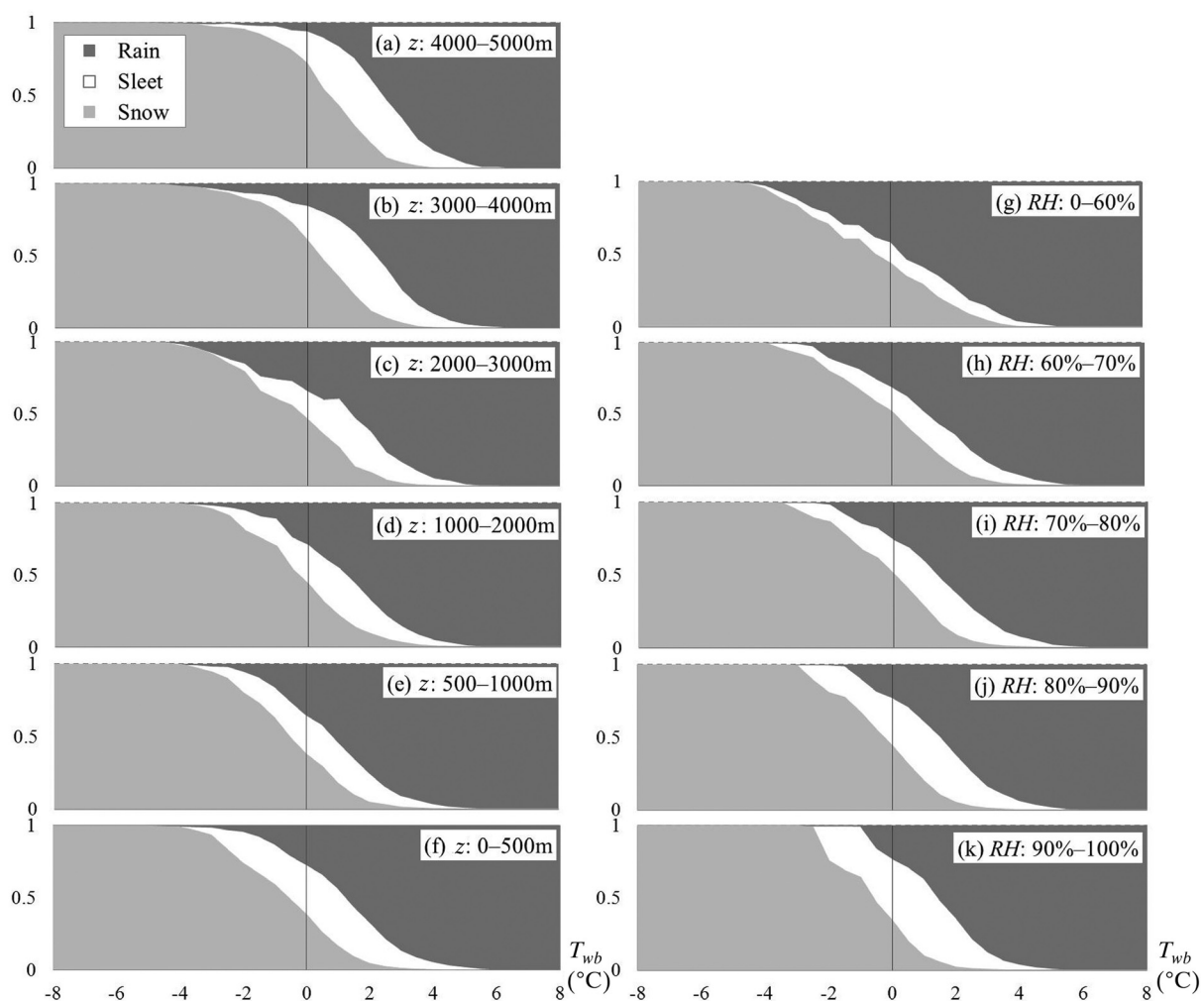


Figure 4.16 Fraction of observations of rain, sleet, and snow (vertical axes) as a function of wet-bulb temperature, T_{wb} , in different ranges of station elevation, z [(a)–(f)] and relative humidity, RH [(g)–(k)] [Ding et al. (2014)]. The dependence of precipitation types on surface elevation and meteorological conditions and its parameterization. *Journal of Hydrology* 513:154–163, with permission of Elsevier].

periodically (typically every 15 minutes) on a punch-paper tape; newer versions use direct electronic recording. Typical precision is 1 to 2.5 mm, but vibrating wire weighing devices are being introduced that improve this to 0.25 mm.

- **Tipping-bucket gauges** collect precipitation in one of a pair of small-capacity (typically 0.2 mm) vessels that are balanced on a fulcrum; when one vessel is filled, it tips and empties and records the time of this event and the other vessel is brought into position for filling.
- **Float gauges** collect precipitation in a vessel containing a float that is connected to an analog or digital recording device. Precision depends on the float and recording mechanism.

Frozen precipitation must be melted before measurement; this is often done by placing a charge of antifreeze in the collecting vessel or by heating elements. Less tractable problems arise when snow piles up at the gauge orifice and subsequently blows off or, as will be discussed more fully below, when wind eddies prevent significant amounts of snow from entering the gauge. For these reasons, it is usually preferable to measure the water content of snow by means other than standard precipitation gauges, as discussed in chapter 5.

Newer technologies have made possible **unconventional recording gauges** that do not use a collecting vessel:

- **Optical gauges** measure precipitation rate as proportional to the continuously recorded disturbance of a light beam emitted by a sensor. The intensity variation due to raindrops is proportional to rainfall rate. Some optical gauges can measure rain and snow separately.
- **Capacitance gauges** collect precipitation in a vessel containing a Teflon-coated stainless steel rod that, along with the collected water, creates an electrical capacitor. The capacitance, which increases with water depth, is recorded electronically.
- **Acoustical gauges** record the underwater sound made by raindrops falling into a body of water (e.g., a pond). Because the sound signatures produced by different sizes of drops are unique, the sound spectra can be used to infer rainfall rates.
- **Disdrometers** measure raindrop size by recording the momentum of drops striking a sensor. The number of drops per minute in each size class is counted and used to calculate total volume.

4.2.1.2 Factors Affecting Measurement Accuracy

In virtually all countries, gauge networks for climate and weather observations consist of conventional nonrecording and recording gauges, and each country has its own standards for gauge installations and observations. The World Meteorological Organization (2008) and references therein provide measurement guidelines and comparisons that are based on **reference gauges**. Ground-level gauges are used as reference gauges for liquid-precipitation measurement; the gauge is in the center of a pit with an anti-splash grid covering the pit (figure 4.17). The reference gauge for solid precipitation is the double fence intercomparison reference (DFIR), which has octagonal vertical double fences surrounding a cylindrical gauge with a conical wind-deflecting shield (figure 4.18).

Point-precipitation measurement in conventional gauges is subject to significant systematic (bias) error and random error (section 1.11). Errors due to wind, evaporation, and splashing result in measured values being systematically less than the true value; those due to faulty calibration, siting, and reporting can be positive or negative. The following sections provide guidance in siting precipitation gauges to minimize these errors and adjusting measurements to account for them.

4.2.1.2.1 Orifice Size

Studies by Huff (1955) and Brakensiek et al. (1979) indicate that orifice diameter should not be less than about 30 mm (area about 700 mm²), but above this limit, the size of opening has little effect on gauge catch of rain in most circumstances. All national standard gauges exceed this minimum.

Small-orifice gauges are not suitable for snow, and many of the measurement errors discussed in the following sections become more serious with smaller orifice size, especially losses due to wetting, evaporation, and splashing.

4.2.1.2.2 Orifice Orientation

For general hydrologic and climatic purposes, precipitation-gauge orifices should be horizontal to measure the water input to watersheds.

However, a given amount of horizontally measured precipitation may result in differing hydrologic inputs to slopes with differing steepness and orientation, and this should be accounted for in studies comparing agricultural conditions, runoff generation, or soil erosion in mountainous areas. To do this, de Lima (1990) prepared a nomograph for adjusting measured precipitation as a function of wind

speed and direction, type of rainfall, and slope inclination and aspect.

4.2.1.2.3 Orifice Height and Wind Shielding

Most precipitation gauges project above the ground surface and cause wind eddies that tend to reduce the catch, especially of smaller raindrops and snowflakes (figure 4.19). These effects are the most common and serious causes of precipitation-meas-

urement errors, and have been the subject of several studies (Larson and Peck 1974; Legates and DeLiberty 1993; Yang et al. 1998a, 1998b; Michelson 2004; Wagner 2009). Several types of wind shields are used to reduce wind effects (figure 4.20 on p. 153). The Alter shield is used in the United States (though most network gauges are unshielded), the Nipher shield is the standard in Canada, and the Tretyakov shield is widely used in Russia.



Figure 4.17
Rain gauge with
orifice at ground
level and sur-
rounded by plas-
tic "egg-crate"
structure to elim-
inate in-splash-
ing (photo by
author).

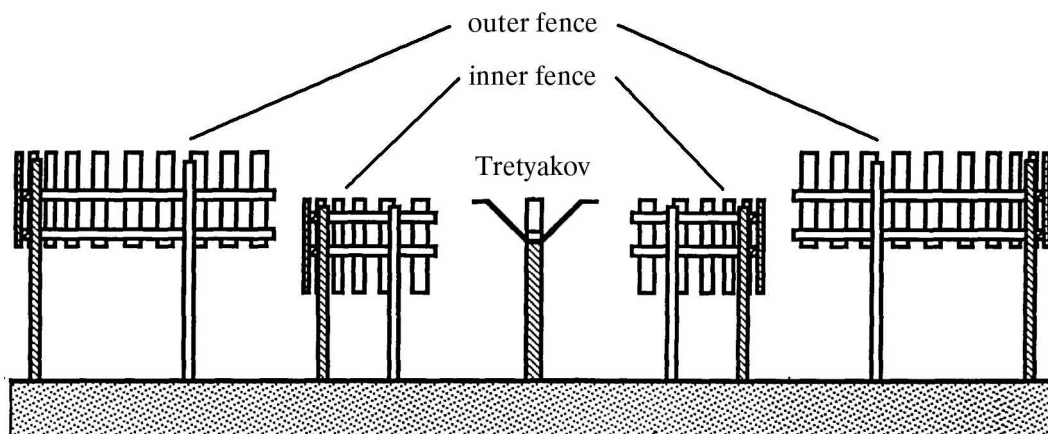


Figure 4.18 Cross section of WMO DFIR precipitation gauge [Goodison et al. (1998). *WMO Solid Precipitation Measurement Intercomparison Final Report*. WMO/TD No. 872, courtesy of World Meteorological Organization].

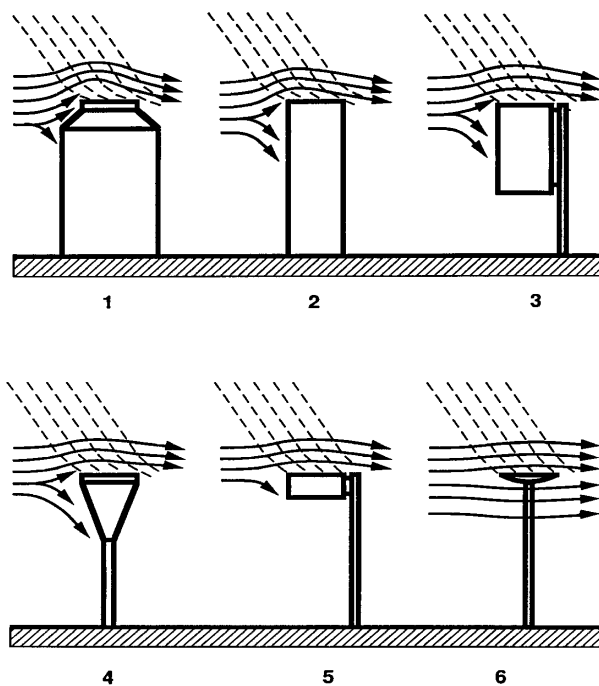


Figure 4.19 Shapes of precipitation gauges used in various countries (example 2 is the standard US nonrecording gauge) showing their effects on wind eddies that reduce gauge catches [courtesy of World Meteorological Organization (2008), *Guide to Meteorological Instruments and Methods of Observation*].

Detailed studies of wind effects and other errors on various types of gauges under various conditions are reported by Nystuen et al. (1996), Michelson (2004), Wagner (2009), and Habib et al. (2010). As an example, figure 4.21 on p. 154 shows average wind-induced catch ratios (ratio of gauge catch to reference-gauge precipitation) for daily observations via the standard US 8-in (203-mm) nonrecording gauge for rain, snow, and mixed precipitation as determined by Yang et al. (1998b). That study found that catch ratios varied considerably from event to event; the best-fit equations for these ratios, R (%), as functions of wind speed at gauge height z_g , $u(z_g)$ (m/s), with subscripts indicating rain (r), snow (s), or mixed precipitation (m); and unshielded (u) or Alter-shielded (A) gauges were

$$R_{ru} = \exp[4.605 - 0.062 \cdot u(z_g)^{0.58}]; \quad (4.1a)$$

$$R_{rA} = \exp[4.606 - 0.041 \cdot u(z_g)^{0.69}]; \quad (4.1b)$$

$$R_{mu} = 100.77 - 8.34 \cdot u(z_g); \quad (4.1c)$$

$$R_{mA} = 101.04 - 5.62 \cdot u(z_g); \quad (4.1d)$$

$$R_{su} = \exp[4.606 - 0.157 \cdot u(z_g)^{1.28}]; \quad (4.1e)$$

$$R_{sA} = \exp[4.606 - 0.036 \cdot u(z_g)^{1.75}]. \quad (4.1f)$$

Note that daily catch deficiencies of 10% for rain and well over 50% for snow are common in unshielded gauges.

Wind speed is usually measured at a height z_m that is above the gauge orifice, and the World Meteorological Organization (2008) recommends using the following relation to estimate the wind speed at the height of the gauge orifice:

$$u(z_g) = \frac{\ln(z_g/z_0)}{\ln(z_m/z_0)} \cdot (1 - 0.024 \cdot \alpha_o) \cdot u(z_m), \quad (4.2)$$

where z_0 is roughness height (taken as 0.01 m in winter and 0.03 m in summer), and α_o is the average vertical angle ($^{\circ}$) of obstacles near the gauge, which in practice can be estimated from table 4.3 on p. 154. Equation (4.2) is based on the Prandtl-von Kármán vertical-velocity profile [equation (3.27)].

It is important to note that gauge-catch ratios are different for different time-averaging periods; for example, Legates and DeLiberty (1993) found much smaller wind-induced deficiencies for monthly 8-in gauge values than those of equations (4.1a-f). For shorter time intervals, some studies have attempted to develop catch-deficiency estimates as functions of rainfall intensity and rain type as well as wind speed (Habib et al. 2010).

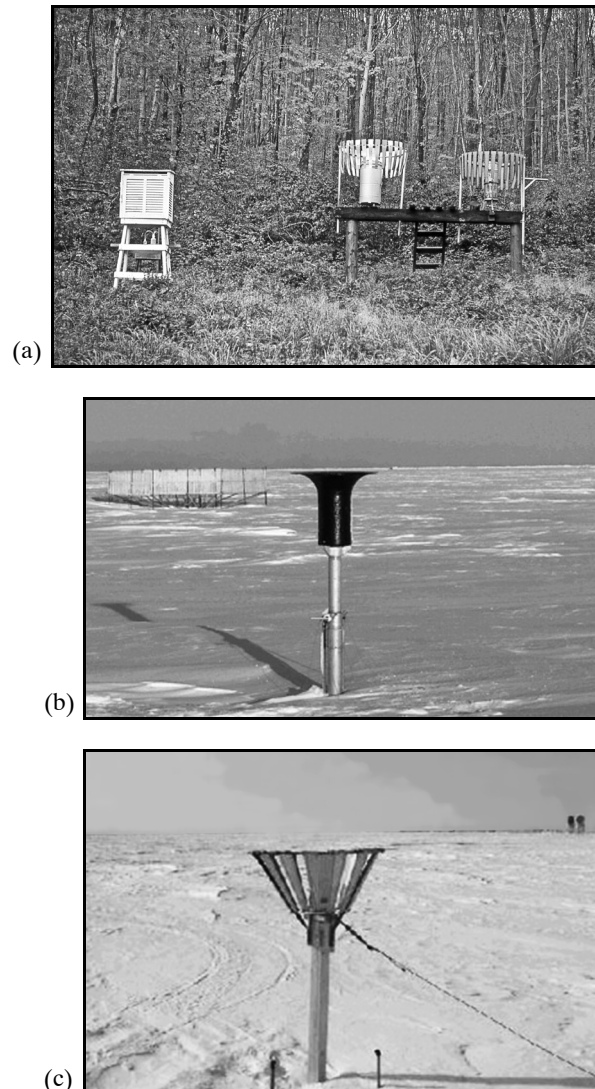


Figure 4.20 Commonly used precipitation-gauge wind shields. (a) Alter (United States); (b) Nipher (Canada); (c) Tretyakov (Russia).

Adam and Lettenmaier (2003) adjusted for wind-induced undercatch and wetting losses in developing a global $0.5^\circ \times 0.5^\circ$ gridded time series of precipitation for hydrological and other modeling studies. Figure 4.22 on p. 155 shows the country-specific catch ratios as a function of wind speed that they used for adjustment of daily snow measurements.

4.2.1.2.4 Distance to Obstructions

Individual trees, buildings, fences, or other isolated objects may produce wind eddies that can signif-

icantly affect (usually reduce) gauge catch, especially if they are appreciably taller than the gauge. Thus the best location for a gauge is within an open space in a fairly uniform enclosure of trees, shrubs, fences, or other objects of about the same height as the gauge opening, so that wind effects are reduced. No surrounding object should be closer to the gauge than twice (preferably four times) its height above the gauge (Brakensiek et al. 1979).

4.2.1.2.5 Splash, Evaporation, and Wetting Losses

If the surface of the water captured in a rain gauge is too near the orifice, in-falling drops can cause water to splash out, adding to the catch deficiency. This can be largely prevented by using deep gauges or gauges with walls that are vertical or slope outward below the orifice, by conducting the collected water to a covered vessel, and/or by emptying the gauge frequently (see Shaw 1988).

For ground-level gauges one must also prevent in-splashing from drops falling near the gauge. This is done either by: (1) placing the gauge in a small excavation so that its orifice is coincident with the general surface, but well above the immediately adjacent ground, (2) placing the gauge in a shallow excavation in which the near-surface soil has been replaced by an “egg-crate” structure (figure 4.17), or (3) covering the soil surface within several meters of the gauge with a mat of coarse fiber that prevents splashing (e.g., Neff 1977; Helvey and Patric 1983).

For small-orifice gauges and all nonrecording gauges that are read only at intervals of several days or more, one must prevent catch deficiencies due to evaporation from the water surface and the walls of the gauge (wetting losses). Such losses can be as much as 0.8 mm/day in hot weather (Habib et al. 2010). Again, use of a gauge in which the water is conducted to a closed vessel is one remedy. Another commonly used technique is to introduce a nonvolatile immiscible oil that prevents evaporation by floating on the collected water.

Errors due to splashing and evaporation in US-standard gauges are usually small and can be neglected; however, evaporative losses can be significant where low-intensity precipitation is common (Yang et al. 1998a). Correction for wetting losses in US-standard gauges can be made by adding 0.03 mm for each rainfall event and 0.15 mm for each snowfall event (Groisman and Legates 1994).

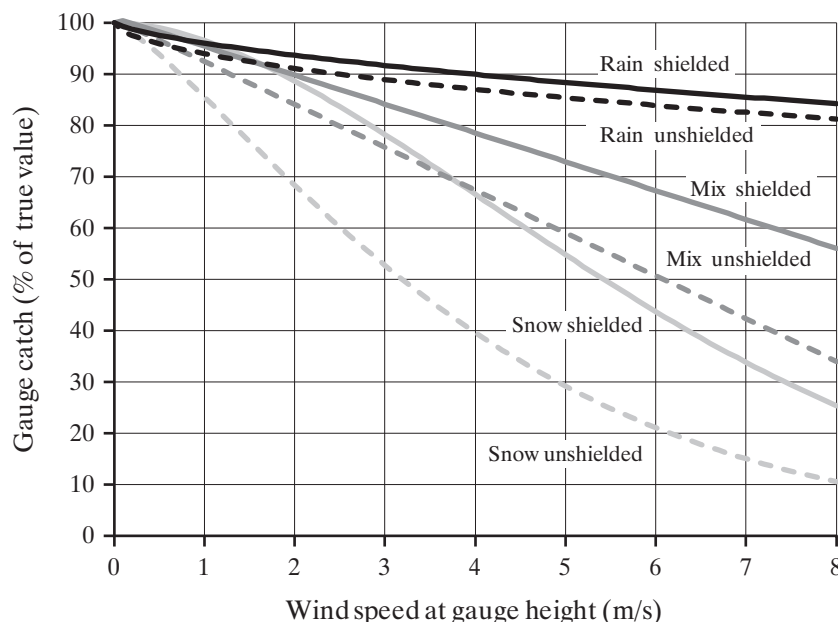


Figure 4.21 Average wind-induced catch ratios (ratio of gauge catch to reference-gauge precipitation) for daily observations via the standard US 8-in (203-mm) nonrecording gauge for rain, snow, and mixed precipitation as determined by Yang et al. (1998b) [equations (4.1a)–(4.1f)].

Table 4.3 Adjustment Angle for Effect of Obstructions on Wind Speed at Gauge Height [Equation (4.2)].

Class	Description	Angle, α_0 (°)
Exposed site	Only a few small obstacles such as bushes, group of trees, a house	0–5
Mainly exposed site	Small groups of trees or bushes or one or two houses	6–12
Mainly protected site	Parks, forest edges, village centers, farms, group of houses, yards	13–19
Protected site	Young forest, small forest clearing, park with big trees, city centers, closed deep valleys, strongly rugged terrain, leeward of big hills	20–26

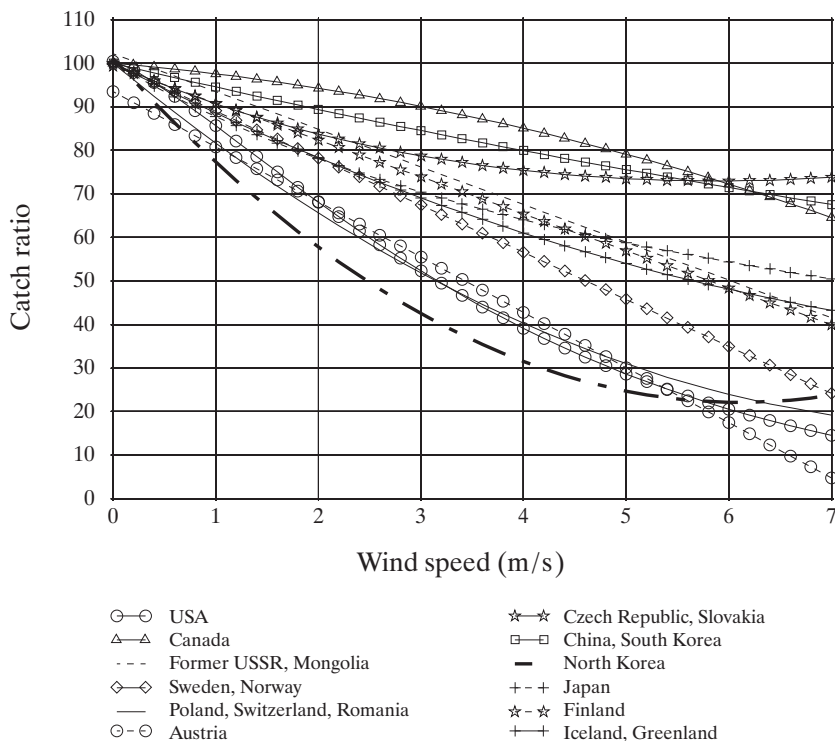
Source: World Meteorological Organization (2008).

4.2.1.2.6 Errors Due to Occult and Low-Intensity Precipitation

Special techniques for measurement of occult precipitation and dew are described in references cited in section 4.1.6. Failure to measure these inputs introduces another form of gauge-catch deficiency in environments where they are important.

In environments where a significant fraction of precipitation comes as very low intensity rain and snow, the observer may often note that some precipitation has entered the gauge since the last observation, but not enough to measure accurately. For example, in the United States observers measure rainfall in standard nonrecording gauges to the nearest 0.01 in (0.25 mm), and an observation of less than 0.005 in (0.13 mm) is called a “trace.” Traces are counted as zeros in totaling rainfall, so if there are many traces recorded, reported rainfall totals could be significantly less than the actual input.

This form of observation error is especially important in the high Arctic: Traces accounted for 10% of the summer precipitation on average in northern Alaska and could be as much as one-third of the total in some years. Brown et al. (1968) and Woo and Steer (1979) found similar results in northern Canada. Thus corrections for this effect have to be made in assessing the region’s water balance; these corrections can be made by multiplying the number of trace observations times one-half the maximum amount designated as a “trace” (i.e., by 0.0025 in or 0.065 mm in the United States) and adding the result to the recorded total precipitation (Dingman et al. 1980; see also Yang et al. 1998a and Yang et al. 2005).



4.2.1.2.7 Instrument and Recording Errors

In the United States and other countries, a significant portion of precipitation measurements are made and recorded manually and are subject to observer error.

Automated systems can experience equipment malfunctions and power outages, often at times of heavy precipitation. Systematic as well as random errors are often associated with recording rain-gauge measurements due to the mechanics of their operation. Tipping-bucket gauges miss rain in the process of tipping, so they underrecord during heavy rains; the use of heating elements to record snowfall greatly increases evaporative losses (Groisman and Legates 1994); and clogging and other malfunctions can reduce gauge catch. Weighing gauges can have mechanical malfunctions, and tend to have reduced sensitivity as the weight of collected water increases. Winter (1981) estimated that instrument errors are typically 1 to 5% of total catch.

To detect and correct for instrument error, it is recommended that a nonrecording gauge be installed adjacent to each recording gauge to assure that at least the total precipitation can be determined.

4.2.1.2.8 Errors Due to Differences in Observation Time

A large portion of precipitation measurements in the United States and worldwide are made in nonrecording gauges that are observed daily. The total gauge catch at the time of observation is recorded as the precipitation associated with that calendar day. In analyzing such data, and in checking for errors, one must be aware that the times of daily observations can vary widely from gauge to gauge within a region. Thus the precipitation from a storm on a given day might be recorded as occurring on that day at some gauges, and as occurring on the next day at other gauges. If a large storm occurred on the last day of a month, a discrepancy in observation times could lead to significantly different recorded monthly precipitation.

4.2.1.2.9 Errors Due to Changes in Gauge Siting

Changes in the type, exact location, and/or environment of the gauge associated with a weather station with a particular name designation are quite common. For example, many US first-order weather stations were relocated from metropolitan centers to suburban airports between 1930 and 1960, many of the gauges have been shifted between ground-level and rooftop sites, and many have had wind shields

added and/or removed (Groisman and Legates 1994). At cooperative stations in the US network the exact gauge location may change when a new observer is appointed, and trees may grow up or buildings be constructed around a gauge.

In the United States, detailed studies of meteorological data in West Virginia (Chang and Lee 1974) and Iowa (Carlson et al. 1994) found many inhomogeneities due to changes in measurement conditions, and emphasized the importance of examining data quality before undertaking climatic analyses. Such changes may alter the values of regional averages and trends, confounding attempts to detect climate change or to characterize meteorological statistics. A striking example of this was reported by Keim et al. (2003), who documented changes in the number of stations and the average latitude, longitude, and ele-

vation of stations over 70 years within a climatically homogeneous region in Massachusetts (figure 4.23). The observed cooling trend calculated from these data, which was opposite to the warming trend calculated from a group of stable stations (figure 4.23a), may be an artifact due to changes in average location (especially the increases in average latitude and elevation, figure 4.23c and figure 4.23e).

4.2.1.2.10 Quality Control

Because of the many potential sources of error, any use of precipitation data, whether for historical climatic analysis or real-time flood forecasting, requires a rigorous program of quality control. Thus an analysis of precipitation records should begin with a review of station history to see if changes in the type, location, or immediate environment of a

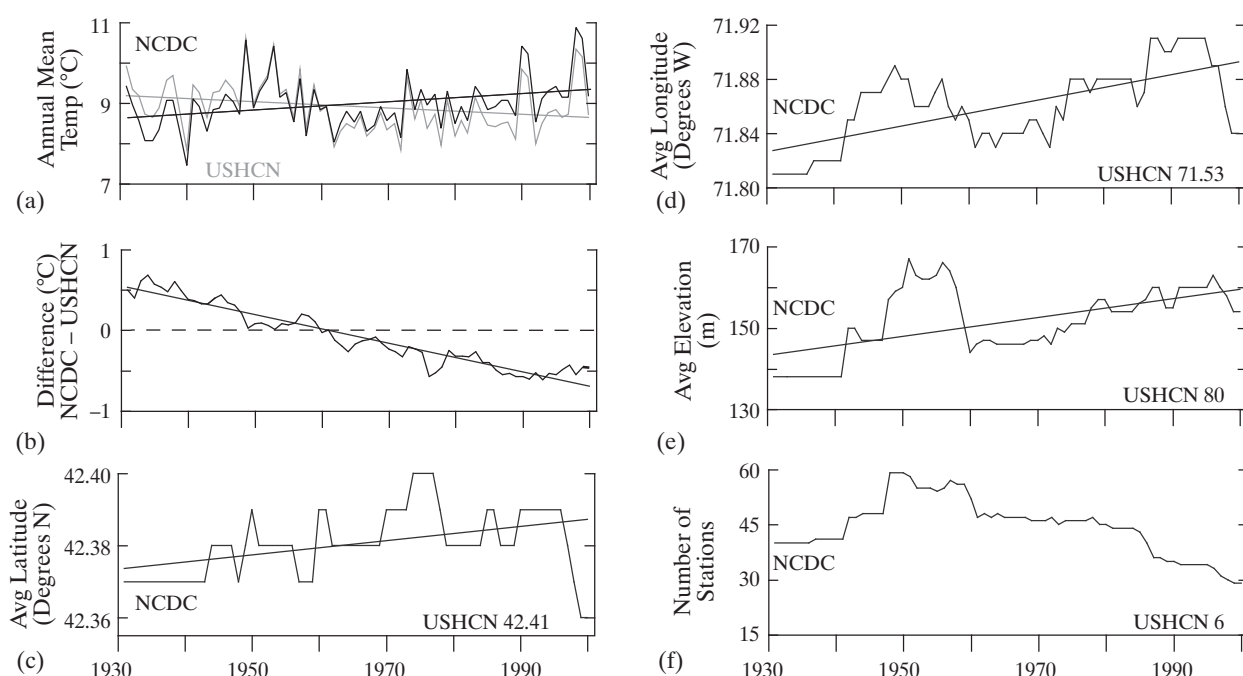


Figure 4.23 Changes in the number and locations of gauges in the observing network over time can induce spurious trends in climatic variables. In Massachusetts Climatic Division 2, the numbers and locations of stations in the US Historical Climate Network (USHCN) remained constant from 1931 to 2000, while stations in the National Climatic Data Center (NCDC) network changed. The cooling trend calculated from NCDC data (figure 4.23a), may be an artifact due to changes in average latitude and elevation (figures 4.23c and e). (a) Mean annual temperatures as determined from NCDC and USHCN networks. (b) Difference between NCDC and USHCN averages. (c) Mean latitude of NCDC stations. (d) Mean longitude of NCDC stations. (e) Mean elevation of NCDC stations. (f) Number of stations used for NCDC averages [Keim et al. (2003)]. Are there spurious temperature trends in the United States Climate Division database? *Geophysical Research Letters* 30(7), with permission of the American Geophysical Union].

gauge have occurred and, if so, to adjust the data to make a more consistent record. A common technique for detecting and correcting for inconsistent precipitation data is via a **double-mass curve**, as described in box 4.2.

Common errors in historical data include data gaps, impossible (e.g., negative) values, and unlikely high or low values (Habib et al. 2010). Anomalous values can often be detected by periodically comparing the records from a number of gauges in a region and noting observations that do not conform to the overall areal pattern of precipitation. If a particular

observation seems anomalously high, one can check weather maps to see if, for example, small-scale thunderstorm activity was occurring during the period of interest. It may also be possible to examine streamflow records for the region to see if high flows occurred. Probably the most effective quality-control strategy, and perhaps the most cost-effective, is to install pairs of gauges at each measurement site (Habib et al. 2010).

In the context of real-time flood forecasting, automated quality-control methods are essential; often these involve comparison of gauge measurements

Box 4.2 Double-Mass Curves

A **double-mass curve** is a plot, on arithmetic graph paper, of the successive cumulative annual^a precipitation collected at a gauge where measurement conditions may have changed significantly versus the successive cumulative average of the annual precipitation for the same period of years collected at several gauges in the same region that have not experienced such changes. The method attempts to detect a change in the proportionality between the measurements at the suspect station and those of the region, which is reflected in a change in the slope of the trend of the plotted points. Note that slope breaks in double-mass curves can occur because of climatic shifts; thus adjustments should only be made if there is reason to believe the break is due to a change in the measurement conditions.

If a double-mass curve reveals a change in slope that is significant (see the following discussion) and is due to changed measurement conditions at a particular station, the annual values of the earlier portion of the record should be adjusted to be consistent with the later portion before computing regional averages and other statistics. This adjustment is accomplished simply by multiplying the data for the period before the slope change by the factor K , where

$$K = \frac{\text{slope for period AFTER slope change}}{\text{slope for period BEFORE slope change}}. \quad (4B2.1)$$

Most analysts recommend that a break in slope be considered significant only if it persists for five or more years, and then only if it: (1) is clearly associated with a change in measurement conditions and (2) is determined to be statistically significant (Searcy and Hardison 1960).

Statistical significance of slope changes in double-mass curves can be detected by techniques called analyses of variance and covariance. These techniques are described in most introductory statistical texts, and

their application to double-mass curves was given by Searcy and Hardison (1960).^b Chang and Lee (1974) described a computerized objective approach to double-mass curve analysis that incorporates analyses of variance and covariance.

The following example illustrates the basic procedure. Table 4.4 shows the annual precipitation values for 1976 to 1992 at five gauges in a region. Gauge E was moved in 1981. To determine how the annual values for 1976–1980 should be adjusted to be consistent with the subsequent period of record, the cumulative annual values for station E are plotted against the cumulative values of the mean of the other four stations as a double-mass curve (figure 4.24 on p. 159). The slope of a straight line through the points prior to 1981 has a slope of 0.77 compared to a slope of 1.05 for a line through the points for succeeding years. The adjustment ratio K_{2X} is therefore

$$K_{2X} = \frac{1.05}{0.77} = 1.36.$$

Thus the annual precipitation values at station E before 1981 are multiplied by 1.36 to produce a consistent record for the entire period of measurement. The appropriately adjusted values are given in the last column of table 4.4(A).

Notes

^a The double-mass curve analysis is virtually always applied only to annual precipitation data. Data for shorter periods are naturally highly variable and tend to mask the kinds of measurement inconsistencies one is trying to identify.

^b However, the usual statistical tests of significance for differences in slope for regressions are not directly applicable for double-mass curves because the process of accumulation introduces a high degree of correlation between successive values. Because of this correlation, the conventional tests will often fail to detect statistically significant slope changes (see Matalas and Benson 1961).

Table 4.4 Data for Double-Mass Curve Example of Box 4.2 and Figure 4.24.

(A) This table gives measured annual precipitation (mm) for gauges A–E and adjusted values for gauge E prior to its being moved in 1981.

Year	A	B	C	D	E	Adj E
1976	1,010	1,161	780	949	834	1,373
1977	1,005	978	1,041	784	713	1,367
1978	1,067	1,226	1,027	1,067	851	1,451
1979	1,051	880	825	1,014	751	1,430
1980	801	1,146	933	923	604	1,090
1981	1,411	1,353	1,584	930	1,483	
1982	1,222	1,018	1,215	981	1,174	
1983	1,012	751	832	683	771	
1984	1,153	1,059	918	824	1,188	
1985	1,140	1,223	781	1,056	967	
1986	829	1,003	899	796	1,088	
1987	1,165	1,120	995	1,121	963	
1988	1,170	989	1,099	1,286	1,287	
1989	1,264	1,056	1,266	1,044	1,190	
1990	1,200	1,261	1,216	991	1,283	
1991	942	811	817	875	873	
1992	1,166	969	1,331	1,202	1,209	

(B) This table gives average and accumulated average values for gauges A–D and accumulated values for gauge E.

Year	Avg A–D	Cum A–D	Cum E
1976	975	975	834
1977	952	1,927	1,548
1978	1,097	3,024	2,399
1979	943	3,966	3,150
1980	951	4,917	3,754
1981	1,319	6,236	5,237
1982	1,109	7,345	6,411
1983	819	8,165	7,182
1984	988	9,153	8,370
1985	1,050	10,203	9,337
1986	882	11,085	10,424
1987	1,100	12,185	11,388
1988	1,136	13,321	12,675
1989	1,157	14,478	13,865
1990	1,167	15,645	15,148
1991	861	16,506	16,021
1992	1,167	17,673	17,230

with radar and/or satellite observations. A detailed description of the method used by the Lower Mississippi River Forecast Center is given by Caldwell and Palmer (2009).

4.2.1.11 Summary

While conceptually simple to make, point measurements of precipitation are subject to significant errors of several types. The most common and largest

errors are those due to wind effects for gauges that project above the ground surface, both shielded and unshielded. These errors are especially large for measurements of snow in standard cylindrical gauges.²

Following a thorough review of the problem, Winter (1981) concluded that errors in point measurements can be in the range of 5 to 15% for long-term data, and as high as 75% for individual storms.

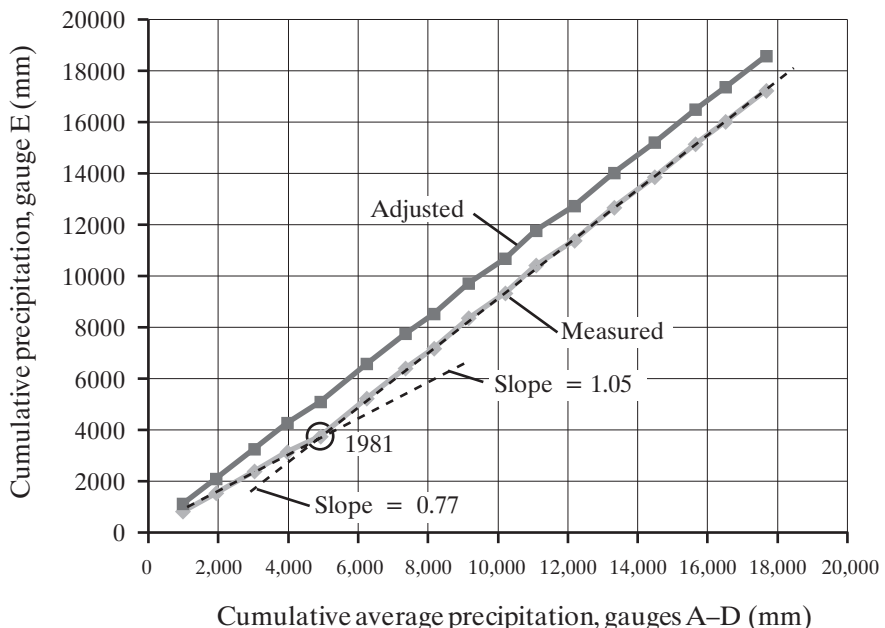


Figure 4.24 Double-mass curve for station E, example of box 4.2.

Rodda (1985) stated similarly discouraging findings: Catch deficiencies for rain collected in standard gauges were found to vary from 3 to 30% for annual totals and over a wider range for individual storms, with far larger errors for snow. In the United States the undermeasurement of annual-average precipitation at gauges averages 9%, and ranges from less than 6% where snow is absent to over 14% where snow is important (figure 4.25) (Groisman and Legates 1994). However, the underestimation varies seasonally and from year to year, and should be corrected on a monthly or daily basis. The implications of errors in precipitation data for water-balance computations are discussed in section 1.11.2.4. Clearly, using erroneous precipitation values as inputs to hydrologic models can lead to faulty calibration and validation decisions and faulty predictions and forecasts.

Thus it is usually unwise to accept reported point precipitation data without rigorous quality control. In spite of this,

well-maintained rain gauges provide the most accurate measurements of the true surface rainfall accumulations and intensities [and], despite the steady increase of using radars and satellites for rainfall estimation, rain gauges are expected to remain an important source of information for a variety of applications that require relatively accurate rainfall data. (Habib et al., 2010, p. 74)

4.2.2 Radar Measurement

Ground-based radar can be used to estimate the areal distribution of instantaneous precipitation rates in clouds, and these rates can be electronically integrated to provide estimates of total precipitation for any time period. Energy in the wavelength band between 1 and 10 cm (microwaves) is reflected by raindrops and snowflakes (collectively called **hydrometeors**). The strength of the signal reflected from a given distance depends on the size distribution, number per unit volume, state (liquid or solid), and shape of the hydrometeors, along with characteristics of the radar system, and the signal strength is related to precipitation intensity by empirical relations. Doppler radar systems also measure the horizontal velocity of the hydrometeors, and hence the movement of the storm.

In contrast to point measurements, ground-based radar systems provide spatially continuous estimates at small time intervals. This has revolutionized quantitative rainfall estimation globally, and radar is the primary observing system in many countries (Seo et al. 2010).

However, radar has inherent limitations: (1) it measures backscattering from hydrometeors in clouds rather than rainfall reaching the ground and (2) the radar beam gets wider with distance and cannot penetrate topographic barriers and buildings, and so has range-dependent biases. Although a constant cover-

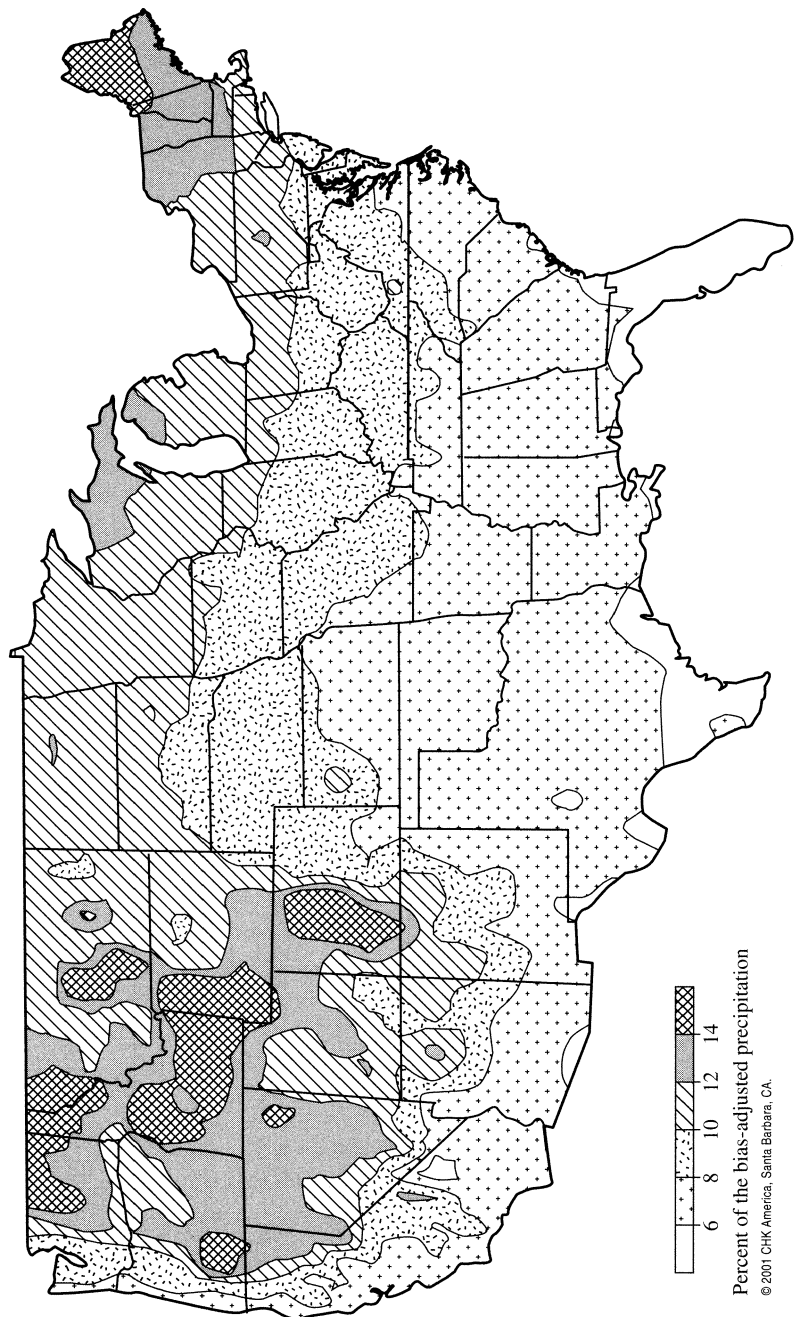


Figure 4.25 Estimated bias of precipitation measurements in the conterminous United States [Groisman and Legates (1994). The accuracy of United States precipitation data. *Bulletin of the American Meteorological Society* 75:215–227, reproduced with permission of American Meteorological Society].

age area is developed for each radar, in fact effective coverage varies with storm conditions, in part because vertical variations in reflectivity and the presence of hail or snow complicate the relation between reflectivity and rainfall rate.

Because of these limitations, it is necessary to use rain-gauge observations for bias correction of radar data. In the United States, River Forecast Centers of the National Weather Service have been developing quantitative precipitation-estimation procedures that combine data from radar and gauge networks since the early 1990s. A detailed review of these procedures and the state of the art is given by Seo et al. (2010). In the United States, the NEXRAD system of WSR-88D weather-radar stations provides information on precipitation distribution at over 130 sites, each with a range of 230 km. This system yields real-time images with qualitative indications of precipitation intensity and summary quantitative estimates of daily or storm total precipitation with a spatial resolution of about 2×2 km. The locations of these systems and the information they produce can be accessed at Internet sites maintained by the US National Weather Service (<http://radar.weather.gov>) and commercial weather enterprises. Global radar images are available through <http://weather.org/radar.htm>.

To date, radar systems have used single-polarization beams. Dual-polarization systems have several advantages, including more accurate detection of drop sizes, the ability to distinguish between rain and snow, improved correction for beam attenuation, and improved detection of spurious beam reflections. These systems are now being integrated into radar networks globally, including the US National Weather Service Weather Surveillance Radar System (Cifelli and Chandrasekar 2010).

4.2.3 Satellite Measurement

Satellites obtain information about the distribution and amounts of precipitation via both direct and indirect means (Arkin and Ardanuy 1989; Kidd et al. 2010). Direct observation is by passive and active (radar) sensing of microwave (MW) energy absorbed and scattered by hydrometeors; conversion of these observations into estimates of rainfall rates is done by accounting for the background radiation from the earth's surface and making assumptions about the size distribution of the hydrometeors. Indirect observation is by sensing visible (VIS) and infrared (IR) radiation emitted by clouds, converting the radiation flux to cloud-top temperature via the Stefan-

Boltzmann law [equation (2.1)], and making use of empirical correlations between the spatial and temporal coverage of clouds with temperatures below a threshold value and rainfall. Currently, geostationary satellites using infrared observations provide rainfall data every 30 minutes, and passive-microwave sensors provide data at < 3-hr intervals at a spatial resolution of 0.25° latitude $\times 0.25^\circ$ longitude (≈ 25 km $\times 25$ km) (Kidd et al. 2010).

Major programs have been instituted to refine satellite estimates of precipitation, including the Global Precipitation Climatology Project (GPCP), which collects and synthesizes information from polar-orbiting and geostationary satellites and surface stations; a series of NOAA polar-orbiting satellites with an advanced microwave sounding unit (AMSU); and the NASA Earth Observing System (EOS). NASA's Tropical Rainfall Measuring Mission (TRMM) is a low-orbiting satellite that includes precipitation radar as well as passive sensing of visible, infrared, and microwave radiation. These capabilities will be extended to cover the earth between the Arctic and Antarctic circles in NASA's Global Precipitation Mission, scheduled to launch in early 2014.

Several recent studies have evaluated satellite-precipitation estimation in various contexts. DiTomaso et al. (2009) developed a procedure to estimate precipitation using different frequencies of the US AMSU-B satellite, and found "very good agreement" with ground-based gauge and radar measurements. Tian et al. (2009) evaluated six satellite-precipitation data sets versus rain-gauge data in the United States. They found that satellites did well at detecting rainfalls > 40 mm/d, but had substantial biases, including missed precipitation (especially rainfall < 10 mm/d), up to 50% overestimation in summer and underestimation in winter, and very little ability to measure snowfall. Tian and Peters-Lidard (2010) evaluated six TRMM data sets at 0.25° as well as daily resolution and reported uncertainties of 40 to 60% over oceans and 100 to 140% at high latitudes and over complex topography and coastlines. Uncertainties were highest in winter and with light precipitation. AghaKouchak et al. (2011) found serious shortcomings in the ability of four satellite-based precipitation products to capture precipitation extremes, which are critical for flood forecasting. New methods for removal of bias from merged rain-gauge and satellite rainfall estimates were described by Li and Shao (2010) in Australia, Xie and Xiong (2011) in China, and Lin and Wang (2011) in Canada.

The utility of satellite-based precipitation estimates as inputs to hydrologic models is an important question. Yong et al. (2010) found that one TRMM precipitation-estimation product provided realistic hydrologic predictions, but another had almost no utility, and suggested corrections for future IR estimates. Pan et al. (2010) used satellite MW and MW + IR and ground-based precipitation data sets as inputs to a hydrologic model to compare predictions of soil moisture, evapotranspiration, and streamflow over the continental United States. They found that integrating rain-gauge data significantly improved predictions, and that rainfall-estimation errors have a large effect on estimates of soil moisture and streamflow, but only weak effect on evapotranspiration. In a similar study in Illinois, Behrangi et al. (2011) found that 6-hr and monthly streamflow predictions based on five satellite-based precipitation products were useful if biases toward overestimation in summer and underestimation in winter were corrected.

Considerable progress is being made in correcting for inherent biases in satellite-based precipitation data, and satellites will have an extremely important and growing role in assessing global precipitation. The earth's surface is 70% ocean and much of the land surface is virtually uninhabited, so that the percentage of the earth's surface on which precipitation-gauge measurements are available is very small and gauge densities are generally very sparse. Thus it is only with the advent of satellites that scientists have been able to obtain a global perspective on precipitation and other aspects of the hydrologic cycle, and satellite-based information will play an increasing role in providing precipitation data for hydrologic science and applications. More detailed descriptions of new programs are given by Kidd et al. (2010) and the Committee on Earth Observation Satellites' website (<http://www.ceos.org>).

4.3 Areal Estimation from Point Measurements

Hydrologists are almost always interested in precipitation over a region rather than at a point. The long-term average precipitation over a watershed, lake, or ground-water recharge area is the input to water-balance computations (section 1.8.1); the total precipitation over a watershed for a particular storm is the input for analyses of hydrologic response (chapter 10). As we have just seen, radar and satellite

measurements provide valuable information about areal precipitation extent and are increasingly used along with gauge measurements to develop information on spatial distribution. However, rain gauges usually provide the most accurate measurements and are often the only sources of historical information, so methods that derive spatial-distribution estimates using only gauge measurements remain essential tools. Furthermore, the methods are applicable to other types of hydrologically important point observations, such as soil moisture and aquifer properties.

Conceptually, the spatial average precipitation, P , over the region depicted in figure 4.26 is

$$P = \frac{1}{A} \cdot \iint_{x,y \in A} p(x,y) \cdot dx \cdot dy, \quad (4.3)$$

where A is the area of the region, (x,y) are coordinates of points in A , and $p(x,y)$ is the precipitation (average or total over a time period) at point (x,y) . Measurements of precipitation have been made at G gauges, $g = 1, 2, \dots, G$, in and near the region, and are designated $p_g \equiv p(x_g, y_g)$. This section introduces approaches to estimating areal averages and distribution from point measurements and assessing the uncertainty of such estimates.

Note that the values at each gauge may be a single observation (e.g., rainfall in a single storm) or a climatological statistic, in which the values at each point are calculated from time series [e.g., the long-term average annual precipitation (section 4.4.1) or an extreme rainfall quantity (section 4.4.3)]. If a climatologic statistic, estimations of uncertainty must account for temporal as well as spatial uncertainty, as described in section 4.3.5.

Approaches to computing an estimate of P , \hat{P} , can be divided into two classes:

1. Methods that compute \hat{P} directly as a weighted average of the measured values; and
2. Surface-fitting methods that first use the measured values to estimate the precipitation at regularly spaced grid-points in A , and then compute the average of these values. These methods also provide a model of the areal distribution.

4.3.1 Direct Weighted Averages

Methods of this type estimate the spatial average directly as the weighted average of the measured values:

$$\hat{P} = \sum_{g=1}^G w_g \cdot p_g, \quad (4.4)$$

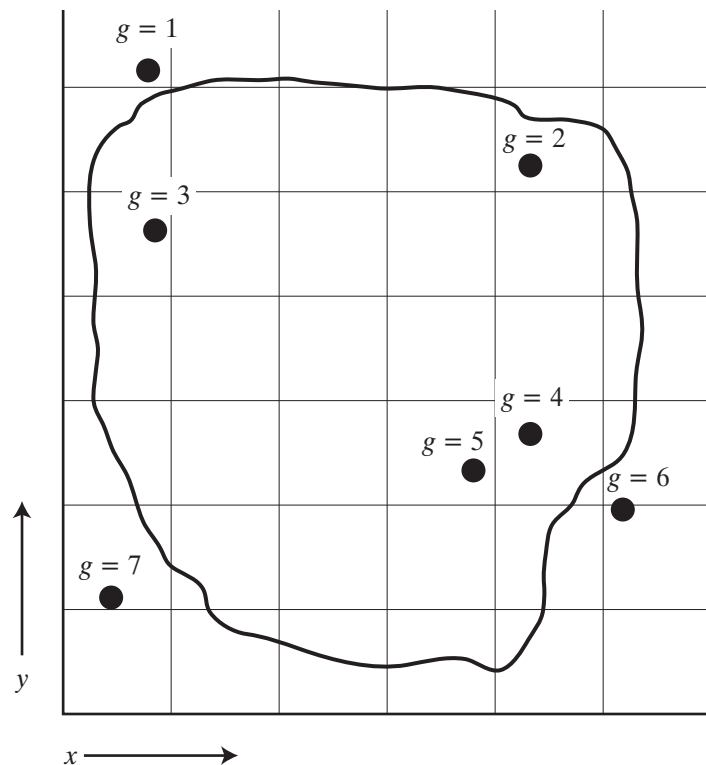


Figure 4.26 The problem of areal interpolation. Measurements of precipitation have been made at gauges (black dots) in and near the region, and are designated $p_g = p(x_g, y_g)$. The areal average is given by the integral of equation (4.3).

where w_g are **weights** that satisfy

$$\sum_{g=1}^G w_g = 1, \quad 0 \leq w_g \leq 1. \quad (4.5)$$

We will examine four methods of this type, which differ in the way in which the weights w_g are estimated.

4.3.1.1 Arithmetic Average

In this method, the weights in equation (4.4) are assigned a value, $w_g = 1/G$, for all gauges and the regional average becomes the arithmetic mean of the values measured at all the gauges in (and perhaps adjacent to) the region:

$$\hat{P} = \frac{1}{G} \cdot \sum_{g=1}^G p_g. \quad (4.6)$$

Assuming no error in the measurements, the spatial uncertainty in \hat{P} is calculated as described in box 1.1, and the spatial and temporal uncertainty assessed together as described in section 4.3.5.

Use of equation (4.6) is warranted only when it is safe to assume that the gauges constitute a representative sample of the areal precipitation for the time period of interest; i.e., where the gauges are well-distributed and there is little spatial variability.

4.3.1.2 Thiessen Polygons

In this approach, the precipitation at a point is assumed to be best estimated by the gauge that is closest to that point. Thus the region is divided into G subregions approximately centered on each gauge, and the subregions are defined such that all points in each subregion are closer to their “central” gauge than they are to any other gauge.³ Once these subregions are identified and their areas, a_g , measured, the weights are determined as $w_g = a_g/A$ and the spatial average is computed as

$$\hat{P} = \frac{1}{A} \cdot \sum_{g=1}^G a_g \cdot p_g. \quad (4.7)$$

Equation (4.5) is satisfied because

$$\sum_{g=1}^G a_g = A. \quad (4.8)$$

Assuming no error in the measurements of precipitation or area, the uncertainty in \hat{P} is calculated as described in box 1.1, and the spatial and temporal uncertainty assessed together as described in section 4.3.5.

The graphical method for delineating the boundaries of the subregions that are closest to each of the G rain gauges was developed by Thiessen (1911) (figure 4.27). First, straight lines are drawn between adjacent gauges to form a network of triangles; then perpendicular bisectors of each line are constructed and extended until they intersect to form irregular **Thiessen polygons**. Polygon areas can be measured by counting evenly spaced points on a grid overlay, by planimeter, or by using a computer-attached digitizing tablet. Diskin (1970) and Croley and Hartmann (1985) have developed computer algorithms for calculating Thiessen subregions that for a given point (x_u, y_u) find the gauge location that minimizes

$$[(x_u - x_g)^2 + (y_u - y_g)^2]^{1/2}. \quad (4.9)$$

The Thiessen method is an objective method of estimating a spatial average that takes some account of gauge distribution, but clearly it has no physical basis and does not give a model of the actual spatial variability of precipitation. It is most suitable for situations in which spatial variability is small and gauge distribution is irregular.

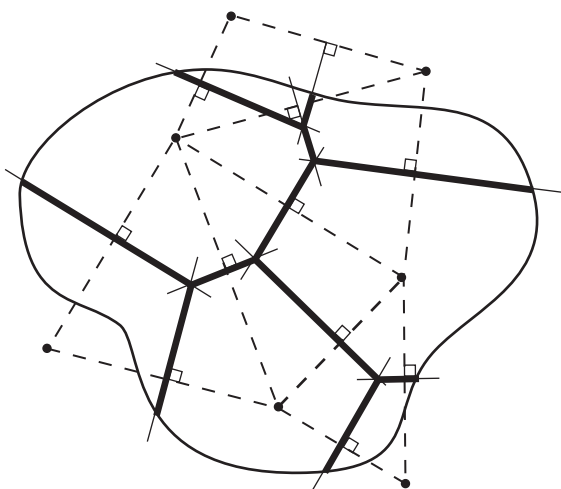


Figure 4.27 Construction of Thiessen polygons. The dashed lines connect adjacent gauges, the solid lines are perpendicular bisectors of those lines, and the heavy solid lines are the portions of the bisectors that constitute polygon boundaries. Points in each polygon are closer to the gauge near the polygon center than to any other gauge.

4.3.1.3 Two-Axis Method

The two-axis method developed by Bethlahmy (1976) derives w_g values that reflect the nearness of each gauge to the center of the region, rather than the relative area associated with each gauge (figure 4.28). To derive the weights, one first draws the longest straight line that can be drawn on a map of the region. The perpendicular bisector of this longest line is then drawn; this is called the **minor axis**. The **major axis** is then drawn as the perpendicular bisector of the minor axis. Next draw two lines from each of the gauges, one line to the farther end of the major axis, the other to the farther end of the minor axis. The angle between these two lines, α_g , is measured (it is always $< 90^\circ$). The sum of all the angles, \AA , is then computed:

$$\AA = \sum_{g=1}^G \alpha_g. \quad (4.10)$$

The weights are then defined as $w_g = \alpha_g / \AA$, and the average precipitation is calculated as

$$\hat{P} = \frac{1}{\AA} \cdot \sum_{g=1}^G \alpha_g \cdot p_g. \quad (4.11)$$

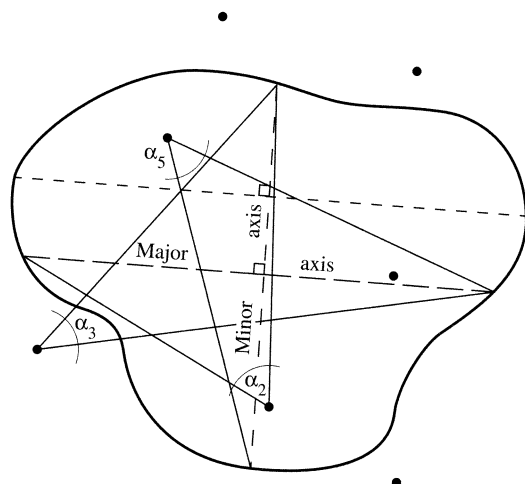


Figure 4.28 Construction of angles for the two-axis method. The region of interest is bisected horizontally at its widest point; the minor axis is drawn perpendicularly from that line. The major axis is the perpendicular bisector of the minor axis. Solid lines are drawn from each gauge to the farther end of the two axes to define the angles α_g . Angles are shown only for gauges 2, 3, and 5 for clarity.

Assuming no error in the measurements of precipitation or angle, the uncertainty in \hat{P} is calculated as described in box 1.1, and the spatial and temporal uncertainty assessed together as described in section 4.3.5.

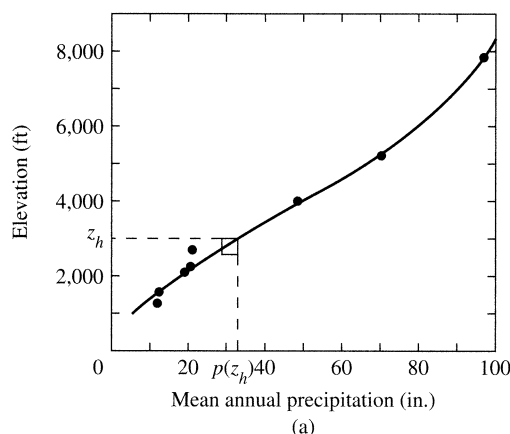
Although it has not been widely used, the two-axis method is simple and flexible—i.e., it is easy to adjust the weights when a gauge is added or deleted. A comparison study by Court and Bare (1984) concluded that the method is as acceptable as any of the other methods. Thus it could be an expedient alternative to the Thiessen-polygon method.

4.3.1.4 Hypsometric Method

The **hypsometric method** is a method of determining the weights in equation (4.4) in regions where orographic effects (section 4.1.5) dominate the spatial variability of precipitation. A topographic map or a digital elevation model (DEM) is required to apply the method.

The first step in applying this approach is to plot the measured p_g values against station elevation, z_g , and to establish a regional relationship between precipitation (p) and elevation (z). This functional relation, the “orographic equation,” can be determined by statistical techniques such as regression analysis (figure 4.29a). Commonly, it is approximated as a linear relation:

$$p(z) = a_z + b_z \cdot z \quad (4.12)$$



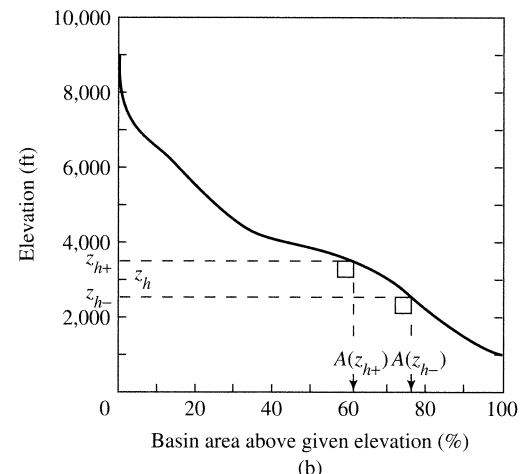
(a)

(e.g., Dingman et al. 1988). In some cases, the relation between $p(z)$ and z may vary systematically in the region—the windward side of a mountain range may have a more rapid elevational increase of precipitation than the leeward side (e.g., Troxell et al. 1942)—and in these cases the hypsometric method should be applied separately for each identified subregion.

Once the precipitation-elevation relation is established, a graph-relating elevation, z , to the area above a given elevation, $A(z)$, called a **hypsometric curve**, is constructed (figure 4.29b). These curves can be developed manually from a topographic map or automatically from a DEM. Average precipitation for the region is then computed via the following steps:

1. Select an elevation interval, Δz , and divide the total elevation range into H increments of Δz .
2. From the hypsometric curve, determine the area within each increment of elevation; designate these areas as a_h , $h = 1, 2, \dots, H$.
3. Use the precipitation-elevation relation [equation (4.12)] to estimate the precipitation, $\hat{p}(z_h)$, at elevations z_h , where z_h is the central elevation of each elevation increment.
4. Compute the estimated areal average precipitation as

$$\hat{P} = \frac{1}{A} \cdot \sum_{h=1}^H a_h \cdot \hat{p}(z_h). \quad (4.13)$$



(b)

Figure 4.29 Application of the hypsometric method to the Delta River Watershed, central Alaska (Dingman et al. 1971). (a) The estimated relation between mean annual precipitation and elevation. (b) The hypsometric curve z_{h-} and z_{h+} are boundaries of elevation increment, $A(z_{h-})$ and $A(z_{h+})$ areas above given elevations, and $a_h = [A(z_h) - A(z_{h+})]/A$. Other symbols as defined in text.

Equation (4.5) is satisfied because

$$\sum_{h=1}^H a_h = A. \quad (4.14)$$

Assuming no error in the measurements of precipitation, area, or elevation, the areal uncertainty in \hat{P} is chiefly due to the uncertainty in the orographic relation. This can be quantitatively evaluated if equation (4.12) is established by standard regression techniques (see, e.g., Haan 2002). If the precipitation being analyzed is a climatic quantity, temporal uncertainty must also be accounted for as described in section 4.3.5.

4.3.2 Spatial Interpolation (Surface Fitting)

4.3.2.1 General Features

Spatial interpolation (also called **spatial prediction**) is the process of estimating precipitation at grid points covering the region, $\hat{p}(x, y)$, from the measured values:

$$\hat{p}(x, y) = F_I(p_1, p_2, \dots, p_G), \quad (4.15)$$

where (x, y) are the rectangular coordinates of points in the region⁴ and F_I is an **interpolation function**. The $\hat{p}(x, y)$ values define a surface that is an estimate of the spatial variability, which can be depicted by contours of equal precipitation called **isohyets**. Thus spatial-interpolation methods are also called **surface-fitting methods**. Once the estimates are made at all grid points, the spatial average [equation (4.3)] can be estimated as

$$\hat{P} = \frac{1}{I} \cdot \sum_{x, y \in A} \hat{p}(x, y), \quad (4.16)$$

where I is the number of grid points in A .

All interpolation methods are based on the assumptions that the surface being modeled is continuous (no gaps or breaks) and has a single value at each coordinate point, and that the precipitation at an arbitrary grid point has some relationship to the measured values; this relationship is modeled by the interpolation function. The various surface-fitting approaches differ in the form of the interpolation function and can be classified as

1. **Deterministic methods**, which use arbitrary mathematical relations, or
2. **Statistical (or stochastic) methods**, which are based on minimum-estimation-error criteria.

Methods can be further categorized as

1. **Interpolation methods**, in which the fitted surface passes exactly through the measured values

$$[\hat{p}(x_g, y_g) = p_g], \text{ or}$$

2. **Smoothing methods**, in which the fitted surface does not pass exactly through the measured values.

Table 4.5 summarizes the classification of the methods discussed here and gives references for more detailed discussions.

In the discussion of these methods, we use the following notation: There are $g = 1, 2, \dots, G$ measured values and $i = 1, 2, \dots, I$ grid points in the area of interest. Specific locations in the area of interest are designated u and v , i.e., $u \equiv (x_u, y_u)$, $v \equiv (x_v, y_v)$; thus the measured precipitation at a given gauge is designated $p_g \equiv p(x_g, y_g)$ and the estimated precipitation at point u is $\hat{p}(u)$. The distance between any two points u and v is $d(u, v)$, where

$$d(u, v) \equiv [(x_u - x_v)^2 + (y_u - y_v)^2]^{1/2}. \quad (4.17)$$

4.3.2.2 Polynomial Trend Surfaces

Standard multiple-regression techniques can be used to determine a surface that “best fits” the measured values; i.e., that minimizes

$$\sum_{g=1}^G [p(x_g, y_g) - \hat{p}(x_g, y_g)]^2. \quad (4.18)$$

Surfaces can be of varying complexity. The simplest model is a plane,

$$\hat{p}(x, y) = b_0 + b_1 \cdot x + b_2 \cdot y, \quad (4.19)$$

and polynomials of higher order give increasingly irregular surfaces. Statistical tests can be applied to determine whether increasing complexity improves the fit to the data (see, e.g., Swan and Sandilands 1995). Since the degree of polynomial is selected a priori, this is a deterministic method; typically polynomial surfaces contain spurious highs and lows. And, unless the number of terms in the polynomial equals the number of measured values, it is a smoothing method. An alternative approach is the Lagrange polynomial method, in which the surface coincides with the measured values (Tabios and Salas 1985).

4.3.2.3 Inverse-Distance Weighting

In this technique, the interpolation function is based on the distance between the grid point and each gauge:

Table 4.5 Summary of Methods for Estimating Areal Precipitation from Point Measurements.

Method	Weighted Average/ Surface Fitting	Interpolation/ Smoothing	Deterministic/ Stochastic	Computational Complexity	Source for Full Description
Arithmetic average	Weighted average	NA	NA	Very low	This text
Thiessen polygons	Weighted average	NA	NA	Low	This text
Two-axis	Weighted average	NA	NA	Low	This text
Hypsometric	Weighted average	NA	NA	Low	This text
Polynomial-trend surface	Surface fitting	Smoothing	Deterministic	Moderate	Tabios and Salas (1985); Swan and Sandilands (1995)
Inverse-distance weighting	Surface fitting	Interpolation	Deterministic	Moderate to high	Tabios and Salas (1985); Swan and Sandilands (1995)
Spline functions	Surface fitting	Interpolation	Deterministic	Moderate to high	Creutin and Obled (1982); Lebel et al. (1987); Swan and Sandilands (1995); Hengl et al. (2010)
Multiquadric interpolation	Surface fitting	Interpolation	Deterministic	Moderate to high	Tabios and Salas (1985); Shaw (1988)
Geostatistical methods	Surface fitting	Interpolation	Stochastic	High	Tabios and Salas (1985); Creutin and Obled (1982); Lebel et al. (1987); Kitanidis (1992); Swan and Sandilands (1995); Haan (2002); Hengl et al. (2010)
Kriging					
Empirical orthogonal functions					
Optimal interpolation					

$$w_{ug} = \frac{1}{\sum_{i=1}^I \frac{1}{d(u,i)^c}} \cdot \sum_{g=1}^G \frac{1}{d(u,g)^c}, \quad (4.20)$$

where w_{ug} is the weight of gauge g on location u , c is an exponent, and $d(\cdot)$ is given by (4.17). The value of c is arbitrarily selected; typical weighting values are $c = 1$ (inverse distance) or $c = 2$ (inverse distance squared). Note that equation (4.20) gives infinite weight at a gauge site [$d(u,g) = 0$]; this means that $\hat{p}(g) = p(g)$, so this is a deterministic interpolation method. A drawback of this method is that it fails to account for redundant information in gauges that are close together.

4.3.2.4 Spline Functions

Splines are typically cubic functions whose derivatives are minimized such that they describe smooth surfaces. Conventional splines are a deterministic interpolation method [i.e., $\hat{p}(g) = p(g)$], however, the user can determine the distance over which the derivatives are calculated and adjust the degree of smoothing. Details of their mathematical structure are given by Creutin and Obled (1982) and Hengl et al. (2010).

4.3.2.5 Multiquadric Interpolation

Tabios and Salas (1985) describe an interpolation method in which the areal influence of each gauge observation is represented by a surface called a

multiquadric cone. The estimate at a given point is the weighted sum of the contributions of the cones for each gauge. Although this method has not been widely applied in hydrology, the method performed well in the tests described by Tabios and Salas (1985).

4.3.2.6 Geostatistical Methods

Geostatistics is a general term for a group of statistical methods in which the interpolation function equation (4.15) takes the form

$$\hat{p}(u) = \sum_{g=1}^G w_{ug} \cdot p_g, \quad (4.21)$$

where the weights w_{ug} are determined by applying statistical criteria (unbiasedness and minimization of estimation error) and are dependent on the **spatial correlation**, i.e., the degree of similarity of precipita-

tion values at two points as a function of the distance between them (box 4.3).

If the average and the variance of the precipitation are not functions of location, the precipitation process is **second-order stationary**, and we have for all points in A

$$E\{p(u)\} = P, \quad (4.22)$$

and

$$E\left[\left[p(u) - P\right]^2\right] = \sigma_p^2, \quad (4.23)$$

where $E\{\cdot\}$ denotes the **expected value** (i.e., the average) and σ_p^2 is the overall spatial variance of precipitation.

The core concept of geostatistics is that, on average, the difference in precipitation at points sepa-

Box 4.3 Spatial Correlation

The general statistical concept of correlation is discussed in section C.6 of appendix C. Here we apply the concept to assess the similarity of precipitation measurements made at various distances from each other.

Consider a region in which we have G gauges at which precipitation has been measured for T years. At each gauge, we can measure the total precipitation for each year, p_{gt} , and compute the average annual precipitation, m_{pg} , and the standard deviation of the annual precipitation, s_{pg} , as

$$m_{pg} = \frac{1}{T} \cdot \sum_{t=1}^T p_{gt} \quad (4B3.1)$$

and

$$s_{pg} = \left[\frac{1}{T-1} \cdot \sum_{t=1}^T (p_{gt} - m_{pg})^2 \right]^{1/2}. \quad (4B3.2)$$

(See box C.2 on the disk accompanying the text.)

There are a total of $G(G - 1)/2$ pairs of gauges. For each pair, say the two gauges $g = a$ and $g = b$, the correlation between annual values r_{ab} is

$$r_{ab} = \frac{\sum_{t=1}^T (p_{at} - m_{pa}) \cdot (p_{bt} - m_{pb})}{(T-1) \cdot s_{pa} \cdot s_{pb}}. \quad (4B3.3)$$

(See box C.6 on the disk.)

If $|r_{ab}|$ exceeds a critical value r^* that depends on T [equation (CB6.2)], we conclude that there is a significant linear relation between annual values of precipitation at

points a and b : Positive values of r_{ab} indicate a tendency for a given year to have relatively high or relatively low values of precipitation at both gauges, and negative values indicate a tendency for precipitation at both gauges to vary in opposite ways (a low year at one gauge tends to be a high year at the other, and vice versa).

When r_{ab} has been calculated for all pairs of gauges, the values accepted as significant can be plotted against the distance between each pair, d_{ab} , which is given by

$$d_{ab} = [(x_a - x_b)^2 + (y_a - y_b)^2]^{1/2}, \quad (4B3.4)$$

where (x_a, y_a) and (x_b, y_b) are the map coordinates of gauges a and b , respectively.

Figure 4.38 shows an r_{ab} versus d_{ab} plot for 29 precipitation gauges (406 gauge pairs) in Nebraska and Kansas. As is common for such plots, it shows considerable scatter. However, in order to use the optimal interpolation methods described in the text, the relation between r_{ab} and d_{ab} has to be described as a simple function. Tabios and Salas (1985) suggested the following alternative functional forms:

$$r_{ab} = [1 + c \cdot d_{ab}]^{-1}, \quad (4B3.5a)$$

$$r_{ab} = [1 + c \cdot d_{ab}]^{-1/2}, \quad (4B3.5b)$$

and

$$r_{ab} = \exp[-c \cdot d_{ab}], \quad (4B3.5c)$$

where c is a parameter to be determined from the data. Figure 4.38 shows equation (4B3.5c) with $c = 0.0031 \text{ km}^{-1}$ fit to the data of Tabios and Salas (1985). (See box 4.5.)

rated by a distance d increases as d increases. The relationship can be quantified in the **variogram**,⁵ $\gamma(d)$, which depicts the average squared difference in precipitation as a function of d :

$$\gamma(d) \equiv \frac{1}{2} \cdot E\{[p(u + d) - p(u)]^2\}. \quad (4.24)$$

Alternatively, the spatial relation can be expressed as the **spatial-correlation coefficient**, $\rho(d)$, which is given by

$$\rho(d) \equiv \frac{E\{p(u + d) \cdot p(u)\} - P^2}{\sigma_p^2}. \quad (4.25)$$

Note that $\rho(d)$ and $\gamma(d)$ are related as

$$\gamma(d) = 0.5 \cdot \sigma_p^2 \cdot [1 - \rho(d)]. \quad (4.26)$$

The variogram is a dimensional quantity that increases with separation, the spatial-correlation coefficient is a dimensionless quantity that decreases with separation.

The most widely used version of geostatistics, called **kriging**,⁶ is based on the variogram, so the discussion here will focus on that approach. The methods called **optimal interpolation** and **empirical orthogonal functions**, which are similar approaches that use spatial correlation, are described in Creutin and Obled (1982).

In practice, the statistics must be estimated from the sample of measured precipitation values. The mean and variance are estimated by standard statistical formulas (appendix C):

$$\hat{P} = \frac{1}{G} \cdot \sum_{g=1}^G p_g; \quad (4.27)$$

$$\hat{\sigma}_P^2 = \frac{1}{G-1} \cdot \sum_{g=1}^G (p_g - \hat{P})^2, \quad (4.28)$$

and the variogram as

$$\hat{\gamma}(d) = \frac{1}{2 \cdot G_d} \cdot \sum \left[p(u_g + d) - p(u_g) \right]^2, \quad (4.29)$$

where u_g represents a gauge location and G_d is the number of gauges separated by d .

$\hat{\gamma}(d)$ is called the **experimental variogram**. For a sample of G gauges, there are $G \cdot (G - 1)/2$ pairs and hence that number of d values. In general these

values will all be different, so the number G_d is determined by “binning” in intervals of Δd , i.e., G_d is the number of gauges in the range $(d - \Delta d/2) \leq d < (d + \Delta d/2)$, and the $p(u_g + d)$ and $p(u_g)$ values in equation (4.29) are replaced by averages for the pairs of stations included in each bin.

Typically, $\hat{\gamma}(d) = 0$ when $d = 0$, it increases with d , and levels off at some distance $d = D$, which is called the **range**. Note that this typical variogram relation will only be evident if:

1. There is an underlying relation between precipitation and separation;
2. Precipitation is not significantly affected by factors other than separation, such as elevation or distance from the coast (this is discussed further below);
3. Measurements errors are reasonably small (section 4.2.1.2); and
4. The average spacing of gauges is small enough to reveal the relation.

In kriging, the interpolation function is determined by a **model**, or **theoretical variogram** that is selected based on the form of the experimental variogram, and is a model of the spatial-covariance structure of the data. Only certain functional forms satisfy the mathematical requirements for an interpolation function (see, e.g., Kitanidis 1992; Haan 2002); some of the most commonly used are illustrated in figure 4.30. The interpolation function takes the form

$$\hat{p}(x, y) = \hat{p}(u) = \sum_{g=1}^G w_{ug} \cdot p_g, \quad (4.30)$$

where the weights w_{ug} are determined by the theoretical variogram (see Haan 2002 for details), and

$$\sum_{g=1}^G w_{ug} = 1. \quad (4.31)$$

Note that $w_{ug} = 0$ if

$$[(x_u - x_g)^2 + (y_u - y_g)^2]^{1/2} \geq D. \quad (4.32)$$

Figure 4.31 shows examples of experimental and theoretical variograms for mean annual precipitation in New Hampshire and Vermont.

Minimization of the estimation-variance function with the assumption that the theoretical variogram portrays the spatial covariance and the sum of the weights equals unity [equation (4.31)] leads to a system of simultaneous equations that can be solved for the weights, and another set of equations that ex-

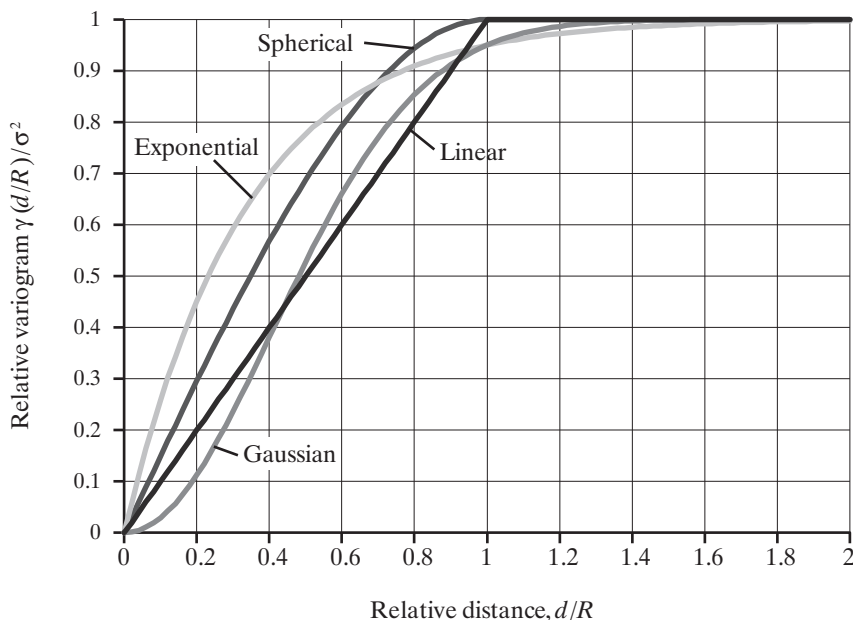


Figure 4.30 The forms of commonly used variogram models. The variogram value, $\gamma(d)$, is defined in equation (4.24). The vertical axis is the ratio of $\gamma(d/R)/\sigma^2$, where d is distance, R is the range, and σ^2 is the variance. When $d > R$, $\gamma(d/R) = \sigma^2$.

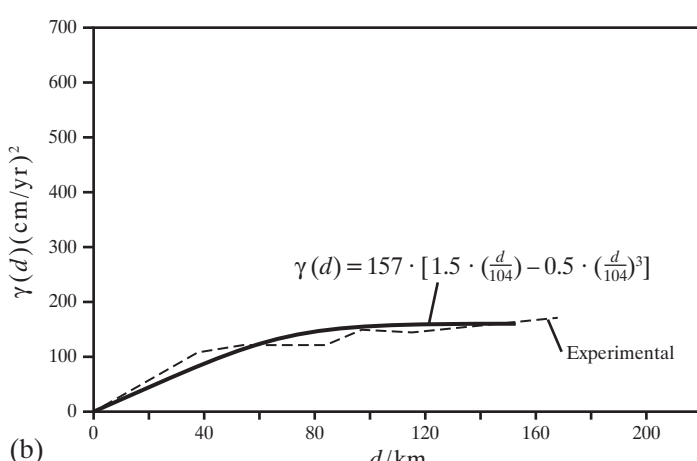
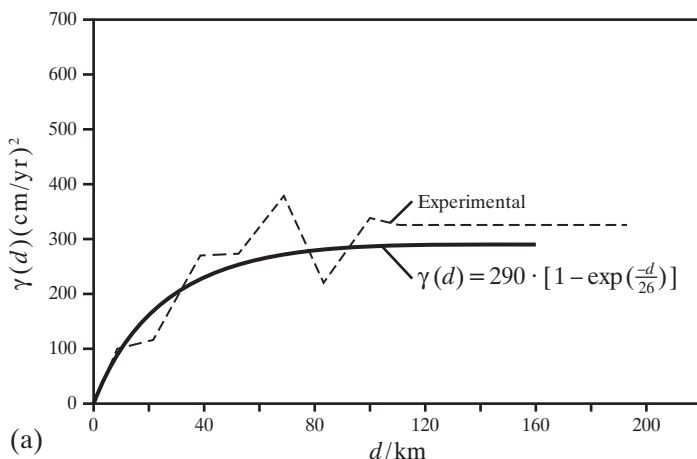


Figure 4.31 Experimental and theoretical variograms for mean annual precipitation in New Hampshire and Vermont. (a) Variograms for measured mean annual precipitation. The theoretical variogram is exponential (figure 4.30). (b) Variograms of mean annual precipitation minus elevation effect [variable $\rho(u)$ in equation (4.34)]. The theoretical variogram is spherical (figure 4.30) [reproduced from Dingman et al. (1988)]. Application of kriging to estimating mean annual precipitation in a region of orographic influence. *Water Resources Bulletin* 24:329–339, with permission from Wiley].

presses the magnitude of the interpolation error variance at each grid point.

In situations where elevation, distance from the coast, or other factors influence the spatial variability of precipitation, equation (4.22) no longer holds, and instead

$$\mathbb{E}\{p(u)\} = P(x_u, y_u). \quad (4.33)$$

If the dependence on location (called **drift**) can be modeled, for example, as a function of elevation as in equation (4.12), one can incorporate the relation in deriving the weights (Kitanidis 1992; Goovaerts 2000; Haan 2002). Another approach is to subtract the elevation, $z(u)$, or other effect from precipitation to define a new spatial variable, $p(u)$, e.g.,

$$p(u) \equiv p(u) - [a_z + b_z \cdot z(u)], \quad (4.34)$$

and conduct the geostatistical analysis on $p(u)$, as done by Dingman et al. (1988). Figure 4.31b shows examples of experimental and theoretical variograms for mean annual precipitation minus the elevation effect in New Hampshire and Vermont.

The critical properties of the weights derived via kriging are that

1. They give *unbiased* estimates;
2. The estimates minimize the error variance
 $\sigma_{\hat{p}}^2 \equiv \sum [\hat{p}(u) - p(u)]^2;$
3. The estimates incorporate the spatial structure of the process as modeled in the theoretical semivariogram; and
4. The error variance $\sigma_{\hat{p}}^2$ is estimated for each point, allowing an assessment of uncertainty.

4.3.2.7 The PRISM Model

PRISM (Precipitation-Elevation Regressions on Independent Slopes Model) is an analytical model that computes estimates of monthly, annual, or single-storm precipitation. The model first uses a DEM to generate a smoothed version of the actual topography (the “orographic elevations”), then a windowing technique to group precipitation gauges onto topographic facets. Using these, a regression model is developed to estimate precipitation for each grid cell as a function of its orographic elevation, with the functions varying depending on location and orientation (Daly et al. 1994). Tests of the approach in its original application in Oregon indicated that it performed better than kriging (Taylor et al. 1993).

As noted by its originators, PRISM is not a traditional statistical model. “Rather, it is a coordinated

set of rules, decisions, and calculations, designed to approximate the decision-making process an expert climatologist would invoke when creating a climate map” (<http://prism.oregonstate.edu>). The approach is under continuing development, and is now widely used for producing maps of precipitation and other climate variables, including temperature, snowfall, and growing degree-days.

PRISM can be classed as a deterministic smoothing method, and it does have a procedure for estimating the uncertainty of its estimates.

4.3.2.8 Satellite Reanalysis

Reanalyses integrate a variety of satellite observing systems with numerical models to produce a spatially and temporally consistent synthesis of atmospheric and hydrologic variables that are not easily observed. One of these is the Modern-Era Retrospective Analysis for Research and Applications (MERRA), a program of NASA (<http://gmao.gsfc.nasa.gov/research/merra>), that provides global estimates of precipitation, soil moisture, latent-heat flux, snow, and runoff. MERRA uses areal-precipitation analyses based on an updated version of the Global Precipitation Climatology Project to provide estimates of land-surface hydrological variables and root-zone soil moisture at hourly intervals. It employs a spatial scale of 1/2-degree latitude and 2/3-degree longitude for 1979 to the present (Reichle et al. 2011).

4.3.3 Comparison of Methods and Summary

Comparative studies of subsets of the areal-estimation methods described above have been made by Shaw and Lynn (1972), Creutin and Obled (1982), Court and Bare (1984), Tabios and Salas (1985), Singh and Chowdhury (1986), Lebel et al. (1987), Custer et al. (1996), Johnson et al. (1999), and Goovaerts (2000).

The choice of a method for computing areal precipitation depends on several factors, including: (1) the objective of the analysis; (2) the nature of the region; and (3) the time and computing resources available. When only areal averages are needed and time and resources are limited, or only reconnaissance-level estimates are required, one would usually apply one of the direct-weighted-average methods or the hypsometric method. The arithmetic-average, Thiessen, or two-axis methods are not well suited to regions where topographic or other factors strongly influence precipitation unless gauges are well distrib-

uted, but simple weighting approaches accounting for topography can be developed (see Singh and Chowdhury 1986). Otherwise, the hypsometric or surface-fitting methods can be used.

However, most of the comparative studies reviewed above have concluded that optimal-interpolation/kriging methods provide the best estimates of regional precipitation in a variety of situations. Presumably this is because these methods are based on the spatial correlation structure of precipitation in the region of application rather than on essentially arbitrary spatial structures. A number of inexpensive optimal interpolation/kriging programs are now available (e.g., Grundy 1988; Kitanidis 1992) so that the feasibility of using these approaches is much enhanced.

The geostatistical methods have the additional advantages of providing explicit estimates of interpolation error along with a model of the spatial variability. However, uncertainty for deterministic as well as statistical methods can be assessed by **cross validation**, in which the predictive model is developed using a subset of the available measured data, and tested by comparing the model predictions against the values not used in the development. Often this is done by suppressing one measured value, developing the predictive model with the remaining $G - 1$ values, and comparing the model's prediction for the suppressed value with the measured value. The process is repeated G times, suppressing each measured value in turn, and computing a statistic such as the average absolute difference between measured and estimated values. Note, however, that none of the methods accounts for errors in point measurements (section 4.2.1.2), so these must always be evaluated separately.

The PRISM model incorporates a number of aspects of the spatial structure of precipitation, not simply the spatial covariance, and may be the best approach for generating climatologic maps of precipitation (and other climatic parameters) and inputs for hydrologic models. It also allows assessment of interpolation uncertainty.

4.3.4 Precipitation-Gauge Networks

Box 4.4 provides information about current precipitation-gauge networks globally; metadata and data for most stations can be readily obtained via the Internet addresses given there.

In general, precipitation for a given region will have higher spatial variability for hourly or daily values than for monthly or annual values, and regions of

convective rainfall and varying topography will tend to have relatively high variability. Based on these general considerations, the WMO recommends the minimum gauge densities shown in table 4.6 on p. 174 for general hydrometeorological purposes in various climatic regions. In fact, there are many regions of the world—including much of the United States—where these criteria are not met (table 4.7 on p. 175). Furthermore, the spatial distribution of gauges within a region such as a watershed is usually extremely uneven, with stations typically concentrated in populated areas, along roads, and at lower elevations. This uneven distribution introduces particular challenges for estimating areal precipitation.

4.3.5 Uncertainty Analysis of Gauge Networks

The importance and basic aspects of assessing uncertainty in hydrology were introduced in section 1.11. Recall that all measurements contain *random errors*, which are unavoidable, unpredictable fluctuations in values obtained in a given measurement situation that are equally likely to be greater than or less than the true value; these are reflected in the measurement *precision*. Many types of measurements are also subject to *systematic errors*, which are biases due to inherent tendencies for instrumentation or methods of observation to consistently record values that are on average higher or lower than the “true” values. Errors are particularly critical concerns for precipitation, which is the input to the land phase of the hydrologic cycle.

As noted in section 4.2.1, there are many causes of (mostly negative) bias in measurements at individual rain gauges. In addition, spatial averages derived from any irregularly distributed station network contain biases due to unavoidable errors in any of the spatial-interpolation methods discussed in section 4.3.2. These biases are usually difficult to assess, and may be especially large when the overall gauge density is insufficient to resolve the actual spatial variability. This is illustrated in figure 4.33 on p. 176, which compares 1985 precipitation in North Carolina based on the first-order network and the cooperative network. Figure 4.33 illustrates that the density of a precipitation-gauge network can make a large difference in estimates of areal precipitation: The differences exceed 762 mm in the mountainous regions, and are over 254 mm even in the relatively flat piedmont portions of the state. In one of the few studies

Box 4.4 Global and US Precipitation-Gauge Networks

Maps of station locations, climatological maps, and station-specific precipitation and other climate data are available for the world through the National Climatic Data Center of the NOAA (<http://www.ncdc.noaa.gov/oa/climate/climatedata.html>). The table below includes a brief list of the major systems/networks around the globe and in the United States.

WMO Networks

The World Meteorological Organization (WMO) reports that there are some 200,000 surface weather stations on land, a gauge density of about $1.5 \times 10^{-3}/\text{km}^2$ ($700 \text{ km}^2/\text{gauge}$). There are several official WMO networks with differing purposes and reporting protocols; further information is available at <http://www.wmo.int/pages/prog/www/OSY/Gos-components.html>.

NCAR Networks

The World Monthly Surface Station Climatology of the National Center for Atmospheric Research (NCAR) is a time-varying network that dates back to the 1800s, with stations selected to provide the most reliable assessment of climate. The network contained 636 stations in 1900, 2,327 stations in 1960, and about 1,500 in 1990 (figure 4.32). Further information about data availability is available at: <https://ncar.ucar.edu/home>.

US Networks

Weather and climate observations for the United States are managed by the National Weather Service (NWS) of the NOAA, which maintains several networks with differing purposes and reporting protocols (<http://www.ncdc.noaa.gov/homr>). Locations of the NWS COOP and USHCN stations are given in Menne et al. (2009), and can be viewed at <ftp://ftp.ncdc.noaa.gov/pub/data/ushcn/v2/monthly/menne-etal2009.pdf>.

The following descriptions of the COOP and ASOS precipitation-gauge networks operated by the NWS is taken directly from Kuligowski (1997), with abridgements. Information about other special-purpose precipitation-gauge networks can be found in that report.

NWS COOP

Automated hourly observations of precipitation are taken at approximately 2,700 cooperative-observer locations throughout the United States and some of its territorial possessions. These gauges are operated by the NWS or the FAA. The records are retrieved once per month (less often for remote gauges) for processing and quality control and are generally not available in real time. Approximately 1,000 of these gauges have been equipped with telephone telemetry systems that are routinely collected four times per day. In addition to hourly observations of precipitation by recording gauges, obser-

Global				
Name	Acronym	Number of Stations	Gauges/km ² (a)	km ² /Gauge
Global Climate Observing System	GCOS	1,040	7.0×10^{-6}	140,000
Global Observation System	GOS	~11,000	$\sim 7.4 \times 10^{-5}$	14,000
Regional Basic Synoptic Network	RBSN	~4,000	$\sim 2.7 \times 10^{-5}$	37,000
Regional Basic Climatological Network	RBCN	~3,000	$\sim 2.0 \times 10^{-5}$	50,000
United States				
Name	Acronym	Number of Stations	Gauges/km ² (b)	km ² /Gauge
NWS Cooperative Network	NWS COOP	> 32,000	$< 3.5 \times 10^{-3}$	290
Global Historical Climatological Network-Daily	GHCN-D	> 70,000	$< 7.6 \times 10^{-3}$	130
Automated Surface Observing System	ASOS	> 900	$< 9.8 \times 10^{-5}$	10,000
Local Climatological Data	LCD	274	$< 3.0 \times 10^{-5}$	33,000
US Climate Reference Network	USCRN	> 120	$< 1.3 \times 10^{-5}$	76,000
US Regional Climate Reference Network	USR CRN	> 60	$< 6.5 \times 10^{-6}$	150,000
US Historical Climatological Network	USHCN	1,218	1.3×10^{-4}	7,500
Automated Surface Observing System	ASOS	> 700	$< 7.6 \times 10^{-5}$	13,000

^aBased on a global land area of 148,910,000 km².

^bBased on total US land area of 9,161,924 km².

gauges, observations of 24-hr precipitation amounts and other variables are made once per day by a network of cooperative observers, mainly using standard nonrecording gauges. These observations are sent once per month to the National Climatic Data Center (NCDC). Data from approximately 7,600 gauges are processed at NCDC. As with the hourly cooperative observations, much of this data is not available in real time; however, a number of these observations are transmitted in real time to a collection system, such as remote automatic meteorological observing system (RAMOS).

ASOS

The ASOS network provides most of the basic hydro-meteorological observations, including precipitation

amount, and serves two primary purposes: (1) to replace manual observations in locations where readings had previously been made using nonrecording gauges and (2) to provide observations in locations where readings had not been previously available. These platforms use heated tipping-bucket gauges to measure precipitation. In regions where snow accounts for more than 20% of the total annual precipitation, Alter shields are used to reduce wind-produced errors in measurement. Precipitation measurements are taken once per minute, with total amounts reported for 1-, 3-, and 24-hr periods.

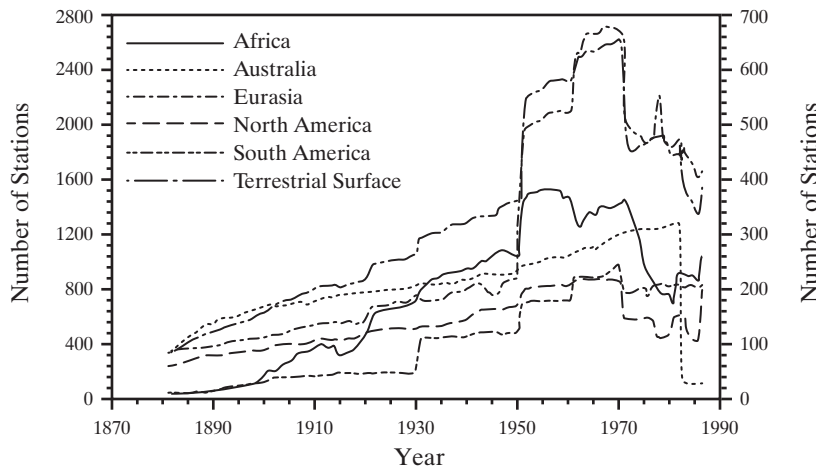


Figure 4.32 Number of stations per year in the NCAR World Monthly Surface Station Climatology from 1881 to 1987 for the global land surface (left axis) and for each continent (right axis) [Spangler and Jenne (1988)].

Table 4.6 WMO–Recommended Rain-Gauge Densities.

Type of Region	km ² /Gauge	Gauges/km ²
Flat regions with temperate, Mediterranean, and tropical climate	Ideal: 1.1×10^{-3} to 1.7×10^{-3} Acceptable: 3.3×10^{-4} to 1.1×10^{-3}	Ideal: 1/600 to 1/900 Acceptable: 1/900 to 1/3,000
Mountainous regions with temperate, Mediterranean, and tropical climate	Ideal: 4.0×10^{-3} to 1.0×10^{-2} Acceptable: 1.0×10^{-3} to 4.0×10^{-3}	Ideal: 1/100 to 1/250 Acceptable: 1/250 to 1/1,000
Arid and polar regions	Ideal: 1.0×10^{-4} to 6.7×10^{-4}	Ideal: 1/1,500 to 1/10,000

Table 4.7 Densities of Precipitation Gauges in Countries that Receive Significant Snowfall.

Country	km ² /Gauge	Gauge/km ²
Mongolia	30,686	3.26×10 ⁻⁵
Former USSR	13,791	7.25×10 ⁻⁵
China	12,529	7.98×10 ⁻⁵
Greenland	10,095	9.91×10 ⁻⁵
United States	9,816	1.02×10 ⁻⁴
Finland	6,241	1.60×10 ⁻⁴
Poland	4,667	2.14×10 ⁻⁴
North Korea	4,305	2.32×10 ⁻⁴
Iceland	2,711	3.69×10 ⁻⁴
Former Czechoslovakia	2,241	4.46×10 ⁻⁴
Norway	2,014	4.97×10 ⁻⁴
South Korea	1,824	5.48×10 ⁻⁴
Japan	1,749	5.72×10 ⁻⁴
Sweden	1,601	6.25×10 ⁻⁴
Canada	1,491	6.71×10 ⁻⁴
Romania	1,389	7.20×10 ⁻⁴
Switzerland	1,007	9.93×10 ⁻⁴
Austria	655	1.53×10 ⁻³

Source: Adam and Lettenmaier (2003).

of the effects of gauge-network density on measurement bias, Willmott et al. (1994) found that sparse densities introduced large positive bias for all continents except South America, where the bias was strongly negative; however, they found that long-term continental averages could be reasonably assessed with densities of 5 to 20 gauges per 10⁶ km² (5×10⁴ to 2×10⁵ km²/gauge).

In contrast, the effect of the density and spacing of gauges on the precision of areal rainfall estimates has been widely investigated. Recall from section 1.11.2 that precision is expressed as a confidence interval about the estimate, which is a multiple $k(p)$ of the *standard deviation of the estimate* (also called the **standard error of estimate**), $\sigma_{\hat{P}}$:

$$\begin{aligned} & \text{"I am } p\% \text{ sure that} \\ & \hat{P} - k(p) \cdot \sigma_{\hat{P}} \leq P \leq \hat{P} + k(p) \cdot \sigma_{\hat{P}}, \end{aligned} \quad (4.35)$$

Where p or p is selected by the investigator and $k(p)$ is determined by properties of the normal distribution [$k(p) = 1, 2$ for $p = 68\%, 95\%$, respectively]. The

value of $\sigma_{\hat{P}}$ is determined by applying basic statistical theory to repeated measurements. Clearly, the value of $\sigma_{\hat{P}}$ is inversely related to precision and to the **information content** of the estimated mean.

An early study by Huff (1970) explored the effects of gauge density on the standard error of estimate of average areal rainfall using a dense, evenly distributed gauge network on a flat prairie area in Illinois. His results are summarized in terms of average absolute (standard error in mm) and relative (standard error in percent) error in figure 4.34 (on p. 177): On average, absolute error increased and relative error decreased with total precipitation, while both types of error decreased with storm duration and gauge density. He also found that a given sampling error could be achieved with a much smaller gauge density when calculating monthly, seasonal, or annual rainfall than for the shorter durations represented in figure 4.34. These general trends have been widely observed, but of course the quantitative relationships differ greatly with location—and in fact Huff (1970) reported large variability from storm to storm, more areal variability for summer convective storms than for winter storms, and a difference in the relationships between the two 5-yr time periods he observed.

Here we describe the general approach to assessing random uncertainty in areal average precipitation estimates developed by Rodriguez-Iturbe and Mejia (1974) (see also Bras and Rodriguez-Iturbe 1984). The precision of a rain-gauge network can be improved by (1) increasing the density of the gauge network and (2) extending the period of measurement; the trade-off between the increase in information and gauge density or time takes the form shown in figure 4.35 on p. 178. Note that the rate of increase of precision decreases as gauge density and observation time increase.

As noted in box 1.1 [equation (1B1.1)], statistical theory shows that the standard error of estimate of an average value decreases with the number of *independent* observations, N , as

$$\sigma_{\hat{P}} = \frac{\sigma_p}{N^{1/2}}, \quad (4.36)$$

where σ_p is the standard deviation of the N individual observations. Independence here means that, for a given time period, measurements at one gauge are not systematically related to those at another gauge (spatial independence); and that for a given gauge, observations in one time period are not systemati-

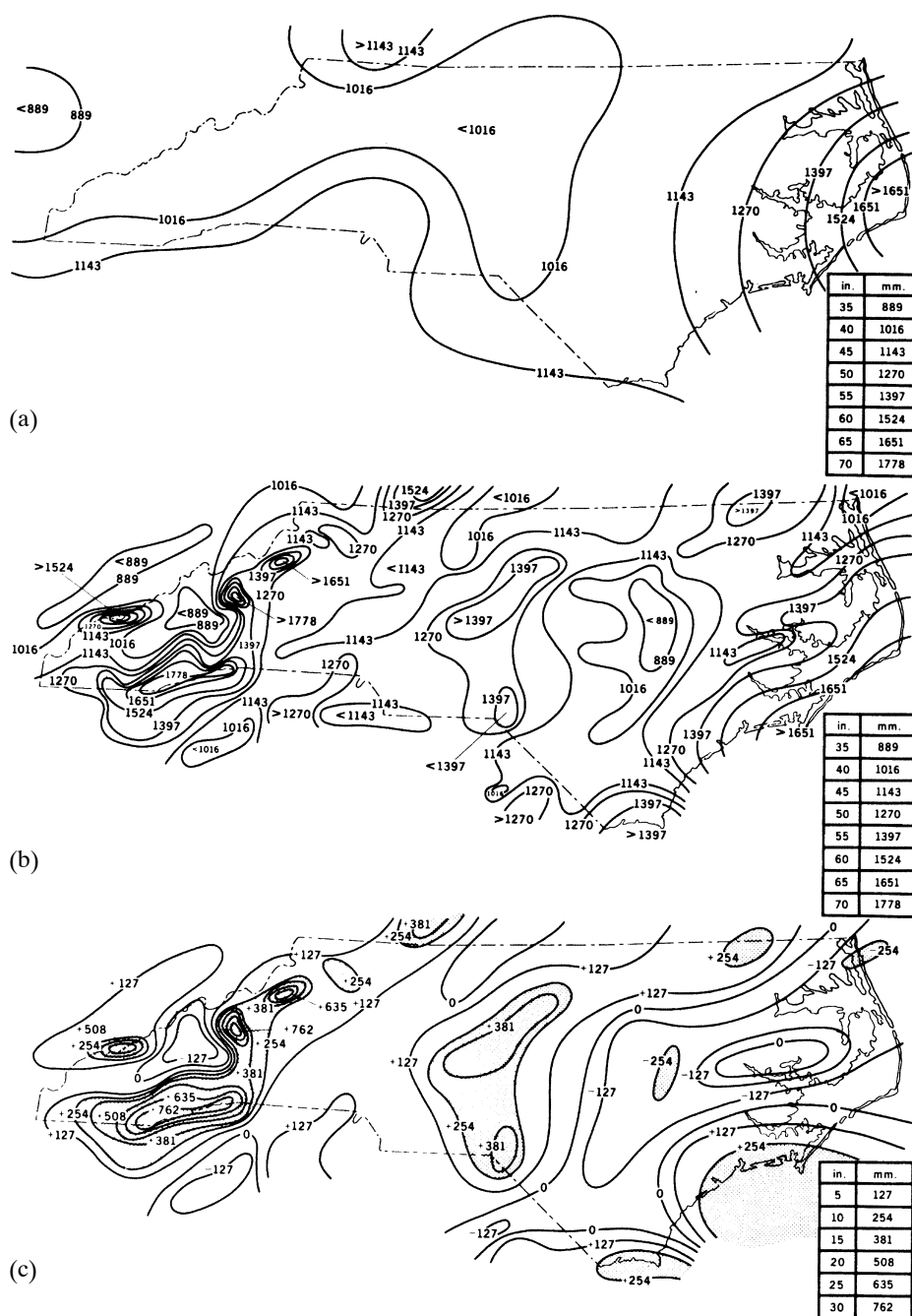


Figure 4.33 Annual precipitation in North Carolina in 1985 based on (a) the primary network and (b) the cooperative network. (c) Differences between the two estimates [Karl and Quayle (1988). Climate change in fact and theory: Are we collecting the facts? *Climatic Change* 13:5–17. With kind permission from Springer Science and Business Media].

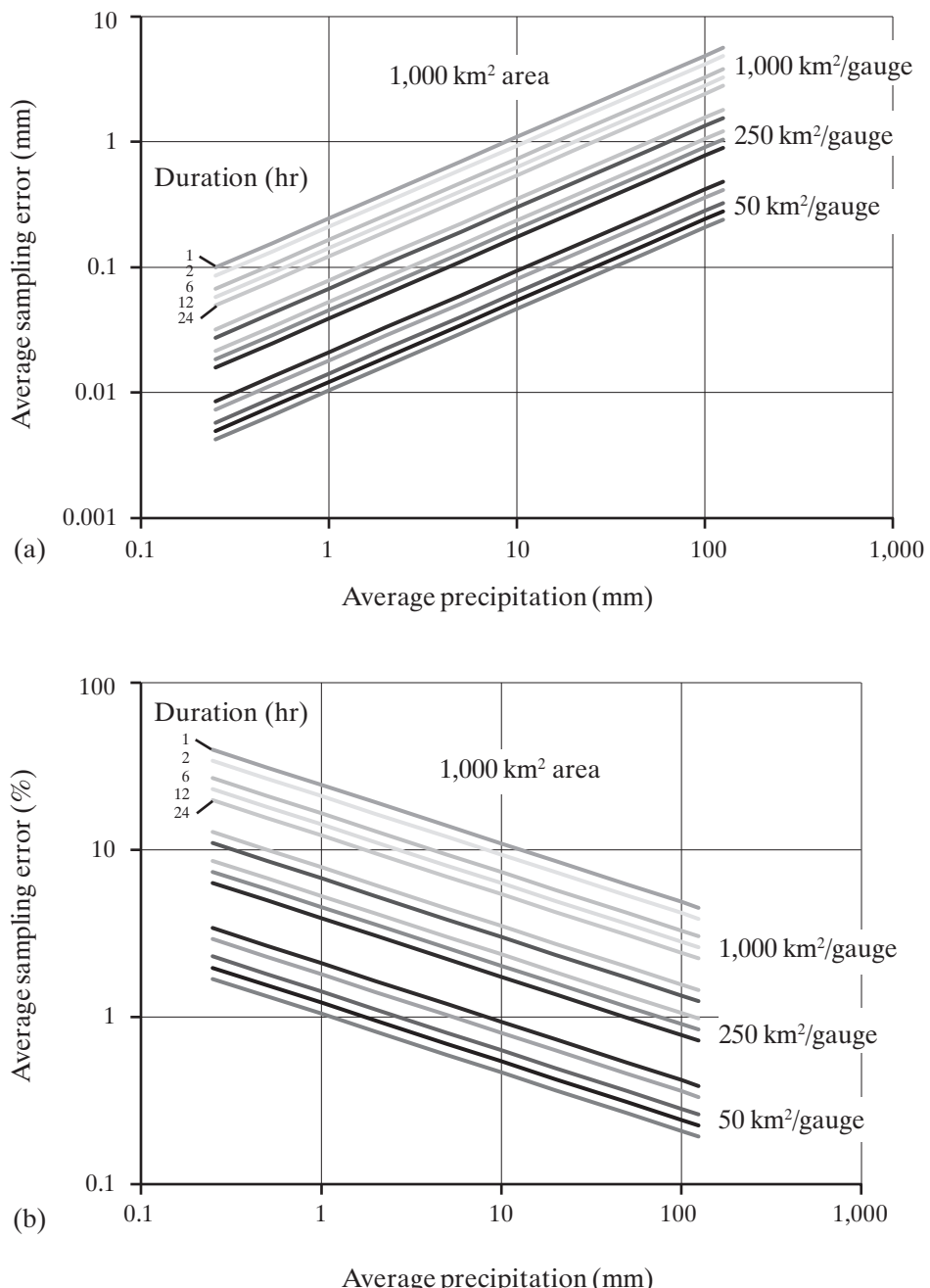


Figure 4.34 Sampling errors on an area of $1,000 \text{ km}^2$ as a function of seasonal precipitation, gauge density, and storm duration. (a) Absolute error. (b) Relative error. Based on analyses of Huff (1970) in Illinois. Errors in most regions follow these general trends, but may differ greatly due to differences in climate and topography.

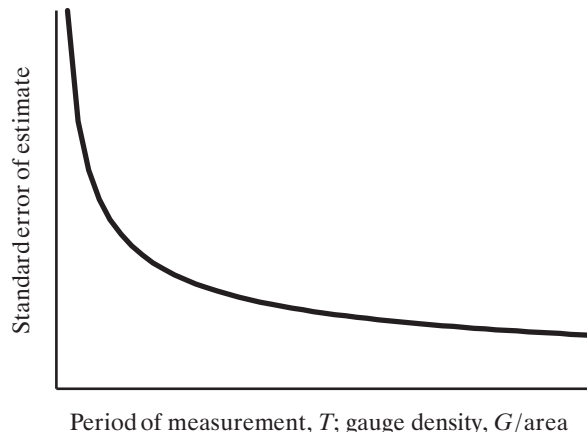


Figure 4.35 Precipitation-estimation error declines quasi-exponentially as (1) period of measurement and (2) gauge density increase.

cally related to those in another period (temporal independence). Thus for spatially and temporally independent observations, the curve in figure 4.35 is given by the inverse square root of the number of gauges, G , and the number of observation periods, T .

However, as we saw in section 4.3.2.6, there is typically a relationship between measurements at gauges spaced a distance d apart, which is quantified in the variogram, $\gamma(d)$ [equation (4.24)], or the spatial-correlation coefficient $\rho(d)$ [equation (4.25)]. If the average spatial correlation is high,⁷ the information provided by the G gauges is less than would be provided by G independent gauges [$\rho(d) = 0$]. Thus the curve in figure 4.35 will decline less steeply than the inverse square root.

Similarly, if precipitation values in one time period are systematically related to those in the following time period, the standard error will decline less rapidly than $T^{-1/2}$. To describe this situation, we use the analogous concept of **autocorrelation (persistence)**,⁸ $\rho_T(1)$:

$$\rho_T(1) \equiv \frac{\text{E}\{p(t+1) - p(t)\}^2 - P^2}{\sigma_P^2}, \quad (4.37)$$

where $p(t)$, $p(t+1)$ represent the areal average precipitation separated by one time unit, called the **lag-1 autocorrelation coefficient**.⁹

To formulate a general relation that accounts for the effects of spatial and temporal dependence on the standard error of estimates of areal average precipitation, Rodriguez-Iturbe and Mejia (1974) wrote

$$\sigma_P^2 = F_1(T) \cdot F_2(G) \cdot \hat{\sigma}_p^2, \quad (4.38)$$

where $\hat{\sigma}_p^2$ is the aggregate variance of the annual precipitation measurements at all gauges in a region over the period of record; $F_1(T)$ is a **temporal variance-reduction function** that depends on the number of years of observation, T , and the average value of the autocorrelation coefficient for all gauges; and $F_2(G)$ is a **spatial variance-reduction function** that depends on the number of gauges, G , the spatial correlation of precipitation, the shape of the area, and the spatial distribution of the gauges. To illustrate the approach, we assume a random distribution of gauges in a square area; Morrissey et al. (1995) explore the effects of other network configurations.

Figure 4.36 shows how $F_1(T)$ decreases with T for various values of $\rho_T(1)$. These curves are calculated from equation (C.51) for the standard error of the mean (= square root of the error variance), accounting for the effect of autocorrelation on the effective record length [equation (C.68) with N replaced by T], so that the variance reduction is less as $\rho_T(1)$ increases for a given T .

In order to evaluate $F_2(G)$, we need to model the dependence of spatial correlation on separation, d . This can be done as described for the experimental variogram in section 4.3.2.6: first the experimental autocorrelation relation $\hat{\rho}(d)$ is developed, then a model relating $\rho(d)$ to d is fit to the experimental values. A common model is

$$\rho(d) = \exp(-c \cdot d), \quad (4.39)$$

where c is the decay constant [L^{-1}] that best fits the data. With this model, Rodriguez-Iturbe and Mejia (1974) developed the relation between $F_2(G)$ and the dimensionless variable $A \cdot c^2$, where A is the area of the region (figure 4.37).

Box 4.5 on p. 180 applies the approach of Rodriguez-Iturbe and Mejia (1974) to a region in the central United States. The important implication of equation (4.38) and figures 4.33, 4.34, and 4.37 is that we can increase the precision of areal precipitation measurements by either: (1) increasing the period of observation, T , and/or (2) increasing the number of stations, G , and box 4.5 illustrates an important conclusion:

We can trade time versus space in hydrologic data collection when we do not reduce the time interval too much, but no miracles can be expected in short times even from the most dense of all possible networks. (Bras and Rodriguez-Iturbe 1984, p. 349)

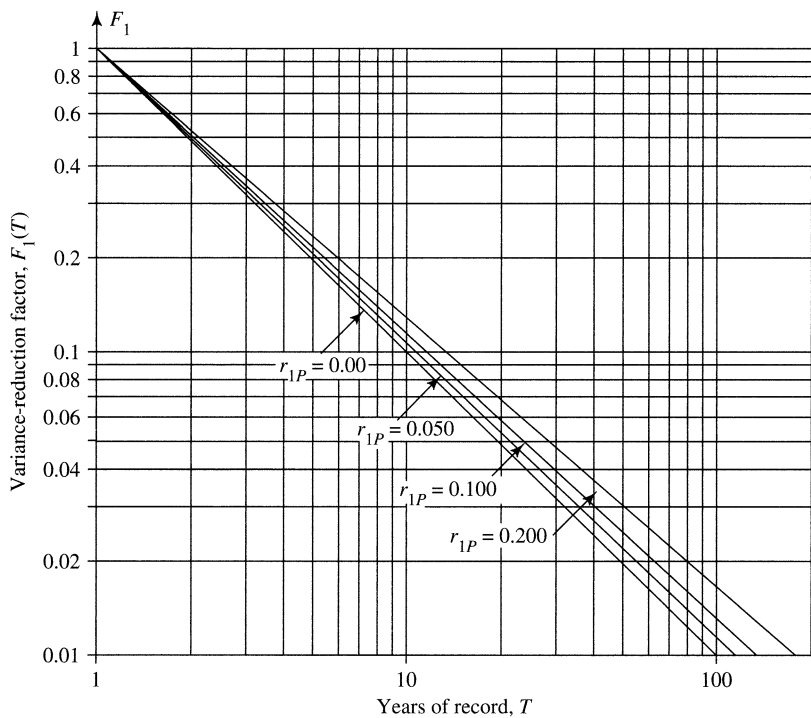


Figure 4.36 Variance-reduction function $F_1(T)$ as a function of number of years of record, T , and average regional correlation, r_{1P} [Rodriguez-Iturbe and Mejia (1974). Design of rainfall networks in time and space.

Water Resources Research 10:713–728, with permission of the American Geophysical Union].

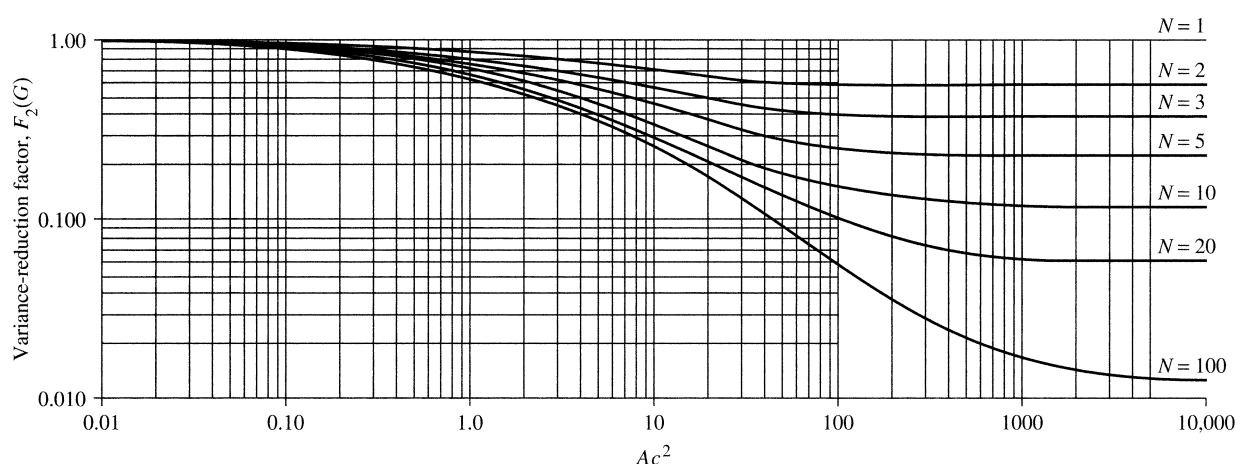


Figure 4.37 Variance-reduction function $F_2(G)$ as a function of number of stations, G ; area, A ; and spatial-correlation factor [c in equation (4.39)] [Rodriguez-Iturbe and Mejia (1974). Design of rainfall networks in time and space. *Water Resources Research* 10:713–728, with permission of the American Geophysical Union].

Box 4.5 Example Application of Information Analysis of a Precipitation-Gauge Network

For the region of eastern Nebraska and northern Kansas ($A = 52,000 \text{ km}^2$) studied by Tabios and Salas (1985), mean annual precipitation for a 30-yr period was determined at 29 stations. The overall mean value (mean of the means at all stations) $\hat{P} = 619 \text{ mm/yr}$, and the overall variance $\hat{\sigma}_P^2 = 25,445 \text{ mm}^2/\text{yr}^2$. The autocorrelation coefficient for annual rainfall [equation (4.37)] was not significantly different from 0, so we assume that $\rho_T(1) = 0$. Spatial correlation was calculated as described in box 4.3. The values are plotted in figure 4.38 as a function of gauge separation; although there is much scatter, the spatial correlation can be modeled via equation (4.39) with $c = 0.0031 \text{ km}^{-1}$.

To calculate the standard error of estimate in the areal average 30-yr mean precipitation, we find from figure 4.36 for $\rho_T(1) = 0$ that $F_1(30) = 0.033$. The value of $A \cdot c^2 = 52,000 \times 0.0031^2 = 0.500$, and from figure 4.37, we find $F_2(29) = 0.73$. Thus, we calculate the standard error of estimate of average annual precipitation for this situation via equation (4.38) as

$$\sigma_{\hat{P}} = \left(0.033 \cdot 0.73 \cdot 25,445 \text{ mm}^2/\text{yr}^2 \right)^{1/2} \\ = 24.8 \rightarrow 25 \text{ mm/yr.}$$

Following the discussion in section 1.11.2.3 and equation (4.35), we can thus state:

"I am 95% sure that the average annual precipitation is between $619 - 2 \cdot 25 = 569 \text{ mm}$ and $619 + 2 \cdot 25 = 669 \text{ mm}$."

We can also compare the value, in terms of variance reduction, of additional years of record with the value of additional gauges in this situation. To do this, we read values of $F_1(T)$ as a function of T directly from the $\rho_T(1) = 0$ curve in figure 4.36; these are plotted in figure 4.39. Then entering figure 4.37 at a value of $A \cdot c = 0.50$, we read the values of $F_2(G)$ for $G = 1, 2, 3, 5, \dots$ and plot these on figure 4.39. Comparing the two curves in figure 4.39, we see that an additional year of record is generally much more valuable in reducing uncertainty (increasing information) than an additional gauge. In fact, for estimating mean annual precipitation, there is little to be gained by having more than about 20 gauges in the region, and additional years of record beyond the present 30 add variance reduction only very slowly.

However, we cannot conclude from this example that there is no need for more precipitation data collection in this region: the analysis applies only to mean annual precipitation, and we are also interested in values for other time periods and for hydrologic analysis of future storms and drought periods. Also, the analysis only applies for a situation in which climate is not changing, and we are interested in maintaining measurements to detect such change.

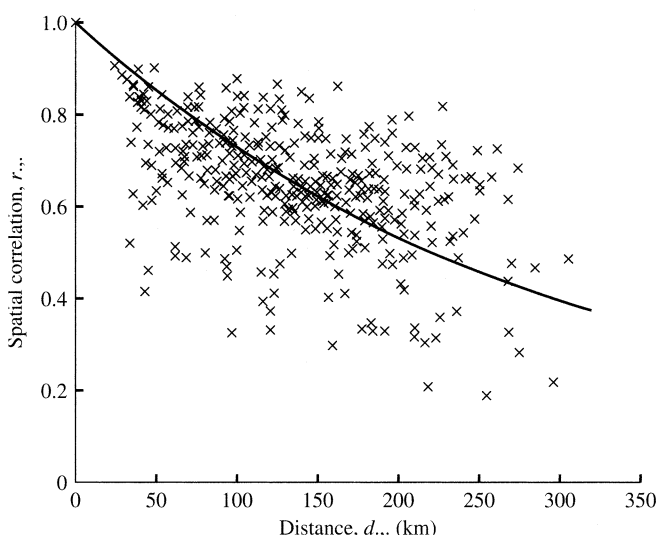


Figure 4.38 Spatial correlation of annual precipitation for the 29 stations studied by Tabios and Salas (1985). Curve is equation (4.39) with $c = 0.0031 \text{ km}^{-1}$ [Tabios and Salas (1985)]. A comparative analysis of techniques for spatial interpolation of precipitation. *Water Resources Bulletin* 21:365–380, courtesy of American Water Resources Association].

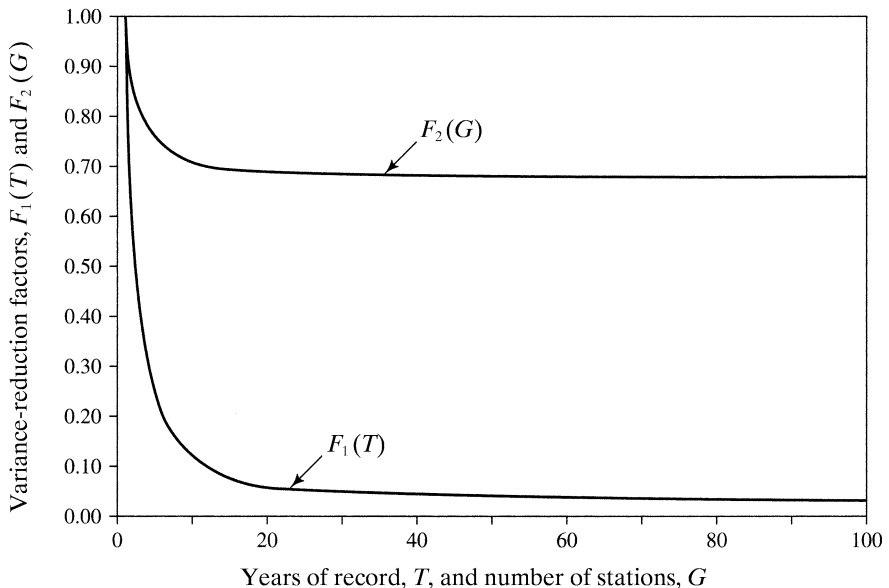


Figure 4.39 Variance-reduction factors $F_1(T)$ and $F_2(G)$ for the example in box 4.5.

4.4 Precipitation Climatology

As discussed in chapters 1 and 2, long-term average precipitation and its characteristic seasonal variability are fundamental determinants of regional hydrology, soils, and vegetation. In addition, estimates of regional **extreme values** of precipitation are required for the prediction of flood magnitudes required for designing structures such as culverts, bridges, storm sewers, and dams, and for delineating areas subject to flooding. This section describes how these climatological averages and extreme values are developed at individual precipitation-gauge stations and how these values are related to general meteorological conditions.

As noted in section 1.9.2.3, climatological computations are traditionally based on the implicit assumption that time series are *stationary*, i.e., that the underlying processes generating precipitation are unchanging and historical measurements are representative of future behavior. If stationarity can be assumed, the computation of averages and other statistics from past data are meaningful, and it can be assumed that increasing sample size (i.e., length of observation period) decreases uncertainty indefinitely, as in standard statistical theory.

Because it is now clear that global climate is changing, the assumption of strict stationarity is no longer warranted. However, it is not clear how to in-

corporate nonstationarity in climatological computations, so the climatological computations presented here are based on the traditional formulations. This practice may provide a reasonable basis for near-term future expectations if the data on which the climatological calculations are based are continually updated, for instance, by using the 30-yr normal concept as described in the following section.

4.4.1 Long-Term Average Precipitation

Average annual precipitation, \hat{P} , is estimated for an individual gauge site by totaling the measured precipitation (corrected for bias due to wind and other factors as discussed in section 4.2.1) for a number, Y , of complete years of record and dividing the sum by the number of years:

$$\hat{P} = \frac{1}{Y} \cdot \sum_{y=1}^Y p_y, \quad (4.40)$$

where p_y is the total precipitation for year y . In the United States, the National Weather Service computes the **30-year normal precipitation** as the average annual precipitation computed for specific 30-year periods, which are updated every 10 years; these values are published in *Climatology of the United States* (<http://www.ncdc.noaa.gov/data-access/land-based-station-data/land-based-datasets/climate-normals>). Average annual or 30-year normal precipitation is often used as an estimate of the long-

term average precipitation rate at a station; areal values may be computed from values for individual gauges using the methods described in the previous section.

The global distribution of average precipitation and its relation to large-scale climatic and topographic features were described in section 2.2. More detailed relationships between average precipitation rate and the time and space characteristics of the precipitation types discussed above are reflected in figure 4.40, which is a map of the US average annual precipitation [a more recent map prepared by the PRISM method (section 4.3.2.7) is available at <http://prism.oregonstate.edu>]. Note the strong orographic effects in western Washington and Oregon and the Sierra Nevada of California, along the crest of the Appalachians from northern Georgia to Pennsylvania, and in the Adirondacks of New York. The importance of the Gulf of Mexico as a source of moisture for the cyclonic systems that move across the country is clear in the roughly concentric pattern of isohyets extending northward from the Gulf Coast and westward to about longitude 105°W. The role of the Atlantic Ocean as a moisture source is also apparent, but because the prevailing storm movements are from the west its effect is limited to the immediate coastal area. The irregular isohyetal patterns between longitude 105°W and the mountains of California and western Washington and Oregon reflect the influence of orography in the Rockies and other mountains and the importance of local convective storms; the low average values in that region are due to the rain-shadow effects of the West Coast mountains and distance from the Gulf of Mexico.

4.4.2 Variability of Precipitation

4.4.2.1 Interannual Variability

The **interannual variability** of precipitation is a measure of the reliability of water inputs to maintain ecosystems and provide human water supplies. It can be expressed as the standard deviation, $\hat{\sigma}_P$, of the annual values:

$$\hat{\sigma}_P = \left[\frac{1}{Y-1} \cdot \sum_{y=1}^Y (p_y - \hat{P})^2 \right]^{1/2}. \quad (4.41)$$

The relative variability of annual precipitation at different locations can be compared via the **coefficient of variation** of annual precipitation, $CV_{\hat{P}}$,

$$CV_{\hat{P}} \equiv \frac{\hat{\sigma}_P}{\hat{P}}, \quad (4.42)$$

or via the **normalized annual precipitation**, \tilde{p}_y , where

$$\tilde{p}_y \equiv \frac{p_y - \hat{P}}{\hat{\sigma}_P}. \quad (4.43)$$

The value of \tilde{p}_y expresses the degree to which a given year's precipitation was above or below its long-term mean in units of standard deviations. Normalized values are particularly useful in comparing concurrent values of quantities with different measurement scales—for instance, in comparing the synchronicity of annual precipitation with annual streamflow, as in figure 4.41 on p. 184.

4.4.2.2 Intra-Annual Variability

The seasonal, or **intra-annual**, variability of precipitation is an important aspect of hydroclimatolgy because it largely determines the seasonality of other hydrologic quantities, such as streamflow and ground-water recharge. Characterization of intra-annual variability is often based on average, or normal, monthly precipitation \hat{P}_m , calculated for each month ($m = 1, 2, \dots, 12$) as

$$\hat{P}_m = \frac{1}{Y} \cdot \sum_{y=1}^Y p_{my}, \quad (4.44)$$

where p_{my} is the total precipitation for month m in year y .

Seasonality at different locations can be compared by simply comparing the monthly values of \hat{P}_m or \hat{P}_m/\hat{P} , or by means of **circular statistics** (Fisher 1993). To use circular statistics, time through the year is represented on a circle and each month is assigned an angle ϕ_m , measured clockwise from 1 January, of its mid-month date (table 4.8 on. p. 185). The computations begin by calculating

$$S \equiv \sum_{m=1}^{12} \hat{P}_m \cdot \sin(\phi_m), \quad (4.45)$$

and

$$C \equiv \sum_{m=1}^{12} \hat{P}_m \cdot \cos(\phi_m). \quad (4.46)$$

The 12 monthly vectors are added to give a resultant vector with a magnitude P_R [L],

$$P_R = (S^2 + C^2)^{1/2}, \quad (4.47)$$

and a direction $\bar{\phi}$,

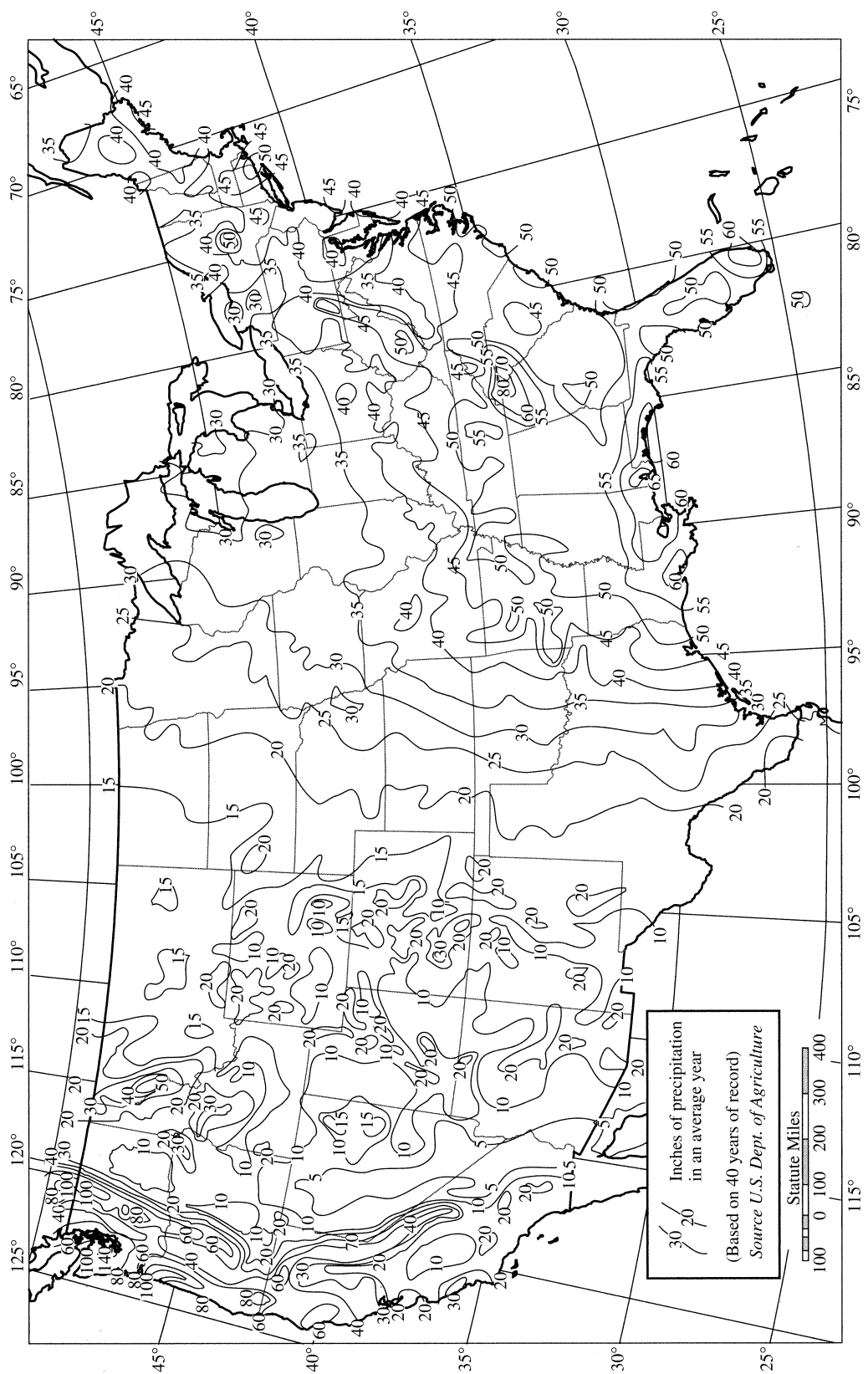


Figure 4.40 Long-term average annual precipitation (in = 25.4 mm) for the conterminous United States (US Department of Agriculture).

$$\bar{\phi} = \text{atan}(S/C) \quad \text{if } S > 0 \text{ and } C > 0; \quad (4.48a)$$

$$\bar{\phi} = \text{atan}(S/C) + 180^\circ \quad \text{if } C < 0; \quad (4.48b)$$

$$\bar{\phi} = \text{atan}(S/C) + 360^\circ \quad \text{if } S < 0 \text{ and } C > 0. \quad (4.48c)$$

$\bar{\phi}$ is the **average time of occurrence**. (Note that since the angles ϕ_m are the central values for each month, we can only resolve $\bar{\phi}$ to the nearest month.)

The **seasonality index**, I_S , which expresses the degree to which precipitation is concentrated in time (Markham 1970), is given by

$$I_S \equiv \frac{P_R}{\sum_{m=1}^{12} P_m} = \frac{P_R}{\hat{P}}. \quad (4.49)$$

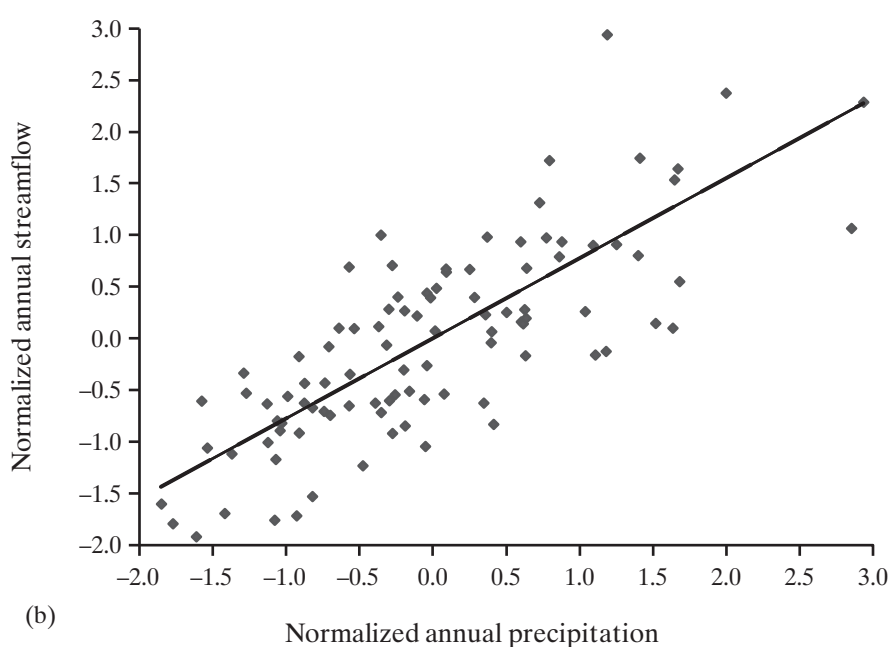
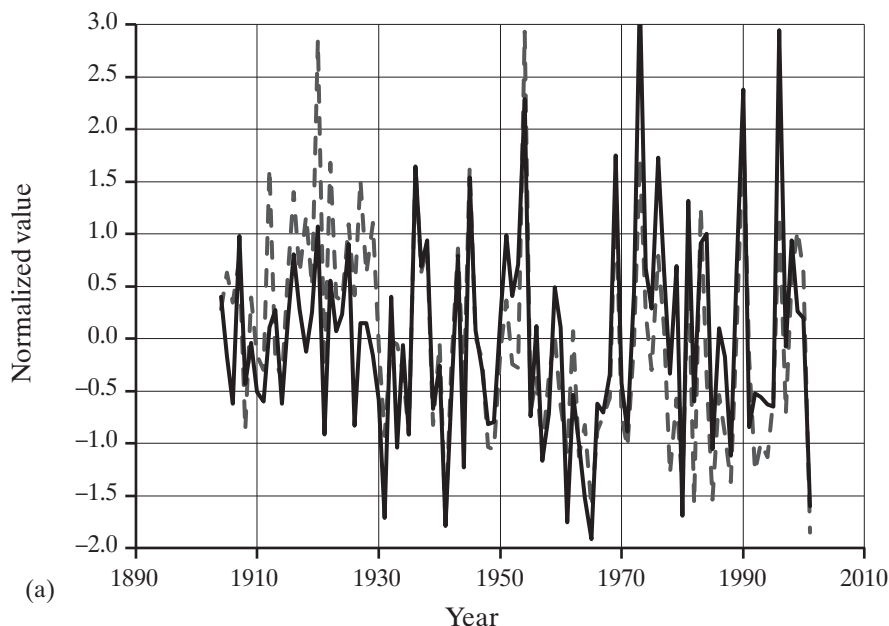


Figure 4.41 Comparison of annual precipitation and streamflow values for the Pemigewasset River at Plymouth, New Hampshire, via normalized values [equation (4.43)]. (a) Time series of normalized precipitation (dashed line) and streamflow (solid line). (b) Scatter plot of annual normalized values of precipitation and streamflow. The straight line is the best-fit linear relation between annual streamflow (\hat{Q}) and annual precipitation (\hat{P}); the correlation is quite strong ($\hat{Q} = 0.76 \cdot \hat{P}, r^2 = 60$).

Table 4.8 Angles and Angle Functions for Computing Seasonality Index and Average Time of Occurrence for Monthly Data.

Month	Day of Year	Mid-Month		First of Month	
		Angle, ϕ_m (degrees)	Sine	Cosine	Day of Year
January	16.0	15.8	0.272	0.962	1
February	45.5	44.9	0.706	0.708	32
March	75.0	74.0	0.961	0.276	60
April	105.5	104.1	0.970	-0.244	91
May	136.0	134.1	0.718	-0.696	121
June	166.5	164.2	0.272	-0.962	152
July	197.0	194.3	-0.247	-0.969	182
August	228.0	224.9	-0.706	-0.708	213
September	258.5	255.0	-0.966	-0.259	244
October	289.0	285.0	-0.966	0.259	274
November	319.5	315.1	-0.706	0.708	305
December	350.0	345.2	-0.255	0.967	335

Note that $0 \leq I_S \leq 1$; $I_S = 0$ when \hat{P}_m is identical for all months, and $I_S = 1$ when all precipitation occurs in a single month.

Box 4.6 gives examples of calculated circular statistics, and figure 4.42 (on p. 187) shows maps of precipitation seasonality in the United States based on circular statistics. The January maximum of precipitation on the West Coast is associated with the position and intensity of the North Pacific high-pressure cell and the Aleutian low-pressure cell (figure 2.12a), which produces an eastward flow of moisture-laden air in winter. In the summer (figure 2.12b), the high-pressure cell has expanded, leading to subsidence and a northerly wind flow parallel to the coast. The June maximum of precipitation in the mid-continent is produced by the springtime northward extension of moist air from the Gulf of Mexico into the zone of intense cyclogenesis in the westerly winds. By July this zone has migrated farther north with the Arctic front (Barry and Chorley 1982). The August maximum in the tropics is due to the northward migration of moist air from the Gulf of Mexico and Gulf of California, increased thermal-convective thunderstorm activity, and, in the Southeast, rain from tropical cyclones. The mild August Arctic maximum results from the northward position of cyclogenesis associated with the Arctic front and the increased amount of moisture that can be held in the warmer air of late summer.

4.4.3 Extreme Rainfalls

The statistical analysis of extreme values has the goal of estimating the probability of exceptionally high (or low) values of a given quantity. It is a central topic in hydrology because of the importance of floods and droughts for water-resource management. Here we focus on extreme high rainfalls,¹⁰ which are used as **design rainfalls** that are input to hydrologic models to generate **design floods**, which are then used as a basis for designing drainage systems, culverts, flood-control structures, and floodplain-management plans.

Extreme-value analysis of rainfall requires separate analyses of the largest rainfall amounts that have been recorded for specified **durations** in the region of interest. To provide an overall context, we begin by examining the record rainfalls that have been recorded for various durations globally. We then introduce the deterministic concept of “probable maximum precipitation,” and conclude with the statistical (probabilistic) treatment of extreme rainfall values.

4.4.3.1 Global Record Rainfalls

The largest amounts of rainfall recorded globally, P_{max} , for various durations, D , are listed in table 4.9 on p. 188. The record rainfalls for various durations can be directly related to the characteristics of the meteorological processes that produced them:

Box 4.6 Example Application of Circular Statistics for Quantifying Precipitation Seasonality

The table below lists the 1931–1960 average monthly precipitation (mm) for San Francisco, California (SFO), and Boston, Massachusetts (BOS). We want to compare the average times of occurrence and the seasonality indices for these stations.

	Jan	Feb	Mar	Apr	May	Jun	Jul	Aug	Sep	Oct	Nov	Dec	Total
SFO	102	88	68	33	12	3	0	1	5	19	40	104	475
BOS	114	95	115	102	88	95	83	103	100	95	115	101	1,206

SFO

$$\begin{aligned} S &= 119.4 \text{ mm} \\ C &= 291.9 \text{ mm} \\ P_R &= (119.4^2 + 291.9^2)^{1/2} = 315.4 \text{ mm} \\ I_S &= 315.4/475 = 0.664 \\ \text{atan}(S/C) &= 0.388 \end{aligned}$$

The I_S value indicates a high degree of seasonality. Since S and C are both > 0 , $\phi = \text{atan}(S/C) = 0.388$ [equation (4.48a)]. Referring to the last column of table 4.8, we see that the average month of occurrence is January.

BOS

$$\begin{aligned} S &= 8.10 \text{ mm} \\ C &= 55.6 \text{ mm} \\ P_R &= (8.10^2 + 55.6^2)^{1/2} = 56.2 \text{ mm} \\ I_S &= 56.2/1,206 = 0.047 \\ \text{atan}(S/C) &= 0.145 \end{aligned}$$

The I_S value is close to 0, so the degree of seasonality is very low. Since S and C are both > 0 , $\phi = \text{atan}(S/C) = 0.145$. This also falls in January, but since the degree of seasonality is so low, this is not very meaningful.

For durations up to about 4.5 hr, the record amounts were produced by convective storms; for those between 9 hr and 15 days they were from tropical cyclones (often enhanced by orographic effects; see Paulhus 1965); and for the longest durations they are the product of the unusually intense orographic enhancement described earlier for Cherrapunji, India.

As shown in figure 4.43 on p. 189, an envelope curve that describes an upper bound for the values of table 4.9 is given by

$$P_{max} = 500 \cdot D^{1/2}, \quad (4.50)$$

where P_{max} is in mm and D is in hr. This apparently universal scaling relation suggests that there is an upper bound on the rain-generating capacity of the atmosphere, and that is the basis for the concept of “probable maximum precipitation” discussed in the next section.

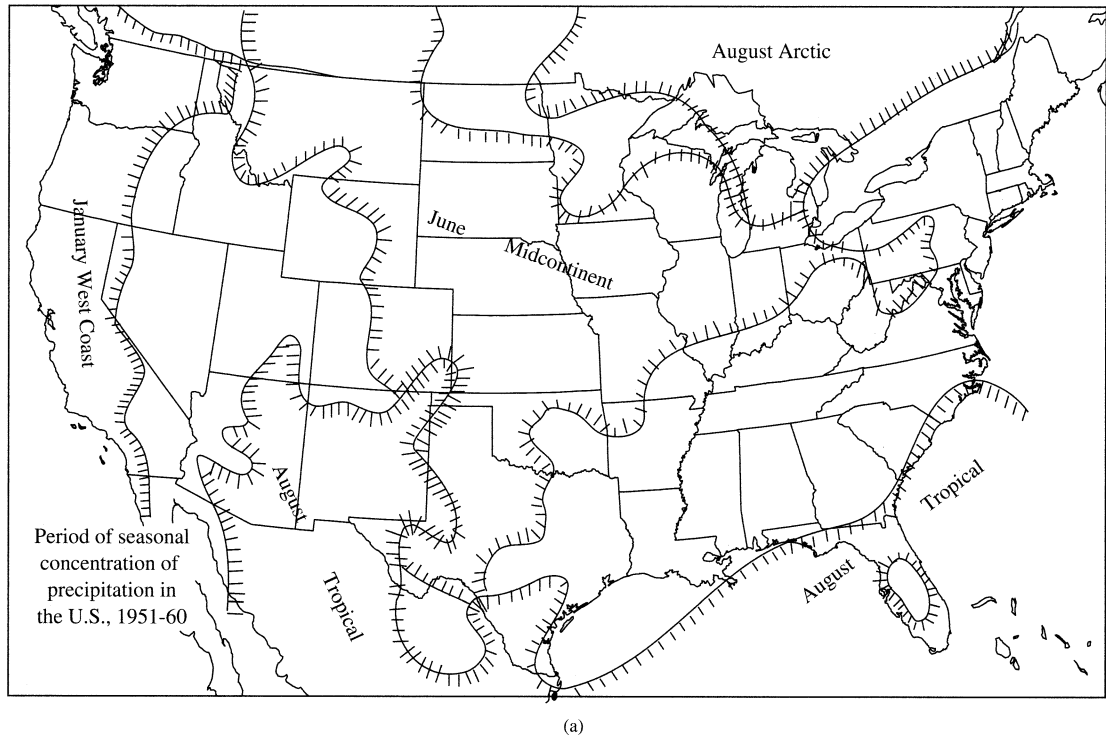
4.4.3.2 Probable Maximum Precipitation

The **probable maximum flood (PMF)** is an estimate of the largest flood that could occur from a given drainage basin. The PMF is often used as the design flood to determine the required capacity of the emergency spillway of a dam whose failure

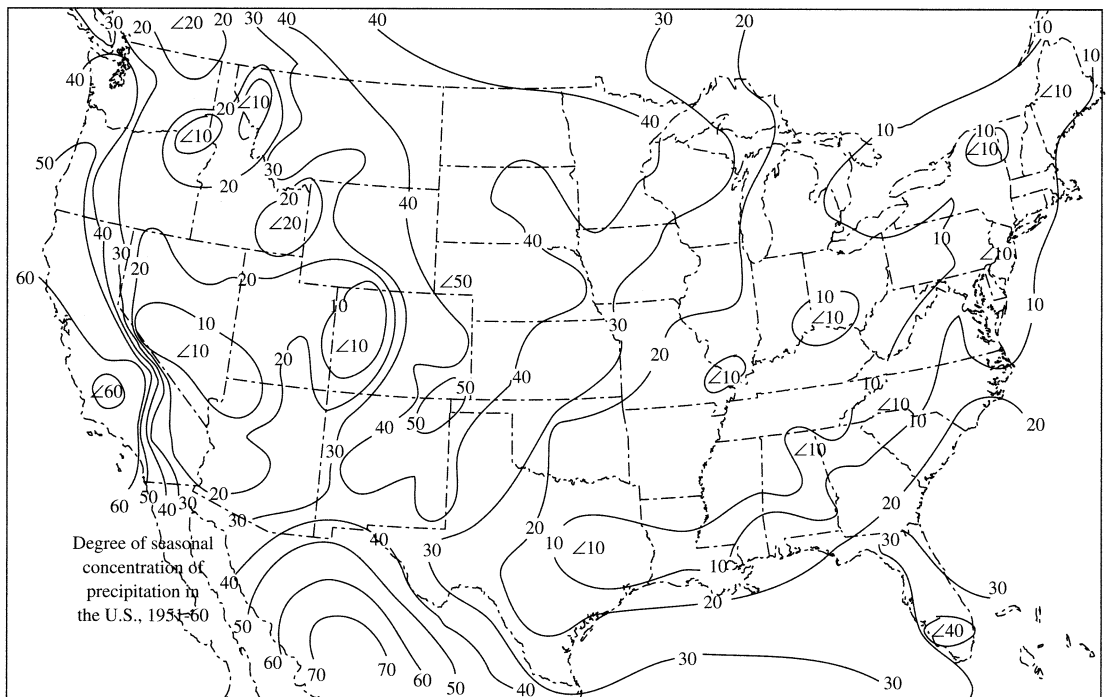
would cause massive economic damage and/or loss of life. To determine the PMF, a design rainfall called **probable maximum precipitation (PMP)** is estimated, which is used as input to a hydrological model to predict the resulting flood flow.

The PMP is “theoretically the greatest depth of precipitation for a given duration that is physically possible over a given size storm area at a particular geographical location at a certain time of year” (Hansen 1987).

Although the PMP concept uses the word “probable,” it is based on the deterministic premise that there is a theoretical maximum to rainfall generation that is meteorologically possible in a given region. In practice, PMP estimates are developed by estimating the maximum values of (1) precipitable water, (2) vertical uplift rates, and (3) convergence of moisture-laden air (see section 3.4), guided by analysis of the largest recorded rainfalls in the region (WMO 1986b; Smith 1992; Papalexiou and Koutsoyiannis 2006; Casas et al. 2008). Maximum rainfall depth P_{max} for



(a)



(b)

Figure 4.42 (a) Average month of occurrence and (b) seasonality index of annual precipitation calculated from monthly precipitation data using methods of circular statistics (box 4.6) [adapted from Markham (1970)].

a given duration is typically estimated from observed values of precipitable water and rainfall in extreme storms as

$$P_{max} = \frac{W_{max}}{W_{obs}} \cdot P_{obs}, \quad (4.51)$$

where P_{obs} is the observed precipitation, W_{obs} is the observed concurrent precipitable water content [usually estimated from observed dew point, as in equation (3.14)], and W_{max} is maximum probable precipitable water estimated from historical measurements of dew points for the appropriate region and season.

Table 4.9 Largest Rainfalls Recorded Globally for Various Durations.

Duration	Amount (in)	Amount (mm)	Location	Start Date
1 min	1.23	31	Unionville, Maryland, USA	4 Jul 1956
3 min	1.75	44	Haughton Grove, Jamaica	30 Sep 1925
5 min	2.48	63	Porto Bello, Panama	29 Nov 1911
8 min	4.96	126	Fussen, Bavaria, Germany	25 May 1920
15 min	7.8	198	Plumb Point, Jamaica	12 May 1916
20 min	8.1	206	Curtea-de-Arges, Romania	7 Jul 1889
30 min	11.02	280	Sikeshugou, Hebei, China	3 Jul 1974
42 min	12	305	Holt, Missouri, USA	22 Jun 1947
60 min	15.78*	401*	Shangdi, Nei Monggol, China	3 Jul 1975
72 min	17.32	440	Gaoj, Gansu, China	12 Aug 1985
2 hr	19.25	489	Yujianwanzi, Nei Monggol, China	19 Jul 1975
3 hr	28.50*	724*	Smethport, Pennsylvania, USA	18 Jul 1942
6 hr	33.07*	840*	Muduocaidang, Nei Monggol, China	1 Aug 1977
9 hr	42.79	1,087	Belouve, La Réunion	28 Feb 1964
18 hr	62.56	1,589	Foc-Foc, La Réunion	7 Jan 1966
1 day	71.85	1,825	Foc-Foc, La Réunion	7 Jan 1966
2 day	97.13	2,467	Auré re, La Réunion	7 Jan 1958
3 day	154.69	3,929	Commerson, La Réunion	24 Feb 2007
6 day	199.8	5,075	Commerson, La Réunion	24 Feb 2007
9 day	217.01	5,512	Commerson, La Réunion	24 Feb 2007
12 day	234.21	5,949	Commerson, La Réunion	16 Jan 1980
15 day	239.49	6,083	Commerson, La Réunion	14 Jan 1980
1 month	366.14	9,300	Cherrapunji, Meghalaya, India	1 Jul 1861
2 month	502.63	12,767	Cherrapunji, Meghalaya, India	1 Jun 1861
3 month	644.44	16,369	Cherrapunji, Meghalaya, India	1 May 1861
4 month	737.7	18,738	Cherrapunji, Meghalaya, India	1 Apr 1861
5 month	803.62	20,412	Cherrapunji, Meghalaya, India	1 Apr 1861
6 month	884.03	22,454	Cherrapunji, Meghalaya, India	1 Apr 1861
1 year	1,041.78	26,461	Cherrapunji, Meghalaya, India	1 Aug 1860
2 year	1,605.05	40,768	Cherrapunji, Meghalaya, India	1 Jan 1860

*Estimated value.

Source: NWS Hydrometeorological Design Studies Center, July 3, 2013, Word Record Point Precipitation Measurements (http://www.nws.noaa.gov/oh/hdsc/record_precip/record_precip_world.html).

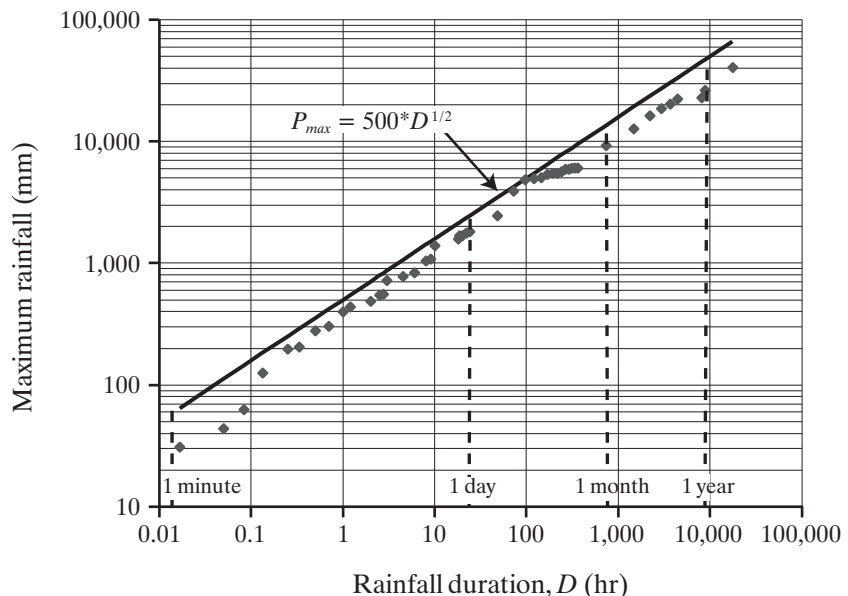


Figure 4.43 Maximum amounts of recorded rainfall as a function of duration. Data are listed in table 4.9.

The storm size and duration appropriate for a given situation are determined by the size of the drainage basin of interest: In general, the critical storm size is approximately equal to the basin size, and the critical duration is approximately equal to the “time of concentration” of the basin (the time it takes storm runoff to travel from the most distant part of the drainage basin to the outlet; discussed in chapter 10). As a general guide, figure 4.44 gives approximate relationships between time of concentration and drainage area.

Schreiner and Reidel (1978) developed generalized PMP maps for portions of the United States east of the 105th meridian, where orographic effects are negligible. Maps were given for storms of 4, 12, 24, 48, and 72 hours in duration and areas of 10, 200, 1,000, 5,000, 10,000, and 20,000 mi² (26, 520, 2,600, 13,000, 26,000, and 52,000 km²). Figure 4.45 on p. 191 shows three of these maps; Schreiner and Reidel (1978) gave methods for developing PMP estimates for durations and areas other than those mapped. The National Academy of Sciences (1983) identified sources for estimating PMP for regions west of the 105th meridian, and Hansen et al. (1982) and Hansen (1987) gave detailed instructions for developing the **probable maximum storm**, which incorporates estimates of the timing and areal distribution of rainfall for use in hydrologic models. For more historical and current information on PMP, see the Hydrometeorological Design Studies Center’s website (http://www.nws.noaa.gov/oh/hdsc/studies/pmp.html#PMP_documents).

The concepts of PMP and PMF are controversial: Can we really specify an upper bound to the amount of rain that can fall in a given time? The consistent square-root scaling relationship in figure 4.43 for rainfalls measured over very different precipitation regimes suggests this possibility. However, we must recognize that the plotted values are only those that have been observed in the last 150 years over the infinitesimal fraction of the earth covered by rain gauges; it is likely that higher amounts must have fallen at ungauged locations at other times and places.

And, conceptually, we can always imagine that a few more molecules of water could fall beyond any limit that is specified. In support of this view, Papalexiou and Koutsoyiannis (2006) conducted statistical analyses of humidity and rainfall data at five locations in Europe, and found no evidence for an upper bound for dew point or precipitation. They concluded that supposed PMP values had a small but nonnegligible probability of being exceeded, and suggested that design rainfalls should be based on a probabilistic analysis of extreme rainfalls. This reasoning now prevails in many countries: In a review of rainfall-frequency estimation methods, Svensson and Jones (2010) reported that the PMP has been re-

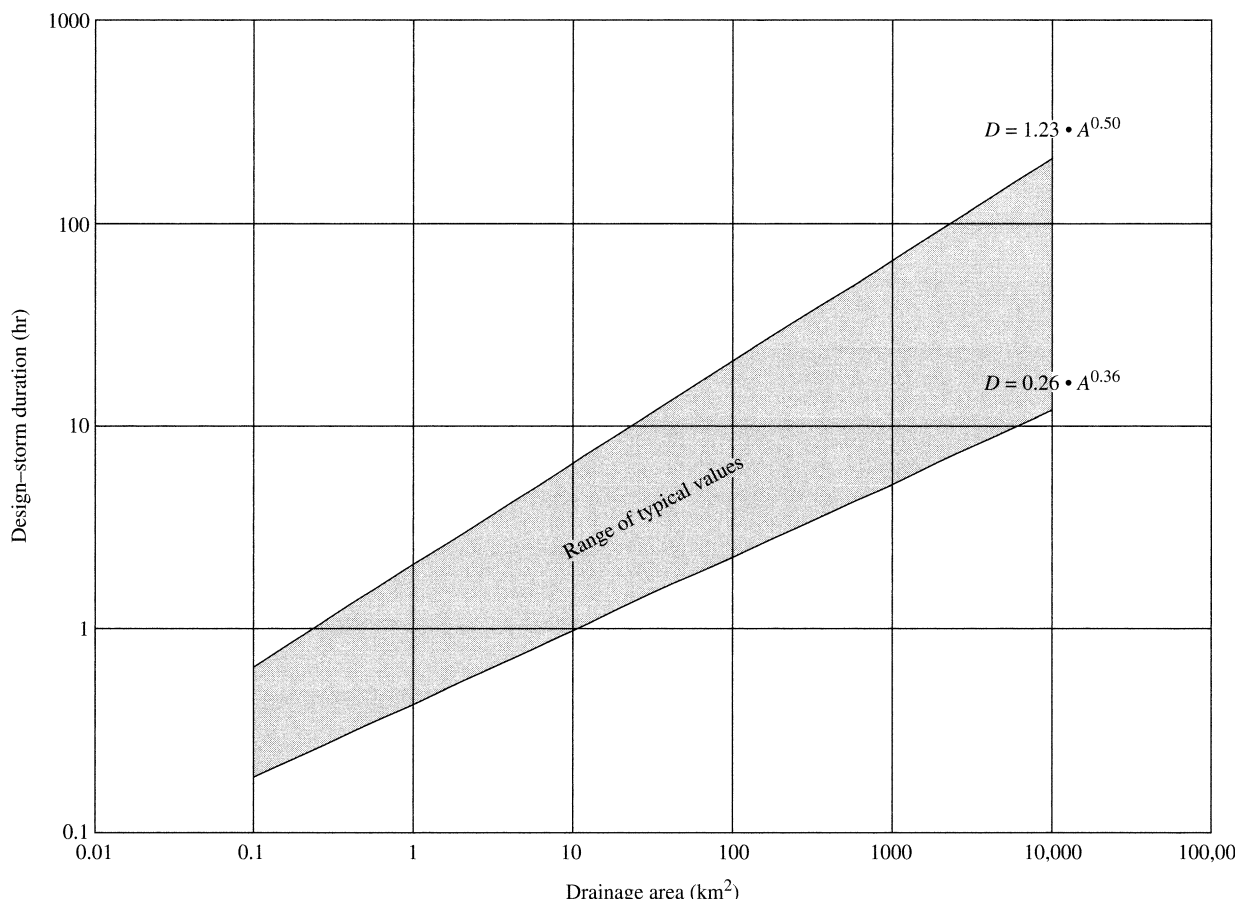


Figure 4.44 Typical values of design-storm duration as a function of drainage area based on relations in McCuen (1998) and Pilgrim and Cordery (1992).

placed by the use of rainfalls of very small exceedence probability in Canada, France, South Africa, New Zealand, the United Kingdom, and the United States, although they are still used as a basis for designing critical structures in Sweden, Germany, Australia, and Spain (Casas et al. 2008, 2010). The following section introduces the probabilistic analysis of extreme rainfalls.

4.4.3.3 Depth-Duration-Frequency Analysis

Most engineering and land-use planning situations do not involve the risk of catastrophic economic damage or loss of life that warrants design to PMF levels. For these less extreme circumstances—and, as noted above, increasingly for the entire range of design conditions—the design flood is the flood with a specified annual **exceedence probability**:

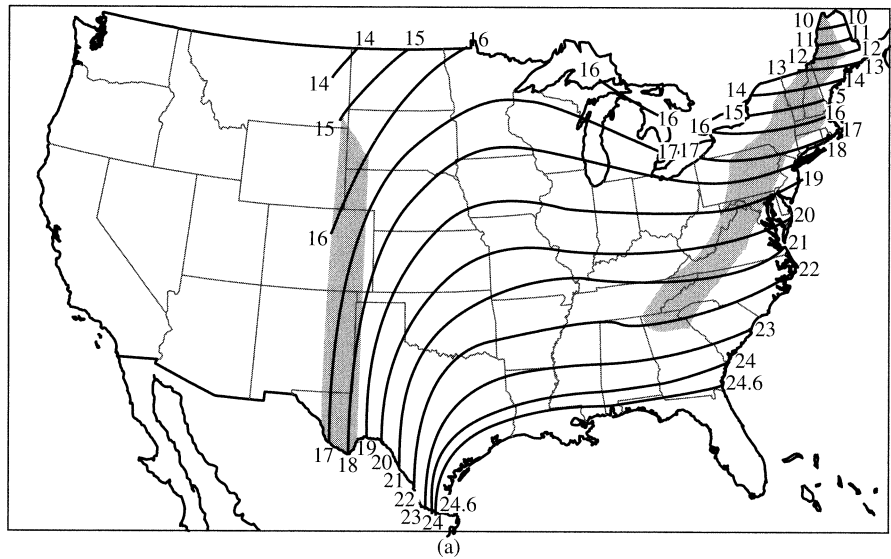
For a random variable X , the annual exceedence probability of an event of magnitude x^* , $EPr\{x^*\}$, is the probability that $X > x^*$ in any year.

That is,

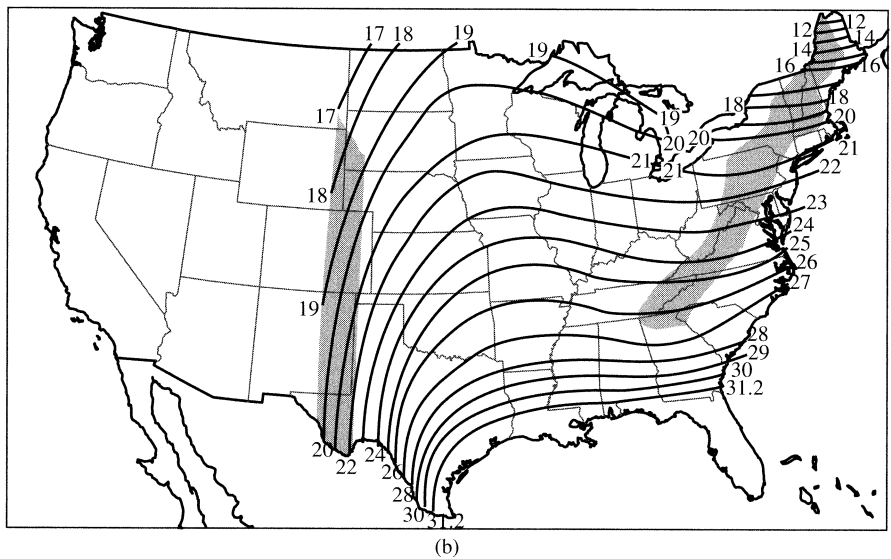
$$EPr\{x^*\} \equiv Pr\{X > x^*\} \text{ in any year. } (4.52)$$

The variable X is either

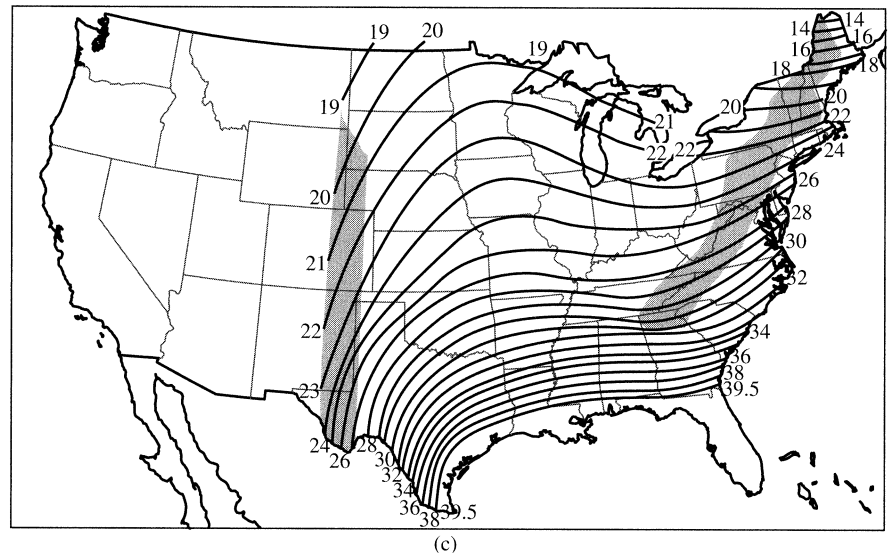
1. an **annual maximum time series**; i.e., the largest value of a quantity in a year, in which case a statistical sample consists of one value for each year (e.g., the annual maximum 1-hr rainfall), or
2. a **partial-duration time series**; i.e., the values of a quantity that exceed a specified threshold, x_{min} , in



(a)



(b)



(c)

Figure 4.45 Generalized all-season PMP ($1 \text{ in} = 25.4 \text{ mm}$) for the eastern United States for a storm area of 200 mi^2 ($\sim 500 \text{ km}^2$) and durations of (a) 6 hr, (b) 12 hr, and (c) 24 hr. Shaded areas require correction for orographic effects [Schreiner and Reidel (1978)].

which case a sample consists of all values such that $X > x_{min}$ (e.g., all 1-hr rainfalls > 25 mm) regardless of when they occur.

Exceedence probability is the complement of the **cumulative distribution function** of a variable X , $F\{x^*\}$, defined as

$$F\{x^*\} \equiv Pr\{X \leq x^*\} = 1 - EPr\{x^*\} \quad (4.53)$$

(section C.5). Exceedence probabilities are often expressed in inverse form as return periods or recurrence intervals:

The **return period** (or **recurrence interval**) of an event of magnitude x^* , $TR\{x^*\}$, is the *average* number of years between exceedences of x^* ,

which is given by

$$TR\{x^*\} = \frac{1}{EPr\{x^*\}}. \quad (4.54)$$

Exceedence probability for a given x^* calculated for a partial-duration series is always greater than for an annual series, but the two are nearly equal for exceedence probabilities < 0.1 (return periods > 10 yr).

Analogously with PMFs, the design flood is estimated by using a design rainfall with the appropriate duration and a specified exceedence probability as input to a hydrologic model.

Estimation of the rainfall depths with a given exceedence probability for various durations is called **depth-duration-frequency (DDF) analysis**. An equivalent procedure differs only in using rainfall intensities (depth divided by duration) rather than depth, and is called **intensity-duration-frequency (IDF) analysis**.

Standard engineering practice dictates the return period appropriate for a given situation, with higher return periods for projects that have higher costs of failure. For example, the flood with a return period of 25 yr (annual exceedence probability of 0.04) is commonly used for designing culverts, while the “100-yr flood” (annual exceedence probability of 0.01) is used to delineate floodplains for land-use planning.

The appropriate design duration is that which produces the largest peak flood from the area of interest.

In general, the critical duration increases with drainage area; figure 4.44 indicates a range of typical values. DDF/IDF analyses are usually carried out for several return periods and durations and the appropriate duration is determined by comparing the floods predicted by the simulation model.

In most cases the hydrologist requires rainfall frequency analysis for a finite area, such as a watershed. Thus there are two parts to DDF/IDF procedure:

1. Determine depth or intensity—probability relations for one or more representative rain-gauge locations in or near the region of interest.
2. Adjust the point values to give depth—or intensity—probability relations for the region of interest.

In the United States, the first step of DDF/IDF analyses have been carried out by the National Weather Service for much of the country, and are readily available on the Internet, as described in box 4.7.

4.4.3.3.1. DDF/IDF Analysis at Gauges

The analysis should begin with a review of the history of the weather station to assure the quality of the observations (section 4.2.1.2.10) and that measurement conditions have not changed significantly. Assuming that conditions have been stable, or observations are suitably adjusted, the annual maximum rainfalls for each duration of interest are extracted from the record. As noted in box 4.7, these steps have been carried out for many stations in the United States by the NWS, and the data can be readily downloaded. An example of a DDF/IDF analysis for a single gauge site and a single duration using these data is given in box 4.8 on p. 196 (figures 4.47, 4.48, and 4.49, all on p. 197).

In practice, DDF/IDF analyses are done for a range of durations, and the appropriate probability distribution is usually determined via a regional analysis rather than for a single station. Recent research has explored new approaches to probability analysis of rainfall extremes (Castellarin et al. 2009; Ceresetti et al. 2010; Haerter et al. 2010). Svensson and Jones (2010) reviewed the rainfall-frequency estimation methods used in nine countries; they noted that it is inherently difficult to estimate long return-period rainfalls from short data records, and that there is no obvious “best” way of doing it. Most countries use a preferred regional probability distribution function, with the GEV distribution (table C.1) being the most common. Parameters are usually estimated regionally; regional boundaries may be fixed, or the regions can be centered on the point of interest.

Box 4.7 Procedure for DDF/IDF Analyses Using the Precipitation Frequency Data Server

Accessing Completed DDF/IDF Analyses

The Precipitation Frequency Data Server (PFDS) is a point-and-click interface developed to deliver NOAA Atlas 14 precipitation frequency estimates and associated information for DDF/IDF analyses. To begin, go to <http://dipper.nws.noaa.gov/hdsc/pfds/>. This will display a map showing the states for which (1) updated analyses are available (those listed in table 4B7.1), (2) updates are in progress, and (3) updates are not underway or completed.

Table 4B7.1 DDF/IDF Analyses Available in NOAA Atlas 14 as of Mid-2012.

Volume	Region	States
1	Semiarid Southwest	AZ, NM, NV, UT
2	Ohio River Basin and Surrounding States	DE, IL, IN, KY, MD, NC, NJ, OH, PA, SC, TN, WV, VA
3	Puerto Rico and the US Virgin Islands	
4	Hawaiian Islands	HI
5	Selected Pacific Islands	
6	California	CA
7	Alaska	AK

To obtain an analysis, click to select the state of interest. Then select (1) depth (DDF) or intensity (IDF) analysis; (2) English or metric (SI) units, and (3) analysis based on annual maximum or partial-duration time series. Data for sites of interest can be selected by (1) specifying latitude and longitude, (2) clicking on a list of stations, or (3) double-clicking on an area of the map.

When you select a station, a table is generated below the map containing precipitation estimates for a range of durations (typically 5 min to 60 days) and recurrence intervals (typically 1 to 1,000 yr), along with 90% confidence intervals for those estimates. You can also access the information graphically as (1) a plot of depth or

intensity versus duration and (2) a plot of depth or intensity versus recurrence interval. Supplemental information about the analyses is also available.

For regions for which analyses have not been updated, you can access earlier analyses and maps that were originally published as paper copies. Hershfield (1961) covered the entire country for durations of 0.5 to 24 hr and return periods up to 100 yr; Miller et al. (1973) updated Hershfield's maps for the 11 western states; and Frederick et al. (1977) gave maps for the central and eastern states for durations of 5 min to 1 hr. Examples of these maps are given in figure 4.46. These maps are generalizations of analyses done in many locations, and are intended for use in design situations where local data are unavailable or where a complete DDF analysis is not economically justified. One must use caution in accepting these generalized map values in areas where precipitation is highly variable spatially due to variations in relief and exposure, and in large metropolitan areas where the urban "heat-island" effects may increase the frequency of heavy rainfalls.

Accessing Maximum Precipitation Time-Series Data

Time-series data for stations used in the Atlas 14 analyses can be downloaded at http://hdsc.nws.noaa.gov/hdsc/pfds/pfds_series.html. First, select the appropriate volume of Atlas 14, then specify (1) annual maximum or partial-duration series and (2) duration from drop-down menus. Then click to download the time-series data for all stations in the region in text (.txt) format. Data for specific stations (the date of the observation and the depth in inches) can be selected from the downloaded file and transferred as a text file into a single column in an Excel spreadsheet. Then using the "text-to-columns" feature for width-delimited fields, the date and amount can be entered into separate columns. An entry of "-9.99" in the depth column indicates missing data for that year. Unit conversion and conversion from depth to intensity (depth divided by duration) can then be accomplished in the spreadsheet if desired.

Regional relations between intensity, duration, and frequency are sometimes represented by equations of the form

$$I = \frac{a \cdot TR^b}{(D^c + d)} \quad (4.55a)$$

or

$$I = \frac{a \cdot TR^b}{(D + d)^c}, \quad (4.55b)$$

where I is intensity, D is duration, and a, b, c, d are empirical constants (Wenzel 1982; Durrans 2010). These equations have no theoretical basis and, as the

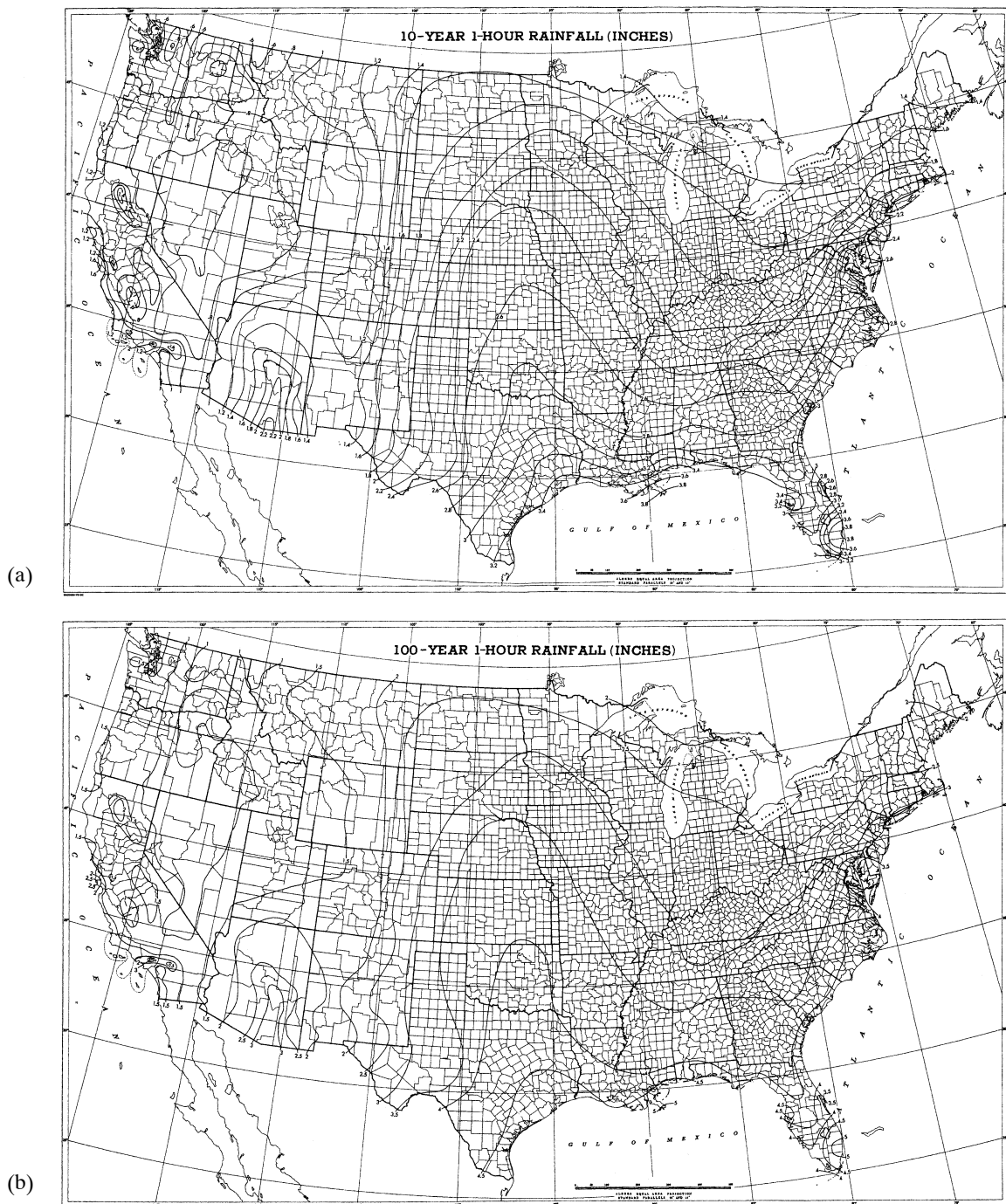
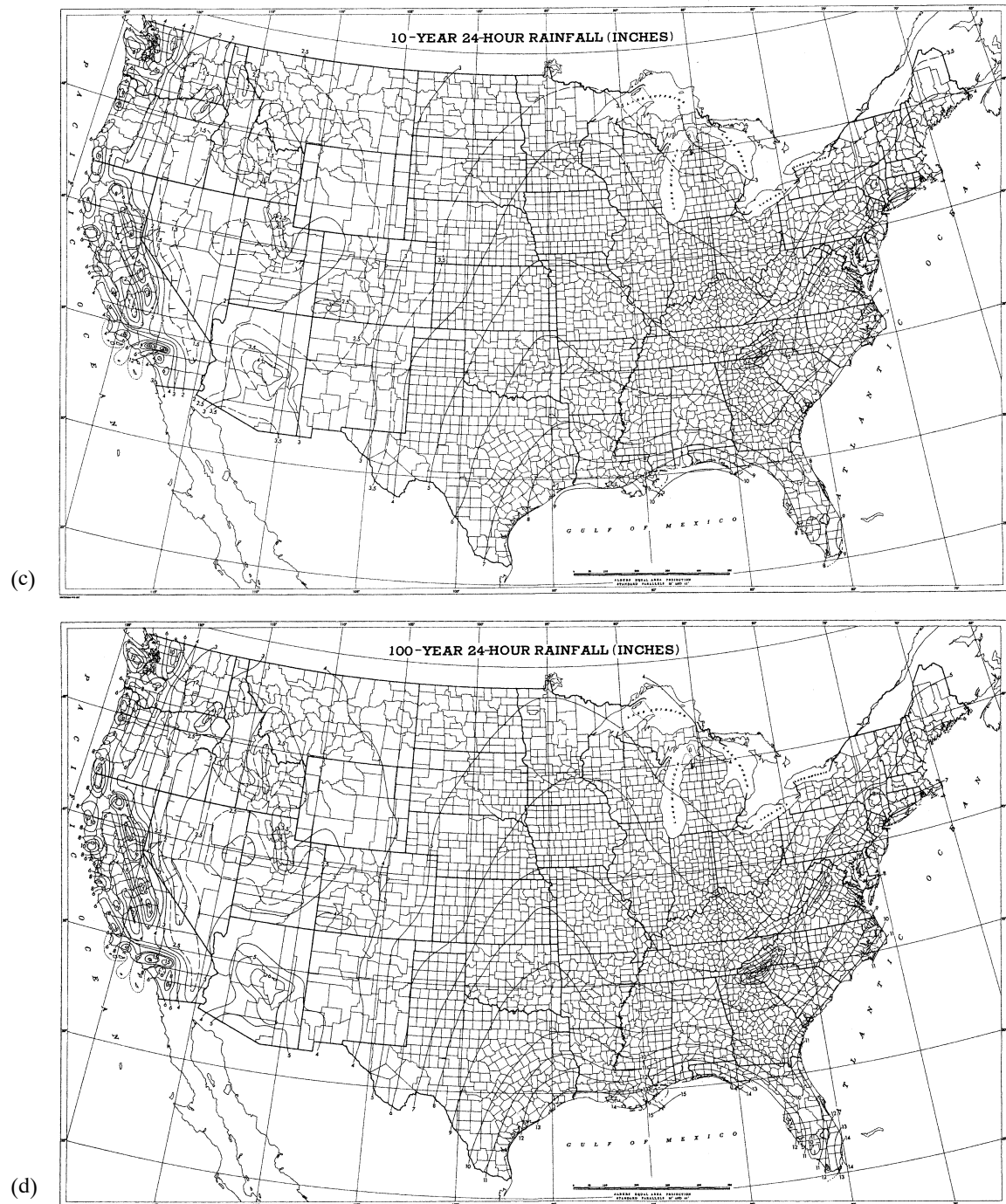


Figure 4.46 Examples of generalized depth-duration-frequency maps for the United States (1 in = 25.4 mm). (a) 10-yr, 1-hr rainfall; (b) 100-yr, 1-hr rainfall; (c) 10-yr, 24-hr rainfall; (d) 100-yr, 24-hr rainfall [Hershfield (1961)].



Box 4.8 Point DDF/IDF Analysis Example

To illustrate the basic DDF procedure for an individual rain gauge, here we will carry out a DDF analysis for 1-hr rainfalls in Philadelphia, Pennsylvania. The annual maximum 1-hr rainfalls for 1900–2000 at that location can be found on the disk accompanying this text (see Max Rainfalls Philadelphia PA.doc). The data were obtained as described in box 4.7.

Before conducting the DDF analysis, the time series of annual maxima should be plotted for visual examination and statistically tested to assure that the time series is homogeneous and stationary, i.e., that it does not contain trends, jumps, or cycles that might be caused by changes in measurement conditions or climatic fluctuations. Non-stationarity due to climatic change is a real concern, as recent studies have shown increases in extreme precipitation in the United States (Knight and Davis 2009; Villarini et al. 2011) and Europe (Zolina et al. 2010; Shiu et al. 2012). Several statistical tests that can detect time-series anomalies are described in section C.11. The plot of figure 4.47 and statistical tests do not suggest any trends, jumps, or cycles, so the Philadelphia time series can be considered homogeneous and stationary.

To provide an introduction to DDF/IDF analysis, we will fit a probability distribution to the Philadelphia data and estimate the return periods of annual maximum 1-hr rainfalls. We do this via the “L-moment” approach (section C.9.2), which is widely accepted as the preferred method for identifying an appropriate probability distribution for hydrologic and climatic data. The sample L-moment values are calculated as described in box C.3 (see disk); for the Philadelphia data we find the following sample L-moment values: $\hat{\lambda}_1 = 31.6$ mm, $\hat{\lambda}_2 = 5.54$ mm, $\hat{\lambda}_3 = 0.628$ mm, and $\hat{\lambda}_4 = 0.874$. To identify the appropriate distribution we calculate the L-skewness

$$\hat{\tau}_3 \equiv \hat{\lambda}_3 / \hat{\lambda}_2 = 0.113, \text{ and the L-kurtosis}$$

$\hat{\tau}_4 \equiv \hat{\lambda}_4 / \hat{\lambda}_2 = 0.158$; referring to the L-moment diagram of figure C.10, we see that these values determine a point close to the point “G” for the Gumbel distribution

[a special case of the generalized extreme-value (GEV) distribution]. Assuming that the Gumbel distribution applies, we see from table C.1 that this distribution relates x and $F_G\{x\}$ as

$$F_G\{x\} = \exp\left[-\exp\left(\frac{x-\xi}{\alpha}\right)\right], \quad (4B8.1)$$

where ξ and α are parameters, and these parameters are estimated from the L-moments as

$$\hat{\alpha} = \frac{\hat{\lambda}_2}{0.6931} = \frac{5.54}{0.6931} = 7.99 \text{ mm}$$

and

$$\begin{aligned} \hat{\xi} &= \hat{\lambda}_1 - 0.5772 \cdot \hat{\alpha} \\ &= 31.6 - 0.5772 \cdot 7.99 \\ &= 27.0 \text{ mm}. \end{aligned}$$

To show that this distribution fits the Philadelphia data, we calculate the empirical distribution function $\hat{F}\{x\}$ using the Cunnane plotting-position formula described in box C.1 (see disk):

$$\hat{F}\{x_{(i)}\} = \frac{i - 0.4}{N + 0.2}, \quad (4B8.2)$$

where N is the number of observations and $x_{(i)}$ indicates the i th-ranked value of precipitation (ranking from lowest $i = 1$ to highest $i = N$). $\hat{F}\{x_{(i)}\}$ and $F_G\{x\}$ are compared in figure 4.48; they show that the Gumbel distribution fits the observations well. We can now convert the $F_G\{x\}$ values to return-period values via equations (4.53) and (4.54) and plot return period versus 1-hr maximum rainfall (figure 4.49). Design rainfalls could then be selected from this graph; for example, the 25-yr, 1-hr rainfall ≈ 53 mm and the 100-yr, 1-hr rainfall ≈ 65 mm. For a project requiring a very low probability of failure, one might design for the 10,000-yr, 1-hr rainfall, ≈ 100 mm.

constants may vary strongly over short distances, it is preferable to base design rainfalls on direct DDF/IDF analyses if suitable data are available for nearby rain gauges.

4.4.3.3.2 Adjustment of Point Estimates to Areal Estimates

DDF analyses and the generalized maps developed from such analyses are for precipitation at a point. For use as input to simulation models, the

point values of depth for a given duration and return period must be multiplied by an **areal reduction factor, ARF**, to give the corresponding average depth over the watershed being modeled. *ARF* is a function of the duration (D) and area (A).

Studies to determine appropriate values of *ARFs* have been of limited geographical extent, and hydrologists often use the curves developed by the NWS and those thought to be generally applicable to the

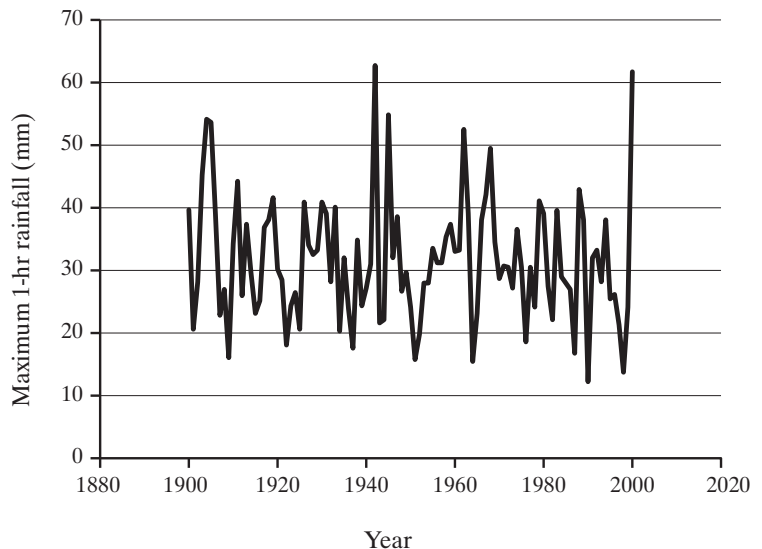


Figure 4.47 Time series of annual maximum 1-hr rainfall at Philadelphia, Pennsylvania (box 4.8). The data do not show evidence of trends or periodicities, and so are suitable for DDF/IDF analysis.

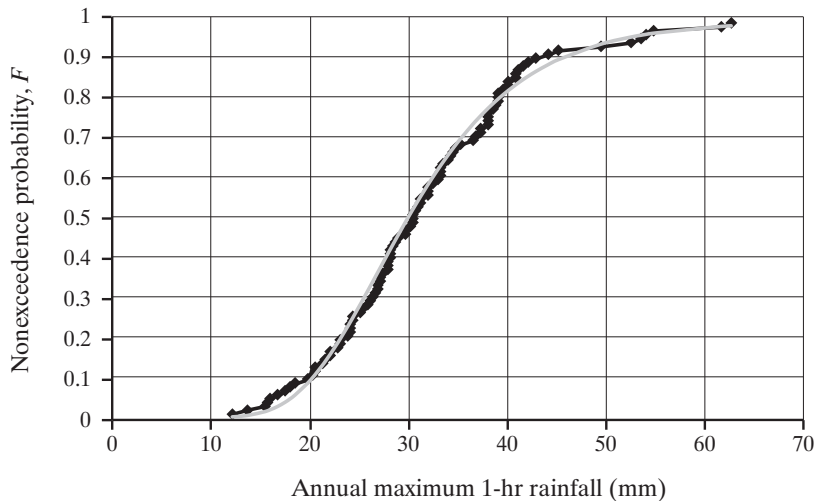


Figure 4.48 Fit of annual maximum 1-hr rainfall at Philadelphia, Pennsylvania (points), to the Gumbel frequency distribution (smooth curve) with parameters determined via L-moment analysis (box 4.8).

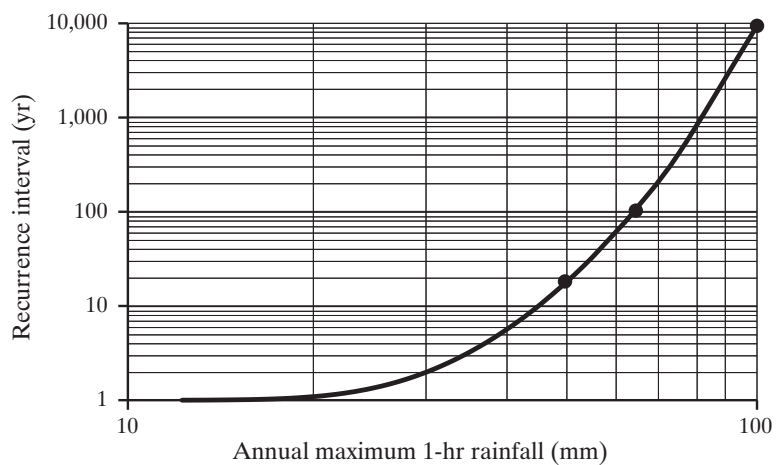


Figure 4.49 Curve relating recurrence interval and annual maximum 1-hr rainfall at Philadelphia, Pennsylvania (box 4.8). The dots show the 25-yr, 1-hr rainfall (53 mm), the 100-yr, 1-hr rainfall (65 mm), and the 10,000-yr, 1-hr rainfall (100 mm).

United States (figure 4.50). Note that these relations reflect the meteorological characteristics of various types of storms discussed earlier: The heaviest short-duration rainfalls come from convective storms that are almost always of small areal extent, and the heaviest longer-duration storms are usually generated by cyclonic storms that cover thousands of square kilometers.

Eagleson (1972) presented an empirical relation that approximates the empirical curves of figure 4.50:

$$ARF = 1 - \exp(-1.1 \cdot D^{0.25}) + \exp(-1.1 \cdot D^{0.25} - 0.0039 \cdot A), \quad (4.56)$$

where D is duration in hours and A is area in km^2 . Omolayo (1993) compared factors for Australia, the United Kingdom, and the United States, and Huff (1995) found that the urbanization effects discussed in the next section alter areal reduction factors.

A theoretical basis for ARF relations was developed by Rodriguez-Iturbe and Mejia (1974), who related ARF to the spatial correlation structure of precipitation as represented by a relation of the form of equation (4.39) and figure 4.37. Sivapalan and Blöschl (1998) expanded this approach to apply to extreme values. De Michele et al. (2001) used the concept of dynamic space-time scaling to derive a physically based formula for $ARFs$.

4.4.3.4 Time Distribution of Rainfall

Hydrologic models generally require the time distribution of rainfall inputs, not just the total storm

rainfall, to generate design floods from design rainfalls. Wenzel (1982) described various approaches to developing appropriate time distributions for design storms, and other aspects of developing design storms for hydrologic analyses. The US Natural Resources Conservation Service has developed typical patterns of time distribution of rainfall for design storms in the United States; these are described in many engineering-hydrology texts (e.g., McCuen 1998). Information on estimating time distributions developed by the NWS can be accessed at the PFDS website (http://dipper.nws.noaa.gov/hdsc/pfds/pfds_temporal.html).

4.4.4 Anthropogenic Effects on Precipitation Climatology

4.4.4.1 Inadvertent Effects

Evapotranspiration from land contributes 40% of annual land precipitation globally (section 4.1.7), so large-scale land-use modifications associated with agriculture and urban development will significantly impact precipitation climatology: Irrigation and large reservoirs increase the potential for precipitation by increasing humidity and modifying surface albedo and temperature (DeAngelis et al. 2010; Degu et al. 2011), overgrazing and deforestation have the opposite effect by reducing humidity, and air pollution changes the concentration and size of cloud condensation nuclei. In its policy statement on planned and inadvertent weather modification, the

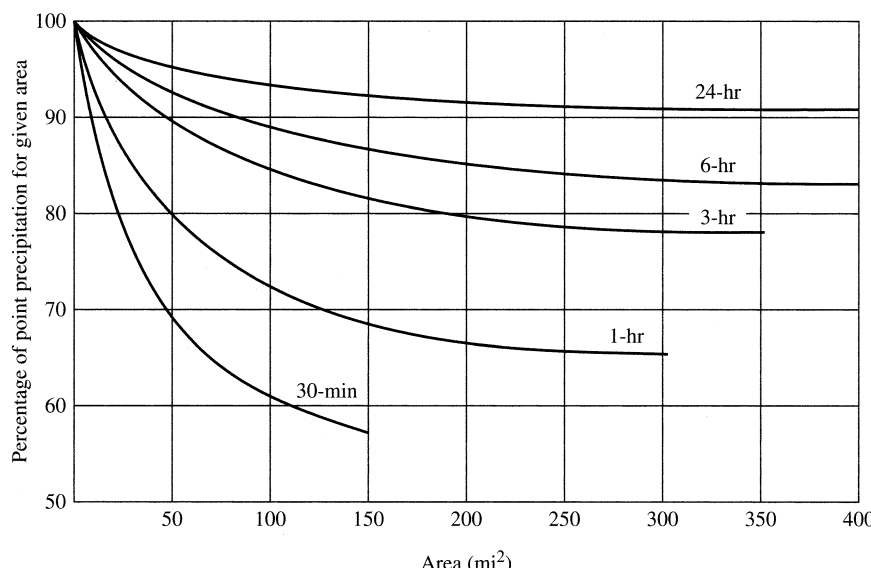


Figure 4.50 Reduction of point rainfalls for application to watersheds up to 400 mi^2 ($\sim 1,000 \text{ km}^2$) as recommended by the NWS [Miller et al. (1973)]. Curve labels indicate storm durations.

American Meteorological Society (AMS 1992) found that agricultural practices, urbanization, industrial activity, and condensation trails (“contrails”) from jet aircraft modify local and regional weather.

Urban effects on precipitation have been studied in detail in the United States. Huff and Changnon (1973) and Changnon (1981) found increases of 9 to 17% in total precipitation and an increase in the number of heavy (> 25 mm) rain storms associated with six of eight large US urban areas. These effects were greater in summer than in winter, and were greatest over and immediately downwind of the urban centers. Although these heavy storms were associated largely with cold fronts, the major cause of the increase appears to be the enhanced convective uplift induced by higher surface temperatures. These higher temperatures are due in turn to the greater absorption of solar radiation by buildings and pavements and to heat emissions from industries and motor vehicles. The urban “heat-island” effect on precipitation was found to be of definite hydrologic significance: It was reflected in increased summertime streamflow, increased ground-water recharge, increased flow in sewers, and increased flooding (Huff 1977). Qian et al. (2009) reported that the increased production of precipitation nuclei in pollution has resulted in fewer light rains in China, and increases in extreme precipitation in the United States (Knight and Davis 2009; Villarini et al. 2011) and Europe (Zolina et al. 2010; Shiu et al. 2012) are likely exacerbated by human-caused climate change.

4.4.4.2 Intentional Weather Modification

Human attempts to modify weather—particularly to increase rainfall when needed for agriculture—are as old as civilization. However, only since the 1940s, when scientific understanding of the precipitation process accelerated, has intentional **weather modification** become a realistic management alternative.

The main goals of precipitation-augmentation activities in the United States have been to increase snowfall from winter cyclonic/orographic storms and rainfall from summertime convective clouds. Both cases involve **cloud seeding**—the introduction of artificial cloud-condensation nuclei (CCN) in the form of crystals of silver iodide (AgI) that serve as templates for the formation of ice crystals, or of common salt (NaCl) that induce droplet growth by hygroscopic action (section 3.4). In the first case, it has been found that snowfall from orographic clouds with temperatures from -10 to -23°C can be in-

creased by providing the additional nuclei; however, seeding colder clouds in otherwise similar conditions may cause overseeding, which reduces precipitation because the available cloud water is spread over the more abundant nuclei and few of the ice crystals grow large enough to fall. In supercooled convective clouds the additional nuclei trigger the formation of ice crystals, and the resulting evolution of latent heat accelerates uplift within the cloud and triggers the process of precipitation formation.

One of the requirements for the formation of significant precipitation is the continuing importation of water vapor into the precipitating cloud (section 3.4). This requirement imposes limitations on the usefulness of cloud seeding for precipitation enhancement—where this importation does not occur, the introduction of CCN may cause most of the cloud moisture to precipitate, resulting in minor precipitation and the disappearance of the cloud. In fact, cloud seeding is sometimes done under these conditions in order to dissipate fogs and stratiform clouds. Attempts also have been made to exploit the overseeding phenomenon to prevent or reduce hail formation and to reduce the intensity of hurricanes (see Mather 1984; AMS 1992).

Reviews of the status of weather modification (AMS 1992; Orville 1995) found that (1) AgI seeding has produced significant precipitation increases in several experiments; (2) seasonal precipitation increases of 10 to 30% have been produced by seeding supercooled orographic clouds; (3) seeding may increase or decrease precipitation from convective clouds, and the conditions contributing to positive or negative results are not well understood; and (4) rainfall can be increased by seeding warm-based ($> 10^{\circ}\text{C}$) convective clouds under certain conditions. These reviews also noted that increases or decreases in precipitation may be induced beyond the target areas, with potential negative impacts, and that the economic viability of precipitation augmentation has not been demonstrated.

A more recent review by the US National Research Council (2003) reported that operational weather-modification programs were underway in 24 countries and 21 US states. However, the report found that very little scientific research was being done, and that “there is still no convincing scientific proof of the efficacy of intentional weather modification” (p. 3). It noted that weather modification does have potential for alleviating water-resource stresses and weather hazards and recommended that, be-

cause observational techniques and scientific understanding of cloud physics have advanced considerably in recent years, the United States should invest in a research program to improve understanding of precipitation microphysics, cloud dynamics, efficacy of cloud-seeding agents, and testing of cloud models.

The AMS (1992) review concluded that the ecological, hydrological, socioeconomic, and legal impacts of weather modification are potentially far-reaching, and that assessment of these impacts should be included in field studies. Certainly the potential for conflicts of interest in deciding whether, how, and where to increase precipitation, and for issues of liability resulting from increasing (or failing to increase) precipitation in a given instance, would appear to be limitless. As Mather (1984) noted, lawyers might well reap the only real benefits of cloud seeding.

4.4.4.3 Effects on Climatological Statistics

As we have seen, evidence of nonstationarity due to natural and/or anthropogenic climate change has appeared in precipitation data in several regions, and introduces serious issues in determining probabilities of extreme precipitation. However, neither the AMS (1992) or the US National Research Council (2003) reviews discussed the impact of the opera-

tional use of weather modification in undermining the value of hydrologic statistics as a scientific basis for water-resource management. As noted by Kazmann (1988), this could well be the most serious impact, because most water-management decisions rely in significant part on statistical quantities such as averages, return periods, and probable maximum values of precipitation and the resulting streamflow. These statistics are based on past records and are only useful insofar as they are indicative of future behavior. If future precipitation is to be governed in part by administrative actions, court decisions, or private economic interests, the uncertainty in these statistics could grow to the point of meaninglessness.

Without meaningful statistics, we have no basis for designing water-supply systems, bridges, wastewater treatment plants, or flood damage reduction measures. The economic costs of losing this basis would appear both as money wasted in overdesigning and as money spent in repairing measures that are too frequently damaged due to their underdesign. These costs, and the potential legal entanglements, should be included in assessing the economic viability and overall wisdom of weather-modification schemes.

▼ EXERCISES

1. Identify and locate the nearest precipitation-gauging station. If possible, visit the station to note the type of gauge, type of wind shield (if any), exposure with respect to surrounding obstructions, and frequency and timing of observation. Find out from the observer, state climatologist, or weather-agency official the history of the station, including length of record and changes in location or immediate surroundings (trees, buildings, etc.).
2. Obtain from the state climatologist, weather-agency official, or other source a map showing the locations of precipitation gauges in your region. How does the gauge density compare with those shown in table 4.6? Does the network appear to adequately sample the region (consider topographic effects, distance from coast, storm directions, etc.)?
3. Select a portion of the precipitation-gauge map you found for exercise 4.2 that contains at least six gauges for which average annual (or annual) precipitation data are available. Compare the regional average precipitation using: (a) the arithmetic average; (b) Thiessen polygons; (c) the two-axis method; and (d) if there appears to be a relation between precipitation and elevation, the isohyetal approach.
4. If you have access to a computer-based surface-generating and -contouring program, enter the data used in exercise 4.3. Compare the regional average calculated from the computer-generated isohyets with the regional averages computed in exercise 4.3.
5. The tables below give area-elevation data for a drainage basin and the average annual precipitation measured at six gauges in the basin. The basin has an area of 269 km², a minimum elevation of 311 m, and a maximum elevation of 1,600 m.
 - a. Compute the average annual precipitation for the basin using the hypsometric method.
 - b. Compare the value computed in (a) with the arithmetic average.

Area-Elevation Data

Elevation Range (m)	Fraction of Area in Range
311–400	0.028
400–600	0.159
600–800	0.341
800–1,000	0.271
1,000–1,200	0.151
1,200–1,400	0.042
1,400–1,600	0.008

Precipitation Data

Gauge	Elevation (m)	Average Annual Precipitation (mm)
1	442	1,392
2	548	1,246
3	736	1,495
4	770	1,698
5	852	1,717
6	1,031	1,752

6. The table below gives annual precipitation measured over a 17-yr period at five gauges in a region. Gauge C was moved at the end of 1974. Carry out a double-mass curve analysis to check for consistency in that gauge's record, and make appropriate adjustments to correct for any inconsistencies discovered. (The data can be found on the disk accompanying this text (see 2MassCurv.xls).

Year	A	B	C	D	E
1970	1,010	1,161	780	949	1,135
1971	1,005	978	1,041	784	970
1972	1,067	1,226	1,027	1,067	1,158
1973	1,051	880	825	1,014	1,022
1974	801	1,146	933	923	821
1975	1,411	1,353	1,584	930	1,483
1976	1,222	1,018	1,215	981	1,174
1977	1,012	751	832	683	771
1978	1,153	1,059	918	824	1,188
1979	1,140	1,223	781	1,056	967
1980	829	1,003	782	796	1,088
1981	1,165	1,120	865	1,121	963
1982	1,170	989	956	1,286	1,287
1983	1,264	1,056	1,102	1,044	1,190
1984	1,200	1,261	1,058	991	1,283
1985	942	811	710	875	873
1986	1,166	969	1,158	1,202	1,209

7. Consider a drainage basin area of 1,611 km² in which three precipitation gauges have been operating for 20 yr. The average annual precipitation, \hat{P} , at the three gauges is 1,198 mm/yr and the overall variance of annual precipitation, $\hat{S}^2(p)$, is 47,698 mm²/yr². An analysis of the spatial correlation structure of annual precipitation in the region gives a value of $c = 0.0386 \text{ km}^{-1}$ [equation (4B3.5c)]. Compute the variance reduction achieved by this measurement program and compare the variance reduction that would have been achieved by having four, rather than three, gauges in the region during the 20-yr period.
8. Compute and compare the (a) seasonality index and (b) average time of occurrence for monthly precipitation at the following stations. The data can be found on the disk accompanying this text (see PptnSeas.xls).

Average Monthly Precipitation (mm)

Station	J	F	M	A	M	J	J	A	S	O	N	D
New Orleans, LA	97	102	135	117	112	112	170	135	127	71	84	104
Seattle, WA	145	107	97	61	43	41	20	25	53	102	137	160
Fairbanks, AK	23	13	10	8	18	36	46	56	28	23	15	13
Mexico City, Mexico	5	8	13	18	48	104	114	109	104	41	13	8
Belem, Brazil	318	358	358	320	259	170	150	112	89	84	66	155
St. Petersburg, Russia	25	23	23	25	41	51	64	71	53	46	36	30
Addis Ababa, Ethiopia	13	38	66	86	86	137	279	300	191	20	15	5
Cherrapunji (Sohra), India	18	53	185	665	1,280	2,695	2,446	1,781	1,101	493	69	13

9. Following the instructions in box 4.7, download a DDF/IDF analysis for a US location and a watershed area specified by your instructor.
- Use figure 4.44 to determine the appropriate design-storm duration for the watershed.
 - Determine and graph the 10-, 25-, 50-, and 100-yr point rainfalls for that duration.
 - Using figure 4.50, determine and graph the 10-, 25-, 50-, and 100-yr rainfalls for that duration on the given watershed area.

▼ NOTES

¹ There is evidence that this approach has been in use at least since 400 BCE in India, where the rainfall data were used in managing agriculture (Neff 1977).

² Other approaches for measuring water inputs due to snow are discussed in chapter 5.

³ Mathematically, this is called a **Dirichlet tessellation** (Diggle 1983).

⁴ If the region is a large portion of the earth's surface, x and y represent latitude and longitude and interpolation must be over a spherical surface.

⁵ Also called the **semivariogram**.

⁶ Pronounced with a hard "g"; it is named for D. J. Krige, who developed the method, along with Georges Matheron, originally to map gold deposits in South Africa.

⁷ Correlation coefficients can range from -1 to +1 (section C.6); here we consider only positive values.

⁸ See equation (C.44) and box C.7 (see disk).

⁹ Autocorrelation can be defined for lags > 1, but since $\rho_T(t) = \rho_T(1)^t$, this is not necessary.

¹⁰ Although snowmelt floods are important in many regions, rates of snowmelt are controlled by energy inputs from the atmosphere (chapter 5), so the discussion here deals only with rainfalls.



5

Snow and Snowmelt

The goal of this chapter is to develop an understanding of the hydrologically important aspects of snow and snowmelt. We begin with an overview of the role of snow in the hydrologic cycle, then examine the nature of snow as a material, define critical snow properties, review techniques for measuring these properties, and survey the distribution of snow at local scales. The major focus of the chapter is a quantitative understanding of the processes that control the melting of snow (relying extensively on the physical principles discussed in chapter 3) and the movement of meltwater through the snowpack to the ground surface. This understanding is the basis for models used to predict and forecast snowmelt runoff, and we conclude with a review of approaches to snowmelt modeling.

5.1 Hydrologic Importance of Snow

Over much of the land above 45°N latitude (figure 2.26), a significant portion of precipitation falls as snow that is stored on the surface for periods ranging from hours to months before melting and continuing through the land phase of the hydrologic cycle. Figure 5.1 shows the steep latitudinal increase in the fraction of average annual precipitation falling as snow in North America; this fraction reaches about 65% on

the north coast of Alaska (Dingman et al. 1980). Location relative to oceans and elevation also influence the portion of precipitation occurring as snow.

As noted by Frei et al. (2012), annual snow accumulation and melt are among the most dramatic environmental changes on the earth's surface. These phenomena influence a range of oceanographic, climatic, and ecological, as well as hydrologic, processes, including (1) the surface energy balance, (2) the stability of permafrost and consequent effects on global carbon budgets, and (3) fresh-water flux to the oceans and the strength of oceanic circulations.

In areas with a significant seasonal snowpack, it is the amount and timing of **water input** (i.e., snowmelt plus rain) rather than of precipitation, that largely determines the availability of water to vegetation and the amount and timing of streamflow (including floods) and ground-water recharge (figure 5.2 on p. 205). Since a smaller proportion of snowmelt than of rainfall is evaporated and transpired, snowfall contributes proportionally more to runoff and ground-water recharge; L'vovich (1974) estimated that more than half the annual runoff is derived from snowmelt in much of the Northern Hemisphere (figure 5.3 on p. 206). For mountain regions, as much as 85% of the annual runoff may come from snowmelt (Shafer and Dezman 1982).

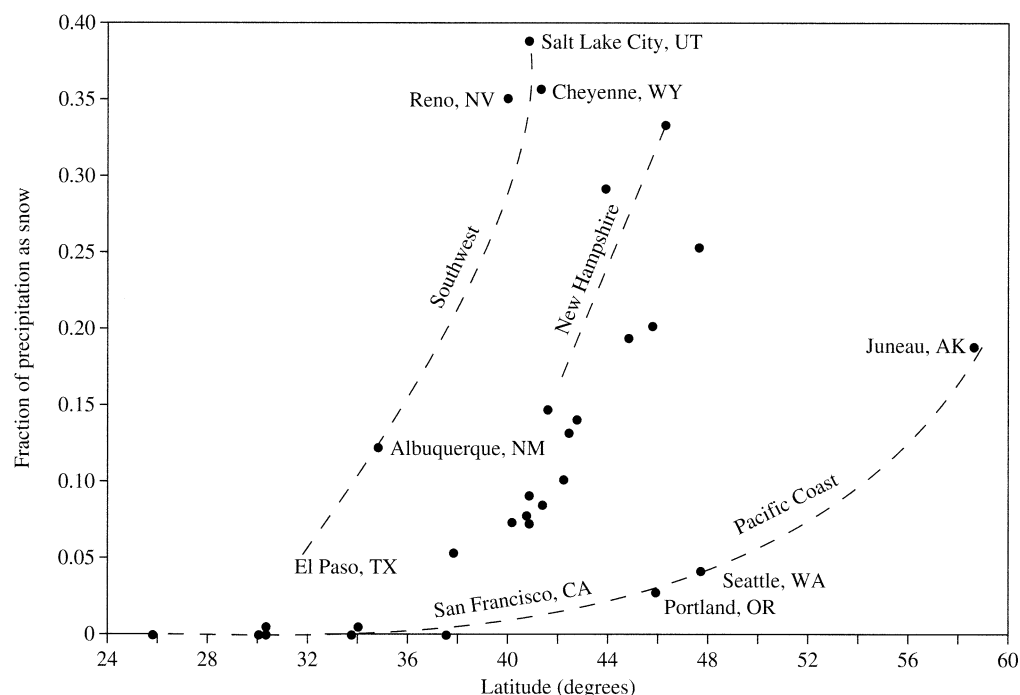


Figure 5.1
Fraction of precipitation occurring as snow as a function of latitude in the United States. City data from Todd (1970); unidentified points are for cities east of the Rocky Mountains. These fractions have probably decreased since these data were assembled due to warming (section 2.2.8.2).

In spite of the hydrologic importance of the melting of seasonal snow, there have been few studies characterizing water-input climatology. An early regional study showed that water-input climatology in New England is determined by latitude and elevation, and it developed a method for determining climatic and synoptic patterns of water input from standard network observations of temperature and precipitation (Hendrick and DeAngelis 1976). More recently, Bookhagen and Burbank (2010) quantified the hydrologic importance of snowmelt in the Himalayas, where changes in the timing or amount of snowmelt due to increasing temperatures or decreasing winter precipitation may have far-reaching societal consequences.

The overwhelming evidence of general global warming (section 2.1.3.2) makes a broader understanding of the role of snow in the hydrologic cycle of critical importance. To provide a general framework for this understanding, Molini et al. (2011) used a simple model of climate and watershed response to explore the relation between streamflow and water-input climatology. They found that, while increased air temperatures reduce winter snow accumulation and reduce total snowmelt amounts, they intensify snowmelt rate and thus increase the annual peak discharge. Thus there is an optimal warm-sea-

son length for which the annual peak discharge reaches a maximum; this length is a function of the watershed residence time¹ (figure 5.4 on p. 206). Where warm-season length is less than this optimum, peak discharge is limited by slow melting dynamics; where it is greater, peak discharge is reduced by decreased winter snow accumulation. Thus although global snow cover has been declining markedly over the last two decades and the average annual duration of Northern Hemisphere snow cover has decreased by 15 to 18 days since the early 1970s (box 2.3), the magnitudes of snowmelt floods could increase or decrease depending on warm-season length and watershed characteristics.

The dynamics of floods due to heavy rain and accompanying warm temperatures on an extensive snowpack ("rain-on-snow floods") are not well understood, and are likely to become an increasing hazard due to global warming, especially in Arctic regions (Putkonen et al. 2009). Jones and Perkins (2010) examined the effects of snow, event size, basin size, and forest harvest on floods in three small ($< 1 \text{ km}^2$) and six large ($60\text{--}600 \text{ km}^2$) watersheds in the western Cascades of Oregon. Rain-on-snow events delivered 75% more water to soils than rain events; peak discharges of rain-on-snow events were almost twice as high as rain-event peaks in large basins, but

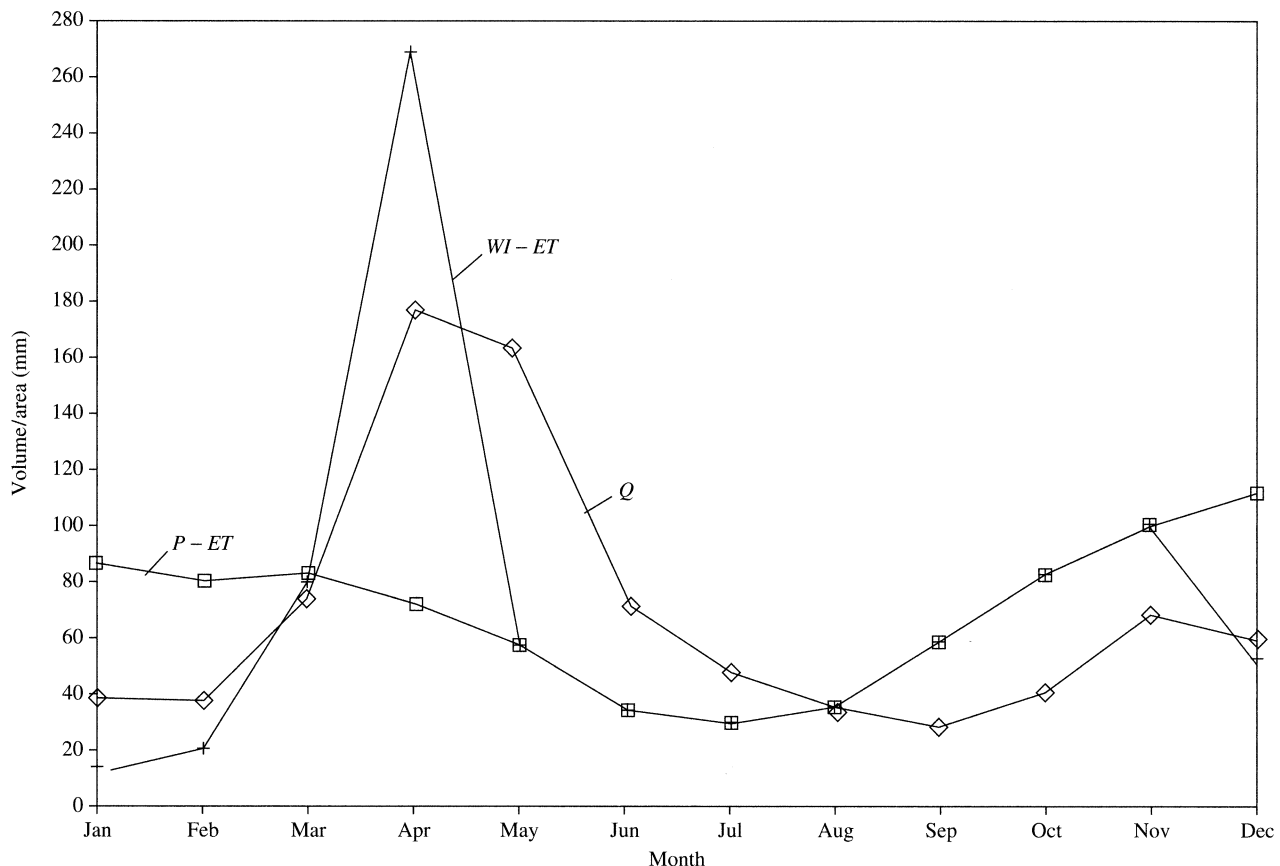


Figure 5.2 Average monthly precipitation minus evapotranspiration ($P - ET$) and water input (snowmelt plus rainfall) minus evapotranspiration ($WI - ET$) compared with streamflow (Q) in the Pemigewasset River basin, New Hampshire. The timing of streamflow is more closely related to $WI - ET$ than to $P - ET$.

only slightly higher in small basins. In extreme floods, prolonged precipitation and synchronous snowmelt produced rapid, synchronized hydrograph responses to small variations in precipitation intensity. They found that the evolving structure of forests has an important influence on extreme rain-on-snow floods, and that further work is needed to delineate areas experiencing snowmelt and describe flow paths in melting snowpacks.

5.2 Material Characteristics of Snow

5.2.1 Snow Properties

Snow is a granular, porous medium consisting of ice and pore spaces. The size of a snow particle, d , is measured at its largest dimension (Colbeck et al.

1990) and covers the ranges shown in table 5.1 on p. 207. When snow is **cold** (i.e., its temperature is below the melting point of ice, 0°C), the pore spaces contain only air (including water vapor). At the melting point, the pore spaces can contain liquid water as well as air, and snow becomes a three-phase system.

Snow depth is the vertical distance from the ground surface to the snow surface. Using the symbols M to designate mass [M], V for volume [L^3], h for height [L], and ρ for mass density [M L^{-3}], and the subscripts s for snow, i for ice, w for liquid water, swe for water substance (water plus ice), and a for air, we consider a representative portion of a snowpack of surface area A (figure 5.5 on p. 208) and volume

$$V_s = V_i + V_w + V_a = h_s \cdot A \quad (5.1)$$

to define quantities that characterize a snowpack:

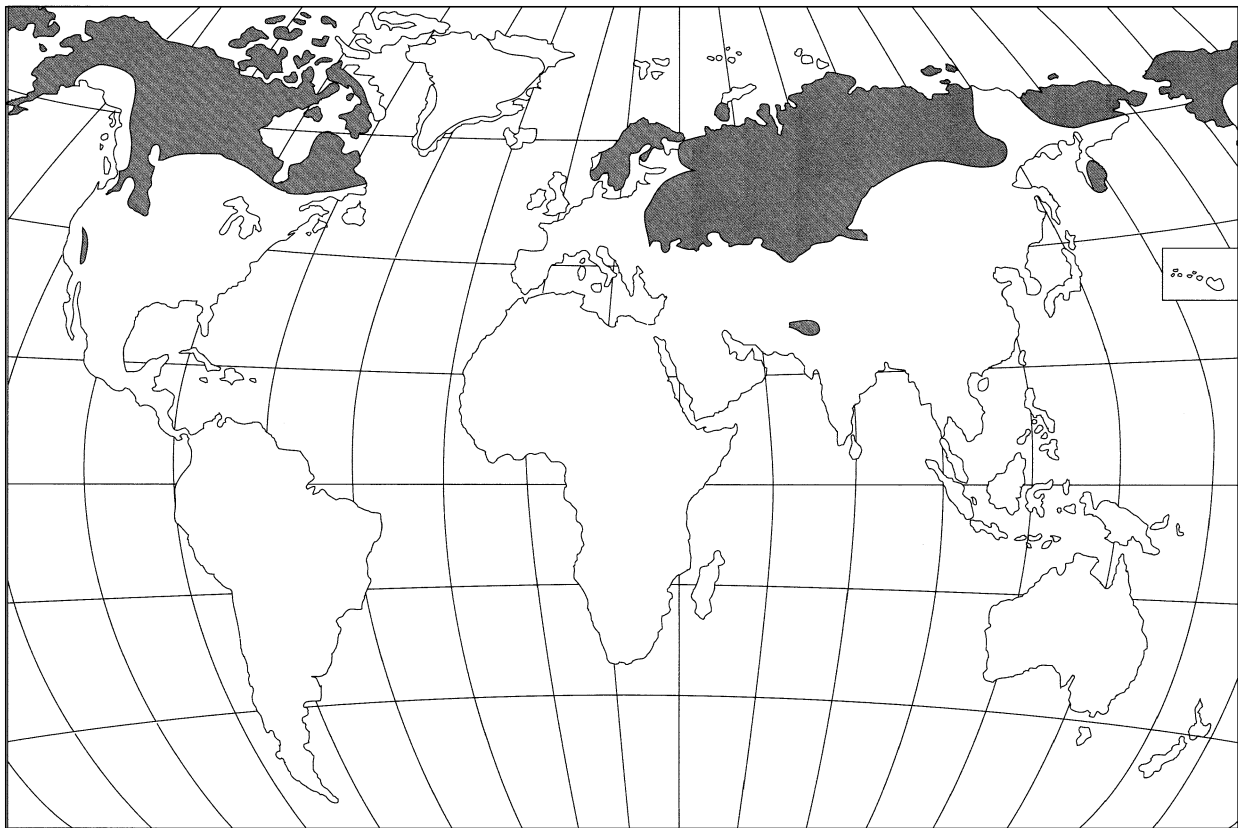


Figure 5.3 Regions in which more than half the annual runoff is derived from snowmelt [L'vovich (1974). *World Water Resources and Their Future*. Trans. by R. L. Nace, with permission of the American Geophysical Union].

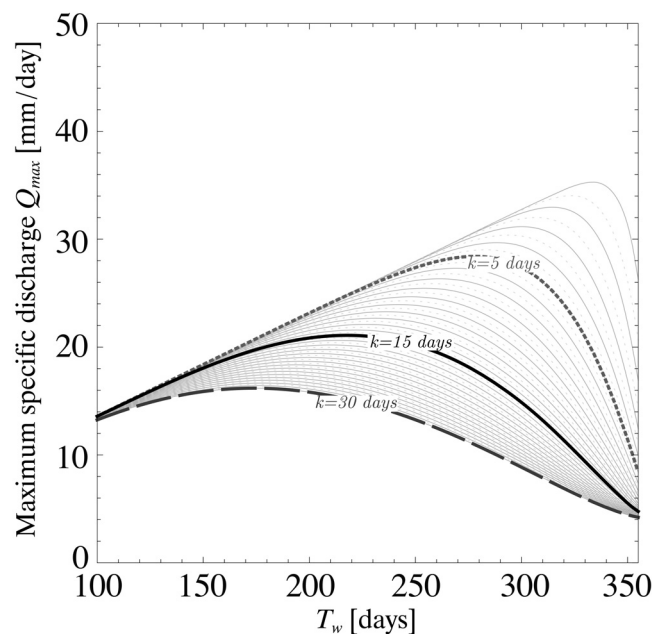


Figure 5.4 Peak discharge (Q_{max}) as a function of melting-season duration, T_w , and basin residence time, k , as modeled by Molini et al. (2011) (Maximum discharge from snowmelt in a changing climate. *Geophysical Research Letters* 38, with permission of the American Geophysical Union).

- **Porosity** (ratio of pore volume to total volume)

$$\phi \equiv \frac{V_w + V_a}{V_s}; \quad (5.2)$$

- **Snow density** (mass per unit volume of snow)

$$\rho_s = \frac{M_i + M_w}{V_s} = \frac{\rho_i \cdot V_i + \rho_w \cdot V_w}{V_s}; \quad (5.3)$$

- **Liquid-water content** (ratio of liquid-water volume to total snow volume)

$$\theta_w \equiv \frac{V_w}{V_s}. \quad (5.4)$$

Table 5.1 shows the ranges of snowpack liquid-water contents.

Table 5.1 Snow Properties.

(A) **Grain Size (d)**

Term	d (mm)
Very fine	< 0.2
Fine	0.2 to 0.5
Medium	0.5 to 1.0
Coarse	1.0 to 2.0
Very coarse	2.0 to 5.0
Extreme	> 5.0

Source: Colbeck et al. (1990).

(B) **Liquid-Water Content (θ_w)**

Term	Description ^a	Range of θ_w
Dry	$T_s < 0$ usually, but can occur at $T_s = 0$. Snow grains have little tendency to stick together when pressed.	0
Moist	$T_s = 0$. Water not visible even at 10× magnification. Snow grains tend to adhere when lightly crushed.	< 0.03
Wet	$T_s = 0$. Water visible as inter-grain menisci at 10× magnification, but cannot be squeezed out.	0.03 to 0.08
Very wet	$T_s = 0$. Water can be squeezed out by moderate pressing, but significant air spaces present.	0.08 to 0.15
Slush	$T_s = 0$. Snow flooded with water, few air spaces.	> 0.15

^a T_s = snowpack temperature (°C)

Source: Colbeck et al. (1990).

(C) **Field Estimation of Snowpack Density (ρ_s)**

Observation	Density (kg/m ³)
Supports an adult without skis.	320 to 350
Foot leaves only a slight impression.	350 to 380
Foot leaves no mark on the surface.	> 400

Source: Rikhter (1954).

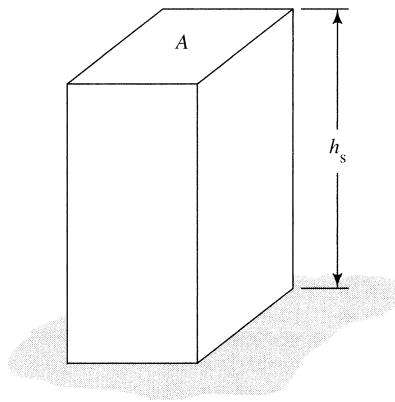


Figure 5.5 Dimensions of a representative portion of a snowpack used in defining snowpack properties. A is the area of the upper surface, h_s is the snow depth.

Combining equations (5.2)–(5.4) allows us to relate snow density, liquid-water content, and porosity as

$$\rho_s = (1 - \phi) \cdot \rho_i + \theta_w \cdot \rho_w, \quad (5.5)$$

where $\rho_i = 917 \text{ kg/m}^3$ and $\rho_w = 1,000 \text{ kg/m}^3$ (at 0°C).

For the hydrologist, the most important property of a snowpack is the amount of water substance it contains, i.e., the depth of water that would result from the complete melting of the snow in place.

This is the **snow-water equivalent (SWE)** of the snowpack, h_{swe} :

$$h_{swe} \equiv \frac{V_w + V_i \cdot (\rho_i / \rho_w)}{A}. \quad (5.6)$$

Noting that

$$V_i = (1 - \phi) \cdot V_s, \quad (5.7)$$

and substituting equations (5.4) and (5.7), equation (5.6) becomes

$$V_{swe} = \theta_w \cdot V_s + (1 - \phi) \cdot V_s \cdot \frac{\rho_i}{\rho_w}. \quad (5.8)$$

We can now utilize equations (5.1) and (5.6) to rewrite equation (5.8) as

$$\begin{aligned} h_{swe} &= \theta_w \cdot h_s + (1 - \phi) \cdot h_s \cdot \frac{\rho_i}{\rho_w} \\ &= \left[\theta_w + (1 - \phi) \cdot \frac{\rho_i}{\rho_w} \right] \cdot h_s. \end{aligned} \quad (5.9)$$

Finally, we see from equation (5.5) that equation (5.9) can be written as

$$h_{swe} = \frac{\rho_s}{\rho_w} \cdot h_s. \quad (5.10)$$

In words, equation (5.10) is expressed as

"water equivalent equals density times depth,"

where density is understood to mean *relative* density (i.e., specific gravity).

5.2.2 Snowpack Metamorphism

The density of new-fallen snow is determined by the configuration of the snowflakes, which is largely a function of air temperature, the degree of supersaturation in the precipitating cloud, and the wind speed at the surface of deposition (Mellor 1964). Higher wind speeds tend to break snowflakes that formed in stellar or needle-like shapes and to pack them together into denser layers. Observed relative densities (ρ_s / ρ_w) of freshly fallen snow range from 0.004 to 0.34 (McKay 1970), with the lower values occurring under calm, very cold conditions and higher values accompanying higher winds and higher temperatures; the usual range is $0.07 \leq \rho_s / \rho_w \leq 0.15$ (Garstka 1964).

Because of the difficulty in measuring the density of new snow,

an average relative density of 0.1 is often assumed to apply when converting snowfall observations to SWE.

However, the user of water-equivalent data should be aware of the potential for significant errors in estimates based on an assumed density (Goodison et al. 1981). New-snow density (kg/m^3) can be estimated as a function of wet-bulb temperature, T_{wb} , as

$$\rho_s = 50 + 1.7 \cdot (T_{wb} + 15)^{1.5} \quad (5.11)$$

(Melloh et al. 2002), where

$$T_{wb} \approx (2 \cdot T_a + T_{dp})/3; 0 \leq T_a \leq 10^\circ\text{C}, \quad (5.12)$$

T_a is air temperature ($^\circ\text{C}$), and T_{dp} is dew-point temperature ($^\circ\text{C}$) (section 3.2.5).

As soon as snow accumulates on the surface it begins a process of metamorphism that continues

until melting is complete. Four mechanisms are largely responsible for this process: (1) gravitational settling; (2) destructive metamorphism; (3) constructive metamorphism; and (4) melt metamorphism.

Gravitational settling in a given snow layer takes place at rates that increase with the weight of the overlying snow and the temperature of the layer and decrease with the density of the layer. According to relations given by Anderson (1976), one can expect gravitational settling to increase density at rates on the order of 2 to $50 \text{ kg/m}^3 \cdot \text{d}$ in shallow snowpacks. On glaciers, the pressure of thick layers of accumulating snow is the principal factor leading to the formation of solid ice.

Destructive metamorphism occurs because vapor pressures are higher over convex ice surfaces with smaller radii of curvature, so the points and projections of snowflakes tend to evaporate (sublimate) and the vapor to redeposit on nearby, less convex surfaces. This leads to the formation of larger, more spherical snow grains with time. This process is primarily important in snowflakes that have recently fallen, causing the density of a new-snow layer to increase at about 1% per hour. The process ceases to be important when densities reach about 250 kg/m^3 (Anderson 1976).

Constructive metamorphism is the most important pre-melt densification process in seasonal snowpacks. Over short distances, this process occurs by **sintering**, in which water molecules are deposited in concavities where two snow grains touch, gradually building a “neck” between adjacent grains. Over longer distances, constructive metamorphism can occur as a result of vapor transfer within a snowpack due to temperature gradients; sublimation occurs in warmer portions of the snowpack and the water vapor moves toward colder portions where condensation occurs. Very cold air overlying a relatively shallow snowpack often produces a strong upward-decreasing temperature gradient within the snow, with a concomitant upward-decreasing vapor-pressure gradient. Under these conditions, snow near the base of the pack evaporates at a high rate, often resulting in a basal layer of characteristic large planar crystals with very low density and strength called **depth hoar**.

Melt metamorphism occurs via two processes. In the first, liquid water formed by melting at the surface or introduced as rain freezes as it percolates downward into the cold snowpack. This results in densification, and may produce layers of essentially

solid ice that extend over long distances. The freezing at depth also liberates latent heat, which contributes to the warming of the snowpack and the acceleration of vapor transfer. The second metamorphic process accompanying melt is the rapid disappearance of smaller snow grains and growth of larger grains that occurs in the presence of liquid water. Because of this phenomenon, an actively melting snowpack is typically an aggregation of rounded grains the size of coarse sand (1 to 2 mm diameter) (Colbeck 1978).

Except for the temporary formation of depth hoar, all the processes of metamorphism lead to a progressive increase in density throughout the snow-accumulation season (figure 5.6). It should be noted, however, that there is much year-to-year variability in snowpack characteristics and that both snowfall and the processes causing metamorphism occur at highly variable rates over short distances due largely to differences in slope, aspect, and vegetative cover.

At the beginning of the melt season, the snowpack is typically vertically heterogeneous as well, with perhaps several layers of markedly contrasting grain sizes and densities. During melt, density continues to increase and the vertical inhomogeneities tend to disappear. During this period, density can fluctuate on an hourly or daily time scale due to the formation and drainage of meltwater. Snowpacks that are at 0°C and well drained tend to have relative densities near 0.35 (McKay 1970).

5.3 Measurement of Snow and Snowmelt

Discussion of measurement of snow and snowmelt requires definition of several terms:

- **Precipitation** is the incremental *water-equivalent depth* of rainfall, snow, sleet, and hail falling during a given storm or measurement period.
- **Snowfall** is the incremental *depth* of snow and other forms of solid precipitation that accumulates on the surface during a given storm or measurement period.
- **Snowpack** is the accumulated snow on the ground at a time of measurement. Its *water-equivalent depth* (h_{swe}) (SWE) is of particular hydrologic interest; its depth (h_s) and density (ρ_s or ρ_s/ρ_w) are also measured.
- **Snow cover** is the *areal extent* of snow-covered land surface. It may be measured in absolute terms [L^2] or as a fraction of a particular area.

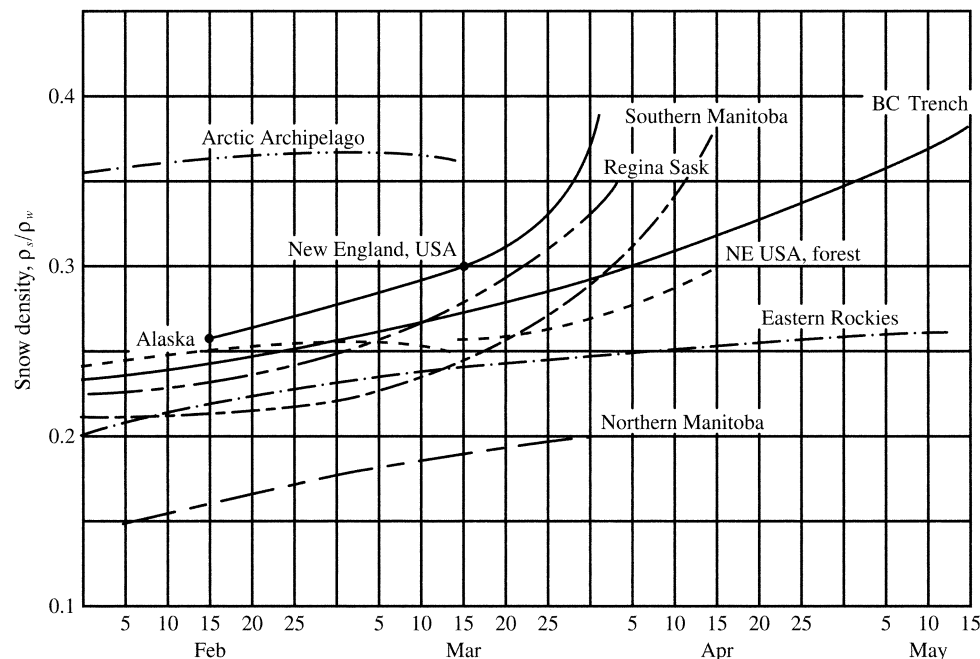


Figure 5.6
Seasonal variation in
snowpack relative
densities in various
regions of North
America [adapted
from McKay (1970)].

- **Ablation** is the incremental *water-equivalent depth* (volume per unit area) that leaves the snowpack during a given time period. It is the sum of snowmelt plus evaporation/sublimation.
- **Snowmelt** is the incremental *water-equivalent depth* (volume per unit area) that is produced by melting and leaves the snowpack during a given time period.
- **Water output** is the incremental *water-equivalent depth* (volume per unit area) that leaves the snowpack during a given time period. It is the sum of rain plus snowmelt that has percolated through the snowpack.

Approaches to measurement of each of the quantities listed above are discussed below and summa-

rized in table 5.2. Sources of snow data are listed in box 5.1.

5.3.1 Precipitation

5.3.1.1 Standard Gauges

As discussed in section 4.2.1.1, standard network measurements of precipitation are made via collecting gauges that weigh the total in-falling water substance or melt the snow and ice that is collected. In most cases, the form of the precipitation is not recorded. As noted in section 4.2.1.2, measurements in such gauges are subject to several sources of error, the most important of which is due to wind, and

Box 5.1 Snow-Data Sources

- Monthly reports and maps of Northern Hemisphere snow-cover extent are available at <http://www.ncdc.noaa.gov/sotc/global-snow> http://earthobservatory.nasa.gov/GlobalMaps/view.php?d1=MOD10C1_M_SNOW
- Daily, weekly, and monthly maps of Northern Hemisphere snow-cover extent and maps of monthly snow-cover climatology are available at <http://climate.rutgers.edu/snowcover/>
- Daily maps of snow cover for the United States and the Northern Hemisphere are available at http://www.nohrsc.noaa.gov/nh_snowcover/
- Preliminary daily snowfall and snow-depth observations collected from NWS Cooperative Observer Program stations and NWS First Order stations can be found at <http://www.ncdc.noaa.gov/snow-and-ice/dly-data.php>
- Current SNOTEL data and maps are available at <http://www.wrcc.dri.edu/snotel.html>

Table 5.2 Methods of Measuring Depth, Water Equivalent, and Areal Extent of Precipitation, Snowfall, Snowpack, and Snowmelt.

Parameter	Depth	Water Equivalent	Areal Extent
Precipitation		Standard storage gauges (G) Universal gauge (G)	Gauge networks (G) Radar (G, S)
Snowfall	Ruler and board (G)	Melt snow on board (G)	Observation networks (G)
		Use estimated density (G)	Radar (G, S)
		Universal gauge (G)	Visible/infrared (S)
		Snow pillow (G)	
Snowpack	Snow stake (G, A)	Universal gauge (G)	Snow surveys (G)
	Snow tube (G)	Snow tube (G)	Aerial observation (A)
	Ultrasonic gauge (G)	Snow pillow (G)	Visible/infrared (S)
	GPS receivers (S)	Radioisotope gauge (G)	Microwave (A, S)
		Natural gamma radiation (G, A)	
		Microwave (A, S)	
		GRACE ^a (S)	
Snowmelt and water output		Snow pillow (G) Lysimeter (G) Universal gauge (G)	Snow-pillow network (G)

A = airborne

G = ground-based

S = satellite-borne

^aGRACE = Gravity Recovery and Climate Experiment

gauge-catch deficiencies are especially large for snow (figure 4.22). A World Meteorological Organization (WMO) study (Goodison et al. 1998) compared gauge-catch deficiencies for snow and mixed precipitation of the standard gauges used in 16 countries; the standard was a Tretyakov gauge (figure 4.18) surrounded by bushes at the same height. The results, summarized in table 5.3 and figure 5.7, show that standard network precipitation-gauge measurements must be significantly adjusted for wind in periods in which snow is important (Legates and DeLiberty 1993; Yang et al. 1998). In the extreme cold of the high Arctic and high elevations, where snow particles are small and subject to especially high winds, gauge-catch deficiencies are even greater than those found in the WMO study (Sugiura et al. 2006).

5.3.1.2 Universal Gauges

Cox (1971) developed a “universal surface precipitation gauge” that measures all the quantities listed in table 5.2 simultaneously. Waring and Jones (1980) modified Cox’s design to make it more suitable for shallow snowpacks (figure 5.8 on p. 213). This gauge measures snowfall and SWE by weight and collects and measures water output. An increase

in the weight recorded by a snow pillow (see below) would usually indicate a snowfall event, although rainfall that stayed in the snowpack would also cause a weight increase. Clearly the installation of these gauges is considerably more elaborate and expensive than that of standard gauges, and they have not been widely used in observation networks.

Recently, several commercial companies have developed “universal precipitation gauges” that are designed to accurately measure the water equivalent of snowfall as well as rain, but are less elaborate than the installation shown in figure 5.8. Many of these are precipitation collectors with aerodynamic designs and are heated for snow collection. These instruments may provide improved gauge-catches in windy conditions, but are not in wide network use. Information about various designs can be found by searching the Internet for “universal precipitation gauges.”

5.3.1.3 Radar

The use of radar in precipitation measurement was described in section 4.2.2. Although it provides spatially continuous observations at small time intervals, it measures falling precipitation rather than that reaching the ground, and the single-polarization sys-

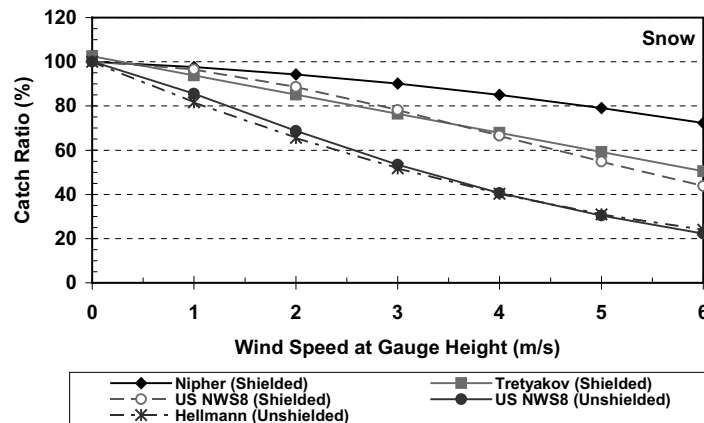


Figure 5.7 Average catch ratios for snow measured for five gauge types [Goodison et al. (1998). *WMO Solid Precipitation Measurement Intercomparison Final Report*. WMO/TD No. 872, courtesy of World Meteorological Organization)].

Table 5.3 Catch Ratios as a Function of Gauge-Height Wind Speed and Air Temperature for Standard Precipitation Gauges.

(A) Snow

Gauge Type	Used in	Equation	n	r ²	Standard Error (%) ^a
Nipher shielded	Canada	$R = 100 - 0.44 \cdot u(z_g)^2 - 1.98 \cdot u(z_g)$	241	0.40	11.05
Tretyakov	Russia	$R = 103.11 - 8.67 \cdot u(z_g) + 0.30 \cdot T_{max}$	381	0.66	10.84
US 8-in shielded	United States	$R = \exp[4.61 - 0.04 \cdot u(z_g)^{1.75}]$	107	0.72	9.77
US 8-in unshielded	United States	$R = \exp[4.61 - 0.16 \cdot u(z_g)^{1.28}]$	55	0.77	9.41
Hellmann unshielded	Germany, Denmark, Croatia	$R = 100 - 1.13 \cdot u(z_g)^2 - 19.45 \cdot u(z_g)$	172	0.75	11.97

(B) Mixed Precipitation

Gauge Type	Used in	Equation	n	r ²	Standard Error (%) ^a
Nipher shielded	Canada	$R = 97.29 - 3.18 \cdot u(z_g) + 0.58 \cdot T_{max} - 0.67 \cdot T_{min}$	177	0.38	8.02
Tretyakov	Russia	$R = 96.99 - 4.46 \cdot u(z_g) + 0.88 \cdot T_{max} + 0.22 \cdot T_{min}$	433	0.46	9.15
US 8-in shielded	United States	$R = 101.04 - 5.62 \cdot u(z_g)$	75	0.59	7.56
US 8-in unshielded	United States	$R = 100.77 - 8.34 \cdot u(z_g)$	59	0.37	13.66
Hellmann unshielded	Germany, Denmark, Croatia	$R = 96.63 + 0.41 \cdot u(z_g)^2 - 9.84 \cdot u(z_g) + 5.95 \cdot T_{avg}$	285	0.48	15.14

R ≡ gauge-catch ratio (%)

$u(z_g)$ ≡ wind speed at gauge height (m/s)

T_{max} ≡ maximum air temperature (°C)

T_{min} ≡ minimum air temperature (°C)

T_{avg} ≡ average air temperature (°C)

n ≡ number of observations

r ≡ correlation coefficient (see section C.4)

^a95% of observed R values are within 2 standard errors of the value given by the equation.

Source: Goodison et al. (1998).

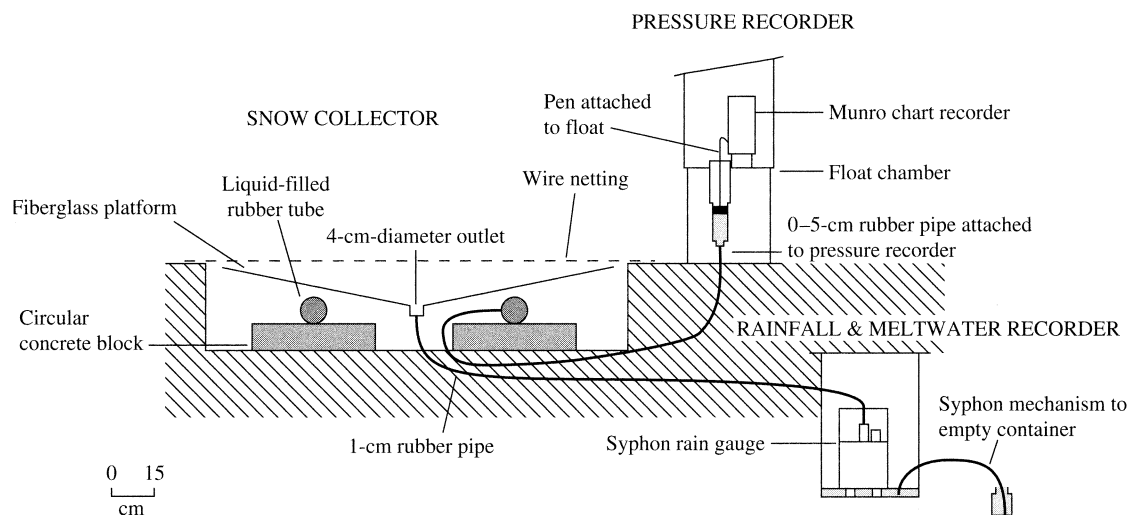


Figure 5.8 Diagram of the universal gauge, which can measure precipitation, snowfall, water equivalent, and water output [Waring and Jones (1980). A snowmelt and water equivalent gauge for British conditions. *Hydrological Sciences Bulletin* 25:129–134, courtesy of International Association of Hydrological Sciences].

tems currently used cannot reliably separate rain from snow. Dual-polarization systems, which are now being integrated into radar networks, will provide improved detection of snow.

5.3.2 Snowfall

5.3.2.1 Rulers

Snowfall is usually measured simply by a ruler placed vertically on a board that was set on the previous snow surface.

5.3.2.2 Ultrasonic Sensors

Ultrasonic snow-depth sensors measure the time for high-frequency (50 kHz) sound waves to travel and return from a source mounted above the snow to the snow surface. Air temperature is monitored, and the time is converted to a distance by multiplying distance by the temperature-adjusted sound velocity. Tests have shown that this technology is a practical and reliable means of obtaining snow-fall and snow-depth information from remote locations (Chow 1992; Ryan et al. 2008; Rice and Bales 2010).

5.3.3 Snowpack and Snow Cover

5.3.3.1 Snow Stakes

The depth of snow cover can be simply observed by inserting a ruler through the snow to the ground surface, or by observing the height of the snow surface against a fixed ruler, called a **snow stake**, with

its zero point at the ground surface. In some remote areas, permanent snow stakes are designed with large markings so that readings can be made from aircraft.

5.3.3.2 Ultrasonic Sensors

The ultrasonic snow-depth sensors described in section 5.3.2.2 provide generally reliable monitoring of snowpack depth.

5.3.3.3 Snow Surveys

As noted, the most important snow information for the hydrologist is the water equivalent of the snow cover. Network measurements of this quantity are most commonly obtained via periodic **snow surveys** at fixed locations called **snow courses**, coupled with automated snow-pillow stations (section 5.3.3.4).

A snow course is a path between two fixed end points over which a series of measurements of snow depth and SWE are made. The length of the path is typically 150 to 250 m, with measurements made at about six points (more if snow conditions are highly variable) spaced at a fixed interval of at least 30 m. At each point, a coring tube equipped with a toothed cutting rim, called a **snow tube** (figure 5.9), is inserted vertically to the surface. After the snow depth is read against markings on the outside of the tube, the tube is pushed a few centimeters into the soil and twisted to secure a small plug of soil that retains the snow in the tube. The tube is then extracted and weighed on a specially calibrated scale that is pre-tared and reads

directly in centimeters or inches of water equivalent. Density at each point can be calculated via equation (5.10), and SWE for the course is the average of the values at the measurement points. A detailed guide for snow-survey techniques was published by the US Soil Conservation Service (1984) and can be accessed at <http://www.wcc.nrcs.usda.gov/factpub/ah169/ah169.htm>.

Several different designs of snow tube are available; they may be made of aluminum or fiberglass and range in diameter from 3.8 to 7.6 cm. Comparisons with snow carefully excavated and weighed have shown a tendency for snow tubes to overestimate SWE by up to 10% (Work et al. 1965; Goodison et al. 1981).

In shallow (i.e., less than about 1 m) snowpacks, depth and density have been found to be essentially independent, and there is typically less temporal and spatial variability in density than in depth (Goodison et al. 1981). Under these conditions, little precision is lost and considerable time may be gained by making more depth measurements than SWE measurements (Jonas et al. 2009).

A snow-course network, like a precipitation-gauge network, should be designed to provide a representative picture of the snowpack in the region of interest. However, since measurements are labor intensive, snow courses are usually considerably more widely spaced than gauges and are usually read at longer time intervals—e.g., every two weeks during the snow season. Because snowpack conditions are largely determined by local conditions, snow-course networks should be designed to sample representative ranges of land use (vegetative cover), slope, aspect, and elevation. Areal averages may then be

estimated by extrapolating from these measurements on the basis of the distribution of the various conditions in the region of interest. For operational purposes such as forecasting runoff, measurement agencies commonly rely on only a few snow-course sites that have been calibrated over a period of years to provide an index, rather than a sample estimate, of the watershed snow cover.

5.3.3.4 Snow Pillows

The water equivalent of snow cover can also be measured with **snow pillows**, which are circular or octagonal membranes made of rubber or flexible metal and contain a liquid with a low freezing point (figure 5.10). The weight of the snow on the pillow controls the pressure of the liquid, which is recorded or monitored via a manometer or pressure transducer.

The diameter of snow pillows ranges from 1 to 4 m, with larger diameters recommended for deeper snowpacks (Barton 1974). Several factors influence the accuracy and continuity of readings, including (1) leaks; (2) temperature variations that affect the density of the liquid; (3) the formation of ice layers within the snowpack, which can support a portion of the snow and lead to undermeasurement of SWE (called “bridging”); (4) disruption of the contact between the snow and the ground, which can distort the snowpack energy and water balances; and, in remote installations, (5) instability of power supply to sensors and recorders. Detailed considerations for installation and maintenance of snow pillows were given by Davis (1973) and Cox et al. (1978), and measurement problems were discussed by McGurk and Azuma (1992) and McGurk et al. (1993). If read frequently enough, snow pillows can be used to measure the water equivalent of individual snowfalls.



Figure 5.9 Measuring snow depth and water equivalent via a snow tube. (a) Teeth for securing a soil plug at the base of the snow tube. (b) Snow tube is pushed through snowpack to ground to measure depth and capture core. (c) Water equivalent is determined by weighing the tube and snow and subtracting the weight of tube (US Natural Resources Conservation Service, n.d.).



Figure 5.10 A snow pillow (foreground) and a water-output lysimeter (background) installed at the US National Weather Service snow-research site at Danville, Vermont. Buried lines transmit the fluid pressure from the pillow to a sensor, and the water released by the snowpack to a measuring device, both of which are in an instrument shelter. The metal ring is electrically heated, and is melted down through the snowpack to isolate the cylinder of snow above the lysimeter (photo by author).

The universal gauge (figure 5.8) measures SWE using the same basic principle as the snow pillow.

Snow pillows are well suited for remote installation. Since 1980, in the United States the NRCS has operated the SNOTEL network in 12 western states and Alaska, which consists of over 600 remotely located snow pillows that provide data on SWE with an accuracy of about 2.5 mm (Schaefer and Werner 1996), along with storage precipitation gauges and air-temperature recorders. Data are recorded every 15 minutes and reported daily via meteor-burst radio communications technology. The current generation of remote sites, master stations, and central computer facilities allows for hourly interrogation. Sites are battery powered with solar-cell recharge, and are designed to operate unattended and without maintenance for a year.

5.3.3.5 Self-Recording Ground-Temperature Sensors

Lundquist and Lott (2008) showed that small, inexpensive self-recording temperature sensors can be used to monitor spatial and temporal patterns of snow accumulation and melt in complex environments. The sensors are buried slightly below the soil

surface, and provide a record of the presence or absence of snow cover, which can be detected because near-surface soil temperatures only experience diurnal temperature oscillations when they are not covered by an insulating layer of snow. When combined with an air temperature record and snowmelt model, the date snow cover disappears can be used to estimate the amount of snow that accumulated at the start of the melt season.

5.3.3.6 Radioactive Gauges

Several types of instruments exploiting the attenuation of gamma rays or neutrons by water substance can be used for nondestructive measurement of SWE. One version involves an artificial gamma-ray source (^{60}Co or ^{137}Cs) and a detector, one of which is at the ground surface with the other suspended above; the readings from the detector are typically transmitted by telemetry from a remote location to the observer. Bland et al. (1997) reported a method by which a portable gamma-ray source is inserted into permanent structures in the field at the time of measurement, and a handheld detector is

used to make a nondestructive determination of SWE with a precision of 3 mm.

For snowpacks with SWE less than about 40 cm, it is also possible to measure the attenuation by snow of natural gamma radiation emitted from the soil surface using a detector that is either fixed a few meters above the surface (Bissell and Peck 1973) or mounted on an aircraft (Loijens and Grasty 1973). Use of an airborne detector requires low-altitude (< 150 m) flights following a route over which the snow-free gamma emission has been previously determined; corrections for soil moisture and radioactive emissions can then be made from the air (Goodison et al. 1981; Foster et al. 1987). However, work by Grasty (1979) suggested that a simpler single-flight technique can give results of high accuracy. Carroll and Voss (1984) found good correlation between SWE determined from airborne gamma-radiation sensors and snow tubes in forested regions of the northern United States and Canada (figure 5.11a), as did Bergstrom and Brandt (1985) in Sweden. The NWS Airborne Snow Survey Program (<http://www.nohrsc.noaa.gov/snowsurvey>) uses low-flying aircraft to estimate SWE via natural gamma radiation (Carroll and Carroll 1989).

5.3.3.7 Airborne Microwave and Radar

Microwave radiation (wavelengths of 0.1 to 50 cm), including radar, can be used to remotely measure SWE, areal extent, and other properties of snow cover. Airborne systems exploiting these wavelengths have the advantage of being able to “see through” clouds; however, some of the many variables that affect the observations and methods for interpreting data are still being worked out.

The flux of microwave radiation emitted by a snowpack depends on its density, temperature, grain size, and the underlying soil conditions. Thus considerable information about ground conditions is required for translating “passive” microwave emissions to estimates of SWE (Foster et al. 1987).

Radar involves directing a beam of microwave radiation at the snowpack and measuring the reflected energy to determine snow cover characteristics. Since this radiation can penetrate into the pack, it can be used to provide information about snowpack stratigraphy and liquid-water content as well as SWE if sufficient information about surface cover and topography is available.

5.3.3.8 Satellite Observation

Satellite imagery using visible, infrared, and microwave wavelengths provides information on the areal

extent of snow cover for large areas (Frei et al. 2012). The most accurate maps of areal snow cover to date have been produced from visible-wavelength images, although careful interpretation is required to distinguish snow from clouds and to identify snow in areas of forest and highly reflective land surfaces. Weekly maps have been produced since 1966 for Northern Hemisphere land with a resolution of about 1.2 km² (Robinson et al. 1993; <http://climate.rutgers.edu/snowcover/>). The National Operational Hydrologic Remote Sensing Center (NOHRSC) provides daily maps of snow cover for the United States and the Northern Hemisphere developed from satellite data on its website (http://www.nohrsc.noaa.gov/nh_snowcover). These maps are based on automated analyses of satellite-borne radiometer data using reflected and emitted energy in several visible and infrared wavelengths to differentiate between clouds and snow and to correctly interpret variations produced by forest cover and shading. NOHRSC also assimilates daily ground-based, airborne, and satellite snow observations into a snow model that computes information on snow cover and SWE, snow depth, snowpack temperatures, snowmelt, sublimation, snow-surface energy exchanges, and precipitation at 1-km² spatial resolution and hourly temporal resolution.

Parajka et al. (2010a) developed a method for snow-cover mapping using daily MODIS/Terra satellite observations, even with cloud covers as high as 90%. Larson et al. (2009) showed that GPS receivers installed for studies of plate tectonics, geodetic surveying, and weather monitoring can be used to measure snow depth, and possibly density (and therefore SWE) as well. As there are hundreds of such receivers in snowy regions of the United States, these stations may provide a useful supplement for remote observation of snow properties. Two more recent studies (Seo et al. 2010; Su et al. 2010) indicate that observations from the GRACE satellite system, which measures total water-storage change (see section 1.8.2.4), can be used in conjunction with other satellite observations to infer SWE.

5.3.3.9 Overview

In spite of their slight tendency to over measure, snow-survey observations are usually considered the most accurate “routine” measurements of SWE. However, they are labor intensive and impractical for routine use in remote areas. Snow pillows are generally accurate and are widely used in the western United States for remote monitoring of mountain

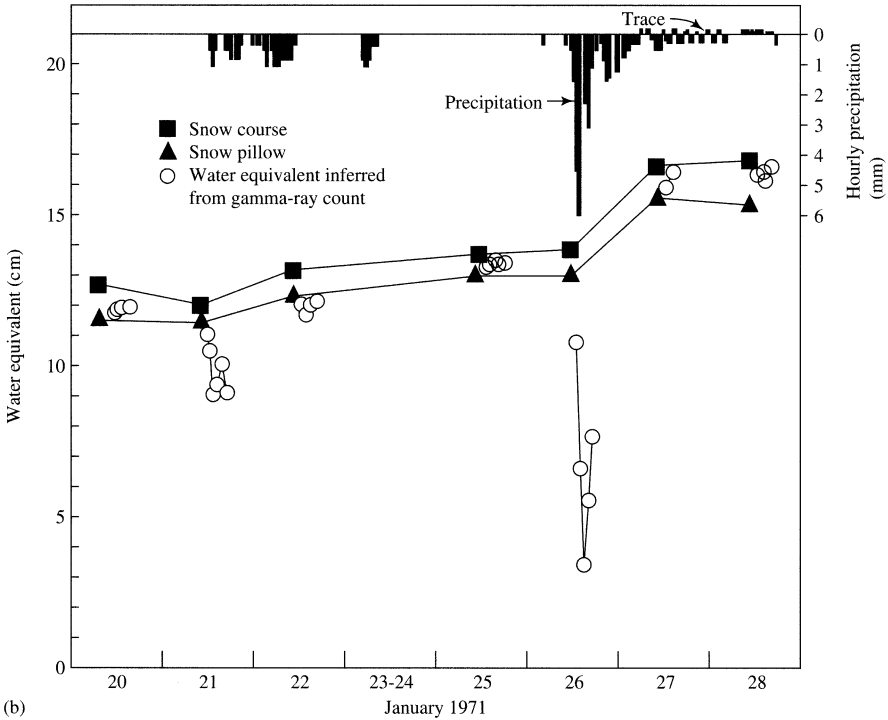
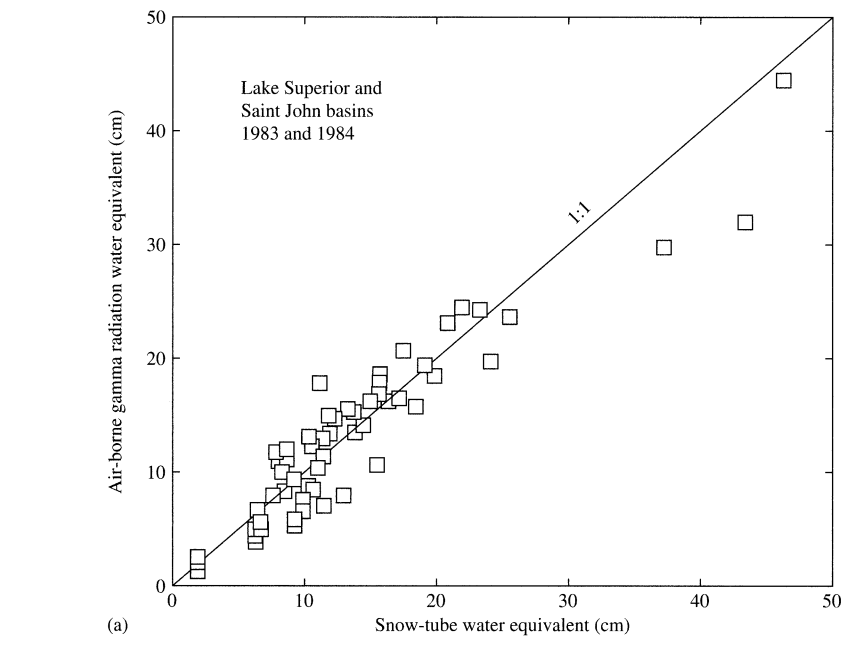


Figure 5.11 (a) Comparison of water equivalent determined by airborne gamma-radiation sensors and snow-tube measurements in the Lake Superior and St. John River basins, United States and Canada [Carroll and Voss (1984)]. (b) Water equivalent of snowpack at Danville, Vermont, measured over 9 days by snow tube, snow pillow, and attenuation of natural gamma radiation. The false low readings of the radiation detector were due to radioactivity deposited during snow storms and could easily be corrected for [Bissell and Peck (1973)]. Monitoring snow water equivalent by using natural soil radioactivity. *Water Resources Research* 9:885–890, with permission of the American Geophysical Union].

snowpacks (SNOWTEL); however, they are subject to bridging, temperature effects, and failures of instrument components (Goodison et al. 1981; McGurk et al. 1993).

Figure 5.11b compares SWE measured via snow tube, snow pillow, and a fixed radio-isotope gauge over several days at one location. Natural radioactivity deposited with falling snow caused false low readings by the gamma detector, but this was found to decay rapidly and could readily be corrected for (Bissell and Peck 1973). Thus all three methods appear to give similar results. Goodison (1981) compared snow-survey and snowfall data in Canada and found that compatible estimates of regional SWE were possible only if: (1) snow-survey data are weighted to account for the variability of SWE as a function of land use and (2) precipitation-gauge measurements of snowfall are corrected for gauge-catch deficiencies due to wind.

Techniques involving spatial interpolation similar to those described for mapping of areal precipitation (section 4.3.2) have been developed and are routinely used for mapping the areal distribution of SWE in the United States (Carroll and Cressie 1996).

Remotely sensed observations via aircraft or satellite using active or passive microwave, infrared, or visible wavelengths are now the main source of information on the areal extent of snow cover. As noted, the NOHRSC program makes these readily available for the United States and the Northern Hemisphere. Such observations, along with water-equivalent information developed from telemetered remote snow pillows and airborne detection of gamma radiation, are widely used for water-resource management decisions, especially in the western United States.

5.3.4 Snowmelt, Ablation, and Water Output

5.3.4.1 Lysimeters

The most straightforward method for measuring water output is via a **lysimeter** (figure 5.10), which collects the water draining from the overlying snow and directs it to a device that records the flow (Haupt 1969). This instrument may be fitted with a circular metal ring that can be electrically heated and lowered through the snow to isolate the cylinder of snow above the collecting surface to avoid gaining or losing water that might be moving horizontally along ice layers in the snowpack. As with snow pillows, snow conditions above a lysimeter may differ from

those in the natural snowpack due to interruption of the snow-ground connection.

5.3.4.2 Snow Pillows

Snow pillows detect ablation as a decrease in weight (assuming the water runs off the pillow); in many cases evaporation can be considered negligible and the weight change can be attributed to water output.

5.3.4.3 Universal Gauge

As noted in section 5.3.1.2, universal gauges collect and measure water output. Water output occurring at the same time as a corresponding weight decrease would indicate snowmelt; water output in the absence of a weight decrease indicates rainfall; and a weight decrease in the absence of water output indicates evaporation.

5.3.4.4 Pans

Specific measurement of snowpack evaporation and sublimation can be made using pans that are periodically weighed. Slaughter (1966) reviewed studies that employed various types of pans, and concluded that good measurements can be obtained using pans made of plastic or metal as long as the edge of the pan is flush with the snow surface and the surface roughness of the snow in the pan is the same as that of the surrounding snowpack. The pan should be at least 10 cm deep to avoid absorption of radiation by the pan bottom and, if significant melt is occurring, should be designed to allow meltwater to drain into a collector for separate measurement.

5.4 Distribution of Snow

Snow accumulation and properties are highly dependent on local topography and site factors such as aspect (slope orientation) and vegetation cover. For example, Rice and Bales (2010) found that snow depths during both accumulation and ablation periods varied by up to 50% due to the variability of topography and vegetation across a small (0.4 ha) study area in the Sierra Nevada of California. In general, local variability will be greatest in regions where periods of melting occur during the winter, where there are pronounced spatial changes in land cover and topography, and where much of the heat input to the snow is from solar radiation. Snow drifting during storms can produce large variations in snow depth and density over short distances, and variations in subsequent snow metamorphism, melt-

ing, and evaporation due to local wind, temperature, radiation, and other microclimatic conditions can further modify the distribution of these properties.

Clark et al. (2011a) reviewed field studies in different snow environments globally. They found that spatial variability of SWE is shaped by several processes that occur across a range of spatial scales. At the watershed scale, spatial variability is shaped by variability in meteorological factors such as elevational gradients in temperature, which can be estimated by spatial interpolation. However, spatial variability of SWE at the hillslope scale is caused by very local processes such as drifting, sloughing of snow from steep slopes, trapping of snow by shrubs, and the unloading of snow by the forest canopy, which are more difficult to resolve explicitly. Based on their analysis, Clark et al. (2011a) provided guidance on approaches to representing these local processes and on the suitability of several common snow-modeling approaches.

Mizukami et al. (2011) developed a simple regional regression-based approach using readily available geographic and meteorological parameters as predictors to map SWE climatology in the mountainous areas of the western United States. The spatial and temporal resolution of the analysis was based on the resolution of available meteorological data, 4 km and 1 month, respectively. The method provided reliable predictions from October to March, but broke down in April because processes at finer space and time scales affected SWE.

Noting that snow-distribution patterns are similar from one year to the next because they are largely controlled by the interaction of topography, vegetation, and consistent synoptic weather patterns, Sturm and Wagner (2010) identified climatological snow distribution patterns for a tundra watershed. Using these empirically based patterns, along with a few depth measurements, they could model the snow-depth distribution as well or better than the output from a weather-driven, physically based snow model. The distribution patterns can be captured via aerial photography or satellite remote sensing.

Thus snow characteristics will be highly variable in space due largely to variations in vegetative cover, slope, and aspect; consequently, obtaining a representative picture of the distribution of snow and snow properties is important, and usually difficult. Remotely sensed information that simply identifies areas with and without snow cover can be extremely valuable in assessing the amount of water present as

snow. Peck (1997) emphasized that particular care is needed in obtaining reliable hydrometeorological measurements in cold regions, and stressed that a smaller number of high-quality records may be more valuable than a larger number of records of questionable quality.

5.4.1 Effects of Elevation and Aspect

Because of the general decrease of air temperature with altitude (figure 2.2), the amount and fraction of precipitation falling as snow are usually strong functions of elevation in a region (figure 5.12). Rates of increase of SWE with elevation vary regionally and with local factors such as aspect, and may vary from year to year at a given location. Meiman (1968) reviewed a number of studies on the elevational distribution of snow in North America, and reported rates of increase of SWE ranging from 5.8 to 220 mm per 100 m elevation. Caine (1975) found that the year-to-year variability of SWE decreased with elevation in the southern Rocky Mountains of the United States.

The main effect of aspect is on energy inputs from solar radiation, resulting in faster densification and melting on south-facing slopes. Aspect may also affect the wind microclimate, which in turn affects snow deposition and densification and energy exchanges of sensible and latent heats. These energy exchanges are discussed quantitatively in section 5.5; Donald et al. (1995) developed relations between land-cover types and SWE and other snow properties in Ontario, Canada, that are useful for snowmelt modeling.

5.4.2 Effects of Vegetation

The accumulation of precipitation on the leaves and branches of vegetation is called **canopy interception**. Some intercepted snow eventually falls to the ground either before or after melting and is added to the snowpack; the rest evaporates and is called **canopy interception loss**.² Deciduous trees intercept less snow than do conifers, and various conifer species differ in their capture of snow. Schmidt and Gluns (1991) found that (1) individual conifer branches intercepted 11 to 80% of SWE in 22 storms, (2) the fraction intercepted was inversely related to snow density and to total storm precipitation, and (3) the maximum intercepted water equivalent was about 7 mm. Thus, although forests intercept a large proportion of snowfall, most studies have found that this is of minor hydrologic import-

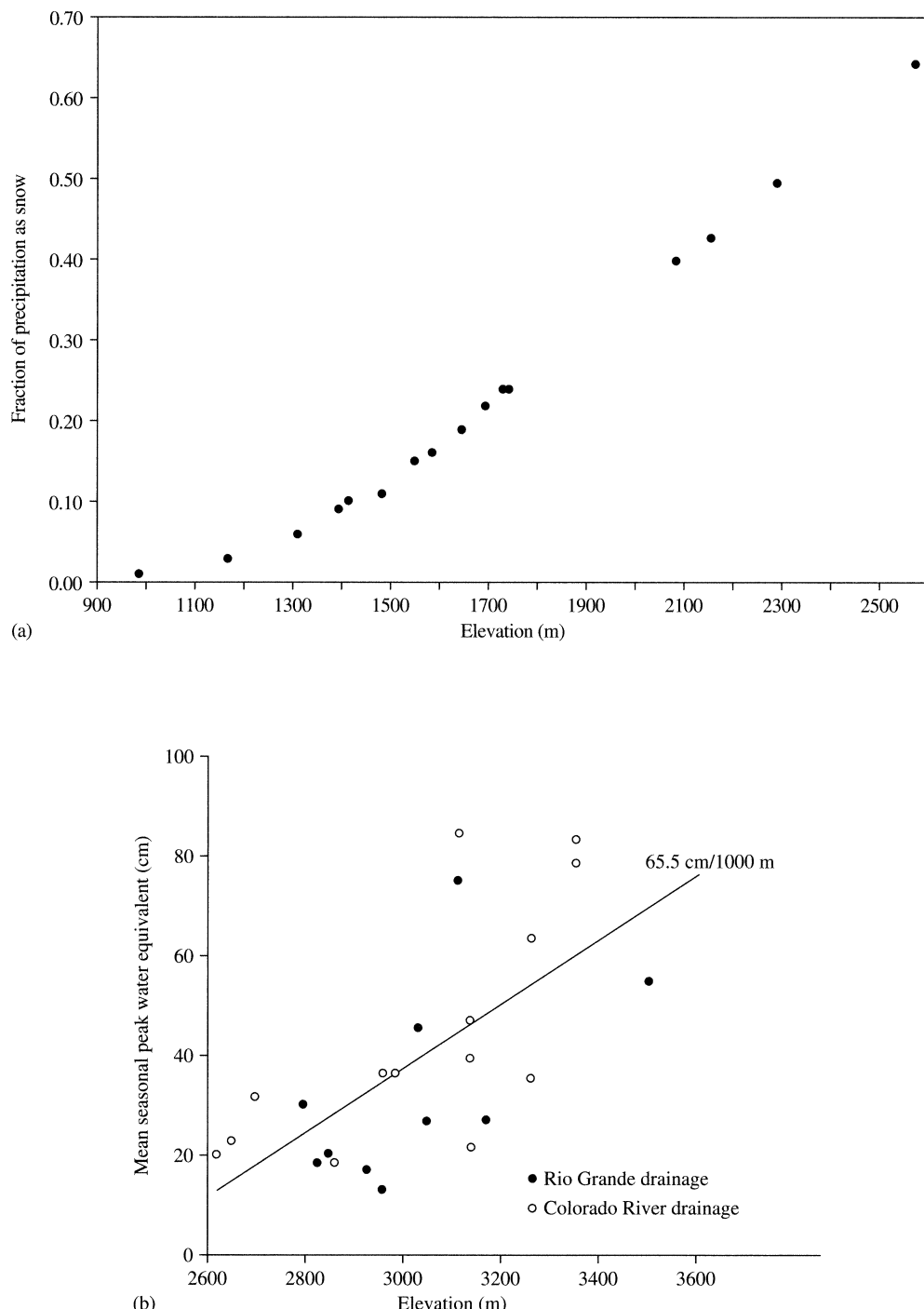


Figure 5.12 (a) Fraction of precipitation occurring as snow as a function of elevation in the San Bernardino Mountains of southern California [data from Minnich (1986)]. (b) Annual peak water equivalent as a function of elevation, San Juan Mountains, Colorado [Caine (1975). An elevational control of peak snowpack variability. *Water Resources Research* 11:613–621, courtesy of American Water Resources Association].

tance because most intercepted snow falls to the ground in solid or liquid form rather than evaporates (Hoover 1971; Tennyson et al. 1974).

In a study in New Mexico, Veach et al. (2009) found that SWE is significantly correlated with canopy density and that maximum snow accumulation occurred in forests with canopy densities between 25 and 40%. Forest edges affected snow depth, with clearings shaded by forest to their immediate south having ~25% deeper snow than either large open areas or densely forested areas.

Forest clearings disrupt the typical upward-increasing wind velocities above a canopy (section 3.5.2) and affect snow deposition. Accumulation tends to be greater in small clearings (i.e., those with diameters less than 20 times the height of surrounding trees) than in the surrounding forest, but the pattern is typically reversed in larger clearings because wind speed tends to be higher, blowing snow into the surrounding forest and causing higher evaporation in the clearing (Golding and Swanson 1986). Watershed-scale experiments have shown that tree harvesting tends to increase SWE and snowmelt runoff (Schmidt and Troendle 1989). This increase is attributed to a reduction in the evaporation of intercepted snow and increased snow deposition into clearings and thinned forests, which is only partially offset by increased evaporation from the ground snowpack.

Figure 5.13 on the following page shows the variability of seasonal peak depth, density, and SWE on a range of vegetation types in Ontario, Canada. Overall these observations are consistent with those just described for forest clearings: the highest depths and water equivalents were in an open forest with shrub understory (vegetation zone B), and the lowest values were in areas without forest cover, including grass (vegetation zone A) and marsh (Adams 1976). Density tended to vary little with land-cover type. Note also that there was considerable year-to-year variability in the relative values.

Varhola et al. (2010) reviewed studies of the overall effects of forest cover on snow accumulation and melt rates at 65 locations, mostly in the United States and Canada. They were able to summarize the results in two simple empirical relations between fractional changes in forest cover, ΔF , and fractional changes in seasonal accumulation, ΔAcc , and melt rates, ΔM :

$$\Delta Acc = -0.40 \cdot \Delta F \quad (5.13)$$

$$\Delta M = -0.53 \cdot \Delta F \quad (5.14)$$

The negative relation in accumulation is attributed to increased sublimation of snow intercepted in the forest canopy; the negative relation in melt rates is largely due to the effects of shading in reducing energy flux from solar radiation. They noted that there was considerable scatter around these relations due to local conditions.

On a very local scale, Woo and Steer (1986) presented data on variations of snow depth around individual trees in a subarctic spruce forest in northern Ontario. The data were used along with information on tree spacing to compute average snow depth for the forest. As shown in figure 5.14, depth increases away from the trunk and reaches the clearing value at a distance of 2 to 4 m from the tree. Presumably, this pattern is produced by snow interception and by added heat inputs due to longwave radiation from the tree trunk, which can accelerate the processes that increase snow density and produce melt.

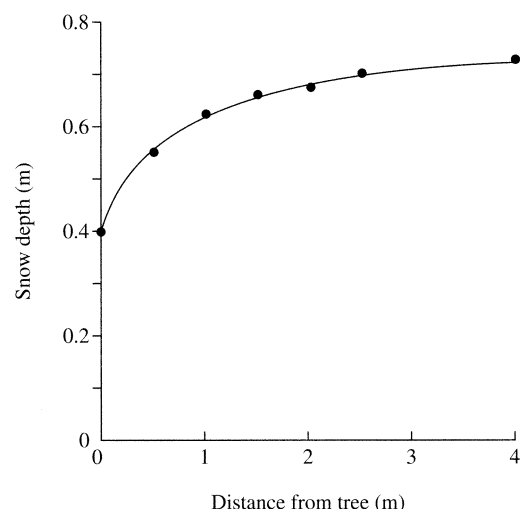


Figure 5.14 Snow depth as a function of distance from a tree in a spruce forest in northern Ontario [data of Woo and Steer (1986)].

5.5 Snowmelt Processes

Much of our understanding of snowmelt processes and the forecasting of snowmelt runoff originated with an intensive, several-year research program conducted by the US Army Corps of Engineers at the Central Sierra Snow Laboratory (Cal-

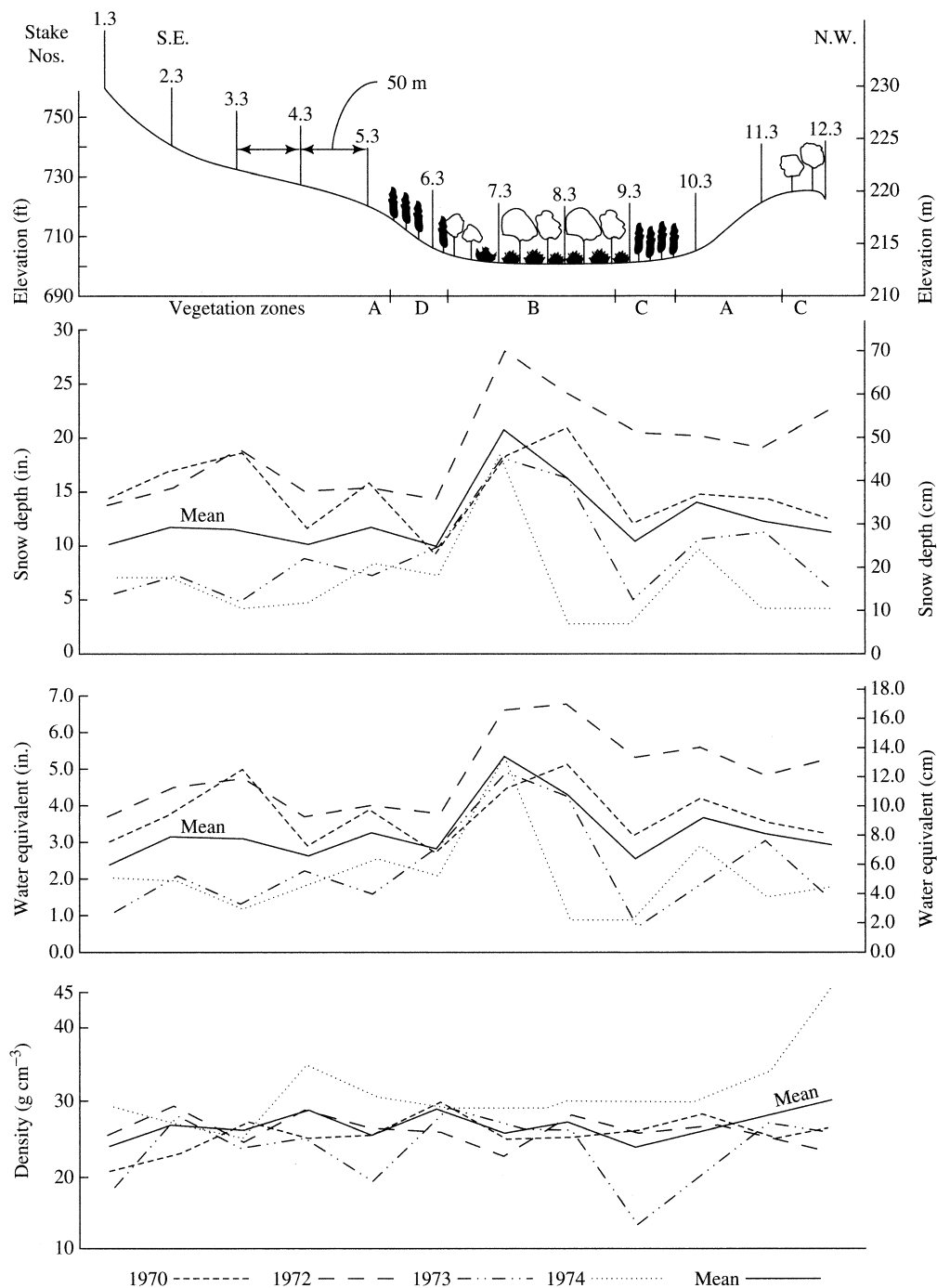


Figure 5.13 Peak seasonal snow properties along a transect near Peterborough, Ontario, for four winters. Vegetation zones: A = grass; B = open deciduous forest with shrub understory; C = moderately dense deciduous and coniferous forest; D = dense cedar forest [Adams (1976)]. Areal differentiation of snow cover in east central Ontario. *Water Resources Research* 12:1226–1234, with permission of the American Geophysical Union].

fornia) in the early 1950s; the results of this research are summarized in the iconic US Army Corps of Engineers (1956) report entitled *Snow Hydrology*. That and subsequent work on snowmelt dynamics sponsored by the NWS (Anderson 1973, 1976), and on the flow of water through snow by the US Army Cold Regions Research and Engineering Laboratory (Colbeck 1971, 1978), form the basis of our current understanding of snowmelt processes.

5.5.1 The Snowpack Energy Balance

The energy balance for the snowpack element of figure 5.5 is

$$Q_{melt} + \frac{\Delta U}{\Delta t} = F_E, \quad (5.15)$$

where Q_{melt} [$\text{E L}^{-2} \text{T}^{-1}$] is the rate at which energy becomes available for snowmelt, F_E is the net flux of energy [$\text{E L}^{-2} \text{T}^{-1}$] from the atmosphere and ground, and $\Delta U/\Delta t$ is the change in internal energy (temperature) in time period Δt . The components of the energy flux are

$$F_E = K + L + \lambda E + H + R + G, \quad (5.16)$$

where K is net shortwave (solar) radiation flux, L is net longwave radiation flux, λE is net flux of latent heat from the atmosphere via turbulent diffusion, H is net flux of sensible heat from the atmosphere via turbulent diffusion, R is flux of sensible heat from rain, and G is the net flux of sensible heat via conduction with the ground.

A seasonal snowpack begins to form when average air temperatures are more or less continually below 0°C . As the snowpack accumulates, net inputs of energy from the atmosphere are generally negative, average snowpack temperature decreases, and water equivalent typically increases. The period of general increase of snowpack water equivalent prior to the melt period is called the **accumulation period**. The **melt period** of a seasonal snowpack begins when the net input of energy becomes more or less continually positive. The melt period can usually be separated into three phases:³

1. **Warming phase**, during which the average snowpack temperature increases more or less steadily until the snowpack is isothermal at 0°C .
2. **Ripening phase**, during which melting occurs but the meltwater is retained in the snowpack. At the end of this phase the snowpack is **ripe**, i.e., it is isothermal and cannot retain any more liquid water.

3. **Output phase**, during which further inputs of energy cause melting that leaves the snowpack as water output.

In most situations, the snowpack does not progress steadily through this sequence: Some melting usually occurs at the surface of a snowpack from time to time prior to the ripening phase, when air temperature rises above 0°C for periods of hours or days. The meltwater thus produced percolates into the cold snow at depth and refreezes, releasing latent heat, which raises the snow temperature. Similarly, snow-surface temperatures may fall below freezing during the melt period, and the surface layer must warm again before melting can continue. Even where daytime temperatures are continuously above freezing, temperatures commonly fall below 0°C at night and it may take several hours for the snowpack to warm and resume melting each day (Bengtsson 1982; Tseng et al. 1994). Nevertheless, the above phases provide a useful context for understanding the melt process. Examples of calculations of the net energy inputs required for completion of each of the melt phases are given in box 5.2.

5.5.1.1 Warming Phase

During the warming phase there is no melt, and net energy inputs warm the snowpack, so from (5.15) and (5.16),

$$\frac{\Delta U}{\Delta t} = F_E = K + L + \lambda E + H + R + G. \quad (5.17)$$

At any point prior to the warming phase, the **internal energy**, or **cold content**, of a snowpack, U_{cc} [E/L^2], is the amount of energy per unit area required to raise its average temperature to the melting point. Considering again the snowpack of figure 5.5, noting that a cold snowpack contains no liquid water, and neglecting the heat capacity of the air within it,

$$U_{cc} = -c_i \cdot \rho_i \cdot (V_i / A) \cdot (T_s - T_{mp}), \quad (5.18a)$$

where c_i is the heat capacity of ice ($2,102 \text{ J/kg} \cdot \text{K}$), T_s is the average temperature of the snowpack ($\leq 0^\circ\text{C}$), T_{mp} is the melting-point temperature (0°C), and the other symbols are as previously defined. Making use of equations (5.1) and (5.7), (5.18a) becomes

$$U_{cc} = -h_s \cdot c_i \cdot \rho_i \cdot (1 - \phi) \cdot (T_s - T_{mp}), \quad (5.18b)$$

which with (5.5) can be written as

$$U_{cc} = -h_s \cdot c_i \cdot \rho_s \cdot (T_s - T_{mp}), \quad (5.18c)$$

or with (5.10) as

$$U_{cc} = -c_i \cdot \rho_w \cdot h_{swe} \cdot (T_s - T_{mp}). \quad (5.18d)$$

Box 5.2 Example Calculations of Energy Involved in Melt Phases

Warming Phase

Consider a snowpack with $h_s = 72.5 \text{ cm}$, $\rho_s = 400 \text{ kg/m}^3$, $h_{\text{swe}} = 29 \text{ cm}$, and $T_s = -9^\circ\text{C}$. Its cold content is given by equation (5.18c):

$$U_{cc} = -(2,102 \cdot \text{J/kg} \cdot \text{K}) \times (1,000 \text{ kg/m}^3) \times (0.29 \text{ m}) \times (-9^\circ\text{C} - 0^\circ\text{C}) = 5.49 \text{ MJ/m}^2.$$

If the net energy flux is $F_E = 10.8 \text{ MJ/m}^2 \cdot \text{day}$, the snowpack temperature increase in one day is given by equation (5.20) as

$$\Delta T_s = \frac{(1 \text{ day}) \cdot (10.8 \times 10^6 \text{ J/m}^2 \cdot \text{day})}{(2,102 \text{ J/kg} \cdot \text{C}) \cdot (1,000 \text{ kg/m}^3) \cdot (0.29 \text{ m})} = 2.95 \text{ }^\circ\text{C}.$$

At this rate it would take

$$\frac{5.49 \text{ MJ/m}^2}{10.8 \text{ MJ/m}^2 \cdot \text{day}} = \frac{9 \text{ }^\circ\text{C}}{17.7 \text{ }^\circ\text{C/day}} = 0.508 \text{ days}$$

to complete the warming phase.

Ripening Phase

When the net energy inputs from the atmosphere and ground equal U_{cc} and the snowpack has become isothermal at the melting point, melting and the ripening phase begin. Assuming snowpack density remains at 400 kg/m^3 , its liquid-water-holding capacity is estimated via equation (5.25) as

$$\theta_{ret} = 3 \times 10^{-10} \cdot (400 \text{ kg/m}^3)^{3.23} = 0.077.$$

Then from equation (5.23),

$$h_{wret} = 0.077 \cdot (0.725 \text{ m}) = 0.055 \text{ m} = 55 \text{ mm}.$$

The energy required to produce melt that fills this capacity and brings the snowpack to a ripe condition is then found from equation (5.26) with $\lambda_f = 0.334 \text{ MJ/kg}$:

$$U_r = (0.055 \text{ m}) \times (1,000 \text{ kg/m}^3) \times (0.334 \text{ MJ/kg}) = 18.4 \text{ MJ/m}^2.$$

Again assuming $F_E = 10.8 \text{ MJ/m}^2 \cdot \text{day}$, we can calculate the amount of melt water produced in 1 day via equation (5.22):

$$\Delta h_w = \frac{(1 \text{ day}) \cdot (10.8 \text{ MJ/m}^2 \cdot \text{day})}{(1,000 \text{ kg/m}^3) \cdot (0.334 \text{ MJ/kg})} = 0.0323 \text{ m} = 32.3 \text{ mm}.$$

At this rate the ripening phase would take

$$\frac{55 \text{ mm}}{32.3 \text{ mm/day}} = 1.70 \text{ days}.$$

Output Phase

The net energy input required to complete the melting of the snowpack is found from equation (5.27):

$$U_o = [(0.29 - 0.055) \text{ m}] \cdot (1,000 \text{ kg/m}^3) \cdot (0.334 \text{ MJ/kg}) = 78 \text{ MJ/m}^2.$$

If the energy flux remained constant at $F_E = 10.8 \text{ MJ/m}^2 \cdot \text{day}$, it would take

$$\frac{78 \text{ MJ/m}^2}{10.8 \text{ MJ/m}^2 \cdot \text{day}} = 7.22 \text{ days}$$

to completely melt the snowpack.

The cold content can be computed at any time prior to the ripening phase, and the net energy input required to complete the warming phase equals the cold content at that time.

During the warming phase an increment of energy input ΔU corresponds to an increase in average temperature of the snowpack, ΔT_s , so from equation (5.18d),

$$\Delta U = c_i \cdot \rho_w \cdot h_{swe} \cdot \Delta T_s. \quad (5.19)$$

Substitution of equation (5.17) into (5.19) relates the temperature change in a time interval Δt to the net energy flux:

$$\Delta T_s = \frac{\Delta t \cdot F_E}{c_i \cdot \rho_w \cdot h_{swe}}. \quad (5.20)$$

5.5.1.2 Ripening Phase

The ripening phase begins when the snowpack becomes isothermal at 0°C. At this point, there is no further temperature change and further net inputs of energy produce meltwater that is initially retained in the pore spaces by surface-tension forces (figure 5.15). During this phase equations (5.15) and (5.16) become

$$Q_{melt} = F_E = K + L + \lambda E + H + R + G. \quad (5.21)$$

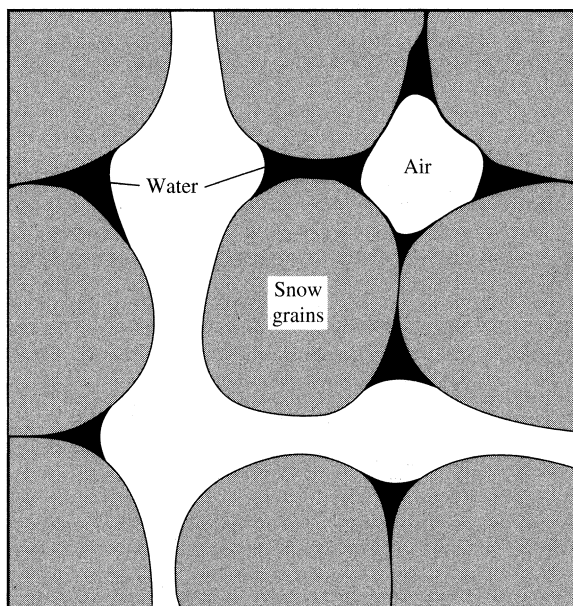


Figure 5.15 An idealized thin section of snow showing snow grains, water retained by surface tension, and continuous pores filled with air [adapted from Colbeck (1971)].

The increase in liquid-water content produced by a given energy flux in a time increment Δt is

$$\Delta h_w = \frac{\Delta t \cdot F_E}{\rho_w \cdot \lambda_f}, \quad (5.22)$$

where λ_f is the latent heat of freezing. The maximum amount of meltwater that can be retained is the **liquid-water-holding capacity**, h_{wret} , which is given by

$$h_{wret} = \theta_{ret} \cdot h_s \quad (5.23)$$

where θ_{ret} is the maximum volumetric water content that the snow can retain against gravity.⁴ Experiments show that θ_{ret} increases with snow density and decreases with grain size, i.e.,

$$\theta_{ret} = f(\rho_s / d) \quad (5.24)$$

(Yamaguchi et al. 2012). However, Goto et al. (2012) found the following empirical relation between θ_{ret} and density for ripe snow, when grain size tends to vary little:

$$\theta_{ret} = 3 \times 10^{-10} \cdot \rho_s^{3.23}, \quad (5.25)$$

where ρ_s is in kg/m³ (figure 5.16).

We can use equation (5.25) with previously derived expressions to compute the proportion of pore spaces that are filled with water when $\theta = \theta_{ret}$. For example, for a ripe snowpack with $\rho_s = 400$ kg/m³, equation (5.25) gives $\theta_{ret} = 0.077$. Substituting these quantities into equation (5.5) allows us to compute the corresponding porosity, $\phi = 0.647$. The ratio θ_{ret}/ϕ is the proportion of pore spaces filled with water at the end of the ripening phase [see equations (5.2) and (5.4)], which for this case is $0.077/0.647 = 0.119$. Thus less than 12% of the pore spaces in a typical ripe snowpack contain water, and such snowpacks are far from being saturated.

The net energy input required to complete the ripening phase, U_r , can be computed as

$$U_r = h_{wret} \cdot \rho_w \cdot \lambda_f = \theta_{ret} \cdot h_s \cdot \rho_w \cdot \lambda_f. \quad (5.26)$$

5.5.1.3 Output Phase

Once the snowpack is ripe, further net energy inputs produce meltwater that cannot be held by surface-tension forces against the pull of gravity, and water begins to percolate downward, ultimately to become water output. This flow is more fully described in section 5.6.

The net energy input required to complete the output phase, U_o , is the amount of energy needed to melt the snow remaining at the end of the ripening phase:

$$U_o = (h_{swe} - h_{wret}) \cdot \rho_w \cdot \lambda_f. \quad (5.27)$$

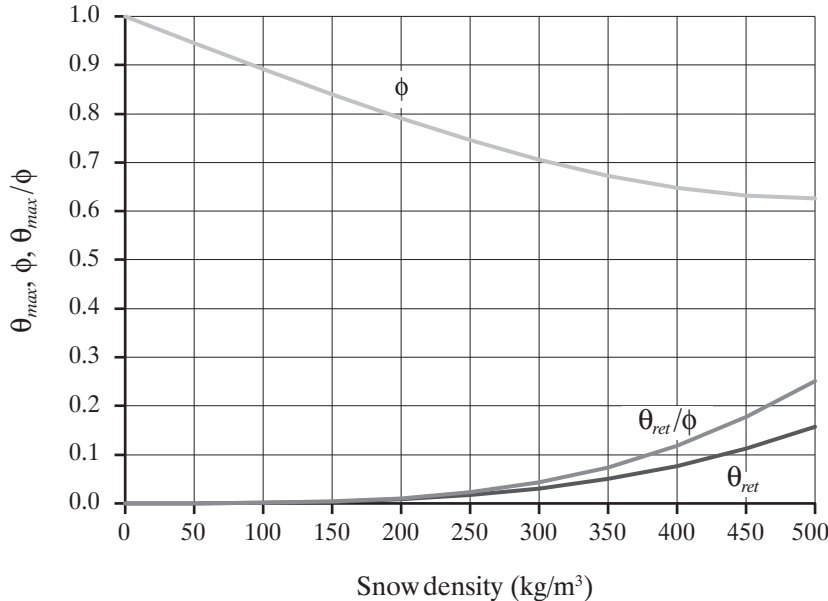


Figure 5.16 Snow porosity, ϕ , maximum water-holding capacity, θ_{ret} , and θ_{ret}/ϕ as a function of snow density, ρ_s . The θ_{ret}/ρ_s relation was measured by Goto et al. (2012) [equation (5.25)]; the other relations were calculated via equation (5.5).

During the output phase, an increase of net energy input, ΔQ_{melt} , is related to a decrease in SWE, $-\Delta h_{swe}$ and an increment of meltwater output, Δw , as

$$\Delta Q_{melt} = -\rho_w \cdot \lambda_f \cdot \Delta h_{swe} \quad (5.28)$$

and

$$\Delta w = -\Delta h_{swe}; \quad (5.29)$$

so that

$$\Delta w = \frac{\Delta Q_{melt}}{\rho_w \cdot \lambda_f}. \quad (5.30)$$

The rate of meltwater production is given by equation (5.22).

5.5.2 Energy-Exchange Processes

The following sections review the basic physics of each of the energy-flux processes of equation (5.16) and introduce approaches to determining their magnitudes. All these energy fluxes vary continuously; the treatment here focuses on *daily* totals or averages, which is a common time-step in hydrologic modeling.

5.5.2.1 Shortwave (Solar) Radiation

The sun's energy is electromagnetic radiation with wavelengths less than 4 μm ; most of this energy is concentrated in the visible range between 0.4 and 0.7 μm (figure 2.4). K is the net flux of solar energy entering the snowpack, so

$$K \equiv K_{in} - K_{out} = K_{in} \cdot (1 - a), \quad (5.31)$$

where K_{in} is the flux of solar energy incident on the snowpack surface (**insolation**), K_{out} is the reflected flux, and a is the shortwave reflectance, or **albedo** [equation (2.7), table 2.4]. Continuous measurements of K values representative of local areas can be obtained with **pyranometers** [described in Iqbal (1983)], facing upward to measure K_{in} and downward to measure K_{out} . However, pyranometers are installed at only a few permanent locations (see figure D.1) and research stations. Hourly, daily, and monthly insolation values representative of large areas ($\sim 0.5^\circ$ latitude \times 0.5° longitude) can be obtained from Geostationary Operational Environmental Satellite (GOES) observations (Justus et al. 1986), but the data are subject to error over areas with significant snow cover (Lindsey and Farnsworth 1997).

Because of the difficulty in obtaining reliable insolation measurements at appropriate space and time scales, other approaches are usually needed to provide values of K or K_{in} . These approaches begin with values of the flux of solar radiation arriving at the outer edge of the earth's atmosphere, the **extraterrestrial solar radiation** which, as described in appendix D, is an astronomically determined function of (1) latitude; (2) declination angle of the sun, which varies sinusoidally through the year (figure 5.17); and (3) the zenith angle of the sun, which varies with time of day. Total daily extraterrestrial radiation is computed by integrating the instantaneous values between the times of sunrise and sunset, which are functions of latitude and declination.

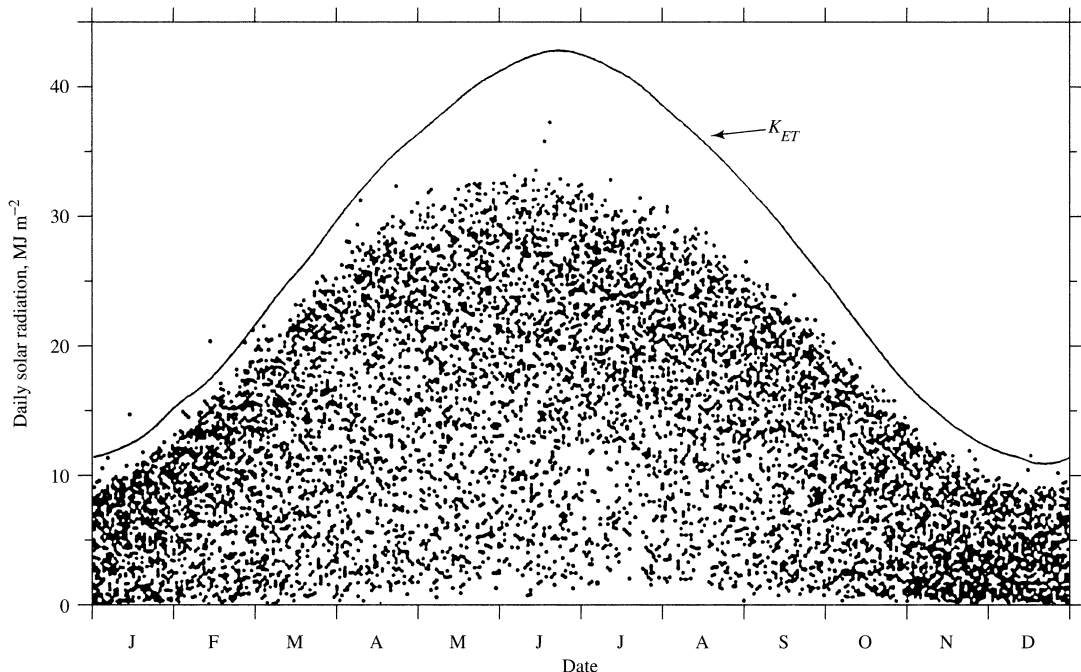


Figure 5.17 Extraterrestrial, K_{ET} , and incident, K_{in} , solar radiation on a horizontal surface, at West Thornton, New Hampshire, for 1960 through 1987. Each dot represents measured K_{in} for a day [Federer et al. (1990)].

5.5.2.1.1 Clear-Sky Shortwave Radiation

Figure 5.18 illustrates the factors affecting the flux of solar radiation incident at the surface. As it passes through the atmosphere, the energy in the solar beam is diminished by absorption and reflectance (scattering) by atmospheric gases and aerosols, reflection by clouds, and shading by vegetation. In the absence of clouds, vegetation, and any topographic shading (which can be important in mountainous areas), the *clear-sky* solar flux on a horizontal surface, K_{CSH} , includes both the energy in the direct solar beam, K_{dir} , diffuse radiation, K_{dif} , and backscattered radiation, K_{BS} :

$$K_{CSH} = K_{dir} + K_{dif} + K_{BS}. \quad (5.32)$$

As developed in appendix D, the terms on the right-hand side of (5.32) can be expressed as fractions of extraterrestrial radiation, so we can write

$$K_{CSH} = \tau_{atm} \cdot K_{ET} \quad (5.33)$$

where τ_{atm} represents the total atmospheric effect on extraterrestrial radiation ($0 < \tau_{atm} < 1$). The effects of clouds and vegetation can be similarly represented as

$$K_{inh} = \tau_C \cdot \tau_F \cdot K_{CSH} = \tau_C \cdot \tau_F \cdot \tau_{atm} \cdot K_{ET} \quad (5.34)$$

where K_{inh} is the insolation on a horizontal surface, $(1 - \tau_C)$ and $(1 - \tau_F)$ are the effects of shading by clouds and forest, respectively, and $0 \leq \tau_C, \tau_F \leq 1$.

5.5.2.1.2 Effect of Cloud Cover

The effect of clouds on insolation can be estimated using several empirical approaches:

- **Estimation based on sky cover:** The fraction of sky covered by clouds, C , was formerly recorded manually by weather observers at about 250 weather stations in the United States. These observations can be used to estimate the effect of cloud cover using empirical relations such as

$$\tau_C = 0.355 + 0.68 \cdot (1 - C) \quad (5.35)$$

(Croley 1989). In snow studies, the US Army Corps of Engineers (1956) used a relation involving cloud height:

$$\tau_C = 1 - (0.82 - 7.9 \times 10^{-5} \cdot Z_C) \cdot C, \quad (5.36)$$

where Z_C is cloud-base height in meters. However, manual observations of C are no longer being made in the United States because human weather observers are being replaced by automated stations (ASOS; box 4.4).

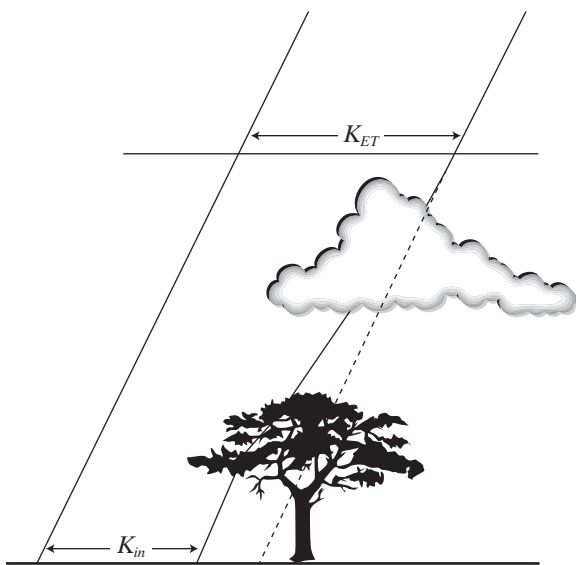


Figure 5.18 Schematic diagram of factors affecting the flux of solar radiation incident at the surface. As it passes through the atmosphere, the energy in the solar beam is diminished by absorption and reflectance (scattering) by atmospheric gases and aerosols, reflection and absorption by clouds, and shading by vegetation.

- **Estimation based on “percent possible sunshine”:** Where available, daily observations of the fraction of daylight hours receiving bright sunshine, \mathcal{S} , have been used to estimate insolation via nomographs (Hamon et al. 1954), or empirical formulas such as

$$\tau_C = k_1 + k_2 \cdot \mathcal{S}, \quad (5.37)$$

where $0.18 \leq k_1 \leq 0.40$ and $0.42 \leq k_2 \leq 0.56$ (Gray and Prowse 1992); Shuttleworth (1992) recommended using $k_1 = 0.25$ and $k_2 = 0.50$. Daily observations of \mathcal{S} have been made at some US weather stations, but the availability of these is decreasing as stations become automated (Lindsey and Farnsworth 1997).

- **Estimation based on maximum and minimum temperature and precipitation:** Daily temperature range tends to be inversely related to cloud cover, and there have been several attempts to use this relation to develop empirical relations between insolation and daily temperature range. Hunt et al. (1998) proposed a relation based on measurements in Canada:

$$K_{inh} = k_0 \cdot (T_M - T_m)^{1/2} \cdot K_{ET} + \\ k_1 \cdot T_M + k_2 \cdot P + k_3 \cdot P^2 + k_4, \quad (5.38)$$

where T_M is daily maximum temperature ($^{\circ}\text{C}$), T_m is daily minimum temperature ($^{\circ}\text{C}$), P is daily precipitation (mm), and k_0-k_4 are empirical constants. Unfortunately, the values of the coefficients in (5.38) were not given; however, the form of the model may be applicable generally. Hunt et al. (1998) found that if the location at which estimates are required is less than 400 km from a station where there are pyranometer measurements, the measured values should be used; otherwise equation (5.38) using local meteorological data gave better estimates.

5.5.2.1.3 Effect of Forest Canopy

The effect of forest canopy on insolation is related to (1) the ratio of the horizontally projected area of forest canopy to the total area of interest, F , which can be determined from air photographs, satellite images, or ground-based hemispherical photography; and (2) the thickness and type of canopy. These relations are complicated by multiple reflections and differing effects of the canopy on direct and diffuse radiation (Hardy et al. 2004; Mahat and Tarboton 2012). A commonly used quantity that reflects both canopy extent and thickness is the **leaf-area index (LAI)**, which is the ratio of total leaf area to ground-surface area; typical values of LAI for common forest types are tabulated in table 6.4.

Figure 5.19 shows values of τ_F for four types of conifer forest and leafless deciduous forest as a function of forest cover only; the relationship for lodgepole pine can be approximated as

$$\tau_F = \exp(-3.91 \cdot F). \quad (5.39)$$

Mahat and Tarboton (2012) measured seasonal average values of $\tau_F = 0.36$ for conifer forest and $\tau_F = 0.79$ for deciduous forest. Wang et al. (2010) suggested a general model for τ_F as a function of leaf-area index:

$$\tau_F = (1 - a_F) \cdot (1 - a_s) \cdot \exp(-LAI), \quad (5.40)$$

where a_F is the albedo of the vegetation (assumed = 0.13) and a_s is the albedo of snow under the canopy (assumed = 0.5). Because the effect of vegetative cover in reducing incident shortwave radiation depends on the type, height, and spacing of the plants, these relations must be applied with caution for other situations.

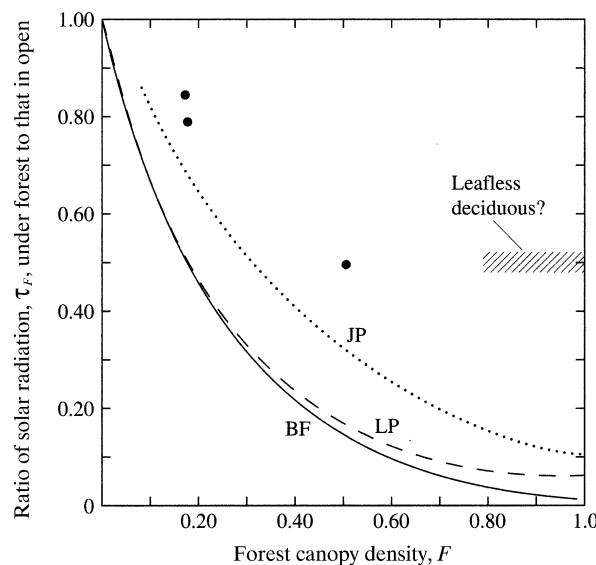


Figure 5.19 Ratio of incident solar radiation, τ_F , under various types of forest canopies to that received in the open for four forest types. BF = balsam fir, JP = jack pine, LP = lodgepole pine, circles = open boreal spruce forest [Dunne and Leopold (1978)].

5.5.2.1.4 Effect of Slope and Aspect

As shown in appendix D, incident solar-radiation flux on a slope is a function of the slope azimuth angle (**aspect**, α) and angle of inclination (slope, β) relative to the solar beam. This effect can be calculated by noting that a sloping surface at a given location is parallel to a horizontal surface at another location, and receives the same flux of direct clear-sky solar radiation

as that horizontal surface. The **equivalent latitude** (figure 5.20) and **equivalent longitude** of this slope can be calculated as functions of latitude, day-of-year (the number of days since the calendar year began, sometimes called the “Julian date”), slope azimuth angle, and slope inclination angle [equations (D.24) and (D.25)]. Figure 5.21 shows the very large differences in insolation on north- and south-facing slopes at a midlatitude location during the snowmelt season.

5.5.2.1.5 Albedo

The physics of reflection are complicated (see, for example, Melloh et al. 2002; Yasunari et al. 2011); snow-surface albedo depends on wavelength, snow depth, grain size and shape, liquid-water content, sun angle, and impurities (Gardner and Sharp 2010). Its value ranges from about 0.2 to 0.9, and is thus an important determinant of the net input of energy to the snowpack. Albedo generally decreases with the age of the snow surface (time since last snowfall) as density, grain size, and liquid-water content increase and impurities accumulate (figure 5.22b).

Because of the porous nature of snow, solar radiation is reflected not at the surface plane, but over a finite depth. There is little penetration of solar radiation below about 10 cm, so figure 5.22a applies only when $h_s > 10$ cm. For shallower snowpacks, significant amounts of radiation are absorbed by the ground and may heat the snow from below. Leonard and Eschner (1968) found that albedo measured for snow intercepted on a conifer forest was considerably lower ($a \approx 0.2$) than for a ground snowpack, resulting in more rapid melting and greater evaporation for intercepted snow.

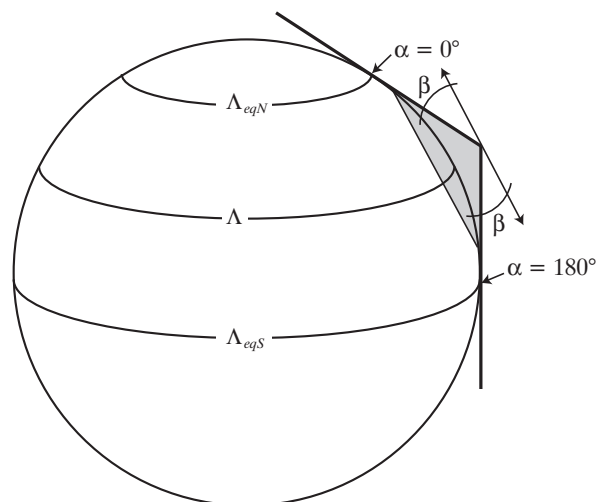


Figure 5.20 Diagram illustrating the equivalent-latitude concept. The shaded triangle represents north- ($\alpha = 0^\circ$) and south- ($\alpha = 180^\circ$) facing hillslopes at latitude Λ . The north-facing hillslope is parallel to a horizontal surface at Λ_{eqN} , the south-facing hillslope is parallel to a horizontal surface at Λ_{eqS} . Λ_{eqN} and Λ_{eqS} are the respective equivalent latitudes that are a function of Λ , the slope direction, α , and the slope inclination, β (section D.3).

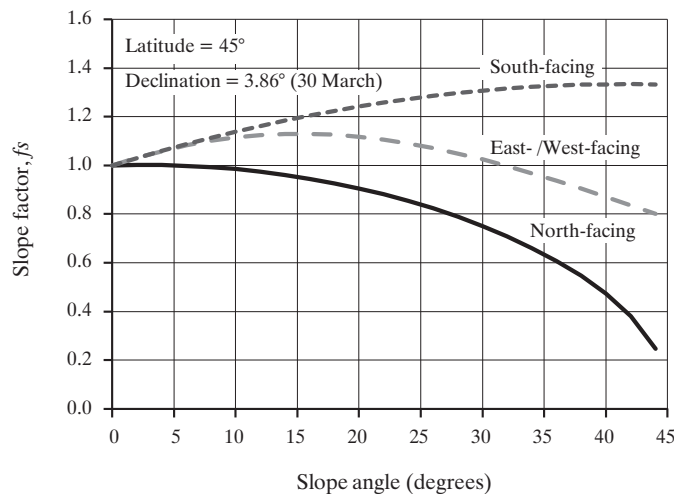


Figure 5.21 Slope factor (= ratio of incident solar radiation on slope to that on a horizontal surface) for north-, east- or west-, and south-facing slopes at latitude 45°N on 30 March.

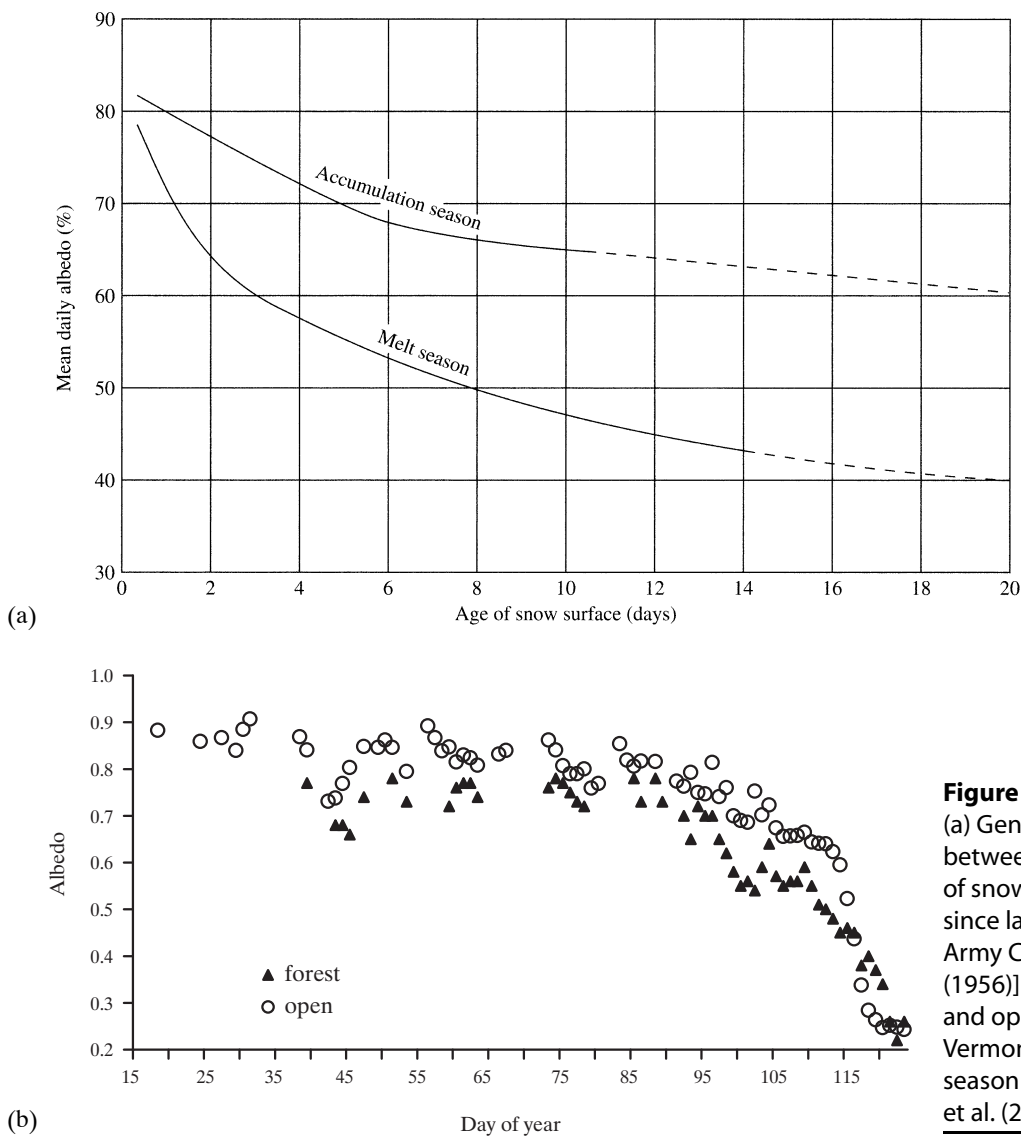


Figure 5.22
 (a) General relation between albedo and age of snow surface (i.e., time since last snowfall) [US Army Corps of Engineers (1956)]. (b) Albedo at forest and open sites at Danville, Vermont, during the snow season of 2001 [Melloh et al. (2002)].

5.5.2.2 Longwave Radiation Exchange

Longwave (also called terrestrial, thermal, or infrared) radiation is electromagnetic radiation with wavelengths of 4 to 60 μm emitted by materials at near-earth-surface temperatures (section 2.1.3.2; figures 2.3 and 2.4). The net input of longwave energy, L , is the difference between the incident flux, L_{in} emitted by the atmosphere, clouds, and overlying forest canopy and the outgoing radiation from the snowpack, L_{out} :

$$L \equiv L_{in} - L_{out}. \quad (5.41)$$

Longwave radiation can be measured directly by means of **pyrgeometers** or as the difference between all-wave radiation measured by a **radiometer** and shortwave radiation measured by a pyranometer. However, such instruments are seldom installed except at sites of intensive research, and routine measurements of longwave radiation are available at only a few locations. Thus, as with shortwave radiation, the longwave component of the energy balance is usually estimated from more readily available meteorological information; this estimation is based on the following considerations.

The flux of electromagnetic radiation emitted by a surface is given by the Stefan–Boltzmann equation [equation (2.1)]. Hence we can write

$$L_{in} = \varepsilon_{at} \cdot \sigma \cdot F_{at}^4, \quad (5.42)$$

where ε_{at} is the integrated effective emissivity of the atmosphere and forest canopy, σ is the Stefan–Boltzmann constant ($\sigma = 4.90 \times 10^{-9} \cdot \text{MJ/m}^2 \cdot \text{K}^4 \cdot \text{d}$), and F_{at} is the effective radiating temperature of the atmosphere and canopy (K). The outgoing flux is the sum of the radiation emitted by the snow surface and the portion of the incident radiation reflected by the surface. Since the longwave reflectivity of a surface equals one minus its longwave emissivity, we have

$$L_{out} = \varepsilon_{ss} \cdot \sigma \cdot T_{ss}^4 + (1 - \varepsilon_{ss}) \cdot L_{in}, \quad (5.43)$$

where the subscript *ss* designates the values of emissivity and temperature for the snow surface.

Combining equations (5.41)–(5.43), expanding and simplifying gives

$$L = \varepsilon_{ss} \cdot \varepsilon_{at} \cdot \sigma \cdot F_{at}^4 - \varepsilon_{ss} \cdot \sigma \cdot T_{ss}^4; \quad (5.44a)$$

however, since the emissivity of snow is very close to 1 (table 2.1), equation (5.44a) can be simplified to

$$L = \varepsilon_{at} \cdot \sigma \cdot F_{at}^4 - \sigma \cdot T_{ss}^4. \quad (5.44b)$$

The major problem in applying equation (5.44) is to find expressions for ε_{at} and F_{at} or, equivalently, to estimate the value of L_{in} under various conditions of cloudiness and forest cover. This problem is addressed in the following sections.

5.5.2.2.1 Clear-Sky Longwave Radiation

Expressions for estimating L_{in} are usually developed by noting that the most important absorbers and emitters of longwave radiation in the atmosphere are carbon dioxide and water vapor (figure 2.4). Since the concentration of carbon dioxide is effectively constant over time periods relevant to snowmelt modeling, variations in the downward flux of longwave radiation under clear skies and no forest canopy are largely due to fluctuations in humidity. Flerchinger et al. (2009) tested the performance of several empirical relations expressing this relation at 21 sites in North America and China, and found the following relation was among those that performed best:

$$L_{in} = \varepsilon_{clr} \cdot \sigma \cdot F_a^4, \quad (5.45)$$

where F_a is near-surface air temperature (K) and the clear-sky emissivity ε_{clr} is estimated as

$$\varepsilon_{clr} = 0.83 - 0.18 \cdot \exp(-1.54 \cdot e_a), \quad e_a > 0.285 \text{ kPa}, \quad (5.46)$$

where e_a is the near-surface vapor pressure in kPa. [Vapor pressure can be calculated from air temperature and relative humidity via equations (3.9) and (3.12).] Flerchinger et al. (2009) found that adjustment for elevation did not significantly improve estimates of ε_{clr} .

In another recent comparison of methodologies, Abramowitz et al. (2012) found that the best estimates of L_{in} were given by a simple empirical relation:

$$L_{in} = 2.7 \cdot e_a + 0.245 \cdot F_a - 45.14, \quad (5.47)$$

where L_{in} is in $\text{MJ/m}^2 \cdot \text{d}$ and e_a is in kPa.

5.5.2.2.2 Effect of Cloud Cover

Clouds are black-body radiators emitting longwave radiation at a rate determined by the cloud-base temperature, and their presence greatly increases the effective emissivity of the atmosphere. Thus under cloudy conditions, the emissivity ε_{sky} will be determined by the degree of cloud cover. Flerchinger et al.'s (2009) review found the following two empirical relations were best at accounting for the effect of clouds:

$$\varepsilon_{sky} = (1 - 0.84 \cdot C) \cdot \varepsilon_{clr} + 0.84 \cdot C \quad (5.48)$$

and

$$\varepsilon_{sky} = (1 - \mathcal{S}) + \mathcal{S} \cdot \varepsilon_{clr} \quad (5.49)$$

where C is fractional cloud cover and \mathcal{S} is the ratio of actual insolation to clear-sky insolation. Surprisingly, however, Abramowitz et al. (2012) found that equation (5.47) performed best for both clear and cloudy conditions, and suggested its use without correcting for clouds.

5.5.2.2.3 Effect of Forest Canopy

Like clouds, trees are very nearly blackbodies with respect to longwave radiation (table 2.1), and they can be considered to be emitting radiant energy at a rate determined by their temperature. Since their temperature is close to the near-surface air temperature, their effect on the total integrated atmospheric emissivity can be modeled as

$$\varepsilon_{at} = (1 - F) \cdot \varepsilon_{sky} + F, \quad (5.50)$$

where F is fractional forest cover as defined for short-wave radiation.

5.5.2.2.4 Longwave Radiation Emitted by Snow Surface

The second term on the right side of equation (5.44) is the radiation flux emitted by the snow surface. Brubaker et al. (1996) showed that average daily snow-surface temperature is well approximated by

$$T_{ss} = \min[(T_a - 2.5), 273.16]. \quad (5.51)$$

During the ripening and output phases of melting, the snow surface is at the freezing point, $T_{ss} = 273.16$ K.

5.5.2.2.5 Summary

When forest cover is absent, values of $\varepsilon_{at} = \varepsilon_{sky}$ as given by equation (5.46) are < 1 ; however, $\varepsilon_{at} = 1$ for complete forest cover [equation (5.50) with $F = 1$]. Thus from equation (5.44b), L will be positive with $F = 1$ when $T_a > T_{ss}$. In most situations, however, $\varepsilon_{at} < 1$ and L is negative.

5.5.2.3 Turbulent Exchange of Sensible Heat

The physics of turbulent exchange of sensible heat were developed in section 3.5.3.6. Combining equations (3.54) and (3.55) gives the flux of sensible heat from the atmosphere into a snowpack, H [E L⁻² T⁻¹], as

$$H = \frac{0.622 \cdot \kappa^2 \cdot \rho_a \cdot c_p \cdot u(z_m) \cdot [T(z_m) - T_{ss}]}{\left[\ln\left(\frac{z_m - z_d}{z_0}\right) \right]^2}, \quad (5.52)$$

where $\kappa = 0.4$, ρ_a is the density of air (≈ 1.292 kg/m³), c_p is the heat capacity of air ($\approx 1.005 \times 10^{-3}$ MJ/kg · K),

z_m is the measurement height above the snow surface, z_d is the zero-plane displacement height, z_0 is the surface-roughness height, $u(z_m)$ is the wind speed, $T(z_m)$ is the air temperature, and T_{ss} is the surface temperature.

To modify this equation for snow, we can assume that z_d is negligibly small. The roughness height, z_0 , depends on the irregularity of the snow surface, and so can be highly variable from place to place and with time at a given location. For example, Anderson (1976) measured values between 0.0001 and 0.038 m for his research site in Vermont. However, his data show a strong decrease in z_0 as the season progressed, and values during the melt season did not exceed 0.005 m. In the absence of other information, a value between 0.0005 and 0.005 m may be selected; however, it should be noted that for special situations, such as vegetation projecting above the snow surface or patchy snow, z_0 could be considerably higher.

Assuming that z_m is a standard measurement height (2 m), we designate $T(z_m) = T_a$ and $u(z_m) = u_a$, so that with $c_p = 0.001005$ MJ/kg · K, $\rho_a = 1.29$ kg/m³, and $z_0 = 0.002$ m, equation (5.52) becomes

$$H = 4.303 \times 10^{-6} \cdot u_a \cdot (T_a - T_{ss}) \text{ MJ/m}^2 \cdot \text{s} \quad (5.53a)$$

$$H = 0.372 \cdot u_a \cdot (T_a - T_{ss}) \text{ MJ/m}^2 \cdot \text{d} \quad (5.53b)$$

where u_a is in m/s and temperatures are in °C. Equation (5.53) is analogous to equation (3.55).

There are two additional considerations in the application of equations (5.52) and (5.53). First, as explained in section 3.5.3.7, those equations apply strictly to conditions of neutral atmospheric stability, i.e., when the actual temperature gradient in the air near the surface equals the adiabatic lapse rate. When warm air overlies a snowpack, the actual lapse rate is typically less steep than adiabatic and temperatures may even *increase* with elevation (a “temperature inversion”), so stable conditions exist that tend to suppress turbulent exchange (see figure 3.13). To account for this, the value of H can be adjusted, as explained in box 3.2.

The second consideration in applying equations (5.52) and (5.53) is that wind speeds are virtually always measured in fields or clearings, and such measurements must be adjusted for calculating turbulent exchange in forested areas. Few data are available on which to base an adjustment factor; Dunne and Leopold (1978) suggested the following simple relation:

$$\frac{u_{aF}}{u_{ao}} = 1 - 0.8 \cdot F, \quad (5.54)$$

where F is the fractional forest cover and the subscripts F and O indicate wind speed in and outside of the forest, respectively. Wang et al. (2010) proposed a relation that depends on temperature, forest-cover fraction, and leaf-area index (LAI):

$$\frac{u_{aF}}{u_{aO}} = \left\{ F \cdot \text{Min}\left(\frac{T_a - T_{ss}}{5}, 1\right) \cdot [1 - \exp(-LAI)] \right\}^{-1}, \quad (5.55)$$

where $\text{Min}(.,.)$ denotes the lesser of the quantities in parentheses.

5.5.2.4 Turbulent Exchange of Latent Heat

Latent-heat exchange with the atmosphere is governed by the same turbulent process that produces sensible-heat exchange; this process is described in section 3.5.3.5 and leads to equation (3.49) for neutral stability:

$$\lambda E = \frac{0.622 \cdot \rho_a \cdot \lambda \cdot \kappa^2 \cdot u(z_m) \cdot [e(z_m) - e_{ss}]}{p \cdot \rho_w \cdot \left[\ln\left(\frac{z_m - z_d}{z_0}\right) \right]^2}, \quad (5.56)$$

where λ is the latent heat of sublimation, ρ_w is density of water, p is atmospheric pressure, $e(z_m)$ is vapor pressure at the measurement height, e_{ss} is the vapor pressure at the snow surface, and the other symbols are as for equation (5.52).

If the vapor-pressure gradient is directed upward [$e(z_m) < e_{ss}$], evaporation/sublimation occurs and latent heat will be lost; if directed downward [$e(z_m) > e_{ss}$] condensation occurs along with an input of latent heat. In applying this equation to snow two phase changes may be involved: For cold snowpacks [$T(0) < 0^\circ\text{C}$], evaporation and condensation involve the solid-vapor or vapor-solid phase change (sublimation) and the latent heat involved is the sum of the latent heats of vaporization, λ_v , and fusion, λ_f , so $\lambda = \lambda_v + \lambda_f$. For melting snowpacks [$T(0) = 0^\circ\text{C}$], no solid-liquid or liquid-solid phase change occurs and only λ_v is involved.

Again, assuming a standard measurement height, near-surface values of ρ_a , ρ_w , κ , p , $z_d = 0$, and $z_0 = 0.002$ m, $\lambda_v = 2.47$ MJ/kg, $\lambda_f = 0.334$ MJ/kg, equation (5.56) becomes

Cold Snow ($T_{ss} < 0^\circ\text{C}$):

$$\lambda E = 6.86 \times 10^{-5} \cdot u_a \cdot (e_a - e_{ss}) \text{ MJ/m}^2 \cdot \text{s} \quad (5.57\text{a})$$

$$\lambda E = 5.93 \cdot u_a \cdot (e_a - e_{ss}) \text{ MJ/m}^2 \cdot \text{d} \quad (5.57\text{b})$$

Melting Snow ($T_{ss} = 0^\circ\text{C}$):

$$\lambda E = 6.05 \times 10^{-5} \cdot u_a \cdot (e_a - e_{ss}) \text{ MJ/m}^2 \cdot \text{s} \quad (5.57\text{c})$$

$$\lambda E = 5.22 \cdot u_a \cdot (e_a - e_{ss}) \text{ MJ/m}^2 \cdot \text{d} \quad (5.57\text{d})$$

where u_a is the wind speed (m/s) and e_a is the vapor pressure (kPa) at the measurement height. Equation (5.57) is analogous to equation (3.50).

As with the sensible heat, (1) these relations are valid for neutral conditions and may need to be adjusted to account for stability effects (section 3.5.3.7; box 3.2) and (2) equation (5.54) or (5.55) may be appropriate for estimating wind speeds in forests. Note also that values of the numerical coefficients in equations (5.53) and (5.57) change with measurement height and roughness height.

In forests, snow evaporation occurs from the snow intercepted on the canopy, and evaporation from the ground becomes important only after the intercepted snow has disappeared via ablation or falling or blowing off (Lundberg and Halldin 1994). There is evidence that evaporation of intercepted snow may occur at rates of up to 3.3 mm/d and be an important component of the snow ablation in forests, perhaps amounting to 200 mm or more per winter (Lundberg et al. 1998).

5.5.2.5 Heat Input by Rain

When rain falls on a snowpack that is at the freezing point ($T_s = T_{mp}$), the rainwater is cooled to the snow temperature and the heat given up by the water is used in melting. Thus for this situation, we can calculate the heat contributed by rain, R , as

$$R = \rho_w \cdot c_p \cdot r \cdot (T_r - T_{mp}) \quad (5.58\text{a})$$

where c_p is heat capacity of water (4.187×10^{-3} MJ/kg · K), r is rainfall rate [L T^{-1}] and T_r is the temperature of the rain.

When rain falls on snow that is below freezing, it will first cool to the freezing point, giving up sensible heat according to equation (5.58a), and then freeze, liberating latent heat. In this case we have

$$R = \rho_w \cdot c_p \cdot r \cdot (T_r - T_{mp}) + \rho_w \cdot \lambda_f \cdot r. \quad (5.58\text{b})$$

If humidity information as well as air temperature is available, T_r can be estimated as the wet-bulb temperature T_{wb} [equation (5.12)]. However, since relative humidity is usually close to 1 when rain occurs, $T_{dp} \approx T_a$ and $T_{wb} \approx T_a$, so the usual practice is to assume $T_r = T_a$.

5.5.2.6 Conductive Exchange of Sensible Heat with the Ground

Temperatures in the soil under snowpacks usually increase downward due to thermal energy stored during the summer and geothermal heat and the insulating effect of snow. In these circumstances, heat is conducted upward to the base of the snowpack at a rate G given by

$$G = k_G \cdot \frac{dT_G}{dz}, \quad (5.59)$$

where k_G is the thermal conductivity of the soil [$\text{E L}^{-1} \Theta^{-1} \text{T}^{-1}$], T_G is soil temperature, and z is distance below the ground surface.

Thermal conductivities of soils depend on soil texture, soil density, and moisture content and vary widely spatially and temporally. For example, the US Army Corps of Engineers (1956) reported a more than tenfold increase in k_G during the melt season in the soil they studied, from 8.37×10^{-3} to $0.100 \text{ MJ/m} \cdot \text{d}$. This variability, along with the general lack of information about thermal conductivity and ground-temperature gradients, often precludes accurate computation of G . This usually has little practical effect on energy-balance estimates during the snowmelt season, however, because G is usually negligible compared to other terms.

In spite of its generally negligible contribution during the melt season, the energy conducted to the snowpack from the ground during the accumulation season can be hydrologically significant: Studies from various localities (Federer and Lash 1978a; Male and Gray 1981) indicate that this heat produces continual melting at the base of the snowpack, called **groundmelt**, at rates up to 2 mm/d (a heat input of $0.668 \text{ MJ/m}^2 \cdot \text{d}$). Groundmelt can add significantly to moisture in the soil, increasing the percentage of snowmelt that will runoff during the snowmelt season, and, in regions like New England, groundmelt may be the principal source of flow in upland streams during the winter.

5.5.3 Relative Importance of Energy-Balance Terms

5.5.3.1 Effects of Forest Cover and Weather

We can use the relations developed in section 5.5.2 to explore the relative importance of the energy-balance components under various conditions of forest cover and weather. As an example, we specify a ripe snowpack on a horizontal location at latitude

45°N on 21 March. Using the relations in appendix D, which are incorporated in the SolarRad.xls program found on the disk accompanying this text, the daily clear-sky solar-radiation input is calculated to be $K_{CSH} = 16.721 \text{ MJ/m}^2 \cdot \text{d}$.

To emphasize contrasts, we will use energy-balance computations at two sites for two forest-cover conditions as an example. At site 1, $F = 0$; at site 2, $F = 1$. Both sites will be compared under two sets of weather conditions. Condition A is a clear day with low humidity and no rain ($C = 0$, $RH = 0.7$, $r = 0 \text{ mm/d}$) and condition B is a cloudy day with high humidity and heavy rain ($C = 1$, $RH = 1$, $r = 25 \text{ mm/d}$). For all conditions we assume air temperature $T_a = 4^\circ\text{C}$, wind speed in the open is $u_{ao} = 3 \text{ m/s}$, albedo $a = 0.5$ (typical for an 8-day-old snow surface; figure 5.22), and a constant ground-heat input of $G = 0.25 \text{ MJ/m}^2 \cdot \text{d}$.

The calculations have been carried out using the SnowMelt.xls program on the accompanying disk using the relations developed in section 5.5.2. Stability adjustments were made as described in box 3.2. The results are shown in table 5.4. Note that by far the highest energy input and melt occur at the open site under cloudy, rainy, and humid conditions when the dominant energy input is latent heat from condensation ("condensation melt"). The second highest input occurs under similar conditions at the forested site, when latent-heat input also dominates. Note that the rain, even though a relatively large amount, contributes only minor heat input at both sites. Solar radiation is the largest input only at the open site under clear skies, but this is balanced by heat loss due to longwave radiation and latent heat.

Note that the relative importance of the solar-radiation term would be much greater on south-facing slopes, and much less on north-facing slopes, than shown in table 5.4, but the other terms would not be affected by slope and aspect. This largely explains why the largest snowmelt floods are usually due to condensation melt, which occurs quasi-uniformly on all slopes and is less affected by forest cover than are solar and longwave radiation.

5.5.3.2 Case Study of Snowmelt at Danville, Vermont

During a typical winter (1972–1973), the NWS, in conjunction with the USDA's Agricultural Research Service, measured the accumulation and melt of a snowpack at the Sleepers River Research Watershed in Danville, Vermont (figure 5.23 on p. 236). Although average snowpack temperature was not measured, the

beginnings and ends of the accumulation period and the phases of the melt period can be approximated from the traces of depth, average snowpack density, water equivalent, and average air temperature.

Air temperature was above 0°C only occasionally between mid-November and late February, and the water equivalent of the pack increased more or less continually during this period due to snowfalls and minor rain. The maximum snow depth of 72 cm was reached in late February. Density was initially about 100 to 150 kg/m³, jumped to about 250 kg/m³ in early December, and increased gradually thereafter to about 300 kg/m³ when the melt season began. Density increases were due largely to constructive metamorphism and occasionally to refreezing at depth of rain and surface melt.

The accumulation period ended when air temperature began a final rise on 26 February; temperature was above freezing from 4 to 17 March, and water equivalent began to decline on 4 March. Significant water output was measured in a snowmelt lysimeter from 9 through 18 March. Density climbed

from about 300 kg/m³ to 400 kg/m³ during the first two phases of melt; it then fluctuated between 350 and 450 kg/m³ and eventually reached 520 kg/m³ just before melting was complete.

Table 5.5 on p. 237 gives the amounts of energy involved in each of the components of the energy budget during the accumulation and melt periods for six seasons at the Danville site. For all accumulation seasons, L was negative and more than balanced K , resulting in negative net radiation. H was positive and LE negative in all accumulation seasons, but the magnitude of H was several times greater than that of LE , so there was a net input of heat from turbulent exchange. There was a very small contribution from rain. The overall positive net input is largely due to ground heat, which was sufficient to produce about 87 mm of groundmelt.

In all melt seasons, the input from K was about twice the loss via L , resulting in a strongly positive net radiation. This was augmented slightly by G and negligibly by R . Again, sensible-heat exchange was positive and latent-heat exchange negative, but of considerably

Table 5.4 Example Energy-Balance Computations Using Relations of Section 5.5.2.

Conditions	Site 1 Condition A	Site 1 Condition B	Site 2 Condition A	Site 2 Condition B
F	0.00	0.00	1.00	1.00
C	0.00	1.00	0.00	1.00
T_a (°C)	4.00	4.00	4.00	4.00
RH	0.70	1.00	0.70	1.00
u_{ao} (m/s)	3.00	3.00	3.00	3.00
R (mm/d)	0.00	25.00	0.00	25.00
a	0.50	0.50	0.50	0.50
Energy-Balance Terms (MJ/m² · d)				
K	8.65	2.97	0.17	0.06
L	-3.28	0.85	1.63	1.63
$K + L$	5.37	3.81	1.81	1.69
H	4.43	4.43	0.89	0.89
LE	-6.99	34.4	-1.40	6.87
R	0.00	0.42	0.00	0.42
G	0.25	0.25	0.25	0.25
F_E	3.07	43.3	1.55	10.1
Water Production (mm/d)				
Snowmelt	9.2	129.6	4.6	30.3
Total ablation	12.0	129.6	5.2	30.3
Snowmelt + Condensation + Rain	9.2	168.4	4.6	58.1

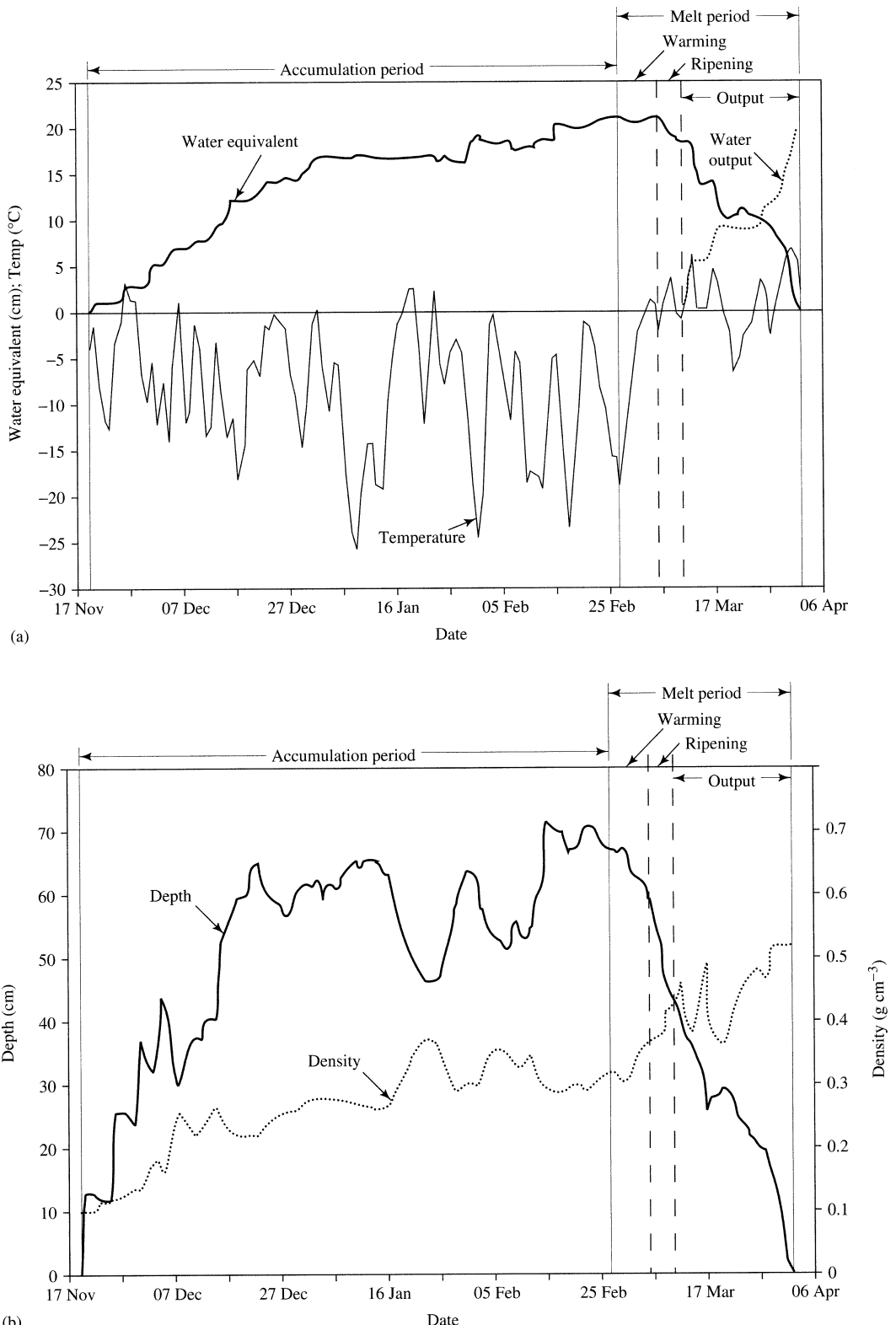


Figure 5.23 (a) Snowpack water equivalent, average air temperature, and cumulative water output and (b) snowpack depth and density at the Sleepers River Research Watershed in Danville, Vermont, for 1972–1973. The accumulation period and three phases of the melt period are shown; the boundary between the warming and ripening phases is uncertain [data from Anderson et al. (1977)].

Table 5.5 Energy-Balance Components (MJ/m^2) for Six Seasons at the NWS Snow Research Station, Danville, Vermont.

	68–69	69–70	70–71	71–72	72–73	73–74	Average
Accumulation Season							
Net shortwave radiation, K	167.94	171.50	195.28	169.70	115.14	191.76	168.55
Net longwave radiation, L	-264.49	-259.64	-282.87	-238.95	-174.39	-225.85	-241.03
Net radiation, $K + L$	-96.55	-88.14	-87.59	-69.25	-59.25	-34.08	-72.48
Heat from rain, R	0.08	0.84	0.25	0.38	0.71	1.00	0.54
Heat from ground, G	30.77	53.89	32.24	25.00	26.29	29.73	32.99
$K + L + R + G$	-65.69	-33.41	-55.10	-43.88	-32.24	-3.35	-38.95
Turbulent exchange, sensible, H	96.76	84.37	112.92	92.49	65.40	81.86	88.97
Turbulent exchange, latent, LE	-11.97	-25.88	-27.13	-24.45	-16.08	-20.39	-20.98
$H + LE$	84.79	58.49	85.79	68.04	49.32	61.47	67.98
Net heat input, F_E	19.09	25.08	30.69	24.16	17.08	58.12	29.04
Melt Season							
Net shortwave radiation, K	191.97	129.00	162.83	150.73	149.69	168.78	158.83
Net longwave radiation, L	-101.12	-67.49	-77.29	-74.78	-92.45	-109.99	-87.19
Net radiation, $K + L$	90.86	61.51	85.54	75.95	57.24	58.79	71.65
Heat from rain, R	0.46	0.63	0.71	1.26	0.67	1.17	0.82
Heat from ground, G	5.23	3.56	5.07	4.27	9.55	9.30	6.16
$K + L + R + G$	96.55	65.69	91.32	81.48	67.45	69.25	78.62
Turbulent exchange, sensible, H	66.57	43.13	67.12	65.86	56.32	60.80	59.96
Turbulent exchange, latent, LE	-28.35	-17.88	-23.66	-28.85	-35.00	-31.90	-27.61
$H + LE$	38.23	25.25	43.46	37.01	21.31	28.89	32.36
Net heat input, F_E	134.78	90.94	134.78	118.49	88.76	98.14	110.98

Source: Anderson (1976).

smaller magnitude, giving a net input from turbulent-exchange processes. The positive net heat input for melt seasons is the energy used in melting.

5.5.3.3 Comparison of Energy Balances in Different Environments

Kuusisto (1986) reviewed over 20 studies of melt-period energy balances; his summary is given in table 5.6. The comparable information for Anderson's (1976) study (computed for the melt season from table 5.5) has been added. Kuusisto (1986) made the following generalizations based on his survey:

- Net radiation and turbulent exchange play a major role in the energy balance, and heat from rain and from the ground are small or negligible.
- Net radiation and sensible-heat exchange are positive during snowmelt in most locations.

- Latent-heat exchange is positive in some places, but negative in others. This is likely the result of contrasting humidity and wind conditions.
- The net radiation is the most important component in forests, probably due to the less-negative or positive longwave radiation and reduced windspeeds.
- On cloudy or rainy days, turbulent exchange of latent heat dominates.
- Very high areal snowmelt rates are usually caused by intense positive turbulent heat exchange under humid, windy, and warm conditions.

This last generalization has important implications for forecasting conditions that can cause snowmelt flooding. Very warm, humid air and high winds above a ripe snowpack can produce very high rates of melt due to latent-heat input. The potential for

Table 5.6 Relative Contributions of Energy-Balance Components to Snowmelt in Different Environments^a

Study	Site ^b	Period ^c	Percent Contribution from			
			K + L	H	L.E.	R
1	Open field, CA, 37°N		72	28	-18	
2	Open field, Canada, 45°N (100 m)	Mar 59 (0.7)	75	25	-74	
3	Open field, AK, 67°N	Mar-Apr 66	86	14	24	
4	Open field in mts., CA, 37°N	Apr-May 47-51 (daytime)	73	23	4	
5	Open field, MI, 46°N	23 Jan 69 (1.5)	17	47	36	
6	Forest opening, CO, 39°N (3,260 m)	Jun 68 (5.0)	56	44	-3	0
7	Open field in mts., France, 46°N (3,550 m)	Jul 68 (1.6)	85	15	-15	
8	Open field in mts., Spain, 41°N (1,860 m)	Apr 70 (1.0)	100	-11	-42	
9	Open field, AK, 71°N (10 m)	Jun 71	100	-19	-10	-22
10	Open field in prairie, Canada, 51°N	Melt season 74 (0.8)	59	41	-10	-6
11	Open field in prairie, Canada, 51°N	Melt season 75 (0.5)	95	5	-29	-1
12	Open field in prairie, Canada, 51°N	Melt season 76 (0.3)	67	33	-14	-4
13	Deciduous forest, Ontario, 46°N	Apr 78 (1.0)	100	0	0	
14	Open field, Finland (60 m)	Melt seasons 68-73 (0.7)	46	53	-4	1
15	Open field in mts., Norway, 60°N	Apr-May 79-80 (1.2) cloudy days (2.3) clear days (0.7)	35 20 37	65 54 63	0 26 -24	
16	Small basin, 23% forest, Switzerland, 47°N (800 m)	Days with intense snowmelt, 77-80 (2.3)	8	65	20	7
17	Open field, AK, 65°N	Apr 80 (0.3)	67	33	-68	0
18	Open field, Finland, 61°N	Days with intense snowmelt, 59-78 (1.4)	48	47	2	3
19	Open field, Finland, 67°N	Days with intense snowmelt, 59-78 (1.5)	58	40	-23	2
20	Open tundra, NWT, Canada, 79°N (200 m)	Melt seasons 69-70	100	90	-77	-45
21	Open field in mts., New Zealand, 43°S (1,500 m)	Oct-Nov 76-80 Rainy days Days with greatest heat input	30 17 16	57 55 60	13 25 23	< 1 3 1
22	Open field in mts., New Zealand, 43°S (1,450 m)	Melt season 82 (3.1)	16	57	25	2
23	Open field, WI, 3 sites, 43-45°N	Melt seasons 53-64	-31	100	-12	
24	Small basin, 82% forest, Finland 64°N (120 m)	Melt seasons 71-81 (0.5)	86	14	-13	< 1
25	Open field, hilly area, VT, 45°N (550 m)	Melt seasons 69-74 (1.3)	52	43	-20	< 1
						4

^a 100% is the sum of all positive components.^b Number in parentheses is site elevation.^c Number in parentheses is average melt in cm/d.

Sources: Data from Kuusisto (1986); see that paper for references to individual studies. Data from Anderson (1976) added as study 25.

flooding under these conditions is high because this situation would typically exist generally over a watershed, whereas rapid melting due to solar radiation is largely restricted to south-facing, nonforested slopes. When rain accompanies warm winds, the flooding potential may be further exacerbated by the rain to produce a “rain-on-snow event,” which is common in the western United States (McCabe et al. 2007) and elsewhere (Sui and Koehler 2001), and which generated the record floods of March 1936 in central New England. As can be seen in tables 5.4–5.6, the heat introduced by the rain plays only a small role in generating melt; but in some cases the rain itself, with little melt, can produce floods (Singh et al. 1997).

One severe flooding case in which melt due to solar radiation did play a large role was that of the Red River in North Dakota and Minnesota in the spring of 1997. The watershed of the Red River is flat and largely unforested; the flood severity was exacerbated because of a record snowpack, the fact that the river flows northward, and the interruption of the melt season by a major blizzard (Macek-Rowland 1997).

5.6 Snowmelt Runoff Generation

We saw earlier that a ripe snowpack typically retains only a small fraction of its water equivalent as liquid water, which is present as thin films held by surface tension occupying less than 10% of the pore

space (figures 5.15 and 5.16). As additional water is produced during the last phase of melting it can no longer be held against gravity, and downward percolation begins. Natural snowpacks are seldom homogeneous, and usually contain discontinuous layers of varying density that temporarily store and horizontally divert the percolating water (Marsh and Woo 1985; Conway and Benedict 1994; Hirashima et al. 2010). Figure 5.24 shows that the distribution of liquid water in a melting snowpack is far from uniform vertically or horizontally. However, ice layers usually disappear as melt progresses, and melting snowpacks tend to become fairly uniform assemblages of quasi-spherical grains of 1 to 3 mm diameter. Thus to gain a basic understanding of the physical processes involved we can treat melting snowpacks as *homogeneous porous media*, physically identical to coarse-grained soils.

Water arriving at the bottom of the snowpack infiltrates into the soil and/or accumulates to form a saturated zone at the base of the snowpack, moving toward a surface-water body by one of the paths illustrated in figure 5.25. In figure 5.25a, the water table is at depth and the ground above it is unsaturated, so all of the water output infiltrates and moves streamward as subsurface flow. In figure 5.25b, the infiltration rate is less than the water-output rate, so a basal saturated zone develops within the snowpack through which water flows toward the stream. In figure 5.25c, ground conditions are simi-

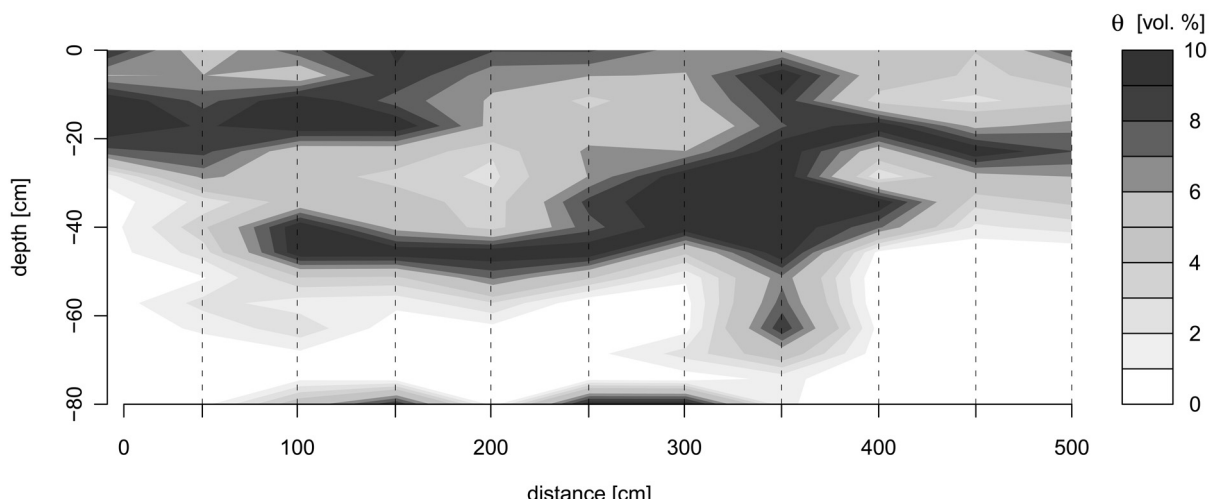


Figure 5.24 Contour plot showing cross section of snow wetness (θ) to a depth of 80 cm over 5-m wide areas across a slope in the Swiss Alps in the early stages of snowmelt [Techel and Pielmeier (2011)].

lar to those of 5.25a, but the water table has risen above the ground surface on the lower part of the slope so that water moves streamward by both surface and subsurface routes.

The process of infiltration will be discussed in detail in chapter 8, and runoff generation by processes similar to those shown in figure 5.25c will be examined in chapter 10. Here we focus on snowmelt-runoff generation by the process shown in figure 5.25b, following Dunne et al. (1976) (figure 5.26).

5.6.1 Flow in the Unsaturated Zone

Above any basal saturated zone, which may form where meltwater accumulates at an ice layer or at the ground surface, the pores of snowpacks are only partially filled with liquid water. Thus the vertical percolation of water in the snowpack is a form of *unsaturated porous-media flow*, which is governed by the basic law of flow in porous media, *Darcy's law* (discussed in detail in section 7.3). Colbeck (1974,

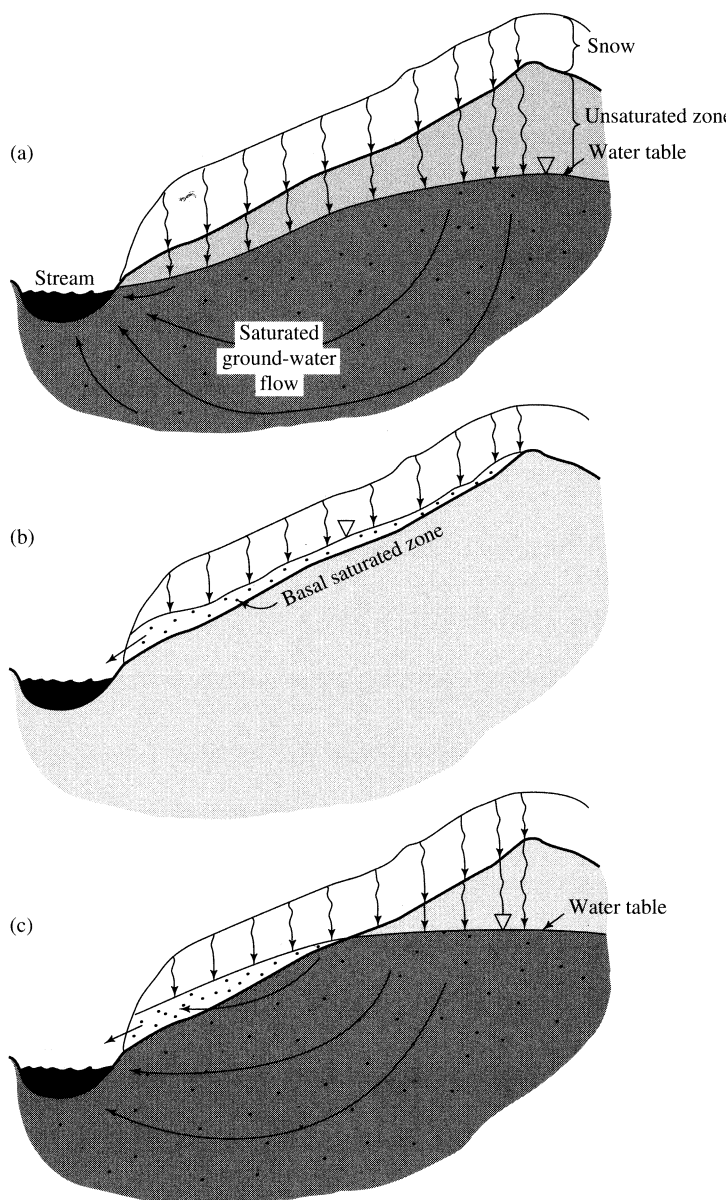


Figure 5.25 Three modes of snowmelt-runoff generation. (a) The top of the saturated zone in the soil (water table) is at depth; percolating meltwater infiltrates and percolates to the saturated zone to raise the water table and thereby induce increased ground-water flow to the stream. (b) The water table is at the soil surface or the soil surface is impermeable (perhaps due to solid soil frost); percolating meltwater accumulates to form a basal saturated zone through which water drains to the stream. (c) The lower portion of the water table has risen above the ground surface into the snowpack; water in the upper part of the slope moves as in (a), water in the lower part as in (b) [adapted from Dunne and Leopold (1978)].

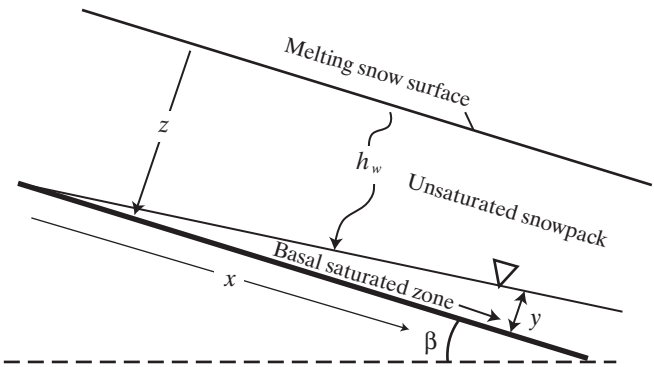


Figure 5.26 Definition diagram for snowmelt runoff processes.

1978) gave a detailed description and experimental validation of the application of Darcy's law to snowmelt percolation, and his treatment is followed here.

Because of the relatively large grain sizes, surface-tension forces in snow are usually negligible in relation to gravitational forces. Thus Darcy's law can be simplified to

$$q_z = K_{hun}, \quad (5.60)$$

where q_z is the downward vertical flux rate (volume of water per unit horizontal area per unit time [L T^{-1}]) and K_{hun} is the **unsaturated hydraulic conductivity** of the snow [L T^{-1}]. As in soils, unsaturated hydraulic conductivity is a function of the **saturated conductivity**, K_h , and the degree to which the pores contain water;

$$K_{hun} = K_h \cdot S^c, \quad (5.61)$$

where S is the fraction of pore space containing mobile water,

$$S \equiv \frac{\theta_w - \theta_{ret}}{\phi - \theta_{ret}}, \quad (5.62)$$

and the exponent has been found experimentally to be $c \approx 3$. K_h in turn is a function of snow density (inversely related to pore-space size) and grain size, d , and can be estimated as

$$\begin{aligned} K_h &= 0.077 \cdot d^2 \cdot (g/v) \cdot \exp(-7.8 \times 10^{-3} \cdot \rho_s) \\ &= 4.4 \times 10^5 \cdot d^2 \cdot \exp(-7.8 \times 10^{-3} \cdot \rho_s), \end{aligned} \quad (5.63)$$

where K_h is in m/s , d is in m , g is gravitational acceleration (9.81 m/s^2), v is kinematic viscosity of water at 0°C ($1.79 \times 10^{-6} \text{ m}^2/\text{s}$), and ρ_s is snow density in kg/m^3 (Shimizu 1970; Hirashima et al. 2010). Combining equations (5.60)–(5.62),

$$q_z = K_h \cdot S^3 = K_h \cdot \left(\frac{\theta_w - \theta_{ret}}{\phi - \theta_{ret}} \right)^3. \quad (5.64)$$

Energy inputs to the surface of a ripe snowpack vary diurnally, usually approximating a sine curve with a peak input in the early afternoon. Thus the rate of meltwater production (assumed to originate at the surface) varies continually. This variation generates a daily wave of meltwater originating near the surface and percolating downward (figure 5.27). We designate the melt rate at any instant $h_w(t)$, and a given melt rate travels vertically downward at a rate

$$\frac{dz}{dt} \Big|_{h_w(t)} = \left(\frac{c}{\phi \cdot (1 - \theta_{ret})} \right) \cdot K_{hun}^{1/c} \cdot h_w(t)^{(c-1)/c}. \quad (5.65)$$

Because the speed of these melt waves increases as the melt rate increases, percolating water produced during the period of peak melting near midday overtakes water produced earlier in the day. Thus the waves tend to accumulate water and develop a sharp wave front, as in figures 5.27 and 5.28. Equation (5.65) can be integrated to show that the depth of penetration, z , of a flux of meltwater with constant flux rate is linearly related to time t :

$$z = \left(\frac{c}{\phi \cdot (1 - \theta_{ret})} \right) \cdot K_{hun}^{1/c} \cdot h_w(t)^{(c-1)/c} \cdot t. \quad (5.66)$$

An example calculation of the travel time of water generated at a particular melt rate is given in box 5.3 on p. 243. To illustrate the overall melt-percolation phenomenon, we use the results of Dunne et al. (1976) over two days of snowmelt at their experimental site at Schefferville, Quebec, Canada. With their measured values, equation (5.66) becomes

$$z = 0.59 \cdot h_w(t)^{2/3} \cdot t, \quad (5.67)$$

where z is in m . Figure 5.29 on p. 243 shows the downward percolation of various melt rates as given by equation (5.67): higher melt rate waves travel

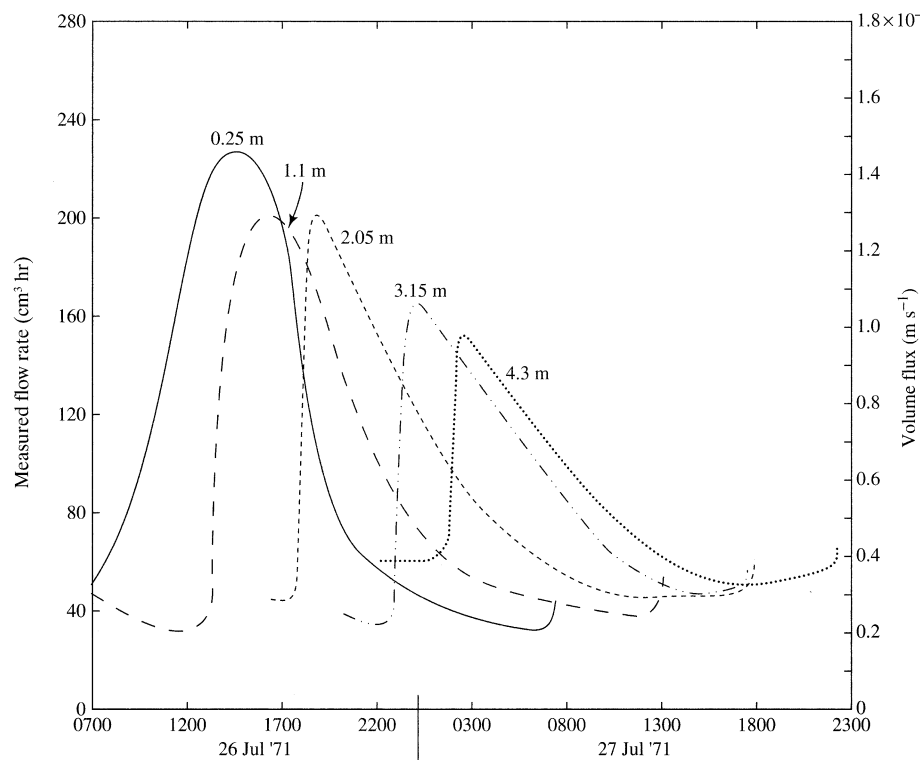


Figure 5.27 Volume rates of flow at different depths in a homogeneous snowpack produced by a day of intense fair-weather melting [Colbeck (1978)].

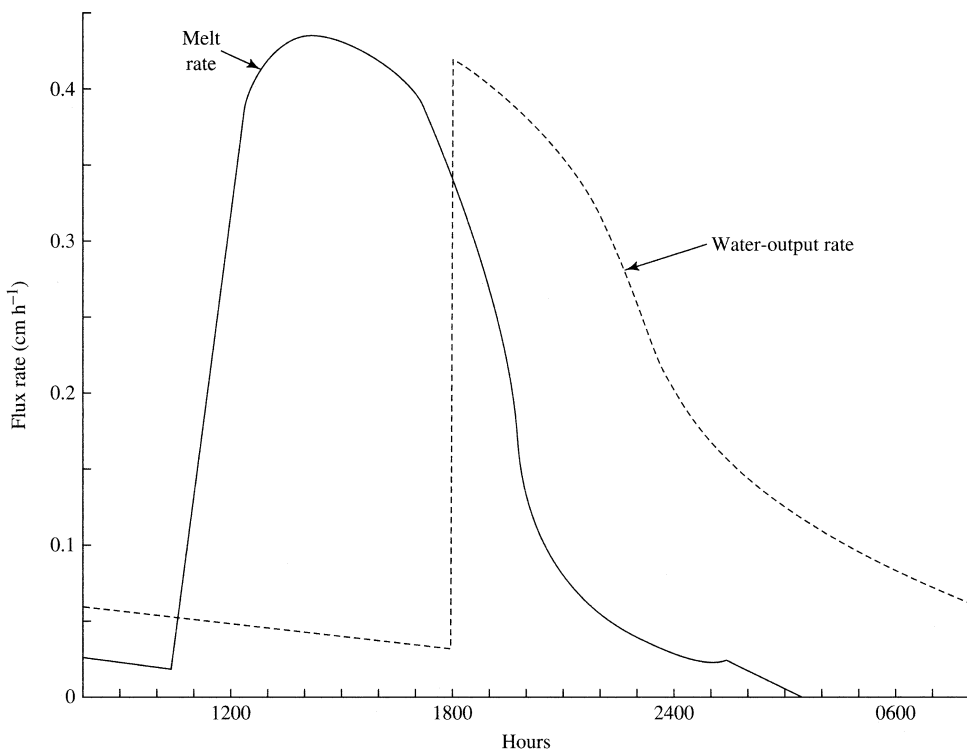


Figure 5.28
Comparison of timing of rate of melting at the surface (the "input") and rate of vertical unsaturated flow at the base of a 101-cm deep tundra snowpack (water output) [Dunne et al. (1976)]. The generation of runoff from subarctic snowpacks. *Water Resources Research* 12:675–694, with permission of the American Geophysical Union].

Box 5.3 Example Computation of Meltwater Percolation

Consider a ripe snowpack with a depth $h_s = 1.00$ m, a density $\rho_s = 400 \text{ kg/m}^3$, and a grain size $d = 2 \text{ mm}$. Then from equation (5.63),

$$K_h = (4.4 \times 10^5 \text{ m/s}) \cdot (0.002 \text{ m})^2 \cdot \exp(-7.8 \times 10^{-3} \cdot 400 \text{ kg/m}^3) = 7.77 \times 10^{-2} \text{ m/s.} \quad (5B3.1)$$

From equation (5.25),

$$\theta_{ret} = 3 \times 10^{-10} \cdot 400^{3.23} = 0.076. \quad (5B3.2)$$

From equation (5.5),

$$\begin{aligned} \phi &= 1 - \frac{\rho_s - \theta_w \cdot \rho_w}{\rho_i} \\ &= 1 - \frac{400 \text{ kg/m}^3 - 0.076 \cdot (1,000 \text{ kg/m}^3)}{917 \text{ kg/m}^3} \\ &= 0.647 \text{ kg/m}^3. \end{aligned} \quad (5B3.3)$$

Equation (5.65) then gives

$$\begin{aligned} \left. \frac{dz}{dt} \right|_{h_w(t)} &= \left(\frac{3}{0.647 \cdot (1 - 0.076)} \right) \cdot (7.77 \times 10^{-2} \text{ m/s})^{1/3} \cdot [h_w(t) \text{ m/s}]^{2/3} \\ &= 2.14 \cdot h_w(t)^{2/3} \text{ m/s.} \end{aligned} \quad (5B3.4)$$

Dunne et al. (1976) measured mid-day melt rates of around $q_z = 0.400 \text{ cm/hr} = 1.11 \times 10^{-6} \text{ m/s}$. Equation (5B3.4) gives the percolation velocity of water generated at this rate as

$$\begin{aligned} \left. \frac{dz}{dt} \right|_{h_w(t)} &= 2.14 \cdot (1.11 \times 10^{-6})^{2/3} \\ &= 2.3 \times 10^{-4} \text{ m/s.} \end{aligned} \quad (5B3.5)$$

At this velocity, it takes

$$\frac{1 \text{ m}}{2.3 \times 10^{-4} \text{ m/s}} = 4,356 \text{ s} = 1.21 \text{ hr} \quad (5B3.6)$$

for this water to reach the bottom of the snowpack.

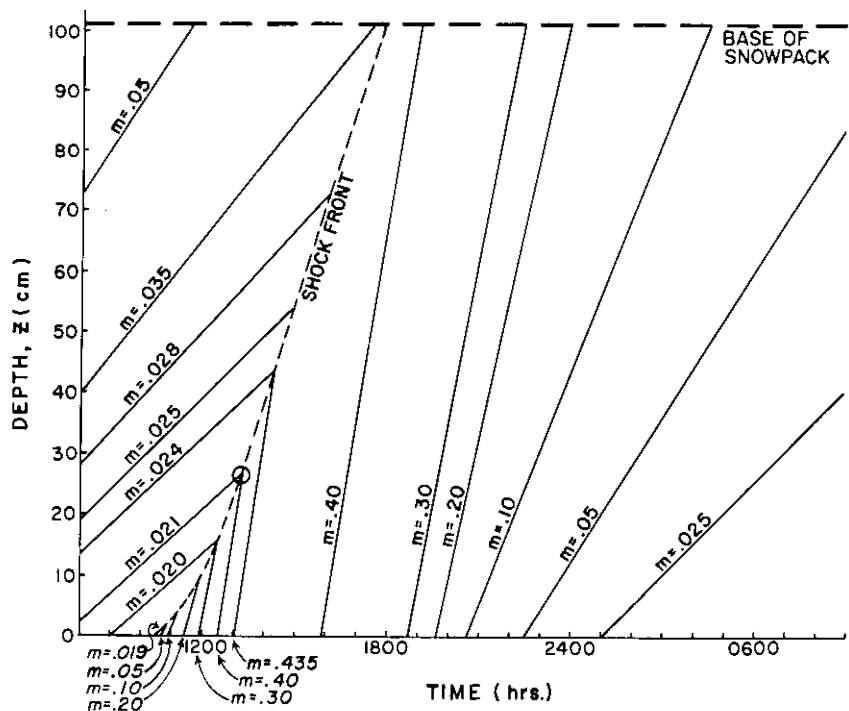


Figure 5.29 Downward percolation of various melt rates ($m \equiv dz/dt, \text{ cm/hr}$) as given by equation (5.67). The times at which these flux rates intersect the base of the snowpack determines the hydrograph of the input to the saturated layer [Dunne et al. (1976). The generation of runoff from subarctic snowpacks. *Water Resources Research* 12:675–694, with permission of the American Geophysical Union].

faster (steeper curves), and faster-moving waves overtake earlier-generated slower waves to form a shock front (dashed line), which travels at an intermediate speed.

The shock wave in figure 5.29 takes about 7 hr to reach the base of the 1.01-m deep snowpack, so its speed is 0.14 m/hr; the peak of the wave in figure 5.27 moves at a velocity of 0.2 to 0.3 m/hr, and Anderson (1968) found average time lags of ~ 0.35 m hr (figure 5.30). Thus for most shallow seasonal snowpacks, the peak water output will occur within a few hours of the peak melt rate. Anderson (1973) developed an empirical expression for the time lag of snow melt, i.e., the elapsed time between the beginning of daily melt and the beginning of water output:

$$\Delta t = 5.33 \cdot \left[1.00 - \exp\left(-\frac{0.03 \cdot h_{swe}}{\Delta h_{w6}}\right) \right], \quad (5.68)$$

where Δt is the time lag (hr), h_{swe} is the water equivalent of the snowpack when melt begins (m), and Δh_{w6} is the amount of melt generated in a 6-hr period (m).

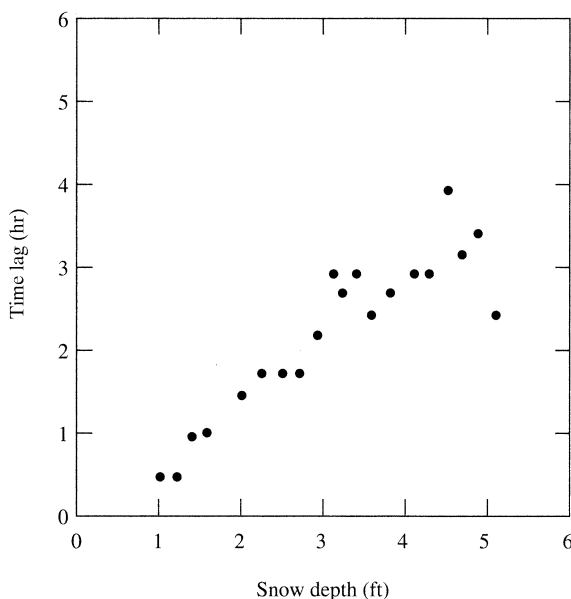


Figure 5.30 Approximate time lag between the time of peak surface melting and the time of peak flow from the bottom of a snowpack as a function of snow depth [Anderson (1968). Development and testing of snow pack energy balance equations. *Water Resources Research* 4:19–37, with permission of the American Geophysical Union].

5.6.2 Flow in the Basal Saturated Zone

Assuming a constant snow depth and uniform conditions above it, the daily wave of water output arrives at the base of the snowpack at the same time all along the slope. This input produces daily waves that travel downslope in the basal saturated zone at a velocity, U_s , where

$$U_s = \frac{K_h}{\phi - \theta_{ret}} \cdot \tan(\beta), \quad (5.69)$$

K_h is the saturated hydraulic conductivity of the basal snow layer, and β is the slope angle. K_h is estimated via equation (5.63). However, it should be noted that the size of snow grains in the saturated zone can be significantly larger than that in the unsaturated zone due to more rapid metamorphism: For a subarctic snowpack, Dunne et al. (1976) found $d = 6$ mm in the basal saturated zone and $d = 2$ mm in the unsaturated zone.

Using the wave velocity U_s , one can calculate the average time of travel of water in the basal saturated zone, t_s , as

$$t_s = \frac{X}{U_s} = \frac{X \cdot (\phi - \theta_{ret})}{K_h \cdot \tan(\beta)}, \quad (5.70)$$

where X is the slope length. t_s is typically on the order of 1% of the travel time through the unsaturated zone (Male and Gray 1981). Thus where a basal saturated zone forms, the lag time between peak melt rates and peak inputs to small upland streams is determined largely by the travel time associated with the vertical percolation through the snowpack and is typically on the order of several hours. In contrast, infiltrating snowmelt that percolates through the soil to the ground water (figure 5.25a) may not appear in streamflow for months (Bengtsson 1988).

5.7 Snowmelt Modeling

5.7.1 Importance of Modeling

Snow is a critical water resource in many regions, and the extent and depth of snow cover are major influences on energy and water balances. Because of difficulties in accessing remote regions, especially mountainous areas, and limited resources for obtaining ground measurements, satellite observations are widely used for assessing the extent and water equivalent of snow cover. However, interpretation of both optical and passive microwave satellite observations

is far from straightforward, particularly in forested areas. Thus modeling of snow accumulation and melt is an essential tool for water-resource management, simulating global climate, and weather forecasting.

5.7.2 Approaches to Snowmelt Modeling

5.7.2.1 Energy-Balance Approach

The energy-balance relations discussed in section 5.5 form the basis for one class of models of snowmelt at a point. These models are often characterized as “physically based” because the energy balance is a fundamental physical principle (conservation of energy) and because they use equations that describe the physics of processes in each component of the energy balance. However, different models use different representations of these processes, which may be simpler or more complex than described in section 5.5. For example, some models may consider the visible and near-infrared portions of the solar spectrum separately, use different ways of characterizing forest effects on wind and/or snow interception, and consider different layers within the snowpack. Furthermore, the processes can be modeled at different spatial and temporal discretizations; for example, the JULES model described by Parajka et al. (2010a) operates at an hourly time step and a spatial resolution of 25 km × 25 km, and each grid cell contains a variable fraction of nine surface-vegetation types, each of which can be set to have different properties.

Anderson (1976) made a thorough and extensive study and testing of point snowmelt-modeling techniques in a large clearing at an elevation of 550 m in Danville, Vermont, over a period of six years. He found only minor differences in results using time steps of 1, 3, and 6 hr. Maximum time steps should probably not exceed 12 hr in order to capture the drastic differences between daytime and nighttime energy balances. Anderson (1976) also compared model results using snowpack-depth increments of 1, 2.5, 5, and 10 cm, and found that predicted water equivalent at a given time increased as the thickness increased because the thicker layers introduced distortions in the diurnal warming-cooling cycles. Although there is little further evidence on which to base definitive guidelines, one could probably expect significant distortions to appear in energy-balance models using thicknesses exceeding 50 to 100 cm. However, many models treat the snowpack as a single layer.

Andreadis et al. (2009) gave a fairly detailed description of a modern energy-balance-based snow

model, others are described by Cline (1997), Melloh (1999), and Wang et al. (2010).

5.7.2.2 Temperature-Index Approach

The empirical **temperature-index approach** to snowmelt modeling was developed because (1) measurements of the many variables required for energy-balance computations are commonly unavailable and (2) the computational resources to implement energy-balance computations are limited. Although the second reason is rapidly becoming less of an issue, some current models use the approach (Rutter et al. 2009).

The temperature-index approach estimates snowmelt, Δw , for a time period as a linear function of air temperature:

$$\begin{aligned}\Delta w &= M \cdot (T_I - T_b), \quad T_I \geq T_b; \\ \Delta w &= 0, \quad T_I < T_b,\end{aligned}\quad (5.71)$$

where M is a **melt coefficient** (or **melt factor** or **degree-day factor**), T_I is an **index temperature**, and T_b is a **base temperature**. The base temperature used is almost always the melting point, 0°C, and the index temperature is the average or maximum temperature for the time period.

This approach is justified because the snow-surface temperature is at or near 0°C during melting, energy inputs from longwave radiation and turbulent exchange are approximately linear functions of air temperature, and there is a general correlation between insolation and air temperature. Figure 5.31 shows that equation (5.71) approximates daily melt at the Danville, Vermont, snow research site—although there is considerable scatter. The value of M that best fits these data is $M = 3.6 \text{ mm/d} \cdot ^\circ\text{C}$, and the intercept value, -1.4 mm/d , is not significantly different from 0.

The value of M varies with latitude, elevation, slope inclination and aspect, forest cover, and time of year, and should ideally be empirically determined for a given watershed. In the absence of site-specific data, several studies have suggested generalized approaches to estimating M (table 5.7).

5.7.2.3 Hybrid Approach

The dependence of the melt factor on time of year, land cover, and slope factor (table 5.7) largely reflects the importance of solar radiation on snowmelt. To reduce this variability and improve prediction accuracy while retaining practical data requirements, Kustas et al. (1994) and Brubaker et

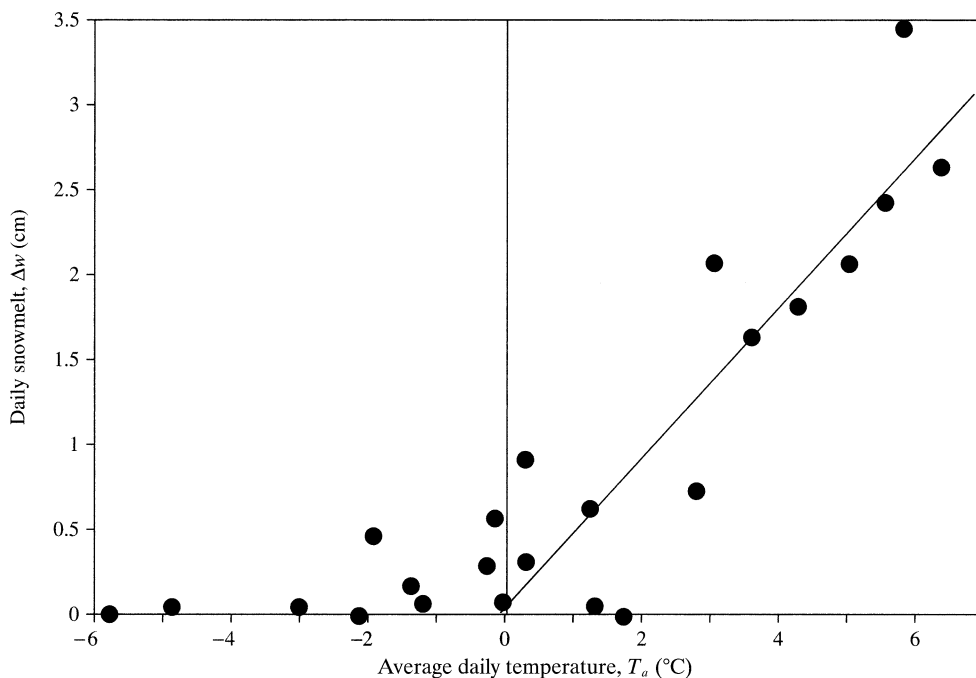


Figure 5.31 Daily snowmelt, Δw , as a function of daily average air temperature, T_a , at Danville, Vermont, March 1973. The line is the best-fit linear relation between the two variables for days when $T_a > 0^{\circ}\text{C}$ [data from Anderson et al. (1977)].

Table 5.7 General Melt-Factor Equations.

Male and Gray (1981)

$$M = 4.0 \cdot (1 - a) \cdot \exp(-4 \cdot F) \cdot f_{sl}$$

Federer and Lash (1978a) (forests in the eastern United States)

$$M = f_F \cdot (0.7 + 0.0088 \cdot J) \cdot f_{sl}, J < 183$$

Kuusisto (1986)

$$\text{Forest: } M = 10.4 \cdot \frac{\rho_s}{\rho_w} - 0.7;$$

$$\text{Open: } M = 19.6 \cdot \frac{\rho_s}{\rho_w} - 2.39$$

Symbols

M ≡ melt factor ($\text{mm}/\text{C}^{\circ} \cdot \text{day}$)

a ≡ albedo

F ≡ fraction of forest cover

f_{sl} ≡ **slope factor** ≡ ratio of solar radiation received on the site of interest to that on a horizontal surface [equation (D.27); a function of latitude, day-of-year, slope inclination, and slope aspect]

f_F ≡ vegetative-cover factor = 30.0 for open areas, 17.5 for hardwood forests, and 10.0 for conifer forests

J ≡ day-of-year ("Julian date")

ρ_s ≡ snow density (kg/m^3)

ρ_w ≡ water density ($= 1,000 \text{ kg}/\text{m}^3$)

al. (1996) evaluated an approach that computes daily snowmelt, Δw , as

$$\Delta w = \frac{K + L}{\rho_w \cdot \lambda_f} + M_r \cdot T_a, \quad (5.72)$$

where M_r is a "restricted" melt factor with a constant value of $2.0 \text{ mm}/\text{C}^{\circ} \cdot \text{d}$ and T_a is average daily temperature ($^{\circ}\text{C}$). In this method the radiation terms are measured or evaluated as described in sections 5.5.2.1 and 5.5.2.2, and M_r accounts for the turbulent-exchange processes. Brubaker et al. (1996) showed that the value of $M_r \approx 2.0 \text{ mm}/\text{C}^{\circ} \cdot \text{d}$ can be derived from the basic equations for those processes.

5.7.3 Evaluation of Snowmelt Models

Anderson (1976) made a thorough comparison of point energy-balance and temperature-index models with measured snowpack properties and snowmelt production over six snow seasons at the Danville, Vermont, research site. His complete model included simulation of snowpack settling and compaction as well as the snowpack energy balance, and was used for both accumulation and melt seasons. The temperature-index model, calibrated for the Danville site, is applicable only for the output phase of the melt season. Figure 5.32 compares snow-

course measurements of snowpack water equivalent and density with values simulated by Anderson's complete energy-balance model for the accumulation season and the warming and ripening phases of the melt season in 1972–1973. Figure 5.33 shows the same comparison for the output phase, and includes the predictions of the temperature-index model. Computed daily water output is compared with values measured in a lysimeter in figure 5.34. Clearly, both models perform very well in simulating density and water equivalent for the 1972–1973 snow season; this was true also in 1971–1972. In three of the other melt seasons examined, the energy-balance model gave somewhat better results, while the temperature-index model was slightly better during one season. Except for two of the highest-output days, predictions of water output were also good.

Figure 5.35 on p. 249 compares streamflow from a small (8.42 km^2) watershed at the Danville site with flow predicted with a model called the Snowmelt Runoff Model (SRM) (Brubaker et al. 1996) for six seasons. Two versions of the SRM are compared, one with melt predicted by the seasonally varying temperature-index approach [equation (5.71)], and

the other with the hybrid approach [equation (5.72)]. The hybrid approach predicted daily runoff better in only two of the six years, but predicted total runoff volume significantly better in all years.

Kustas et al. (1994) compared lysimeter-measured snowmelt with melt estimated via (1) a complete energy balance, (2) the temperature-index approach with a seasonally increasing melt coefficient, and (3) the hybrid approach with radiation terms estimated as in sections 5.5.2.1 and 5.5.2.2 for a research site in Switzerland (figure 5.36 on p. 250). The accuracy of the hybrid approach was almost identical to that of the complete energy balance, and both were considerably better than the temperature-index estimates.

Anderson (1976) concluded that in heavily forested watersheds, a temperature-index model that includes a way to account for decreases in areal snow cover during melt should give results similar to an energy-balance model. However, an energy-balance model should perform better than a temperature-index model when applied to a relatively open (unforested) watershed where there is considerable variability in meteorological conditions, and in watersheds with considerable physiographic and climatic

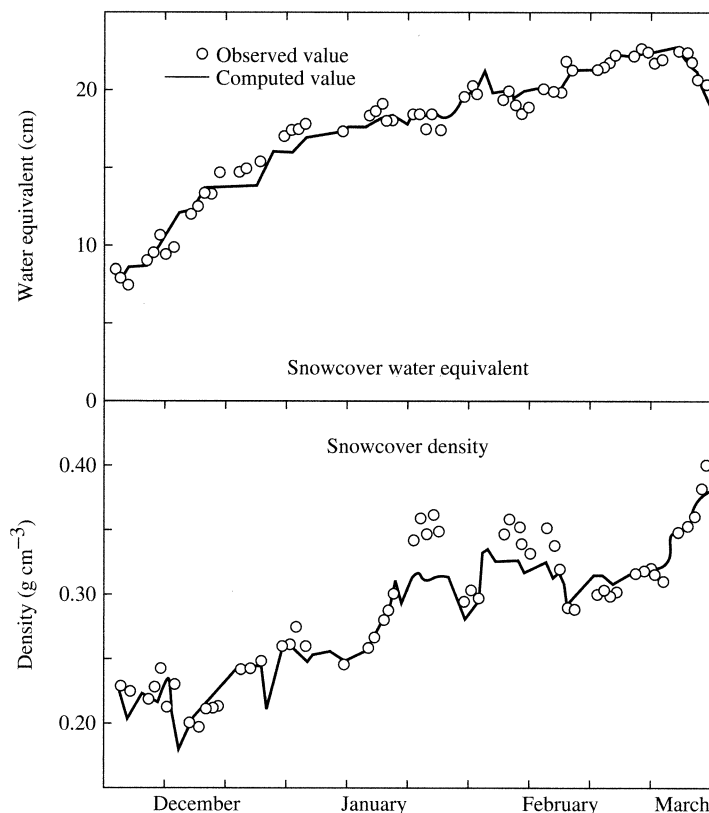


Figure 5.32 Comparison of observed and simulated (energy-balance model) snowpack water equivalent and density for the 1972–1973 accumulation season and warming and ripening phases of the melt season at Danville, Vermont. Observed values are snow-course observations [Anderson (1976)].

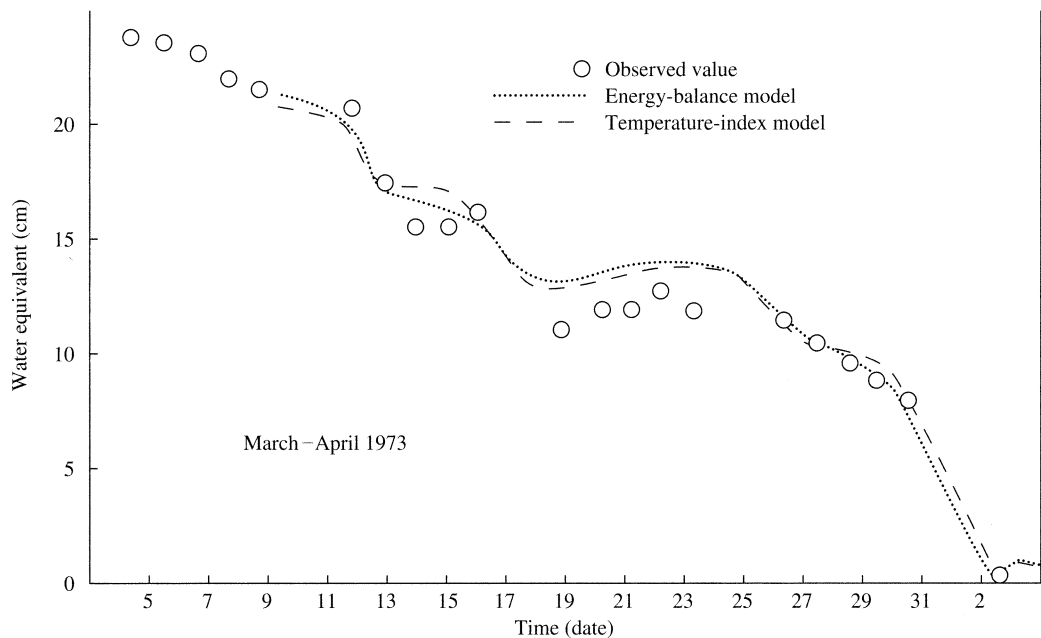


Figure 5.33 Comparison of observed and simulated (energy-balance and temperature-index models) snowpack water equivalent for the output phase of the 1973 melt season at Danville, Vermont. Observed values are snow-course observations [Anderson (1976)].

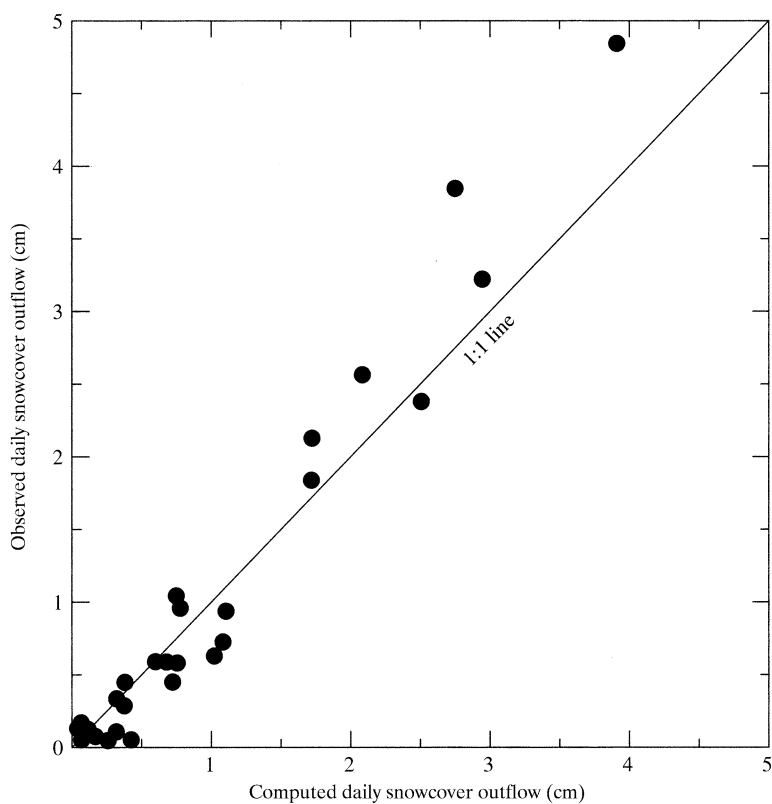


Figure 5.34 Water output observed in lysimeter versus simulated via energy-balance model at Danville, Vermont [Anderson (1976)].

variability. He found that the minimal data requirements for use of an energy-balance model are an accurate and representative estimate of incoming solar radiation, plus measurements of air temperature, vapor pressure, and wind speed.

Promising approaches to snowmelt that would be especially useful in predicting the effects of global

warming on snow and snowmelt runoff include: (1) a model of the areal depletion of snow cover in a forested catchment (Buttle and McDonnell 1987), (2) a model that simulates the growth and disappearance of the seasonal snow cover from daily air temperature and precipitation data (Motoyama 1990), and (3) a model that uses areally averaged versions of the basic

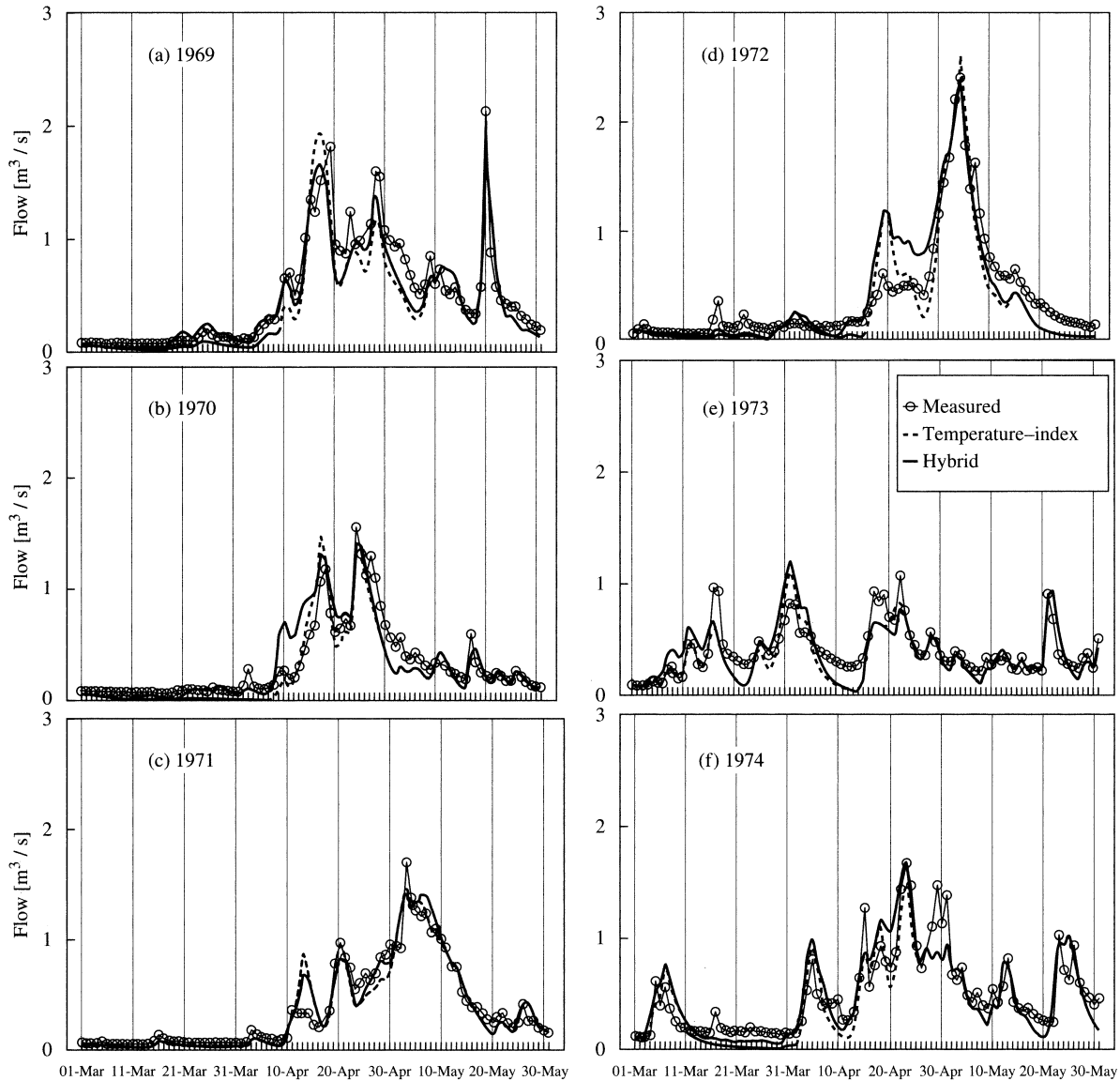


Figure 5.35 1969–1974 snowmelt runoff hydrographs at Sleepers River Research Watershed, Vermont. Open circles = measured; dashed line = modeled via temperature-index approach; solid line = modeled via hybrid approach [Brubaker et al. (1996). Incorporating radiation inputs into the Snowmelt Runoff Model. *Hydrological Processes* 10:1329–1343, with permission from Wiley].

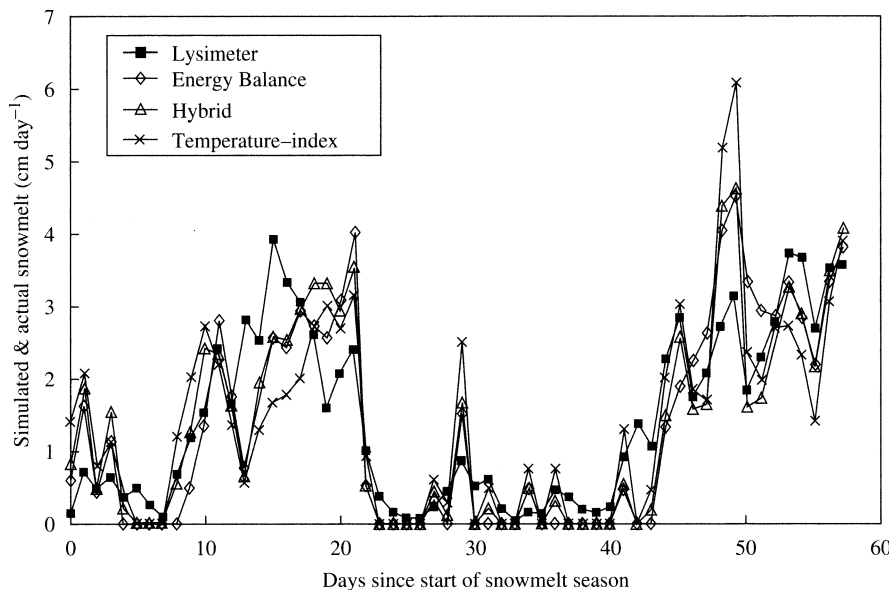


Figure 5.36 Daily snowmelt measured by lysimeter and simulated by the temperature-index approach, the hybrid approach, and the energy-balance approach at Weissfluhjoch, Switzerland, for the 1985 melt season [Kustas et al. (1994). A simple energy budget algorithm for the snowmelt runoff model. *Water Resources Research* 30:1515–1527, with permission of the American Geophysical Union].

energy-balance relations to predict areal snow cover and snowmelt runoff (Horne and Kavvas 1997).

The World Meteorological Organization (1986a) compared 11 temperature-index models using common data sets for six different watersheds, and other model comparisons were reported by Rango and Martinec (1994) and Blöschl et al. (1991a, 1991b). Rutter et al. (2009) evaluated 33 snowpack models of varying complexity and purpose across a wide range of hydrometeorological and forest-canopy conditions at five Northern Hemisphere locations, and compared modeled estimates of snow water equivalent or depth to observations at forest and open sites at each location. They found a great deal of variability in model performance from year to year and site to site, and concluded that there is no universal “best” model for all sites or locations.

5.7.4 Summary

Snowmelt is a significant contributor to runoff and water supplies over much of the Northern Hemisphere, and changes in snowmelt runoff will be one of the most pronounced hydrologic responses to global warming. Thus it is important that the processes of snow accumulation and melt are accurately captured in land-surface models. Many agencies have developed models that are specifically designed for particular regions, data sources, and purposes. However, they all attempt to simulate melt processes on the basis of meteorological data to account for the typically

wide range of topography, land use, and weather over watersheds, and to integrate the processes of water movement over hillslopes and in stream channels. Because of the wide variability of conditions, the sparseness of surface meteorological data, and the need to provide operational forecasts at relatively short time intervals (usually less than 24 hr), some of these models use semi-empirical relations rather than physically based models of melt and water movement. Many watershed-scale models use some form of temperature-index model or hybrid approach to predict melt.

These results lead to the following conclusions:

- The understanding of snowpack processes as developed in sections 5.5 and 5.6 can be used to simulate point snowmelt to a high degree of precision given careful measurements of the meteorological inputs at the point of interest.
- The temperature-index approach can provide useful estimates of daily snowmelt, but the value of the melt coefficient should reflect local conditions and seasonal changes.
- The hybrid approach appears to predict daily snowmelt with a precision equivalent to the complete energy balance and, since good estimates of the radiation components of the energy balance can usually be made with commonly available data, this approach will often be attractive for modeling.

However, recent reviews of approaches to modeling snow processes (Roesch 2006; Andreadis et al.

2009; Parajka et al. 2010b; Rutter et al. 2009) have noted that the representation of snow processes in land-surface models is a key area in which improvements are required. Part of the difficulty arises because the physics of snow accumulation and ablation operate at much finer temporal and spatial scales than those resolved in most models. This problem is particularly important in mountainous areas, where orographic effects influence local precipitation, and in forested areas, where the canopy affects all aspects of the energy balance in complex ways.

Important challenges in modeling snowmelt over large areas remain, including:

- Accounting for differences in snow accumulation and melt over the typically large range of variations in topography, elevation, and vegetation.

- Achieving the correct partitioning of rain/snow (section 4.1.8). This problem is exacerbated in watersheds that have a wide range of elevation.
- Accounting for spatial and temporal variations in the areal extent of snow cover. Improvements in the interpretation of satellite imagery are evolving and will improve the estimation of areal snow cover (Dozier 2011).
- Accounting for the movement of water output to the watershed outlet. Empirical and semi-empirical techniques, some of which are discussed in chapter 10, are used for this.

▼ EXERCISES

1. Snow surveyors using a snow tube and thermometer recorded the following data from a snow course on two different dates (temperature was taken at the mid-point of the snow depth to represent the average snowpack temperature):

2 March 2013	Station 1	Station 2	Station 3	Station 4	Station 5
Depth (cm)	92	94	105	93	96
Water equivalent (cm)	29	30	33	29	32
Temperature (°C)	-6	-5	-6	-6	-6

7 March 2013	Station 1	Station 2	Station 3	Station 4	Station 5
Depth (cm)	88	89	102	88	91
Water equivalent (cm)	35	36	40	35	37
Temperature (°C)	-2	-2	-3	-2	-3

- a. Compute the snow density and cold content for both dates.
 - b. How much energy needs to be added to the snowpack before water output begins?
2. The following snow-tube and temperature data were collected at five stations spaced 30 m apart on the University of New Hampshire baseball field:

31 January 2005	Station 1	Station 2	Station 3	Station 4	Station 5
Depth (cm)	20.1	18.3	18.2	16.4	24.5
Water equivalent (cm)	4.0	2.0	3.0	3.5	4.5
Temperature (°C)	0.0	0.0	0.0	0.0	-1.0

At station 3, an undisturbed sample of snow measuring 33 cm wide by 50 cm long by 18.2 cm deep was collected in a plastic container with an empty weight of 1,284 g. The weight of the container with snow was 6,246 g.

- a. Calculate the average depth, density, and water equivalent of the snowpack.
- b. Compare the average density calculated from the snow tube with that calculated from the bulk sample.

3. Using a snow tube, make a survey of snow depths, densities, and water equivalents under various conditions of slope, aspect, and forest cover. If a snow tube is not available, measure depths with a meter stick and collect samples to be melted to determine water equivalents. Write a brief report comparing observations in different environments.
4. For one or more snow storms, compare the catch of a rain gauge with the increment of water equivalent as determined with a snow tube or by collecting and melting the snowfall. Compare the results with the information in figure 4.16. Write a brief report discussing your findings.
5. The spreadsheet program SolarRad.xls (see appendix D) on the disk accompanying this text computes the daily clear-sky incident solar radiation, K_{in} , as a function of latitude, date, slope steepness, and orientation. Select fixed values for four of these factors and a range of values for the fifth, and use the program to compute how K_{in} varies as a function of this fifth factor. Summarize your results with appropriate tables and/or figures and a brief discussion.
6. The program SnowMelt.xls on the disk accompanying this text computes the daily snowmelt and water output as a function of a number of environmental variables using the relations described in section 5.5.2.
 - a. Using this spreadsheet and SolarRad.xls to estimate clear-sky solar radiation, compare snowmelt at sites with varying forest cover and slopes under varying weather conditions as specified by your instructor.
 - b. Write a brief report comparing the relative importance of the various energy-balance components under the differing site and weather conditions.
 - c. Write a paragraph comparing the melt and water output computed by the energy balance, the temperature-index approach, and the hybrid approach under the various conditions. Describe the reasons for any significant differences.
7. Use the approach described in section 5.6 and box 5.3 to compute the time lag for the water output from ripe snowpacks under the following conditions:

Case	Snow Depth (cm)	Density (kg/m ³)	Grain Size (mm)	Melt Rate (cm/hr)
1	1	400	2	1
2	2	500	1	2
3	5	400	2	5
4	1	350	1	2

▼ NOTES

¹ See section 1.10.

² Rainfall interception and interception loss are discussed in detail in chapter 6.

³ In some regions and some years, snow covers may form and melt more than once during the winter; in these cases each successive snowpack will go through an accumulation period and the three phases of the melt period.

⁴ θ_{ret} is directly analogous to the “field capacity” of a soil, defined in chapter 8.



6

Evapotranspiration

Evapotranspiration is the collective term for all the processes by which water in the liquid or solid phase at or near the earth's land surfaces becomes atmospheric water vapor. The term thus includes evaporation from rivers and lakes (open water), bare soil, and vegetative surfaces (**interception loss**); evaporation from within the leaves of plants (**transpiration**); and sublimation from ice and snow surfaces.

Globally, about 62% of the precipitation that falls on the continents is evapotranspired, amounting to 73,000 km³/yr (table 2.6). Of this, about 42% (29,000 km³/yr) is transpiration (various models estimate a range from 25 to 64%; Wang and Dickinson 2012) and about 3% (2,000 km³/yr) is open-water evaporation. Most of the remainder is interception loss; soil evaporation is a minor component of the total. Figure 2.27 shows the global distribution of evapotranspiration, and tables 2.7 and 2.8 give data on evapotranspiration from the continents and from major river basins. Note that evapotranspiration exceeds runoff in most of the river basins and on all the continents except Antarctica.

A quantitative understanding of evapotranspiration is of vital practical importance:

- Evapotranspiration is a major component of energy as well as water-vapor exchange between land surfaces and atmosphere (figure 2.3). Understanding

relations between evapotranspiration and ecosystem type is a requirement for predicting ecosystem response to climate change (Woodward 1987).

- Evapotranspiration is essential to the growth of plants that form the base of natural ecosystems and agriculture.
- Over the long term, the difference between continental precipitation and evapotranspiration is the water available for direct human use and management. Thus quantitative assessments of water resources and the effects of climate and land-use change on those resources require a quantitative understanding of evapotranspiration.
- Much of the world's food supply is grown on irrigated land, and irrigation is one of the largest uses of water in the United States and many other countries. Efficient irrigation requires knowledge of crop water use (transpiration), so that water will be applied only as needed.
- Evaporation has a significant influence on the yield of water-supply reservoirs, and thus on the economics of building reservoirs of various sizes.
- The fraction of water falling in a given rain storm that contributes to streamflow and to ground-water recharge is in large part determined by the "wetness" of the land; this wetness depends on the

amount of evapotranspiration that has occurred since the previous storm.

Direct measurement of evapotranspiration is much more difficult and expensive than of precipitation and streamflow, and is usually impractical. Thus hydrologists have developed an array of methods that provide estimates of evapotranspiration based on measurements of more readily measured quantities. A major goal of this chapter is to show how these methods are based on the basic physics of radiant-energy exchange (section 2.1.3), the laws of gases (sections 3.1 and 3.2), and the physics of turbulent mass and energy exchange (turbulent diffusion) at the earth's surface (sections 3.3 and 3.5). These relations are involved in liquid-vapor and solid-vapor phase changes at all surfaces, including transpiring leaves, and the chapter begins by reviewing and extending those basic relations. Following this we define the basic types of evapotranspiration, and then focus on methods of estimation appropriate for each type in various situations. We concentrate here on the liquid-vapor transition, since evaporation from snow was discussed in chapter 5.

6.1 Evaporation and Heat-Exchange Processes

6.1.1. Vapor-Pressure Relations

The vapor pressure of an evaporating surface, e_s , is equal to the saturation vapor pressure at the surface temperature, $e^*(T_s)$, so

$$e_s = e^*(T_s), \quad (6.1)$$

where $e^*(T_s)$ is given to good approximation by

$$e^*(T) = 0.611 \cdot \exp\left(\frac{17.3 \cdot T}{T + 237.3}\right), \quad (6.2)$$

with $T = T_s$ in °C and vapor pressure is in kPa.

The vapor pressure at height z above the surface, $e(z)$, depends on the relative humidity, $RH(z)$, as well as the air temperature, $T(z)$:

$$e(z) = RH(z) \cdot e^*[T(z)], \quad (6.3)$$

where $e^*[T(z)] = e^*(z)$ is the saturation vapor pressure at the air temperature.

Some approaches to estimating evapotranspiration make use of the slope of the relation between saturation vapor pressure and temperature, Δ . Its value can be found by taking the derivative of equation (6.2):

$$\Delta(T) \equiv \frac{de^*(T)}{dT} = \frac{2,508.3}{(T + 237.3)^2} \cdot \exp\left(\frac{17.3 \cdot T}{T + 237.3}\right), \quad (6.4)$$

where $\Delta(T)$ is in kPa/C° and T is in °C. Note that, like $e^*(T)$, $\Delta(T)$ increases exponentially with temperature.

6.1.2 Evaporation as a Diffusive Process

The physical mechanism by which water vapor is transferred from a water or leaf surface to the atmosphere is turbulent diffusion, as described in section 3.5. Fick's law of diffusion states that the rate of transfer (flux), F_S , of a constituent S in the z -direction, is directly proportional to the gradient of concentration, χ_S , of S in that direction:

$$F_S = -D_S(z) \cdot \frac{d\chi_S(z)}{dz}. \quad (6.5)$$

The proportionality parameter D_S is the **diffusivity** of S in the fluid (figure 3.12). For our purposes, the quantity S may represent water vapor, latent heat, or sensible heat, and the z -coordinate is directed vertically upward.

The diffusivity characterizes the vertical transport effected by turbulent eddies that result from (1) surface friction acting on horizontal winds (**forced convection**) and/or (2) buoyancy due to heating at the surface (**free convection**). In the absence of buoyancy effects (**neutral stability**), the vertical distribution of wind velocity is given by the **Prandtl-von Kármán universal velocity distribution**:

$$u(z) = \frac{1}{\kappa} \cdot u_* \cdot \ln\left(\frac{z - z_d}{z_0}\right), \quad z_d + z_0 \leq z, \quad (6.6)$$

where $u(z)$ is the time-averaged wind velocity at height z above the ground surface, u_* is the “friction velocity” [which must be determined from measured values of $u(z)$], κ is a dimensionless constant ≈ 0.4 , the height z_d is called the **zero-plane displacement height**, and z_0 is the **roughness height** (figure 3.10). As noted in section 3.5.2, z_d and z_0 can be taken to be proportional to the average height of the roughness elements on the surface. Note from (6.6) that $u(z) = 0$ at $z = z_d + z_0$, which is the virtual surface. Typical z_0 and z_d values for water and various vegetation categories are given later in this chapter.

As developed in section 3.5.3.4, the combination of equations (6.5) and (6.6) and ideal gas laws gives the **mass-transfer equation** for evaporation rate, E [L T⁻¹]:

$$E = -\frac{0.622 \cdot \rho_a}{p \cdot \rho_w} \cdot \frac{\kappa^2 \cdot [u(z_2) - u(z_1)] \cdot [e(z_2) - e(z_1)]}{\left[\ln\left(\frac{z_2 - z_d}{z_1 - z_d}\right) \right]^2}, \quad (6.7)$$

where p is atmospheric pressure, ρ_a and ρ_w are the mass densities of air and water, respectively, and $e(z_1)$ and $e(z_2)$ are vapor pressures at heights z_1 and z_2 . Note that, since $u(z_2) > u(z_1)$, evaporation occurs ($E > 0$) when $e(z_1) > e(z_2)$; when $e(z_1) < e(z_2)$, condensation occurs at the surface ($E < 0$).

If we assume that the surface velocity $u_s \equiv u(z_d + z_0) = 0$ and designate e_s as the vapor pressure at the evaporating surface, we can simplify (6.7) to

$$E = -\frac{0.622 \cdot \rho_a}{p \cdot \rho_w} \cdot \frac{\kappa^2 \cdot u(z_m) \cdot [e(z_m) - e_s]}{\left[\ln\left(\frac{z_m - z_d}{z_0}\right) \right]^2}. \quad (6.8)$$

Note that κ is a constant, and that typical near-surface values for $\rho_a = 1.220 \text{ kg/m}^3$, $\rho_w = 1,000 \text{ kg/m}^3$, and $p = 101.3 \text{ kPa}$, can often be assumed (table 3.1). In this case the evaporation rate can be estimated via equation (6.7) using measurements of wind velocity, temperature, and humidity at two levels as

$$E = 1.20 \times 10^{-6} \cdot \frac{[u(z_2) - u(z_1)] \cdot [e(z_1) - e(z_2)]}{\left[\ln\left(\frac{z_2 - z_d}{z_1 - z_d}\right) \right]^2}, \quad (6.9)$$

where the vapor pressures are in kPa; or via equation (6.8) by measuring those quantities at one level, z_m , and vapor pressure (e_s^*) at the surface:

$$E = 1.20 \times 10^{-6} \cdot \frac{u(z_m) \cdot [e_s^* - e(z_m)]}{\left[\ln\left(\frac{z_m - z_d}{z_0}\right) \right]^2}. \quad (6.10)$$

Further simplification is possible if we assume a standard measurement height (e.g., $z_m = 2 \text{ m}$ typically) and, for a given surface, typical values of z_d and z_0 . In this case we can define a **water-vapor transfer coefficient** K_E with dimensions [$\text{L}^2 \text{ F}^{-1}$],

$$\begin{aligned} K_E &\equiv \frac{0.622 \cdot \kappa^2 \cdot \rho_a}{\rho_w \cdot p \cdot \left[\ln\left(\frac{z_m - z_d}{z_0}\right) \right]^2} \\ &= \frac{1.20 \times 10^{-6}}{\left[\ln\left(\frac{z_m - z_d}{z_0}\right) \right]^2} \cdot \text{kPa}^{-1}, \end{aligned} \quad (6.11)$$

and write the mass-transfer relation for evapotranspiration in its most simplified form as:

$$E = K_E \cdot u(z_m) \cdot [e_s - e(z_m)]. \quad (6.12)$$

This shows that, for a given surface,

Evaporation/condensation rate is proportional
to the product of near-surface vapor-pressure
difference and wind speed.

6.1.3 Latent-Heat Exchange

As explained in section 3.3.2, evaporation/condensation is always accompanied by a transfer of latent heat from/to the evaporating body to/from the air. The rate (flux) of latent-heat transfer, λE [$\text{E L}^{-2} \text{ T}^{-1}$], is found simply by multiplying the evaporation rate by the latent heat of vaporization, λ_v , and the mass density of water, ρ_w :

$$\lambda E = \rho_w \cdot \lambda_v \cdot E. \quad (6.13)$$

The latent heat of vaporization decreases as the temperature of the evaporating surface increases; this relation is given approximately by

$$\lambda_v = 2.50 - 2.36 \times 10^{-3} \cdot T, \quad (6.14)$$

where λ_v is in MJ/kg and T is in °C.

6.1.4 Sensible-Heat Exchange

As developed in section 3.5.3.6, the upward rate (flux) of sensible-heat exchange by turbulent diffusion under neutral-buoyancy conditions, H , is

$$H = \rho_a \cdot c_p \cdot \frac{\kappa^2 \cdot [u(z_2) - u(z_1)] \cdot [T(z_1) - T(z_2)]}{\left[\ln\left(\frac{z_2 - z_d}{z_1 - z_d}\right) \right]^2}, \quad (6.15)$$

where $T(z)$ is temperature at height z . As in equation (6.8), this can be written for use with measurements at the surface and one level,

$$H = \rho_a \cdot c_p \cdot \frac{\kappa^2 \cdot u(z_m) \cdot [T_s - T(z_m)]}{\left[\ln\left(\frac{z_m - z_d}{z_0}\right) \right]^2}, \quad (6.16)$$

where T_s is surface temperature.

And, as in equation (6.11) we can use standard surface values of $c_a = 1.00 \times 10^{-3}$ MJ/kg · K, $\rho_a = 1.220$ kg/m³, and $\kappa = 0.4$, to define a **sensible-heat-transfer coefficient**, K_H :

$$\begin{aligned} K_H &\equiv c_a \cdot \rho_a \cdot \frac{\kappa^2}{\left[\ln\left(\frac{z_m - z_d}{z_0}\right) \right]^2} \\ &= \frac{1.95 \times 10^{-4}}{\left[\ln\left(\frac{z_m - z_d}{z_0}\right) \right]^2} \text{ MJ/m}^3 \cdot \text{K}, \end{aligned} \quad (6.17)$$

to show that, for a given surface,

Sensible-heat flux is proportional to the product of near-surface temperature difference and wind speed:

$$H = K_H \cdot u(z_m) \cdot [T_s - T(z_m)]. \quad (6.18)$$

6.1.5 The Bowen Ratio, the Psychrometric Constant, and the Evaporative Fraction

In developing approaches to estimating evapotranspiration based on energy balances we will see that it is sometimes useful to incorporate the ratio of sensible-heat exchange to latent-heat exchange. This quantity, originally formulated by Bowen (1926), is called the **Bowen ratio**, B :

$$B \equiv \frac{H}{\lambda E}. \quad (6.19)$$

Combining equations (6.8), (6.16), and (6.19), we have

$$B = \frac{c_a \cdot p \cdot [T_s - T(z_m)]}{0.622 \cdot \lambda_v \cdot [e_s - e(z_m)]} = \gamma \cdot \frac{[T_s - T(z_m)]}{[e_s - e(z_m)]}. \quad (6.20)$$

Thus the Bowen ratio depends on the ratio of surface-air temperature difference to surface-air vapor-pressure difference, multiplied by a factor γ , where

$$\gamma \equiv \frac{c_a \cdot p}{0.622 \cdot \lambda_v}. \quad (6.21)$$

The factor γ [F L⁻² Θ⁻¹] enters separately into some expressions for estimating evapotranspiration, and is called the **psychrometric constant**.¹ Using typical values of $c_a = 1.00 \times 10^{-3}$ MJ/kg · K, $p = 101.3$ kPa, and $\lambda_v = 2.47$ MJ/kg, $\gamma = 0.066$ kPa/K, and that value is commonly used. However, γ is not strictly a constant: Its value should be adjusted for the effect of elevation on pressure (figure 2.2) and the effect of temperature on latent heat [equation (6.14)].

It has also proved useful in studies of regional evapotranspiration to define the **evaporative fraction**, EF , as the ratio of latent-heat flux to total turbulent-heat flux:

$$EF \equiv \frac{\lambda E}{\lambda E + H} = \frac{1}{B + 1}. \quad (6.22)$$

6.1.6 The Energy Balance

Both evaporation/condensation as a latent-heat flux and the transfer of sensible heat between a surface and the atmosphere involve the removal or addition of energy from the surface. Thus these processes are intimately involved with the energy balance of the surface. The general energy balance for an evapotranspiring body during a time period Δt can be written as

$$\lambda E = K + L - G - H + A_w - \frac{\Delta U}{\Delta t}, \quad (6.23)$$

where the first six terms represent average energy fluxes (energy per unit area of evaporating surface per unit time) via the following modes: (1) evaporation, λE ; (2) net shortwave radiation input, K ; (3) net longwave radiation input, L ; (4) net output via conduction downward from the surface, G ; (5) net output of sensible-heat exchange with the atmosphere, H ; and (6) net input associated with inflows and outflows of water (**water-advedted energy**), A_w . ΔU is the change in the amount of heat stored in the body per unit area between the beginning and end of Δt .² Where appropriate, a term representing the energy used in photosynthesis can be included in equation (6.23), but this term is usually small ($\leq 3\%$ of $K + L$ for crops; C. A. Federer, pers. comm.).

From equation (6.23) we see that any evaporation occurring during Δt must be balanced by some combination of heat inputs from radiation or sensible heat from the atmosphere, from below, or from inflowing water, and/or a loss of heat energy (i.e., a temperature reduction) in the evaporating body.

6.2 Classification of Evapotranspiration Processes

Various methods for estimating evapotranspiration have been developed for specific surfaces and energy-exchange situations determined by the following conditions:

- **Type of surface:** open water, bare soil, leaf or leaf canopy, a specific *reference crop* (usually a complete cover of well-watered grass, as discussed later), or land region (generally including vegetated surfaces, surface-water bodies, and areas of bare soil);
- **Availability of water:** unlimited water available to evaporate, or water supply to the air, may be limited because water vapor must pass through plant openings or soil pores;
- **Stored-energy use:** ΔU in equation (6.23) may be significant or negligible; and
- **Water-advedted energy use:** A_w in equation (6.23) may be significant or negligible.

Table 6.1 shows how the various “types” of evapotranspiration are distinguished with respect to the above conditions, and the methods described in subsequent sections of this chapter are classified according to these types.

Additional considerations in choosing a method for use in a given circumstance are: (1) the purpose of the analysis (e.g., determination of the amount of evapotranspiration that has actually occurred in a given situation, incorporation in a hydrologic model, reservoir design, general water-resources assessment, etc.); (2) the available data (particular meteorological parameters measured and whether measurements were made at the area of interest or are estimated regional values); and (3) the time period of interest (hourly, daily, monthly, annual, climatic average). We will indicate the applicability of the various methods with respect to these considerations.

6.3 Free-Water and Lake Evaporation

In natural water bodies, water-advedted heat and changes in heat storage may play a significant role in the energy balance [equation (6.23)]. The magnitude of these components in a particular case depends in large part on the area, volume, and residence time of water in the lake relative to the time period of the analysis. Because of the variable importance of these nonmeteorologic factors in the energy balance, it is not generally possible to develop equations for predicting the evaporation for a particular lake from meteorologic data alone. In order to develop general methods for estimating evaporation from surface-water bodies, hydrometeorologists have formulated the theoretical concept of *free-water evaporation*:

Table 6.1 Classification of Types of Evapotranspiration.

Evapotranspiration Type	Type of Surface	Availability of Water to Surface	Stored Energy Use	Water-Advedted Energy Use
Free-water evaporation ^a	Open water	Unlimited	None	None
Lake evaporation	Open water	Unlimited	May be involved	May be involved
Bare-soil evaporation	Bare soil	Limited to unlimited	Negligible	None
Transpiration	Leaf or leaf canopy	Limited	Negligible	None
Interception loss	Leaf or leaf canopy	Unlimited	Negligible	None
Potential evapotranspiration	Reference crop ^b	Limited to air, unlimited to plants	None	None
Actual evapotranspiration	Land area ^c	Varies in space and time	Negligible	None

^aAlso called **potential evaporation**.

^bUsually a complete ground cover of uniform short vegetation (e.g., grass); discussed further in section 6.7.1.

^cMay include surface-water bodies and areas of bare soil.

Free-water, or potential, evaporation (E_0) is the rate (flux) of evaporation that would occur from an extended open-water surface under current meteorologic conditions without heat-storage or water-adverted-energy effects.

Lake evaporation is determined by adjusting free-water evaporation to account for the advection and heat-storage effects in a given water body. In the following discussion of methods, we will indicate how each approach can be applied to estimating free-water evaporation and lake evaporation.

6.3.1 Eddy Correlation

6.3.1.1 Theoretical Basis

As described in section 3.5.4, turbulence theory indicates that the flux of upward movement of water vapor near the surface (i.e., the local evaporation rate) is proportional to the time average of the product of the instantaneous fluctuations of upward air velocity, v' , and of absolute humidity, q' , around their respective mean values:

$$E_0 = \frac{\rho_a}{\rho_w} \cdot \overline{v' \cdot q'}, \quad (6.24)$$

where the overbar denotes time averaging.

If sensors capable of accurately recording and integrating high-frequency (on the order of 10 s^{-1}) fluctuations in humidity and vertical velocity are used, equation (6.24) is often considered to give the “true” evaporation rate because the method has a sound theoretical foundation and requires no assumptions about parameter values, the shape of the velocity profile, or atmospheric stability.

6.3.1.2 Practical Considerations

The eddy-correlation approach is mathematically complex and has stringent instrumentation requirements. It is increasingly used in studies of land evapotranspiration, but the additional difficulties of modifying the instrumentation for installation on rafts make it impractical for operational evaporation estimates over open water.

The eddy-correlation approach can give measurements of free-water evaporation representative of limited ($\sim 1 \text{ ha}$) areas upwind of the sensors, with accuracies of about 10% for time periods as short as 0.5 hr (Stannard and Rosenberry 1991). However, recent comparative studies indicate that the method tends to

give evaporation rates only about 80% of the rates given by energy-balance approaches, perhaps because it does not measure fluctuations over the full range of turbulent-eddy sizes (Wang and Dickinson 2012).

6.3.2 Mass Transfer

6.3.2.1 Theoretical Basis

The mass-transfer approach makes direct use of equation (6.12), often in the form

$$E_0 = [b_0 + b_1 \cdot u(z_m)] \cdot [e_s - e(z_m)], \quad (6.25)$$

where b_0 accounts for any free-convection effects and b_1 depends chiefly on the height and location at which wind speed and air vapor pressure are measured.

The theoretical analysis leading to equations (6.11) and (6.12) indicates that, in the absence of buoyancy effects, $b_0 = 0$ and $b_1 = K_E$. Thus we can evaluate b_1 by inserting appropriate numerical values for the quantities in equation (6.11). Published values of z_0 for water surfaces range from 1×10^{-4} to $1.2 \times 10^{-3} \text{ m}$. Using $z_0 = 5 \times 10^{-4} \text{ m}$ and $z_d = 0 \text{ m}$ (Brutsaert 1982) along with standard values for air and water properties and a measurement height of 2 m, we find

$$E_0 = 1.7 \times 10^{-8} \cdot u(2 \text{ m}) \cdot [e_s - e(2 \text{ m})], \quad (6.26a)$$

where E_0 and $u(2 \text{ m})$ are in the same units and vapor pressures are in kPa. When $u(2 \text{ m})$ is in m/s and E_0 is in mm/day, the relation becomes

$$E_0 = 1.5 \cdot u(2 \text{ m}) \cdot [e_s - e(2 \text{ m})]. \quad (6.26b)$$

The evaporation rate is also affected by atmospheric stability (section 3.5.3.7). When the water surface is warmer than the air, the air in contact with the surface is warmed by conduction and tends to rise, so that there is turbulent transport of water vapor (and heat) away from the surface even in the absence of wind ($b_0 > 0$). This **free convection** is most common in situations where the water body has been artificially heated, as in a cooling pond or a river reach receiving heated water from a power plant. However, it also occurs in large lakes because of thermal inertia: Derecki (1981) found considerable seasonal variation for Lake Superior, with $b < 0$ in summer when the lake is colder than the air, and $b > 0$ in fall and winter when the lake is warmer. One approach to account for the effect of atmospheric instability on K_E when $T_s > T_a$ is to model b_0 in equation (6.25) as a positive quantity that increases with the temperature difference between the surface and

the air. In a comparative study of several evaporation equations, Rasmussen et al. (1995) found that the following gave the best results:

$$E_0 = \frac{\left[2,330 \cdot [T_s - T(z_m)]^{1/3} + 2,680 \cdot u(z_m) \right] \cdot [e_s - e(z_m)]}{\rho_w \cdot \lambda_v}, \quad T_s > T(z_m), \quad (6.27)$$

where E_0 is evaporation rate in mm/day; T_s and $T(z_m)$ are in °C; $u(z_m)$ is in m/s; e_s and $e(z_m)$ are in kPa, ρ_w is in kg/m³, and λ_v is in MJ/kg.

6.3.2.2 Practical Considerations

Use of equation (6.26) or (6.27) requires measurement of wind speed, air temperature, and humidity at a height above the surface, and of surface temperature. Clearly all measured values should be representative of the entire water body, which may be difficult to accomplish using shore-based observation stations (Sene et al. 1991). In fact, in a comparative study, Winter et al. (1995, p. 991) concluded that “the mass transfer equation is acceptable only if a raft station is used so that water temperature and wind speed data can be obtained near the center of the lake.” If the lake surface is highly irregular with many inlets, it may be difficult to obtain measurements representative of the entire water body, although surface temperature may be obtained from satellite observations of outgoing thermal radiation (Croley 1989).

Many studies have been done to verify the appropriate values for b_0 and b_1 and, because of variations in lake size, measurement height, instrument location, atmospheric stability, and time scale, each study has obtained a different set of values. The Lake Hefner project (Harbeck et al. 1954) and a study by Ficke (1972) in Indiana were among the most detailed and careful of these studies because accurate estimates of daily evaporation could be independently obtained via the water balance. In both cases, $e(z_m)$ represents the vapor pressure of the air unmodified by passage over the lake. Both studies confirmed that $b_0 = 0$, and Harbeck et al. (1954) found K_E almost identical to the value in equation (6.26) while Ficke (1972) found K_E about 15% smaller. A later study of Lake Erie found K_E very close to Harbeck’s Lake Hefner value (Derecki 1976).

It appears that much of the variability in K_E found in various studies is a function of lake area. Harbeck (1962) found that the empirical relation

$$K_E = 1.26 \cdot A_L^{-0.05} \quad (6.28)$$

can be used in equation (6.26) when lake area A_L is in km², $u(2\text{ m})$ is in m/s, vapor pressures are in kPa, and E_0 is in mm/day. There are two reasons for this area effect: (1) since water surfaces are smoother than land surfaces, the efficiency of turbulent eddies in the vertical transport of water vapor decreases as the wind travels longer distances over a lake and (2) the vapor pressure will increase with downwind distance as evaporation occurs, decreasing the effective vapor-pressure difference over the lake compared with the value measured anywhere except on the downwind shore.

Thus the mass-transfer approach is potentially useful for determining the amount of free-water evaporation that has occurred during a given time period during which $u(z_m)$, T_s , $T(z_m)$, and $RH(z_m)$ have been measured at a representative location. However, the mass-transfer equation is derived for the *instantaneous* rate of evaporation under given *instantaneous* values of wind speed and vapor pressure. Because the vapor pressures are determined from measured temperatures via the nonlinear relation of equation (6.2), and because wind speed and vapor-pressure differences may be correlated, one cannot assume that the approach will give the correct *time-averaged* rate of evaporation when time-averaged temperatures and wind speeds are used as independent variables. Using Lake Hefner data, Jobson (1972) determined the errors that are introduced in calculating average evaporation from averaged temperatures and wind speeds for averaging periods of 3 hr, 1 day, and 1 month. The results, shown in table 6.2, indicate that little error is introduced for averaging periods up to 1 day, but that a bias is introduced with monthly averaging.

Table 6.2 Errors in Computing Time-Averaged Evaporation Using Time-Averaged Temperatures and Wind Speeds.

	Averaging Period		
	3 hr	1 day	1 month
Median % error	0	0	+4
% of time periods with less than 5% error	97	79	—
% of time periods with less than 10% error	>99	93	—

Source: Data from Jobson (1972), based on Lake Hefner studies.

In general, the mass-transfer method can be used to predict, forecast, or model free-water evaporation based on predicted, forecast, or modeled values of the independent variables. It is particularly useful for modeling artificially heated water bodies, for which surface temperatures can usually be readily calculated. However, it is difficult to apply the method for predicting evaporation in naturally heated water bodies, because there are virtually no climatic data on water-surface temperatures, and modeling such temperatures is difficult. In a comparative study on a small lake Rosenberry et al. (2007) found that mass-transfer methods often showed large deviations from evaporation rates calculated by other methods.

6.3.3 Energy Balance

6.3.3.1 Theoretical Basis

Equation (6.23) is the energy-balance equation for an evaporating water body. Solving this for evaporation rate,

$$E = \frac{K + L - H - G + A_w - \Delta U/\Delta t}{\rho_w \cdot \lambda_v}, \quad (6.29)$$

where E has dimensions [L T^{-1}]. By definition, free-water evaporation is calculated by including only the terms involving energy exchange at the surface:

$$E_0 = \frac{K + L - H}{\rho_w \cdot \lambda_v}. \quad (6.30)$$

Equations (6.29) and (6.30) can be written in a different and often more useful form by using the Bowen ratio [equation (6.19)]: The sensible heat-loss rate, H , is replaced by

$$H = B \cdot \lambda E = B \cdot \rho_w \cdot \lambda_v \cdot E, \quad (6.31)$$

so that (6.29) becomes

$$E = \frac{K + L - G + A_w - \Delta U/\Delta t}{\rho_w \cdot \lambda_v \cdot (1 + B)}, \quad (6.32)$$

and (6.30) becomes

$$E_0 = \frac{K + L}{\rho_w \cdot \lambda_v \cdot (1 + B)}. \quad (6.33)$$

Use of (6.32) or (6.33) is usually preferable to (6.29) or (6.30) because it does not require measurements of wind speed, only the near-surface temperature and vapor-pressure differences, and does not require adjustments for nonneutral stability conditions except in extreme cases (Wang and Dickinson

2012). However, problems arise when the vapor-pressure difference becomes very small, such that $B \rightarrow \infty$.

Conceptually, net water-adverted energy is found from

$$A_w = c_w \cdot \rho_w \cdot (P \cdot T_P + Q_{in} \cdot T_{Qin} - Q_{out} \cdot T_{Qout} + GW_{in} \cdot T_{GWin} - GW_{out} \cdot T_{GWout}), \quad (6.34)$$

where c_w is the specific heat of water, P is precipitation rate, Q and GW , respectively, represent surface-water and ground-water inflows and outflows expressed as volumes per time per unit lake area, and T represents the various temperatures of the respective inflows and outflows. All the quantities in (6.34) represent averages over the measurement period.

The change in energy storage in a lake is found from the volumes and average temperatures of the lake water at the beginning and end of Δt :

$$\Delta U = c_w \cdot \rho_w \cdot (V_2 \cdot T_{L2} - V_1 \cdot T_{L1}), \quad (6.35)$$

where V is lake volume, T_L is average lake temperature, and the subscripts 1 and 2 designate values at the beginning and end of Δt , respectively.

6.3.3.2 Practical Considerations

The energy-balance approach requires precise determination of all the nonnegligible quantities in the basic equation because all measurement errors are included in the final computation of evaporation. However, it is often possible to determine values of the surface energy-balance components with greater accuracy than possible for other approaches, and the energy-balance/Bowen-ratio approach is often used as the standard determination of free-water evaporation against which other methods are compared (Winter et al. 1995; Rosenberry et al. 2007). Ways of determining values of the radiation components when direct measurements are lacking were introduced in section 5.5.2; these are reviewed and extended in box 6.1.

In most situations, the heat exchange by conduction between a lake and the underlying sediments (G) is not measured and is assumed negligible. Rosenberry et al. (1993) found that this term accounted for about 7% of evaporation.

For determining lake evaporation, the magnitude of the advection and heat-storage terms must be assessed. These depend on the climate, geologic and hydrologic setting, and the area, volume, and residence time of water in the lake relative to the time

period of the analysis. Clearly, a detailed evaluation of the advection term is a formidable measurement challenge. However, Kohler and Parmele (1967) stated that the effects of advected energy are small—unless inflows and outflows are large relative to evaporation, and even then only if inflow and outflow temperatures differ appreciably. In many cases, errors may be minimized by choosing Δt so that the term in parentheses in equation (6.34) is likely to be

Box 6.1 Determination of Shortwave and Longwave Radiation Fluxes for Energy-Balance Computations

Shortwave (Solar)

Net shortwave, or solar, radiation, K , is given by

$$K = K_{in} \cdot (1 - a), \quad (6B1.1)$$

where K_{in} is incident solar radiation and a is the albedo (shortwave reflectivity) of the water surface. Incident and reflected solar radiation can be measured with pyranometers, but this is routinely done at only scattered locations. Where K_{in} is not directly measured, it is best determined from hourly, daily, and monthly insolation values representative of large areas ($\sim 0.5^\circ$ latitude \times 0.5° longitude) developed from Geostationary Operational Environmental Satellite (GOES) imagery (Justus et al. 1986). When observations of the fraction of sky covered by cloud, C , are available, K_{in} can be determined from empirical relations such as

$$K_{in} = [0.355 + 0.68 \cdot (1 - C)] \cdot K_{cs} \quad (6B1.2)$$

(Croley 1989), where K_{cs} is the incident clear-sky solar radiation determined from the latitude, time of year, and humidity using the relations given in appendix D. However, manual observations of C are no longer routinely available in the United States.

Koberg (1964) presented an empirical relation giving the albedo of a water surface as a function of K_{in} :

$$a = 0.127 \cdot \exp(-0.0258 \cdot K_{in}), \quad (6B1.3)$$

where K_{in} is in $\text{MJ/m}^2 \cdot \text{day}$; other studies have assumed a constant albedo value in the range $0.05 \leq a \leq 0.10$.

Longwave

The net input of longwave energy, L , is the difference between the incident flux, L_{in} , emitted by the atmosphere and clouds and the outgoing radiation from the surface, L_{out} :

$$L \equiv L_{in} - L_{out}. \quad (6B1.4)$$

L_{in} and L_{out} can be measured directly by means of **pyrgeometers** or as the difference between all-wave radiation measured by a **radiometer** and shortwave

small. In most situations this will be true if $\Delta t = 1 \text{ yr}$ unless the residence time of water in the lake is greater than 1 yr.

The ΔU term may be quite well constrained by measuring water-temperature profiles and lake volume at the beginning and end of the measurement period. In regions that experience cold winters, lakes become isothermal at the temperature of maximum density (3.98°C) in the fall and spring, so those times

radiation measured by a pyranometer. However, such measurements are available at only a few locations, so the longwave component of the energy balance is usually estimated using the Stefan–Boltzmann equation [equation (2.1)] and readily available meteorological observations as described below.

Incident longwave energy flux is given by

$$L_{in} = \varepsilon_{at} \cdot \sigma \cdot T_a^4, \quad (6B1.5)$$

where ε_{at} is the integrated effective emissivity of the atmosphere, σ is the Stefan–Boltzmann constant ($\sigma = 4.90 \times 10^{-9} \text{ MJ/m}^2 \cdot \text{K}^4 \cdot \text{d}$), and T_a is the air temperature (K). The outgoing longwave flux is the sum of the radiation emitted by the lake surface and the portion of the incident radiation reflected by the surface. Since the longwave reflectivity of a surface equals one minus its longwave emissivity,

$$L_{out} = \varepsilon_s \cdot \sigma \cdot T_s^4 + (1 - \varepsilon_s) \cdot L_{in}, \quad (6B1.6)$$

where the subscript s designates surface values. Combining equations (6B1.4)–(6B1.6), expanding, and simplifying gives

$$L = \varepsilon_s \cdot \varepsilon_{at} \cdot \sigma \cdot T_a^4 - \varepsilon_s \cdot \sigma \cdot T_s^4, \quad (6B1.7)$$

where $\varepsilon_s = 0.95$ for water.

As discussed in section 5.5.2.2, ε_{at} is largely a function of humidity and cloud cover. Flerchinger et al. (2009) reviewed empirical formulas for estimating ε_{at} and found the best results using

$$\varepsilon_{at} = (1 - 0.84 \cdot C) \cdot [0.83 - 0.18 \cdot \exp(-1.54 \cdot e_a)] + 0.84 \cdot C, \quad (6B1.8)$$

where surface vapor pressure $e_a > 0.285 \text{ kPa}$ and C is fractional cloud cover. However, Abramowitz et al. (2012) found that

$$L_{in} = 2.7 \cdot e_a + 0.245 \cdot T_a - 45.14 \quad (6B1.9)$$

(where L_{in} is in $\text{MJ/m}^2 \cdot \text{day}$ and e_a is in kPa) performed best for both clear and cloudy conditions, and suggested its use without correcting for clouds.

can be used to bound Δt . It may be possible to relate average lake temperature to water-surface temperature (Rosenberry et al. 1993), which can be remotely sensed; however, the relation between the two must be established for each lake, and at least for deep lakes will vary seasonally. This is shown in figure 6.1: Heat storage reaches a maximum in the fall in Lake Superior, shifting the annual peak of evaporation such that it is out of phase with the annual cycles of air temperature, water temperature, and humidity (Croley 1992). Kohler and Parmele (1967) found that heat-storage effects can be neglected in computing long-term average evaporation for all lakes, and annual evaporation for lakes with residence times less than 1 yr.

Even if there are significant advection and/or heat-storage effects on the water temperature in a given lake, only a portion of that energy affects evaporation; the rest affects sensible-heat exchange and longwave radiation emission. Kohler and Parmele (1967) developed a general approach for assessing the fraction of the advection and heat-storage effects that is reflected in lake evaporation; this is summarized in box 6.2 and figure 6.2, both on p. 264. It suggests that in many cases, less than half the energy inputs or losses due to advection and storage are reflected in

the evaporation rate, reducing the difference between lake evaporation and free-water evaporation.

L. J. Anderson, who conducted the elaborate energy-balance studies at Lake Hefner, concluded that “the energy-budget equation, when applied to periods greater than 7 days, will result in a maximum accuracy approaching ± 5 per cent of the mean . . . evaporation, providing all terms in the energy budget have been evaluated with the utmost accuracy, particularly changes in energy storage” (Harbeck et al. 1954, p. 117). He found that considerable error in evaluating the change in energy storage may occur if the method is applied to periods of less than seven days. Rosenberry et al. (1993) found that the energy-budget approach gave the best estimates of lake evaporation for a small lake in Minnesota and investigated the effects of using various instrumentation and approaches to determining energy-budget components.

As with the mass-transfer method, it is difficult to apply the energy-budget approach in the prediction, forecasting, or modeling mode because of the requirement for water-surface temperatures. However, Hostetler and Bartlein (1990) developed a model that simulates the vertical distribution of lake temperatures through time coupled to energy-balance computations, and this appears promising as an

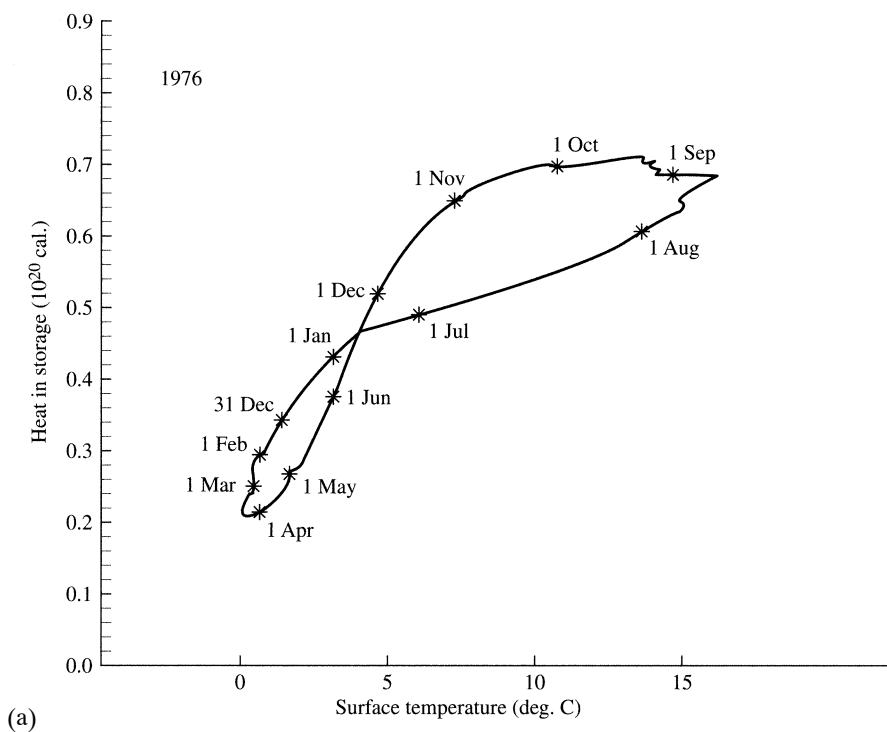


Figure 6.1 (a) Variation of total heat storage with surface temperature in Lake Superior in 1976. (b) Annual cycles of air temperature, humidity, wind speed, water temperature, and evaporation in Lake Superior, 1975–1977 [Croley (1992). Long-term heat storage in the Great Lakes. *Water Resources Research* 28:69–81, with permission of the American Geophysical Union].

approach to estimating the effects of past and future climate change on lake evaporation.

As we will see in the next section, the most useful applications of the energy-balance approach are in combination with the mass-transfer method, whereby one can eliminate the need for surface data in estimating free-water evaporation.

6.3.4 Penman or Combination Method

6.3.4.1 Theoretical Basis

Penman (1948) was the first to show that the mass-transfer and energy-balance approaches could be combined to arrive at an evaporation equation that did not require surface-temperature data. Fol-

lowing the steps shown in box 6.3 on p. 265, Van Bavel (1966) generalized Penman's original development by replacing an empirical wind function with equation (6.9), resulting in the following theoretically sound relation for free-water evaporation:

$$E_0 = \frac{\Delta \cdot (K + L) + \gamma \cdot K_E \cdot \rho_w \cdot \lambda_v \cdot u(z_m) \cdot [e^*(z_m) - e(z_m)]}{\rho_w \cdot \lambda_v \cdot (\Delta + \gamma)}, \quad (6.36a)$$

$$= \frac{\Delta \cdot (K + L) + \gamma \cdot K_E \cdot \rho_w \cdot \lambda_v \cdot u(z_m) \cdot e^*(z_m) \cdot [1 - RH(z_m)]}{\rho_w \cdot \lambda_v \cdot (\Delta + \gamma)}. \quad (6.36b)$$

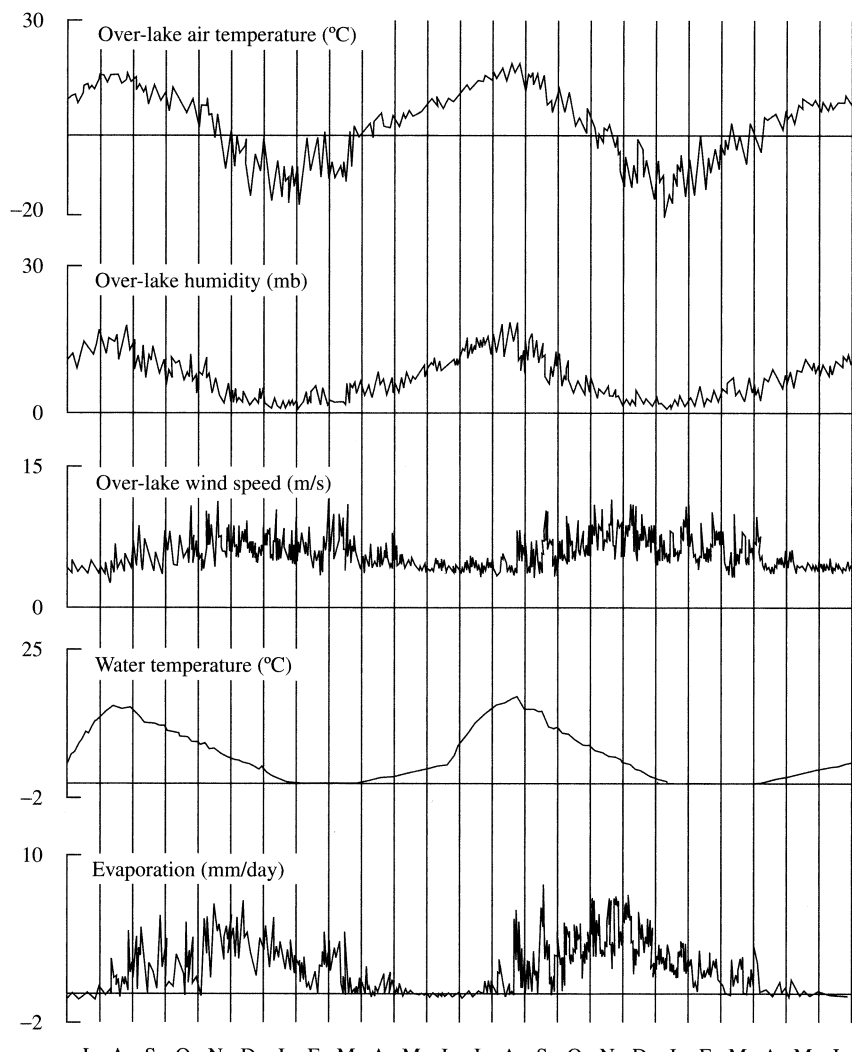


Figure 6.1 (continued) (b)

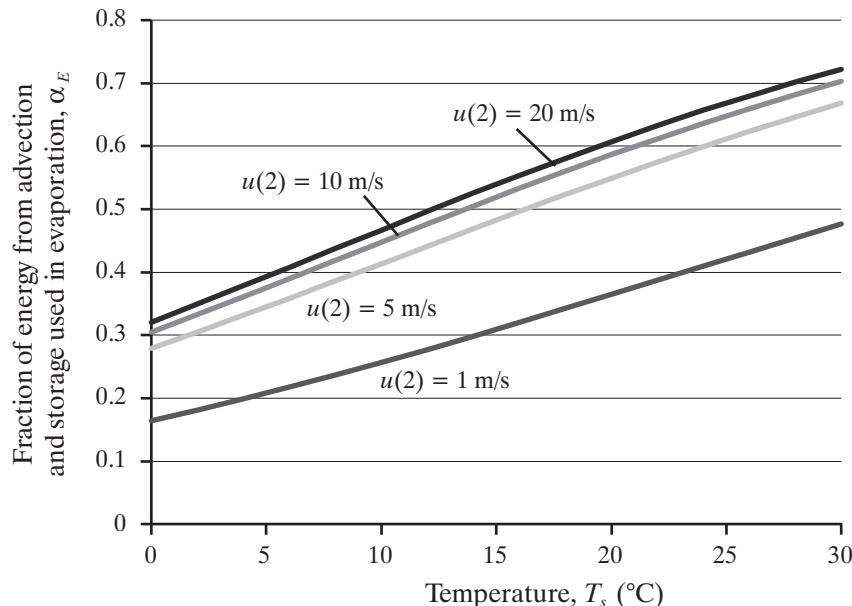


Figure 6.2 Fraction of energy from advection and storage used in lake evaporation, α_E , as estimated via equation (6B2.6).

Box 6.2 Fraction of Lake Evaporation Attributable to Advection and Heat Storage

Kohler and Parmele (1967) developed a general expression for the proportion of lake evaporation that can be attributed to the effects of water-adverted energy and changes in heat storage. They began by relating lake evaporation, E_L , to free-water evaporation, E_0 , as

$$E_L = E_0 + \alpha_E \cdot (A_w - \Delta U / \Delta t), \quad (6B2.1)$$

where A_w and ΔU are as in equation (6.29), and α_E is the fraction of the net addition of energy from advection and storage used in evaporation during Δt . They reasoned that changes in advection and heat storage are reflected in changes in water-surface temperature (T_s), and the total net addition ($A_w - \Delta U / \Delta t$) is allocated among evaporation (E_L), sensible-heat transfer (H), and longwave radiation emitted from the surface (L_{out}). Thus the portion affecting evaporation, α_E , is

$$\alpha_E = \frac{\partial E_L / \partial T_s}{\partial E_L / \partial T_s + \partial H / \partial T_s + \partial L_{out} / \partial T_s}. \quad (6B2.2)$$

Then they showed from equations (6.4) and (6.12) that

$$\frac{\partial E_L}{\partial T_s} = K_E \cdot u(z_m) \cdot \Delta; \quad (6B2.3)$$

from equations (6.18)–(6.21) that

$$\frac{\partial H}{\partial T_s} = K_E \cdot u(z_m) \cdot \gamma; \quad (6B2.4)$$

and from the Stefan–Boltzmann law [equation (2.1)] that

$$\frac{\partial L_{out}}{\partial T_s} = \frac{4 \cdot \varepsilon_w \cdot \sigma \cdot \bar{T}_s^3}{\rho_w \cdot \lambda_v}, \quad (6B2.5)$$

where ε_w is the emissivity of water, and σ is the Stefan–Boltzmann constant. Then substituting (6B2.3)–(6B2.5) into (6B2.2), α_E can be found as

$$\alpha_E = \frac{K_E \cdot u(z_m) \cdot \Delta}{K_E \cdot u(z_m) \cdot \Delta + K_E \cdot u(z_m) \cdot \gamma + 4 \cdot \varepsilon_w \cdot \sigma \cdot \bar{T}_s^3 / (\rho_w \cdot \lambda_v)}. \quad (6B2.6)$$

A plot of α_E as a function of 2-m wind speed and surface temperature is shown in figure 6.2; its value is < 0.5 except at high surface temperatures and wind speeds.

Box 6.3 Derivation of the Penman Combination Equation

The sensible-heat transfer flux is given by equation (6.18):

$$H = K_H \cdot u(z_m) \cdot [T_s - T(z_m)]. \quad (6B3.1)$$

The slope of the saturation-vapor versus temperature curve at the air temperature, Δ [equation (6.4)], can be approximated as

$$\Delta = \frac{e_s^* - e^*(z_m)}{T_s - T(z_m)}, \quad (6B3.2)$$

from which

$$T_s - T(z_m) = \frac{e_s^* - e^*(z_m)}{\Delta}. \quad (6B3.3)$$

Equation (6B3.3) can now be substituted into (6B3.1):

$$H = \frac{K_H \cdot u(z_m)}{\Delta} \cdot [e_s^* - e^*(z_m)]. \quad (6B3.4)$$

Equation (6B3.4) remains true if $e(z_m)$ is added and subtracted from each of the terms in brackets:

$$H = \frac{K_H \cdot u(z_m)}{\Delta} \cdot [e_s^* - e(z_m)] - \frac{K_H \cdot u(z_m)}{\Delta} \cdot [e^*(z_m) - e(z_m)]. \quad (6B3.5)$$

We can rearrange equation (6.12) to give

$$e_s^* - e(z_m) = \frac{E_0}{K_E \cdot u(z_m)}, \quad (6B3.6)$$

This relation has become known as the **Penman equation or combination equation**.

The essence of the Penman equation can be represented as

$$E_0 = \frac{\Delta \times \text{net radiation} + \gamma \times \text{mass transfer}}{\Delta + \gamma}, \quad (6.37)$$

i.e., evaporation rate is the sum of a rate due to net radiation weighted by a temperature-dependent term Δ [equation (6.4)], and a rate due to mass transfer weighted by a pressure-dependent term γ [equation (6.21)]. Note, though, that the mass-transfer relation here depends on the difference between the actual vapor pressure and the saturation vapor pressure at the *air temperature*, rather than at the water-surface temperature.

Penman (1948) intended his equation to eliminate the need for water-surface-temperature data,

and substituting (6B3.6) into (6B3.5) yields

$$H = \frac{K_H \cdot u(z_m)}{\Delta} \cdot \frac{E_0}{K_E \cdot u(z_m)} - \frac{K_H \cdot u(z_m)}{\Delta} \cdot [e^*(z_m) - e(z_m)]. \quad (6B3.7)$$

Now equation (6B3.7) can be substituted into the energy-balance equation (6.30), and the result solved for E_0 :

$$E_0 = \frac{K + L + [K_H \cdot u(z_m) / \Delta] \cdot [e^*(z_m) - e(z_m)]}{\rho_w \cdot \lambda_v + (K_H / K_E) \cdot \Delta}. \quad (6B3.8)$$

From the definitions of K_H [equation (6.17)], K_E [equation (6.11)], and γ [equation (6.21)], we see that

$$K_H = \gamma \cdot \rho_w \cdot \lambda_v \cdot K_E \quad (6B3.9)$$

and substituting this relation into (6B3.8), multiplying the numerator and denominator by Δ , and making use of equation (6.13) yields

$$E_{0P} = \frac{\Delta \cdot (K + L) + \gamma \cdot K_E \cdot \rho_w \cdot \lambda_v \cdot u(z_m) \cdot [e^*(z_m) - e(z_m)]}{\rho_w \cdot \lambda_v \cdot (\Delta + \gamma)}. \quad (6B3.10)$$

Source: Van Bavel 1966.

which is required for estimating surface vapor pressure in the mass-transfer equation [equation (6.12)]. However, surface temperature is in fact required to evaluate the longwave energy exchange, L [equation (6B1.7)], except in the very rare instances where measured radiation values are available. Kohler and Parmele (1967) showed that another approximation could be made to avoid this problem with little error, and arrived at the following modifications of the terms in equation (6.36):

1. replace L with L' , where

$$L' \equiv \varepsilon_w \cdot L_{in} - \varepsilon_w \cdot \sigma \cdot [T(z_m) + 273.16]^4; \quad (6.38)$$

2. replace γ with γ' , where

$$\gamma' \equiv \gamma + \frac{4 \cdot \varepsilon_w \cdot \sigma \cdot [T(z_m) + 273.16]^3}{K_E \cdot \rho_w \cdot \lambda_v \cdot u(z_m)}. \quad (6.39)$$

6.3.4.2 Practical Considerations

The combination approach as originally developed for free-water evaporation requires representative data on net shortwave radiation, net longwave radiation, wind speed, air temperature, and relative humidity. As modified by equations (6.38)–(6.39), the need for water temperature for calculating outgoing longwave radiation is eliminated. The radiation terms may be estimated using the relations in box 6.1; however, Van Bavel (1966) found that significant errors can be introduced when empirical radiation relations are used in place of measured values. Where humidity data are lacking, one can assume for nonarid regions that the dew-point temperature equals the daily minimum temperature (Gentilli 1955; Bristow 1992) and use that temperature in equation (6.2) to estimate $e(2\text{ m})$. Linacre (1993) developed an even more simplified empirical version of the Penman equation that does not require direct measurement of radiation or humidity.

Many studies have shown that evaporation estimates made with the combination approach com-

pare well with those determined by other methods. For example, Van Bavel (1966) showed that free-water evaporation calculated with equation (6.36) compared closely with actual evaporation from a shallow pan on an hourly basis (figure 6.3). However, as with all approaches to determining evaporation, calculated values are only valid to the degree that the input data are correct and representative of the evaporating water body. Rosenberry et al. (2007) found that several variations of the combination approach gave good estimates of lake evaporation, even for monthly values, and the Penman method performed well in comparative studies of lake (Winter et al. 1995) and wetland (Souch et al. 1996) evaporation. Kohler and Parmele (1967) tested their generalized version of the combination approach against evaporation determined by water-balance methods at Lake Hefner and other lakes, and found good agreement when evaporation was calculated daily and summed to use with weekly to monthly values of advection and storage.

Because it gives satisfactory results, because it has a theoretical foundation, and because it requires

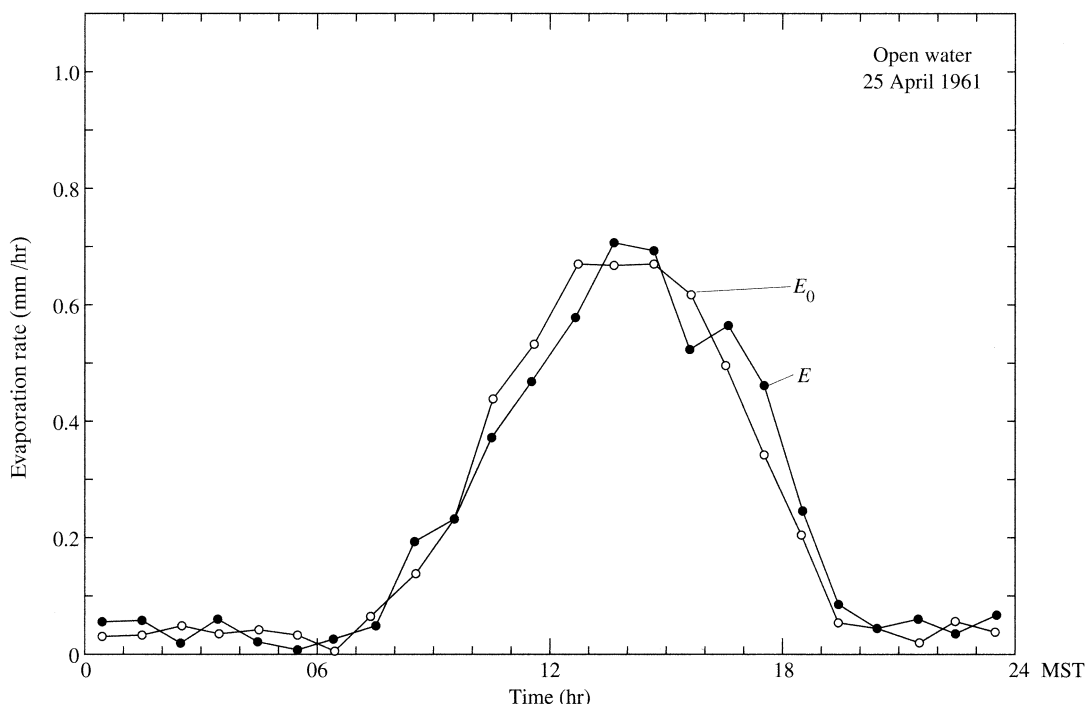


Figure 6.3 Comparison of hourly evaporation rates determined from measurements in a shallow pan (E) with those computed via the combination approach [E_0 , equation (6.36)] at Tempe, Arizona [Van Bavel (1966)]. Potential evaporation: The combination concept and its experimental verification. *Water Resources Research* 2:455–467, with permission of the American Geophysical Union].

meteorological inputs that are widely available or can usually be reasonably well estimated from available data, the combination method has become the “standard” hydrological method for determining free-water evaporation. One of its major advantages is that it eliminates the need for surface-temperature data, so that it can be readily used in the predictive or modeling context as well as for estimating evaporation from meteorological observations.

6.3.5 Pan Evaporation

6.3.5.1 Theoretical Basis

A direct approach to determining free-water evaporation is to expose a shallow pan of water to the atmosphere and solve a simplified water-balance equation for a convenient time period, Δt (usually one day):

$$E = P - [S_2 - S_1], \quad (6.40)$$

where P is precipitation during Δt and S_1 and S_2 are the volumes of water stored at the beginning and end of Δt , respectively. Precipitation is measured in an adjacent nonrecording rain gauge; the storage volumes are determined by measuring the water level in a small **stilling well** in the pan with a high-precision micrometer called a **hook gauge**. Ideally, the water surface is maintained a few centimeters below the pan rim by adding measured amounts of water as necessary.

An evaporation pan approximates the definition of free-water evaporation: it has a reasonably ex-

tended surface, negligible heat storage, and no water-adverted energy except that due to rain. However, heat conduction through the pan sides and bottom may affect the evaporation rate, and recent experimental studies showed that water depth significantly affects observed evaporation (Chu et al. 2010).

6.3.5.2 Practical Considerations

Pans on land are placed in clearings suitable for rain gauges (see chapter 4), surrounded by a fence to prevent animals from drinking, and may be sunken so that the water surface is approximately in the same plane as the ground surface or raised a standard height above the ground. For special studies of lake evaporation, pans are sometimes placed in the center of a floating platform with dimensions large enough to insure stability and prevent water from splashing in, again with the surface either at or above the lake surface.

Several different standard types of pans are used by different countries and agencies. Shaw (1988) described the types used in Great Britain, the former Soviet Union, and the United States, and figure 6.4 shows the standard “Class-A” pan used by the NWS and in Canada.

An evaporation pan differs from a lake in having far less heat-storage capacity, in lacking surface- or ground-water inputs or outputs, and, in raised pans like the Class A, in having sides exposed to the air and sun. These differences significantly affect the energy balance, elevating the warm-season average



Figure 6.4 Standard NWS “Class-A” evaporation pan.

The pan is 4 ft (1.22 m) in diameter by 10 in (25.4 cm) high and set on a low platform. The stilling well in which water level is measured is on the right, and a floating thermometer is on the left. Typically an anemometer is installed next to the pan and a rain gauge must be located nearby (photo by author).

temperature and vapor pressure of the water surface of a pan relative to that of a nearby lake. The ratio of lake evaporation to pan evaporation is called the **pan coefficient**; its annual average over the United States is about 0.7. Within the evaporation season, heat-storage effects cause water temperatures in lakes to be generally lower than those of pans in the spring, and higher in the fall. Thus pan coefficients follow the same pattern, with values lower than the seasonal average in the spring and higher in the fall (e.g., figure 6.5).

The Class-A pan is usually installed with an anemometer and a floating maximum-minimum thermometer, providing data on average daily wind speed and average water-surface temperature. Kohler et al. (1955) developed an empirical equation to use these data along with air temperature to account for the energy exchange through the sides of a pan and thereby adjust daily pan evaporation to daily free-water evaporation:

$$E_0 = 0.7 \cdot [E_{pan} \pm 0.064 \cdot p \cdot \alpha_{pan} \cdot (0.37 + 0.00255 \cdot u_{pan}) \cdot |T_{span} - T_a|^{0.88}], \quad (6.41)$$

where E_0 is in mm/day, E_{pan} is daily pan evaporation (mm/day), p is atmospheric pressure (kPa), u_{pan} is average wind speed at a height of 15 cm above the pan (km/day), T_{span} is water-surface temperature in

the pan ($^{\circ}\text{C}$), T_a is air temperature ($^{\circ}\text{C}$), and the sign following E_{pan} is + when $T_{span} > T_a$ and - when $T_{span} < T_a$. The factor α_{pan} is the proportion of energy exchanged through the sides of the pan that is used for, or lost from, evaporation, which is estimated as

$$\alpha_{pan} = 0.34 + 0.0117 \cdot T_{span} - (3.5 \times 10^{-7}) \cdot (T_{span} + 17.8)^3 + 0.0135 \cdot u_{pan}^{0.36} \quad (6.42)$$

using the same units as in equation (6.41) (Linsley et al. 1982). Because inputs and outputs of energy through the sides of a pan tend to balance out over the course of a year, adjustments via equations (6.41) and (6.42) may not be needed for annual values.

Pan evaporation data provide a useful basis for understanding the regional climatology of seasonal or annual free-water evaporation and long-term average lake evaporation. Pan coefficients and annual free-water evaporation have been summarized and mapped by Farnsworth and Thompson (1982) (figure 6.6).

Since year-to-year variations of pan evaporation are usually not large, observations for a few years can provide a satisfactory estimate of annual values, which can then be adjusted by the appropriate regional pan coefficient to give an estimate of free-water evaporation. While such information might be useful in planning for a water-supply reservoir, advection and storage could cause actual lake evaporation

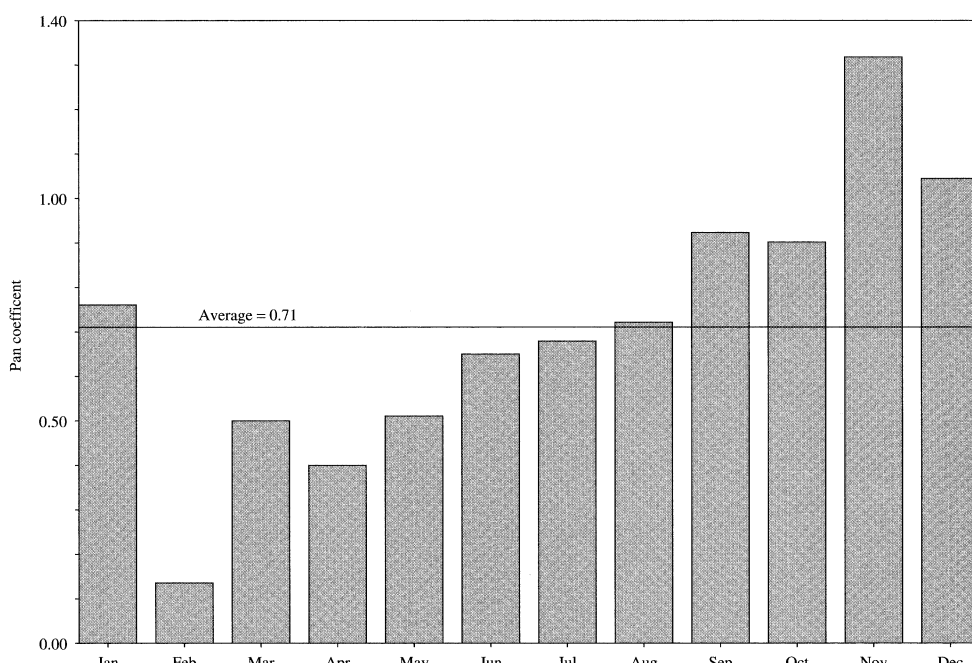


Figure 6.5 Monthly Class-A pan coefficients at Lake Hefner, Oklahoma, June 1950–May 1951 [data from Harbeck et al. (1954)].

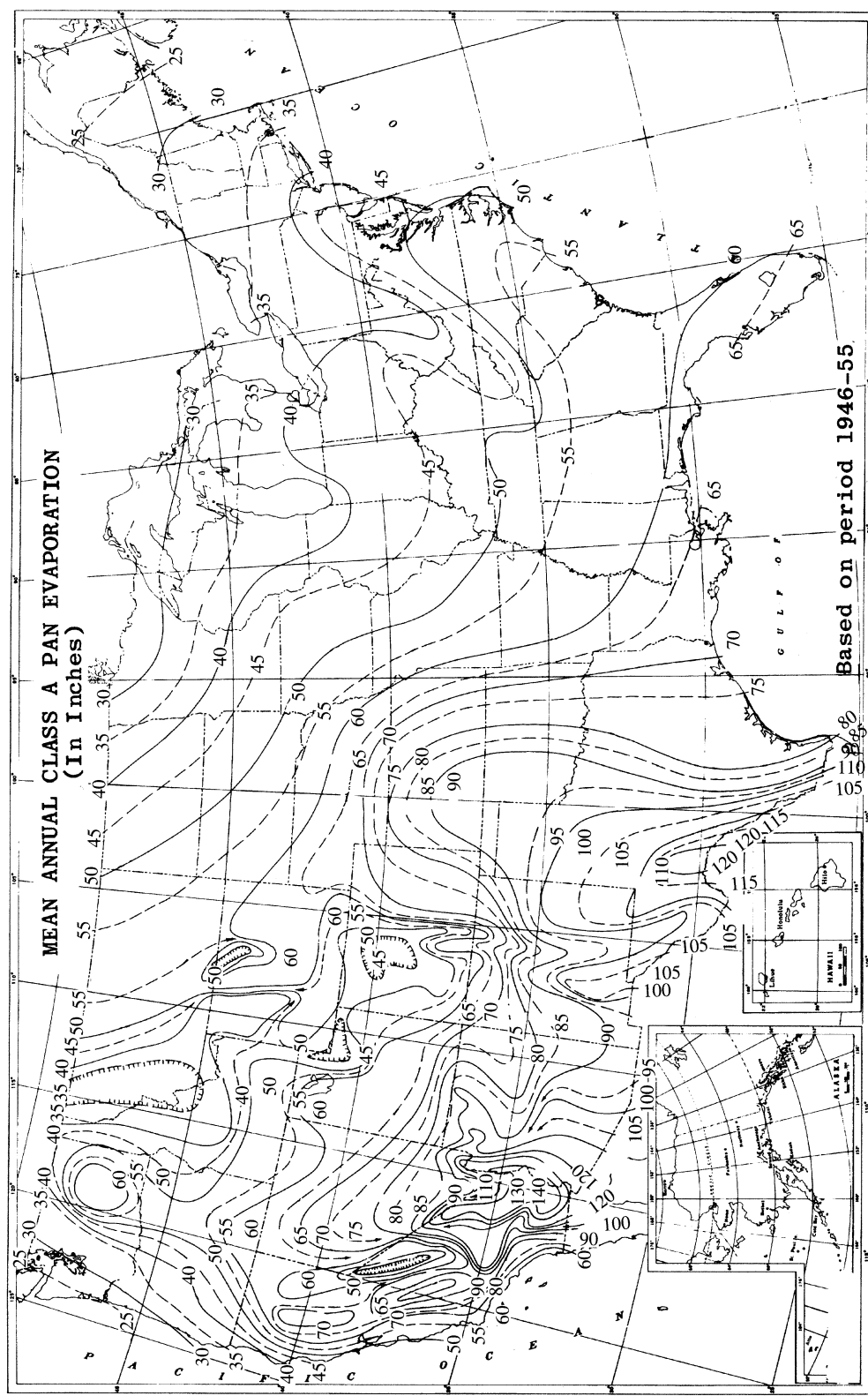


Figure 6.6 Average annual pan (= free-water-surface) evaporation ($\text{in}/\text{yr} \cdot 25.4 = \text{mm}/\text{yr}$) for the 48 contiguous United States based on data for 1946–1955 (map provided by US National Weather Service).

to be considerably different from pan-estimated free-water evaporation: Derecki (1981) computed 483 mm average annual evaporation for Lake Superior by the mass-transfer approach, whereas free-water-surface evaporation is about 554 mm. Based on the Lake Heffner study, M. A. Kohler concluded that “Annual lake evaporation can probably be estimated within 10 to 15% (on the average) by applying an annual coefficient to pan evaporation, provided lake depth and climatic regime are taken into account in selecting the coefficient” (Harbeck et al. 1954, p. 148).

Van Bavel’s (1966) results and other studies indicate that free-water-surface evaporation calculated by the combination method closely approximates pan evaporation on an annual basis and for shorter periods if heat exchange through the pan is accounted for via equations (6.41) and (6.42).

6.3.6 Water-Balance Approach

6.3.6.1 Theoretical Basis

The water-balance approach is applicable to determining actual evaporation from a water body rather than free-water evaporation. It involves applying the water-balance equation (section 1.8) to the water body over a time period, Δt , and solving that equation for evaporation, E :

$$E = P + Q_{in} + GW_{in} - Q_{out} - GW_{out} - \Delta S, \quad (6.43)$$

where P is precipitation; Q_{in} and Q_{out} are the inflows and outflows of surface water, respectively; GW_{in} and GW_{out} are the inflows and outflows of ground water, respectively; ΔS is the change in the amount of water stored in the lake during Δt ; and all quanti-

ties have dimensions of either volume or volume per unit lake area.

6.3.6.2 Practical Considerations

While the water-balance approach is simple in concept, it is generally far from simple in application, because the measurement of all water inputs and outputs for a water body is generally a formidable task:

- All major streams entering the body and the outlet stream must be continuously gauged, and some method must be devised for estimating the amount of any nonchannelized surface-water flow inputs.
- The discussion in section 9.3.2 makes it clear that it is difficult to assess ground-water inflows and outflows to lakes. At best, these are usually estimated from gradients observed in a few observation wells and assumptions about the saturated thickness and hydraulic conductivity of surrounding geologic formations, perhaps supplemented by scattered observations with seepage meters.
- If the lake is large and the surrounding topography irregular, it may be difficult to obtain precise measurements of precipitation (section 4.3).
- Changes in storage can be estimated from careful observations of water levels if one has good information on the lake’s bathymetry, and if corrections are made for changes in water density.

Winter (1981) made a thorough analysis of the uncertainties in estimating lake water balances; even for the “readily” measurable components the results are somewhat discouraging (table 6.3). For other components—overland flows and, especially, ground-

Table 6.3 Range of Uncertainty in Precipitation and Streamflow Values Used in Computing Lake Water Balances.^a

Time Interval	Precipitation	Streamflow Inputs ^b		Streamflow Outputs
		General Range		
Daily	60–75	5–15 (50)		5 (15)
Monthly	10–25	5–15 (50)		5 (15)
Seasonal/annual	5–10	5–15 (30)		5 (15)
Values for a Typical Lake in Northern United States				
Monthly	(26)	(31)		(12)
Seasonal/annual	8 (17)	9(23)		9 (12)

^a Values are percentages of the true values. Those without parentheses are for “best” methodology; those in parentheses are “commonly used” methodology.

^b Does not include overland flow.

water flows—uncertainties on the order of 100% must be generally anticipated. For example, LaBaugh (1985) found that evaporation was a small fraction of the total outflow and less than the uncertainty in the overall balance of a reservoir in Colorado (figure 6.7). If reasonably accurate information on the significant balance components is available, the method can provide a rough—and in rare cases a quite accurate—check on evaporation estimated by other approaches. Table 6.3 indicates that the accuracy of the method generally increases as Δt increases.

Because of the difficulty in finding situations where all the significant terms on the right side of equation (6.43) can be measured with sufficient accuracy, the water-budget approach has only rarely been used to determine lake evaporation. One of the more successful applications of the approach was in an extensive comparison of methods for determining lake evaporation conducted by the USGS in the early 1950s at Lake Hefner, Oklahoma (Harbeck et al. 1954). That lake was selected for the study because it was one of the few—out of more than 100 considered—for which a water balance could be

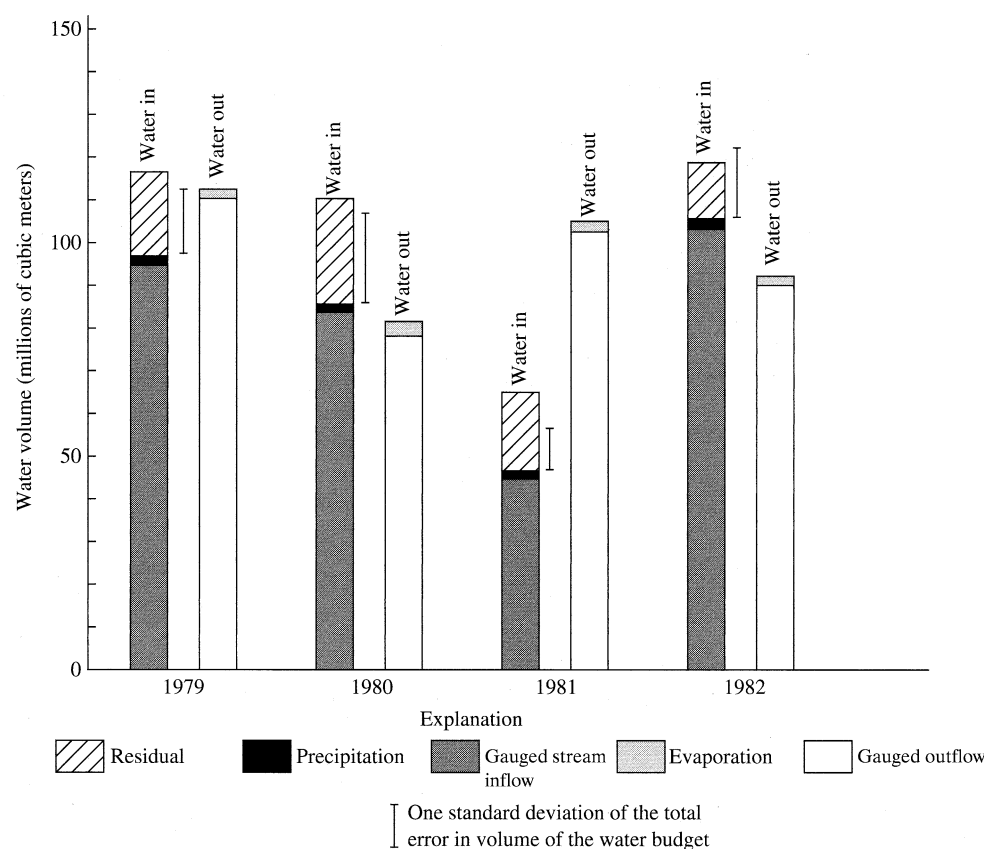
computed with acceptable precision. Harbeck et al. (1954) concluded that daily evaporation calculated via the water balance at Lake Hefner was within 5% of the true value on 29% of the days, and within 10% on 62% of the days.

6.3.7 Summary and Example Calculations

As noted above, detailed multiyear studies comparing lake-evaporation estimates by the various methods discussed here were carried out by the USGS on Lake Hefner, Oklahoma (Harbeck et al. 1954), and Pretty Lake, Indiana (Ficke 1972). Three more-recent studies compared evaporation computed via several approaches on small water bodies:

- Winter et al. (1995) compared 11 evaporation equations with evaporation determined via the energy budget on a small (0.36 km^2) lake in Minnesota. The approaches included mass-transfer and combination-type equations and several empirical methods. One useful aspect of this study was the comparison of results using data collected on a raft in the lake, on land near the lake, and from a sta-

Figure 6.7 Water balance for the Williams Fork Reservoir, Colorado, for four years. The vertical bars represent the uncertainty in the overall budget (standard deviation of total error); note that this is several times larger than annual evaporation [LaBaugh (1985). Uncertainty in phosphorus retention, Williams Fork Reservoir, Colorado. *Water Resources Research* 21:1684–1692, with permission of the American Geophysical Union].



tion 60 km distant. They concluded that net radiation, air temperature, wind speed, and relative humidity need to be measured near the lake and that the energy budget needs to include an assessment of heat-storage changes.

- Rosenberry et al. (2007) compared evaporation as calculated by 14 equations against the Bowen-ratio/energy-budget method on a 0.15-km² New Hampshire lake. Their equations included various versions of combination and mass-transfer approaches, plus several semi-empirical methods that use only solar radiation and temperature. Combination methods requiring measurement of net radiation, air temperature, and vapor pressure performed best, but heat-storage changes had to be accounted for. They also found that some simple methods re-

quiring only measurement of air temperature, or air temperature and solar radiation, performed well, particularly over longer time periods.

- Tanney et al. (2008) made comparisons of five equations and Class-A pan data on a 0.36-km² reservoir in Israel, using eddy-correlation measurements as the standard. Combination methods and energy-balance methods performed best.

While all these comparisons are instructive, it is difficult to generalize from them because of the differences in climate, lake sizes, sources of data, and averaging periods used. To illustrate the use of the various approaches described here and to give a sense of the range of values likely to result from these approaches, box 6.4 compares example calculations of evaporation for one day at Lake Hefner, Oklahoma.

Box 6.4 Example Calculations of Free-Water Evaporation

Tables 6B4.1 and 6B4.2 summarize daily average and total values of various quantities measured by the US Geological Survey (1954) at Lake Hefner, Oklahoma, on 12 July 1951. The lake's area is 9.4 km².

Table 6B4.1 Daily Average Values.

T(2 m) (°C)	T _s (°C)	RH(2 m)	P (kPa)	u(2 m) (m/s)	T _{span} (°C)	u _{pan} (m/s)
27.2	26.9	0.69	97.3	5.81	27.5	2.79

Table 6B4.2 Daily Total Values.

K _{in} (MJ/m ² · day)	a	L _{in} (MJ/m ² · day)	Water-Balance Evaporation (mm)	Class-A Pan Evaporation (mm)
30.6	0.052	34.4	5.58	12.4

Here we calculate the daily free-water evaporation via the mass-transfer, energy-balance, Bowen ratio, combination, and evaporation-pan methods and compare the results with the evaporation given by the lake water balance, which is thought to provide an accurate value for this lake.

Mass Transfer

The basic mass-transfer relation is

$$E_0 = K_E \cdot u(2 \text{ m}) \cdot [e_s - e(2 \text{ m})]. \quad (6B4.1)$$

Substituting the lake's area into equation (6.28) gives

$$\begin{aligned} K_E &= 1.26 \cdot (9.4 \text{ km}^2)^{-0.05} \\ &= 1.13 \text{ mm} \cdot \text{s/day} \cdot \text{m} \cdot \text{kPa} \end{aligned}$$

The surface-vapor pressure is given by equations (6.1) and (6.2):

$$e_s = 0.611 \cdot \exp\left(\frac{17.3 \cdot 26.9}{26.9 + 237.3}\right) = 3.56 \text{ kPa}.$$

The air-vapor pressure is given by equations (6.2) and (6.3):

$$e^*(2 \text{ m}) = 0.611 \cdot \exp\left(\frac{17.3 \cdot 27.2}{27.2 + 237.3}\right) = 3.62 \text{ kPa};$$

$$e(2 \text{ m}) = 0.69 \cdot 3.62 \text{ kPa} = 2.50 \text{ kPa}.$$

Then from equation (6B4.1),

$$\begin{aligned} E_0 &= (1.13 \text{ mm} \cdot \text{s/day} \cdot \text{m} \cdot \text{kPa}) \cdot (5.81 \text{ m/s}) \cdot (3.56 \text{ kPa} - 2.50 \text{ kPa}) \\ &= 6.96 \text{ mm/day}. \end{aligned}$$

Energy Balance

The energy-balance relation is equation (6.30). Net shortwave radiation, K , is found via equation (6B1.1):

$$\begin{aligned} K &= K_{in} \cdot (1 - a) \\ &= (30.6 \text{ MJ/m}^2 \cdot \text{day}) \times (1 - 0.052) \\ &= 29.0 \text{ MJ/m}^2 \cdot \text{day}. \end{aligned}$$

Incoming longwave radiation, L_{in} , was measured, so net longwave radiation, L , is found via equations (6B1.4) and (6B1.6) as

$$\begin{aligned} L &= L_{in} - 0.05 \times L_{in} - 0.95 \times (4.90 \times 10^{-9}) \times (T_s + 273.15)^4 \\ &= 0.95 \times 34.4 \text{ MJ/m}^2 \cdot \text{day} - 0.95 \times \\ &\quad (4.90 \times 10^{-9} \text{ MJ/m}^2 \cdot \text{K}^4 \cdot \text{day}) \times (26.9 \text{ K} + 273.15 \text{ K})^4 \\ &= -5.05 \text{ MJ/m}^2 \cdot \text{day}. \end{aligned}$$

Sensible-heat exchange is found via equation (6.16), with K_H given by equation (6.17) with $z_m = 2 \text{ m}$, $z_d = 0$, and $z_0 = 0.0012 \text{ m}$ (table 6.1):

$$\begin{aligned} K_H &= \frac{1.95 \times 10^{-4} \text{ MJ/m}^3 \cdot \text{K}}{\left[\ln\left(\frac{2 \text{ m}}{0.0012 \text{ m}}\right) \right]^2} \\ &= 3.54 \times 10^{-6} \text{ MJ/m}^3 \cdot \text{K}; \end{aligned}$$

$$\begin{aligned} H &= (3.54 \times 10^{-6} \text{ MJ/m}^3 \cdot \text{K}) \cdot (5.81 \text{ m/s}) \cdot [(26.9 - 27.2) \text{ K}] \\ &= -6.18 \times 10^{-6} \text{ MJ/m}^2 \cdot \text{s} = -0.534 \text{ MJ/m}^2 \cdot \text{day}. \end{aligned}$$

From equation (6.14),

$$\lambda_v = 2.50 \text{ MJ/kg} - (2.36 \times 10^{-3} \text{ MJ/kg} \cdot ^\circ\text{C}) \times (26.9^\circ\text{C}) = 2.43 \text{ MJ/kg}.$$

Now with $\rho_w = 996 \text{ kg/m}^3$, equation (6.30) gives

$$\begin{aligned} E_0 &= \frac{(29.0 - 5.05 - 0.534) \text{ MJ/m}^2 \cdot \text{day}}{(996 \text{ kg/m}^3) \cdot (2.43 \text{ MJ/kg})} \\ &= 0.00967 \text{ m/day} = 9.67 \text{ mm/day}. \end{aligned}$$

Energy Balance with Bowen Ratio

The energy-balance relation using the Bowen ratio is given by equation (6.32). With the vapor pressures and radiation terms as calculated above, the Bowen ratio, B , is found from equations (6.19) and (6.20):

$$\begin{aligned} B &= \frac{c_a \cdot P \cdot [T_s - T(z_m)]}{0.622 \cdot \lambda_v \cdot [e_s - e(z_m)]} \\ &= \frac{(1.00 \times 10^{-3} \text{ MJ/kg} \cdot \text{K}) \cdot (97.3 \text{ kPa}) \cdot [(26.9 - 27.2) \text{ K}]}{0.622 \cdot (2.43 \text{ MJ/kg}) \cdot [(3.56 - 2.50) \text{ kPa}]} \\ &= -0.182. \end{aligned}$$

Then from equation (6.33),

$$\begin{aligned} E_0 &= \frac{29.0 \text{ MJ/m}^2 \cdot \text{day} - 5.05 \text{ MJ/m}^2 \cdot \text{day}}{(996 \text{ kg/m}^3) \cdot (2.43 \text{ MJ/kg}) \cdot (1 - 0.0182)} \\ &= 0.0101 \text{ m/day} = 10.1 \text{ mm/day}. \end{aligned}$$

Combination

The combination approach is given by equation (6.37). The values of Δ and γ are found from equations (6.4) and (6.21), respectively:

$$\begin{aligned} \Delta(T) &= \frac{2,508.3}{[T(2 \text{ m}) + 237.3]^2} \cdot \exp\left(\frac{17.3 \cdot T(2 \text{ m})}{T(2 \text{ m}) + 237.3}\right) \\ &= \frac{2,508.3}{[27.2^\circ\text{C} + 237.3]^2} \cdot \exp\left(\frac{17.3 \cdot 27.2^\circ\text{C}}{27.2^\circ\text{C} + 237.3}\right) \\ &= 0.212 \text{ kPa}/^\circ\text{C}; \\ \gamma &\equiv \frac{c_a \cdot P}{0.622 \cdot \lambda_v} \\ &= \frac{1.00 \times 10^{-3} \text{ MJ/kg} \cdot \text{K} \cdot 97.3 \text{ kPa}}{0.622 \cdot 2.43 \text{ MJ/kg}} \\ &= 0.0644 \text{ kPa}/^\circ\text{C}. \end{aligned}$$

All other values needed for equation (6.37) are available from tables 6B4.1 and 6B4.2 and previous calculations. However, the value of K_E given above must be multiplied by 10^{-3} m/mm to give consistent units ($s/\text{kPa} \cdot \text{day}$). Then we find

$$\begin{aligned} E_0 &= \frac{0.212 \cdot (29.0 - 5.05) + 0.0644 \cdot (1.13 \times 10^{-3}) \cdot 996 \cdot 2.43 \cdot 5.81 \cdot 3.62 \cdot (1 - 0.69)}{996 \cdot 2.43 \cdot (0.212 + 0.0644)} \\ &= 0.00806 \text{ m/day} = 8.06 \text{ mm/day}. \end{aligned}$$

It is also of interest to compare this result with that obtained from the combination approach using the modifications of Kohler and Parmele (1967). To do this, we replace L with L' from equation (6.38):

$$\begin{aligned} L' &= 0.95 \cdot (34.4 \text{ MJ/m}^2 \cdot \text{day}) - 0.95 \cdot \\ &\quad (4.90 \times 10^{-9} \text{ MJ/m}^2 \cdot \text{K}^4 \cdot \text{day}) \cdot [(27.2 + 273.15) \text{ K}]^4 \\ &= -5.20 \text{ MJ/m}^2 \cdot \text{day}, \end{aligned}$$

and replace γ with γ' from equation (6.39):

$$\begin{aligned} \gamma' &= 0.0644 \text{ kPa/K} + \\ &\quad \frac{4 \cdot 0.95 \cdot (4.90 \times 10^{-9} \text{ MJ/m}^2 \cdot \text{K}^4 \cdot \text{day}) \cdot [(27.2 + 273.16) \text{ K}]^3}{(1.13 \times 10^{-3} \text{ s/day} \cdot \text{kPa}) \cdot 996 \text{ kg/m}^3 \cdot 2.43 \text{ MJ/kg} \cdot 5.81 \text{ m/s}} \\ &= 0.0958 \text{ kPa/K}. \end{aligned}$$

Substituting these quantities into the Penman–Monieth equation yields

$$\begin{aligned} E_0 &= \frac{0.212 \cdot (29.0 - 5.20) + 0.0958 \cdot (1.13 \times 10^{-3}) \cdot 996 \cdot 2.43 \cdot 5.81 \cdot 3.62 \cdot (1 - 0.69)}{996 \cdot 2.43 \cdot (0.212 + 0.0958)} \\ &= 0.00907 \text{ m/day} = 9.07 \text{ mm/day}. \end{aligned}$$

(continued)

Pan Evaporation

To adjust the measured Class-A pan evaporation at Lake Hefner to give an estimate of the free-water evaporation on 12 July 1951, we first convert u_{pan} from m/s to km/day:

$$u_{pan} = (2.79 \text{ m/s}) \cdot (1 \text{ km}/1,000 \text{ m}) \cdot (86,400 \text{ s/day}) = 241 \text{ km/day.}$$

Next compute α_{pan} via equation (6.42):

$$\alpha_{pan} = 0.34 + 0.0117 \cdot 27.5 - (3.5 \times 10^{-7}) \cdot (27.5 + 17.8)^3 + 0.0135 \cdot 241^{0.36} = 0.726.$$

Substituting this value into equation (6.41) yields

$$E_0 = 0.7 \cdot [12.4 + 0.064 \cdot 97.3 \cdot 0.726 \cdot (0.37 + 0.00255 \cdot 241) \cdot |27.5 - 27.2|^{0.88}] = 9.76 \text{ mm/day.}$$

Summary

Table 6B4.3 compares the daily evaporation values calculated by the various approaches.

Obviously, the comparison for one day on one lake does not indicate which approach is most accurate; all calculated values are substantially higher than the value given by the water balance. However, the range of values does suggest the uncertainty involved in estimating evaporation.

Table 6B4.3 Daily Free-Water Evaporation, E_0 (mm/day).

Mass Transfer	Energy Balance	Energy Balance-Bowen Ratio	Combination	Combination with Equations (6.38) and (6.39)	Class-A Pan	Class-A Pan Adjusted	Water Balance
6.96	9.67	10.1	8.06	9.07	12.4	9.76	5.58

6.4 Bare-Soil Evaporation

More than one-third of the earth's land surface consists of soil orders that support little or no vegetation: Entisols, Inceptisols, and Aridisols (table 2.14; figure 2.47). In addition, most agricultural lands have meager vegetative cover much of the time. Thus evaporation from bare soil is globally significant and vitally important to farmers, especially in the management of irrigation.

Following infiltration due to significant rain, snowmelt, or irrigation, evaporation from a wet bare soil (also called **exfiltration**) above a water table generally occurs in two distinct stages (figure 6.8).

Stage 1: Atmosphere-Controlled. In this stage, the evaporation rate (E_1) is largely determined by the surface energy balance and mass-transfer conditions (wind and humidity) and occurs at or near the rate of free-water evaporation. Water moves to the surface as a liquid by capillary action and vaporizes at the surface. Soil evaporation during stage 1 can be estimated by the approaches appropriate for free-water evaporation (section 6.3), of which the Penman equation [equation (6.36)] usually gives the best results (Parlange and Katul 1992a).

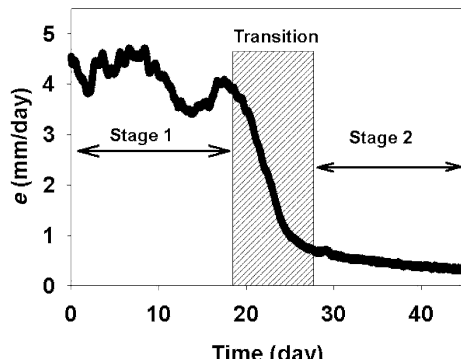


Figure 6.8 The drying rate measured during evaporation from a column packed with sand with an average particle size of 0.224 mm. Following infiltration due to significant rain, snowmelt, or irrigation, evaporation from a wet bare soil above a water table generally occurs in two distinct stages. During stage 1, the evaporation rate is relatively high and constant, followed by a much lower value [Shokri and Or (2011)]. What determines drying rates at the onset of diffusion controlled stage-2 evaporation from porous media? *Water Resources Research* 47, with permission of the American Geophysical Union].

Transition. As the soil dries, the menisci begin to detach from the surface to form a drying front, disrupting the hydraulic connection to the surface (figure 6.9). From experimental studies, Shokri and Or (2011) showed that the depth at which this front forms is inversely proportional to the soil pore (grain) size (i.e., larger for clays than for sands), and is typically between 3 and 14 mm. Evaporation then declines from E_1 , asymptotically approaching a constant rate (figure 6.8). The transition period may last for several days as the drying front descends.

Stage 2: Soil-Controlled. In this stage, the evaporation rate (E_2) is nearly constant at a rate much lower than E_1 , typically 0.7 (sand) to 3.5 (clay) mm/day (Shokri and Or 2011). Water movement is primarily by vapor diffusion and by **film-flow** in the water held on soil particles by surface tension. E_2 is controlled largely by the soil's physical characteristics and not by E_1 (Hillel 1998; Shokri and Or 2011; Sadeghi et al. 2012; Smits et al. 2012).

Following an infiltration event, the soil dries both by drainage and by evaporation. Accounting for this, Salvucci (1997) showed that the modeling of stage-2 soil evaporation can be greatly simplified by (1) invoking a relationship between the duration of stage-1 evaporation, soil properties, and soil moisture and (2) assuming that the rate of soil drainage due to gravity is greater than the evaporation rate. His analysis led to simple expressions for evaporation rate beginning at the end of stage 1 (i.e., during the transition and stage 2), E_2 :

$$E_2 = \bar{E}_1 \cdot \frac{8}{\pi^2} \cdot \frac{t_1}{t}, \quad t > t_1, \quad (6.44)$$

where \bar{E}_1 is the average stage-1 evaporation rate and t_1 is the duration of stage 1. With equation (6.44) one can estimate stage-2 evaporation based only on estimates of the stage-1 evaporation rate and observation of the time at which stage 1 ends. This simplified approach gave estimates that compared well with observations in several field experimental situations (figure 6.10a). One practical advantage of this approach is that the time t_1 can often be visually detected as an increase in the brightness (albedo) of the soil surface (figure 6.10b), which can be observed via remote sensing.

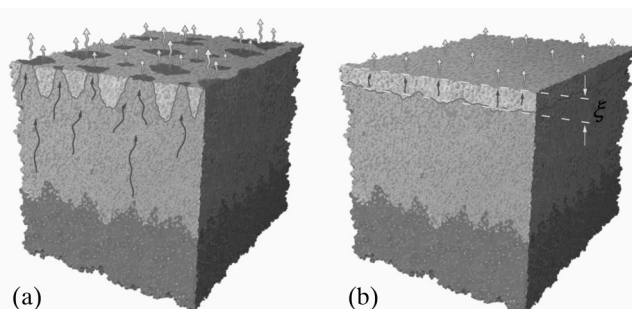
6.5 Transpiration

6.5.1 The Transpiration Process

Transpiration is the evaporation of water from the vascular system of plants into the atmosphere. The entire process (figure 6.11 on p. 277) involves **absorption** of soil water by plant roots; **translocation** in liquid form through the vascular system of the roots, stem, and branches to the leaves; and through the vascular system of the leaf to the walls of tiny **stomatal cavities**, where evaporation takes place. The water vapor in these cavities then moves into the ambient air through openings in the leaf surface called **stomata**.

Plants live by absorbing carbon dioxide (CO_2) from the air to make carbohydrates, and that gas can enter the plant only when dissolved in water. The essential function of the stomatal cavities is to provide a place where CO_2 dissolution can occur and enter plant tissue; the evaporation of water is an unavoidable concomitant of that process. Transpiration also

Figure 6.9 Sketch illustrating the jump of the liquid meniscus from the surface and formation of the secondary drying front during the transition from stage-1 to stage-2 evaporation. (a) Detachment of the liquid meniscus from the surface to a level below. (b) Formation of the secondary drying front at the onset of stage 2. The evaporation is preceded by the capillary flow up to the secondary drying front, vaporization at that level, and vapor diffusion through the dry layer [Shokri and Or (2011). What determines drying rates at the onset of diffusion controlled stage-2 evaporation from porous media? *Water Resources Research* 47, with permission of the American Geophysical Union].



performs the essential functions of maintaining the turgor of plant cells and delivering mineral nutrients from the soil to growing tissue.

Air in stomatal cavities is saturated at the temperature of the leaf, and water moves from the cavities into the air due to a vapor-pressure difference, just as in open-water evaporation. The major difference between transpiration and open-water evaporation is that plants can exert some physiological control over the size of the stomatal openings, and hence the ease of vapor movement to the air, by the action of **guard cells** (figure 6.12 on p. 278). The major factors affecting the opening and closing of guard cells are: (1) light (most plants open stomata during the day and close them at night); (2) humidity (stomatal openings tend to decrease as humidity decreases below its saturation value); and (3) the water content of the leaf cells (if daytime water contents become too low, stomata tend to close). Several other factors also affect the opening and closing of stomata,

including wind, CO₂ levels, temperature, and certain chemicals. A mathematical representation of the effects of the factors most important in hydrological modeling is given later.

It is important to emphasize that transpiration is a physical, not a metabolic, process: Water in the **transpiration stream** is pulled through the plant by potential-energy gradients that originate with the movement of water vapor into the air through the stomata in response to a vapor-pressure difference. When vapor exits through the stomata, water evaporates from the walls of the stomatal cavity to replace the loss; this loss of liquid water causes a potential-energy decrease that induces the movement of replacement water up through the vascular system; this movement ultimately produces a water-content gradient between the root and the soil; and this gradient induces movement of soil water into the root. Absorption at the root surface decreases soil-water content in the adjacent soil, inducing some flow of water

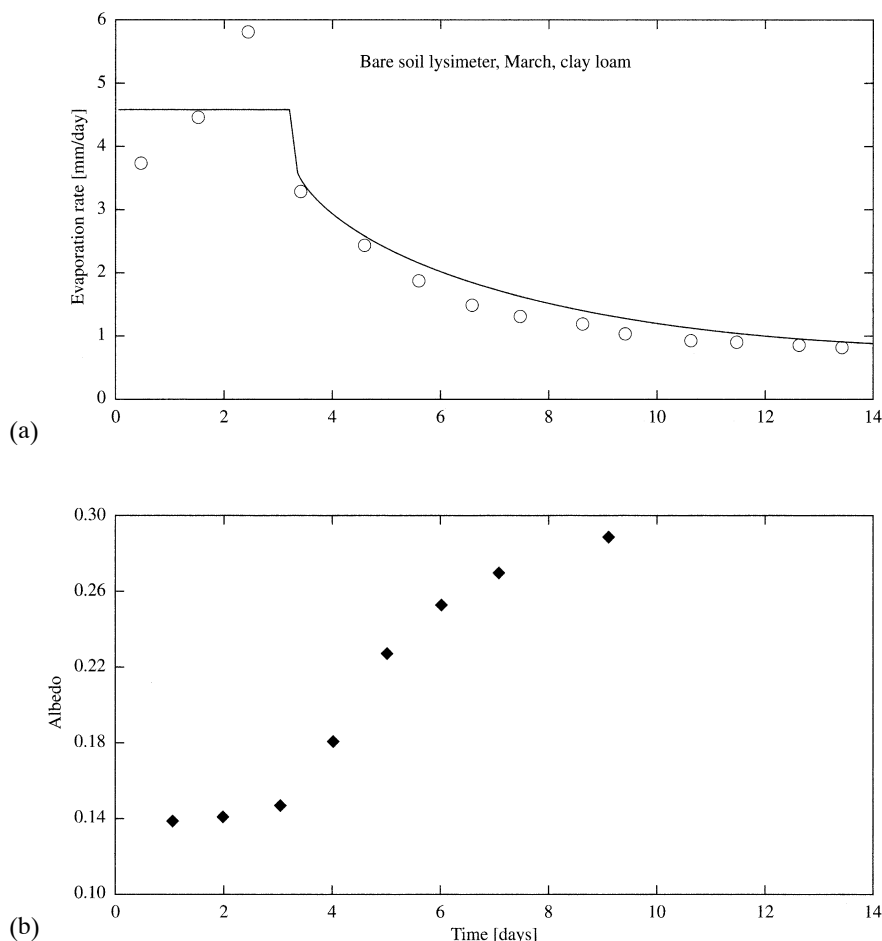


Figure 6.10 (a) Bare-soil evaporation following irrigation as measured in a lysimeter (circles) and computed via equation (6.44) (line). (b) Concurrent soil-surface albedo (provided by Guido Salvucci, Boston University).

toward the root following Darcy's law. However, roots come into contact with soil water mostly by growing toward the water: During the growing season roots typically grow several tens of millimeters per day (Raven et al. 1976).

The great cohesive strength of water due to its intermolecular hydrogen bonds (see appendix B) generally maintains the integrity of the transpiration stream to heights of the tallest trees. Although bubbles can form in the stream, trees have evolved mechanisms for healing them to maintain transpiration (Pickard and Melcher 2005).

6.5.2 Measurement of Transpiration

The two approaches to direct measurement of transpiration are briefly described here. Further details can be found in the review by Wang and Dickinson (2012) and the literature cited therein.

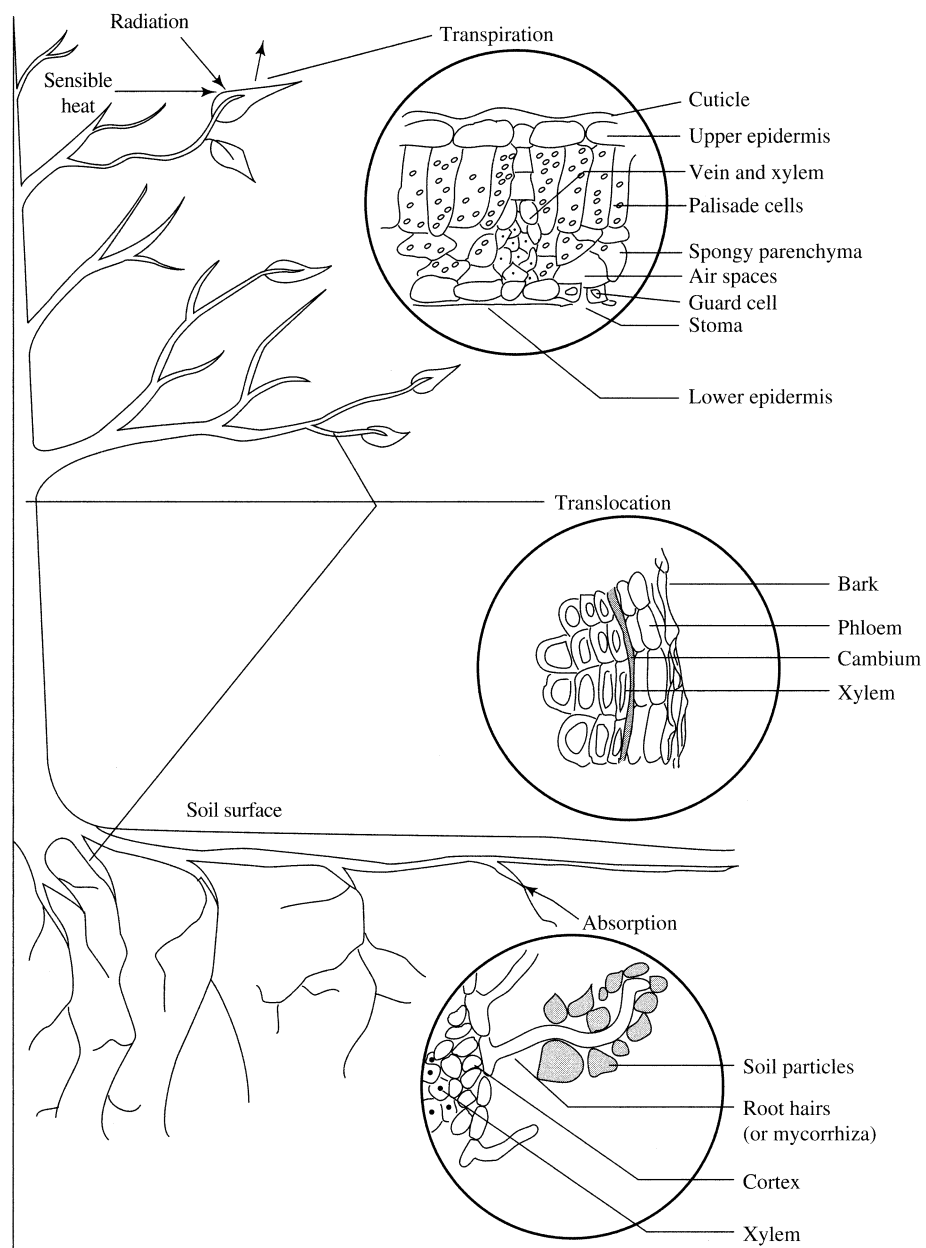


Figure 6.11 Diagram of the transpiration process and enlarged views of plant cellular structure where absorption, translocation, and transpiration occur [Hewlett (1982). *Principles of Forest Hydrology* (2nd ed.), with permission of The University of Georgia Press].

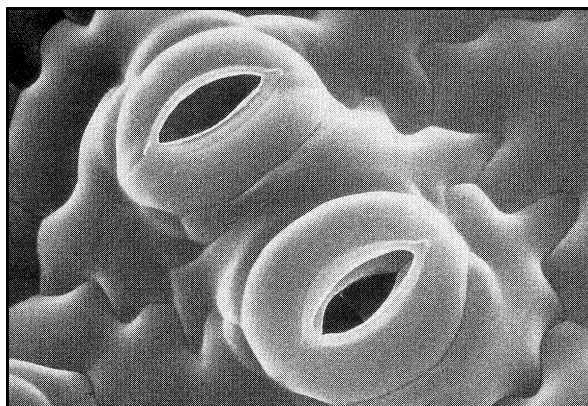


Figure 6.12 Photomicrograph of leaf surface showing stomata and the crescent-shaped guard cells that regulate their openings (Dr. Jeremy Burgess/Science Photo Laboratory).

6.5.2.1 Sap-Flow Measurement

Transpiration rates for whole trees can be determined by measuring the velocity of sap ascension. This is done by applying heat, either continuously or in pulses, at one level on the tree trunk and measuring the rate at which the heat travels upward. The conversion of sap velocity to flux rates depends on the cross-sectional area of sapwood, which varies with tree species and site conditions. Typically, simultaneous measurements on about 10 trees provide an accurate estimate of transpiration flux for a forest stand, but more may be required depending on the species and spatial heterogeneity of the site. In some regions, significant stand transpiration may occur in shorter understory vegetation in which sap-flow measurements are difficult. Intercomparisons indicate that sap-flow measurements generally compare well to estimates obtained by water-balance and isotopic techniques.

6.5.2.2 Stable-Isotope Techniques

As discussed in appendix B, about 0.015% of water molecules contain an atom of deuterium (^2H) in place of one atom of ^1H , and about 0.2% contain an atom of ^{18}O in place of the ^{16}O atom. Since various natural processes preferentially **fractionate** these stable (nonradioactive) isotopes, their concentration at different stages in the hydrologic cycle can be measured and used to determine the amounts of water involved in those stages. Assuming that the isotopic composition of water in a plant is the same as that in the water extracted by its roots, continuous measurements of near-

surface variations in the isotopic composition of water vapor can be used to partition total evaporation into evaporation from soil and water surfaces, evaporation from intercepted rainfall, and transpiration.

6.5.3 Modeling Transpiration

Since transpiration is essentially the same physical process as open-water evaporation, it can be represented by a mass-transfer equation of the form of equation (6.12). In order to develop an equivalent relation for transpiration, it is convenient first to recast the mass-transfer relation for evaporation using the concept of atmospheric conductance. This allows us to use some electric-circuit analogies for “scaling up” from a leaf to an entire vegetated surface.

6.5.3.1 Atmospheric Conductance/Resistance

We can represent the process of evaporation from open water by combining equation (6.11) and (6.12) and defining an **atmospheric constant**, K_{at} , as

$$K_{at} \equiv \frac{0.622 \cdot \rho_a}{p \cdot \rho_w}, \quad (6.45)$$

so that

$$E = K_{at} \cdot \left\{ \frac{u(z_m)}{6.25 \cdot \left[\ln \left(\frac{z_m - z_d}{z_0} \right) \right]^2} \right\} \cdot [e_s - e(z_m)], \quad (6.46)$$

where z_d is the zero-plane displacement height and z_0 is the roughness height.

The term in braces in equation (6.46) represents the efficacy of the turbulent eddies in the lower atmosphere in transporting water vapor from the surface to the ambient air, assuming equal efficacy for water vapor and momentum.³ This efficacy can also be viewed as an **atmospheric conductance** for water vapor, C_{at} , so that the mass-transfer equation for evaporation can be written as:

$$\begin{array}{lll} E & = & K_{at} \cdot C_{at} \cdot [e_s - e(z_m)], \\ \text{evaporation} & \text{atmospheric} & \text{atmospheric} \cdot \text{driving} \\ \text{rate} & \text{constant} & \text{conductivity} \text{ gradient} \end{array} \quad (6.47)$$

and C_{at} is given explicitly as

$$C_{at} \equiv \frac{u(z_m)}{6.25 \cdot \left[\ln \left(\frac{z_m - z_d}{z_0} \right) \right]^2} \quad (6.48)$$

and has the dimensions $[L T^{-1}]$. Sometimes it is more convenient to express the evaporation relation using **atmospheric resistance**, $R_{at} [T L^{-1}]$, where

$$R_{at} \equiv \frac{1}{C_{at}} = \frac{6.25 \cdot \left[\ln\left(\frac{z_m - z_d}{z_0}\right) \right]^2}{u(z_m)}, \quad (6.49)$$

so that

$$E = K_{at} \cdot \frac{1}{R_{at}} \cdot [e_s - e(z_m)]. \quad (6.50)$$

Typical values of z_d and z_0 for various land-cover types are given in table 6.4. The zero-plane displace-

ment height, z_d , and roughness height, z_0 , can be approximately related to the height of vegetation, z_{veg} , as

$$z_d = 0.7 \cdot z_{veg} \quad (6.51)$$

and

$$z_0 = 0.1 \cdot z_{veg} \quad (6.52)$$

If it is assumed that z_m is a fixed distance, say 2 m, above the top of the vegetation, equations (6.48), (6.51), and (6.52) can be used to generate a relation between atmospheric conductance and wind speed for various values of z_{veg} , as shown in figure 6.13.

Evaporation from an open-water surface is a “one-step” process in which water molecules pass directly

Table 6.4 Characteristic Surface Parameters.

Surface	Top of Canopy, z_{veg} (m)	Bottom of Canopy (m)	z_0 (m)	z_d (m)	Minimum R_{leaf} (s/m)	Maximum C_{leaf} (m/s)	Leaf-Area Index (LAI)	Stem-Area Index (SAI)	Albedo ^a α
Water			0.0012	0					0.070
Evergreen needle-leaf forest	17	6	0.98	10.2	0.01	100	5–6	2.0	0.062
Evergreen broad-leaf forest	35	1	2.2	20.7	0.01	100	5–6	2.0	0.076
Deciduous needle-leaf forest	14	2	0.9	9.2	0.01	100	1–6	2.0	0.062
Deciduous broad-leaf forest	20	11	0.9	7.2	0.01	100	1–6	2.0	0.092
Mixed cover	8	4	0.9	6.5	0.01	100	2.9–6	2.0	0.069
Woodland	14	6	0.8	7.4	0.01	100	3.4–5.7	2.1	0.075
Wooded grassland	8	4	0.5	3.6	0.015	67	2.0–4.6	2.6	0.091
Closed shrubland	5	2	0.1	1.4	0.015	67	1.4–5.1	2.4	0.099
Open shrubland	4	0	0.08	0.2	0.01	100	0.6–6	1.9	0.121
Grassland	0.6	0	0.04	0.2	0.02	50	0.7–2.6	3.7	0.107
Cropland	0.6	0	0.11	0.2	0.01	100	0.8–6	0.7	0.101
Bare ground			0.05	0.2					0.159
Urban and built-up			0.2	1.1					0.097

^aLive leaves.

Source: Data from “Mapped Static Vegetation Data.” NASA Land Data Assimilation Systems (<http://ldas.gfsc.nasa.gov/nldas/web/web.veg.table.html>).

from the liquid surface into the atmosphere, so it can be conceptually represented by the electric-circuit analogy shown in figure 6.14a. In this analogy a “current” (water vapor) moves in response to a “voltage” (vapor-pressure difference) across an atmospheric resistance.

6.5.3.2 Leaf Conductance/Resistance

Transpiration is a “two-step” process, in which water molecules pass: (1) from the stomatal cavity to the leaf surface and (2) from the leaf surface into the atmosphere. Continuing the electric-circuit analogy, the same driving force in this case operates across two resistances linked in series: leaf and atmospheric (figure 6.14b).

Leaf conductance/resistance is determined by the number of stomata per unit area and the size of the stomatal openings. Stomatal densities range from 10,000 to 100,000 stomata per square centimeter of leaf surface, depending on species (Hewlett 1982). Table 6.4 lists leaf conductances at maximum stomatal opening for various land-cover types. As noted earlier, plants control the size of the stomatal openings, and hence leaf conductance, by the response of the guard cells. These cells have been found to respond to: (1) light intensity; (2) ambient CO_2 concentration; (3) leaf/air vapor-pressure difference; (4) leaf temperature; and (5) leaf water content (Stewart

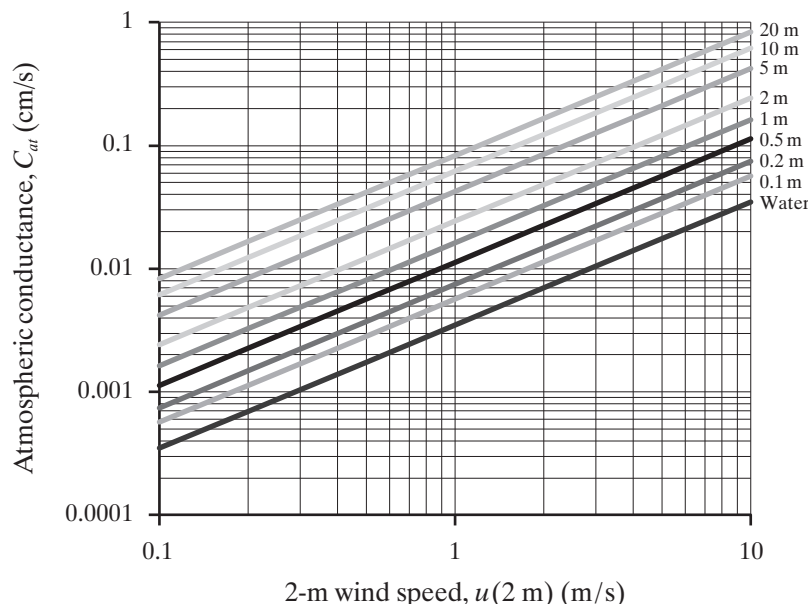


Figure 6.13 Relation between atmospheric conductance, C_{at} , and wind velocity measured 2 m above the canopy, $u(2 \text{ m})$, for vegetation of various heights, z_{veg} , and at a typical water surface. It is assumed that atmospheric stability is near neutral.

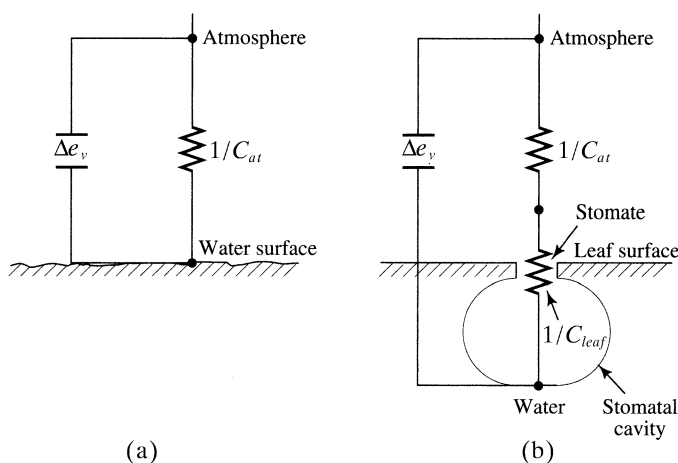


Figure 6.14 Conceptualization of (a) open-water evaporation and (b) transpiration in terms of atmospheric resistance ($1/C_{at}$) and leaf resistance ($1/C_{leaf}$). Δe_v is the driving vapor-pressure difference between the evaporating surface and the atmosphere.

1989). We first examine how these factors affect leaf conductance, and then incorporate them in a model for the transpiration from a vegetative canopy.

Stewart (1988) developed and tested a model for estimating hourly evapotranspiration that incorporates four of the five factors that determine leaf conductance—the effect of CO₂ concentration was not included because it usually varies little with time.⁴ As shown in table 6.5, he substituted more commonly measured hydrologic variables for some of the controlling factors—in particular, soil-moisture deficit was used as a proxy for leaf-water content. His model has the general form

$$C_{leaf} = C^*_{leaf} \cdot f_K(K_{in}) \cdot f_p(\Delta\rho_v) \cdot f_T[T(z_m)] \cdot f_\theta(\Delta\theta), \quad (6.53)$$

where C^*_{leaf} is the maximum value of leaf conductance (i.e., values from table 6.4), K_{in} is incident shortwave radiation flux, $\Delta\rho_v$ is the humidity deficit [the difference between the saturated and actual absolute humidity of the air, calculated from vapor pressures and temperature via equations (6.2) and (6.3)], $T(z_m)$ is air temperature at the measurement height, and $\Delta\theta$ is the soil-moisture deficit (the difference between the field capacity and the actual water content of the root zone).

The f s in equation (6.53) represent the effects of each environmental factor on relative leaf conductance; they are nonlinear functions that vary from 0 to 1, as shown in figure 6.15. While the constants in

these functions have been derived from studies at only one site (a pine forest in southeast England), controlled studies indicate that their form is quite general (Jarvis 1976; Wang and Dickinson 2012). An abbreviated form of the model incorporating only $f_K(K_{in})$ and $f_p(\Delta\rho_v)$ (but with different constants, determined by calibration at the site) successfully modeled transpiration from prairie grasses in Kansas (Stewart and Gay 1989).

6.5.3.3 Canopy Conductance

A vegetated surface like a grass, crop, or forest canopy can be thought of as a large number of leaf conductances in parallel. Again, from the laws of electric circuits, the total conductance of a number of conductances in parallel equals the sum of the individual conductances. Thus it is possible to represent a reasonably uniform vegetated surface as a single “big leaf” whose total conductance to water vapor is proportional to the sum of the conductances of millions of individual leaves. The relative size of this big leaf is reflected in the **leaf-area index, LAI**, defined as

$$LAI \equiv \frac{\text{total area of leaf surface above ground area } A}{A}. \quad (6.54)$$

Canopy conductance, C_{can} is then given by

$$C_{can} = k_s \cdot LAI \cdot C_{leaf}, \quad (6.55)$$

where k_s is a **shelter factor** that accounts for the fact some leaves are sheltered from the sun and wind and

Table 6.5 Stewart's (1988) Model of Leaf Conductance as a Function of Environmental Factors.^a

Factor Controlling Stomatal Opening	Quantity Representing Controlling Factor in Model	Functional Relation
light	incident solar radiation (MJ m ⁻² day ⁻¹)	$f_K(K_{in}) = \frac{12.78 \cdot K_{in}}{11.57 \cdot K_{in} + 104.4}$ $0 \leq K_{in} \leq 86.5 \text{ MJ m}^{-2} \text{ day}^{-1}$
CO ₂ concentration	(not included)	(none)
vapor-pressure deficit	absolute humidity deficit, $\Delta\rho_v$ (kg/m ³)	$f_p(\Delta\rho_v) = 1 - 66.6 \cdot \Delta\rho_v$ $0 \leq \Delta\rho_v \leq 0.01152 \text{ kg/m}^3$ $f_p(\Delta\rho_v) = 0.233, 0.01152 \text{ kg/m}^3 \leq \Delta\rho_v$
leaf temperature	air temperature, $T(z_m)$ (°C)	$f_T[T(z_m)] = \frac{T(z_m) \cdot [40 - T(z_m)]^{1.18}}{691}$ $0 \leq T(z_m) \leq 40^\circ\text{C}$
leaf water content	soil-moisture deficit, $\Delta\theta$ (cm)	$f_\theta(\Delta\theta) = 1 - 0.00119 \cdot \exp(0.81 \cdot \Delta\theta)$ $0 \leq \Delta\theta \leq 8.4 \text{ cm}$

^aFunctional relations are plotted in figure 6.15.

thus transpire at lower rates. Values of k_s range from 0.5 to 1, and decrease with increasing LAI (Carlson 1991); a value of $k_s = 0.5$ is probably a good estimate for a completely vegetated area (Allen et al. 1989).

Leaf-area indices for various types of plant communities are given in table 6.4. For deciduous forests, leaf area changes through the growing season, rising from near 0 to a maximum and back; figure 6.16 shows examples of the seasonal variation of LAI used in modeling transpiration for three types of forests.

6.5.3.4 The Penman–Monteith Model

Making use of equation (6.12) and the definitions of γ [equation (6.21)], K_{at} [equation (6.45)], and C_{at} [equation (6.48)], the Penman (combination) model for evaporation from a free-water surface [equation (6.36)] can be written in terms of atmospheric conductance as

$$E = \frac{\Delta \cdot (K + L) + \rho_a \cdot c_a \cdot C_{at} \cdot e_a^* \cdot [1 - RH(z_m)]}{\rho_w \cdot \lambda_v \cdot (\Delta + \gamma)} \quad (6.56)$$

Recall that the derivation of this equation assumes no water-advedted energy, no ground-heat conduction, and no heat-storage effects.

Monteith (1965) showed how the Penman equation can be modified to represent the evapotranspiration rate, ET , from a vegetated surface by incorporating canopy conductance:

$$ET = \frac{\Delta \cdot (K + L) + \rho_a \cdot c_a \cdot C_{at} \cdot e_a^* \cdot [1 - RH(z_m)]}{\rho_w \cdot \lambda_v \cdot [\Delta + \gamma \cdot (1 + C_{at}/C_{can})]} \quad (6.57)$$

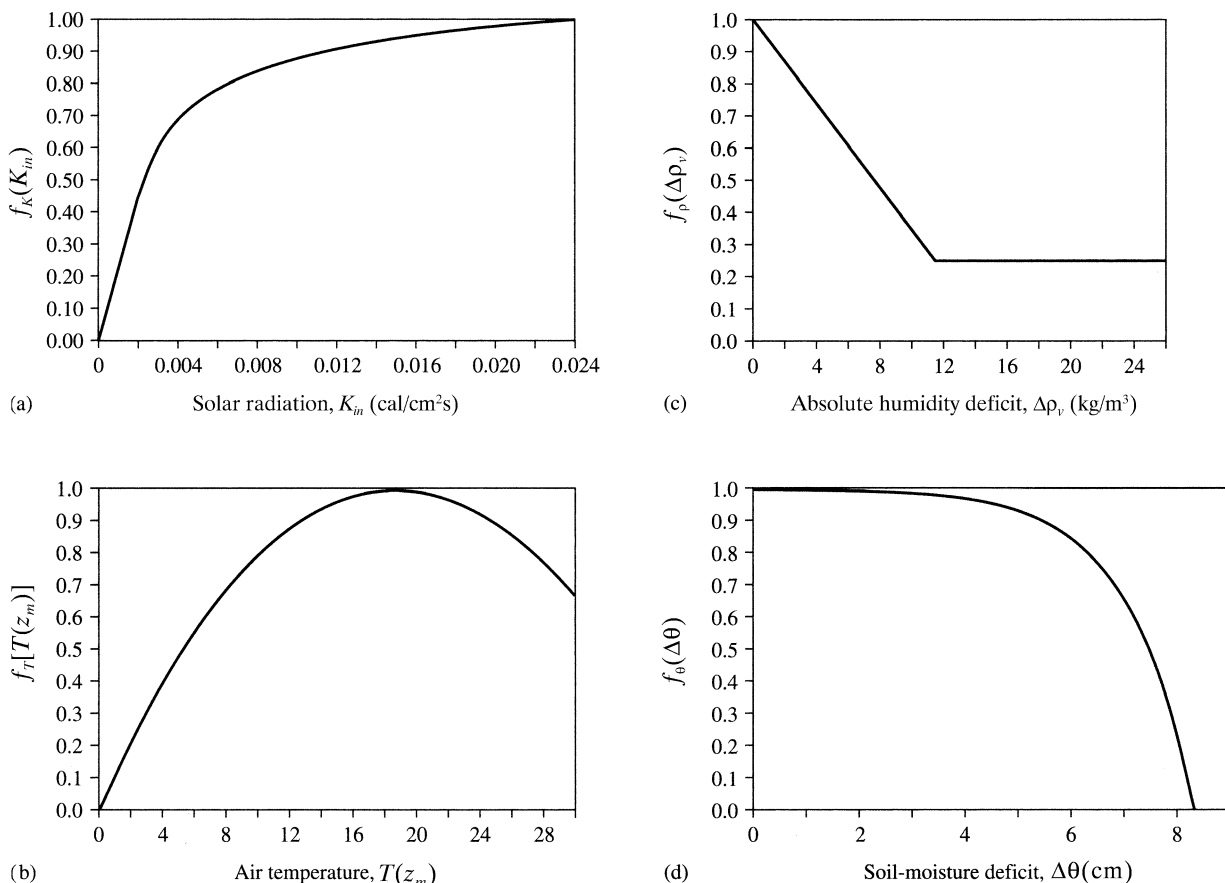


Figure 6.15 Effects of (a) solar radiation, K_m ; (b) air temperature, $T(z_m)$; (c) absolute-humidity deficit, $\Delta\rho_v$; and (d) soil-moisture deficit, $\Delta\theta$ on relative leaf conductances (see table 6.5) [adapted from Stewart (1988)].

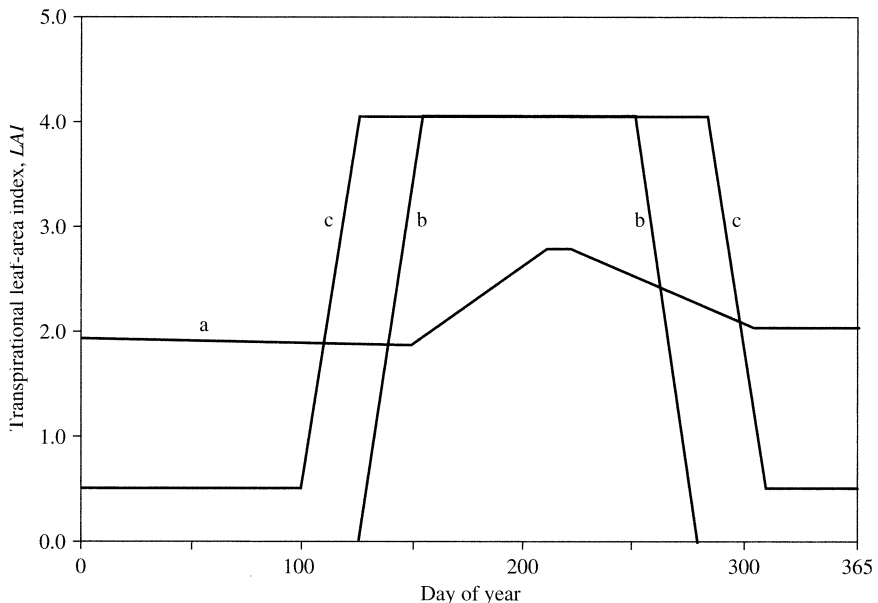


Figure 6.16 Annual variability of transpirational leaf-area index, LAI , in (a) a pine forest in southeast England [Stewart (1988)]; (b) a hardwood forest in New Hampshire [Federer and Lash (1978a)]; and (c) a hardwood forest in North Carolina [Federer and Lash (1978a)].

this has become known as the **Penman–Monteith equation**. The assumptions of no water-adverted energy and no heat-storage effects, which are generally not valid for natural water bodies, are usually reasonable when considering a vegetated surface. Note that equation (6.57) reduces to equation (6.56) when $C_{can} \rightarrow \infty$.

The Penman–Monteith equation has been successfully tested in many environments (see for example Calder 1977, 1978; Berkowicz and Prahm 1982; Lindroth 1985; Dolman et al. 1988; Stewart 1988; Allen et al. 1989; Stewart and Gay 1989; Lemeur and Zhang 1990) and has become the most widely used approach to estimating evapotranspiration from land surfaces. Box 6.5 gives example calculations of the effect of soil moisture on evaporation rate using the Stewart and Penman–Monteith relations. We will consider the Penman–Monteith equation further later in this chapter in discussing methods of estimating areal evapotranspiration.

6.6 Interception and Interception Loss

Interception is the process by which precipitation falls on vegetative surfaces (the **canopy**), where it is subject to evaporation. The portion of intercepted water that evaporates is called **interception**

loss; as we shall see, it is a significant fraction of total evapotranspiration in most regions.

Interception loss depends strongly on: (1) vegetation type, density, and stage of development, which should be well characterized by leaf-area index and (2) the intensity, duration, frequency, and form of precipitation. Vegetation type is commonly altered by human activities (e.g., deforestation), and there is concern that aspects of precipitation climatology may be altered by climate change (Waggoner 1989). A sound physical basis for understanding the interception process is essential in order to sort out and predict how these changes will affect the hydrologic cycle locally and globally. In particular,

The question of whether interception loss is an addition to, as opposed to a replacement for, transpiration loss is important in evaluating the effects of vegetation changes on regional water balances.

Under some weather conditions, vegetation can “comb” water from clouds and fog and thereby add water input to a region. This phenomenon is sometimes called “positive interception”; it is briefly discussed as “occult precipitation” in section 4.1.6. Snow interception is treated in section 5.4.2.

Box 6.5 Example Calculations with the Stewart–Penman–Monteith Model

Here we use the Stewart model of leaf conductance [equation (6.53)] and the Penman–Monteith model [equation (6.57) to compare the transpiration rate from the canopy for soil-moisture deficits ($\Delta\theta$) of (1) 0 cm (wet soil) and (2) 7.0 cm (dry soil) under the conditions in the

pine forest at Thetford, England, studied by Stewart (1988). These relations are programmed in the spreadsheet PenMontX.xls found on the disk accompanying this text. Tables 6B5.1–6B5.3 give the vegetation and environmental conditions.

Table 6B5.1 Vegetation Conditions.^a

Tree Height, z_{veg} (m)	Zero-Plane Displacement, z_d (m)	Roughness Height, z_0 (m)	Leaf-Area Index, LAI	Maximum Leaf Conductance, C^*_{leaf} (m/day)	Shelter Factor, k_s
16.5	11.6	1.65	2.8	199	0.5

^aThe values of z_{veg} , LAI, and C^*_{leaf} were determined for this site and are used in preference to values from table 6.4. Measurement height $z_m = 2$ m above the canopy. z_d and z_0 are calculated via equations (6.51) and (6.52).

Table 6B5.2 Environmental Conditions (Radiation).

Incident Solar Radiation, K_{in} (MJ/m ² · day)	Albedo, α	Net Solar Radiation, K (MJ/m ² · day)	Net Longwave Radiation, L (MJ/m ² · day)
25.1	0.18	20.6	-4.99

Table 6B5.3 Environmental Conditions (Atmosphere).

Atmospheric Pressure, p (kPa)	Air Temperature, $T(z_m)$ (°C)	Saturation Vapor Pressure, $e^*(z_m)$ (kPa)	Relative Humidity, $RH(z_m)$	Wind Speed, $u(z_m)$ (m/day)	Slope of Saturation- Vapor-Pressure Curve, Δ (kPa/°C)	Psychrometric Constant, γ (kPa/°C)
101.3	19.2	2.23	0.54	259,200	0.139	0.067

Values of additional quantities in the Penman–Monteith equation are given in table 6B5.4.

Table 6B5.4 Additional Quantities in Penman–Monteith Equation [Equation (6.57)].

Atmospheric Conductance, C_{at} (m/day)	Air Density, ρ_a (kg/m ³)	Air Specific Heat, c_a (MJ/kg · °C)	Latent Heat, λ_v (MJ/kg)
20,057	1.29	1.005×10^{-3}	2.45

Calculation of the leaf conductance, C_{leaf} , via equation (6.53) requires the absolute humidity deficit, $\Delta\rho_v$, which is found by first calculating the air vapor-pressure deficit $\Delta e(z_m)$ via equation (6.3):

$$\begin{aligned}\Delta e(z_m) &\equiv e^*(z_m) - e(z_m) \\ &= e^*(z_m) \cdot [1 - RH(z_m)] \\ &= 2.23 \cdot (1 - 0.54) = 1.03 \text{ kPa.}\end{aligned}$$

Using relations in section 3.1, vapor-pressure deficit, Δe , is converted to absolute humidity deficit, $\Delta\rho_v$, via

$$\Delta\rho_v (\text{kg/m}^3) = \frac{100 \cdot \Delta e (\text{kPa})}{461 \cdot [T (\text{°C}) + 273.2]} = 0.0076 \text{ kg/m}^3.$$

Using the equations in table 6.5, we compute the values of the f functions of equation (6.53). The results are found in table 6B5.5.

Table 6B5.5 Values of *f* Functions in Equation (6.53) (Table 6.5).

Function	$f_K(K_{in})$	$f_p(\Delta p_v)$	$f_T[T(z_m)]$	$f_\theta(\Delta\theta)$	$f_\theta(\Delta\theta)$
Variable value	25.1 MJ/m ² · day	0.0076 kg/m ³	19.2 °C	0 cm	7 cm
Function value	0.812	0.493	0.998	1.00	0.655

From the above *f* values we calculate the conductances via equations (6.53) and (6.55) and *ET* values via equation (6.57). The results are found in table 6B5.6.

Table 6B5.6 Leaf and Canopy Conductances and *ET*.

$\Delta\theta$ (cm)	C_{leaf} (m/day)	C_{can} (m/day)	ET mm/day
0	79.4	111.1	0.974
7	52.0	72.8	0.642

It is also instructive to compare the latent-heat flux, *LE*, associated with the evaporation of intercepted water with the available energy (net radiation). The net radiation, *K* + *L*, in this example is

$$K + L = (25.1 \text{ MJ/m}^2 \cdot \text{day}) \times (1 - 0.18) - 4.99 \text{ MJ/m}^2 \cdot \text{day} \\ = 16.0 \text{ MJ/m}^2 \cdot \text{day}.$$

The latent-heat flux associated with evaporating the intercepted water is

$$LE = \rho_w \cdot \lambda_v \cdot E \\ = (1,000 \text{ kg/m}^3) \times (2.45 \text{ MJ/kg}) \times (0.0953 \text{ m/day}) \\ = 233 \text{ MJ/m}^2 \cdot \text{day},$$

which is over 15 times the energy available from net radiation. The difference between the latent-heat flux and the net radiation must be provided by downward sensible-heat transfer, and this energy is supplied by air advected from the surrounding region. Several studies (e.g., Stewart 1977) have shown that such energy advection is commonly involved in evaporating intercepted water, that is, interception loss can markedly cool the air regionally.

6.6.1 Definitions

Figure 6.17 illustrates the following definitions used in describing and measuring interception.

- **Gross rainfall**, *R*, is the rainfall measured above the vegetative canopy or in the open.
- **Canopy interception loss**, *Ec*, is water that evaporates from the canopy.
- **Throughfall**, *Rt*, is rainfall that reaches the ground surface directly through spaces in the canopy and by dripping from the canopy.
- **Stemflow**, *Rs*, is water that reaches the ground surface by running down trunks and stems.
- **Litter interception loss**, *EI*, is water that evaporates from the ground surface (usually including near-ground plants and leaf litter).
- **Total interception loss**, *Ei*, is the sum of canopy and litter interception losses.
- **Net rainfall**, *Rn*, is the gross rainfall minus the total interception loss.

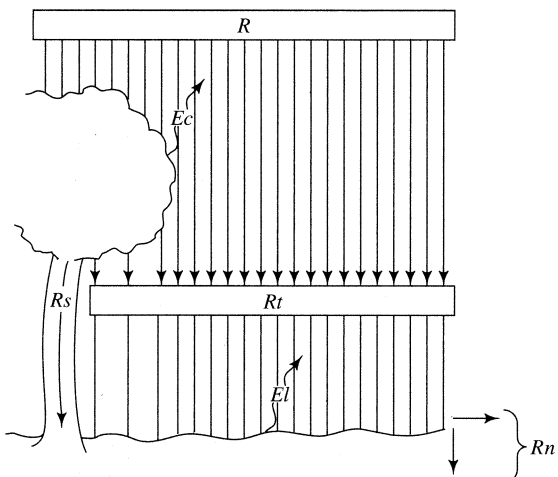


Figure 6.17 Definitions of terms used in describing the interception process. *R* = gross rainfall; *Ec* = canopy interception loss; *Rt* = throughfall; *Rs* = stemflow; *EI* = litter interception loss; *Rn* = net rainfall.

These definitions are applied over a representative area of the plant community of interest, so they take into account the typical spacing between plants. If the symbols given represent volumes of water [L^3] or volumes per unit area [L] during a given time period, we have

$$R_n = R - E_i; \quad (6.58)$$

$$E_i = E_c + E_l; \quad (6.59)$$

$$R = R_t + R_s + E_c; \quad (6.60)$$

and

$$R_n = R_t + R_s - E_l. \quad (6.61)$$

6.6.2 Field Measurement of Interception

As with other components of evapotranspiration, interception loss cannot be measured directly. The most common approach to determining the amounts of canopy interception loss in various plant communities is to measure gross rainfall, throughfall, and stemflow, and solve equation (6.60) for E_c . However, this is not a simple procedure because of: (1) the difficulties in accurately measuring rainfall, particularly at low rainfall intensities when interception losses are relatively large (see section 4.2.1.2); (2) the large spatial variability of throughfall; and (3) the difficulty and expense of measuring stemflow.

Helvey and Patric (1965a) reviewed criteria for measuring interception quantities, and concluded that averaging the catches in 20 rain gauges spaced randomly over a representative portion of the community should give acceptable estimates of throughfall; typical intergauge spacing for forest studies is on the order of 10 to 30 m (Gash et al. 1980). Large plastic sheets have also been used to get an integrated measure of net rainfall (Calder and Rosier 1976).

Stemflow is measured by attaching flexible troughs tightly around the trunks of trees and conducting the water to rain gauges or collecting bottles. Helvey and Patric (1965a) stated that measuring stemflow from all trees on randomly selected plots gives the most representative results, with plot diameters at least 1.5 times the diameter of the crown of the largest trees. However, since stemflow is usually much less than throughfall, most studies have estimated stemflow less rigorously by sampling a few "typical" trees.

The few published studies of grass or litter interception have usually been done using artificial rain, either by measuring the net rainfall from small iso-

lated areas in the field (Merriam 1961) or by collecting undisturbed samples of the surface litter and setting them on recording scales in the laboratory (Pitman 1989; Putuhena and Cordery 1996).

6.6.3 Modeling

6.6.3.1 Regression Analysis

Most of the earlier studies of interception have used results of field or laboratory measurements in particular plant communities to establish equations relating R_t , R_s , E_l , R_n , and/or E_i to R via regression analysis. These equations are usually of the form

$$Y = M_Y \cdot R + B_Y, \quad (6.62)$$

where Y is one of the components of the interception process (R_t , R_s , E_c , E_l , or E_i), R is gross rainfall for an individual storm, and M_Y and B_Y are empirical constants determined by regression analysis. Equations of the form of (6.62) can readily be adapted to give estimates for seasonal or annual periods:

$$\Sigma Y = M_Y \cdot \Sigma R + n \cdot B_Y, \quad (6.63)$$

where the summation sign indicates seasonal or annual totals and n is the number of storms per season or year.

Table 6.6 summarizes published equations for various community types. Unfortunately, few of the studies that developed these equations made concurrent measurements of leaf-area index, so it is difficult to judge the range of applicability of their results. Only a few studies have included estimates of litter interception loss; most of these have found E_l in the range $0.02 \cdot R$ to $0.05 \cdot R$, though some higher values have been reported (Helvey and Patric 1965b; Helvey 1971).

As shown in box 6.6, regression equations can be useful for showing the effects of rainfall amount and number of storms on net rainfall (figure 6.18 on p. 288). However, such equations cannot usually be confidently applied to areas other than where they were developed.

6.6.3.2 Conceptual Models

Because of the uncertain transferability of regression equations and the need for simulating interception loss in predictive models, considerable effort has been expended to develop conceptual models of the process. The **sparse Rutter model** is the most widely used of these; it was originally developed by Rutter et al. (1971) and modified by Gash and Mor-

ton (1978) and Valente et al. (1997). This model operates at a time step (Δt) of one day, and usually assumes that each day's rain occurs in a single storm. A running water balance of the canopy (leaves and

Table 6.6 Regression Equations for Estimating Throughfall, R_t , and Stemflow, R_s , as Functions of Gross Rainfall, R , for Individual Storms [Equation (6.62)], or for Seasons [Equation (6.63)].

Plant Community	Quantity (Y) (cm)	M_Y (cm)	B_Y
Eastern Hardwoods^a			
Full leaf	R_t	0.901	-0.079
	R_s	0.041	-0.013
	$R_t + R_s$	0.941	-0.092
Leafless	R_t	0.914	-0.038
	R_s	0.062	-0.013
	$R_t + R_s$	0.978	-0.051
Conifers^b			
Red pine	$R_t + R_s$	0.89	-0.10
Loblolly pine	$R_t + R_s$	0.88	-0.08
Shortleaf pine	$R_t + R_s$	0.91	-0.10
Eastern white pine	$R_t + R_s$	0.91	-0.13
Ponderosa pine	$R_t + R_s$	0.93	-0.15
Pines (average)	$R_t + R_s$	0.90	-0.10
Spruce-fir-hemlock	$R_t + R_s$	0.79	-0.13

^aEastern hardwood values from Helvey and Patric (1965b).

^bConifer values from Helvey (1971).

branches) and tree trunks is computed using the conceptual scheme shown in figure 6.19 on p. 289. A portion (k_{gap}) of the rain falls through the canopy; of the rain hitting the canopy, a small fraction (k_{tR}) runs down the trunks. The canopy storage (S_c) is filled by rainfall and emptied by evaporation (E_c), at a rate given via the Penman-Monteith equation (E_p), and by drainage (D) as

$$D = D_S \cdot \exp[k_D \cdot (S_c - S_c^*)], S_c \geq S_c^* \\ D = 0, S_c < S_c^*, \quad (6.64)$$

where S_c^* is the canopy storage capacity. A similar relation is used to calculate drainage via trunks, which have storage capacity S_t^* . A portion (k_{tD}) of the rain reaching the trunks also evaporates, the remainder becomes stemflow (R_t). The total interception loss from the canopy-covered area (E_c) is the sum of the evaporation from canopy (E_c) and trunks (E_t).

The structure of the vegetation is reflected in the parameters S_c^* , S_t^* , k_{tR} , and k_{tD} . Valente et al. (1997) discussed how these can be determined from analysis of regression relations of the form of equation (6.62) developed from field measurements. However, Miralles et al. (2010) reviewed a number of studies in various forest types and found that the values of all the model parameters had a surprisingly small range globally (table 6.7 on p. 290), with no clear relation to forest characteristics such as leaf-area index. Several studies have found good agreement between observed interception loss and that simulated by the Rutter-Gash model and its variants (e.g., Gash and Morton 1978; Gash 1979; Lloyd et al. 1988; Valente et al. 1997).

The **Liu model** (Liu 1997, 2001) is a somewhat simpler variant of the Rutter-Gash model, in which the storage and interception loss of the canopy and

Box 6.6 Example Calculations: Effects of Total Rainfall and Number of Storms on Net Rainfall

Summer gross rainfall at Fairbanks, Alaska, ranges from 100 to 400 mm, typically arriving in about 45 low-intensity storms. Although none of the equations listed in table 6.6 applies to birch forests in this region, we use the ones for eastern hardwoods in leaf to illustrate the effects on net rainfall of (1) total summer gross rainfall (ΣR) and (2) number of storms (n):

$$\Sigma(R_t + R_s) = 0.941 \cdot \Sigma R - 0.92 \cdot n \quad (6B6.1)$$

and assume $\Sigma E_l = 0.04 \cdot \Sigma R$. Then from equation (6.61) we have

$$\Sigma R_n = 0.941 \cdot \Sigma R - 0.92 \cdot n - 0.04 \cdot \Sigma R \\ = 0.901 \cdot \Sigma R - 0.92 \cdot n. \quad (6B6.2)$$

Now we can use this relation to estimate ΣR_n and $\Sigma R_n / \Sigma R$ for $n = 10$ to 60 storms per season over the range $100 \leq \Sigma R \leq 400$ mm, with the results shown in figure 6.18.

Although the relations shown in figure 6.18 may not strictly apply to central Alaska, they illustrate the general effects of total seasonal rainfall and number of storms on net rainfall: For a given seasonal rainfall total, the net rainfall decreases markedly with number of storms.

trunks are combined (as they are in figure 6.17). For a period with n storms, this model takes the form

$$E_c = (S_c^* + S_t^*) \cdot \left[1 - \frac{\bar{E}}{(1-F) \cdot \bar{R}} \right] \cdot \left[n - \sum_{i=1}^n D_i \right] + \frac{\bar{E}}{\bar{R}} \cdot \sum_{i=1}^n R_i, \quad (6.65)$$

where

$$D_i = \exp \left[-\frac{(1-F) \cdot R_i}{S_c^* + S_t^*} \right] \quad (6.66)$$

and \bar{E} and \bar{R} are the average rates of evaporation and rainfall, respectively.

In a comparison study, Liu (2001) found that the Rutter-Gash and Liu models both successfully

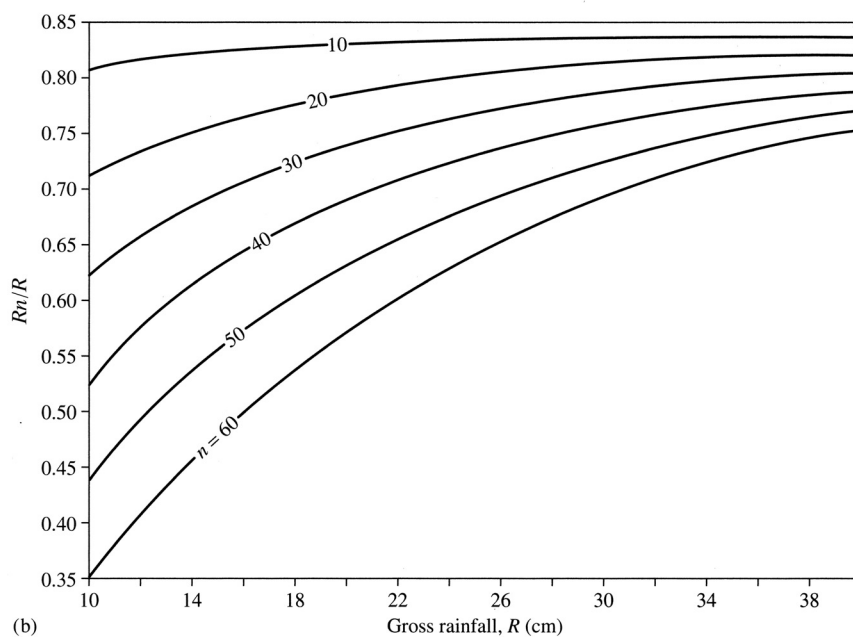
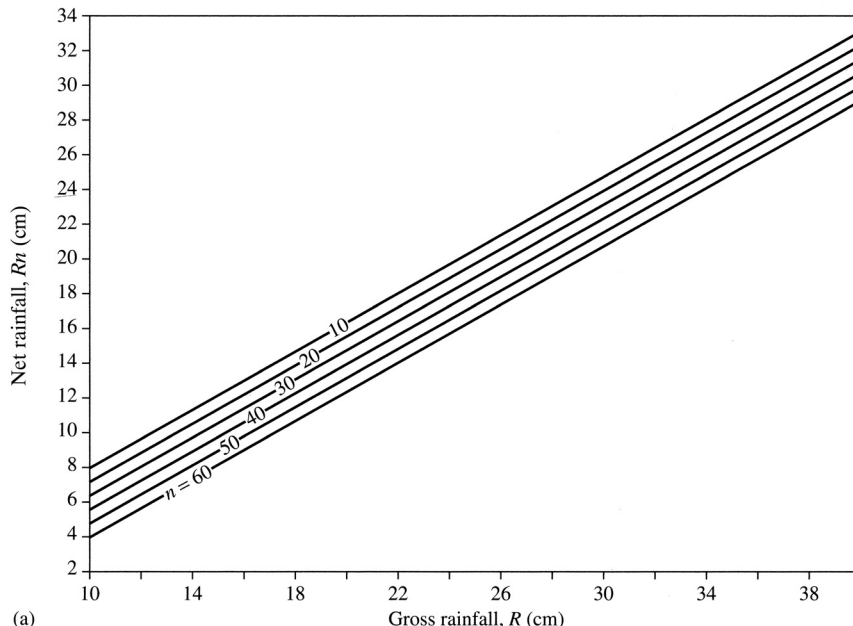


Figure 6.18 (a) Net rainfall, R_n , and (b) the ratio of net rainfall to gross rainfall, R_n/R , as a function of seasonal gross rainfall, R , and number of storms per season, n , estimated for a central Alaskan birch forest. (See box 6.6.)

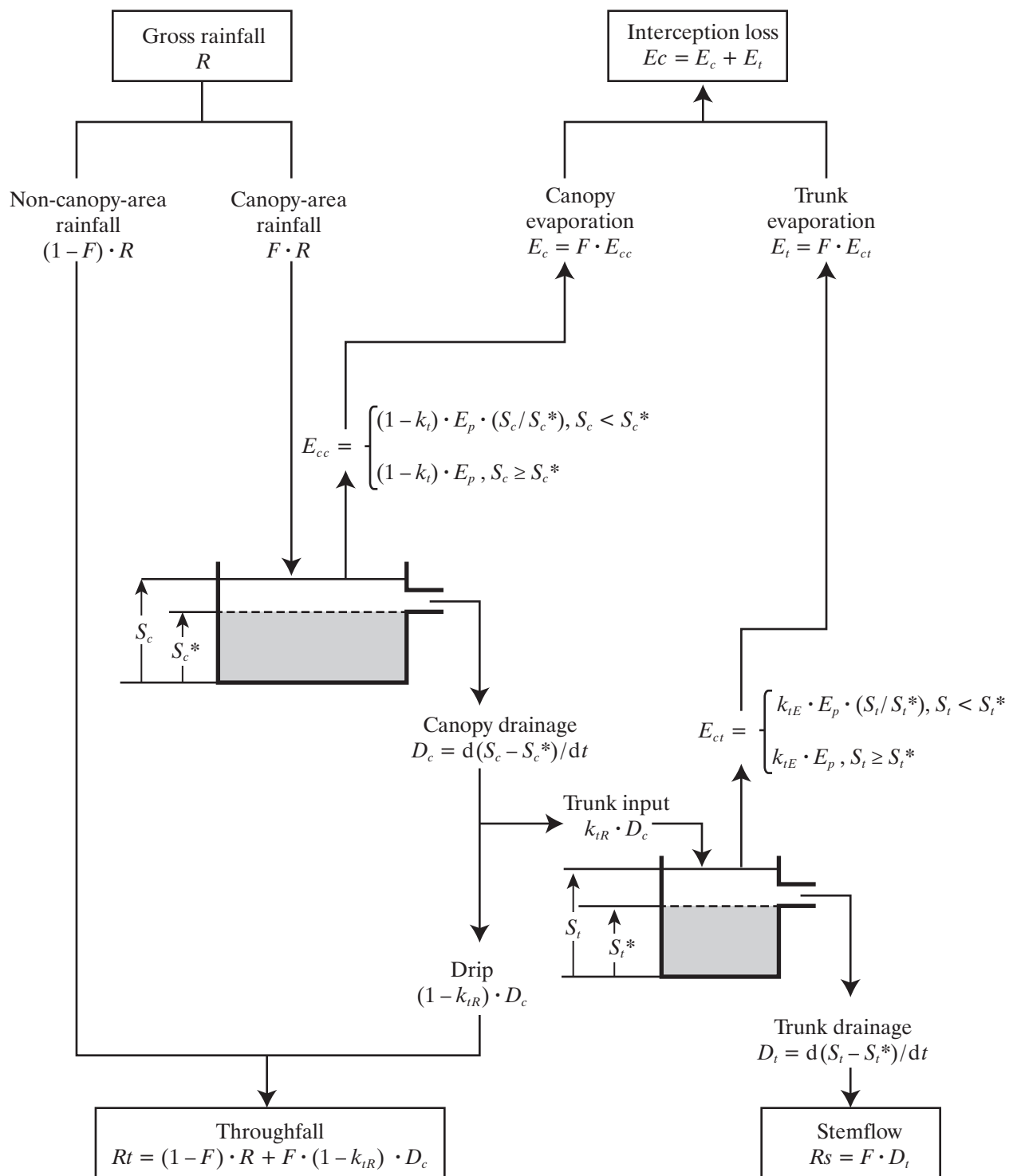


Figure 6.19 The “sparse” Rutter conceptual model of interception as developed by Valente et al. (1997) [adapted from Valente et al. (1997)].

Table 6.7 Parameters of Gash Interception Model and Values Used in Global Simulation by Miralles et al. (2010).

Parameter	Symbol	Average Value ± Standard Deviation
Canopy storage capacity	S_c^*	$1.2 \pm 0.4 \text{ mm}$
Trunk storage capacity	S_t^*	0.02 mm
Fraction of rain to trunks	k_{tR}	0.02
Fraction of trunk evaporation	k_{tE}	0.02

modeled long-term interception losses from a broad range of 20 forests globally, and suggested that the Liu model might be preferable because it has a simpler form and fewer data requirements. Buttle and Farnsworth (2012) found that the Liu model gave good predictions of seasonal interception in red pine plantations of different ages and in mature mixed hardwood forest stands in southern Ontario, Canada.

6.6.4 Evaporation of Intercepted Water

As noted, the Penman equation [equation (6.56)] is used to calculate the rate of evaporation of intercepted water in the Rutter–Gash and Liu models. This is equivalent to using the Penman–Monteith equation [equation (6.57)] with infinite canopy conductance, which is appropriate because the evaporation is from the leaf surface with no effect from the stomata. Thus only atmospheric conductance affects the evaporation rates of intercepted water, and intercepted water will evaporate faster than transpiration that occurs under the same conditions.

Note from figure 6.13 that atmospheric conductance increases markedly with vegetation height for a given wind speed: When $u(2 \text{ m}) = 1 \text{ m/s}$, $C_{at} \approx 0.006 \text{ m/s}$ above 0.1-m high grass, but $C_{at} \approx 0.06 \text{ m/s}$ above 10-m high trees. This is due to the effects of surface roughness on the efficiency of turbulent transfer (section 3.5.3). Thus for forests the difference between the evaporation rates of intercepted water and transpired water is considerable, as illustrated by the following example.

In the example of box 6.5, the atmospheric conductance C_{at} is 20,057 m/day (0.232 m/s) (table 6B5.4), canopy conductance C_{can} for a pine forest is 111.1 m/day (table 6B5.6), and with $\Delta\theta = 0 \text{ cm}$ the Penman–Monteith equation gives a transpiration

rate of 0.974 mm/day (table 6B5.6). With an infinite canopy conductance, equation (6.57) yields a canopy evaporation rate of 95.3 mm/day, almost 100 times greater than the transpiration rate! Thus if there is 1 mm of intercepted water on the canopy, it will be completely evaporated in $(1 \text{ mm})/(95.3 \text{ mm/day}) = 0.0105 \text{ day} = 0.252 \text{ hr}$.

The contrast between rates of evaporation of intercepted water and rates of transpiration has an important bearing on understanding the hydrologic impacts of land-use changes, as discussed in the following section.

6.6.5 Hydrologic Importance of Interception Loss

6.6.5.1 Observed Values of Interception Loss

Table 6.8 summarizes measurements of seasonal interception loss (E_c) in various plant communities; values range from 10 to 40% of gross precipitation. A recent study by Miralles et al. (2010) used the sparse Rutter model with the parameter values of table 6.7 to model forest rainfall interception loss globally at a spatial resolution of about 300 km². Satellite observations were used to classify rainfall events as “synoptic” (average rainfall rate $\bar{R} = 1.5 \text{ mm/hr}$) or “convective” (average rainfall rate $\bar{R} = 5.6 \text{ mm/hr}$). They found that average evaporation rate of intercepted water varied little with forest type, and had an average value $E_c = 0.3 \text{ mm/hr}$. Using these values, they found that average values of interception loss ranged from 0 to about 500 mm/yr and 0 to 30% of rainfall, comparable to the range in table 6.8, and mapped the global distribution of these values.

The Miralles et al. (2010) study found that the main determinant of interception loss was the volume and intensity of rainfall (as suggested by the example in box 6.6): Rates are highest where rain tends to come in long-duration (synoptic) storms and lowest where short-duration (convective) storms dominate. Because of the association of forest types and climate (figures 2.48 and 2.49), the highest average percentages of interception loss are associated with conifer forests (22%), and interception in tropical broadleaf evergreen forests (13%) is lower than in temperate deciduous broadleaf forests (22%), despite the lower canopy cover of deciduous forests in winter.

6.6.5.2 Does Interception Loss Add To or Replace Transpiration?

There has been considerable debate concerning the extent to which this loss is an addition to, as op-

Table 6.8 Annual Canopy Interception Loss as a Fraction of Gross Precipitation for Various Plant Communities.

Latitude	Location	Community	Annual Ptn. (cm) ^a	<i>Ec/R</i>
	Tropics	Lowland forest		0.22
	Tropics	Montane forest		0.18
3.0	Manaus, Brazil	Amazonian rain forest	281	0.09
4.0	Malaysia	Lowland forest		0.23
5.9	Ivory Coast	Evergreen hardwoods		0.09
6.5	W Java	Lowland tropical rain forest		0.21
7.0	Ghana	Semideciduous moist forest		0.16
10.0	Nigeria	Forest-savannah boundary		0.05
11.3	Kottamparamba, India	Cashew	300	0.31
18.3	Mts., E Puerto Rico	Tabonuco et al.	575	0.42
18.3	Mts., E Puerto Rico	Dwarf forest		0.09
34.5	Mts., AR, US	Pine-hardwood		0.13
35.0	W NC, US	60-yr-old white pine	203	0.09
35.0	W NC, US	Mixed hardwoods	203	0.12
35.0	W NC, US	35-yr-old white pine	203	0.19
35.0	W NC, US	10-yr-old white pine	203	0.15
42.2	S Is. New Zealand	Mixed evergreen hardwood	260	0.24
43.9	Mts., N NH, US	Mixed hardwoods	130	0.13
~45.0	NW US	Douglas fir		0.24
~45.0	NW US	Douglas fir et al.		0.32
~45.0	NW US	Sitka spruce-hemlock et al.		0.35
~45.0	NW US	Mature Douglas fir		0.34
~45.0	NW US	White pine-hemlock		0.21
~45.0	NW US	Douglas fir-hemlock		0.24
51.4	SE UK	Corsican pine	79	0.35
51.4	Hampshire, UK	Hornbeam		0.36
51.4	Hampshire, UK	Douglas fir		0.39
51.4	Hampshire, UK	Oak		0.18
51.4	Hampshire, UK	Oak-defoliated		0.12
51.4	Hampshire, UK	Norway spruce		0.48
51.4	Hampshire, UK	Corsican pine		0.35
52.3	Norfolk, U	Scots & Corsican pine	60	0.36
52.5	Wales, UK	Sitka spruce	187	0.27
52.5	Castricum, Holland	Oak forest	31	0.22
55.0	S Scotland, UK	Sitka spruce	160	0.30
55.0	Northumberland, UK	Sitka spruce-mature	100	0.49
55.0	Northumberland, UK	Sitka spruce-pole timber	100	0.29
55.2	S Scotland, UK	Sitka spruce	97	0.32
56.4	Scotland, UK	Sitka spruce	213	0.28
57.7	NE Scotland, UK	Scots pine	64	0.42
58.3	SE AK, US	Hemlock-Sitka spruce		0.25

^aAnnual precipitation during period of measurement or climatic average, as given in source. Data from published sources.

posed to a replacement for, water loss by transpiration. Clearly most of the interception loss that occurs in seasons when vegetation is dormant is a net addition to evapotranspiration. When intercepted water is present during the growing season, it evaporates in preference to water in stomatal cavities because it does not encounter stomatal resistance. For short vegetation, atmospheric conductances are much lower than over forests (figure 6.13) and interception loss occurs at rates comparable to transpiration. Thus

For grasses and other short vegetation,
interception loss is to a large extent
compensated by reduction in transpiration and
makes little net addition to evapotranspiration
(McMillan and Burgy 1960).

However, as we have just seen, the evaporation of intercepted water in forests occurs at rates several times greater than for transpiration under identical conditions. Thus intercepted water disappears quickly and interception loss replaces transpiration only for short periods. Thus

For forests, interception loss is largely a
net addition to evapotranspiration.

For example, Stewart (1977) found that annual interception loss for the forest he studied was 214 mm, and that 69 mm would have transpired during the time this loss was occurring. Thus the net additional evapotranspiration due to interception was 145 mm; this was 26% of the total annual evapotranspiration.

Because forest interception is a significant additional component of seasonal evapotranspiration, tree removal by logging, forest fire, or wind damage increases the average runoff from the affected area, and afforestation decreases runoff (e.g., Hewlett and Hibbert 1961; Bosch and Hewlett 1982). The magnitude of the change is roughly proportional to the percentage change in forest cover (figure 6.20) and is largely due to increased or decreased interception loss. Change in the vertical extent of the root zone from which transpired water is extracted adds to the effect.

6.7 Potential and Reference-Crop Evapotranspiration

6.7.1 Conceptual Definition

The concept of *potential evapotranspiration* was introduced in section 2.2.8.3 in the discussion of the effects of climate change on hydrology. The concept originated as part of a scheme for climate classification by Thornthwaite (1948), who intended it to depend essentially on climate or weather, independent of surface characteristics:

Potential evapotranspiration (PET) is the rate at which evapotranspiration would occur from a large area completely and uniformly covered with growing vegetation with access to an unlimited supply of soil water and without advection or heat-storage effects (table 6.1).

However, this concept is problematical because there are several characteristics of a vegetative surface that have a strong influence on evapotranspiration rate even when there is no limit to the available water (see table 6.4 and figure 6.13): (1) the albedo of the surface, which determines the net radiation; (2) the maximum leaf conductance; (3) the atmospheric conductance, which is largely determined by vegetation height; and (4) the presence or absence of intercepted water. Because of these surface effects, Penman (1956) suggested replacing the PET concept with *reference-crop evapotranspiration*:

Reference-crop evapotranspiration (RET) is the amount of water transpired by a short green crop, completely shading the ground, of uniform height, and never short of water.

Another concern about the concept of PET is that its magnitude is often calculated from meteorological data collected under conditions in which the actual evapotranspiration rate is less than the potential rate. However, if evapotranspiration had been occurring at the potential rate, the latent- and sensible-heat exchanges between the air and the surface, and hence the air temperature and humidity, would have been considerably different (Brutsaert 1982).

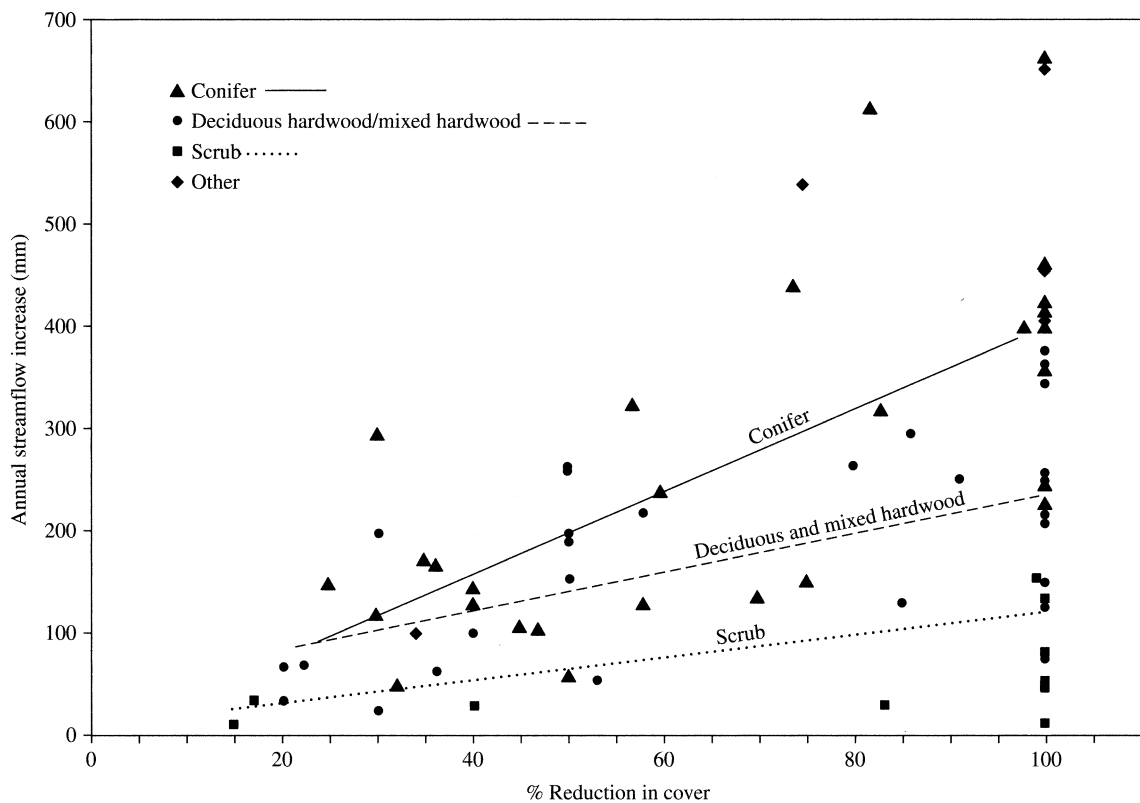


Figure 6.20 Annual streamflow increases due to reductions in vegetative cover as measured in watershed experiments [Bosch and Hewlett (1982). A review of catchment experiments to determine the effect of vegetation changes on water yield and evapotranspiration. *Journal of Hydrology* 55:3–23, with permission of Elsevier].

In spite of these ambiguities, it has proven useful to retain the concept of PET as an index of the “drying power” of the climate or the ambient meteorological conditions, and we now examine some operational definitions that have been applied in climate classification and hydrologic modeling. The last section of this chapter will describe how estimates of actual evapotranspiration are derived from calculated values of potential evapotranspiration in hydrologic analysis.

6.7.2 Operational Definitions

In practice, PET/RET is defined by the method used to calculate it, and many methods have been proffered. We limit our discussion to the methods most commonly applied in hydrologic studies; other methods are summarized and compared by Winter et al. (1995), Federer et al. (1996), Vörösmarty et al. (1998), and Rosenberry et al. (2007). Following Jensen et al. (1990), these methods can be classified on the basis of their data requirements:

- **Temperature-based:** Uses only air temperature (often climatic averages) and sometimes day length (time from sunrise to sunset).
- **Radiation-based:** Uses net radiation and air temperature.
- **Combination:** Based on the Penman combination equation; uses net radiation, air temperature, wind speed, and relative humidity.
- **Pan evaporation:** Uses pan evaporation, sometimes with modifications depending on wind speed, temperature, and humidity.

Some of the methods do not require information about the nature of the surface and can be considered to give a version of reference-crop evapotranspiration, others are surface-specific and require information about albedo, vegetation height, maximum stomatal conductance, leaf-area index, and/or other factors.

6.7.2.1 Temperature-Based Methods

Thornthwaite (1948) developed a complex empirical formula for calculating average monthly PET, PET_{Th} , as a function of climatic average monthly temperature:

$$PET_{Th} = \frac{16}{n_m} \cdot \left(\frac{10 \cdot T_m}{I} \right)^\zeta, \quad (6.67a)$$

where n_m is number of days in month m , T_m is mean monthly temperature ($^{\circ}\text{C}$), I is the “annual heat index” given by

$$I \equiv \sum_{m=1}^{12} \left(\frac{T_m}{5} \right)^{1.514}, \quad (6.67b)$$

and

$$\zeta \equiv 6.75 \times 10^{-7} \cdot I^3 - 7.71 \times 10^{-5} \cdot I^2 + 1.79 \times 10^{-2} \cdot I + 0.49. \quad (6.67c)$$

In spite of its highly empirical nature, the Thornthwaite formula has been widely used.

It turns out that Thornthwaite's temperature function has a form similar to the saturation vapor-pressure relation [equation (6.2)], and some simplifications of his approach are based on this similarity. For example, Hamon (1963) estimated daily PET as

$$PET_H = 29.8 \cdot D \cdot \frac{e^*(T_a)}{T_a + 273.2}, \quad (6.68)$$

where PET_H is in mm/day, D is day length in hr [calculated via equation (D.7)], and $e^*(T_a)$ is the saturation vapor pressure at the mean daily temperature, T_a ($^{\circ}\text{C}$), in kPa. Equation (6.68) gives values close to those given by the original Thornthwaite formulation and has been used in several hydrologic models.

6.7.2.2 Radiation-Based Methods

Slatyer and McIlroy (1961) reasoned that air moving large distances over a homogeneous, well-watered surface would become saturated, so that the mass-transfer term in the Penman equation [equation (6.56)] would disappear. They defined the evapotranspiration rate under these conditions as the **equilibrium potential evapotranspiration**, PET_{eq} . Subsequently Priestley and Taylor (1972) compared PET_{eq} with values determined by energy-balance methods over well-watered surfaces, and found a close fit if PET_{eq} was multiplied by a factor α_{PT} to give

$$PET_{PT} = \frac{\alpha_{PT} \cdot \Delta \cdot (K + L)}{\rho_w \cdot \lambda_v \cdot (\Delta + \gamma)}. \quad (6.69)$$

A number of field studies of evapotranspiration in humid regions have found $\alpha_{PT} = 1.26$, and theoretical examination has shown that that value in fact represents equilibrium evapotranspiration over well-watered surfaces under a wide range of conditions (Eichinger et al. 1996). Thus PET_{PT} is often referred to as the equilibrium potential evapotranspiration, and equation (6.69) gives an estimate of PET that depends only on net radiation and air temperature, which has proven useful in hydrologic analysis.

6.7.2.3 Combination Methods

If the required data are available, the Penman-Monteith equation [equation (6.57)] is the preferred method for calculating PET. To simulate well-watered vegetation, a C_{can} value calculated from equations (6.53) and (6.55) with $f_0(\Delta\theta) = 1$ can be used. To quantify the definition of reference-crop evapotranspiration (section 6.7.1), recall that the Penman-Monteith equation relates evapotranspiration rate to atmospheric and surface characteristics (heat exchange with the ground, G , is added to the energy balance here, but it can usually be neglected when calculating daily or several-day ET):

$$ET = \frac{\Delta \cdot [K_{in}(1-a) + L - G] + \rho_a \cdot c_a \cdot C_{at} \cdot [e^*(z_m) - e(z_m)]}{\rho_w \cdot \lambda_v \cdot [\Delta + \gamma \cdot (1 + C_{at}/C_{can})]} \quad (6.70)$$

Table 6.9 shows the dependences of the terms in equation (6.70) on weather/climate and surface characteristics. The terms that are determined by surface characteristics are albedo (a), atmospheric conductance (C_{at}) and canopy conductance (C_{can}). Thus reference-crop evapotranspiration is defined precisely as a function only of average or current weather conditions by specifying values for those three terms (Shuttleworth 1992):

Reference-crop evapotranspiration (RET) is the rate of evaporation from an idealized grass crop with $z_{veg} = 0.12$ m, $a = 0.23$, and $C_{can} = 0.16$ m/s ($1/C_{can} = 70$ s/m).

Box 6.7 on p. 296 derives the formula recommended by the Food and Agriculture Organization (FAO) for calculating RET:

$$RET = \frac{0.408 \cdot (K + L - G) + \gamma \cdot \left(\frac{900}{T(2\text{ m}) + 273.2} \right) \cdot u(2\text{ m}) \cdot [e^*(2\text{ m}) - e(2\text{ m})]}{\Delta + \gamma \cdot [1 + 0.34 \cdot u(2\text{ m})]} \quad (6.71)$$

Table 6.9 Terms in the Penman–Monteith Equation [Equation (6.70)] and Their Dependences on Weather/Climate and Surface Characteristics.

Term	Definition	Weather/Climate Dependence	Surface Dependence
Δ	slope of saturation vapor pressure–temperature relation	T_a (air temperature) [equation (6.4)]	
K_{in}	incident shortwave radiation	cloud cover [equation (6B1.2)]	
a	albedo		type of vegetation (table 6.4)
L	net longwave radiation	T_a , humidity, cloud cover [equations (6B1.8) and (6B1.9)]	
ρ_a	air density	slight T_a dependence	
c_a	specific heat of air	slight T_a dependence	
C_{at}	atmospheric conductivity	wind speed [equation (6.48), figure 6.13]	vegetation height (figure 6.13)
$e^*(z_m)$	saturation vapor pressure	T_a [equation (6.2)]	
$e(z_m)$	vapor pressure	T_a , humidity [equations (6.2) and (6.3)]	
ρ_w	water density	slight T_a dependence	
λ_v	latent heat of vaporization	slight T_a dependence	
γ	psychrometric constant	slight T_a and pressure dependence	
C_{can}	canopy conductance	K_{in}, T_a , humidity, soil moisture [equation (6.53)]	vegetation type [equation (6.55), table 6.4]

where RET is in mm/day, the energy-budget terms are in $MJ/m^2 \cdot day$, Δ and γ are in $kPa/^\circ C$, T is in $^\circ C$, u is in m/s , and e^* and e are in kPa .

6.7.3 Direct Measurement: Lysimeters, Pans, and Atmometers

The potential evapotranspiration for short vegetation is commonly very similar to free-water evaporation (Brutsaert 1982; Linsley et al. 1982). This may be because lower canopy conductance over the vegetation fortuitously compensates for the lower atmospheric conductance over the pan. In any case, annual values of pan evaporation (= free-water evaporation as shown in figure 6.6) are essentially equal to annual PET, and pan evaporation corrected via equations (6.41) and (6.42) can be used to estimate PET for shorter periods. Farnsworth et al. (1982) have published maps of annual (May–October) Class-A pan evaporation for the United States.

A **lysimeter** is an artificially enclosed volume of soil, usually planted with grass or similar vegetation, for which the inflows and outflows of liquid water can be measured and changes in storage can be monitored by weighing. Lysimeters range from $1 m^2$ or less to over $150 m^2$ in size and are usually designed so that their soil and vegetation are as closely as pos-

sible identical to those of the surrounding area. Details of standard lysimeter construction can be found in Dunne and Leopold (1978), Brutsaert (1982), and Shaw (1988); Grimmond et al. (1992) describe a portable mini-lysimeter ($< 0.2 m^2$ area). Goss and Ehlers (2009) provide a detailed review of the use of lysimeters in measuring evapotranspiration.

Carefully obtained lysimeter measurements are usually considered to give the best determinations of actual evapotranspiration or, if well-watered conditions are maintained, PET or RET, and are often taken as standards against which other methods are compared (e.g., Jensen et al. 1990). However, lysimeters must be carefully constructed to reproduce surrounding soil and vegetation. They must have provisions for drainage that closely mimic drainage in the natural soil so that the water-content profile, and hence the evapotranspiration rate, are similar to those in the surrounding soil. It is virtually impossible to use the technique for forest vegetation.

Potential evapotranspiration can also be directly measured by various forms of **atmometers** or **evaporimeters** where the evaporation that occurs from porous surfaces is supplied from a water reservoir (Giambelluca et al. 1992; Fontaine and Todd 1993; Alam and Trooien 2001; Gavilán and Castillo-

Box 6.7 FAO Formula for Calculating Reference-Crop Evapotranspiration

Here we reproduce the derivation of the FAO formula for calculating reference-crop evapotranspiration (RET) from Allen et al. (1998). Starting with the Penman–Monteith equation [equation (6.57)]:

$$RET = \frac{\Delta \cdot (K + L - G) + \rho_a \cdot c_a \cdot C_{at} \cdot [e^*(z_{mh}) - e(z_{mh})]}{\rho_w \cdot \lambda_v \cdot [\Delta + \gamma \cdot (1 + C_{at}/C_{can})]}, \quad (6B7.1)$$

where z_{mh} is the height at which humidity measurements are made. The atmospheric conductance is written as

$$C_{at} = \frac{\kappa^2 \cdot u(z_{mu})}{\ln\left(\frac{z_{mu} - z_d}{z_{0u}}\right) \cdot \ln\left(\frac{z_{mh} - z_d}{z_{0h}}\right)}, \quad (6B7.2)$$

where z_{mu} is the height at which wind speed is measured, and z_{0u} and z_{0h} are the roughness heights governing momentum and vapor transfer, respectively. Terms in (6B7.2) are related to vegetation height, z_{veg} , as $z_d = 0.67 \cdot z_{veg}$, $z_{0m} = 0.123 \cdot z_{veg}$, and $z_{0h} = 0.012 \cdot z_{veg}$. Then assuming $\kappa = 0.41$, $z_{mu} = z_{mh} = 2$ m, and the standard crop height $z_{veg} = 0.12$ m,

$$C_{at} = \frac{u(2 \text{ m})}{208}, \quad (6B7.3)$$

where $u(2 \text{ m})$ and C_{at} are in m/s. Comparing equation (6B7.2) to equation (6.48), note that here the roughness heights for vapor transfer is assumed to be 0.1 of the roughness height for momentum, rather than identical to it [equation (6.52)]. Also, the zero-plane displacement

Llanque 2009). These are especially useful in scheduling applications of irrigation water, but may also have scientific application.

6.7.4 Comparison of PET/RET Estimation Methods

Jensen et al. (1990) compared PET computed by 19 different approaches with measured reference-crop evapotranspiration in weighing lysimeters at 11 locations covering a range of latitudes and elevations. The Penman–Monteith method gave the best overall results (figure 6.21a). Equilibrium evapotranspiration [equation (6.69) with $\alpha_{PT} = 1.26$] gave reasonable agreement up to rates of 4 mm/day but considerable underestimation at higher rates (figure 6.21b). Monthly Class-A pan evaporation correlated well with measured PET, but

has a slightly different relation to vegetation height than given by equation (6.51).

In this formulation, the canopy conductance includes the conductance for water-vapor flow through the transpiring crop and the evaporation from the soil surface. For grass, the leaf-area index is related to plant height approximately as

$$LAI = 24 \cdot z_{veg}, \quad (6B7.4)$$

where z_{veg} is in m. The “active” leaf-area index (portion of leaves exposed to sunlight; equivalent to the shelter factor [equation (6.55)]) is approximated as

$$LAI_{act} = 0.5 \cdot LAI. \quad (6B7.5)$$

Thus C_{can} is related to “active” leaf-area index and the conductance for a well-illuminated leaf, C^*_{leaf} , as

$$C_{can} = C^*_{leaf} \cdot LAI_{act}. \quad (6B7.6)$$

The stomatal conductance of a single leaf, C^*_{leaf} , has a value of about 0.01 m/s under well-watered conditions. Combining equations (6B7.4)–(6B7.6) and assuming a crop height of 0.12 m, the surface conductance C_{can} for the grass reference surface becomes:

$$\begin{aligned} C_{can} &= C^*_{leaf} \cdot 0.5 \cdot 24 \cdot z_{veg} \\ &= 0.01 \text{ m/s} \cdot 0.5 \cdot 24 \text{ 1/m} \cdot 0.12 \text{ m} = 0.0144 \text{ m/s}. \end{aligned} \quad (6B7.7)$$

Substituting the above relations into the Penman–Monteith equation yields equation (6.71), which is the operational relation for calculating RET as a function only of atmospheric conditions.

with considerable scatter presumably due to variability of heat exchange through the pan walls (figure 6.21c).

For short vegetation, the Penman equation [equation (6.56)] gives nearly the same estimates as the Penman–Monteith equation, and Van Bavel (1966) found a close correspondence for hourly and daily evapotranspiration computed by the Penman equation and that measured for well-watered alfalfa growing in a lysimeter (figure 6.22).

Vörösmarty et al. (1998) compared the estimates of annual PET given by nine different methods. The various methods were used as a basis for estimating actual evapotranspiration in a global-scale monthly water-balance model (as discussed in the following section), and these estimates were compared with the difference between measured precipitation and measured stream-

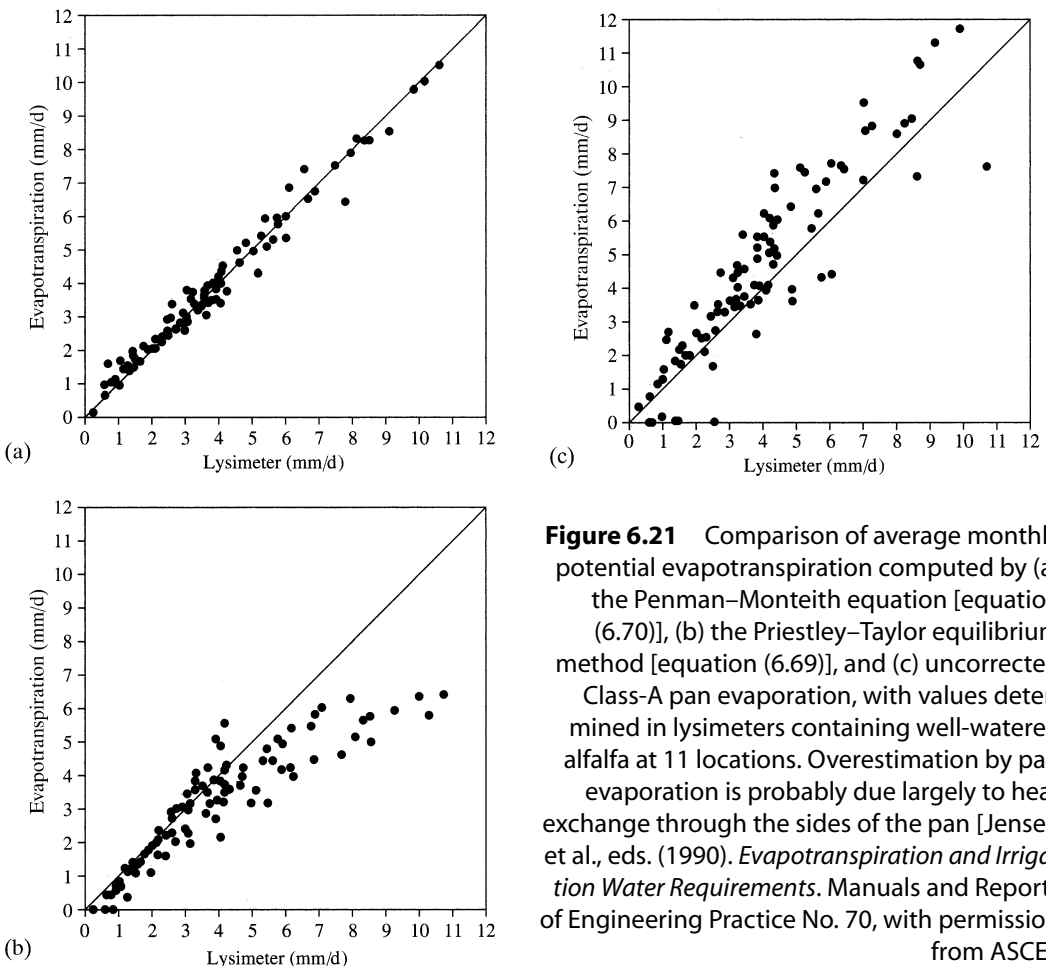


Figure 6.21 Comparison of average monthly potential evapotranspiration computed by (a) the Penman–Monteith equation [equation (6.70)], (b) the Priestley–Taylor equilibrium method [equation (6.69)], and (c) uncorrected Class-A pan evaporation, with values determined in lysimeters containing well-watered alfalfa at 11 locations. Overestimation by pan evaporation is probably due largely to heat exchange through the sides of the pan [Jensen et al., eds. (1990). *Evapotranspiration and Irrigation Water Requirements*. Manuals and Reports of Engineering Practice No. 70, with permission from ASCE].

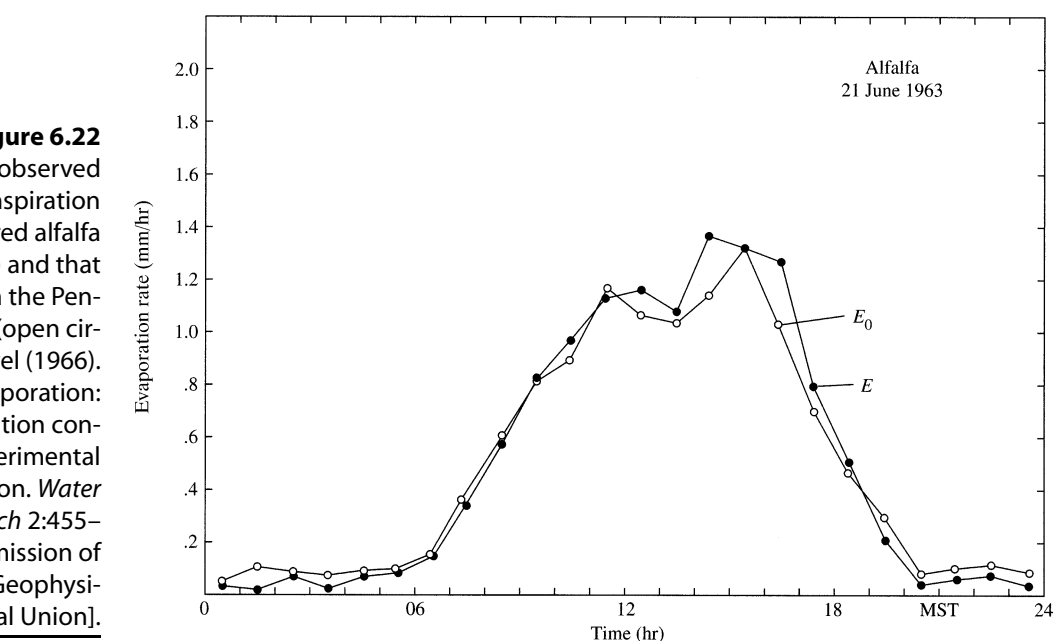


Figure 6.22
Comparison of observed hourly evapotranspiration for well-watered alfalfa (closed circles) and that calculated via the Penman equation (open circles) [Van Bavel (1966)]. Potential evaporation: The combination concept and its experimental verification. *Water Resources Research* 2:455–467, with permission of the American Geophysical Union].

flow. Considering the differences in conceptual basis and data requirements, the various methods gave surprisingly similar results overall. Interestingly, the Hamon method [equation (6.68)], which is based only on temperature and day length, performed best. Several variations of the Penman–Monteith method [equation (6.57)] performed well, while the equilibrium method [equation (6.69)] tended to overestimate in regions with higher ET rates and the Penman equation [equation (6.56)] overestimated for all locations.

6.8 Actual Evapotranspiration

6.8.1 Potential-Evapotranspiration Approaches

6.8.1.1 Relation to Precipitation/PET Ratio

In hot arid regions, potential evapotranspiration greatly exceeds precipitation so that average actual evapotranspiration is water-limited, and is nearly equal to average precipitation. In regions with abundant

rainfall in all seasons, evapotranspiration is limited by the available energy, so that average evapotranspiration is essentially equal to average potential evapotranspiration. As discussed in section 2.2.8.3, this relation is modeled via a “Budyko-type” equation:

$$ET = \frac{P}{\left[1 + \left(\frac{P}{PET}\right)^w\right]^{1/w}}, \quad (6.72)$$

where w is a parameter that depends on watershed characteristics that affect storage: regions with low values of w have relatively small storage, while those with high w values represent watersheds with high storage. The ratio PET/P is called the **aridity index**; actual evapotranspiration is **energy-limited** in humid regions ($PET/P < 1$) and **water-limited** in arid regions ($PET/P > 1$).

In the original form of equation (6.72), Pike (1964) assumed $w = 2$ generally, and figure 6.23 shows that that value provides a reasonably accurate

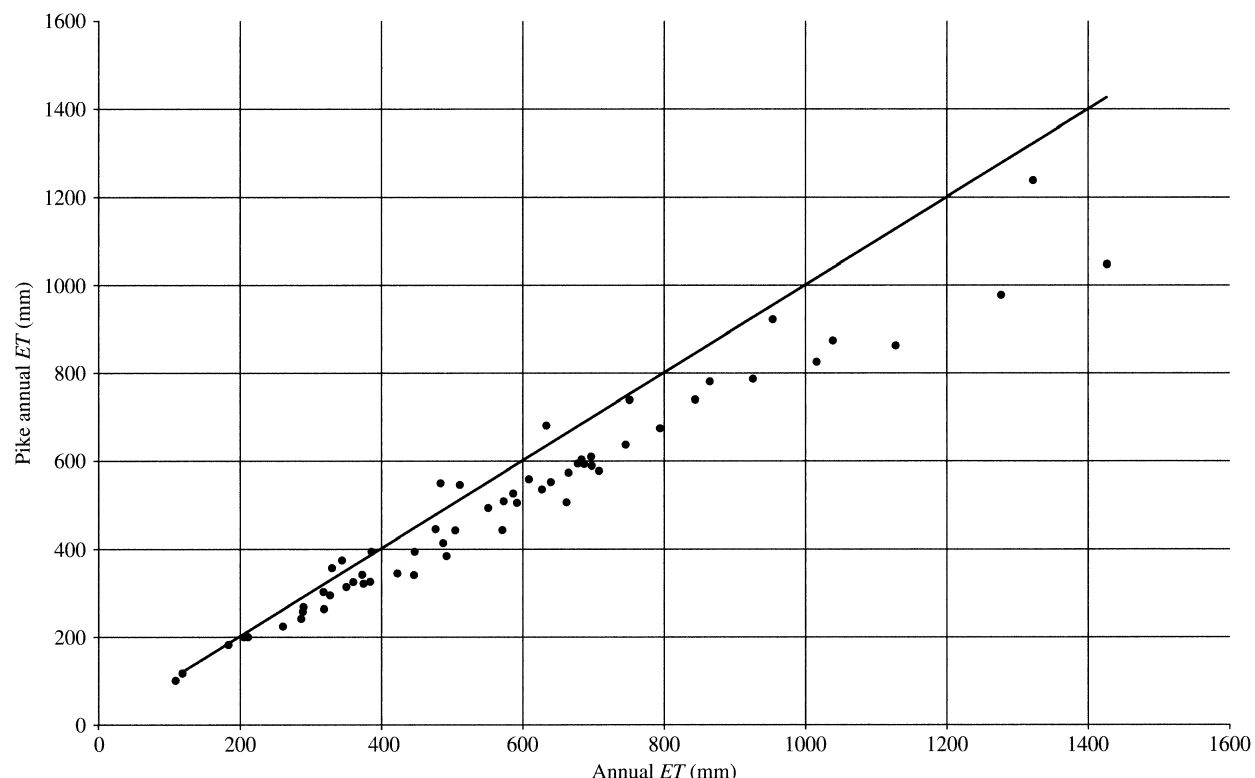


Figure 6.23 Comparison of annual evapotranspiration computed by the Pike equation [equation (6.72)] with that computed via a monthly water-balance model for selected North American stations.

model for estimating annual average ET for locations in North America. However, there is no a priori method of determining w for a particular watershed or region, and the Budyko relationship must be viewed as a broad climatic generalization that is not suited for estimating ET for short time periods at specific locations.

6.8.1.2 Monthly Water-Balance Models

Thornthwaite and Mather (1955) developed a water-balance model that estimates monthly ET from monthly PET , where PET is calculated from monthly average temperature using equation (6.67), equation (6.68), or another temperature-based approach. Monthly precipitation is input to a simple heuristic model that computes monthly actual ET as a function of soil-moisture storage and monthly average temperature and updates soil moisture via a “bookkeeping” procedure. Monthly values of ET are

summed to give the annual value. One version of this approach is described in detail in box 6.8, and table 6.10 and figure 6.24 (on p. 301) give an example of its application. The method can be used with monthly climatic-average values of precipitation and temperature, or with actual monthly values over a period of years. In spite of their extremely simple structure and empirical nature, models of the Thornthwaite type generally estimate monthly runoff values reasonably well (Alley 1984; Calvo 1986), and this correspondence suggests that their estimates of actual evapotranspiration are also generally reasonable.

“Thornthwaite-type” monthly ET models can be extended to estimate monthly ground-water recharge and runoff, and one can verify ET estimates by comparing estimated and measured runoff. Somewhat more elaborate versions of the basic monthly water-balance model described in box 6.8 have been used to

Box 6.8 Thornthwaite-Type Monthly Water-Balance Model

Thornthwaite-type monthly water-balance models are conceptual models that can be used to simulate steady-state seasonal (climatic average) or continuous values of watershed or regional water input, snowpack, soil moisture, and evapotranspiration. Input for such models consists of monthly values of precipitation, P_m , and temperature, T_m , representative of the region of interest. For steady-state applications, these values are monthly climatic averages, in which case $m = 1, 2, \dots, 12$; for continuous simulations they are actual monthly averages, in which case $m = 1, 2, \dots, 12 \cdot N$, where N is the number of years of record. Such models typically have a single parameter, the soil-water storage capacity of the soil in the region, $SOIL_{max}$, which is defined as

$$SOIL_{max} = \theta_{fc} \cdot Z_{rz} \quad (6B8.1)$$

where θ_{fc} is the field capacity and Z_{rz} the vertical extent of the root zone. Typically $SOIL_{max} = 100$ or 150 mm. For continuous applications an initial value of soil moisture, $SOIL_0$, must also be specified.

All water quantities in the model represent depths (volumes per unit area) of liquid water; inputs and outputs are monthly totals and snowpack and soil storage are end-of-month values.

Snowpack, Snowmelt, and Water Input

Monthly precipitation is divided into rain, $RAIN_m$, and snow, $SNOW_m$, where

$$RAIN_m = F_m \cdot P_m, \quad (6B8.2)$$

$$SNOW_m = (1 - F_m) \cdot P_m, \quad (6B8.3)$$

and F_m is the **melt factor**. A simple approach to calculating F_m is

$$\begin{aligned} F_m &= 0, T_m \leq 0^\circ\text{C}; \\ F_m &= 0.167 \cdot T_m, 0^\circ\text{C} < T_m < 6^\circ\text{C}; \\ F_m &= 1, T_m \geq 6^\circ\text{C}. \end{aligned} \quad (6B8.4)$$

The melt factor is also used in a temperature-index snowmelt model [equation (5.71)] to determine the monthly snowmelt, $MELT_m$, as

$$MELT_m = F_m \cdot (PACK_{m-1} + SNOW_m), \quad (6B8.5)$$

where $PACK_{m-1}$ is the snowpack water equivalent at the end of month $m - 1$. The snowpack at the end of month m is then computed as

$$PACK_m = (1 - F_m)^2 \cdot P_m + (1 - F_m) \cdot PACK_{m-1}. \quad (6B8.6)$$

By definition, the water input, W_m , is

$$W_m = RAIN_m + MELT_m. \quad (6B8.7)$$

Evapotranspiration and Soil Moisture

Following Alley (1984), if $W_m \geq PET_m$, ET takes place at the potential rate,

$$ET_m = PET_m \quad (6B8.8)$$

(continued)

and soil moisture increases or, if already at $SOIL_{max}$, remains constant. Thus

$$SOIL_m = \min\{[(W_m - PET_m) + SOIL_{m-1}], SOIL_{max}\}, \quad (6B8.9)$$

where $\min\{\dots\}$ indicates the smaller of the quantities in the braces. In the original formulation, Thornthwaite (1948) used equation (6.67) to calculate PET_m . Most current applications of the method use a simpler temperature-based method [e.g., equation (6.68)] or, if data are available, one of the other approaches for estimating PET_m .

If $W_m < PET_m$, ET_m is the sum of water input and an increment removed from soil storage,

$$ET_m = W_m + SOIL_{m-1} - SOIL_m, \quad (6B8.10)$$

where the decrease in soil storage is computed via the following conceptual model:

$$SOIL_{m-1} - SOIL_m = SOIL_{m-1} \cdot \left[1 - \exp\left(-\frac{PET_m - W_m}{SOIL_{max}}\right) \right]. \quad (6B8.11)$$

Computation

If the model is used with climatic monthly averages, the computations in equations (6B8.5), (6B8.9), (6B8.10), and (6B8.11) are “wrapped around” from $m = 12$ to $m = 1$ so that $m - 1 = 12$ when $m = 1$. Thus the computations are cir-

cular and must be iterated until all the monthly quantities converge to constant values. This iteration is automatically carried out in Excel spreadsheets when the “Enable iterative calculations” option is activated. Otherwise you will get an error message: “Cannot resolve circular references.”

Overall Water Balance

The model output is a table of monthly values that can be graphed to give a concise picture of the annual cycle of inputs, soil and snowpack storage, evaporation, and water available for ground-water recharge and streamflow at any location. Table 6.10 is a completed water-balance spreadsheet for Omaha, Nebraska, at 41.3°N latitude; the annual values are the sums of the monthly values. Note that the annual precipitation and water input are equal, as must be the case. As shown in figure 6.24, the snowpack begins to build up in December, reaches a peak in February, and melts in March and April. $ET = PET$ for the months when $W > PET$ (March–June). Soil-water storage is recharged by rain and snowmelt beginning in February and reaches its capacity in April. It declines in July–October because $PET > P$ and some of the evaporative demand is satisfied by withdrawal of water from soil storage. The last line, $W-ET-\Delta SOIL$, is the average monthly “water surplus,” i.e., the water available for recharge and runoff.

This model has been programmed in a spreadsheet called ThornEx.xls, which can be found on the disk accompanying this text.

Table 6.10 Thornthwaite-Type Monthly Water Balance for Omaha, Nebraska.^a

	J	F	M	A	M	J	J	A	S	O	N	D	Year
P	21	24	37	65	88	115	86	101	67	44	32	20	700
T	-5.4	-3.1	2.7	10.9	17.2	22.8	25.8	24.6	19.4	13.2	3.8	-2.1	
F	0	0	0.45	1	1	1	1	1	1	1	0.63	0	
RAIN	0	0	17	65	88	115	86	101	67	44	20	0	603
SNOW	21	24	20	0	0	0	0	0	0	0	12	20	97
PACK	45	69	49	0	0	0	0	0	0	0	4	24	
MELT	0	0	40	49	0	0	0	0	0	0	7	0	97
W	0	0	57	114	88	115	86	101	67	44	28	0	700
PET	0	0	29	56	90	130	151	131	88	54	26	0	755
W-PET	0	0	27	61	8	1	-50	-26	-25	-18	-5	0	
SOIL	29	29	55	100	100	100	60	47	36	30	29	29	
$\Delta SOIL$	0	0	27	45	0	0	-40	-14	-10	-6	-2	0	
ET	0	0	29	56	90	129	126	113	73	46	26	0	688
$W-ET-\Delta SOIL$	0	0	0	12	0	0	0	0	0	0	0	0	12

^aSee box 6.8. Computed by ThornEx.xls spreadsheet model found on the accompanying CD.

Temperatures in °C; water-balance terms in mm; $SOIL_{max} = 100$ mm.

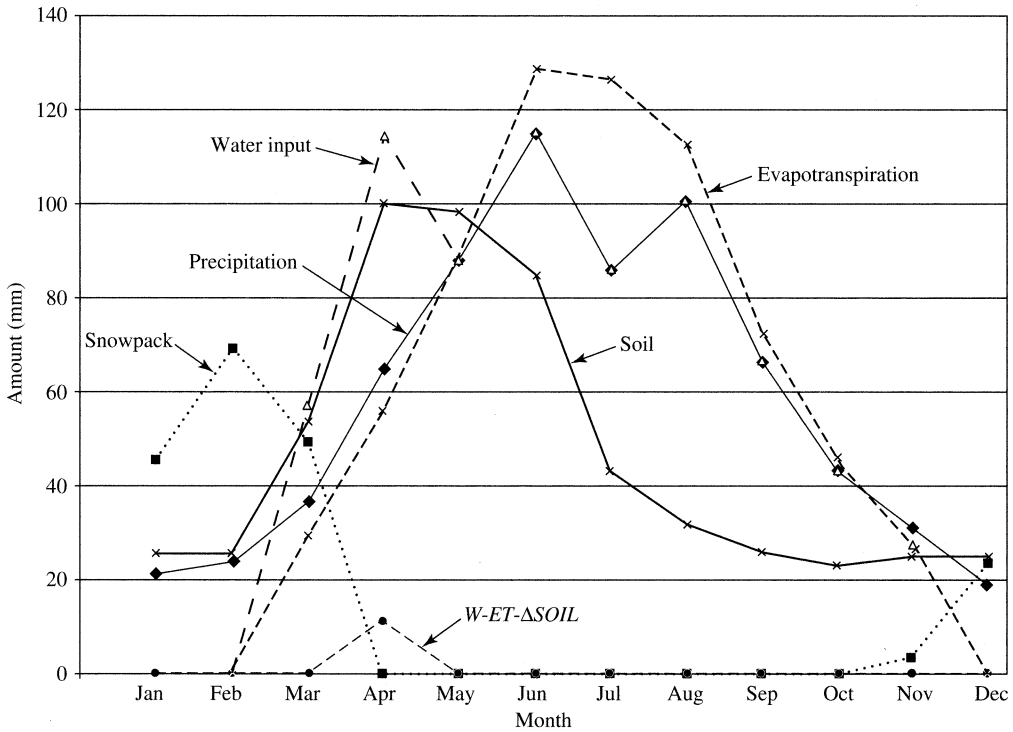


Figure 6.24
Annual cycle of water-balance components as computed by Thornthwaite-type monthly water-balance model for Omaha, Nebraska (see table 6.10).

simulate land-surface hydrology in many of the general circulation models used to forecast the impacts of climate change (e.g., Vörösmarty et al. 1998).

6.8.1.3 Use of Soil-Moisture Functions

One of the most widely used approaches for estimating actual evapotranspiration makes use of meteorologic data to estimate potential evapotranspiration via relations like those discussed in section 6.7.2, then computes actual evapotranspiration as a function of soil-water content, θ :

$$ET = f(\theta^*) \cdot PET, \quad (6.73)$$

where θ^* is the effective saturation,

$$\theta^* \equiv \frac{\theta - \theta_r}{\phi - \theta_r}, \quad (6.74)$$

θ_r is the permanent residual water content (typically $\theta_r \approx 0.05$), and ϕ is soil porosity (soil-moisture terms are defined in sections 7.1 and 7.2). The relation between ET/PET and θ^* usually has a form like that shown in figure 6.25: ET/PET increases quasi-linearly as θ^* increases, and reaches 1 at some water content θ_{PET}^* (e.g., Davies and Allen 1973; Federer 1979, 1982; Spittlehouse and Black 1981). Typically

$0.5 \cdot \theta_{fc} \leq \theta_{PET}^* \leq 0.8 \cdot \theta_{fc}$ where θ_{fc} is the water content at field capacity (see section 8.1.1).

Assuming that $ET = PET$ when there is no soil-moisture deficit, the Stewart (1988) model of canopy conductance can be used with the Penman–Monteith equation to give ET/PET as a function of soil moisture. In that model, the function $f_\theta(\Delta\theta)$ reflects the effect of soil-moisture deficit, $\Delta\theta$, on ET (table 6.5) [$f_\theta(\Delta\theta) = 1$ when there is no deficit]. Combining equations (6.53) and (6.55) with equation (6.57),

$$ET/PET = \frac{\Delta + \gamma \cdot \left\{ 1 + \frac{C_{at}}{C_{can}[f_\theta(\Delta\theta) = 1]} \right\}}{\Delta + \gamma \cdot \left\{ 1 + \frac{C_{at}}{C_{can}[f_\theta(\Delta\theta)]} \right\}}. \quad (6.75)$$

Figure 6.26 shows ET/PET as a function of $\Delta\theta$ given by this relation using the functions in table 6.5 for the conditions described in box 6.5.

A third approach to estimating ET from PET relates the value of a_{PT} in the Priestley–Taylor equation [equation (6.69)] to some measure of soil-water content (e.g., Mukammal and Neumann 1977).

These or other methods of estimating ET from PET and soil moisture are well suited to use in “real-

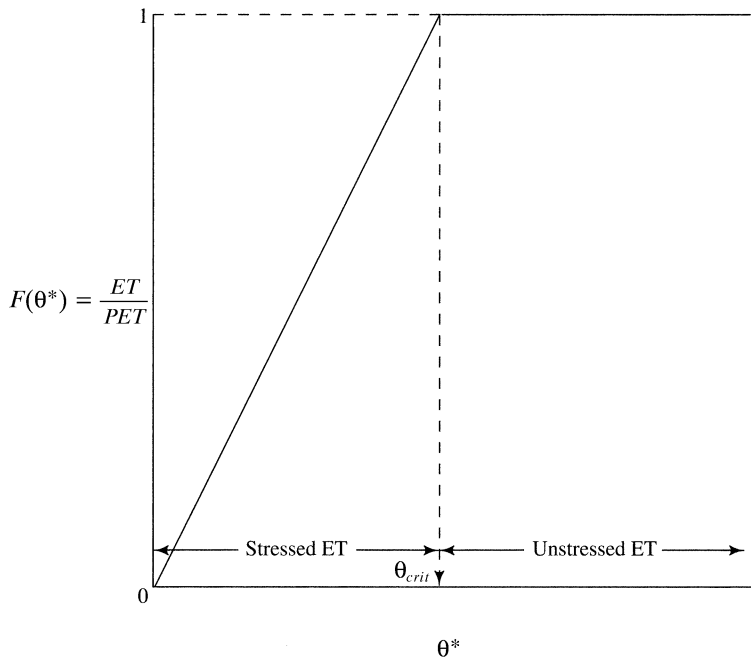


Figure 6.25 General form of relations between ET/PET and soil-water content, θ , used to estimate ET . Different studies have used different functions to express soil wetness. When the soil-water content variable is less than the critical value θ_{crit} , ET is less than PET and plants are considered under water stress.

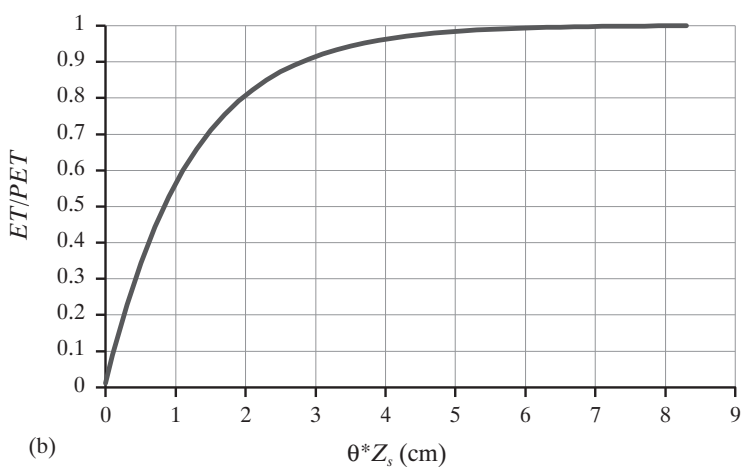
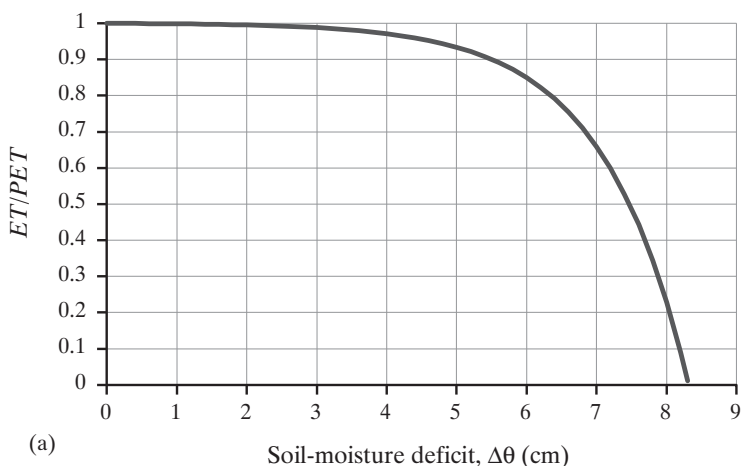


Figure 6.26 ET/PET as a function of soil moisture using the Stewart equation (table 6.5) with $\Delta\theta$ given by equation (6.75) for the conditions described in box 6.5. (a) ET/PET versus $\Delta\theta$; (b) ET/PET versus root-zone soil moisture, $\theta \cdot Z_s$, to show similarity to figure 6.25.

time” estimation, where θ is measured every few days, and in hydrologic models where θ is tracked by a “bookkeeping” algorithm along with equations for infiltration and deep drainage.

6.8.1.4 Complementary (Advection-Aridity) Approach

Following Bouchet (1963), consider a well-watered uniform surface of 1 to 100 km² area evapotranspiring at the potential rate $ET = PET_0$ under a steady set of meteorological conditions. If these conditions remained constant, eventually the soil moisture would fall below field capacity and ET would be less than PET_0 . A flux of energy, Q [E L⁻² T⁻¹], equivalent to the difference between PET_0 and ET would then not be used for evapotranspiration, and would become available to warm the atmosphere. Thus

$$PET_0 - ET = \frac{Q}{\rho_w \cdot \lambda_v}. \quad (6.76)$$

The reduced evapotranspiration decreases the humidity and the warming increases the air temperature. Under these circumstances one would calculate a new potential evapotranspiration, PET , that is larger than PET_0 by the amount $Q/(\rho_w \cdot \lambda_v)$:

$$PET = PET_0 + \frac{Q}{\rho_w \cdot \lambda_v}. \quad (6.77)$$

Combining equations (6.76) and (6.77) yields the **complementary relationship** between ET and PET :

$$ET = 2 \cdot PET_0 - PET \quad (6.78)$$

(see figure 6.27).

Brutsaert and Stricker (1979) reasoned that PET_0 is the PET under equilibrium conditions [equation (6.69)] and PET is the “actual” PET given by the Penman equation using measured current values of the meteorological variables [equation (6.37)]. Substitution of those relationships into equation (6.78) yields

$$ET = \frac{(2 \cdot \alpha_{PT} - 1) \cdot \Delta \cdot (K + L - G) - \gamma \cdot K_E \cdot \rho_w \cdot \lambda_v \cdot u(z_m) \cdot e^*(z_m) \cdot [1 - RH(z_m)]}{\rho_w \cdot \lambda_v \cdot (\Delta + \gamma)} \quad (6.79)$$

which Brutsaert and Stricker (1979) called the **advection-aridity** interpretation of the complementary approach. Its main advantage is that it uses readily available meteorological data and does not require calibration to a specific site. It has been found to give estimates of daily ET that compare well with those using other approaches (figure 6.28; see also Parlange and Katul 1992b).

Kahler and Brutsaert (2006) used the basic reasoning of the complementary approach to develop a method for estimating daily ET from temperature,

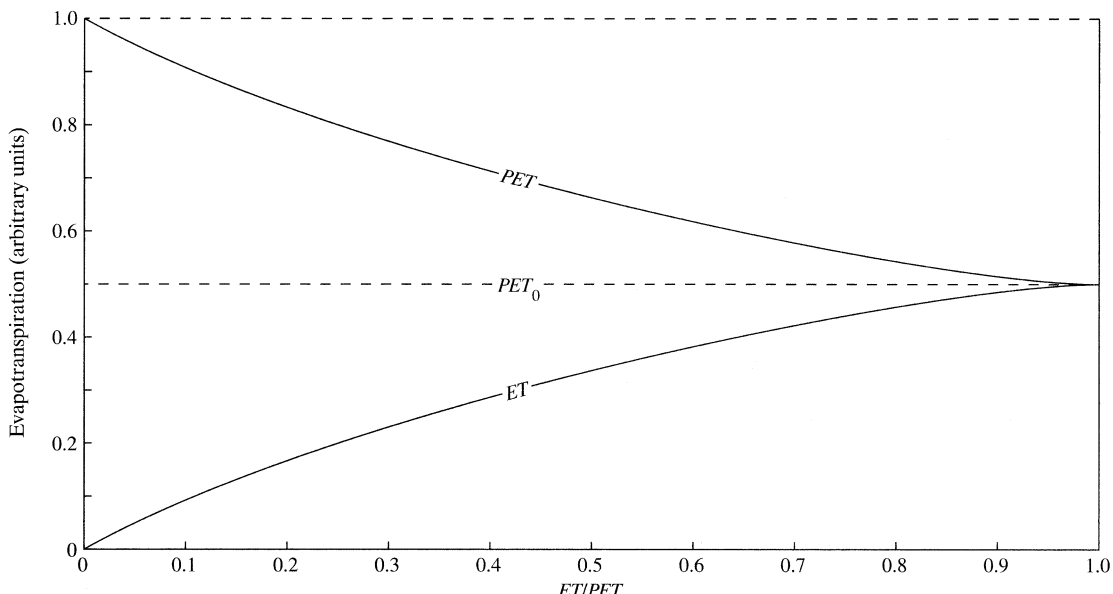


Figure 6.27 Bouchet’s (1963) complementary relationship: $ET = 2 \cdot PET_0 - PET$ [equation (6.78)] [adapted from Brutsaert (1982)].

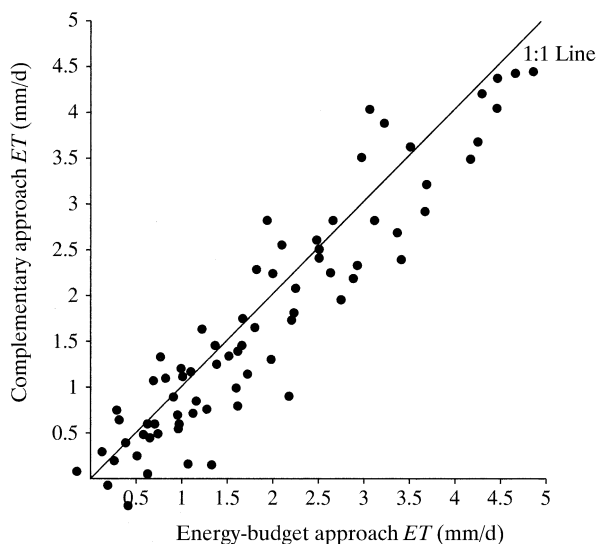


Figure 6.28 Comparison between estimates of daily ET obtained by the complementary (advection-aridity) approach [equation (6.79)] and an energy-budget method [Brutsaert (1982)]. *Evaporation into the Atmosphere*. Used with permission of Kluwer Academic Publishers].

net radiation, and pan evaporation data. Their general relation takes the form

$$ET = \alpha_{PT} \cdot (1 - c_R) \cdot \left(\frac{1+b}{b} \right) \cdot \left(\frac{\Delta}{\Delta + \gamma} \right) \cdot (K + L) - \left(\frac{C_{pan}}{b} \right) \cdot E_{pan}, \quad (6.80a)$$

where α_{PT} is the Priestley–Taylor coefficient [equation (6.69)], c_R is a coefficient that accounts for ground-heat exchange, b accounts for heat exchange through the sides of the pan, and C_{pan} is a constant of proportionality that relates pan evaporation to evaporation from the surrounding vegetation under potential conditions, E_{pan} is Class-A pan evaporation, and the other symbols are as in the Penman equation [equation (6.56)]. They tested their relation against daily and monthly ET determined by the Bowen-ratio method (see section 6.3.1) for two experimental sites and concluded that, although the coefficients should ideally be determined via on-site calibration, it appears that useful results can be obtained by assuming $\alpha_{PT} = 1.26$, $c_R = 0.15$ (for dense vegetation), $b = 5$, and $C_{pan} = 1$. Using these values, equation (6.80a) becomes

$$ET = 1.29 \cdot \left(\frac{\Delta}{\Delta + \gamma} \right) \cdot (K + L) - 0.20 \cdot E_{pan}. \quad (6.80b)$$

Note that the complementary relation is reflected in the fact that an increase in pan evaporation results in a decrease in actual evapotranspiration.

6.8.2 Water-Balance Approaches

Actual evapotranspiration from a region over a time period Δt can in principle be determined by defining a control volume, measuring liquid-water inputs and outputs and changes in storage, and solving the water-balance equation, just as for open-water evaporation. The application of this principle to various types of control volumes is discussed in the following sections; in all cases the precision of the determination is dictated by the precision with which all the other water-balance components can be measured (section 1.8).

6.8.2.1 Land-Area Water Balance

The most common method of estimating actual evapotranspiration from a land area is the application of the water-balance equation (section 1.8.1),

$$ET = P + GW_{in} - Q - GW_{out} - \Delta S, \quad (6.81)$$

where P is precipitation, Q is streamflow, GW_{in} and GW_{out} are ground-water inflows and outflows, and ΔS is change in storage.

The major problems in applying equation (6.81) are obtaining reliable estimates of regional precipitation, ground-water terms, and changes in storage; as discussed in section 1.8.2, these are usually formidable problems. Often the ground-water terms are assumed negligible or to cancel out and storage changes are assumed to be negligible for annual or longer time periods, so that

$$ET = P - Q. \quad (6.82)$$

However, these assumptions should not be casually made, because:

- As described in section 9.5.5.2.3, one study found that half the watersheds in the United States were net importers and half net exporters of ground water, making the neglect of ground-water terms questionable.
- The levels of the Great Lakes and Great Salt Lake in the United States show periods of several decades of steadily declining or rising levels (US Geological Survey 1984). These trends suggest that

significant errors are possible in estimating ET from equation (6.81) for some large drainage basins, even when quantities are averaged over long periods. Fortunately, the 2002 launch of the Gravity Recovery and Climate Experiment (GRACE) satellite now makes measurement of storage changes possible for large regions (section 1.8.2.4).

6.8.2.2 Lysimeter and Pan Measurement

The use of lysimeters for measuring potential evapotranspiration was described in section 6.7.3. They can also be used to make direct measurements of actual evapotranspiration over a wide range of time scales, to the extent that the conditions in the lysimeter are representative of the region of interest. As noted, this is not possible for forested regions.

Equation (6.80) provides a relation for estimating daily to monthly ET from observations of temperature, net radiation, and pan evaporation.

6.8.2.3 Soil-Moisture Balance

One can estimate the total evapotranspiration in a rain-free time period Δt by carefully monitoring soil-water content profiles [$\theta(z)$] at spatially representative locations. As shown in figure 6.29, the total soil-water loss is the difference in water content through the soil profile between times t_0 and $t_0 + \Delta t$. The portion of this loss due to evapotranspiration is determined by identifying the “zero-flux plane,” which is the bound-

ary between upward-directed water movement due to evapotranspiration and downward-directed movement due to drainage. The average location of the zero-flux plane is found by plotting profiles of the vertical soil-water potential $\psi(\theta) + z$, which is determined from the $\theta(z')$ values and the moisture-characteristic curve for the soil (section 7.4.3).

This method essentially creates a “lysimeter without walls” that does not distort the soil water-content profile and can be especially useful in forests. However, obtaining representative values of $\theta(z')$ is not easy, and the method will not give good results if the water table is near the surface, if there is horizontal water movement, or if soil properties are highly variable. Rouse and Wilson (1972) found that the minimum length of Δt for reliable results is four days, and is considerably longer under many conditions.

6.8.2.4 Atmospheric Water Balance

Evaporation can also be estimated by applying the water-balance equation to a control volume of the lower atmosphere. For a control volume of height z_a and perimeter X above an area A and a time interval Δt , this equation becomes

$$\bar{ET} = \bar{P} - \frac{1}{A \cdot \rho_w} \cdot \int_0^{z_a} \int_X (\bar{\rho}_v \cdot \bar{u}_n) \cdot dx \cdot dz - M_2 + M_1, \quad (6.83)$$

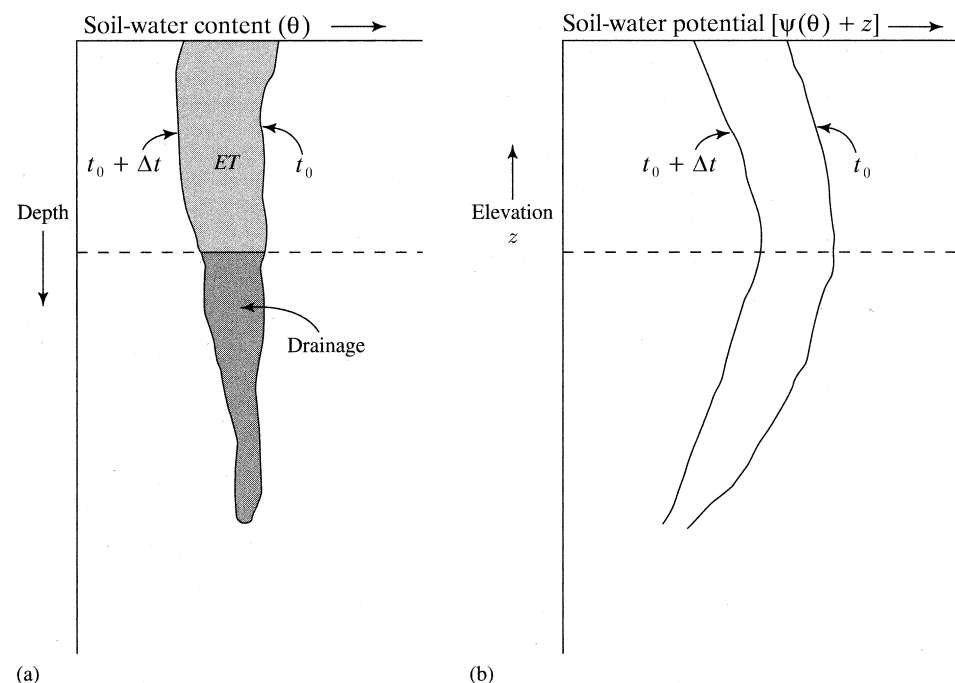


Figure 6.29

Conceptual basis for estimating evapotranspiration from the soil-water balance. (a) Change in soil-water content with depth during time period Δt . (b) Profiles of soil-water potential defining the zero-flux plane (dashed line) that divides water lost to evapotranspiration (ET) from that lost to drainage [adapted from Shuttleworth (1992)].

Change in soil-water content with depth during time period Δt . (b)

Profiles of soil-water potential defining the zero-flux plane (dashed line) that divides water lost to evapotranspiration (ET) from that lost to drainage [adapted from Shuttleworth (1992)].

where \bar{ET} and \bar{P} are the average rates of evapotranspiration into and precipitation out of the volume (per unit area), respectively, $(\bar{\rho}_v \cdot \bar{u}_n)$ is the time-averaged product of the absolute humidity and the outward-directed wind velocity normal to the perimeter, and M_1 and M_2 are the total water content per unit area of the control volume at the beginning and end of Δt , respectively.

As summarized by Brutsaert (1982), this method has been applied in several studies using both routine and specially collected atmospheric data. Typically, $7 < z_a < 8$ km. The spatial and temporal coarseness of network upper-air observations limit its routine application to areas of 2.5×10^5 km² or more to provide estimates of monthly to annual evaporation. Munley and Hipps (1991) showed the importance of vertical resolution in obtaining accurate estimates, and Wang and Dickinson (2012) caution that errors in integration accumulate as longer time periods are included in the analysis.

Several recent research efforts have applied the atmospheric water balance to estimate evapotranspiration from large areas of land, and it appears that the method will play an increasing role in expanding understanding of global-scale hydrology (Brutsaert 1988; Shuttleworth 1988). Kuznetsova (1990) summarized several applications of the approach at the large river basin, subcontinental, and continental scales.

6.8.3 Turbulent-Exchange and Energy-Balance Approaches

6.8.3.1 Penman–Monteith Approach

The Penman–Monteith equation [equation (6.57)], with the vegetative canopy treated as a “big leaf” via equations (6.53)–(6.55), is commonly used to estimate land-area evapotranspiration. This approach can be refined by treating the vegetated and unvegetated (bare-soil) portions of a given area separately.

A detailed methodology combining canopy and bare-soil evapotranspiration was developed by Shuttleworth and Wallace (1985). Briefly, this approach applies the Penman–Monteith equation twice, once to compute transpiration for the vegetated fraction of the region (as in box 6.5) and again for the unvegetated fraction. In computing bare-soil evaporation, atmospheric conductance is modified by appropriate adjustments of the surface roughness and zero-plane displacement height, and the surface conductance decreases as surface soil-water content decreases.

Evapotranspiration is computed separately for the daylight and nondaylight hours using different values for air temperature and wind speed and, of course, solar radiation for the two periods. Total daily evapotranspiration is an appropriately weighted sum of daytime transpiration and nighttime and daytime soil evaporation.

6.8.3.2 Bowen-Ratio Approach

Direct application of the mass-transfer equation [equation (6.25)] to estimating actual evapotranspiration from a land surface is generally infeasible because of the absence of surface-temperature data and, most of the time, the absence of a surface that is at saturation.

However, evapotranspiration can in principle be evaluated by applying the mass-transfer equation in the form that makes use of measurements of wind speed and humidity at two levels in the air near the surface [equation (6.9)]. Alternatively, we can eliminate the need for wind-speed data and for estimates of the roughness height by making use of the Bowen-ratio approach [as in the development of equation (6.32)] and an energy-balance relation. Using measurements at two levels, the Bowen ratio B is

$$\begin{aligned} B &\equiv \frac{H}{\rho_w \cdot \lambda_v \cdot ET} \\ &= \frac{c_a \cdot p \cdot [T(z_1) - T(z_2)]}{0.622 \cdot \lambda_v \cdot [e(z_1) - e(z_2)]}. \end{aligned} \quad (6.84)$$

Combining (6.84) with the surface-energy balance,

$$ET = \frac{K + L - G}{\rho_w \cdot \lambda_v \cdot (1 + B)}. \quad (6.85)$$

Because of the need for measurements at two levels, equation (6.85) is useful only in an elaborately instrumented research setting. In such situations it is often used as a standard for determining ET at time scales from less than an hour to annual and is representative of regions up to hundreds of meters in extent. However, the approach may not give good results for forest evapotranspiration because the diffusivities of momentum and water vapor may differ significantly over rough surfaces.

6.8.3.3 Eddy-Correlation Approach

Eddy-correlation (section 6.3.1) techniques over representative surfaces can also provide direct observations of land-surface evapotranspiration, and are often considered to be measurements of the “true” evapo-

transpiration rate because the method has a sound theoretical foundation and requires no assumptions about parameter values, the shape of the vertical velocity profile, or atmospheric stability. However, instrumentation requirements are stringent and measurements are subject to interruption and to failure to capture vapor transfer in large eddies (Wang and Dickinson 2012). A full theoretical development and discussion of instrumentation was given by Brutsaert (1982).

6.8.3.4 Scintillometry

Evapotranspiration can also be measured via **scintillometers**. These are instruments that transmit horizontal optical or radio-frequency beams to receivers through the turbulent mixed layer (figure 3.7) above the surface of interest. As the beams propagate through the turbulent air the intensity of the radiation varies because the refractive index varies due to temperature and humidity fluctuations.

Scintillometry is becoming an increasingly common tool for measuring fluxes of heat, water vapor, and momentum on large spatial scales (Moene et al. 2009). Liu et al. (2013) employed a scintillometer system using near-infrared wavelengths to measure the turbulent transfer of sensible heat along with measurements of net radiation to determine evapotranspiration via the energy balance [equation (6.30)].

6.8.4 Methods Based on Water Quality

Approaches based on chemical and isotopic composition can provide very useful estimates of space- and time-integrated evapotranspiration. However, their application appears limited to situations where the hydrology is fairly simple.

6.8.4.1 Methods Based on Dissolved-Solids Composition

Water evaporates as individual H_2O molecules, and any dissolved solids remain in the liquid water. Thus there is a tendency for the concentration of dissolved solids in unevaporated water to increase in proportion to the amount of water that has evaporated, and this tendency can be used to estimate the amount of evaporation if other complicating factors (e.g., sporadic additions of water of varying concentration, dissolution of new materials) can be accounted for.

Margaritz et al. (1990) were able to use isotopes to determine the source of dissolved chloride, and then examined the increase in concentration of the chloride that came with precipitation to estimate evapotranspiration in the Jordan River basin. Claassen and Halm (1996) found that annual evapotranspiration in a number of Rocky Mountain watersheds could be well estimated from the chloride concentration in a single sample of stream water where the chloride concentrations of precipitation were well known.

6.8.4.2 Methods Based on Isotopic Composition

Isotopically lighter water molecules are more likely to evaporate than heavier ones, so the liquid water left behind tends to become enriched in the heavier isotopes of hydrogen and oxygen (appendix B). Several studies have taken advantage of this enrichment to estimate evapotranspiration from land surfaces (e.g., Allison and Barnes 1983; Walker and Brunel 1990). Gat (1996) provides a thorough review of the fractionation of hydrogen and oxygen isotopes in hydrologic processes.

▼ EXERCISES

1. Measurements of water-balance components have been made for a one-year period on a lake with an area of 4.2 km^2 and a drainage basin of 52.1 km^2 (including the lake), with the following results: $P = 1,083 \text{ mm}$; $Q_{in} = 2.33 \times 10^7 \text{ m}^3$; $GW_{in} = 2.2 \times 10^5 \text{ m}^3$; $GW_{out} = 0.6 \times 10^5 \text{ m}^3$; $Q_{out} = 2.70 \times 10^7 \text{ m}^3$. The lake-surface elevation, h , at the end of the year was 108 mm higher than at the beginning.
 - a. What is the water-balance estimate of the lake evaporation for that year?
 - b. Referring to table 6.3, give a qualitative evaluation of the uncertainty of this estimate.
2. The table on the following page gives the hourly air temperature, T_a , relative humidity, RH , wind speed, $u(2 \text{ m})$, and water-surface temperatures, T_s , for Lake Hefner, Oklahoma, on 3 May 1951. The lake area is 9.4 km^2 . Compare the average evaporation rate for that day via the mass-transfer approach by
 - a. calculating the evaporation rate for each hour and averaging the results; and

- b. averaging the values in the table and using those averages in the mass-transfer equation.

Hour →	1	2	3	4	5	6	7	8
T_a (°C)	20.8	21.0	21.3	21.9	22.6	23.5	26.4	28.2
RH	0.92	0.92	0.91	0.90	0.88	0.87	0.72	0.62
$u(2 \text{ m})$ (m/s)	8.14	7.83	7.62	7.94	8.53	9.47	9.68	9.84
T_s (°C)	16.2	16.2	16.2	16.3	16.8	17.4	18.0	18.9
Hour →	9	10	11	12	13	14	15	16
T_a (°C)	28.2	29.1	30.9	32.6	32.4	32.0	31.9	30.3
RH	0.58	0.49	0.41	0.30	0.33	0.38	0.42	0.57
$u(2 \text{ m})$ (m/s)	10.71	10.05	9.46	9.37	9.02	8.88	8.55	8.34
T_s (°C)	19.5	19.7	19.8	20.2	20.1	20.0	19.8	19.5
Hour →	17	18	19	20	21	22	23	24
T_a (°C)	29.6	26.2	25.8	24.9	23.6	23.3	22.8	22.5
RH	0.64	0.75	0.79	0.81	0.84	0.86	0.88	0.92
$u(2 \text{ m})$ (m/s)	8.01	8.03	7.99	8.15	8.24	8.00	7.84	7.62
T_s (°C)	19.1	18.9	18.7	18.4	18.3	18.0	17.6	17.4

3. Given the following meteorological conditions (average or total daily values for 10 September 1950 at Lake Hefner, Oklahoma), compare the open-water evaporation rates given by (a) the mass-transfer; (b) energy-balance; and (c) combination approaches.

T_a (°C)	RH	$u(2 \text{ m})$ (m/s)	T_s (°C)	P (kPa)	K_{in} (MJ/m ² · d)	Albedo	L_{in} (MJ/m ² · d)
22.3	0.68	2.16	23.7	97.3	16.2	0.057	30.6

4. For the conditions given in exercise 6.3, compute the open-water evaporation rate given by the combination approach with the Kohler–Parmele modifications [equations (6.38)–(6.39)].

5. Given the following conditions at the Class-A pan at Lake Hefner on 10 September 1950, compute the free-water evaporation [pan evaporation adjusted via equations (6.41) and (6.42)] and compare it with the results of exercises 6.3 and 6.4.

Pan Evaporation, E_{pan} (mm/d)	Pan Water-Surface Temperature, T_{span} (°C)	Average Wind Speed, u_{pan} (m/s)
6.1	25.3	0.89

6. Use the spreadsheet program PenMontX.xls on the disk accompanying this text to explore the effects of any two of the variables listed as “Input Data” on the evapotranspiration rate computed via the Penman–Monteith equation. Write a paragraph or two, supplemented with appropriate graphs, describing the sensitivity of ET to the variables you selected.
7. In central Alaska, spruce forests typically occupy north-facing slopes, with birch forests on the south-facing slopes. Redo the example found in box 6.6 using the regression equation for spruce–fir–hemlock from table 6.6, compare the results with figure 6.18, and write a paragraph comparing the runoff-producing potential of north- versus south-facing slopes in this region.
8. Pick a set of meteorological conditions and vegetation characteristics typical of the growing season in the region in which you live, and use the spreadsheet program PenMontX.xls to compare the rate of transpiration with the rate of evaporation of intercepted water, as in box 6.5. How long would it take to evaporate 1 mm of intercepted water at the computed rate? Does the evaporation rate exceed the net radiation? If so, what are the implications for energy supply?

9. For the following conditions, compare the potential evapotranspiration as given by equations (6.56), (6.68), and (6.69).

T_a (°C)	RH	$K + L$ (MJ/m ² · d)	z_m (m)	z_{veg} (m)	$u(z_m)$ (m/s)	P (kPa)	D (hr)	C^*_{stom} (m/s)	LAI
20.7	0.49	13.9	3.66	0.50	2.48	101.3	14.8	0.0050	4.5

10. Do an Internet search to determine what Class-A pan evaporation data are available for your region. If data are available, examine the seasonal and year-to-year variability of selected stations.
11. The file ThornEx.xls on the disk accompanying this text is a spreadsheet implementing a Thornthwaite-type monthly water-balance model for climatic-average data. The file ThornData.xls contains monthly average precipitation and temperature for many locations throughout the world. These can be used to compute actual evapotranspiration and to explore a range of hydrologic questions, such as:
- How does ET and the ratio ET/PET vary with latitude on each continent? (Compare with figures 2.27 and 2.28.)
 - How does ET/PET vary with annual precipitation?
 - How does annual runoff vary with latitude? (Compare with figures 2.29 and 2.30.)
 - How does annual ET computed via ThornEx.xls compare with that given by the Pike equation [equation (6.72) with $w = 2$] for selected stations?
 - What proportion of annual precipitation falls as snow as a function of latitude for selected continents? (Compare with figure 5.1.)
 - How would a 2°C average temperature increase (as projected due to increased atmospheric CO₂) affect annual ET and runoff for selected stations? Is the relative response of ET or runoff more sensitive to a temperature increase? What are the implications for water resources?
 - How would a 2°C average temperature increase affect the timing of water “surplus” (monthly $W-ET-\Delta SOIL$) for selected stations? What are the implications for water resources?

▼ NOTES

¹ “Psychrometry” is the measurement of humidity.

² Equation (6.23) is analogous to the energy-balance relation for a snowpack, equation (5.16). Note, however, that the signs of H , λE , and G are reversed here because we are considering outward latent- and sensible-heat flows to be positive. Heat input due to rain [R in equation (5.16)] is usually negligible in considering evaporation, but could be included in A_w in equation (6.23).

³ This assumption is justified for short vegetation, but becomes less so for forests because z_0 and z_d for water vapor transfer increasingly differ from their values for momentum transfer as the surface gets rougher (C. A. Federer, pers. comm.). In the interests of simplicity, we assume this equality in the developments herein.

⁴ However, a long-term decrease in leaf conductance is a possible response of plants to the anthropogenic increase in atmospheric CO₂ concentration (Rosenberg et al. 1989).



Part III

Water Movement on the Land

7



Principles of Subsurface Flow

L'vovich (1974) estimated that 76% of the world's land-area precipitation enters the soil, providing all the water used by natural and cultivated plants and almost all the water that enters ground-water reservoirs.

Figure 7.1 shows terms describing water paths in porous subsurface materials. If the soil pores at the surface are not completely filled with water, a portion of rain and snowmelt enters the soil via the process of **infiltration**, where it is subject to the forces of gravity and pressure. Gravity is, of course, omnipresent and constant and directed downward. The pores of soils in the **unsaturated zone** (also called the **vadose¹ zone**) contain air and water; pressure forces are due to surface tension (section 1.5.3) and pressures are less than atmospheric. Pressure gradients arise due to spatial variations in water content, which operate at scales up to ~ 0.01 m and can act in any direction, resulting in redistribution, evaporation at the soil surface (**exfiltration**), downslope flow (**interflow**), or downward flow to an underlying **saturated zone**.

Water moving vertically downward arrives at the **saturated zone** as **ground-water recharge**. The **water table** is the fluctuating upper boundary of the saturated zone, at which pressure is atmospheric. Soil pores in the saturated zone are completely filled with

water and pressures are greater than atmospheric due to the weight of the overlying water. The combination of pressure- and gravity-force gradients move water generally from higher to lower elevations at scales $>> 1$ m, but local flow directions may range from vertically downward to vertically upward.

This chapter introduces the basic physics of the storage and movement of water in porous earth materials (**porous media**). Chapter 8 focuses on the application of these principles to the process of infiltration and redistribution in the unsaturated zone, typically at vertical scales of ~ 1 m and horizontal scales of up to $10^3 \cdot m^2$. Chapter 9 applies these principles to saturated flow in the ground-water zone, typically at much larger scales.

7.1 Material Properties of Porous Media

7.1.1 Distribution of Particle Sizes and Pores

7.1.1.1 Definition

Our model of a quasi-homogeneous soil is a three-phase system consisting of a matrix of individual solid grains (mineral or organic) between which are interconnected pore spaces that can contain varying

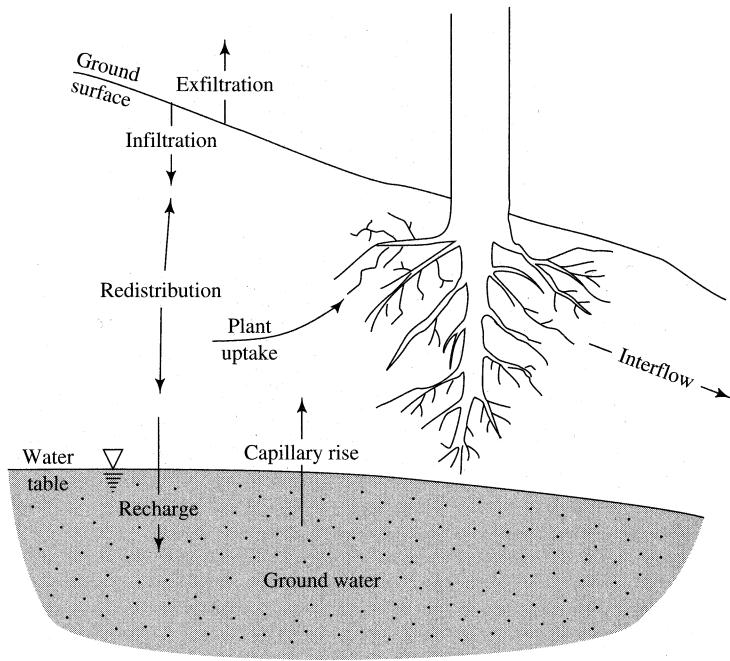


Figure 7.1 Definitions of terms used to describe water movement in the unsaturated zone.

proportions of water and air. To simplify discussion, we will not consider the organic component separately. The volume of water vapor contained in the air in soil pores is insignificant and can be neglected.

Thus we can define soil properties using the symbols M to designate mass [M], V for volume [L^3], and ρ for mass density [$M\ L^{-3}$]; and the subscripts s for soil, m for soil mineral, w for liquid water, a for air, and v for voids (i.e., pores). Thus for a representative portion of a soil,

$$V_s = V_m + V_w + V_a = V_m + V_v. \quad (7.1)$$

As described in section 2.3.1, near-surface soils usually have a distinct vertical zonation, so soil properties may differ significantly over short vertical distances.

For uniform spheres, it can be shown that the volume of an individual pore space ranges from 0.35 (close-packed) to 0.91 (open-packed) times the volume of the individual spheres (figure 7.2). Thus the sizes of the pores through which water flows are approximately equal to the grain size (characterized by the grain diameter, d) and the distribution of pore sizes is determined largely by the grain-size distribution. Note that the range of diameters of natural soil particles is extremely large (figure 7.3). A given soil has a mixture of grain sizes, and its grain-size distribution is portrayed as a cumulative-frequency plot of grain diameter (logarithmic scale) versus weight-

fraction of grains with smaller diameter (figure 7.4 on p. 314). The steeper the slope of such a plot, the more uniform the grain-size distribution.

The US Department of Agriculture has developed a widely used scheme that assigns **soil-texture terms** to soils on the basis of their proportions by weight of clay ($d < 0.002\text{ mm}$), silt ($0.002 \leq d < 0.05\text{ mm}$), and sand ($0.05 \leq d < 2\text{ mm}$) (often called **separates**); this scheme can be shown on a ternary dia-

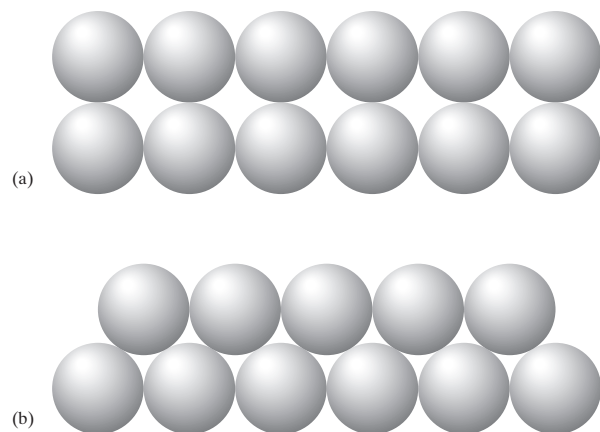


Figure 7.2 Packing of uniform spheres. (a) Open-packed; porosity = 0.91. (b) Close-packed; porosity = 0.35.

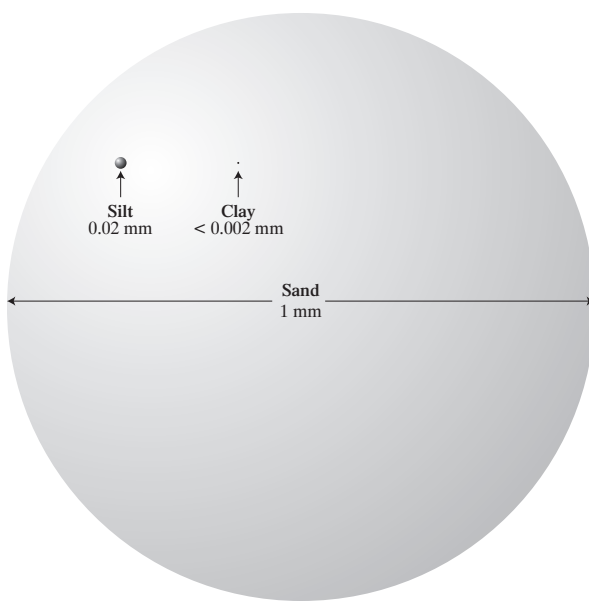


Figure 7.3 Relative sizes of sand, silt, and clay particles.

gram (figure 7.5a on p. 315) or, since the totals of the three separates adds to 100%, as in figure 7.5b. Note that the texture is determined by the proportions of sand, silt, and clay *after* particles larger than sand (i.e., $d > 2 \text{ mm}$) are removed. If a significant proportion of the soil ($> 15\%$) is gravel or larger, an adjective such as “gravelly” or “stony” is added to the soil-texture term. Box 7.1 on p. 316 illustrates the determination of soil texture from grain-size analysis. The NRCS provides an automated soil-texture calculator on its website (<http://www.nrcs.usda.gov/wps/portal/nrcs/detail/soils/survey>).

7.1.1.2 Measurement

Weight fractions of soils of various diameters are measured by sieve analysis for particles larger than 0.05 mm, and by sedimentation in water for the smaller grain sizes (Hillel 1980a; Burt 2004).

7.1.2 Particle Density

7.1.2.1 Definition

Particle density, ρ_m , is the weighted average density of the mineral grains making up a soil:

$$\rho_m \equiv \frac{M_m}{V_m}. \quad (7.2)$$

7.1.2.2 Measurement

The value of ρ_m for a given soil is not usually measured, but is estimated based on the mineral composition of the soil. A value of $2,650 \text{ kg/m}^3$, which is the density of the most common soil, mineral quartz, is assumed for most soils.

7.1.3 Bulk Density

7.1.3.1 Definition

Bulk density, ρ_b , is the *dry* density of the soil; i.e., when $V_w = 0$,

$$\rho_b \equiv \frac{M_m}{V_s} = \frac{M_m}{V_a + V_m} = \frac{M_m}{V_v + V_m}. \quad (7.3)$$

In most hydrologic situations, bulk density in any layer is constant in time; however, it commonly increases with depth due to compaction by the weight of overlying soil and decreasing amounts of organic matter.

7.1.3.2 Measurement

In practice, bulk density is determined as the weight of a volume of soil that has been dried for an extended period (16 hr or longer) at 105°C , divided by the original volume.

7.1.4 Porosity

7.1.4.1 Definition

Porosity, ϕ , is the proportion of pore spaces in a volume of soil:

$$\phi \equiv \frac{V_v}{V_s} = \frac{V_a + V_w}{V_s}. \quad (7.4)$$

Like bulk density, porosity at a given location and depth is constant over the time periods considered in most hydrologic analyses. However, in many soils, it decreases with depth due to compaction and the presence of **macropores** due to near-surface biological activity.

7.1.4.2 Measurement

From equations (7.1)–(7.4),

$$\phi = 1 - \frac{\rho_b}{\rho_m} \quad (7.5)$$

and ϕ is usually determined by measuring ρ_b and assuming an appropriate value for ρ_m (usually $2,650 \text{ kg/m}^3$).

The range of porosities in soils is shown in figure 7.6 on p. 317; in general, finer-grained soils have

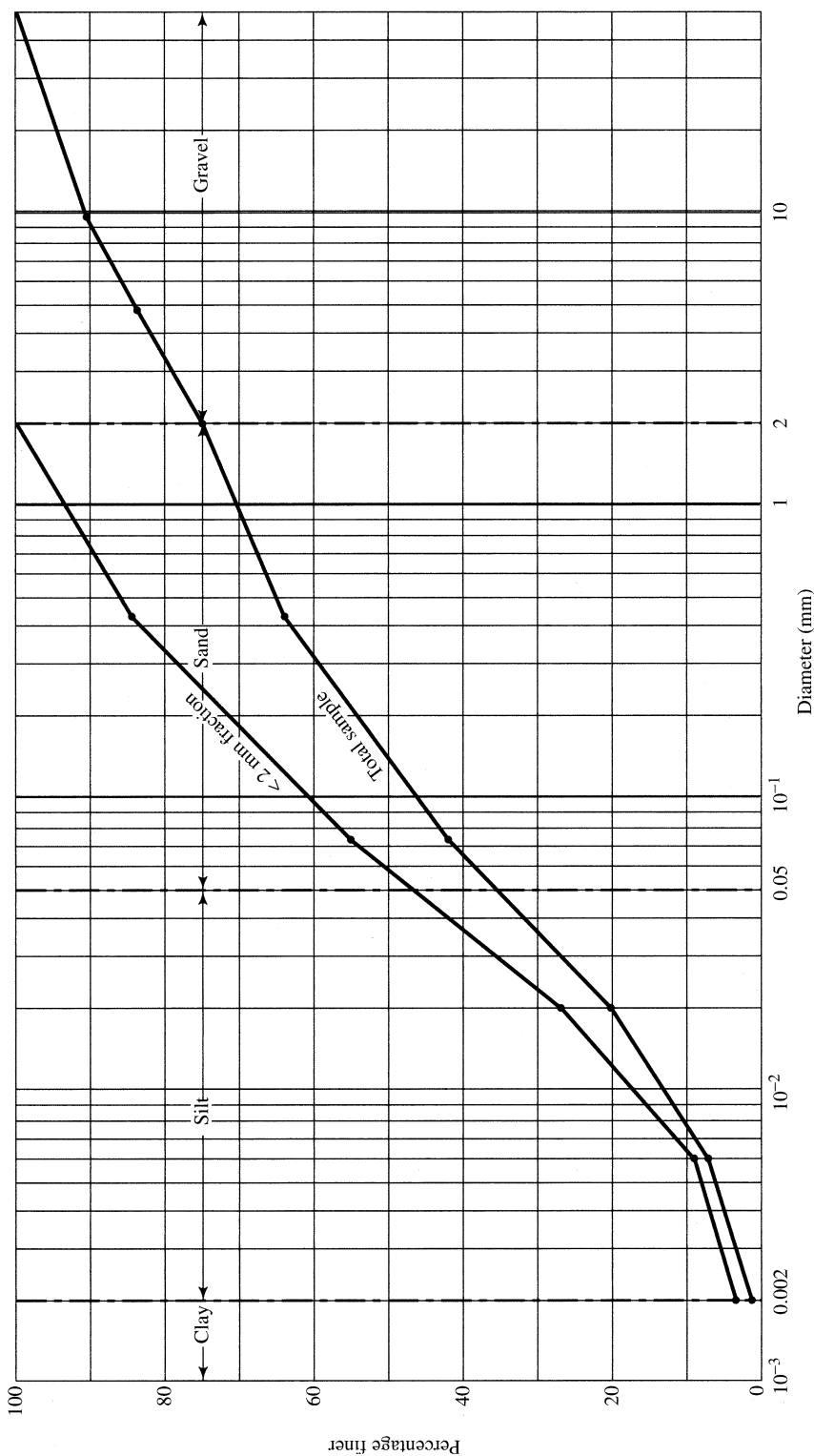


Figure 7.4 Grain-size distribution curve for a soil formed on glacial till in southwestern New Hampshire (see box 7.1). The boundaries between size classes designated clay, silt, sand, and gravel are shown as vertical lines.

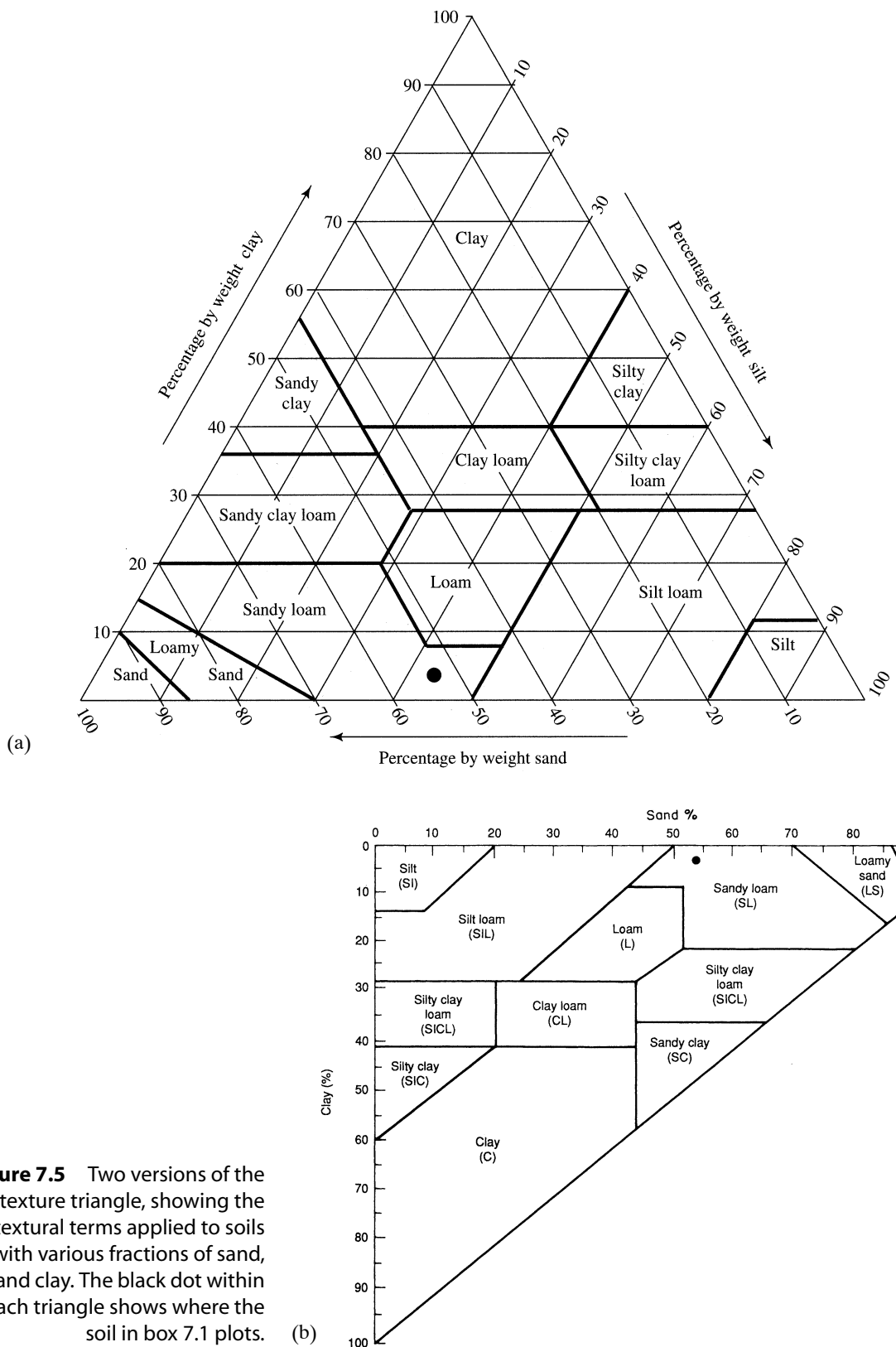


Figure 7.5 Two versions of the soil-texture triangle, showing the textural terms applied to soils with various fractions of sand, silt, and clay. The black dot within each triangle shows where the soil in box 7.1 plots.

Box 7.1 Soil-Property Example Calculations

Soil-Texture Determination

To determine the texture designation of a soil formed on glacial till in southwestern New Hampshire, the grain-

size distribution found in table 7B1.1 was determined by sieving and sedimentation.

Table 7B1.1 Total and Recalculated Grain-Size Distribution.

Diameter, d (mm)	50	19	9.5	4.76	2	0.42	0.074	0.02	0.005	0.002
% finer (total sample)	100	95	90	84	75	64	42	20	7	2
% finer (< 2 mm part)					100	85	56	27	9	3

The total grain-size distribution is plotted as the lower curve in figure 7.4. Since > 15% of the grains have $d > 2$ mm (gravel), the distribution for the portion with $d < 2$ mm is recalculated as shown in the bottom row of table 7B1.1 and plotted as the upper curve in figure 7.4. From this we determine the textural proportions, as shown in table 7B1.2.

Using the soil-texture triangle in figure 7.5, this soil is a sandy loam (as shown by the black dot). However, since more than 15% of the particles are in the gravel range, the soil would be called a gravelly sandy loam.

Table 7B1.2 Total and Recalculated Textural Proportions.

Texture	Gravel $d > 2$ mm	Sand $0.05 \leq d < 2$ mm	Silt $0.002 \leq d < 0.05$ mm	Clay $d < 0.002$ mm
Total sample (%)	25	40	33	2
< 2 mm part (%)		53	44	3

Computation of Bulk Density, Porosity, and Water Content

A 10-cm long sample of a soil is taken with a cylindrical sampling tube having a 5-cm diameter. On removal from the tube, the sample weighs 331.8 g. After oven drying at 105°C, the sample weighs 302.4 g. To compute the bulk density, porosity, water content, and wetness, first determine the sample volume, V_s :

$$V_s = (10 \text{ cm}) \times (2.5 \text{ cm}^2) \times 3.1416 \\ = 196 \text{ cm}^3 = 1.96 \times 10^{-4} \text{ m}^3.$$

The bulk density is found from equation (7.3) as

$$\rho_b = \frac{302.4 \text{ g}}{196.3 \text{ cm}^3} = 1.54 \text{ g/cm}^3 = 1,540 \text{ kg/m}^3.$$

The porosity can be calculated from equation (7.5) assuming $\rho_m = 2,650 \text{ kg/m}^3$:

$$\phi = 1 - \frac{1,540 \text{ kg/m}^3}{2,650 \text{ kg/m}^3} = 0.419.$$

The water content is found via equation (7.7):

$$\theta = \frac{(0.3318 \text{ kg} - 0.3024 \text{ kg}) / (1,000 \text{ kg/m}^3)}{1.96 \times 10^{-4} \text{ m}^3} = 0.150.$$

The saturation Θ is then found using equation (7.8):

$$\Theta = \frac{0.150}{0.419} = 0.358.$$

Although the residual water content θ_r was not measured, θ_r is typically about 0.05 for soils of this texture, so we calculate the effective saturation via equation (7.8b) as

$$\theta^* = \frac{0.150 - 0.05}{0.419 - 0.05} = 0.271.$$

higher porosities than coarser-grained soils. This is in part due to the very open “house-of-cards” arrangement of clays, which is maintained by electrostatic forces between the roughly disk-shaped grains;

in contrast, quasi-spherical sand and silt grains are in a more closely packed grain-to-grain architecture (figure 7.7). Peats, which are highly organic soils, may have porosities as high as 0.80.

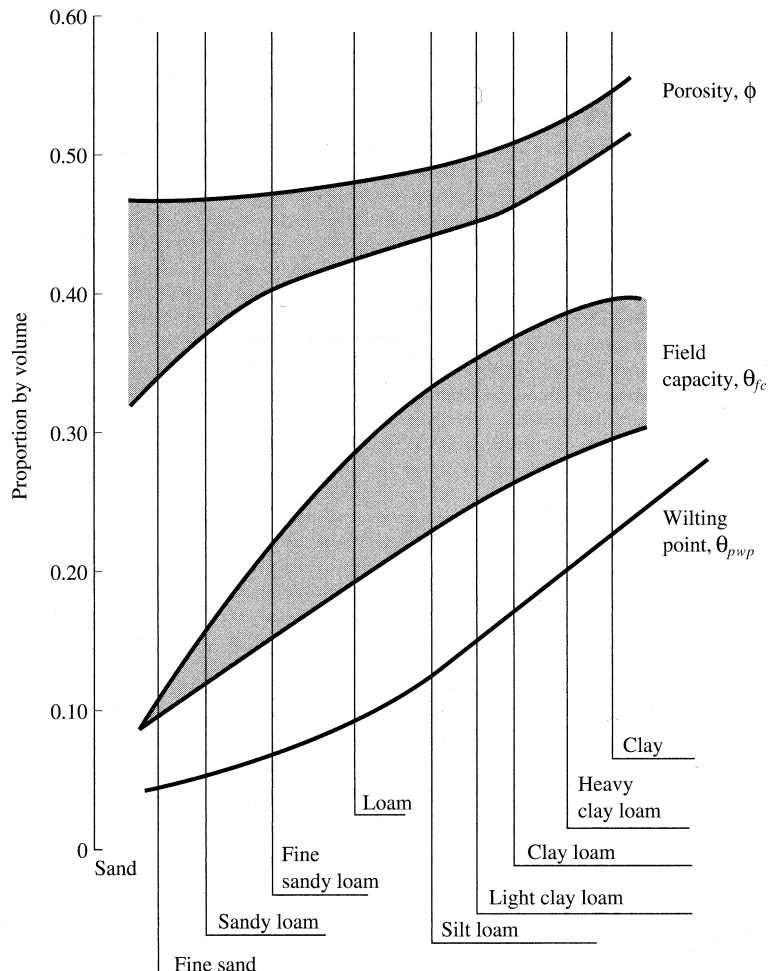
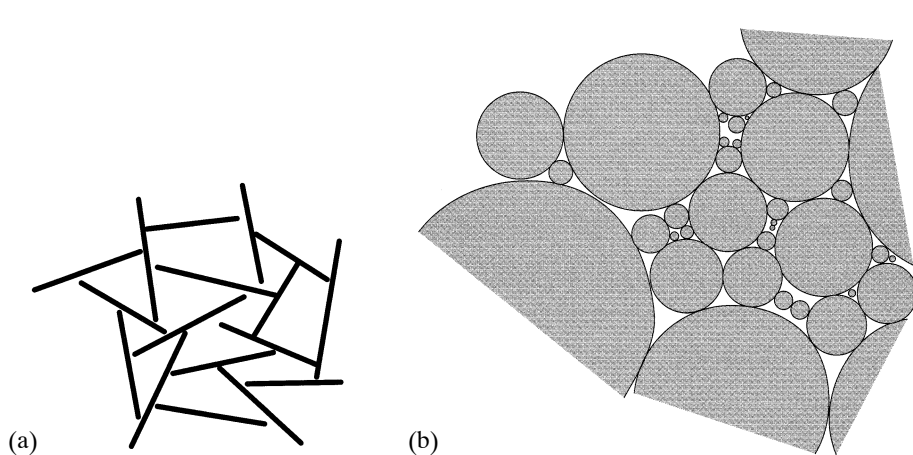


Figure 7.6 Ranges of porosities, field capacities, and permanent wilting points for soils of various textures [Dunne and Leopold (1978)].

Figure 7.7 Schematic diagrams of structures of aggregates of (a) clay (shown as tabular particles viewed edge-on) and (b) sand (shown as spherical particles). The architecture of clay particles is maintained by intergrain electrostatic forces [adapted from Hillel (1980a)].



7.2 Water Storage

7.2.1 Volumetric Water Content

7.2.1.1 Definition

Volumetric water content, θ , (also called **water content** or **soil-moisture content**) is the ratio of water volume to soil volume:

$$\theta \equiv \frac{V_w}{V_s}. \quad (7.6)$$

Water content in natural soils typically varies widely vertically, horizontally, and with time. The theoretical range of θ is from 0 (completely dry) to ϕ (saturation), but, as will be seen later, the lower limit for natural soils is greater than 0.

The total amount of water stored in any layer of soil (i.e., **soil-water storage**) is usually expressed as a depth [L] (volume per unit area), which is the product of the volumetric water content times the thickness of the layer.

7.2.1.2 Measurement

Standard laboratory measurements of small (~ 100 g) soil samples are made by the **gravimetric method**: A small soil sample of known volume V_s is collected in the field, weighed, oven-dried at 105°C for 24 hr, and reweighed. θ is calculated as

$$\theta = \frac{M_{swet} - M_{sdry}}{\rho_w \cdot V_s}, \quad (7.7)$$

where M_{swet} and M_{sdry} are the soil masses (weights) before and after drying, respectively.

Nondestructive field measurements of water content can be achieved by a number of approaches that vary in cost, accuracy, spatial scale, and response time. These are described in box 7.2 and summarized in table 7.1 on p. 320; more detailed descriptions can be found in Zazueta and Xin (1994), Robinson et al. (2008), and Dobriyal et al. (2012) and the literature cited therein.

Box 7.2 Field Soil Water-Content Measurement Methods

Local In-Situ Measurement

The paragraphs below briefly describe various techniques for determining water content at specific locations in the field. Robinson et al. (2008) provided a review of ways in which individual site measurements can be linked in networks that provide information over areas, which is usually required for hydrologic research. Their review includes a discussion of the new technology called **motes**, which are small (about the size of a pack of cards), low-cost sensors that determine water content based on time-domain reflectometry, frequency-domain reflectometry, or capacitance and can be wirelessly linked to a central data logger. Sayde et al. (2010) and Rosenbaum et al. (2012) described other approaches to obtaining watershed-scale measurements of water content.

Electrical resistance blocks utilize the inverse relation between water content and electrical resistance. Resistance is measured across a volume of porous material (gypsum, nylon, or fiberglass) placed in the soil and allowed to equilibrate with the water content of the surrounding soil.

Neutron moisture meters are combined sources and detectors of neutrons that are inserted into access tubes. The radioactive source releases high-energy neutrons; these are slowed by collisions with hydrogen

atoms, and the detector counts the returns of the scattered slower neutrons. Readings are unaffected by the state of the soil water. Restrictions on the use of radioactive materials are increasingly stringent, so use of this technology is decreasing.

Gamma-ray instruments consist of a radioactive source surrounded by a beam collimator that can be lowered into the soil at a fixed location. A detector measures the absorption of gamma rays by water molecules in the soil between a source and a detector. Readings are unaffected by the state of the soil water. Restrictions on the use of radioactive materials are increasingly stringent, so use of this technology has decreased.

Time-domain reflectometry (TDR) measures the propagation velocity of very short electromagnetic energy pulses sent through a probe. The pulse velocity decreases with soil-moisture content due to the relatively large dielectric value of water (Topp et al. 1980; Zegelin et al. 1989; Roth et al. 1990; Jacobsen and Schjønning 1993; Yu et al. 1997).

Frequency-domain reflectometry (FDR) is similar to TDR, but measures soil-moisture content based on variation in the frequency of a radio-frequency signal that depends on the dielectric properties, which in turn depend on water content (Bell et al. 1987; Dean et al. 1987; Eller and Denoth 1996).

Capacitance probes determine water content by measuring the electrical capacitance between soil-implanted electrodes.

Heat pulse probes consist of thin (approximately 1 mm) heater and temperature probes mounted in parallel with a 6-mm separation distance. A short-duration heat pulse is applied and the temperature response is recorded. The soil heat capacity and water content can then be estimated from theoretical heat-flow relations. Sayde et al. (2010) explored a promising technique that uses fiber-optic cables as thermal sensors to passively measure propagation of temperature changes due to the diurnal cycle. These cables can be more than 10 km long, with measurements every 1 m.

Tensiometers are probes that measure the moisture potential as a function of the pressure (suction) force exerted on water by soil. These instruments are described more fully in section 7.4.3.1. The water content is determined from the pressure-water content relation, which is discussed in section 7.4.3.2.

Geophysical Methods

The geophysical methods described below are ground-based techniques that provide measurements of water content over transects or areas, which is usually essential for hydrologic analysis. Robinson et al. (2008) provide more detail on these methods, and also describe mobile TDR systems mounted on all-terrain vehicles that can provide similar spatial information.

Ground-penetrating radar (GPR) uses the transmission and reflection of high-frequency (1 MHz–1 GHz) electromagnetic waves within the subsurface to estimate θ to depths of up to tens of meters, depending on water content and soil texture. A simple application of GPR involves measuring the travel time of a direct ground wave from source to antenna through the surface layer to measure θ along transects. GPR can also be used in a surface-based system, where the transmitter and receiver antennas are moved across the surface, or where the antennas are positioned in boreholes.

Electromagnetic induction (EMI) instruments measure ground electrical conductivity between a transmitter loop and a receiver. The greater the spacing of the loops, the deeper the penetration into the ground. This method is well suited for field use and can be linked to global positioning systems to provide detailed water-content data over areas as large as 500 ha (Robinson et al. 2008).

Direct-current resistivity is measured via evenly spaced electrodes inserted in the ground along a line, typically at 0.5- to 5-m spacing. Although resistivity depends on soil properties as well as water content, new electronic advances make the technique highly useful for monitoring spatial processes, and when calibrated or linked to point measurements with water-content sen-

sors, it can provide strong insight into subsurface processes, including changes in θ (Robinson et al. 2008).

Nuclear magnetic resonance (NMR) determines water content via the response of hydrogen nuclei to magnetic fields. Paetzold et al. (1985) developed and tested a system consisting of an electromagnet, detection coil, and tuning capacitor that was tractor-mounted to provide a continuous measurement of water content at depths to 63 mm.

Remote-Sensing Methods

Remote-sensing measurements are made by instruments not in contact with the ground, and involve crane-, aircraft- or satellite-mounted detection of electromagnetic fields whose strength is correlated with water content. The methods discussed here can provide measurements at the field-plot or small-watershed scale; methods based on detection of gravity fields can resolve water contents only at scales larger than 600 to 1,000 km (see section 1.8.2.4). The review by Robinson et al. (2008) provides more detail on these methods.

Passive microwave measurements use radiometers to measure the **brightness temperature**, F_B , of the land surface. Brightness temperature is related to surface temperature, F_s , as

$$F_B = \varepsilon \cdot F_s, \quad (7B2.1)$$

where ε is emissivity. At infrared wavelengths, $\varepsilon = 1$, so those wavelengths can be used to determine the temperature, F_s , of a very thin (< 0.001 m) surface layer. At microwave wavelengths (~ 0.01 to 0.20 m), ε is approximately an inverse linear function of θ , but it also depends on soil texture, the surface roughness, vegetation, the angle of view, and the wave polarization (horizontal or vertical). The emitted microwave flux “sees” water content over depths of from 0.02 to 0.2 m. Water content can be mapped at scales of tens to hundreds of meters from aircraft, and tens of kilometers from satellites. However, infrared radiation cannot pass through clouds. Approaches to accounting for the effect of vegetation are described by Robinson et al. (2008). Piles et al. (2010) present an in-depth study of the retrieval configurations and ancillary data needed for the retrieval of soil moisture by the Soil Moisture and Ocean Salinity (SMOS) satellite mission of the European Space Agency, which was launched in November 2009.

Active microwave (radar) measurements determine soil-water content by emitting a radiation flux and measuring the ratio of flux reflected by the surface to that emitted. Radiation at low radar frequencies can integrate water content over depths of ~ 0.05 m, can pass through clouds and low-density vegetation, and can be used at night as well as during the day. Aircraft-mounted radar can map at scales of tens to hundreds of meters, while minimum satellite-borne radar resolution is on the order of a kilometer.

Table 7.1 Comparison of Methods Used for Measurement of Water Content.^a**Field Site**

Method	Quantity Observed	Support Volume (m³)^b	Response Time	Accuracy	Calibration Required?	Cost Effectiveness
electrical resistance blocks	electrical resistance	2×10 ⁻³	2–3 hr	low	yes	economical
neutron probe	slow neutrons	10 ⁻¹	1–2 min	high	yes	expensive
gamma-ray attenuation	gamma-ray absorption	10 ⁻⁶	1 min	high	no	expensive
time-domain reflectometry	electrical-pulse velocity	1.5×10 ⁻⁵ to 3×10 ⁻⁴	instantaneous	high	no	economical
frequency-domain reflectometry	radio frequency	6×10 ⁻⁵	instantaneous	high	yes	expensive
capacitance	dielectric constant	6×10 ⁻⁵	instantaneous	high	yes	expensive
heat pulse	temperature response	10 ⁻⁵	1 min	high	yes	expensive
tensiometer	soil-water potential	< 10 ⁻³	2–3 hr	high	yes	economical

Geophysical

Method	Quantity Observed	Depth Sampled (m)	Response Time	Accuracy	Calibration Required?	Cost Effectiveness
ground-penetrating radar	refraction of microwaves	< 1 to > 10	instantaneous	high	yes	expensive
electromagnetic induction	electrical conductivity	depends on configuration	instantaneous	low	yes	expensive
direct-current resistivity	electrical conductivity	depends on configuration	instantaneous	low	yes	expensive
nuclear magnetic resonance	radio frequency	< 0.1 m; can be tractor mounted	1–2 min	high	yes	expensive

Remote Sensing

Method	Quantity Observed	Depth Sampled (m)^c	Horizontal Scale (m)	Response Time	Accuracy	Calibration Required?
passive microwave	emitted microwave flux	0.02 to 0.2	10 to 100 ^d to 10 ^{4(e)}	instantaneous	low	yes
active microwave (radar)	reflected microwave flux	~0.05	10 to 100 ^d to 1,000 ^e	instantaneous	low	yes

^aSee section 7.2.1.2 for further discussion.^bApproximate volume sampled; for most methods, this varies with soil texture and water content.^cVaries with soil texture, water content, and surface properties.^dAircraft-mounted.^eSatellite-mounted

7.2.2 Saturation

The **saturation**, or **wetness**, Θ , is the proportion of pores that contain water:

$$\Theta \equiv \frac{V_w}{V_v} = \frac{V_w}{V_a + V_w} = \frac{\theta}{\phi}. \quad (7.8a)$$

However, soils usually contain water that is held so tightly by surface tension and electrochemical forces that it is immobile. Thus it is useful to define **effective saturation**, θ^* , as

$$\theta^* \equiv \frac{\theta - \theta_r}{\phi - \theta_r}, \quad (7.8b)$$

where θ_r is the permanent residual water content (typically $\theta_r \approx 0.05$). We will use θ^* to express the relative saturation of field soils.

7.3 Basic Principles of Saturated Subsurface Flow

7.3.1 Darcy's Law

The law governing water flow through a porous medium was discovered in 1856 by Henri Darcy, a French engineer. As a basis for designing a sand-filtration system for the water supply of the city of Dijon, Darcy did experiments on flow through saturated sand using an apparatus like that shown in figure 7.8. His results can be summarized in the relation now known as **Darcy's law**:

$$q_x \equiv \frac{Q_x}{A_x} = -K_{hx} \cdot \frac{dh}{dx}, \quad (7.9)$$

where q_x [$L T^{-1}$] is the **specific discharge**, which is the volume rate of flow, Q_x [$L^3 T^{-1}$], per unit area of porous medium at right angles to the x -direction, A_x [L^2]; K_{hx} [$L T^{-1}$] is a proportionality factor called the **saturated hydraulic conductivity** of the medium in the x -direction; and dh/dx is the gradient of **total hydraulic head**, h , of the fluid in the x -direction. The minus sign indicates that flow moves from higher values of h to lower values.

Hydraulic head (usually called simply "head") represents the **fluid potential**, which is the mechanical energy per unit weight of fluid [$E F^{-1}$] = [L]. The hydraulic-head gradient is the gradient of potential energy that induces the flow.

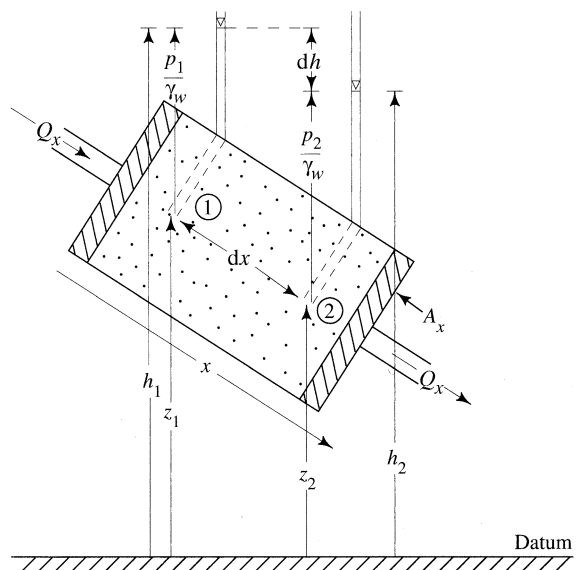


Figure 7.8 A simple experimental device illustrating the terms in Darcy's law [equation (7.9)]. The tubes measuring water levels at points 1 and 2 are piezometers. The subscripts 1 and 2 refer to "upstream" and "downstream" points, respectively.

At a point, hydraulic head is the sum of (1) **gravitational head**, given by the elevation of the point above an arbitrary horizontal datum, z [L]; and (2) **pressure head**, ψ [L], which is equal to the pressure of the fluid at the point, p [$F L^{-2}$], divided by the weight density of the fluid, γ [$F L^{-3}$]; thus

$$h = z + \psi = z + \frac{p}{\gamma}. \quad (7.10)$$

Pressure is conventionally measured as **gauge pressure**, which is the difference between actual pressure and atmospheric pressure. As noted earlier, pressures in saturated porous media are greater than atmospheric, so that $p > 0$ and $\psi > 0$ in saturated flow. For a fluid of constant density (which we assume throughout this chapter),

The total head $z + \psi$ at a "point" in a *saturated* flow can be measured as the height above an arbitrary datum to which water rises in a **piezometer**, which is a tube connecting the point to the atmosphere (see figure 7.8).

Combining equations (7.9) and (7.10), Darcy's law can be written as

$$\begin{aligned} q_x &= -K_{hx} \cdot \frac{dh}{dx} = -K_{hx} \cdot \left[\frac{dz}{dx} + \frac{d\psi}{dx} \right] \\ &= -K_{hx} \cdot \left[\frac{dz}{dx} + \frac{d(p/\gamma)}{dx} \right]. \end{aligned} \quad (7.11)$$

The actual flow of water through a porous medium is extremely complex, with individual tiny "parcels" of water flowing with varying velocities along tortuous paths through the pores. In contrast, note that

Darcy's law describes the *bulk flow* in a particular direction through a "small" volume that is representative of the local medium, over which interpore and intrapore variations of velocity are averaged.

This hypothetical "small" volume is called a **representative elementary volume (REV)**; its dimensions are on the order of several grain diameters. In diagrams of saturated flow systems, such a volume is represented as a point.

The specific discharge, $q_x \equiv Q_x/A_x$, has the dimensions of a velocity and is sometimes called the **Darcy velocity**. The actual average velocity of the water is found by dividing the discharge by the cross-sectional area occupied by the flowing water. In a saturated porous medium, that area is given by $\phi \cdot A_x$, where ϕ is porosity, so the average water velocity, U_x , is given by

$$U_x = \frac{Q_x}{\phi \cdot A_x} = \frac{q_x}{\phi}. \quad (7.12)$$

7.3.2 Limitations of Darcy's Law

Darcy's law does not apply to flows at scales smaller than the REV; i.e., the REV must be large enough to permit meaningful flow averaging. As noted by Freeze and Cherry (1979), the REV concept also has upper limits of validity in heterogeneous or fractured porous media.

A second important limitation arises because the linear relation between flow rate and head gradient expressed in Darcy's law is valid only for flow velocities that are low enough such that intrapore flow paths of individual water "parcels" are mutually par-

allel; i.e., for **laminar flows**. If flow velocities are large enough, inertial forces arise that disrupt this parallelism and produce a nonlinear relation between flow rate and head gradient. The likely presence of this nonlinearity can be detected by calculating the dimensionless **Reynolds number** for the flow, Re , where

$$Re \equiv \frac{q_x \cdot d}{v}, \quad (7.13)$$

q_x is the specific discharge [$L T^{-1}$], d is the average grain diameter of the medium [L], and v is the kinematic viscosity of the fluid [$L^2 T^{-1}$] ($v \approx 1.7 \times 10^{-6} m^2/s$; see appendix B). Experience has shown that Darcy's law is valid when $Re < \sim 1$. Most natural ground-water flows meet this criterion, and we will assume this is true for the saturated and unsaturated porous-media flows discussed in this text. However, non-Darcian flow can occur in very large soil pores ("macropores"; see chapter 10), in large openings produced by fracturing or dissolution of earth materials, and in the immediate vicinity of pumped wells.

7.3.3 Permeability and Hydraulic Conductivity

Consider again the experiment of figure 7.8. Suppose the experiment was run twice with water under identical head gradients, first using a medium of uniform spheres of diameter $d = 1$ mm, and then with $d = 4$ mm. It is intuitively clear that the flow rate q would be larger for the larger particles because water would move more rapidly through larger pores. Now imagine that the experiment was repeated with $d = 1$ mm, but first with water and then with a fluid with a higher viscosity, like motor oil, maintaining the same head gradient for both flows. Again, it's clear that the flow rate would be higher for the water flow.

Thus we see that the hydraulic conductivity depends on both the nature of the medium and the nature of the fluid. The relationship is

$$K_h = C \cdot d^2 \cdot \frac{\rho \cdot g}{\mu} = C \cdot d^2 \cdot \frac{g}{v}, \quad (7.14)$$

where d is average grain diameter, g is gravitational acceleration, ρ is fluid mass density, μ is dynamic viscosity, v is kinematic viscosity ($\equiv \mu/\rho$), and C is a proportionality parameter that depends on properties of the medium such as grain shape, size distribution, and packing.

The portion of conductivity that depends only on the medium is called the **intrinsic permeability**, k_I :

$$k_I \equiv C \cdot d^2. \quad (7.15)$$

From (7.14) and (7.15),

$$K_h = k_I \cdot \frac{g}{\nu}. \quad (7.16)$$

K_h varies over an extremely large ($> 10^{12}$ -fold) range for earth materials (figure 7.9). This variability is due almost exclusively to the $> 10^6$ -fold range of d ; viscosity varies with temperature, but only by a factor of two under typical near-surface conditions.

Values of saturated hydraulic conductivity for small samples can be readily determined in **permeameters** similar to the device shown in figure 7.8, where A_x and dx are known, Q_x and dh are measured, and K_{hx} is calculated via equation (7.9). However, conductivities measured in permeameters may differ greatly from field values because: (1) it is often difficult to avoid disturbing the structure of materials when transferring samples to a permeameter and (2)

conductivities measured in small samples do not include the effects of fractures and larger-scale geologic variability, and hence are generally smaller than effective regional-scale values.

Larger-scale values of K_h can be measured in the field by pumping water from a well and observing the rate at which water level changes in one or more nearby observation wells. Details of these methods can be found in most ground-water-hydrology texts (e.g., Todd and Mays 2014). As noted in chapter 9, hydraulic conductivity usually has significant spatial variability, even in a given geologic unit, and may vary in different directions.

7.3.4 General Saturated-Flow Equation

The general equation for saturated ground-water flow is derived in box 7.3 (figure 7.10) by combining Darcy's law with the law of conservation of fluid mass, leading to

$$\begin{aligned} & \frac{\partial}{\partial x} \left(K_{hx} \cdot \frac{\partial h}{\partial x} \right) + \frac{\partial}{\partial y} \left(K_{hy} \cdot \frac{\partial h}{\partial y} \right) + \frac{\partial}{\partial z} \left(K_{hz} \cdot \frac{\partial h}{\partial z} \right) \\ &= S_s \cdot \frac{\partial h}{\partial t}. \end{aligned} \quad (7.17)$$

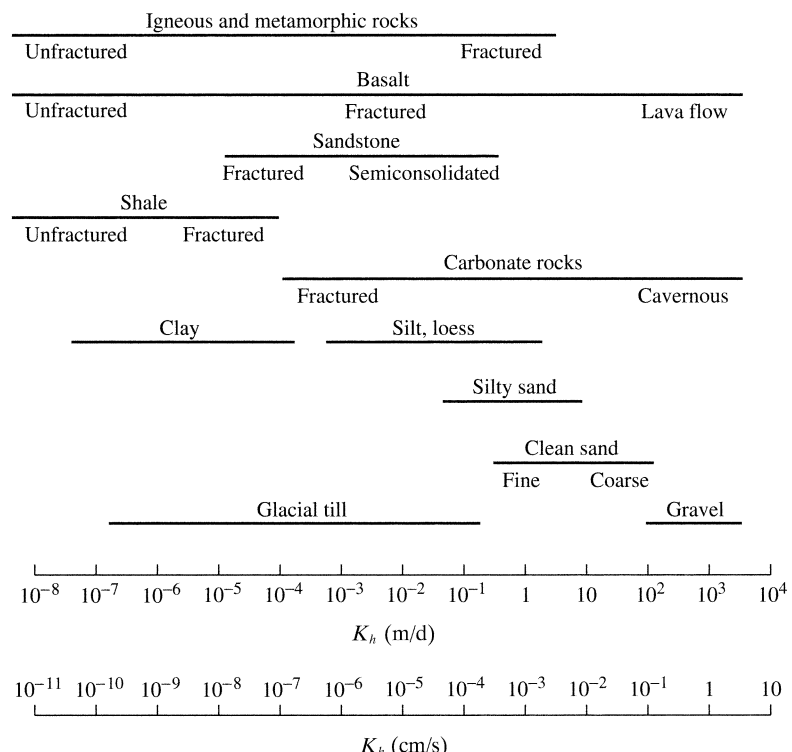


Figure 7.9 Ranges of saturated hydraulic conductivities for various geologic materials [Heath (1982)].

Box 7.3 Derivation of General Equation for Saturated Ground-Water Flow

Conservation of Mass

Following the principles discussed in section 1.6.2, the conservation-of-mass equation for saturated porous-media flow is derived by considering a control volume in the form of a rectangular parallelepiped $dx \cdot dy \cdot dz$ within a saturated porous medium (figure 7.10). The volume must be large enough to contain many typical pore spaces, but small enough to allow the use of continuous mathematics (i.e., a REV). For this volume over time period dt ,

$$M_{in} - M_{out} = \Delta M, \quad (7B3.1)$$

where M_{in} is the mass of water flowing into the volume, M_{out} is the mass of water flowing out of the volume, and ΔM is the change in mass storage.

The flow can be in any direction, and the specific-discharge vector can be resolved into vectors parallel to the sides of the volume, q_x , q_y , and q_z . Then M_{in} (entering the volume through faces 1, 2, and 3) is

$$\begin{array}{ccc} \text{Face 1} & \text{Face 2} & \text{Face 3} \\ M_{in} = \rho \cdot q_x \cdot dy \cdot dz \cdot dt + \rho \cdot q_y \cdot dx \cdot dz \cdot dt + \rho \cdot q_z \cdot dx \cdot dy \cdot dt, \end{array} \quad (7B3.2)$$

where ρ is the mass density of water. In general, the rate of flow changes in space, so that M_{out} (leaving through faces 4, 5, and 6) is given by

$$\begin{array}{ccc} \text{Face 4} & & \text{Face 5} \\ M_{out} = \left[\rho \cdot q_x + \frac{\partial(\rho \cdot q_x)}{\partial x} \cdot dx \right] \cdot dy \cdot dz \cdot dt + \left[\rho \cdot q_y + \frac{\partial(\rho \cdot q_y)}{\partial y} \cdot dy \right] \cdot dx \cdot dz \cdot dt \\ & & \\ & \text{Face 6} & \\ & + \left[\rho \cdot q_z + \frac{\partial(\rho \cdot q_z)}{\partial z} \cdot dz \right] \cdot dx \cdot dy \cdot dt. \end{array} \quad (7B3.3)$$

The change in storage, ΔM is

$$\Delta M = \rho \cdot S_s \cdot \frac{\partial h}{\partial t} \cdot dx \cdot dy \cdot dz \cdot dt, \quad (7B3.4)$$

where h is head and S_s is the **specific storage**, defined as

$$\begin{aligned} S_s &\equiv \frac{\text{volume of water entering or leaving control volume } [L^3]}{\text{increase or decrease in head } [L] \times \text{control volume } [L^3]} \\ &= \frac{\text{volume of water entering or leaving control volume}}{dh \cdot dx \cdot dy \cdot dz}. \end{aligned} \quad (7B3.5)$$

Note that specific storage has dimensions $[L^{-1}]$. In saturated media its magnitude is determined by the compressibility of the fluid and of the medium (section 9.1.3).

Substituting equations (7B3.2)–(7B3.5) into (7B3.1), assuming constant density and simplifying, yields the conservation-of-mass equation for three-dimensional time-varying ground-water flow:

$$\frac{\partial q_x}{\partial x} + \frac{\partial q_y}{\partial y} + \frac{\partial q_z}{\partial z} = -S_s \cdot \frac{\partial h}{\partial t}. \quad (7B3.6)$$

Combination with Darcy's Law

When Darcy's law in the form of equation (7.9) for each of the three coordinate directions is inserted into equation (7B3.6), we have the equation that must be satisfied for a time-varying Darcian flow at all points in a saturated medium (assuming constant density):

$$\frac{\partial}{\partial x} \left(K_{hx} \cdot \frac{\partial h}{\partial x} \right) + \frac{\partial}{\partial y} \left(K_{hy} \cdot \frac{\partial h}{\partial y} \right) + \frac{\partial}{\partial z} \left(K_{hz} \cdot \frac{\partial h}{\partial z} \right) = S_s \cdot \frac{\partial h}{\partial t}. \quad (7B3.7)$$

Equation (7B3.7) describes time-varying ground-water flow in a porous medium in which the head, head gradient, conductivity, and specific storage may change with location. Note, though, that in (7B3.7) K_{hi} for each of the coordinate directions $i = x, y, z$ varies only in the i -direction, whereas in the most general case K_{hx} , for example, might also change in the y - and z -directions. As noted by Freeze and Cherry (1979), this does not usually need to be taken into account, and (7B3.7) can be considered general.

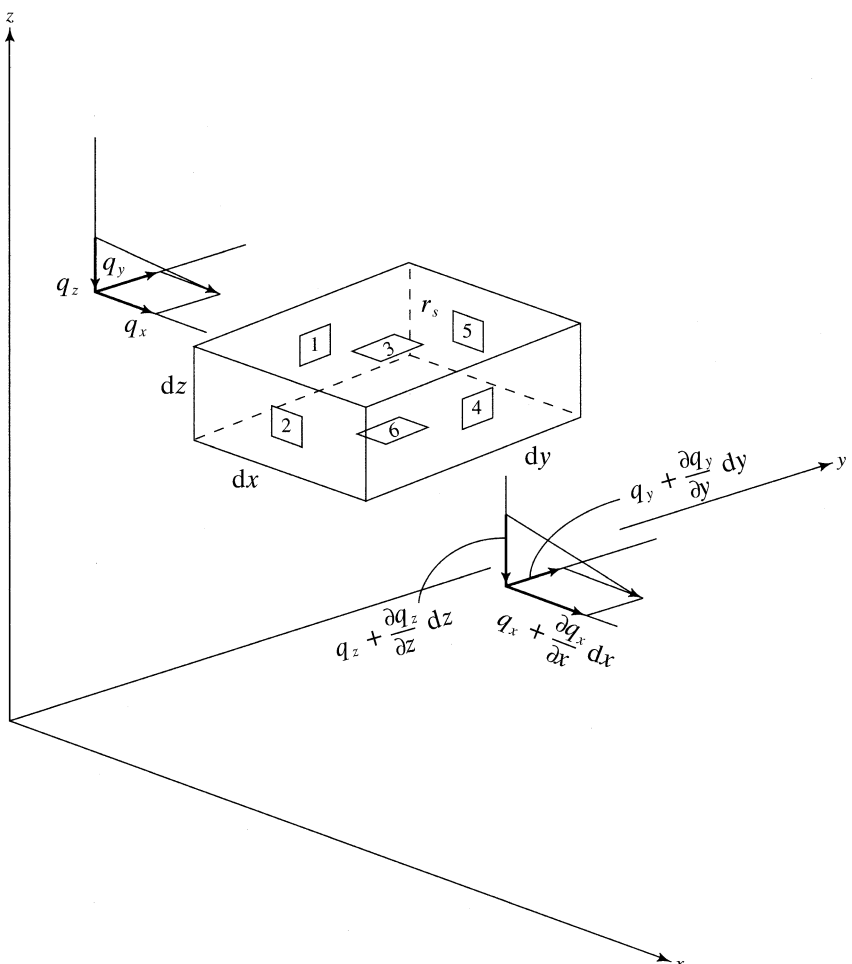


Figure 7.10 Definitions of terms for derivation of the continuity equation for ground-water flow (see box 7.3).

There are many instances when the equation can be simplified:

- Steady-state flow, $\partial h / \partial t = 0$

$$\frac{\partial}{\partial x} \left(K_{hx} \cdot \frac{\partial h}{\partial x} \right) + \frac{\partial}{\partial y} \left(K_{hy} \cdot \frac{\partial h}{\partial y} \right) + \frac{\partial}{\partial z} \left(K_{hz} \cdot \frac{\partial h}{\partial z} \right) = 0; \quad (7.18)$$

- Isotropic and homogeneous medium, $K_{hx} = K_{hy} = K_{hz} = K_h$ ("diffusion equation")

$$\frac{\partial^2 h}{\partial x^2} + \frac{\partial^2 h}{\partial y^2} + \frac{\partial^2 h}{\partial z^2} = \frac{S_s}{K_h} \cdot \frac{\partial h}{\partial t}; \quad (7.19)$$

- Steady-state flow, isotropic and homogeneous medium ("Laplace equation")

$$\frac{\partial^2 h}{\partial x^2} + \frac{\partial^2 h}{\partial y^2} + \frac{\partial^2 h}{\partial z^2} = 0. \quad (7.20)$$

Solutions to equation (7.17) and its various simplifications consist of a coherent potential-energy [$h(x,y,z,t)$] field, and are largely determined by the **boundary conditions** of the flow system. The boundary conditions are specified in terms of: (1) the configuration of the system's boundaries, expressed as the coordinates of points on the boundaries, (x_b, y_b, z_b) and (2) at boundary points, either the head $h(x_b, y_b, z_b)$ or their designation as impermeable barriers. In general, we must also specify as parameters the values of hydraulic conductivity and storage coefficient at all points and, for time-varying flows, the initial conditions, $h(x, y, z, 0)$.

For most situations, solutions must be numerically approximated by transforming the partial-differential equations to a system of algebraic equations and solving for h at selected points throughout the flow system and at successive times.² The points are the nodes of an x, y, z coordinate system separated by finite distances, and the equations are solved at suc-

cessive finite time steps. Once solutions have been obtained, contour lines (if two-dimensional) or surfaces (if three-dimensional) of equal values of h (**equipotentials**) can be drawn, and vectors of ground-water flow (**streamlines**) are perpendicular to the equipotentials. In section 9.2, numerical solutions to the general ground-water equation are used to illustrate the effects of topography and geology on regional ground-water flows.

7.4 Basic Principles of Unsaturated Subsurface Flow

7.4.1 Surface Tension and Capillarity

7.4.1.1 Surface Tension

Soil pores in the unsaturated zone contain water and air. Water molecules at the air-water interface are subjected to a net inward force due to hydrogen bonding with the molecules below the surface (figure 7.11). **Surface tension**, σ , is equal to the magnitude of that force divided by the distance over which it acts; thus its dimensions are $[F L^{-1}]$. It can also be viewed as the energy required to increase the surface area of a liquid by a unit amount ($[F L]/[L^2] = [F L^{-1}]$). Surface tension and the closely related phenomenon of **capillarity** significantly influence fluid dynamics where a water surface is present and where the flow scale is less than a few millimeters—i.e., in porous media that are partially saturated or in which there is an interface between water and an immiscible liquid (e.g., hydrocarbons).

Water has a surface tension higher than most other liquids; its value at 0°C is 0.0756 N/m , and decreases slightly as temperature increases (appendix B). Dissolved substances can also increase or decrease surface tension, and certain organic compounds have a major effect on its value.

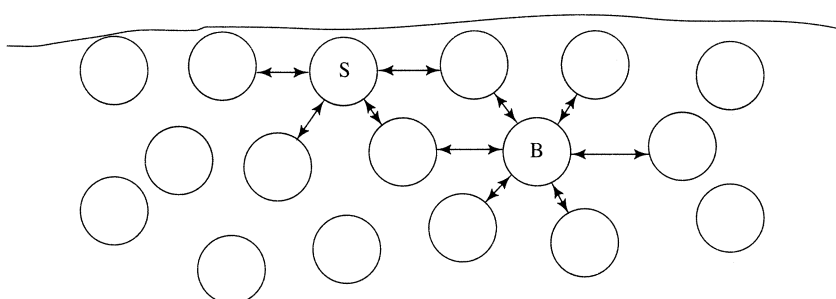


Figure 7.11 Intermolecular forces acting on typical surface (S) and nonsurface (B) molecules.

7.4.1.2 Capillary Rise and the Tension-Saturated Zone

Consider a small (diameter of a few millimeters or less) cylindrical tube immersed in a body of water with a surface at atmospheric pressure (figure 7.12). If the material of the tube is such that the hydrogen bonds of the water are attracted to it, the molecules in contact with the tube are drawn upward. The degree of attraction between the water and the tube is reflected in the **contact angle** between the upper edge of the water surface, or **meniscus**, and the tube: the stronger the attraction, the smaller the angle. Because of the intermolecular hydrogen bonds, the entire mass of water within the tube is drawn upward until the adhesive force between the molecules of the tube and those of the water is balanced by the downward force due to the weight of the water suspended within the tube.

The height to which the water will rise in the tube can thus be calculated by equating the upward and downward forces. The upward force, F_u , equals the vertical component of the surface tension times the distance over which that force acts (the tube circumference):

$$F_u = \sigma \cdot \cos(\beta_c) \cdot 2 \cdot \pi \cdot r, \quad (7.21)$$

where β_c is the contact angle and r is the radius of the tube. The downward force due to the weight of the column of water, F_d , is

$$F_d = \gamma \cdot \pi \cdot r^2 \cdot h_{cr}, \quad (7.22)$$

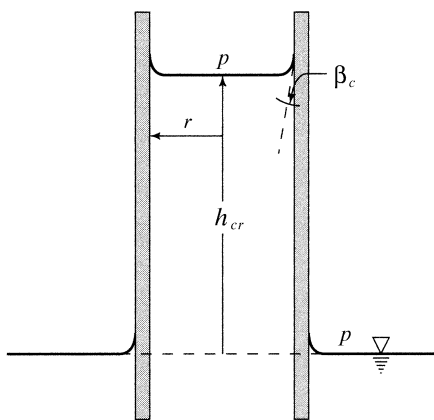


Figure 7.12 Sketch of phenomenon of capillary rise in a circular tube of radius r ; β_c is the contact angle between the meniscus and the wall, p is atmospheric pressure, and h_{cr} is the height of capillary rise.

where γ is the weight density of water and h_{cr} is the height of the column. Equating F_u and F_d and solving for h_{cr} yields

$$h_{cr} = \frac{2 \cdot \sigma \cdot \cos(\beta_c)}{\gamma \cdot r}. \quad (7.23)$$

Thus the **height of capillary rise** is inversely proportional to the radius of the tube and directly proportional to the surface tension and the cosine of the contact angle. The contact angle for common minerals is close to 0° (table B.4), so $\cos(\beta_c) \approx 1$ typically.

As noted earlier, the water table is a surface at atmospheric pressure. The interconnected soil pores above that surface act as capillary tubes, pulling water upward to produce a **tension-saturated zone** or **capillary fringe** above the free surface. The height of this zone can be approximately calculated via equation (7.23) with r equal to the average radius of the soil particles; it ranges from a few centimeters in gravel and sand to well over a meter in silt. For clay soils, however, additional electrical forces become significant and equation (7.23) does not strictly hold.

7.4.1.3 Pressure Relations

When capillary rise has ceased (see figure 7.12), the column of water is suspended from the meniscus, which is attached to the walls by hydrogen bonds. Thus the water is under **tension**, which is negative (i.e., less than atmospheric) pressure. In porous media of silt size and larger ($d \geq 0.002$ mm), pressure in the unsaturated zone is determined by the radius of curvature of menisci in the pore spaces. The relation between the radius of curvature and pressure can be developed from further consideration of the capillary-rise phenomenon.

In figure 7.12, the weight of the water suspended beneath the plane that is tangent to the lowest point of the meniscus is equal to F_d [equation (7.22)]. Since the area of that plane is $\pi \cdot r^2$, the pressure in the suspended water at that plane, p_m , is

$$p_m = -\frac{\gamma \cdot \pi \cdot r^2 \cdot h_{cr}}{\pi \cdot r^2} = -\gamma \cdot h_{cr}. \quad (7.24)$$

Substituting equation (7.23) into equation (7.24) gives

$$p_m = -\frac{2 \cdot \sigma \cdot \cos(\beta_c)}{r}. \quad (7.25)$$

Thus the pressure difference across a meniscus, like the height of capillary rise, is inversely proportional to the radius of curvature of the meniscus. In unsaturated soils of silt size or larger, this radius is determined by

(1) the pore (grain) size and (2) the pore water content (figure 7.13). For $r = 0.001$ mm (the lower boundary for silts), equation (7.25) gives a pressure of about -1.5 atmospheres. Tensions stronger than that can exist in clay soils, but are due to electrical forces between the water and the mineral grains and do not represent capillary forces alone (Gray and Hassanzadeh 1991). The moisture-characteristics curve discussed in section 7.4.3.2 is the empirical manifestation of the pressure-radius relation of equation (7.25).

Here we use “pressure head” to refer to both positive and negative values of ψ ; when ψ is negative,

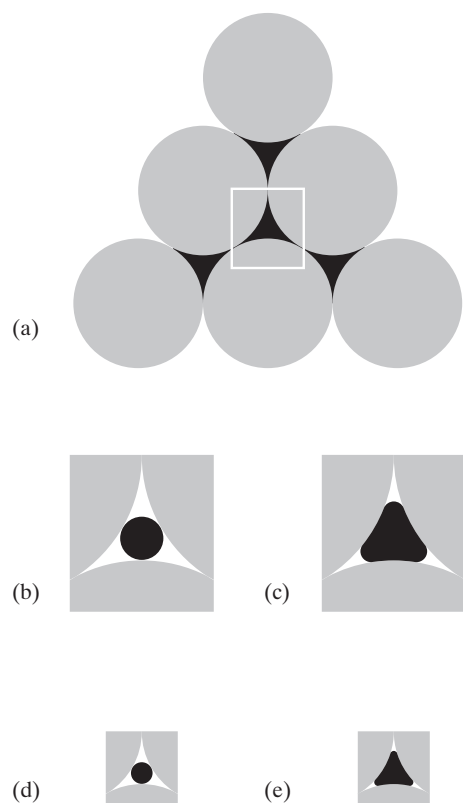


Figure 7.13 The pressure difference across a meniscus is inversely proportional to the radius of curvature of the meniscus. In unsaturated soils of silt size or larger, this radius is determined by the pore (grain) size and the pore water content. To illustrate this, we have modeled a pore space as a triangle (a); (b) shows a relatively coarse-grained soil with high water content; (c) is a relatively coarse-grained soil with low water content; (d) is a relatively fine-grained soil with high water content, and (e) is a relatively fine-grained soil with low water content.

$|\psi|$ is called **tension head** (also called **suction head** or **matric potential**).

7.4.2 Darcy's Law for Unsaturated Flow

Darcy's law in the form of equation (7.11) applies to both unsaturated and saturated porous-media flows. The major difference between porous-media flows in unsaturated and saturated media is that

In unsaturated flows both the pressure head ψ and the hydraulic conductivity K_h are functions of the local water content θ (alternatively expressed as effective saturation θ^*).

To reflect this, we write Darcy's law for unsaturated flow as

$$q_x = -K_{hx}(\theta) \cdot \frac{d[z + \psi(\theta)]}{dx}. \quad (7.26)$$

Both $K_{hx}(\theta)$ and $\psi(\theta)$ increase (algebraically) as θ increases. The quantitative relations between pressure and water content and between hydraulic conductivity and water content are crucial determinants of unsaturated flow in soils, and these are examined in more detail in the following sections.

7.4.3 Soil-Water Pressure

7.4.3.1 Measurement

Piezometers cannot be used to measure h in the unsaturated zone. Instead, the pressure head ψ of soil moisture under field conditions is measured by **tensiometers** (figure 7.14). These devices consist of a hollow metal tube, one end of which is closed off by a cup of porous ceramic material and the other end is fitted with a removable air-tight seal. A manometer, vacuum gauge, or pressure transducer is attached to the tube. The tube is inserted into the soil to the depth of measurement and filled with water. Since the water in the tube is initially at a pressure above atmospheric, there is a pressure-induced flow through the porous cup into the unsaturated soil that continues until the (negative) pressure inside the tube equilibrates and equals that in a roughly spherical region immediately surrounding the cup. The value of ψ is then read on the manometer or gauge and h is determined by adding that value to the elevation of the point, z . Box 7.4 shows how tensiometer readings are used to determine potential gradients in unsaturated soils.

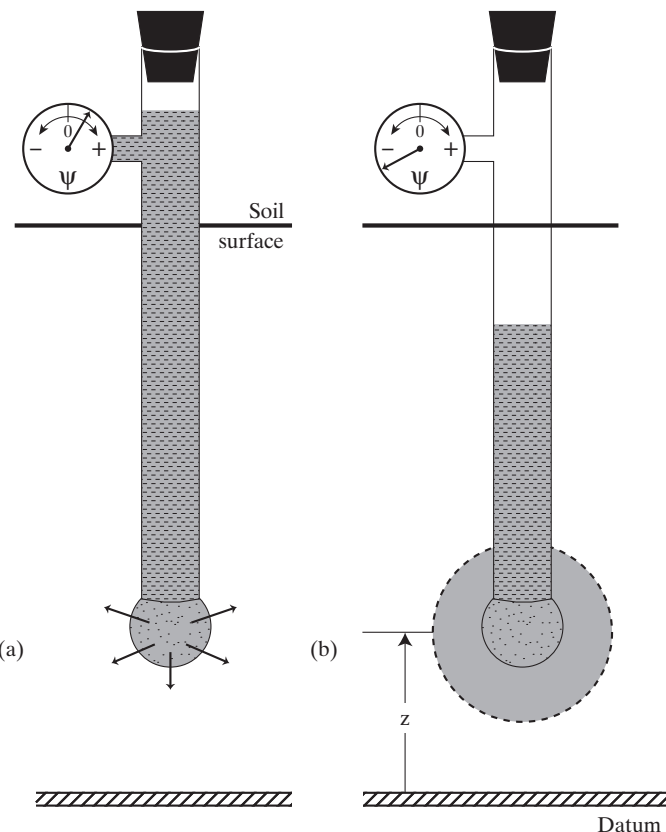


Figure 7.14 The pressure head ψ of soil moisture under field conditions is measured by tensiometers. (a) Pressure-induced flow enters the soil until the pressure inside the tube equilibrates with that in a region surrounding the cup. (b) The value of ψ is read on the manometer or gauge and h is determined by adding that value to the elevation of the point, z .

Box 7.4 Example Tensiometer Computations

Consider two adjacent tensiometers inserted into unsaturated soil to determine whether water flow is toward or away from the surface. The bulb of tensiometer A is installed at a depth of 20 cm; the bulb of tensiometer B is installed at a depth of 50 cm. The following

readings are obtained on days 1–5. Assuming that no maximum or minimum of tension occurs between the two sensor depths, which way is the water flowing in each condition?

Tensiometer Reading (cm)	Depth (cm)	Day 1	Day 2	Day 3	Day 4	Day 5
ψ_A	20	-93	-76	-151	-217	-71
ψ_B	50	-83	-71	-117	-173	-71

The value of h is determined by adding the elevation head at the depth of each measurement. If we take the elevation of the deeper tensiometer B as the datum,

$z_B = 0$ cm and $z_A = +30$ cm. The flow direction is from algebraically higher to lower h . Thus

Total Head (cm)	Depth (cm)	Day 1	Day 2	Day 3	Day 4	Day 5
h_A	20	-63	-46	-111	-187	-41
h_B	50	-83	-71	-117	-173	-71
Flow direction		down	down	down	up	down

The practical range of pressure measurable in a tensiometer is from 0 to -8 m (0 to -78 kPa), which covers only a small part of the range observed in nature (Hillel 1980a). However, this covers a large part of the range for coarser-grained soils, and tensiometers are often used in hydrologic field studies. They are often installed in clusters of two or three extending to different depths to provide information on vertical pressure gradients, with readings recorded continuously on a data logger (Walkotten 1972; Williams 1978; Cooper 1980; Robinson et al. 2008). Soil-water pressure is often determined by measuring water content (see box 7.2) and referring to the *moisture-characteristic curve* described in the following section.

7.4.3.2 Pressure–Water-Content Relations

The relation between pressure head, $|\psi|$, (often plotted on a logarithmic scale) and water content, θ , (or saturation, θ^*) for a given soil is its **moisture-characteristic curve**.

The relationship is highly nonlinear and typically has the form shown in figure 7.15. Note that the pressure head is zero (i.e., pressure is atmospheric) when the water content equals the porosity (saturation), and that the water content changes little as $|\psi|$ increases up to a point of inflection. This more-or-less distinct point represents the pressure head at which significant volumes of air begin to appear in the soil pores, and is called the **air-entry pressure** (or **tension**) **head** (also called **bubbling pressure**), ψ_{ae} .

The absolute value of the air-entry pressure head, $|\psi_{ae}|$, equals the height of the tension-saturated zone, or capillary fringe.

As $|\psi|$ increases beyond its air-entry value, the water content begins to decrease rapidly and then more gradually. At very high tensions the curve again becomes nearly vertical, reflecting a residual water content that is very tightly held in the soil pores by surface tension and electrochemical forces.

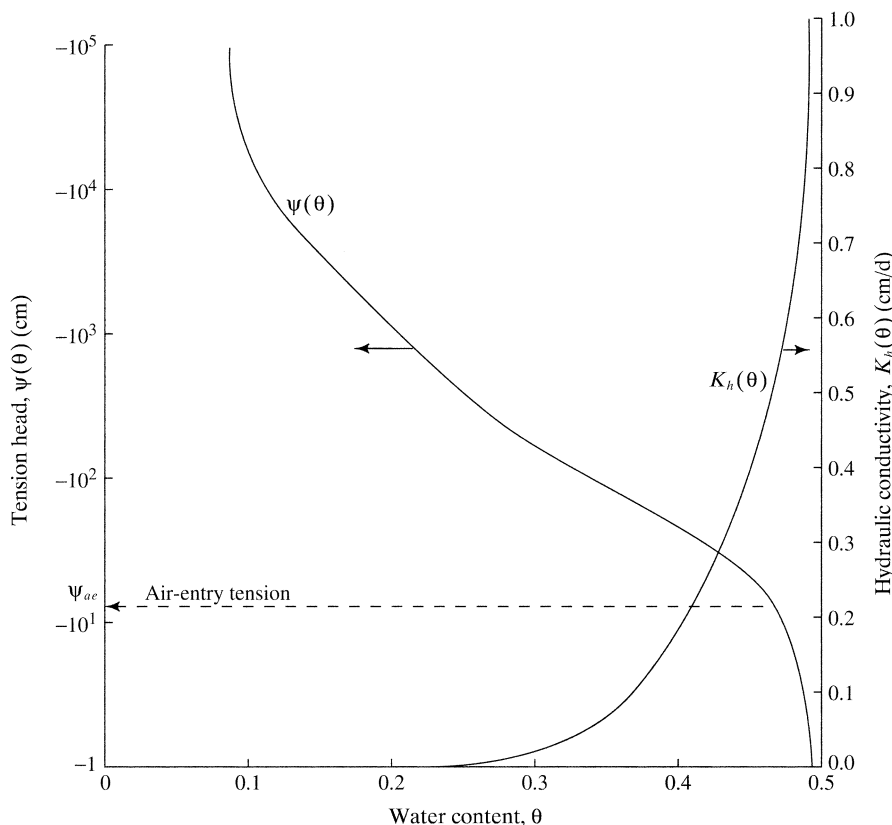


Figure 7.15 Typical forms of hydraulic relations $\psi(\theta)-\theta$ and $K_h(\theta)-\theta$ for unsaturated soils. For this soil, porosity $\phi = 0.5$.

The shape of moisture-characteristic curves is highly dependent on soil texture: figure 7.16 shows that, at a given degree of saturation, $|\psi|$ is much higher in finer-grained than in coarser-grained soils. In real soils $|\psi|$ is not a single-valued function of θ , but depends also on the soil's history of wetting and drying (figure 7.17). While this **hysteresis** can have a significant influence on soil-moisture movement (Rubin 1967; Perrens and Watson 1977), it is difficult to model mathematically and is therefore not commonly incorporated in hydrologic models.

7.4.4 Unsaturated Hydraulic Conductivity

Hydraulic conductivity is the rate (volume per unit time per unit area) at which water moves through a porous medium under a unit potential-energy gradient ($dh/dx = 1$). Under saturated conditions this rate is determined by the cross-sectional area of the pathways available for water transmission, which is proportional to d^2 [equation (7.14)]. For unsaturated flows this area is determined by both grain size and the degree of saturation (figure 7.13).

In discussing unsaturated flows we use the symbol K_h to denote the saturated hydraulic conductivity.

7.4.4.1 Measurement

Hillel (1980a) and Stephens (1995) described various approaches to field and laboratory measurement

of unsaturated hydraulic conductivity. One such approach involves measurement of water content at several depths as the soil drains for extended periods following irrigation, with evaporation prevented. The flux of water and the vertical water-content gradients can be determined from these measurements, and the hydraulic conductivity calculated by substituting the measured values into Darcy's law (Khosla 1980). The infiltrometer measurements described in chapter 8 can also be used to estimate saturated hydraulic conductivity (Scotter et al. 1982; Elrick et al. 1990; Moret et al. 2004; Cheng et al. 2011).

Mualem (1976) derived a method for calculating $K_h(\theta)$ based on the moisture-characteristic curve and the value of K_h , which can be measured using various laboratory and field techniques.

7.4.4.2 Hydraulic Conductivity–Water Content Relations

The relation between hydraulic conductivity, $K_h(\theta)$, (often plotted on a logarithmic scale) and water content, θ , (or saturation, θ^*) for a given soil is its **moisture-conductivity curve**.

For a typical soil, unsaturated hydraulic conductivity is very low at low to moderate water contents;

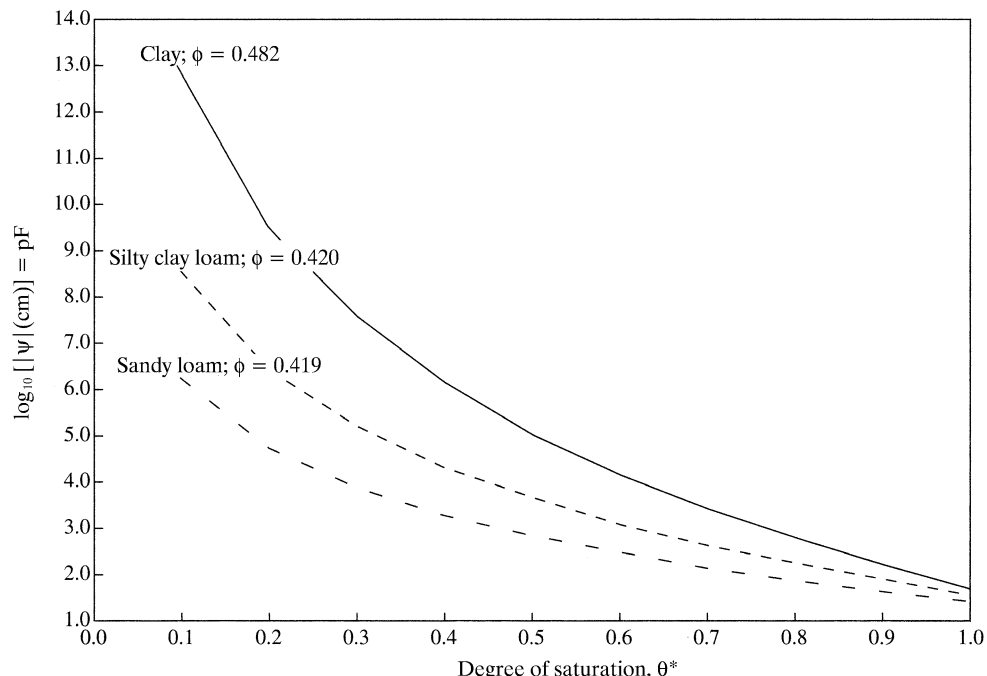


Figure 7.16 Soil-water pressure (tension), $|\psi|$, versus degree of saturation, θ^* , for soils of three different textures. Note that the vertical axis gives the base-10 logarithm of the tension expressed in cm of water (pF). Curves are based on typical values given by Clapp and Hornberger (1978).

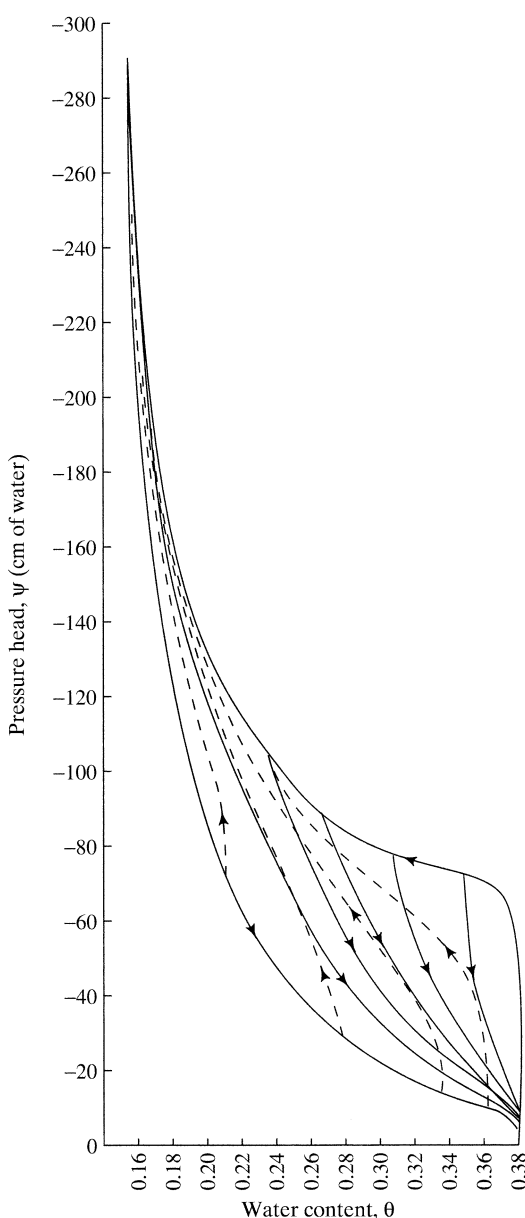


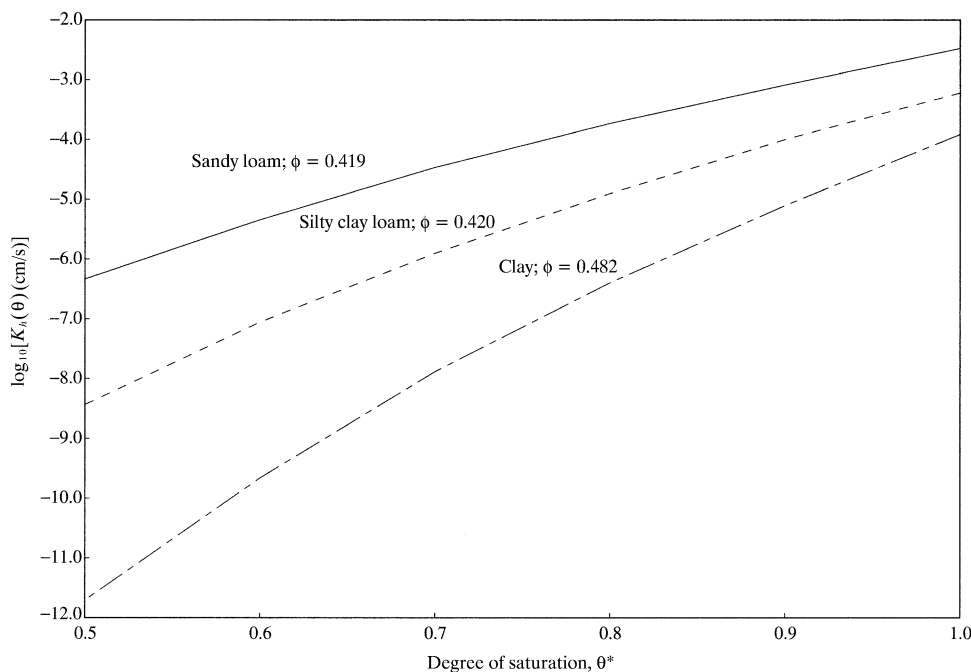
Figure 7.17 Hysteresis in the $\psi(\theta)$ - θ relation for Rubicon sandy loam. The paths with arrows trace the relation as the soil undergoes successive cycles of wetting (arrows pointing to right) and drying (arrows pointing to left) [Perrens and Watson (1977)]. Numerical analysis of two-dimensional infiltration and redistribution. *Water Resources Research* 13:781–790, with permission of the American Geophysical Union].

it increases nonlinearly to its saturated value as water content increases to saturation (figure 7.15). A comparison of $K_h(\theta^*)$ relations for soils of different textures is shown in figure 7.18; the form of these curves differs from that in figure 7.15 because here the $K_h(\theta^*)$ scale is logarithmic. Note that, for a given θ^* , $K_h(\theta^*)$ increases by several orders of magnitude in going from clay to silty clay loam to sandy loam; and that, for a given soil, $K_h(\theta^*)$ increases by several orders of magnitude over the range of θ^* values. The hysteresis effect in the $K_h(\theta)$ relation is less marked than in the $\psi(\theta)$ relation and is usually neglected.

7.4.5 Analytic Approximation of $\psi(\theta)$ and $K_h(\theta)$ Relations

$\psi(\theta)$ and $K_h(\theta)$ relations control all the near-surface hydrologic processes shown in figure 7.1: infiltration, redistribution, surface runoff, water available for plants, and ground-water recharge. These relations are unique for each soil, and are difficult and time-consuming to measure. Thus to simulate the dynamics of water movement in the unsaturated zone that control watershed responses to rain and snowmelt, the $\psi(\theta)$ and $K_h(\theta)$ relations are (1) modeled in analytical form and (2) related to soil texture and other properties.

Analytical approximations of $\psi(\theta)$ and $K_h(\theta)$ relations have been proposed by Brooks and Corey (1964), Campbell (1974), and van Genuchten (1980); these are summarized in table 7.2 on p. 336. Note that all these models are single-valued functions that ignore hysteresis. The van Genuchten model is the most widely used; note that it models the complete moisture-characteristic curve except for the point corresponding to $\theta_{vG}^* = 1$, for which $\psi = 0$. In contrast, the Brooks–Corey and Campbell equations apply for $|\psi| > |\psi_{ae}|$; the values at $|\psi_{ae}|$ are represented by vertical lines extending from 0 to $|\psi_{ae}|$. In the van Genuchten model, the parameters θ_{vG} and α should be viewed as “fitting parameters” whose values are chosen so that the modeled curves provide a best fit to measured values: θ_{vG}^* is typically somewhat less than the actual porosity ϕ , reflecting the fact that field soils typically do not reach full saturation due to air entrapped in pores; α may approximate but does not equal the inverse of the air-entry tension, $1/\psi_{ae}$. Figure 7.19 on p. 336 shows the fit of the Brooks–Corey and van Genuchten models to the measurements of the moisture-characteristic relation for a sand soil.

**Figure 7.18**

Hydraulic conductivity, K_h , versus degree of saturation, θ^* , for soils of three different textures. Note that the vertical axis gives the base-10 logarithm of the hydraulic conductivity expressed in cm/s. Curves are based on typical values given by Clapp and Hornberger (1978).

7.4.6 $\psi(\theta)$ and $K_h(\theta)$ Relations and Soil Texture

The parameters of the models in table 7.2 (b , n , K_h , a , θ_r , θ_{vG}^* , ϕ , ϕ_{vG} , ψ_{ae}) depend primarily on the soil grain-size distribution (texture), but also on organic content, chemistry, and other factors (Clapp and Hornberger 1978; Cosby et al. 1984; Mishra et al. 1989; Rawls et al. 1992; Wösten et al. 2001). There are two basic approaches used to relate model parameters to texture:

- Pedotransfer functions (PTFs)** are continuous functions that relate soil-hydraulic parameters to measured soil properties such as bulk density and the proportions of clay, silt, sand, and organic matter (carbon). The functions are established by regression-type analyses of large data sets.
- Soil-hydraulic classes** are discontinuous categories, each with a characteristic suite of soil-hydraulic parameters. The categories are determined by the proportions of clay, silt, and sand, as in the soil-texture triangle.

Table 7.3 on p. 337 gives an example of PTFs for the van Genuchten parameters; others can be found in Rawls et al. (1992), Wösten et al. (2001), and Loosvelt et al. (2011). PTFs can be “mapped” on the soil-texture triangle, as shown in figure 7.20 on p.

337. Wösten et al. (2001) extensively reviewed the derivation and application of PTFs and concluded that, although significant variability and uncertainty in some of the relationships must be recognized, they are a “powerful tool” for predicting soil-hydraulic properties.

Table 7.4 on p. 338 gives the Brooks–Corey and Campbell parameters for various soil textures (figure 7.5). The most recent exploration of soil-hydraulic classes was by Twarakavi et al. (2010) using the van Genuchten model. They estimated the parameters (n , K_h , a , θ_r , and ϕ_{vG}) as functions of fraction of sand, silt, and clay, then used objective methods to determine the optimal number of soil-hydraulic classes for estimating the suite of values. These turned out to be the 12 classes shown on the **soil-hydraulic triangle** of figure 7.21 on p. 338: Sand-dominated soils are represented by the letter A, with a number that increases (from 1 to 4) as the sand fraction decreases; silt-dominated soils are represented by “B”; and clay-dominated soils by “C”, also with numbers ranging from 1 to 4. Interestingly, the optimal soil-hydraulic classification is very similar to the soil-texture classification, especially for soils in which the sand fraction is dominant; the similarities between the soil-texture triangle and the soil-hydraulic triangle are less pronounced for finer soils, where capillary forces have a greater impact on the wa-

Table 7.2 Analytic Approximations of $\psi(\theta)$ and $K_h(\theta)$ Relations.

Moisture Characteristic	Moisture Conductivity
$ \psi(\theta^*) = \psi_{ae} \cdot \left(\frac{1}{\theta^*} \right)^b, \quad \theta^* < 1;$ $ \psi(\theta^*) = \psi_{ae} , \theta^* = 1.$	Brooks and Corey (1964) $K_h(\theta) = \theta^{*2-b+3} \cdot K_h$
$ \psi(\theta) = \psi_{ae} \cdot \left(\frac{\phi}{\theta} \right)^b, \quad \theta^* < 1;$ $ \psi(\theta^*) = \psi_{ae} , \theta^* = 1.$	Campbell (1974) $K_h(\theta) = \left(\frac{\theta}{\phi} \right)^{2-b+3} \cdot K_h$
$ \psi(\theta^*_{VG}) = \left(\frac{1}{\alpha} \right) \cdot \left[\theta^{*(n-1)/n} - 1 \right]^{1/n}, \quad \theta^*_{VG} < 1;$ $ \psi(\theta^*_{VG}) = 0, \theta^*_{VG} = 1.$	van Genuchten (1980) $K_h(\theta) = \theta^{*1/2} \cdot \left\{ 1 - \left[1 - \theta_{VG}^{n/(n-1)} \right]^{(n-1)/n} \right\}^2 \cdot K_h$

Symbols

b ≡ parameter that depends on pore-size distribution [1]	θ^*_{VG} ≡ van Genuchten saturation parameter [1] ≡ $\frac{\theta - \theta_r}{\phi_{VG} - \theta_r}$
K_h ≡ saturated hydraulic conductivity [$L T^{-1}$]	ϕ ≡ porosity [1]
n ≡ parameter that depends on pore-size distribution [1]	ϕ_{VG} ≡ van Genuchten porosity parameter [1]
α ≡ van Genuchten pressure-head parameter [L^{-1}]	ψ ≡ pressure head [L]
θ ≡ volumetric water content [1]	ψ_{ae} ≡ air-entry pressure head [L]
θ_r ≡ residual water content [1]	
θ^* ≡ degree of saturation [1] ≡ $\frac{\theta - \theta_r}{\phi - \theta_r}$	

Source: Modified after Rawls et al. (1992).

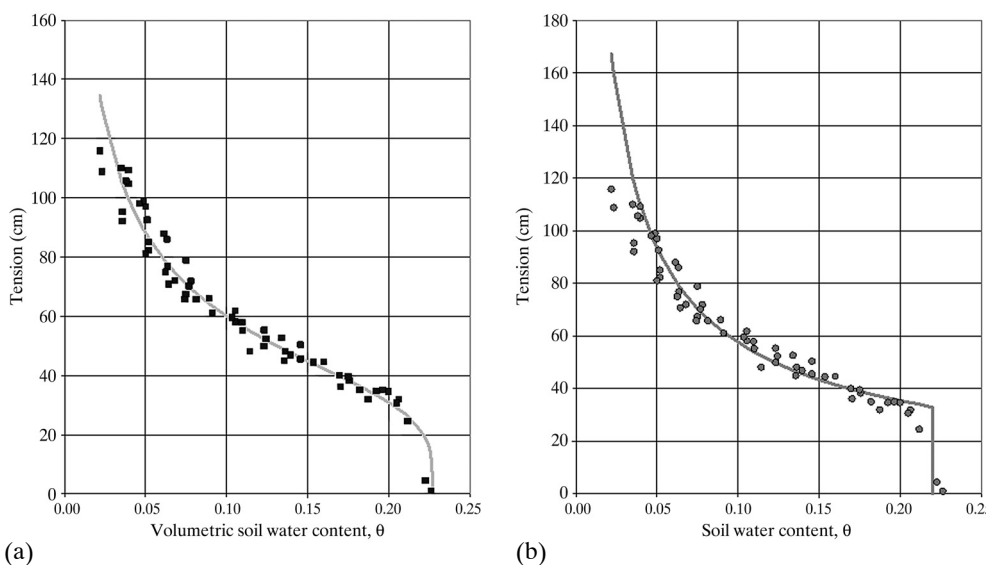


Figure 7.19 Fit of the (a) van Genuchten and (b) Brooks–Corey models (table 7.2) to measurements of the moisture-characteristic relation for a sand soil (plots courtesy of R. H. Cuenca, Oregon State University).

Table 7.3 Example of Pedotransfer Functions for Modeling Soil Hydraulic Behavior via the van Genuchten Model (Table 7.2).

$$\theta_r = 0.015 + 0.005 \cdot CLAY + 0.014 \cdot C$$

$$\phi_{vG} = 0.810 - 0.283 \cdot \rho_b + 0.001 \cdot CLAY$$

$$\alpha = \exp(-2.486 + 0.025 \cdot SAND - 0.352 \cdot C - 2.617 \cdot \rho_b - 0.023 \cdot CLAY)$$

$$n = \exp(0.053 - 0.009 \cdot SAND - 0.013 \cdot CLAY + 0.00015 \cdot SAND^2)$$

$$K_h = 1.1574 \times 10^{-5} - \exp[20.62 - 0.96 \cdot \ln(CLAY) - 0.66 \cdot \ln(SAND) - 0.046 \cdot \ln(C) - 8.43 \cdot \rho_b]$$

Symbols

C = organic carbon content (%)

$CLAY$ = clay fraction (%)

K_h = saturated hydraulic conductivity (cm/s)

n = van Genuchten exponent

$SAND$ = sand fraction (%)

α = van Genuchten pressure-head parameter (cm^{-1})

ρ_b = bulk density (g/cm^3)

ϕ_{vG} = van Genuchten porosity parameter

Source: Loosvelt et al. (2011).

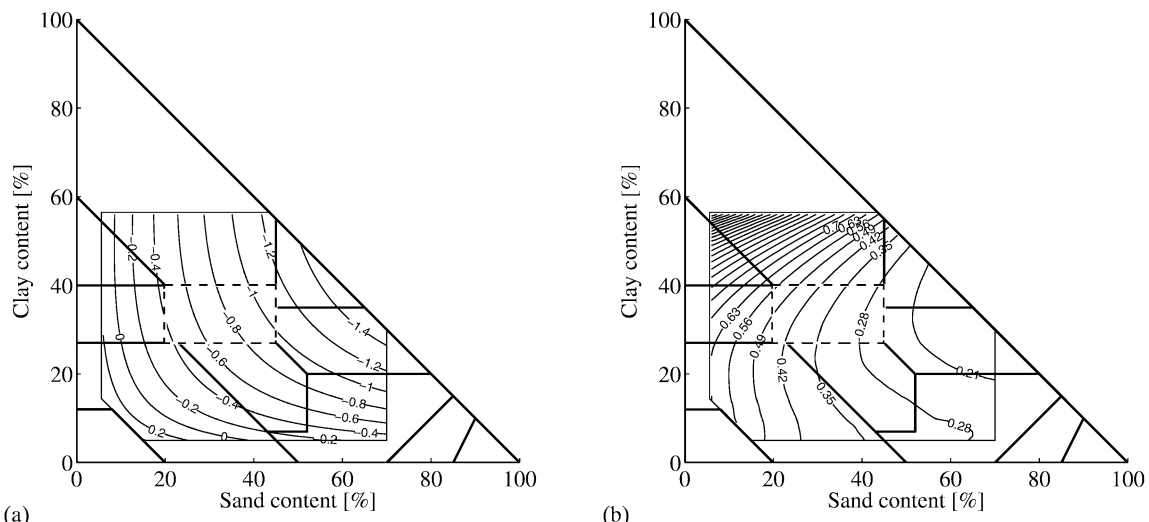


Figure 7.20 (a) Contour plot of the logarithm (\log_{10}) of the saturated hydraulic conductivity K_h predicted with a PTF. (b) Contour plot of the bubbling pressure $|\psi_{ae}|$ predicted with a PTF. The clay loam soil class is highlighted with a dashed line [Loosvelt et al. (2011)]. Impact of soil hydraulic parameter uncertainty on soil moisture modeling. *Water Resources Research* 47, with permission of the American Geophysical Union].

Table 7.4 Brooks–Corey and Campbell Parameters (Table 7.2) for Various Soil Textures Based on Analysis of 1845 Soils.^a

Soil Texture	ϕ	K_h (cm/s)	$ \psi_{aef} $ (cm)	b
Sand	0.395 (0.056)	1.76×10^{-2}	12.1 (14.3)	4.05 (1.78)
Loamy sand	0.410 (0.068)	1.56×10^{-2}	9.0 (12.4)	4.38 (1.47)
Sandy loam	0.435 (0.086)	3.47×10^{-3}	21.8 (31.0)	4.90 (1.75)
Silt loam	0.485 (0.059)	7.20×10^{-4}	78.6 (51.2)	5.30 (1.96)
Loam	0.451 (0.078)	6.95×10^{-4}	47.8 (51.2)	5.39 (1.87)
Sandy clay loam	0.420 (0.059)	6.30×10^{-4}	29.9 (37.8)	7.12 (2.43)
Silty clay loam	0.477 (0.057)	1.70×10^{-4}	35.6 (37.8)	7.75 (2.77)
Clay loam	0.476 (0.053)	2.45×10^{-4}	63.0 (51.0)	8.52 (3.44)
Sandy clay	0.426 (0.057)	2.17×10^{-4}	15.3 (17.3)	10.4 (1.64)
Silty clay	0.492 (0.064)	1.03×10^{-4}	49.0 (62.1)	10.4 (4.45)
Clay	0.482 (0.050)	1.28×10^{-4}	40.5 (39.7)	11.4 (3.70)

^aValues in parentheses are standard deviations.

Source: Data from Clapp and Hornberger (1978).

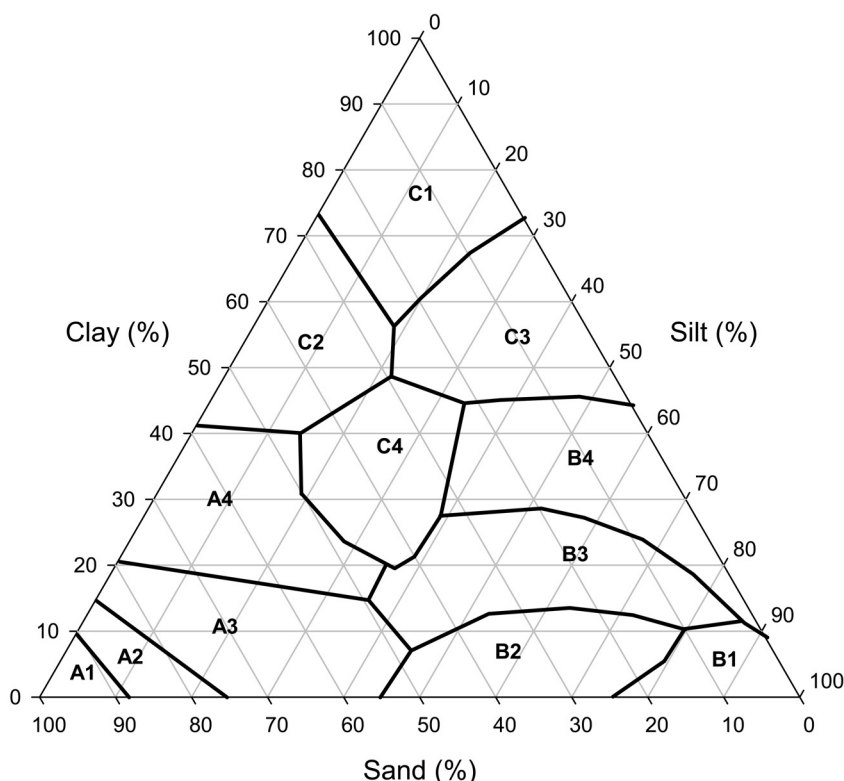


Figure 7.21 Soil hydraulic classes of Twarakavi et al. (2010) plotted on the soil-texture triangle [Twarakavi et al. (2010). Can texture-based classification optimally classify soils with respect to soil hydraulics? *Water Resources Research* 46, with permission of the American Geophysical Union].

ter flow. The average values and standard deviations of the van Genuchten parameters for each soil-hydraulic class are given in table 7.5. The relative uncertainty in these relations, reflected in the standard deviations, is quite large, especially for saturated hydraulic conductivity. This uncertainty is due to variations in the exact grain-size distributions, grain shape, organic content, wetting history (hysteresis), and other factors. An example of the use of the soil-hydraulic relations is provided in box 7.5 and figure 7.22 (on p. 341).

Data sets of worldwide soil texture, water-holding capacities, and other properties are available in Zobler (1986), Webb et al. (2000), and at the Distributed Active Archive Center (DAAC) for Biogeochemical Dynamics' website (<http://ftp.daac.ornl.gov/SOILS/guides/igbp-surfaces.html>).

7.4.7 General Unsaturated-Flow Equation

The general equation for unsaturated flow is derived by combining the conservation-of-mass relation with Darcy's law, as for saturated flow in box 7.3. If we assume constant fluid density, the storage coefficient defined in equation (7B3.5) is due to a change in water content in the control volume in response to a change in head, rather than to the compressibility of the medium or fluid; i.e.,

$$S_s = \frac{\partial \theta}{\partial h}. \quad (7.27)$$

Note that the dimensions of S_s remain $[L^{-1}]$. Substituting (7.27) into (7B3.6),

$$\frac{\partial q_x}{\partial x} + \frac{\partial q_y}{\partial y} + \frac{\partial q_z}{\partial z} = -\frac{\partial \theta}{\partial h} \cdot \frac{\partial h}{\partial t} = -\frac{\partial \theta}{\partial t}. \quad (7.28)$$

Now substituting Darcy's law for unsaturated flow [equation (7.26)] for each of the coordinate directions into (7.28), and assuming that (1) the z -direction is oriented vertically³ and (2) the $K_h(\theta)$ relation is isotropic, yields the general equation:

$$\begin{aligned} & \frac{\partial}{\partial x} \left[K_h(\theta) \cdot \frac{\partial \psi(\theta)}{\partial x} \right] + \frac{\partial}{\partial y} \left[K_h(\theta) \cdot \frac{\partial \psi(\theta)}{\partial y} \right] \\ & + \frac{\partial}{\partial z} \left[K_h(\theta) \cdot \left(\frac{\partial \psi(\theta)}{\partial z} + 1 \right) \right] = \frac{\partial \theta}{\partial t}. \end{aligned} \quad (7.29)$$

Equation (7.29) was first derived by Richards (1931), and is known as the **Richards equation**.

In principle, solutions to the Richards equation are found by specifying boundary conditions and the $K_h(\theta)$ and $\psi(\theta)$ relations and using numerical methods, as for the general saturated-flow equation. In (7.29), the solutions would be values of $\psi(x,y,z)$ and require specification of the $\psi(\theta)$ and $K_h(\theta)$ relations as discussed in sections 7.4.5 and 7.4.6; total heads would be found as $h(x,y,z) = \psi(x,y,z) + z$.

There have been some attempts to combine the general saturated and unsaturated flow equations and solve them together numerically to simulate subsurface flow in fairly simple two- or three-dimensional boundary-value problems (e.g., Freeze 1971; Weill et al. 2009). However, the Richards equation is mostly applied for *vertical downward flow* as a starting point for quantifying infiltration and redistribution in the unsaturated zone. To do this, we write the last term on the left side in the form

$$-\frac{\partial K_h(\theta)}{\partial z'} - \frac{\partial}{\partial z'} \left[K_h(\theta) \cdot \left(\frac{\partial \psi(\theta)}{\partial z'} \right) \right] = \frac{\partial \theta}{\partial t}, \quad (7.30)$$

where z' is the vertical *downward* direction, i.e., $z' \equiv -z$ and $\partial z/\partial z' = -1$. Because it is nonlinear, there is no closed-form analytical solution to (7.30) except for highly simplified $\psi(\theta)$ and $K_h(\theta)$ relations and boundary conditions. However, the equation can be used as a basis for numerical modeling by specifying appropriate boundary and initial conditions, dividing the soil into thin layers, and applying the equation to each layer sequentially at small increments of time. Tests have shown good agreement between the predictions of the numerically solved Richards equation and field and laboratory measurements (Nielsen et al. 1961; Whisler and Bouwer 1970). Šimůnek and van Genuchten (2009) described a flexible numerical model for solving the Richards equation in a variety of applications. Various approaches to developing approximate analytical solutions to the Richards equation that can be applied to infiltration (Wang and Dooge 1994) will be examined in chapter 8.

Table 7.5 Average Values of Parameters for Modeling Soil Hydraulic Behavior via the van Genuchten Model (Table 7.2).^a

Soil Hydraulic Class^b	θ_r	ϕ_{vG}	$\log_{10}[\alpha (\text{cm}^{-1})]$	$\log_{10}(n)$	$\log_{10}[K_h(\text{cm/day})]$
A1	0.055 (0.002)	0.374 (0.008)	-1.479 (0.036)	0.511 (0.060)	2.853 (0.544)
A2	0.053 (0.002)	0.386 (0.007)	-1.474 (0.076)	0.276 (0.055)	2.093 (0.696)
A3	0.051 (0.002)	0.382 (0.010)	-1.540 (0.176)	0.171 (0.015)	1.641 (0.659)
A4	0.055 (0.003)	0.387 (0.009)	-1.672 (0.183)	0.140 (0.019)	1.242 (0.764)
B1	0.057 (0.011)	0.487 (0.031)	-2.034 (0.045)	0.208 (0.009)	1.641 (0.273)
B2	0.053 (0.003)	0.425 (0.030)	-2.278 (0.124)	0.206 (0.024)	1.714 (0.594)
B3	0.056 (0.007)	0.413 (0.026)	-2.234 (0.193)	0.186 (0.021)	1.197 (0.757)
B4	0.072 (0.015)	0.470 (0.026)	-2.016 (0.141)	0.160 (0.024)	1.115 (0.875)
C1	0.072 (0.012)	0.475 (0.013)	-1.940 (0.070)	0.135 (0.010)	1.206 (0.110)
C2	0.091 (0.013)	0.436 (0.025)	-1.444 (0.174)	0.106 (0.008)	1.263 (0.649)
C3	0.069 (0.016)	0.500 (0.037)	-1.888 (0.057)	0.124 (0.010)	1.324 (0.972)
C4	0.064 (0.005)	0.421 (0.012)	-1.830 (0.068)	0.137 (0.017)	0.642 (1.090)

^aValues in parentheses are standard deviations.^bSoil hydraulic classes determined from figure 7.21.

Source: Twarakavi et al. (2010).

Box 7.5 Example of Use of Analytical Soil-Hydraulic Functions

Here we show how the van Genuchten equations (table 7.2) and the soil-hydraulic triangle (figure 7.21) are used to estimate the moisture-characteristic and hydraulic-conductivity characteristic curves for the soil described in box 7.1.

The porosity of this soil was measured at $\phi = 0.419$. The sand fraction = 53%, silt fraction = 44%, and clay fraction = 3%. From figure 7.21 we see that this soil falls into hydraulic class A3, but is close to the boundary

between A3 and B2. Given the uncertainty in the texture-hydraulic parameter relations, it is instructive to compare the moisture- and conductivity-characteristic curves for both those classes. We do this by calculating three curves for each class, one using the average values, one using the average values plus one standard deviation (denoted by $+1 \cdot \sigma$), and one using average values minus one standard deviation ($-1 \cdot \sigma$).

Class A3	θ_r	ϕ_{vG}	$\log(\alpha)$	$ \alpha (\text{cm})$	$\log n$	n	$\log(K_h)$	$K_h (\text{cm/day})$
$+1 \cdot \sigma$	0.053	0.392	1.716	52.000	0.186	1.535	2.300	199.526
average	0.051	0.382	1.540	34.674	0.171	1.483	1.641	43.752
$-1 \cdot \sigma$	0.049	0.372	1.364	23.121	0.156	1.432	0.982	9.594

Class B2	θ_r	ϕ_{vG}	$\log(\alpha)$	$ \alpha (\text{cm})$	$\log n$	n	$\log(K_h)$	$K_h (\text{cm/day})$
$+1 \cdot \sigma$	0.056	0.455	2.402	252.348	0.230	1.698	2.308	203.236
average	0.053	0.425	2.278	189.671	0.206	1.607	1.714	51.761
$-1 \cdot \sigma$	0.050	0.395	2.154	142.561	0.182	1.521	1.120	13.183

The curves are plotted in figure 7.22. Note that for each soil type there is a wide spread for the three curves reflecting plus and minus one standard deviation, and a very large difference between the curves for the two soil

types, especially for the moisture-characteristic curves. Clearly there is much uncertainty inherent in estimating soil-hydraulic relations from texture.

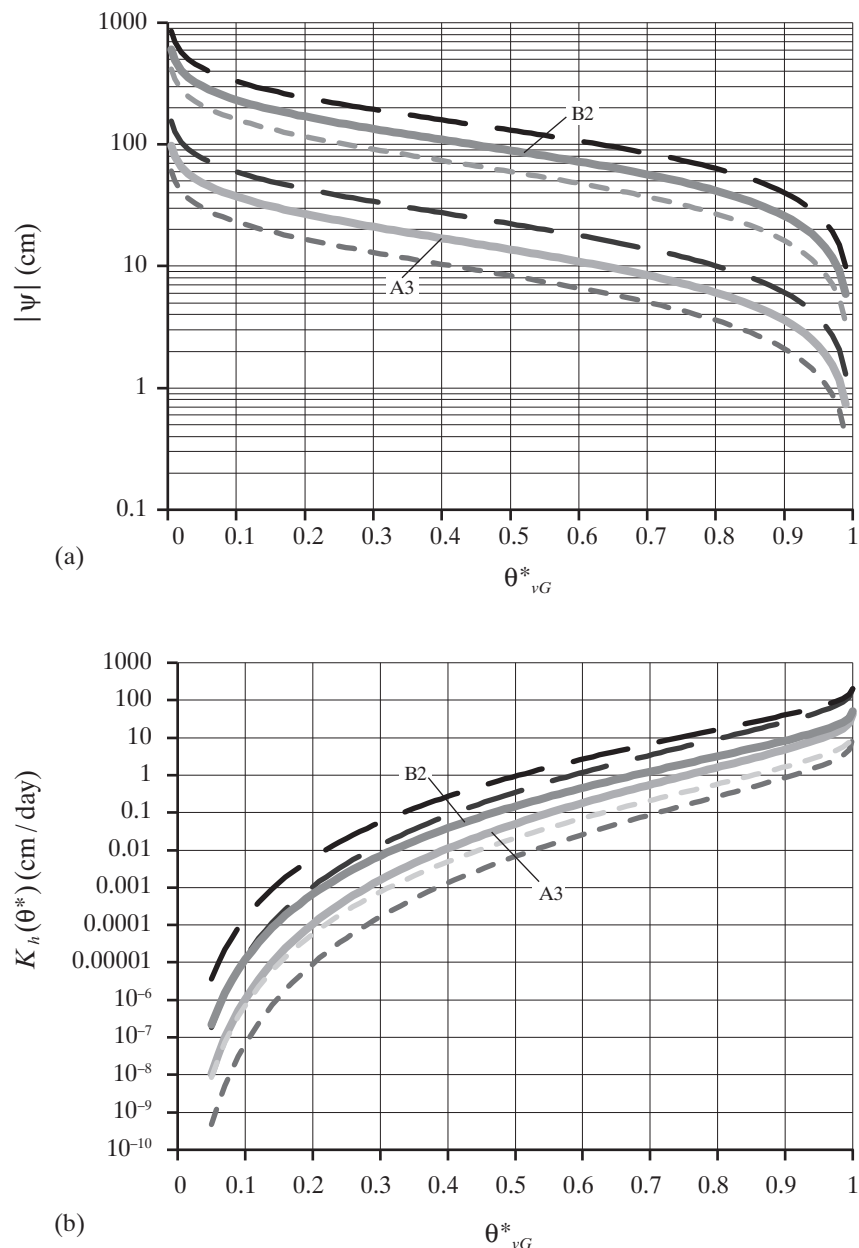


Figure 7.22 Estimated soil-hydraulic curves for example in box 7.5. (a) $|\psi|$ versus θ^* for soil-hydraulic classes A3 and B2. (b) K_h versus θ^* for soil-hydraulic classes A3 and B2. Dashed lines show curves for ± 1 standard deviation values.

▼ EXERCISES

1. Plot the grain-size distributions for the following soils, then determine the texture classes for each soil.

Soil	Percent by Weight Finer Than Indicated Diameter (mm)									
	50	19	9.5	4.76	2.00	0.420	0.074	0.020	0.005	0.002
1.1	100	100	100	100	100	100	97	79	45	16
1.2	100	100	98	94	70	19	15	8	3	2
1.3	93	91	88	85	69	44	40	27	13	6
1.4	100	100	100	100	100	97	92	75	47	31

2. Field and oven-dry weights of four soil samples taken with a 10-cm-long by 5-cm-diameter cylindrical tube are given in the following table. Assuming $\rho_m = 2,650 \text{ kg/m}^3$, calculate the field water contents and degrees of saturation and the bulk densities and porosities of these soils.

Soil	Field Weight (g)	Oven-Dry Weight (g)
2.1	302.5	264.8
2.2	376.3	308.0
2.3	422.6	388.6
2.4	468.3	441.7

3. Consider two adjacent tensiometers inserted into unsaturated sandy-loam soil to determine whether water flow is toward or away from the surface. Tensiometer A is placed at a depth of 20 cm; tensiometer B at 60 cm. The following readings are obtained at different times. Which way is the water flowing at each time (assuming that no maximum or minimum of tension exists between the two levels)?

Time →	1	2	3	4	5
ψ at A (cm)	123	106	9	211	20
ψ at B (cm)	22	51	65	185	6

4. Use the Brooks and Corey relations of table 7.2 and table 7.4 to estimate the $|\psi|-\theta$ and $K_h-\theta$ relations for the soils in exercise 7.1. Plot these relations.
5. Access a soils map of your area. In the United States, soils maps are published for each county in soil-survey reports that are available online from the NRCS of the USDA (<http://www.nrcs.usda.gov/wps/portal/nrcs/surveystatus/soils/survey/state/?state>).

Data sets of worldwide soil texture, water-holding capacities, and other properties are available in Zobler (1986), Webb et al. (2000), and at the DAAC's website (<http://ftp.daac.ornl.gov/SOILS/guides/igbp-surfaces.html>).

Read the descriptions of typical soil profiles and identify information about hydrologically critical properties in your region, such as porosity, hydraulic conductivity, depth to water table, presence of impermeable layers, etc.

6. Using the map(s) identified in exercise 7.5, locate one or more suitable areas in which to excavate a pit to observe soil profiles and properties. (Be sure you have the landowner's permission before entering an area and digging a pit!) Identify soil horizons (see sections 2.3.1.2 and 8.1.4) and take samples to measure or estimate grain size, bulk density, and water content.
7. Figure 7.8 shows a Darcy tube, the experimental device that can be used to measure the hydraulic conductivity, K_h , of a porous material. Below are the results of experiments for measuring K_h of glass beads of uniform diameter, d . For all experiments, the diameter of the

Darcy tube is 6.0 cm, the spacing between the piezometer openings 1 and 2 is $dz = 45.5$ cm, and the tube is horizontal, with $z_1 = z_2 = 7.0$ cm. The kinematic viscosity $\nu = 0.0179$ cm/s².

Four experiments are run, using two flow rates for each bead size; h_1 and h_2 are measured for each experiment after the levels have stabilized at a given flow rate:

Experiment	d (mm)	Q (cm ³ /s)	h_1 (cm)	h_2 (cm)
1A	1.5	3.30	27.2	14.8
1B	1.5	0.50	23.0	21.4
2A	0.75	3.30	37.8	19.1
2B	0.75	0.50	22.8	19.0

- Compute the elevation head and pressure head at each piezometer in each experiment.
- Compute the Reynolds numbers for each experiment to determine whether the flows are in the range for which Darcy's law is valid (section 7.3.2).
- Calculate the hydraulic conductivity for all experiments. Are there consistent values for each material? How do the values compare with those given for medium to coarse sand in figure 7.9?

▼ NOTES

¹ From the Latin word *vados*, meaning “shallow.”

² Wang and Anderson (1982) provided an excellent introduction to the two approaches for finding numerical solutions to the ground-water flow equation: the finite-difference approach and the finite-element method.

³ $\partial x/\partial z = 0$; $\partial y/\partial z = 0$; $\partial z/\partial z = 1$.



8

Infiltration and Water Movement in Soils

This chapter applies the principles of unsaturated porous-media flow (section 7.4) to the processes of **infiltration**, which is the movement of water from the soil surface into the soil, and **percolation**, which is a general term for downward flow in the unsaturated zone. Understanding these linked processes is an essential basis for forecasting and predicting hydrologic response to rain or snowmelt events: Water that does not infiltrate typically moves relatively quickly as *overland flow* toward a stream channel and contributes to short-term stream response, perhaps causing soil erosion and flooding. In contrast, infiltrated water either (1) moves, usually much more slowly, to the surface-water system via underground paths, (2) is retained in the soil and ultimately evapotranspired, or (3) becomes ground-water recharge. Crucial aspects of water-resource management require understanding of these processes, including developing strategies for crop irrigation and the movement of contaminants to ground and surface waters.

Other aspects of the redistribution of water in the unsaturated zone (see figure 7.1) are discussed elsewhere: exfiltration (soil evaporation) (chapter 6), uptake by plant roots (transpiration) (chapter 6),

ground-water recharge (chapter 9), and interflow (chapter 10).

8.1 Water Conditions in Soils

8.1.1 Field Capacity

If a soil is saturated and then allowed to drain without being subject to evapotranspiration, its water content will decrease indefinitely in a quasi-exponential manner, following Darcy's law [equation (7.26)], which can be written for vertical downward unsaturated flow as

$$q_z' = K_h(\theta) - K_h(\theta) \cdot \frac{d\psi(\theta)}{dz'}, \quad (8.1)$$

where z' is the vertical down-directed coordinate, q_z' is the vertical downward flow rate, $K_h(\theta)$ is the hydraulic conductivity, θ is the water content, and $\psi(\theta)$ is the pressure head. An example of gravity drainage is shown in figure 8.1: Note that the water content is still decreasing after 156 days of drainage, although the drainage rate also declines quasi-exponentially and becomes negligible within at most a few days.

Thus although gravity drainage is an indefinitely continuing process, it has proven useful to define a soil's *field capacity*:

Field capacity, θ_{fc} , is the water-content at which the gravity-drainage rate becomes "negligible."

The field capacity is thus a measure of the water content that can be held against the force of gravity; when water content reaches this point, downward movement essentially ceases, and water content can only be further reduced by evapotranspiration. Note that from (8.1), when $q'_z = 0$,

$$\frac{d\psi(\theta)}{dz'} = 1, \quad (8.2)$$

i.e., the vertical pressure gradient balances the unit downward gravitational gradient, dz/dz' .

Because gravity drainage in real soils continues indefinitely, it is impractical to define field capacity as the water content when $q'_z = 0$, and various operational definitions of field capacity have been proposed: (1) the water content remaining after a specified number of days of drainage (typically three days for sandy soils and six or more days for finer-grained soils); (2) the water content corresponding to a specific tension (commonly $\psi = -33 \text{ kPa} = -340 \text{ cm}$); or (3) the water content corresponding to a specific small drainage rate. The last of these is most consistent with the conceptual definition, and after examining various possibilities, Twarakavi et al. (2009) concluded that specifying a limiting rate of $q'_z = 0.1 \text{ mm/d}$ (the smallest amount of precipitation

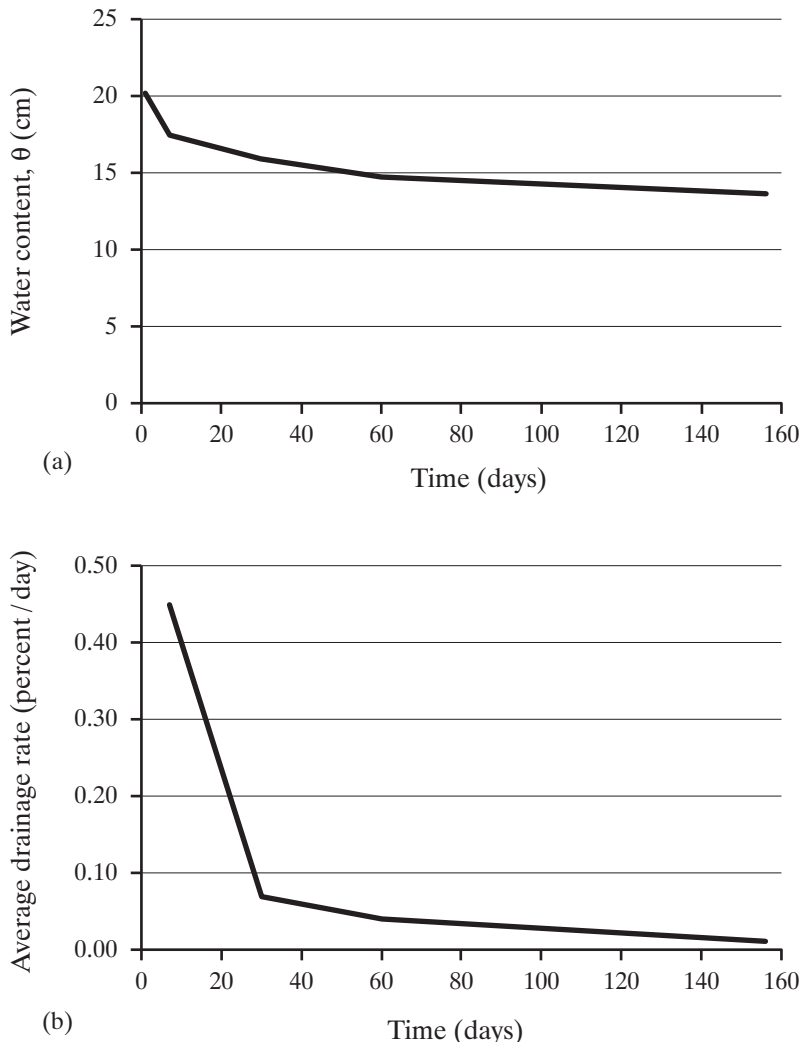


Figure 8.1 Gravity drainage of a silt-loam soil. (a) Water content (θ) versus time (t). (b) Drainage rate ($d\theta/dt$) [data from Hillel (1971)].

that is practically measurable) is the most hydrologically meaningful.

Using this latter definition and the van Genuchten soil-hydraulic relations (table 7.2), Twarakavi et al. (2009) showed that field capacity can be estimated as

$$\theta_{fc}^* = n^{-0.60 \cdot [2 + \log_{10}(K_h)]}, \quad (8.3)$$

where

$$\theta_{fc}^* \equiv \frac{\theta_{fc} - \theta_r}{\theta_{vG} - \theta_r}; \quad (8.4)$$

n , θ_r , and θ_{vG} are van Genuchten parameters; and K_h is saturated hydraulic conductivity (cm/d). These relations then also allowed computation of the time for a soil to drain from saturation to field capacity, T_{fc} , and the pressure head at field capacity, $|\psi_{fc}|$.

Finally, using pedotransfer functions (PTFs) as described in section 7.4.6, Twarakavi et al. (2009) mapped average values θ_{fc} , T_{fc} , and $|\psi_{fc}|$ on the soil-texture triangle, as shown in figure 8.2. Note that θ_{fc} ranges from < 0.1 to > 0.4, $|\psi_{fc}|$ from < 100 cm to > 1,000 cm, and T_{fc} from ~0.5 to > 2 days, with generally smaller values for sandier soils, and higher values for clays and silt-clay mixtures. Figure 8.3 compares drainage curves for two soils with contrasting textures.

8.1.2 Permanent Wilting Point

In nature, water can be removed from a soil that has reached field capacity by surface evaporation (exfiltration) or by plant uptake as part of the process of transpiration (section 6.5). However, there is a species-variable limit to the suction (negative pressure)

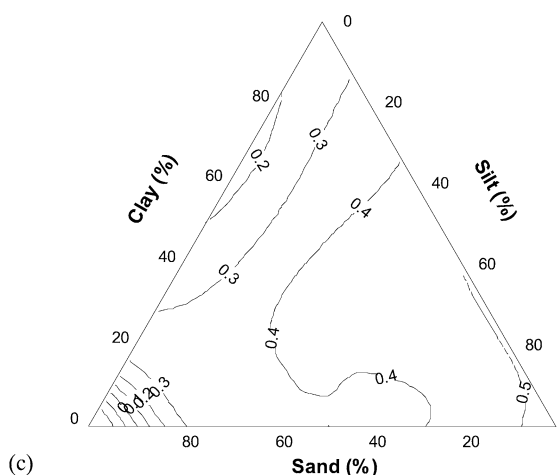
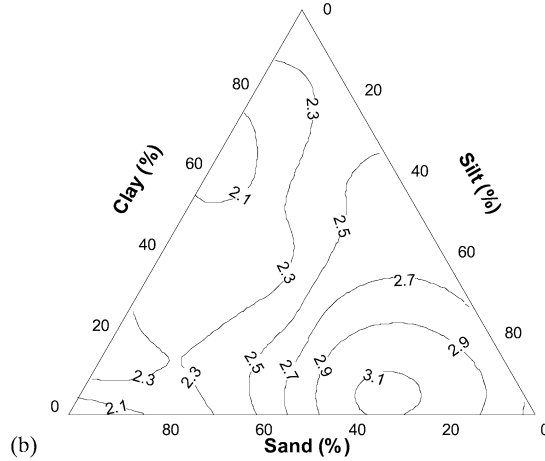
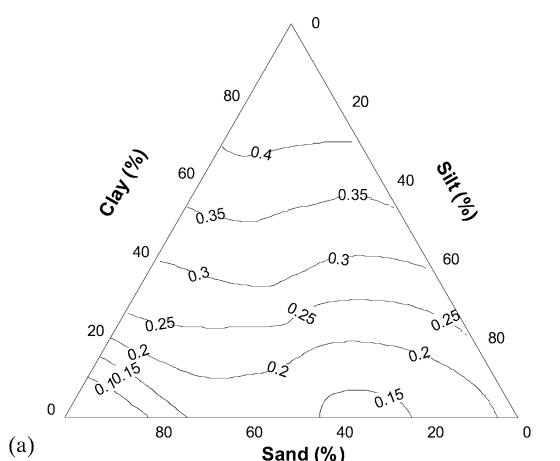


Figure 8.2 Mean values of (a) field capacity, θ_{fc} ; (b) tension at field capacity, $\log_{10}(|\psi_{fc}|)$ (cm); and (c) time to drain to field capacity, $\log_{10}(T_{fc})$ (days), as a function of sand, silt, and clay percentages [Twarakavi et al. (2009). An objective analysis of the dynamic nature of field capacity. *Water Resources Research* 45, with permission of the American Geophysical Union].

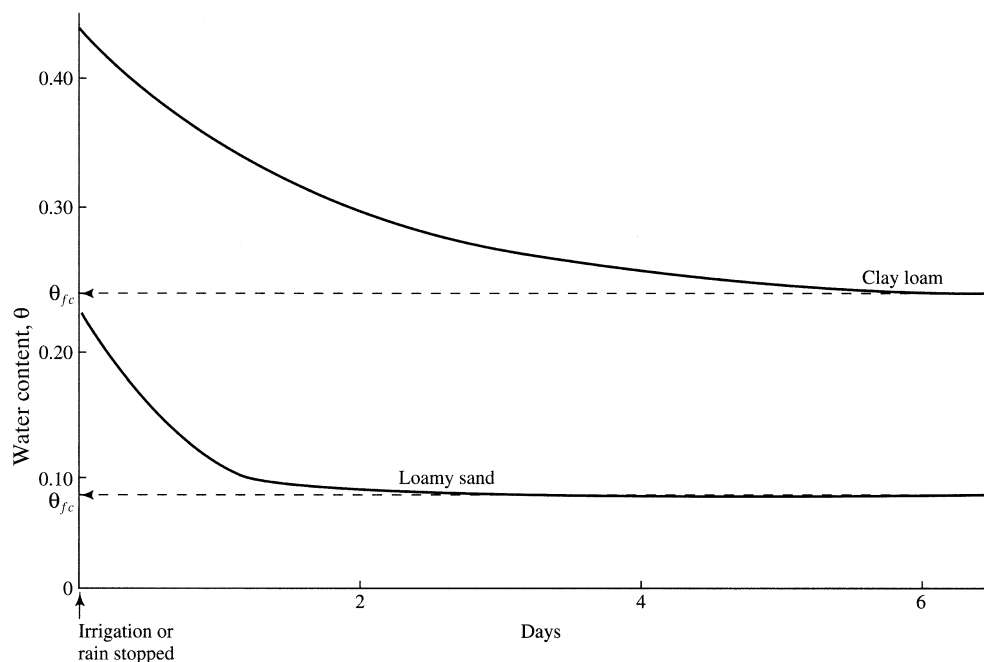


Figure 8.3
Drainage of two soils (schematic); the arrows indicate the values of field capacity [adapted from Donahue et al. (1983)].

that plants can exert. For hydrologic purposes, this limit is usually considered to be -15 bar ($= -15,000$ cm of water $= -1,470$ kPa $= -14.5$ atm) and, when the water content is reduced to the point corresponding to that value on the moisture-characteristic curve, transpiration ceases and plants wilt. Thus it is useful to define the **permanent wilting point**, θ_{pwp} , as

$$\theta_{pwp} \equiv \theta(-15 \text{ bar}). \quad (8.5)$$

Using the van Genuchten relations (table 7.2), θ_{pwp} can be estimated for a particular soil as

$$\begin{aligned} \theta_{pwp} &= \theta(-15,000 \text{ cm}) \\ &= \theta_r + \frac{\theta_{vG} - \theta_r}{\left[1 + (\alpha \cdot 15,000)^n\right]^{(n-1)/n}}. \end{aligned} \quad (8.6)$$

The value of θ_{pwp} ranges from about 0.06 for sands to 0.27 for clays (figure 8.4).

8.1.3 Soil-Water Status

The difference between the field capacity and permanent wilting point is considered to be the water available for plant use, called the **available water content**, θ_a :

$$\theta_a = \theta_{fc} - \theta_{pwp}. \quad (8.7)$$

Figure 8.5 shows a classification of water status in soils based on pressure head. Clearly natural soils will always have water contents $> \theta_{pwp}$, and most of the time in the range $\theta_{pwp} \leq \theta \leq \theta_{fc}$. Soils in nature do

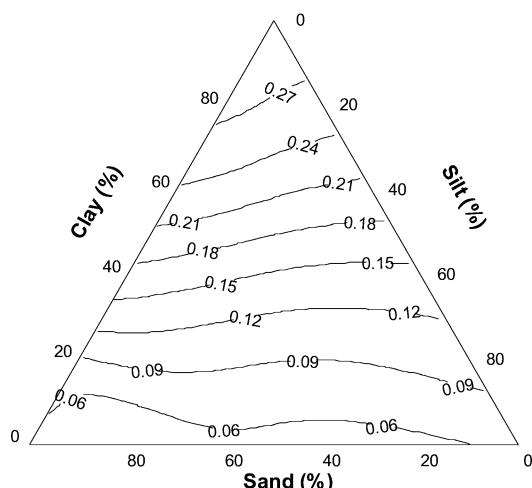


Figure 8.4 Average value of permanent wilting point, θ_{pwp} , plotted on the soil-texture triangle [Twarakavi et al. (2010)]. Can texture-based classification optimally classify soils with respect to soil hydraulics? *Water Resources Research* 46, with permission of the American Geophysical Union].

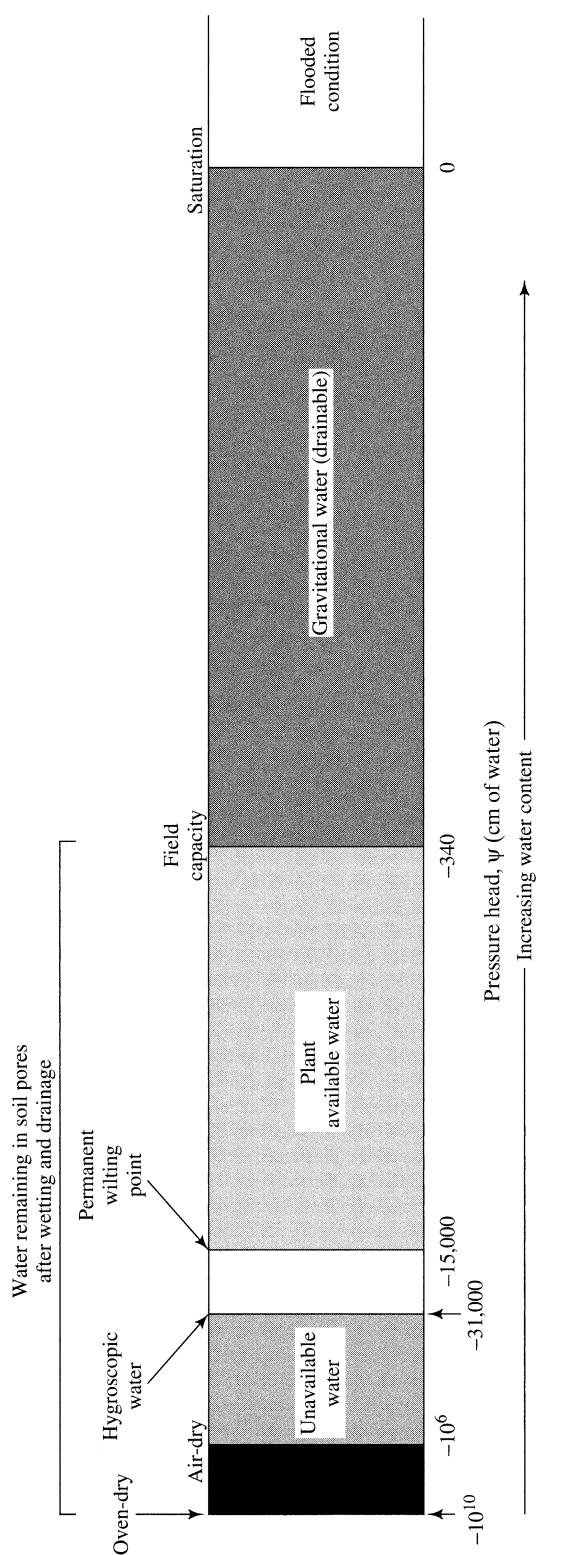


Figure 8.5 Soil-water status as a function of pressure (tension). Natural soils do not have tensions exceeding about $-31,000$ cm; in this range water is absorbed from the air [adapted from Donahue et al. (1983)].

not have water contents lower than that corresponding to **hygroscopic**, since at this extreme dryness water is absorbed directly from the air. Water contents corresponding to θ_{fc} , θ_{pwp} , and θ_a for a particular soil can be determined from its moisture-characteristic curve, soil-hydraulic class (figure 7.21), or PTFs and equations (8.3)–(8.6), as shown in box 8.1.

8.1.4 Hydrologic Soil Horizons

For purposes of describing water movement, it is useful to define **soil-hydrologic horizons** based on

the normal range of water contents and soil-water pressures, as shown in figure 8.6. The depths and thicknesses of these hydrologic horizons vary in both time and space, and one or more of them may be absent in a given situation.

8.1.4.1 Ground-Water Zone

The **ground-water zone** (sometimes called the **phreatic zone**¹⁾) is saturated and the pressure is positive. *If there is no ground-water flow, the pressure is hydrostatic*, i.e., it increases linearly with depth as

Box 8.1 Example Computation of Field Capacity, Permanent Wilting Point, and Available Water Content

Here we use the PTF relationships of table 7.3 to estimate the van Genuchten parameters and the (a) field capacity, (b) permanent wilting point, and (c) available water content for a soil with a bulk density $\rho_b = 1,600 \text{ kg/m}^3 = 1.6 \text{ g/cm}^3$; sand fraction = 70%, clay fraction = 3%, and organic carbon fraction = 1%. The PTF relationships are

$$\begin{aligned}\theta_r &= 0.015 + 0.005 \cdot \text{CLAY}(\%) + 0.014 \cdot C(\%) \\ \theta_r &= 0.015 + 0.005 \cdot 3 + 0.014 \cdot 1 = 0.044;\end{aligned}$$

$$\begin{aligned}\phi_{VG} &= 0.810 - 0.283 \cdot \rho_b \left(\text{g/cm}^3 \right) + 0.001 \cdot \text{CLAY} (\%) \\ \phi_{VG} &= 0.810 - 0.283 \cdot 1.6 + 0.001 \cdot 1 = 0.363;\end{aligned}$$

$$\begin{aligned}\alpha (1/\text{cm}) &= \exp[-2.486 + 0.025 \cdot \text{SAND}(\%) - 0.352 \cdot C(\%) - 2.617 \cdot \rho_b (\text{g/cm}^3) - 0.023 \cdot \text{CLAY}(\%)] \\ \alpha &= \exp[-2.486 + 0.025 \cdot 70 - 0.352 \cdot 1 - 2.617 \cdot 1.6 - 0.023 \cdot 3] = 4.78 \times 10^{-3} \text{ 1/cm};\end{aligned}$$

$$\begin{aligned}n &= \exp[0.053 - 0.009 \cdot \text{SAND}(\%) - 0.013 \cdot \text{CLAY}(\%) + 0.00015 \cdot \text{SAND}(\%)^2] \\ n &= \exp[0.053 - 0.009 \cdot 70 - 0.013 \cdot 3 + 0.00015 \cdot 70^2] = 1.13;\end{aligned}$$

$$\begin{aligned}K_h (\text{cm/s}) &= 1.1574 \times 10^{-5} - \exp[20.62 - 0.96 \cdot \ln[\text{CLAY}(\%)] - 0.66 \cdot \ln[\text{SAND}(\%)] - 0.046 \cdot \ln[C(\%)] \\ &\quad - 8.43 \cdot \rho_b (\text{g/cm}^3)] \\ K_h &= 1.1574 \times 10^{-5} - \exp[20.62 - 0.96 \cdot \ln[3] - 0.66 \cdot \ln[70] - 0.046 \cdot \ln[1] - 8.43 \cdot 1.6] \\ &= 3.06 \times 10^{-4} \text{ cm/s} = 26.4 \text{ cm/d}.\end{aligned}$$

From equation (8.3),

$$\theta_{fc}^* = n^{-0.60 \cdot [2 + \log_{10}(K_h)]} = 1.13^{-0.60 \cdot [2 + \log_{10}(26.4)]} = 0.738.$$

From equation (8.4),

$$\theta_{fc} = \theta_{fc}^* \cdot (\theta_{VG} - \theta_r) + \theta_r = 0.783 \cdot (0.363 - 0.044) + 0.044 = 0.294.$$

From equation (8.5),

$$\theta_{pwp} = \theta_r + \frac{\theta_{VG} - \theta_r}{\left[1 + (\alpha \cdot 15,000)^n \right]^{(n-1)/n}} = 0.044 + \frac{0.363 - 0.044}{\left[1 + (4.78 \times 10^{-3} \cdot 15,000)^{1.13} \right]^{(0.13/1.13)}} = 0.230.$$

From equation (8.6),

$$\theta_a = \theta_{fc} - \theta_{pwp} = 0.294 - 0.230 = 0.064.$$

$$p(z') = \gamma \cdot (z' - z_0'), z' > z_0'; \quad (8.8)$$

where p is gauge pressure, γ is the weight density of water, z' is distance measured vertically downward, and z_0' is the value of z' at the water table. In general, ground water is flowing; then the pressure at a point is determined by the overall configuration of the regional flow system, i.e., by the value that satisfies the general ground-water equation [equation (7.17)].

The water table is at atmospheric pressure; it is the level at which water would stand in a well. In general, the water table rises and falls in response to seasonal climatic variations and to recharge from individual storm events. In arid regions it may be at depths of many tens of meters, while elsewhere (e.g., where the soil is developed in a thin layer of glacial till overlying dense crystalline bedrock), there may be no water table in the soil all or most of the time.

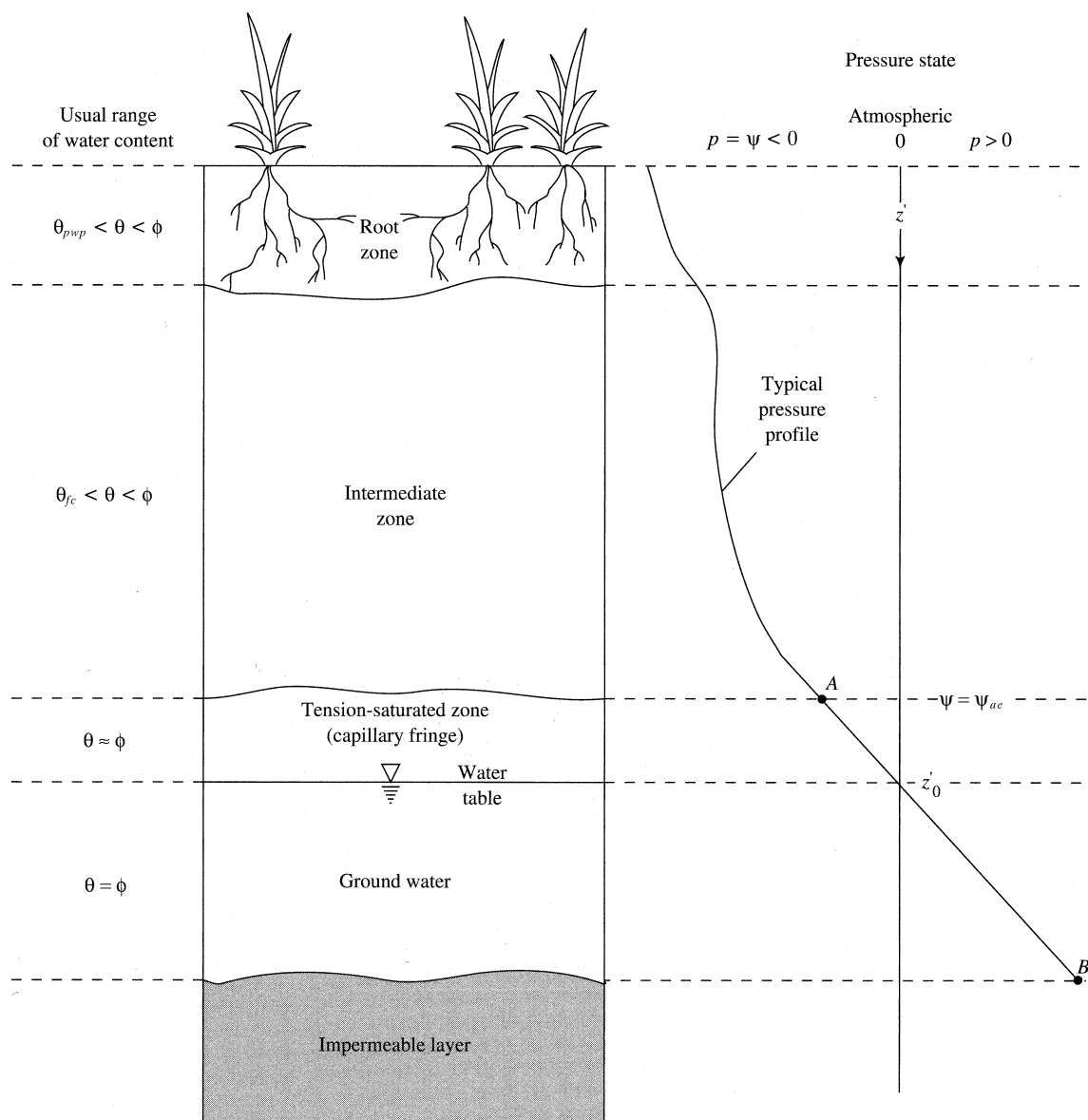


Figure 8.6 Designation of hydrologic soil-profile horizons. Note that this figure is idealized, and that one or more of these horizons may be absent in a given situation [adapted from Todd (1959)].

Water may enter the upper ground-water zone as flow from below, in which case the region is in a *ground-water discharge zone*, or as recharge from above. Water may leave the zone as downward flow in a *ground-water recharge zone*, or as upward flow into the tension-saturated zone as **capillary rise**. Discharge and recharge zones are major components of regional ground-water flow, as discussed in section 9.2.

8.1.4.2 Tension-Saturated Zone

The term **vadose zone** is commonly used to refer to the entire zone of negative pressures above the water table. As discussed in section 7.4.1, a portion of this zone immediately above the water table is saturated or nearly saturated as a result of capillary forces, creating the **tension-saturated zone** or **capillary fringe**. Water in this zone is under tension [$p(z') < 0$], but the pressure distribution remains hydrostatic, and is given by

$$p(z') = \gamma \cdot (z' - z_{ts}'), z_{ts}' < z' < z_0'. \quad (8.9)$$

The pressure head at top of this zone ($z' = z_{ts}'$) is the air-entry tension, ψ_{ae} , which is equal to the height of capillary rise. Typically ψ_{ae} = about 10 mm for gravel to 1.5 m for silt to several meters for clay.

Water enters the tension-saturated zone as recharge from above or capillary rise from below. It leaves downward, as ground-water recharge, or upward, in response to head gradients induced by surface evaporation or water withdrawal by roots to supply plant transpiration. When inflows occur, the entire zone moves upward; when withdrawals occur, it moves downward. In either case the thickness of the zone is maintained at $z_0' - z_{ts}' = \psi_{ae}$.

8.1.4.3 Intermediate Zone

The **intermediate zone** is the portion of the vadose zone between the top of the tension-saturated zone and the base of the root zone. In arid regions this zone may occupy much of the soil profile and extend many tens of meters. In other situations it may be absent at least seasonally; for example, in wetlands and where the root zone extends to the water table or to impermeable bedrock.

Water enters the intermediate zone as percolation from above and leaves by gravity drainage. Thus water content in this zone does not go below field capacity; it may rise above field capacity when water from rain or snowmelt passes through the root zone, after which it gradually returns toward field capacity following a curve like those in figure 8.3. Tensions in this zone are usually stronger than ψ_{ae} and depend

on the soil texture and the water content, as given by the moisture-characteristic curve.

8.1.4.4 Root Zone

The **root zone** is the layer from which plant roots can extract water during transpiration; its upper boundary is the soil surface, while its lower boundary is indefinite and irregular, but effectively constant in time (except in agricultural situations). Table 8.1 gives root-zone depths for various vegetation types.

Table 8.1 Typical Root-Zone Depths for Vegetation Types.

Vegetation Type	Rooting Depth (m)
Evergreen Needleleaf Forest	1.2
Evergreen Broadleaf Forest	1.0
Deciduous Needleleaf Forest	0.5
Deciduous Broadleaf Forest	1.2
Mixed Cover	1.2
Woodland	1.1
Wooded Grassland	1.2
Closed Shrubland	1.2
Open Shrubland	0.7
Grassland	1.2

Source: NASA Land Data Assimilation Systems (<http://ldas.gsfc.nasa.gov/nldas>).

Water enters the root zone chiefly by infiltration, although it may enter from below in ground-water-discharge zones and when evapotranspiration creates gradients that draw water from the intermediate zone; it leaves via evapotranspiration and gravity drainage. The water content is above the permanent wilting point; in non-wetland soils it might occasionally approach saturation following extensive water input and infiltration but would be below field capacity much of the time between water-input events.

As noted above, there are many places (including wetlands) in which the root zone extends to the water table, and it may extend throughout a thin soil lacking a subjacent water table.

8.1.5 Equilibrium Soil-Water Profiles

The **equilibrium water-content profile** is the vertical water-content profile that will transmit to the

water table a constant flux of water equal to the local climatic-average rate of recharge. It is determined by (1) the climatic-average recharge, or net infiltration, rate (= average infiltration rate minus average evapotranspiration rate), (2) the depth to the water table, and (3) the soil-hydraulic properties (Salvucci and Entekhabi 1995). Although the actual water-content profile varies with time at a given location, the equilibrium profile is useful for portraying the characteristic soil-hydraulic conditions for a given climate, soil type, and water-table depth and for specifying typical initial conditions when modeling infiltration.

In many regions the average recharge rate, R , is close to the average annual precipitation, so

$$R \approx P - ET, \quad (8.10)$$

where P is average precipitation rate and ET is average evapotranspiration rate. For a soil with known or estimated air-entry tension (ψ_{ae}) and saturated hydraulic conductivity, K_h , and a given depth to water table, z_0' , the average depth to the top of the tension-saturated zone, z_{ts}' , is

$$z_{ts}' = z_0' - |\psi_{ae}| \cdot (1 + R/K_h). \quad (8.11)$$

Thus the effect of recharge is to increase the height of the tension-saturated zone above its static value $|\psi_{ae}|$. However, typically $R \ll K_h$, so the effect is usually small.

Below z_{ts}' , the soil is effectively saturated so

$$\theta(z') = \phi, \quad z' > z_{ts}'. \quad (8.12a)$$

For $z' \leq z_{ts}'$, Darcy's law [equation (8.1) with $q_z' = R$] and the analytical relations for the soil-hydraulic properties can be used to compute the equilibrium profile. Salvucci (1993) and Salvucci and Entekhabi (1995) used the Brooks–Corey relations (tables 7.2 and 7.4) to derive

$$\begin{aligned} \theta(z') = \phi \cdot \left[\frac{R}{K_h} + \left(1 - \frac{R}{K_h} \right) \cdot \left(\frac{z_0' - z'}{|\psi_{ae}| \cdot (1 + R/K_h)} \right)^{-(2+b+3)/b} \right]^{1/(2+b+3)}, \\ , z' \leq z_{ts}'. \end{aligned} \quad (8.12b)$$

Using equations (8.11)–(8.12), the general effects of soil type, water-table depth, and climate on equilibrium profiles can be illustrated. Figure 8.7 shows that the finer the soil texture, the higher the typical water content for a given recharge rate and

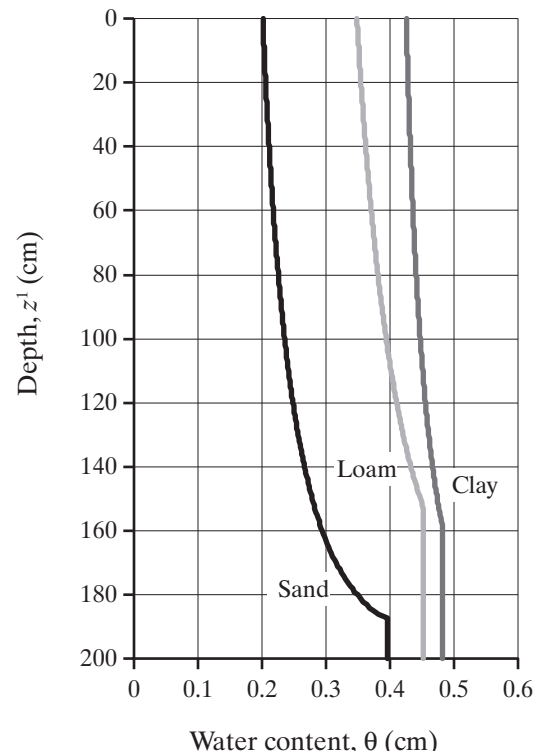


Figure 8.7 Climatic-equilibrium water-content profiles for typical clay, loam, and sand soils with a net recharge rate of 50 cm/yr and a water table at a depth of 200 cm [equation (8.12b)]. The finer the soil texture, the higher the typical water content for a given recharge rate and depth to water table.

depth to water table. The equilibrium water contents for all three soils are above typical field-capacity values (0.07 for sand, 0.22 for loam, and 0.39 for clay; see figure 8.2) over the entire profiles, suggesting that gravity drainage is a common occurrence. Figure 8.8 shows that a higher water table acts to maintain the overlying soil in a wetter state, and figure 8.9 suggests that the effect of recharge rate (net infiltration) on soil-water content is minor.

8.1.6 Relation between Hydrologic and Pedologic Horizons

As described in section 2.3, soils are characterized by a typical sequence of pedologic horizons that constitutes the *soil profile*. Pedologic horizons are distinguished by the proportion of organic material and the degree to which geologic parent material has been altered, removed (*eluviated*), or added to (*illuviated*).

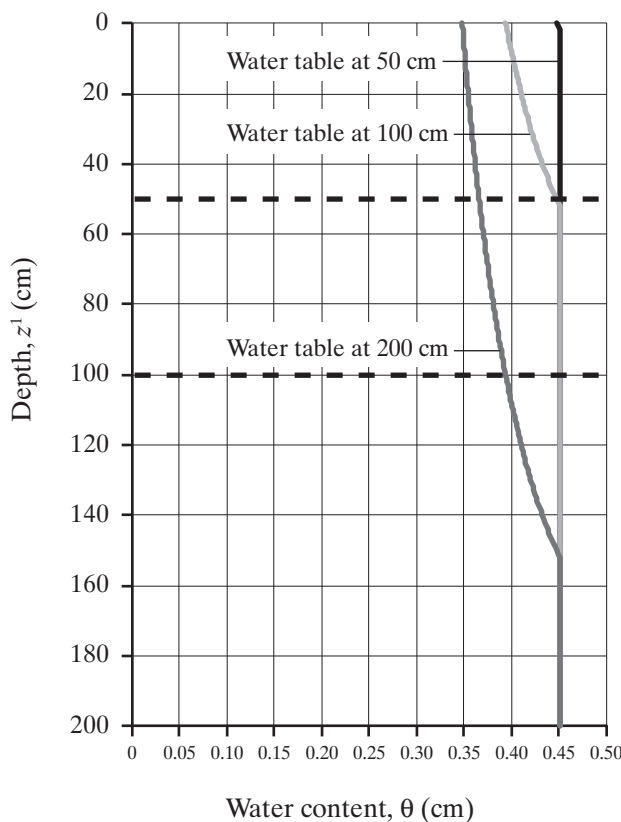


Figure 8.8 Effect of water-table depth on the climatic-equilibrium water-content profile for a loam soil with a net recharge rate of 50 cm/yr [equation (8.12b)]. A higher water table maintains a wetter soil.

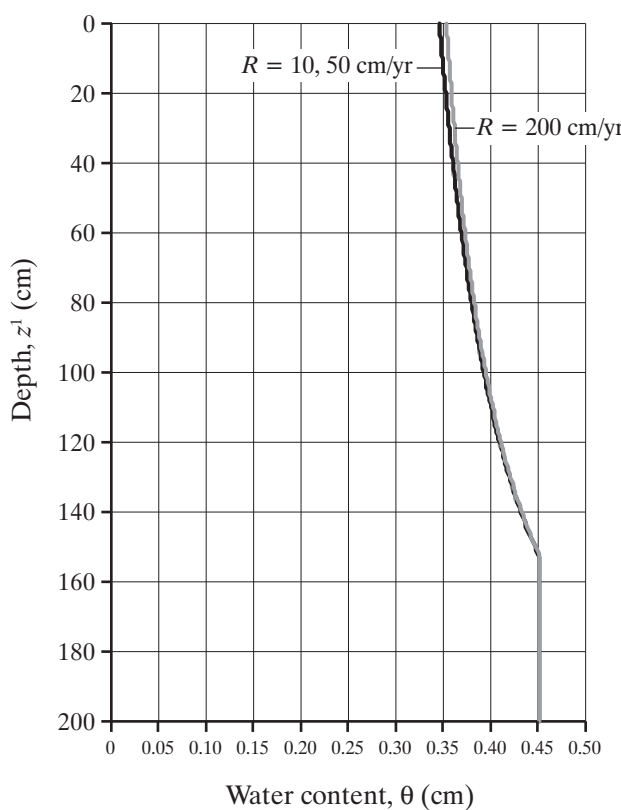


Figure 8.9 Effect of net recharge rate, R , on the climatic-equilibrium water-content profile for a loam soil with a water table depth of 200 cm [equation (8.12b)]. Curves are plotted for $R = 10, 50$, and 200 cm/yr ; the curves for 10 and 50 cm/yr are virtually identical, the curve for 200 cm/yr gives only slightly higher water content in the upper portion of the profile.

ated) by chemical and physical processes. The upper, highly altered horizons constitute the *solum*.

Pedologists identify soil horizons on the basis of color, texture, and structure and designate them by letters, as shown in figure 2.47. Not all horizons are present in all soils, and the boundaries between layers are commonly gradational. The relative development of these horizons is the basis for identifying soil orders (table 2.14) and for more detailed pedologic classification. The development of pedologic horizons is determined largely by climate, but depends also on: (1) local topography; (2) the effects of erosion, deposition, and other disturbances; (3) the type of parent material; and (4) the time over which soil-forming processes have been operating. The development of these horizons may vary significantly over short distances depending on local conditions, but does not vary temporally over the time scale of most hydrologic analyses.

Because of the variability in development of pedologic and hydrologic horizons, only a few generalizations can be made about the relations between them. In non-wetland soils, the root zone usually occupies the zone of eluviation and may extend throughout the solum. Ordinarily the zones of eluviation and illuviation develop only in the unsaturated zone above the capillary fringe, but in some soils the seasonal high water table may move into the solum. Large water-conducting pores called **macropores**, produced by roots and animal activity, may occur in the root zone.

Bluish, grayish, and greenish mottling of subsoils, called **gleying**, usually indicates reduced aeration because the horizon is below the water table for a significant fraction of the year. In wetlands, where the water table is at or near the ground surface, the soil may consist almost entirely of organic layers or, where mineral soils are present, the solum may be absent or poorly developed.

Soil-hydraulic properties may change relatively abruptly in successive pedologic horizons. In some cases impermeable or nearly impermeable layers called **hardpan** or **fragipan** develop at or below the B layer, and percolating water may accumulate above these layers, forming a **perched water table** above the general regional water table. However, other soils show a more or less gradual decrease in hydraulic conductivity and porosity with depth (Beven 1984).

In general, soil-water pressure changes smoothly across the boundary between layers of contrasting hydraulic conductivity, even though there are abrupt changes in water content.

8.2 The Infiltration Process

As noted, infiltration is the process by which water arriving at the soil surface as rain or snowmelt enters the soil. Here we define terms and conditions essential to understanding the process, describe the basic aspects of this process at a “point” (i.e., a plot that is a few m^2 in size) during a single water-input event, and qualitatively describe the factors that control the process. Later sections describe approaches to the field measurement of infiltration and develop quantitative descriptions of infiltration that sharpen our understanding of the process and can be used in modeling this critical component of the hydrologic cycle. To simplify the discussion, we focus on flow in a uniform soil matrix governed by Darcy’s law (**Darcian flow**); i.e., soils without vertical contrasts in texture and without macropores.

8.2.1 Definitions

- The **water-input rate**, $w(t)$ [L T^{-1}], is the rate at which water arrives at the surface due to rain, snowmelt, or irrigation. A water-input event begins at time $t = 0$ and ends at $t = T_w$.
- The **infiltration rate**, $f(t)$ [L T^{-1}], is the rate at which water enters the soil from the surface.
- The **infiltrability** (also called **infiltration capacity**), $f^*(t)$ [L T^{-1}], is the maximum rate at which infiltration could occur at any time; note that this changes during the infiltration event.
- The **depth of ponding**, $H(t)$ [L], is the depth of water standing on the surface.

We distinguish three conditions:

- No ponding:** Infiltration rate equals water-input rate and is less than or equal to infiltrability;

$$H(t) = 0, f(t) = w(t) \leq f^*(t). \quad (8.13)$$

In this situation, infiltration is said to be **supply-controlled** or **flux-controlled**.

- Saturation from above:** Ponding is present because the water-input rate exceeds the infiltrability, and infiltration rate equals infiltrability;

$$H(t) > 0, f(t) = f^*(t) \leq w(t). \quad (8.14)$$

In this situation, the rate of infiltration is determined by the soil type and wetness, and is said to be **profile-controlled** (Hillel 1980b). When ponding occurs due to saturation from above, the infil-

tration process may be complicated by the upward flow of air in some of the soil pores.

3. **Saturation from below:** Ponding is present because the water table has risen to or above the surface and the entire soil is saturated. In this case, infiltration rate and infiltrability are zero;

$$H(t) \geq 0, f(t) = f^*(t) = 0. \quad (8.15)$$

8.2.2 General Features

Recalling the Richards equation for vertical downward flow [equation (7.30)],

$$\underbrace{\frac{\partial K_h(\theta)}{\partial z'}}_{\text{gravity}} - \underbrace{\frac{\partial}{\partial z'} \left[K_h(\theta) \cdot \left(\frac{\partial \psi(\theta)}{\partial z'} \right) \right]}_{\text{pressure gradient}} = \frac{\partial \theta}{\partial t}, \quad (8.16)$$

note that the first term represents flow due to gravity and the second represents flow due to the pressure gradient. As water enters a dry soil in the first stages of infiltration, the pressure gradient at the surface is much larger than the unit gravitational gradient, and the infiltration rate is almost entirely due to pressure forces and tends to be large. Thus infiltration into unsaturated soils typically occurs at high rates at the beginning of the event. As the process continues, near-surface water content increases, causing the pressure-gradient forces and the infiltration rate to decline; if water input continues for a long enough time, the pressure forces become small and the infiltration rate declines quasi-exponentially to a near-constant value that approximates the rate due to gravity alone (figure 8.10).

Typical vertical profiles of water content during an infiltration event are shown in figure 8.11. The region of rapid downward decrease in water content is called a **wetting front**, which in this case was at a depth of about 3 cm after 0.83 hr and had progressed to about 33 cm after 83 hr of steady infiltration. Wetting fronts in clay soils like that in figure 8.11 tend to be relatively diffuse due to the effect of capillarity, but are quite sharp (i.e., quasi-horizontal) in sandy soils (figure 8.12). When the pressure gradient opposes the flow ($d\psi/dz' > 0$), which may occur when hydraulic conductivity increases with depth, the wetting front may become unstable and the downward flow becomes concentrated into vertical “fingers” (Hillel 1980b).

Symbol	Water-input rate, w (mm h ⁻¹)
○	312
▲	234
×	156
●	78

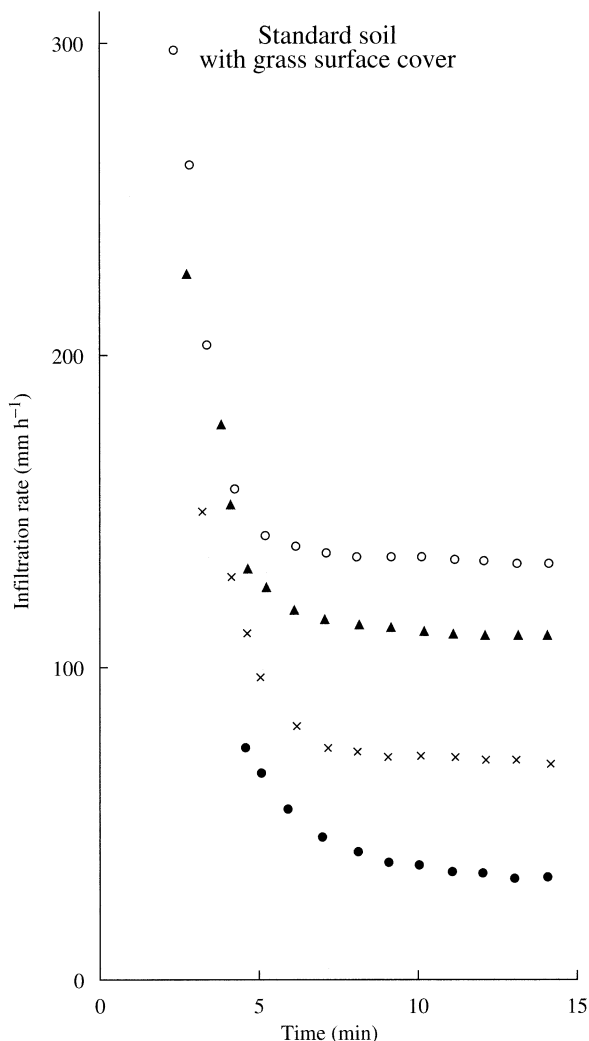


Figure 8.10 Infiltration rate into bare and grassed loam plots as a function of time for various water-input rates as measured in laboratory studies using artificial rainstorms of 15-min duration [adapted from Nassif and Wilson (1975)].

8.2.3 Factors Affecting Infiltration Rate

The infiltration rate $f(t)$ is determined by the gravity and pressure forces on water arriving at the surface, which are in turn determined by the following factors:

8.2.3.1 Water-Input Rate or Depth of Ponding

Equations (8.13)–(8.15) state the conditions under which the water-input rate $w(t)$, the depth of

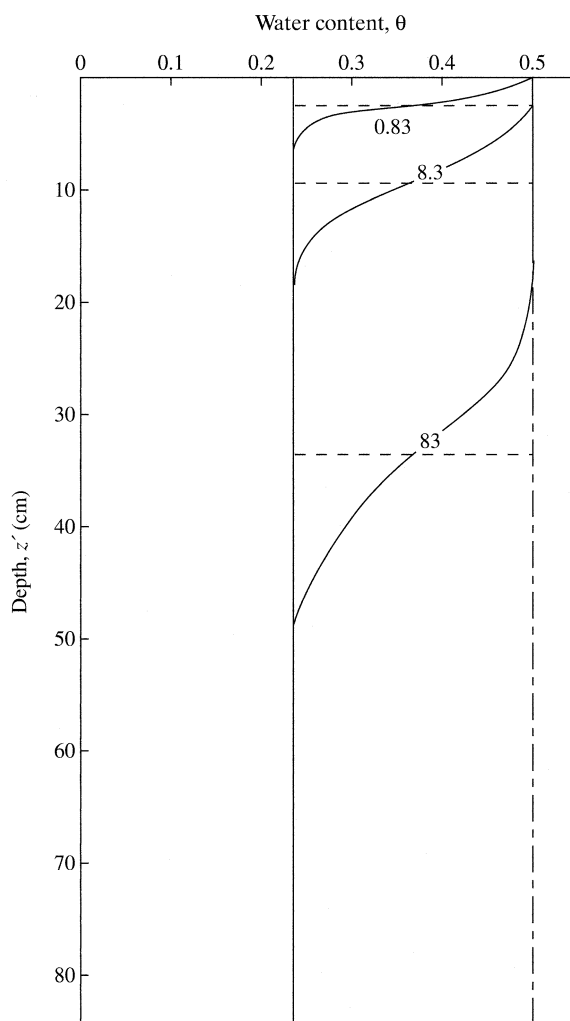


Figure 8.11 Soil-moisture profiles in a light clay soil with $\phi = 0.50$ at various times during steady infiltration with no ponding. The number on the curve is the time since infiltration began in hours. Initial water content was 0.23. The dashed lines mark the average positions of the wetting front at the indicated times [data from Freyberg et al. (1980)].

ponding, $H(t)$, and the presence of saturation from above or below determine the range of possible values for $f(t)$.

8.2.3.2 Hydraulic Conductivity of the Surface

Subsequent analysis will show that the minimum value of the infiltrability of a soil approximately equals its saturated hydraulic conductivity, K_h . As noted earlier, K_h for uniform mineral soils is determined primarily by grain size. However, there are many factors that can cause the pore size, and hence K_h , at the surface of soils to be greater or less than those of the underlying undisturbed mineral soil, as described below.

Organic surface layers: If the soil supports natural vegetation, particularly a forest, the near-surface soil will usually consist largely of leaf litter, humus,



Figure 8.12 Wetting front in a sandy soil exposed after an intense rain (photo by author).

and other organic matter that has a large number of large openings, and hence a high hydraulic conductivity, regardless of the texture of the mineral soil beneath (Tricker 1981). Root growth and decay and the action of worms, soil insects, and burrowing mammals contribute to the surface porosity. This effect occurs also in grass (Hino et al. 1987) and even in arid scrubland, where infiltration was found to be nearly three times higher under individual bushes than in the open (Lyford and Qashu 1969). In deciduous broad-leaved forests, the leaf litter can produce a “shingling” effect that can have the opposite result and prevent infiltration, at least locally.

Frost: If surface soil with a high water content freezes, “concrete frost” can form, making the surface nearly impermeable. However, frost action associated with lower water contents can sometimes markedly increase the surface permeability (Schumm and Lusby 1963; Dingman 1975). In some permafrost areas, seasonal freezing at the surface produces a polygonal network of cracks that can admit much of the spring melt water.

Swelling-drying: Some soils, especially Vertisols (section 2.3.1), contain clay minerals that swell when wet and shrink when dry. During the rainy season, or during a single rain storm, swelling can reduce effective surface porosity and permeability and limit infiltration; during dry periods polygonal cracks develop that can accept high infiltration rates.

Rain compaction: The impact of rain on bare soils causes the surface to compact, producing a soil seal that markedly decreases infiltration. The intensity of the effect is determined by the kinetic energy of the rain modified by the physical and chemical nature of the soil (Assouline and Mualem 1997).

Inwashing of fine sediment: Where surface erosion occurs due to flow over the surface, or where mineral grains are brought into suspension by the splashing of raindrops, fine sediment may be carried into larger pores and effectively reduce the surface pore size and permeability. These situations are most likely to occur where vegetative cover is sparse, either naturally or due to cultivation practices.

Human modification of the soil surface: Many human activities have a direct effect on surface porosity, most obviously the construction of roads

and parking lots. Plowing may increase or decrease surface porosity temporarily, but equipment used for spreading fertilizers and pesticides tends to compact the soil and reduce porosity. Grazing animals also tend to compact the surface soil.

8.2.3.3 Water Content of Surface Pores

Saturation from below occurs when local recharge and/or ground-water flow from upslope causes the local water table to rise to the surface. It can also occur in the absence of a local water table at the beginning of an event where there is a more-or-less gradual decrease of porosity and hydraulic conductivity with depth, or where there is a distinct layer with significantly reduced permeability at depth. Either situation may reduce or prevent percolation at depth, which in turn causes an accumulation of water arriving from above and may lead to creation of a saturated zone. If water input continues at a high enough rate, the saturated zone can reach the surface and prevent further infiltration regardless of the hydraulic conductivity, the rate of input, or any other factor.

Even when surface saturation does not occur, the antecedent water content affects the infiltration rate. A higher water content increases hydraulic conductivity and reduces the space available for storage of infiltrating water, both of which tend to increase the speed at which the wetting front descends. However, a soil that is relatively wet at the beginning of a water-input event will be more likely to become saturated during the event, resulting in a longer period of reduced infiltration.

The net effect of antecedent water content on infiltration thus depends on the specific conditions of water-input rate and duration, the distribution of soil-hydraulic conductivity with depth, the depth of the local water table, and the initial water content itself. The model developed in section 8.4.3 will allow us to evaluate some of these factors quantitatively.

8.2.3.4 Surface Slope and Roughness

As long as ponding does not occur during a water-input event, the infiltration rate is governed by the water-input rate, and the roughness of the soil surface has no direct effect on infiltration. However, once ponding begins the ponding depth will increase until it is sufficient to overcome the hydraulic resistance of the surface, at which time downslope runoff or *overland flow* begins. The rate of overland flow increases with increasing slope and decreases with increasing roughness. Thus steeper slopes and smoother sur-

faces promote more rapid overland flow, and hence less accumulation of ponded water on the surface and, other things equal, lower infiltration rates (Nasif and Wilson 1975).

8.2.3.5 Chemical Characteristics of the Soil Surface

Waxy organic substances produced by vegetation and microorganisms have been found on ground surfaces under a variety of vegetation types. Since the contact angle between a water surface and waxes is negative (table B.4), water falling on these surfaces tends to “bead up” instead of being drawn into the pores by surface-tension forces. Soils with such surfaces are called **hydrophobic** (i.e., water-repellent).

The effects of hydrophobic compounds on infiltration seem to be minor under undisturbed vegetation. However, when forest or range fires occur the organic surface layer is burned off, these substances vaporize and subsequently condense on the bare soil, and the wetability and infiltrability of the surface is significantly reduced (Branson et al. 1981).

8.2.3.6 Physical and Chemical Properties of Water

The movement of liquid water in the unsaturated zone is affected by the surface tension, density, and viscosity of water, all properties that depend on temperature (table B.2). Viscosity is especially sensitive: Its value at 30°C is less than half its value at 0°C, thus the hydraulic conductivity at 30°C is about twice as large as it is at 0°C, other things equal [equation (7.16)]. This effect was observed by Klock (1972), who measured infiltration rates twice as large with 25°C water as with 0°C water in laboratory experiments.

8.3 Measurement of Infiltration

8.3.1 Ring Infiltrometers

A **ring infiltrometer** is a device for direct field measurement of infiltration over a small area ($0.02\text{--}1\text{ m}^2$). The area is defined by an impermeable boundary, usually a cylindrical ring extending several centimeters above the surface, and sealed at the surface or extending several centimeters into the soil.

A condition of ponding due to saturation from above is created within the ring by direct flooding of the surface or by applying a sufficiently high rate of simulated rainfall. The rate of infiltration is obtained by: (1) measuring the rate at which the level of ponded water decreases; (2) measuring the rate at which water has to be added to maintain a constant level of

ponding; or (3) solving a water-balance equation for the ponded surface:

$$f(t) = \frac{W - Q - \Delta H \cdot A}{\Delta t}, \quad (8.17)$$

where $f(t)$ is the average infiltration rate over the period of measurement, Δt , W is the volume of water applied in Δt , Q is the volume of ponded water removed from the plot (usually by a small pump) during Δt , ΔH is the change in ponded-water level during Δt , and A is the area covered by the infiltrometer.

As noted, infiltration rates during the early stages of the process are usually high, and gradually decrease to a nearly constant value; it is this constant value that is usually taken as the infiltrability at a particular location. We will see later that this rate is approximately equal to the saturated hydraulic conductivity of the near-surface soil.

Because water infiltrating into an unsaturated soil is influenced by both capillary (pressure) and gravity forces, the water applied within an infiltrometer ring moves laterally as well as vertically (figure 8.13) and the measured infiltration rate thus exceeds the rate that would be obtained if the entire surface were ponded. One way of reducing this effect is to use concentric rings (a **double-ring infiltrometer**) in which areas within both rings are ponded; the area between the two rings acts as a “buffer zone” and measurements on the inner ring only are used to calculate the infiltration rate (figure 8.14). Swartzendruber and Olson (1961a, 1961b) suggested that the inner- and outer-ring diameters be at least 100 and 120 cm, respectively.

A more convenient approach is to use a single-ring infiltrometer and apply a correction for the capillary effect; Tricker (1978) showed that this gave satisfactory results using a single ring of 15-cm diameter and correction factors that depend on the measured rate and the duration of the measurement. Detailed information on the design of various types of infiltrometers can be found in Johnson (1963), McQueen (1963), Tricker (1979), Wilcock and Essery (1984), Bouwer (1986), and Loague (1990). Cheng et al. (2011) described a new version of the single-ring infiltrometer and analysis methods for interpreting the results.

Infiltrability tends to have considerable spatial variability, so that the value for a given soil should be the average of several measurements at different locations. Burgy and Luthin (1956) found that the average of six single-ring infiltrometer measurements

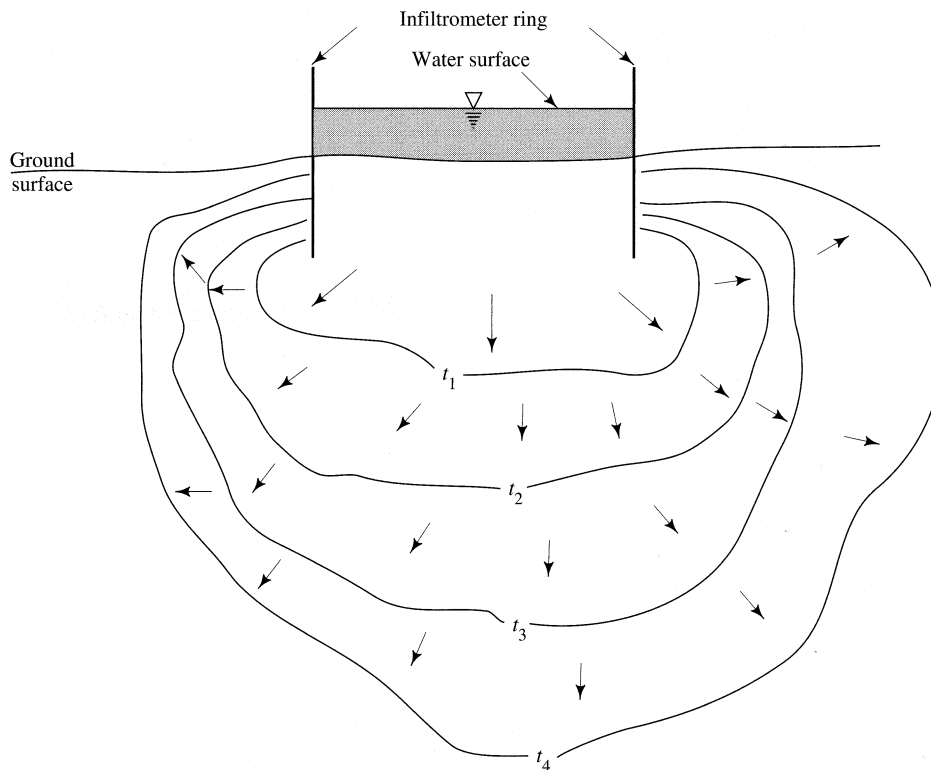


Figure 8.13 Pattern of wetting-front movement into an unsaturated soil from an infiltrometer; t_1, \dots, t_4 represent successive times. Because the front moves laterally due to capillary forces, the rate of inflow at the surface exceeds the infiltration rate that would be obtained if the entire surface were flooded [adapted from Hills (1971)].

of infiltrability was within 30% of the true value for a soil with uniform characteristics.

8.3.2 Tension (Disc) Infiltrometers

In **tension**, or **disc infiltrometers**, the infiltrating water enters the soil through a porous disk placed beneath a reservoir, with the volume of water remaining in the reservoir recorded at successive times (Perroux and White 1988). These instruments are more portable and more readily installed than ring infiltrometers, and are available commercially. Recent innovations include use of time-domain reflectometry (box 7.2) (Moret et al. 2004) and a constant-flow reservoir (Moret-Fernández and González-Cebollada 2009) for accurate measurement of the rate of infiltration.

8.3.3 Sprinkler-Plot Studies

Infiltration rates can also be determined by recording the rates of runoff from well-defined plots on which a known constant rate of artificial rainfall, w , is applied at a constant rate high enough to produce saturation from above. The infiltration rate $f(t)$ is computed as

$$f(t) = w - q(t) \quad (8.18)$$

where $q(t)$ is the rate of surface runoff from the plot (Nassif and Wilson 1975). Langhans et al. (2011) described a portable **drop infiltrometer** that can produce a wide range of simulated rainfall intensities and allows detailed observation of ponding via concomitant photographs.



Figure 8.14 A double-ring infiltrometer connected to an apparatus that maintains a constant water level in each ring (photo by author).

8.3.4 Observation of Soil-Water Changes

Infiltration rates can be measured by recording changes in pressure in tensiometers (section 7.4.3.1) installed at several depths during a natural or artificial water-input event. The moisture-characteristic curve is used to relate tension to water content, and infiltration rate is determined from the increase in soil-water content at various depths during the event.

8.3.5 Preferential Flow

As noted, infiltration in natural soils commonly takes place in macropores produced by plant roots, animal activity, drying, or frost action, rather than via Darcian flow through a uniform soil matrix. Allaure et al. (2009) reviewed laboratory and field techniques for measuring such preferential flow.

8.4 Quantitative Modeling of Infiltration at a Point

8.4.1 Idealized Conditions

Here we introduce approaches to the quantitative modeling of infiltration under idealized conditions, most importantly:

1. Water moves as Darcian flow through interconnected intergrain pores that are uniformly distributed throughout a quasi-homogeneous soil, and our analysis applies to representative soil volumes that are large relative to the typical pore size. Infiltration and vertical flow concentrated in macropores caused by frost action, drying, animal burrowing, or decayed roots may not be well modeled by this idealized approach (Beven and Germann 1982, 2013; Wagenet and Germann 1989). The importance of macropore flow in runoff generation is discussed in section 10.4.3.
2. Upward air flow, which may complicate infiltration under ponded conditions, can usually be neglected for natural infiltration events (Youngs 1988) and is not treated here.
3. Water movement that may occur in response to thermal and osmotic gradients during freezing or thawing is not considered here.

8.4.2 Solutions to the Richards Equation

The Richards equation [equation (8.16)] is the basic theoretical equation for infiltration into a homogeneous porous medium. Because it is nonlinear,

there is no closed-form analytical solution except for highly simplified $\psi-\theta$ and $K_h-\theta$ relations and boundary conditions.

However, as noted in section 7.4.7, the Richards equation can be used as a basis for numerical modeling of infiltration, exfiltration, and redistribution by specifying appropriate boundary and initial conditions, dividing the soil into thin layers, and applying the equation to each layer sequentially at small increments of time. Tests have shown good agreement between the predictions of the numerically solved Richards equation and field and laboratory measurements (Nielsen et al. 1961; Whisler and Bouwer 1970). Šimůnek and van Genuchten (2009) described a flexible numerical model for solving the Richards equation in a variety of applications.

Numerical solutions, however, are not very useful for providing a conceptual overview of the ways in which various factors influence infiltration, and they are generally too computationally intensive for inclusion in operational hydrologic models. Thus there have been many attempts to develop approximate analytical solutions to the Richards equation that can be applied to specific situations such as infiltration (Wang and Dooge 1994). The first and best known of these was developed by Philip (1957, 1969), who formulated an infinite-series solution for ponded infiltration into an indefinitely deep soil with a uniform initial water content:

$$f(t) = \frac{S_p}{2} \cdot t^{-1/2} + A_2 + A_3 \cdot t^{1/2} + A_4 \cdot t + \dots + A_n^{n/2-1}, \quad (8.19)$$

where S_p is the soil **sorptivity** (box 8.2, figure 8.16). As noted in box 8.2, the first term of (8.19) comes from an analytical solution to the Richards equation that applies to the early stages of infiltration when the process is controlled almost exclusively by the pressure gradient. Inclusion of subsequent terms extends the applicability to longer durations, but usually only the first two terms are used. A_2 has the dimensions of a hydraulic conductivity [$L T^{-1}$] and is designated K_p , so that the **Philip equation** is usually written as

$$f(t) = \frac{S_p}{2} \cdot t^{-1/2} + K_p. \quad (8.20a)$$

The cumulative infiltration $F(t)$ is given by the time-integral of equation (8.20a):

$$F(t) = S_p \cdot t^{1/2} + K_p \cdot t. \quad (8.20b)$$

Box 8.2 Approach to Analytical Solutions of the Richards Equation: Diffusivity, Sorptivity, and the Boltzmann Transformation

Diffusivity

In some situations, problems of soil-water movement can be more readily solved by defining the **hydraulic diffusivity**, $D_h(\theta)$, as

$$D_h(\theta) \equiv K_h(\theta) \cdot \frac{\partial \psi(\theta)}{\partial \theta}. \quad (8B2.1)$$

Note that $D_h(\theta)$ has appropriate dimensions of a diffusivity [$L^2 T^{-1}$] (section 3.5.3.2). Equation (8B2.1) allows us to write Darcy's law for vertical unsaturated flow [equation (7.26)] as

$$\begin{aligned} q_{z'} &= K_x(\theta) \cdot \frac{d[z + \psi(\theta)]}{dz'} = K_h(\theta) - K_h(\theta) \cdot \frac{d\psi(\theta)}{dz'} \\ &= K_h(\theta) - D_h(\theta) \cdot \frac{d\theta}{dz'}. \end{aligned} \quad (8B2.2)$$

Using (8B2.1), diffusivity can be expressed as an analytical function of soil properties and water content using the relations in table 7.2. For example, using the Brooks–Corey relations,

$$D_h(\theta^*) = b \cdot |\psi_{ae}| \cdot K_h \cdot \theta^{* b+2}, \quad (8B2.3)$$

thus diffusivity increases with water content for a given soil, and increases as soil-grain size increases (figure 8.15).

Sorptivity

As noted in section 8.2.2, in the earliest stages of vertical infiltration into dry soils, the pressure forces are much greater than the gravity forces. The soil **sorptivity**, S_p , is a measure of the rate at which water will be drawn into an unsaturated soil in the absence of gravity forces (equivalent to horizontal infiltration), and is a function of the initial water content, porosity, hydraulic conductivity, and air-entry tension. Sorptivity arises in formulating analytical solutions for infiltration based on the Richards equation, as described below. Note that the dimensions of S_p are [$L T^{-1/2}$]. Using the Brooks–Corey relations (table 7.2), it can be related to soil properties and the initial soil wetness prior to infiltration, θ_0 , as

$$S_p = \left[(\phi - \theta_0) \cdot K_h \cdot |\psi_{ae}| \cdot \left(\frac{2 \cdot b + 3}{b + 3} \right) \right]^{1/2} \quad (8B2.4)$$

(Rawls et al. 1992). Figure 8.16 shows S_p for sand, loam, and clay soils as a function of initial soil dryness ($\phi - \theta_0$).

Horizontal Infiltration

Figure 8.17 on p. 364 shows an experimental setup for measuring horizontal infiltration. The Richards equation [equation (8.16)] for this situation can be written as

$$\frac{\partial}{\partial x} \left[K_h(\theta) \cdot \left(\frac{\partial \psi(\theta)}{\partial x} \right) \right] = \frac{\partial \theta}{\partial t}, \quad (8B2.5)$$

where x is the horizontal coordinate. This can be written using (8B2.1) as

$$\frac{\partial}{\partial x} \left[D_h(\theta) \cdot \frac{\partial \theta}{\partial x} \right] = \frac{\partial \theta}{\partial t}. \quad (8B2.6)$$

For horizontal infiltration, the conditions for application of (8B2.5) are

$$t = 0, \theta = \theta_0 \text{ at } x > 0;$$

$$x = 0, \theta = \theta_s \text{ at } t \geq 0.$$

The upper graph in figure 8.17 is a schematic plot of data (θ versus x at successive times t_1, t_2, t_3) obtained with the experimental apparatus shown.

The Boltzmann Transform

Boltzmann (1894) formulated a mathematical transform for solving diffusion problems that combines the space and time variables into a single variable Φ :

$$\Phi \equiv x \cdot t^{-1/2}. \quad (8B2.7)$$

This transform allows θ to be expressed as a function of a single variable Φ rather than of both x and t , so that (8B2.5) can be written as an ordinary, rather than a partial, differential equation:

$$\frac{d}{d\Phi} \left[D_h(\theta) \cdot \frac{d\theta}{d\Phi} \right] + \frac{\Phi}{2} \cdot \frac{d\theta}{d\Phi} = 0. \quad (8B2.8)$$

[See Brutsaert (1992) for the steps leading to (8B2.8).] Because of the definition of Φ , the transform is only appropriate when the boundary conditions for $x = 0$ are the same as for $t \rightarrow \infty$, and vice versa. This is true in the present case, and the new boundary conditions are

$$\theta = \theta_0 \text{ for } \Phi \rightarrow \infty,$$

$$\theta = \theta_s \text{ for } \Phi = 0.$$

Now the data can be replotted as a single curve of θ versus Φ , as shown in the lower graph of figure 8.17.

Analytical Solution for Horizontal Infiltration

Following Brutsaert (1992), note that the cumulative volume of infiltrated water, F , is

$$F = \int_{\theta_0}^{\theta_s} x \cdot d\theta. \quad (8B2.9)$$

Substituting the Boltzmann variable [equation (8B2.7)], this becomes

$$F = t^{1/2} \cdot \int_{\theta_0}^{\theta_s} \Phi \cdot d\theta. \quad (8B2.10)$$

Since the integral in (8B2.9) has constant limits, it has a constant value in a given situation, which in fact is the formal definition of the sorptivity (Philip 1957), i.e.,

$$S_p \equiv \int_{\theta_0}^{\theta_s} \Phi \cdot d\theta. \quad (8B2.11)$$

Combining (8B2.9) and (8B2.10) gives a relation for total horizontal infiltration as a function of time:

$$f(t) = S_p \cdot t^{1/2}. \quad (8B2.12)$$

and taking the derivative of this gives an expression for the rate of infiltration as a function of time, $f(t)$:

$$f(t) = \frac{1}{2} \cdot S_p \cdot t^{-1/2}. \quad (8B2.13)$$

These results for horizontal infiltration are applicable to the early stages of vertical infiltration, when the gravitational force is negligible relative to the pressure force that results from the strong contrast in water contents at and near the surface. As discussed in section 8.4.2, additional terms must be added to equations (8B2.11) and (8B2.12) to capture later stages of the process.

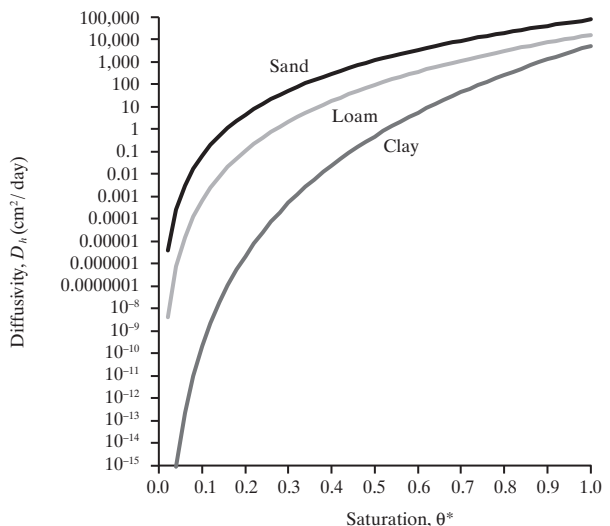


Figure 8.15 Diffusivity, D_h , of typical sand, loam, and clay soils as a function of degree of saturation, θ^* [equation (8B2.3)].

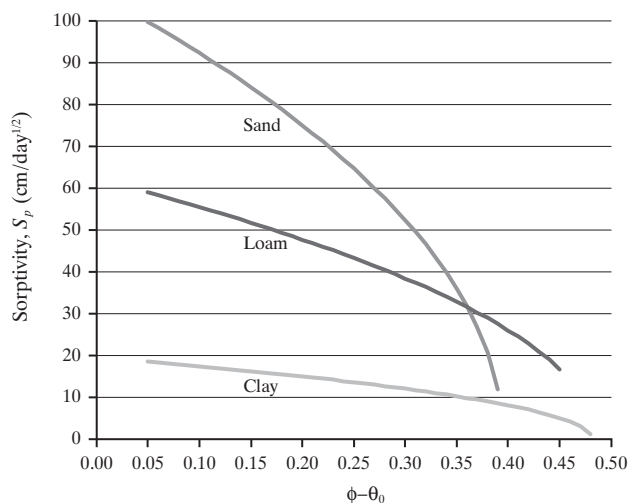


Figure 8.16 Sorptivity, S_p , of typical sand, loam, and clay soils as a function of initial soil dryness, $\phi - \theta_0$ [equation (8B2.4)].

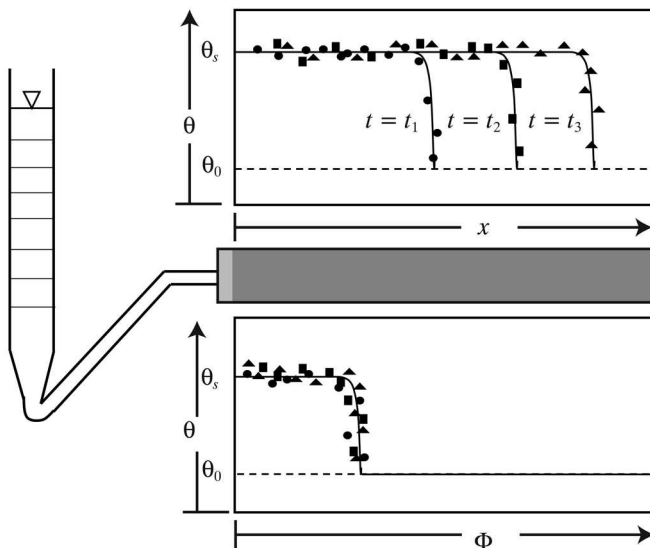


Figure 8.17 Experimental set-up for measuring horizontal infiltration. The upper graph is a schematic plot of θ versus x at successive times t_1, t_2, t_3 obtained with this apparatus. Using the Boltzmann transform (box 8.2), the data can be replotted as a single curve of θ versus Φ , as shown in the lower graph.

Note that equation (8.20a) reproduces the general behavior apparent in figure 8.10: Infiltration rate decreases with time and becomes asymptotic to a constant value. However, Swartzendruber (1997) showed that equation (8.20) is the exact solution of the Richards equation only when $K_h(\theta)$ is a linear function of θ and the level of ponded water increases in proportion to $t^{1/2}$, which are generally unrealistic conditions. Philip's approach has three additional limitations: (1) since it applies only to ponded conditions, it is not directly applicable to flux-controlled infiltration [equation (8.13)], a common situation discussed further below; (2) equations (8.19) and (8.20a) give an infinite initial infiltration rate [$f(0) \rightarrow \infty$]; and (3) the series solution [equation (8.19)] diverges as t increases beyond a certain time and thus ceases to portray the actual behavior.

In spite of these theoretical limitations, the Philip equation has been widely used. It can be applied to modeling flux-controlled infiltration after the time of ponding by applying a time-adjustment approach. To do this, a **compression time**, T_{cp} , is found by solving equation (8.20a) for the time when the infiltration rate equals the water-input rate, w :

$$T_{cp} = \left[\frac{S_p}{2 \cdot (w - K_p)} \right]^2. \quad (8.21)$$

Next, the **apparent time of ponding**, T_{pp} , is calculated as

$$T_{pp} \equiv \frac{F(T_{cp})}{w} = \frac{S_p \cdot T_{cp}^{1/2} + K_p \cdot T_{cp}}{w}. \quad (8.22)$$

Values of $f(t)$ and $F(t)$ are then computed via equation (8.20), but with the **effective time**, t_{ep} , substituted for t , where

$$t_{ep} = t - T_{pp} + T_{cp} \quad (8.23)$$

In application, S_p is usually computed from the soil properties and initial conditions via equation (8B2.4). K_p is often assumed to equal the saturated hydraulic conductivity K_h , although smaller values, in the range $K_h/3 \leq K_p \leq 2 \cdot K_h/3$, may fit measured values better for short time periods (Sharma et al. 1980). Application of equations (8.20)–(8.23) in modeling an infiltration event is illustrated in section 8.4.4.

In many studies S_p and K_p are treated simply as empirical parameters whose values are those that best fit infiltration data measured with infiltrometers as described in box 8.3 and figure 8.18.

Other analytical solutions to the Richards equation have been derived by Swartzendruber (1997), Swartzendruber and Clague (1989), and Salvucci (1996) (among others), but none have proved to be of widespread practical use.

Box 8.3 Least-Squares Estimates of Parameters of the Philip Equation

The Least-Squares Method

Field or laboratory experiments are often conducted to determine the values of parameters that appear in a theoretical equation that characterize a particular process. In such situations, one wants to find the values of the parameters that will give the "best fit" of the equation to the data.

"Best fit" is usually interpreted to mean the parameter values that minimize the sum of the squared differences between the measured values and the values predicted by the theoretical equation. This is called the **least-squares criterion**, and it is represented mathematically as

$$\text{minimize } (SS), \quad (8B3.1)$$

where

$$SS \equiv \sum_{i=1}^N (x_i - \hat{x}_i)^2, \quad (8B3.2)$$

x_i is the i th measured value of the process of interest, \hat{x}_i is the i th value of the process according to the theoretical equation, and N is the number of measured values.

Application to Determining Parameters of the Philip Equation

To determine the values of \hat{S}_p and \hat{K}_p that provide the best fit of the Philip equation [equation (8.20b)] for a particular soil, we measure the cumulative infiltration at successive times using an infiltrometer under ponded (profile-controlled) conditions [equation (8.14)]. In this case equation (8B3.2) becomes

$$SS = \sum_{i=1}^N \left[F(t_i) - \left(\hat{S}_p \cdot t^{1/2} + \hat{K}_p \cdot t \right) \right]^2, \quad (8B3.3)$$

where $F(t_i)$ are the cumulative infiltration amounts measured at N successive times t_i . This expression can be expanded to

$$SS = \sum F_i^2 - 2 \cdot \hat{S}_p \cdot \sum F_i \cdot t_i^{1/2} - 2 \cdot \hat{K}_p \cdot \sum F_i \cdot t_i + \hat{K}_p^2 \cdot \sum t_i^2 + 2 \cdot \hat{K}_p \cdot \hat{S}_p \cdot \sum t_i^{3/2} + \hat{S}_p^2 \cdot \sum t_i, \quad (8B3.4)$$

where $F_i \equiv F(t_i)$ and the summation limits are dropped to simplify the notation.

The values of \hat{S}_p and \hat{K}_p that minimize SS are found by taking the derivative of equation (8B3.4) with respect to each of the parameters, setting the results equal to zero, and solving for the parameters. Taking the derivatives, we find

$$\frac{\partial SS}{\partial \hat{S}_p} = 2 \cdot \hat{S}_p \cdot \sum t_i + 2 \cdot \hat{K}_p \cdot \sum t_i^{3/2} - 2 \cdot \sum F_i \cdot t_i^{1/2} \quad (8B3.5)$$

and

$$\frac{\partial SS}{\partial \hat{K}_p} = -2 \cdot \sum F_i \cdot t_i + 2 \cdot \hat{K}_p \cdot \sum t_i^2 + 2 \cdot \hat{S}_p \cdot \sum t_i^{3/2}. \quad (8B3.6)$$

Setting these expressions equal to zero and solving yields

$$\hat{S}_p = \frac{\sum F_i \cdot t_i^{1/2} - \hat{K}_p \cdot \sum t_i^{3/2}}{\sum t_i} \quad (8B3.7)$$

and

$$\hat{K}_p = \frac{\sum F_i \cdot t_i - \hat{S}_p \cdot \sum t_i^{3/2}}{\sum t_i^2}. \quad (8B3.8)$$

Equation (8B3.8) can be substituted into (8B3.7) and the result solved to give the least-squares estimate of S_p entirely in terms of the measured data, t_i and F_i :

$$\hat{S}_p = \frac{\sum F_i \cdot t_i^{1/2} \cdot \sum t_i^2 - \sum F_i \cdot t \cdot \sum t_i^{3/2}}{\sum t_i^2 \cdot \sum t - (\sum t_i^{3/2})^2}. \quad (8B3.9)$$

Finally, the least-squares estimate of K_p is found by substituting \hat{S}_p from equation (8B3.9) into (8B3.8).

Example Application

The following measurements of cumulative infiltration as a function of time were made via an infiltrometer:

Table 8B3.1

Time, t_i (min)	Cumulative Infiltration (mm)	Time, t_i (min)	Cumulative Infiltration (mm)
1	4	180	21
2	5	240	24
4	6	360	29
6	7	480	34
10	8	600	38
20	10	960	50
30	11	1,140	56
60	14	1,320	61
120	18	1,480	65

(continued)

From these values we calculate the following quantities required for equations (8B3.8) and (8B3.9):

Table 8B3.2

Quantity	Value
$\sum F_i \cdot t_i^{1/2}$	11,512.42 mm · min ^{1/2}
$\sum F_i \cdot t_i$	351,350 mm · min
$\sum t_i^{3/2}$	213,398 min ^{3/2}
$\sum t_i^2$	6,983,457 min ²
$\sum t_i$	7,013 min

Substituting these values into equations (8B3.8) and (8B3.9) gives $\hat{S}_p = 1.58 \text{ mm/min}^{1/2} = 5.98 \text{ cm/d}^{1/2}$; $\hat{K}_p = 0.00212 \text{ mm/min} = 0.306 \text{ cm/d}$. The measured values are compared with those predicted using these parameter estimates in equation (8.20b) in figure 8.18.

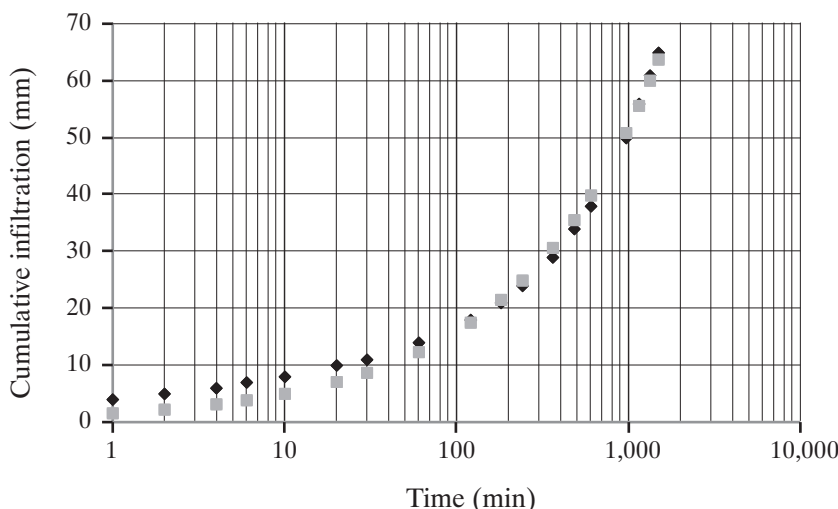


Figure 8.18 Least-squares fit of the Philip equation (squares) to measured infiltration (diamonds) for the example of box 8.3.

8.4.3 The Green-and-Ampt Model

As noted, numerical solutions of the Richards equation are computationally intensive and require detailed soil data that are usually unavailable. Furthermore, they do not succinctly reveal how basic soil properties, initial conditions, and water-input properties affect infiltration. While equation (8.20) gives some insight into how soil properties and initial wetness affect infiltration, it does not reveal the interactions between soil properties, initial conditions, and the characteristics of the rainfall or snowmelt event that determine whether and when ponding develops (section 8.2.2). To better understand these essential aspects of the infiltration process we explore a

model called the **Green-and-Ampt model** after its original formulators (Green and Ampt 1911), following the development of Mein and Larson (1973).

Like the Richards equation, the Green-and-Ampt model applies Darcy's law and the principle of conservation of mass, but in an approximate finite-difference formulation. Although the model applies strictly to highly idealized initial and boundary conditions, it allows informative exploration of varying water-input conditions and shows directly how soil properties and antecedent water-content conditions affect the infiltration process. The predictions of this model have been successfully tested against numerical solutions of the Richards equation (Mein and Larson 1973).

8.4.3.1 Idealized Conditions

As in the derivation of the Richards equation [equation (8.16)], z is the upward-directed vertical axis (elevation), z' indicates the downward vertical direction, $f(t)$ is the infiltration rate at time t [$L T^{-1}$], and $F(t)$ is the total amount of water infiltrated up to time t [L].

Consider a block of soil that is homogeneous to an indefinite depth (i.e., porosity, ϕ , and saturated hydraulic conductivity, K_h , are given parameters that are invariant throughout, and there is no water table, capillary fringe, or impermeable layer) and which has a horizontal surface at which there is no evapotranspiration. The water content just prior to $t = 0$ is also constant with depth at an initial value $\theta(z', 0) = \theta_0 < \theta_{fc}$. (Note that in real situations, the initial water-content profile is likely to look more like an equilibrium profile, as described in section 8.1.5.)

Just before water input begins at $t = 0$, there is no water-content gradient and therefore no pressure gradient, so the downward flux of water, $q_{z'}(z', 0)$, is given by equation (8.1) as

$$q_{z'}(z, 0) = K_h(\theta_0). \quad (8.24)$$

Note that this is not a steady-state situation because the soil is gradually draining, but if we further assume that $\theta_0 \ll \theta_{fc}$, $q_{z'}(z, 0)$ can be considered negligible.

Beginning at time $t = 0$, liquid water (rain or snowmelt) begins arriving at the surface at a specified rate w and continues at this rate for a specified time T_w . We need to consider two cases: (1) $w < K_h$ and (2) $w \geq K_h$.

8.4.3.2 Water-Input Rate Less Than Saturated Hydraulic Conductivity

Consider a soil with the $K_h(\theta)$ relation shown in figure 8.19 that is subject to a constant water-input rate w for a duration T_w . If the initial water content θ_0 is such that $K_h(\theta_0) < w$, water enters the surface layer faster than it is leaving because $q_{z'} = K_h(\theta_0) < w$. Thus water goes into storage in the layer, increasing its water content. The increase in water content causes an increase in hydraulic conductivity (arrows in figure 8.19), so the flux out of the layer, $q_{z'}$, increases. This increase continues until the water content equals θ_w , the value at which $q_{z'} = w$. At this point, the rate of outflow equals the rate of inflow, and there is no further change in water content in the surface layer until water input ceases. This process happens successively in each layer as water input continues, producing a descending wetting front at which water content decreases abruptly: above the front, $\theta = \theta_w$; below it, $\theta = \theta_0$. This process results in the successive water-content profiles shown in figure

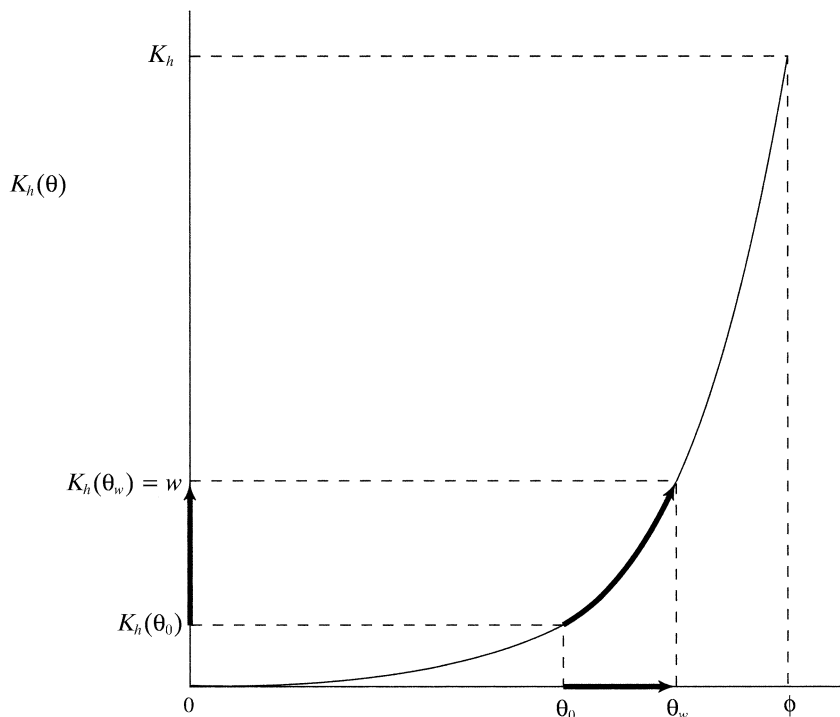


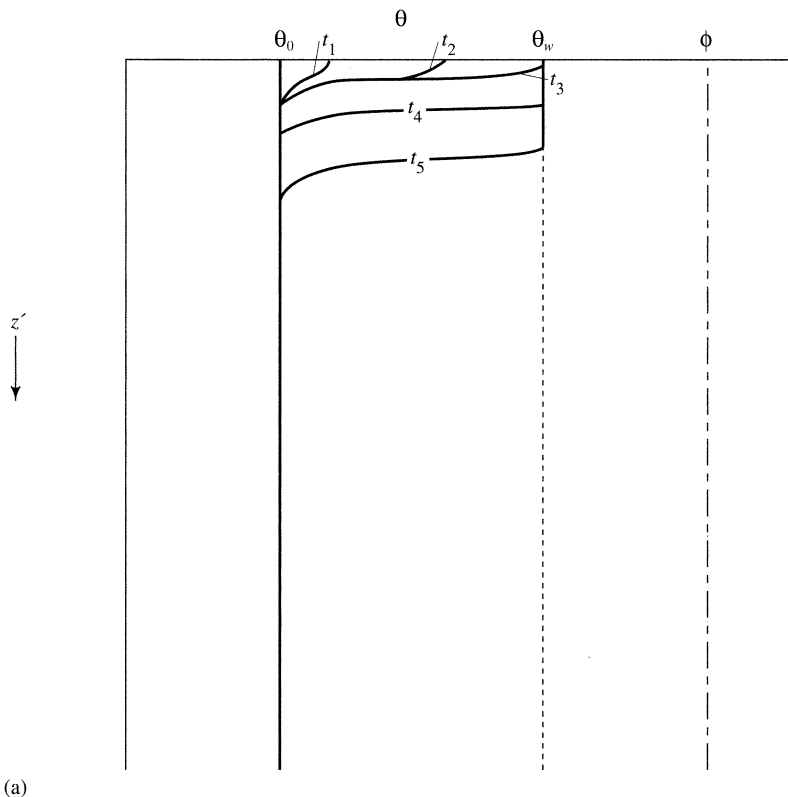
Figure 8.19 Conceptual basis of the Green-and-Ampt model. Arrows show changes in hydraulic conductivity, $K_h(\theta)$, with water content, θ , during water input at a rate w , where $K_h(\theta_0) < w = K_h(\theta_w) < K_h$. Water content at successive depths increases until $K_h(\theta_w) = w$.

8.20a and the corresponding graph of infiltration at the rate $f = w$ shown in figure 8.20b. As the wetting front descends, the importance of the pressure (capillary) forces decreases because the denominator of the $\partial\theta/\partial z'$ term of equation (8.1) increases, thus the rate of downward flow approaches $K_h(\theta_w)$.

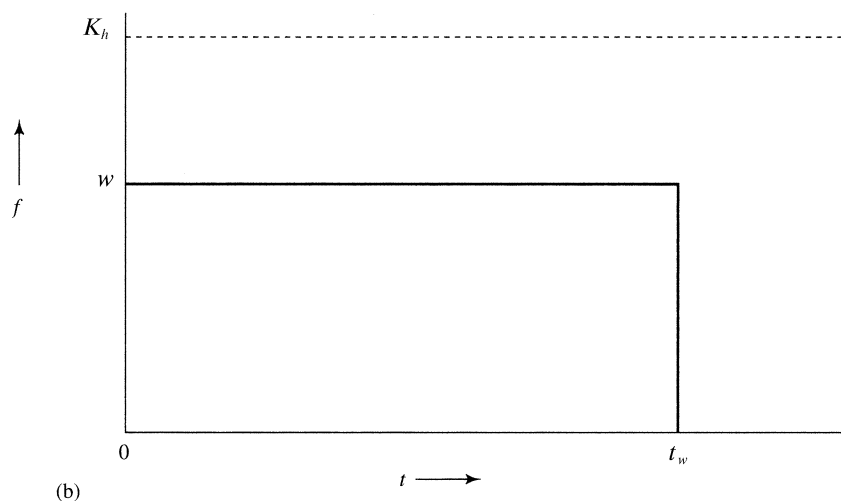
This analysis leads to the following model:

If the water-input rate is less than the saturated hydraulic conductivity ($w < K_h$), the infiltration rate equals the water-input rate until input ceases:

$$f(t) = w; 0 < t \leq T_w. \quad (8.25)$$



(a)



(b)

Figure 8.20 Conceptual basis of the Green-and-Ampt model. (a) Successive water-content profiles (t_1, t_2, \dots denote successive times) and (b) infiltration rate versus time for infiltration into a deep soil when $w < K_h$.

8.4.3.3 Water-Input Rate Greater Than Saturated Hydraulic Conductivity

When $w > K_h$, the process just described will occur in the early stages of infiltration. Water will arrive at each layer faster than it can be transmitted downward and will initially go into storage, raising the water content and the hydraulic conductivity (figure 8.19). However, the water content cannot exceed its value at saturation, ϕ , and the hydraulic conductivity cannot increase beyond K_h . Once the surface layer reaches saturation, the wetting front begins to descend, with $\theta = \phi$ above the wetting front

and $\theta = \theta_0$ below it (figure 8.21a). As in the previous situation, the pressure force decreases as the wetting front descends while the gravity force remains constant; thus the downward flux decreases, approaching $q_z' = K_h$ (figure 8.21b). After the surface reaches saturation, the excess accumulates on the surface as ponding because $w > K_h$. However, some rain continues to infiltrate and the wetting front continues to descend as long as the input continues. (If the ground is sloping, the excess moves downslope as *overland flow* or *surface runoff*, as discussed further in chapter 10.)

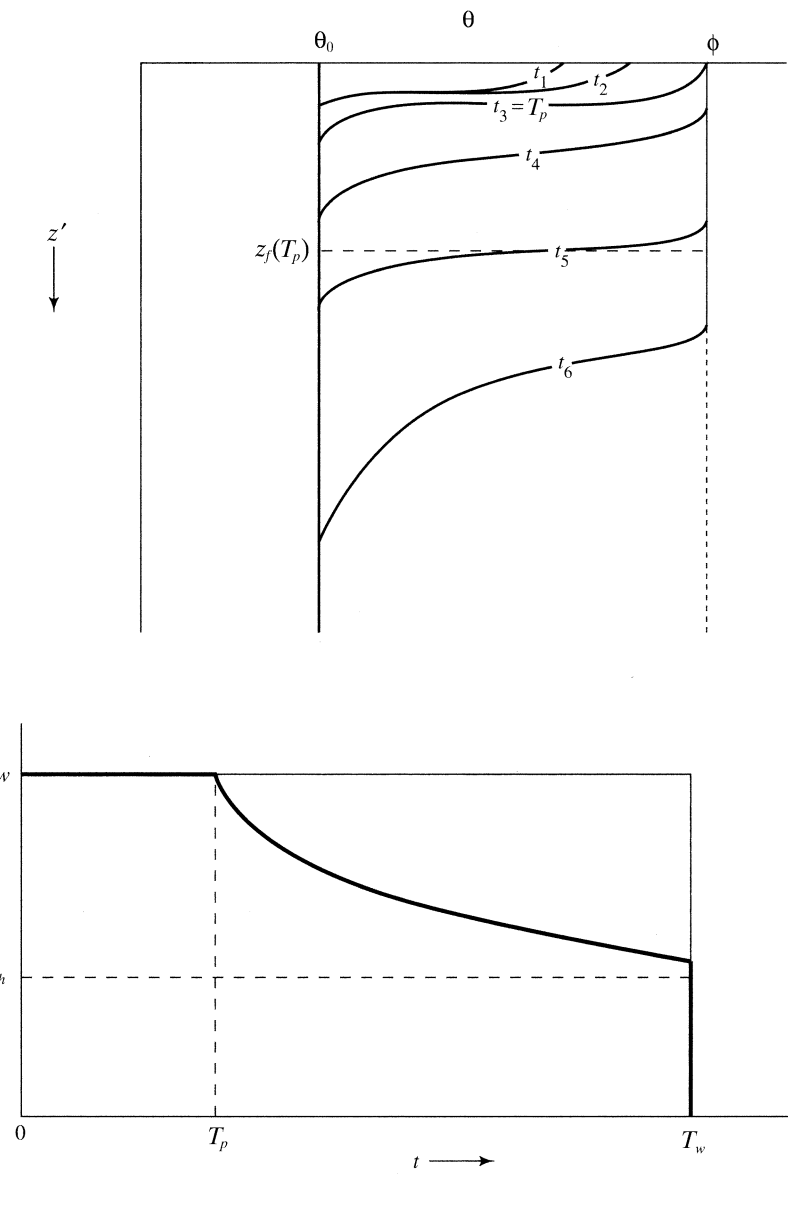


Figure 8.21 Conceptual basis of the Green-and-Ampt model. (a) Successive water-content profiles (t_1, t_2, \dots denote successive times). Dashed lines show average wetting-front depths at the time of ponding, $z_f(T_p)$, and at some arbitrary later time $t_5, z_f(t_5)$. (b) Infiltration rate versus time for infiltration into a deep soil when $w > K_h$.

The instant when the surface layer becomes saturated is called the **time of ponding**, designated T_p . We can develop an equation to compute T_p by approximating the wetting front as a perfectly sharp boundary (horizontal line), which is at a depth $z_f'(T_p)$ at $t = T_p$. Up to this instant, all the rain that has fallen has infiltrated, so

$$F(T_p) = w \cdot T_p. \quad (8.26)$$

All this water occupies the soil between the surface and $z_f'(T_p)$, so

$$F(T_p) = z_f'(T_p) \cdot (\phi - \theta_0). \quad (8.27)$$

Combining equations (8.26) and (8.27) yields

$$T_p = \frac{z_f'(T_p) \cdot (\phi - \theta_0)}{w}. \quad (8.28)$$

In order to use equation (8.28), we need to determine $z_f'(T_p)$. This is done by applying Darcy's law [equation (8.1)] in finite-difference form between the surface and the depth $z_f'(T_p)$:

$$q_{z'}(0, T_p) = f(T_p) = w = K_h - K_h \cdot \frac{\psi_f - 0}{z_f'(T_p)}, \quad (8.29)$$

where ψ_f is the effective tension at the wetting front (discussed further below). This relation is justified because at the instant of ponding we have saturation at the surface, so the tension there is 0, the hydraulic conductivity is equal to its saturation value, and the infiltration rate is just equal to the rainfall rate. Noting that $\psi_f < 0$, we can solve equation (8.29) for $z_f'(T_p)$:

$$z_f'(T_p) = \frac{K_h \cdot |\psi_f|}{w - K_h}. \quad (8.30)$$

Substitution of equation (8.30) into (8.28) then yields

$$T_p = \frac{K_h \cdot |\psi_f| \cdot (\phi - \theta_0)}{w \cdot (w - K_h)} \quad (8.31)$$

as the equation for time of ponding. This expression has a logical form in that T_p increases with increasing K_h , $|\psi_f|$, and the initial soil-water deficit $(\phi - \theta_0)$; and decreases with increasing w .

As water input continues after the time of ponding, infiltration continues at a rate given by Darcy's law as

$$\begin{aligned} f(t) &= q_{z'}[z_f'(t), H(t)] \\ &= K_h - K_h \cdot \frac{\psi_f + H(t)}{z_f'(t)} = f^*(t), \end{aligned} \quad (8.32)$$

where $H(t)$ is the depth of ponding and f^* is the infiltration capacity (infiltrability). Thus the infiltration rate decreases with time (as in figure 8.10 and 8.21b) because the gradient producing the pressure force (capillary suction) decreases with time as the wetting-front depth $z_f'(t)$ increases.

Since $H(t)$ is in general a complicated function that depends on the amount of infiltration up to time t and the surface slope and roughness, and since satisfactory results for many natural situations have been obtained by assuming $H(t)$ is negligible (as will be shown later), our subsequent analysis will assume $H(t) = 0$. Then noting that

$$F(t) = z_f'(t) \cdot (\phi - \theta_0), \quad (8.33)$$

we can solve this expression for $z_f'(t)$ and substitute it into equation (8.32) to yield

$$\begin{aligned} f(t) &= f^*(t) \\ &= K_h \cdot \left[1 + \frac{|\psi_f| \cdot (\phi - \theta_0)}{F(t)} \right], \quad T_p \leq t \leq T_w, \end{aligned} \quad (8.34)$$

which is the Green-and-Ampt equation for infiltration after ponding occurs.

Equation (8.34) gives the infiltration rate as a function of the total infiltration that has occurred after the time of ponding. For this to be useful, we need a relation between $f(t)$ or $F(t)$ and t , and we can derive such a relation if we recognize that

$$f(t) = \frac{dF(t)}{dt}. \quad (8.35)$$

With equation (8.35), we see that equation (8.34) is a differential equation that can be solved to yield a relation for t as a function of $F(t)$ after the time of ponding:

$$\begin{aligned} t &= \frac{F(t) - F(T_p)}{K_h} + \left[\frac{|\psi_f| \cdot (\phi - \theta_0)}{K_h} \right]. \\ \ln \left[\frac{F(T_p) + |\psi_f| \cdot (\phi - \theta_0)}{F(t) + |\psi_f| \cdot (\phi - \theta_0)} \right] &+ T_p \end{aligned} \quad (8.36)$$

for $F(t) > F(T_p)$ ($T_p \leq t \leq T_w$). Thus the Green-and-Ampt model states that

If the water-input rate is greater than or equal to the saturated hydraulic conductivity ($w \geq K_h$), ponding occurs. As input continues the infiltration rate $f(t)$ gradually declines, becoming asymptotic to K_h .

Thus the Green-and-Ampt model predicts the same behavior given by the approximate solutions to the Richards equation in equation (8.20) and observed in nature. Unfortunately, however, equation (8.36) cannot be inverted to give $F(t)$ as an explicit function of t , which would be more convenient. Thus application of equation (8.36) requires arbitrarily choosing values of $F(t)$ and solving for t . If the chosen value of $F(t)$ gives $t < T_p$ or $t > T_w$, it is invalid. The corresponding infiltration rate $f(t)$ is then found by substituting valid values of $F(t)$ in equation (8.34), and the corresponding depth of wetting front, $z_f'(t)$, can be computed from equation (8.33). Explicit relations that closely approximate the Green-Ampt equations are discussed in section 8.4.3.5.

8.4.3.4 Estimation of Effective Soil-Hydraulic Properties

In order to use equation (8.36) we must determine appropriate values of the properties ϕ , K_h , and

ψ_f for the soil of interest. Lacking measurements of ϕ and/or K_h , values can be estimated using the pedo-transfer functions (PTFs) (table 7.3), or the soil-hydraulic triangle (figure 7.20, table 7.4). In general, the wetting-front suction ψ_f is a function of time, ponding depth, initial water content, and soil type. However, Freyberg et al. (1980) explored several definitions of ψ_f that are appropriate in different situations and concluded that they had only minor effects on calculated infiltration rates. Thus for general purposes, the wetting-front suction $|\psi_f|$ can be estimated using the Brooks-Corey parameters (table 7.2) as

$$|\psi_f| = \frac{2 \cdot b + 3}{2 \cdot b + 6} \cdot |\psi_{ae}| \quad (8.37)$$

(Rawls et al. 1992), or by reference to figure 8.22. An example application of the Green-and-Ampt model is given in section 8.4.4.

8.4.3.5 Explicit Form

The need to use a trial-and-error solution method makes direct use of the Green-and-Ampt model inconvenient for incorporation into models of land-surface hydrologic processes. To get around this problem, Salvucci and Entekhabi (1994a) developed a close approximation to the Green-and-Ampt equations that gives $f(t)$ and $F(t)$ as explicit functions of t . Their approach requires computation of three time parameters similar to those developed in section 8.4.2 for the Philip equation:

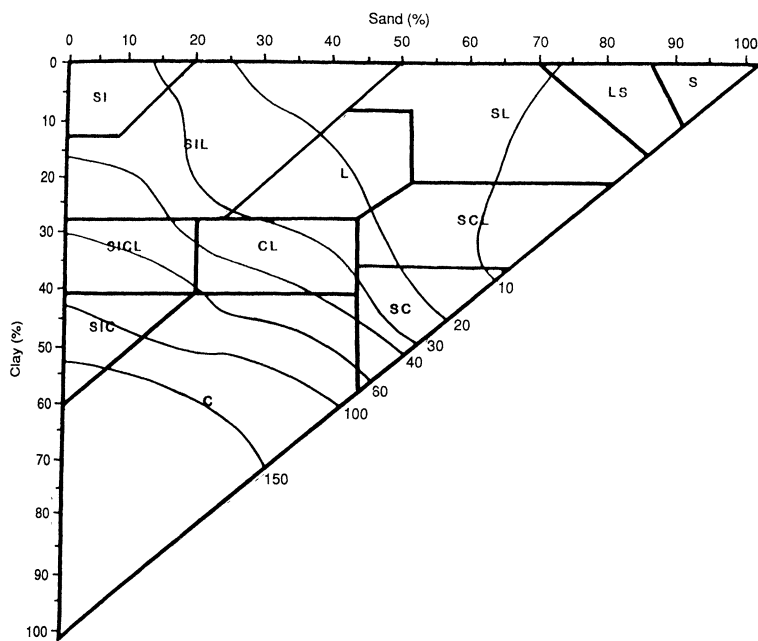


Figure 8.22 Green-Ampt wetting-front suction $|\psi_f|$ as a function of soil texture [reprinted with permission from "A procedure to predict Green Ampt infiltration parameters" by W. J. Rawls and D. L. Brakensiek. In *Advances in Infiltration* (pp. 102–112). Copyright 1983 American Society of Agricultural Engineers].

1. A **characteristic time**, T^* , which depends on soil type and the initial water content:

$$T^* \equiv \frac{|\psi_f| \cdot (\phi - \theta_0)}{K_h}; \quad (8.38)$$

2. A **compression time**, T_c , which is the equivalent time to infiltrate $F(T_p) = w \cdot T_p$ under initially ponded conditions, as given by the Green-and-Ampt relation:

$$T_c \equiv \frac{w \cdot T_p}{K_h} - \left[\frac{|\psi_f| \cdot (\phi - \theta_0)}{K_h} \right] \cdot \ln \left[1 + \frac{w \cdot T_p}{|\psi_f| \cdot (\phi - \theta_0)} \right], \quad (8.39)$$

where T_p is time of ponding computed via equation (8.31); and

3. An **effective time**, t_e , defined as

$$t_e \equiv t - T_p + T_c. \quad (8.40)$$

The complete explicit solution is an infinite series giving the infiltration rate $f(t_e)$ as a function of the effective time, t_e , and the characteristic time, T^* . However, retaining the first four terms gives sufficient accuracy for most purposes:

$$f(t_e) = K_h \cdot \left[0.707 \cdot \left(\frac{t_e + T^*}{t_e} \right)^{1/2} + 0.667 - 0.236 \cdot \left(\frac{t_e}{t_e + T^*} \right)^{1/2} - 0.138 \cdot \left(\frac{t_e}{t_e + T^*} \right) \right]. \quad (8.41)$$

The cumulative infiltration $F(t_e)$ is then found by integrating (8.41):

$$F(t) = K_h \cdot \left\{ 0.529 \cdot t_e + 0.471 \cdot (T^* \cdot t_e + t_e^2)^{1/2} + 0.138 \cdot T^* \cdot [\ln(t_e + T^*) - \ln(T^*)] + 0.471 \cdot T^* \cdot \left\{ \ln \left[t_e + T^*/2 + (T^* \cdot t_e + t_e^2)^{1/2} \right] - \ln(T^*/2) \right\} \right\}. \quad (8.42)$$

Section 8.4.4 gives an example application of the explicit method, and compares the results with the implicit Green-and-Ampt approach.

An alternative approach to deriving an explicit form of the Green-Ampt relation is described by Swamee et al. (2012).

8.4.3.6 Application to Shallow Soils (Saturation from Below)

As we have just seen, the Green-and-Ampt model provides useful insight into infiltration and the phenomenon of potential runoff formation by saturation from above when $w > K_h$ and $t_w > T_p$ in deep homogeneous soils with a uniform initial water content θ_0 . We can use the same approach to explore infiltration in soils underlain by an impermeable layer or by a water table at a relatively shallow depth, which can lead to saturation from below. Once such saturation occurs, infiltration ceases and surface storage builds up; as with saturation from above, this water is potential overland flow (runoff). This situation will be explored in chapter 10.

In this development, Z_u' represents the depth of an impermeable layer or of the top of the tension-saturated zone above a water table. As for the deep-soil case, we examine two cases: (1) water-input rate less than saturated hydraulic conductivity and (2) water-input rate greater than saturated hydraulic conductivity.

8.4.3.6.1 Water-Input Rate Less Than Saturated Hydraulic Conductivity

If $K_h(\theta_0) < w < K_h$, infiltration will occur at the rate w until the time, T_b , at which the soil between the surface and the impermeable layer becomes saturated, i.e.,

$$f(t) = w, 0 < t < T_b \quad (8.43)$$

and

$$F(t) = w \cdot t, 0 < t < T_b, \quad (8.44)$$

where T_b is calculated as developed below.

Water storage will occur at each successive depth until $q_z(\theta) = w$, at which point the water content is designated θ_w . Again assuming a piston-like wetting front, above which $\theta = \theta_w$ and below which $\theta = \theta_0$, we can combine the continuity relation,

$$F(t) = (\theta_w - \theta_0) \cdot z_f'(t), \quad (8.45)$$

with equation (8.44) to get the position of the wetting front, $z_f'(t)$, as a function of time:

$$z_f'(t) = \frac{w \cdot t}{\theta_w - \theta_0}. \quad (8.46)$$

From this we can calculate the time it takes the wetting front to reach the impermeable boundary (i.e., when, $z_f'(t) = Z_u'$):

$$T_u = \frac{(\theta_w - \theta_0) \cdot Z_u'}{w}. \quad (8.47)$$

If $T_w > T_u$, water will continue to arrive at the impermeable layer and the water content just above the layer will increase until it reaches saturation. At this point an upward-moving wetting front will develop, below which $\theta = \phi$ and above which $\theta = \theta_w$. As long as water input continues, the position of this front, $z_f'(t)$, is given by

$$z_f'(t) = Z_u' - \frac{w \cdot (t - T_u)}{\phi - \theta_w}, \quad t > T_u. \quad (8.48)$$

By combining equations (8.47) and (8.48) we can calculate the time, T_b , when the saturated front reaches the surface:

$$T_b = \frac{Z_u' \cdot (\phi - \theta_0)}{w}. \quad (8.49)$$

At the instant the saturation front reaches the surface we have saturation from below, infiltration will decrease abruptly from $f(t) = w$ to $f(t) = 0$, and water will begin to build up on the surface. Note that if Z_u' represents the top of a tension-saturated zone, the pressure state of the zone will change from tension to positive pressure as soon as the water content at Z_u' reaches saturation. As discussed in section 10.4.3.2, this phenomenon can produce sudden ground-water movement to streams.

8.4.3.6.2 Water-Input Rate Greater Than Saturated Hydraulic Conductivity

If $w \geq K_h$ and $T_b \leq T_p$, the analysis of the section immediately preceding applies and we have saturation from below. If $T_b > T_p$, ponding occurs due to saturation from above and infiltration begins to decrease when $t = T_p$, just as in the deep-soil case. The position of the wetting front for $t > T_p$ can be found from equations (8.33) and (8.36), and the instant when $z_f'(t) = Z_u'$ can be identified. Since the Green-and-Ampt model assumes saturation above the wetting front, the entire soil layer is saturated and infiltration ceases at this instant. This situation thus involves simultaneous saturation from above and below.

8.4.3.7 Infiltration with Depth-Varying Water Content

As shown in figure 8.8, the presence of a water table near the surface tends to cause the water-con-

tent profile to be nonuniform. When water content increases with depth as in typical equilibrium profiles, the descending wetting front encounters pores that are increasingly occupied with water. Thus with a constant water-input rate the wetting-front descends more rapidly than with the homogeneous initial water content assumed in the Green-and-Ampt model, and continuously accelerates. The wetting front thus reaches the top of the tension-saturated zone more quickly than calculated in the preceding analysis for uniform initial water content.

Salvucci and Entekhabi (1995) derived a Green-and-Ampt-like approach to calculating the infiltration with nonuniform (i.e., equilibrium) water-content profiles. An example comparing their calculations with simulations using the finite-element solutions to the Richards equations is shown in figure 8.23.

8.4.3.8 Summary

The system of equations (8.26) through (8.36) provides a complete model of the infiltration process for cases where $w > K_h$ and the other assumptions of the idealized situation apply—most importantly, the representation of the wetting front as an abrupt “piston-like” discontinuity and a homogeneous initial water-content profile. Mein and Larson (1973) compared infiltration predictions using this model with those derived by numerical solution of the Richards equation, and found the excellent correspondence shown in figure 8.24.

Thus in spite of its development from idealized conditions, the Green-and-Ampt model captures the essential aspects of the infiltration process, in particular the complete infiltration of rain up to the time of ponding and the quasi-exponential decline of infiltration rate thereafter. This decline is due to the steadily decreasing pressure gradient, $\psi_f/z_f'(t)$, as the wetting front descends, and is asymptotic to K_h . Thus the minimum value of infiltrability for a soil is its saturated hydraulic conductivity. A valuable feature of the model is that its parameters are measurable bulk physical properties of the soil that affect infiltration in intuitively logical ways.

The assumption of a piston-like wetting front is closer to reality for sands than for clays, in which the wetting front tends to be less distinct. The computation of equilibrium water-content profiles (figure 8.7) suggests that the assumption of homogeneous initial water content is better for clays than sands; the profile also becomes more homogeneous for deeper water tables for all soil types (figure 8.8).

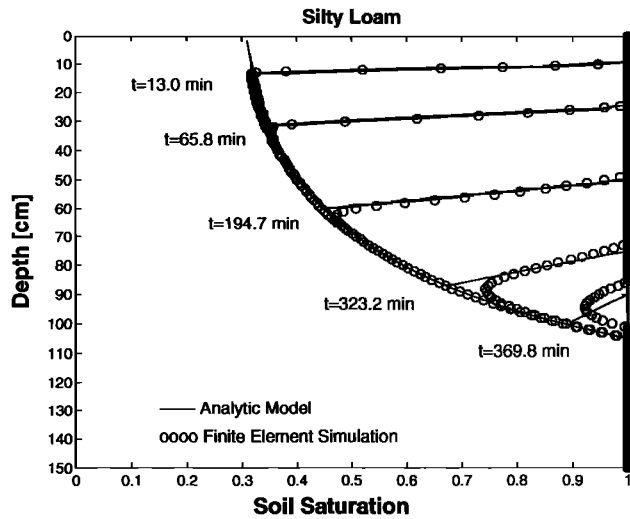


Figure 8.23 Comparison of wetting fronts predicted by the Green-Ampt-type model of Salvucci and Entekhabi (1995) with simulations using finite-element solutions to the Richards equations for a silt-loam soil [Salvucci and Entekhabi (1995)]. Ponded infiltration into soils bounded by a water table. *Water Resources Research* 31:2751–2759, with permission of the American Geophysical Union].

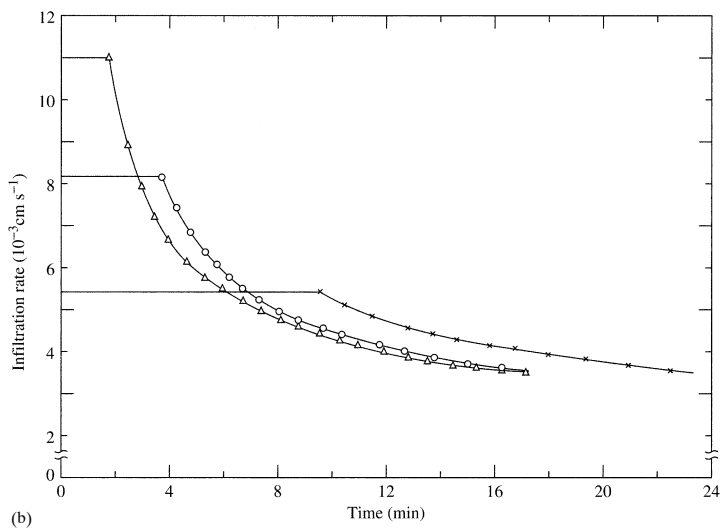
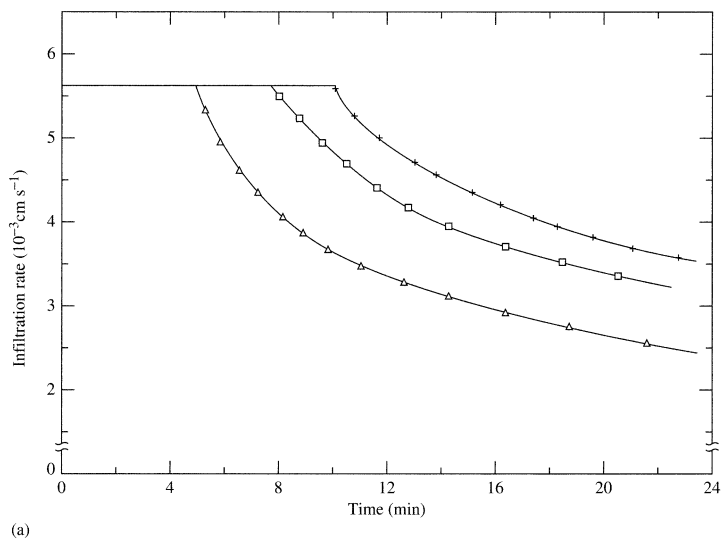


Figure 8.24 Comparison of infiltration rates computed by the Green-and-Ampt model (symbols) with those computed by numerical solution of the Richards equation (lines). (a) The effects of initial water content, θ_0 , for an identical water-input event. (b) The effect of water-input rates, w , for identical θ_0 [Mein and Larson (1973). Modeling infiltration during a steady rain. *Water Resources Research* 9:384–394, with permission of the American Geophysical Union].

The Green-and-Ampt model has been extended for application to conditions of unsteady rain (Chu 1978), time-varying depths of ponding (Freyberg et al. 1980), and soils in which K_h decreases with depth continuously (Beven 1984) or in discrete layers (Rawls et al. 1992). Rawls et al. (1992) also describe an approach that adapts the Green-and-Ampt approach where macropores are important.

8.4.4 Comparison of Green-and-Ampt and Philip Models

Box 8.4 on pp. 376–378 compares infiltration-rate calculations using the Green-and-Ampt implicit, Green-and-Ampt explicit, and Philip approaches. The results are compared in table 8B4.2 and figure 8.25 (on p. 379). In this case, the Green-Ampt explicit model gives rates virtually identical to the original implicit approach, while the Philip relation predicts somewhat higher rates. Using a K_p value slightly less than K_h would bring the Philip predictions very close to those of Green-Ampt.

8.5 Infiltration Over Areas

8.5.1 Spatial and Temporal Variability of Infiltration

Detailed field studies generally show a very high degree of spatial variability of infiltrability and the factors that affect infiltration rates, particularly saturated hydraulic conductivity. The experiments of Burgy and Luthin (1956) give a striking example of this variability. They first measured the infiltrability of an unvegetated clay soil by flooding a 335-m² basin and measured the rate of decline of the water level. After this water had completely infiltrated, they made ring-infiltrometer measurements at 119 sites evenly spaced throughout the basin. The average value for the infiltrometer measurements, 16.8 cm/hr, was reasonably close to the basin value of 10.8 cm/hr, but the infiltrometer values ranged from near zero to over 110 cm/hr.

Sharma et al. (1980) found an 11-fold and 29-fold variation in the Philip-equation parameters S_p and K_p , respectively, and a 7.5-fold variation in total infiltration for a 30-min storm over a 0.096-km² watershed in Oklahoma, with no consistent relation between these quantities and location or soil type. In another detailed study in that same watershed, Loague and Gander (1990) found that the scale of spatial correlation

(defined in section 4.3.2.6) of infiltration was less than 20 m, that there was little spatial structure to the data, and that infiltration rates were strongly influenced by animal activity, vegetation, and climate rather than by soil texture. Buttle and House (1997) found similar results in Ontario, where saturated hydraulic conductivity was largely determined by macropores.

In other small-watershed-scale studies in humid areas, Tricker (1981) measured infiltrability (infiltration rates after 1 hr of ponded infiltration) over a 3.6-km² watershed in England and found values ranging from near zero to 256 cm/hr; these values were positively related to the thickness of the surface organic layer but unrelated to soil texture or soil-water content. Measurements on a 15.7-km² watershed in Northern Ireland found a considerably lower range of variability in infiltrability, but a similar dependence on soil organic matter rather than soil texture (Wilcock and Essery 1984). This latter study also found a substantial seasonal variability, with average infiltrability considerably higher in summer (0.9 cm/hr in June) than in winter (0.06 cm/hr in January).

Springer and Gifford (1980) repeatedly measured infiltrability with infiltrometers at 20 to 25 locations on a plowed and grazed rangeland area in Idaho and found coefficients of spatial correlation [equation (4.25)] in the range of 0.40 to 0.68 and little seasonal variation. In another semiarid area, Berndtsson (1987) found a very high degree of spatial variability in the coefficients of the Philip equation over a 19.6-km² catchment in Tunisia: values of S_p and K_p had coefficients of variation [equation (C.20)] exceeding 1.00. Schumm and Lusby (1963) found wide seasonal variations in infiltrability in a sparsely vegetated badlands area.

The dominant conclusions of these and other field studies are: (1) infiltration varies greatly over short (1- to 20-m) distances and (2) the variations are often not related to soil textures but are instead determined by plant and animal activity and by small-scale topographic variations. These conclusions make it difficult to transfer an understanding of the process at a point to its representation over a watershed. Some approaches to this problem are discussed in the next section.

8.5.2 Modeling Infiltration Over Areas

8.5.2.1 Theoretical Scaling Approaches

A logical approach to “scaling up” a point-process model to an area would be to divide the area into

Box 8.4 Example Calculations Comparing the Green-and-Ampt Implicit, Green-and-Ampt Explicit, and Philip Equations

Here we compare infiltration-rate calculations using the Green-and-Ampt implicit, Green-and-Ampt explicit, and Philip approaches for a constant rain of $w = 2 \text{ cm/hr}$ lasting $T_w = 2 \text{ hr}$ on a soil with 20% sand, 60% silt, and 20% clay and an initial water content of $\theta_0 = 0.350$. From figure 7.5, the soil is a silt loam; referring to figure 7.21, the soil is hydraulic class B3, and from table 7.5 we find $\phi = 0.413$ and $K_h = 10^{1.197} = 15.7 \text{ cm/d} = 0.656 \text{ cm/hr}$. From figure 8.22 we find $|\psi_f| = 30 \text{ cm}$.

Green-Ampt Implicit Method

Since $w > K_h$, there is potential for ponding, and we compute the time of ponding, T_p via equation (8.28):

$$T_p = \frac{(0.656 \text{ cm/hr}) \times (30 \text{ cm}) \times (0.413 - 0.350)}{(2.00 \text{ cm/hr}) \times (2.00 \text{ cm/hr} - 0.656 \text{ cm/hr})} = 0.461 \text{ hr.}$$

Since $T_p < T_w$, there is ponding. The infiltration rate is constant at the rainfall rate, 2.00 cm/hr, from $t = 0$ to $t = 0.461 \text{ hr}$, and the cumulative infiltration during this time is given by equation (8.23) as

$$F(T_p) = (2.00 \text{ cm/hr}) \times (0.461 \text{ hr}) = 0.923 \text{ cm.}$$

Now we select a series of $F(t)$ values such that $F(t) > F(T_p)$ and compute the corresponding t values via equation (8.36), $f(t)$ via equation (8.34), and $z_f'(t)$ via equation (8.27):

Table 8B4.1

$F(t)$ (cm)	$f(t)$ (cm/hr)	$z_f'(t)$ (cm)	t (hr)	Comments
0	2.00	0	0	Begin event
0.92	2.00	14.6	0.46	Time of ponding
1.00	1.89	15.9	0.50	
1.10	1.78	17.5	0.56	
1.20	1.68	19.0	0.61	
1.30	1.61	20.6	0.67	
1.40	1.54	22.2	0.74	
1.50	1.48	23.8	0.80	
1.60	1.43	25.4	0.87	
1.70	1.38	27.0	0.94	
1.80	1.34	28.6	1.02	
1.90	1.30	30.2	1.09	
2.00	1.27	31.7	1.17	
2.10	1.24	33.3	1.25	
2.20	1.22	34.9	1.33	
2.30	1.19	36.5	1.42	
2.40	1.17	38.1	1.50	
2.50	1.15	39.7	1.59	
2.60	1.13	41.3	1.67	
2.70	1.11	42.9	1.76	
2.80	1.10	44.4	1.85	
2.90	1.08	46.0	1.95	
3.00	1.07	47.6	2.04	Calculated $t > T_w$

The last $F(t)$ value selected, 3.00 cm, gives $t > T_w$, so that is not a meaningful value. By trial and error, $F(t) = 2.95$ cm gives $t \approx 2.00$ hr = T_w with corresponding final values of $f(T_w) = 1.07$ cm/hr and $z_f'(T_w) = 46.9$ cm. Thus for this storm under these conditions, 2.95 cm infiltrates and $4.00 - 2.95 = 1.05$ cm runs off.

Green-Ampt Explicit Method

Here we calculate the infiltration rate using the explicit forms of the Green-and-Ampt relations for the same soil, storm, and initial conditions as the previous example.

First compute T^* from equation (8.35):

$$T^* = \frac{30 \text{ cm} \times (0.413 - 0.350)}{0.654 \text{ cm/hr}} = 2.89 \text{ hr.}$$

We found above that $T_p = 0.461$ hr and $F(T_p) = 0.923$ cm. Substituting these values into equation (8.36) yields

$$T_c = \frac{0.923 \text{ cm}}{0.654 \text{ cm/hr}} - \left[\frac{30.0 \text{ cm} \times (0.413 - 0.350)}{0.654 \text{ cm/hr}} \right] \times \\ \ln \left[1 + \frac{0.923 \text{ cm}}{30.0 \text{ cm} \times (0.413 - 0.350)} \right] = 0.260 \text{ hr.}$$

Finally, compute t_e via equation (8.40):

$$t_e = t - 0.461 \text{ hr} + 0.260 \text{ hr} = t - 0.201 \text{ hr.}$$

Now we can select a series of times, $t, T_p \leq t \leq T_w$, calculate the corresponding values of t_e , then compute the corresponding $f(t)$ via equation (8.38), $F(t)$ via equation (8.39), and wetting-front depth, $z_f'(t)$, via equation (8.27).

To compare the explicit and implicit results for this example, we select the times computed by the implicit method in table 8B4.1, and compare the corresponding values of $f(t)$ computed by the two methods here and in figure 8.23:

Table 8B4.2

t (hr)	Green-Ampt Implicit $f(t)$ (cm/hr)	Green-Ampt Explicit $f(t)$ (cm/hr)	Philip $f(t)$ (cm/hr)
0	2.00	2.00	2.00
0.46	2.00	2.00	2.00
0.50	1.89	1.89	1.93
0.56	1.78	1.77	1.83
0.61	1.68	1.68	1.75
0.67	1.61	1.60	1.68
0.74	1.54	1.53	1.62
0.80	1.48	1.47	1.57
0.87	1.43	1.42	1.52
0.94	1.38	1.37	1.48
1.02	1.34	1.33	1.44
1.09	1.30	1.29	1.41
1.17	1.27	1.26	1.38
1.25	1.24	1.23	1.35

(continued)

Table 8B4.2 (cont'd.)

t (hr)	Green-Ampt Implicit $f(t)$ (cm/hr)	Green-Ampt Explicit $f(t)$ (cm/hr)	Philip $f(t)$ (cm/hr)
1.33	1.22	1.20	1.32
1.42	1.19	1.18	1.30
1.50	1.17	1.15	1.28
1.59	1.15	1.13	1.26
1.67	1.13	1.11	1.24
1.76	1.11	1.09	1.22
1.85	1.10	1.08	1.21
1.95	1.08	1.06	1.19
2.00	1.07	1.05	1.19

Philip Equation with Time Adjustment

Here we calculate the infiltration rate using the two-term Philip relation [equation (8.20)] with time adjustment [equations (8.21)–(8.23)] for the same soil, storm, and initial conditions as the previous example.

The sorptivity can be found via equation [8B2.4], but here we use $\psi_{ae} = \psi_f = 30$ cm as found from figure 8.22. The value of $b = 5.3$ for silt loams is taken from table 7.4. Thus

$$S_p = \left[(0.413 - 0.350) \times 0.656 \text{ cm/hr} \times 30 \text{ cm} \times \left(\frac{2 \times 5.3 + 3}{5.3 + 3} \right) \right]^{1/2} = 1.43 \text{ cm/hr}^{1/2}.$$

The time parameters are then found as

$$T_{cp} = \left[\frac{1.43 \text{ cm/hr}^{1/2}}{2 \times (2.0 \text{ cm/hr} - 0.656 \text{ cm/hr})} \right]^2 = 0.28 \text{ hr};$$

$$T_{pp} = \frac{1.43 \text{ cm/hr}^{1/2} \times (0.28 \text{ hr})^{1/2} + 0.656 \text{ cm/hr} \times 0.28 \text{ hr}}{2.0 \text{ cm/hr}} \\ = 0.47 \text{ hr.}$$

The effective time values t_{ep} used in the Philip equation are then found from equation (8.23):

$$t_{ep} = t - 0.47 \text{ hr} + 0.28 \text{ hr} = t - 0.19 \text{ hr.}$$

Using these times in equation (8.20) with $K_p = K_h = 0.656 \text{ cm/hr}$ then gives the infiltration rates shown in the last column of table 8B4.2.

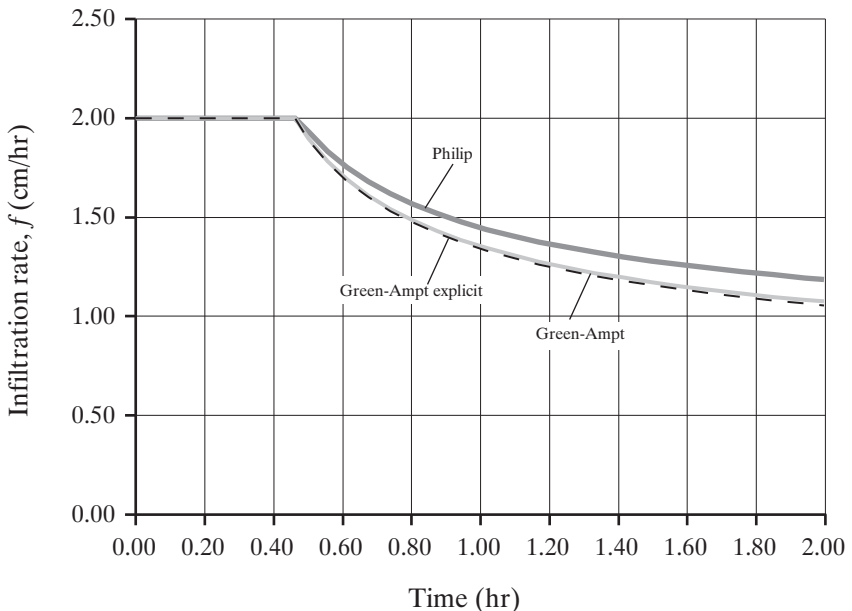


Figure 8.25 Comparison of infiltration rates computed by the Green-Ampt, Green-Ampt explicit, and Philip approaches for the example of box 8.4.

relatively homogeneous subareas, each characterized by its set of parameters, compute areal-average parameter values, and use these averages in the model to characterize the process over the area. This approach is problematical for infiltration because, as we have just seen, soil properties and initial conditions are highly variable spatially and temporally, and sufficient measurements to characterize this variability are usually unavailable. Furthermore, infiltration rates are nonlinearly related to soil properties [equations (8.20) and (8.36)], so using averages of point-parameter values does not provide meaningful areal-average values of infiltration rate. Even more fundamentally, recall that Darcy's law and the Richards equation, on which the Philip and Green-Ampt approaches are based, were derived for *representative elemental volumes*, i.e., at scales many orders of magnitude smaller than of practical hydrologic interest, and it is not clear to what extent these relations can be scaled up. Thus, as Kabat et al. (1997, p. 369) concluded,

An area-average solution for [the Darcy–Richards] equation, which would retain the physical meaning of the soil hydraulic characteristics (i.e. soil water retention and hydraulic conductivity curves), remains computationally laborious, non-trivial and in many cases an almost impossible task, requiring an extended knowledge of local-scale information.

However, Kabat et al. (1997) also concluded that models using a physics-based structure are “too at-

tractive to be discarded” and can be applied to large areas if the parameters that represent hydraulic conductivity, porosity, etc., are treated as calibration parameters that do not necessarily have a direct relation to field-measurable quantities. These parameters can be determined on the basis of *geometric scaling* or *dynamic scaling*.

Geometric scaling is based on the concept that two soils that are geometrically similar are related by a **scale factor** α , where

$$\alpha = \frac{\lambda_x}{\lambda_{ref}}, \quad (8.50)$$

where λ_x and λ_{ref} are the characteristic lengths (grain sizes) of a soil at a given location x and a **reference soil**, respectively. Then other properties are related as powers of this scale factor that depend on their dimensional character; for example,

$$\theta_x = \alpha^0 \cdot \theta_{ref}, \quad (8.51)$$

$$\psi_x = \alpha^{-1} \cdot \psi_{ref}, \quad (8.52)$$

$$K_{hx} = \alpha^2 \cdot K_{href}, \quad (8.53)$$

$$S_{px} = \alpha^{1/2} \cdot S_{pref}. \quad (8.54)$$

These equations imply that the soil-water-retention and hydraulic-conductivity characteristics at a given water content at any location can be related to mean (reference) moisture-characteristic and hydraulic-

characteristic curves. In theory, the α values calculated for all properties should be identical.

Dynamic scaling is based on writing the governing equation in dimensionless form, using dimensionless time and depth variables. For example, after defining a dimensionless cumulative infiltration,

$$\beta(t) \equiv \frac{K_p}{S_p^2} \cdot F(t), \quad (8.55)$$

and a dimensionless time,

$$\tau \equiv \frac{K_p^2}{S_p^2} \cdot t, \quad (8.56)$$

the Philip equation [equation (8.20b)] can be written as

$$\beta(t) = \tau^{1/2} + \tau. \quad (8.57)$$

Sharma et al. (1980) tested the applicability of geometric and dynamic scaling. They found that infiltrometer measurements at 26 sites on a small watershed were well fit by the Philip equation [equation (8.20)], but that the variation in parameters was large: S_p varied by one order of magnitude and K_p by two orders of magnitude (figure 8.26a), and neither was related to soil type or topographic position. In spite of this, the combined data from all 26 infiltrometers was well fit by equation (8.57) (figure 8.26b), suggesting that dynamic scaling is valid.

However, using reference soil properties defined as the averages of the values at the 26 sites, \bar{S}_{pref} and \bar{K}_{pref} , the α values calculated from measured \bar{S}_{pref} and \bar{K}_{pref} values differed, suggesting that strict geometrical scaling was violated. This difference is likely due to spatial differences in initial water content, which affects S_p [equation (8B2.4)] but not K_p . The correspondence between the α values was greatly improved when the harmonic or geometric, rather than arithmetic, mean was used to define S_{pref} , and Sharma et al. (1980) concluded that the concept of geometrical scaling should be investigated further.

Kabat et al. (1997) also found support for dynamic scaling based on the Richards equation. They found that soils with similar hydrologic response have similar values of the characteristic response time δ , where

$$\delta \equiv \frac{D_h(\theta^*)}{K_h^2}. \quad (8.58)$$

Examination of field data showed that the reference curve determined by scaling closely approaches the “effective” area-average curve that reproduces the hydrologic behavior, and that characteristic values of δ can be associated with soil-texture classes.

A recent study by Jana and Mohanty (2012) used a hydrologic model based on the Richards equation to compare four techniques for up-scaling soil-hydraulic parameters from a 30-m to a 1-km resolution. They found that a topographically based scaling algorithm captured much of the variation in soil-hydraulic parameters at the larger scale and was generally successful at reproducing hydrologic behavior at that scale. The mathematics of the algorithm are complex, but the approach appears promising.

8.5.2.2 Heuristic Approaches

A very simple method for incorporating the spatial variability of infiltration in a watershed model was described by Manley (1977). Based on the work of Burgy and Luthin (1956), he assumed a linear cumulative distribution of ultimate infiltrability (K_h) over the watershed (figure 8.27 on p. 382). The intersection of a horizontal line representing the rainfall rate, w , with the line representing this distribution defines an area proportional to the rate of runoff, Q ; this rate can then be calculated as

$$Q = \frac{w^2}{2 \cdot K_{hmax}}, \quad w \leq K_{hmax}; \quad (8.59a)$$

$$Q = \frac{3 \cdot w}{2} - K_{hmax}, \quad w > K_{hmax}, \quad (8.59b)$$

where K_{hmax} is the maximum value of K_h for the watershed.

Many operational watershed models use heuristic schemes that approximate the general form of point infiltration models such as the Philip equation (see Viessman et al. 1989). For example, the widely used SCS model for estimating watershed runoff from soil and land-cover data (section 10.6.4.2) calculates streamflow resulting from a rain as equal to the rainfall rate less an “initial abstraction” and a declining “loss rate.” These abstractions are largely due to infiltration and, as shown in figure 8.28 on p. 382, are modeled as approximations of a watershed-wide effective infiltration curve, though the parameters that determine their magnitudes are related to general soil and land-cover characteristics rather than to soil hydraulic properties.

Somewhat more sophisticated heuristic approaches for incorporating the variability of soil properties and initial conditions in watershed models have also been suggested (e.g., Maller and Sharma 1981; Berndtsson 1987; Berndtsson and Larson 1987; Valdes et al. 1990).

8.6 Redistribution of Soil Water

In moderately deep and deep soils, infiltration following a rain or snowmelt event usually ceases

before the wetting front has penetrated through an entire soil profile. The infiltrated water is then subject to redistribution by gravity and pressure forces and removal by evapotranspiration.

8.6.1. Redistribution without Evapotranspiration

Under the conditions assumed in the Green-Ampt approach (i.e., uniform soil, uniform initial soil moisture, no water table), experiments have shown that there are two basic patterns of soil-water

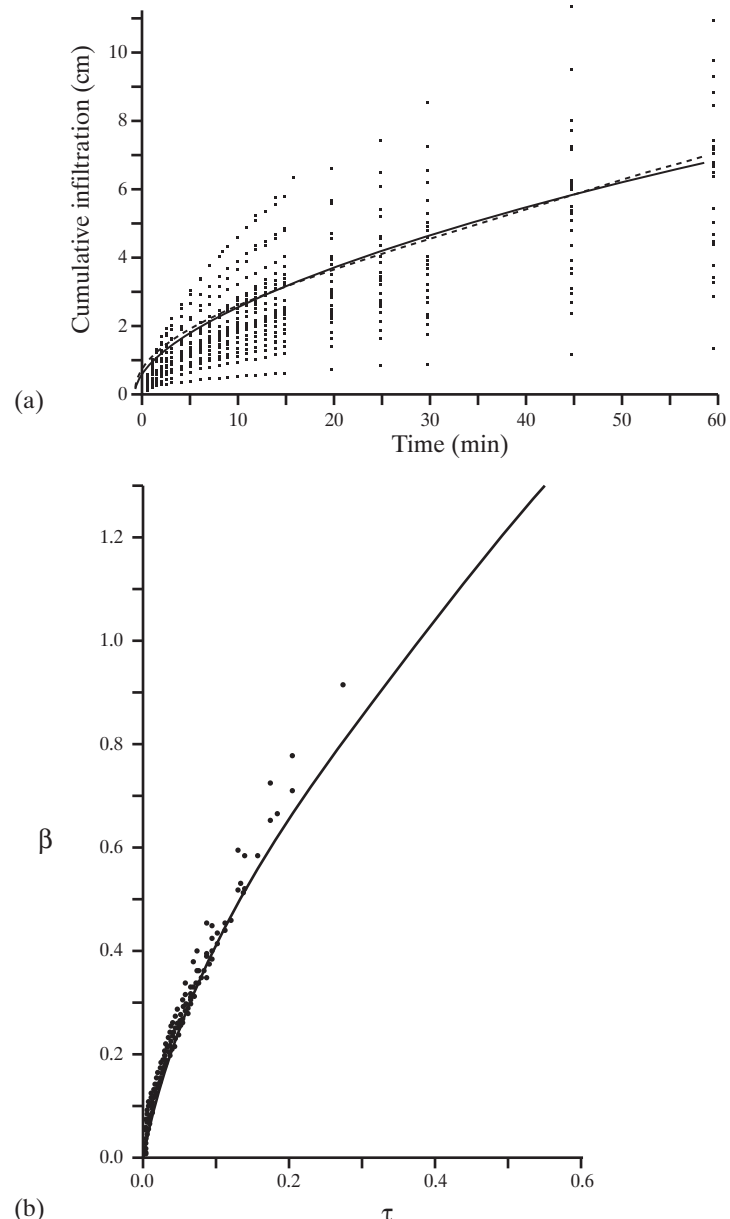


Figure 8.26 Results of testing the applicability of geometric and dynamic scaling by Sharma et al. (1980). (a) Field-measured cumulative infiltration $F(t)$ measurements at 26 sites on a small watershed. Dots are measurements at individual sites, line is Philip equation with average values of S_p and K_p . (b) The combined data from all 26 infiltrometers was well fit by equation (8.57), suggesting that dynamic scaling is valid [reproduced from Sharma et al. (1980), Spatial variability of infiltration in a watershed, *Journal of Hydrology* (45):101–122, with permission from Elsevier].

redistribution following infiltration in the absence of evapotranspiration (figure 8.29). In the first the water content decreases monotonically with depth, and the water-content gradient across the wetting front gradually decreases as the front descends. In this case, the rate of redistribution is faster the

smaller the amount of infiltrated water $F(T_w)$. This situation occurs when the gravitational force is negligible compared to the capillary force (i.e., when the water content above the wetting front at the start of redistribution is less than field capacity), and hence characterizes finer-grained soils and

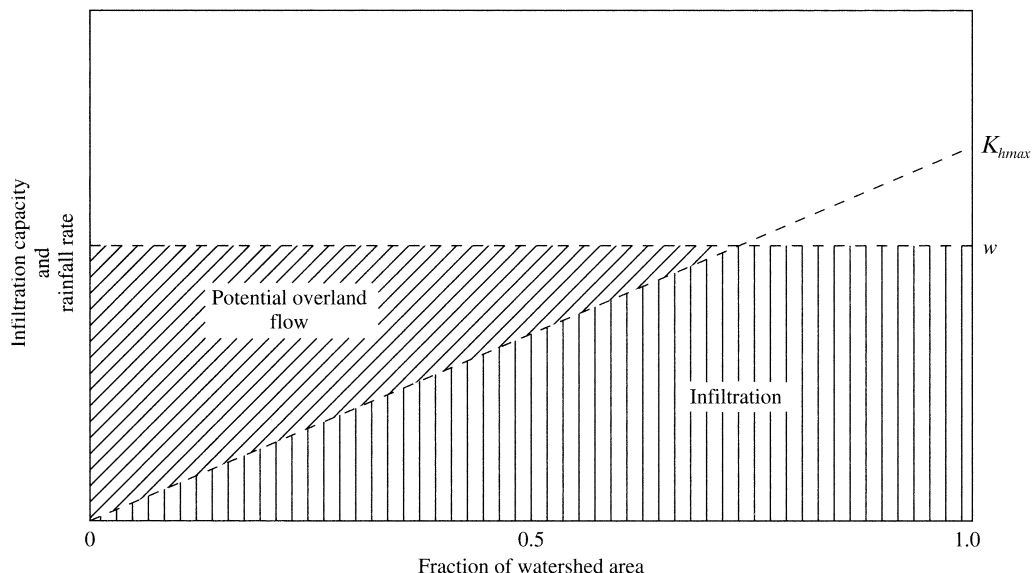


Figure 8.27 Simple approach to estimating watershed infiltration and runoff. The diagonal dashed line represents an approximation of the areal distribution of infiltration, with K_{hmax} the maximum value for the area. The horizontal dashed line is drawn at the rainfall rate, w . The area with the diagonal lines is proportional to the potential overland flow; the geometry of the relation yields equation (8.59) [adapted from Manley (1977)].

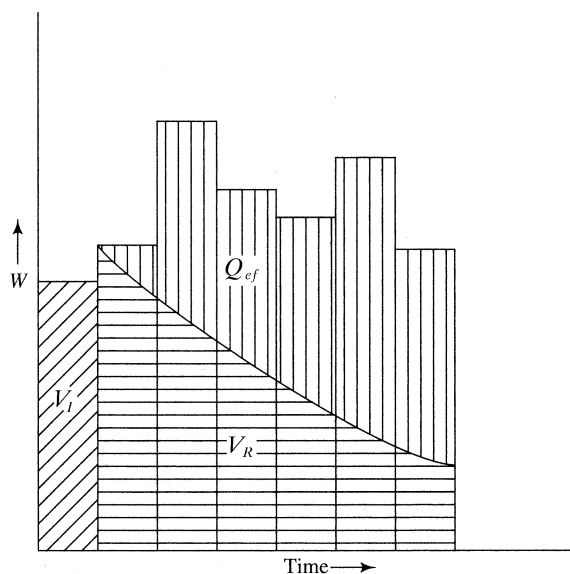
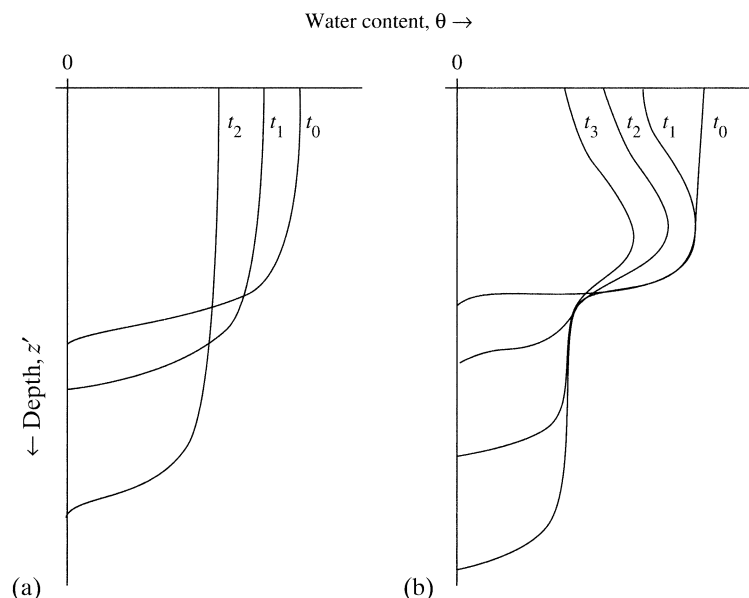


Figure 8.28 Simple rainfall-runoff models typically use the general behavior of infiltration during a storm (e.g., figure 8.10) to model total rainfall “abstractions” (infiltration + interception + surface detention). The scheme used by the SCS model (section 10.6.4.2) is shown here: Vertical histogram bars represent total rainfall, V_t is “initial abstraction,” V_R is subsequent abstraction, and Q_{ef} is event flow.

Figure 8.29 Typical soil-water profiles showing the redistribution of water at successive times (t_0, \dots, t_3) following infiltration into a deep soil with no evaporation.

Time t_0 is when infiltration ceases and redistribution begins. (a) Redistribution when capillary force dominates gravitational force (water content above wetting front at t_0 less than field capacity). (b) Redistribution when gravitational force dominates (water content above wetting front at t_0 greater than field capacity) [Youngs and Poulovassilis (1976)]. The different forms of moisture profile development during the redistribution of soil water after infiltration. *Water Resources Research* 12:1007–1012, with permission of the American Geophysical Union].



smaller initial depths to the wetting front at the cessation of infiltration.

In the second pattern, a “bulge” in water content develops due to rapid gravitational drainage soon after infiltration ceases and persists as redistribution progresses. A sharp wetting front is maintained, but the water contents above the bulge form a gradual “drying front” that is transitional to the field capacity. This situation occurs when the gravitational force is significant (i.e., the water content above the initial wetting front exceeds the field capacity), and hence characterizes coarser-grained soils and higher $F(T_w)$. In this case the rate of redistribution increases with greater $F(T_w)$, and in the “final” condition the infiltrated water is distributed over a depth $z_f'(\infty)$ given by

$$z_f'(\infty) = \frac{F(T_w)}{\theta_{fc} - \theta_0}. \quad (8.60)$$

Once this “final” state is reached, there will be slow redistribution by pressure forces at the wetting front. Biswas et al. (1966) showed several examples of redistribution in the absence of a water table in laboratory experiments.

In the absence of evapotranspiration, the equilibrium profile (figures 8.7–8.9), rather than a uniform water content, more realistically approximates the antecedent conditions encountered by an infiltration event. If infiltration ceased when the wetting front was

at one of the levels shown in figure 8.23, subsequent redistribution due to gravity and pressure gradients would cause the profile to “rotate” counterclockwise toward the equilibrium curve.

Using numerical solutions to the Richards equation, Rubin (1967) showed that hysteresis has a significant effect on soil-water profiles during redistribution. Interestingly, he found that profiles accounting for hysteresis were not intermediate between those using nonhysteretic wetting and nonhysteretic drying moisture-characteristic curves (figure 8.30).

8.6.2. Redistribution with Evapotranspiration

In many natural situations, extraction of water from the upper soil layers by evapotranspiration strongly affects water redistribution following infiltration. This process is governed by and can be numerically modeled via the Richards equation, adding a “sink” term to represent uptake of water by plants in the root zone:

$$\frac{\partial \theta}{\partial t} = -\frac{\partial}{\partial z'} \left[K_h(\theta) \cdot \left(\frac{\partial \psi(\theta)}{\partial z'} \right) \right] - \frac{\partial K_h(\theta)}{\partial z'} - S, \quad (8.61)$$

where S is the rate of uptake per unit volume ($[L^3 T^{-1} / L^3] = [T^{-1}]$). In numerical models, the soil is divided into a number of layers (generally on the order of a few centimeters thick) and the equations are solved for successive time steps (generally on the order of

minutes to hours) (e.g., Rubin 1967; Milly 1988; Muusake et al. 1988).

However, numerical solutions of (8.61) are computationally expensive, and sufficient data to capture the variability in soil properties in a watershed are seldom available. Thus for many purposes, the drainage from a soil layer can be satisfactorily modeled using a simpler approach based on an approximation of Darcy's law in which the capillary gradient is ig-

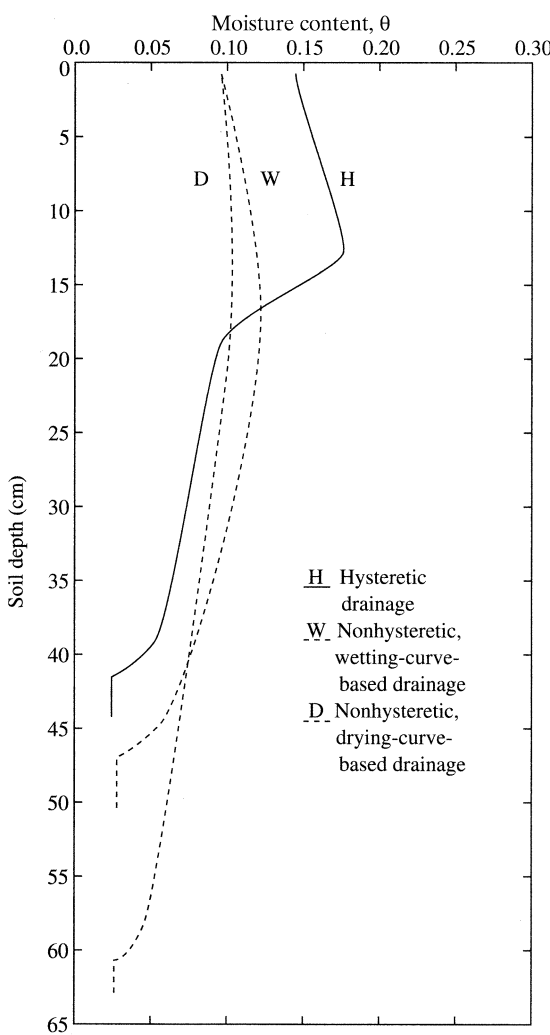


Figure 8.30 Numerically simulated water-content profiles 2 hr after cessation of rain on a sandy soil. Note that the profile that accounts for hysteresis in the moisture-characteristic curve (H) is not intermediate between those assuming nonhysteretic curves characterizing wetting (W) and drying (D) [adapted from Rubin (1967)].

nored, the water content is averaged over the soil layer, and the $K_h(\theta)$ relation can be represented analytically (table 7.2). For example, Black et al. (1970) used equation (8.24) in a simple water-balance procedure applied to a soil layer supporting a vegetable crop. In their application, the change in water content of the soil layer over time period t , $\Delta\bar{\theta}_t$, was calculated as

$$\Delta\bar{\theta}_t = \frac{-K_h(\bar{\theta}_{t-1}) \cdot \Delta t - ET_t - F_t}{\Delta z}, \quad (8.62)$$

where ET_t and F_t are the evapotranspiration and total infiltration during period t , respectively, Δt is the time step, and Δz is the thickness of the layer. The average soil-water content at the end of period t , $\bar{\theta}_t$, was then found as

$$\bar{\theta}_t = \bar{\theta}_{t-1} + \Delta\bar{\theta}_t. \quad (8.63)$$

Black et al. (1970) found that water contents estimated in this way compared well with measured values even with $\Delta t = 1$ day and $\Delta z = 150$ cm. However, this approach can become numerically unstable unless $\Delta\bar{\theta}_t \ll \bar{\theta}_{t-1}$, so it may be necessary to make $\Delta t < 1$ day. With this modification, equations (8.62) and (8.63) appear to be sound bases for simulating percolation in general hydrologic models (see also Groves 1989), although the problem of adequately accounting for the variability of soil properties remains.

When evapotranspiration occurs following an infiltration event, an upward-decreasing water-content gradient is produced similar to that of figure 8.29b. Figure 8.31 shows total head (water-content) changes following infiltration in a forest soil; most of the water loss in this case was due to evapotranspiration rather than to gravitational drainage, as in figure 8.29b. The importance of evapotranspiration to the seasonal variation of soil-water content is evident in figure 8.32, which shows a wide range of θ in the root zone of a silt-loam soil in an agricultural watershed and a much narrower range below this zone.

8.7 Summary

Infiltration and soil-water movement are critical hydrologic processes since they determine the rates and amounts of water available for surface and subsurface runoff, evapotranspiration, and recharge to ground water. These processes are also crucial in determining water quality (see Nielsen et al. 1986 for a review of solute transport in the vadose zone). In

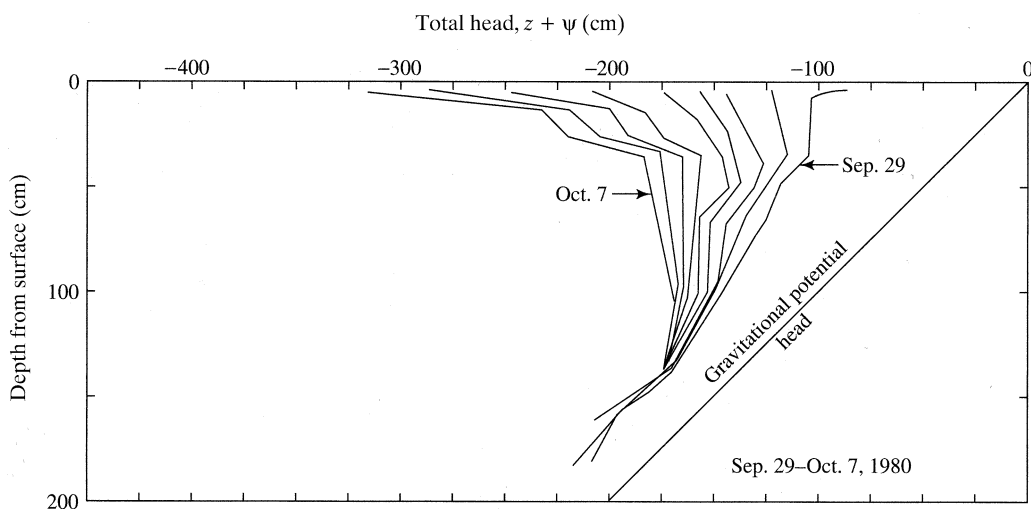


Figure 8.31 Daily profiles of total head changes due largely to evapotranspiration from a forest soil during a rainless period. The soil-water tension, which reflects the water content, is the horizontal distance between each profile and the gravitational head line [reproduced from Musiak et al. (1988), Unsaturated zone soil moisture behavior under temperate humid conditions—tensiometric observations and numerical simulations, *Journal of Hydrology* (102):179–200, with permission from Elsevier].

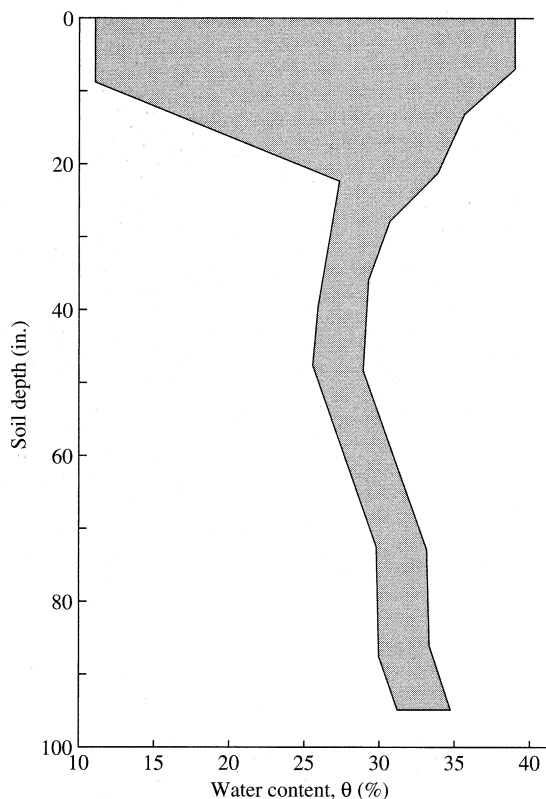


Figure 8.32 Annual range of soil-water content, θ , in a silt-loam soil supporting grass and clover in Ohio [Dreibelbis (1962). Some aspects of watershed hydrology as determined from soil moisture data. *Journal of Geophysical Research* 67:3425–3435, with permission of the American Geophysical Union].

fact, it has been said that “hydrology is mostly soil physics” (Youngs 1988).

The classical theory of unsaturated flow based on Darcy’s law and the Richards equation is well developed and tested, and has been successfully incorporated in hydrologic models in various forms. Some of these models employ approximate analytical solutions or numerical approximations of the basic equations, while others use simpler but physically based representations like the Green-Ampt and Philip approaches. However, we need to be aware that the classical theory may inadequately represent soil-water processes in many situations. This is especially true where macropores are important routes of water and solute transport and where soil-water movement is affected by temperature gradients and freezing and thawing.

The quantitative characterizations of equilibrium soil-water profiles developed by Salvucci and Entekhabi (1994b, 1995) [equations (8.10)–(8.12)] are important contributions to understanding how soil-water conditions are affected by climate, soil type, and water-table depth, and appear to be very useful for large-scale water-balance modeling and for rainfall-runoff modeling (discussed further in chapter 10).

The most critical theoretical and practical questions in the application of theory concern the representation of the typically wide variability in the conditions that determine infiltration. Because of our limited understanding of this variability and the paucity of field data, we are often led to highly simplified model representations of the process. Promising approaches in this area include the application of various statistical methods (e.g., Berndtsson and Larson 1987) and scaling and similarity theory (e.g., Sharma et al. 1980; Wood et al. 1990; Kabat et al. 1997; Jana and Mohanty 2012). There is a continuing need for field data so that we can understand what we are attempting to model, and the remote sensing of soil moisture and other surface factors will be essential in this regard.

▼ EXERCISES

1. As noted in section 8.1, field capacity can be defined as (1) the moisture content at which $\psi = -340$ cm or (2) the moisture content at which $q_s = 0.1$ mm/d.
 - a. Use the Brooks and Corey relations of table 7.2 and the parameters of table 7.4 to compute field capacities for a sand, a silt loam, a loam, and a clay using each of these definitions.

- b. Write a brief report comparing the values given by the two definitions.
2. Use the Brooks and Corey relations of table 7.2 and the parameters of table 7.4 to estimate the $|\psi|-\theta$ and $K_h-\theta$ relations for the soils in exercise 8.1.
 - a. Plot the $|\psi|-\theta$ relation for all four soils on a single graph, with $|\psi|$ on the logarithmic axis (vertical). Label the curves for each soil and show θ_f and θ_{wp} .
 - b. Plot the $K_h-\theta$ relation for all four soils on a single graph, with K_h on the logarithmic axis (vertical). Label the curves for each soil and show saturated K_h .
 - c. Write a brief report comparing the curves and specific values for the four soils.
3. The table below contains data collected during a double-ring infiltrometer experiment on a silt loam with an antecedent moisture content of 0.10 (Akinbile 2010).

Time, t_i (min)	Cumulative Infiltration (mm)	Time, t_i (min)	Cumulative Infiltration (mm)
2	4.8	22	26.0
4	8.8	26	28.3
6	11.8	30	30.2
8	14.3	34	31.7
10	16.5	38	32.8
12	18.5	44	33.8
14	20.2	50	34.4
18	23.3	60	34.9

- a. Implement the least-squares methodology described in box 8.3 in a spreadsheet to estimate the parameters of the Philip infiltration equation [equation (8.20)], where sorptivity, S_p , is in $\text{mm}/\text{hr}^{1/2}$ and the hydraulic conductivity, K_p , is in mm/hr .
- b. Compare the calculated K_p value with the value of K_h given for silt-loam soils in table 7.4.
4. If an infiltrometer is available, make observations of infiltration in the field. Use the data to estimate S_p and K_p as described in box 8.3.
5. Using the spreadsheet program GreenAmpt.xls on the disk accompanying this text, this exercise will give you experience in applying the Green-and-Ampt model (section 8.4.3) for computing infiltration during a rainfall event. It will provide insight into (1) how infiltration and surface detention (potential Hortonian overland runoff; see section 10.4.2.1) vary with time during a storm and (2) how total infiltration and runoff vary with (a) antecedent soil water content (experiment A), and (b) storm rainfall (experiment B).

Soil Properties

The soil is Columbia Sandy Loam, with the following properties:

Porosity, ϕ	Air-Entry Tension, $ \Psi_{ae} $ (cm)	Saturated Hydraulic Conductivity, K_h (cm/hr)	Pore-Size Distribution Exponent, b
0.52	22	5	4.9

Experiment A

The object of this experiment is to demonstrate the effect of **initial water content** ("antecedent conditions") on the timing and amount of infiltration and runoff from a rain storm of a given intensity: $w = 10$ cm/hr; and duration: $t_w = 1$ hr.

Procedure

- A1. Enter the above values in the appropriate cells in the spreadsheet.
 - A2. Make three runs, each with a different initial soil-water content, θ_0 :
- | Run | A1 | A2 | A3 |
|------------|------|------|------|
| θ_0 | 0.40 | 0.32 | 0.25 |
- A3. Enter the first θ_0 value under "Initial Conditions." The "Calculated Quantities" are computed, including t_p and $F(t_p)$ in the second line of the Infiltration table.
 - A4. Enter six to 10 $F(t)$ values, with the last one as close as possible (when rounded to three significant figures) to the value that gives $t = t_w$. Ignore error messages below the rows in which you have entered $F(t)$ values. The calculated values of $f(t)$, $z_f(t)$, and t appear in the other columns.
 - A5. Print out the spreadsheet.
 - A6. Use the charting feature in Excel to create graphs of $F(t)$ and $f(t)$ versus t (see "Analysis" below).
 - A7. Repeat steps A3–A6 for the θ_0 values for runs 2 and 3.

Analysis

- A8. Use the program output to plot graphs of (a) $f(t)$ versus t for all three runs and (b) $F(t)$ versus t for all three runs. Indicate the values of w and K_h on graph a. Show all quantities from $t = 0$ to $t = t_w$. Note that infiltration ceases at t_w .
- A9. Determine $F(t_w)$ for each run from the output. Then compute total runoff, $Q(t_w) = w \cdot t_w - F(t_w)$, for each run and plot graphs of (a) $Q(t_w)/(w \cdot t_w)$ versus θ_0 , and (b) t_p versus θ_0 .

Experiment B

The object of this experiment is to demonstrate the effect of **rainfall amount** on the timing and amount of infiltration and runoff from a rainstorm of a given duration: $t_w = 1$ hr, for a given initial water content: $\theta_0 = 0.32$.

Procedure

- B1. Enter the above values in the appropriate cells in the spreadsheet.
- B2. You will make five runs, each with a different rainfall rate, w :

Run	B1	B2	B3	B4	B5
w (cm/hr)	6	7	8	9	10

Analysis

- B3. Determine $F(t_w)$ for each run from the output. Then compute total runoff, $Q(t_w) = w \cdot t_w - F(t_w)$, for each run and plot graphs of (a) $Q(t_w)/(w \cdot t_w)$ versus w and (b) t_p versus w .

Discussion

Write brief paragraphs discussing the effects of θ_0 and w on the timing and relative and absolute amounts of infiltration and storm runoff as revealed in these experiments.

6. Construct a spreadsheet model of the explicit Green-and-Ampt model and apply it to experiment A in exercise 8.5.
 - a. Create graphs comparing $f(t)$ versus t and $F(t)$ versus t as calculated by the explicit approach with the values given by the implicit approach in exercise 8.5.
 - b. Write a brief paragraph comparing the results of the explicit and implicit approaches.
7. Consider a layer of sandy-loam soil 1.0 m thick, with a porosity of 0.38 and $K_h = 0.0025$ cm/s, above an impermeable bedrock surface. Use equation (8.49) to explore how the time to saturation from below varies as a function of: (a) initial water content and (b) rainfall rate.
8. Using the method described in box 8.3, estimate S_p and K_p using the results for one event simulated in exercise 8.5. Compare the estimated value of K_p with K_h for the soil chosen.
9. Access a soils map of your area (see exercise 7.5). Read the descriptions of typical soil profiles and identify information about porosity, saturated hydraulic conductivity, air-entry tension, depth to water table, presence of impermeable layers, etc. Then, using regional climatic information, use equation (8.12) to generate equilibrium soil-moisture profiles for one or more of these soils, as directed by your instructor.

NOTE

¹ "Phreatic" comes from the Greek word for "well."

9



Ground Water in the Hydrologic Cycle

Ground water is water under positive (i.e., greater than atmospheric) pressure in the saturated zone of earth materials. The water table is the fluctuating upper boundary of the ground-water zone at which pressure is atmospheric (denoted on diagrams by the **hydrat** symbol, $\underline{\underline{v}}$). Figure 9.1 shows the general relations between ground water and surface water. Most water enters the ground-water reservoir when infiltrated water arrives at the **water table** as **recharge**; recharge can also occur by horizontal or vertical seepage from surface-water bodies. Under natural conditions ground water eventually discharges into rivers or lakes or, in coastal areas, directly into the ocean; water can also leave the ground-water reservoir by moving upward from the water table into the capillary fringe and thence into the unsaturated zone, where it is subject to evapotranspiration.

Ground water constitutes about 30% of the world's total fresh water and 99% of its total stock of liquid fresh water (table 2.5). As with all hydrologic stocks, ground water is in continual motion, albeit slow (typically much less than 1 m/d). Using the values from figure 2.20 in equation (1.25), one can calculate that the overall residence time for the global ground-water reservoir is about 235 yr; for moderate-

to large-scale regional flow systems in various parts of the world residence time varies from a few years to 1,000 years or more. In spite of its slow pace, ground water is a crucial link in the hydrologic cycle because it is the source of most of the water in rivers and lakes.

Ground water is, of course, also important as the direct source of water withdrawn for domestic water use, irrigation, and industrial uses worldwide. In the United States, about one-fourth of the water used for these purposes comes from ground water, and the proportion is much higher for many regions; concern about the quantity and quality of ground water is one of the major water-resource issues in many parts of the world.

The material properties of porous media were described in sections 7.1 and 7.2, and the basic physics of ground-water flow were developed in section 7.3. For convenience, the basic equations and concepts of ground-water flow are summarized in box 9.1 on p. 391.

Our focus in this chapter is on ground water as a link in the hydrologic cycle. We will examine the effects of topography and geology on natural ground-water flows in drainage basins; how ground water in-

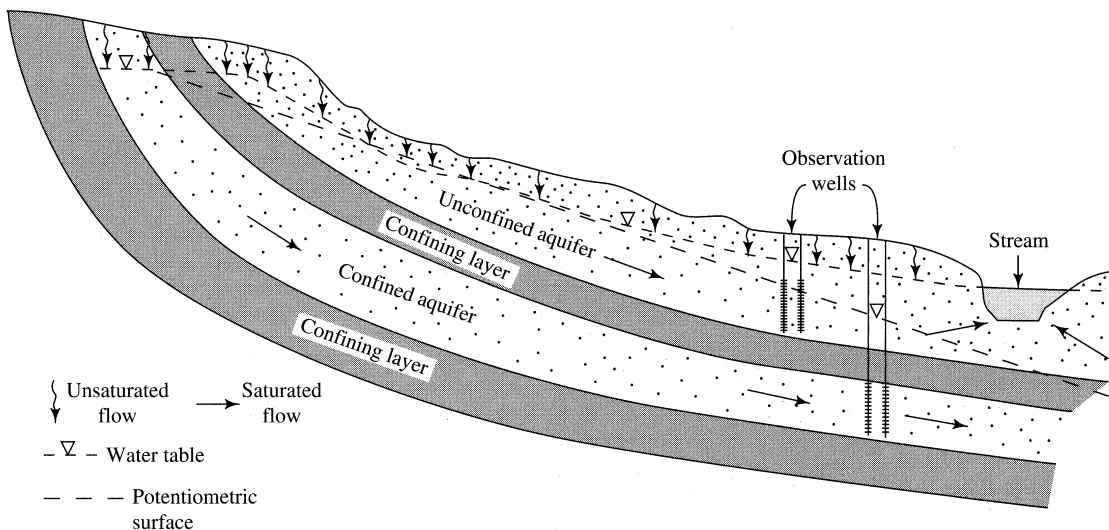


Figure 9.1 Unconfined and confined aquifers in a region of folded sedimentary rocks. Note relations of water levels in wells penetrating unconfined and confined aquifers.

teracts with streams, lakes, wetlands, and the ocean; the role of ground water in the drainage-basin water balance; and approaches to the quantitative evaluation of components of the ground-water budget. We will also briefly examine the hydraulics of wells, how human use of ground water affects the basin water balance, and the concept of “safe yield.” We do not explore the chemical evolution of ground water or its relation to geotechnical problems or geologic processes; these topics are well covered in many texts devoted exclusively to hydrogeology (e.g., Freeze and Cherry 1979; Fetter 2001).

9.1 Aquifers and Aquitards

9.1.1 Definitions

A **geologic formation** is a regionally extensive, mappable geologic unit with a characteristic lithology. For our purposes, an **aquifer** is a formation that can store enough water and transmit it at a rate fast enough to be hydrologically significant. A given aquifer has reasonably uniform water-storage and transmitting properties, and the ground-water movement within it can be considered to be the flow field induced by a single coherent potential-energy field.

Formations that do not transmit water at hydrologically significant rates are called **aquitards**. The term **aquiclude** is sometimes used to describe an “im-

permeable” formation, but it is now recognized that few, if any, geologic materials are strictly impermeable.

Note that the definitions of aquifer and aquitard are relative, and depend on the particular regional context: In an area of interbedded sands and silts, the sands would be considered aquifers and the silts aquitards; in an area of interbedded silts and clays, the silts would be aquifers and the clays aquitards. In the context of runoff generation, the aquifer of interest may be a thin surficial layer capable of conducting infiltrated water to streams. In the context of water resources, an aquifer is a geologic unit that is a significant source of water.

9.1.2 Unconfined and Confined Aquifers

Figure 9.1 illustrates the two major classes of ground-water flows, which are distinguished by the nature of the upper boundary of the flow:

1. **Unconfined aquifers:** If the upper boundary of a ground-water flow is a water surface at atmospheric pressure (the water table), the flow and the aquifer in which it occurs are **unconfined**. At the water table, the pressure is atmospheric, the gauge pressure $p = 0$, and the total head is equal to its elevation above the selected datum, z . The elevation of the water table can be determined as that of the water surface in a well open along its length and extending just deep enough to encounter standing

Box 9.1 Basic Ground-Water Definitions and Equations

Hydraulic Head

The total potential energy per unit weight of a fluid at a point is given by the **total head**, h [L], which is the sum of the **gravitational head**, z [L], and the **pressure head**, ψ [L]:

$$h = z + \psi. \quad (9B1.1)$$

Pressure head is the local fluid gauge pressure, p [F L⁻²], divided by the weight density of the fluid, γ [F L⁻³]:

$$\psi = \frac{p}{\gamma}. \quad (9B1.2)$$

Total head at a point in a saturated porous medium is measured as the elevation of the water surface in a **piezometer**, which is a tube connecting the point to the atmosphere (see figure 7.8).

Gravitational head at the point is measured as the elevation of the point above an arbitrary datum. Pressure head at the point can be determined as $\psi = h - z$.

Darcy's Law

At any point, ground-water flow rate in coordinate direction x equals the product of the local total head gradient and the local **hydraulic conductivity** of the medium in direction x , K_{hx} [L T⁻¹]:

$$q_x \equiv \frac{Q_x}{A_x} = -K_{hx} \cdot \frac{dh}{dx}, \quad (9B1.3)$$

where q_x [L T⁻¹] is the **Darcy velocity**, Q_x is the volumetric flow rate [L³ T⁻¹], and A_x [L²] is the cross-sectional area of the medium through which flow occurs. Darcy's law is valid for laminar (viscous) flow, which occurs when

$$Re \equiv \frac{q_x \cdot d}{v} < 1, \quad (9B1.4)$$

where Re is the **Reynolds number** [1], d is the characteristic (average) grain size of the porous medium [L], and v is the fluid kinematic viscosity [L² T⁻¹].

water (Freeze and Cherry 1979). Recharge to unconfined aquifers usually occurs from infiltrated water percolating vertically to the water table over a significant portion of the upper surface. The elevation of the water table changes as the flow through the aquifer varies; thus flow and storage in unconfined aquifers are correlated, as in streams.

2. **Confined aquifers:** If an aquifer is saturated throughout and bounded above and below by formations with significantly lower hydraulic conduc-

Permeability and Hydraulic Conductivity

Intrinsic permeability k_i [L²] is determined by properties of the medium,

$$k_i = C \cdot d^2, \quad (9B1.5)$$

where C [1] is a parameter that depends on grain shape, size distribution, and packing of the medium. Hydraulic conductivity K_h is determined by properties of the medium and of the fluid:

$$K_h = C \cdot d^2 \cdot \frac{\rho \cdot g}{\mu} = k_i \cdot \frac{\rho \cdot g}{\mu} = k_i \cdot \frac{g}{v}, \quad (9B1.6)$$

where ρ is fluid mass density [M L⁻³], g is gravitational acceleration [L T⁻²], and μ is fluid dynamic viscosity [M L⁻¹ T⁻¹]. Grain diameters of geologic materials range over more than six orders of magnitude (< 10⁻⁶ m to > 1 m); at near-surface conditions, viscosity varies approximately twofold as a function of temperature, and water density is essentially constant. Thus K_h of granular geologic materials varies over 12 orders of magnitude (figure 7.9).

Specific Storage

Specific storage, S_s [L⁻¹], is defined as

$$S_s \equiv \frac{\text{volume of water entering or leaving control volume [L}^3\text{]}}{\text{increase or decrease in head [L] } \times \text{control volume [L}^3\text{]}} \quad (9B1.7)$$

General Equation of Ground-Water Flow

$$\frac{\partial}{\partial x} \left(K_{hx} \cdot \frac{\partial h}{\partial x} \right) + \frac{\partial}{\partial y} \left(K_{hy} \cdot \frac{\partial h}{\partial y} \right) + \frac{\partial}{\partial z} \left(K_{hz} \cdot \frac{\partial h}{\partial z} \right) = S_s \cdot \frac{\partial h}{\partial t}, \quad (9B1.8)$$

where x, y, z are Cartesian coordinate directions and t is time.

tivity, the flow and the aquifer are **confined**; the bounding aquitards are called **confining layers**. The pressure throughout is greater than atmospheric, and the water level in an observation well penetrating a confined aquifer will rise above the upper boundary to coincide with the **potentiometric surface**, an imaginary surface analogous to the water table. Major recharge to a confined aquifer occurs from water infiltrating at its “upstream” end, where the flow is not confined and a water table is present.

The boundary of the flow in a confined aquifer does not change with time; thus flow and storage in confined aquifers are not correlated, as in pipes.

It is important to recognize that the unconfined/confined categories are idealizations, and that the three-dimensional spatial variability of geologic conditions produces flows that may have some of the characteristics of both types. As noted, most confining layers can transmit some ground water, and if the amount transmitted is significant such layers are called **leaky aquitards**.

9.1.3 Storage Properties of Aquifers

9.1.3.1 Specific Storage and Storage Coefficient

The volume of water stored in a saturated porous medium per unit volume of medium equals the porosity, ϕ [equation (7.4)], and the degree of saturation, θ^* [equation (7.8)], equals unity.¹ However, the actual volume of water in a unit volume of porous medium may change in response to changes in head; these changes are reflected in the values of the *specific storage* and the *specific head*.

Consider a small unit area (say 1 m^2) on the earth's surface above an aquifer. The saturated thick-

ness of the aquifer beneath that area is designated H [L]. When the hydraulic head in the aquifer increases or decreases, water is taken into or released from storage. The increase or decrease in volume of water stored beneath the unit area per unit increase or decrease in head is the **specific storage**, S_s [L^{-1}], of the aquifer [equation (9B1.7)].

We can also define a dimensionless measure of storage, equal to the change in volume of stored water per unit aquifer surface area per unit change in head; this is the **storage coefficient**, S [1]:

$$S \equiv \frac{\text{Increase or decrease in volume of water stored } [\text{L}^3]}{\text{Surface area of aquifer } [\text{L}^2] \times \text{Increase or decrease in head } [\text{L}]} \quad (9.1)$$

Specific storage and storage coefficient are related as

$$S = H \cdot S_s. \quad (9.2)$$

The mechanisms relating changes in head and changes in storage, and the relative magnitudes of these changes, differ for unconfined and confined aquifers, as described in the following sections (figure 9.2).

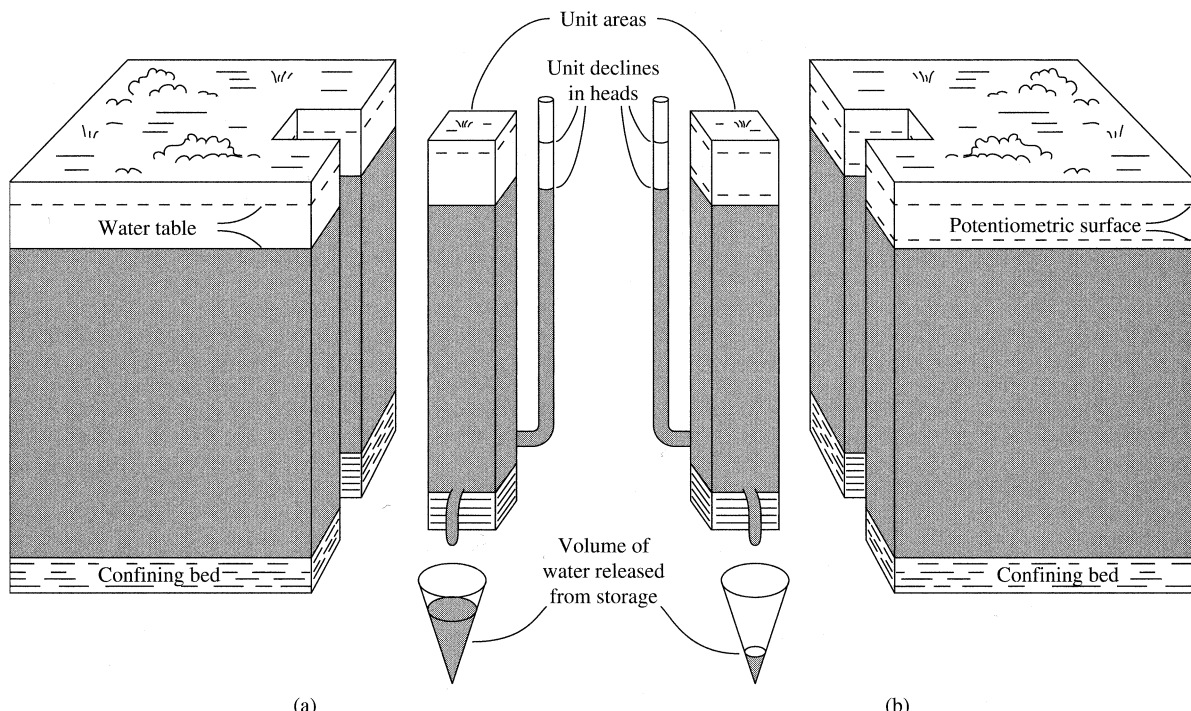


Figure 9.2 Definition of storativity in (a) unconfined and (b) confined aquifers. See equation (9.1) [Heath (1982)].

9.1.3.2 Unconfined Aquifers

In an unconfined aquifer, a change in head produces a change in the volume of water in the medium (figure 9.2a). A decrease in head is reflected in the lowering of the water table and a concomitant decrease in water content of the portion of the aquifer through which the water table descends and in the overlying unsaturated zone (figure 9.3). The opposite occurs for an increase in head. The amount of water-content change is characterized by the **specific yield**, S_y , defined as the volume of water released per unit surface area per unit decline of water table (figure 9.2a). Thus for an unconfined aquifer,

$$S = S_y. \quad (9.3)$$

Typical values of S_y are shown in table 9.1.

The relative volume of water retained in the portion of the aquifer experiencing a head decline is the **specific retention**, S_r . Thus

$$\phi = S_y + S_r. \quad (9.4)$$

The water remaining in the portion of the medium experiencing a water-table decline is held by surface-tension against gravity, so specific retention is essentially identical to field capacity (section 8.1.1). Recall also that soil drainage is not instantaneous, and many days may be required for water content to decline to S_r in a draining aquifer (figure 8.1).

9.1.3.3 Confined Aquifers

In a confined aquifer, a decrease in head is reflected in a lowering of the piezometric surface, but the aquifer beneath the unit surface area remains sat-

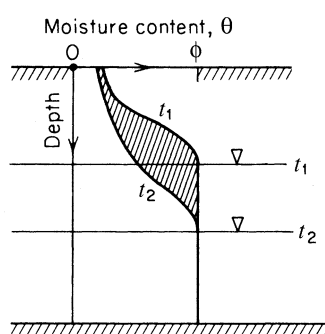


Figure 9.3 Specific yield (shaded area) in an unconfined aquifer [reproduced from Freeze and Cherry (1979), *Groundwater*, with permission from Prentice Hall].

urated (figure 9.2b). In this case, the decrease of storage accompanying the head decrease is due to: (1) compaction of the aquifer as part of the weight of the overlying material is transferred from the liquid to the solid grains, resulting in an increase in **effective stress** and a slight decrease in porosity and (2) expansion of the water due to the lowered pressure (box 9.2 on p. 395). The changes are reversed for an increase in head.

Following Freeze and Cherry (1979), when a volume V_T of a saturated aquifer is subjected to an increase in effective stress $d\sigma_{eff}$, it is compacted by an amount $-dV_T$, and an equal volume of water dV_w is expelled. Thus from equations (9B2.5) and (9B2.6),

$$dV_w = -dV_T = \alpha \cdot V_T \cdot d\sigma_{eff} = -\alpha \cdot V_T \cdot \gamma \cdot dh, \quad (9.5)$$

where α [$L^2 F^{-1}$] is the aquifer compressibility and γ [$F L^{-3}$] is the weight density of water. Thus for a unit volume ($V_T = 1$) and a unit head decline ($dh = -1$), the volume of water expelled becomes

$$dV_w = \alpha \cdot \gamma. \quad (9.6)$$

The increase in effective stress produces a decrease in fluid pressure and head [equations (9B2.3) and (9B2.4)], which produces an expansion in the water. From equation (9B2.1), this is given by

$$dV_w = -\beta \cdot V_w \cdot dp. \quad (9.7)$$

The total volume of water in the unit volume of medium is $\phi \cdot V_B$ where ϕ is porosity. Thus using equation (9B2.4), equation (9.7) becomes

$$dV_w = \beta \cdot \phi \cdot \gamma. \quad (9.8)$$

Thus the specific storage for a confined aquifer is the sum of the water-volume changes due to compaction/expansion of the medium [equation (9.6)] and of the water [equation (9.8)].

$$S_s = (\alpha + \phi \cdot \beta) \cdot \gamma. \quad (9.9)$$

The dimensionless storage coefficient, S , for a confined aquifer is often called the **storativity**; combining equations (9.2) and (9.9) gives

$$S = (\alpha + \phi \cdot \beta) \cdot \gamma \cdot H. \quad (9.10)$$

Storativities for confined aquifers are usually in the range 5×10^{-5} to 5×10^{-3} ; i.e., at least an order of magnitude less than the specific yield for unconfined aquifers.

Table 9.1 Porosities, Specific Yields, and Specific Retentions of Geologic Materials.^a

Material	Porosity			Specific Yield			Specific Retention		
	Min.	Avg.	Max.	Min.	Avg.	Max.	Min.	Avg.	Max.
Unconsolidated Alluvial Deposits									
Clay	0.34	0.42	0.57	0.01	0.06	0.18	0.25	0.38	0.47
Silt	0.34	0.46	0.61	0.01	0.20	0.39	0.03	0.28	0.45
Fine sand	0.26	0.43	0.53	0.01	0.33	0.46	0.03	0.08	0.43
Medium sand	0.29	0.39	0.49	0.16	0.32	0.46	0.01	0.04	0.18
Coarse sand	0.31	0.39	0.46	0.18	0.30	0.43	0.05	0.07	0.18
Fine gravel	0.25	0.34	0.39	0.13	0.28	0.40	0.00	0.07	0.17
Medium gravel	0.24	0.32	0.44	0.17	0.24	0.44	0.01	0.07	0.15
Coarse gravel	0.24	0.28	0.37	0.13	0.21	0.25	0.03	0.09	0.14
Unconsolidated Glacial Deposits									
Silty till	0.30	0.34	0.41	0.01	0.06	0.13	0.23	0.28	0.33
Sandy till	0.22	0.31	0.37	0.02	0.16	0.31	0.03	0.14	0.29
Gravelly till	0.22	0.26	0.30	0.05	0.16	0.34	0.01	0.12	0.25
Unconsolidated Aeolian Deposits									
Loess	0.44	0.49	0.57	0.14	0.18	0.22	0.22	0.27	0.30
Aeolian sand	0.40	0.45	0.51	0.32	0.38	0.47	0.01	0.03	0.06
Unconsolidated Biogenic Deposits									
Peat		0.92			0.44			0.44	
Weathered Rock (Saprolites)									
Granite	0.34	0.45	0.57						
Gabbro	0.42	0.43	0.45						
Clastic Sedimentary Rocks									
Fine sandstone	0.14	0.33	0.49	0.02	0.21	0.40	0.01	0.13	0.31
Med. sandstone	0.30	0.37	0.44	0.12	0.27	0.41	0.05	0.10	0.19
Siltstone	0.29	0.35	0.48	0.01	0.12	0.33	0.05	0.29	0.45
Claystone	0.41	0.43	0.45						
Shale	0.01	0.06	0.10						
Carbonate Rocks									
Limestone	0.07	0.30	0.56	0.02	0.14	0.36	0.05	0.13	0.29
Dolomite	0.19	0.26	0.33						
Igneous and Metamorphic Rocks									
Basalt	0.03	0.17	0.35						
Volcanic tuff	0.07	0.41	0.55	0.02	0.21	0.47	0.06	0.21	0.38
Schist	0.04	0.38	0.49	0.22	0.26	0.33	0.22	0.26	0.33

^aValues measured in small samples by Morris and Johnson (1967).

Box 9.2 Effective Stress and the Compressibility of Water and Aquifers

Compressibility of Water

Consider a volume of water V_w at a pressure p . If the pressure is increased by an amount dp , the volume will decrease by an amount $-dV_w$. The compressibility of water, β , is defined as the relative decrease in volume per unit increase in pressure [$L^2 F^{-1}$]:

$$\beta \equiv \frac{-dV_w/V_w}{dp} \quad (9B2.1)$$

This is a reversible process, so a decrease in pressure ($dp < 0$) causes a concomitant expansion ($dV_w > 0$). β for water is very small and is effectively constant at near-surface pressures and temperatures at $\beta = 4.4 \times 10^{-10} \text{ m}^2/\text{N}$.

Effective Stress

Consider a horizontal plane within a saturated porous medium. The total stress (\equiv force per unit area [$F L^{-2}$]) acting on the plane is due to the weight of the overlying mineral medium and water. Part of this stress is borne by the solid particles of the medium and part by the fluid, which is reflected in the fluid pressure. Thus

$$\sigma_T = p + \sigma_{eff}, \quad (9B2.2)$$

where σ_T is total stress, p is fluid pressure, and σ_{eff} is the stress borne by the medium, which is called the **effective stress**.

In most hydrologic situations, the weight of the overlying rock and water do not change, so that $d\sigma_T = 0$ and

$$d\sigma_{eff} = -dp. \quad (9B2.3)$$

Thus if pressure decreases, stress is transferred from the fluid to the medium, and effective stress increases. This increase causes the grains of the medium to become somewhat more densely packed, so the medium compacts. If pressure increases, the effective stress decreases, and the medium tends to expand. However, the process is not quantitatively reversible, and the expansion is less than the compaction in response to a given dp . This means that a medium tends to become increasingly compacted in response to repeated cycles of increasing and decreasing pressure changes.

Since

$$p = \gamma \cdot \psi = \gamma \cdot (h - z), \quad (9B2.4)$$

and z is constant at any level,

$$d\sigma_{eff} = -\gamma \cdot d\psi = -\gamma \cdot dh; \quad (9B2.5)$$

that is, changes in effective stress are determined by changes in hydraulic head.

Note that changes in effective stress do not respond immediately to changes in pressure; water flow in response to a change in pressure may take considerable time (months to years in some cases).

Compressibility of Porous Media

The compressibility of the medium, α [$L^2 F^{-1}$], is defined analogously to that of water:

$$\alpha \equiv \frac{-dV_T/V_T}{d\sigma_{eff}}, \quad (9B2.6)$$

where V_T is the total volume of the medium (solid plus pore space).

Because of the nonreversibility of porous-media compaction, α is a function of the applied stress and of the history of stress changes. The table below gives ranges of α values for porous media. Note that these are generally much larger than for water, especially for unconsolidated materials.

Table 9B2.1

Medium	Compressibility, α (m^2/N)
Clay	10^{-8} to 10^{-6}
Sand	10^{-9} to 10^{-7}
Gravel	10^{-10} to 10^{-8}
Jointed rock	10^{-10} to 10^{-8}
Sound rock	10^{-11} to 10^{-9}

Source: Freeze and Cherry (1979).

9.1.4 Transmission Properties of Aquifers

The fundamental transmission property of a porous medium is its saturated hydraulic conductivity, K_h , which is the volume rate of flow per unit area transmitted through the medium by a unit hydraulic-head gradient [equation (9B1.2)]. Methods of mea-

surement and ranges of values of K_h were described in section 7.3. As noted there, K_h has significant spatial variability, even within a given aquifer, and conductivity at a “point” may be different in different directions. Figure 9.4 illustrates the four possible combinations of anisotropy and heterogeneity: If K_h at a “point” is the

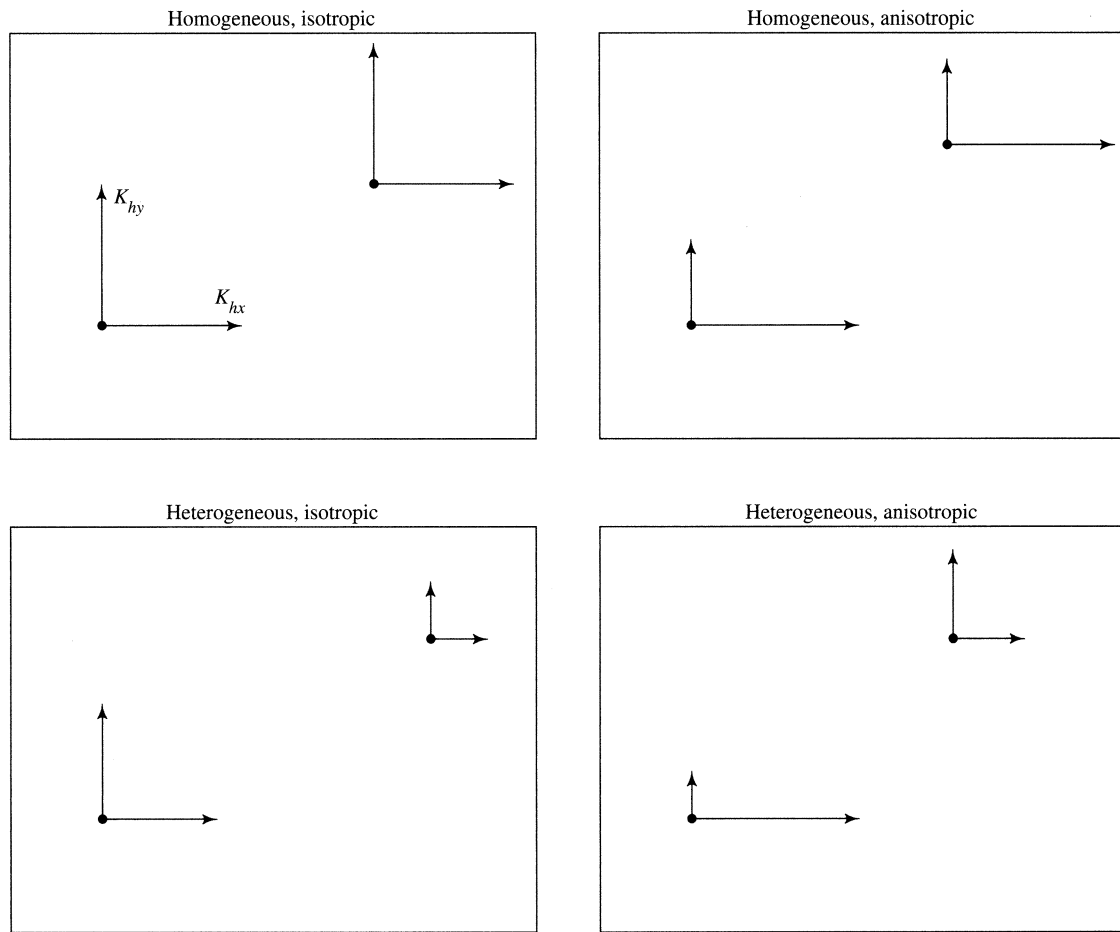


Figure 9.4 Four possible combinations of heterogeneity and anisotropy in saturated hydraulic conductivity [adapted from Freeze and Cherry (1979)].

same for all directions, the medium is **isotropic**; otherwise it is **anisotropic**. If the conductivity in all directions is the same at all “points,” the medium is **homogeneous**; otherwise it is **heterogeneous**.

When dealing with flows to wells in confined aquifers in which K_h and the saturated thickness, H , are only slightly variable and the flow paths are approximately horizontal, ground-water hydrologists often use the concept of aquifer **transmissivity**, T [$L^2 \cdot T^{-1}$], defined as

$$T \equiv H \cdot K_h. \quad (9.11)$$

9.1.5 Aquifer Response Time and Residence Time

Unconfined aquifers are reservoirs in which outflow is related to storage [equation (1.23)], and stor-

age is related to inflow and outflow. A relative measure of the time scale at which aquifer storage and outflow vary is given by

$$\tau = \frac{L^2 \cdot S}{H \cdot K_h} = \frac{L^2 \cdot S}{T}, \quad (9.12)$$

where τ is **aquifer response time** [T], L is a measure of the horizontal extent of the aquifer [L], and the other symbols are as defined earlier. The inverse of τ is often called the **aquifer response rate** (Erskine and Papaioannou 1997). These response characteristics appear in various contexts later in this chapter.

As noted, the S values, and hence response times, for unconfined aquifers are orders of magnitude greater than those for confined aquifers, because changes in storage in unconfined aquifers reflect the

actual filling and emptying of soil pores rather than the very minor effects of water and aquifer compressibility. Unconfined aquifers may also be subject to recharge by infiltration and water loss in response to evapotranspiration over their entire extents. Thus

Unconfined aquifers are much more
interactively related to the regional
hydrologic cycle than are confined aquifers,

and unconfined aquifers will be the sole focus of subsequent ground-water treatments in this text.

As discussed in section 1.10.3, the residence time of water in a reservoir is the average length of time a “parcel” of water spends in the reservoir. Aquifer residence time also characterizes the timing of aquifer responses to changes in recharge and the fate of contaminants that are subject to chemical and biological processes as they move through aquifers to surface-water bodies (Haitjema 1995). From equation (1.25), the general definition of residence time, T_R , is

$$T_R = \frac{\text{average storage in reservoir } [L^3]}{\text{average rate of input/output } [L^3 T^{-1}]} \quad (9.13)$$

For an unconfined aquifer of average saturated thickness H , this becomes

$$T_R = \frac{S_y \cdot H}{R}, \quad (9.14)$$

where R is average recharge rate per unit area $[L T^{-1}]$.

9.2 Regional Ground-Water Flow

9.2.1 Equation for Steady Ground-Water Flow

Recall that the general ground-water flow equation [equation (9B1.8)] is derived by combining Darcy's law with the conservation of mass. To illustrate the essential features of regional ground-water flow systems, we will use solutions of that equation that represent *steady flow* in *two-dimensional* vertical slices through unconfined aquifers (like figure 9.1), imposing simple boundary conditions that represent idealized configurations of topography and geology. For these conditions, the general equation becomes

$$\frac{\partial}{\partial x} \left(K_{hx} \cdot \frac{\partial h}{\partial x} \right) + \frac{\partial}{\partial z} \left(K_{hz} \cdot \frac{\partial h}{\partial z} \right) = 0, \quad (9.15a)$$

where x is the horizontal coordinate and z is the vertical coordinate. In many of our examples, we assume that the hydraulic-conductivity field is isotropic (i.e., $K_{hx} = K_{hz}$), and the general equation reduces to the **Laplace equation**,

$$\frac{\partial^2 h}{\partial x^2} + \frac{\partial^2 h}{\partial z^2} = 0. \quad (9.15b)$$

As noted in section 7.3.4, solutions to these equations are shown as flow nets giving the pattern of equipotentials and streamlines that is consistent with the boundary conditions and the distribution of conductivity values. The spacing of the equipotentials is inversely related to the head gradient, so the relative intensity of the circulation is larger where the equipotentials are closely spaced. The rate of flow in the direction of the streamline at any point can be calculated by determining the head gradient in that direction and multiplying it by the local value of hydraulic conductivity.

In nature, topography, conductivity, and climate influence infiltration, recharge, evapotranspiration, and discharge of ground water to streams, and hence the water-table configuration. The water-table configuration in turn influences the distribution of recharge and discharge conditions, as discussed in section 9.5. These interactive processes are not incorporated in the solutions we examine here; instead, water-table configurations typical of those observed in nature are specified as imposed boundary conditions. However, if the general configuration of the water table does not greatly change through the year, and if the fluctuations of the water table at any point are small relative to the thickness of the saturated zone (as is often the case), equation (9.15) provides an instructive picture of the essential features of regional ground-water flow under various topographic and geologic conditions. Note that these features are independent of the scale of the flow system.

9.2.2 General Features of Regional Ground-Water Flow

Figure 9.5 shows the effects of overall aquifer geometry on solutions to equation (9.15). In both cases, the upper flow boundary is a gently sloping water table, the lower boundary is a horizontal impermeable layer, the right boundary is a **divide** where flow is vertically downward, and the left boundary is a **valley** where flow is vertically upward. In relatively thin aquifers, the flow is essentially horizontal except at

the divide and valley (figure 9.5a); in relatively thick aquifers the vertical components of the streamlines are much greater throughout (figure 9.5b).

The flowlines represent flow from *recharge areas* to *discharge areas*:

- **Recharge areas** are regions in which the ground-water flow is directed away from the water table.
- **Discharge areas** are regions in which the ground-water flow is directed toward the water table.
- The line separating recharge and discharge areas is called a **hinge line**.

The water table is usually at some depth in recharge areas and at or near the surface in discharge areas. Thus discharge areas are usually the sites of surface-water bodies: streams, lakes, wetlands, or, if highly localized, springs.

Note that basic water-balance considerations dictate that the average rate of discharge from a regional aquifer must be equal to the average rate of recharge. Since recharge rate (\approx precipitation less evapotranspiration) is determined largely by climate, topography and geology determine only the spatial distributions of discharge and recharge, not the absolute rates.

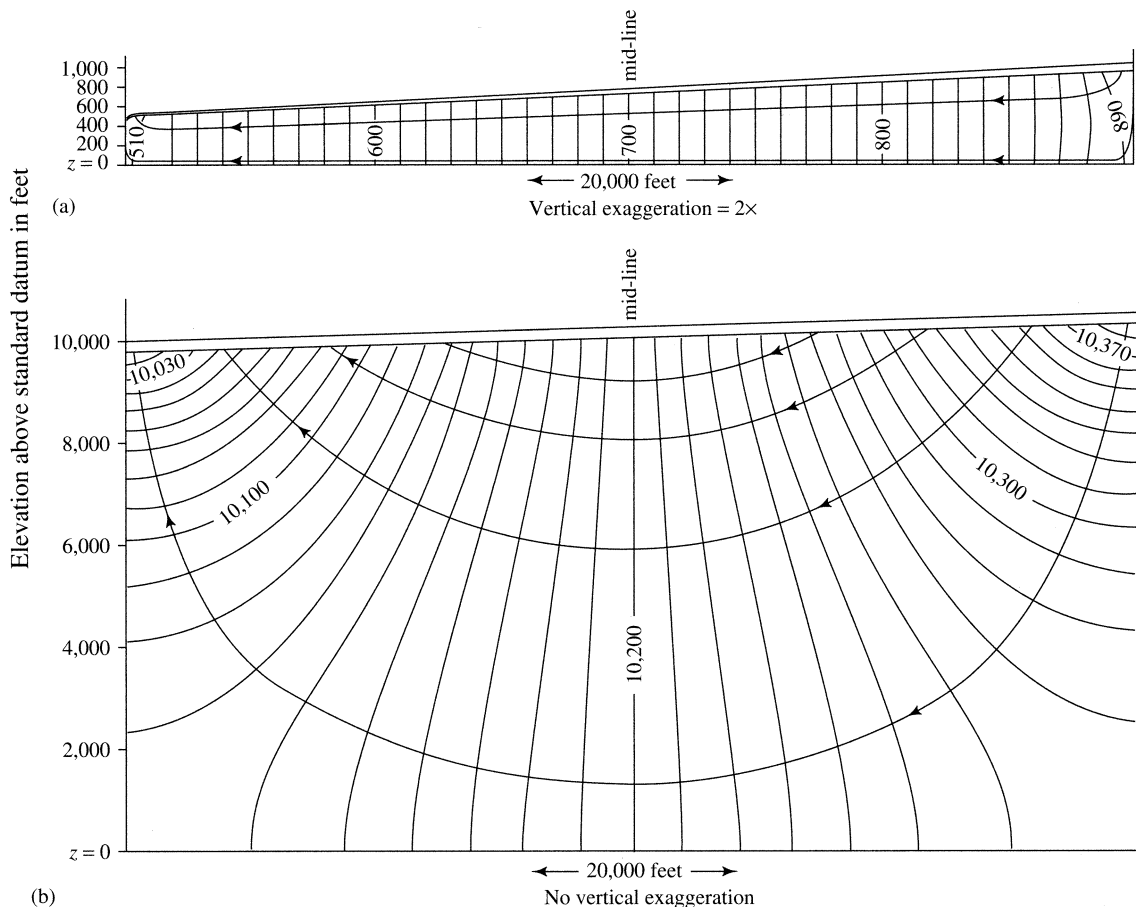


Figure 9.5 Flow-net configurations computed by applying the Laplace equation [equation (9.15b)] to idealized approximations of unconfined ground-water flow to a stream where: (a) the aquifer is relatively shallow (note flow is essentially horizontal) and (b) the aquifer is relatively deep (note flow has a significant vertical component, except near the mid-line). Contours are equipotentials; lines with arrows are streamlines [Tóth (1962)]. A theory of groundwater motion in small drainage basins in central Alberta, Canada. *Journal of Geophysical Research* 67:4375–4387, with permission of the American Geophysical Union].

9.2.3 Effects of Topography

Figure 9.6 shows a cross section through an idealized hilly upland area in a humid region, underlain by permeable deposits with homogeneous and isotropic conductivity resting on an impermeable base. Under these conditions, the solution of equation (9.15) results in a general head gradient from the divides toward the streams, with the flow moving downward and diverging near the divide and then upward and converging toward the valleys, where ground-water discharge produces streams. A boundary streamline flows vertically downward at the divides, horizontally along the impermeable base, and vertically upward under the streams. Thus in hilly humid areas,

- Surface divides and streams are usually the boundaries of ground-water flow systems;
- The balance between net vertical recharge and lateral ground-water flow produces a water table that is a subdued replica of the ground surface;
- The higher the ratio of recharge rate to hydraulic conductivity, the more closely the water table replicates the topography.

However, in arid regions or areas of asymmetric topography or heterogeneous geology, ground-water divides may not coincide with surface-water divides and surface-water bodies.

Figure 9.7 shows the flow nets for two situations of identical geology, depth to impermeable base, and lateral dimension. Both have a major valley on the left and an upland area toward the right, but the smaller-scale topography (as represented by the wa-

ter table) differs. In figure 9.7a the water table is a gently sloping plane, such as might be found beneath a region of undeformed lake or coastal-plain sediments; the water table in figure 9.7b reflects a hilly upland superimposed on the general leftward-sloping topographic trend, such as might be found in a region of glacial deposits.

The plane water table of figure 9.7a results in a single flow system, with the recharge area extending down to the central valley. In figure 9.7b, on the other hand, each hill in the water table produces a small-scale recharge-discharge system that circulates above a larger-scale flow in the left half of the system, and both these systems circulate above a still larger-scale flow system extending from the major divide to the major valley.

Patterns like that in figure 9.7b led Tóth (1963) to conclude that, in many situations, one can identify **local flow systems**, in which water moves from a recharge area to the next adjacent discharge area; **regional flow systems**, in which the flow is from the recharge area farthest from the main valley to the discharge area in the main valley; and **intermediate flow systems**, in which the flow path is longer than local but shorter than regional (figure 9.8 on p. 401).

Regions with little local relief typically have only regional systems, and regions with pronounced local relief typically have only local systems. However, the pattern of development of flow systems of various scales is affected also by the overall system geometry: Development of local flow systems is favored where the depth to the impermeable layer is small relative to

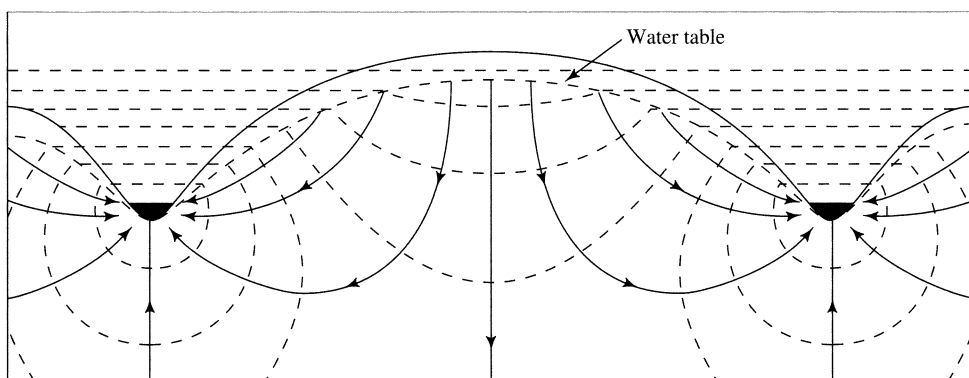


Figure 9.6 Ground-water flow net as given by solving the Laplace equation [equation (9.15b)] for a vertical section through idealized hills and valleys in a permeable material resting on an impermeable base. Dashed lines are equipotentials; arrows are streamlines. Streams, lakes, or wetlands are present in valleys where the water table intersects the land surface [adapted from Hubbert (1940)].

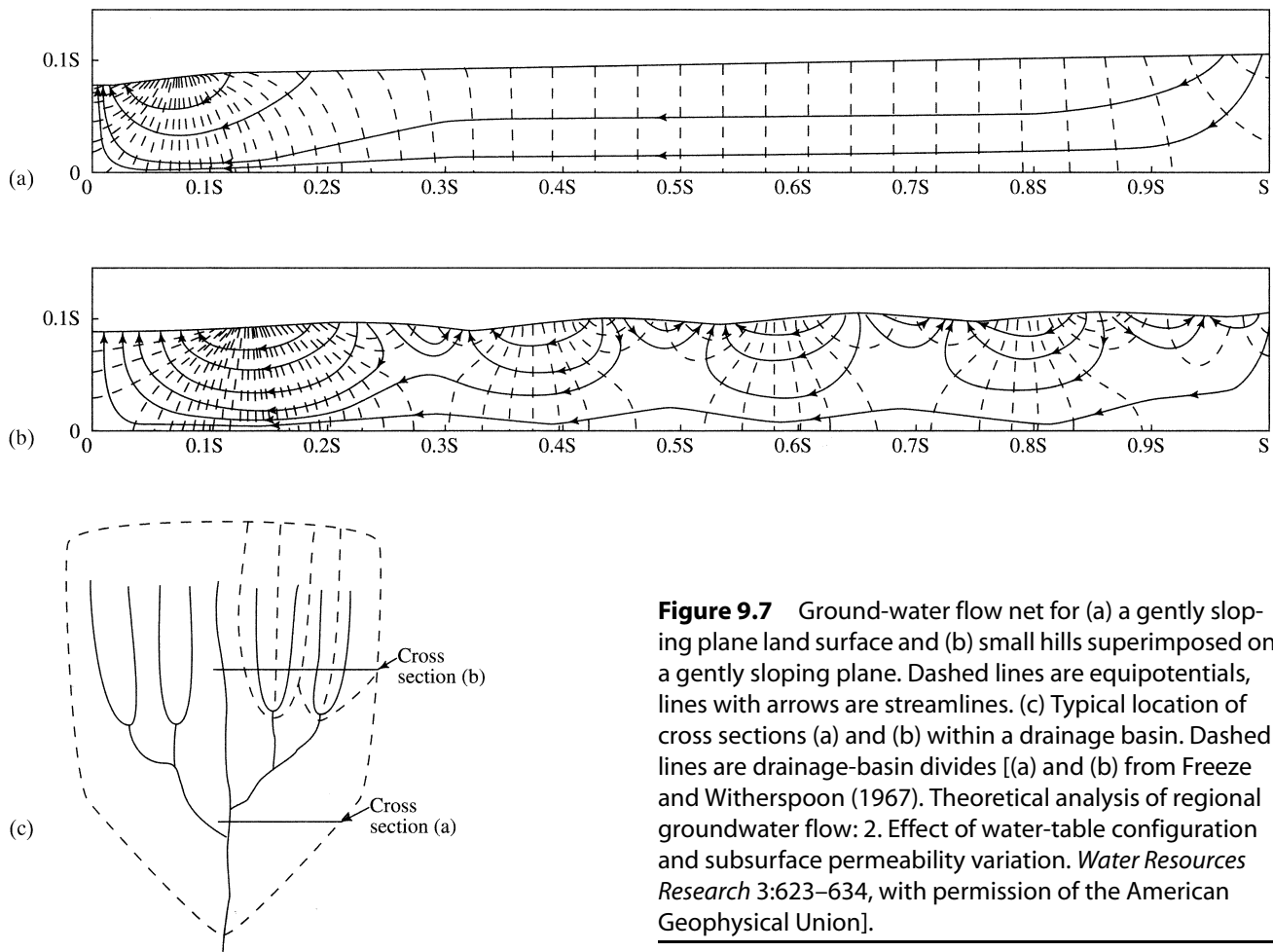


Figure 9.7 Ground-water flow net for (a) a gently sloping plane land surface and (b) small hills superimposed on a gently sloping plane. Dashed lines are equipotentials, lines with arrows are streamlines. (c) Typical location of cross sections (a) and (b) within a drainage basin. Dashed lines are drainage-basin divides [(a) and (b) from Freeze and Witherspoon (1967). Theoretical analysis of regional groundwater flow: 2. Effect of water-table configuration and subsurface permeability variation. *Water Resources Research* 3:623–634, with permission of the American Geophysical Union].

the distance from the main valley to the divide, and the more pronounced the relief, the deeper the local systems extend; regional systems are favored where the impermeable layer is deep relative to that distance. (These relations are examined further in section 9.2.5.)

Thus, as noted by Freeze and Cherry (1979), topography alone can create complex ground-water flow patterns. In general, uplands are recharge areas and lowlands are discharge areas; hinge lines are usually closer to the valleys than to the divides and discharge areas typically constitute less than 30% of a given drainage basin.

9.2.4 Effects of Geology

The most important geologic factors controlling the directions and relative rates of ground-water movement are:

1. **Lithology:** The mineral composition, grain-size distribution, and grain-shape characteristics of rocks and unconsolidated geologic materials that control the hydraulic conductivity distribution.
2. **Stratigraphy:** The geometrical relations among the various formations which, except for intrusive igneous or highly metamorphosed rocks, are typically layered.
3. **Structure:** The general arrangement and relative positions of formations, especially as modified by deformational processes such as folding, faulting, and jointing (formation of cracks) and intrusion of igneous rocks.

As noted by Freeze and Cherry (1979), an understanding of the lithology, stratigraphy, and structure of a region usually leads directly to an understanding of the distribution of aquifers and

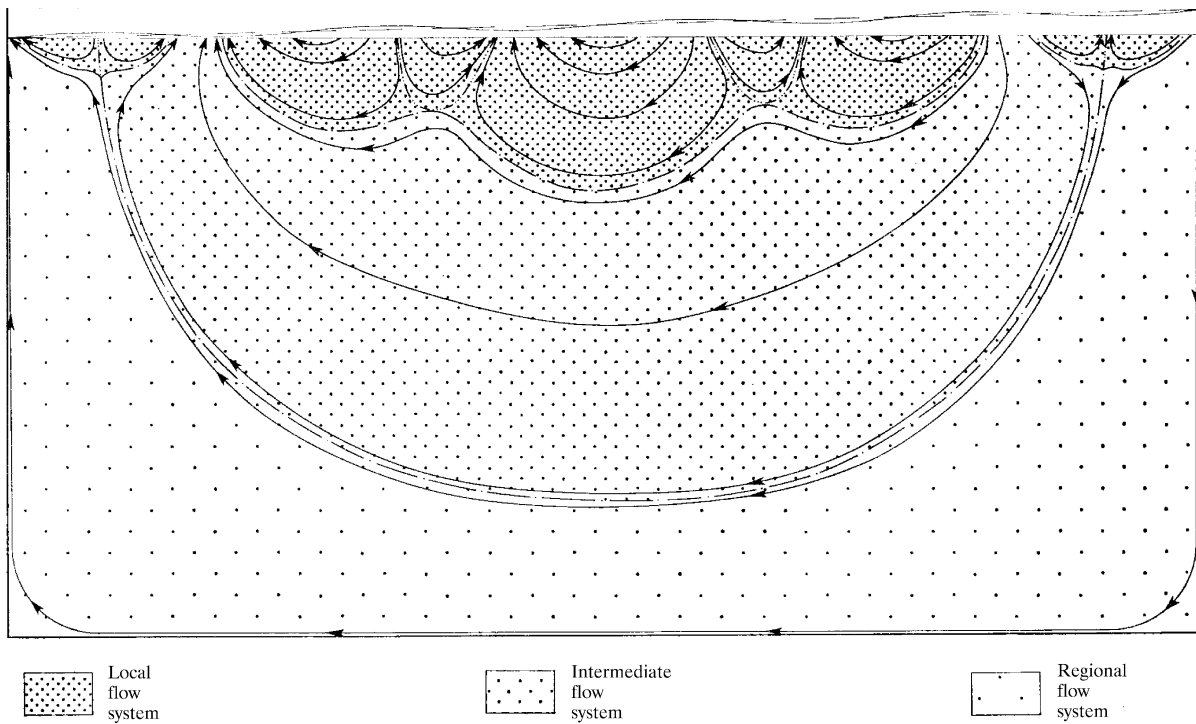


Figure 9.8. Local, intermediate, and regional ground-water flow systems [Tóth (1963). A theoretical analysis of groundwater flow in small drainage basins. *Journal of Geophysical Research* 68:4795–4812, with permission of the American Geophysical Union].

confining beds, and hence to a qualitative understanding of at least the major characteristics of ground-water movement. Complete understanding of the role of ground water in a region's hydrology must be based on detailed geologic mapping, subsurface exploration, and modeling.

Figure 7.9 shows the ranges of saturated hydraulic conductivity and table 9.1 gives some typical values of porosity, specific yield, and specific retention for various geologic materials. Figure 9.9 shows the distribution of the principal types of aquifers in the conterminous United States. More detailed information about regional ground-water geology and the ground-water characteristics of various types of geologic materials can be found in McGuinness (1963), Freeze and Cherry (1979), US Geological Survey (1985), and Fetter (2001).

Geologic conditions display infinite variability, so we can only suggest the types and magnitudes of geologic effects on ground-water flow patterns by examining a few idealized situations. In these depictions, variations in geology are represented by differences in

the relative magnitudes of saturated hydraulic conductivity.

Figure 9.10 on p. 403 shows the effects of a buried layer with hydraulic conductivity 100 times greater than the overlying layer on the flow net for a sloping-plane topography. Comparing this net with figure 9.7a, where the flow is essentially horizontal, the flow in the upper layer now has a strong vertical component and the hinge line moves upslope.

The effect of a buried high-conductivity layer in a region of hilly topography can be seen by comparing figure 9.11 with figure 9.7b. In figure 9.11 on p. 403, the buried layer changes the local flow systems near the divide to intermediate systems, reduces the flow intensities in the remaining local systems, and increases the intensity and extent of the discharge area in the main valley.

Figure 9.12 on p. 404 shows the effect of a basal lens of high-conductivity material in the upper portion of a system with flat topography. The flow net is much altered from that in figure 9.7a, with a discharge zone in mid-basin.

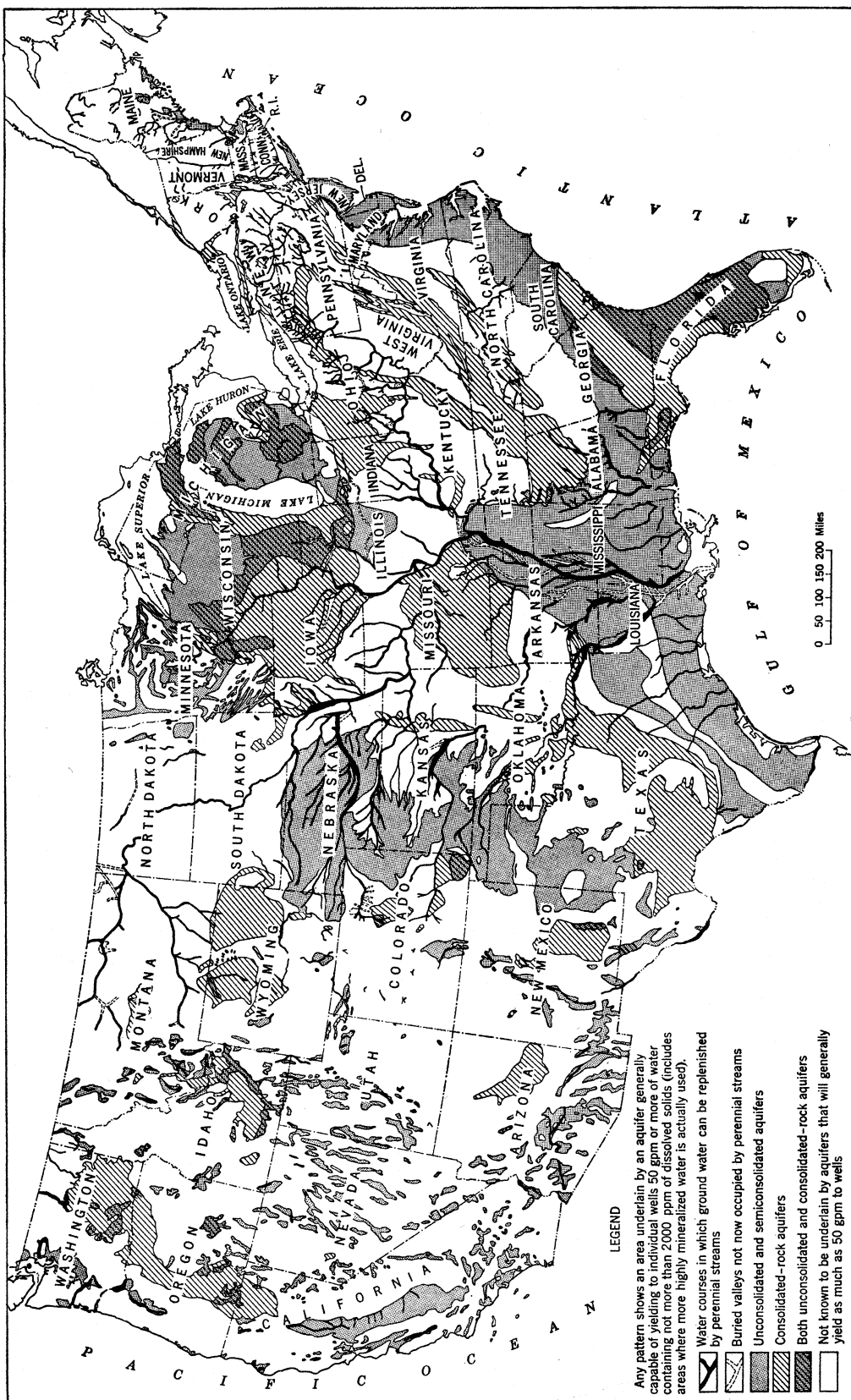


Figure 9.9 Major aquifers of the conterminous United States [McGuinness (1963)].

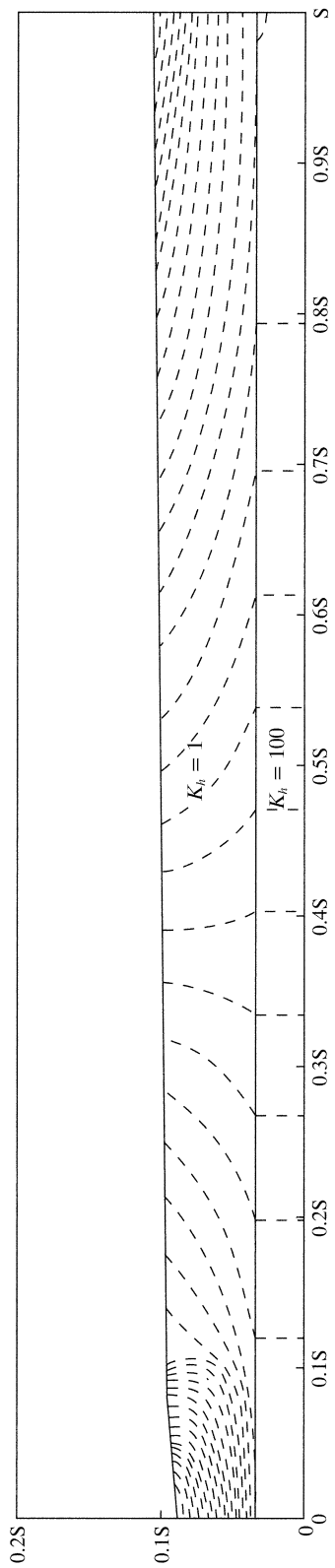


Figure 9.10 Equipotentials for topography of figure 9.7a, but with a buried layer with hydraulic conductivity 100 times greater than that of the overlying material [Freeze and Witherspoon (1967)]. Theoretical analysis of regional groundwater flow: 2. Effect of water-table configuration and subsurface permeability variation. *Water Resources Research* 3:623–634, with permission of the American Geophysical Union.

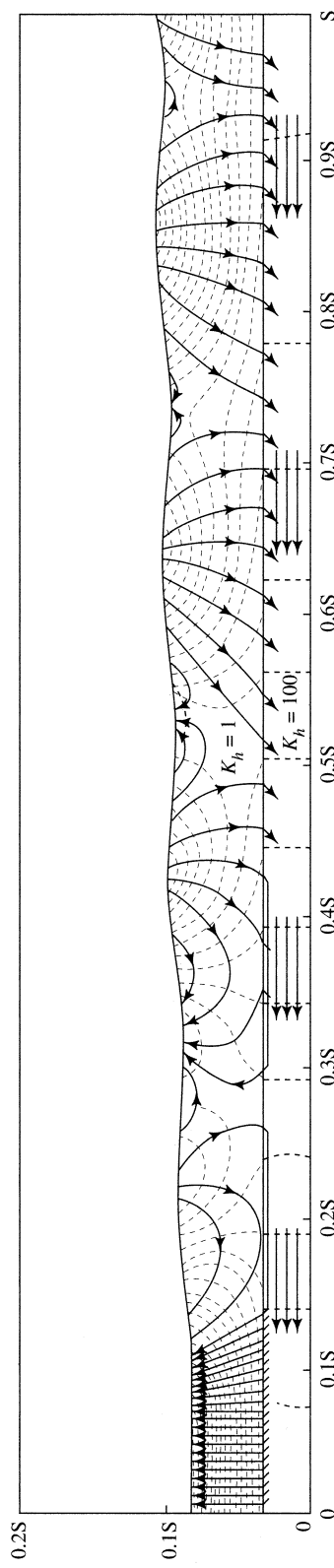


Figure 9.11 Flow net for hilly topography of figure 9.7b, but with a buried layer with hydraulic conductivity 100 times greater than that of the overlying material. Dashed lines are equipotentials, arrows are streamlines [Freeze and Witherspoon (1967)]. Theoretical analysis of regional groundwater flow: 2. Effect of water-table configuration and subsurface permeability variation. *Water Resources Research* 3:623–634, with permission of the American Geophysical Union.

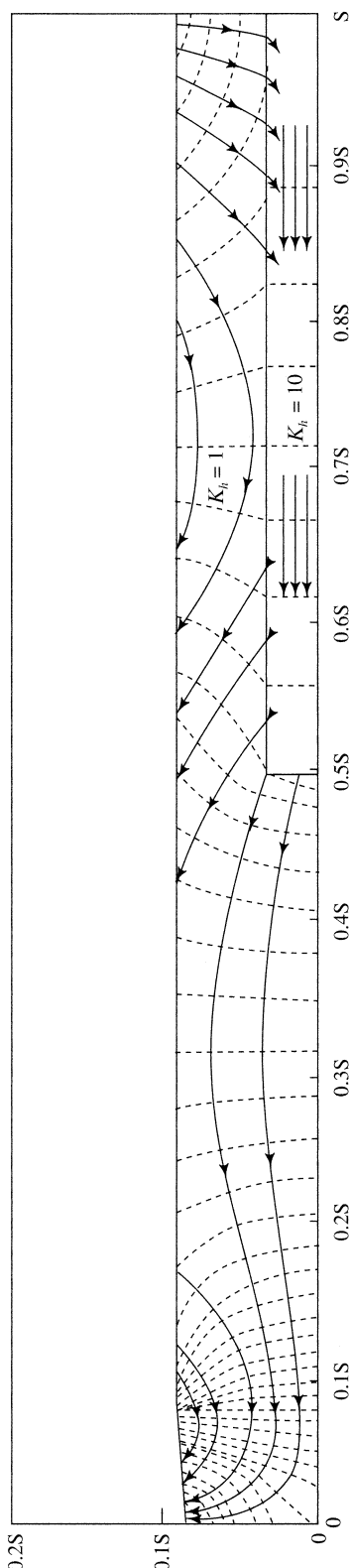


Figure 9.13 is a cross section of an actual flow system in glacial deposits in Saskatchewan, Canada, that illustrates the complexity of flow patterns that can exist in nature. Note that recharge occurs over almost the entire section, and that Notukeu Creek is a site of recharge, not discharge. Discharge occurs only to Wiwa Creek, but there is also flow beneath that stream and the northern upland to some other regional discharge site to the northeast.

Freeze and Witherspoon (1967) presented flow nets for combinations of idealized topography and geology other than those shown here. All these examples show clearly that variations in geology, which might not be apparent without detailed subsurface exploration, can produce a wide range of possible flow-net configurations consistent with a given water-table configuration. Thus information about subsurface geologic conditions and hydraulic head is necessary for formulating an accurate picture of regional ground-water flow.

9.2.5 Synthesis: Effects of Topography, Geology, and Climate

9.2.5.1 Hydrologic Landscapes

Winter (2001) introduced the concept of **hydrologic landscape** as a framework for synthesis and analysis of the interactions between topography, geology, and climate. This concept is based on the idea that a simple landform—an upland adjacent to a lowland separated by an intervening steeper slope (figure 9.14 on p. 406)—along with its geology and climate, is the basic building block of all hydrologic landscapes. Winter (2001) called this feature a **fundamental hydrologic landscape unit (FHLU)**.

The central hydrologic feature of an FHLU is a simple ground-water flow cell from the upland to the lowland, involving the movement of water between the atmosphere (precipitation and evapotranspiration), surface water (controlled by the slopes and permeability of the unit's surfaces), and ground water (controlled by the hydraulic characteristics of the unit's geologic framework). Thus in a given context,

Figure 9.12 Flow nets for topography of figure 9.7a, but with a buried lens with hydraulic conductivity 10 times greater than that of the overlying material in different positions [Freeze and Witherspoon (1967)]. Theoretical analysis of regional groundwater flow: 2. Effect of water-table configuration and subsurface permeability variation. *Water Resources Research* 3:623–634, with permission of the American Geophysical Union].

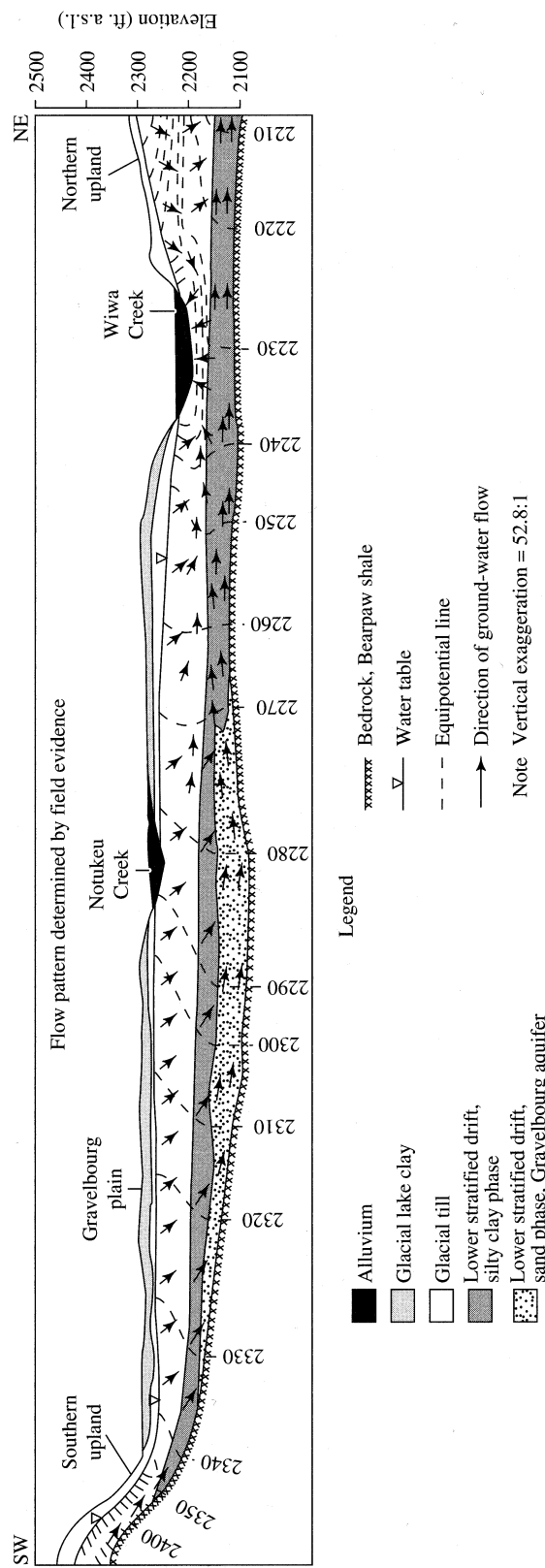


Figure 9.13 Geologic cross section and ground-water flow pattern in glacial deposits in the Wiwa Creek drainage basin, Saskatchewan, Canada, as determined from field measurements [Freeze and Witherspoon (1968)]. Theoretical analysis of regional groundwater flow: 3. Quantitative interpretations. *Water Resources Research* 4:581–590, with permission of the American Geophysical Union.

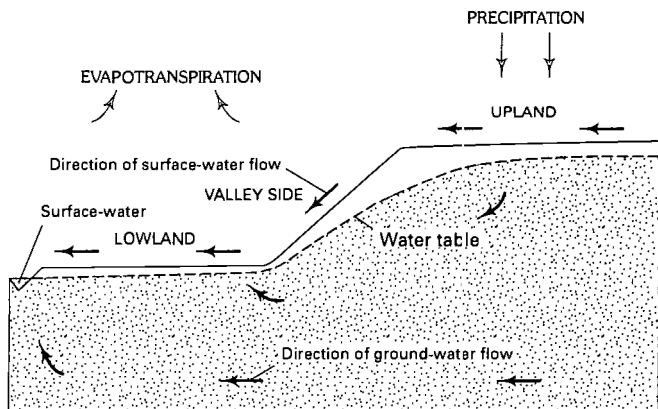


Figure 9.14 The fundamental hydrologic landscape unit (FHLU) consists of an upland adjacent to a lowland separated by an intervening steeper slope, along with its geology and climate [reproduced from Winter (2001). The concept of hydrologic landscapes. *Journal of the American Water Resources Association* 37(2):335–349, with permission of Wiley].

the characterization of the FHLU would involve a description of climate; the surface slopes and areas of the upland, lowland, and intervening steeper slopes; and the hydraulic properties of the geologic units.

Figure 9.15 shows six general FHLU types that occur commonly in various parts of the world. In all these systems

- The water table is a subdued replica of the topography; and
- Downward components of ground-water flow occur at downward breaks-in-slope of the water table, and upward components at upward breaks-in-slope.

In some settings, this may result in wetlands in the area of lower slope; wetlands may also occur where the water table intersects the lower part of the steeper land-surface slope.

The FHLU concept provides useful generalizations about the nature of ground-water–surface-water interactions in various physiographic, geologic, and climatic settings. It also provides a basis for subdivision of a region of any scale into areas likely to have similar surface-runoff and/or ground-water flow fields for hydrologic analysis and hypothesis testing.

The hypotheses can then be tested by study of a particular area, or they can be the foundation for plans of study, design, and evaluation of data networks, syntheses of existing information, enhancing transfer value of information from well studied to unstudied sites, or comparisons of research results from a wide variety of small research sites. (Winter 2001, p. 341)

9.2.5.2 Water-Table Ratio

A recent quantitative approach to regional ground-water analysis (Gleeson et al. 2011) com-

bines the influences of topography, geology, and climate into a dimensionless **water-table ratio (WTR)**:

$$WTR \equiv \frac{R \cdot X^2}{8 \cdot K_h \cdot H \cdot Z}, \quad (9.16)$$

where R is average recharge rate [L T^{-1}], X is average horizontal distance between streams [L], K_h is hydraulic conductivity [L T^{-1}], H is average vertical extent of the aquifer flow system [L], and Z is maximum watershed relief [L] (figure 9.16 on p. 408). Where $WTR > 1$, the water table is **topography-controlled**: the water table is relatively shallow and closely associated with topography. Where $WTR < 1$, the water table is **recharge-controlled**: the water table is deep and largely unrelated to topography.

Using available databases for values of R (0 to 2.2 m/yr), K_h (0 to 4,000 m/yr), and Z (0 to 4,000 m), Gleeson et al. (2011) calculated WTR for watersheds of $\sim 100 \text{ km}^2$ area in the contiguous United States (H and X were assumed to be essentially constant because all the watersheds were of similar size). These values varied over ~ 11 orders of magnitude, largely because of the variability of K_h , so values of $\log(WTR)$ were mapped. Although there was very little correlation among the R , K_h , and Z values, there was strong regional coherence in $\log(WTR)$ values. They found that areas with topography-controlled water tables [$\log(WTR) > 0$] occur in humid (high-recharge) regions with subdued topography, low hydraulic conductivity, and shallow and less variable water-table depths; local rather than regional ground-water flow is typical of these areas (e.g., in the Northeast). Conversely, recharge-controlled water tables [$\log(WTR) < 0$] occur in arid re-

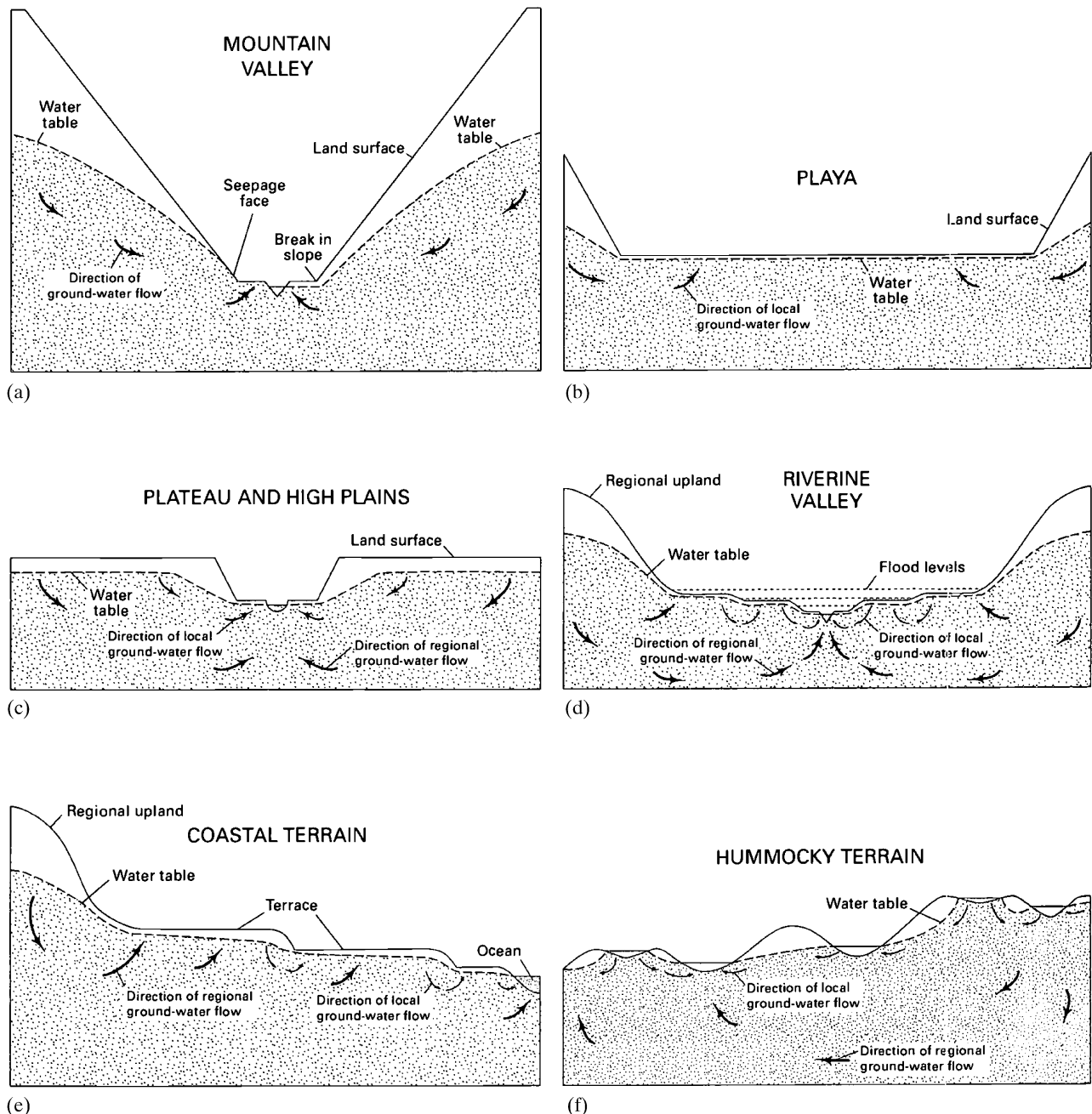


Figure 9.15 Generalized hydrologic landscapes: (a) narrow uplands and lowlands separated by a large, steep valley side (mountainous terrain); (b) large, broad lowland separated from narrow uplands by steeper valley sides (playas and basins of interior drainage); (c) small, narrow lowlands separated from large, broad uplands by steeper valley side (plateaus and high plains); (d) small FHLUs nested within a larger fundamental hydrologic landscape unit (large riverine valley with terraces); (e) small FHLUs superimposed on a larger fundamental hydrologic landscape unit (coastal plain with terraces and scarps); (f) small FHLUs superimposed at random on larger, fundamental hydrologic landscape units (hummocky glacial and dune terrain) [reproduced from Winter (2001). The concept of hydrologic landscapes. *Journal of the American Water Resources Association* 37(2):335–349, with permission of Wiley].

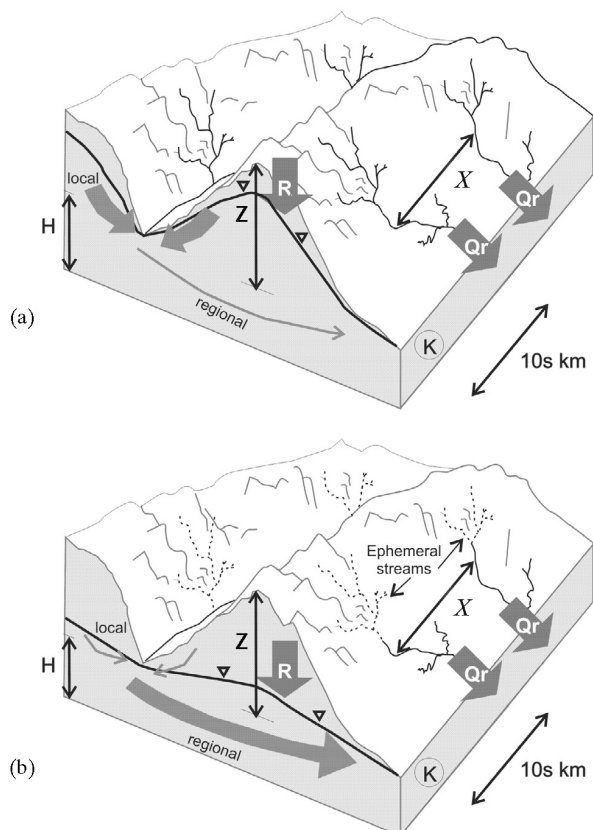


Figure 9.16 Regional water-table types classified by Gleeson et al. (2011). The arrow thickness represents the relative magnitude of regional ground-water flow. (a) Topography-controlled. (b) Recharge-controlled. The water-table depth is generally deeper and more variable in recharge-controlled water tables [Gleeson et al. (2011)]. Classifying the water table at regional to continental scales. *Geophysical Research Letters* 38, with permission of the American Geophysical Union].

gions with mountainous topography and high hydraulic conductivity; water tables are deep, and regional rather than local flow systems dominate (e.g., in the Southwest and Rocky Mountains).

Gleeson et al. (2011) concluded that differentiating water-table types on the basis of *WTR* provides a basis for conceptualizing regional ground-water flow systems, understanding the relation between ground water and surface water, and understanding the coupling of land-surface processes (precipitation, snowmelt, and evapotranspiration) to ground-water circulation. Thus in many respects, *WTR* is a quantification of Winter's (2001) hydrologic landscape approach.

9.3 Ground-Water-Surface-Water Relations

9.3.1 Ground Water and Streams

Streams range in size from rills to brooks to rivers, and there are no strict quantitative boundaries to the application of these terms. The channel geometry, bank and bed materials, and flow characteristics of a given stream as identified by a single name (e.g., Beaver Brook, Mekong River) usually change significantly along its length. Thus for purposes of describing and understanding natural streams we focus on the **stream reach**, which is a stream segment with fairly uniform size and shape, water-surface slope, channel materials, and relation to ground-water inflows and outflows. The length of a reach depends on the scale and purposes of a study. The volumetric flow rate (volume per unit time) within a channel is the **discharge** or **streamflow** [$L^3 T^{-1}$]; this quantity varies along a stream and with time at a given location.

Here we examine the types of relations that can exist between stream reaches and ground water, define some useful terms, and introduce a simple but useful quantitative model of the relation between recharge, ground-water flow, and streamflow. Approaches to quantifying ground-water contributions to streamflow are discussed in section 9.5.3.

9.3.1.1 Event Flow and Base Flow

Water that enters streams promptly in response to individual water-input events (rain and/or snowmelt) is called **event flow**, **direct flow**, **storm flow**, or **quick flow**. This is distinguished from **base flow**, which is water that enters from persistent, slowly varying (long-residence-time) sources and maintains streamflow between water-input events. Stream reaches that receive large proportions of their flow as base flow tend to have relatively low temporal flow variability, and hence provide a more reliable source of water for various water-resource purposes (water supply, waste-water dilution, navigation, hydropower generation, etc.).

It is usually assumed that most, if not all, base flow is supplied by ground-water discharge, as depicted in figures 9.5–9.7 and 9.10–9.12. However, base flow can also come from lakes or wetlands, or even from the slow drainage of relatively thin soils on upland hillslopes (Hewlett and Hibbert 1963). Conversely, ground water can also contribute to quick flow; these aspects of ground-water-surface-water relations are examined in chapter 10.

9.3.1.2 Stream Types

A stream reach that occurs in a discharge area and receives ground-water flow is called a **gaining** (or **effluent**) **reach**; its discharge increases downstream. The surface of gaining reaches is generally very slightly below the out-cropping of the water table, with a thin **seepage face** between the two surfaces (figure 9.17a).

A **losing** (or **influent**) **reach** is one in which discharge decreases downstream; such a reach typically occurs in a recharge zone and may either be connected to (figure 9.17b) or “perched” above (figure 9.17c) the general ground-water flow. A **flow-through** **reach** is one that simultaneously receives and loses ground water (figure 9.17d).

Relations between ground water and streams are highly dynamic, especially in humid regions. During wet seasons, when recharge exceeds evapotranspira-

tion, the water table rises and intersects stream channels widely over the watershed, converting dry, losing reaches to gaining and making the watershed more responsive to water-input events (section 10.4). In seasons when precipitation is less or evapotranspiration greater, the water table recedes and upstream gaining reaches become losing. A stream reach that contains flow all year is **perennial**; one with flow only during wet seasons is **intermittent**; one with flow only in response to a water-input event is **ephemeral**. Perennial and intermittent reaches are usually sustained by ground-water flow between water-input events (gaining), while ephemeral reaches are usually losing.

9.3.1.3 Hyporheic Flow

Hyporheic flow is the exchange of stream water and ground water that occurs in the stream bed. The

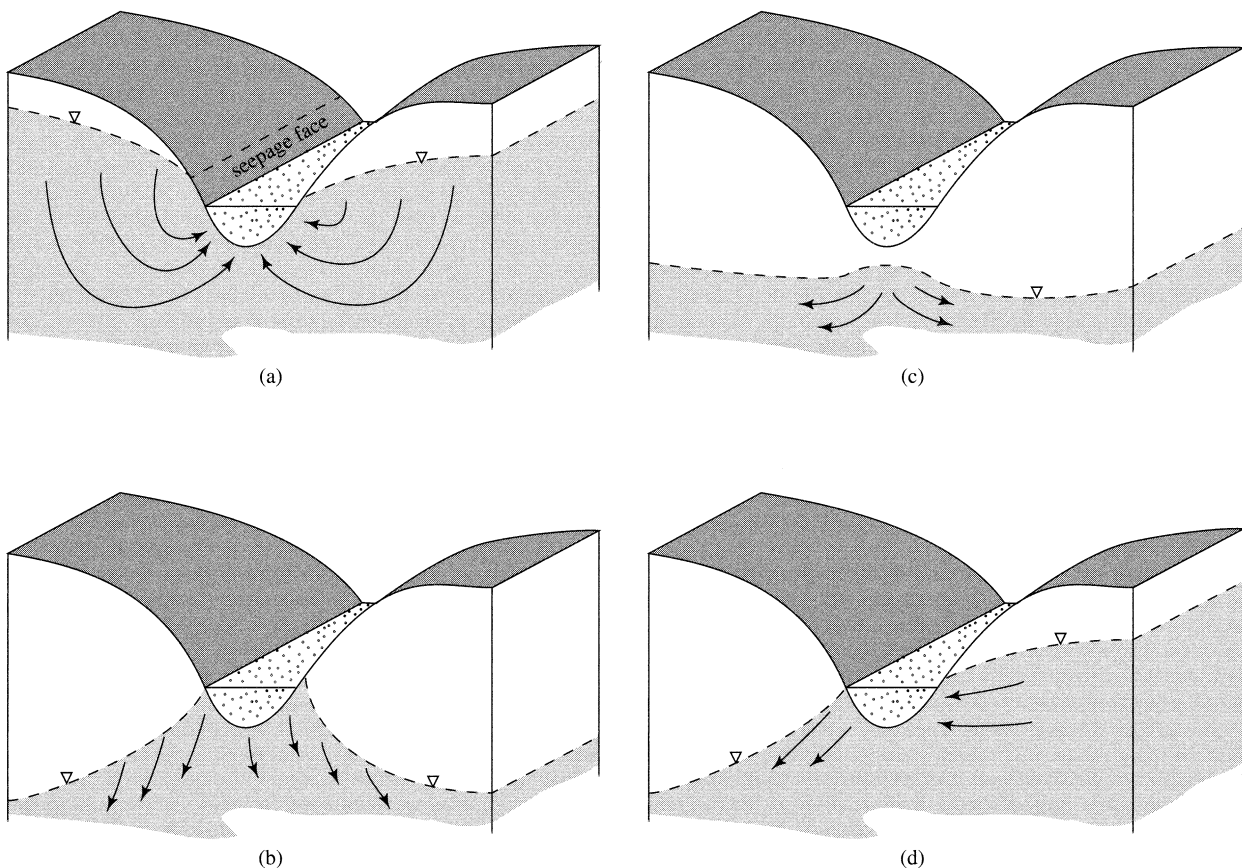


Figure 9.17 Stream-aquifer relations. (a) Gaining stream receiving water from local, intermediate, or regional ground-water flow; (b) losing stream connected to water table; (c) losing stream perched above water table; (d) flow-through stream.

hyporheic zone can extend laterally from the stream up to hundreds of meters under the floodplain (e.g., Jones et al. 2007), and vertically several meters into the stream bed (Tonina and Buffington 2011). Buried paleochannels can create high-conductivity zones that conduct hyporheic flow away from and back toward the active channel (e.g., Kasahara and Wondzell 2003). The importance of the hyporheic zone to water quality and aquatic organisms, including fish spawning, is increasingly being recognized (e.g., Hakenkamp et al. 1993).

Hyporheic flow is produced by variations in bed topography that create pressure-head differences: Flow enters the bed in zones of high pressure, and re-enters the channel in zones of low pressure. Based on flume experiments and modeling, Tonina and Buffington (2011) found that the depth of the hyporheic zone was about 0.3 times the streamwise spacing of the bedforms, and that the characteristics of hyporheic exchange vary with stream discharge, bedform amplitude, and depth of alluvium, as summarized in table 9.2. The depth of alluvium is the primary control on the character of hyporheic flow when an impermeable sublayer is present at a depth less than 0.3 times the bedform spacing. Stream discharge controls the pressure distribution at the sediment interface and bedform amplitude influences pressure distribution and the area of bed available for exchange.

9.3.1.4 Bank Storage

The lateral exchange of water between the channel and banks is commonly significant during high

flows, and is termed **bank storage**. When an event flow enters a gaining reach, a flood wave forms and travels downstream (section 10.5). As the leading edge of the wave passes, the stream-water level rises above the water table in the bank, reversing the head gradient and inducing flow from the stream into the bank (figure 9.18b). After the peak of the wave passes, the stream level declines and a streamward gradient is once again established (figure 9.18c). Now the wedge of stream-water storage created by the rapid rise drains in both directions, but ultimately all returns to the stream.

By temporarily removing water from the channel, bank storage reduces the magnitude and delays the peak of the flood wave that would otherwise have occurred in response to the water-input event (figure 9.19). The importance of this natural flood-control process varies depending on the channel configuration and material, the extent of the permeable banks, and the rate of rise, magnitude, and duration of the flood wave. Approaches to quantitative modeling of bank storage have been developed by Rorabaugh (1964), Pinder and Sauer (1971), Moench et al. (1974), Hunt (1990), and Whiting and Pomeranets (1997).

9.3.1.5 The Dupuit Approximation

In gaining streams, which are typical of humid regions, streamflow consists largely of drainage from unconfined aquifers (figures 9.6 and 9.17a). Flow in unconfined aquifers is inherently difficult to characterize because the position of the upper flow boundary (the water table) changes with time. However,

Table 9.2 Relations between Hyporheic-Flow Characteristics and Stream Discharge, Bedform Amplitude, and Depth of Alluvium.

Characteristic	Stream Discharge (Q)	Bedform Amplitude (Z_{BF})	Depth of Alluvium ^a (Z_A)
Average depth of hyporheic zone (Z_{HZ})	$Z_{HZ} \downarrow$ as $Q \uparrow$ when bedforms partially submerged.	$Z_{HZ} \downarrow$ as $Z_{BF} \downarrow$	$Z_{HZ} \downarrow$ as $Z_A \downarrow$
	$Z_{HZ} \uparrow$ as $Q \uparrow$ when bedforms fully submerged.		
Average residence time in hyporheic zone (T_{HZ})	$T_{HZ} \downarrow$ as $Q \uparrow$	$T_{HZ} \downarrow$ as $Z_{BF} \downarrow$ when bedforms partially submerged.	$T_{HZ} \downarrow$ as $Z_A \downarrow$
Average downward hyporheic flux, (Q_{HZ})	$Q_{HZ} \uparrow$ as $Q \uparrow$	$Q_{HZ} \uparrow$ as $Z_{BF} \uparrow$	$Q_{HZ} \downarrow$ as $Z_A \downarrow$

↑ = increases

↓ = decreases

^aWhen $Z_A > Z_{HZ}$, Z_A does not affect hyporheic-flow characteristics.

Source: Adapted from Tonina and Buffington (2011).

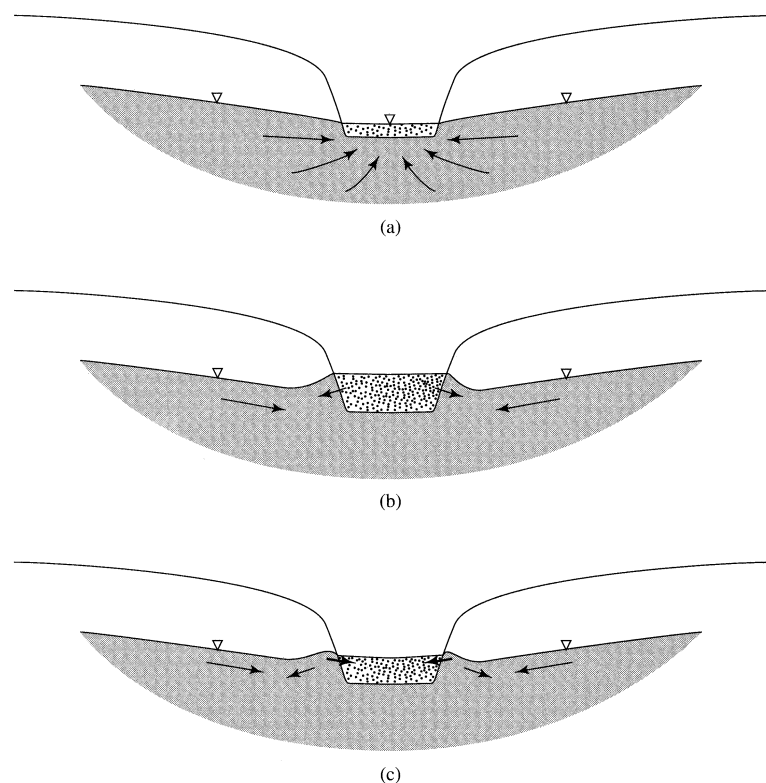


Figure 9.18 The bank-storage process.

In (a) the stream is receiving base flow only. In (b) a flood peak is passing, and flow is induced into the banks. In (c) the peak has passed and the bank-storage wedge is draining.

useful approximate analytical solutions to many unconfined flow problems can be developed using assumptions formulated by the French engineer A. J. E. J. Dupuit in 1863. The **Dupuit equations** are derived in box 9.3 (figure 9.20), and are applied to a simplified steady-state model of an aquifer draining to streams in box 9.4 (figure 9.21 on p. 413).

Equation (9B4.9) gives significant insight into the water-balance relations between ground-water and surface-water flows: It shows that average ground-water discharge to streams depends only on the average rate of recharge from infiltration, which is essentially climatically determined, and the stream spacing. The hydraulic conductivity determines the configuration of the water table required to transmit the recharge to streams [equation (9B4.5)], but not the flow rate.

Note that q_{GW} in equation (9B4.9) is the ground-water contribution to streamflow *per unit length of stream* from one-half of the drainage basin above the cross section. Thus for a drainage basin,

$$q_{GW} = \frac{Q_{GW}}{2 \cdot L}, \quad (9.17)$$

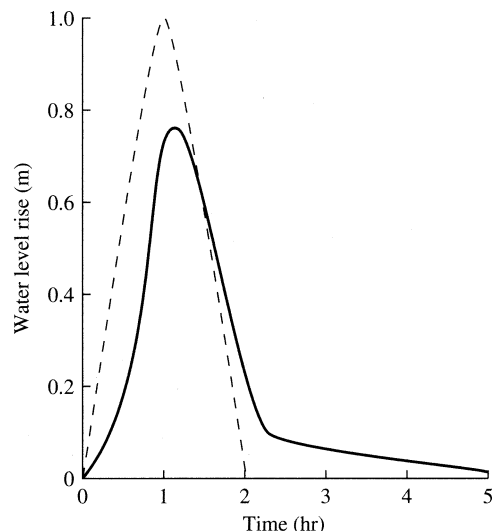


Figure 9.19 Flood-control effect of bank storage. The dashed line shows the magnitude of a hypothetical flood wave in the absence of bank storage; the solid line shows the peak reduction and delay due to bank storage for conditions modeled by Hunt (1990). Bank storage is filling/draining when the dashed hydrograph is above/below the solid-line hydrograph.

Box 9.3 Dupuit Approximation for Unconfined Flow

The Dupuit formulation follows the reasoning used in deriving the general equation for ground-water flow in box 7.3, but with the following simplifying assumptions (see figure 9.20): (1) the control volume extends from a horizontal impermeable base in the x - y plane up to the water table; (2) at any point in the x - y plane the total head, h , is constant in the vertical (z) direction so that the vertical flow rate $q_z = 0$; and (3) the head gradients are assumed equal to the slope of the water table. These assumptions do not introduce significant errors for water-table slopes < 0.18 (Smith and Wheatcraft 1992).

Under these conditions, the mass inflow, M_{in} , (through faces 1, 2, and 3) during time period dt is

$$M_{in} = \rho \cdot q_x \cdot h \cdot dy \cdot dt + \rho \cdot q_y \cdot h \cdot dx \cdot dt + \rho \cdot R_I \cdot dx \cdot dy \cdot dt, \quad (9B3.1)$$

where R_I is the net rate of recharge from infiltration per unit area [$L T^{-1}$] and q_x and q_y are the Darcy velocities [$L T^{-1}$] in the x - and y -directions, respectively. Since both q and h may change in the x - and y -directions, the outflow (through faces 3 and 4 only, since face 6 is impermeable) in dt , M_{out} , is

$$M_{out} = \rho \cdot \left[q_x \cdot h + \frac{\partial(q_x \cdot h)}{\partial x} \cdot dx \right] \cdot dy \cdot dt + \rho \cdot \left[q_y \cdot h + \frac{\partial(q_y \cdot h)}{\partial y} \cdot dy \right] \cdot dx \cdot dt. \quad (9B3.2)$$

The change in storage during dt is

$$\rho \cdot S_y \cdot \frac{\partial h}{\partial t} \cdot dx \cdot dy \cdot dt, \quad (9B3.3)$$

where S_y is the aquifer specific yield. Thus

$$M_{in} - M_{out} = R_I - \frac{\partial(q_x \cdot h)}{\partial x} - \frac{\partial(q_y \cdot h)}{\partial y} = S_y \cdot \frac{\partial h}{\partial t}. \quad (9B3.4)$$

Replacing q_x and q_y with the flow rates given by Darcy's law then yields

$$R_I - \frac{\partial}{\partial x} \left(-K_{hx} \cdot \frac{\partial h}{\partial x} \cdot h \right) - \frac{\partial}{\partial y} \left(-K_{hy} \cdot \frac{\partial h}{\partial y} \cdot h \right) = S_y \cdot \frac{\partial h}{\partial t}. \quad (9B3.5)$$

If the aquifer is homogeneous and isotropic ($K_{hx} = K_{hy} = K_h$), this is further simplified to

$$\frac{R_I}{K_h} + \frac{\partial}{\partial x} \left(h \cdot \frac{\partial h}{\partial x} \right) + \frac{\partial}{\partial y} \left(h \cdot \frac{\partial h}{\partial y} \right) = \frac{S_y}{K_h} \cdot \frac{\partial h}{\partial t}. \quad (9B3.6)$$

Now we can make use of the mathematical identities

$$h \cdot \frac{\partial h}{\partial x} = \frac{1}{2} \cdot \frac{\partial(h^2)}{\partial x}; \quad h \cdot \frac{\partial h}{\partial y} = \frac{1}{2} \cdot \frac{\partial(h^2)}{\partial y} \quad (9B3.7)$$

to rewrite equation (9B3.6) as

$$\frac{2 \cdot R_I}{K_h} + \frac{\partial^2(h^2)}{\partial x^2} + \frac{\partial^2(h^2)}{\partial y^2} = \frac{2 \cdot S_y}{K_h} \cdot \frac{\partial h}{\partial t}, \quad (9B3.8)$$

which is the Dupuit equation for time-varying flow in a homogeneous isotropic aquifer. For steady flow in a homogeneous isotropic aquifer, equation (9B3.8) becomes

$$\frac{2 \cdot R_I}{K_h} + \frac{\partial^2(h^2)}{\partial x^2} + \frac{\partial^2(h^2)}{\partial y^2} = 0. \quad (9B3.9)$$

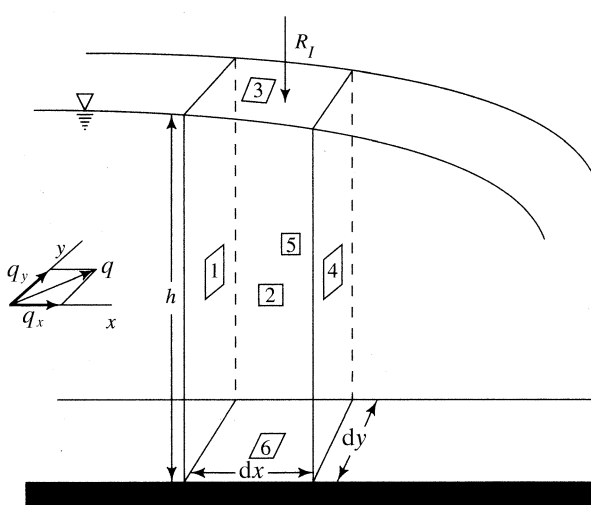


Figure 9.20 Definition diagram for derivation of the Dupuit equation (box 9.3).

Box 9.4 Dupuit Approximation for Steady-State Unconfined Aquifer Drainage to Streams

Figure 9.21 is a simplified version of figure 9.6, in which the land surface between streams is horizontal and the streams are **fully penetrating**, i.e., they extend downward to the basal impermeable layer. We consider long-term average (i.e., steady-state) conditions, and to make the development more general we show an asymmetrical situation, with $h_0 \neq h_X$. Since flow is in the x -direction only, equation (9B3.9) becomes

$$\frac{\partial^2(h^2)}{\partial x^2} = 0. \quad (9B4.1)$$

Separating variables and integrating twice yields

$$h^2 = -\frac{R_I}{K_h} \cdot x^2 + C_1 \cdot x + C_2. \quad (9B4.2)$$

The constants of integration, C_1 and C_2 , are evaluated by noting that

$$h = h_0 \text{ at } x = 0 \quad (9B4.3)$$

and

$$h = h_X \text{ at } x = X, \quad (9B4.4)$$

so that

$$h^2 = -\frac{R_I}{K_h} \cdot x^2 + \left(\frac{h_X^2 - h_0^2}{X} + \frac{R_I \cdot X}{K_h} \right) \cdot x + h_0^2. \quad (9B4.5)$$

Equation (9B4.5) states that the water table in this situation is a curved surface whose shape is determined by

the stream spacing (X), the hydraulic conductivity (K_h), the recharge rate (R_I), and the stream elevations h_0 and h_X . By manipulation of this relation, we can show that the maximum water-table elevation (i.e., the ground-water divide), h_{max} occurs at $x = X_d$, where

$$X_d = \left[\frac{X}{2} - \frac{K_h \cdot (h_0^2 - h_X^2)}{2 \cdot R_I \cdot X} \right] \quad (9B4.6)$$

and has a value

$$h_{max} = \left[h_0^2 - \frac{(h_0^2 - h_X^2) \cdot X_d}{X} - \frac{R_I \cdot (X - X_d) \cdot X_d}{K_h} \right]^{1/2}. \quad (9B4.7)$$

Note that for $h_0 = h_X$ the configuration becomes symmetrical, analogous to figure 9.6. Under these conditions, the discharge to the streams (per unit stream length), q_{GW} , is

$$q_{GW} = q_{GW0} = q_{GWX} = -K_h \cdot h_X \cdot \frac{dh}{dx} \Big|_X. \quad (9B4.8)$$

Evaluating dh/dx from equation (9B4.5) and substituting into equation (9B4.8) then leads to

$$q_{GW} = \frac{R_I \cdot X}{2}. \quad (9B4.9)$$

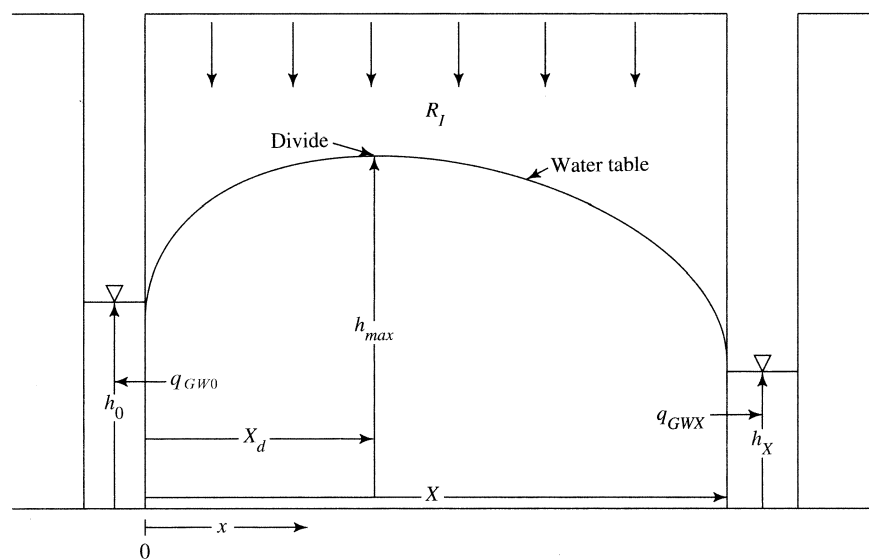


Figure 9.21 Definition sketch for Dupuit flow to streams (box 9.4). Under the Dupuit assumptions (box 9.3), equipotential lines are vertical and streamlines are horizontal, in contrast to figure 9.6.

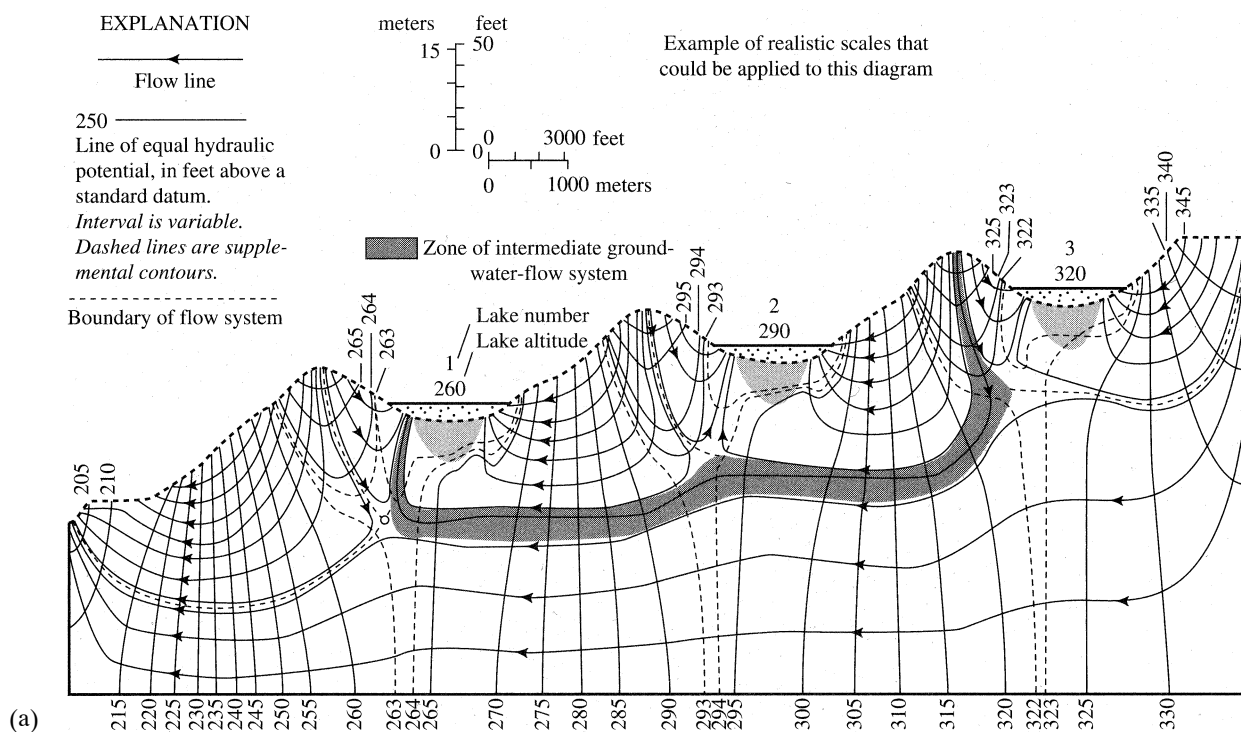


Figure 9.22 Hypothetical ground-water–lake relations. (a) Flow net for a system of three lakes above a main stream. With a homogeneous aquifer there are local, intermediate, and regional flow systems and the lakes are zones of discharge for local systems [Winter (1976)].

where Q_{GW} is the ground-water contribution to streamflow from the drainage basin above the cross section and L is the length of the main stream above the cross section (perpendicular to the cross section). An important implication of equation (9B4.9) is that one can estimate recharge from infiltration as

$$R_I = \frac{Q_{GW}}{X \cdot L}. \quad (9.18)$$

Methods for evaluating Q_{GW} are discussed in section 9.5.3.

9.3.2 Ground Water and Lakes and Wetlands

Lakes have the same range of relations to ground water as shown for streams in figure 9.17. Like gaining streams, perennial lakes usually occur in discharge zones, although some are flow-through systems. Seasonal lakes can be local sources of recharge, like losing streams. In gaining and flow-through situations, the lake surface is at the water-table elevation.

Most fresh-water wetlands are on the borders of streams or lakes, or are former lakes that have been largely or wholly filled with mineral and organic soil and vegetation in various proportions. Thus they are hydrologically similar to lakes, and the discussion here can also be applied to bogs, swamps, and marshes. Dooge (1975) and LaBaugh (1986) provide useful reviews of wetland hydrology and Doss (1993), Hunt et al. (1996), and Rosenberry and Winter (1997) describe field investigations.

As with regional flow systems, much of our understanding of ground-water–lake interactions is based on mathematical simulations of idealized situations (McBride and Pfannkuch 1975; Winter 1976, 1978, 1983; Cheng and Anderson 1994), supplemented increasingly by field studies (e.g., Crowe and Schwartz 1985; Cherkauer and Zager 1989; Shaw and Prepas 1990; Winter 1999; Winter et al. 2003). Figure 9.22 shows examples of some of the complex ground-water–lake interactions that can exist in a simple topographic setting as revealed by modeling studies. In figure 9.22a the subsurface has uniform

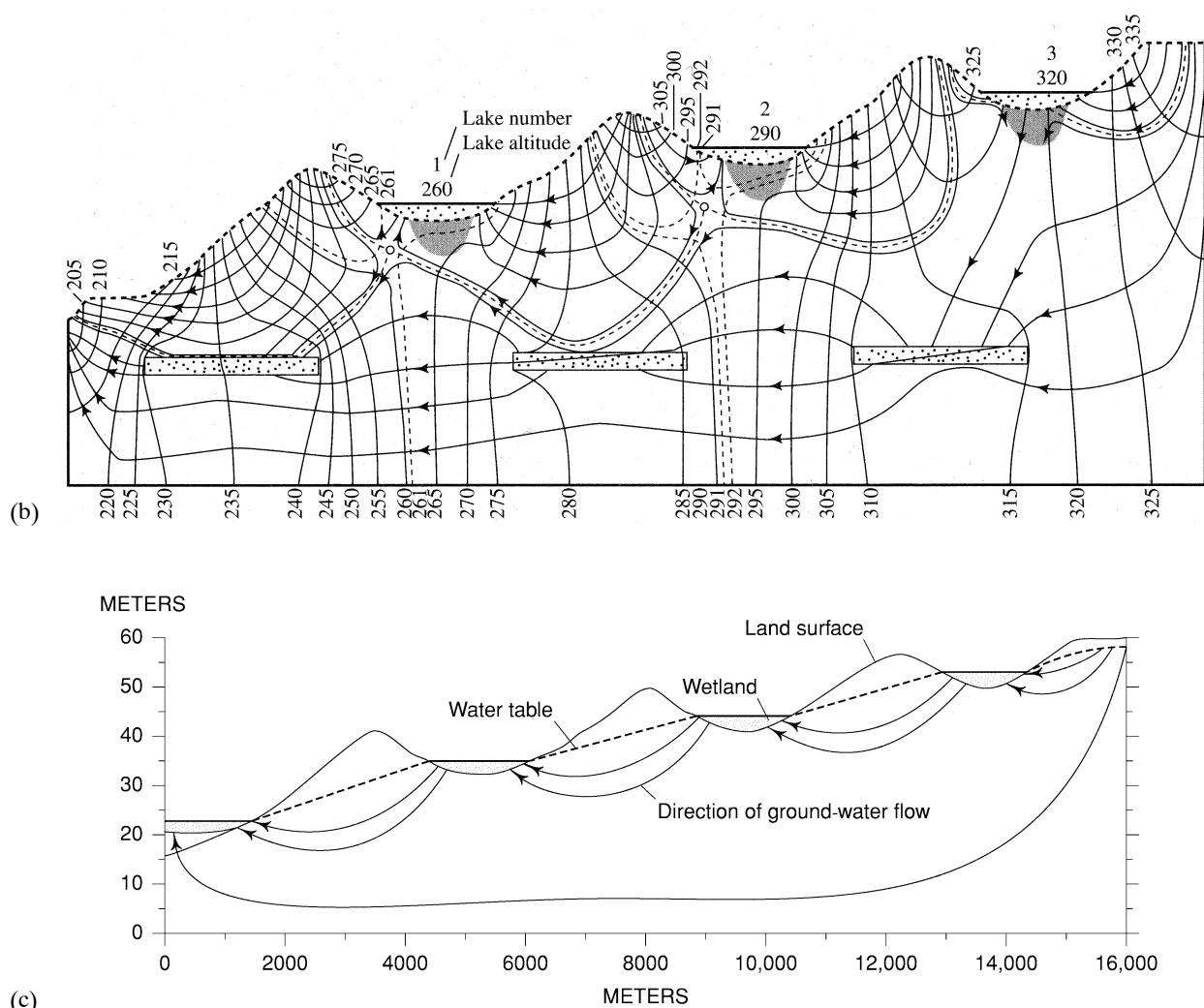


Figure 9.22 (continued) (b) Same as (a), but with three high-conductivity lenses at depth. Now the intermediate system disappears and the highest lake receives discharge near its edge and contributes recharge in its center [Winter (1976)]. (c) Ground-water flow systems where water table highs do not underlie topographic highs. The surface water bodies are flow-through with respect to ground water [reproduced from Winter et al. (2003), *Where does the ground water in small watersheds come from?* *Ground Water* 41(7):989–1000, with permission from Wiley].

and isotropic hydraulic conductivity and the water table slopes toward the three lakes from all sides. Here the lakes are in the discharge zones of local flow systems; there is a regional flow system at depth, and an intermediate system that discharges into the lowest lake. Figure 9.22b shows a situation topographically identical to figure 9.22a, but here discontinuous lenses of high hydraulic conductivity at depth change the flow net so that the highest lake contributes recharge through its bottom while receiv-

ing discharge around its perimeter. Flow-through lakes tend to occur where water tables do not rise under topographic highs (figure 9.22c).

Modeling and field studies have also shown that, even where the surrounding geologic materials are homogeneous, ground-water inflow to lakes is concentrated in the littoral zone whether or not there are relatively impermeable sediments present in the deeper part of the lake. However, high-conductivity zones in the lake bed can be loci of local

concentration of inflows (springs), or zones of outflow (recharge), depending on the regional ground-water configuration (Cherkauer and Nader 1989; Winter 1999).

In some situations, lakes can be recharge sites exclusively, at least at certain seasons. Meyboom (1966) showed that, in southern Saskatchewan, Canada, spring snowmelt runoff accumulates in small depressions (prairie potholes) that are above the recharge zone of a regional flow system. The subsequent leaking of these small ponds produces localized ground-water mounds representing recharge to this system. This local ground-water flow pattern reverses in the summer, when trees growing around the edges of the potholes extract ground water and thereby make the potholes sites of discharge for temporary local flow systems.

Studies by Winter (1983), Sacks et al. (1992), and Anderson and Cheng (1993) also showed significant seasonal changes in local ground-water flow systems adjacent to lakes. Winter et al. (2003) reviewed field studies of ground-water–lake interactions and noted that surface-water and ground-water watersheds of lakes commonly do not coincide. It is often difficult to determine the extents of subsurface contributing areas because of the lack of detailed subsurface information, the coexistence of ground-water circulations of local to regional scales, and often the effects of seasonal variability on system boundaries. They found that lakes and wetlands in small watersheds at the lower end of extensive ground-water flow systems may receive subsurface inflow from shallow flow systems that extend far beyond their surface watershed, and may also receive ground-water inflow from deeper regional flow systems.

The above review makes it clear that the hydrologic setting of lakes and wetlands may be complex and very difficult to determine without detailed subsurface information, perhaps over an extensive area. This makes it difficult to quantify the most basic hydrologic characterization—the water-balance equation relating inflows, outflows, and storage changes.

9.3.3 Ground Water and the Ocean

Figure 9.23 depicts the relations between fresh and salt ground water in a simple coastal aquifer. The Ghyben–Herzberg relation (box 9.5 on pp. 418–419) indicates that the salt/fresh interface lies at a depth below sea level equal to 40 times the height of the water table above sea level, and the water-table elevation decreases to zero at the coast. Equation

(9B5.6) gives the depth of the interface as a function of distance from the coast.

In real situations the position of the interface differs somewhat from the static equilibrium given by the Ghyben–Herzberg relation because the aquifer receives recharge from infiltration, and water-balance considerations dictate that the average net recharge rate must be balanced by an equal average discharge to the ocean. This discharge occurs through an outflow face that extends seaward from the coast, the width of which is given by equation (9B5.9). The average discharge, q_{GW} , per unit length of coastline is given by

$$q_{GW} = R \cdot X, \quad (9.19)$$

where R is the net recharge rate [L T^{-1}] and X is the distance inland to the ground-water divide. Equation (9B5.10) gives the depth of the interface when the outflow face is accounted for.

As the example in box 9.5 shows, the width of the outflow face is usually small compared to the scale of the flow system, and the Ghyben–Herzberg relation gives a useful approximation, except very near the coast, in many situations.

9.4 Ground Water in the Regional Water Balance

In this section we apply the basic water-balance equation (section 1.8.1) to the ground water of a region. The main purposes of the analysis are to (1) define the ground-water balance components and (2) show how the ground-water balance relates to the overall regional water balance. Section 9.5 then describes approaches to quantifying the various components.

The surface extent of the control volume for the water-balance equation can be defined arbitrarily—it could be a political division, an aquifer, or a topographically defined watershed. The lower boundary of the control volume is usually defined as the “depth at which ground-water flow is negligible”; if the geology is known, this can be more precisely specified.

Choosing a watershed as a control volume has one important advantage: It is usually possible to measure at least one of the balance components, surface-water outflow (streamflow), accurately. However,

researchers studying small watersheds need to be aware that ground water flow divides do not underlie surface divides in many settings. Only if a surface watershed of a research site is at the highest ridge

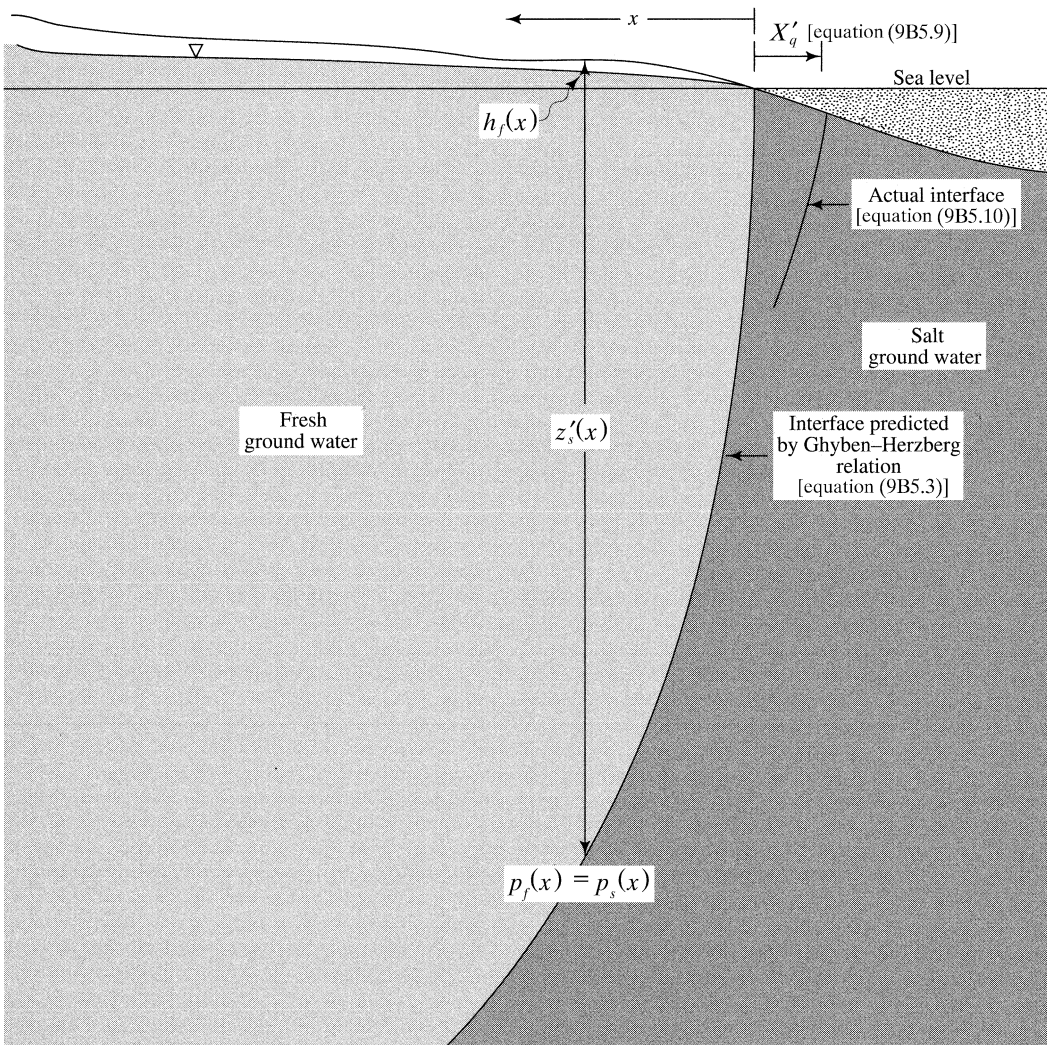


Figure 9.23 Definition sketch for deriving the Ghyben–Herzberg relation (box 9.5). The salt-water–fresh-water interface position predicted by this hydrostatic relation differs somewhat from the actual position near the coast due to the dynamics of the flow, which produces an outflow face of width X_q' , which can be estimated via equation (9B5.8).

away from major hydrologic sinks such as regional rivers, can one be sure that ground water is not moving into the area from distant sources. For most other watersheds, ground water can move into watersheds either because ground water divides are not present beneath the surface divides or because ground water moves into the area from deeper flow systems. Ground water divides move in response to changing recharge conditions, which in turn is related to the dynamics of climate and precipitation. (Winter et al. 2003, pp. 998–999)

An example of a situation where ground-water and surface-water divides do not coincide is shown in figure 9.24 on p. 419.

Thus, although the water-balance equations are straightforward, recall from section 1.11.2 that measurement errors, which are inevitable, are propagated through calculations and can lead to large uncertainty in final estimates. For regional water balances, these errors are likely to result from (1) insufficient knowledge of the system boundaries and (2) failure to fully account for regional variability.

Box 9.5 The Fresh/Salt Ground-Water Interface in Coastal Aquifers

Ghyben–Herzberg Relation

Figure 9.23 shows the interface between fresh and salt ground water in a homogeneous unconfined aquifer at a coastline. If we assume that this interface is a static sharp boundary, the hydrostatic pressure on the fresh-water side of the fresh/salt interface, $p_f(x)$, is

$$p_f(x) = \gamma_f \cdot [h_f(x) + z_s'(x)], \quad (9B5.1)$$

where x is distance inland from the coast, γ_f is the weight density of fresh water, $h_f(x)$ is the elevation above sea level of the water table, and $z_s'(x)$ is the distance below sea level of the interface. The hydrostatic pressure on the sea-water side of the interface, $p_s(x)$, is

$$p_s(x) = \gamma_s \cdot z_s'(x), \quad (9B5.2)$$

where γ_s is the weight density of sea water.

At hydrostatic equilibrium $p_f(x) = p_s(x)$, so equating equations (9B5.1) and (9B5.2) and solving for $z_s'(x)$ yields

$$z_s'(x) = \Gamma \cdot h_f(x), \quad (9B5.3)$$

where

$$\Gamma \equiv \frac{\gamma_f}{\gamma_s - \gamma_f} = \frac{9,800 \text{ N/m}^3}{10,045 \text{ N/m}^3 - 9,800 \text{ N/m}^3} = 40. \quad (9B5.4)$$

Thus

$$z_s'(x) = 40 \cdot h_f(x); \quad (9B5.5)$$

i.e., at any distance inland, x , the depth below sea level to the salt/fresh interface is 40 times the height above sea level of the water table. This analysis of the fresh/salt ground-water interface was formulated over 100 years ago, and is known as the **Ghyben–Herzberg relation**.

Todd (1953) used the Ghyben–Herzberg assumptions along with the Dupuit equation (box 9.4) to give the depth to the interface as a function of the ground-water discharge and the hydraulic conductivity of the aquifer:

$$z_s'(x) = \left(\frac{2 \cdot \Gamma \cdot q_{GW} \cdot x}{K_h} \right)^{1/2}, \quad (9B5.6)$$

where q_{GW} is the ground-water discharge to the ocean per unit length of coastline [$\text{L}^2 \text{T}^{-1}$] and K_h is hydraulic conductivity. Equating (9B5.3) and (9B5.6) gives relations for the height of the water table as a function of distance from the coast, discharge, and conductivity:

$$h_f(x) = \left(\frac{2 \cdot q_{GW} \cdot x}{\Gamma \cdot K_h} \right)^{1/2}. \quad (9B5.7)$$

Ground-Water Outflow to Ocean

Analogously to equation (9.17), q_{GW} is the product of the average recharge rate, R [L T^{-1}], and the distance from the ground-water flow divide to the coast, X [L]:

$$q_{GW} = R \cdot X. \quad (9B5.8)$$

The Ghyben–Herzberg analysis does not provide for a sub-sea zone in which this discharge must occur. To account for this, Glover (1964) developed a simple model that gives the seaward extent of the **outflow face**, X_q' , as

$$X_q' = \frac{\Gamma \cdot q_{GW}}{2 \cdot K_h} = 20 \cdot \frac{q_{GW}}{K_h}. \quad (9B5.9)$$

To account for this, an additional term is included in equation (9B5.6) giving the depth to the salt/fresh interface:

$$z_s'(x') = \left(\frac{2 \cdot \Gamma \cdot q_{GW} \cdot x'}{K_h} + \frac{\Gamma^2 \cdot q_{GW}^2}{K_h^2} \right)^{1/2}, \quad 0 \leq x', \quad (9B5.10)$$

where x' is the distance seaward from the coast. The relative importance of this additional term increases toward the coast, and at the coast ($x' = 0$) the interface depth is

$$z_s(0) = \frac{\Gamma \cdot q_{GW}}{K_h}. \quad (9B5.11)$$

Example

Here we use the relations derived above to calculate aspects of the ground-water discharge to the Atlantic Ocean from the southern part of Long Island, New York. The region is underlain by relatively homogeneous glacial sands and gravels about 120 m thick overlying coastal-plain sedimentary rocks, which are relatively impermeable. The distance from the central ground-water divide to the south coast is about 16 km. The average annual recharge is about 0.57 m/yr, the hydraulic conductivity of the aquifer is about 50 m/day = 18,250 m/yr. Thus using equation (9B5.8), the discharge to the ocean is

$$q_{GW} = 0.57 \text{ m/yr} \times 16,000 \text{ m} \\ = 9,120 \text{ m}^2/\text{yr} \text{ per m of coastline.}$$

Our analysis will not be valid for points landward of where the fresh/salt interface depth equals the aquifer thickness; to calculate that distance, X^* , we rearrange equation (9B5.6) and find the distance corresponding to the aquifer thickness:

$$X^* = \frac{K_h \cdot z_s(X^*)^2}{2 \cdot \Gamma \cdot q_{GW}} = \frac{(18,250 \text{ m/yr}) \times (120 \text{ m})^2}{2 \times 40 \times (9,120 \text{ m}^2/\text{yr})} = 360 \text{ m};$$

Table 9B5.1 compares the depths to the interface at increasing distances from the coast computed via equations (9B5.7) and (9B5.10) for $x \leq X^*$.

The width of the outflow face, X_q' , extending seaward from the south coast is found from equation (9B5.9):

$$X_q' = \frac{40 \times 9,120 \text{ m}^2/\text{yr}}{2 \times 18,250 \text{ m}/\text{yr}} = 9.99 \text{ m.}$$

Table 9B5.1

Distance, x (m)	Equation (9B5.7)		Equation (9B5.9)	
	Interface Depth, z_s' (m)	Water-Table Height, h_f (m)	Interface Depth, z_s' (m)	Water-Table Height, h_f (m)
0	0	0.0	20	0.5
10	20	0.5	40	1.0
20	28	0.7	48	1.2
50	45	1.1	65	1.6
100	63	1.6	83	2.1
200	89	2.2	109	2.7
250	100	2.5	120	3.0
300	110	2.7	120	—
360	120	3.0	120	—

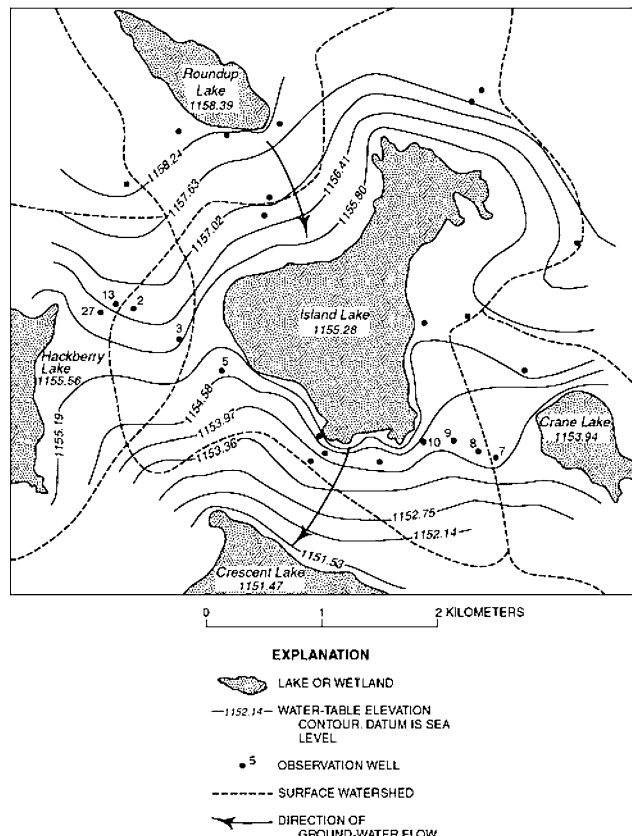


Figure 9.24 Island Lake area in Nebraska showing surface-water bodies, surface watersheds, contours of the water table (m), and direction of ground-water flow on October 28, 1982. Note ground-water flow across surface-water divides [reproduced from Winter et al. (2003), Where does the ground water in small watersheds come from? *Ground Water* 41(7):989–1000, with permission from Wiley].

Under natural (i.e., no pumping or artificial water imports or exports) conditions,² the regional water balance can be written as

$$P + G_{in} = Q + ET + G_{out} \quad (9.20)$$

where P is precipitation, Q is stream outflow, ET is evapotranspiration, G_{in} is water entering as ground water, G_{out} is water leaving as ground water, and all quantities are long-term average values (i.e., storage changes are assumed zero) (figure 9.25). Note that the terms in

these water-balance relations can be expressed as volumes [L^3] or volumes per unit area [L] during a specific time period, or as average rates [$L^3 T^{-1}$] or [L T⁻¹].

Under the same conditions, the long-term average water balance for the aggregated ground-water reservoir in the basin is

$$R_I + R_{SW} + G_{in} = CR + Q_{GW} + G_{out} \quad (9.21)$$

where R_I is recharge from infiltration, R_{SW} is recharge from surface-water bodies, CR is the move-

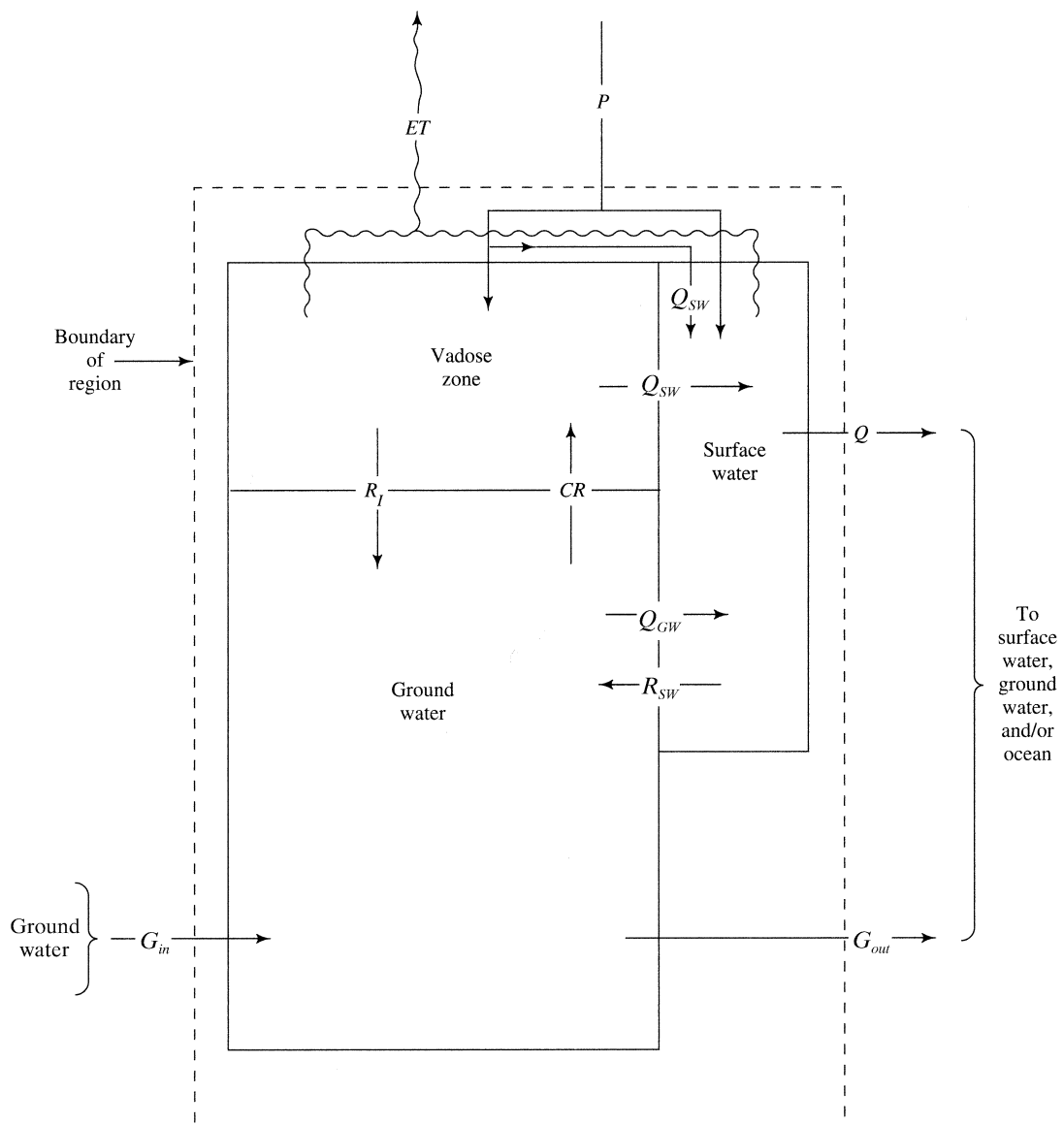


Figure 9.25 Schematic water balance for a drainage basin.

ment of water from ground water into the capillary fringe (capillary rise),³ and Q_{GW} is the ground-water contribution to streamflow. We can then define **net recharge**, R , as

$$R \equiv R_I + R_{SW} - CR. \quad (9.22)$$

Equations (9.20)–(9.22) can be combined to give

$$P - Q - ET = R_I + R_{SW} - CR - Q_{GW} = R - Q_{GW} \quad (9.23a)$$

or

$$P - Q_{SW} - ET = R_I + R_{SW} - CR = R, \quad (9.23b)$$

where Q_{SW} is the non-ground-water contribution to streamflow.

Box 9.6 provides an example of a very simple “first-cut” approach to estimating the ground-water balance, in which standard network hydroclimato-

logical data and general knowledge of basin geology and water-table configurations are used to estimate various ground-water balance terms. In general, this approach has severe limitations, usually because of incomplete knowledge of ground-water divides. These are probably fairly well known in this case, but even if we also make the assumptions that long-term average values of P , Q , and ET are well known, we can at best use equation (9.20) to estimate $(G_{out} - G_{in})$, and equations (9.21) and (9.22) to estimate $(R_I + R_{SW} - CR - Q_{GW}) = (R - Q_{GW})$.

Thus even under ideal conditions where standard network data provides good estimates of P , ET , and Q , firm knowledge of a basin’s water balance usually requires independently evaluating at least some of the terms in equation (9.21). Approaches to obtaining quantitative estimates of these terms are described in the following section.

Box 9.6 Ground-Water-Balance Example

Cohen et al. (1968) developed a water balance for the aquifer described in the example in box 9.5 based on standard network meteorologic and hydrologic data collected over the period 1940–1965. Long-term average water-balance data are given in table 9B6.1. P estimates were based on data collected at five stations and Q estimates on records at five gauging stations. ET was estimated based on average monthly temperatures via the Thornthwaite approach (see chapter 6). Estimates of CR (here assumed equal to direct evapotranspiration from ground water), Q_{GW} , R_{SW} , and G_{in} were based on hydrologic judgment and the configuration of the water table.

Estimates of G_{out} , R_I , and R are found by substitution of the appropriate values from table 9B6.1 into the appropriate water-balance equations, as shown in table 9B6.2.

Table 9B6.2

Quantity	Equation	Value (mm/yr)
G_{out}	9.16	328
R_I	9.17	561
R	9.18	551

Note that G_{out} here represents direct ground-water flow to the ocean plus outflow across the drainage-basin boundaries; these were estimated by Cohen et al. (1968) as 237 mm/yr and 91 mm/yr, respectively.

The aquifer has an average thickness of 60 m. From table 9.1, the specific yield of unconsolidated sand and gravel $S_y \approx 0.30$. Thus the average residence time of ground water is estimated via equation (9.14) as

$$T_R = \frac{60 \text{ m} \times 0.30}{0.551 \text{ m/yr}} \approx 33 \text{ yr.}$$

Table 9B6.1

Quantity	Value (mm/yr)	Source
P	1,120	m
ET	541	em, eh
Q	249	m
CR	10	eh
Q_{GW}	224	eq
R_{SW}	0	eh
G_{in}	0	eh

m = measured

em = estimated from meteorological measurements

eh = estimated based on water-table configuration

eq = estimated via base-flow analysis (section 9.5.3.6)

9.5 Evaluation of Ground-Water Balance Components

This section reviews approaches to quantitative evaluation of the components of the ground-water balance [equation (9.21), figure 9.25] in a given location from field measurements. Most of these approaches are based on application of basic water-balance concepts and/or Darcy's law, in some cases employing various water-quality constituents as tracers and/or remotely sensed observations. A still useful and historically interesting review of early (1686–1931) approaches to estimating ground-water components was compiled by Meinzer (1932). Smerdon et al. (2009) described a modern comprehensive approach that integrates a range of tools, including ground-water modeling, to assess the ground-water budget in a mountain watershed.

9.5.1 Recharge from Infiltration, R_I

Infiltrated water can carry contaminants from agriculture, industries, and waste-disposal sites to the ground-water reservoir, so quantification of R_I has important implications for the study of water quality as well as quantity.

As noted, the water-table configurations in the regional ground-water flows depicted in figures 9.5 to 9.7 and 9.10 to 9.12 were specified as boundary conditions to illustrate typical flow configurations, and these conditions determined the locations of recharge and discharge zones. Since recharge from infiltration is the principal source of water to unconfined aquifers and is the ultimate source of most streamflow, it is of interest to explore further the natural factors that determine the regional distribution of recharge and discharge.

Direct measurement of recharge requires elaborate instrumentation and is feasible only in a research setting. In one of the few such studies, Wu et al. (1996) installed lysimeters consisting of 60-cm diameter soil-filled cylinders in which the water table was kept at depths ranging from 1.5 to 5 m. At the shallowest depth almost every water-input event caused a separate recharge event that was reflected in a rise, peak, and decline of the water table; but at 5 m individual events were not identifiable and there was a single annual peak. At intermediate depths, individual recharge events were associated with input events separated by a "critical" time interval that increased with depth. The relationship between re-

charge, precipitation (P), and evapotranspiration (ET) for individual events were

$$\text{1.5-m depth: } R_I = 0.87 \cdot (P - 5.25) \quad (9.24\text{a})$$

$$\text{4.5-m depth: } R_I = 0.87 \cdot (P - ET - 27.4) \quad (9.24\text{b})$$

where all quantities are in cm.

In nature the depth of the water table at a given location is determined by feedbacks among precipitation, infiltration, runoff, and evapotranspiration at that location along with the regional flow, which integrates those quantities throughout the drainage basin under the influence of topography and geology. On average, the water table is at an equilibrium depth such that the net recharge (i.e., percolation minus capillary rise to supply evapotranspiration) from above is just balanced by the net ground-water flow away from (recharge areas) or toward (discharge areas) the water table. When the water table is above this depth, losses to evapotranspiration exceed recharge and a discharge zone exists; when below this depth, recharge exceeds evapotranspiration and a recharge zone exists.

Levine and Salvucci (1999) quantitatively modeled these relations and showed how water-table depth is related to net recharge for various soil types. They found that net recharge increases and evapotranspiration and surface runoff generally decrease as water-table depth increases (figure 9.26). Figure 9.27 on p. 424 shows regional ground-water flow and recharge and discharge zones modeled using these more realistic relationships in climatic, topographic, and geologic conditions similar to those assumed in figure 9.7b. Note that local, intermediate, and regional circulations occur in both, but that discharge zones are more concentrated in figure 9.27. Salama et al. (1994) showed that aerial photographs and satellite imagery can be used to map regional recharge and discharge areas.

Because of the difficulty in direct measurement of recharge, hydrologists have attempted to evaluate R_I by applying various combinations of water-balance concepts, applications of Darcy's law, soil-physics principles, mathematical systems models, and water-quality measurements. The major methodological approaches are briefly described here, following in part the review of Van Tonder and Kirchner (1990). Most of these methods require elaborate and careful data collection, and Sophocleous and Perry (1984) provide a useful overview of considerations in selecting instrumentation for recharge studies.

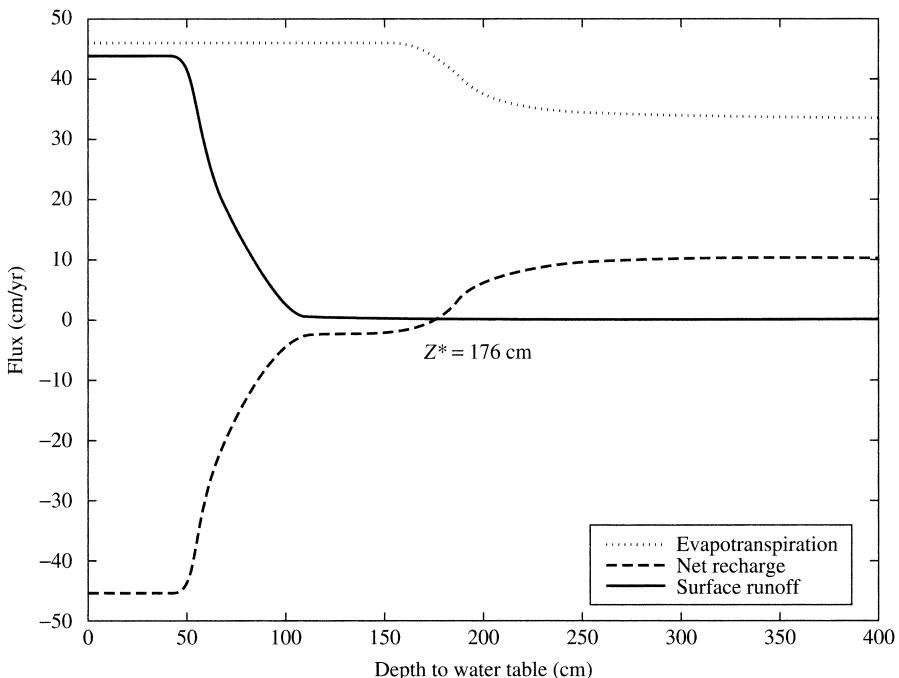


Figure 9.26 Variations of evapotranspiration, net recharge, and surface runoff as a function of water-table depth for a silt-loam soil [Levine and Salvucci (1999)].

Equilibrium analysis of groundwater-vadose zone interactions and the resulting spatial distribution of hydrologic fluxes across a Canadian prairie. *Water Resources Research* 35:1369–1383, with permission of the American Geophysical Union].

9.5.1.1 Soil-Water Balance Method

The water balance for the root zone of a soil for a time period Δt can be written as

$$R_I = P - ET - Q_{SW} - R_{SW} + CR + \Delta S, \quad (9.25)$$

where Q_{SW} represents surface outflow, ΔS is the change in soil-water storage during Δt , and the other symbols are as defined for equation (9.20) and (9.21). Equation (9.25) is usually applied to a small plot where P and Q_{SW} are directly measured, ET is determined by measuring meteorological parameters and applying one of the approaches discussed in chapter 6, R_{SW} and CR are assumed negligible, and ΔS is calculated from measurements of water content at several depths using one of the approaches discussed in section 7.2.1.2. Rushton and Ward (1979) found that Δt should not exceed 1 day to minimize propagation of measurement errors. Steenhuis et al. (1985) used equation (9.25), assuming that all terms except P and ET were negligible, and estimated regional R_I on Long Island, New York, as simply

$$R_I = P - ET, \quad (9.26)$$

where P was measured and ET was calculated from detailed energy-balance measurements at the site (section 6.8.3).

As noted, the major concerns in applying various forms of the water-balance equation are (1) making measurements with sufficient precision such that errors in the final computations are within acceptable limits and (2) acquiring sufficient measurements to characterize the regional situation. Finch (1998) found that recharge estimates are highly sensitive to soil characteristics, and Rushton and Ward (1979) concluded that uncertainties of $\pm 15\%$ should be expected with this approach.

In spite of these caveats, the basic method—with varying approaches to modeling ET and soil-water storage—has been successful in estimating R_I in a small coastal-plain drainage basin in Maryland (Rasmussen and Andreasen 1959), chalk and sandstone aquifers of England (Wellings 1984; Ragab et al. 1997) and France (Thiery 1988), glacial deposits on Long Island, New York (Steenhuis et al. 1985; Steenhuis and Van Der Molen 1986), and Sweden (Johansson 1987), and in a large drainage basin in Australia (Chiew and McMahon 1990).

9.5.1.2 Analysis of Well Hydrographs

Well hydrographs are observations of water levels in monitoring wells plotted against time. To evaluate recharge, the hydrographs are combined with hyetographs showing the timing and amount of water input

(figure 9.28). Recharge is reflected in the rise of the hydrograph following a water-input event, after which drainage to surface-water bodies is reflected in a gradual decline. There are several approaches to estimating

recharge from well hydrographs; most of these assume that unconfined aquifers can be modeled as linear reservoirs (box 9.7; figure 9.29, both on p. 426), which is often approximately true (Brutsaert and Lopez 1998).

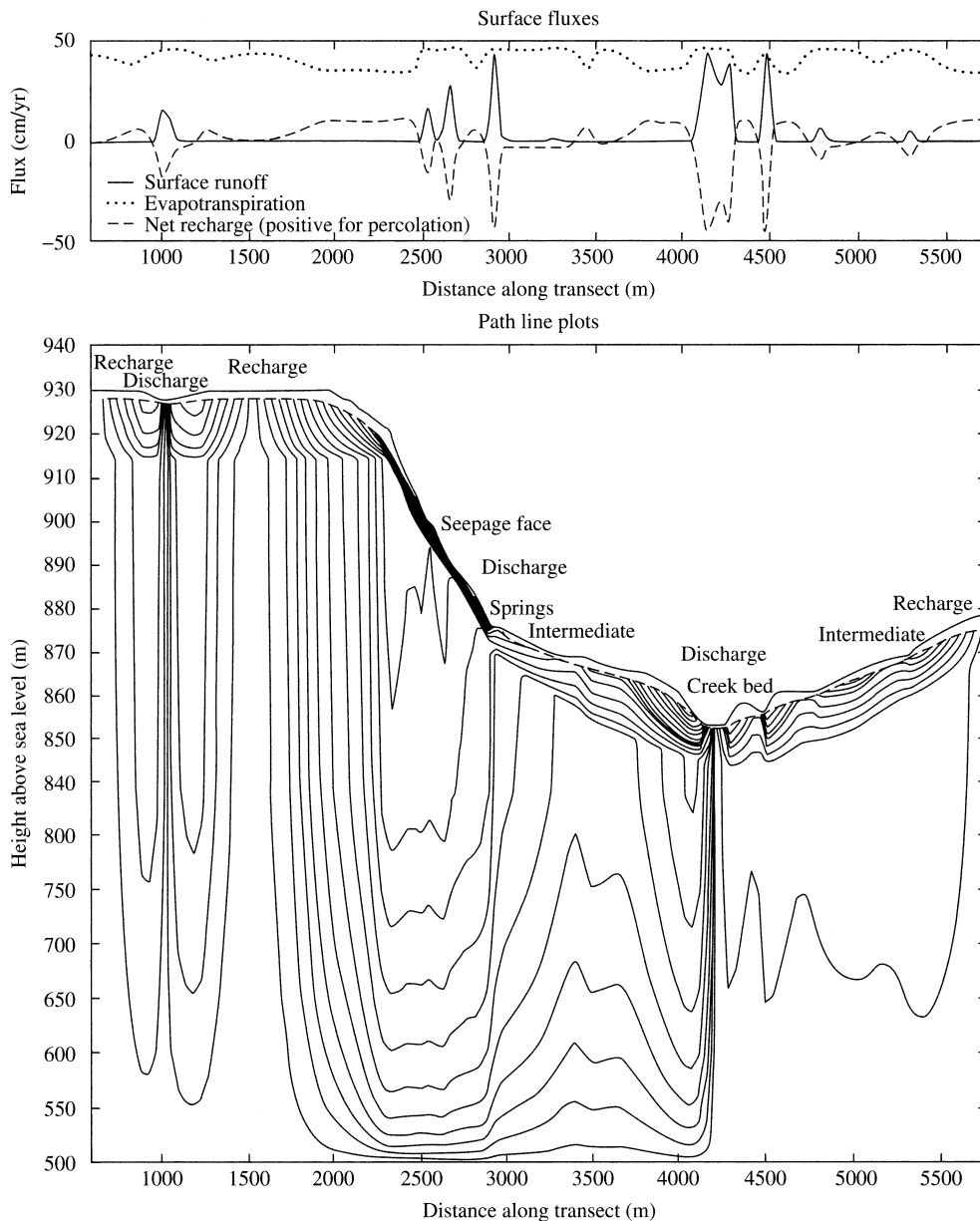


Figure 9.27 Recharge areas, discharge areas, and streamlines for a cross section of a drainage basin in Alberta, Canada, as determined by coupling recharge estimated via unsaturated flow modeling with a ground-water flow model. Note that the discharge areas are more concentrated than predicted from ground-water flow modeling with imposed water-table configuration (compare figure 9.7) [Levine and Salvucci (1999). Equilibrium analysis of groundwater-vadose zone interactions and the resulting spatial distribution of hydrologic fluxes across a Canadian prairie. *Water Resources Research* 35:1369–1383, with permission of the American Geophysical Union].

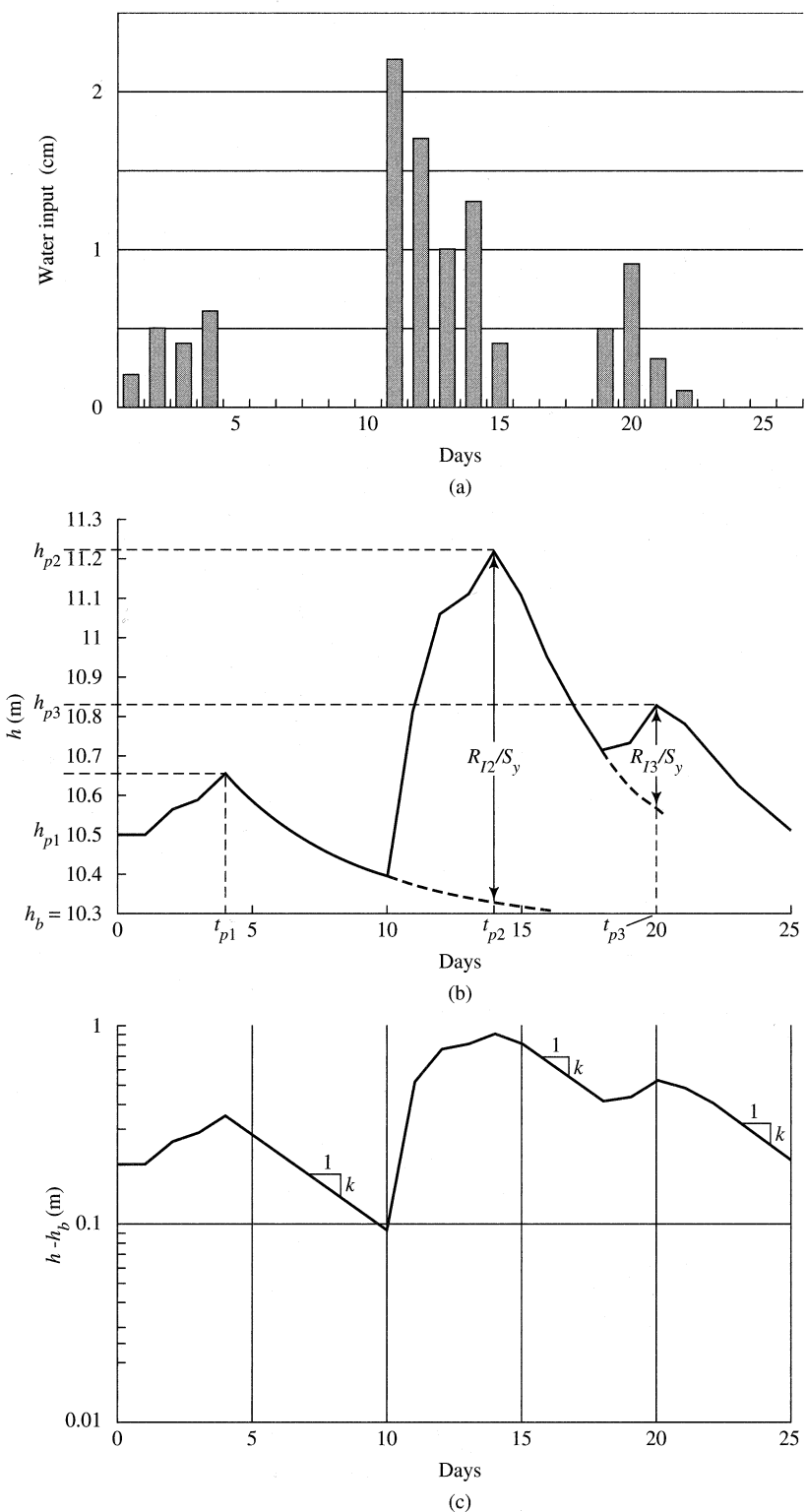


Figure 9.28 Typical plot for estimation of recharge via well-hydrograph analysis. (a) Rainfall hyetograph. (b) Well hydrograph plotted on arithmetic scale. Dashed lines are the extensions of hydrograph recessions (assumed exponential decay). R_{12} and R_{13} are recharge from storm events 2 and 3, respectively, estimated as the vertical distance between the extended recession and the hydrograph peak times the specific yield [see equation (9.29)]. (c) Well hydrograph plotted on logarithmic scale.

Box 9.7 Drainage of a Linear-Reservoir Aquifer

Figure 9.29 shows an idealized unconfined aquifer of area A and specific yield S_y receiving recharge from infiltration, R_I [L T^{-1}], and discharging to a stream at a rate Q_{GW} [$\text{L}^3 \text{T}^{-1}$]. Assuming constant density, the conservation-of-mass equation for a time period dt for this situation is

$$A \cdot R_I \cdot dt - Q_{GW} \cdot dt = A \cdot S_y \cdot dh. \quad (9B7.1)$$

Defining $q_{GW} \equiv Q_{GW}/A$, this becomes

$$R_I - q_{GW} = S_y \cdot \frac{dh}{dt}. \quad (9B7.2)$$

If the aquifer behaves as a linear reservoir, outflow rate is proportional to storage [see equation (1.24)],

$$q_{GW} = k \cdot S_y \cdot (h - h_b), \quad (9B7.3)$$

where h_b is a level below which no discharge occurs and k [T^{-1}] is the inverse of the residence time [equation (9.14)] of the aquifer. With equation (9B7.3), (9B7.2) becomes

$$R_I - k \cdot S_y \cdot (h - h_b) = S_y \cdot \frac{dh}{dt}. \quad (9B7.4)$$

If there is no recharge or capillary rise and the aquifer is draining, $R_I = 0$ and equation (9B7.4) can be written as

$$-k \cdot dt = \frac{dh}{h - h_b}. \quad (9B7.5)$$

Integrating (9B7.5) yields

$$-k \cdot t = \ln(h - h_b) + C, \quad (9B7.6)$$

and evaluating the constant of integration, C , from the initial condition $h = h_0$ when $t = 0$ leads to

$$h = h_b + (h_0 - h_b) \cdot \exp(-k \cdot t). \quad (9B7.7)$$

Equation (9B7.7) shows that drainage of a linear aquifer follows an exponential decay asymptotic to h_b with decay constant k . Substituting equation (9B7.7) into equation (9B7.3) yields

$$q_{GW} = k \cdot S_y \cdot h_0 \cdot \exp(-k \cdot t), \quad (9B7.8)$$

and we see that a linear aquifer produces ground-water outflow that also follows an exponential decay with the same decay constant. For well-hydrograph analysis, k is usually evaluated empirically as the slope of the hydrograph when plotted on a semilogarithmic graph.

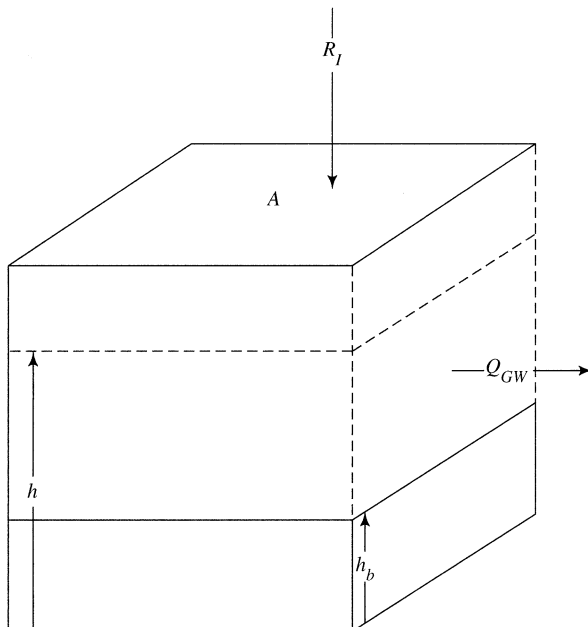


Figure 9.29 Definition diagram for analysis of drainage of a horizontal aquifer (box 9.7).

If recharge from streams and capillary rise are negligible, the ground-water balance equation, accounting for storage changes, is

$$R_I = Q_{GW} + \Delta S, \quad (9.27)$$

where ΔS now denotes the change in storage in the aquifer. If the aquifer behaves as a linear reservoir, the analysis in box 9.7 shows that equation (9.27) becomes

$$R_I = k \cdot S_y \cdot (h - h_b) + S_y \cdot \frac{dh}{dt}, \quad (9.28)$$

where R_I has units of $[\text{L T}^{-1}]$, h is the water level in the aquifer, and h_b is the level at which Q_{GW} becomes negligible. As shown in figure 9.28, the parameter k is evaluated as the slope of the straight line that best defines the hydrograph recessions when plotted on a semilogarithmic graph, and h_b can be evaluated as the level to which the recessions become asymptotic during extended periods of no recharge. The seasonal variation of R_I can then be estimated by observing water-table elevations in monitoring wells and using equation (9.28). Figure 9.30 is an example of this approach as applied to a glacial aquifer in Sweden.

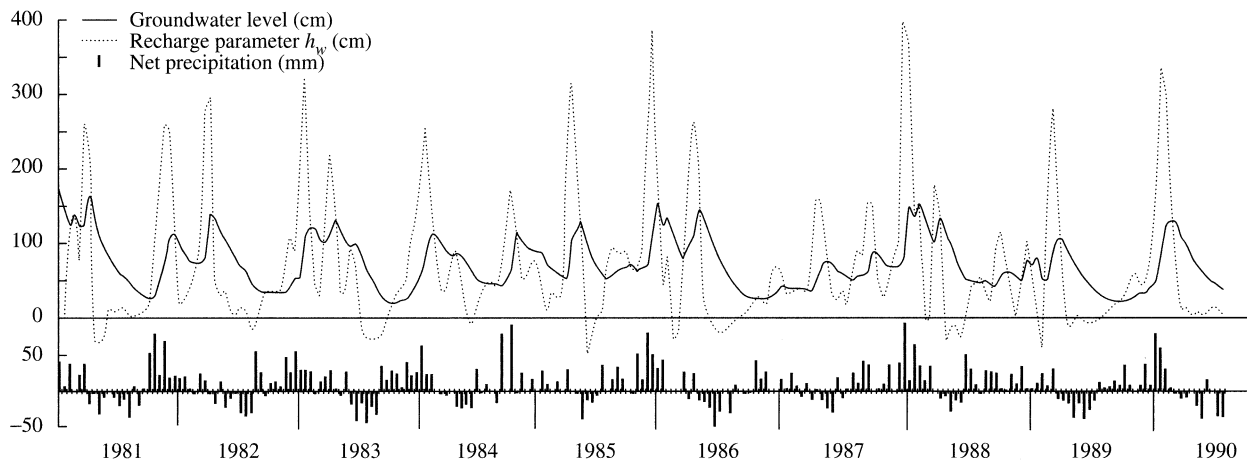


Figure 9.30 Hyetograph (histogram), well hydrograph (solid line), and recharge as estimated via equation (9.28) (dashed line) in Sweden over a 10-yr period [reproduced from Olin and Svensson (1992), Evaluation of geological and recharge parameters for an aquifer in southern Sweden, *Nordic Hydrology* 23:305–314, with permission from the copyright holders, IWA Publishing].

Another approach to well-hydrograph analysis applies the linear-reservoir model in a somewhat different way. Again, assuming an exponential recession and referring to figure 9.28, recharge for event i , $R_{I,i}$ [L], becomes

$$R_{I,i} = \{h_{p,i} - h_{p,i-1} \cdot \exp[-k \cdot (t_{p,i} - t_{p,i-1})]\} \cdot S_y, \quad (9.29)$$

where $h_{p,i}$ and $h_{p,i-1}$ are the peak water levels associated with events i and $i - 1$, respectively; $t_{p,i}$ and $t_{p,i-1}$ are the times of occurrence of the successive peak water levels; and S_y is the specific yield. Rasmussen and Andreasen (1959) obtained reasonable results with this method in Maryland, with a constant S_y determined via successive approximations as the value most consistent with weekly water-balance data.

A third approach to estimating recharge from well hydrographs applies a simplified water-balance equation to the entire aquifer of area A :

$$R_I = S_y \cdot \Delta h_+ \cdot A - (G_{in} - G_{out}), \quad (9.30)$$

where Δh_+ is the spatial average increase in aquifer water level in response to a water-input event and G_{in} and G_{out} are the ground-water inflows and outflows, respectively, to the aquifer. Van Tonder and Kirchner (1990) suggested estimating the G terms by approximating Darcy's law as

$$G = T \cdot L \cdot \frac{i_1 + i_2}{2}, \quad (9.31)$$

where G is the appropriate flow rate, T is the transmissivity [equation (9.11)] for the inflow or outflow boundary, L is the width of the boundary, and i_1 and i_2 are the hydraulic gradients at the boundary at the beginning and end of the observation period, respectively. Van Tonder and Kirchner (1990) found that this method was the only one to give reliable estimates of recharge in clastic sedimentary rock aquifers in South Africa. Das Gupta and Paudyal (1988) showed how an approximate analytical solution of the one-dimensional ground-water flow equation could be used to account for the G terms when equation (9.31) is applied to an aquifer.

Although the studies cited above have claimed success in estimating recharge from well-hydrograph analysis, the approach is subject to two sources of potentially large uncertainty:

1. **Difficulty of determining the appropriate areal value of specific yield:** A characteristic value of S_y for the aquifer material is often assumed, but this can range widely (table 9.1). Furthermore, the specific yield cannot in general be assumed constant in the near-surface zones of aquifers. This is especially true if the water table is within a few meters of the surface, where water contents are a function of depth due to the complex interplay of infiltration, percolation, and capillary rise. In general, the equilibrium water-content profile varies with the water-table elevation (figure 8.8), so a

given water-table rise represents different amounts of recharge depending on the elevation range covered. Another cause of inconstancy in S_y is related to the wetting/drying hysteresis in soils (figure 7.17): In a wetting soil, air bubbles are typically trapped in the pores, so that S_y for a rising water table is generally less than S_y for a falling water table. Sophocleous and Perry (1985) showed that recharge estimates based on the assumption of a constant S_y can be seriously in error.

- 2. Uncertainty that an increase in water level actually represents an increment of recharge:** Increases in water-table elevation unrelated to recharge may occur due to: (a) fluctuations in atmospheric pressure due to the expansion and contraction of air trapped beneath the water table; (b) thermal effects, including freezing and thawing; and (c) pressurization of the capillary fringe. This latter phenomenon is especially likely to occur where the capillary fringe extends up to the soil surface; infiltrating water can then cause an almost instantaneous rise of the water table to the surface with virtually no change in ground-water storage (Novakowski and Gillham 1988; this is discussed further in section 10.4.3.2).

9.5.1.3 Direct Application of Darcy's Law

This approach requires (1) careful determination of the $K_h(\theta)$ - θ and $\psi(\theta)$ - θ relations for the soil of interest (table 7.4), and (2) periodic measurement of the vertical water-content gradient in the unsaturated zone of that soil. Recharge is then computed as the flux across the base of the root zone, $q_{z'}$, as given by Darcy's law for vertical unsaturated flow:

$$R_I = q_{z'} = K_h(\theta) - K_h(\theta) \cdot \frac{\partial \psi(\theta)}{\partial z'} \quad (9.32)$$

Sophocleous and Perry (1985) and Stephens and Knowlton (1986) obtained reasonable recharge estimates using this approach in humid and semiarid environments, respectively. Steenhuis et al. (1985) also successfully applied this method in a humid region, using biweekly observations of soil-water content at depths of 90 and 120 cm in a sandy loam soil. They found that the hydraulic gradient across the soil layer varied linearly with time following a rainstorm, and the hydraulic conductivity varied linearly with the square root of time. Thus the average rate of recharge between two observation times t_1 and t_2 was calculated from a modified version of Darcy's law for unsaturated flow:

$$R_I = -\left[K_h(\theta_{t1}) \cdot K_h(\theta_{t2}) \right]^{1/2} \cdot \left(\frac{1}{2} \right) \cdot \left[\left(\frac{dh}{dz} \right)_{t1} + \left(\frac{dh}{dz} \right)_{t2} \right] \cdot (t_2 - t_1), \quad (9.33)$$

where h is the hydraulic head [= $\psi(\theta) + z$] and the subscripts indicate the time of measurement.

A variation on this method involves ignoring the capillary-force gradient in the one-dimensional form of Darcy's law and estimating recharge as a function of water content:

$$R_I = K_h(\theta). \quad (9.34)$$

Stephens and Knowlton (1986) found good agreement between results obtained with equation (9.34) and those using the more complete version of Darcy's law.

Principal limitations of this approach are the spatial variability of soils in a typical drainage basin, the difficulty in establishing precise $K_h(\theta)$ - θ relations for a given soil, and the possibility that recharge can occur via macropores or fissures in which flow is not well modeled by Darcy's law (Van Tonder and Kirchner 1990).

9.5.1.4 Inverse Application of Ground-Water Flow Equation

The general equation for steady-state ground-water flow [equation (7.18)] can be incorporated into a model that accounts for an assumed regional distribution of recharge. The inverse application of such a model involves finding the values of recharge by calibration: The values of recharge in the model are changed until the computed head distribution corresponds to the values observed in piezometers in the region.

A number of studies have shown that useful estimates of recharge can be obtained via the inverse method, including those of Smith and Wikramaratna (1981), Wikramaratna and Reeve (1984), Chiew et al. (1992), Boonstra and Bhutta (1996), and Levine and Salvucci (1999).

However, the inherent problem of the inverse approach is the nonuniqueness of solutions: There may be many distributions of recharge that give head distributions that match the field observations within the uncertainty of those observations. The problem is exacerbated by the difficulties in obtaining a precise picture of the distribution of hydraulic conductivities.

9.5.1.5 Impulse-Response Analysis

The objective of impulse-response analysis is to determine recharge from the relation between water inputs (the impulse) and water-table rises (the response) using the principles of the mathematical analysis of time series. Given a series of daily observations of water level in an observation well and water input, the level on a given day, h_i , is assumed to depend on the previous day's level and the previous days' water inputs as

$$h_i = a_0 + a_1 \cdot h_{i-1} + b_0 \cdot W_i + b_1 \cdot W_{i-1} + \dots + b_n \cdot W_{i-n}, \quad (9.35)$$

where a s and b s are constants, the W s are water inputs (rain plus snowmelt), the subscripts are day counters, and n is the maximum number of days required for water to percolate to the water table.

The values of the constants in equation (9.35) are found by mathematical techniques that minimize the differences between estimated and observed h_i values over some period of observation of the particular wells of interest. Viswanathan (1984) showed that the average fraction of water input that becomes recharge is given by

$$\frac{R_I}{W} = S_y \cdot \sum_{j=0}^n b_j, \quad (9.36)$$

so that the method can be used to estimate long-term average recharge from long-term average water input (= average precipitation). Note, though, that this relation is also based on the uncertain assumption of a constant specific yield.

9.5.1.6 Methods Based on Water Quality

Under some circumstances, recharge rates can be estimated from the concentrations of certain chemicals and stable and radioactive isotopes that function as natural tracers of water movement.

9.5.1.6.1 Chemical Tracers

A chemical tracer suitable for estimating recharge must be: (1) present in measurable amounts in precipitation or, if deposited in solid form from the atmosphere, highly soluble; (2) not taken up or released in the vadose zone; and (3) not taken up or released by vegetation. For a column of the vadose zone in which no horizontal flow occurs above a water table, the balance for such a tracer is

$$C_w \cdot W = C_{GW} \cdot R_I \quad (9.37)$$

where W is water input, C_w is the concentration of the tracer in the water input as it infiltrates, C_{GW} is

the concentration in ground water at the water table, and all terms represent long-term averages. Recharge can thus be directly calculated if all other terms are determined from observations.

One candidate tracer is the chloride ion (Cl^{-1}), which is commonly present in precipitation, is not used by plants, and is not commonly involved in soil-chemical reactions. Recharge has been estimated from Cl^{-1} concentrations in Colorado (Claassen et al. 1986), Australia (Thorburn et al. 1991; Walker et al. 1991), and Niger (Bromley et al. 1997). Detailed aspects of using Cl^{-1} to estimate recharge were discussed by Allison et al. (1984) and Taniguchi and Sharma (1990).

Chlorofluorocarbons (CFCs) are chemically stable man-made compounds that have been accumulating in the atmosphere since their introduction as propellants and refrigerants in the 1930s. Detectable concentrations of CFCs are present in ground water that fell as precipitation since 1945, and their concentration can be used to compute recharge rates. Busenberg and Plummer (1992) and Dunkle et al. (1993) discuss the methodology in detail. However, due to the effects of CFCs on stratospheric ozone, their manufacture ceased by international agreement in the 1990s, so their future use as tracers is infeasible.

9.5.1.6.2 Stable Isotopes

A small fraction of water molecules contain the heavy oxygen isotope ^{18}O , or the heavy hydrogen isotope ^2H (deuterium) (see appendix B). The concentrations of these isotopes in precipitation tend to vary seasonally at a given location, but they are not affected by soil-chemical reactions or by plant uptake. Thus comparisons of concentrations in ground water with those in precipitation at various times of the year can provide qualitative information on the seasonality of recharge.

It is usually difficult to use stable isotopes for quantitative estimates of R_I without additional information or assumptions about the percolation mechanism, i.e., whether a piston-like wetting front occurs, whether macropores are important, or whether isotopic equilibration takes place between percolating and immobile water. Darling and Bath (1988) cited several studies in which ^{18}O and ^2H were used to obtain information about the seasonality and rate of recharge.

9.5.1.6.3 Radioactive Isotopes

Atmospheric testing of nuclear weapons in the 1950s and 1960s increased concentrations of tritium (^3H) in precipitation by orders of magnitude above

its natural levels. In subsequent decades, ${}^3\text{H}$ proved very useful for recharge studies, as it is part of the water molecule and its concentration is not affected by chemical reactions (e.g., Larson et al. 1987 and studies cited therein). However, atmospheric nuclear testing has been banned since the 1960s, and ${}^3\text{H}$ concentrations have decreased to the point where it is no longer usable as a tracer.

9.5.2 Recharge from Surface Water, R_{SW}

Although there are few published studies in which R_{SW} has been estimated, we can outline the principal approaches that can be applied to evaluation of this quantity.

9.5.2.1 Ground-Water Balance Computation

In arid regions, average evapotranspiration is nearly equal to average precipitation, so most infiltrating water evaporates and most recharge is from losing streams (figure 9.17b and c) rather than infiltration. For example, Osterkamp et al. (1994) applied water-balance computations along with streamflow measurements (see below) and ground-water modeling techniques to a 20,000-km² river basin in Nevada and California to estimate that only 1.6% of basin precipitation became recharge and that 90% of recharge was from streams.

9.5.2.2 Direct Measurement of Ground-Water Potential or Flux

The gradient of ground-water flow out of (or into) a stream can be measured by comparing (1) the water level of the stream with the head measured in a piezometer inserted into the subjacent bed or (2) the levels in two piezometers inserted to different distances below the bed (figure 9.31). If the gradient is directed downward, the ground-water flux out of the stream can be calculated directly via Darcy's law using measured or estimated hydraulic conductivities. However, there is likely to be considerable spatial and temporal variability in local values (and even direction) of gradients as well as conductivities, so such measured values must be extrapolated with caution. Winter et al. (1988) give details on the construction of piezometers used for this purpose.

Workman and Serrano (1999) combined measurements of near-stream water levels with a simple ground-water flow model to estimate that 65% of the recharge to alluvial aquifers in Ohio came from overbank flow due to floods, and hence was highly sporadic.

9.5.2.3 Direct Measurement of Streamflow Increments

The difference between stream discharge at the upstream and downstream limits of a stream reach

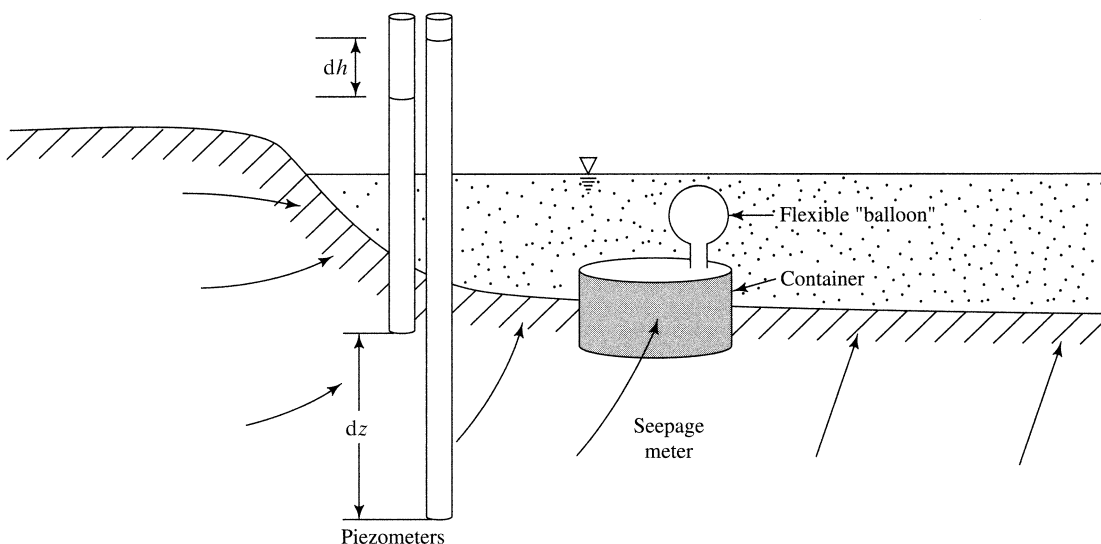


Figure 9.31 Sketch showing installation of piezometers and seepage meter to measure ground-water flux to a stream. Arrows indicate flow direction. dh is the head difference and dz is the elevation difference between the two piezometers; vertical flow is calculated via Darcy's law. Water flowing into the container of the seepage meter is collected in the flexible "balloon."

that receives no overland or tributary flow can be attributed to ground-water inflow or outflow. Techniques for measuring streamflow are discussed in appendix E; typically “velocity-area” methods, in which flow depth and average flow velocity are measured at a number of points across the stream width, are most applicable since they do not require fixed installations.

The accuracy of an estimate of R_{SW} or Q_{GW} using this approach depends on the precision of the streamflow measurements (see appendix E) and is increased by maximizing the difference between the upstream and downstream discharges (i.e., by making the measurement reach as long as possible while not including inflow from tributaries). Here again one must be aware that rates and directions of ground-water–surface-water exchange may be highly variable in space and time.

9.5.2.4 Water-Temperature Measurements

Stream temperatures are temporally highly variable due to daily and seasonal cycles. Where streams are losing water to subjacent ground water, this variability becomes progressively damped with distance below the stream bed. The outflow flux can be evaluated by measuring temperature fluctuations a short distance below the channel bottom, measuring the thermal properties of the bed sediment, and applying basic heat-flow relations (Silliman et al. 1995). Analytical methods that are commonly used in this approach are limited by uncertainties in the effective thermal properties of the sediments at the ground-water–surface-water interface.

McCallum et al. (2012) developed a new analytical method that utilizes both the amplitude ratio and phase shift of pairs of temperature measurements at the interface to estimate the magnitude and direction of the Darcy velocity. They applied the method to a stream reach in Australia, and were able to accurately measure ground-water–surface-water exchanges in both directions (bank storage).

9.5.3 Ground-Water Contribution to Streamflow, Q_{GW}

9.5.3.1 Application of Dupuit Approximation

As described in boxes 9.3 and 9.4, steady flow in horizontal unconfined aquifers draining to streams can often be usefully described by the Dupuit approximation. If significant water is not being pumped from such aquifers (section 9.6.2.2), and if capillary rise is negligible, these equations state that $Q_{GW} = R_I$ on a long-term average, per unit area basis

[equation (9.18)]. Thus under these conditions, the techniques described above for estimating R_I also provide information about Q_{GW} . Note, however, that the Dupuit formulation assumes fully penetrating streams, which seldom occur in nature, and that application of equation (9.18) assumes that the recharge area coincides with the surface watershed.

9.5.3.2 Flow Nets

Principles of graphical flow-net construction are developed in most ground-water texts (e.g., Freeze and Cherry 1979; Fetter 2001) and are discussed in detail by Cedergren (1989). If enough information on the spatial distribution of hydraulic conductivities and average water-table elevations is available, one can develop a numerical or graphical solution to equation (9.15) and sketch one or more flow nets that represent the major ground-water flow features of the basin along various stream reaches. Referring to figure 9.32, the discharge per unit length of stream Δq_{GW} into a stream for each streamtube can then be calculated as

$$\Delta q_{GW} = K_h \cdot \Delta h, \quad (9.38)$$

where K_h is the appropriate conductivity and Δh is the head difference between the stream and the next up-gradient equipotential line; the total discharge per unit stream length for a reach, q_{GW} , is given by

$$q_{GW} = n \cdot \Delta q_{GW}, \quad (9.39)$$

where n is the number of streamtubes discharging to the stream. The total flow into the stream for the reach, Q_{GW} , is then found as

$$Q_{GW} = L \cdot q_{GW}, \quad (9.40)$$

where L is the length of the reach.

Flow nets constructed in the horizontal plane can also be used to estimate ground-water inflow to streams. In practice, however, it is usually difficult to obtain enough information about subsurface geology and conductivities to warrant computations based on a flow net, and there are only a few published studies that have used this approach (Freeze 1968; Freeze and Witherspoon 1968; Ophori and Tóth 1990).

9.5.3.3 Direct Measurement of Ground-Water Potential or Flux

As for R_{SW} , Q_{GW} can be evaluated by measuring the heads in adjacent piezometers in the stream bed or banks or comparing the stream water level with the sub-bed hydraulic head (Winter et al. 1988) and

using those values along with information about conductivities to calculate the ground-water flux into the stream via Darcy's law.

Direct local measurement of Q_{GW} can be made using seepage meters, which are devices that capture water flowing upward into a portion of a water body over some time period (figure 9.31). The flux into the container is simply the volume collected divided by the time period. Lee (1977) described the construction and use of seepage meters.

As noted earlier, the main concern in using piezometer or seepage meter measurements is whether the sampling is spatially and temporally representative. Piezometer observations in stream beds in relatively homogeneous glacial deposits on Long Island, New York, were consistent with mathematical simulations (Prince et al. 1989). However, Lee and Hynes

(1978) found very large spatial variability of ground-water input to a small stream in Ontario, Canada, and concluded that determination of average rates of ground-water input to streams from point measurements of seepage flux was not generally possible.

9.5.3.4 Direct Measurement of Streamflow Increments

As described for evaluating R_{SW} , the difference between streamflow measured via velocity-area stream gauging (appendix E) at the upstream and downstream ends of a stream reach in which no tributaries enter provides a direct measurement of Q_{GW} . For gaining streams, the longer the distance between measurement cross sections, the lower the absolute error in the difference in the measured flow rates. However, the applicability of this approach is limited because of the frequent occurrence of tributaries, which must also be gauged. Cey et al. (1998) found

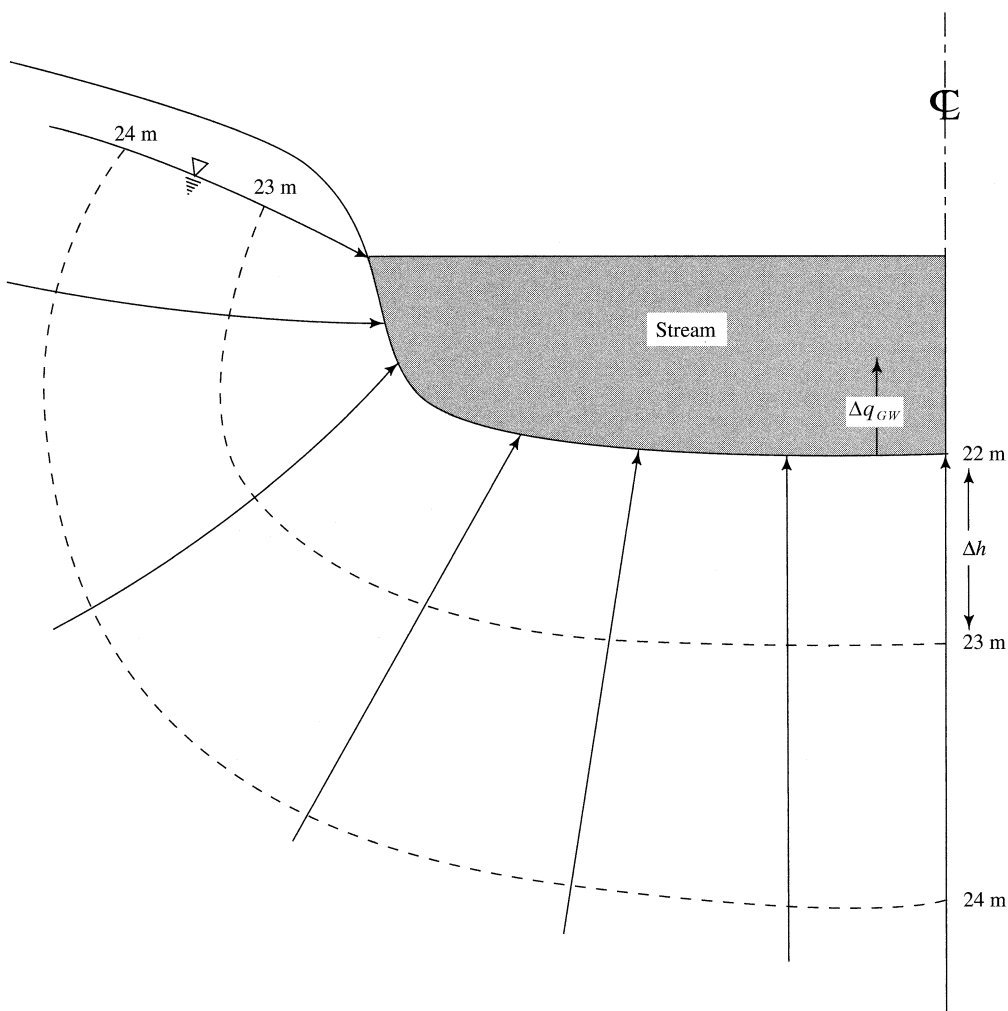


Figure 9.32
Flow net in the vicinity of a stream receiving ground water; defining terms in equations (9.38)–(9.40).

that this approach gave the most reliable results in their study of a small Canadian stream.

9.5.3.5 Methods Based on Water Quality

If streamflow, Q , at any instant is assumed to be a mixture of water from two sources, e.g., (1) surface water, Q_{SW} , and (2) ground water, Q_{GW} , each of which has a characteristic concentration of some chemical or isotope, C_{SW} and C_{GW} , then

$$Q = Q_{SW} + Q_{GW} \quad (9.41)$$

and

$$C \cdot Q = C_{SW} \cdot Q_{SW} + C_{GW} \cdot Q_{GW}, \quad (9.42)$$

where C is the concentration in the streamflow. If Q and C are measured and C_{SW} and C_{GW} determined from sampling the respective sources in the watershed, Q_{GW} can be found by combining equations (9.41) and (9.42):

$$Q_{GW} = Q \cdot \left(\frac{C - C_{SW}}{C_{GW} - C_{SW}} \right). \quad (9.43)$$

Use of equation (9.43) assumes that there are only two sources of streamflow, that each source has a constant concentration of tracer, and that these concentrations are significantly different. To relax some of these constraints, Pilgrim et al. (1979) showed how the relation could be modified when the concentration of one of the components is a function of time since the beginning of the event, and Swistock et al. (1989) derived a version of equation (9.43) for use when there are three runoff components.

Equation (9.43) has been used with apparent success in several studies, using as tracers various anions and cations (e.g., Newbury et al. 1969; Pinder and Jones 1969), stable isotopes ^{18}O and ^2H (e.g., Sklash and Farvolden 1979; Space et al. 1991), and the radioactive gas radon (^{222}Rn) (e.g., Ellins et al. 1990). Figure 9.33 shows the estimated ground-water contribution to streamflow in a case where the sulfate ion (SO_4^{2-}) was used as the tracer in equation (9.43). This approach is discussed further in section 10.3.

9.5.3.6 Base-Flow Analysis

9.5.3.6.1 Definitions

In figure 9.34 on p. 435, **streamflow hydrographs** show the typical response of a stream to an isolated water-input event: There is a relatively rapid flow increase (the **hydrograph rise**) to a **peak**, which usually occurs at or soon after the input ceases, followed by a more gradual decline (the **hydrograph re-**

cession). If the recession continues long enough before the next event, at some point recession flow equals **base flow**. As discussed in section 9.3.1.1,

Base flow is the portion of streamflow that is presumed to have entered the watershed in previous events and is derived from persistent, slowly varying sources.

Base flow is usually assumed to be from aquifers that drain to the stream network within the stream's watershed, i.e., Q_{GW} (e.g., Wolock 2003), and the attempt to identify ground-water contributions to streamflow by analysis of stream hydrographs, usually called **base-flow analysis**, **base-flow separation**, or **recession analysis**, has a long history (Hall 1968; Tallaksen 1995) and remains a common practice (Chapman 1999; Santhi et al. 2008). However, it is important to recognize that

- The concept of base flow has no scientific basis; and
- The actual source of base flow is seldom known, and may include the drainage of surface water (lakes, reservoirs, wetlands), the slow drainage of soils (e.g., Hewlett and Hibbert 1963; Dingman 1970), late-melting snow, regional ground-water flow that originated outside the watershed, or anthropogenic stream inputs.

Here we introduce some theoretical links between recession flow and ground-water inflows to streams, and some more arbitrary methods that have been used to separate base flow from event flow.

9.5.3.6.2 Recession Flow and Aquifer Drainage

If flow (Q_R) during the recession represents drainage from watershed storage—some of which is water that entered in the current event and some in past events—and declines as storage decreases, we can infer that

$$Q_R = f(S), \quad (9.44)$$

where S is the volume of water in storage and f is a positive function (i.e., flow decreases as storage decreases). The form of this function is assumed to be determined largely by watershed characteristics (e.g., size, geology, slope, etc.) [see equation (1.23)], but can only be inferred empirically. The function is often assumed to be a power law:

$$Q_R = k \cdot S^b; \quad (9.45)$$

if $b = 1$, this leads to

$$Q_R = Q_{R0} \cdot \exp[-k \cdot (t - t_0)] \quad (9.46)$$

(the linear reservoir of box 9.7); if $b > 1$,

$$Q_R = Q_{R0} \cdot [1 + d \cdot (t - t_0)]^{b/(1-b)}, \quad (9.47)$$

where k , b , and d are constants, t is time, and Q_{R0} is the flow rate at the selected initial time t_0 . Values of the constants are found empirically by choosing t_0 (the time of peak flow or later) and finding values of b and d that give a line that best fits the subsequent recession.

In fact, because total watershed storage S cannot actually be determined, flow-storage relations are best inferred from relations between concurrent values of the rate of change of flow and flow during re-

cessions, which can also commonly be approximated as power-law relations:

$$-\frac{dQ_R}{dt} = a \cdot Q_R^b, \quad (9.48)$$

where a and b are characteristic of a given watershed that can be estimated by plotting dQ_R/dt versus Q_R on logarithmic graph paper and determining a and b from the slope and intercept of the line that best fits the plot (Brutsaert and Nieber 1977). [This approach was used in the analysis of section 1.12; see equation (1.48).] Note that although equations (9.46)–(9.48) may give the form of the recession hydrograph, they provide no information about the actual source of the water.

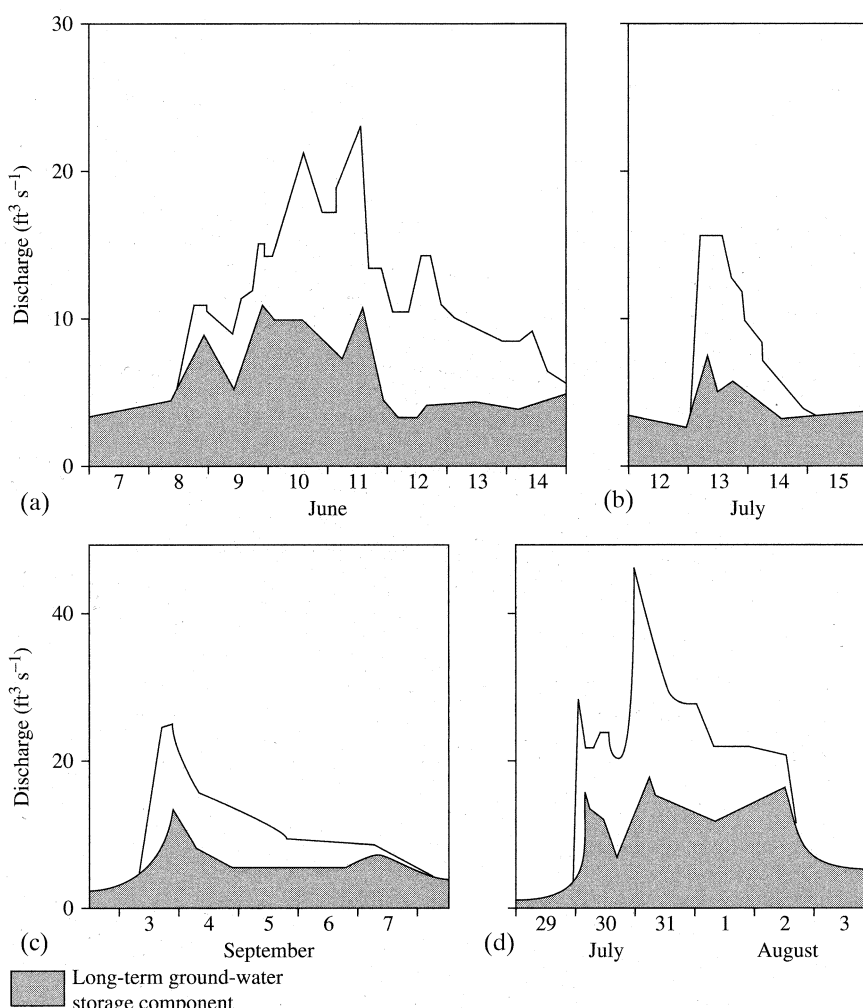


Figure 9.33 Total streamflow and streamflow attributed to ground-water base flow for four runoff events in Wilson Creek, Manitoba, as estimated using equation (9.43) with SO_4^{2-} as a tracer [reproduced from Newbury et al. (1969), Groundwater-streamflow systems in Wilson Creek Experimental Watershed, Manitoba, *Canadian Journal of Earth Sciences* 6:613–623, © Canadian Science Publishing or its licensors].

As shown by Brutsaert (1992, 1994), drainage from a horizontal aquifer under the Dupuit assumptions (box 9.3) can be approximated as an exponential decay with the parameters related to aquifer properties as

$$q_{GW} = \frac{h_0^2 \cdot K_h}{X} \cdot \exp\left(\frac{1.23 \cdot K_h \cdot h_0}{X^2 \cdot S_y} \cdot t\right), \quad (9.49)$$

where q_{GW} is ground-water flow per unit stream length and the other symbols are as in boxes 9.3 and

9.4. If recession flow is drainage from quasi-horizontal watershed aquifers, this provides a theoretical basis for the exponential-decay recession [equation (9.46)] and a possible basis for estimating recession flow on the basis of aquifer properties (or vice versa, if some of the properties are known). These possibilities are explored further by Harman et al. (2009).

9.5.3.6.3 Arbitrary Base-Flow Separation Methods

In practice, base-flow separation is assumed to represent Q_{GW} , and base-flow separation is usually

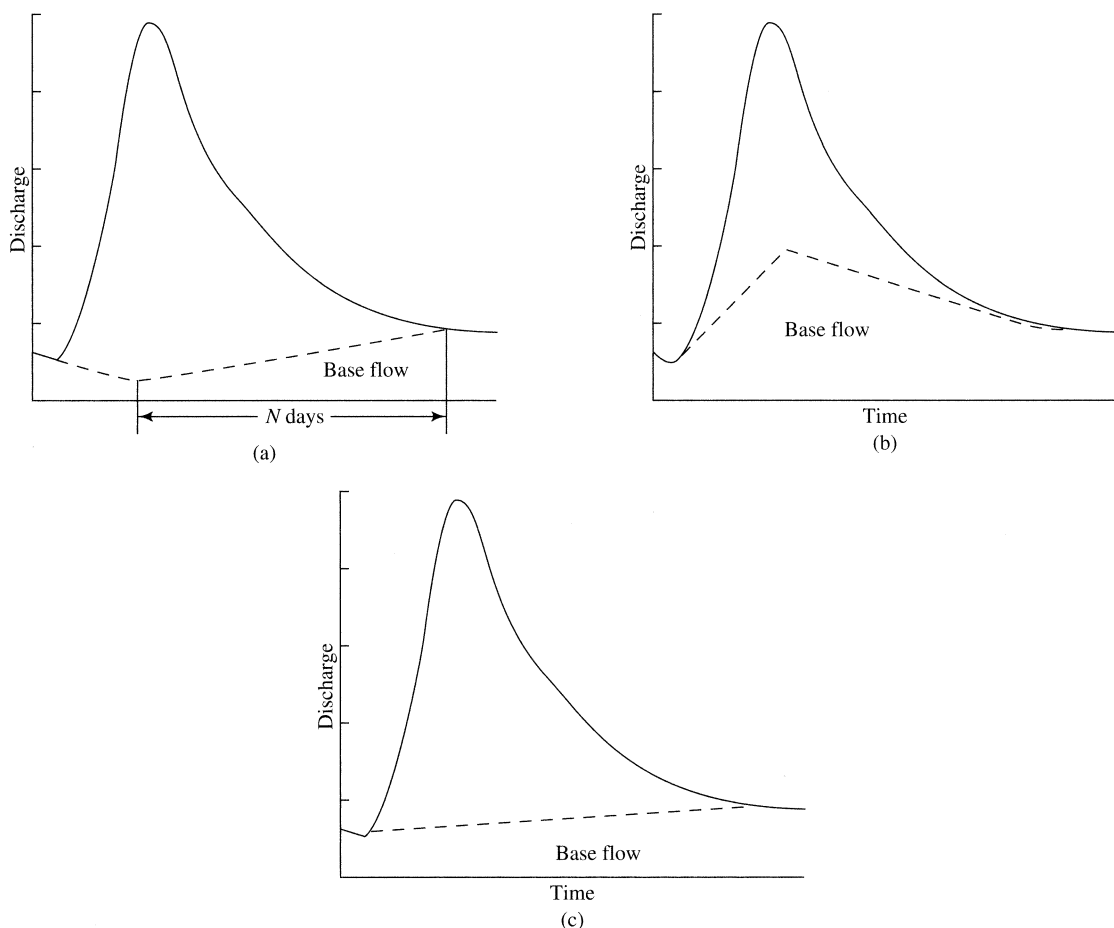


Figure 9.34 Methods of graphical base-flow separation. (a) The preevent flow trend is projected until the time of peak, after which the base-flow hydrograph is connected by a straight line that intersects the total-flow hydrograph N days after the peak, where N (days) = $0.82 \cdot A^{0.2}$, and A is drainage area in km^2 . (b) The hydrograph is plotted on semi-logarithmic paper ($\log[Q(t)]$ versus t). A straight line is fitted to the end of the hydrograph recession on this graph and projected backward in time under the peak. This projected line is transferred onto arithmetic graph paper and a smooth line is sketched connecting it to the end of the preceding recession. (c) From the point of initial hydrograph rise, a line that slopes upward at a rate of $0.0014 \text{ m}^3/\text{s} \cdot \text{A km}^2$ per hour is drawn and extended until it intercepts the hydrograph ($A < 50 \text{ km}^2$) [Dunne and Leopold (1978)].

done by plotting the measured stream hydrograph and constructing by arbitrary methods a line coincident with or below the hydrograph that is designated the base flow. Construction of the line requires answers to the following questions: (1) How does base flow behave while the stream is responding to water input? and (2) At what point does base flow become equal to total flow?

The theoretical analyses just described may provide plausible guidance in answering these questions. However, because no information as to the true sources of stream flow is usually available, many purely arbitrary approaches to separation have been proposed. In fact, base-flow separation has been called “one of the most desperate analysis techniques in use in hydrology” (Hewlett and Hibbert, 1967, p. 276).

Three arbitrary separation methods that have been used on relatively small watersheds are described in figure 9.34; others are described by Nathan and McMahon (1990), Tallaksen (1995), Arnold and Allen (1999), and Chapman (1999). One of the most widely used methods for larger watersheds was developed by the Institute of Hydrology (UK) (now the Centre for Ecology and Hydrology); this is described in box 9.8 and illustrated in figure 9.35. This method is usually used to calculate the **base-flow index (BFI)**, defined as

$$BFI \equiv \frac{\sum_{i=1}^N Q_{Bi}}{\sum_{i=1}^N Q_i}, \quad (9.50)$$

where Q_{Bi} are daily base-flow values determined by the method, and Q_i are average daily streamflows. Similar computations of the relative magnitude of base flow can be based on other separation methods.

In a region of generally similar geology, larger watersheds tend to have more storage and a higher proportion of base flow. A watershed containing very permeable soils or low slopes typically has a high proportion of base flow (e.g., $BFI > 0.95$), while one with high slopes underlain by impermeable material has a low proportion ($BFI < 0.2$). If relations between BFI and watershed properties can be established, they may provide a basis for inferring stream behavior in watersheds where flow measurements have not been made. Kling and Nachtnebel (2009) presented a simple method for the regional estimation of runoff-separation parameters for the monthly water-balance model using the BFI and catchment

characteristics, and Santhi et al. (2008) mapped BFI values for the United States and related them to hydrologic landscape regions and watershed properties such as relief and percentage of sand.

Note that the total volume of base flow varies greatly depending on the separation method used. This illustrates the crucial point: If a consistent method is applied, base-flow separation can be a useful tool for comparing the relative contributions of ground water to streamflow in different watersheds. However,

All base-flow separation methods are based on assumptions and require arbitrary decisions; thus, by themselves they cannot be used to identify the actual ground-water component of streamflow
(Freeze 1972a; Anderson and Burt 1980).

The topic of base-flow separation is also important for the study of event flow, and is examined further in section 10.2.2.

9.5.4 Capillary Rise, CR

Capillary rise is induced by extraction of water from the unsaturated zone and capillary fringe by evapotranspiration, and by migration of water to a freezing front. Capillary rise is usually considered to be a minor to negligible component of the water budget in humid regions, but may be a significant proportion of evapotranspiration in semiarid and arid areas. Net capillary rise may be difficult to estimate as a separate component, and it is often tacitly included as part of basin evapotranspiration, as done here.

One approach to estimating capillary rise is to identify those portions of the drainage basin where the water table is close enough to the surface that plants can obtain water from the capillary fringe or the saturated zone below. The presence of wetland vegetation and plants that are known **phreatophytes** can be used in this identification. One can then assume that evapotranspiration from these areas will always be at the potential rate, and use one of the methods described in chapter 6 to estimate PET. Nichols (1993, 1994) applied such methods in estimating CR in the western United States.

In areas where plants are extracting water from the capillary fringe, the water table may show a diurnal fluctuation (figure 9.36 on p. 438). Johansson (1986) showed that transpiration could produce such

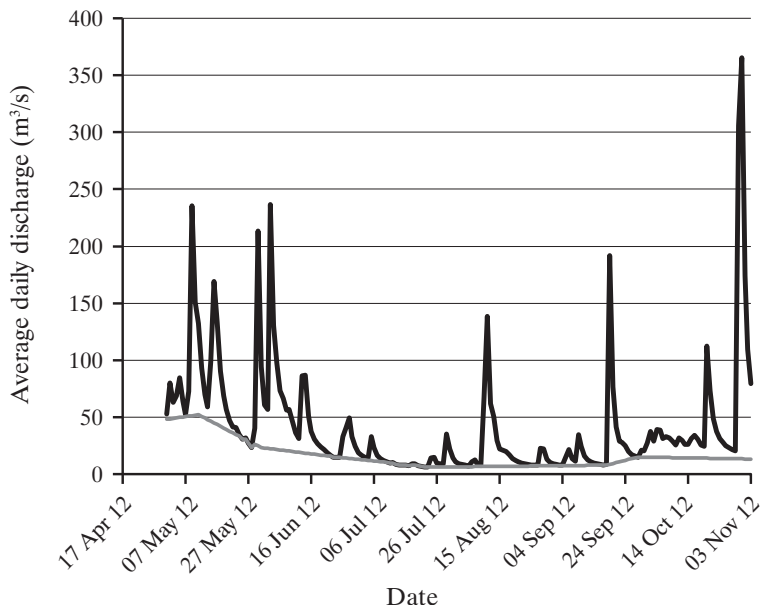


Figure 9.35 Measured discharge and base flow as calculated by the Institute of Hydrology base-flow separation method (box 9.8) for the Pemigewasset River at Plymouth, New Hampshire, for 17 April 2012 to 3 November 2012.

Box 9.8 Institute of Hydrology Base-Flow Separation Method

This base-flow separation method was developed by the Institute of Hydrology (1980) and is implemented via a computer program or in a spreadsheet. The initial data required are a time series of mean *daily* streamflow rates. The method is not appropriate for small "flashy" streams in which hydrograph rises take place over hours rather than days.

To access such data for stream gauges in the United States, go to the National Water Information System website (<http://waterdata.usgs.gov>) and follow these steps:

1. Select "Surface Water."
2. Select "Daily Data."
3. Under "Site Identifier," enter site (stream) name.
4. Under "Water Level/Flow Parameters," select "Streamflow ft³/s."
5. Scroll down to "Choose Output Format" and select an appropriate format, then go to "Retrieve USGS Surface-Water Daily Data for Selected Sites" and enter the first date and last date of the time period of interest.
6. Scroll down and select "Tab-separated data" and "Save to file" to save the data in a spreadsheet.
7. In the spreadsheet, convert flows from ft³/s to m³/s by dividing by 35.31.

Given a sequence of N mean daily flows Q_1, Q_2, \dots, Q_N , the basic procedure is to determine the minima of nonoverlapping consecutive 5-day periods and identify "turning points" in the sequence of minima. The turning

points, which are separated by varying numbers of days, are then connected by straight lines that define the ordinate of the daily base-flow hydrograph, $Q_{BF1}, Q_{BF2}, \dots, Q_{BFN}$, with the constraint that $Q_{BFi} \leq Q_i$. The detailed steps in the procedure are:

1. Divide the daily flows into nonoverlapping blocks of 5 days.
2. Determine the minimum value for each block, designate these Q_{m1}, Q_{m2} , etc.
3. For each group of three successive minima $(Q_{m1}, Q_{m2}, Q_{m3}), (Q_{m2}, Q_{m3}, Q_{m4}), (Q_{m3}, Q_{m4}, Q_{m5})$, etc., determine whether the central value is < 0.9 times both outer values. If this is true for day i , $Q_{BFi} = Q_{mj}$; i.e., the central value is an ordinate of the base-flow hydrograph, designated Q_{BFi} . These will be separated by varying numbers of days.
4. Linearly interpolate between successive Q_{BFi} values to determine the potential base-flow ordinates for the intervening days.
5. If any Q_{BFi} value determined in step 4 is greater than the actual flow, Q_i , set $Q_{BFi} = Q_i$.

An example is shown in figure 9.35.

Aksoy et al. (2009) developed a modification of the Institute of Hydrology method that removes sharp peaks and troughs in the base-flow line via digital filtering and smoothing.

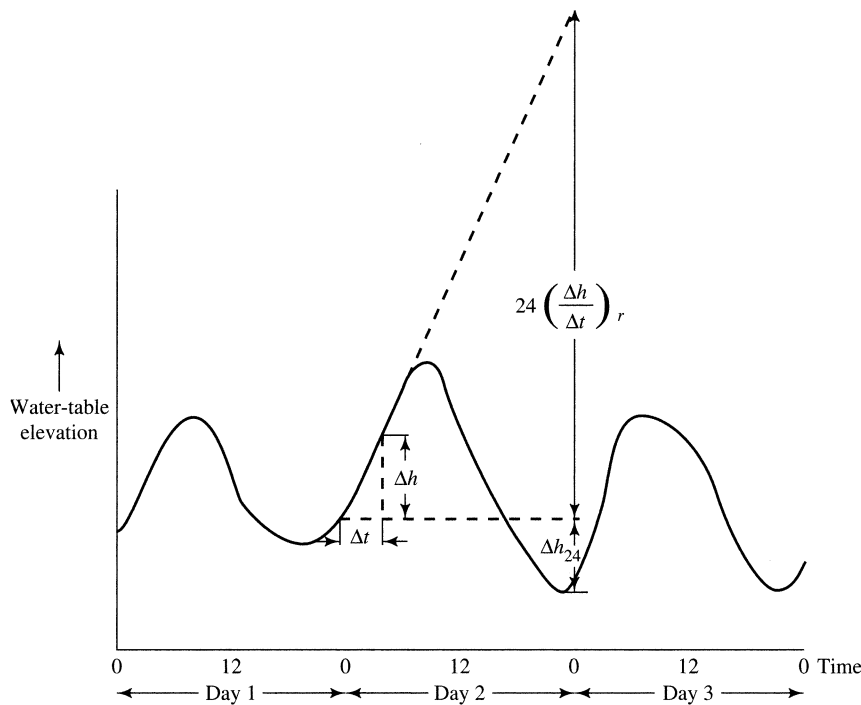


Figure 9.36 Estimation of evapotranspiration from the capillary fringe (capillary rise) using diurnal water-table fluctuations [equation (9.51)] [adapted from Freeze and Cherry (1979)].

fluctuations even with water tables at depths of 2 m or more. White (1932) suggested that evapotranspiration could be estimated from such diurnal water-table fluctuations as

$$ET = \left[24 \cdot \left(\frac{\Delta h}{\Delta t} \right)_r + \Delta h_{24} \right] \cdot S_y, \quad (9.51)$$

where ET is the daily evapotranspiration [L], $(\Delta h / \Delta t)_r$ is the rate of rise of the water table during the period midnight to 4:00 AM, and Δh_{24} is the net fall in water level over the 24-hr period. This method was successfully used by Meyboom (as cited in Freeze and Cherry 1979), who suggested that the appropriate value of S_y used in equation (9.51) is one-half the conventional value.

Daniel (1976) developed a method for estimating evaporative extractions of ground water based on theoretical aquifer-drainage relations, and applied it successfully in Alabama.

9.5.5 Deep Seepage, G_{in} and G_{out}

In the context of the water-balance relations developed earlier [equations (9.21)–(9.23)], **deep seepage** refers to the ground-water inflow and outflow terms G_{in} and G_{out} , respectively. The magnitudes of these terms are very difficult to determine, and they

are often assumed to be negligible or to cancel (i.e., $G_{out} = G_{in}$). However, the earlier discussion of regional ground-water flow suggests that it is often unwise to cavalierly adopt such assumptions.

9.5.5.1 Piezometer Measurements and Flow Nets

Installation of piezometers and observation wells at strategic locations gives the most definitive information about the magnitude of deep seepage. This information is most effectively used in combination with flow-net construction, as by Freeze and Witherspoon (1968). Winter et al. (1989) and Winter et al. (2003) combined piezometer observations with hydroclimatologic observations to develop information on the magnitude of deep seepage in smaller watersheds in many regions (see section 9.3.2), and found that it is often significant.

9.5.5.2 Water-Balance Analyses

9.5.5.2.1 Watershed Segments

Figure 9.37 shows a hypothetical drainage basin in which the main stream is gauged at N successive downstream locations. Starting at each of these locations, topographic divides can be delineated that define N subbasin segments, numbered $i = 1, 2, \dots, N$ from upstream to downstream. If we assume that there is no flow across the main basin divides, and

that ground water as well as surface water moves only in the down-basin direction, the long-term average water balance for the i th segment is

$$Q_i = (P_i - ET_i) \cdot A_i + G_{i-1} - G_i + Q_{i-1}, \quad (9.52)$$

where Q is stream outflow [$L^3 T^{-1}$], P and ET are areal average precipitation and evapotranspiration rates, respectively [$L T^{-1}$], A is the area of the segment [L^2], and G is ground-water outflow rate [$L^3 T^{-1}$].

If we assume that all the quantities in equation (9.52) can be determined with reasonable precision except the G terms, there are N equations of the form of (9.52) with $N + 1$ unknowns (including G_0). However, if G_0 as well as $Q_0 = 0$ as assumed, there are actually only N unknowns, and the ground-water outflow for the i th segment can be found as

$$G_i = (P_i - ET_i) \cdot A_i + G_{i-1} + Q_{i-1} - Q_i. \quad (9.53)$$

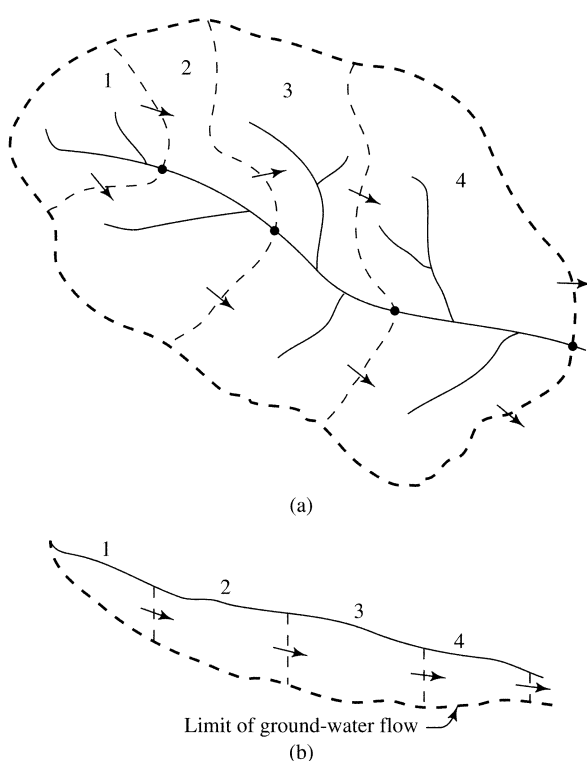


Figure 9.37 Schematic diagram defining terms for derivation of water-balance estimates of deep seepage [equations (9.52)–(9.53)]. Arrows indicate general direction of ground-water flow, dots are gauging stations. (a) Plan view of basin showing segments. (b) Longitudinal cross section.

Box 9.9 gives an example application of equation (9.53). However, as with all water-balance approaches, the uncertainty in all the “known” terms is hidden in the terms found by subtraction.

9.5.5.2.2 Water Balance as a Function of Basin Elevation

As discussed in section 4.1.5, average precipitation (P) is a strong function of elevation in many regions. Since average evapotranspiration (ET) is strongly related to average air temperature, which decreases with elevation, ET usually decreases with elevation. Dingman (1981) developed relations for estimating P and ET as functions of elevation in northern New England and then compared values of $P - Q$ with ET , where Q is measured average streamflow for small watersheds that each span a limited range of elevation. The results are shown in figure 9.38 on p. 441: The presence of ground-water outflow is indicated for watersheds in which $(P - Q) > ET$. The data suggest that many higher-elevation watersheds in northern New England have deep-seepage outflows on the order of 100 mm/yr.

9.5.5.2.3 Regional Water Balance

Schaller and Fan (2009) presented a quantitative survey of ground-water inflows and outflows based on a simple water-balance analysis for some 1,555 watersheds over the contiguous United States. Watershed surplus (recharge, R) was calculated at a resolution of ~ 10 km as

$$R = P - ET, \quad (9.54)$$

where P was determined from gridded observations, and ET from a 50-year simulation using a hydrologic model. The recharge was partitioned into streamflow, Q , and ground-water outflow, G_{out} :

$$R = Q + G_{out}, \quad (9.55a)$$

i.e., G_{out} was calculated as

$$G_{out} = R - Q = P - ET - Q, \quad (9.55b)$$

where Q was measured at gauging stations selected to minimize the effects of reservoir operations, ground-water extraction, and other artificial influences. The ratio Q/R (the fraction of recharge that leaves the watershed as streamflow) was used to characterize this partition: If $Q/R > 1$, the observed river flow includes ground-water inflow from other watersheds, and the basin is a ground-water importer; if $Q/R < 1$, the watershed is a ground-water exporter.

The results are shown in figure 9.39 on p. 442. Values of Q/R ranged from < 0.1 ($> 90\%$ of recharge exits as ground-water outflow, G_{out}) to > 2 ($> 50\%$ of the streamflow is imported ground water, G_{in}). Half (49.6%) of the watersheds examined are ground-water exporters and half are importers. As would be expected, Q/R values greater or less than 1 were more frequent in arid regions ($P < 500$ mm/yr; figure

9.39b); they are more common in watersheds with recharge-controlled water tables as indicated by the water-table ratio (WTR) described in section 9.2.5.2. There is a tendency of the Q/R ratio to be closer to 1 with increasing watershed area (figure 9.39c), consistent with regional ground-water flow dynamics. There is no clear relation between Q/R and elevation (figure 9.38d). However, the watersheds studied were

Box 9.9 Example Calculation of G_{in} and G_{out} from Watershed-Segment Water Balances

Table 9B9.1 gives areas and long-term average values of precipitation, evapotranspiration, and streamflow for four segments of the Contoocook River basin in central New Hampshire.

Table 9B9.1

Watershed segment, i	Stream Gauge at	Area, A (km 2)	Average Streamflow (m 3 /s)	Precipitation, P (mm/yr)	Evapotranspiration, ET (mm/yr)
1	Peterboro	176	3.31	1,300	500
2	Henniker	777	18.0	1,180	500
3	W. Hopkinton	153	10.7	1,020	550
4	Penacook	878	35.5	1,070	550

We want to estimate the ground-water outflow, G_i , from each segment using the method and assumptions of section 9.5.5.2.1. For the first (upstream-most) segment, we assume no stream or ground-water inflow, and equation (9.53) gives

$$G_1 = [(1,300 - 500) \text{ mm/yr}] \times (176 \text{ km}^2) \times [3.17 \times 10^{-5} \text{ m}^3/\text{yr}/(\text{mm} \cdot \text{km}^2 \cdot \text{s})] \\ + 0 \text{ m}^3/\text{s} + 0 \text{ m}^3/\text{s} - 3.31 \text{ m}^3/\text{s} = 1.15 \text{ m}^3/\text{s}.$$

For the second segment, we have

$$G_2 = [(1,180 - 500) \text{ mm/yr}] \times (777 \text{ km}^2) \times [3.17 \times 10^{-5} \text{ m}^3/\text{yr}/(\text{mm} \cdot \text{km}^2 \cdot \text{s})] \\ + 1.15 \text{ m}^3/\text{s} + 3.31 \text{ m}^3/\text{s} - 18.0 \text{ m}^3/\text{s} = 3.21 \text{ m}^3/\text{s}.$$

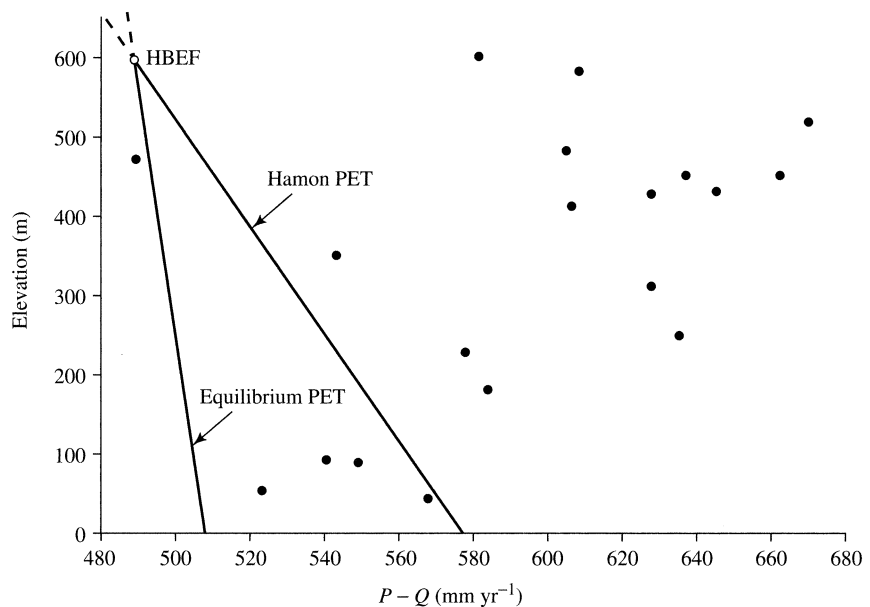
Similarly, the third and fourth segments yield the results in table 9B9.2.

Table 9B9.2

Segment, i	G_i (m 3 /s)	G_i/Q_i
1	1.15	0.35
2	3.21	0.18
3	3.76	0.19
4	2.50	0.07

These computations suggest that deep seepage is a significant component of the water balance in the Contoocook River basin. Note that the calculated proportion of outflow occurring as ground water decreases downstream, as would be expected as larger watersheds capture more ground water. The uncertainties in these estimates should be assessed (section 1.11.2) before accepting these conclusions (see exercise 9.12).

Figure 9.38 Long-term average precipitation (P) minus streamflow (Q) versus mean basin elevation for 19 small gauged basins in New Hampshire and Vermont. The lines are estimates of potential evapotranspiration (PET) using the Hamon and equilibrium estimates (see section 6.7.2.2), with the value determined at Hubbard Brook Experimental Forest (HBEF) as control. The existence of deep seepage is suggested for basins that plot to the right of the PET lines [reproduced from Dingman (1981), Elevation: A major influence on the hydrology of New Hampshire and Vermont, USA. *Hydrological Sciences Bulletin* 26:399–413, courtesy of International Association of Hydrological Sciences].



not characterized geologically or examined regionally, and doing so might have brought out that relation.

Although unaccounted for, artificial water transfers and uncertainty in the estimates of precipitation and evapotranspiration could have affected Schaller and Fan's (2009) Q/R values. However, their results suggest that ground-water outflow or inflow can be a significant portion of a watershed's water budget and emphasize the need for careful assessment of watershed water-budget components.

9.6 Impacts of Ground-Water Development on Areal Hydrology

Ground water is of course a major source of water for domestic, industrial, and agricultural uses. In many regions, the extraction of ground water has major impacts on local and regional hydrology, affecting streamflow, lake and wetland levels, coastal ecology, water quality, and land subsidence (box 9.2). The goal of this section is to provide a basic understanding of these impacts.

We focus on unconfined aquifers, because they have the most direct connections with other portions of the land phase of the hydrologic cycle and their exploitation as water sources has the most direct im-

pacts on regional hydrology. However, we will use the mathematically simpler but essentially similar behavior of confined aquifers to illustrate the most basic features of the effects of the extraction of ground water on drainage-basin hydrology. This is justified because the behavior of unconfined aquifers is nearly identical to that of confined aquifers as long as the changes in water-table elevation are small relative to the saturated thickness.

To further simplify the discussion we consider only homogeneous, isotropic aquifers, simple aquifer configurations, and fully-penetrating wells. General ground-water texts such as Bear (1979), Freeze and Cherry (1979), and Fetter (2001) explore more exact models of ground-water development in unconfined flows and in more complex boundary conditions.

9.6.1 Hydraulics of Ground-Water Development

9.6.1.1 Radial Flow to a Well

Consider the highly idealized case of a well completely penetrating a homogeneous unconfined aquifer of infinite extent resting on a horizontal impermeable base (figure 9.40 on p. 443). The water table is initially horizontal everywhere at a height h_0 above the base and there is no recharge or capillary rise.

When the well is pumped at a constant rate Q_w , water is withdrawn from aquifer storage, the water table declines toward the well, and flow is induced toward the well from all directions. Thus the flow has radial symmetry, and if we approximate the unconfined case by equivalent confined conditions (i.e., assume negligible water-table decline and horizontal streamlines and ignore a transient initial period prior to the establishment of gravity drainage), it can be described by transforming the two-dimensional form of the general ground-water equation [equation (9B1.8)] to polar coordinates (Freeze and Cherry 1979):

$$\frac{\partial^2 h}{\partial r^2} + \frac{1}{r} \cdot \frac{\partial h}{\partial r} = \frac{S_y}{K_h \cdot h_0} \cdot \frac{\partial h}{\partial t}, \quad (9.56)$$

where r is the radial distance measured outward from the well.

Theis (1935) showed that an analytical solution for equation (9.56) is

$$h_0 - h(r, t) = \frac{Q_w}{4 \cdot \pi \cdot K_h \cdot h_0} \cdot W[u(r, t)], \quad (9.57)$$

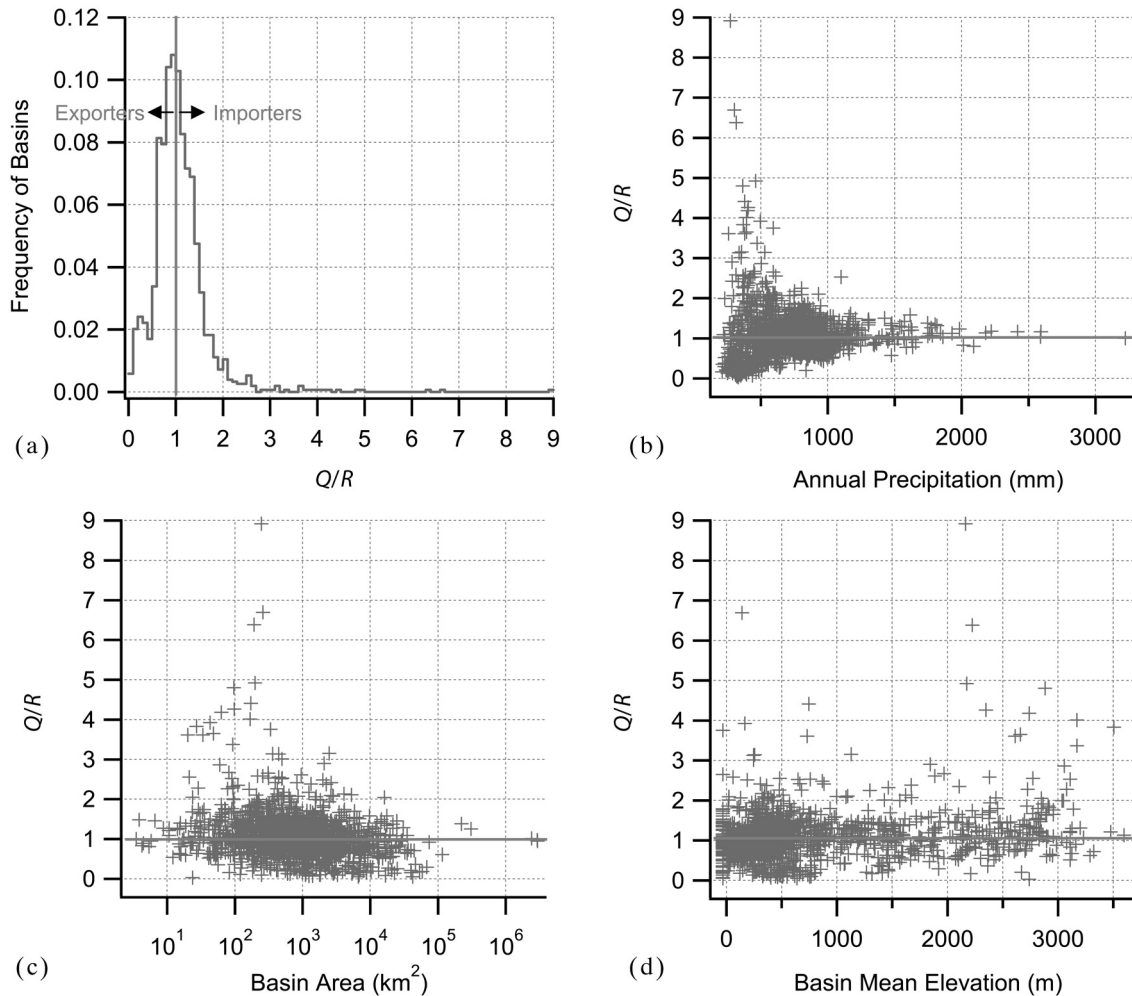


Figure 9.39 (a) The frequency of basins found at a given Q/R ratio, (b) the ratio as a function of annual precipitation, (c) the ratio as a function of basin area, and (d) the ratio as a function of mean basin elevation [Schaller and Fan (2009). River basins as groundwater exporters and importers: Implications for water cycle and climate modeling. *Journal of Geophysical Research* 114, with permission of the American Geophysical Union].

where

$$W[u(r,t)] \equiv \int_{u(r,t)}^{\infty} \frac{\exp[-u(r,t)]}{u(r,t)} \cdot du(r,t) \quad (9.58)$$

and $u(r,t)$ is a measure of the aquifer response time similar to equation (9.12):

$$u_{r,t} \equiv \frac{S_y \cdot r^2}{4 \cdot K_h \cdot h_0 \cdot t}. \quad (9.59)$$

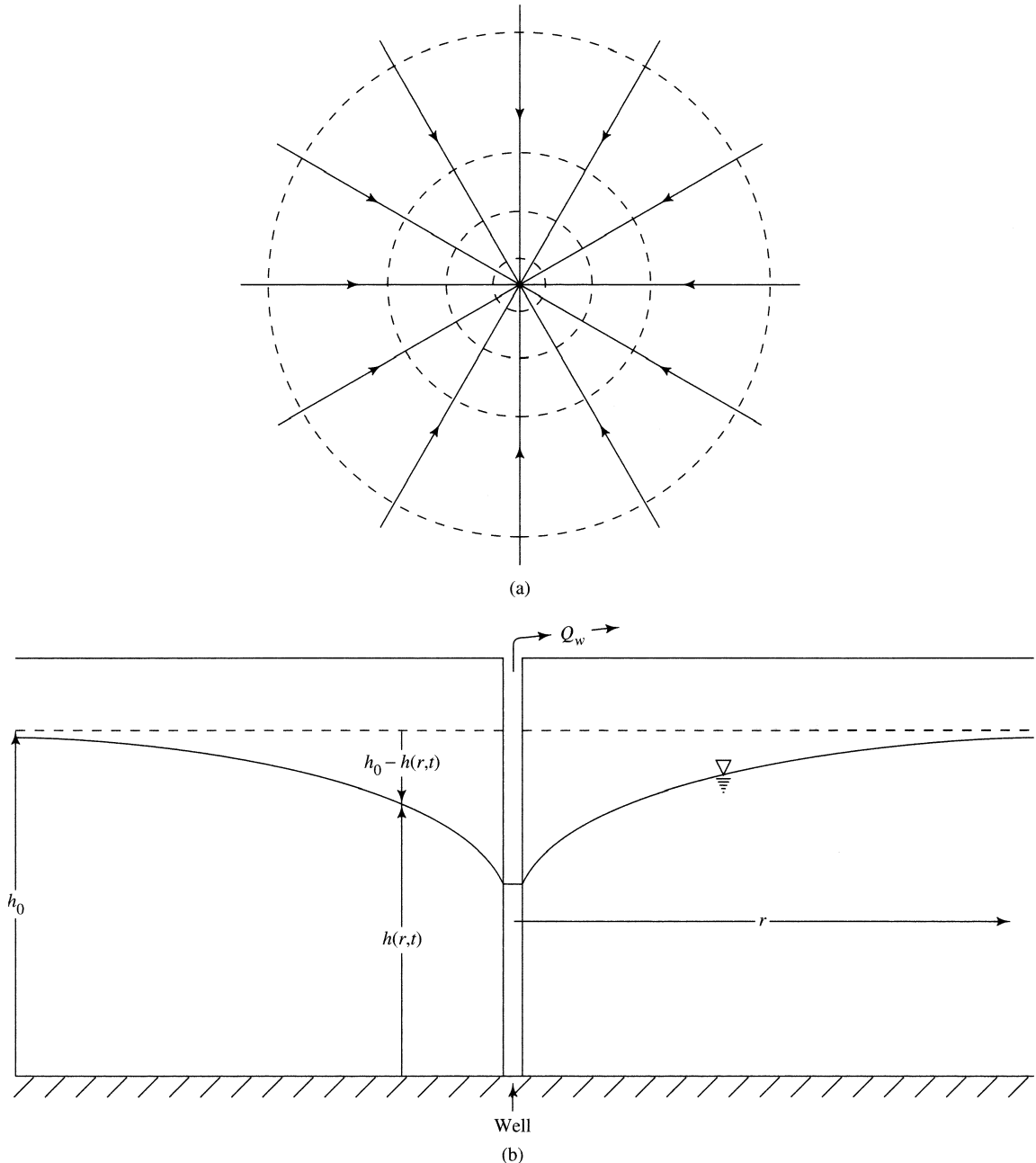


Figure 9.40 Definitions of terms for equations describing radial flow to a well in an unconfined aquifer [equations (9.56)–(9.59)]. (a) Plan view; dashed lines are equipotentials, arrows show flow directions. (b) Cross section.

The function $W[u(r,t)]$ is known as the **well function**; its values are tabulated in table 9.3. The quantity $[h_0 - h(r,t)]$ is the **drawdown**, and when its values are plotted as a function of distance at any time they define a **drawdown curve** or, in three dimensions, a **cone of depression** that is asymptotic to h_0 . Box 9.10 shows how this relation is applied.

The area over which the pumping causes drawdown is called the **area of influence**. For the idealized situation of figure 9.40, the lines of equal drawdown and the extent of the cone of depression are circular in plan view and the area of influence coincides with the projected area of the cone.

Clearly, the drawdown is proportional to pumping rate, and it decreases with distance at any time and increases with time at any distance. For a given pumping rate and a given duration of pumping, the rates of change are controlled by the aquifer properties. At a given time,

- lower $K_h \rightarrow$ larger drawdown spread over a smaller area
- higher $K_h \rightarrow$ smaller drawdown spread over a greater area

- lower $S_y \rightarrow$ larger drawdown spread over a greater area
- higher $S_y \rightarrow$ smaller drawdown spread over a smaller area

An interesting and useful property of the solution to equation (9.56) is that the drawdown at any location due to the pumping of more than one well is equal to the sum of the drawdowns that would be produced at that location by each of the wells individually.

9.6.1.2 Contributing Areas

The **contributing area** of a well is the area on the land surface above the portion of aquifer from which water is flowing to the well. Identification of this area for unconfined aquifers receiving recharge from infiltration and/or surface-water bodies is important because (1) the levels of ground-water-fed lakes or streams in the contributing area will be affected by pumping and (2) any water-contaminating substances introduced into the contributing area will eventually reach the well. The delineation of these areas by analytical and numerical methods was reviewed by Morrissey (1987).

Table 9.3 Values of $W[u(r,t)]$ for Various Values of $u(r,t)$.^a

Example: For $u(r,t) = 4.0 \times 10^{-5}$, $W[u(r,t)] = 9.55$.

$u(r,t)$	1.0	2.0	3.0	4.0	5.0	6.0	7.0	8.0	9.0
$\times 1$	0.219	0.049	0.013	0.0038	0.0011	0.00036	0.00012	0.000038	0.000012
$\times 10^{-1}$	1.82	1.22	0.91	0.70	0.56	0.45	0.37	0.31	0.26
$\times 10^{-2}$	4.04	3.35	2.96	2.68	2.47	2.30	2.15	2.03	1.92
$\times 10^{-3}$	6.33	5.64	5.23	4.95	4.73	4.54	4.39	4.26	4.14
$\times 10^{-4}$	8.63	7.94	7.53	7.25	7.02	6.84	6.69	6.55	6.44
$\times 10^{-5}$	10.94	10.24	9.84	9.55	9.33	9.14	8.99	8.86	8.74
$\times 10^{-6}$	13.24	12.55	12.14	11.85	11.63	11.45	11.29	11.16	11.04
$\times 10^{-7}$	15.54	14.85	14.44	14.15	13.93	13.75	13.60	13.46	13.34
$\times 10^{-8}$	17.84	17.15	16.74	16.46	16.23	16.05	15.90	15.76	15.65
$\times 10^{-9}$	20.15	19.45	19.05	18.76	18.54	18.35	18.20	18.07	17.95
$\times 10^{-10}$	22.45	21.76	21.35	21.06	20.84	20.66	20.50	20.37	20.25
$\times 10^{-11}$	24.75	24.06	23.65	23.36	23.14	22.96	22.81	22.67	22.55
$\times 10^{-12}$	27.05	26.36	25.96	25.67	25.44	25.26	25.11	24.97	24.86
$\times 10^{-13}$	29.36	28.66	28.26	27.97	27.75	27.56	27.41	27.28	27.16
$\times 10^{-14}$	31.66	30.97	30.56	30.27	30.05	29.87	29.71	29.58	29.46
$\times 10^{-15}$	33.96	33.27	32.86	32.58	32.35	32.17	32.02	31.88	31.76

^aInterpolated values can be estimated using the method of Barry et al. (2000).

Source: Wenzel (1942).

Box 9.10 Example Calculations: Drawdown and Stream Depletion**Example Drawdown Calculation**

Here we compute the drawdown at various distances from a well ($r = 1, 5, 10, 50$, and 100 m) at various times after pumping begins ($t = 1, 2, 40$, and 80 hr). We assume an ideal homogeneous horizontal aquifer with $K_h = 10^{-5}\text{ m/s}$, $h_0 = 20\text{ m}$, $S_y = 0.20$, a constant pumping rate $Q_w = 0.001\text{ m}^3/\text{s}$ ($= 86.4\text{ m}^3/\text{day}$), and no interaction with surface-water bodies. For the first values of time and distance we use equation (9.59) to find $u(r,t)$ as

$$u(1\text{ m}, 3,600\text{ s}) = \frac{0.2 \times (1\text{ m})^2}{4 \times (10^{-5}\text{ m/s}) \times (20\text{ m}) \times (3,600\text{ s})} = 0.07. \quad (9B10.1)$$

Repeating this for all combinations of time and distance gives the values of $u(r,t)$ in table 9B10.1.

Table 9B10.1 $u(r,t)$

$t\text{ (s)}$	$r = 1\text{ m}$	$r = 5\text{ m}$	$r = 10\text{ m}$	$r = 50\text{ m}$	$r = 100\text{ m}$
3,600	0.07	1.74	6.94	173.61	694.44
7,200	0.03	0.87	3.47	86.81	347.22
144,000	0.00	0.04	0.17	4.34	17.36
288,000	0.00	0.02	0.09	2.17	8.68

From table 9.3 we find the values of $W[u(r,t)]$ that correspond to the above values of $u(r,t)$ [table 9B10.2; interpolated using approximation of Barry et al. (2000)].

Table 9B10.2 $W[u(r,t)]$

$t\text{ (s)}$	$r = 1\text{ m}$	$r = 5\text{ m}$	$r = 10\text{ m}$	$r = 50\text{ m}$	$r = 100\text{ m}$
3,600	2.16	0.07	0.00	0.00	0.00
7,200	2.82	0.28	0.01	0.00	0.00
144,000	5.78	2.60	1.34	0.00	0.00
288,000	6.47	3.27	1.96	0.04	0.00

Finally, the drawdown is calculated by multiplying the above values of $W[u(r,t)]$ by

$$\frac{Q_w}{4 \cdot \pi \cdot K_h \cdot h_0} = \frac{0.001\text{ m}^3/\text{s}}{4 \times 3.14 \times (10^{-5}\text{ m/s}) \times (20\text{ m})} = 0.398\text{ m} \quad (9B10.2)$$

to give $h_0 - h(r,t)$ in m. The results are found in table 9B10.3.

Table 9B10.3 Drawdown, $h_0 - h(r,t)$ (m)

$t\text{ (s)}$	$r = 1\text{ m}$	$r = 5\text{ m}$	$r = 10\text{ m}$	$r = 50\text{ m}$	$r = 100\text{ m}$
3,600	0.86	0.03	0.00	0.00	0.00
7,200	1.12	0.11	0.00	0.00	0.00
144,000	2.30	1.04	0.53	0.00	0.00
288,000	2.58	1.30	0.78	0.02	0.00

(continued)

Example Stream-Depletion Calculation

Consider a well in an aquifer with the same properties as in the previous example, except it is located 20 m from a stream. To determine the streamflow depletion rate D_w at 1, 10, 30, 60, 180, and 365 days of continuous pumping, refer to equation (9.64) and calculate

$$\frac{K_h \cdot h_0}{x^2 \cdot S_y} = \frac{(10^{-5} \text{ m/s}) \times (20 \text{ m})}{(20 \text{ m})^2 \times (0.20)} = 2.5 \times 10^{-6} \text{ s}^{-1}. \quad (9B10.3)$$

Table 9B10.4 shows the arguments of $D()$ obtained by multiplying the value of equation (9B10.3) by the times of interest. The values of $D_w(t)/Q_w$ are then found from the curve in figure 9.43, and D_w is found by multiplying those values by Q_w .

Table 9B10.4 Argument of Depletion Function

Quantity	$t = 1 \text{ day} = 8.64 \times 10^4 \text{ s}$	$t = 10 \text{ days} = 8.64 \times 10^5 \text{ s}$	$t = 30 \text{ days} = 2.59 \times 10^6 \text{ s}$	$t = 60 \text{ days} = 5.18 \times 10^6 \text{ s}$	$t = 180 \text{ days} = 1.56 \times 10^7 \text{ s}$	$t = 365 \text{ days} = 3.15 \times 10^7 \text{ s}$
argument	0.216	2.16	6.48	13.0	38.9	78.8
$D_w(t)/Q_w$	0.11	0.62	0.77	0.82	0.90	0.92
$D_w (\text{m}^3/\text{s})$	1.1×10^{-4}	6.2×10^{-4}	7.7×10^{-4}	8.2×10^{-4}	9.0×10^{-4}	9.2×10^{-4}

For the ideal, infinite, homogeneous aquifer with an initially horizontal water table described in the preceding section all the water extracted from the cone of depression eventually arrives at the well, and the contributing area at any time is identical to the area of influence. However, actual aquifers do not have horizontal water tables (which would imply no flow) and do not extend infinitely. If the water table is initially sloping, the cone of depression is no longer circular and the contributing area does not coincide with the area of influence (figure 9.41). If the aquifer is in a river valley, the contributing area may extend to or even beyond the river (figure 9.42 on pp. 448–449).

9.6.2 Effects of Ground-Water Extraction

9.6.2.1 Effects on Natural Recharge and Discharge

Consider the ground-water system of a drainage basin in which there is no ground-water flow in or out. Under natural (no development) conditions, the long-term average recharge and discharge for this system must be in balance, and from equation (9.23):

$$R_{nat} - Q_{GWnat} = 0, \quad (9.60)$$

where the subscript “*nat*” denotes the natural recharge and discharge rates.

If one or more wells begins pumping from the system, water will be removed from aquifer storage as the cones of depression develop. In addition, the

natural rates of recharge and/or discharge will in general be changed as the water-table configuration is altered by the pumping. Thus, during development, the water-balance for the system becomes

$$(R_{nat} + \Delta R) - (Q_{GWnat} + \Delta Q_{GW}) - \Sigma Q_w = \frac{\Delta S}{\Delta t}, \quad (9.61)$$

where ΔR and ΔQ_{GW} are the changes in recharge and discharge, respectively, due to the water-table lowering induced by the pumping; ΣQ_w is the total pumping rate; and $\Delta S/\Delta t$ is the rate of change of aquifer storage ($\Delta S/\Delta t < 0$). Combining equations (9.60) and (9.61) yields

$$\Sigma Q_w = \Delta R - \Delta Q_{GW} - \frac{\Delta S}{\Delta t}. \quad (9.62)$$

Equation (9.62) states that ground-water extraction must be balanced by a decrease in storage ($-\Delta S$, which always occurs) and, in general, by some combination of increased (induced) recharge ($+\Delta R$) and/or decreased ground-water discharge ($-\Delta Q_{GW}$). We now examine how water tables lowered by pumping affect ΔR and ΔQ_{GW} .

From the definition of recharge [equation (9.22)], we see that ΔR must be due to some combination of: (1) increased recharge from infiltration, R_I ; (2) increased recharge from surface-water bodies,

R_{SW} ; and (3) decreased capillary rise, CR . Lowered water tables due to pumping affect these components in the following ways:

R_I : As shown in figure 9.26, net recharge from infiltration tends to increase with water-

table depth up to a point, beyond which there is little change.

R_{SW} : As shown in figure 9.42, the cone of depression from wells near streams can extend to the stream, locally reverse the

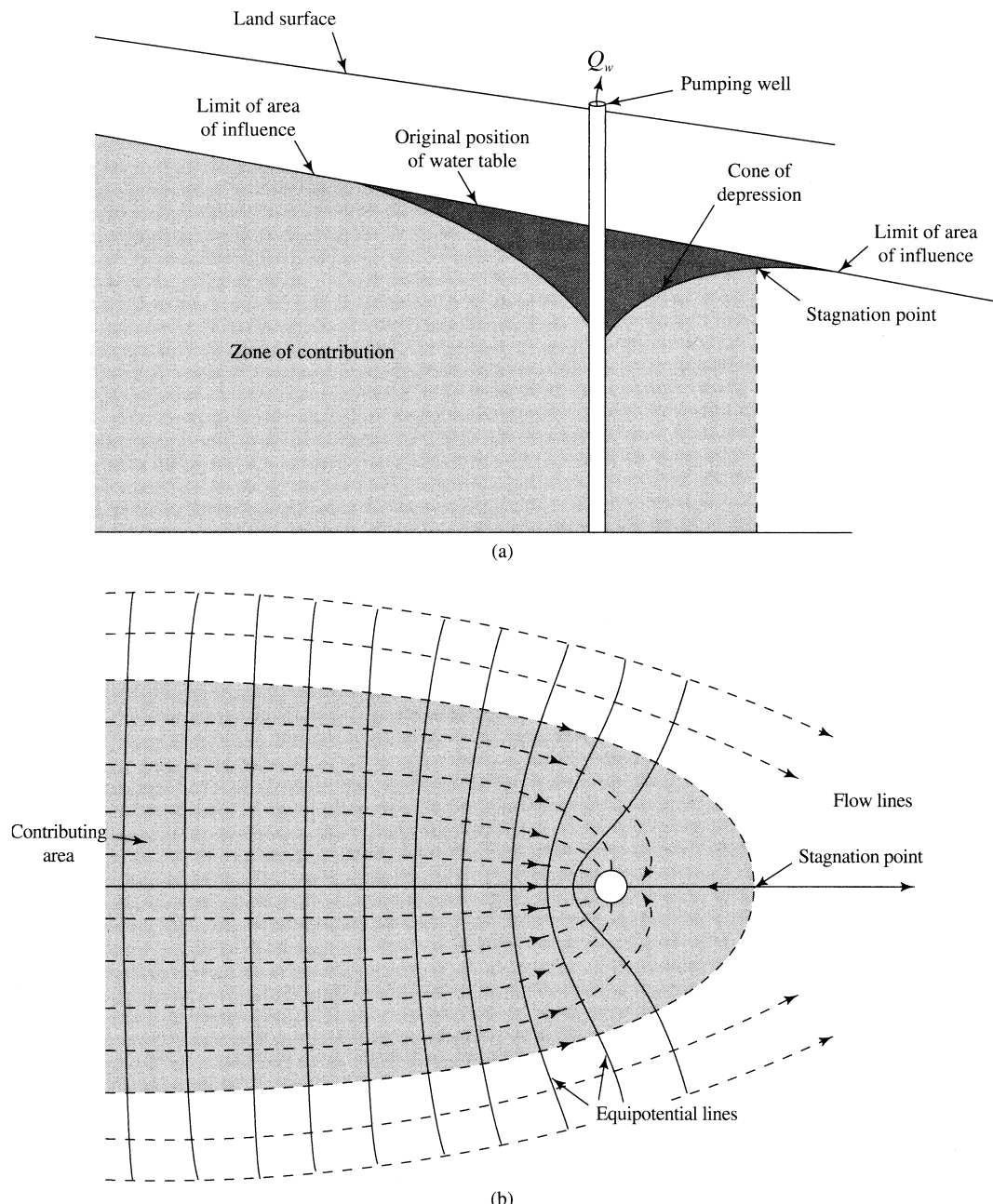


Figure 9.41 The cone of depression, area of influence, and contributing area for an aquifer with a sloping water table. (a) Cross section. (b) Plan view [adapted from Morrissey (1987)].

potential gradient, and induce recharge from the stream. (This effect is discussed further in the next section.)

CR: Again from figure 9.26, lowered water tables tend to decrease capillary rise by lowering the capillary fringe beyond the reach of plant roots.

Thus the overall effect of ground-water development tends to be a net increase in recharge; the magnitude of the effect will be highly dependent on the drainage-basin geology, topography, and climate and the placement and pumping rates of wells. In humid regions with gaining streams, lakes, and wetlands, much of this will be due to water loss from surface water (ΔR_{SW}).

It should be clear from the preceding discussion that some “mining”—i.e., removal of water from

aquifer storage—occurs with any extraction rate. However, if a constant rate of ground-water extraction is imposed on a region for a sufficient time, a new equilibrium state *may* eventually be reached in which there is no further change in storage ($\Delta S/\Delta t = 0$); if this occurs, the extraction rate (ΣQ_w) is supplied by increased recharge ($\Delta R_I + \Delta R_{SW} > 0$) and/or reduced discharge ($\Delta C_R + \Delta Q_{GW} < 0$). Bredehoeft et al. (1982) pointed out that the time required to reach this equilibrium may be very long indeed (hundreds of years), depending on the region’s size, hydrology, and geology and on the locations and pumping rates of wells. In some situations, it is not possible to reach an equilibrium state before drawdown at wells equals its maximum value, i.e., the water table is drawn down to the bottom of the deepest well. Only detailed ground-water modeling studies can evaluate a given situation.

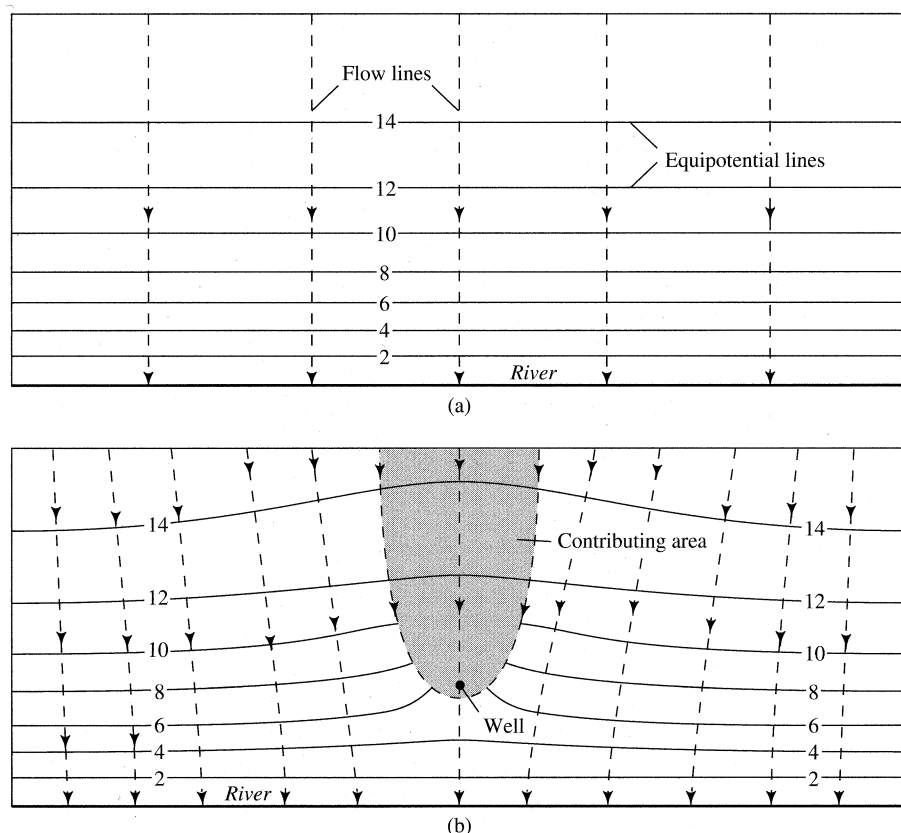


Figure 9.42 Contributing areas and water-table contours for wells near a river. (a) Natural condition before pumping. (b) Well intercepts water that was flowing to the river. (c) Well intercepts water and extracts flow from the river. (d) Well intercepts water from both sides of the valley and extracts water from the river. Existence of conditions (b), (c), or (d) depends on pumping rate and aquifer configuration and properties [Morrissey (1987)].

9.6.2.2 Effects on Streams

As shown in figure 9.42, ground-water extraction can reduce streamflow by: (1) inducing local recharge from a gaining stream ($\Delta R_{SW} > 0$) and (2) intercepting water that would naturally discharge to streams ($\Delta Q_{GW} < 0$). The net of these two effects is called **stream depletion**, D_w :

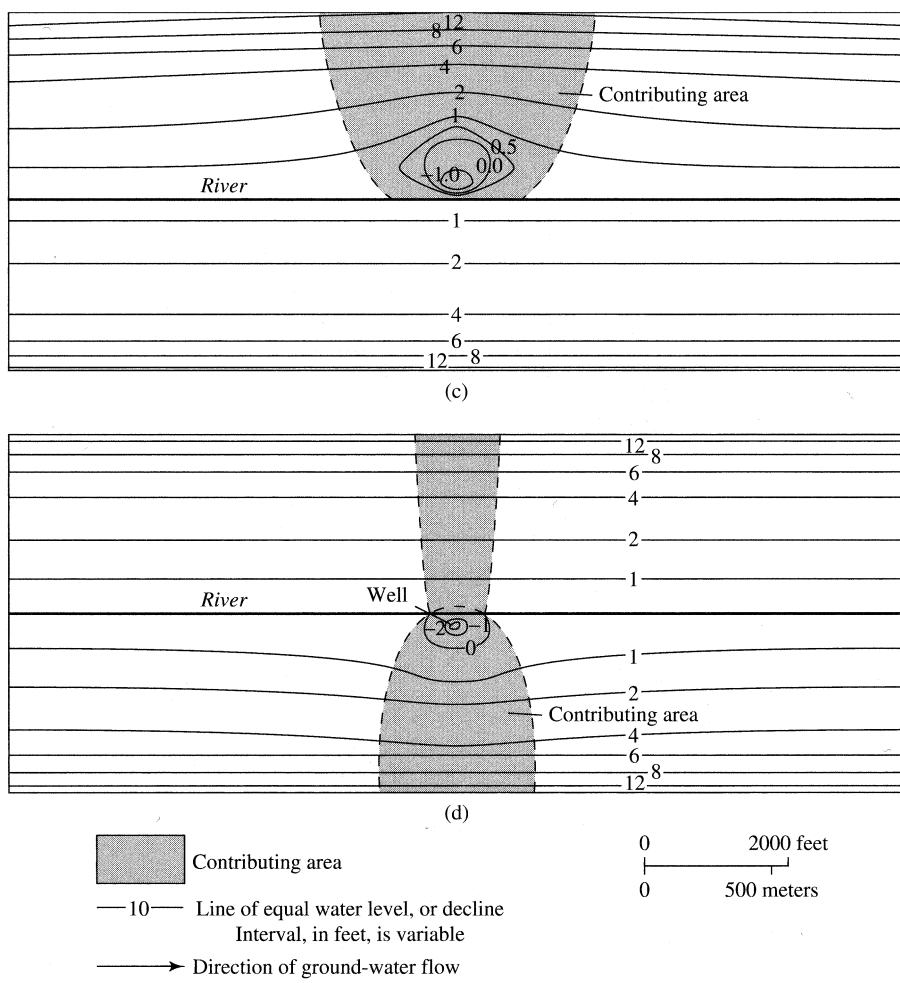
$$D_w \equiv \Delta R_{SW} - \Delta Q_{GW}. \quad (9.63)$$

Jenkins (1968) showed that, under the same idealized aquifer conditions used to solve equation (9.56), the ratio of stream depletion rate to a constant rate of pumping, Q_w , from a well located a dis-

tance x from a stream is given by a **depletion function**, D , where

$$\frac{D_w(t)}{Q_w} = D\left(\frac{K_h \cdot h_0 \cdot t}{x^2 \cdot S_y}\right). \quad (9.64)$$

Figure 9.43 gives the form of this depletion function; note that depletion rate is a function of the aquifer properties (K_h , S_y , h_0) and the distance of the well from the stream (x), and that the function is asymptotic to $D_w(t)/Q_w = 1$. Thus the fraction of pumpage that comes from the river increases with time until ultimately all the water withdrawn by the well comes from streamflow.



For all figures, units of head and drawdown expressed in feet relative to river stage

Figure 9.42 (continued)

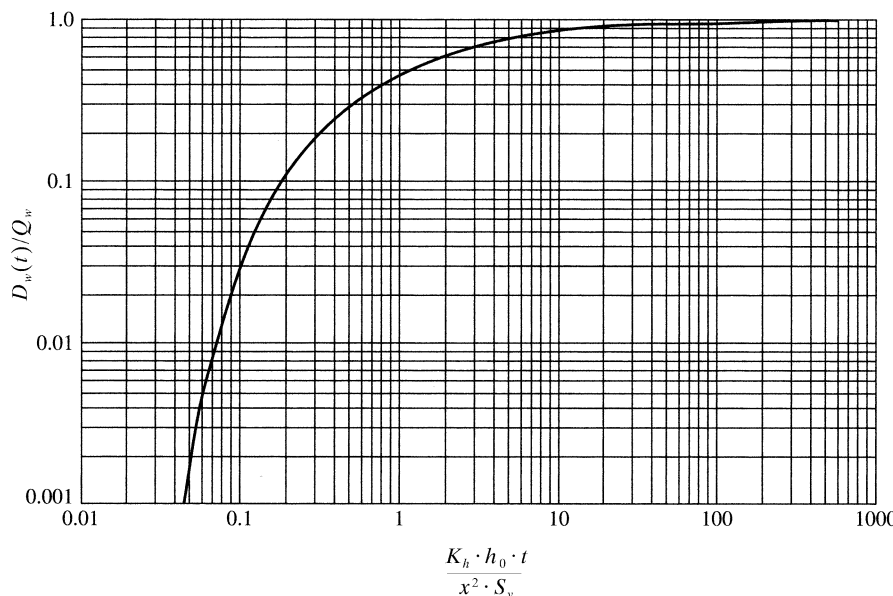


Figure 9.43 The stream-depletion function, $D_w(t)/Q_w$, as a function of $K_h \cdot h_0 \cdot t / (x^2 \cdot S_y)$. See example in box 9.10 [reproduced from Jenkins (1968), Techniques for computing rate and volume of stream depletion by wells. *Ground Water* 6(2):37–46, with permission from Wiley].

Box 9.10 gives an example of the application of this relation to estimating streamflow depletion rates. Jenkins (1968) gave additional examples, and showed how the relation can be used to estimate depletion rates and volumes due to continual and intermittent pumping.

9.6.2.3 Salt-Water Intrusion

Consider a well located above the fresh-salt interface in a coastal aquifer like that shown in figure 9.23. By the Ghyben-Herzberg principle (box 9.5), the elevation of the interface will increase by 40 m for every 1 m in drawdown caused by pumping. Thus if the drawdown at the well approaches 1/40th of the vertical distance between the bottom of the well and the interface, the well is likely to pump salt water.

To the extent that the idealized conditions assumed in deriving them are not satisfied, equations (9.57)–(9.59) will not exactly predict the drawdown in a coastal aquifer. This may occur when the aquifer is not quasi-infinite, the well is not fully penetrating, or the interface between fresh and salt water is not sharp. Modified versions of those equations are available to account for these complicating conditions (Freeze and Cherry 1979).

9.6.3 “Safe Yield”

It is widely believed, even by many hydrologists and water-resource managers, that the sustainable rate of extraction—or “safe yield”—of ground water

from a basin equals the rate of natural recharge, R_{nat} . It should be clear from the preceding discussion that this is not true: Equation (9.62) shows that the rate of extraction is supplied by a decrease in storage and, in general, by changes in recharge and/or discharge. R_{nat} itself does not enter into that equation, and in fact is relevant to the determination of safe yield only to the extent that it should be accounted for in ground-water models (Bredehoeft et al. 1982; Bredehoeft 1997, 2002; Zhou 2009). Instead,

Safe yield (or sustainable yield) is best defined as the rate at which ground water can be withdrawn without producing undesirable effects (Lohman 1979).

The preceding discussion has identified the most important hydrologic impacts of ground-water extraction, and most of these have potentially undesirable effects:

- Reductions of streamflow may seriously reduce surface water available for instream (e.g., wildlife habitat, waste dilution, hydropower, recreation, navigation) and withdrawal (water supply, irrigation) uses.
- Levels and/or extents of lakes and wetlands may be reduced, with consequent loss of valued habitat and recreational value.

- Extent of areas where water is available to plants that exploit the capillary fringe (phreatophytes) may be reduced, with consequent loss of habitat.
- Ground-water outflow to the ocean may be reduced, with consequent effect on coastal wetlands and/or nearshore benthic marine habitats.
- Lowered water table may cause land subsidence as some of the overburden stresses formerly supported by ground water are transferred to the mineral grains (box 9.2). Land subsidence of up to 9 m has occurred due to extraction of ground water for irrigation in the Central Valley of California.
- Costs of pumping, which are proportional to depth of water table, rise.
- Water tables lowered by one developer may fall below depths of nearby wells belonging to others, perhaps resulting in legal action.

- The fresh-salt interface may be raised, increasing the likelihood of salt-water intrusion.

Because of the varying importance of all these hydrologic effects and their economic, social, environmental, and legal consequences in different regions, and within a given region, there is no general formula for computing “safe yield.” Acceptable rates of development can only be determined by: (1) determining the likely hydrologic effects of various combinations of rates, timing, and location of ground-water extraction, which requires ground-water modeling; (2) assessing the environmental, economic, legal, and social impacts of these effects; and (3) balancing the benefits afforded by the ground water against the undesirable consequences of the various schemes.

▼ EXERCISES

- Given the following measurements at individual piezometers, calculate (a) the hydraulic head, (b) the pressure head, (c) the elevation head, and (d) the pressure:

Piezometer→	A	B	C	D	E
Ground surface elevation (m)	450	100	320	65	210
Piezometer depth (m)	150	100	80	120	20
Depth to water surface (m)	27	65	55	40	10

- Piezometers A, B, and C are located 1,000 m apart in a horizontal aquifer. A is due south of B, and C is due east of a line between A and B. Given the data in the table below, determine (a) the direction of ground-water through the triangle ABC and (b) the hydraulic gradient.

Piezometer→	A	B	C
Ground surface elevation (m)	95	110	135
Depth to water surface (m)	5	30	35

- A horizontal aquifer with a thickness of 45 m is subjected to pumping that lowers the pressure head by 25 m. Assuming an aquifer compressibility of $\alpha = 1.8 \times 10^{-8} \text{ m}^2/\text{N}$, how much does the aquifer compact?
- Obtain information about the general geology and ground-water environment of your region. For the United States, information can be accessed at <http://water.usgs.gov/ogw/gwrp/activities/regional.html>. Write a brief report summarizing the general geology and regional ground-water flow, including:
 - Typical values of ground-water residence times [equation (9.14)].
 - Which of the fundamental hydrologic landscape units (FHLUs) shown in figure 9.15 most closely applies to your region?
 - Likely typical values of the water-table ratio (*WTR*) [equation (9.16)].
 - The implication of regional *WTR* values for computation of watershed water budgets.

5. Which of the stream types shown in figure 9.17 characterizes streams in your region? Are different types associated with streams of different sizes?
6. a. To what extent do streams in your area seem to conform to the Dupuit approximation (box 9.4)?
 - b. Locate a stream-gauging station in your region and obtain annual flow data with which to estimate long-term average discharge, Q . In the United States, gauging stations can be located via the USGS website (<http://www.usgs.gov/water>) and average discharge data can be directly obtained through the WaterWatch website (<http://waterwatch.usgs.gov>) by clicking on “Toolkit,” followed by entering the name or number of the stream-gauging station of interest. Estimate the proportion of streamflow from ground water, Q_{GW}/Q , via equation (9.18), using topographic maps or Google Earth to estimate a regional value of interstream spacing X and stream length L for the selected gauge.
7. It is often stated that riparian wetlands reduce downstream flooding by acting as “sponges” that absorb flood water from upstream. Evaluate that belief based on the discussion in section 9.3.2.
8. Compute the base-flow index (BFI) for one year for a USGS stream gauge as specified by your instructor, following the instructions in box 9.8 to download the data and compute the BFI in a spreadsheet. (Ideally, different students could compute values for different streams for the same year and compare BFI values.)
9. A series of observation wells (piezometers) are installed in a straight line at varying distances from the edge of a small reservoir in Durham, New Hampshire. The table below gives the distances from the reservoir, the heights of the top of the well casing (TOC) above the ground surface, the ground-surface elevations, and the depth to water table from TOC as measured in October 2000 and October 2001.

Location →	Reservoir	Well 1	Well 2	Well 3	Well 4	Well 5
Distance from reservoir (m)	—	4.79	32.62	53.87	75.03	105.88
Ground elevation (m.a.s.l.)	24.16	25.35	26.18	26.28	26.23	27.98
TOC elevation (m.a.s.l.)		25.95	26.82	27.08	26.93	29.20
Depth to water table from TOC (m) in 2000	0.87*	0.88	1.38	1.38	1.11	2.76
Depth to water table from TOC (m) in 2001	0.38*	1.40	2.27	2.51	2.35	4.49

*Depth of water above point of ground-elevation measurement at edge of reservoir.

- a. Calculate the water-table elevations at each well and the reservoir water-surface elevations for the two years.
- b. Graph the ground and water-table elevations along the profile for the two years. Use an appropriate degree of vertical exaggeration. Show the locations of all measurements and the calculated elevations.
- c. Write a paragraph summarizing your observations. Is the relation of ground water to surface water typical of humid regions?
10. Outer Cape Cod at Eastham, Massachusetts, is a 4,800-m wide north/south-trending peninsula consisting of glacially deposited sands and gravels. Ground water discharges into the Atlantic Ocean to the east and Cape Cod Bay to the west. Recharge from precipitation = 0.46 m/yr; the aquifer specific yield is 0.15 and hydraulic conductivity is 75 m/day.
 - a. Calculate and graph the water-table profile and depth to salt-water/fresh-water interface from the center of the peninsula to either coast, accounting for the outflow face.
 - b. Calculate the width of the outflow face.
 - c. Calculate the discharge per length of coastline through the outflow face.
11. Figure 9.32 shows a portion of a flow net adjacent to one-half a symmetrical stream. Assume that the flow net is spatially and temporally representative of a reach of length L = 1,500 m, that the aquifer is homogeneous and isotropic with a hydraulic conductivity K_h =

- 10^{-5} m/s, and that the equipotentials are drawn at $\Delta h = 1$ m intervals. What is the ground-water contribution to streamflow Q_{GW} for this reach?
12. Construct a spreadsheet program to explore the effects of various degrees of relative uncertainty in estimates of precipitation and evapotranspiration on the G terms estimated in the example in box 9.9 (see section 1.11.2). Typical 95% confidence levels for relative errors are 5% for streamflow and 10% for precipitation and evapotranspiration. Does your analysis tend to confirm or cast doubt on the hypothesis that deep seepage is important in this region?
 13. Find a drainage basin in your region in which an analysis like that of box 9.9 can be done. Carry out the analysis and test for the effects of uncertainty on your estimates of deep seepage.
 14. Using the WellFunc.xls spreadsheet on the disk accompanying the text, compute the drawdown for a well pumping 3,000 m³/day for distances up to 3 km and times up to 10 yr from an aquifer with a hydraulic conductivity of $K_h = 30.5$ m/day and a specific yield of $S_y = 0.15$.
 15. Use the spreadsheet program WellFunc.xls to compute drawdowns as a function of distance and time for an aquifer typical of your region. How well do the assumptions involved in deriving the well function apply for this case?
 16. Use WellFunc.xls to explore the effects of varying at least two of the variables Q_w , K_h , S_y , and h_0 on drawdown for a typical aquifer in your region and write a paragraph describing your results.
 17. What are the most important potential adverse impacts of ground-water development in your region? Is there evidence that any of these impacts have occurred? What studies would you recommend for determining safe yield in your region?

▼ NOTES

¹ Ground-water hydrologists often distinguish between the **primary porosity**, which is the original intergranular porosity of a soil or sedimentary deposit, and the **secondary porosity**, which is due to void spaces developed subsequently by fracturing and/or dissolution.

² The effect of pumping on the ground-water balance is considered in the last section of this chapter.

³ As described in sections 7.4.1 and 8.1.4, this water movement occurs in response to pressure gradients created by evapotranspiration that reduces the liquid water content in the vadose zone. Capillary rise can be a significant portion of basin evapotranspiration in many semiarid and arid regions where a class of vascular plants called **phreatophytes** grows near streams and obtains water via roots that extend to the capillary fringe. Saltcedar, arrowweed, cottonwood, cattails, and willows are common phreatophytes.



10

Runoff Generation and Streamflow

Streams are the routes by which almost all the **runoff** on the continents (i.e., the portion of precipitation not ultimately evaporated or transpired) is returned to the oceans to complete the global hydrologic cycle (tables 2.5, 2.6; figure 2.20).¹ There are three principal scientific and practical motivations for understanding the processes by which rainfall and snowmelt travel to streams:

1. **Water Resources.** The flow in streams constitutes the sustainable water resource available for human use and management (section 1.8.1) and for stream organisms. (Note that this includes the ground-water resource, because virtually all ground water discharges to surface-water bodies.)
2. **Flood Prediction and Forecasting.** **Flood predictions** are estimates of the *probabilities* of floods of various magnitudes; they are the basis for the design of bridges, dams, and levees and the formulation of floodplain land-use plans and regulations. **Flood forecasts** are estimates of the *actual magnitudes* of flooding produced by a rain or snowmelt event that is occurring or is forecast to occur; these are used to guide the operation of reservoir systems and to provide flood warnings to floodplain occupants.

3. **Water Quality.** Water quality (temperature, inorganic and organic dissolved constituents, and particulate material), which affects the suitability of water for use by humans and natural organisms, is strongly influenced by physical processes and chemical and biological reactions that occur as water moves over and through the land surface toward streams.

The principal focuses of this chapter are: (1) a review of the watershed concept and a description of stream networks; (2) a conceptual overview of the essential characteristics of stream responses to water inputs; (3) a survey of the processes and routes by which water enters streams and moves through the watershed stream network in response to rain and snowmelt events; and (4) an introduction to some commonly used approaches to forecasting and predicting stream responses (“rainfall-runoff modeling”).

10.1 The Watershed and the Stream Network

10.1.1 The Watershed

As defined in section 1.7, a **watershed** (also called drainage basin, river basin, or catchment) is

the area that topographically appears to contribute all the water that passes through a specified cross section of a stream (the **watershed outlet**; figure 1.10). The surface trace of the boundary that delimits a watershed is called a **divide**. The horizontal projection of the area of a watershed is called the **drainage area** of the stream at (or above) the outlet.

At least most of the water passing through the stream cross section at the watershed outlet originates as precipitation on the watershed. Thus

Watershed geology, soils, topography, and land cover determine the magnitude, timing, and quality of water entering the stream network and of the streamflow leaving the watershed.²

10.1.2 The Stream Network

10.1.2.1 Stream Orders and the “Laws” of Network Composition

Within any watershed larger than a minimum size (which is a function of geology, soils, topography, and climate), drainage of excess precipitation occurs via a hierarchical **stream network**. Figure 10.1 shows the most common approach to quantitatively describing stream networks (Strahler 1952): Streams with no tributaries are designated **first-order streams**; the confluence of two first-order streams is the beginning of a **second-order stream**; the confluence of two second-order streams produces a **third-order stream**, etc. When a stream of a given order receives a tributary of a lower order, its order does not change. The **watershed order** is the order of the stream at the watershed outlet. The actual size of the streams designated a particular order depends on the scale of the map or image used and the conventions used in defining stream channels (perennial, intermittent, ephemeral; section 9.3.1.2). A scale of about 1:25,000 is common; at that scale the Mississippi River is a twelfth-order stream at its mouth (Leopold et al. 1964).

Within a given watershed, the numbers, N_ω , average lengths, L_ω , and average drainage areas, A_ω , of streams of successive orders ω can usually be closely described by relations of the form

$$N_\omega = K_N \cdot \exp(-k_N \cdot \omega), \quad (10.1)$$

$$L_\omega = K_L \cdot \exp(k_L \cdot \omega), \quad (10.2)$$

$$A_\omega = K_A \cdot \exp(k_A \cdot \omega), \quad (10.3)$$

where K_N , K_L , K_A , k_N , k_L , and k_A are fitting parameters that vary regionally (figure 10.2). The **bifurcation ratio**, R_B , the **length ratio**, R_L , and the **area ratio**, R_A , are defined in table 10.1, and the water-

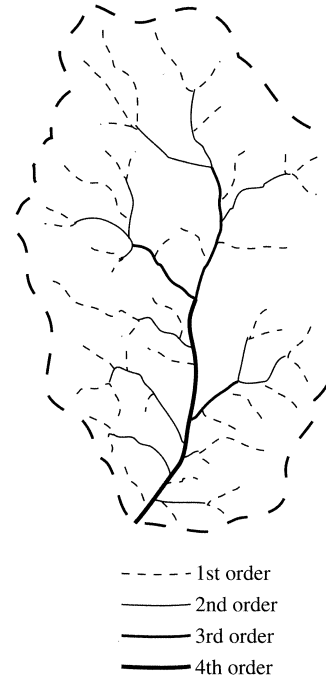


Figure 10.1 Strahler (1952) system of designating stream orders.

Table 10.1 The Laws of Drainage-Network Composition.

Law	Relation	Usual Range	Source
Law of stream numbers	$R_B \equiv \frac{N_\omega}{N_{\omega+1}}$	$3 < R_B < 5$	Horton (1945)
Law of stream lengths	$R_L \equiv \frac{L_{\omega+1}}{L_\omega}$	$1.5 < R_L < 3.5$	Horton (1945)
Law of drainage areas	$R_A \equiv \frac{A_{\omega+1}}{A_\omega}$	$3 < R_A < 6$	Schumm (1956)

R_B ≡ bifurcation ratio

R_L ≡ length ratio

R_A ≡ drainage-area ratio

N_ω ≡ number of streams of order ω

L_ω ≡ average length of streams of order ω

A_ω ≡ average drainage area of streams of order ω

order: $\omega = 1, 2, 3, \dots, \Omega$.

shed average values of these ratios are related to the parameters of equations (10.1)–(10.3) as

$$R_B = \exp(k_N), \quad (10.4)$$

$$R_L = \exp(k_L), \quad (10.5)$$

$$R_A = \exp(k_A). \quad (10.6)$$

The values of these ratios are usually constrained within fairly narrow ranges, as summarized in table 10.1; these typical ranges are called the “**laws**” of **drainage-network composition**.

The physical processes that produce stream networks are complex and operate at a range of spatial and temporal scales. Thus the development of net-

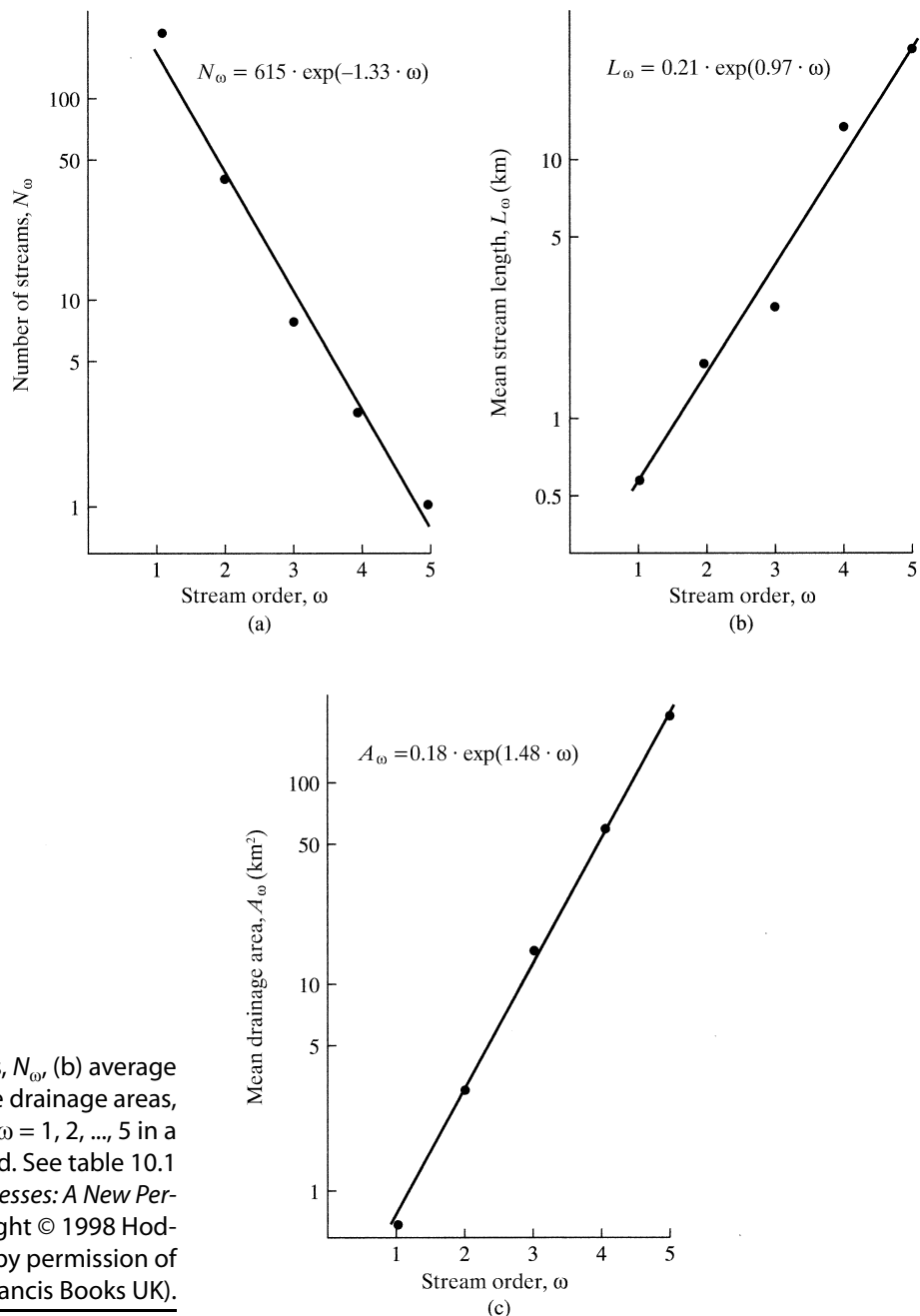


Figure 10.2 (a) Numbers, N_ω , (b) average lengths, L_ω , and (c) average drainage areas, A_ω , of streams of order $\omega = 1, 2, \dots, 5$ in a drainage basin in England. See table 10.1 (from *Fluvial Forms and Processes: A New Perspective*, D. Knighton, copyright © 1998 Hodder Arnold, reproduced by permission of Taylor & Francis Books UK).

works that lead to equations (10.1)–(10.3) can be modeled as a random process (Leopold 1994; Knighton 1998), and the values of the ratios summarized in table 10.1 are not physical laws, but typical ranges of statistical averages.

10.1.2.2 Links, Nodes, and Network Magnitude

A stream network can also be quantitatively described by designating the junctions of streams as **nodes** and the channel segments between nodes as **links**. Links connecting to only one node (i.e., first-order streams) are called **exterior links**, the others are **interior links**. The **magnitude** of a stream network is the total number of exterior links (= first-order streams) it contains; thus the network of figure 10.1 is of magnitude 43. Typically the number of links of a given order is about one-half the number for the next lowest order (Kirkby 1993).

10.1.3 Drainage Density

The **drainage density**, D , of an area, A , is the total length of streams draining that area, ΣL , divided by the area:

$$D \equiv \frac{\Sigma L}{A}. \quad (10.7)$$

Drainage density thus has dimensions [L^{-1}].

Drainage density is usually measured on maps or aerial photographs, and this can now be done relatively easily using digitizers or geographic information systems (GIS). Sellmann and Dingman (1970) showed that drainage density can also be readily measured by constructing a number of straight lines over the region of interest and counting the number of times the lines cross streams. Then

$$D = \frac{\pi}{2} \cdot \frac{N_x}{\Sigma L_x}, \quad (10.8)$$

where N_x is the total number of crossings, and ΣL_x is the total length of lines.

The value of D for a given region will increase as the scale of the map on which measurements are made increases. Sellmann and Dingman (1970) found that drainage densities measured on standard USGS topographic maps at a scale of 1:24,000 were close to true values observed in the field.

Channel networks form by erosion initiated where surface water accumulates, which is a function of both precipitation, climate, surface permeability, and soil erodibility. Thus drainage density tends to be low in arid regions, but also in humid ar-

eas, where vegetation tends to increase surface permeability and reduce erodibility; the largest values occur in semiarid regions. In a given climate, drainage density is higher on less permeable soils. Drainage density values ranging from less than 2 km^{-1} to over 100 km^{-1} have been reported, and an area of similar geology in a given climatic region tends to have a characteristic value.

10.1.4 Relations between Network Properties and Stream Response

Stream-network characteristics provide information about the relative importance of hillslope and channel processes in determining the response of a given watershed to rainfall. It can be shown from straightforward geometry that the average spacing of streams, X , is

$$X \approx \frac{1}{D}. \quad (10.9)$$

Therefore the divide-to-stream distance (i.e., the average hillslope length) is approximately $1/(2 \cdot D)$ and the average distance that a drop of water travels to a stream is about $1/(4 \cdot D)$. Thus drainage density is an indicator of the efficiency of a stream network in draining an area, especially if its definition is modified to eliminate the effects of stream sinuosity:

$$D_{eff} \equiv \frac{\Sigma L_v}{A}, \quad (10.10)$$

where ΣL_v is the total length of stream *valleys* and D_{eff} is called the **effective drainage density** (Dingman 1978).

As we will see in this chapter, water travels to streams at widely varying rates by various surface and subsurface routes, and many factors other than distance affect drainage efficiency. Thus although many studies have attempted to use drainage density as a predictor of hydrologic characteristics, such as the magnitudes of flood flows or low flows, these relations have limited regional application (Dingman 1978; Harlin 1984).

The **network width** is the number of links as a function of distance upstream from the basin outlet. For watersheds in which the time of travel in the stream network dominates over that in the hillslopes (typically watersheds with areas exceeding about 50 km^2), the shape of the network-width function is related to the time between the occurrence of water input and the occurrence of the peak of the response hydrograph at the watershed outlet: The closer the maximum in the width

function is to the watershed outlet, the shorter the time between input and peak response (Kirkby 1976).

The values of the bifurcation, length, and drainage-area ratios can be used to calculate some hydrologically important characteristics of watersheds. Rodriguez-Iturbe and Valdes (1979) derived formulas relating R_B , R_A , and R_L to (1) the fraction of a watershed draining directly to streams of a given order and (2) the fraction of streams of any order that are tributary directly to streams of any higher order. They also showed that those ratios can be used to predict the characteristic response of a watershed to rainfall inputs (section 10.6.4.3.5).

10.2 General Characteristics of Stream Response

10.2.1 Basic Features

Figure 10.3 shows possible flow paths in a small upland watershed during a rain or snowmelt event. Inputs [L] during a time period are measured at one or more points and spatially averaged (section 4.3); a

graph (usually a histogram) of water input versus time is called a **hyetograph** (P_i , where $i = 1, 2, \dots, n$ is the time-period indicator). Watershed response to the event (output) is characterized by measuring the stream discharge $q(t)$ (the volume rate of flow [$L^3 T^{-1}$]) at a single “point” in the stream network—i.e., a stream cross section whose location is the watershed outlet (section 1.7). A continuous graph of stream discharge versus time is a **streamflow hydrograph**; for direct comparison with the input, discharge may be divided by watershed area and expressed as [$L T^{-1}$].

The hydrograph of a stream responding to an isolated period of rain or snowmelt of significant magnitude and areal extent usually has the characteristic form shown in figure 10.4a: At some time after the beginning of the event the flow rate begins to increase relatively rapidly from the preevent rate to a well-defined **peak discharge**; this period is called the **hydrograph rise**. Following the peak, flow declines more slowly to a rate near its preevent value; this is the **hydrograph recession**. The streamflow hydrograph is the trace of a **flood wave**³ passing a point in the stream network. In general, the magnitude and

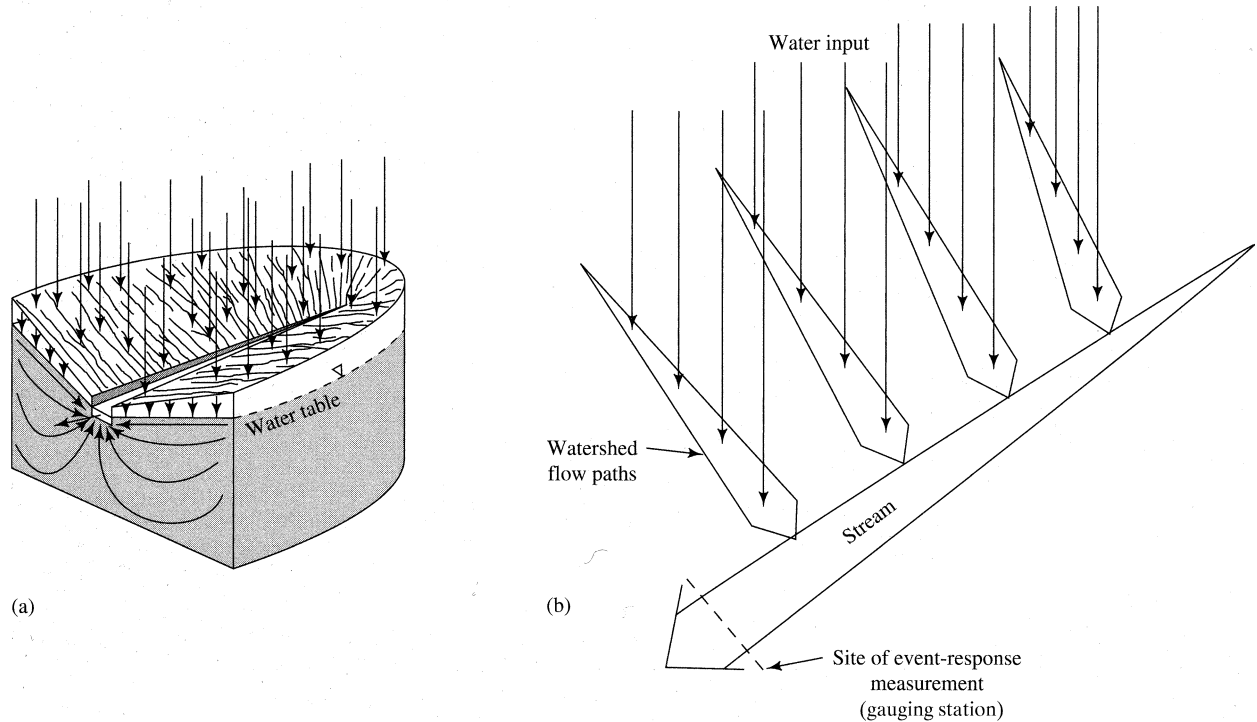


Figure 10.3 (a) Schematic flow paths in a small upland watershed receiving water input. (b) The essence of watershed response as the space- and time-integrated result of flow with lateral inflows.

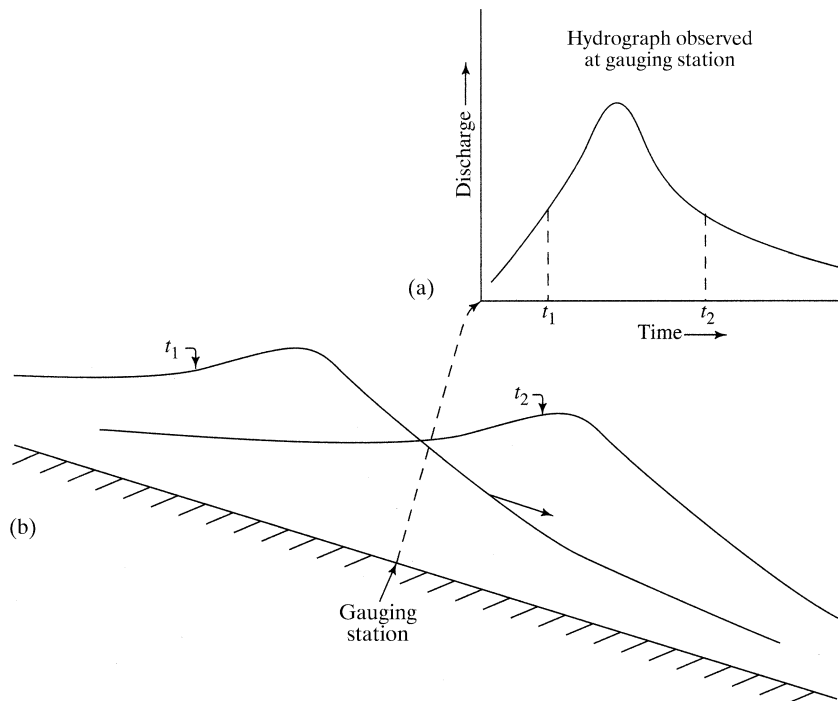


Figure 10.4 (a) Example of a hydrograph. (b) A storm hydrograph is the time trace made by an observer at a fixed point of a flood wave moving downstream.

shape of the flood wave changes as it moves through the network due to additional inputs, hydraulic effects induced by the channel configuration, and bank and floodplain storage (section 10.5).

Figure 10.3 shows that streamflow is a spatially and temporally integrated response determined by: (1) the spatially and temporally varying input rates; (2) the time required for each drop of water to travel from where it strikes the watershed surface to the stream network (determined by the length, slope, vegetative cover, soils, and geology of the watershed hillslopes); and (3) the time required for water to travel from its entrance into the channel to the point of measurement (determined by the length and nature of the channel network).

In small watersheds (less than about 50 km^2 area), the travel time to the watershed outlet is typically determined mostly by the hillslope travel time; for larger watersheds the travel time in the stream network becomes increasingly important (Kirkby 1993).

Once the flood wave leaves the portion of the stream network that has been affected by a given input

event, its shape is determined by channel characteristics (geometry, slope, bed and bank material), tributary inputs, and exchanges of water with the banks and the floodplain.

Figure 10.5 shows a typical example of how the effects of hillslope-response mechanisms are gradually modified by the effects of spatial and temporal integration and channel hydraulics through a stream network. The hydrograph shape for the smallest watershed (figure 10.5b) is strongly influenced by the form of the hydrograph (figure 10.5a). Subsequently, the hydrograph is increasingly affected by tributary inputs and by the storage effects of the watershed and stream channels, and the net result is an increase in the lag time between the rainfall inputs and the peaks and a decrease in hydrograph ordinates (when scaled by drainage area). The hydrograph also becomes smoother, and at the lowest two gauges the formerly multiple-peaked hydrograph has become single-peaked.

In attempting to analyze and model these event-response processes, it is important to keep the following points in mind.

On the hillslopes:

- Water moves in an infinite number of surface and/or subsurface flow paths of varying length and character.

- During the water-input event, each flow path is an accumulation of **lateral inflows** of precipitation and/or snowmelt that vary in space and time (figure 10.3b).
- Flow in each path can in principle be described by invoking the conservation of mass and an equation of motion appropriate to the mode of flow. The principles of unsaturated and saturated subsurface flow were discussed in chapter 7; the principles of surface overland flow are discussed in section 10.4.2.

In the stream network:

- During the event, and while the land surface is draining, flow is an accumulation of temporally and spatially varying lateral inflows from the hillslope flow paths distributed along the channel length (figure 10.3b).
- Movement of water in the stream can be described by invoking the conservation of mass and the equation of motion for open-channel flow. These principles are introduced in section 10.5.

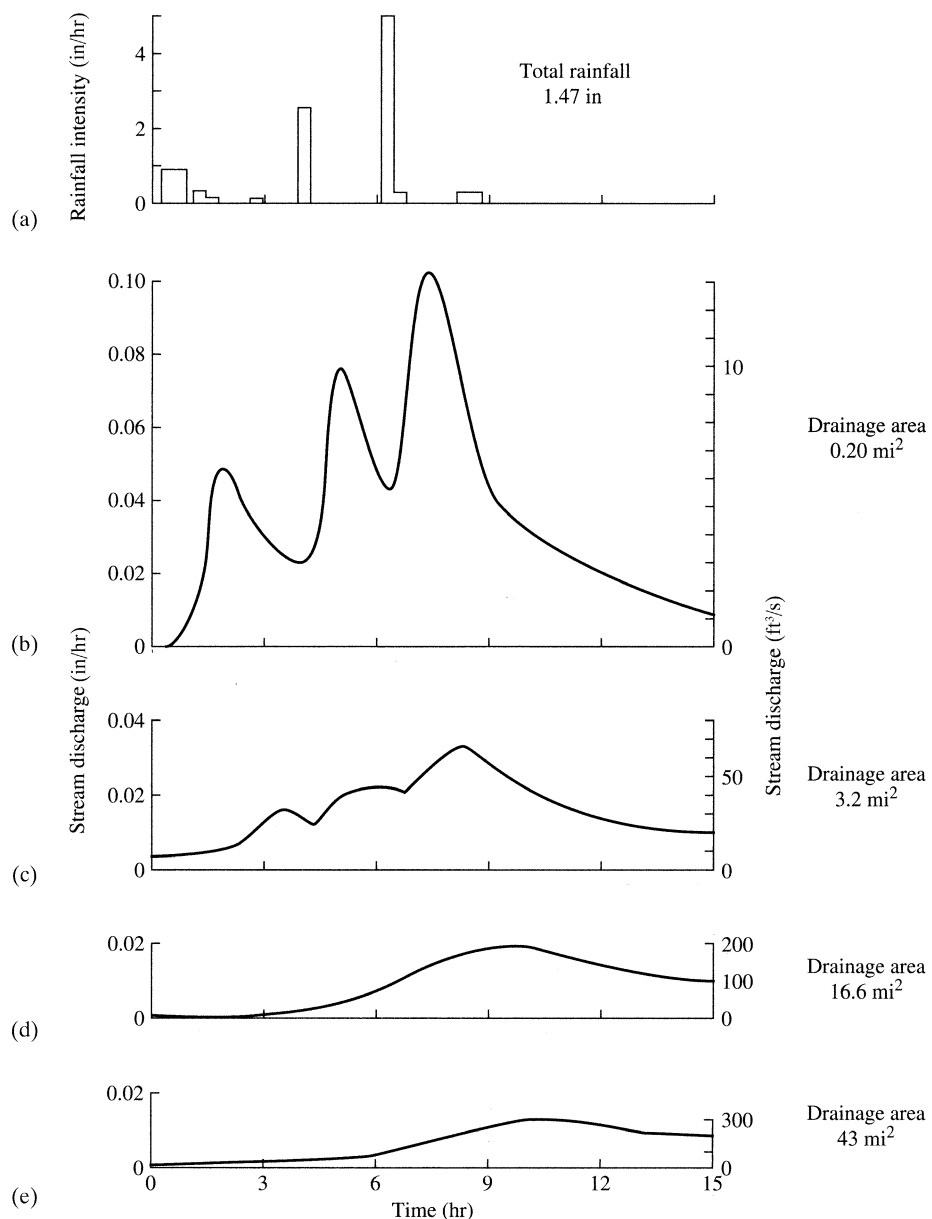


Figure 10.5 Changes in hydrograph shape at a series of gauging stations along the Sleepers River in Danville, Vermont, in response to an intense rainstorm [(a) is a hyetograph]. Note that the left-hand hydrograph ordinates show flow rates per unit drainage area, while right-hand ordinates show actual flow rates. 1 in = 25.4 mm; 1 mi² = 2.59 km². [Dunne and Leopold (1978)].

- Flow in the stream takes the form of a flood wave that moves downstream through the stream network (figure 10.4).
- The observed hydrograph records the movement of the flood wave past the stream-gauging station at the watershed outlet (figure 10.4).

In the overall watershed response:

- The volume of water appearing in the apparent response hydrograph for a given event is usually only a fraction (often a very small fraction) of the total input. The remainder of the water input ultimately leaves the watershed as: (1) evapotranspiration; (2) streamflow that occurs so long after the event that it cannot be associated with that event; or (3) ground-water outflow from the watershed.
- The water identified as the response to a given event may originate on only a fraction of the watershed; this fraction is called the **contributing area**.
- The extent of the contributing area may vary from event to event and during an event.
- At least some of the water identified as the response to a given event may be “old water” that entered the watershed in a previous event.

These points are elaborated in subsequent sections of this chapter.

10.2.2 Heuristic Hydrograph Separation

Box 10.1 summarizes the notation used in this chapter. Figure 10.6 shows the response of a small watershed to an isolated rainfall lasting about 15 hr. As in most humid-region streams, there is nonzero flow before the event and gradually declining flow

persisting long after the event and the obvious hydrograph response. Clearly some of the flow during the hydrograph rise must have entered the watershed in previous events, and some of the water that entered during the current event will flow out of the watershed well after the identifiable hydrograph response. In the context of analyzing stream responses to rain events,⁴ usually for the purpose of developing methods for predicting or forecasting floods, this raises a central question:

How do we identify the portion of stream response that is associated with a given event?

Note that this practical question is different from, but related to, the more scientific question, “What are the sources of streamflow and the routes by which water enters streams?” This latter question is addressed in sections 10.3 and 10.4.

Except in specialized research situations, the only data available on which to base the quantification of event flow are measurements of total rainfall and total streamflow. Since this streamflow includes water from the event of interest plus an indeterminate number of preceding events, the problem of identifying response to a particular event arises. This problem is the complement of the question of **base-flow separation**, used to identify probable ground-water contributions to streamflow discussed in section 9.5.3.6. To review:

- In the absence of other information, graphical techniques such as those discussed in box 9.8 and figure 9.34 are used to separate total streamflow into two components, base flow and event flow.

Box 10.1 Notation

In this chapter, we use the following notation:

- | | |
|-------|--|
| p | rate of water input (rain plus snowmelt) in a storm event [$L T^{-1}$] |
| p^* | rate of effective water input (\equiv water that appears as streamflow in response to a water-input event) [$L T^{-1}$] |
| P | total volume of water input in a storm event [L] or [L^3] |
| P^* | total volume of effective water input in a storm event [L] or [L^3] |

- | | |
|-------------|---|
| $q(t)$ | total streamflow rate as a continuous function of time [$L T^{-1}$] or [$L^3 T^{-1}$] |
| $q^*(t)$ | event-flow rate as a continuous function of time [$L T^{-1}$] or [$L^3 T^{-1}$] |
| $q_{BF}(t)$ | base-flow rate as a continuous function of time [$L T^{-1}$] or [$L^3 T^{-1}$] |
| Q | total volume of streamflow in a storm event [L^3] or [L] |
| Q^* | total volume of event flow in a storm event [L^3] or [L] |

- **Base flow** is the portion of streamflow that is presumed to have entered the watershed in previous events and to be derived from persistent, slowly varying sources. (Ground water is usually assumed to be the main, if not the only, such source.)
- **Event flow** (also called **direct runoff**, **storm runoff**, **quick flow**, or **storm flow**) is considered to be the direct response to a given water-input event.
- Total flow rate at any instant $q(t)$ is the sum of event-flow rate $q^*(t)$ and base-flow rate $q_{BF}(t)$:

$$q(t) = q^*(t) + q_{BF}(t). \quad (10.11)$$

- Graphical flow separation techniques are heuristic and have no direct scientific basis.

Graphical hydrograph separation must therefore be regarded as a “convenient fiction” that is invoked in order to analyze and model the ways in which event response is influenced by watershed characteristics and by the spatial and temporal variability of water input. However, there may be a reasonably constant (if unknown) relation between the true event flow and the event flow identified by a particular method on a particular watershed (see, for example, Bloomfield et al. 2009 and Norbiato et al. 2009); therefore,

In applying graphical flow separation in a given study, it is most important to use a consistent separation scheme.

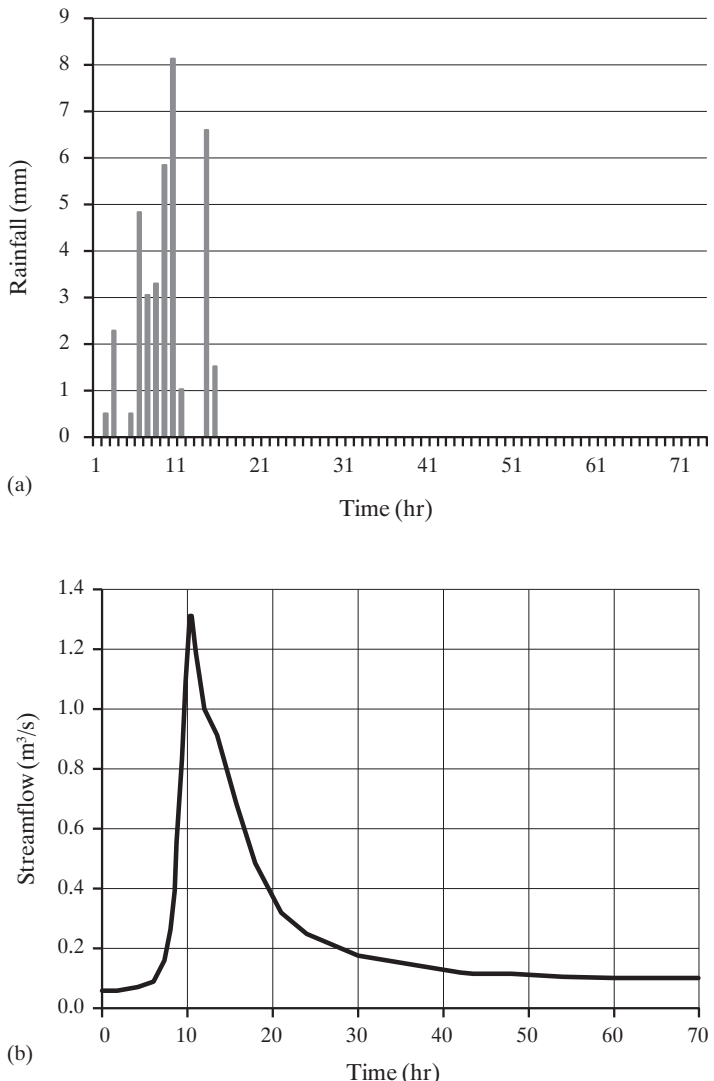


Figure 10.6 (a) Hyetograph and (b) hydrograph for an isolated storm on Watershed W-3, Sleepers River Research Watershed, Vermont, 18 September 1973.

However,

One must not fall into the trap of thinking that heuristic graphical separation actually identifies flow from different sources.

Box 10.2 and figure 10.7 (on p. 466) give an example of graphical flow separation. The remainder of this section gives examples of the spatial variability of the ratio of event-flow volume to precipitation (Q^*/P) and the temporal variability of that ratio at a given location, which are due to spatial and temporal variability in the mechanisms generating runoff. These mechanisms are discussed in sections 10.3 and 10.4.

Box 10.2 Example Graphical Flow Separation and Centroid Calculation

Flow Separation

Figure 10.7a shows the hydrograph of Watershed W-3 (drainage area = 8.37 km²) in the Sleepers River Research Watershed in northeastern Vermont in response to a rainstorm with a total area-averaged storm depth $P = 38$ mm on 18 September 1973. To find the volume of event flow, Q^* , we use the graphical separation method shown in figure 9.34c. For this method, the separation line (dashed line in figure 10.7a) slopes upward from the time of initial hydrograph rise at a rate of

$$(0.000547 \text{ m}^3/\text{s} \cdot \text{km}^2 \cdot \text{hr}) \times (8.37 \text{ km}^2) = 0.00457 \text{ m}^3/\text{s} \cdot \text{hr}$$

and is extended until it intersects the measured hydrograph at 29 hr (0500 on 19 September). Using a digitizer or planimeter, we measure the area between the total hydrograph and the separation line and find that this represents an event-flow volume of $Q^* = 31,200$ m³. Dividing by watershed area,

$$Q^* = \frac{31,200 \text{ m}^3}{8.37 \text{ km}^2} \times \frac{1 \text{ km}^2}{10^6 \text{ m}^2} = 0.00372 \text{ m} = 3.72 \text{ mm}.$$

Thus the ratio of event flow to total rainfall, Q^*/P , is 3.72 mm/38 mm = 0.098.

Centroid of Precipitation

The hyetograph for the rain storm recorded at Watershed W-3 of the Sleepers River Research Watershed, Vermont, on 18 September 1973 is shown in figure 10.6a and summarized in table 10B2.1.

Table 10B2.1

Clock time	0	1	2	3	4	5	6	7	8
P_i (mm)	0	0.5	2.3	0	0.5	4.8	3.1	3.3	
t_i (hr)	0.5	1.5	2.5	3.5	4.5	5.5	6.5	7.5	

Clock time	9	10	11	12	13	14	15	16
P_i (mm)	5.8	8.1	1.0	0	0	6.6	1.5	0
t_i (hr)	8.5	9.5	10.5	11.5	12.5	13.5	14.5	15.5

To calculate the centroid of effective precipitation via equation (10.13), we first need to estimate effective precipitation. Various approaches to this are described in section 10.6.3.2; for purposes of illustration we here apply a simple ad hoc method that results in $P^* \approx Q^*$:

If $P_i > 3$ mm, $P_i^* = 0.12 \cdot P_i$;

If $P_i \leq 3$ mm, $P_i^* = 0$.

Table 10B2.2 summarizes the P_i^* values and shows the calculation of the centroid of effective precipitation; these are plotted in figure 10.7b.

Table 10B2.2

Clock time	0	1	2	3	4	5	6	7	8
P_i^* (mm)	0	0.061	0.275	0	0.061	0.055	0.366	0.343	
t_i (hr)	0.5	1.5	2.5	3.5	4.5	5.5	6.5	7.5	
$P^* \cdot t_i$ (mm · hr)	0	0.092	0.687	0	0.275	0.304	2.379	2.574	
Clock time	8	9	10	11	12	13	14	15	16
P_i^* (mm)	0.419	0.976	0.122	0	0	0.792	0.182	0	
t_i (hr)	8.5	9.5	10.5	11.5	12.5	13.5	14.5	15.5	
$P^* \cdot t_i$ (mm · hr)	3.558	9.268	1.285	0	0	10.692	2.645	0	

The sums $\sum P_i^* = 3.65$ mm, $\sum P_i^* \cdot t_i = 33.8$ mm · hr. Then from equation (10.13),

$$t_{pc} = \frac{\sum_{i=1}^n P_i^* \cdot t_i}{\sum_{i=1}^n P_i^*} = \frac{33.8 \text{ mm} \cdot \text{hr}}{3.65 \text{ mm}} \approx 9.2 \text{ hr.}$$

Since $t_0 = 00:00$ clock time on 18 September, the centroid of effective rainfall for this storm occurred at $00:00 + 9.2$ hr = 09:12 clock time.

Centroid Lag-to-Peak

Figure 10.7c is a plot of the $q^*(t)$ hydrograph; its peak occurs at 10.5 hr. Thus the centroid lag-to-peak for this storm is $10.5 \text{ hr} - 9.2 \text{ hr} = 1.3 \text{ hr}$.

10.2.3 Event-Flow Volume

10.2.3.1 Spatial Variability

The results of the example of figure 10.7 and box 10.2 are quite typical for most regions: The ratio Q^*/P for individual events is usually considerably less than 0.5 and commonly less than 0.1. Woodruff and Hewlett (1970) investigated the long-term-average values of Q^*/P for a large sample of small to moderate-sized watersheds in the southeastern United States (where snow is negligible). As in box 10.2, they used the method of figure 9.34c to identify event-flow volumes. Their results, summarized in figure 10.8 on p. 467, reinforce the conclusion that the amount of water involved in event response is a small fraction of inputs, and illustrate that average values of Q^*/P are highly variable in space. Colonell and Higgins (1973) found similar ratios in New England.

Woodruff and Hewlett's (1970) results can also be used to show that for the region they studied, the ratio of event flow to total runoff, Q^*/Q , is considerably less than 0.5 (figure 10.9 on p. 468). This sug-

gests that more than half of streamflow typically travels to streams via delayed routes as base flow, presumably in large part as regional ground-water flow.

One implication of these results is that forecasts and predictions of runoff response are very sensitive to estimates of total event flow—a small error in estimating Q^*/P could lead to a large relative error in the predicted runoff peak and volume.

10.2.3.2 Temporal Variability

Figure 10.10 on p. 468 shows Q^* as a function of P for 16 rainstorms during four summers on a research watershed in central Alaska. (The separation in this case was done using the method of figure 9.34b.) For this period the Q^*/P ratio varied over an order of magnitude, from 0.03 to 0.42; Dingman (1973) showed that the ratio for a given storm was positively related to the amount of rain received in previous storms—i.e., the watershed wetness.

An even more striking example of the range of variability of Q^*/P for a given watershed is shown in figure 10.11 on p. 469. Figure 10.11a is the response

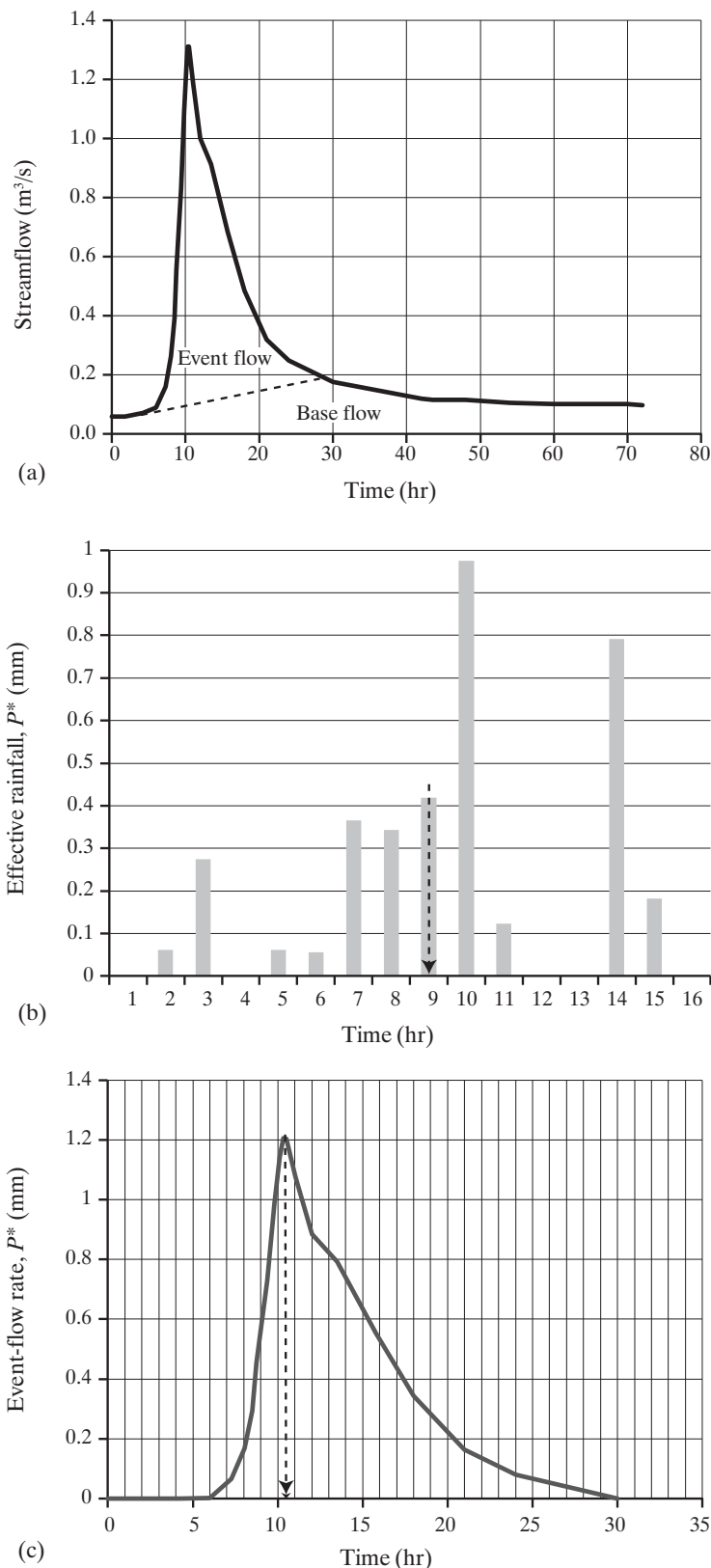


Figure 10.7 Event flow and effective rainfall of Watershed W-3 (drainage area = 8.37 km^2) in the Sleepers River Research Watershed in northeastern Vermont in response to a rainstorm with a total area-averaged storm depth $P = 38 \text{ mm}$ on 18 September 1973. See box 10.2. (a) Hydrograph showing base-flow separation. (b) Hyetograph of effective rainfall; arrow shows centroid. (c) Hydrograph of event flow; arrow shows centroid.

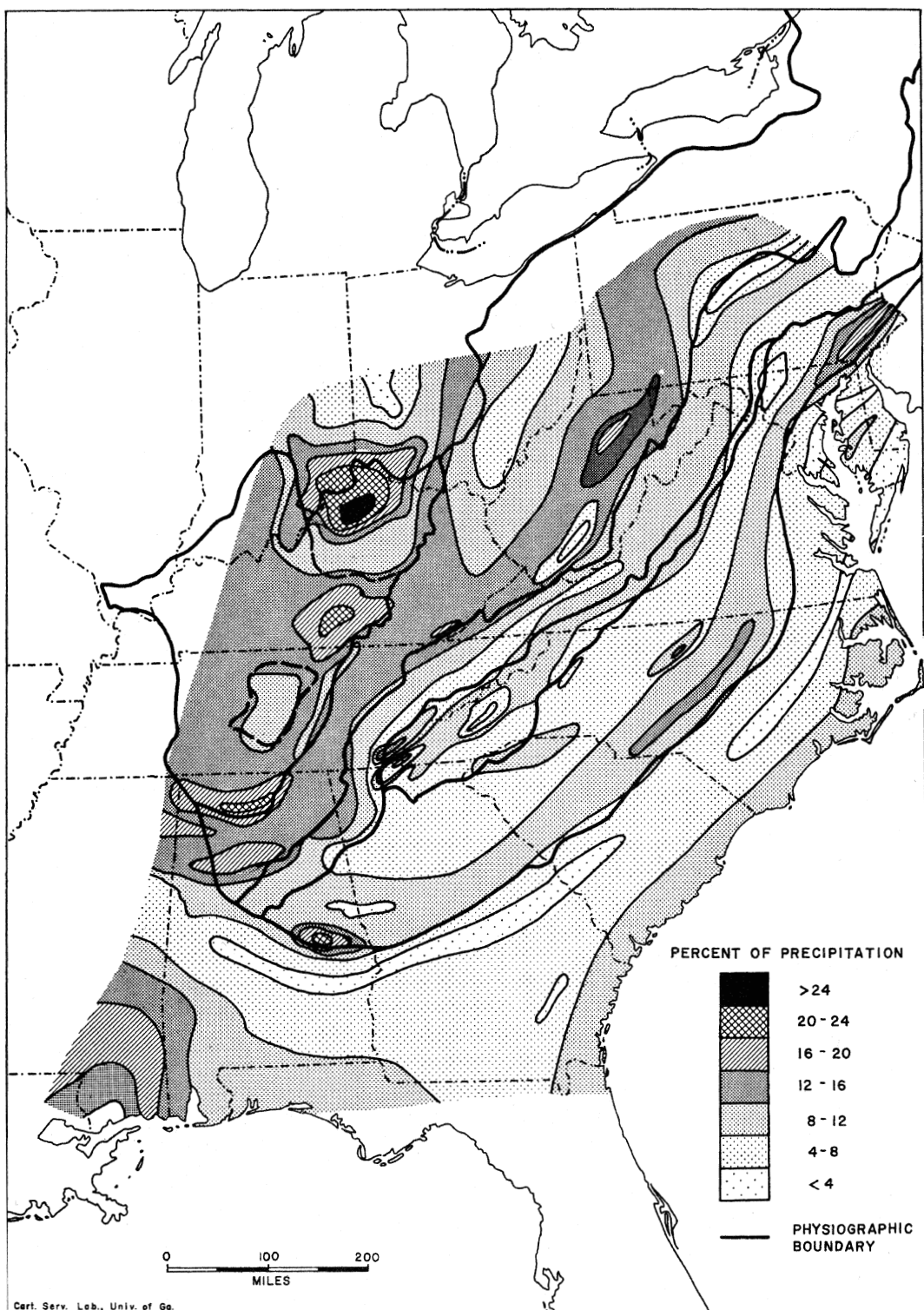


Figure 10.8 Spatial distribution of average annual event-flow volume for watersheds less than 200 mi² (500 km²) in area in the southeastern United States expressed as a ratio to average annual precipitation. [Woodruff and Hewlett (1970). Predicting and mapping the average hydrologic response for the eastern United States. *Water Resources Research* 6:1312–1326, with permission of the American Geophysical Union].

of this watershed to an isolated storm in August 1963, a very wet summer in northern Alaska; $Q^*/P = 0.63$. In the very dry summer of 1965, a storm of similar intensity and total volume resulted in the hydrograph of figure 10.11b, in which $Q^*/P = 0.01$ —less than 1/50th of the earlier value!

A high degree of temporal variability in Q^*/P in a single watershed is common in most regions, and

the implication of these results is that watershed wetness, or **antecedent condition**, has a major influence on the ratio. The physical processes that produce this relation will be discussed in section 10.4. Clearly, failure to account for time-varying watershed conditions may result in significant forecasting or prediction errors. Interestingly, it may be less important to account for temporal variability if one restricts con-

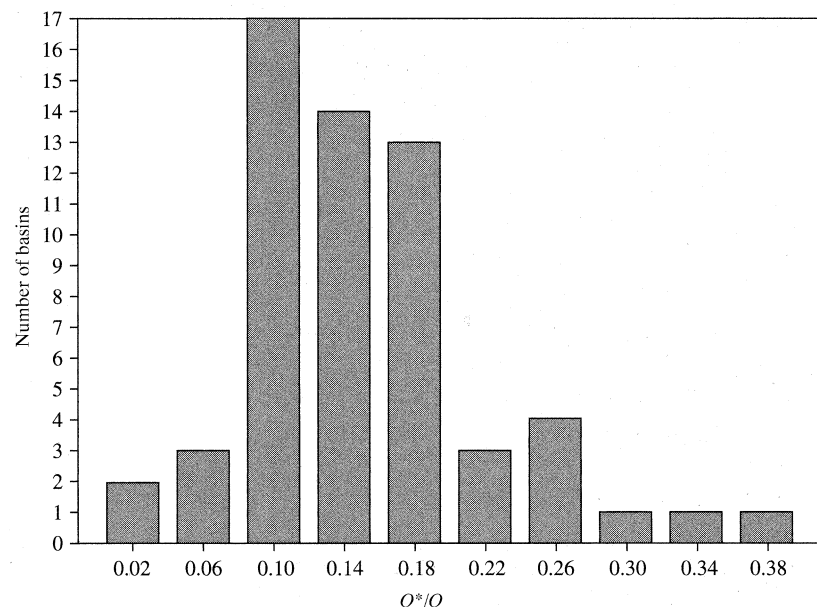


Figure 10.9 Frequency distribution of average annual Q^*/Q for 59 watersheds in the southeastern United States. Q^* data from Woodruff and Hewlett (1970).

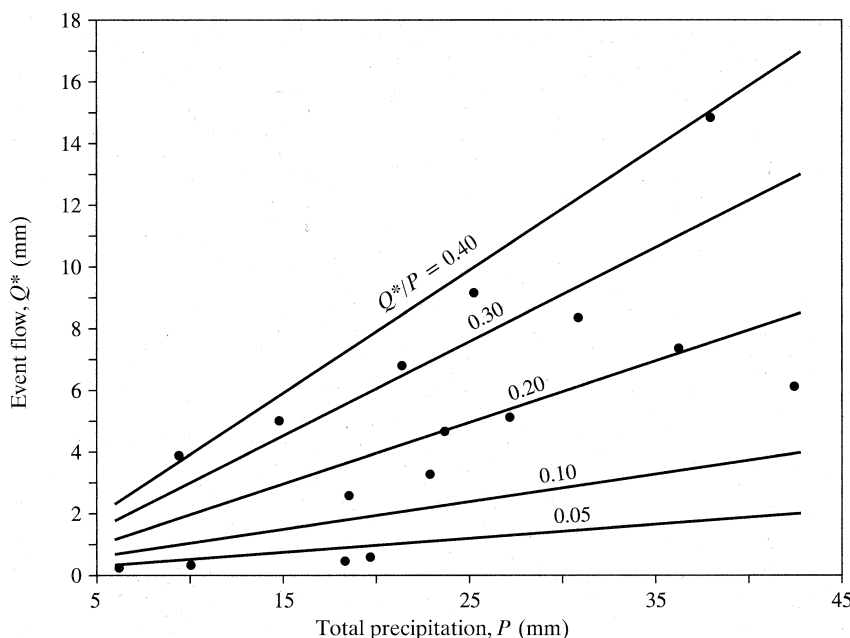


Figure 10.10 Event flow, Q^* , versus total precipitation, P , for 16 summer rainstorms on a 1.8- km^2 watershed in central Alaska [data from Dingman (1970)].

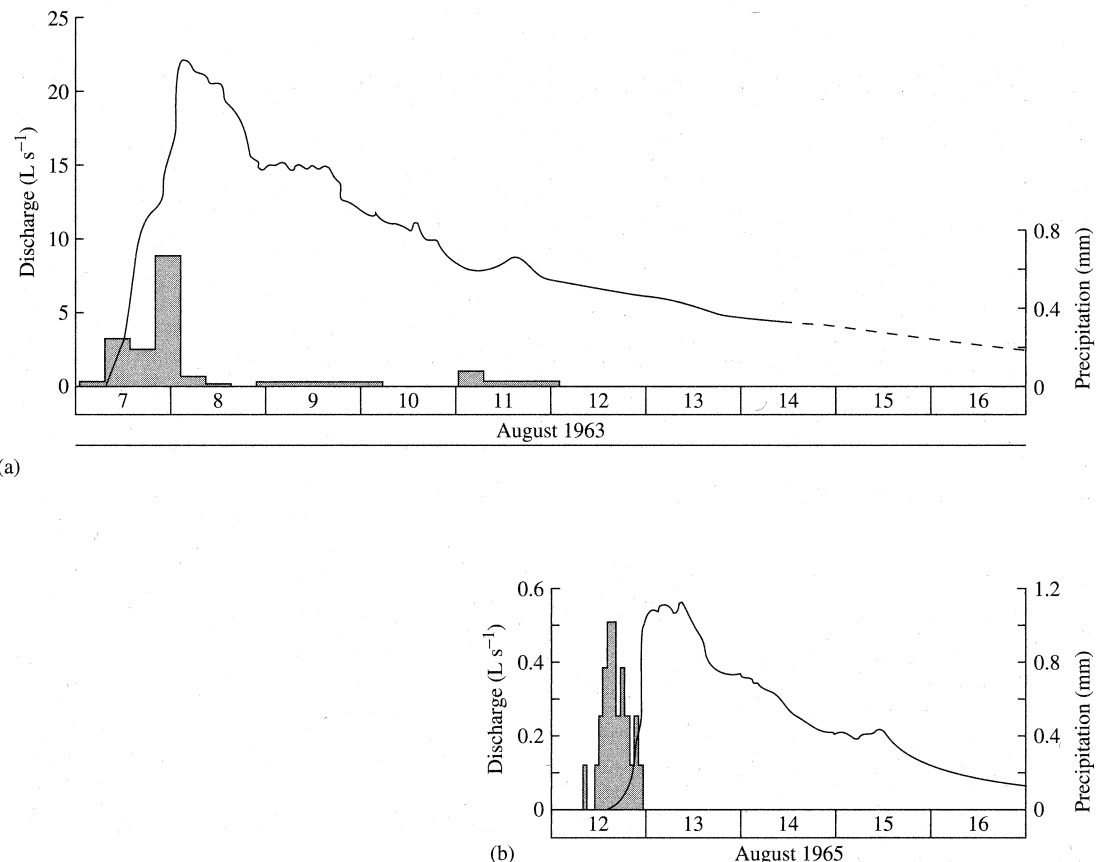


Figure 10.11 Hydrographs and hyetographs for two similar storms on a 1.6-km² watershed at Barrow, Alaska. Note different scales. (a) August 1963: $P = 7.9$ mm, $T_p = 24$ hr; $Q^* = 5.0$ mm, $Q^*/P = 0.63$. (b) August 1965: $P = 6.9$ mm, $T_p = 13.5$ hr; $Q^* = 0.08$ mm, $Q^*/P = 0.012$.

sideration to large floods, when the watershed is generally wet and contributing area may be fairly constant (Askew 1970; Pilgrim 1976).

10.2.4 Quantitative Description of Response Hydrographs

The terms used to analyze response hydrographs and relate them to event hyetographs are defined on figure 10.12 and in table 10.2 and are discussed below. Note that here we are focusing only on (1) the portion of streamflow identified as event flow, Q^* , and (2) the fraction of water input that appears as event flow, called the **effective rainfall** or **excess rainfall**, P^* . These volumes are equal:

$$P^* = Q^*. \quad (10.12)$$

For forecasting or predicting the runoff response to rainfall, we need some a priori method of separating P^* from total P for a given storm. Various approaches to this problem are discussed in sections 10.6.3 and 10.6.4.

In figure 10.12, water input begins at time t_{p0} and ends at t_{pe} ; the input duration (often called **storm duration**), is $T_p \equiv t_{pe} - t_{p0}$. Stream response, or **hydrograph rise**, begins at t_{q0} and usually continues more or less steadily to a peak flow, q_{pk} , at time t_{pk} . Typically the peak occurs when or soon after input ceases. The delay between the beginning of input and the beginning of the rise is the **response lag**, $T_{LR} \equiv t_{q0} - t_{p0}$. The time between the beginning of input and peak is the **lag-to-peak**, $T_{LP} \equiv t_{pk} - t_{p0}$. The duration of the hydrograph rise is called the **time of rise**,

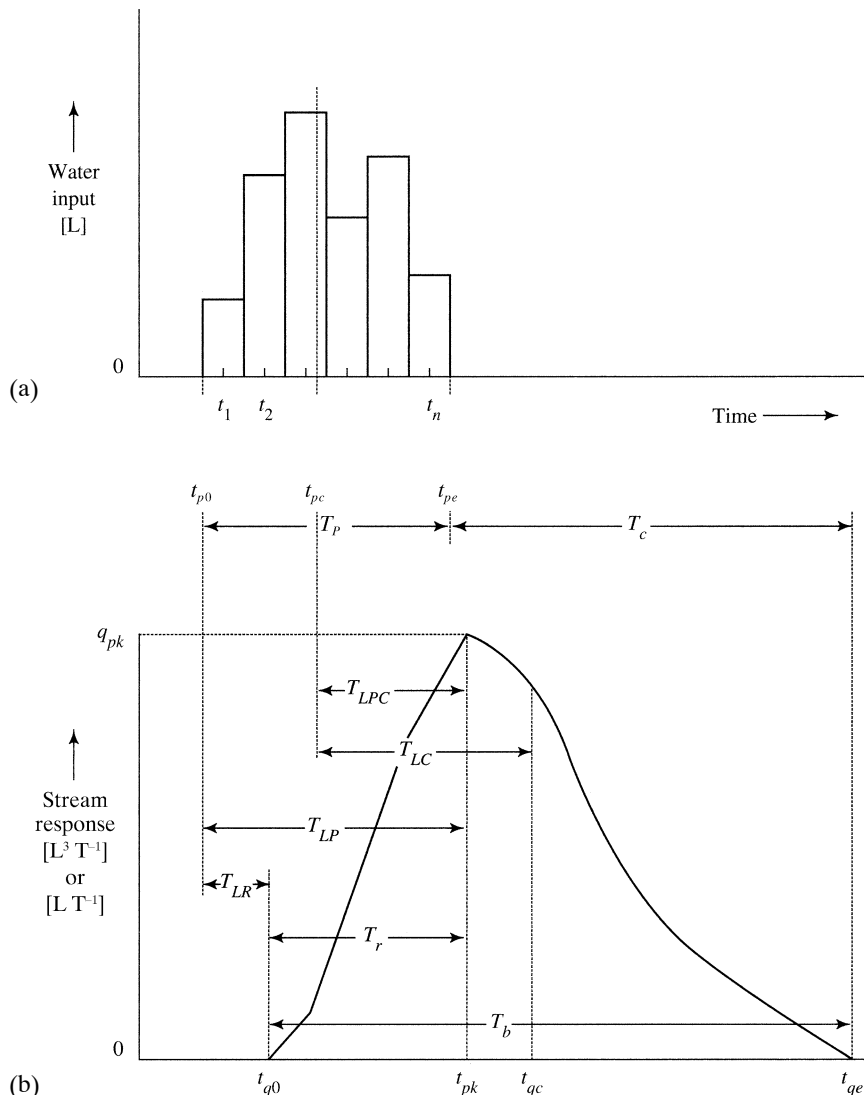


Figure 10.12 Definitions of terms used to describe (a) hyetographs and (b) response hydrographs. See table 10.2.

Table 10.2 Definitions of Terms Used to Describe Hyetographs and Response Hydrographs (see figure 10.12).

Time Instants	Time Durations
t_{p0} ≡ beginning of effective water input	T_p ≡ duration of effective water input = $t_{p0} - t_{pe}$
t_{pc} ≡ centroid of effective water input	T_{LR} ≡ response lag = $t_{q0} - t_{p0}$
t_{pe} ≡ end of effective water input	T_r ≡ time of rise = $t_{pk} - t_{q0}$
t_{q0} ≡ beginning of hydrograph rise	T_{LP} ≡ lag-to-peak = $t_{pk} - t_{p0}$
t_{pk} ≡ time of peak discharge	T_{LPC} ≡ centroid lag-to-peak = $t_{pk} - t_{pc}$
t_{qc} ≡ centroid of response hydrograph	T_{LC} ≡ centroid lag = $t_{qc} - t_{pc}$
t_{qe} ≡ end of response	T_b ≡ time base = $t_{qe} - t_{q0}$
	T_c ≡ time of concentration = $t_{qe} - t_{pe}$
	T_{eq} ≡ time to equilibrium ≈ T_c

or **time to peak**, $T_r \equiv t_{pk} - t_{q0}$. Following the peak, the response declines quasi-exponentially as water input drains from watershed storage; response ceases at time t_{qe} . The total duration of the response hydrograph is called the **time base**, $T_b \equiv t_{qe} - t_{q0}$.

The **centroid**, or **center of mass**, of the input, t_{pc} , is the weighted-average time of occurrence of the input hyetograph. If we have values of input, P_i^* , measured for $i = 1, 2, \dots, n$ time periods of equal length, the centroid of effective precipitation, t_{pc} , is calculated as

$$t_{pc} = \frac{\sum_{i=1}^n P_i^* \cdot t_i}{P^*} \quad (10.13)$$

where t_i is the time from the beginning of effective precipitation to halfway through period i . If the hyetograph is imagined to represent the distribution of masses on a bar, the centroid is the balance-point. The centroid of a response hydrograph, t_{qc} , can be estimated by approximating the continuous curve with a histogram and substituting the appropriate values into equation (10.13).

The **centroid lag**, T_{LC} , is defined as the time between the centroids of input and response: $T_{LC} \equiv t_{qc} - t_{pc}$. As will be discussed more fully below, the centroid lag is a theoretically meaningful value characterizing the response time of a watershed. However, a more commonly used measure of watershed response time is the time between the centroid of input and the peak, called the **centroid lag-to-peak**, $T_{LPC} \equiv t_{pk} - t_{pc}$.

It is commonly assumed that $T_{LPC} \approx 0.60 \cdot T_c$, where T_c is the **time of concentration**, i.e., the time it takes water to travel from the hydraulically most distant part of the contributing area to the outlet. Thus $T_c = t_{qe} - t_{pe}$. However, it is virtually impossible to define the true time of concentration because of uncertainties about the nature of the flow paths. Formulas for estimating nominal values of T_c from watershed and storm characteristics are discussed in section 10.6.

In spite of the difficulty in obtaining a precise a priori definition of time of concentration in most natural situations, the concept is useful in visualizing hydrologic response: If effective precipitation continues at a constant rate for a duration equal to T_c , the outflow rate will become equal to the input rate and the hydrograph peak will be effectively constant at that rate until input ceases (figure 10.13). This condition is called **equilibrium runoff**, and the time at

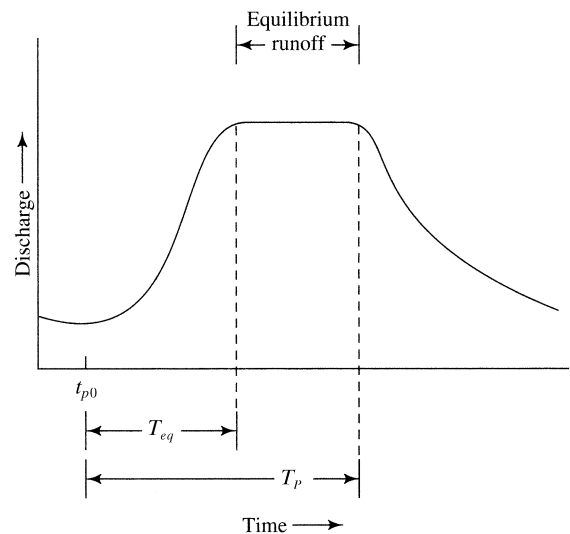


Figure 10.13 Schematic hydrograph for equilibrium runoff resulting when input duration, T_P exceeds the watershed's time of equilibrium, T_{eq} .

which the input and output rates become effectively equal is an apparent time of concentration, called the **time to equilibrium**, T_{eq} . When equilibrium runoff is occurring, all parts of the contributing area are contributing to the output, and

$$q^{*}(t) = q_{pk}^* = p^* \cdot A_c, \quad T_{eq} < t - t_{p0} < T_P, \quad (10.14)$$

where q_{pk}^* is the peak event-flow rate [$L^3 T^{-1}$], p^* is the effective water-input rate [$L T^{-1}$], and A_c is the contributing area [L^2].

Equilibrium runoff almost never occurs in natural watersheds, but it can occur from small areas with short times of concentration, such as parking lots. Thus most hydrographs from natural areas have an instantaneous peak, as in figure 10.13, and the peak flow rate will be less than the input rate. This implies that the entire contributing area does not contribute runoff simultaneously and that

$$q_{pk}^* < p^* \cdot A_c. \quad (10.15)$$

10.2.5 Effects of Input and Basin Characteristics on the Hydrograph: Exploration via a Simple Model

The objective of this section is to explore in a general way how (1) storm size and timing and (2) drainage-basin characteristics affect the hydrograph

characteristics defined in table 10.2 and figure 10.12. To do this we use the simple **linear-watershed model** developed in box 10.3. This model is based on the principle of conservation of mass [equation (10B3.1)] and on a very simple heuristic concept of watershed function: the linear-reservoir model [equation (10B3.2)].

A linear watershed is characterized by a single parameter, T^* , called the **response time**: the larger the value of T^* , the longer it takes water to travel to the watershed outlet and the more sluggish the response of the watershed. Thus T^* integrates the effects of all the factors that affect the travel time of water input to the basin outlet: permanent conditions such as watershed size, shape, slope, soils, and

geology, and changing conditions that affect the nature of the various flow paths, such as vegetative cover and watershed wetness. The discussion later in this chapter of the physical processes that produce a response hydrograph will provide more detailed insight into these relationships.

In the examples used here to illustrate basic hydrograph features, the input, output, and time values are arbitrary. Thus although T^* is given in "hr," this is an arbitrary measure of watershed response time, and all times are relative. Inputs and outputs are also in arbitrary units with dimensions $[L^3 T^{-1}]$ or $[L T^{-1}]$. Inputs to the model represent effective water input, and in all the simulations examined here the total volume of input, P^* , is the same: 1 unit. Because the

Box 10.3 Linear-Reservoir Model of Watershed Response

We can develop a very simple conceptual model of the response of a watershed to effective precipitation based on: (1) the principle of conservation of mass,

$$p^* - q^* = \frac{dS^*}{dt}; \quad (10B3.1)$$

(section 1.6.2) and (2) the linear-reservoir conceptual model of watershed behavior (section 1.10.2):

$$q^* = \frac{1}{T^*} \cdot S^*, \quad (10B3.2)$$

where p^* is effective rainfall rate ($[L^3 T^{-1}]$ or $[L T^{-1}]$), q^* is event-flow rate ($[L^3 T^{-1}]$ or $[L T^{-1}]$), S^* is storage of event-flow water ($[L^3]$ or $[L]$), t is time, and T^* is a time constant that characterizes the watershed response [T]. Real watersheds are not strictly linear reservoirs, but equation (10B3.2) captures the most basic aspects of watershed response and is mathematically tractable.

Combining equations (10B3.1) and (10B3.2) yields

$$p^* - q^* = T^* \cdot \frac{dq^*}{dt}, \quad (10B3.3)$$

which for constant p^* has the solution

$$q^* = p^* + (q_0^* - p^*) \cdot \exp(-t/T^*), \quad (10B3.4)$$

where q_0^* is the outflow at $t = 0$.

To model an isolated hydrograph rise in response to a constant input beginning at $t = 0$ and lasting until time T_p , we can set $q_0^* = 0$ at $t = 0$ so that equation (10B3.4) becomes

$$q^* = p^* \cdot [1 - \exp(-t/T^*)], t \leq T_p \quad (10B3.5)$$

The peak discharge, q_{pk}^* , occurs when water input ceases, i.e., when $t = T_p$; q_{pk}^* is then given by

$$q_{pk}^* = p^* \cdot [1 - \exp(-T_p/T^*)]. \quad (10B3.6)$$

When input ceases the hydrograph recession begins and we have new conditions: $p^* = 0$ and the "initial" discharge is q_{pk}^* at time $t = T_p$. Thus for the recession equation (10B3.4) becomes

$$q^* = q_{pk}^* \cdot \exp[-(t - T_p)/T^*], t \geq T_p. \quad (10B3.7)$$

The properties of this model are:

1. The model preserves continuity; i.e., the volume of event response Q^* equals the volume of effective water input, $P^* = p^* \cdot T_p$.
2. T^* can be shown to be equal to the centroid lag of the watershed (i.e., $t_{qc} - t_{pc} = T^*$).
3. The hydrograph rise begins as soon as input begins ($T_{LR} = 0$) and peaks exactly at $t_{pk} = T_p$.
4. Because outflow decreases exponentially after input ceases and approaches zero asymptotically, time of concentration is infinite. However, if we define the time to equilibrium, T_{eq} as the time it takes for the outflow rate to reach 99% of a constant inflow rate, it can be shown that

$$T_{eq} = -\ln(0.01) \cdot T^* = 4.605 \cdot T^*. \quad (10B3.8)$$

model preserves continuity, the total volume of outflow, Q^* , is also always 1 unit [equation (10.12)].

10.2.5.1 Basic Hydrograph Shape

Figure 10.14 shows the response of the linear watershed with $T^* = 1$ hr to a constant unit input rate $p^* = 1$ unit/hr for 1 hr, after which $p^* = 0$. The general form of this hydrograph is similar to that for natural watersheds, suggesting that the typical pattern of quick rise to an instantaneous peak followed by gradual recession is inherent to the general form of storage-out-

flow relations for watersheds in which $T_P < T_{eq}$, as expressed in equations (1.24) and (10B3.2).

Figure 10.15 shows the same input volume applied to the same watershed, but with T_P equal to T_{eq} as given by equation (10B3.8). This produces equilibrium runoff as described earlier.

Figure 10.16 shows the same input amount and timing as in figure 10.14, but to a watershed with $T^* = 5$ hr. Note that in this case the peak is much lower and the recession much longer.

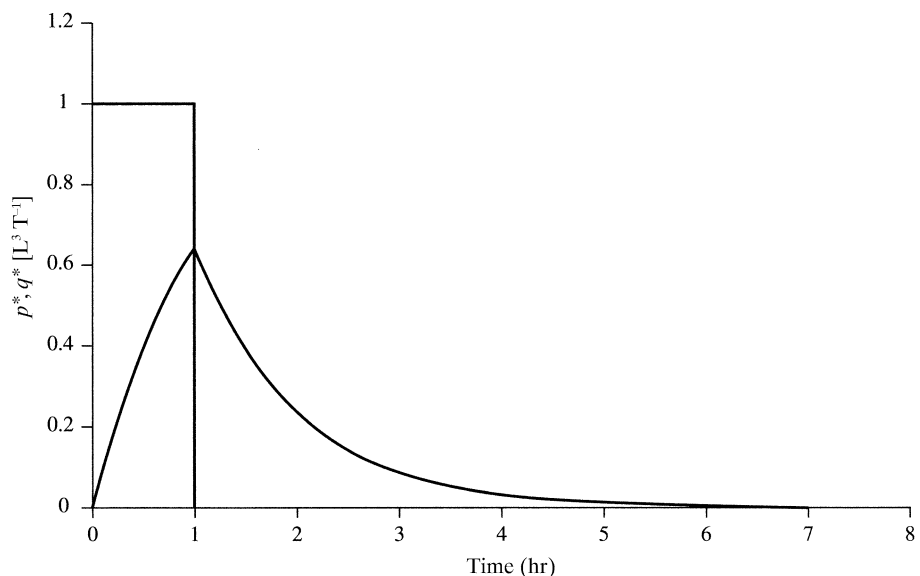


Figure 10.14 Response, q^* , of linear watershed with $T^* = 1$ hr to 1 unit of input, P^* , in 1 hr. Input rate $p^* = 1$ unit/hr.

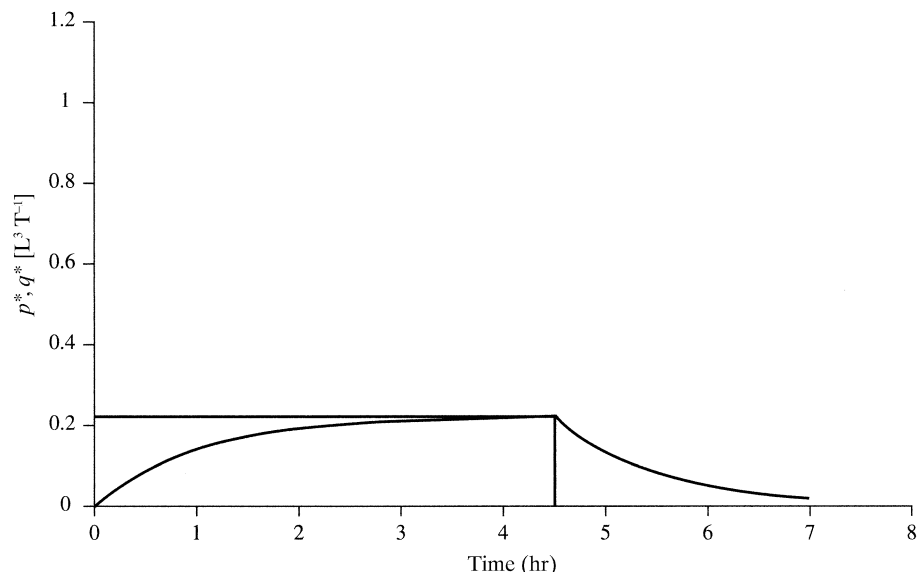


Figure 10.15 Response, q^* , of linear watershed with $T^* = 1$ hr to 1 unit of input, P^* , in 4.5 hr. Input rate $p^* = 0.222$ unit/hr.

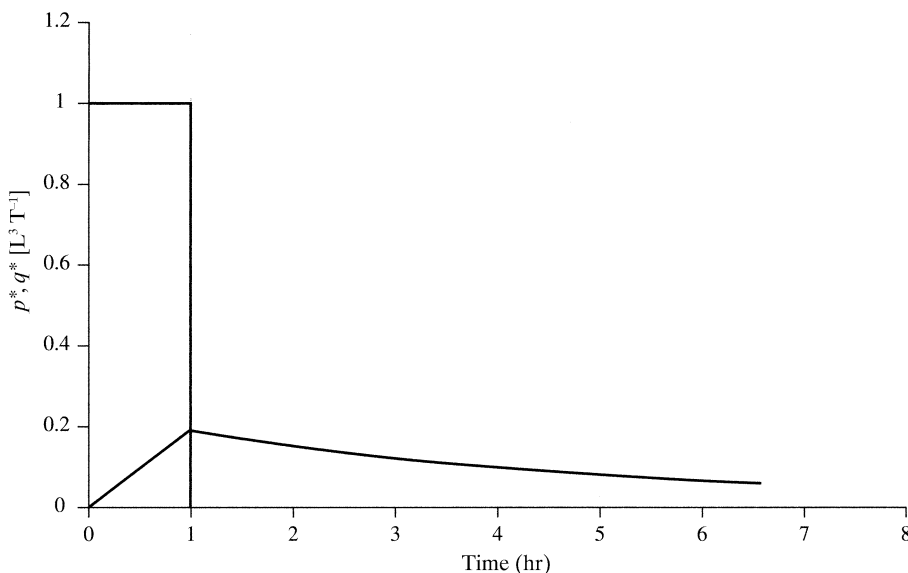


Figure 10.16 Response, q^* , of linear watershed with $T^* = 5$ hr to 1 unit of input, P^* , in 1 hr. Input rate $p^* = 1$ unit/hr.

10.2.5.2 Response Time and Centroid Lag

As noted earlier, T^* is related to the time required for water to travel to the watershed outlet, so that its value is determined largely by the following factors:

Watershed Size: Larger watersheds have larger T^* , other things equal. Analyses of large floods by Holtan and Overton (1963) indicated that T^* is strongly related to drainage area; however, the relationship varies from region to region, presumably largely because of differences in watershed geology, soils, and topography.

Soils and Geology: Water moves fastest toward streams as overland flow and slowest as subsurface flow (as discussed more fully later in this chapter). Thus watersheds with low surface hydraulic conductivities (e.g., clay soils), where less infiltration and more overland flow occur, should have smaller T^* than those with higher conductivities (e.g., sandy soils). If flow paths are predominantly in the subsurface, watersheds with higher hydraulic conductivities will have smaller values of T^* .

Slope: Steeper slopes should be associated with faster surface and subsurface water movement and hence smaller T^* .

Land Use: In general, watersheds with heavy vegetation, especially forests, have permeable surface soils that allow rapid infiltration and subsurface flow to streams, resulting in larger T^* . In contrast, sparsely vegetated watersheds tend to have lower T^* because their lower surface permeability makes

overland flow more common. Watersheds with intensive urbanization (more impermeable areas and storm sewers) generally have faster water movement and smaller T^* .

Watershed Wetness: As seen in section 10.2.3.2, the wetness of the watershed at the time of a rainfall event (antecedent condition) usually has a significant influence on the connectivity of surface and subsurface flow paths and the extent of the contributing area, so that a given watershed will have a smaller T^* when wet than when drier. The physical relations underlying this are discussed in section 10.4.

In the linear-watershed model the centroid lag, T_{LC} , is equal to T^* , regardless of the timing of inputs. Thus if the timing and amounts of effective water input and output can be determined, average T_{LC} would appear to be the best estimate of the characteristic response time for a given watershed.

10.2.5.3 Response Lag

In the linear-watershed model response begins as soon as input begins. The time between the beginning of water input and the beginning of measurable response in real watersheds is largely determined by the time required to fill storage (canopy interception, infiltration, surface depressions) plus the average travel time to the basin outlet. Very short response times can result when water inputs cause a nearly immediate change in hydraulic conditions that cause channelward flow of “old” water held in soil storage near streams (section 10.4).

10.2.5.4 Time of Rise

Experiments with the linear-watershed model show that, for a constant input rate, the time of rise equals the duration of effective precipitation (compare figures 10.14 and 10.15). Observations on real watersheds also show a close correspondence between T_r and storm duration for large storms (Holtan and Overton 1963, 1964). If effective precipitation rates vary markedly during an event, the time of peak is usually determined by the timing of the

highest rates, as illustrated in figures 10.17 and 10.18 and, for a real watershed, figure 10.5.

10.2.5.5 Lag-to-Peak and Centroid Lag-to-Peak

Some hydrologists have considered T_{LP} or T_{LPC} to be a characteristic time of a watershed, determined by the same factors that control T^* . However, experiments with the watershed model show that the timing of the inputs is at least as important in determining these lags: For a constant input rate, the lag-

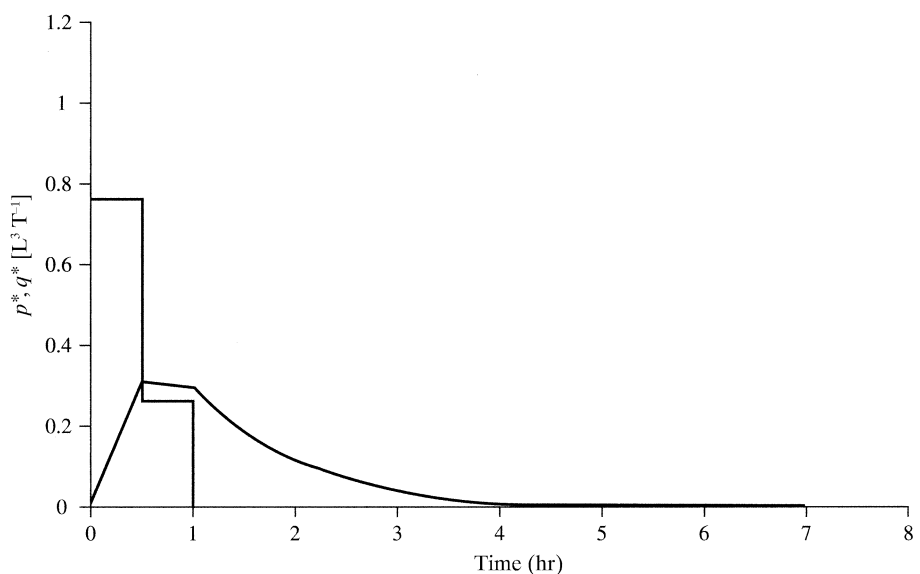


Figure 10.17 Response, q^* , of linear watershed with $T^* = 1$ hr to 1 unit of input, P^* , in 1 hr. Input rate $p^* = 0.75$ unit/hr for first 0.5 hr and 0.25 unit/hr for second 0.5 hr.

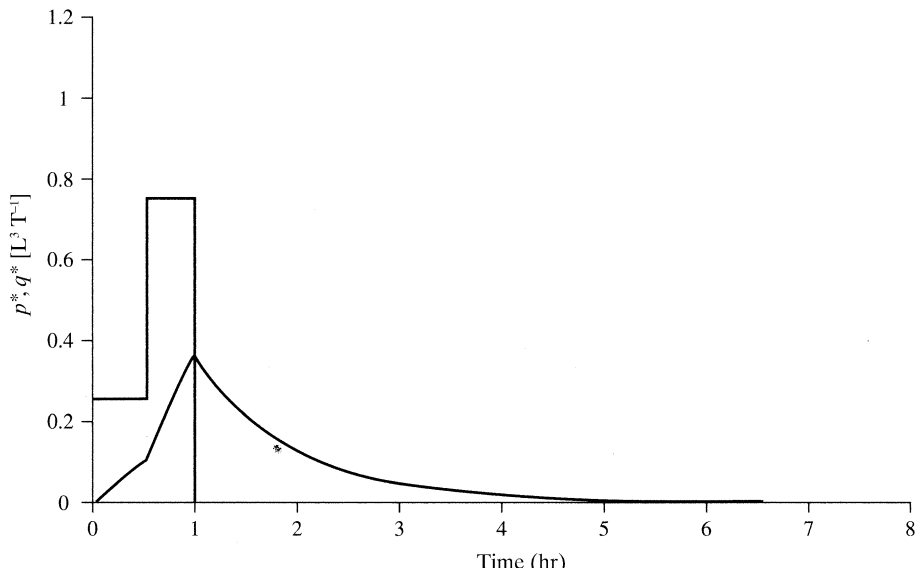


Figure 10.18 Response, q^* , of linear watershed with $T^* = 1$ hr to 1 unit of input, P^* , in 1 hr. Input rate $p^* = 0.25$ unit/hr for first 0.5 hr and 0.75 unit/hr for second 0.5 hr.

to-peak and the centroid lag-to-peak of the linear watershed are equal to one-half the input duration; when input rates vary, these times are determined by both the exact timing of the inputs and the watershed characteristics as reflected in the value of T^* .

10.2.5.6 Time of Concentration

Conceptually, the time of concentration is a characteristic time for a given watershed, given by the time between the end of effective input and the end of response. Usually this time will be approximately equal to the duration of the recession, and from box 10.3 we see that this is given by

$$T_c = 4.605 \cdot T^*. \quad (10.16)$$

Empirical formulas for estimating T_c typically have the general form

$$T_c \propto \frac{L^a}{S^b}, \quad (10.17)$$

where L is some measure of the length of watershed flow paths, S is some measure of watershed slope, and a and b are positive empirical constants; several such formulas are given in section 10.6.

10.2.5.7 Time Base and Recession

The recession of the linear watershed follows an exponential decay with decay constant equal to T^* [equation (10B3.7)]; thus the theoretical time base is infinite. However, defining the end of runoff when $q^* = 0.01 \cdot p^*$, as in box 10.3, we see that $T_b = T_p + 4.605 \cdot T^*$, and is thus determined by both the duration of input and by watershed characteristics.

To the extent the recession for a given stream approximates exponential decay, the decay constant

can be used to estimate T^* [equation (10B3.7)]. However, recessions for a given watershed often appear to have different decay-constant values in different discharge ranges and at different seasons, making it difficult to identify a “fundamental” time constant for a watershed. As noted in section 9.5.3.6, the exponential-decay model has been used as a basis for graphical hydrograph separation (figure 9.34b).

10.2.5.8 Peak Discharge

Equation (10B3.6) shows that, for a constant water-input rate, the peak discharge rate is determined by the rate and duration of input and the basin characteristics as reflected in T^* . Interestingly, Holtan and Overton (1963) found that peaks of large floods on actual watersheds could be well estimated by a relation almost identical to equation (10B3.6).

The effect of T^* on q_{pk} can be seen by comparing figure 10.16 with figure 10.14: For a watershed with $T^* = 1$ hr the peak rises to more than 60% of the input rate, then recedes to near zero 5.5 hr after input ceases. When the same input is applied to a basin with $T^* = 5$ hr, the peak is about 20% the input rate and the recession is much slower—outflow is still well above zero 7 hr after input stops.

Comparison of figures 10.17 and 10.18 shows that the temporal variability of input affects the magnitude as well as the timing of peaks.

10.2.5.9 Summary

Table 10.3 summarizes the conclusions gleaned from applying the linear-reservoir model. Conceptually, the centroid lag and time of concentration are characteristic watershed times that depend on the time of travel of water to the basin outlet, and hence on both quasi-permanent conditions (basin size, to-

Table 10.3 Dependence of Response Hydrograph Characteristics on Watershed and Input Characteristics as Predicted by the Linear-Watershed Model.

Hydrograph Characteristic	Watershed Characteristics, T^*	Input Duration, T_p	Input Timing
Centroid lag, T_{LC}	X		
Response lag, T_{LR}			
Time of rise, T_r		X	X
Lag-to-peak, T_{LP}	X		X
Centroid lag-to-peak, T_{LPC}	X		X
Time base, T_b	X	X	
Time of concentration, T_c	X		
Peak discharge, q_{pk}	X	X	X

topography, geology, land use) and time-variable watershed wetness. Other time characteristics of the response hydrograph depend on both these same properties and on the duration or timing of input. Peak flow—the most important hydrograph feature for flood forecasting and prediction—also depends on watershed characteristics, antecedent conditions, and the duration and timing of inputs.

10.3 Identification of Runoff Sources

The actual sources of streamflow can be identified with confidence only if water entering the stream from specific sources (e.g., direct rain onto the channel, flow from the watershed surface, ground water) has a characteristic water-quality “signature” and if the components of this signature in streamflow are monitored during an event. The basic approach to this problem is **end-member mixing analysis (EMMA)**; this involves (1) identifying two or more streamflow sources (**end members**); (2) characterizing the unique chemical or isotopic characteristics of each end member; (3) measuring the concentrations of those characteristic components in streamflow; and (4) using mathematical analysis to determine the proportion of each end member present. The analysis is based on the assumption that the characteristic components are “conservative”; i.e., that their concentrations are affected only by mixing in the stream, and not by chemical reactions or isotopic fractionation while en route to the point of measurement.

The simplest case involves two end members (e.g., surface flow and ground water), each with a characteristic concentration of a particular constituent. In this case we can write the mass-balance equation for water as

$$q(t) = q_1(t) + q_2(t), \quad (10.18)$$

and for the constituent as

$$c(t) \cdot q(t) = c_1 \cdot q_1(t) + c_2 \cdot q_2(t), \quad (10.19)$$

where the c s represent the characteristic concentrations, the q s represent discharges, the subscripts denote the two components, and (t) denotes variability with time. Then if the total flow rate, $q(t)$, and its concentration, $c(t)$, are measured, we can combine equations (10.18) and (10.19) to calculate the discharge contributed by each component:

$$q_2(t) = \frac{c(t) - c_1}{c_2 - c_1} \cdot q(t), \quad (10.20a)$$

$$q_1(t) = q(t) - q_2(t). \quad (10.20b)$$

Contributions of three end members can be determined if one can measure the flow rate contributed by one of them, as well as the total flow rate and total concentration. For example, Swistock et al. (1989) used rainfall measurements to determine the contribution of precipitation directly on a channel, $q_{cp}(t)$, and were able to determine the contributions of soil water, $q_s(t)$, and ground water, $q_{gw}(t)$, as

$$q_s(t) = q(t) \cdot \frac{c(t) - c_{gw}}{c_s - c_{gw}} - q_{cp}(t) \cdot \frac{c_{cp} - c_{gw}}{c_s - c_{gw}} \quad (10.21a)$$

and

$$q_{gw}(t) = q(t) - q_{cp}(t) - q_s(t), \quad (10.21b)$$

where the subscripts cp , s , and gw denote channel precipitation, soil, and ground water, respectively, and ^{18}O was the tracer.

The most commonly used chemical tracers are Ca, Mg, K, Na, Fe, Cl, HCO_3^- , CO_3^{2-} , NO_3^- , Si, alkalinity, and the stable isotopes ^{18}O and ^2H . Very precise measurements of concentrations are usually needed to get meaningful hydrograph separations because small errors in concentrations can lead to large errors in computed flow rates (Rice and Hornberger 1998).

Because a given tracer is seldom strictly conservative, one can solve the above equations using several tracers, and construct a composite curve. For example, Pinder and Jones (1969) applied equation (10.20) using HCO_3^- , Mg, Ca, and SO_4^{2-} as tracers, and constructed a composite curve showing ground-water contribution on a small watershed in Canada (figure 10.19). Interestingly, the analysis indicated that ground water contributed significantly to the peak discharge (compare figure 10.19 with figure 9.34). Figure 10.20 shows an example of EMMA for a small watershed in Georgia, where the sources are ground water (sampled via wells), the surface organic layer of the soil (sampled via a suction lysimeter), and water draining from the hillslopes (sampled via a shallow well at the hillslope base); the constituents are silica (SiO_2) and magnesium (Mg). (Similar diagrams were constructed using other constituents.) Note that the points outside the triangle do not fit the EMMA model using these constituents; this could be because (1) the compositions are not strictly conservative (i.e., chemical reactions may alter the water chemistry); (2) the end members are not correctly characterized due to inadequate sampling; or (3) there are unsampled streamflow sources. However, the percentage of varia-

tion in the streamwater solute concentrations explained by the analysis ranged from 82 to > 97%, and the hydrograph separation was physically reasonable.

Figure 10.21 is a **Stiff diagram** that shows end-member chemical compositions in an alpine watershed in Colorado. Chemical analyses of runoff on this watershed indicate that long-residence-time ground water is an important component of streamflow, becoming more important as watershed size increases (Frisbee et al. 2011).

Special issues of the *Journal of Hydrology* (volume 116, 1990) and *Water Resources Research* (volume 26, number 12, 1990) are dedicated to this topic, and Bonell (1993) provided a useful review. Two more recent studies provide approaches to objective identification of end-member models: (1) Hooper (2003) developed diagnostic tools to identify processes that violate the assumptions of the model and suggest how models can be refined and (2) Barthold et al. (2011) found that models of runoff sources are

highly sensitive to the tracer-set size and composition, and developed an automated procedure that identifies appropriate models by conducting EMMA while iteratively changing tracer-set size and composition. They found that the major elements are not always the most useful tracers, and that larger tracer sets have an enhanced capacity to avoid misleading conclusions about runoff sources.

10.4 Event-Flow-Generation Processes

In this section we explore the physical mechanisms by which water produced at the ground surface by rain or snowmelt travels to a stream to produce an event hydrograph (storm runoff). These mechanisms are classified in table 10.4, and the climatic, topographic, and pedologic-geologic conditions in which they occur are described further below. Some or all of these mecha-

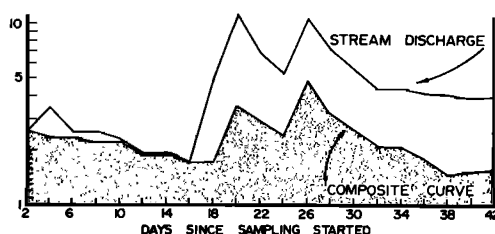


Figure 10.19 Composite curve showing ground-water contribution on a small watershed in Canada based on HCO_3^- , Mg , Ca , and SO_4^{2-} as tracers. Note logarithmic discharge scale [Pinder and Jones (1969). Determination of the ground-water component of peak discharge from the chemistry of total runoff. *Water Resources Research* 5(2):438–445, with permission of the American Geophysical Union].

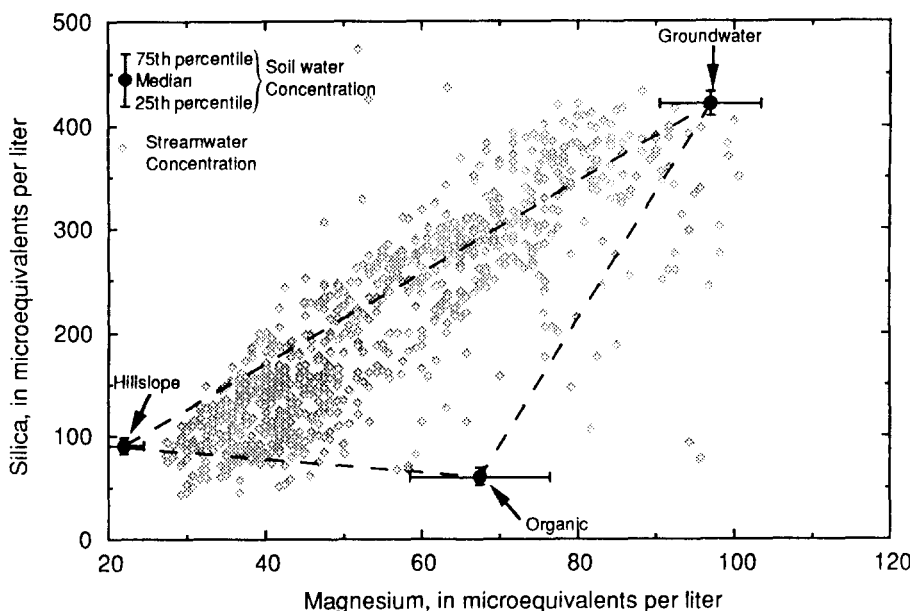


Figure 10.20 Three-component EMMA plot based on silica (SiO_2) and magnesium (Mg) for Panola Mountain Research Watershed, Georgia [reproduced from Hooper et al. (1990), Modeling streamwater chemistry as a mixture of soil-water end-members—an application to the Panola Mountain catchment, Georgia, U.S.A., *Journal of Hydrology* 116:321–343, with permission from Elsevier].

Figure 10.21 End-member chemical compositions in an alpine watershed in Colorado displayed on a Stiff diagram. Concentrations of all ions, but especially Ca, Na, K, HCO₃, and CO₃, increase with residence time in the watershed [Frisbee et al. (2011). Streamflow generation in a large, alpine watershed in the southern Rocky Mountains of Colorado: Is streamflow generation simply the aggregation of hillslope runoff responses? *Water Resources Research* 47, with permission of the American Geophysical Union].

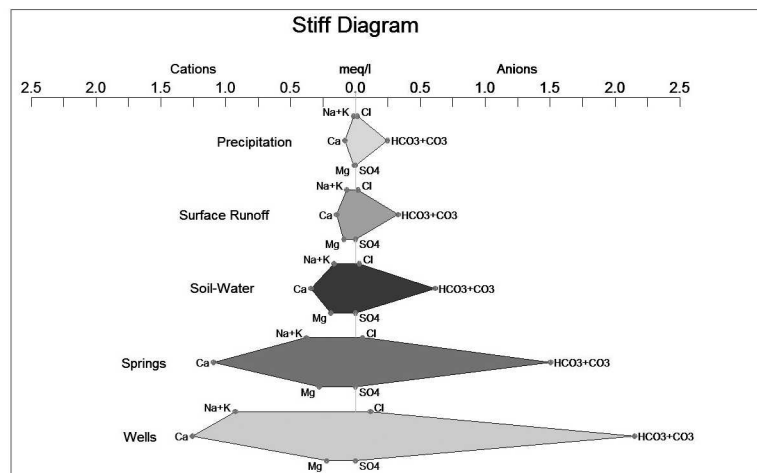


Table 10.4 Classification of Flow Mechanisms That Produce Event Responses.

- I. Channel precipitation
- II. Overland flow (surface runoff)
 - A. Hortonian overland flow
 - B. Saturation (Dunne) overland flow
- III. Subsurface flow
 - A. Flow in the saturated zone
 - 1. Flow from near-stream ground-water mounds
 - a. Gradual ground-water-mound development
 - b. Sudden ground-water-mound development by pressurization of capillary fringe
 - 2. Flow from perched saturated zones
 - a. Matrix (Darcian) flow
 - b. Macropore flow
 - B. Flow in the unsaturated zone^a
 - 1. Matrix (Darcian) flow
 - 2. Macropore flow

^aCannot enter surface flow directly.

nisms may operate simultaneously on a given watershed, and their relative importances may fluctuate seasonally or even during a single water-input event. Much of our understanding of the importance of these sources in various climatic, geologic, and topographic contexts has come from studies using various chemical and/or isotopic tracers as described in section 10.3.

10.4.1 Channel Precipitation

Channel precipitation (also called **channel interception**) is the rain that falls directly on the stream to become incorporated in channel flow.

Runoff from this source occurs in all rainstorms and in all regions and, although the total area of stream channels is almost always less than 1% of the total drainage area, it can be a significant component of peak flow and total event flow.

The volume of channel precipitation, P_{cp} , for an event can be calculated as

$$P_{cp} = P \cdot A_{cn}, \quad (10.22)$$

where P is total rainfall and A_{cn} is the surface area of stream channels above the point of measurement, which can be estimated on the basis of ground- or aerial-photo sampling and stream-network analysis (section 10.1.2). To estimate the hydrograph of runoff from channel precipitation, one can approximate it as a triangle so that

$$P_{cp} = 0.5 \cdot q_{pkc} \cdot (T_p + T_{cn}), \quad (10.23)$$

where q_{pkc} is the peak discharge from channel precipitation; T_p is storm duration; and T_{cn} is the time of concentration for the channel network (figure 10.22), which can usually be estimated from stream network and channel characteristics (section 10.5.1). Equating equations (10.22) and (10.23) leads to an expression for q_{pkc} :

$$q_{pkc} = \frac{2 \cdot P \cdot A_{cn}}{T_p + T_{cn}}. \quad (10.24)$$

Because of the crude approximation of the hydrograph as a triangle, q_{pkc} calculated via (10.24) is probably somewhat larger than the true value.

Using equation (10.24), Dingman (1970) calculated that up to 5% of total event flow and 40% of

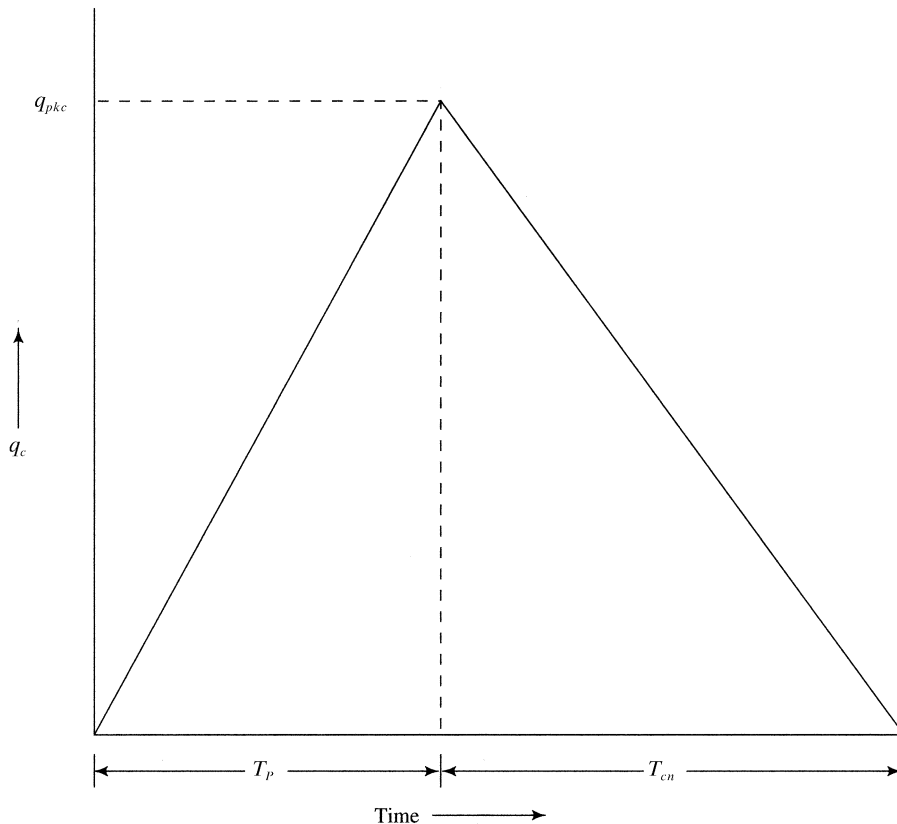


Figure 10.22
Approximation of the hydrograph of channel precipitation, q_c , as a triangle. The total area of the triangle is the volume of channel precipitation, $P \cdot A_{cn}$ [equations (10.22)–(10.24)].

peak discharge were due to channel interception for a small Alaskan watershed. Beven and Wood (1993) cited several studies in which channel precipitation was a significant part of the response hydrograph, and Crayosky et al. (1999) found that channel precipitation accounted for all of the rising limbs of storm hydrographs during the dry season and up to 29% of total storm flow for a small stream in Pennsylvania.

10.4.2 Overland Flow

Overland flow (or surface runoff) occurs when rain or snowmelt accumulates on a sloping surface. This occurs when the surface layer of soil becomes saturated either (1) from above, when the rainfall rate exceeds the infiltration rate (section 8.2.1), or (2) from below, when the water table rises to the surface (section 8.4.3.6).

The discussion here focuses on qualitative descriptions of these two major overland-flow-generating processes. Emmett (1978) and Abrahams et al. (1986) described methods of measuring overland flow on hillslopes. The hydraulics of overland flows is explored by Woolhiser and Liggett (1967) and re-

viewed by Brutsaert (1992). Eagleson (1970) and Stephenson and Meadows (1986) presented approaches for computing overland-flow hydrographs as a function of slope conditions and rainfall rates.

10.4.2.1 Saturation from Above: Hortonian Overland Flow

Overland flow that results from saturation from above is called **Hortonian overland flow** (figure 10.23), which was named for Robert E. Horton, a pioneer of quantitative hydrology who described the process in a series of papers (Horton 1933, 1945). The mechanism is also called **infiltration-excess runoff**.

The process of saturation from above on an initially unsaturated soil is quantitatively modeled in section 8.4.3. As water input at a rate exceeding the saturated hydraulic conductivity of the surface begins, infiltration occurs and the infiltrating water creates a descending wetting front. As input and infiltration continue, the near-surface water content increases and the wetting front descends. If input persists long enough, the surface soil becomes saturated, infiltration ceases, and the water that accumu-

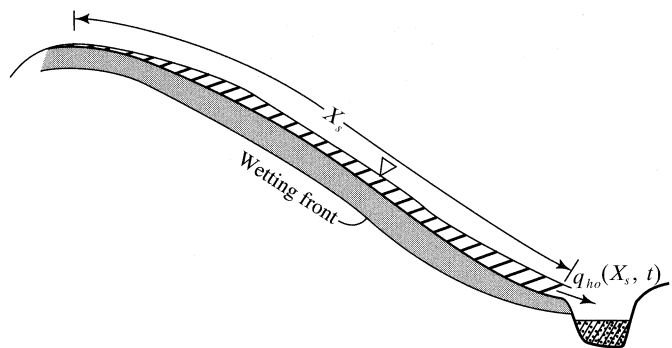


Figure 10.23 Hortonian overland flow over an entire slope of length X_s . $q_{ho}(X_s, t)$ is the lateral inflow to the stream at time t .

lates on the surface runs off downslope. The instant when surface saturation occurs is called the **time of ponding**. Thus

-
- Hortonian overland flow occurs when and where
1. the water-input rate exceeds the surface saturated hydraulic conductivity and
 2. storm duration exceeds the time of ponding.
-

As shown in section 8.4.3, time of ponding, T_p , for a constant input rate, p , can be calculated as a function of soil saturated hydraulic conductivity, K_h , capillary suction at the wetting front, ψ_f , and antecedent soil wetness (i.e., porosity less initial water content, $\phi - \theta_0$):

$$T_p = \frac{K_h \cdot |\psi_f| \cdot (\phi - \theta_0)}{p \cdot (p - K_h)}. \quad (10.25)$$

The infiltration rate, $f(t)$, under these conditions is given by equation (8.34), and the rate at which water becomes available for Hortonian overland flow, $q_{ho}(t)$, is

$$q_{ho}(t) = p - f(t), \quad t > T_p \quad (10.26)$$

(figure 10.24). The development in section 8.4.3 showed that $f(t)$ decreases asymptotically to K_h as input continues after the time of ponding. Thus Hortonian overland flow tends to increase during a storm with constant water-input rate.

Figure 10.25 compares the range of natural rainfall intensities⁵ with K_h values of various soils and geologic materials, and indicates that $p > K_h$ only for relatively intense rains on relatively fine-grained

soils. In fact, actual occurrences of Hortonian overland flow may be even rarer than figure 10.25 implies because the K_h values indicated there are for the mineral soil horizons, and the surface horizons of many soils have considerably larger hydraulic conductivities because of organic matter and biological activity. Thus

-
- Hortonian overland flow is typically an important response mechanism in:
- (1) semiarid to arid regions, where rainfalls tend to be intense and natural surface conductivities are low due to lack of surface vegetation;
 - (2) areas where soil frost or human or animal activity has reduced surface conductivity (see section 8.2.3);
 - and (3) impermeable areas.
-

Horton (1933, 1945) postulated that overland flow due to saturation from above would occur from virtually an entire upland watershed. This view was modified by Betson (1964), who proposed the **partial-area concept**:

-
- Event response may originate as Hortonian overland flow on a limited, low-permeability **contributing area** that varies from watershed to watershed but, except for the possibility of some expansion during extreme events, remains fairly constant on a given watershed.
-

Betson (1964) found that the stable contributing area ranged from 4.6% to 46% on agricultural watersheds in the southern Appalachian Mountains.

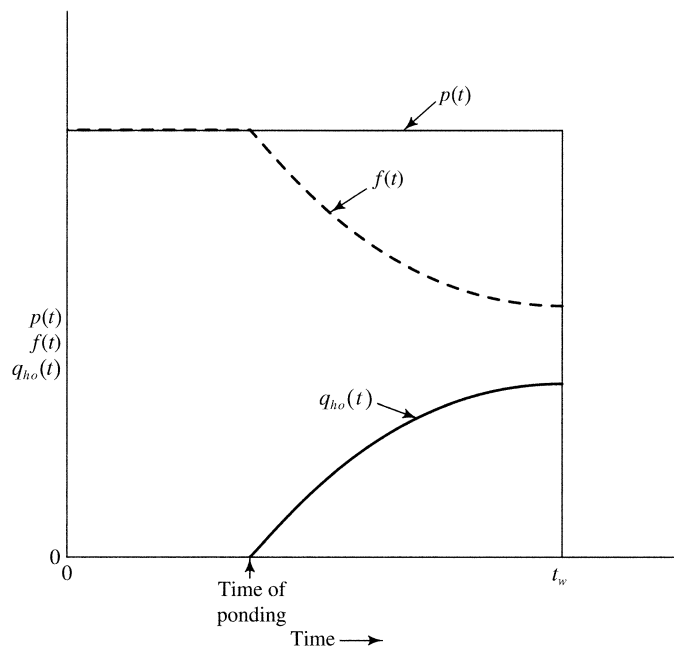


Figure 10.24 Hortonian overland flow, $q_{ho}(t)$, at a point on a hillslope during a water-input event. $p(t)$ is water-input rate (shown as constant), $f(t)$ is infiltration rate given by equation (8.34).

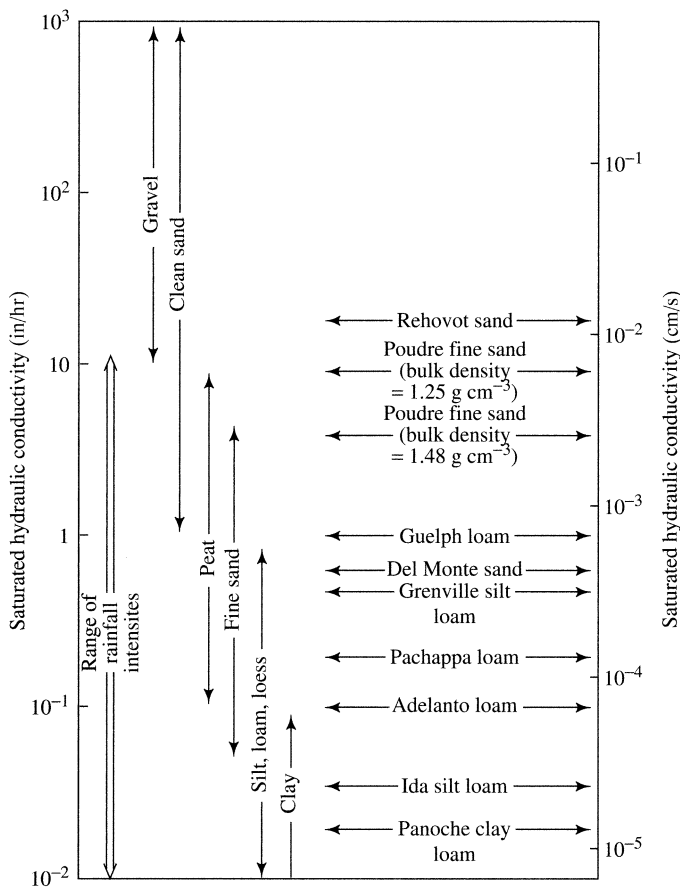


Figure 10.25 Saturated hydraulic conductivities for several soils and geologic materials compared to usual range of rainfall intensities [Freeze (1972b). Role of subsurface flow in generating surface runoff: 2. Upstream source areas. *Water Resources Research* 8:1272–1283, with permission of the American Geophysical Union].

10.4.2.2 Saturation from Below: Saturation (Dunne) Overland Flow

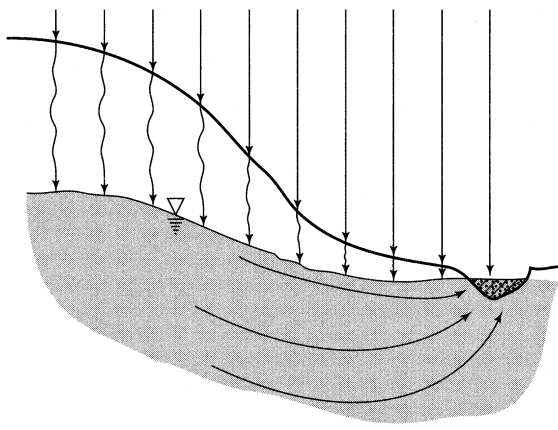
Saturation overland flow (also called **saturation-excess runoff**) (figure 10.26) is overland flow that occurs when the water table rises to the surface due to saturation from below. This occurs where the downward percolation of infiltrated water is impeded by

1. a preexisting shallow water table;
2. a shallow impervious layer (section 8.4.3.6); or
3. a decrease of hydraulic conductivity with depth.

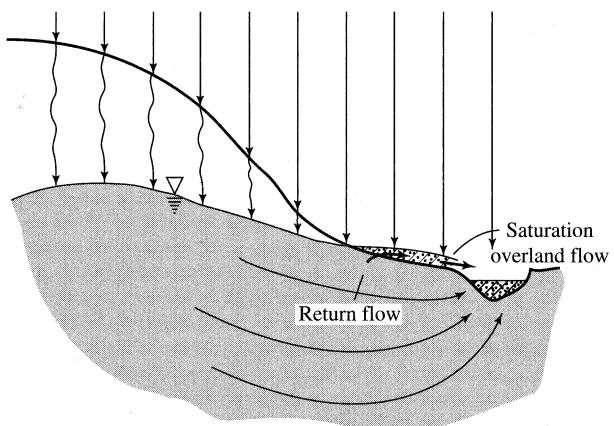
The accumulating water at these barriers causes the water table to rise; when it reaches the surface no

further infiltration is possible and overland flow begins. As the rising water table intersects the surface, ground water from upslope, called **return flow**, breaks out and becomes part of overland flow (figure 10.26b). Thus saturation overland flow consists of (1) direct water input on the saturated area, plus (2) return flow contributed by the breakout of ground water from upslope on to the saturated area. During an event, return flow is usually much less important than direct water input on the saturated zone, especially in areas distant from the stream. However, return flow can be a significant contributor to streamflow when it persists after input ceases (Whipkey and Kirkby 1978).

Streams in humid areas are typically gaining (section 9.3.1); the water table is usually coincident with the stream surface and not far below the ground surface in near-stream areas, as in figure 10.26. When water input occurs over the drainage basin, all or part of it infiltrates and some of this infiltration re-



(a)



(b)

Figure 10.26 Saturation overland flow and subsurface event flow due to near-stream ground-water mounding. (a) Early stages of event; overland flow is absent and only regional ground-water flow (base flow) is occurring. (b) Later, the water table has risen to the surface in near-stream areas due to local and upslope recharge; infiltration ceases and saturation overland flow results along with subsurface event flow. Return flow is the portion of saturation overland flow contributed by the “breakout” of ground water. Flow contributing to mounding results from both vertical recharge and downslope flow in the saturated zone [adapted from Ward (1984)].

charges ground water and raises the water table. Since the water table is close to the surface near streams, it commonly rises to the surface in riparian areas. Once this happens, all further water input on the saturated zone travels as overland flow to the stream, regardless of water-input rate. The process often occurs during snowmelt (figure 5.25).

The importance of near-stream saturation overland flow as a runoff-generating mechanism in humid regions was first established by the intensive field studies of Thomas Dunne (Dunne 1970, 1978; Dunne and Black 1970), and the process is sometimes called **Dunne overland flow**. A number of field (Ragan 1966; Dunne and Black 1970; Dunne 1978; Ward 1984) and modeling (Freeze 1972b, 1974) studies indicate that

Saturation overland flow is usually one of several, if not the only, mechanisms producing event response in humid regions.

Concomitantly, these studies have established the **variable source area concept**:

Within a given watershed, the extent of areas saturated from below varies widely with time, reflecting the overall watershed wetness (figure 10.27).

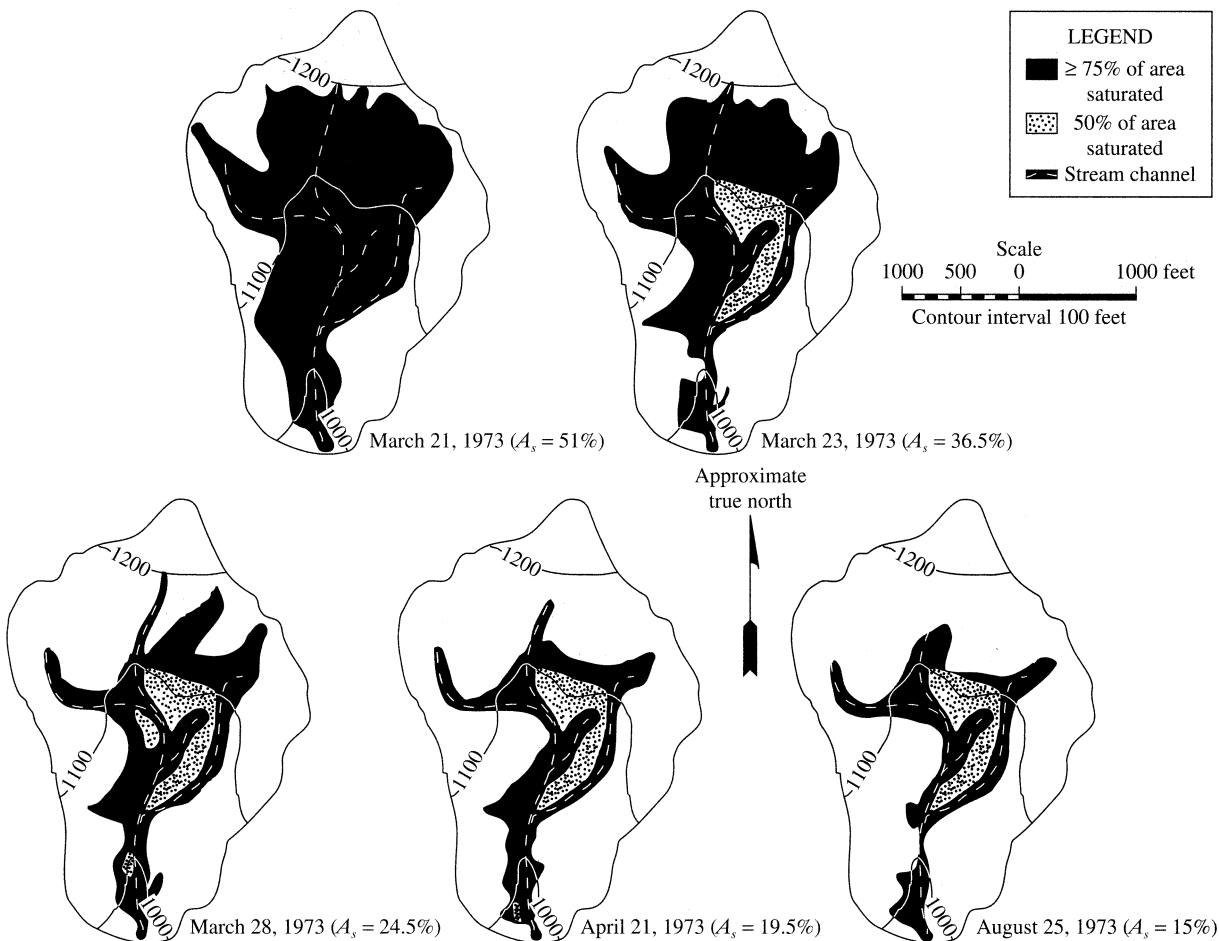


Figure 10.27 Seasonal variation of extent of areas saturated from below in a drainage basin with gentle slopes and moderately to poorly drained soils in northeastern Vermont. A_s is percent of total area that is saturated [Dunne et al. (1975), used with permission of the International Association of Hydrologic Sciences].

This variability is in large part responsible for the tremendous temporal variability of storm runoff that is observed in many regions (e.g., figures 10.10 and 10.11), and thus has extremely important implications for understanding and modeling event response.

Near-stream saturated zones will be most extensive in drainage basins with concave hillslope profiles and wide, flat valleys. A number of studies (see Ward 1984) have shown that saturation overland flow can also occur: (1) where subsurface flow lines converge

in slope concavities ("hillslope hollows") and water arrives faster than it can be transmitted downslope as subsurface flow (figure 10.28a); (2) at concave slope breaks, where the hydraulic gradient inducing subsurface flow from upslope is greater than that inducing downslope transmission (figure 10.28b); (3) where soil layers conducting subsurface flow are locally thin (figure 10.28c); and (4) where hydraulic conductivity decreases abruptly or gradually with depth, and percolating water accumulates above the

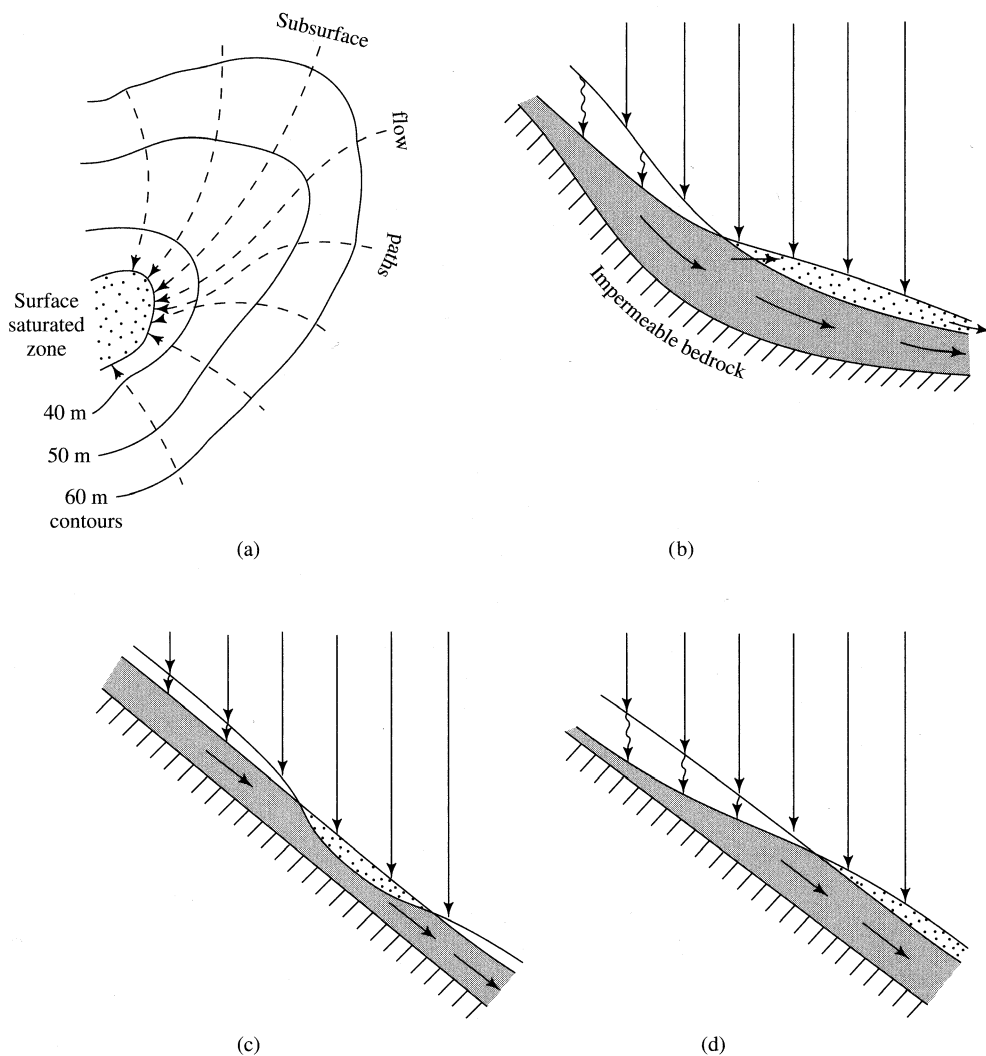


Figure 10.28 Situations in which saturation overland flow may arise on hillslopes outside of near-stream areas. (a) Plan view showing convergence of subsurface flow paths. (b) Cross section showing downslope reduction in hydraulic gradient associated with slope break. (c) Cross section showing local area of thin soil. (d) Cross section showing formation of perched saturated zone above low-conductivity layer with constant slope and soil thickness [adapted from Ward (1984)].

low-conductivity layers to form “perched” zones of saturation that reach the surface (figure 10.28d).

Thus we see from figure 10.28 that the propensity for saturation from below to occur is related to local topography. At each “point” in the watershed (represented by a pixel of finite area), this propensity is directly proportional to the tendency to collect subsurface flow from upslope areas, and inversely proportional to the tendency to transmit that flow downslope; these effects can be quantified as the **topographic index**, TI_i :

$$TI_i \equiv \ln\left(\frac{a_i}{\tan \beta_i}\right), \quad (10.27)$$

where a_i is the area draining to pixel i per unit contour length ($a_i \equiv A_i / \delta c_i$ in figure 10.29), and β_i is the local slope angle (Beven and Kirkby 1979). Thus pixels that collect drainage from large areas and have flat slopes have high TI values. Typically the distri-

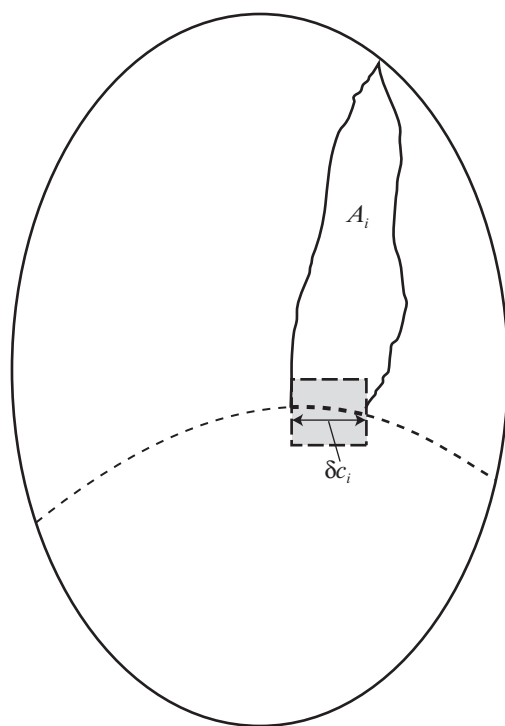


Figure 10.29 Subsurface-flow convergence in the topographic index concept, TI [equation (10.27)]. The outer oval represents the watershed divide; the outlet is at the bottom. A_i is the area draining to the square pixel i . The short-dashed line is a contour line; δc_i is the length of the contour within the pixel. $a_i = A_i / \delta c_i$.

bution of TI is computed from a digital elevation model (DEM) (Quinn et al. 1995), as in figure 10.30.

TI is the basis for “TOPMODEL,” a runoff-modeling approach that has been widely applied to small watersheds in humid regions (e.g., Beven and Kirkby 1979; Wood et al. 1990; Beven and Wood 1993; Ambroise et al. 1996; Beven 1997; Kirkby 1997; Blazkova et al. 2002; Kavetski et al. 2003). In this approach, the portion of the watershed producing saturation overland flow at any time is modeled by calculating the soil-moisture-storage deficit for pixel i , d_i , as

$$d_i = \bar{d} + M \cdot (\bar{TI} - TI_i), \quad (10.28)$$

where \bar{d} is watershed mean soil-moisture-storage deficit, \bar{TI} is the watershed mean value of TI , and M characterizes the rate at which hydraulic conductivity decreases with depth. The value of \bar{d} is computed at successive time steps by keeping track of the watershed water balance (precipitation, evapotranspiration, and outflow). Then at each time step, the points capable of generating saturation overland flow are those at which $d_i = 0$ (i.e., $TI_i = \bar{TI} - \bar{d}/M$). Given the spatial pattern of values of d_i and the percentage of the watershed that is saturated, the spatial pattern of saturated points can be determined and the rate of saturation overland flow computed.

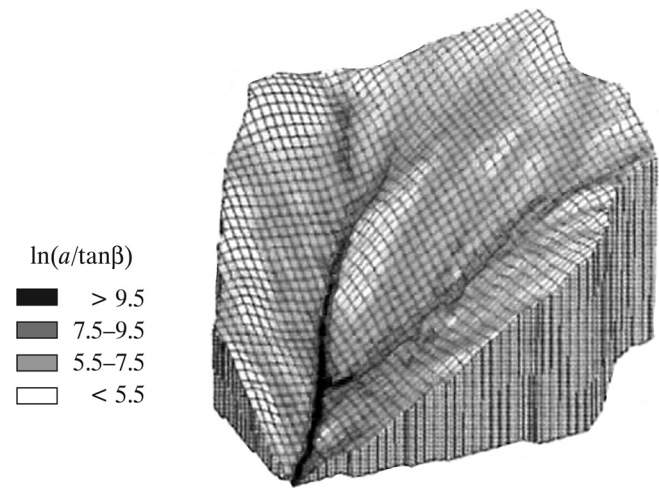
Dunne et al. (1975) have shown how the extent of source areas for saturation overland flow can be identified in the field, and Van de Greind and Engman (1985) reviewed approaches for identifying such areas via remote sensing. O’Loughlin (1981) developed generalized relations that give the extent of saturated zones as a function of hillslope gradient, planform geometry (diverging, planar, or converging), hydraulic conductivity, depth, and flow rate, as in figure 10.28.

10.4.2.3 Surface Detention (Depression Storage)

Land surfaces are highly irregular, with many depressions of varying size (microrelief) in which overland flow, however generated, collects. During water input, these depressions fill, spill, and merge, delaying and complicating the movement of overland flow toward streams. This phenomenon is called **surface detention** or **depression storage**.

Although long recognized, the phenomenon has been studied in detail only relatively recently (see references cited in Chu et al. 2013). Overall, the effect of surface detention is to delay the onset of event flow at the watershed outlet and to reduce event-flow

Figure 10.30 Distribution of the topographic index, Tl , for the Ringelbach Watershed, French Alps [Ambroise et al. (1996). Toward a generalization of the TOPMODEL concepts: Topographic indices of hydrological similarity. *Water Resources Research* 32:2135–2145, with permission of the American Geophysical Union].



volume by providing enhanced opportunities for evaporation and infiltration of overland flow. But because the process operates at small horizontal and vertical spatial scales and short time scales, it is difficult to measure and to develop general quantitative models. Consequently, surface detention is usually accounted for heuristically in rainfall-runoff models, as described in section 10.6.

10.4.3 Subsurface Flow

Discussion in section 9.5.3 makes it clear that regional ground-water flow is usually the source of streamflow between event responses (i.e., base flow). The water in base flow enters the drainage basin in the same rainfall and snowmelt events that produce event responses, but travels to the stream through ground-water reservoirs with residence times that are so large that short-term pulses of input are damped out. Here we examine mechanisms by which subsurface flow may move toward streams rapidly enough to generate event flow.

10.4.3.1 Flow in the Unsaturated Zone

Water in the unsaturated zone is under tension (i.e., less-than-atmospheric) pressure. Thus water cannot move from the unsaturated zone, including the tension-saturated zone, directly onto a seepage face (which is at atmospheric pressure) or into a stream (which is at greater-than-atmospheric pressure). Therefore,

The unsaturated zone cannot be a direct (proximal) source of streamflow.

However, the movement of infiltrated water through the unsaturated zone to the water table is a critical link in the land phase of the hydrologic cycle. Here we explore the nature of this link and its role in runoff generation.

In the discussion of infiltration in chapter 8, the ground surface was horizontal, the water-content contours were parallel to the surface, and the potential gradients driving flow were vertical. In the larger context of natural landscapes, infiltration takes place on slopes; downslope flow occurring between the ground surface and water table is called **interflow**. Under certain conditions, such flow can occur as (1) unsaturated Darcian flow through the soil matrix, or (2) as pipe flow in macropores that largely bypasses the unsaturated soil matrix.

10.4.3.1.1 Matrix (Darcian) Flow

Figure 10.31 shows the hydraulic-head contours during and following infiltration on a slope underlain by a homogeneous and isotropic soil. In the initial stages of water input, the wetting front remains essentially parallel to the surface (figure 10.31a); as infiltration continues, the near-surface hydraulic-head contours gradually rotate clockwise toward the horizontal (figure 10.31b). The flow direction is normal to the total-head contours; thus initial infiltration is normal to the slope, but becomes nearly vertical if the event continues long enough. These simulations indicate that significant downslope Darcian unsaturated flow does not occur during a storm or snowmelt event. Thus Darcian unsaturated flow does not appear to be a likely source of water to near-stream saturated zones during water-input events under most circumstances.

However, the study by Jackson (1992) and others show that a downslope component of drainage can emerge *following* a water-input event on deep homogeneous soils. After water input ceases, the near-surface head contours continue to rotate clockwise, ultimately becoming nearly normal to the surface (figure 10.31c, d), indicating downslope flow. This was confirmed in the experimental studies of Lv et al. (2013) and has been observed in field studies in upland watersheds in many regions (Hewlett and Hibbert 1963; Weyman 1970; Nutter 1975; Anderson and Burt 1977).

This phenomenon is strikingly illustrated in figure 10.32, which shows the drainage of an isolated 1 m ×

1 m column of homogeneous sandy clay loam soil extending 15 m on a 40° slope, with an outlet at the slope base. The soil was initially saturated and covered to prevent evaporation or water input. After 1.5 days the saturated zone had retreated to within a few cm of the outlet and flow into that zone came from unsaturated downslope flow. Note that discharge rates declined very rapidly in the first few days, but drainage persisted until the experiment was terminated at 145 days. The total change in water content over this period was relatively small, from about 0.50 at saturation to 0.38 at 145 days. Thus it is clear that unsaturated matrix flow can contribute to, and may be the

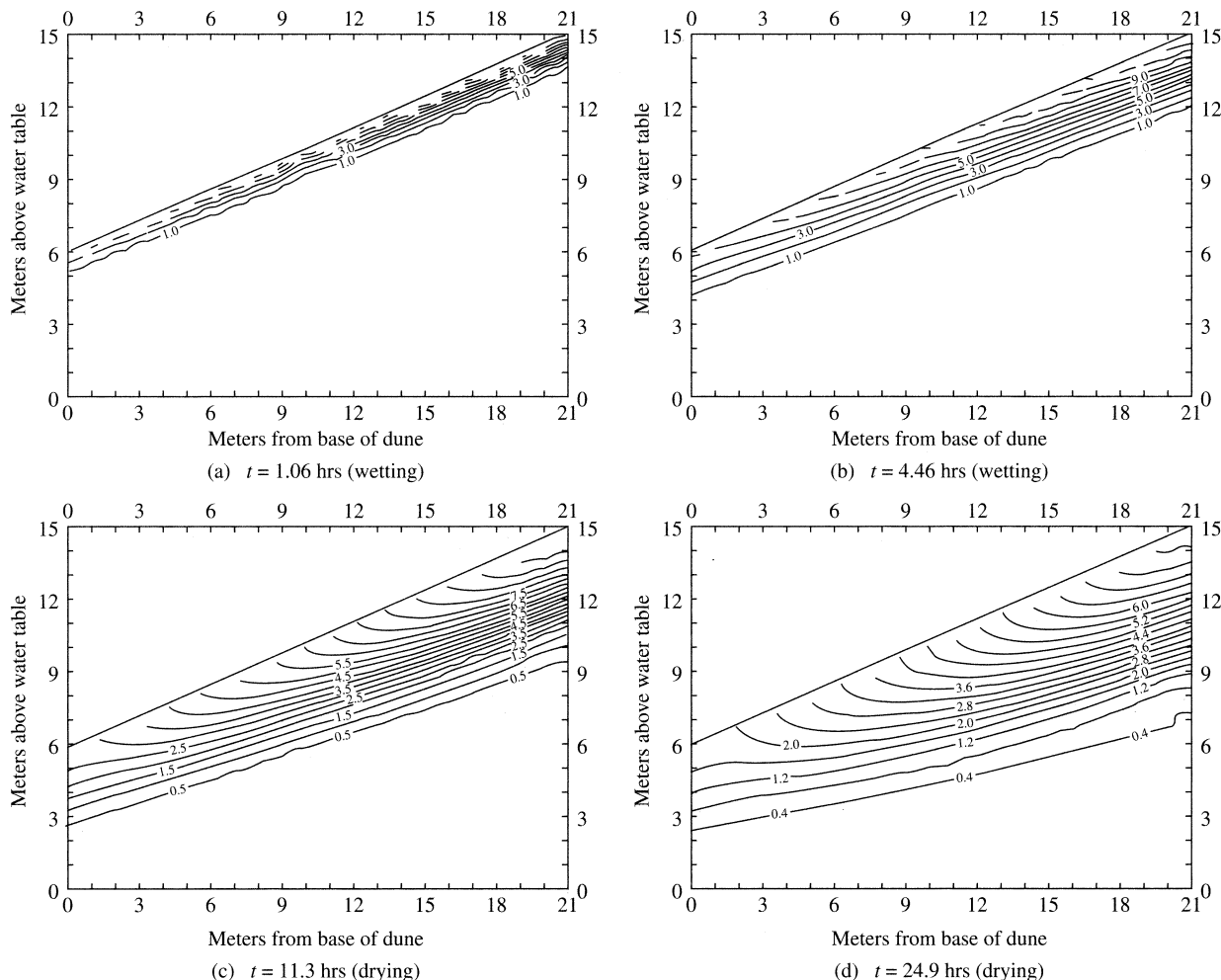
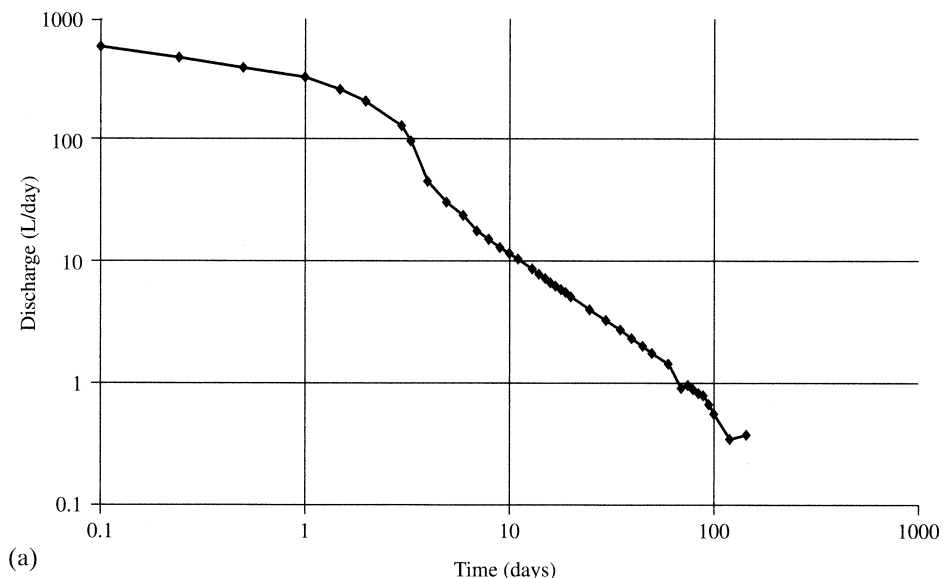


Figure 10.31 Modeled total-head contours in an isotropic soil draining after rainfall at a rate of 1 cm/hr for $0 < t < 5$ hr. (a) $t = 1.06$ hr; (b) $t = 4.46$ hr; (c) $t = 11.3$ hr; (d) $t = 24.9$ hr [Jackson (1992). Hillslope infiltration and lateral downslope unsaturated flow. *Water Resources Research* 28:2533–2539, with permission of the American Geophysical Union].

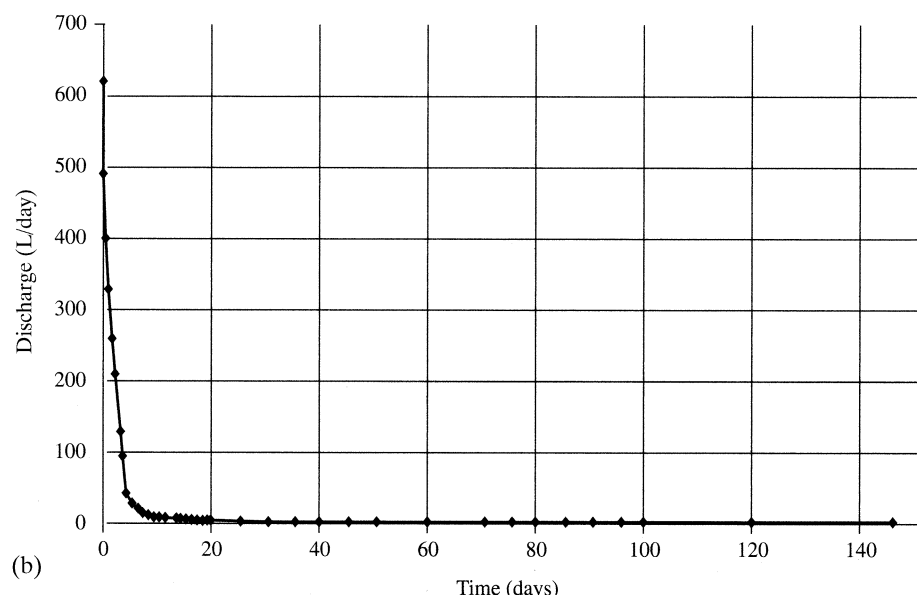
major source of streamflow recessions (base flow) in upland watersheds. A similar situation is shown in figure 10.33, which shows water-content and hydraulic-head contours measured after more than 30 days of drainage of a sloping soil mass, confirming the existence of a downslope-oriented hydraulic-head gradient and showing the development of a saturated wedge at the slope base.

10.4.3.1.2 Macropores and Preferential Flow

The simulations and experiments just described suggest that unsaturated Darcian flow through a homogeneous, isotropic soil matrix is seldom, if ever, rapid enough to link infiltrated water directly to event flow (Buttle and McDonald 2002). However, natural soils are not generally homogeneous or isotropic: biological activity (root growth and decay



(a)

**Figure 10.32**

Drainage for 145 days from a 1 m x 1 m column of sandy clay loam soil extending 15 m down a 40° slope. Soil was initially saturated and covered to prevent surface inputs or outputs. (a) Log-log plot. (b) Arithmetic plot [data from Hewlett and Hibbert (1963)].

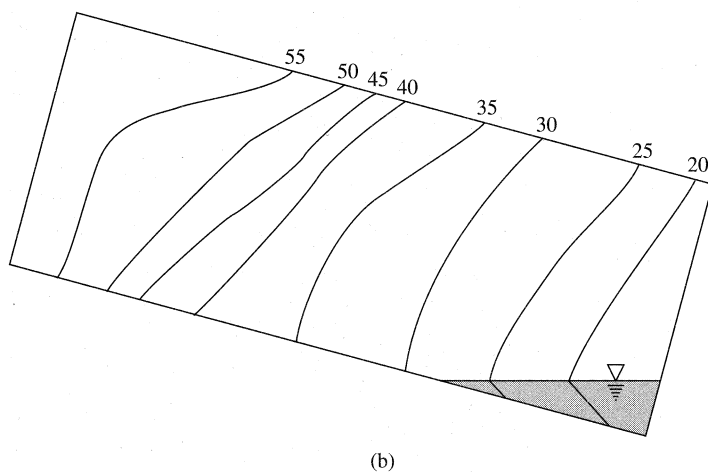
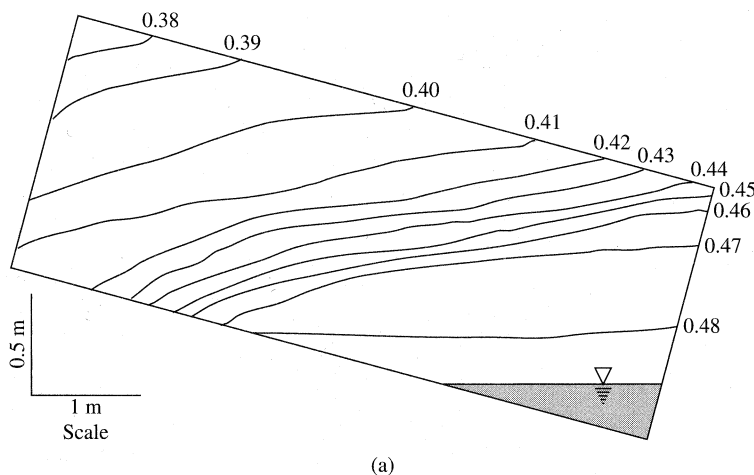


Figure 10.33 (a) Water content and (b) hydraulic-head distribution in a sloping slab after 749 hr of drainage. Slope = 15°. Note the saturated wedge at the slope base [Nutter (1975)].

and burrowing animals), desiccation, and frost action commonly occur near the surface to produce **macropores** (also called **soil pipes**), which are larger than the pores of the undisturbed soil matrix (figure 10.34). Flow through macropores is usually much more rapid than unsaturated or saturated Darcian flow through the soil matrix (Kirkby 1988), and is called **preferential flow** or **bypass flow**. Macropores can conduct water downslope considerable distances through otherwise unsaturated soils at velocities of several millimeters per second (Mosley 1979, 1982; Beven and Germann 1982, 2013).

Macropores are typically on the order of 3 to 100 mm in diameter and are interconnected to varying degrees (figure 10.34). They typically occur in the upper soil layers (the solum in figure 2.46), but may link to openings at depth that can extend over tens or hundreds of meters in fractured rock. In a de-

tailed study in a New Hampshire forest, Stresky (1991) found that more than 60% of the macropores were in the upper 0.15 m of the soil, and were created by live roots, decayed roots, and animal burrows. More than 70% of them were less than 20 mm in diameter—though conduits exceeding 25 mm were present. Macropore networks were generally oriented downslope and were interconnected over distances of at least tens of meters.

The soil matrix surrounding the macropores is often unsaturated, so the potential gradient causing preferential flow is not in equilibrium with the gradient in the soil matrix. For example, Beven and Germann (2013) reported that preferential flow can occur regardless of the antecedent soil-water content, and cited experiments in which 95% of infiltration occurred in pores wider than 0.25 mm, which constituted less than 0.5% of pore volume. Kirkby (1988)

presented a general relation between the minimum pore diameter that will cause bypassing and the pore (grain) size of the soil matrix (figure 10.35): In a clay soil (0.0001 mm), a pore of 0.1-mm diameter will act as a macropore; in a sand of 0.5-mm diameter, the minimum macropore size is about 1 mm. As noted by Ward (1984, p. 181), the functioning of a thatched roof provides an apt analogy for the functioning of preferential flow paths provided by macropores in an unsaturated matrix:

No hydrologist, having measured the infiltration characteristics of bundles of straw, would recom-

mend their use as roofing material. And yet, in even the heaviest rain, the building remains dry, no water runs over the thatch as “overland” flow, there is no “ground water” and no evidence of zones of “temporary saturation,” i.e. all the rainfall is evacuated along the narrow layer of the thatch itself. The thatched roof works because the alignment of straw imparts a preferential permeability along the stems and because the roof slopes.

Networks of visible macropores are often disconnected (figure 10.34), so continuous downslope flows require some mechanism for transmitting flow

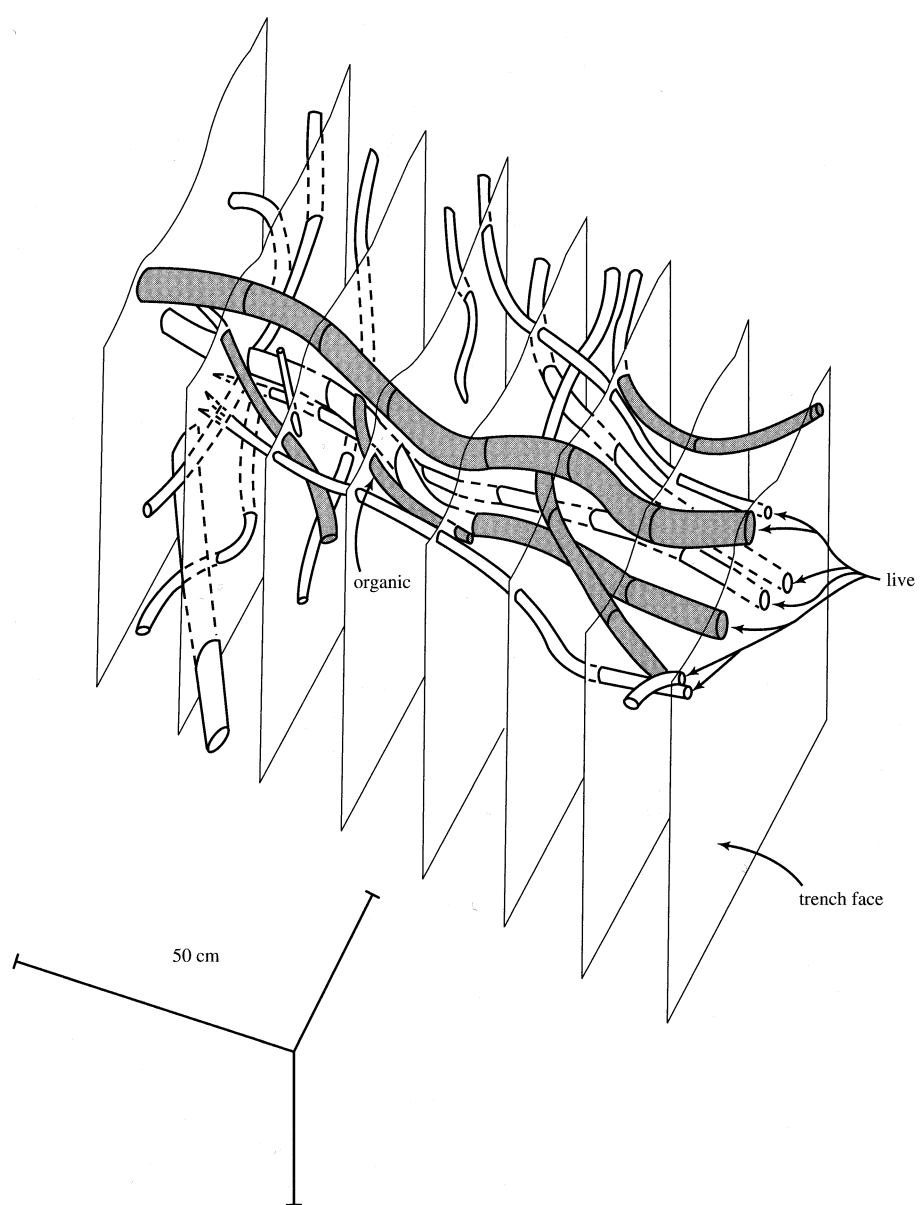


Figure 10.34 Macropores in an approximately 1-m portion of hillslope in a New Hampshire forest floor. Live-root and organic macropores are indicated; other macropores are decayed roots. For live-root macropores, the entire root is shown; flow occurs in the space between the roots and the soil matrix. Dark portions show tracer-dye paths [Stresky (1991)].

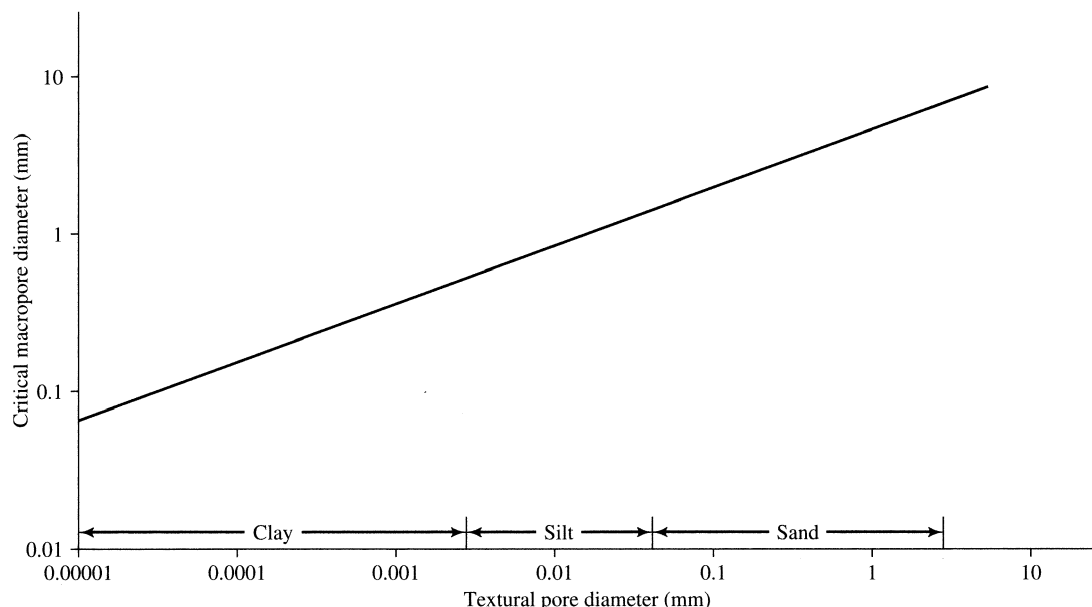


Figure 10.35 Relation between critical minimum macropore diameter that will allow bypassing and pore (grain) diameter of soil matrix. Thus for a fine sand (diameter = 0.1 mm), bypassing would occur in macropores exceeding about 1 mm diameter [reproduced from Kirkby (1988), Hillslope runoff processes and models, *Journal of Hydrology* 100:315–339, with permission from Elsevier].

from one part of the network to another. Where the soil is saturated, this happens via the propagation of pressure waves, such that an increase in pressure in an upslope macropore causes the displacement of stored water into a pathway farther downslope. This can also be a mechanism for the displacement of water from the matrix into an empty macropore (Beven and Germann 2013).

Preferential flows have been documented in numerous environments from the Amazon to Alaska, and are often an important part of hillslope runoff generation and, by implication, important in solute transport (Chappell 2010; Jones 2010; Beven and Germann 2013). Macropore flow has been found to contribute to event flow in northern Quebec (Roberge and Plamondon 1987), New Zealand (McDonnell 1990), Wales (Chapman et al. 1993), Denmark (Villholth et al. 1998), New Mexico (Newman et al. 1998), and in the humid tropics (Jones 2010). An entire issue of *Hydrological Processes* (volume 24, issue 12, 2010) was devoted to preferential flows. It is clear from these studies that macropores play an important role in delivering water input to streams in many regions, particularly forested areas; in some places, preferential flows may contribute up to 50% of event

flow (Jones 2010). Many studies indicate that their importance increases with the amount of rain or snowmelt in an event.

Because the number, orientation, size, and interconnectedness of macropores are highly dependent on local geology, soils, vegetation, and fauna, it is difficult to generalize about their importance or to simulate their effects in models. Ward's thatched-roof analogy emphasizes the contrast between preferential-flow processes and the traditional modeling of infiltration as an equilibrium process through a soil matrix via Darcy's law and the Richards equation, as in section 7.4.7. Recognizing this, Beven and Germann (2013, p. 8) argued that the widespread use of the Richards equation as a basis for modeling hill-slope hydrologic response is inappropriate, and called for a new approach that includes “the interaction between input variability, surface characteristics, antecedent conditions, and the generation of preferential flow in ways that reflect the (non-Richards) dynamics of . . . flow in a heterogeneous matrix. . . .” Attempts to model preferential flow have been made by Ormsbee and Khan (1989), Jones and Connally (2002), and Beckers and Alila (2004), among others (see Beven and Germann 2013).

10.4.3.2 Flow in the Saturated Zone

Model studies incorporating the ground-water flow equations lead to the conclusion that basinwide regional ground-water flow (as depicted, for example, in figures 9.5 and 9.6) cannot usually respond quickly enough to contribute to event response (Freeze 1974). However, field studies using various tracers have indicated that ground water can be a significant component of event response under some circumstances (see figures 9.33 and 10.19); such flow is called **subsurface event flow** or **subsurface storm flow**. These ground-water contributions to event flow must arise from mechanisms that quickly produce steep hydraulic gradients in materials of high hydraulic conductivity in near-stream areas. Such mechanisms are described here.

10.4.3.2.1 Flow from Near-Stream Ground-Water Mounds

Because the water table adjacent to streams in humid regions is near the surface, infiltration recharges ground water in near-stream areas before it does so at upslope locations. This can produce contributions to event flow by two mechanisms.

In **gradual ground-water-mound development**, recharge produces a mound, or ridge, that steepens the hydraulic gradient both toward and away from the stream (figure 10.26b). The steepened streamward gradient can produce a reasonably prompt and sustained contribution to streamflow if hydraulic conductivity is high enough.

Sudden ground-water-mound development involves rapid pressurization of the tension-saturated zone (capillary fringe) that extends above the water table. As noted, water under tension cannot flow to streams. However, laboratory and field studies (Abdul and Gillham 1984, 1989; Gillham 1984; Jayatilaka et al. 1996) show that when even a small amount of water percolates to the top of this zone, the menisci that maintain the tension are obliterated and the pressure state of the water is immediately changed from negative (tension) to positive (pressure) (figure 10.36). This phenomenon can thus produce an almost instantaneous rise in the near-stream water table (figure 10.37 on p. 495) to the top of the tension-saturated zone, forming a ground-water mound and inducing streamward ground-water flow. Note that the resulting streamflow contribution may greatly exceed the quantity of water input that induced it, and that event flow produced in this way is “old” water—water that fell in previous events.

As with saturation overland flow, subsurface event flow due to near-stream ground-water mounding is most likely to occur in watersheds with concave slopes and wide, flat valleys.

10.4.3.2.2 Flow from Shallow Saturated Layers (*The Sloping Slab*)

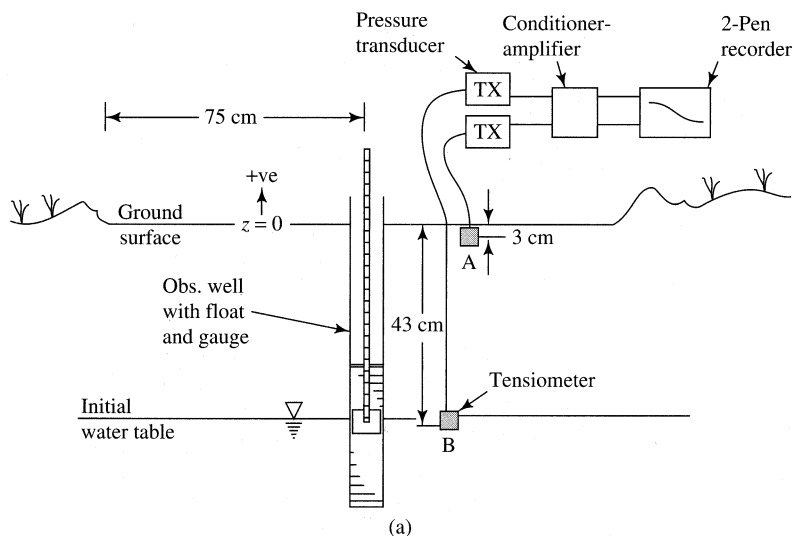
In many regions, hillslopes consist of a thin layer of permeable soil overlying relatively impermeable materials, or soils in which the hydraulic conductivity decreases markedly with depth. In these situations, infiltration and percolation of water input commonly produce a thin saturated zone that is not connected to a regional ground-water flow (i.e., a **perched water table**), and downslope flow in this zone can contribute to event response. This situation is often referred to as a **sloping slab**.

The time required for a saturated layer to begin forming in a sloping slab can be estimated by applying the same reasoning used to develop the Green-and-Ampt approach to modeling infiltration in shallow soils (section 8.4.3.6). We consider an initially unsaturated soil layer of uniform depth, hydraulic properties, and initial water content overlying a uniformly sloping impermeable base (figure 10.38 on p. 495). For these conditions, the time, T_u , required for a wetting front due to the complete infiltration of input at a constant water-input rate, p , to reach the base can be determined from equation (8.47):

$$T_u = \frac{(\theta_p - \theta_0) \cdot Y}{p \cdot \cos(\beta)}, \quad (10.29)$$

where θ_p is the soil-water content at which the hydraulic conductivity equals p , θ_0 is initial water content, Y is soil depth, β is the slope angle, and the cosine accounts for the fact that infiltration is vertical. Beven (1982a) showed how equation (10.29) can be modified to give T_u when hydraulic conductivity decreases with depth.

Beven (1981) reviewed the hydraulics of downslope saturated flows in a sloping slab (box 10.4 on p. 496). The simplest representation is called the **kinematic-wave approximation**, in which the flow paths and hydraulic gradient are assumed parallel to the slope [equations (10B4.8)–(10B4.10)]. This yields a water table that is a linear function of distance upslope, represented by the dashed line in figure 10.38. The solutions to the flow equations are developed in nondimensional form, in which the input rate is scaled to the slope and hydraulic conductivity to define the dimensionless input parameter λ :



(a)

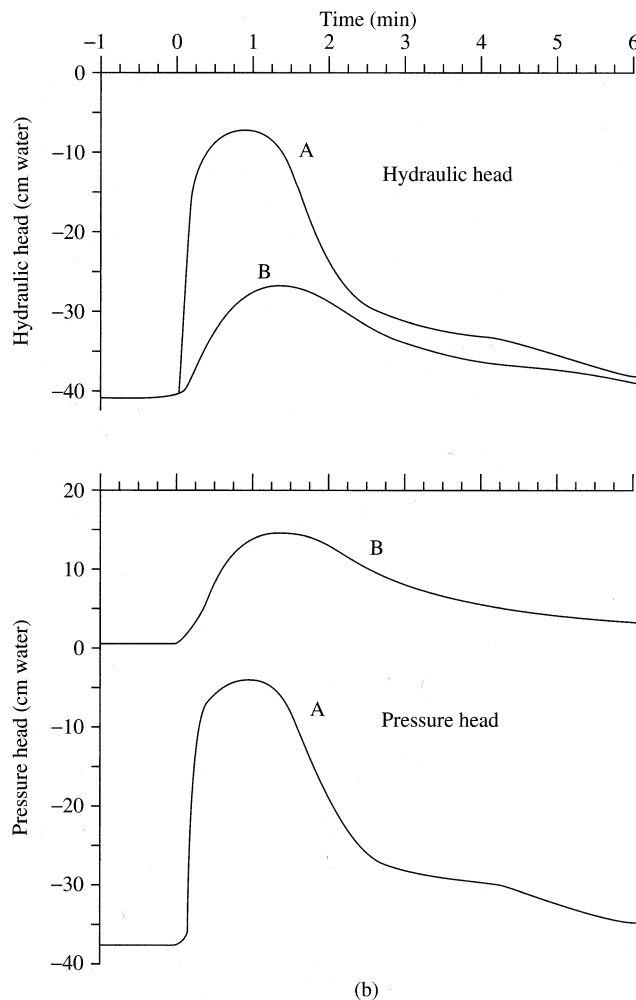


Figure 10.36 (a) Field instrumentation used to record rapid pressurization of the tension-saturated zone in a sandy soil. (b) Response of pressure head and total hydraulic head to sudden application of 3 mm of water to the surface in (a). [reproduced from Gillham (1984), *The capillary fringe and its effect on water-table response*, *Journal of Hydrology* 67:307–324, with permission from Elsevier].

$$\lambda \equiv \frac{4 \cdot p}{K_h \cdot \sin^2 \beta}. \quad (10.30)$$

Beven (1981) showed that for values of $\lambda < 0.75$, the runoff-generation hydrograph from a sloping slab can be well approximated by the kinematic-wave approximation. Figure 10.39 on p. 497 shows the combination of p/K_h and slope values for which $\lambda < 0.75$. It indicates that the kinematic-wave representation of the rising hydrograph is a good approximation for values of $p/K_h < 0.01$ on low slopes, and up to $p/K_h \approx 0.1$ on slopes near 45° . For values of $\lambda > 0.75$, runoff generated from a sloping slab must be modeled via the Dupuit–Forchheimer equations or the extended Dupuit–Forchheimer equations.

Here we explore analytical solutions for the sloping-slab hydrograph [i.e., the outflow at the base of the slab, $Q(0,t)$] under the kinematic-wave approximation, considering the hydrograph rise, equilibrium runoff (section 10.2.4), and the hydrograph recession separately:

Hydrograph Rise

For $\lambda > 0.75$, the hydrograph rise can be well approximated as a linear increase with time:

$$Q(0,t) = \frac{K_h}{\sin \beta \cdot S} \cdot p \cdot t; \quad t \leq \min(T_P, T_c), \quad (10.31)$$

where S is soil-storage coefficient, T_P is the storm duration, and T_c is the time of concentration (section

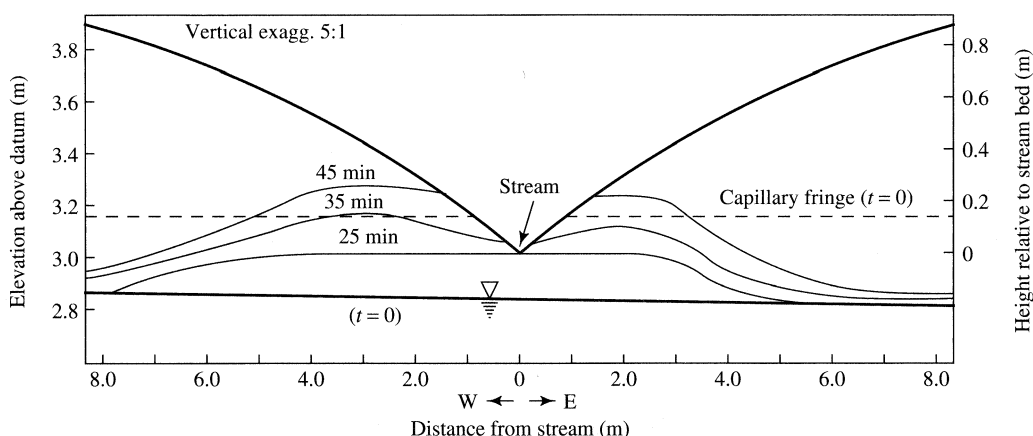


Figure 10.37 Response of near-stream water table due to pressurization of the capillary fringe during a simulated rain of $p = 2.0 \text{ cm/hr}$, $T_P = 50 \text{ min}$, in a sandy soil. Lines show position of water table at successive times after onset of rain [reproduced from Abdul and Gillham (1989), Field studies of the effects of the capillary fringe on streamflow generation, *Journal of Hydrology* 112:1–18, with permission from Elsevier].

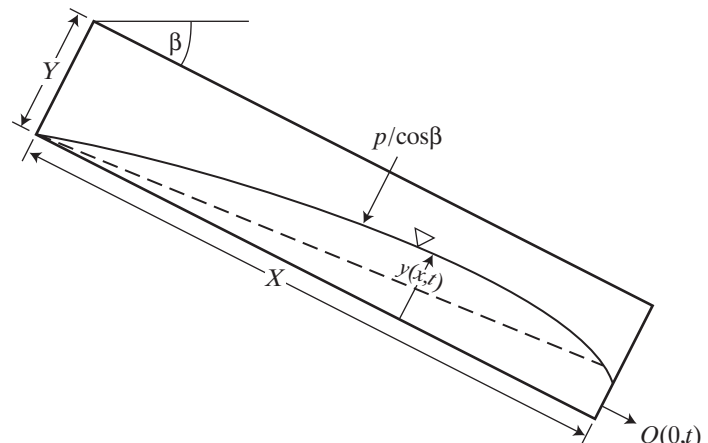


Figure 10.38 Definition diagram for hydraulics of sloping-slab drainage. The solid curve with the triangle is the water table given by the Dupuit model; the dashed line is the water table assumed in the kinematic-wave approximation. See box 10.4.

10.2.4) for the slope. The flow depth at the slope base is

$$y(0,t) = \frac{\cos\beta}{\sin^2\beta \cdot S} \cdot p \cdot t, \quad t \leq \min(T_P, T_{eq}). \quad (10.32)$$

Note that if $y(0,t) > Y$ the flow breaks out onto the surface and the surface flow must be separately accounted for; this happens if

$$\frac{\cos\beta \cdot p \cdot T_P}{\sin^2\beta \cdot S \cdot Y} > 1. \quad (10.33)$$

Box 10.4 Hydraulics of Sloping-Slab Flow

Beven (1981) explored hydraulic relations for sloping-slab flows, based on earlier work by Dupuit and Henderson and Wooding (1964). The flow geometry is shown in figure 10.38.

Basic Equations

Darcy's law is

$$q(x,t) = -K_h \cdot \frac{dh(x,t)}{dx}, \quad (10B4.1)$$

where $q(x,t)$ is Darcy velocity [$L T^{-1}$], $h(x,t)$ is hydraulic head [L], and K_h is hydraulic conductivity [$L T^{-1}$]. The one-dimensional conservation-of-mass (continuity) relation is

$$S \cdot \frac{\partial y(x,t)}{\partial t} = -\frac{\partial Q(x,t)}{\partial x} + \frac{p}{\cos\beta}, \quad (10B4.2)$$

where $y(x,t)$ is height of water table above the bed, S is soil-moisture-storage coefficient [1], $Q(x,t)$ is downslope flow rate per unit width [$L^2 T^{-1}$], and p is input rate per unit horizontal area [$L T^{-1}$].

To formulate the various flow representations, equation (10B4.1) is integrated over the saturated depth and substituted into equation (10B4.2), incorporating various assumptions about the flow paths and hydraulic gradient, as shown below.

Dupuit Assumptions (Dupuit–Forchheimer Equations)

Assuming horizontal flow paths and a hydraulic gradient equal to the slope of the water table yields

$$\text{Flow law: } Q(x,t) = -K_h \cdot y(x,t) \cdot \frac{\partial y(x,t)}{\partial x} \quad (10B4.3)$$

and

$$\begin{aligned} \text{Continuity: } S \cdot \frac{\partial y(x,t)}{\partial t} &= \\ K_h \cdot \frac{\partial}{\partial x} \left(y(x,t) \cdot \frac{\partial y(x,t)}{\partial x} \right) + \frac{p}{\cos\beta}. \end{aligned} \quad (10B4.4)$$

These relations have been found to be good representations of sloping-slab flow when $\tan\beta < 0.2$ ($\beta < 11.3^\circ$) and $X \gg Y$. They were applied to a horizontal aquifer in boxes 8.3 and 8.4.

Extended Dupuit–Forchheimer Equations

When slopes are steeper than 0.2, a better approximation of the flow is possible by assuming that the flow paths are parallel to the slope, so that

$$\frac{\partial h(x,t)}{\partial t} = \frac{\partial y(x,t)}{\partial x} \cdot \cos\beta - \sin\beta, \quad (10B4.5)$$

Flow law: $Q(x,t) =$

$$-K_h \cdot y(x,t) \cdot \left(\frac{\partial y(x,t)}{\partial x} \cdot \cos\beta - \sin\beta \right), \quad (10B4.6)$$

and

$$\begin{aligned} \text{Continuity: } S \cdot \frac{\partial y(x,t)}{\partial t} &= K_h \cdot \cos\beta \cdot \frac{\partial}{\partial x} \left(y(x,t) \cdot \frac{\partial y(x,t)}{\partial x} \right) - \\ K_h \cdot \sin\beta \cdot \frac{\partial y(x,t)}{\partial x} + \frac{p}{\cos\beta}. \end{aligned} \quad (10B4.7)$$

Kinematic-Wave Approximation

The simplest approach assumes that flowlines and the hydraulic gradient are parallel to the slope, so that Darcy's law can be written as

$$q(x,t) = K_h \cdot \tan\beta, \quad (10B4.8)$$

where $q(0,t)$ is the Darcy velocity at the base of the slope. Thus the outflow rate at the slope base is

$$\text{Flow law: } Q(x,t) = K_h \cdot \tan\beta \cdot y(x,t), \quad (10B4.9)$$

and

$$\begin{aligned} \text{Continuity: } S \cdot \frac{\partial y(x,t)}{\partial t} &= -K_h \cdot \sin\beta \cdot \frac{\partial y(x,t)}{\partial x} + \frac{p}{\cos\beta}. \end{aligned} \quad (10B4.10)$$

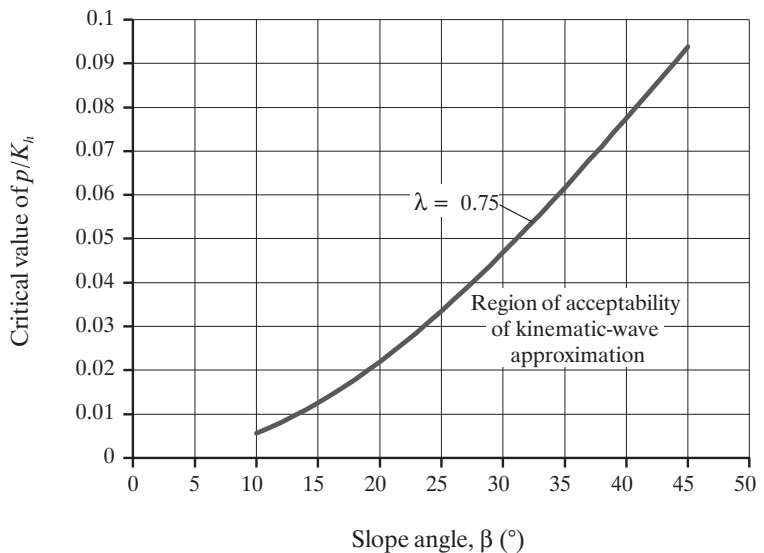


Figure 10.39 Combination of p/K_h and slope values for which $\lambda < 0.75$ and the kinematic-wave representation is a good approximation of runoff from a sloping slab.

Equilibrium Runoff

If input continues for a period exceeding the time of concentration (the time it takes water from the most distant part of the slope to travel to the outlet), the flow rate becomes constant and we have equilibrium runoff (figure 10.13). From equation (7.12), the velocity of the water in the slab, U , is

$$U = \frac{K_h \cdot \tan \beta}{S}, \quad (10.34)$$

so the time of concentration, T_c , is

$$T_c = \frac{S \cdot X}{K_h \cdot \tan \beta}. \quad (10.35)$$

If $T_p > T_c$, substitution of (10.35) into (10.32) gives the outflow height at equilibrium:

$$y(0, t) = \frac{\cos^2 \beta \cdot X}{\sin^3 \beta \cdot K_h} \cdot p; \quad T_{eq} < t < T_p. \quad (10.36)$$

Substituting this into (10.31) gives the equilibrium flow as

$$Q(0, t) = \frac{\cos \beta \cdot X}{\sin^2 \beta} \cdot p; \quad T_{eq} < t < T_p. \quad (10.37)$$

The flow continues at this rate until the storm ends and the recession begins.

Hydrograph Recession

During recession, flow from the slope is supplied by gravity drainage of the saturated zone. Note

from figure 10.38 that if equilibrium runoff does not occur, the kinematic-wave approximation assumes that this zone is triangular. Thus the continuity relation for the saturated portion of the slope during recession is

$$Q(0, t) = K_h \cdot y(0, t) \cdot \tan \beta \\ = -\frac{X \cdot (\phi - \theta_{fc})}{2} \cdot \frac{dy(0, t)}{dt}, \quad t > T_p, \quad (10.38)$$

Where ϕ is porosity and θ_{fc} is the field capacity of the soil. Integration of (10.38) leads to an exponential recession:

$$Q(0, t) = Q(0, T_p) \cdot \\ \exp \left[-\frac{2 \cdot K_h \cdot \tan \beta}{X \cdot (\phi - \theta_{fc})} \cdot (t - T_p) \right], \quad t > T_p. \quad (10.39)$$

Note that equation (10.39) is exactly the same as the recession for the linear-watershed model of box 10.3, with the characteristic time constant T^* equal to

$$T^* = \frac{X \cdot (\phi - \theta_{fc})}{2 \cdot K_h \cdot \tan \beta}. \quad (10.40)$$

Box 10.5 and figure 10.40 give an example application of these relations for a relatively rapidly draining (sandy) soil. Note that the recession is of long duration even for this relatively high-conductivity soil, consistent

Box 10.5 Example Calculations of Sloping-Slab Runoff

Here we give an example application of the analytical relations of sloping-slab runoff developed in section 10.4.3.2.2.

Table 10B5.1 Slope Properties

Slope Length, X (m)	Soil Thickness, Y (m)	Slope Angle, β (degrees)	Slope Angle, β (radians)	$\sin \beta$	$\cos \beta$	$\tan \beta$
30	1	32	0.559	0.530	0.848	0.625

Table 10B5.2 Soil Properties (Sand Soil)

Hydraulic Conductivity, K_h (m/hr)	Storage Coefficient, S	Porosity, ϕ	Field Capacity, θ_{fc}
0.5	0.25	0.4	0.1

Table 10B5.3 Storm Conditions

Rainfall Rate, p (mm/hr)	Storm Duration, T_p (hr)
25	1

- Calculate λ via equation (10.30) to verify that the situation is appropriately modeled via the kinematic-wave approximation:

$$\lambda = \frac{4 \cdot 0.025 \text{ m/hr}}{0.5 \text{ m hr} \cdot 0.530^2} = 0.712.$$

$0.712 < 0.75$, so kinematic-wave approximation appropriate.

- Calculate T_c via equation (10.35) to determine if equilibrium outflow occurs:

$$T_{eq} = \frac{0.25 \cdot 30 \text{ m}}{0.5 \text{ m hr} \cdot 0.625} = 24.0 \text{ hr} > T_p = 1.0 \text{ hr},$$

so equilibrium flow does not occur.

- Use equation (10.31) to calculate the outflow rate $Q(0,t)$ for $0 \leq t \leq T_p$:

$$Q(0,t) = \frac{0.5 \text{ m hr} \cdot 0.025 \text{ m hr}}{0.530 \cdot 0.25} \cdot t = 0.094 \text{ m}^2/\text{hr}^2 \cdot t.$$

- Use equation (10.33) to determine if breakout occurs

$$\frac{0.848 \cdot 0.025 \text{ m hr} \cdot 1 \text{ hr}}{(0.530)^2 \cdot 0.25 \cdot 1 \text{ m}} = 0.302 < 1,$$

so breakout does not occur.

- Use equation (10.39) to calculate recession flow:

$$\begin{aligned} Q(0,t) &= 0.0944 \text{ m}^2/\text{hr} \cdot \exp \left[-\frac{2 \cdot 0.5 \text{ m hr} \cdot 0.625}{30 \text{ m} \cdot (0.4 - 0.1)} \cdot t \right] \\ &= 0.0944 \text{ m}^2/\text{hr} \cdot \exp(0.0694 \text{ hr}^{-1} \cdot t). \end{aligned}$$

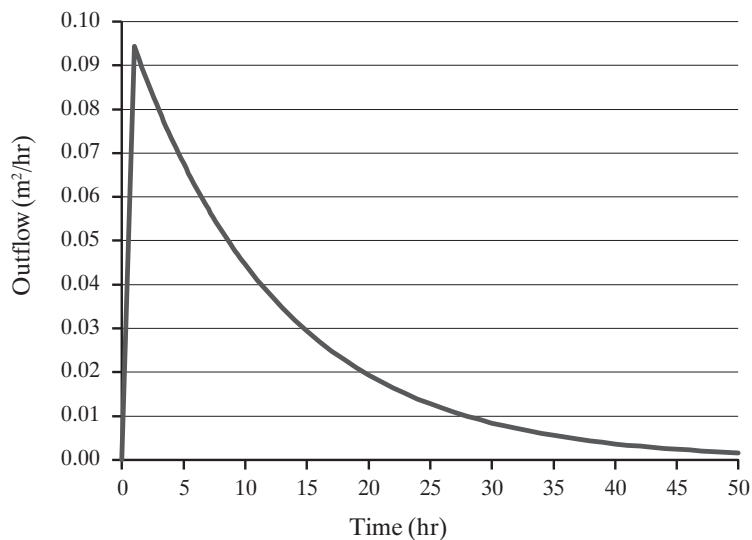


Figure 10.40 Hydrograph of kinematic-wave approximation of subsurface flow from a sloping-slab hillslope with slope $\beta = 32^\circ$ and a rapidly draining (sandy) soil ($K_h = 0.5 \text{ m/hr}^{-1}$, $S = 0.25$, $\theta_{fc} = 0.1$) for a rainfall of $p = 25 \text{ mm hr}^{-1}$ for 1 hr.

with the soil-drainage measurements shown in figure 10.32. Note also that this example does not include calculation of the descent of the wetting front to the impermeable base, which might introduce a significant lag in output. Studies by Freeze (1972b) and Beven (1982b) suggest that the response of even a relatively shallow, permeable, and steeply sloping slab to a relatively intense water-input rate is usually quite sluggish where percolation and downslope flow occur via Darcy's law through the soil matrix. However, rapid subsurface response to water input can occur on slopes containing macropores as described in section 10.4.3.1.2.

Sloan and Moore (1984) developed a model of flow from the base of a steeply sloping slab based on kinematic-wave concepts. Ormsbee and Khan (1989) incorporated that approach into a watershed model that explicitly considers both macropore and Darcian matrix flow. Application of the new model to selected watersheds produced good correlations between the observed and predicted watershed responses (runoff volume, peak discharge, and time to peak). However, model parameters varied seasonally, and they concluded that the runoff-response mechanisms are highly influenced by seasonal changes in surface and subsurface watershed characteristics.

10.4.4 Overview of Hillslope Processes

Understanding of watershed event-response mechanisms has been evolving rapidly since the mid-1960s, and has accelerated in recent years as studies based on chemical and isotopic flow separations (section 10.3) and detailed measurements of soil and

ground water are conducted in new environments. Bonell (1993) provided a comprehensive review of studies investigating runoff mechanisms in forests, and table 10.5 summarizes a sample of such studies.

A recent study by Inamdar et al. (2013) provides insight into the temporal changes in runoff sources and processes that are reflected in the wide range of event-flow response seen in most watersheds (as in figures 10.10 and 10.11). EMMA was used to determine runoff mixing patterns for base flow and 42 storms on a small forested watershed in the Piedmont region of Maryland. They were able to identify 11 runoff sources: precipitation, throughfall, stemflow, litter leachate, wetland soil water, soil water, shallow ground water, ground-water seeps, hyporheic (subchannel) water, riparian ground water, and deep ground water. Base-flow chemistry of stream waters was similar to ground-water seeps. Event runoff was attributed to contributions from surficial sources (precipitation, throughfall, stemflow, and litter leachate) on the rising limb of the hydrograph and to soil and shallow ground-water sources on the recession limb. As shown in figure 10.41 on p. 501, the shapes of the storm-event hysteresis loops (wide versus tight, quasi-linear patterns) varied with hydrologic conditions from wet, hydrologically well-connected conditions to a dry, disconnected state.

Table 10.6 and figure 10.42 on p. 502 (the "Dunne diagram"; Dunne 1978) summarize the current understanding of the soil/geologic, topographic, vegetative, and climate conditions that favor the various mechanisms of runoff generation. The Hortonian-

overland-flow mechanism that dominated hydrologic thinking and modeling beginning in the 1930s is now known to be common only on natural hillslopes in semiarid to arid regions and on human-disturbed and

impermeable areas, where rainfall rates commonly exceed surface infiltration capacities (figure 10.25). Hortonian overland flow can also occur on ground rendered impermeable by soil frost.

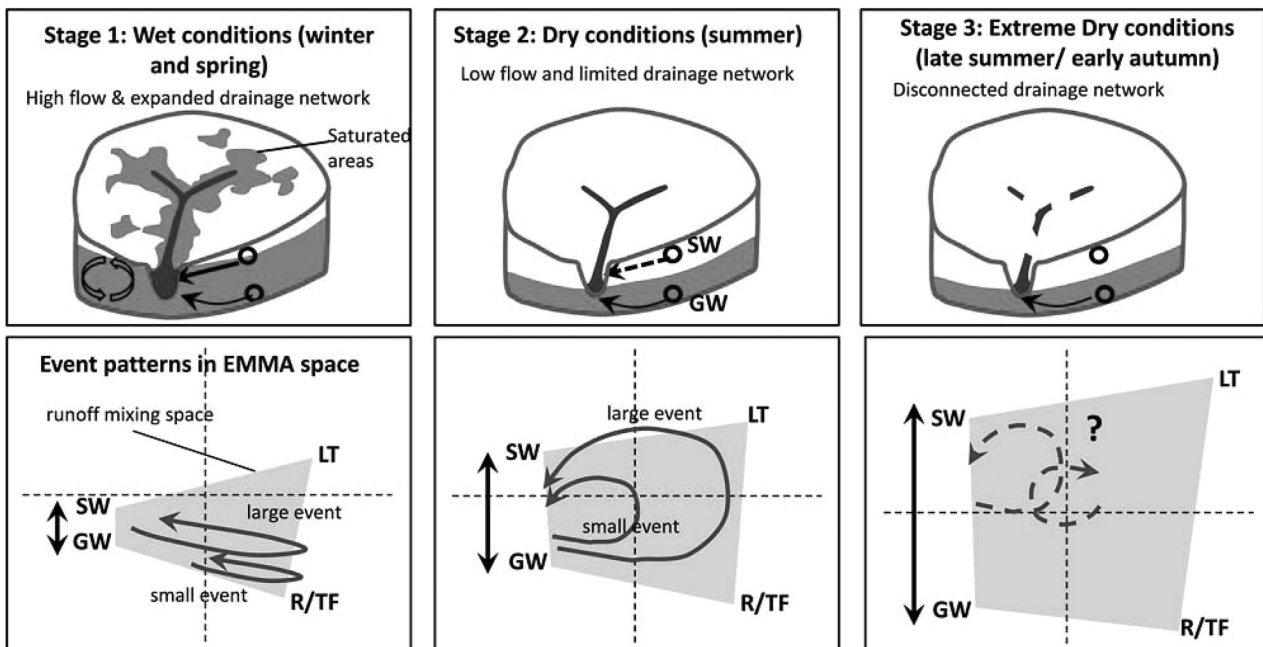
Table 10.5 A Sampling of Field Studies of Runoff Mechanisms.

Location	Mechanisms	Separation Basis	Source
Upland forest, Pennsylvania	Ground-water mounding; pressurization of capillary fringe; minor channel precipitation	^{18}O	Swistock et al. (1989)
Upland forest, Georgia	Sloping slab (mineral soil); sloping slab (organic soil); ground-water mounding	Six chemical constituents	Hooper et al. (1990)
Gently sloping forested hillside, Australia	Sloping slab (macropores)	^2H ; Cl^{-1}	Leaney et al. (1993)
Coastal Plain, Virginia	Saturation overland flow	Cl^{-1}	Eshleman et al. (1993)
Forested swamp, Ontario, Canada	Saturation overland flow; ground water (macropore flow)	^{18}O , Cl^{-1} , Li^{+1}	Waddington et al. (1993)
Forested upland, deep soils, Tennessee	Bedrock (dolomite) ground water; ground-water mounding; sloping slab	Flow measurement; Ca , SO_4	Mulholland (1993)
Upland unforested watershed, Scotland	Hortonian overland flow; sloping slab; ground water	ANC	Giusti and Neal (1993)
Forest and pasture watershed, Switzerland	Saturation overland flow; ground water; Hortonian overland flow	^{18}O	Jordan (1994)
Upland forest, Virginia	Saturation overland flow; subsurface flow	^{18}O , Cl^{-1}	Bazemore et al. (1994)
Tropical rain forest, Australia	Saturation overland flow; sloping slab; ground-water mounding	K^{+1} , ANC, ^{18}O , DOC	Eisenbeer et al. (1995)
Shallow-soil forest, Canadian Shield	Saturation overland flow; sloping slab		Peters et al. (1995)
Mixed forest, New Brunswick, Canada	Ground water	Conductivity, alkalinity, pH, Na^{+1} , Mg^{+2} , Ca^{+2}	Caissie et al. (1996)
Unforested permafrost watershed, northern Alaska	Water tracks ^a	Conductivity, ^{18}O	McNamara et al. (1997)
Steep forested slope, Japan	Sloping slab	Flow measurement; tensiometers	Tani (1997)
Catskill Mountains, New York	Sloping slab; ground-water mounding	Several solutes	Evans et al. (1998)
Steep, forested watershed, Maryland	Subsurface flow; channel precipitation	^2H , ^{18}O , Cl^{-1} , SiO_2 , Na^{+1}	Rice and Hornberger (1998)

ANC = acid-neutralizing capacity

DOC = dissolved organic carbon

^aSubsurface "channels" of enhanced soil moisture that conduct flow directly downslope to streams.



- Near-surface groundwater results in greater solute mixing and similar soil water (SW) and groundwater (GW) chemistry.
- Runoff mixing space is constrained.
- Mixing loops are tight and linear with greater expression of surficial sources.

- Dry catchment conditions results in greater chemical separation in potential end-members.
- Runoff mixing space expands.
- Mixing loops are wider. Large events produce bigger loops.

- Extremely dry conditions lead to hydrologic disconnectivity in the catchment.
- Mixing space expands further.
- Mixing loops show complex and mixed responses without influence of any specific end-member, especially, if the event is not large enough to re-establish hydrologic connectivity.

End-members:

SW- soil water LT - litter leachate
 GW- groundwater TF - throughfall
 R- precipitation

Figure 10.41 Conceptual model illustrating how end-member chemistry, extent of mixing space, and storm-event hysteresis loops evolve as a watershed transitions from a wet, hydrologically well-connected system (stage 1) to a very dry, disconnected state (stage 3) [Inamdar et al. (2013)]. Temporal variation in end-member chemistry and its influence on runoff mixing patterns in a forested, Piedmont catchment. *Water Resources Research* 49, with permission of the American Geophysical Union].

In most humid forested watersheds a very large proportion of rain and snowmelt usually infiltrates, and response hydrographs are dominated by subsurface flow supplemented to varying extents by saturation overland flow. The relative importance of the various subsurface mechanisms is determined by watershed geology, soils, topography, and the amount, intensity, and spatial and temporal distribution of water input, but the exact mechanism that contributes the subsurface flow is often unclear. Whatever the mechanism, it is widely accepted that the water that gives rise to response hydrographs usually comes from only a limited portion of the topographi-

cally defined watershed, that this contributing area generally varies strongly as a function of watershed wetness, and that in many cases much of the event response consists of “old” water.

The concepts of the Dunne diagram were explored quantitatively by Mirus and Loague (2013) to provide deeper insight into watershed processes. Using a well-tested, process-based model of coupled surface and subsurface flow, they applied 140 simulation scenarios of varying rainfall intensity and amount to four actual small watersheds with a range of permeability contrasts, soil-characteristic curves, and topography. They found that the processes by which runoff

begins and ends are defined by the relative rates of rainfall, infiltration, lateral flow convergence, and storage dynamics within variably saturated soil layers. Saturated hydraulic conductivity has the strongest influence on runoff generation, while porosity, antecedent soil wetness, and soil-characteristic curves have a lesser but significant influence on the available storage in the unsaturated zone and, subsequently, on

surface runoff response. Their results also quantitatively confirm the importance of topography on surface runoff: Hillslope gradients exert a very strong control on lateral drainage through permeable soil layers, and topographic convergence and average slope influence the transition between subsurface storm flow and saturation overland flow (figures 10.29 and 10.30).

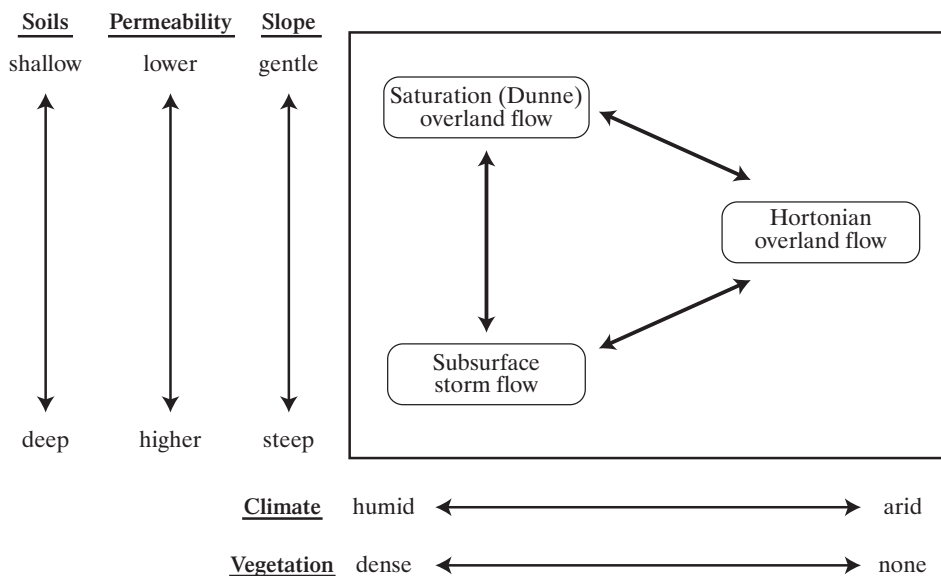


Figure 10.42 The Dunne diagram summarizes the soil/geologic, topographic, vegetative, and climate conditions that favor the various mechanisms of runoff generation [adapted from Mirus and Loague (2013)]. How runoff begins (and ends): Characterizing hydrologic response at the catchment scale. *Water Resources Research* 49, with permission of the American Geophysical Union].

Table 10.6 Environmental Factors Favoring Hillslope Event-Response Mechanisms.

Mechanism	Soils/Geology	Water Table	Topography	Vegetation	Water-Input Rate ^a
Hortonian overland flow	Low surface K_h .	Deep	Steep slopes	Absent to sparse	High
Saturation overland flow	Slopes: High surface K_h , decreasing gradually or abruptly at shallow depth; conditions of figure 10.28. Valley bottoms: Low to high K_h .	Near surface	Concave, convergent slopes; wide valleys	Absent to abundant	Low to high
Ground-water mounding	Slopes: Deep soils with high surface K_h . Valley bottoms: High K_h . Silty soils enhance flow from pressurized capillary fringe.	Slopes: Deep Valley bottoms: Near surface	Concave slopes, wide valleys	Absent to abundant	Low to moderate
Perched ground water (sloping slab)	Slopes: High surface K_h , decreasing gradually or abruptly at shallow depth; macropores present.	Absent to present in high K_h layer	Steep slopes; straight to convex	Absent to abundant	Low to moderate

K_h = saturated hydraulic conductivity

^aRelative to K_h .

Figure 10.43 quantitatively summarizes the results of Mirus and Loague (2013) on the Dunne diagram. On a given watershed, rainfall depth largely controls the transition from subsurface storm flow to saturation overland flow, and rainfall intensity largely controls the occurrence of Hortonian overland flow, as expected (figure 10.25). Surface runoff (filled dots in figure 10.43) can occur over the entire range of rainfall-intensity values, but occurs only above a minimum value of rainfall depths. This suggests that the Hortonian and saturation overland flow mechanisms are end members of a continuum of subsurface-controlled runoff-generation processes, while subsurface stormflow and saturation overland flow are competing mechanisms.

10.5 Channel Processes

10.5.1 Hydraulic Relations

10.5.1.1 Basic Equations

As described in section 10.2.2, the event-flow hydrograph is increasingly modified as the flood wave travels through the stream network due to (1) the varied timing and amounts of inflows and outflows and (2) intrinsic hydraulic effects due to the wave-like nature of the hydrograph (figure 10.4), modified by changes in channel resistance and geometry. These effects can be seen in the following basic equations of one-dimensional (downstream) open-channel flow: the conservation of mass:

$$\frac{\partial Q}{\partial x} = \frac{\partial A}{\partial t} + q_L; \quad (10.41)$$

Figure 10.43 Summary of results for 140 simulation scenarios plotted on a quantitative version of the Dunne diagram. The x-axis is a dimensionless rate term; the y-axis a dimensionless storage term. DOF = Dunne (saturation) overland flow; HOF = Hortonian overland flow; SSSF = subsurface storm flow. Each of the four watersheds (R5, TW, C3, CB) is represented by a different symbol, numbers in parentheses are average slopes along stream channels. Closed and open symbols indicate the occurrence and absence of surface runoff, respectively [Mirus and Loague (2013)]. How runoff begins (and ends): Characterizing hydrologic response at the catchment scale. *Water Resources Research* 49, with permission of the American Geophysical Union].

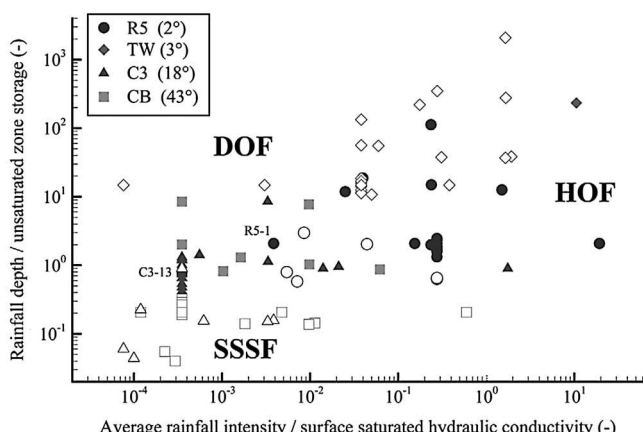
and the conservation of energy, which is incorporated into a flow equation analogous to Darcy's law:

$$Q = \frac{g^{1/2}}{\xi} \cdot A \cdot y^{1/2} \cdot \left[\zeta - \frac{\partial y}{\partial x} - \frac{u}{g} \cdot \frac{\partial u}{\partial x} - \frac{1}{g} \cdot \frac{\partial u}{\partial t} \right]^{1/2}, \quad (10.42)$$

where Q is streamflow rate [$L^3 T^{-1}$], q_L is lateral inflow rate per unit channel length [$L^2 T^{-1}$], g is gravitational acceleration [$L T^{-2}$], ξ is channel resistance [1], A is the cross-sectional area of the flow [L^2], y is flow depth [L], ζ is channel slope [1], x is channelwise distance [L], u is average flow velocity [$L T^{-1}$], and t is time [T]. (See Dingman 2009 for derivation of these relations.)

In equation (10.41), we see that subsurface, surface, and tributary inflows ($q_L > 0$) increase discharge in the downstream direction. Conversely, if the stream rises above its banks and there are outflows onto the floodplain ($q_L < 0$), the discharge tends to decrease downstream.

The intrinsic hydraulic effects are represented in the term in brackets in equation (10.42), which is the energy gradient driving the flow. To see this, we can ignore the last two terms, which are usually much smaller than ζ and $\partial y / \partial x$ (Dingman 2009), and consider the response hydrograph as the flood wave shown in figure 10.4: On the rising limb of the wave, depth decreases downstream ($\partial y / \partial x < 0$), so that the gradient driving the flow is greater than the channel slope, tending to accelerate the flow; on the recession limb depth increases downstream ($\partial y / \partial x > 0$), so the total gradient is less than the slope, tending to slow the flow. These two effects combine to flatten the flood wave, so that the hydrograph usually becomes



smoother and peak flows per unit watershed area tend to decrease and become delayed as the wave travels downstream (as in figure 10.5).

10.5.1.2 Uniform Flow

Flow in stream channels is often approximated by assuming **uniform flow**, i.e., that the last three terms in the brackets in equation (10.42) are small relative to channel slope, ζ , so that

$$Q = \frac{g^{1/2}}{\xi} \cdot A \cdot y^{1/2} \cdot \zeta^{1/2}, \quad (10.43a)$$

or, since $Q/A = u$,

$$u = \frac{g^{1/2}}{\xi} \cdot y^{1/2} \cdot \zeta^{1/2}. \quad (10.43b)$$

The value of ξ depends essentially on channel roughness and irregularity, and is difficult to estimate quantitatively (Dingman 2009). The most common practice is to characterize resistance as

$$\xi = \frac{g^{1/2} \cdot n_M}{\epsilon \cdot y^{1/6}}, \quad (10.44)$$

where n_M is called **Manning's roughness factor** [1] and ϵ is a unit conversion factor [$L^{1/3} T^{-1}$] ($\epsilon = 1 \text{ m}^{1/3}/\text{s}$ for SI units). The value of n_M is usually estimated by comparison with photographs of channels with measured n_M values (Barnes 1967; Hicks and Mason 1991; Dingman 2009).

10.5.1.3 Flood-Wave Velocity

It can be shown from equation (10.41) that the velocity of a flood wave, U , is given by

$$U = \frac{1}{w} \cdot \frac{\partial Q}{\partial y}, \quad (10.45)$$

where w is stream width (see Dingman 2009). Noting that $A = w \cdot y$, equation (10.43a) can be written as

$$Q = \frac{g^{1/2}}{\xi} \cdot w \cdot y^{3/2} \cdot \zeta^{1/2} \quad (10.46)$$

so that

$$\frac{\partial Q}{\partial y} = \frac{3}{2} \cdot \left(\frac{g^{1/2} \cdot w \cdot \zeta^{1/2} \cdot y^{1/2}}{\xi} \right). \quad (10.47)$$

Substituting equations (10.43) and (10.47) into equation (10.45) yields

$$U = \frac{3}{2} \cdot u. \quad (10.48)$$

Thus we have the interesting result that a flood wave travels with a velocity about 1.5 times that of the water itself.

Equations (10.46)–(10.48) are valid for flood waves that remain within the channel and can be considered to have a single representative average velocity. However, the relation between flow velocity and flood-wave velocity may be altered when a flood overtops the channel banks and inundates the floodplain. Typically the velocities of the overbank portions of a flow are much lower than in-channel flows because they are shallower and encounter much higher resistance due to vegetation. Referring to figure 10.44, we can rewrite equation (10.48) as

$$U = \frac{3}{2} \cdot \frac{U_{LB} \cdot w_{LB} + U_C \cdot w_C + U_{RB} \cdot w_{RB}}{w_{LB} + w_C + w_{RB}}, \quad (10.49)$$

where the subscripts LB and RB refer to the left and right overbank portions of the flow and C to the central channel. If the floodplain velocities U_{LB} and U_{RB} are negligible, equation (10.49) becomes

$$U = \frac{3}{2} \cdot \frac{U_C \cdot w_C}{w_{LB} + w_C + w_{RB}} = \frac{3}{2} \cdot \frac{U_C \cdot w_C}{w}. \quad (10.50)$$

Because w_C/w is less than 1, equation (10.50) shows that the flood-wave velocity U will be less than 1.5 times the channel velocity; and if $w_C/w < 2/3$, the flood-wave velocity will be less than the central channel velocity. Thus by providing areas for storage of water as a flood wave moves downstream, floodplains reduce the velocity of the flood wave. And, be-

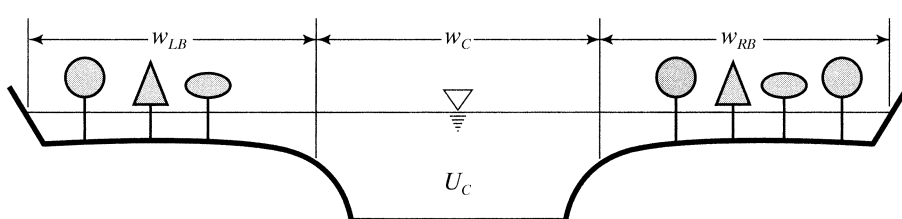


Figure 10.44 Definitions of terms used in deriving effects of overbank flows on flood-wave velocity [equations (10.49) and (10.50)] [adapted from Gray and Wigham (1970)].

cause the water spreads over the floodplain, they also reduce the height of the flood peak [i.e., there is lateral *outflow* so that q_L in equation (10.41) is negative].

10.5.2 Simple Streamflow Routing

Streamflow routing is the computational procedure for modeling the modification of hydrographs traveling through the stream network. The **outflow hydrograph** at the downstream end of a stream segment (“reach”) is predicted, given an **inflow hydrograph** for the upstream end of the reach, the hydraulic characteristics of the reach, and a **lateral-inflow hydrograph**. The most general approaches to this problem are based directly on discretization of equations (10.41) and (10.42). However, such approaches are generally time-consuming and data-intensive, and engineers have developed simpler routing methods that can usefully model the movement of flood waves under many conditions. In order to get a basic understanding of the hydraulic factors that affect response hydrographs, we explore the simplest of these methods. Gupta et al. (1979), Weinman and Laurenson (1979), and Nwaogazie and Tyagi (1984) discussed more elaborate routing methods.

The **convex routing method** is based on very simplified versions of equations (10.41) and (10.42) applied to a stream reach of a specified length (X), constant slope (ζ), width (w), and resistance (ξ). A hydrograph of inflow at the upstream end of the reach, QI_t , as a function of time, t , is also specified. (A lateral-inflow hydrograph may be specified as well.) The conservation-of-mass relation is written in discrete form as

$$QI_t - QO_t = \frac{V_{t+1} - V_t}{\Delta t}, \quad (10.51)$$

where QO_t is the rate of outflow from the reach at time t , V_t is the volume of water stored in the reach at time t , and $t_{i+1} = t_i + \Delta t$. The dynamic relation of equation (10.42) is written for the outflow in very simple form:

$$QO_t = \frac{1}{T^*} \cdot V_t, \quad (10.52)$$

where T^* is the time it takes a flood wave to travel through the reach, i.e.,

$$T^* = \frac{X}{U}, \quad (10.53)$$

where U can be estimated from the reach properties via equations (10.43b), (10.44), (10.48), and, if appropriate, (10.49).

Equation (10.52) portrays the reach as a **linear reservoir**, as was done for the watershed model of box 10.3. Real stream reaches are not strictly linear reservoirs, but equation (10.52) captures the most basic aspects of the storage-outflow relation and is mathematically tractable. The model is implemented by selecting the **routing time step**, $\Delta t \leq T^*$, which defines a **routing coefficient**, CX , where

$$CX \equiv \frac{\Delta t}{T^*}. \quad (10.54)$$

Substitution of equation (10.53) into (10.52) yields

$$QI_t - QO_t = \frac{T^* \cdot (QO_{t+1} - QO_t)}{\Delta t}, \quad (10.55)$$

and incorporating (10.54) and solving for QO_{t+1} gives the routing equation:

$$QO_{t+1} = CX \cdot QI_t + (1 - CX) \cdot QO_t. \quad (10.56)$$

Note that an initial value, QO_0 , must be specified.

The value of CX determines the degree to which flow through the reach reduces and delays the peak (figure 10.45a): If $CX = 1$, the outflow at the end of a time step equals the inflow at the end of the preceding step, and the flood wave travels through the reach at the velocity U but does not change shape during transit. Such motion is called **purely translatory**. From equations (10.43b), (10.44), (10.48), (10.53), and (10.54) we find

$$CX = \frac{1.5 \cdot \varepsilon \cdot y^{2/3} \cdot \zeta^{1/2} \cdot \Delta t}{n_M \cdot X}, \quad (10.57)$$

so that flatter slopes, lower flow depth, and higher resistance reduce the speed of the flood wave and increase the value of CX , which increases peak flattening and delay. Box 10.6 and figure 10.45b show how the convex routing process is carried out in practice.

10.6 Rainfall-Runoff Modeling

Largely because of the need to predict floods in the absence of detailed field data, engineering hydrologists have developed rainfall-runoff models. Using the terminology of appendix F (table F.1),

A **rainfall-runoff model** is a conceptual, lumped simulation model applied to a watershed to estimate the streamflow hydrograph in response to a specified rainfall event.

In this section we introduce some of the basic considerations involved in developing rainfall-runoff (RF-RO) models and introduce three models that have been widely used for runoff prediction. Although these heuristic models do not incorporate explicit simulations of the hydrologic processes we have examined in this book, they have value as quantitative abstractions of the runoff-producing process (section 10.2) as well as potential for practical application. Further detailed discussion of rainfall-runoff models can be found in the review by Pilgrim and Cordery

(1992) and in the many textbooks on engineering hydrology (e.g., Ponce 1989; McCuen 1998). More elaborate models used for flood forecasting and for design of large structures were reviewed by DeVries and Hromadka (1992) and Lettenmaier and Wood (1992).

10.6.1 Runoff Processes and Rainfall-Runoff Models

Ideally, one might assume that RF-RO models should simulate the physical processes by which wa-

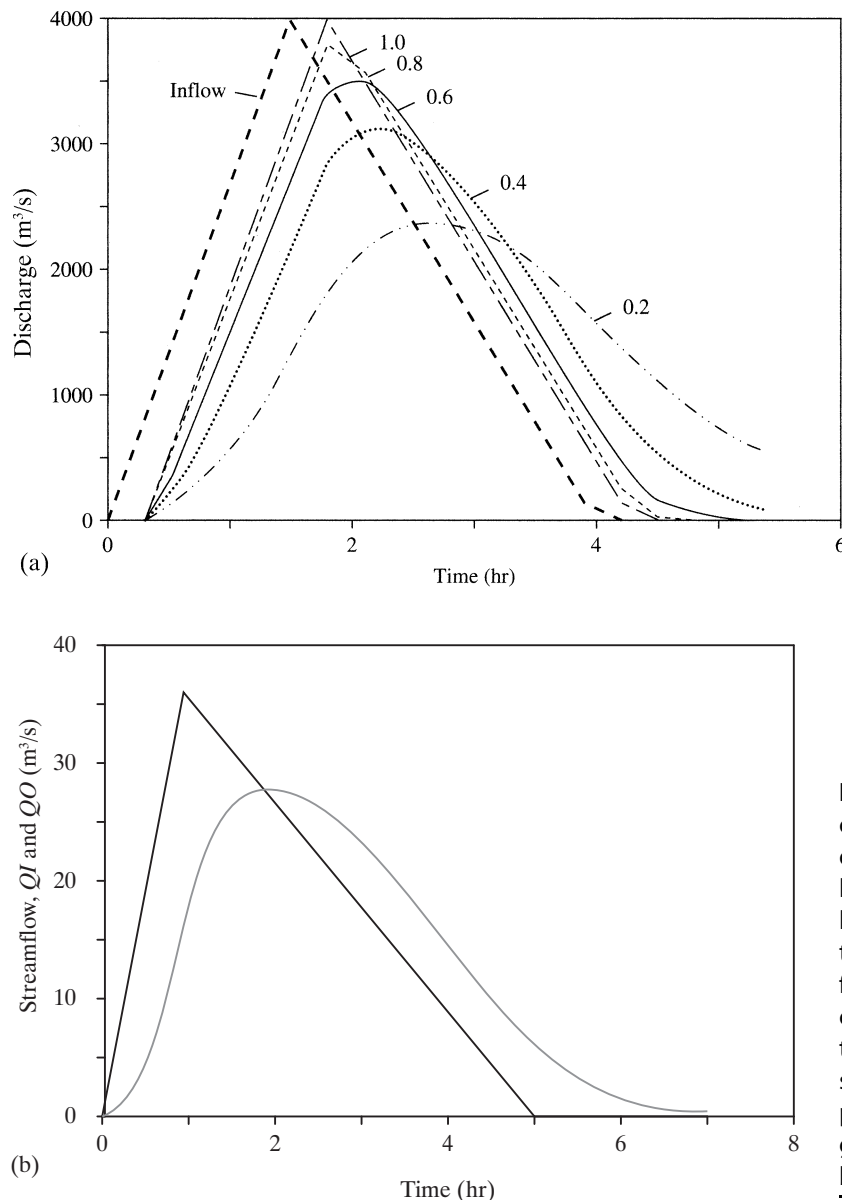


Figure 10.45 (a) Effect of routing coefficient, CX , in the convex method on the outflow hydrograph from a hypothetical channel reach. Curve labels are values of CX . When $CX = 1$ there is no diffusive effect and the flood wave is purely translatory. Successively smaller values of CX (longer travel times for a given reach) successively flatten and delay the outflow peak. (b) Inflow and outflow hydrographs for convex routing example of box 10.6.

Box 10.6 Example Application of Convex Routing Method

Here we apply the convex routing procedure to a fictitious inflow hydrograph and river reach. The steps follow the methods described in US Department of Agriculture (1982). SI units are assumed. The hydrograph of inflow to the channel reach is given, either as values of QI_t or as a graph from which values of QI_t can be determined. The development here does not consider lateral inflows; when required, these can be included as described in the above reference.

Input Information

Reach Characteristics

Length, X (m)	Width, w (m)	Slope, ζ	Manning's n_M
2,500	20	0.0005	0.05

Inflow-Hydrograph Characteristics

Initial QI (m^3/s)	Peak Flow (m^3/s)	Time of Rise (hr)	Duration of Recession (hr)
0	36	1.00	4.00

Compute Reach Travel Time, T^*

The flood-wave travel time through the reach is that associated with 3/4 of the peak-inflow discharge, $QI_{3/4} \equiv 0.75 \cdot QI_{pk}$. For this example,

$$QI_{3/4} = 0.75 \cdot 36 \text{ m}^3/\text{s} = 27.00 \text{ m}^3/\text{s}.$$

Using the uniform-flow relations [equations (10.45) and (10.46)], we first find the depth associated with this discharge, $y_{3/4}$, as

$$\begin{aligned} y_{3/4} &= \left(\frac{Q_{3/4} \cdot n_M}{\varepsilon \cdot w \cdot \zeta^{1/2}} \right)^{3/5} \\ &= \left(\frac{27.00 \text{ m}^3/\text{s} \cdot 0.05}{1 \text{ m}^{1/3}/\text{s} \cdot 20 \text{ m} \cdot 0.0005^{1/2}} \right)^{3/5} = 1.94 \text{ m}. \end{aligned}$$

The flow velocity at this discharge, $u_{3/4}$, is given by equations (10.43b) and (10.44):

$$\begin{aligned} u_{3/4} &= \frac{\varepsilon \cdot y_{3/4}^{2/3} \cdot \zeta^{1/2}}{n_M} \\ &= \frac{1 \text{ m}^{1/3}/\text{s} \cdot (1.94 \text{ m})^{2/3} \cdot 0.0005^{1/2}}{0.05} = 0.70 \text{ m/s} \end{aligned}$$

and the flood-wave velocity, $U_{3/4}$, is then computed via equation (10.48):

$$U_{3/4} = 1.5 \cdot 0.70 \text{ m/s} = 1.04 \text{ m/s}.$$

The travel time for the reach, T^* , is given via equation (10.53):

$$T^* = \frac{X}{U_{3/4}} = \frac{2,500 \text{ m}}{1.04 \text{ m/s}} = 2,396 \text{ s} = 0.665 \text{ hr.}$$

Select Routing Time Step, Δt , and Compute Routing Coefficient, CX

To avoid numerical problems, the routing time step Δt must be less than T^* and less than 1/5 the time of rise of the inflow hydrograph. Here the time of rise is 1 hr, so Δt must be less than 0.2 hr. We select $\Delta t = 0.1$ hr, so equation (10.54) gives

$$CX = \frac{\Delta t}{T^*} = \frac{0.1 \text{ hr}}{0.665 \text{ hr}} = 0.15 \text{ hr.}$$

Compute Outflow Hydrograph

The outflow hydrograph, QO_t , is computed via successive application of equation (10.56):

Time Step, i	Time, t (hr)	Inflow, QI_{tr} (m^3/s)	Outflow, QO_t (m^3/s)
0	0.0	0.0	0.0
1	0.1	3.6	0.0
2	0.2	7.2	0.5
3	0.3	10.8	1.5
*	*	*	*
7	0.7	25.2	8.9
8	0.8	28.8	11.4
9	0.9	32.4	14.0
10	1.0	36.0	16.8
*	*	*	*
30	3.0	18.0	23.0
31	3.1	17.1	22.3
32	3.2	16.2	21.5
33	3.3	15.3	20.7
*	*	*	*

The inflow and outflow hydrographs for this example are shown in figure 10.45b.

ter moves from the land surface to and through the stream network: interception, infiltration, subsurface and overland flow, and channel flow. This is especially important for predicting streamflow responses under conditions other than those for which we have recorded experience, including: (1) extreme flood-producing rainfalls; (2) major land-use changes, such as deforestation and urbanization; and (3) altered climatic regimes.

The most general methodology for incorporating the basic physics of hydrologic processes in modeling event response is to use spatially distributed numerical solutions to complete equations of saturated-unsaturated subsurface and open-channel flow, as was done by Freeze (1972a, 1972b, 1974). However, that approach is too computationally intensive and requires too much field data to be a practical approach to runoff modeling. Furthermore, questions have been raised as to whether the physical equations that describe these processes at the “micro” level are applicable at the larger scales that must be used in modeling (e.g., Kirchner 2009; see appendix F).

More practical but still physically based models commonly represent a watershed as a collection of hillslope strips on which simplified representations of the appropriate mechanisms operate—for example, the kinematic-wave model of overland flow (Eagleson 1970; Stephenson and Meadows 1986) or the sloping-slab/saturated overland flow model (section 10.4.2.1; boxes 10.4 and 10.5). And, as discussed earlier, a newer generation of event models incorporates saturation overland flow on variable source areas whose extent depends on basin topography and watershed wetness through the TOPMODEL approach (section 10.4.2.2) (Hornberger et al. 1985; Wood et al. 1990). The coupling of such models with remotely sensed data and geographic information systems is a growing area of research.

The understanding of the physical mechanisms of runoff response developed earlier in this chapter can be applied to guide the development and application of RF-RO models, even when the detailed processes are not explicitly simulated. In general, the processes with the longest residence times control the shape of the hydrograph, and Kirkby (1988) suggested that satisfactory event models can be developed considering only the two processes with the longest residence times on the watershed of interest (table 10.7). Following Woods and Sivapalan (1999), the residence time for watershed runoff for a given event, T_{RQ} , can be expressed as the sum of the residence times of wa-

Table 10.7 Ranges of Residence Times Associated with Event-Response Processes on Hillslopes and in Channels.

Process	Residence Times (hr)
Hillslope processes	
Surface detention	0.1–1
Infiltration	1–20
Percolation	1–50
Downslope flow	1–12
Channel flow	
Watershed area = 1 km ²	0.5
Watershed area = 100 km ²	7
Watershed area = 10,000 km ²	100

Source: Kirkby (1988).

ter input, T_{RP} , hillslope runoff production, T_{RH} , and travel through the stream network, T_{RS} :

$$T_{RQ} = T_{RP} + T_{RH} + T_{RS}. \quad (10.58)$$

T_{RP} can be approximated as one-half the storm duration, T_P ,

$$T_{RP} \approx \frac{T_P}{2}, \quad (10.59)$$

and T_{RS} as

$$T_{RS} \approx \frac{A_D^{1/2}}{u_S}, \quad (10.60)$$

where A_D is drainage area and u_S is the average flow velocity in the stream network. For rough estimates u_S can be taken as ~ 1 m/s; if the appropriate information is available more refined estimates can be obtained via equations (10.43b) and (10.44).

Hillslope residence times might be estimated using knowledge of local topography and geology and the operative runoff mechanism. For example, for runoff due to subsurface flow in a sloping slab,

$$T_{RH} \approx \frac{1}{4 \cdot D \cdot u_H}, \quad (10.61)$$

where D is drainage density (section 10.1.3) and u_H is the typical flow velocity. u_H could be calculated by approximating Darcy's law as

$$u_H \approx K_h \cdot \tan(\beta), \quad (10.62)$$

where K_h is hydraulic conductivity and β is the slope angle, as was done in the kinematic-wave approximation of sloping-slab runoff (boxes 10.4 and 10.5).

Figure 10.46 shows the ranges of lag-to-peak times and peak flow rates measured in field studies for watersheds in which responses were due to Hortonian overland flow, saturation overland flow, and “throughflow.” The exact nature of the throughflow represented in the data is not clear; it probably refers largely to macropore-dominated flow in sloping slabs, but may include other subsurface mechanisms as well (section 10.4.3). Clearly, overland flow results in lag times an order of magnitude shorter and peak flows at least an order of magnitude larger than does subsurface flow. Channel hydraulics significantly affects the peaks and lag times for watersheds larger than a few tens of square kilometers. Thus a small

watershed might be efficiently modeled by taking account of infiltration, percolation, and the appropriate hillslope process. For a larger watershed, the response model might be simplified to include only the dominant hillslope process combined with a channel-routing procedure.

The work of Wood et al. (1990) indicates that actual patterns of soil and water-input variability do not have to be modeled for regions less than about 1 km² in area; instead the spatial variability can be accounted for more simply through the areal means and variances of those quantities. And, because channel processes tend to dominate the response hydrographs of larger watersheds, much of the variability and nonlinearity of hillslope event-response mechanisms can be ignored or averaged when modeling watersheds over about 100 km² in area. For

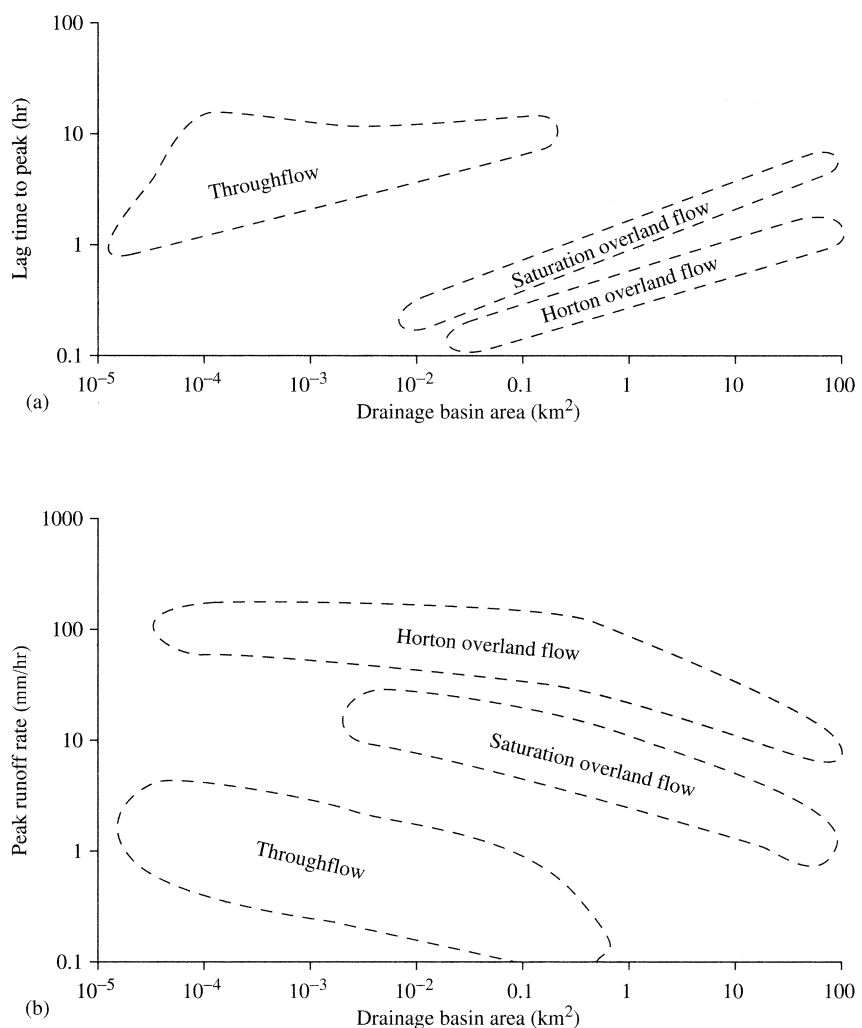


Figure 10.46 Ranges of (a) lag-to-peak and (b) peak flow rates associated with various response mechanisms. “Throughflow” probably includes all subsurface mechanisms in table 10.4 except ground-water mounding [reproduced from Kirkby (1988), Hillslope runoff processes and models, *Journal of Hydrology* 100:315–339, with permission from Elsevier].

these watersheds, simple conceptual approaches like those described in section 10.6.4 may provide a satisfactory model.

10.6.2 The Watershed as an Impulse-Response System

Even simulation models that simplify the runoff process as just described require the specification of many **parameters** characterizing watershed topography (slope, aspect), vegetation (leaf-area index, plant height), soil (porosity, field capacity, water content), and channel configuration (network properties, geometry, slope, resistance), as well as the spatial and temporal distribution of rainfall. As discussed in appendix F, none of these parameters can be known with certainty, so that appropriate values must be determined via *calibration* and *validation*:

Calibration involves use of measured rainfall data as model input, comparison of model outputs with measured streamflow using different sets of parameter values, and selection of the parameter values that give the "best" model performance.

Once a parameter set has been selected, **validation** involves comparing model outputs with measured flows for events not used in calibration.

Although this methodology would seem to be a straightforward approach to determining appropriate parameter sets, experience has shown that significantly differing sets of parameters often give equally good (or bad!) results. This outcome, known as the problem of **equifinality**, severely reduces confidence in the validity of multi-parameter models and provides justification for viewing a watershed as a simple **system**, or "black box," that produces a response (the streamflow hydrograph) in response to an impulse (the rainfall hyetograph), without detailed consideration of the physical processes that produce that response. In general, the systems approach deals only with *effective precipitation*, P^* , and *event flow*, Q^* (figure 10.47), using the concepts and expedient separation techniques discussed in section 10.2.2 and 10.2.3. An implicit assumption of the systems approach is that the water that appears as Q^* is the same water identi-

fied as P^* . [As we have seen, however, many studies of actual runoff sources and mechanisms (table 10.5) have found that a substantial portion of the water appearing as stream response to a given event is "old" water—water that entered the watershed in previous rain or snowmelt events and was hydraulically displaced by the "new" water.]

Application of the systems approach requires: (1) estimation of P^* (and for some methods the time-distribution, P_i^*) (figure 10.47a), and (2) identification of an appropriate **transfer function** for the situation to be modeled. The following section considers the critical problem of estimating effective precipitation; three approaches to formulating transfer functions are described in section 10.6.4.

10.6.3 Inputs to Rainfall-Runoff Models

10.6.3.1 Design Floods vs. Floods from Actual Storms

Rainfall-runoff models are used both to generate both predictions (*design floods*) and forecasts of floods from actual storms (figure 10.48 on p. 512).

10.6.3.1.1 Prediction of Design Floods

A **design flood** is a flood of a specified probability of occurrence that is used in the design of culverts, bridges, flood-retention basins, levees, dam spillways, or floodplain-management plans.

For these situations, the goal is to estimate the design flood using an appropriate design rainfall as the input. The design-flood probability is specified as a return period (also called recurrence interval); this term is defined in section 4.4.3.3 and section C.5. The design return period depends on the consequences of the design flood being exceeded: small culverts may be designed to pass a low return-period flood (e.g., the 10-yr flood), bridges a somewhat larger flood (e.g., the 25-year flood), and spillways of large dams the 100-year or larger flood. As explained in section 4.4.3.2, if the failure of a dam or levee would cause great economic damage and loss of life, the "probable maximum flood" (PMF) is used for the spillway design.

A crucial question in selection of the design rainfall is the determination of the storm duration that will generate the required design flood for a particular watershed. For a given region the critical duration increases with watershed area (see figure

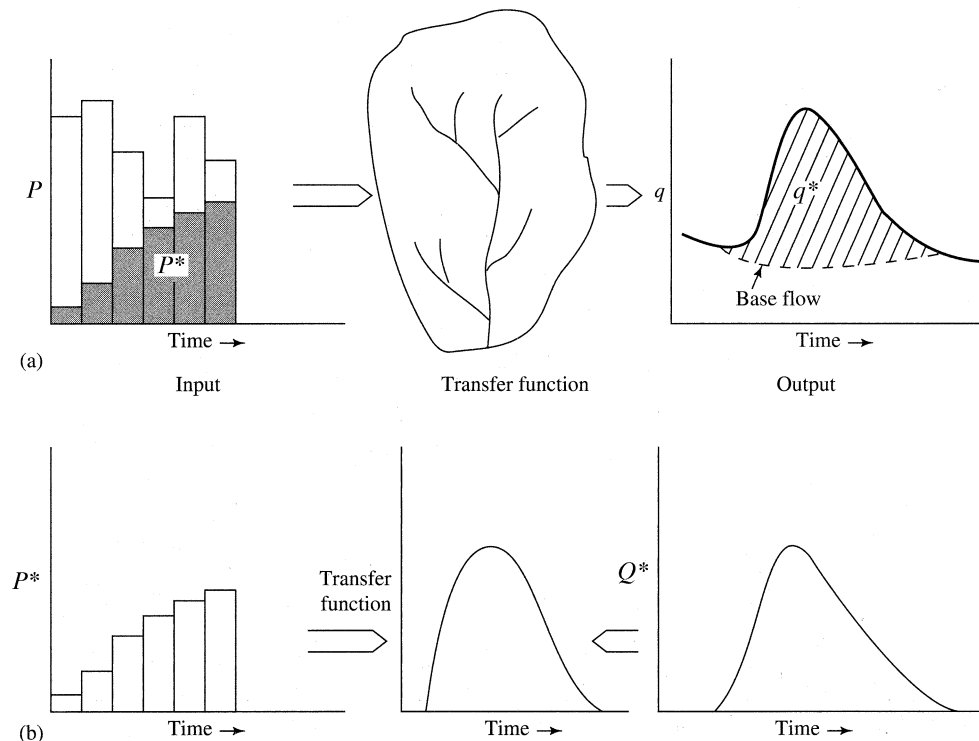


Figure 10.47 In the systems view, watershed response consists only of event flow, Q^* , which is volumetrically equal to effective precipitation, P^* . (a) In practice, the systems approach requires a priori determination of P^* from a measured or specified time distribution of P (see figure 10.49), routing through a specified transfer function, and addition of the predicted response to a specified base flow. (b) The inverse problem involves identification of the transfer function from observed time distributions of input and response. Once the transfer function for a given watershed is determined, it is used to forecast or predict responses to actual or design storms.

4.44); it is generally of the order of the watershed's time of concentration, which can be estimated by formulas like those summarized in table 10.8 on p. 513. The critical duration for a given watershed can also be determined by trial and error. To do this, rainfalls of a given return period and varying durations are used as input to the RF-RO model, and the duration that gives the largest peak is selected.

Another important question in generating design floods is the relationship between the return period of the rainfall used as model input and the return period of the resulting flood. Approaches to developing answers to this question are described in box 10.7.

10.6.3.1.2 Forecasts of Floods from Actual Storms

Estimates of floods from actual storms are generated to forecast flooding from an in-progress or im-

minent storm, as a basis for flood warnings. Such estimates are also used to calibrate and validate rainfall-runoff models using historical storms as inputs.

Flood forecasting is usually done via complex hydrologic models that are to varying degrees physically based, rather than the simple conceptual models discussed in section 10.6.4. These complex models typically divide a larger watershed into subwatersheds that are modeled separately, and contain simulations of the physical processes discussed in previous chapters, particularly snowmelt and infiltration. Such models may specifically simulate the specific runoff processes discussed earlier in this chapter, and generally contain procedures for streamflow routing. Excellent reviews of such models and their use in forecasting have been prepared by DeVries and Hromadka (1992) and Lettenmaier and Wood (1992).

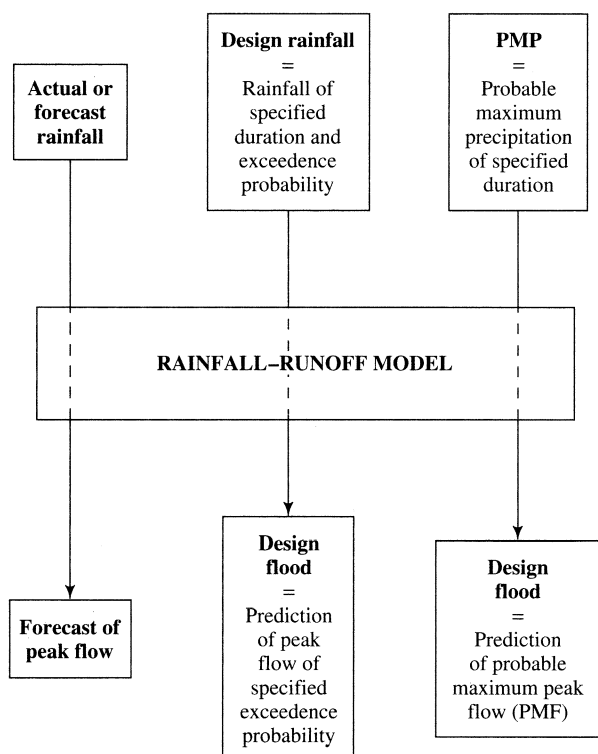


Figure 10.48 Use of systems models for forecasting and prediction. In addition to flood peaks, other characteristics of response, such as total flood volume or duration, may also be forecasted or predicted.

Box 10.7 Approaches to Developing Relations between Rainfall Return Period and Flood Return Period

As noted by Pilgrim and Cordery (1992), there are four general approaches to this problem:

1. The simplest and most direct approach requires (a) frequency analysis of floods at gauging stations in the region of interest, using the methods described in box C.1 (which can be found on the disk accompanying the text) or methods that apply a specific probability distribution and (b) frequency analysis of rainfalls of appropriate durations for the gauged watersheds. By trial and error, determine the model parameters that convert a rainfall of a given return period to a flood peak of the same return period.
2. For a given watershed, determine the model parameters that best reproduce the measured floods for

each of a number of events. Select the median values of these parameters for use; this should result in a close correspondence between the return periods of rainfall and the resulting flood.

3. Calibrate the selected model for the watershed of interest. Then use the model to generate a continuous record of simulated streamflows from a long record of historical rainfall data. Finally, conduct a frequency analysis of the rainfall and flow data, and relate the return periods.
4. Conduct a joint probability analysis of parameters of an appropriate model and inputs.

Table 10.8 Formulas for Estimating Time of Concentration, T_c , from Watershed Characteristics and Rainfall Intensity.

Equation ^a	Remarks	Source ^b
$T_c = 0.0278 \cdot \frac{B^{0.6}}{k^{0.4} \cdot (K_h \cdot i_{eff} \cdot S_s)^{0.2}}$	Sloping slab, steep forested watershed	Loukas and Quick (1996)
$T_c = 0.0664 \cdot \left(\frac{L}{S_c^{0.5}} \right)^{0.77}$	Agricultural watersheds in TN; $0.003 \leq A_D \leq 0.5 \text{ km}^2$	Kirpich (1940)
$T_c = 0.161 \cdot \left(\frac{L}{S_c^{0.5}} \right)^{0.64}$	Midwestern US; $0.012 \leq A_D \leq 18.5 \text{ km}^2$	Chow (1962)
$T_c = 0.927 \cdot \left(\frac{L}{S_c^{0.5}} \right)^{0.47}$	United Kingdom	NERC (1975)
$T_c = 0.700 \cdot \left(\frac{L \cdot L_c}{S_c^{0.5}} \right)^{0.38}$	Appalachian Mountains	Snyder (1938)
$T_c = 0.128 \cdot \left(\frac{L}{S_c^{0.5}} \right)^{0.79}$	US and Canada; $0.01 \leq A_D \leq 5,840 \text{ km}^2$; $0.00121 \leq S_c \leq 0.0978$	Watt and Chow (1985)
$T_c = 0.817 \cdot \frac{L \cdot n^{0.75}}{A_D^{0.25} \cdot k^{0.5} \cdot i_{eff}^{0.25} \cdot S_c}$	Overland flow	Aron et al. (1991)
$T_c = 2.15 \cdot \frac{L^{0.5} \cdot n^{0.52}}{S_c^{0.31} \cdot i_{eff}^{0.38}}$	Rural watersheds; $A_D < 5 \text{ km}^2$	Papadakis and Kazan (1987)

 A_D = drainage area (km^2) B = factor integrating travel times (dimensionless) i_{eff} = effective rainfall intensity (mm/hr) k = channel shape factor (dimensionless) K_h = hydraulic conductivity of slope soil (mm/hr) L = length of main stream (km) L_c = stream distance from basin outlet to point opposite watershed centroid (km) n = Manning's resistance factor for channel S_c = sine of channel slope angle (dimensionless) S_s = sine of hillslope angle (dimensionless) T_c = time of concentration (hr) T_{LPC} = centroid lag-to-peak (table 10.2) (hr)^aAssumes $T_c = 1.67 \cdot T_{LPC}$.^bSee Loukas and Quick (1996) for original references.

10.6.3.2 Determining Effective Rainfall

Since systems models relate *effective* rainfall to storm runoff, calibration and validation of such models requires separation of hyetographs. This is a critical problem, because the total volume of effective rainfall equals the volume of effective runoff and is a major determinant of the magnitude of the flood peak.

Effective water input P^* is conventionally considered to be

$$P^* = P - \text{"losses,"} \quad (10.63)$$

where P is total water input during an event. In equation (10.63),

$$\text{losses} = ET + \Delta S_c + \Delta S_D + \Delta S_\theta, \quad (10.64)$$

where ET is the portion of the event water evapo-transpired during the event; ΔS_c is the net addition to storage on the vegetative canopy (figure 6.19); ΔS_D is the net addition to depression storage, i.e., the water added to lakes, ponds, wetlands, puddles, and smaller depressions (section 10.4.2.3); and ΔS_θ is the net addition to soil-water storage during the event.

Because rainfall events are usually of short duration and are accompanied by high humidity and low solar radiation, ET is usually small. As discussed in section 6.6, canopy-storage capacity is on the order of $1 \text{ mm} \times \text{leaf-area index}$. Thus it is usually filled quickly, and ΔS_c is also usually negligible for storms that generate significant responses.

As noted in section 10.4.2.3, depression storage is spatially variable and difficult to estimate, and only very meager data on depression-storage volumes have been published. Values on the order of 5–10 mm have been estimated for turf (Bras 1990). Evaporation and infiltration usually empty small surface depressions between rain storms (Kirkby 1988); however, they may be maintained full during active snowmelt. Because of the difficulty of evaluating depression storage, it is usually treated conceptually in combination with soil-water storage. These combined storage components are typically modeled as filling in the same way that infiltration occurs (figures 8.10 and 8.21). Thus the ratio P^*/P is largely determined by the degree to which the available near-surface storage capacity is already filled; i.e., by the antecedent soil-water content, θ_0 . Operational methods for relating effective water input to antecedent conditions of watershed wetness are discussed in section 10.6.4.2.1 and box 10.8.

However the transfer function is developed, it is important to emphasize that the validity of the esti-

mate of P^* is at least as important as the exact nature of the transfer function in determining the accuracy of the forecast response (figures 10.10 and 10.11). Unless unusually detailed observations of storage components—especially soil moisture—are available, there is very little basis for physically-based forecasts or predictions of the quantity of effective water input. The need for such forecasts and predictions has thus led to the development of empirical methods for estimating P^* .

Most of these methods are based on one of the conceptual relations shown in figure 10.49. If one is attempting to solve the system-identification problem for a given watershed, one can determine the total losses for various events *a posteriori* by hydrograph separation, and then estimate their time distribution via one of the models in figure 10.49. For future applications in predicting the response of the watershed, one might attempt to relate P^* to a measurable quantity that reflects basin storage via one of the approaches described in box 10.8 (on p. 516) and 10.9 (on p. 517) and figures 10.50 and 10.51 (on p. 518).

10.6.4 Rainfall-Runoff Models

In this section we introduce three simple rainfall-runoff models. The “rational method” and the “SCS method” are commonly used for generating design flows from small watersheds for simple, relatively inexpensive structures such as culverts, small bridges, surface-drainage systems, and runoff-detention basins. The rational method is most often applied to urban areas, and the SCS method to suburban and rural areas. The “unit-hydrograph method” is often applied to generate design flows from larger watersheds where measurements of rainfall and runoff in past events are available. “Synthetic unit hydrographs” are intended for use where such data are not available.

10.6.4.1 The Rational Method

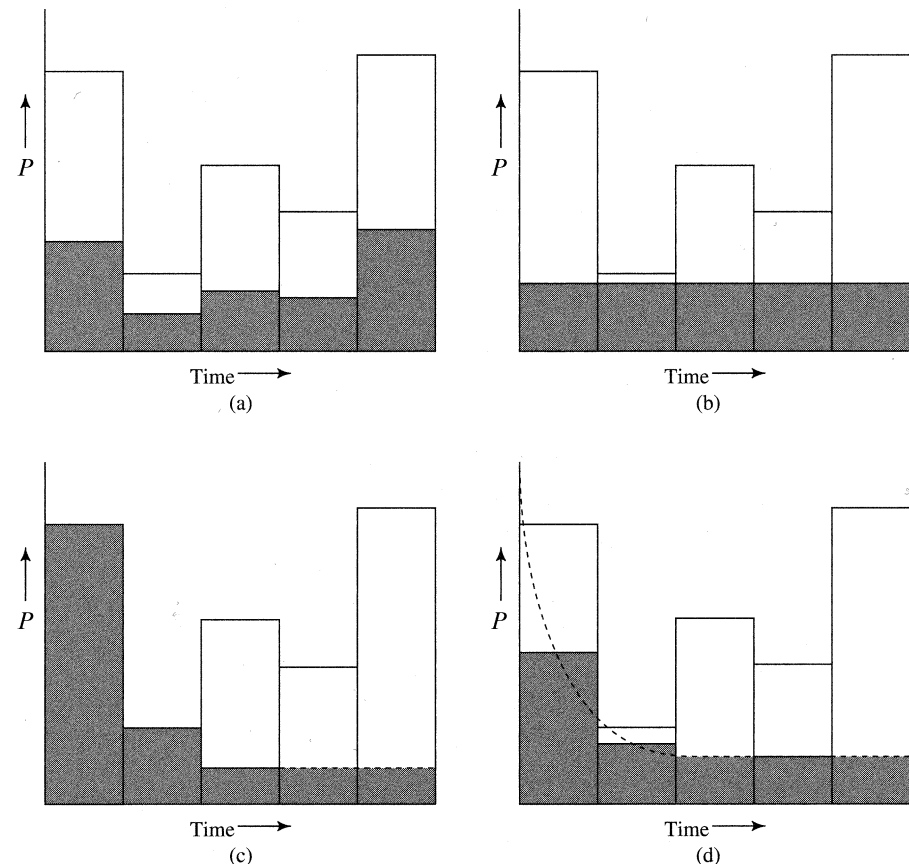
The **rational method** postulates a simple proportionality between peak discharge, q_{pk} , and rainfall intensity, p^* :

$$q_{pk} = \varepsilon_R \cdot C_R \cdot A_D \cdot p^*, \quad (10.65)$$

where ε_R is a unit-conversion factor, A_D is drainage area, and C_R is a dimensionless **runoff coefficient**, which depends on watershed land use. For q_{pk} in m^3/s , p^* in mm/hr , and A_D in km^2 , $\varepsilon_R = 0.278$.

Equation (10.65) was derived from a simplified conceptual model of travel times on basins with neg-

Figure 10.49 Conceptual models for estimating effective water input, P^* , from hyetograph of water input, P . Losses are shaded portions, P^* is unshaded. (a) Losses equal a constant fraction of the water input for each time period. (b) Losses equal a constant rate throughout the event. (c) Losses are given by an initial abstraction (which may be a specified amount or all input over an initial time period) followed by a constant rate (which may be zero). (d) Losses are given by an approximation to an infiltration-type curve (dotted line), such as given by the Green-and-Ampt or Philip approach (see chapter 8) [adapted from Pilgrim and Cordery (1992)].



ligible surface storage, and is widely used for drainage design for small rural and urban watersheds. The duration of the rainfall to be used in equation (10.65) is taken as the time of concentration of the watershed, for which values can be estimated by formulas like those in table 10.8. For design purposes, the return period of the design peak flow is equal to the return period of the rainfall.

One can see from equation (10.65) that the sole model parameter, C_R , is the ratio of peak streamflow per unit area to rainfall intensity. Obviously the results obtained with the method are highly sensitive to the value chosen for C_R ; values range from 0.05 for gently sloping lawns up to 0.95 for highly urbanized areas of roofs and pavement (table 10.9 on p. 519).

The rational method is widely used in urban drainage design, but Pilgrim and Cordery (1992) caution that there are typically few data available to guide the selection of C_R , and that C_R for a given wa-

tershed may vary widely from storm to storm due to differing antecedent conditions, as we saw in figures 10.10 and 10.11.

10.6.4.2 The Soil Conservation Service Curve-Number Method

The most widely used RF-RO model for routine design purposes in the United States is the **Soil Conservation Service Curve-Number** (SCS-CN), or simply **runoff curve-number**, method. This method was developed by the NRCS and makes direct use of soils information routinely mapped by that agency. Given a watershed in which the hydrologic characteristics of the soils (discussed further below) have been mapped and a design rainfall volume, P , is specified, there are two basic computations in the method: (1) estimation of the effective rainfall, P^* (= the event flow volume, Q^*); and (2) estimation of the peak discharge, q_{pk} . If desired, the entire runoff hydrograph can also be estimated.

Box 10.8 Estimating P^*

Empirical Relations with Storm Characteristics

Lacking sufficient data to apply other approaches one can estimate P^* as

$$P^* = a_0 + a_1 \cdot P, \quad (10B8.1)$$

where a_0 and a_1 are empirically determined for a given watershed. Although Loague and Freeze (1985) found that the approach did not yield precise estimates, it may have some predictive value and be useful if data limitations preclude other approaches.

Antecedent Rainfall Indices

Following a storm, the storage components enumerated in equation (10.64) gradually empty. This process is approximated via an empirical **antecedent rainfall index**, $I_a(d)$, which is calculated on a daily basis as

$$I_a(d) = I_a(0) \cdot k^d, \quad (10B8.2)$$

where $I_a(0)$ is the value for a day with rain, k is a constant (usually $0.80 < k < 0.98$), and d is the number of days since the last rainfall. The values of $I_a(0)$ and k are empirically determined for a particular watershed. Conceptually, $I_a(0)$ represents the total watershed near-surface storage (usually expressed as a depth of water), and $I_a(d)$ is the amount of water from the previous storm that remains in that storage on day d . One then identifies the empirical relation between P^* and $I_a(d)$ for past storms.

Indices Related to Ground-Water and/or Soil-Water Levels

Forecasts of P^* for a particular watershed or region can be empirically related to water levels in observation wells or soil-water content measured at one or more index sites (Dunne et al. 1975; Troch et al. 1993).

Empirical Relations with Antecedent Discharge

Assuming that the rate of outflow from a watershed reflects the amount of water stored in it, as in equation (1.42) and the linear-watershed model of box 10.3, it is reasonable to attempt to relate P^* to antecedent discharge, q_0 . Figure 10.50 shows the relation between P^*/P and q_0 for the same watershed portrayed in figure 10.10, and indicates that it has useful predictive ability there. Gburek (1990) reported similar results for a watershed in Pennsylvania, but with considerably greater scatter.

Use of Continuous Watershed Models

If calibrated and validated for a particular watershed, watershed models can be used to keep a running account of the state of the various storage components. When a water-input event occurs, the filling of those components can be estimated using models of the interception, infiltration, and percolation processes as discussed in earlier chapters; P^* is then estimated as the residual. Several such models were described by Viessman et al. (1989).

Probability Models

Beran and Sutcliffe (1972) described how the probability distribution of P^* can be determined from the distribution of P in Britain.

SCS Method

In the absence of specific information on antecedent conditions, the SCS curve-number method described in box 10.9 is widely used in the United States to estimate P^* given total rainfall P and information on watershed soils.

10.6.4.2.1 Estimation of Effective Rainfall

As shown in box 10.9, the original SCS-CN method relating P^* to total rainfall, P , and watershed storage capacity, S_{max} [L], is

$$P^* = \frac{(P - 0.2 \cdot S_{max})^2}{P + 0.8 \cdot S_{max}}. \quad (10.66)$$

A revised relation, based on a more hydrologically consistent analysis, is also given in box 10.9. Note from figure 10.51 that the rationale for the original relation coincides closely with the behavior of infiltration when rainfall rate exceeds the saturated hydraulic conductivity of the surface soil, as modeled

by the Green-and-Ampt approach in section 8.4.3. However, the model is not explicitly an infiltration model, and S_{max} supposedly incorporates all watershed storage, including interception and surface detention as well as subsurface storage.

The NRCS classifies and maps the soils in the United States at various scales, and the wide acceptance of the SCS-CN method is largely because values of S_{max} can be determined from such maps, along with land-cover information. Each mapped soil type is assigned to one of the hydrologic soils groups described in table 10.10 on p. 519. These groups are based largely on minimum infiltration capacity, which should be approximately equal to K_h at the surface (chapter 8).

Box 10.9 SCS Approach to Forecasting P^* for Rainstorms

Original Formulation

Figure 10.51 shows a schematic hyetograph for a rainstorm. The SCS approach assumes that the total storm rainfall volume P is allocated to: (1) **initial abstraction**, S_I , which is the amount of storage that must be satisfied before event flow can begin; (2) **retention**, S_R , which is the amount of rain that falls after the initial abstraction is satisfied but does not contribute to event flow; and (3) total event flow, Q^* , which is equal to the effective precipitation, P^* . It is further assumed that the watershed has a maximum retention capacity S_{max} and that the following relation exists:

$$\frac{S_R}{S_{max}} = \frac{P^*}{P - S_I}. \quad (10B9.1)$$

All the quantities are volumes expressed on a per watershed area basis as lengths.

The actual retention is

$$S_R = P - S_I - P^*. \quad (10B9.2)$$

Combining equations (10B9.1) and (10B9.2) and solving for P^* yields

$$P^* = \frac{(P - S_I)^2}{P - S_I + S_{max}}. \quad (10B9.3)$$

Examination of actual response hydrographs led to the generalization that $S_I = 0.2 \cdot S_{max}$ under conditions of "normal" watershed wetness. Substituting that relation into equation (10B9.3) gives

$$P^* = \frac{(P^* - 0.2 \cdot S_{max})^2}{P + 0.8 \cdot S_{max}}. \quad (10B9.4)$$

As explained in section 10.6.4.2.1, S_{max} is estimated from a *runoff curve number* that is a function of watershed soils and land uses. Curve numbers may be adjusted to reflect unusually dry or wet antecedent conditions (watershed wetness at the beginning of a storm).

Revised Formulation

Although equation (10B9.4) is widely used, there are concerns about "severe structural inconsistencies" in the definitions of some of the quantities involved (Chen

1982; Sabol and Ward 1983; Boughton 1989, 1994). These concerns led Michel et al. (2005) to reexamine the approach and to propose a revision that is hydrologically consistent. This approach involves defining a new parameter, S_0 , which is the volume of water stored in the soil at the beginning of a rainfall event, and characterizing antecedent conditions as the proportion of soil-water-storage capacity that is full at the storm onset, S_0/S_{max} . The revised approach leads to three equations for estimating P^* , depending on general antecedent conditions:

1. "Dry" Conditions ($S_0/S_{max} \approx 0.33$)

$$P^* = \frac{P^2}{(S_{max} + P)}; \quad (10B9.5a)$$

2. "Average" Conditions ($S_0/S_{max} \approx 0.61$)

$$P^* = \frac{P \cdot (0.48 \cdot S_{max} + 0.72 \cdot P)}{(S_{max} + 0.72 \cdot P)}; \quad (10B9.5b)$$

3. "Wet" Conditions ($S_0/S_{max} \approx 0.87$)

$$P^* = \frac{P \cdot (0.79 \cdot S_{max} + 0.46 \cdot P)}{(S_{max} + 0.46 \cdot P)}. \quad (10B9.5c)$$

The value of S_{max} is determined by the runoff curve number, as in the original approach [equation (10.66), section 10.6.4.2].

Although not suggested by Michel et al. (2005), their model can be made more flexible by generalizing equation (10B9.5) as

$$P^* = \frac{P \cdot (k_S \cdot S_{max} + k_P \cdot P)}{(S_{max} + k_P \cdot P)}, \quad (10B9.6)$$

and calculating k_S and k_P as linear functions of S_0/S_{max} :

$$k_S = 1.33 - \frac{S_0}{S_{max}} \quad (10B9.7)$$

and

$$k_P = -0.48 + 1.47 \cdot \frac{S_0}{S_{max}}. \quad (10B9.8)$$

Table 10.11 on p. 520 gives the **curve numbers** assigned to each hydrologic soil group under various land uses. S_{max} is determined from these curve numbers, CN , as

$$S_{max} = \frac{25,400}{CN} - 254, \quad (10.67)$$

where S_{max} is in mm. Note that this is an empirical dimensionally inhomogeneous equation, so the con-

stants differ when other units are used (section 1.4). In the original method, curve numbers may be further adjusted to reflect the antecedent wetness of the watershed, as prescribed in table 10.12 on p. 521; however, the values given in table 10.11 are used for most design purposes. The revised approach described in box 10.9 allows for direct incorporation of antecedent wetness.

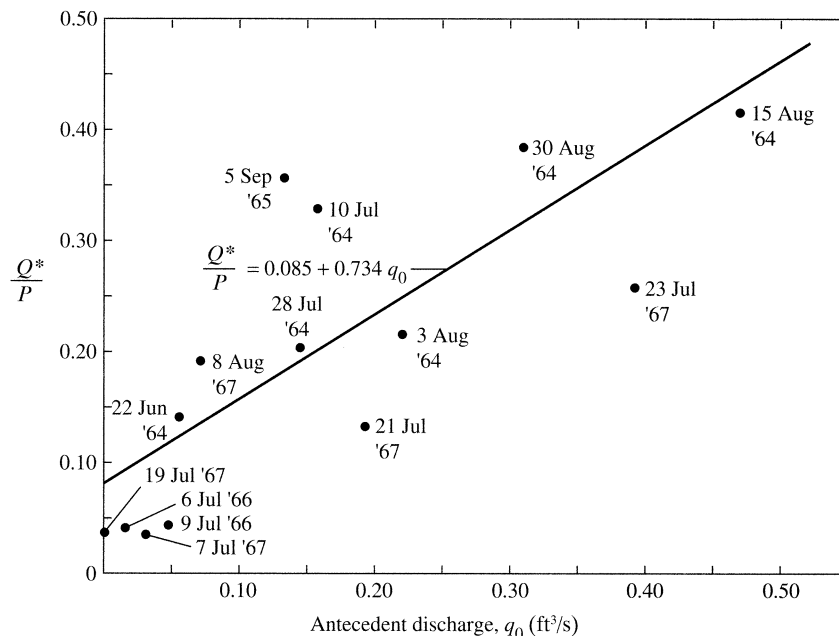


Figure 10.50 Relation between Q^*/P and antecedent discharge, q_0 , for a small watershed in central Alaska for the same 16 storms shown in figure 10.10 [Dingman (1970)].

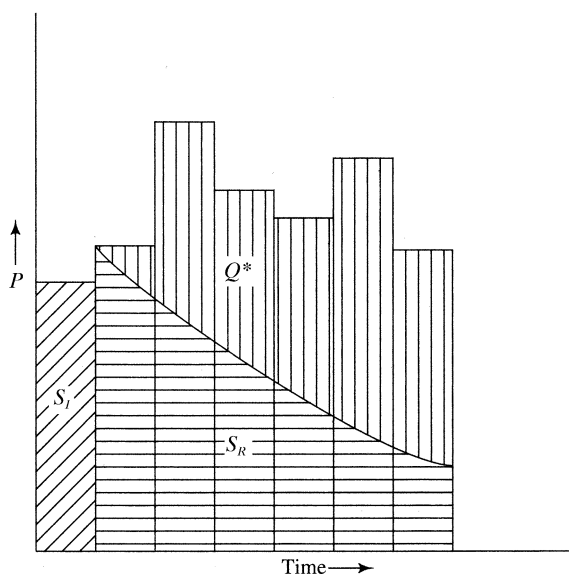


Figure 10.51 Definitions of initial abstraction, S_I , retention, S_R , and event flow, Q^* , in the SCS method.

Table 10.9 Runoff Coefficients, C_R , for the Rational Method [Equation (10.65)].^a

Type of Surface	C_R
Pavement: Asphalt and concrete	0.70–0.95
Pavement: Brick	0.70–0.85
Roofs	0.75–0.95
Lawns (sandy soil): slope < 2%	0.05–0.10
Lawns (sandy soil): slope 2–7%	0.10–0.15
Lawns (sandy soil): slope > 7%	0.15–0.20
Lawns (heavy soil): slope < 2%	0.13–0.17
Lawns (heavy soil): slope 2–7%	0.18–0.22
Lawns (heavy soil): slope > 7%	0.25–0.35
Parks and cemeteries	0.10–0.25
Playgrounds	0.20–0.35
Railroad yards	0.20–0.35
Unimproved	0.10–0.30

^aValues apply to storms with return periods of 5 to 10 yr; higher values should be used for higher return-period storms.

Source: McCuen (1989).

When a watershed consists of more than one soil/land-use complex, the standard approach is to compute a weighted average curve number as in the example in box 10.10 on pp. 522–523 (see also Grove et al. 1998).

10.6.4.2.2 Estimation of Peak Discharge

Peak discharge in the SCS-CN method is computed by assuming that the runoff hydrograph is a triangle, with a time of rise, T_r , (see table 10.2) given by

$$T_r = 0.5 \cdot T_{P^*} + 0.6 \cdot T_c, \quad (10.68)$$

where T_{P^*} is the duration of excess rainfall and T_c is the watershed time of concentration estimated from an appropriate formula from table 10.8. The time base of the hydrograph, T_b , is then given by

$$T_b = 2.67 \cdot T_r. \quad (10.69)$$

The total runoff volume is set equal to the triangular area, so that

$$Q^* = P^* = 0.5 \cdot q_{pk} \cdot T_b. \quad (10.70)$$

Combining equations (10.68)–(10.70), solving for q_{pk} , and adjusting for units then yields

$$q_{pk} = \frac{0.208 \cdot P^* \cdot A_D}{T_r}, \quad (10.71)$$

Table 10.10 Hydrologic Soils Groups as Defined by the NRCS.^a

Soil Group	Characteristics
A	Low overland-flow potential; high minimum infiltration capacity even when thoroughly wetted ($> 0.30 \text{ in/hr} = 0.76 \text{ cm/hr}$). Deep, well-to excessively drained sands and gravels.
B	Moderate minimum infiltration capacity when thoroughly wetted (0.15 to 0.30 in/hr = 0.38 to 0.76 cm/hr). Moderately deep to deep, moderately to well-drained, moderately fine- to moderately coarse-grained (e.g., sandy loam).
C	Low minimum infiltration capacity when thoroughly wetted (0.05 to 0.15 in/hr = 0.13 to 0.38 cm/hr). Moderately fine- to fine-grained soils or soils with an impeding layer (fragipan).
D	High overland-flow potential; very low minimum infiltration capacity when thoroughly wetted ($< 0.05 \text{ in/hr} = 0.13 \text{ cm/hr}$). Clay soils with high swelling potential, soils with permanent high-water table, soils with a clay layer near the surface, shallow soils over impervious bedrock.

^aMinimum infiltration capacities given should approximate saturated hydraulic conductivities. (See section 6.6.2.)

where q_{pk} is in m^3/s , P^* is in mm, A_D is in km^2 , and T_r is in hr. An example calculation is given in box 10.10.

10.6.4.2.3 Estimation of Runoff Hydrograph

The analysis of a large number of hydrographs developed for watersheds over a range of sizes and locations led to the formulation of the **SCS generalized dimensionless synthetic hydrograph** (Mockus 1957). In this approach the time of rise is estimated via equation (10.68) and the peak discharge via equation (10.71). These values are then used to scale the time and discharge axes as indicated in table 10.13 on p. 523.

10.6.4.2.4 Application and Validity

The results of studies comparing SCS-CN method predictions against measured data have been mixed. For example, Kumar and Jain (1982) applied the original method to estimate P^* for 11 storms on a research watershed in Iowa, and found poor agreement with values determined by hydrograph separation (figure 10.52 on p. 524). Wood and Blackburn (1984) also found discrepancies for rangelands; how-

Table 10.11 SCS Curve Numbers for Various Soils/Land-Cover Complexes, Antecedent Wetness Condition II ("Average").

Land Use or Cover	Treatment or Practice	Hydrologic Condition	Hydrologic Soil Group			
			A	B	C	D
Fallow	Straight row	Poor	77	86	91	94
Row crops	Straight row	Poor	72	81	88	81
	Straight row	Good	67	78	85	89
	Contoured	Poor	70	79	84	88
	Contoured	Good	65	75	82	86
	Contoured and terraced	Poor	66	74	80	82
	Contoured and terraced	Good	62	71	78	81
Small grain	Straight row	Poor	65	76	84	88
	Straight row	Good	63	75	83	87
	Contoured	Poor	63	74	82	85
	Contoured	Good	61	73	81	84
	Contoured and terraced	Poor	61	72	79	82
	Contoured and terraced	Good	59	70	78	81
Close-seeded legumes or rotation meadow	Straight row	Poor	66	77	85	89
	Straight row	Good	58	72	81	85
	Contoured	Poor	64	75	83	85
	Contoured	Good	55	69	78	83
	Contoured and terraced	Poor	63	73	80	83
	Contoured and terraced	Good	51	67	76	80
Pasture or range		Poor	68	79	86	89
		Fair	49	69	79	84
		Good	39	61	74	80
	Contoured	Poor	47	67	81	88
	Contoured	Fair	25	59	75	83
	Contoured	Good	6	35	70	79
Meadow (permanent)		Good	30	58	71	78
Woodlands (farm woodlots)		Poor	45	66	77	83
		Fair	36	60	73	79
		Good	25	55	70	77
Forest		Good	25	58	72	77
Farmsteads			59	74	82	86
Roads, dirt			72	82	87	89
Roads, hard-surface			74	84	90	92

Source: US Soil Conservation Service (1964).

Table 10.12 Antecedent Wetness Conditions and Curve-Number Adjustments for the SCS Method.

Curve Numbers		
Condition II	Condition I	Condition III
100	100	100
95	87	98
90	78	96
85	70	94
80	63	91
75	56	88
70	51	85
65	45	82
60	40	78
55	35	74
50	31	70
45	26	65
40	22	60
35	18	55
30	15	50
25	12	43
20	9	37
15	6	30
10	4	22
5	2	13

Condition	Soil Wetness	Total Rain 5 Previous Days (in)	
		Dormant Season	Growing Season
I	Dry but above wilting point	< 0.5	< 1.4
II	Average	0.5–1.1	1.4–2.1
III	Near saturation	> 1.1	> 2.1

Source: US Soil Conservation Service (1964).

ever, others have found satisfactory agreement (e.g., Mostaghimi and Mitchell 1982).

Results like those shown in figure 10.52—for a region in which the method should be well suited—suggest that it is unwise to accept uncritically the predictions of the SCS method. The user of the SCS-CN relations must bear in mind that they are generalized and may not be very accurate for a specific watershed. The NRCS now recognizes that the relation of a given set of soil and land-use conditions to curve number may vary regionally (Miller and Cron-

shey 1989). Thus field observations are always advisable; one can make observations of rise times simply by measuring water levels at the basin outlet during a water-input event.

However, the SCS-CN approach will no doubt continue in use because: (1) it is computationally simple; (2) it uses readily available watershed information; (3) it has been “packaged” in readily available tables, graphs, and computer programs; (4) it appears to give “reasonable” results under many conditions; and (5) in the absence of detailed watershed information, there are few other practicable methodologies for obtaining a priori estimates of P^* that are known to be better (Ponce and Hawkins 1996). Michel et al. (2005, p. 1) characterize the SCS-CN method as “based on a tremendous amount of experimental work, has been widely used in the United States, and has . . . been incorporated into several rainfall-runoff models.” One must be careful, though, not to confuse the use and manipulation of curve numbers and related approaches with the science of hydrology (Klemeš 1986a).

10.6.4.3 The Unit Hydrograph

10.6.4.3.1 Definition

One of the most venerable and widely used transfer functions for RF-RO modeling is the **unit hydrograph** (also called the **unit graph**).

For a given watershed, the “ T_{P^*} -hr unit hydrograph” is its characteristic *event-flow* hydrograph in response to a unit volume (e.g., 1 in or 1 cm) of effective rainfall applied at a constant rate for T_{P^*} hours.

The central hypothesis of the unit-hydrograph approach is that watershed response is *linear*: i.e., the ordinates of the hydrograph responding to a steady input of P^* units for a duration T_{P^*} are equal to P^* times the ordinates of the T_{P^*} -hr unit hydrograph. This means that

The time base T_b of the hydrograph of event flow remains constant for all inputs of duration T_{P^*} .

Example 1 in box 10.11 (on p. 524) and figure 10.53 (on p. 525) show how the basic unit-hydrograph approach is applied.

Box 10.10 Example Application of SCS Method

Estimation of P^*

We apply the SCS method to a rain event of 107 mm in 3.4 hr on a watershed of $A_D = 3.21 \text{ km}^2$, mainstream length of 1.35 km, a main-channel slope of 0.08, and the land-cover characteristics shown in table 10B10.1.

Table 10B10.1 Land-Cover Characteristics

Land Cover	Soil Group	Area (km^2)	Fraction of Total Area	Condition II Curve Number
Forest	B	1.86	0.58	58
Forest	C	0.39	0.12	72
Meadow	A	0.67	0.21	30
Meadow	B	0.28	0.09	58

The curve numbers for condition II were found from table 10.11. The weighted-average curve number for condition II is calculated as

$$0.58 \times 58 + 0.12 \times 72 + 0.21 \times 30 + 0.09 \times 58 = 53.8 \rightarrow 54.$$

Then from equation (10.67)

$$S_{max} = \frac{25,400}{54} - 254 = 216 \text{ mm},$$

and using this value in equation (10.66) gives

$$P^* = \frac{(107 \text{ mm} - 0.2 \times 216 \text{ mm})^2}{(107 \text{ mm} + 0.8 \times 216 \text{ mm})} = 14 \text{ mm.}$$

Repeating the computations using the curve numbers adjusted for conditions I and III gives the results in table 10B10.2.

Table 10B10.2 Comparison of S_{max} and P^* Values for Antecedent Wetness Conditions

Condition	Weighted Curve Number	S_{max} (mm)	P^* (mm)
I	35	472	0.3
II	54	216	14
III	72	99	46

Estimation of Peak Discharge

To compute the peak discharge for the above event for antecedent conditions I, II, and III, we first calculate the time of concentration, T_c , using an appropriate formula from table 10.8. For this example, we select the Watt and Chow formula:

$$T_c = 0.128 \cdot \left(\frac{1.35}{0.08^{0.5}} \right)^{0.79} = 0.44 \text{ hr.}$$

From equation (10.68),

$$T_r = 0.5 \times 3.4 \text{ hr} + 0.6 \times 0.44 \text{ hr} = 1.96 \text{ hr.}$$

From equation (10.71) for condition II:

$$q_{pk} = \frac{0.208 \times 14 \times 3.21}{1.96} = 4.78 \text{ m}^3/\text{s}.$$

The results for conditions I and III are:

Condition I: $q_{pk} = 0.105 \text{ m}^3/\text{s}$;

Condition III: $q_{pk} = 13.9 \text{ m}^3/\text{s}$.

Table 10.13 Ordinates of the SCS Dimensionless Unit Hydrograph.

t/t_{pk}	q/q_{pk}	t/t_{pk}	q/q_{pk}
0.0	0.0	1.4	0.75
0.1	0.015	1.5	0.66
0.2	0.075	1.6	0.56
0.3	0.16	1.8	0.42
0.4	0.28	2.0	0.32
0.5	0.43	2.2	0.24
0.6	0.60	2.4	0.18
0.7	0.77	2.6	0.13
0.8	0.89	2.8	0.098
0.9	0.97	3.0	0.075
1.0	1.00	3.5	0.036
1.1	0.98	4.0	0.018
1.2	0.92	4.5	0.009
1.3	0.84	5.0	0.004

Source: From Viessman et al. (1989).

10.6.4.3.2 Determination of the Unit Hydrograph from Observations

Unit hydrographs for a watershed can be constructed from observations of input and response for several significant storms of approximately equal duration on the watershed. Dunne and Leopold (1978) recommended the following steps:

1. Choose four or five hydrographs from intense storms of approximately equal duration T_{P^*} and at least moderately uniform spatial and temporal distribution.
2. Plot each hydrograph and separate event response from base flow using one of the methods described in figure 9.34.

3. For each hydrograph, determine effective precipitation $P^* = Q^*$ by measuring the area between the measured flow and the separation line.
4. Multiply selected ordinates of each hydrograph by the corresponding value of $1/P^*$ to give the unit hydrograph ordinates for each storm. Note that these ordinates have dimensions of $[T^{-1}]$ (usually units of hr^{-1}).
5. Plot the unit hydrographs on the same graph, each beginning at the same time (figure 10.54a on p. 526).
6. Determine the peak of the composite unit graph as the average of all the peaks, and plot the average peak at the average time of occurrence of all the peaks.
7. Sketch the composite unit graph to conform to the average shape of the plotted unit graphs, with the peak as determined in step 6.
8. Measure the area under the sketched curve, and adjust the curve until this area is satisfactorily close to 1 unit (centimeter or inch) of runoff (figure 10.54b on p. 526).

Theoretically, unit hydrographs can also be determined from observations of rainfall and runoff using matrix algebra (see, for example, Viessman et al. 1989). However, application of the matrix approach is limited in practice because it requires that the time distribution of effective water input be known.

10.6.4.3.3 Deriving Unit Hydrographs of Different Durations

Once the unit graph for a given duration of excess water input, say T'_{P^*} , is obtained, the unit graph for any other duration can be readily derived as described below.

Estimating longer-duration unit hydrographs: Note that, if an event producing 1 unit of effective in-

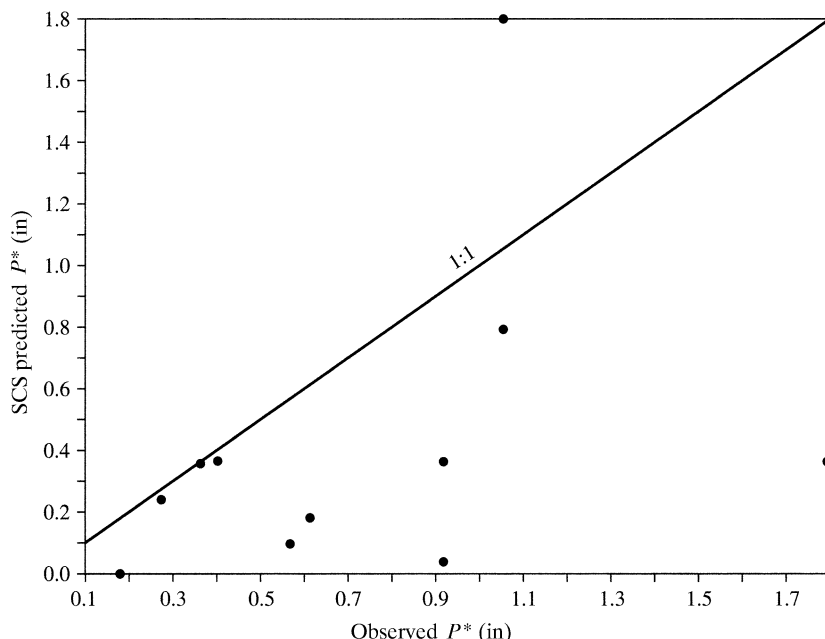


Figure 10.52 P^* estimated a priori by the SCS method versus P^* determined by hydrograph separation for 11 storms on Ralston Creek Research Watershed, Iowa [data from Kumar and Jain (1982)].

Box 10.11 Unit-Hydrograph Examples

Example 1: Peak-Flow Prediction

Figure 10.53 shows the 2.5-hr unit ($1 \text{ in} = 2.54 \text{ cm}$) hydrograph for a 7.2-mi^2 ($= 18.6\text{-km}^2$) watershed; i.e., the event-flow response of the watershed to 1 in of effective rainfall on the watershed over 2.5 hr. The peak flow is $2,980 \text{ ft}^3/\text{s}$ ($= 84.4 \text{ m}^3/\text{s} = 0.43 \text{ cm/hr}$). To find the response hydrograph for an effective rainfall of 2.4 in ($= 6.10 \text{ cm}$) for the same duration, the unit-hydrograph ordinates are multiplied by 2.4, yielding the larger hydrograph in figure 10.53. The predicted peak flow is thus $2.4 \times 2,980 \text{ ft}^3/\text{s} = 7,160 \text{ ft}^3/\text{s}$ ($= 203 \text{ m}^3/\text{s} = 1.04 \text{ cm/hr}$).

Example 2: Deriving Unit Hydrographs of Longer Durations

The 5-hr unit hydrograph for the above watershed is found from the 2.5-hr unit hydrograph as shown in figure 10.55. Figure 10.55a shows the 2.5-hr unit graph lagged by 2.5 hr and summed; this gives the response to 2 in ($= 5.08 \text{ cm}$) of effective rainfall in 5 hr. Figure 10.55b shows the 5-hr unit graph obtained by halving the ordinates of the summed hydrograph of figure 10.55a. Thus the peak flow for 1 in ($= 2.54 \text{ cm}$) in 5 hr is $2,310 \text{ ft}^3/\text{s}$ ($= 65.4 \text{ m}^3/\text{s} = 0.34 \text{ cm/hr}$).

Example 3: Deriving Unit Hydrographs of Shorter Durations

The 1-hr unit hydrograph for this watershed is found from the 2.5-hr unit hydrograph as shown in figure 10.56. In figure 10.56a the S-hydrograph is derived by summing successive 2.5-hr unit hydrographs (figure 10.53) lagged by 2.5 hr. The S-hydrograph constructed from figure 10.56a is the left-hand curve in figure 10.56b. The right-hand curve is that S-hydrograph lagged by 1 hr. Figure 10.56c shows the difference between the two S-hydrographs of figure 10.56b; this difference represents the response to 1 in ($= 2.54 \text{ cm}$) effective rain in 1 hr. Figure 10.56d is the 1-hr unit hydrograph obtained by multiplying the ordinates in figure 10.56c by 2.5. The peak discharge for 1 in ($= 2.54 \text{ cm}$) effective rainfall in 1 hr is $3,000 \text{ ft}^3/\text{s}$ ($= 85.0 \text{ m}^3/\text{s} = 0.44 \text{ cm/hr}$).

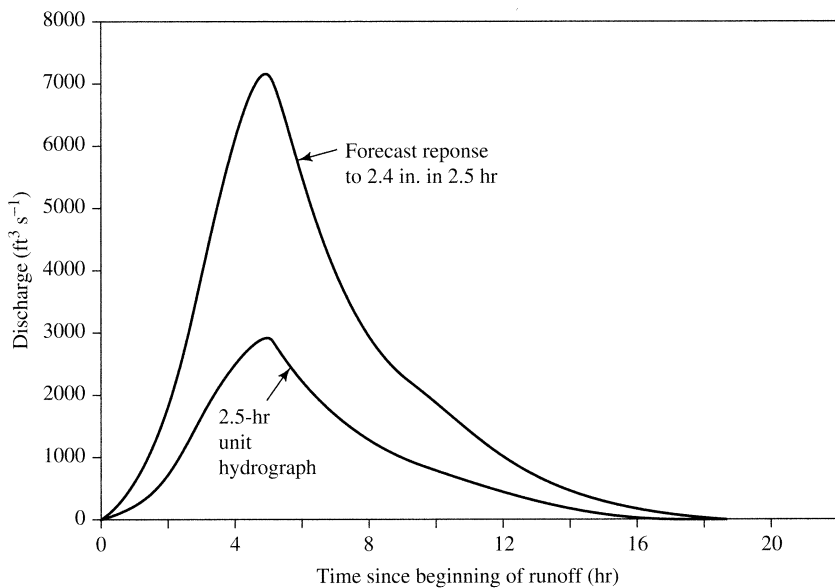


Figure 10.53 The 2.5-hr unit (in) hydrograph for a 7.2-mi² watershed and the hydrograph given by the unit-hydrograph approach for 2.4 in of effective rain applied for 2.5 hr.

put over the period $t = 0$ to $t = T'_{P^*}$ hr is followed by a second identical event over the period $t = T'_{P^*}$ to $t = 2 \cdot T'_{P^*}$ hr, the response hydrograph will be given by the sum of the ordinates of two T'_{P^*} -hr unit hydrographs, one beginning at $t = 0$ hr and the other at $t = T'_{P^*}$ hr. This new hydrograph thus represents the response to 2 units of effective input in $2 \cdot T'_{P^*}$ hr. Thus if we divide the ordinates of this new hydrograph by 2, we have the $2 \cdot T'_{P^*}$ -hr unit hydrograph.

To generalize the above procedure: Given a T'_{P^*} -hr unit graph, the $n \cdot T'_{P^*}$ -hr unit hydrograph for $n = 2, 3, 4, \dots$, can be obtained by adding the n unit graphs, each lagged by T'_{P^*} , and dividing the resulting ordinates by n . See example 2 of box 10.11 and figure 10.55 on p. 527.

Estimating shorter-duration unit hydrographs: Unit hydrographs for a duration T_{P^*} less than T'_{P^*} can be obtained from the T'_{P^*} -hr unit graph by constructing an **S-hydrograph** via the following steps (figure 10.56 on p. 528) (see example 3 of box 10.11):

1. A series of T_{P^*} -hr unit hydrographs are plotted, beginning at successive intervals of

$$t = T'_{P^*}, 2 \cdot T'_{P^*}, 3 \cdot T'_{P^*}, \dots$$

2. Successive lagged unit hydrographs are added until the S-hydrograph ordinate becomes effectively constant to give the ordinates of the S-hydrograph.

3. Plot the S-hydrograph twice, the first beginning at $t = 0$, and the second beginning at $t = T_{P^*}$, and subtract the ordinates for the lagged curve from those of the first curve.

4. Multiply the ordinates found in step 3 by T'_{P^*} to give the ordinates for the T_{P^*} -hr unit graph.

The S-hydrograph thus represents the hydrograph of a storm of infinite duration at an intensity of 1 unit/ T'_{P^*} . Each watershed is characterized by a single S-hydrograph, from which the unit hydrograph for any duration of input can be obtained.

10.6.4.3.4 The Instantaneous Unit Hydrograph

If the input duration T_{P^*} used to define the unit hydrograph is allowed to become infinitesimally small, the resulting response function is called the *instantaneous unit hydrograph*:

The instantaneous unit hydrograph (IUH)

is the response of the watershed to a unit volume of effective precipitation applied instantaneously.

This concept, although obviously theoretical, is useful because it can be used to develop unit hydrographs of any duration. Another advantage of the IUH is that it permits the use of continuous mathematics in developing the transfer function from mea-

surements of the watershed response hydrograph, $q^*(t)$, to a continuous input, $p^*(t)$. Bras (1990) reviewed several approaches to doing this.

10.6.4.3.5 Synthetic Unit Hydrographs

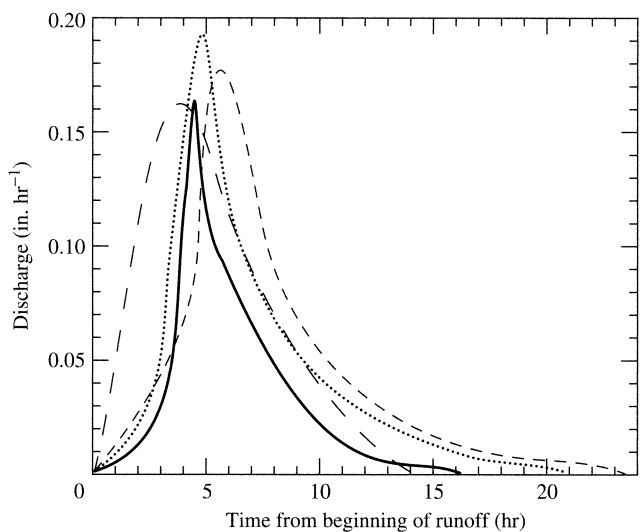
Synthetic unit hydrographs provide a means for estimating the unit hydrograph based on watershed characteristics when measured values of rainfall and runoff for previous storms are not available.

The **linear-watershed instantaneous unit hydrograph** is based on the linear-watershed model (box 10.3). It can be shown that the linear-watershed

model is equivalent to an IUH having ordinates, $h(t)$, given by the simple mathematical form

$$h(t) = \frac{1}{T^*} \cdot \exp\left(-\frac{t}{T^*}\right) \quad (10.72)$$

(Bras 1990). If T^* can be estimated from relations like those in table 10.8 and equation (10.16), then the response of the linear model to a unit input for the duration of interest is the unit hydrograph for that duration. Once T^* is determined, the linear model can be used directly to estimate the response to any



(a)

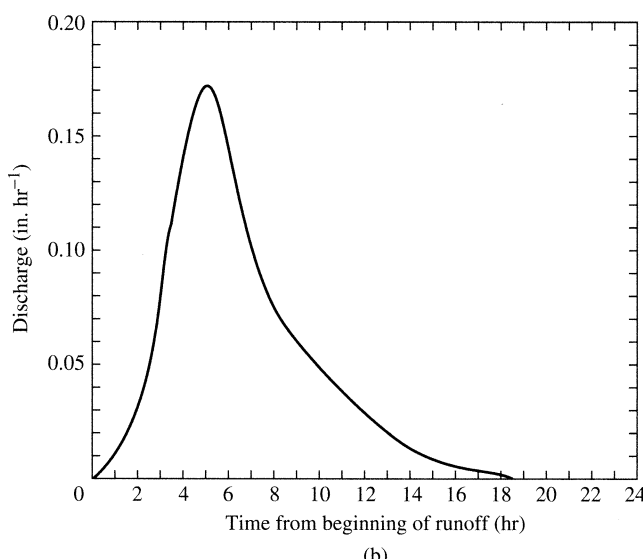


Figure 10.54 (a) Unit hydrographs for the watershed of box 10.11 derived from four storms of $T_{p*} \approx 2.5$ hr. (b) Composite "average" 2.5-hr unit hydrograph derived from (a) as described in section 10.6.4.3. This is the same unit hydrograph shown in figure 10.53 [Dunne and Leopold (1978)].

sequence of inputs without explicitly invoking the unit hydrograph, as done in section 10.2.5.

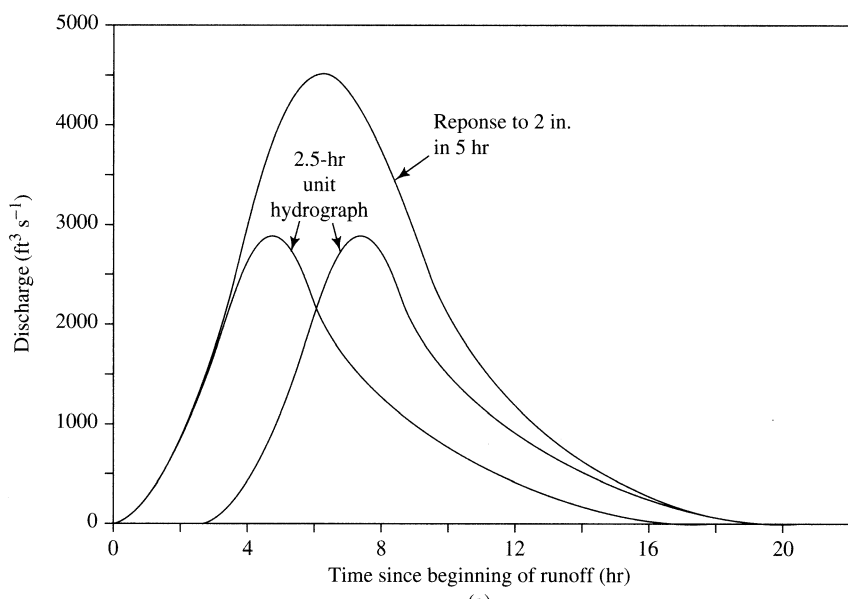
The concept of the **geomorphologic instantaneous unit hydrograph (GIUH)** was introduced in a series of papers by Rodriguez-Iturbe et al. (1979), Rodriguez-Iturbe and Valdes (1979), Valdes et al. (1979), and developed further by Gupta et al. (1980) and Rodriguez-Iturbe (1993). Very briefly, they used statistical concepts and extensions of the laws of drainage composition (table 10.1) to develop the fol-

lowing relations for estimating the peak, q_{pk} , and time-of-rise, T_r , of the IUH:

$$\frac{q_{pk}}{P^*} = 1.31 \cdot \frac{R_L^{0.43} \cdot u_{pk}}{L_\Omega} \quad (10.73)$$

and

$$T_r = 0.44 \cdot \frac{L_\Omega}{u_{pk}} \cdot \left(\frac{R_B}{R_A} \right)^{0.55} \cdot \left(\frac{1}{R_L} \right)^{0.38}, \quad (10.74)$$



(a)

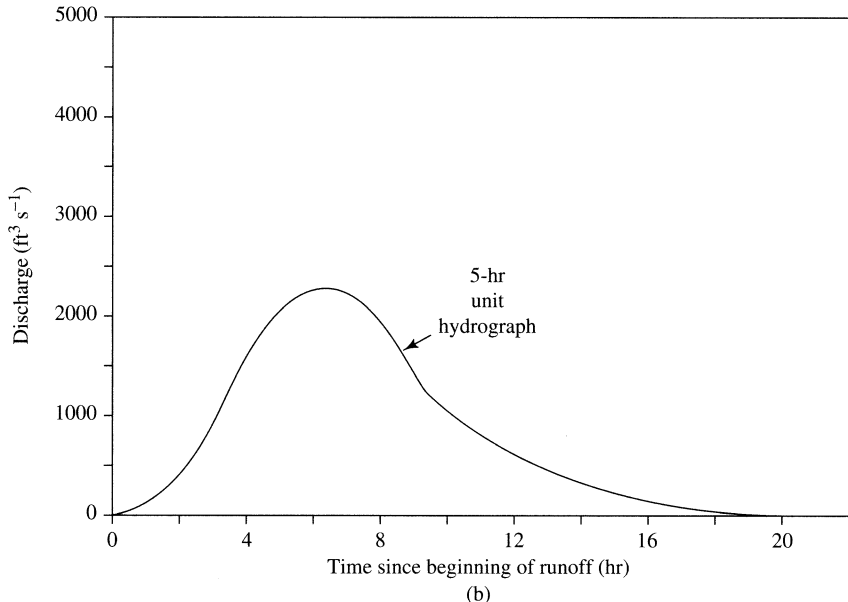


Figure 10.55 (a) The 2.5-hr unit hydrograph of figure 10.54 lagged by 2.5 hr and summed to give the response to 2 in of effective rainfall in 5 hr. (b) The 5-hr unit hydrograph derived by halving the ordinates of the hydrograph of (a).

where q_{pk}/P^* is in hr^{-1} ; T_r is in hr; L_Ω is the length of the highest-order stream in km; R_B , R_A , and R_L are the bifurcation, area, and length ratios defined in table 10.1; and u_{pk} is the velocity of flow in the channel network in m/s, which can be estimated via equation (10.43).

10.6.4.3.6 Application of the Unit-Hydrograph Approach

Freeze (1972a) concluded from a series of experiments with physically based models that “no physical reason seems to exist why watersheds should respond in a linear fashion,” and it is clear that the linear-response assumptions of unit-hydrograph theory are at best only approximated by actual watersheds (see, for example, Valdes et al. 1979).

However, the unit hydrograph is often the only feasible way to approach practical problems. Dunne

and Leopold (1978) stated that the unit-hydrograph method gives estimates of flood peaks that are usually within 25% of their true value; this may be close enough for most planning purposes and about as close as can be expected given the usual lack of detailed information about watershed processes and states. Errors larger than 25% can be expected if synthetic unit graphs are used without verification for the region of application. As noted earlier in this chapter, the assumption of linearity that underlies the unit-hydrograph approach seems most valid for large rainstorms on relatively large watersheds ($A_D > 100 \text{ km}^2$).

The most important difficulties in applying the unit-hydrograph approach are:

1. The rainfall-runoff relationships are between *effective* input and *event* response, and it is often not

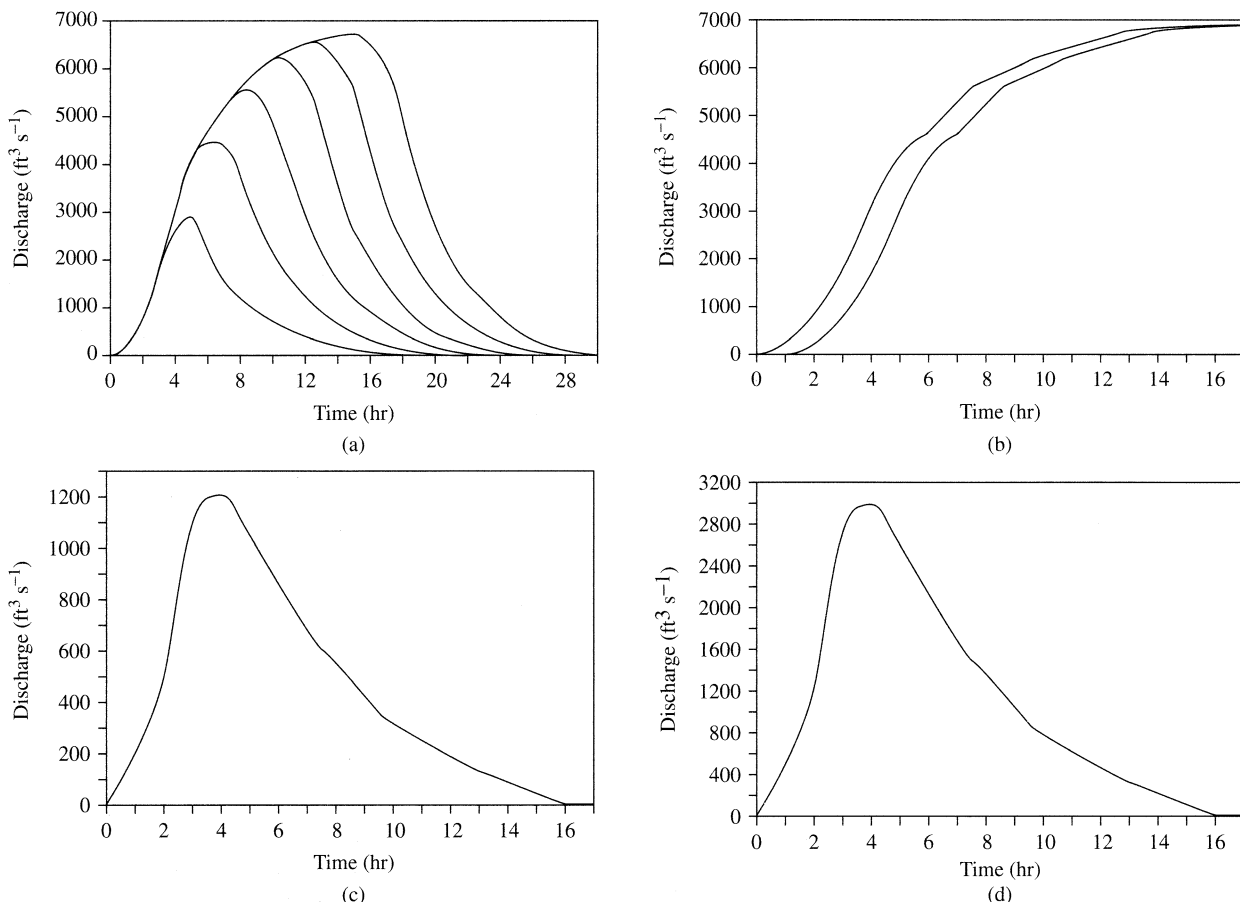


Figure 10.56 (a) The S-hydrograph for the watershed of box 10.11 derived by summing the 2.5-hr unit hydrograph (figure 10.54b) lagged by 2.5 hr. (b) The S-hydrograph lagged by 1 hr. (c) The difference between the two S-hydrographs of (b). (d) The 1-hr unit hydrograph obtained by multiplying the ordinates of (c) by 2.5.

clear how to make reliable a priori estimates of effective input. There is usually little information about the magnitudes of the loss quantities in equation (10.64), and since P^* is usually small relative to P , small relative errors in estimating those quantities lead to large relative errors in estimating event flow.

2. Because of the temporal variability of contributing area and rates of water movement, it is difficult to identify characteristic response times for real watersheds. In fact, unless contributing area in a given watershed follows exactly the same patterns of temporal and spatial change in every storm, the watershed cannot have a single unit hydrograph.
3. In general, the characteristic response of a given drainage basin depends strongly on antecedent conditions (figures 10.10 and 10.11), so the assumption of linearity of response may be grossly in error, except for large storms when it can be assumed that watershed storage is essentially filled.

In spite of these difficulties, Singh et al. (2013) concluded that the geomorphological synthetic unit hydrograph approach has potential for estimating streamflow responses in ungauged watersheds, because it has a sound theoretical basis and can be implemented using geomorphological and stream-network information that can be extracted from digital elevation models and remote-sensing observations.

▼ EXERCISES

1. Consider a stream reach for which $X = 2,500$ m, $w = 10$ m, Manning's $n = 0.042$, and $\zeta = 0.0005$. Using the convex method, compute the outflow hydrograph for this reach given a triangular inflow hydrograph that begins at $QI(0) = 0$ m³/s, reaches a peak, QI_{pk} , of 100.0 m³/s at 3.0 hr, and declines to 0 m³/s at 10.0 hr. Use the spreadsheet program GoConvex.xls, which can be found on the disk that accompanies this text.
2. Obtain topographic maps of a region of interest containing the drainage basin of a fourth- or fifth-order stream.
 - a. Designate stream orders as indicated in figure 10.1, and determine whether the law of stream numbers is followed.
 - b. Determine the average lengths and areas of streams for each order (you need measure only a selected sample of the low-order streams) and see if the laws of stream lengths and areas is followed.

3. Use the method of equation (10.8) to determine the drainage density of a region.

4. Obtain the hydrograph of a stream responding to a known rainfall and use one of the methods depicted in figure 9.34 to determine Q^* , then assume $P^* = Q^*$ and compute P^*/P .

Repeat the example calculations in box 10.10 using the revised SCS-CN method described in box 10.9 and compare the two sets of results.

5. If soils and land-use information are available for the watershed used in exercise 4, compare the "actual" P^* with that given by the SCS curve-number method.
6. Obtain the hyetograph and hydrograph for a rainfall event on a watershed.
 - a. Separate the hydrograph using one of the methods of figure 9.34 and estimate the hyetograph of the effective rainfall (you may use a method similar to the one used in the example of box 10.2).
 - b. Estimate the centroid of the effective rain and calculate the centroid lag.
 - c. Compare the "actual" values of centroid lag, peak-flow rate, and response time with T_c given by one or more of the formulas in table 10.8, T_f given by equation (10.68), and q_{pk} given by equation (10.71).

7. Compare the hydrograph of event flow developed in exercise 6 with that obtained via the linear-watershed model (box 10.3) for the same effective input hyetograph, assuming $T^* =$ the "actual" centroid lag.
8. Compare the hydrograph of event flow developed in exercise 6 with that obtained via the SCS dimensionless unit hydrograph (table 10.13) for the same effective input hyetograph.
9. From the geologic, soils, topographic, and vegetative conditions in your region, which mechanism(s) are likely to contribute water to event responses? Have any studies that shed light on this question been done in the region?

▼ NOTES

¹ Globally, a small fraction of continental runoff occurs as ground water.

² Recall, though, that we have seen (section 9.5.5) that situations in which a portion of streamflow originates as ground-water inflow from outside the topographic watershed are not uncommon.

³ So-called even if no actual flooding (overbank flow) occurs.

⁴ The question of event-flow identification is relevant to snowmelt events also, but since snowmelt is seldom directly measured and snowmelt events are usually analyzed separately, we limit the discussion here to rainfall events.

⁵ Snowmelt rates seldom exceed 0.5 cm/hr (see chapter 5).

Appendix

A

Measurement Precision, Significant Figures, and Unit and Equation Conversion

A.1 Measurement Precision and Significant Figures

A.1.1 Measured Quantities

All measurements are made with finite precision.

Precision is the “fineness,” or degree, to which a quantity is measured. **Absolute precision** may be expressed

1. explicitly as

$$x_{\text{meas}} = x \pm \delta x, \quad (\text{A.1})$$

where x_{meas} is the measured value, x is the observer’s best estimate of the “true” value, and δx is the **error** or **uncertainty** in the measurement, i.e., the bounds of the range in which the observer is “reasonably confident” that the true value lies (see section 1.11);

2. in terms like “measurements were made to the nearest u ,” where u is some measurement unit; or
3. implicitly, as the number of **significant figures** in the reported value, where

The number of **significant figures** in a measured quantity is equal to the number of digits beginning with the leftmost nonzero digit and extending to the right to include all digits warranted by the precision of the measurement.

For example, if we were to measure a distance to the nearest centimeter, we would report it as, say, 21 cm. If we were to report the measurement as 21.0 cm or 21.00 cm, we would be implying that it had been made to the nearest 0.1 cm or 0.01 cm, respectively. However, if a measurement is given as, say, 200 m, the precision is not clear because we don’t know if the measurement was made to the nearest 1 m, 10 m, or 100 m. The best way of avoiding this ambiguity is to use scientific notation and express the quantity as 2×10^2 m, 2.0×10^2 m, or 2.00×10^2 m, as appropriate. Otherwise, additional information, usually in the form of other analogous measurements, is required to clarify the situation. Note that the number of significant figures also indicates the range of *relative precision* in a measured quantity:

Significant Figures	Relative Uncertainty Range
4	1/10,000 to 1/1,000
3	1/1,000 to 1/100
2	1/100 to 1/10

Hydrologic measurements cannot usually be made with great precision, so

RULE 1: Unless it is clear that greater precision is warranted, assume no more than three-significant-figure precision in measured hydrologic quantities.

In many cases, only two significant figures are warranted. For example, it is the policy of the USGS to report discharge (streamflow) measurements with the precision shown in table A.1.

Table A.1 Absolute Precision of Streamflow Data Reported by the USGS.

Discharge Range		Precision	
(ft ³ /s)	(m ³ /s)	(ft ³ /s)	(m ³ /s)
< 1	< 0.028	0.01	0.0003
1 to 9.9	0.028 to 0.28	0.1	0.003
10 to 999	0.28 to 28.3	1	0.028
> 1,000	> 28.3	three significant figures	

A.1.2 Computations with Measured Quantities

It is important that the uncertainty in measured values be appropriately reflected in computations using those values. In computations made with measured quantities, including unit conversions (section A.2), the appropriate level of precision is obtained by observing rules 2 and 3:

RULE 2: The absolute precision of a sum or difference equals the absolute precision of the *least* absolutely precise number involved in the calculation.

RULE 3: The number of significant figures of a product or quotient equals the number of significant figures of the *least* relatively precise number involved in the calculation.

Examples in box A.1 show application of these rules. However, in order to avoid the risk of losing significant figures during calculations, you should observe rule 4:

RULE 4: In computations involving several steps, do not round off to the appropriate number of significant figures until you get to the final answer.

Be sure to do the appropriate rounding at the end, because

RULE 5: The numbers on computer printouts and calculator displays almost always have more digits than is warranted by the precision of measured hydrologic quantities.

As noted by Harte (1985, p. 4),

Nonsignificant figures have a habit of accumulating in the course of a calculation, like mud on a boot, and you must wipe them off at the end. It is still good policy to keep one or two nonsignificant figures during a calculation, however, so that the rounding off at the end will yield a better estimate.

A.2 Unit Conversion

A.2.1 Units with Common Zero

Because of the common use of three systems of units and the proliferation of units within each system, hydrologists must become experts in the skill of converting from one set of units to another.

Table A.2 on pp. 534–536 lists quantities commonly encountered in hydrological practice, in dimensional categories. All quantities listed below each dimensional category are identical and, except for commonly used temperature units (discussed below), a zero value in one unit system is a zero value in the other systems. For these quantities, unit conversions are carried out by chaining quantities as numerators and denominators to make a multiplier (conversion factor) equal to unity, and the decision of whether to put the factor in the numerator or denominator is determined by the direction of the conversion. For example, to convert a pressure of 4.23 mH₂O to kPa,

$$4.23 \text{ mH}_2\text{O} \cdot \frac{1 \times 10^{-3} \text{ kPa}}{1.0198 \times 10^{-4} \text{ mH}_2\text{O}} = 41.47872 \text{ kPa} \rightarrow 41.5 \text{ kPa.}$$

Note that

All conversion factors have infinite precision; it is only the precision of the measured quantities that determines the significant figures of the converted value.

Box A.1 Examples of Correct Treatment of Precision

Computations with Measured Quantities

Example AB1.1

The average flow for two consecutive days is reported as 102 ft³/s and 3.2 ft³/s. What is the total for the two days?

Answer: Adding the reported values gives 105.2 ft³/s, but since the larger flow was measured only to the nearest 1 ft³/s, rule 2 dictates that we report the total as 105 ft³/s.

Example AB1.2

The average flow for two consecutive days is reported as 1,020 ft³/s and 3.2 ft³/s. What is the total for the two days?

Answer: Here rule 2 dictates that the sum be reported as 1,020 ft³/s, because the larger flow was measured to the nearest 10 ft³/s.

Example AB1.3

Given the following daily flows (in ft³/s), what is the total flow for the period?

27 104 12 2,310 6.4 0.11 256

Answer: Adding all these values gives 2,715.51 ft³/s, but since the largest value was measured only to the nearest 10 ft³/s, rule 2 dictates that we report the sum as 2,720 ft³/s.

Example AB1.4

Discharge, Q , at a stream cross section is measured as the product of water-surface width, w , average depth, Y , and average velocity, U . The results of a measurement are $w = 20.4$ m, $Y = 1.2$ m, and $U = 1.7$ m/s.

To report the discharge properly, first calculate

$$Q = 20.4 \text{ m} \times 1.2 \text{ m} \times 1.7 \text{ m/s} = 41.616 \text{ m}^3/\text{s}.$$

However, because of rule 3, we report the discharge to two significant figures as $Q = 42 \text{ m}^3/\text{s}$. To state the uncertainty explicitly, follow rule 7 and write

$$Q = 42 \pm 1 \text{ m}^3/\text{s}.$$

Temperature Conversion

Example AB1.5

To convert a temperature difference of 3.4 F° to C°,

$$3.4 \text{ F}^\circ \cdot \frac{1 \text{ C}^\circ}{1.8 \text{ F}^\circ} = 1.888 \dots \text{ C}^\circ \rightarrow 1.9 \text{ C}^\circ.$$

Example AB1.6

To convert a temperature difference of 3.4 C° to F°,

$$3.4 \text{ C}^\circ \cdot \frac{1.8 \text{ F}^\circ}{1 \text{ C}^\circ} = 6.12 \text{ F}^\circ \rightarrow 6.1 \text{ F}^\circ.$$

Example AB1.7

To convert an actual temperature of -37°C to °F, combine formulas in table A.2 to give

$$\frac{1.8 \text{ F}^\circ}{1 \text{ C}^\circ} \cdot (T \text{ }^\circ\text{C}) + 32 \text{ }^\circ\text{F} = T \text{ }^\circ\text{F},$$

so

$$1.8(-37 \text{ }^\circ\text{C}) + 32 = -34.6 \text{ }^\circ\text{F} \rightarrow -35 \text{ }^\circ\text{F}.$$

Example AB1.8

To convert an actual temperature of -37°F to °C, the formulas in table A.2 can be inverted to give

$$(T \text{ }^\circ\text{F} - 32 \text{ }^\circ\text{F}) \cdot \frac{1 \text{ C}^\circ}{1.8 \text{ F}^\circ} = T \text{ }^\circ\text{C},$$

so

$$(-37 \text{ }^\circ\text{F} - 32 \text{ }^\circ\text{F}) \cdot \frac{1 \text{ C}^\circ}{1.8 \text{ F}^\circ} = -38.33 \dots \text{ }^\circ\text{C} \rightarrow -38 \text{ }^\circ\text{C}.$$

The conversion factors in table A.2 are given to at least five significant figures (those given as "1" are exact, i.e., they have infinite significant figures) so that rule 6 can be observed:

RULE 6: In unit conversions, the number of digits retained in the conversion factors must be greater than the number of significant digits in any of the measured quantities involved.

The above rules must be followed in all unit conversions. However, the process can lead to some am-

biguity in representing uncertainty appropriately. For example, to convert a distance measured as 9.6 mi in m, we use table A.2 to calculate

$$9.6 \text{ mi} \times \frac{1 \text{ m}}{6.2137 \times 10^{-4} \text{ mi}} = 15,449.73 \text{ m}.$$

Clearly it would be misleading to express the result as 15,449.73 m, because this would imply that we know the distance to a precision of 0.01 m, whereas the original measurement was known only to 0.1 mi, or about 161 m. Following rule 3, we round the converted

Table A.2 Unit-Conversion Table.^a

Mass [M]		Force [F]		Length [L]		Time [T]	
1 kg		1 N		1 m		1 s	
1 \times 10 ³ g		1 \times 10 ⁵ dyne		1 \times 10 ² cm		1.6667 \times 10 ⁻² min	
1 \times 10 ⁻³ T		2.2482 \times 10 ⁻¹ lb		1 \times 10 ⁻³ km		2.7778 \times 10 ⁻⁴ hr	
6.8521 \times 10 ⁻² slug		1.0198 \times 10 ⁻¹ kg _f		1 \times 10 ³ mm		1.1574 \times 10 ⁻⁵ d	
2.2046 lb _m				1 \times 10 ⁶ μ m		3.1688 \times 10 ⁻⁸ yr ^b	
1.1023 \times 10 ⁻³ ton _m				1 \times 10 ⁹ nm		3.1710 \times 10 ⁻⁸ yr ^c	
				1 \times 10 ¹⁰ \AA			
				3.9370 \times 10 ¹ in			
				3.2808 ft			
				6.2137 \times 10 ⁻⁴ mi			
				1.0936 yd			
Area [L ²]		Volume [L ³]		Mass Density [M L ⁻³]		Weight Density [F L ⁻³]	
1 m ²		1 m ³		1 kg/m ³		1 N/m ³	
1 \times 10 ⁴ cm ²		1 \times 10 ⁶ cm ³		1 \times 10 ⁻³ g/cm ³		1 \times 10 ⁻¹ dyne/cm ³	
1 \times 10 ⁻⁴ ha		1 \times 10 ⁹ mm ³		1 \times 10 ⁻³ kg/L		1.0198 \times 10 ⁻¹ kg _f /m ³	
1 \times 10 ⁻⁶ km ²		1 \times 10 ⁻⁹ km ³		6.2428 \times 10 ⁻² lb _m /ft ³		6.3666 \times 10 ⁻³ lb/ft ³	
1 \times 10 ⁶ mm ²		1 \times 10 ³ L					
1.5500 \times 10 ³ in ²		6.1024 \times 10 ⁴ in ³					
1.0764 \times 10 ¹ ft ²		3.5314 \times 10 ¹ ft ³					
2.4711 \times 10 ⁻⁴ acre		2.6417 \times 10 ² gal					
3.8611 \times 10 ⁻⁷ mi ²							
Velocity [L T ⁻¹]		Acceleration [L T ⁻²]		Diffusivity [L ² T ⁻¹]		Discharge [L ³ T ⁻¹]	
1 m/s		1 m/s ²		1 m ² /s		1 m ³ /s	
1 \times 10 ² cm/s		1 \times 10 ² cm/s ²		1 \times 10 ⁴ cm ² /s		1 \times 10 ⁶ cm ³ /s	
1 \times 10 ³ mm/s		3.2808 ft/s ²		1 \times 10 ⁴ stoke		1 \times 10 ³ L/s	
3.6000 \times 10 ³ m/hr				3.8750 ft ² /hr		3.1558 \times 10 ⁻² km ³ /yr	
8.6400 \times 10 ⁴ m/d						3.5314 \times 10 ¹ ft ³ /s	
3.6000 \times 10 ⁵ cm/hr						1.5850 \times 10 ⁴ gal/min	
3.6000 \times 10 ⁶ mm/hr						2.2824 \times 10 ⁷ gal/d	
2.2369 mi/hr							
3.2808 ft/s							
1.9425 knot							

Table A.2 (cont'd.)

Dynamic Viscosity [M L ⁻¹ T ⁻¹] = [F L ⁻² T]		Mass Flux [M L ⁻² T ⁻¹]		Pressure [M L ⁻¹ T ⁻²] = [F L ⁻²]	
1 kg/m · s		1 kg/m ² · s		1 kg/m · s ²	
1 Pa · s		1 × 10 ⁻¹ g/cm ² · s		1 N/m ²	
1 N · s/m ²		8.6400 × 10 ⁴ kg/m ² · d		1 Pa	
1 × 10 ¹ dyne · s/cm ²		3.1558 × 10 ¹¹ kg/ha · yr		1 × 10 ¹ dyne/cm ²	
1 × 10 ¹ g/cm · s		2.0476 × 10 ⁻¹ lb _m /ft ² · s		1.0198 × 10 ⁻¹ kg _f /m ²	
1 × 10 ¹ poise				1 × 10 ⁻² mb	
2.0886 × 10 ⁻² lb · s/ft ²				1 × 10 ⁻³ kPa	
6.7197 × 10 ⁻¹ lb _m /ft · s				1 × 10 ⁻⁵ bar	
				9.8717 × 10 ⁻⁶ atm	
				7.5018 × 10 ⁻³ mm Hg	
				1.0198 × 10 ⁻² cm H ₂ O	
				1.0198 × 10 ⁻⁴ m H ₂ O	
				3.3456 × 10 ⁻⁴ ft H ₂ O	
				2.9533 × 10 ⁻⁴ in Hg	
				1.4505 × 10 ⁻⁴ lb/in ²	
				2.0886 × 10 ⁻² lb/ft ²	
Angle [1]	Temperature Unit [Θ]	Actual Temperature, T [Θ]			
1 radian	1 K	T		K	
5.7296 × 10 ¹ degree	1 C°	T - 273.16		°C	
	1.8 F°	1.8 · (T - 273.16) + 32		°F	
Energy [M L ² T ⁻²] = [F L] = [E]		Power [M L ² T ⁻³] = [F L T ⁻¹] = [E T ⁻¹]			
1 kg · m ² /s ²		1 kg · m ² /s ³			
1 N · m		1 N · m/s			
1 J		1 J/s			
1 W · s		1 W			
1 × 10 ⁻⁶ MJ		1 × 10 ⁻³ kW			
1 × 10 ⁷ g · cm ² /s ²		1 × 10 ⁻⁶ MW			
1 × 10 ⁷ erg		1 × 10 ³ mW			
2.7778 × 10 ⁻⁴ W · hr		1 × 10 ⁷ g · cm ² /s ³			
2.7778 × 10 ⁻⁷ kW · hr		1 × 10 ⁷ erg/s			
2.3883 × 10 ⁻¹ cal		2.3883 × 10 ⁻¹ cal/s			
2.3883 × 10 ⁻⁴ kcal		1.4330 × 10 ¹ cal/min			
7.3746 × 10 ⁻¹ ft · lb		2.0634 × 10 ⁴ cal/d			
9.4787 × 10 ⁻⁴ Btu		1.3410 × 10 ⁻³ hp			
3.7258 × 10 ⁻⁷ hp · hr		3.4123 Btu/hr			
		8.5979 × 10 ⁻¹ kcal/hr			

(continued)

Table A.2 (cont'd.)

Surface Tension, Energy/Area $[M\ T^{-2}] = [F\ L^{-1}] = [E\ L^{-2}]$		Energy Flux $[M\ T^{-3}] = [F\ L^{-1}\ T^{-1}] = [E\ L^{-2}\ T^{-1}]$	
1	kg/s ²	1	kg/s ³
1	N/m	1	N/m · s
1	J/m ²	1	J/m ² · s
1	W · s/m ²	1	W/m ²
1	$\times\ 10^3$ dyne/cm	1 $\times\ 10^3$	dyne/cm · s
2.3883	$\times\ 10^{-5}$ cal/cm ²	3.6000 $\times\ 10^{-3}$	MJ/m ² · hr
1	$\times\ 10^3$ g/s ²	8.6400 $\times\ 10^{-2}$	MJ/m ² · d
1	$\times\ 10^3$ erg/cm ²	8.6400 $\times\ 10^2$	MJ/ha · d
6.8532	$\times\ 10^{-2}$ lb/ft	2.3883 $\times\ 10^{-5}$	cal/cm ² · s
		2.0635	cal/cm ² · d
		3.1701 $\times\ 10^{-1}$	Btu/ft ² · hr
Latent Heat $[L^2\ T^{-2}] = [E\ M^{-1}]$		Heat Capacity $[L^2\ T^{-2}\ \Theta^{-1}] = [E\ M^{-1}\ \Theta^{-1}]$	
1	J/kg	1	J/kg · K
1	$\times\ 10^{-6}$ MJ/kg	1 $\times\ 10^{-6}$	MJ/kg · K
2.3883	$\times\ 10^{-4}$ cal/g	2.3883 $\times\ 10^{-4}$	cal/g · C°
4.2995	$\times\ 10^{-4}$ Btu/lb _m	2.3886 $\times\ 10^{-4}$	Btu/lb _m · F°
Thermal Conductivity $[M\ L\ T^{-3}\ \Theta^{-1}] = [F\ T^{-1}\ \Theta^{-1}] = [E\ L^{-1}\ T^{-1}\ \Theta^{-1}]$		Heat Transfer Coefficient $[M\ T^{-3}\ \Theta^{-1}] = [F\ L^{-1}\ T^{-1}\ \Theta^{-1}] = [E\ L^{-2}\ T^{-1}\ \Theta^{-1}]$	
1	J/m · s · K	1	J/m ² · s · K
1	$\times\ 10^{-6}$ MJ/m · s · K	1 $\times\ 10^{-6}$	MJ/m ² · s · K
2.3883	$\times\ 10^{-3}$ cal/cm · s · C°	8.6400 $\times\ 10^{-2}$	MJ/m ² · d · K
5.7782	$\times\ 10^{-1}$ Btu/ft · hr · F°	2.3883 $\times\ 10^{-5}$	cal/cm ² · s · C°
		1.7611 $\times\ 10^{-1}$	Btu/ft ² · hr · F°

^a This table is a modification of one developed by Dr. C. Anthony Federer, formerly of the US Forest Service, Durham, New Hampshire.

^b average year = 365.25 days.

^c 365-day year.

value to two significant figures, and report the result as 15,000 m. Stating the distance as 15,000 m implies an absolute precision of 1,000 m, which is considerably less precise than the original measurement precision of ~ 161 m. It would be appropriate to state the result as 1.5×10^4 m, making the two-significant-figure precision explicit, and implying an absolute precision of about 7% or 100 m, which is close to 161 m. Note that it is incorrect to state the uncertainty as ± 161 m, or even ± 160 m, because this implies a precision of 1 m or 10 m in the original measurement. In fact, Taylor (1997, p. 15) states the following rule:

RULE 7: Measurement uncertainties should almost always be rounded to one significant figure.

Following this rule, one would state the converted value with an explicit absolute precision as $15,000 \pm 200$ m.

A.2.2 Temperature Conversion

Note that actual Celsius and Fahrenheit temperatures are written here with the degree sign before the letter symbol (read “degrees Celsius” or “degrees

Fahrenheit”), while temperature *differences*—distances on the temperature scale—for each system are written with the symbol after the letter (read “Celsius degree” or “Fahrenheit degree”). The zero point for the Kelvin scale is absolute zero, so the degree sign is not used in that system.

Because we are dealing only with distances on the temperature scales,

Conversion of temperature differences does not involve addition or subtraction.

Because the zero points of the Kelvin, Celsius, and Fahrenheit scales differ,

Conversion of actual temperatures involves addition or subtraction.

Examples of temperature conversion are given in box A.1.

A.3 Conversion of Dimensionally Inhomogeneous Equations

As noted in section 1.4.3, an equation that completely and correctly describes a physical relation must be dimensionally and unitarily homogeneous, i.e., it has the same dimensions and units on both sides of the equal sign. However, equations that are not dimensionally homogeneous can be useful approximations of physical relationships, and hydrologists are often forced to develop and rely on relatively simple empirical equations that may be dimensionally inhomogeneous. Examples of such equations are given in table 10.8, and inhomogeneous equations are frequently developed via regression analysis [e.g., equations (9.62) and (9.63)].

Because dimensionally inhomogeneous empirical equations are so frequently encountered, it is extremely important that the practicing hydrologist cultivate the habit of checking every equation for dimensional and unitary homogeneity because

RULE 8: If an inhomogeneous equation is given, the units of each variable in it MUST be specified.

This rule is one of the main reasons you should train yourself to examine each equation you encounter for homogeneity: If you use an inhomogeneous equa-

tion with units other than those for which it was given, you will get the wrong answer. Surprisingly, it is not uncommon to encounter in the earth sciences and engineering literature inhomogeneous equations for which units are not specified—so *caveat calculator!*

Rule 8 has an equally important corollary:

RULE 9: At least one of the coefficients or additive numbers in an inhomogeneous equation must change when the equation is to be used with different systems of units.

In practice, for example, in writing a computer program to make a series of calculations we often want to use an inhomogeneous equation with quantities measured in units different from those used in developing the equation. Or, we may want to compare inhomogeneous empirical equations that were developed using differing units. The steps for determining the new numerical values when an inhomogeneous equation is to be used with different units are detailed below. The guiding principle in equation conversion is that

The dimensions and units of quantities in equations are subjected to the same mathematical operations as the numerical magnitudes.

Careful execution of the following steps will assure that equation conversion is done correctly.

1. Write out the equation with the NEW units next to each term.
2. Next to each new unit, write the factor for converting the NEW units to the OLD units. (This may seem backwards, but it isn’t.)
3. Perform the algebraic manipulations necessary to consolidate and simplify back to the original form of the equation.

In executing steps 2 and 3 note that

Exponents are not changed in equation conversion, and conversion factors are subject to the same exponentiation as the variables they accompany.

Box A.2 gives an example of the conversion of a commonly used inhomogeneous equation.

One should always check to make sure a conversion was done correctly. To do this, follow these steps:

- Pick an arbitrary set of values in the new units for the variables on the right-hand side of the equation, enter them in the new equation, and calculate the value of the dependent variable in the new units.
- Convert the values of the independent variables to the old units. (Dimensionless quantities do not change value.)

- Enter the converted independent variable values from step 2 into the converted equation and calculate the value of the dependent variable in the old units.
- Convert the value of the dependent variable calculated in step 3 to the new units and check to see that it is identical to that calculated in step 1.

These steps are applied to check the equation conversion example in box A.2.

Box A.2 Example of Conversion of a Dimensionally Inhomogeneous Equation for Use with New Units

The Manning equation [a version of equation (10.43)] is a dimensionally inhomogeneous equation that is frequently used to compute the average velocity or discharge of stream flows. It is often written in the form used with British (common) units:

$$u = \frac{1.486 \cdot y^{2/3} \cdot \zeta^{1/2}}{n_M}, \quad (\text{AB2.1})$$

where y is in ft, ζ is water-surface slope (ft/ft), n_M is Manning's roughness factor (a dimensionless factor proportional to flow resistance), and u is average flow velocity in ft/s. To convert equation (AB2.1) for use with SI units (u in m/s and y in m), we follow the steps given in section A.3:

- Write out the equation with the NEW units next to each term:

$$(u \text{ m/s}) = \frac{1.486 \cdot (y \text{ m})^{2/3} \cdot \zeta^{1/2}}{n_M}.$$

- Next to each new unit, write the factor for converting the NEW units to the OLD units:

$$\left(u \text{ m/s} \cdot \frac{3.2808 \text{ ft/s}}{1 \text{ m/s}} \right) = \\ 1.486 \cdot \left(y \text{ m} \cdot \frac{3.2808 \text{ ft}}{1 \text{ m}} \right)^{2/3} \cdot \zeta^{1/2} \\ n_M$$

- Perform the algebraic manipulations necessary to consolidate and simplify back to the original form of the equation.

$$3.2808 \cdot u = \frac{1.486 \cdot y^{2/3} \cdot 2.2079 \cdot \zeta^{1/2}}{n_M}, \\ u = \frac{1.000059 \cdot y^{2/3} \cdot \zeta^{1/2}}{n_M} \rightarrow \frac{y^{2/3} \cdot \zeta^{1/2}}{n_M}$$

Thus the coefficient 1.486 in equation (AB2.1) is changed to 1 for use with the new units.

One should always check to make sure a conversion was done correctly. To do this, follow these steps:

- Enter the arbitrary values $y = 2.40$ m, $\zeta = 0.00500$, and $n_M = 0.040$ into the new equation and calculate u in m/s:

$$u = \frac{2.40^{2/3} \times 0.00500^{1/2}}{0.040} = 3.17 \text{ m/s.}$$

- Using table A.2, convert

$$y = 2.40 \text{ m} \times \frac{3.2808 \text{ ft}}{1 \text{ m}} = 7.8732 \text{ ft} \rightarrow 7.87 \text{ ft.}$$

The ζ and n_M values do not change because they are dimensionless.

- Substitute the converted value into the old equation:

$$u = \frac{1.486 \times 7.87^{2/3} \times 0.00500^{1/2}}{0.040} = 10.42 \text{ ft/s.}$$

- Using table A.2, convert this value of u to the new units and compare with the value in step 1:

$$10.42 \text{ ft/s} \times \frac{1 \text{ m/s}}{3.2808 \text{ ft/s}} = 3.1761 \rightarrow 3.18 \text{ m/s OK.}$$

The difference between this value and the original value is due only to round-off error.

Appendix

B

Water as a Substance

As noted in section 1.5, water is a very unusual substance with anomalous properties—a topic that is entertainingly elaborated on by van Hylckama (1979). This strangeness is the reason it is so common at the earth's surface, and its existence in all three phases makes our planet unique (see figure 1.6) and makes the science of hydrology vital to understanding and managing the environment and our relation to it. Aspects of water's unusual properties were introduced in table 1.2; here we provide more detail about its atomic and molecular structure and additional aspects of its properties.

B.1 Structure of Water

B.1.1 Molecular and Intermolecular Structure

The water molecule is formed by the combination of two hydrogen atoms (Group Ia, with one electron in the outer shell) with one oxygen atom (Group VIA, with six electrons in the outer shell), and hence has the chemical formula H_2O . As shown in figure B.1a, the outer shell of oxygen can accommodate eight electrons, so it has two vacancies. The outer (and only) shell of hydrogen can hold two electrons, so it has one vacancy. The electron vacancies of two hydrogen atoms and one oxygen atom can be mutually filled by sharing outer-shell electrons, as shown schematically in figure B.1b. This sharing is known as a **covalent bond**.

The two most important features of the water molecule are that: (1) its covalent bonds are very

strong (i.e., much energy is needed to break them) and (2) the molecular structure is asymmetric, with the hydrogen atoms attached on one “side” of the oxygen atom and an angle of about 105° between the two hydrogen atoms (figure B.2 on p. 541).

The asymmetry of the water molecule causes it to have a positively charged end (the “side” where the hydrogens are attached) and a negatively charged end (the “side” opposite the hydrogens), much like the poles of a magnet. Most of the unusual properties of water are ultimately the result of its being made up of these **polar molecules**. The polarity produces an attractive force between the positively charged end of one water molecule and the negatively charged end of another, as shown in figure B.3 on p. 541. This force, called a **hydrogen bond**, is absent in most other liquids.

Although the hydrogen bond is only about one-twentieth the strength of the covalent bond (Stillinger 1980), it is far stronger than the intermolecular bonds that are present in liquids with symmetrical, nonpolar molecules. We get an idea of this strength when we compare the melting/freezing temperature and the boiling/condensation temperature of the hydrides of all the Group VIA elements: oxygen (O), sulfur (S), selenium (Se), and tellurium (Te). These elements are all characterized by an outer electron shell that can hold eight electrons, but has two vacancies. Thus they all form covalent bonds with two hydrogens but, except for water, the resulting molecules are nearly symmetrical and therefore nonpolar.

In the absence of strong intermolecular forces that result from polar molecules, the melting/freez-

ing and boiling/condensation temperatures of these compounds would be expected to rise as their atomic weights increased. As shown in figure B.4 on p. 542, these expectations are fulfilled, except—strikingly—in the case of H₂O. The reason for this anomaly is the hydrogen bonds, which attract one molecule to another and which can only be loosened (as in melting) or broken (as in evaporation) when the vibratory energy of the molecules is large—that is, when the temperature is high. Because of its high melting and boiling temperatures, water is one of the very few substances that exists in all three physical states—solid, liquid, and gas—at earth-surface temperatures.

B.1.2 Freezing/Melting

At temperatures below 0°C the vibratory energy of water molecules is sufficiently low that the hydrogen bonds can lock the molecules into the regular

three-dimensional crystal lattice of ice (figure B.5 on p. 542). When this happens, the decreased vibratory energy is released as the **latent heat of freezing/melting** ($\lambda_f = 3.34 \times 10^5 \text{ J/kg}$). Each molecule in the ice lattice is hydrogen-bonded to four adjacent molecules. The angle between the hydrogen atoms in each molecule remains at 105°, but each molecule is oriented so that a puckered honeycomb of perfect hexagons is visible when the lattice is viewed from one direction. Thus ice is a hexagonal crystal, and snowflakes show infinite variation on a theme of six-fold symmetry.

When ice is warmed to 0°C, further additions of heat cause melting, in which about 15% of the hydrogen bonds break (Stillinger 1980); a quantity of energy equal to λ_f is absorbed to melt each kg of ice. Because of the rupturing of some of the hydrogen bonds, the rigid ice lattice partially collapses, and a

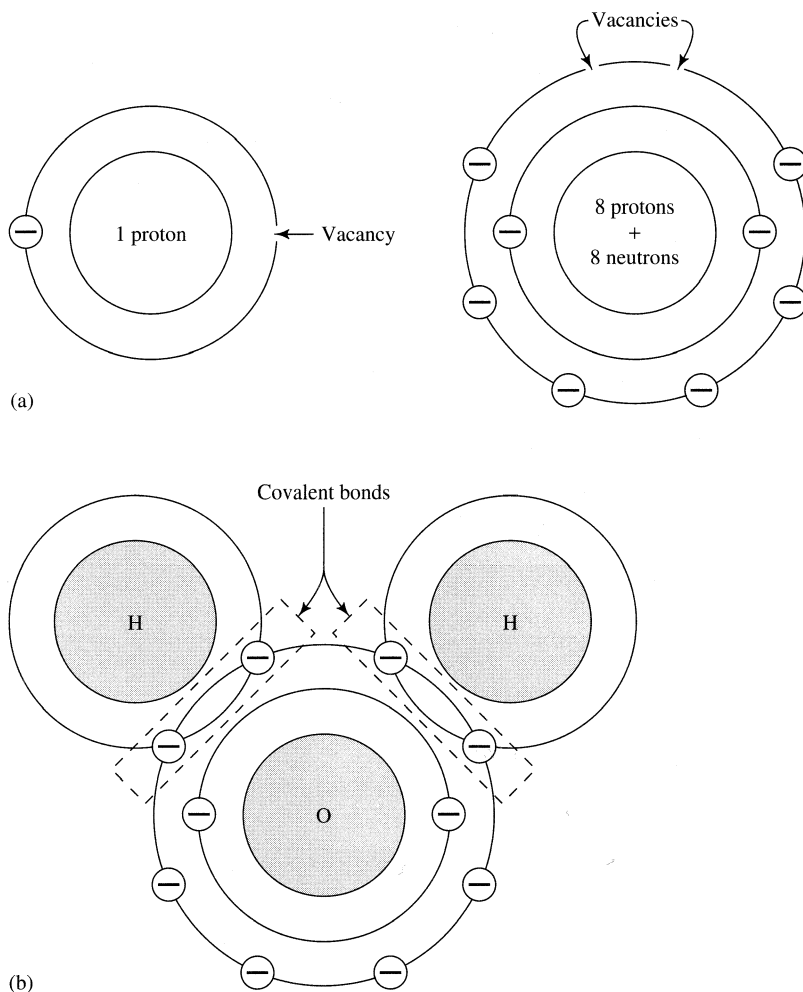


Figure B.1 (a) Schematic diagram of a hydrogen atom (left) and an oxygen atom (right). (b) Schematic diagram of a water molecule showing covalent bonding. \ominus symbols represent electrons [Dingman (1984)].

given number of molecules take up less space in the liquid phase than in the solid. As a result, the density of ice is less than that of water (91.7% of the density of liquid water at 0°C). Very few substances have a lower density in the solid state than in the liquid, and this property is of immense importance: Ice floats

rather than sinks, and if rivers and lakes froze from the bottom up instead of from the top down, biological and hydrological conditions in higher latitudes would be markedly altered.

Although melting always occurs when ice at earth-surface pressure is warmed to 0°C, freezing may

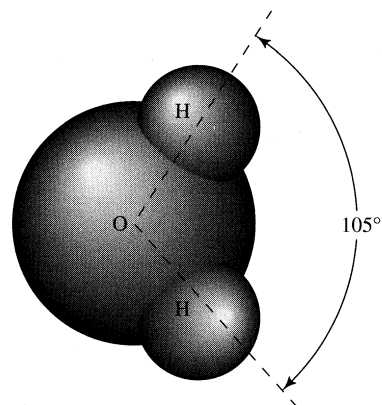


Figure B.2 Diagram of a water molecule showing the angle between the hydrogen atoms [adapted from Davis and Day (1961)].

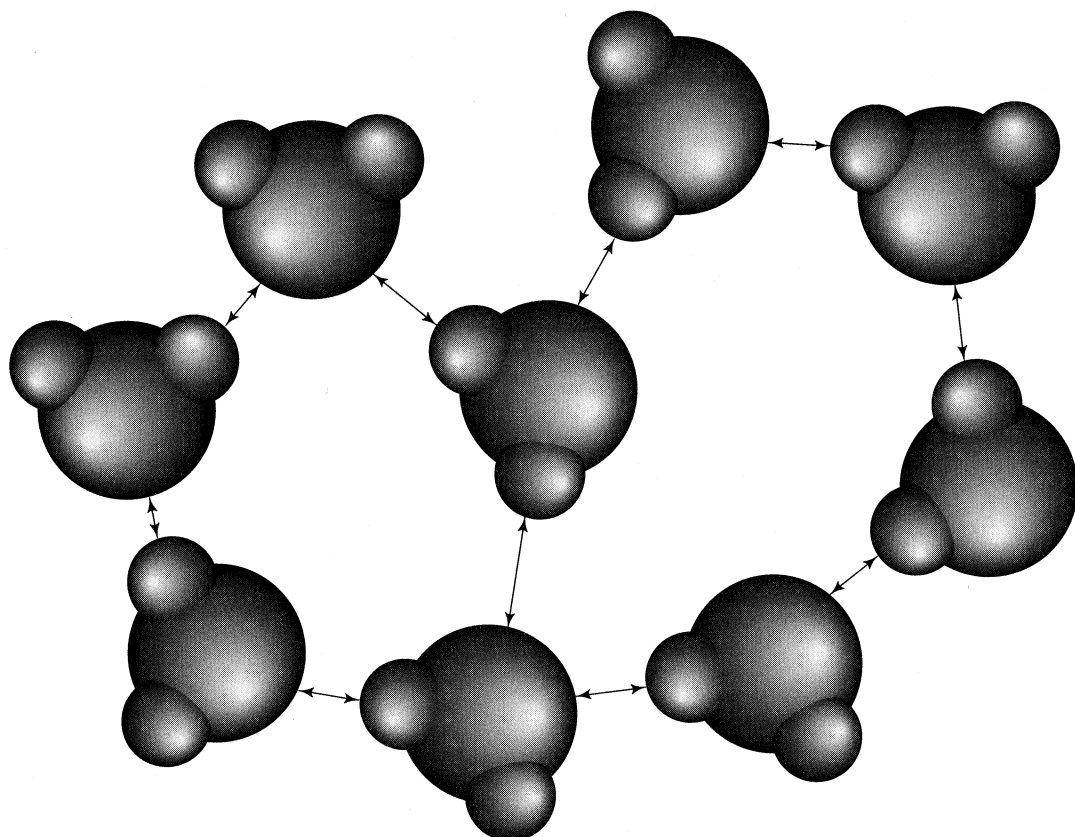


Figure B.3 Schematic diagram of water molecules in the liquid state. Arrows indicate hydrogen bonds between the oppositely charged ends of adjacent molecules [Dingman (1984)].

not always take place when liquid water is cooled to 0°C. If the liquid contains no impurities and is not in contact with preexisting ice, it is possible to supercool it to temperatures as low as -41°C. This resistance to freezing is because the water molecules form various types of nonhexagonal hydrogen-bonded polyhedra (figure B.3), which prevent the formation of the ice lattice. However, if ice particles, snowflakes, or com-

mon impurities like clay minerals (which have a crystal structure like that of ice) are present, they provide templates that act as growth nuclei to trigger the formation of ice at 0°C. Significant supercooling is quite common in clouds, where effective growth nuclei may be lacking, and is an important factor in the development of cloud particles into raindrops and snowflakes (section 3.4). In rivers, supercooling of 0.01 to

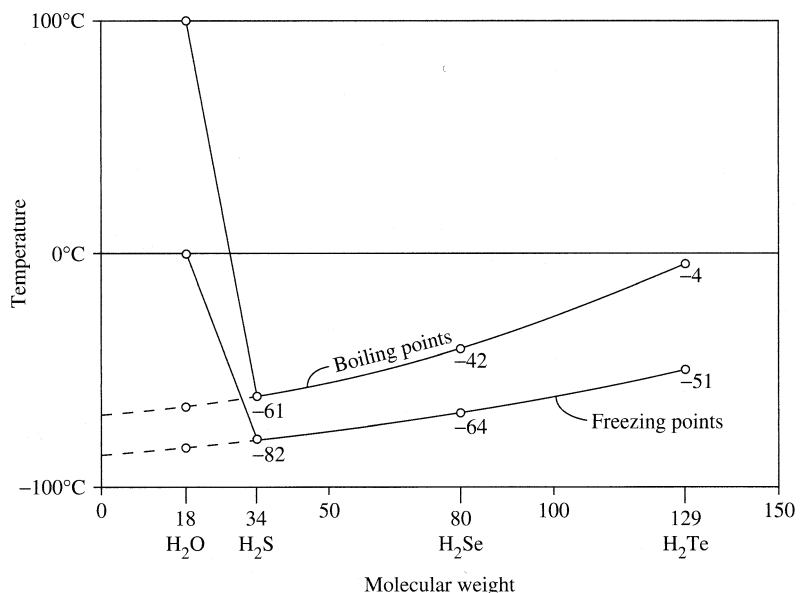


Figure B.4 Melting/freezing and boiling/condensation temperatures of Group VIa hydrides. In the absence of hydrogen bonds, water would have a melting/freezing point of -100°C and a boiling/condensation point of -91°C [adapted from Davis and Day (1961)].

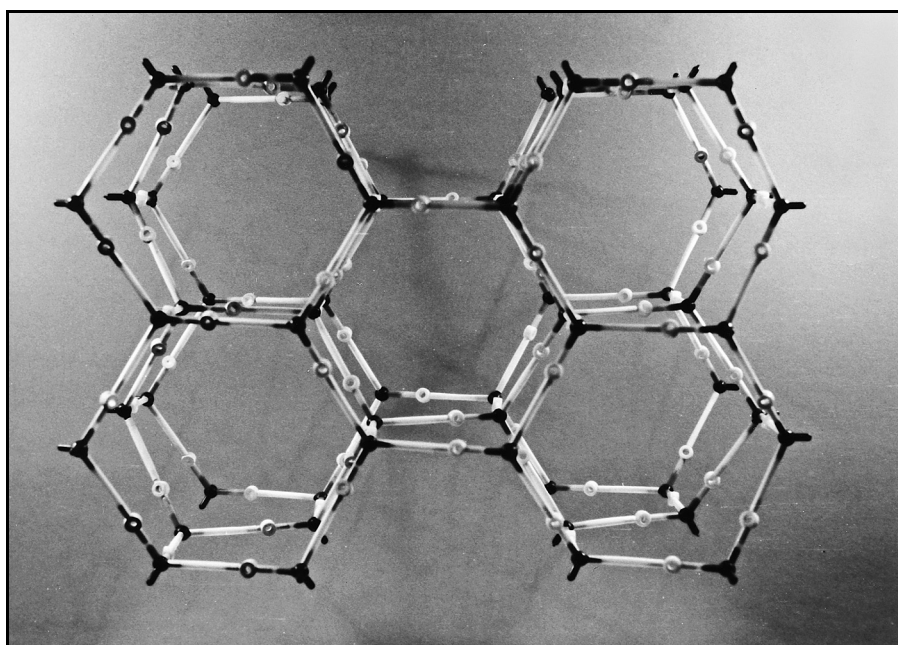


Figure B.5 A model of the crystal lattice of ice, showing its hexagonal structure. White circles are hydrogen atoms, dark circles are oxygen atoms, dashed lines are hydrogen bonds (photo by author).

0.1°C often occurs during the formation of ice in fast-flowing reaches (Michel 1971).

B.1.3 Evaporation/Condensation

The physics of evaporation is described in detail in section 3.3, and the physics of condensation to form precipitation in section 3.4. Due to the breaking/formation of hydrogen bonds, very significant losses/gains of energy are involved in evaporation/condensation (the **latent heat of vaporization/condensation**, λ_v ; section 3.3.2); λ_v depends on the temperature of the evaporating/condensing water [equation (3.18)].

B.1.4 Dissociation

An **ion** is an elemental or molecular species with a net positive or negative electrical charge. At any given instant, a very small fraction of the molecules of liquid water are **dissociated** into positively charged hydrogen ions, designated H^{+1} , and negatively charged hydroxide ions, designated OH^{-1} . In spite of their generally very low concentrations, these ions participate in many important chemical reactions.

Hydrogen ions are responsible for the acidity of water, and acidity is usually measured in terms of the quantity called **pH**, which is defined as

$$pH \equiv -\log_{10}([H^{+1}]), \quad (\text{B.1})$$

where $[H^{+1}]$ designates the concentration of hydrogen ions in mg/L. The concentration of hydrogen ions in pure water at 25°C is $10^{-7.00}$ mg/L ($pH = 7.00$). As $[H^{+1}]$ increases above this value (pH decreases below 7.00), water becomes more acid; as $[H^{+1}]$ decreases ($pH > 7.00$), it becomes more basic.

Certain chemical reactions change the concentration of hydrogen ions, causing the water to become more or less acid. The degree of acidity, in turn, determines the propensity of the water to dissolve many elements. The pH of cloud water in equilibrium with the carbon dioxide in the atmosphere is about 5.7, and other reactions make the natural pH of rainwater in the range 4.5 to 5.6 depending on location (Turk 1983).

B.1.5 Isotopes

Isotopes of an element have the same number of protons and electrons, but differing numbers of neutrons; thus they have similar chemical behavior, but differ in atomic weight. Some isotopes are **radioactive**, and decay naturally to other atomic forms at a

characteristic rate, while others are **stable**. Table B.1 gives the properties and abundances of the isotopes of hydrogen and oxygen, from which it can be calculated that 99.8% of all water consists of “normal” $^1H_2^{16}O$.

Table B.1 Characteristics of Isotopes of Hydrogen and Oxygen.

Isotope	Natural Abundance (%)	Natural Variability (%)	Stability
1H	99.9844		stable
2H (D)	0.0156	~30	stable
3H (T)	Trace		radioactive
^{16}O	99.7795		stable
^{17}O	~0.02		stable
^{18}O	0.2006	~5	stable

Source: Data from Gat (1996).

The isotope 3H , called **tritium** (symbol T), is radioactive and decays with a half-life of 12.5 yr to 3He . It is produced in very small concentrations by natural processes and in larger concentrations by nuclear reactions. For a period of time the testing of nuclear weapons between the mid-1950s and mid-1970s produced enough atmospheric tritium to be useful in dating water in aquifers and glaciers and hence in estimating recharge rates (e.g., Davis and Murphy 1987). Because of the cessation of such tests in recent decades, this is no longer possible.

The stable isotopes 2H (deuterium, D) and ^{18}O , however, are useful hydrologic tracers. The various isotopes are involved in differing proportions in phase changes, and so are **fractionated** as water moves through the hydrologic cycle (see Fritz and Fontes 1980; Drever 1982; Gat 1996): Lighter isotopes evaporate more readily than heavier ones, heavier isotopes condense more readily than lighter ones.

Isotopic composition for both D and ^{18}O is expressed as a δ value in parts per thousand, ‰, where

$$\delta \equiv \left(\frac{R_I}{R_{std}} - 1 \right) \cdot 1,000, \quad (\text{B.2})$$

where R_I is the isotope ratio D/H or $^{18}O/^{16}O$ for a particular sample and R_{std} the standard ratio. For both oxygen and hydrogen isotopes, R_{std} is that of standard mean ocean water (SMOW); from table B.1, R_{std} for

D is 1:6410 (= 0.000156); for ^{18}O it is 1:500 (= 0.002). Positive δ values indicate a relative enrichment of the heavy isotopic species and negative values indicate relative depletion. Because the variability in $\delta(\text{D})$ is typically almost an order of magnitude larger than that of $\delta(^{18}\text{O})$, isotope data of water samples are usually plotted on a graph of $\delta(\text{D})$ versus $\delta(^{18}\text{O})$, with the $\delta(\text{D})$ scale compressed by a factor of ten.

Gat (1996) reviewed the physics of fractionation processes and the isotopic signatures of water in various parts of the hydrologic cycle. Fractionation accompanying evaporation from the ocean and other surface waters and condensation during precipitation formation has the greatest effect on isotopic composition. Thus atmospheric water and precipitation are depleted in D and ^{18}O relative to ocean water ($\delta < 0$), and the average δ values of precipitation decrease with distance from the equator as heavier components are successively depleted by precipitation as air moves poleward. Water in large water bodies subject to evaporation (oceans, lakes, and soil water) is relatively enriched in D and ^{18}O ($\delta > 0$). However, water is not fractionated during uptake by plants or during evaporation from leaves (transpiration) because all the water arriving at the stomatal openings evaporates (Gat 1996). Isotopic fractionation in intercepted water depends on the timing and amounts of precipitation. Isotopic composition is generally unchanged as water moves through the ground-water system.

As noted in section 10.3, the relative concentrations of stable water isotopes can be used in some hydrologic situations to identify the sources of water in glaciers, aquifers, or streams (e.g., Perry and Mont-

gomery 1982; Kendall et al. 1995; Gat 1996). Until recently, isotopic tracing was usually applied to small watersheds, but recent studies have extended it to continental-scale areas (Fekete et al. 2006; Bowen et al. 2011).

B.2 Properties of Water

In this section we briefly describe the bulk properties of liquid water that influence its movement through the hydrologic cycle and its interactions with the terrestrial environment. More detailed discussions of these properties can be found in Dorsey (1940) and Davis and Day (1961). Properties of water in the solid and vapor form are discussed where relevant in the text.

The variation of water's properties with temperature is important in many hydrologic contexts. Thus in the following discussion, the values of each property at 0°C are given in the three unit systems, and their relative variations with temperature are shown in table B.2. Empirical equations for computing the values of some properties as functions of temperature are given in table B.3.

B.2.1 Density

Mass density, ρ , is the mass per unit volume [M L^{-3}] of a substance; **weight density**, γ , is the weight per unit volume [F L^{-3}]. These are related by Newton's second law (i.e., force equals mass times acceleration):

$$\gamma = \rho \cdot g, \quad (\text{B.3})$$

where g is the acceleration due to gravity [L T^{-2}] ($g = 9.81 \text{ m/s}^2$).

Table B.2 Relative Values of Properties of Pure Liquid Water as Functions of Temperature.

Temperature ($^\circ\text{C}$)	ρ, γ	μ	ν	σ	c_p	λ_v
0	1.00000	1.0000	1.0000	1.0000	1.0000	1.0000
3.98	1.00013					
5	1.00012	0.8500	0.8500	0.9907	0.9963	0.9953
10	0.99986	0.7314	0.7315	0.9815	0.9940	0.9904
15	0.99926	0.6374	0.6379	0.9722	0.9924	0.9857
20	0.99836	0.5607	0.5616	0.9630	0.9915	0.9810
25	0.99720	0.4983	0.4997	0.9524	0.9910	0.9763
30	0.99580	0.4463	0.4482	0.9418	0.9907	0.9715

ρ = mass density, γ = weight density, μ = dynamic viscosity, ν = kinematic viscosity, σ = surface tension, c_p = specific heat, λ_v = latent heat of vaporization.

Table B.3 Empirical Equations for Water Properties (SI Units) as Functions of Temperature (°C).

$$\rho = 1,000 - 0.019549 \cdot |T - 3.98|^{1.68}$$

$$\sigma = 0.001 \cdot (20,987 - 92.613 \cdot T)^{0.4348}$$

$$\mu = 2.0319 \times 10^{-4} + 1.5883 \times 10^{-3} \cdot \exp\left[-\left(\frac{T^{0.9}}{22}\right)\right]$$

$$c_p = 4,175 + 1,666 \cdot \left[\exp\left(\frac{34.5 - T}{10.6}\right) + \exp\left(-\frac{34.5 - T}{10.6}\right) \right]$$

Source: Heggen (1983).

In the SI system, the kilogram is the mass of 1 m³ of pure water at its temperature of maximum density, 3.98°C. At 0°C,

$$\rho = 999.87 \text{ kg/m}^3 = 0.99987 \text{ g/cm}^3 = 1.9397 \text{ slug/ft}^3$$

$$\gamma = 9,799 \text{ N/m}^3 = 979.9 \text{ dyn/cm}^3 = 62.46 \text{ lb/ft}^3.$$

The **specific gravity** of a substance is the ratio of its weight density to the weight density of pure water at 3.98°C; thus it is dimensionless.

As noted in section 1.5.2, the change in density of water with temperature is highly unusual and environmentally significant: Liquid water at 0°C is denser than ice. As liquid water is warmed from 0°C its density initially *increases* until density reaches a maximum value of 1,000 kg/m³ at 3.98°C; beyond this, density decreases with temperature, as in most other substances. In lakes where temperatures reach 3.98°C, the density maximum controls the vertical distribution of temperature and causes an annual or semiannual overturn of water that has a major influence on biological and physical processes. However, except for lakes, the variation of density with temperature is small enough that it can usually be neglected in hydrological calculations.

The addition of dissolved or suspended solids to water increases its density in proportion to the density of the solids and their concentration. Again, the effects of dissolved materials can be important in lakes, but are not usually significant in other environments. However, high concentrations of suspended matter can significantly increase the effective density of water in rivers.

B.2.2 Surface Tension

The basic aspects of surface tension are developed in section 1.5.3. Due to its strong intermolecular forces (hydrogen bonds), water has a surface tension, σ , higher than most other liquids. Its value at 0°C is

$$\sigma = 0.0756 \text{ N/m} = 75.6 \text{ dyn/cm} = 0.00518 \text{ lb/ft.}$$

Surface tension decreases rapidly as temperature increases (tables B.2, B.3), and this effect can be important when considering the movement of water in soils (see chapter 8). Dissolved substances can also increase or decrease surface tension, and certain organic compounds have a major effect on its value.

Water's hydrogen bonds cause it to be attracted to surface molecules in many materials, including most earth materials. This attraction causes the phenomenon of capillarity, which is responsible for the pressure status of water in unsaturated soils (section 7.4.1).

Table B.4 gives the contact angle for water in contact with air and selected solids. Note that the contact angle for most soil materials is close to 0°.

Table B.4 Surface-Tension Contact Angles for Water-Air Interfaces against Various Solids.

Solid	Contact Angle, β_c (°)	$\cos (\beta_c)$
Glass	0	1.0000
Most silicate minerals	0	1.0000
Ice	20	0.9397
Platinum	63	0.4540
Gold	68	0.3746
Talc	86	0.0698
Paraffin	105 to 110	-0.2588 to -0.3420
Shellac	107	-0.2924
Carnauba wax	107	-0.2924

Source: Data from Dorsey (1940) and Jellinek (1972).

B.2.3 Viscosity and Turbulence

B.2.3.1 Resistance in Boundary-Layer and Potential Flows

When water flows over a solid boundary, hydrogen bonds cause the fluid molecules adjacent to the boundary to “stick,” so that the velocity at the boundary is zero. This phenomenon is called the **no-slip condition**. This condition produces a frictional drag, or **resistance**, that is transmitted through the fluid for considerable distances normal to the boundary.

In overland flows and flows in stream channels, the retarding effects of the boundary are transmitted throughout the flow by viscosity and, usually, turbulence (described below); such flows are **boundary-layer flows**. Flows within the pores of porous media are also boundary-layer flows, but are not mathematically treated as such. As described in section 7.4.2, Darcy’s law describes bulk flow through a represen-

tative elemental volume of the medium rather than through individual pores. Thus the effect of intrapore resistance is aggregated and represented (inversely) by the bulk hydraulic conductivity; the boundary of the overall flow (i.e., the aquifer boundary) is not a source of flow resistance. Thus porous-media flow is mathematically represented as a **potential flow**, analogous to the flow of electricity (Darcy’s law is a direct analog of Ohm’s law).

B.2.3.2 Viscosity and Laminar Flow

For flows that are very close to a boundary and are very slow, the water moves in parallel layers (figure B.6a) and is described as **laminar**. The **dynamic viscosity**, μ , is the friction between the layers that transmits the boundary friction through the fluid and resists the forces tending to cause flow. The layers move successively faster as one moves away from the boundary, so that a velocity gradient exists, and μ is

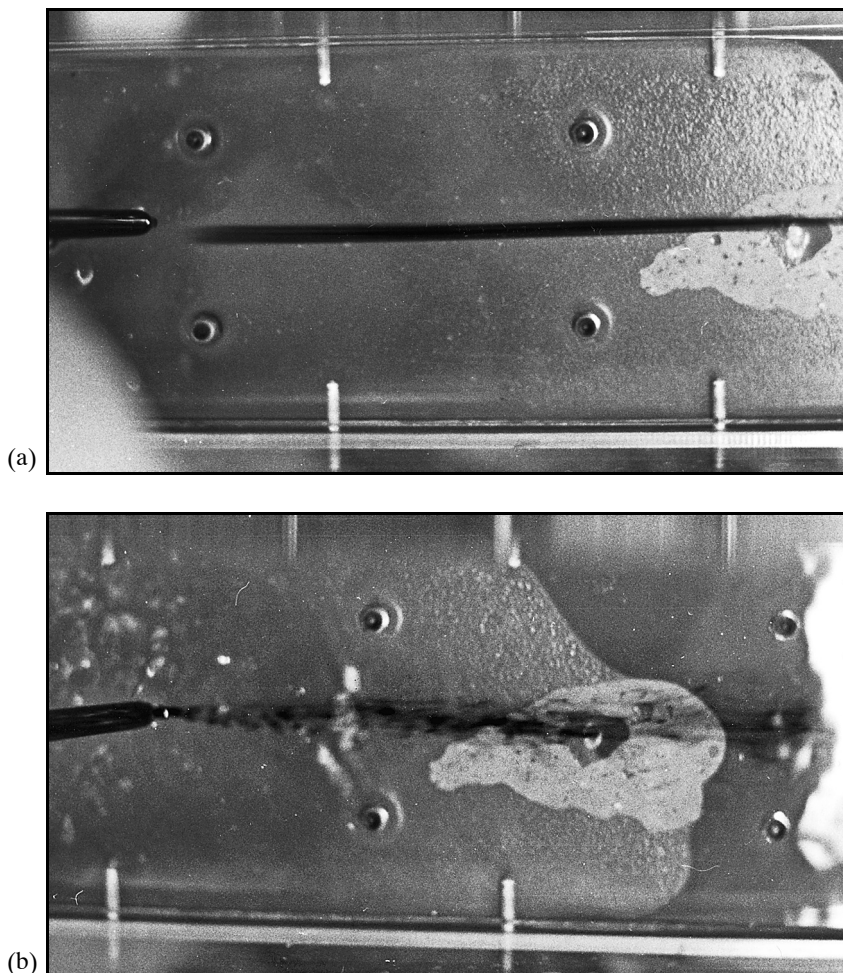


Figure B.6 Dye injected into flows in a laboratory flume showing (a) laminar flow and (b) turbulent flow (photo by author).

the proportionality between this gradient and the frictional force per unit area, called the **shear stress**, $\tau(y)$:

$$\tau(y) = \mu \cdot \frac{du(y)}{dy}, \quad (\text{B.4})$$

where $u(y)$ is the velocity at a distance y from the boundary.

Equation (B.4) shows that, for a given boundary shear stress, a higher viscosity causes a smaller velocity gradient—i.e., the velocity increases more slowly as one moves away from the boundary. Note that, since $\tau(y)$ has the dimensions $[F L^{-2}]$, μ has the dimensions $[F T L^{-2}] = [M L^{-1} T^{-1}]$. The dynamic viscosity is due to intermolecular attractions, and is also called the **molecular viscosity**. In spite of the strength of the hydrogen bonds, water's viscosity is relatively low because of the rapidity with which the hydrogen bonds break and reform (about once every 10^{-12} s). Viscosity at 0°C is

$$\mu = 0.001787 \text{ N} \cdot \text{s/m}^2 = 0.01787 \text{ dyn} \cdot \text{s/cm}^2 = 3.735 \times 10^{-5} \text{ lb} \cdot \text{s/ft}^2.$$

In many contexts the ratio μ/ρ arises; thus it is convenient to define the **kinematic viscosity**, v [$L^2 T^{-1}$]:

$$v \equiv \frac{\mu}{\rho}. \quad (\text{B.5})$$

Values of v at 0°C are

$$v = 1.787 \times 10^{-6} \text{ m}^2/\text{s} = 1.787 \times 10^{-2} \text{ cm}^2/\text{s} = 1.926 \times 10^{-5} \text{ ft}^2/\text{s}.$$

As shown in tables B.2 and B.3, viscosity decreases rapidly as temperature increases. Some dissolved constituents increase viscosity while others decrease it, but these effects are usually negligible at the concentrations found in nature. However, moderate to high concentrations of suspended material can significantly increase the effective viscosity of the fluid.

B.2.3.3 Turbulence

As distance from a boundary and velocity increase, the inertia of the moving water increasingly overcomes viscous friction and the flow paths of individual water “particles” increasingly deviate from the parallel layers of laminar flow. At relatively modest distances and velocities, all semblance of parallel flow disappears and the water moves in highly irregular eddies (figure B.6b). This is the phenomenon of **turbulence**. Because the water in turbulent eddies

moves in directions other than the main flow direction, turbulence consumes some of the energy that would otherwise drive the main flow. Thus although turbulence is not an intrinsic property of water, the energy loss it causes is an addition to the internal frictional resistance to fluid flow and therefore is an addition to the effective viscosity. This effect is called the **eddy viscosity**, η , which is defined as

$$\eta \equiv \kappa^2 \cdot \rho \cdot y^2 \cdot \left[\frac{du(y)}{dy} \right]^2, \quad (\text{B.6})$$

where κ is a dimensionless constant that has been determined by experiment to equal 0.4. Note that the dimensions of η are identical to those of μ .

Physically, the effect of molecular viscosity is always present and is the ultimate mechanism by which the retarding effect of a boundary is transmitted into the fluid. Thus the flow resistances due to eddy viscosity and molecular viscosity are additive. However, the magnitude of η greatly exceeds that of μ for even small values of y and $du(y)/dy$, so μ is usually neglected for turbulent flows.

Replacing μ in equation (B.4) with the analogous quantity η from equation (B.6) gives the shear stress in turbulent flows:

$$\tau(y) = \kappa^2 \cdot \rho \cdot y^2 \cdot \left[\frac{du(y)}{dy} \right]^2. \quad (\text{B.7})$$

Thus when turbulence is present and viscosity can be ignored, the relation between velocity gradient and friction depends on location within the flow, y , and the local velocity gradient. The integration of equation (B.7) yields the Prandtl-von Kármán universal velocity distribution discussed in section 3.5.2.

B.2.3.4 Criteria for Laminar- or Turbulent-Flow State

Comparison of equations (B.4) and (B.7) shows that the nature and magnitude of internal flow resistance differ greatly between laminar and turbulent flows. Because pore spaces and velocities are small, flow in porous media is almost always laminar, and Darcy's law applies only when this is the case. Virtually all flows in stream channels, even small ones, are turbulent, and their velocity is given by equation (10.43). The situation for overland flows is complex; they may be laminar, turbulent, or transitional.

Because of the differing resistance relations for laminar and turbulent flows, it is essential to be able to determine the state of flows in the hydrologic cycle. The basic criterion for distinguishing laminar

and turbulent flow is the ratio of eddy viscosity to molecular viscosity,

$$\frac{\eta}{\mu} = \frac{\kappa^2 \cdot \rho \cdot y^2}{\mu} \cdot \frac{du(y)}{dy}. \quad (\text{B.8})$$

For a given type of flow, it can be shown (Dingman 2009) that this ratio is proportional to Re , where

$$Re \equiv \frac{\rho \cdot L \cdot u}{\mu}, \quad (\text{B.9})$$

and L is a characteristic length and u a characteristic velocity of the flow. Re is called the **Reynolds number**, named after the English hydraulician Osborne Reynolds who studied the transition from laminar to turbulent flow.

For flows in porous media, the Reynolds number Re_{pm} is defined as

$$Re_{pm} \equiv \frac{\rho \cdot q \cdot d}{\mu} = \frac{q \cdot d}{v}, \quad (\text{B.10})$$

where the characteristic velocity is the Darcy velocity, q , (volumetric flow rate per unit cross-sectional area) and the characteristic length is the average diameter of the grains making up the medium, d .

Porous-media flows are laminar when $Re_{pm} < 1$, turbulent when $Re_{pm} > 10$, and transitional in between.

The Reynolds number applicable to open-channel flows, Re_{oc} , is defined as

$$Re_{oc} \equiv \frac{\rho \cdot u \cdot y}{\mu} = \frac{u \cdot y}{v}, \quad (\text{B.11})$$

where the characteristic velocity is the average flow velocity, u , and the characteristic length is the average flow depth, y .

Open-channel flows are laminar when $Re_{oc} < 500$, turbulent when $Re_{oc} > 2,000$, and transitional in between.

B.2.4 Heat Capacity (Specific Heat)

Heat capacity, c_p , relates a temperature change of a substance to a change in its heat-energy content. It is defined as the amount of heat energy, ΔH , absorbed/released by a mass M of a substance when its temperature is raised/lowered by an amount ΔT :

$$c_p \equiv \frac{\Delta H}{M \cdot \Delta T}. \quad (\text{B.12})$$

Thus its dimensions are $[L^2 T^{-2} \Theta^{-1}] = [E M^{-1} \Theta^{-1}]$.

The thermal capacity of water at 0°C is

$$c_p = 4,216 \text{ J/kg} \cdot \text{K} = 1.007 \text{ cal/g} \cdot \text{C}^\circ = \\ 32.43 \text{ Btu/slug} \cdot \text{F}^\circ$$

and, as shown in tables B.2 and B.3, its value decreases slowly with temperature until it reaches a minimum of $4,178.42 \text{ J/kg} \cdot \text{K}$ at 37°C , after which it slowly increases.

The temperature of a substance reflects the vibratory energy of its molecules. The thermal capacity of water is very high relative to that of most other substances because, when heat energy is added to it, much of the energy is used to break hydrogen bonds rather than to increase the rate of molecular vibrations. This high specific heat has a profound influence on organisms and the global environment: It makes it possible for warm-blooded organisms to regulate their temperatures, and makes the oceans and other bodies of water moderators of the rates and magnitudes of ambient temperature changes.

Appendix

C

Statistical Concepts Useful in Hydrology

This appendix summarizes the basic statistical concepts applied in hydrologic analysis in condensed form. More extensive treatment of these topics can be found in the many basic statistics texts and in texts that specifically explore the application of statistics to hydrology, including Yevjevich (1972), Helsel and Hirsch (1992), Hirsch et al. (1992), Kitanidis (1992), Salas (1992), Stedinger et al. (1992), Hosking and Wallis (1997), and Haan (2002). Statistical tests for evaluating and comparing predictions of hydrologic models are discussed in section F.5.

C.1 Random Variables, Populations, and Samples

"If the outcome of an experiment, process, or measurement has an element of uncertainty associated with it, such that its value can only be stated probabilistically, the outcome is a **random variable**" (Haan 2002, p. 31).

Because measurements can only be made with finite precision over a finite time period, or at a finite number of points, there is uncertainty associated with any attempt to characterize typical values or variability of any hydrologic quantity. Thus

Virtually all hydrologic quantities
are random variables.

Note also that

Any function of a random variable (e.g., the average value or a measure of variability of a random variable) is also a random variable.

Statistical analysis is based on the idea that hydrologic observations are spatially or temporally distributed **samples** taken from some underlying **population**. The properties of the population are unknown, and the goal of **statistical inference** is to estimate those properties and assess the degree of uncertainty associated with those estimates based on the laws of probability.

Here and in most statistical texts, the properties of populations are represented by Greek letters (μ , σ , ρ , etc.). These properties are treated as fixed but unknown quantities; they are *not* random variables. Sample values and quantities calculated from sample values are random variables whose values are known (within measurement uncertainty); these are represented by Latin letters or Greek letters under a "hat" (m , s , r , etc., or $\hat{\mu}$, $\hat{\sigma}$, \hat{p} , etc.).

C.2 Probability

If outcome A of an observation (experiment or measurement) is defined as the occurrence of a particular value or range of values of a random variable X , the **probability** of A , $Pr\{A\}$, is defined as

$$Pr\{A\} \equiv \lim_{N \rightarrow \infty} \frac{N(A)}{N}, \quad (\text{C.1})$$

where $N(A)$ is the number of times outcome A occurs in N outcomes. Thus probability is a number between 0 (impossible) and 1 (certain) equal to the relative frequency with which the stated value or range of values would occur in a very large number of outcomes.

If outcomes A, B, C, \dots of a particular experiment or measurement (a **trial**) are mutually exclusive, then

$$Pr\{A \text{ or } B \text{ or } C \text{ or } \dots\} = Pr\{A\} + Pr\{B\} + Pr\{C\} + \dots \quad (\text{C.2})$$

and the sum of the probabilities of all possible outcomes is unity. If the outcomes of successive or separate trials are **independent** (i.e., the results of one trial do not affect the probabilities of outcomes in other trials), then

$$Pr\{A \text{ and } B \text{ and } C \text{ and } \dots\} = Pr\{A\} \cdot Pr\{B\} \cdot Pr\{C\} \dots \quad (\text{C.3})$$

C.3 Probability Distributions

As noted above, the magnitudes of spatially and temporally variable hydrologic quantities are random variables, and their magnitude-frequency relations are quantitatively described in terms of probability distributions.

A **probability distribution** is a relation between the *magnitude* of a random variable and its *probability*.

The exact definition of probability distributions differs for discrete and continuous random variables.

C.3.1 Discrete Random Variables

If a random variable can take on only specific exact numerical values, it is a **discrete random variable**.

Discrete random variables are those that are determined by counting; for example, the number of days with rainfall greater than 25 mm in a year.

For a discrete random variable X , the probability distribution $p_X(x_i)$ is an equation or table that gives the probability that X takes on a particular value x_i :

$$p_X(x_i) \equiv Pr\{X = x_i\}. \quad (\text{C.4})$$

$p_X(x_i)$ is called the **probability function** of X . The sum of the probabilities associated with all possible values of X must equal 1:

$$\sum_{\text{all } X} p_X(x_i) = 1. \quad (\text{C.5})$$

It is common to express a discrete probability distribution in terms of a **cumulative probability function**, $P_X(x_i)$, which is the probability that X takes a value *less than or equal to* x_i :

$$P_X(x_i) \equiv Pr\{X \leq x_i\} = \sum_{\text{all } X \leq x_i} p_X(x_i). \quad (\text{C.6})$$

The probability of occurrence of values of X in the interval between x_j and x_k (inclusive) is

$$Pr\{x_j \leq X \leq x_k\} = \sum_{x_j \leq x_i \leq x_k} p_X(x_i). \quad (\text{C.7})$$

C.3.2 Continuous Random Variables

If a random variable can take on any numerical value over some interval on the real-number line, it is a **continuous random variable**.

For example, streamflow is a continuous random variable because it can potentially assume any nonnegative value. The fact that measurement precision dictates that streamflow can be expressed only to two or three significant figures does not affect this reasoning.

Because continuous random variables can theoretically take on any value within an interval on the real number line, an infinite number of possible values exist and the probability of occurrence of any particular exact value is 0. Thus we cannot define a probability function like equation (C.4) for a continuous variable; probabilities can be defined *only over intervals on the real number line*. To express these probabilities, we define the **cumulative distribution function (cdf)** of a continuous variable X , $F_X(x)$:

$$F_X(x) \equiv Pr\{X \leq x\}, \quad (\text{C.8})$$

where x is a particular value of X . The **probability-density function (pdf)**, $f_X(x)$, of a continuous random variable is defined as

$$f_X(x) = \frac{dF_X(x)}{dx}; \quad (\text{C.9})$$

thus

$$F_X(x) = \int_{-\infty}^x f_X(x) \cdot dx. \quad (\text{C.10})$$

The probability that X takes on a value between $x = a$ and $x = b$, $a < b$, is given by

$$Pr\{a < X \leq b\} = \int_a^b f_X(x) \cdot dx = F_X(b) - F_X(a). \quad (\text{C.11})$$

Clearly,

$$\int_{-\infty}^{+\infty} f_X(x) \cdot dx = 1. \quad (\text{C.12})$$

The cdf is a complete specification of the variability of a random variable, and it is usually expressed as a mathematical function, ϕ , of x and one or more **parameters**, θ_i :

$$F_X(x) = \phi(x, \theta_i), i = 1, 2, \dots, I. \quad (\text{C.13})$$

Since the most common applications of statistics in hydrology involve continuous variables like streamflow, we restrict the subsequent discussion to continuous distributions.

Table C.1 on pp. 552–553 summarizes the formulas for several distributions commonly used for hydrologic variables; most of these are two- or three-parameter distributions (i.e., $I = 2$ or 3). Stedinger et al. (1992), Hosking and Wallis (1997), and Haan (2002) give information on other distributions.

C.3.3 Expectation

As noted, functions of a random variable are also random variables. Denoting an arbitrary function of X as $\psi(X)$, the **expected value** of $\psi(X)$, $E[\psi(X)]$, is defined as

$$E[\psi(X)] \equiv \int_{-\infty}^{+\infty} \psi(x) \cdot f_X(x) \cdot dx. \quad (\text{C.14})$$

As shown below, the expected value of $\psi(X)$ is the mean, or average, value of $\psi(X)$.

C.3.4 Quantiles

One of the simplest ways of describing the distribution of a random variable is to give the values of several **quantiles** of the distribution. The q th quantile of the variable X is the value x_q that is larger than $100 \cdot q$ percent of all values; thus for a continuous variable,

$$F_X(x_q) = q. \quad (\text{C.15})$$

The **quantile function** is the inverse of the probability distribution [i.e., equation (C.13) solved for x]:

$$x = x(F_X) = F_X^{-1}(x) = \phi^{-1}[F_X(x), \theta_i]. \quad (\text{C.16})$$

The most commonly reported quantiles are the **median**, $x_{0.5}$, the **lower quartile**, $x_{0.25}$, and the **upper quartile**, $x_{0.75}$. The median is one measure of **central tendency**; X has a 0.5 probability of being less than $x_{0.5}$. The interval $[x_{0.25}, x_{0.75}]$ is the **interquartile range**; X has a 0.5 probability of being in this interval. Thus the difference $x_{0.75} - x_{0.25}$ is a measure of the **spread**, **variability**, or **dispersion** of the data around the central value, and the ratio of the interquartile range to the median is a relative measure of dispersion.

Since in general we do not know the distribution from which a sample was obtained, we do not know the true values of its quantiles. Thus we are forced to estimate these values from the sample, as described and illustrated in box C.1 and table C.2 (see disk).

Because of the importance of floods and droughts, hydrologists often need to estimate quantiles in the “tails” of the distribution of a precipitation or streamflow time series, e.g., $x_{0.05}$ or $x_{0.99}$. As noted in the subsequent discussion of sampling error, such estimates are subject to considerable uncertainty and in general should not be made by the methods of box C.1 (see disk). Rather they are best made by fitting a probability distribution to the data, as described later.

C.3.5 Product Moments

A probability distribution can also be characterized in terms of its **product moments**. The general definition of the r th product moment about the value x^* , ${}_{x^*} M_X$, is

$${}_{x^*} M_X \equiv E[(X - x^*)^r] = \int_{-\infty}^{+\infty} (x - x^*)^r \cdot f_X(x) \cdot dx. \quad (\text{C.17})$$

The first moment about $x^* = 0$ of a distribution is called the **mean**, or **expected value**, of X , $E(X)$. It is denoted μ_X and defined as:

$${}_1 M_X \equiv E(X) = \mu_X = \int_{-\infty}^{+\infty} x \cdot f_X(x) \cdot dx. \quad (\text{C.18})$$

The mean, like the median, is a measure of central tendency, and determines the location of the central part of the distribution along the real-number line (figure C.1a on p. 554).

Table C.1 Some Probability Distributions Commonly Used in Hydrology.

Distribution cdf and Inverse	Range	Product Moments	L-Moments
Uniform (U):			
$F_{UX}(x) = \frac{x - \alpha}{\beta - \alpha}$	$\alpha \leq x \leq \beta$	$\mu_X = \frac{\alpha + \beta}{2}$	$\lambda_1 = \frac{\alpha + \beta}{2}$
$x(F) = \alpha + (\beta - \alpha) \cdot F$		$\sigma_X^2 = \frac{(\beta - \alpha)^2}{12}$	$\lambda_2 = \frac{\beta - \alpha}{6}$
Normal (N):			
$F_{NZ}(z) = \frac{1}{(2 \cdot \pi)^{1/2}} \cdot \int_{-\infty}^z \exp\left(-\frac{z^2}{2}\right) \cdot dz$	$-\infty < z < \infty$	μ_X	$\lambda_1 = \mu_X$
$z(F) \approx 5.0633 \cdot [F^{0.135} - (1 - F)^{0.135}]$		σ_X	$\lambda_2 = \frac{\sigma_X}{\pi^{1/2}}$
$Z \equiv \frac{X - \mu_X}{\sigma_X}$		$\gamma_X = 0$	$\tau_3 = 0; \tau_4 = 0.1226$
Log-Normal (LN):			
$F_{LNZ'}(z') = \frac{1}{(2 \cdot \pi)^{1/2}} \cdot \int_{-\infty}^{z'} \exp\left(-\frac{z'^2}{2}\right) \cdot dz'$	$x > 0$	$\mu_X = \exp\left(\mu_Y + \frac{\sigma_Y^2}{2}\right)$	$\lambda_1 = \mu_Y$
$z'(F) \approx 5.0633 \cdot [F^{0.135} - (1 - F)^{0.135}]$		$\sigma_X^2 = \mu_X^2 \cdot \left[\exp\left(\sigma_Y^2\right) - 1 \right]$	$\lambda_2 = \exp\left(\mu_Y + \frac{\sigma_Y^2}{2}\right) \cdot \text{erf}\left(\frac{\sigma_Y}{2}\right)$
$Z' \equiv \frac{Y - \mu_Y}{\sigma_Y}$		$\gamma_X = 3 \cdot CV_X + CV_X^2$	τ_3, τ_4 : see Hosking and Wallis (1997)
$Y \equiv \ln(X)$			

Our discussions of product moments for $r > 1$ will always be for $x^* = \mu_X$, so we henceforth shorten the notation to M_X for $r > 1$. The second moment about the mean is called the **variance**, denoted σ_X^2 , and defined as

$$\begin{aligned} {}_2 M_X &\equiv E[(X - \mu_X)^2] = \sigma_X^2 \\ &= \int_{-\infty}^{+\infty} [x_i - \mu_X]^2 \cdot f_X(x_i) \cdot dx. \end{aligned} \quad (\text{C.19})$$

The **standard deviation**, σ_X , is the square root of the variance. Like the interquartile range, it is a measure of the spread or variability of the distribution around the central value (figure C.1b). A relative measure of spread derived from product moments is the dimensionless **coefficient of variation**, CV_X :

$$CV_X \equiv \frac{\sigma_X}{\mu_X}. \quad (\text{C.20})$$

The third moment about the mean, ${}_3 M_X$, is a measure of the symmetry of a distribution. To facilitate comparison among distributions of variables of different magnitudes, symmetry is usually characterized by the dimensionless **skewness**, γ_X :

$$\gamma_X \equiv \frac{{}_3 M_X}{\sigma_X^3}. \quad (\text{C.21})$$

Figure C.1c shows the relation between the sign of the skewness and the shape of a distribution. A non-zero skewness indicates an asymmetrical distribution; a negative/positive skewness means that the lower/upper tail of the distribution is extended.

The fourth moment about the mean provides information about the “peakedness” of the central portion of the distribution. It is usually characterized by the dimensionless ratio κ_X , called the **kurtosis**:

$$\kappa_X \equiv \frac{{}_4 M_X}{\sigma_X^4}. \quad (\text{C.22})$$

Table C.1 (cont'd.)

Distribution cdf and Inverse	Range	Product Moments	L-Moments
Exponential (E):			
$F_{EX}(x) = 1 - \exp[-\eta \cdot (x - \xi)]$ $x(F) = \xi - \frac{1}{\eta} \cdot \ln(1 - F)$	$\eta > 0$ $x > \xi$	$\mu_X = \xi + \frac{1}{\eta}$ $\sigma_X^2 = \frac{1}{\eta^2}$ $\gamma_X = 2$	$\lambda_1 = \xi + \frac{1}{\eta}$ $\lambda_2 = \frac{1}{2 \cdot \eta}$ $\tau_3 = 0.3333; \tau_4 = 0.1667$
Gumbel (G):			
$F_{GX}(x) = \exp\left[-\exp\left(\frac{x - \xi}{\alpha}\right)\right]$ $x(F) = \xi - \alpha \cdot \ln[-\ln(F)]$	$-\infty < x < \infty$	$\mu_X = \xi + 0.5772 \cdot \alpha$ $\sigma_X^2 = 1.645 \cdot \alpha^2$ $\gamma_X = 1.1396$	$\lambda_1 = \xi + 0.5772 \cdot \alpha$ $\lambda_2 = 0.6931 \cdot \alpha$ $\tau_3 = 0.1699$ $\tau_4 = 0.1504$
Generalized Extreme Value (GEV):			
$F_{GEVX}(x) = \exp\left\{-\left[1 - \frac{\kappa \cdot (x - \xi)}{\alpha}\right]^{1/\kappa}\right\}$ $x(F) = \xi + \frac{\alpha}{\kappa} \cdot \left[1 - \left[-\ln(F)\right]^\kappa\right]$	$\kappa > 0:$ $x < \left(\xi + \frac{\alpha}{\kappa}\right)$ $\kappa < 0:$ $x > \left(\xi + \frac{\alpha}{\kappa}\right)$	$\mu_X = \xi + \frac{\alpha}{\kappa} \cdot [1 - \Gamma(1 + \kappa)]$ $\sigma_X^2 = \left(\frac{\alpha}{\kappa}\right)^2 \cdot \left\{\Gamma(1 + 2 \cdot \kappa) - [\Gamma(1 + \kappa)]^2\right\}$	$\lambda_1 = \xi + \frac{\alpha}{\kappa} \cdot [1 - \Gamma(1 + \kappa)]$ $\lambda_2 = \frac{\alpha}{\kappa} \cdot (1 - 2^{-\kappa}) \cdot \Gamma(1 + \kappa)$ $\tau_3, \tau_4:$ see Stedinger et al. (1992)
Generalized Pareto (GPA):			
$F_{GPAX}(x) = 1 - \left[1 - \kappa \cdot \frac{(x - \xi)}{\alpha}\right]^{1/\kappa}$ $x(F) = \xi + \frac{\alpha}{\kappa} \cdot \left[1 - (1 - F)^\kappa\right]$	$\kappa < 0:$ $\xi \leq x$ $\kappa > 0:$ $\xi \leq x \leq \xi + \frac{\alpha}{\kappa}$	$\mu_X = \xi + \frac{\alpha}{1 + \kappa}$ $\sigma_X^2 = \frac{\alpha^2}{(1 + \kappa^2) \cdot (1 + 2 \cdot \kappa)}$	$\lambda_1 = \xi + \frac{\alpha}{1 + \kappa}$ $\lambda_2 = \frac{\alpha}{(1 + \kappa) \cdot (2 + \kappa)}$ $\tau_3 = \frac{1 - \kappa}{3 + \kappa}$ $\tau_4 = \frac{(1 - \kappa) \cdot (2 - \kappa)}{(3 + \kappa) \cdot (4 + \kappa)}$

Sources: Stedinger et al. (1992), Hosking and Wallis (1997), and Haan (2002).

The kurtosis of the normal distribution (section C.4) equals 3; if $\kappa > 3$, the distribution is more peaked than the normal distribution; if $\kappa < 3$, it is flatter.

As with quantiles, we can never know the true values of the moments of a distribution, and must estimate them from the sample. Box C.2 (see disk) shows how this is done.

C.3.6 Probability-Weighted Moments and L-Moments

Because of the generally small sample sizes available for characterizing hydrologic variables, estimates of the third and higher product moments are

usually very uncertain. This has led to the use of an alternative approach for characterizing probability distributions, called **L-moments** (see Stedinger et al. 1992; Hosking and Wallis 1997).

L-moments are based on **probability-weighted moments (PWM)**. The r th PWM, β_X^r , is defined as

$$\begin{aligned} \beta_X^r &\equiv E\left\{X \cdot [F_X(X)]^r\right\} \\ &= \int_{-\infty}^{+\infty} x \cdot [F_X(x)]^r \cdot f_X(x) \cdot dx. \end{aligned} \quad (\text{C.23})$$

L-moments, λ_X^r , are linear combinations of PWMs. The first four L-moments are computed as

$${}_1\lambda_X = {}_0\beta_X \quad (\text{C.24})$$

$${}_2\lambda_X = 2 \cdot {}_1\beta_X - {}_0\beta_X \quad (\text{C.25})$$

$${}_3\lambda_X = 6 \cdot {}_2\beta_X - 6 \cdot {}_1\beta_X + {}_0\beta_X \quad (\text{C.26})$$

$${}_4\lambda_X = 20 \cdot {}_3\beta_X - 30 \cdot {}_2\beta_X + 12 \cdot {}_1\beta_X - {}_0\beta_X. \quad (\text{C.27})$$

From equations (C.18), (C.23), and (C.24), we see that ${}_1\lambda_X = \mu_X$. The higher L-moments also reflect probability-distribution properties analogous to higher product-moment properties: ${}_2\lambda_X$ is a measure of the dispersion, or variability, of the distribution; ${}_3\lambda_X$ is a measure of its asymmetry; and ${}_4\lambda_X$ is a measure of its peakedness (see Hosking and Wallis 1997). We can also define dimensionless ratios of L-

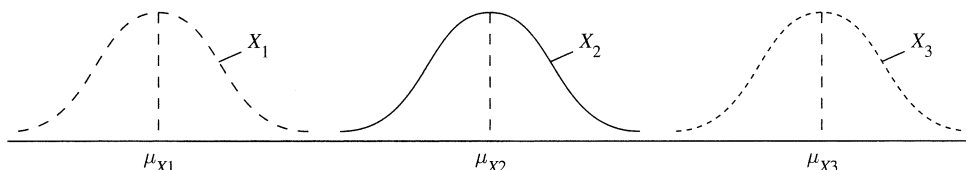
moments that are analogous to the coefficient of variation, skewness, and kurtosis:

$$\text{L-coefficient of variation: } LCV \equiv \frac{2\lambda_X}{1\lambda_X}; \quad (\text{C.28})$$

$$\text{L-skewness: } LSK \equiv \frac{3\lambda_X}{2\lambda_X}; \quad (\text{C.29})$$

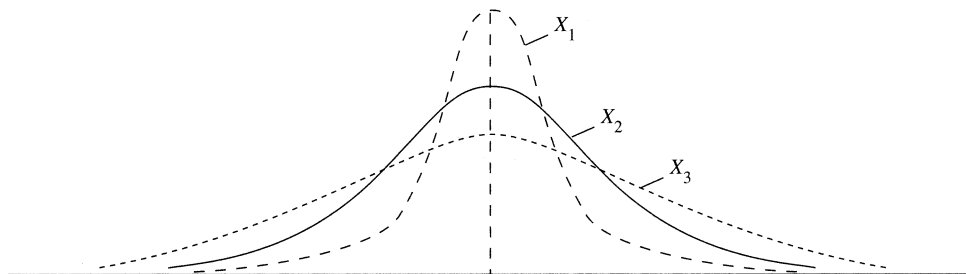
$$\text{L-kurtosis: } LKU \equiv \frac{4\lambda_X}{2\lambda_X}. \quad (\text{C.30})$$

Note that PWMs involve raising values of $F_X(X)$, rather than of X , to powers [equation (C.23)]. Because $F_X(x) \leq 1$, $F_X(x)^r \leq 1$, and estimates of sample PWMs, L-moments, and L-moment ratios are much less sus-



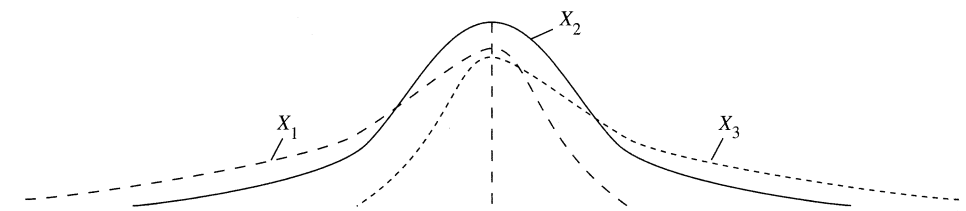
$$\begin{aligned} \mu_{X1} &< \mu_{X2} & \mu_{X3} \\ \sigma_{X1} &= \sigma_{X2} = \sigma_{X3} \\ \gamma_{X1} &= \gamma_{X2} = \gamma_{X3} = 0 \end{aligned}$$

(a)



$$\begin{aligned} \mu_{X1} &= \mu_{X2} = \mu_{X3} \\ \sigma_{X1} &< \sigma_{X2} < \sigma_{X3} \\ \gamma_{X1} &= \gamma_{X2} = \gamma_{X3} = 0 \end{aligned}$$

(b)



$$\begin{aligned} \mu_{X1} &= \mu_{X2} = \mu_{X3} \\ \sigma_{X1} &= \sigma_{X2} = \sigma_{X3} \\ \gamma_{X1} &< 0; \gamma_{X2} = 0; \gamma_{X3} > 0 \end{aligned}$$

(c)

Figure C.1 Effects of increasing magnitudes of (a) mean, μ_X ; (b) standard deviation, σ_X ; and (c) skewness, γ_X , on the location and shape of probability distributions. In each graph the horizontal axis is the value of X , and the vertical axis is the probability-density function (pdf), $f(X)$.

ceptible to the influences of a few large or small values in the sample. Hence they are preferable to product moments for characterizing probability distributions of hydrologic variables, as described in section C.8. Box C.3 (see disk) explains how L-moments are computed and gives an example calculation.

C.4 The Normal Distribution

The **normal**, or **Gaussian, distribution** plays a large role in statistical analysis. It was derived by K. F. Gauss in 1809 from his investigations of estimating the true value of a quantity from uncertain measurements, and one important application is in characterizing measurement error and uncertainty (section 1.11). In addition, many hydrologic variables can be characterized by the normal or log-normal distribution.

C.4.1 Normal pdf and cdf

The normal distribution of a variable X has two parameters, the mean μ_X and the standard deviation σ_X . Its pdf is

$$f_{NX}(x) = \frac{1}{(2\pi)^{1/2} \cdot \sigma_X} \cdot \exp\left[-\frac{1}{2} \cdot \left(\frac{x - \mu_X}{\sigma_X}\right)^2\right]. \quad (\text{C.31})$$

The **standard normal variate**, Z , has a normal distribution with $\mu_Z = 0$ and $\sigma_Z = 1$. Thus its pdf is

$$F_{NZ}(z) = \frac{1}{(2\pi)^{1/2}} \cdot \exp\left(-\frac{z^2}{2}\right). \quad (\text{C.32})$$

By making the transformation

$$Z = \frac{X - \mu_X}{\sigma_X}, \quad (\text{C.33})$$

we can state that

$$f_{NX}(x) = f_{NZ}(z). \quad (\text{C.34a})$$

Note that the normal distribution is symmetrical about the value $x = \mu_X$ or $z = 0$; thus it has skewness $\gamma_X = 0$ and L-skewness $\tau_3 = 0$. The kurtosis, κ_X , of the normal distribution = 3 and the L-kurtosis $\tau_4 = 0.123$.

The normal cdf is the integral of equation (C.31) or (C.32) (table C.1), so

$$F_{NX}(x) = F_{NZ}(z). \quad (\text{C.34b})$$

This integral can be evaluated only as a series expansion, so tables and spreadsheet algorithms are used

to give $F_{NZ}(z)$ as a function of z (table C.3; see disk). The inverse relation can be approximated as

$$z \approx 5.0633 \cdot \{[F_{NZ}(z)]^{0.135} - [1 - F_{NZ}(z)]^{0.135}\}. \quad (\text{C.35})$$

By using equations (C.11), (C.33), and (C.34) and the symmetry property, table C.3 (see disk) can be used to calculate the cdf for any normally distributed variable and the probability that a value will fall into any interval, as demonstrated in box C.4 (see disk). Table C.4 (see disk) gives the probability of Z between $-z^*$ and $+z^*$ for specified values of z^* (see also figure 1.20).

C.4.2 Log-Normal Distribution

Most hydrologic variables cannot be negative numbers, and many have pdfs that are strongly positively skewed like X_3 in figure C.1c. In many cases, such variables can be well represented by the **log-normal distribution**, in which the logarithms of the variable values are normally distributed, rather than the values themselves. Thus, defining

$$LX \equiv \ln(X), \quad (\text{C.36})$$

the pdf for the log-normal distribution is

$$f_{LNX}(x) = \frac{1}{(2\pi)^{1/2} \cdot \sigma_{LX}} \cdot \exp\left[-\frac{1}{2} \cdot \left(\frac{Lx - \mu_{LX}}{\sigma_{LX}}\right)^2\right]. \quad (\text{C.37})$$

It can be shown (Haan 2002) that there are fixed relations between the parameters of the normal and log-normal distributions:

$$\mu_{LX} = \left(\frac{1}{2}\right) \cdot \ln\left(\frac{\mu_X^2}{CV_X^2 + 1}\right) \quad (\text{C.38})$$

and

$$\sigma_{LX}^2 = \ln(CV_X^2 + 1). \quad (\text{C.39})$$

If X is log-normally distributed and μ_X and σ_X are specified, the probability that x is in any range can be readily calculated using the above relations and tables of the normal distribution, as shown in example CB4.4 of box C.4 (see disk).

The example computations in box C.4 assume that the annual flows are normally distributed and the annual maximum flows are log-normally distributed and the means and standard deviations are known. The tests described in section C.8 can be

used to show whether the data are consistent with these assumptions, and the methods of section C.9 can be used to assess uncertainty in the estimates of parameters such as the mean and standard deviation.

C.5 Time Series, Exceedence Probability, and Return Period

Hydrologists commonly apply statistical concepts to samples in the form of a **time series**, which is a sequence of values of a variable associated with successive time periods of equal length Δt . As described in section 1.9.2.1, the variable values are usually totals, averages, maxima, or minima of some quantity (e.g., precipitation, streamflow) for each period. The statistical concepts discussed in this appendix are generally applicable to *stationary* time series, as discussed in section 1.9.2.3. If nonstationarity exists, the validity of statistical inferences about a time series becomes questionable.

Hydrologists commonly express probabilities of time-series variables in terms of **exceedence probability**, $EP_X(x^*)$, defined as

$$EP_X(x^*) \equiv Pr\{X > x^*\} = 1 - F_X(x^*), \quad (\text{C.40})$$

where x^* is a specified value of X . This concept was introduced in the discussion of depth-duration-frequency analysis of precipitation in section 4.4.3.3. For a stationary time series, it can be shown that the *average* number of time intervals between occurrences of the event $X > x^*$ is equal to $1/EP_X(x^*)$. Thus exceedence probability is frequently expressed as **return period** (or **recurrence interval**), $TR_X(x^*)$, where

$$TR_X(x^*) \equiv \frac{1}{EP_X(x^*)} = \frac{1}{1 - F_X(x^*)}. \quad (\text{C.41})$$

When $\Delta t = 1$ yr (the most common choice in hydrologic analysis), $TR_X(x^*)$ is the *average* number of years between years in which $X > x^*$.

In spite of the use of the words “return” or “recurrence,” there is no regularity or periodicity in occurrences of exceedences involved in the definition of $TR_X(x^*)$.

For an annual time series (i.e., $\Delta t = 1$ yr), the “ T -yr event” is the value x^* for which $TR_X(x^*) = T$. Thus for a time series of annual floods (i.e., the annual maximum streamflows), the “100-yr flood” is the an-

nual maximum streamflow x^* for which $EP(x^*) = 0.01$; thus x^* is the 0.99-quantile, $x_{0.99}$.

Box C.5 (see disk) applies the rules of probabilities for independent events [equation (C.3)] to show how various exceedence probabilities are calculated for specified time periods $n \cdot \Delta t$ (e.g., over a period of n yr).

C.6 Covariance, Correlation, and Autocorrelation

C.6.1 Covariance and Correlation

The degree to which two variables X and Y fluctuate in parallel is measured by the **covariance**, $COV_{X,Y}$, defined analogously to the variance [equation (C.19)] as

$$\begin{aligned} COV_{X,Y} &= E\{[X - E(X)] \cdot [Y - E(Y)]\} \\ &= E(X \cdot Y) - E(X) \cdot E(Y). \end{aligned} \quad (\text{C.42})$$

The magnitude of the covariance depends on the scale of the variables and their units of measurement, so a more meaningful measure of this tendency is the dimensionless **correlation coefficient**, $\rho_{X,Y}$:

$$\begin{aligned} \rho_{X,Y} &\equiv \frac{COV_{X,Y}}{\sigma_X \cdot \sigma_Y} = \frac{E(X \cdot Y) - E(X) \cdot E(Y)}{\sigma_X \cdot \sigma_Y} \\ &= \frac{E[(x - \mu_X) \cdot (y - \mu_Y)]}{\sigma_X \cdot \sigma_Y}. \end{aligned} \quad (\text{C.43})$$

Note that $\rho_{X,Y} = \rho_{Y,X}$.

The range of $\rho_{X,Y}$ is $-1 \leq \rho_{X,Y} \leq 1$. As shown in figure C.2, $\rho_{X,Y} > 0$ indicates that relatively high/low values of X tend to be associated with high/low values of Y ; $\rho_{X,Y} < 0$ indicates that high/low values of X are associated with low/high values of Y . When $|\rho_{X,Y}| = 1$ there is a perfect *linear* relation between X and Y (figure C.2a). When $\rho_{X,Y} = 0$ there is no degree of *linear* relation; however, X and Y may be related in other ways (figure C.2f).

Estimates of $\rho_{X,Y}$, the **sample correlation coefficient**, $r_{X,Y}$, are made from samples of pairs of X, Y values as described in box C.6 (see disk) and figure C.3. Most spreadsheets include built-in functions that calculate $r_{X,Y}$.

C.6.2 Autocorrelation and Persistence

C.6.2.1 Definition

Some variables are inherently **ordered**; this is true of all time-series variables and some spatially

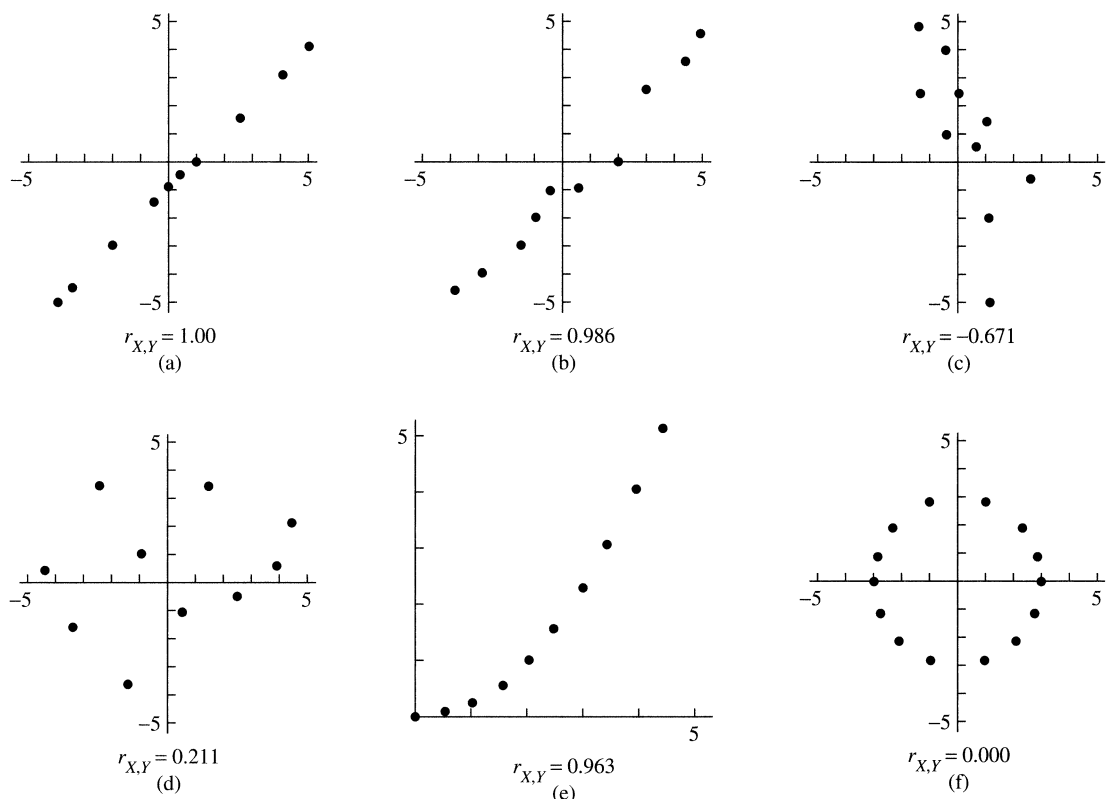


Figure C.2 Values of the sample correlation coefficient, $r_{X,Y}$, for various degrees of linear correlation [reproduced from Haan (2002). *Statistical Methods in Hydrology*, 2nd ed. Ames: Iowa State University Press, with permission of Wiley].

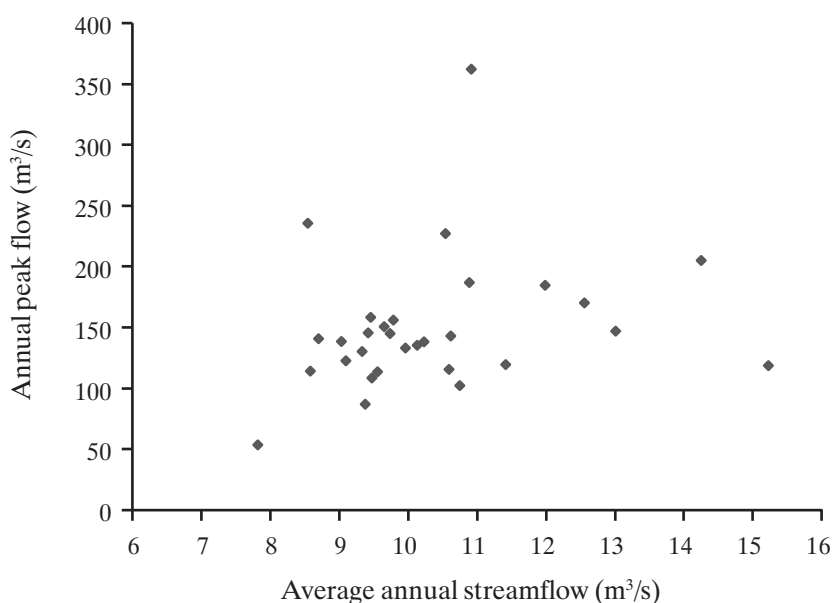


Figure C.3 Scatter plot of annual flood versus average annual streamflow for the Diamond River, Wentworth, New Hampshire, 1971–2000. Although the sample correlation coefficient $r_{X,Y} = 0.230$, the null hypothesis that the population correlation coefficient $\rho_{X,Y} = 0$ cannot be rejected at the $\alpha = 0.05$ significance level (box C.6; see disk).

distributed variables, such as measurements of snow depth or soil-moisture content along a linear transect. For such variables, **persistence** is the tendency for adjacent values to be correlated, i.e., high values to follow high values, and low values to follow low values, where “high” and “low” are determined relative to the average. Thus the presence of persistence indicates that successive values of the time series are not independent, but are instead related in some way to preceding values.

Standard approaches to statistical inference
assume independence, so if persistence
is present it must be accounted for
in statistical analysis.

Ordered variables are written as $x_{(i)}$, where $(i) = (1), (2), \dots$ designates the order in the time or spatial sequence. The most common type of persistence is reflected in the **lag- k autocorrelation coefficient** (or **serial correlation coefficient**), ρ_{kX} , defined analogously to the correlation coefficient [equation (C.43)] as

$$\rho_{kX} \equiv \frac{E[(x_{(i)} - \mu_X)(x_{(i+k)} - \mu_X)]}{\sigma_X^2}, \quad (\text{C.44})$$

where k is the **lag**, or spacing of the variables. By comparison with equation (C.43), we see that ρ_{kX} is simply the correlation coefficient between values of a

single ordered variable at a spacing of k intervals. Thus, like ρ_{XY} , ρ_{kX} is a dimensionless number that can take on values between -1 and $+1$. As with other statistics, the true value of ρ_{kX} cannot be known and must be estimated by calculating r_{kX} as described in box C.7 (see disk). An example is shown in figure C.4.

C.6.2.2 Causes and Significance

By far the most common autocorrelation measure is the lag-1 autocorrelation coefficient. Persistence is reflected in a positive value for ρ_{1X} ; a zero value of ρ_{1X} indicates that successive values of X are not *linearly* related. A negative value of ρ_{1X} indicates that high values of X tend to be followed by low values and vice versa; this reflects the opposite of persistence and is very rare in hydrologic time series.

For time-series variables with no seasonal variation, persistence is usually the result of storage with a residence time at least as great as the time interval of the time series, e.g., outflow from a substantial reservoir (watershed, lake, or aquifer). In this case ρ_{kX} values typically decline quasi-exponentially as k increases (i.e., values are less correlated as they are further apart in time). Variables with seasonal variation tend to have significant autocorrelation at a lag equal to the period of the seasonality. For example, monthly average streamflow values in many regions have significant correlation at lag $k = 12$.

The presence of persistence makes it more likely that a time-series sample was taken from a period when values tended to be higher or lower than aver-

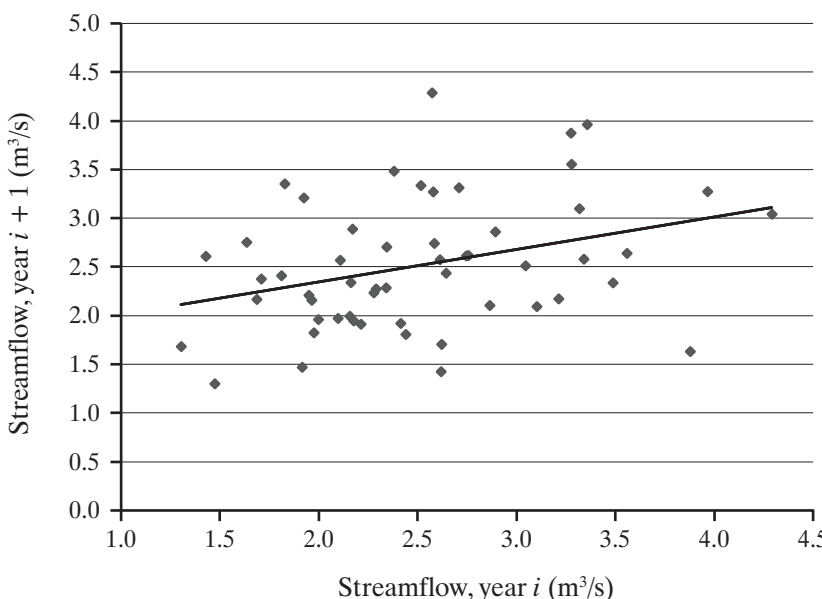


Figure C.4 Scatter plot of 1940–1990 average annual flows of the Squam River, New Hampshire, for year i , $x_{(i)}$, versus the following year's flow, $x_{(i+1)}$. The unbiased estimate of the lag-1 autocorrelation coefficient [equation (CB7.2)] $r_{1X} = 0.380$, significant at $\alpha = 0.05$ (box C.7; see disk). The autocorrelation is due to the large storage in Squam Lake, which has a residence time of about 5 yr.

age, and when the variability was not representative of the population. Thus persistence reduces the confidence with which one can estimate mean, variance, and other statistics of the time series. Approaches to accounting for this are discussed in section C.11.4.

C.7 Data Analysis: Hypothesis Tests

Hypothesis testing—for example, of the hypothesis that the true mean of a variable is in a particular range, or that a variable follows a particular probability distribution—is a central goal of statistical analysis. This is a formal process that has the following structure (Helsel and Hirsch 1992):

1. Choose an appropriate test.

The choice of test depends on the study objectives and the nature of the data. For example, there are tests to detect differences in central values (means, medians) or spreads (standard deviations, interquartile ranges) of two or more variables, whether a sample is from a specified probability distribution, whether two variables are correlated, or whether a time series is autocorrelated, among others. There are two categories of tests: (1) **parametric tests** require an assumption about the probability distribution of the variable (usually that it is normally distributed) and (2) **nonparametric tests**, which do not require such an assumption. Nonparametric tests are generally more appropriate for the types of data and sample sizes encountered by hydrologists; Conover (1980) and Helsel and Hirsch (1992) provide excellent documentation of nonparametric hypothesis tests.

2. Formulate the null hypothesis and the alternate hypothesis.

The **null hypothesis** (designated H_0) is a statement that is assumed to be true until countervail-

ing evidence is found. Usually it is a statement that there is “no difference”; for example, that there is no difference between the population means of two variables, or that the probability distribution of a given variable does not differ from some specified distribution. The **alternate hypothesis** (H_1) is either the negation of H_0 (e.g., there is a difference) or a more specific type of difference (e.g., a particular one of the populations has a higher mean than the other).

3. Decide on an acceptable Type I error probability, α .

As always in science, the true state of nature is not known with 100% confidence. Thus, as shown in figure C.5, there are four possible results of hypothesis testing. The probability of incorrectly concluding that H_0 is false when it is true (called **Type I error**) is selected by the researcher prior to conducting the test. This is called the **significance level**, designated α . The complement of this ($1 - \alpha$), is the probability of correctly concluding that H_0 is true. The probability of concluding that H_0 is false when it is true (**Type II error**) is designated β ; its complement ($1 - \beta$) is the probability of correctly concluding that H_0 is false, and is called the **power** of the test. In general, a numerical value for β cannot be given. However, different tests are known to be more powerful than others under various conditions (see, for example, Helsel and Hirsch 1992).

In a given test situation, the choice of a higher significance level α (smaller likelihood of Type I error) reduces the power of the test (greater likelihood of Type II error).

Unknown state of nature		
Possible conclusions	H_0 True	H_0 False
Fail to reject H_0	Correct decision Probability = $1 - \alpha$	Type II error Probability = β
Reject H_0	Type I error Probability = α Significance Level	Correct decision Probability = $1 - \beta$ Power

Figure C.5 Possible results of hypothesis testing [adapted from Helsel and Hirsch (1992)].

Once a value of α is chosen in a given situation (conventionally, $\alpha = 0.05$), the power of a test can be increased only by using a larger sample size (which is not always possible).

4. Compute the test statistic from the data.

Each test has its own **test statistic**, say ζ , the value of which, ζ^* , is calculated from the data.

5. Compute the probability of the test-statistic value, p .

Tables or graphs are consulted to determine the probability of obtaining the test statistic value ζ^* , or a value of ζ even less likely than ζ^* , given that H_0 is true. The p value of a test should always be reported, as it is a measure of how strong the evidence for rejection/nonrejection is.

6. Reject the null hypothesis if $p < \alpha$.

If $p < \alpha$, H_0 is rejected; otherwise, H_0 is not rejected. Note that a value of $p \geq \alpha$ does not mean that H_0 is accepted or proven to be true, only that the data do not support rejection of H_0 . Note also from figure C.5 that if we decide not to reject H_0 there is still a probability, generally not precisely quantifiable, that H_0 is false (Type II error).

C.8 Data Analysis: Display and Preliminary Assessment

The usual first step in a statistical analysis, often done prior to formal hypothesis testing, is to get a general impression of the basic characteristics of the distribution of values in each data set: its central value, range, and shape and, especially for time-series data, the likely presence of autocorrelation and nonstationarity. This section describes some basic techniques for doing this; others are described in Helsel and Hirsch (1992).

C.8.1 Histograms

A histogram is a plot of the frequency of occurrence of sample values in which the widths of contiguous vertical bars indicate the ranges of sample values (horizontal axis) and the heights of the bars are proportional to the frequency of occurrence of values in each range. It is the sample analog of the theoretical probability-distribution function (pdf).

Construction of a histogram requires arbitrary selection of the number and range of classes, or **bins**; one of the disadvantages of histograms is that the visual impression of the sample distribution is deter-

mined by that choice. There are no widely accepted guidelines for choosing the number of bins; one objective suggestion that appears generally useful is to make a preliminary calculation of the number of bins, m , as

$$m = 1 + 3.3 \cdot \log_{10}(N), \quad (\text{C.45})$$

where N is sample size, then adjust this to a whole number with convenient bin boundaries. Box C.8 (see disk) and figure C.6 give an example of the construction of a histogram.

C.8.2 Boxplots

In a boxplot the vertical axis shows the data values, and the box extends from the 0.25-quantile of the data to the 0.75-quantile (the interquartile range), with the 0.50-quantile (median) shown as a horizontal line within the box. Typically the “tails” of the distribution are shown by lines that extend upward from the box to the 0.90-quantile, and downward to the 0.10-quantile. Dots may be added to show individual sample values beyond those limits. Box C.8 (see disk) and figure C.7 give an example of the construction of a boxplot.

Boxplots are a very convenient way to display the quantiles of a sample distribution. And, because they do not involve arbitrary decisions that affect their appearance, boxplots are better than histograms for characterization of a sample distribution, especially for quick visual comparison of different samples.

C.8.3 Empirical Distribution Function

Another informative way of displaying values of a sample of a variable X is as an **empirical distribution function (edf)**, $\hat{F}_X(x)$. The edf is a plot of the cumulative frequency distribution of the sample values, and is the sample analog of the theoretical cumulative distribution function (cdf).

Given a sample of N observations, x_1, x_2, \dots, x_N , the edf is constructed by sorting the observations in increasing order, designated $x_{[1]}, x_{[2]}, \dots, x_{[N]}$, where i is the **rank** of $x_{[i]}$; $x_{[1]}$ is the smallest value and $x_{[N]}$ the largest. Each sample value $x_{[i]}$ is then plotted (horizontal axis) versus $\hat{F}_X(x)$, where

$$\hat{F}_X(x_{[i]}) = \frac{i}{N}, \quad (\text{C.46})$$

as in figure C.8 on p. 562.

The edf provides a concise picture of the range and spread of the variable, its central value, and the frequency of values within any range. Unlike a his-

togram, its shape is not affected by arbitrary selection of the number of bins and their ranges. Characteristics of different samples can be visually compared by plotting several edfs on the same graph. However, boxplots are probably better than edfs for giving a visual impression of the central value (mean or median), spread (standard deviation or interquartile range), and asymmetry (skewness) of a sample distribution.

C.8.4 Autocorrelation Assessment

As noted in section C.6.2, autocorrelation is common in hydrologic time-series variables. Its presence means that successive sample values are not independent, and the amount of information that the sample provides about the underlying population is less than contained in an independent sample of the same size. Thus it is important to determine the likely presence or absence of autocorrelation in a sample time series.

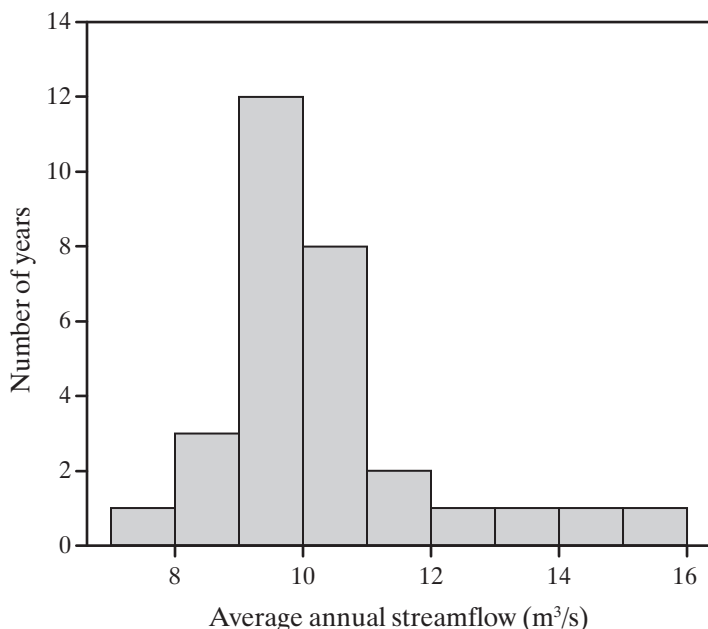


Figure C.6 The histogram of average annual streamflow for the Diamond River, Wentworth, New Hampshire, 1971–2000 indicates that the distribution is positively skewed, consistent with the sample skewness $g_X = 1.33$ calculated in box C.2 (see disk).

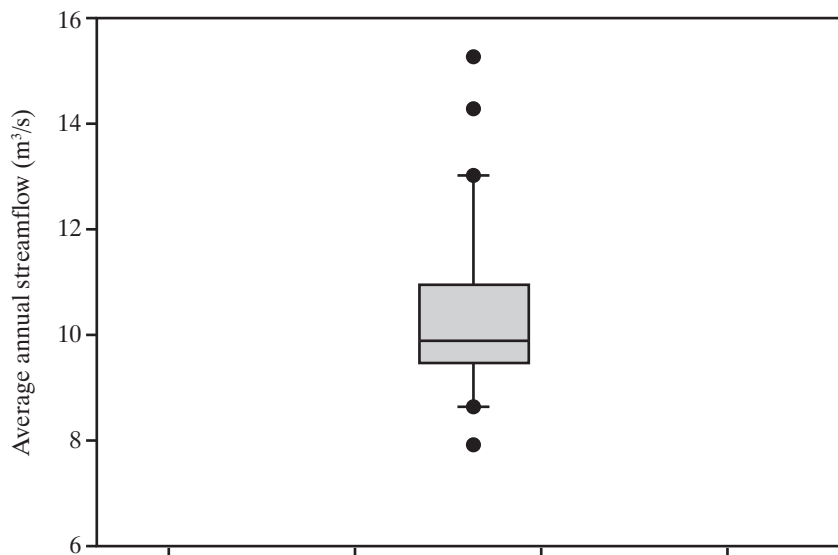


Figure C.7 Boxplot of average annual streamflow for the Diamond River, Wentworth, New Hampshire, 1971–2000. The shaded box extends from the 0.25- to 0.75-quantile (interquartile range); the horizontal line is the median. The vertical lines extend to the 0.10- and 0.90-quantiles and the dots show individual values beyond the 0.10- and 0.90-quantiles.

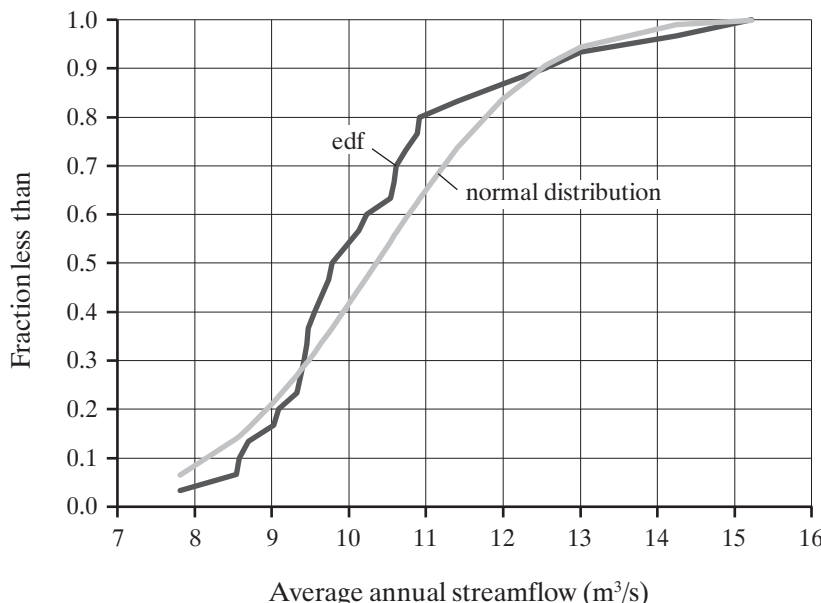


Figure C.8 Empirical distribution function (edf) of annual streamflow for the Diamond River, Wentworth, New Hampshire, 1971–2000. The cdf for a normal distribution with the same mean and standard deviation is shown for comparison.

For preliminary detection of probable autocorrelation, the sample values are arranged in chronological order, $x_{(1)}$, $x_{(2)}$, ..., $x_{(N)}$. A scatter plot of each sample value $x_{(i)}$ versus the following value $x_{(i+1)}$ can then be constructed; the presence of an upward or downward trend in the plot suggests that autocorrelation is present, as in figure C.4. A hypothesis test of the significance of the trend can be conducted as described in box C.9 (see disk).

C.8.5 Stationarity Assessment

As noted in section 1.9, time series are conventionally assumed to be *stationary*; i.e., to be representative samples of long-term behavior of the variable. However, natural phenomena (solar cycles, teleconnections) and human activity (dam building, land-use change, ground-water pumping, climate change due to greenhouse gas emissions, shifts in measurement locations) can induce nonstationarity in the form of trends, cycles, or abrupt shifts in hydrologic data. In order to have confidence in inferences made from statistical analyses, tests of time-series data should be conducted to identify the possible presence of nonstationarity. If stationarity can be assumed, most traditional statistical concepts can be applied to time series, including the idea that the larger the sample size (i.e., length of observation period), the greater the confidence in statistical inferences. Clearly, this idea is questionable if the underlying system is changing over time.

There are three common forms of nonstationarity in hydrologic data: (1) upward or downward *trends* in central values (means, medians) or variability (standard deviation, interquartile range), (2) abrupt upward or downward *shifts* in central values or variability, and (3) *cyclicity*.

It is advisable to make a preliminary assessment to determine its possible presence by plotting the time series as in figure C.9 and noting any visual evidence of one of the forms of nonstationarity. One hypothesis test for detecting a trend in mean values is described in box C.9 (see disk). Many other tests for the various forms of nonstationarity are available, but they are beyond the scope of this text. Note, however, that

Type I and Type II errors are always present, so that no single test is definitive and no combination of tests can absolutely rule out or establish stationarity or nonstationarity.

C.9 Data Analysis: Identifying Candidate Probability Distributions

The most common goal of identification of candidate probability distributions for hydrologic variables is to estimate extreme quantiles in order to assess risks associated with floods and droughts, as

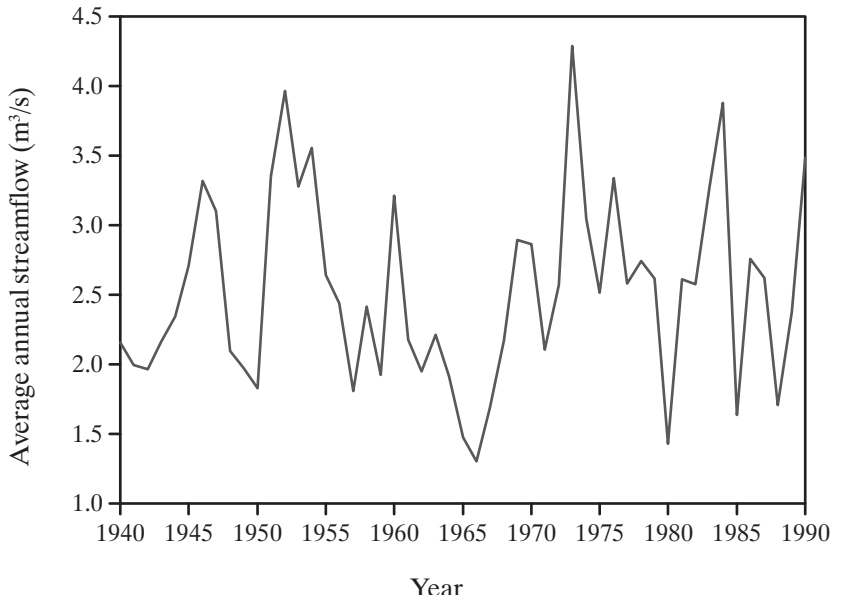


Figure C.9 Time series of the Squam River annual average streamflows, 1940–1990. The plot does not suggest that any trend is present; this is confirmed by the hypothesis test described in box C.9 (see disk).

discussed in sections 4.4.3 and 10.6. As pointed out by Stedinger et al. (1992), the problem of identifying candidate probability distributions can be posed in the form of three distinct questions:

1. *What is the true probability distribution from which the observations are drawn?*

This question is probably unanswerable because actual distributions are not likely to exactly follow relatively simple mathematical formulations such as those in table C.1.

2. *Is a specific probability distribution consistent with a given sample of observations?*

This question can be answered by relatively simple statistical tests. Section C.9.1 introduces a commonly used, relatively powerful **goodness-of-fit analysis** that is widely recommended for this purpose. More detailed discussion of this and other approaches to this question can be found in Helsel and Hirsch (1992), Stedinger et al. (1992), and Haan (2002).

3. *What distribution should be used to provide reasonably accurate regional estimates of design quantiles and risk that are minimally subject to the vagaries of sample variability?*

Section C.9.2 introduces the basic approach to this question, which is often of main interest in water-resource studies. A comprehensive description of this approach, which requires in-depth analysis of data from many sites in the region of interest, is described by Hosking and Wallis (1997).

C.9.1 Goodness-of-Fit: The Probability-Plot Correlation-Coefficient Test

The null hypothesis that a given variable X follows a candidate probability distribution $F_X^*(x)$ can be tested via the **probability-plot correlation-coefficient (PPCC)** goodness-of-fit test. The test is done via the following steps:

1. Sort the sample values in ascending order, designated $x_{[1]}, x_{[2]}, \dots, x_{[N]}$.
2. Calculate the quantile function, $F_X^{*-1}(x_{[i]})$, that would exist for each $x_{[i]}$ if the data followed the candidate distribution. Quantile functions for some distributions are listed in table C.1. If the candidate distribution is the normal distribution, the $x_{[i]}$ values are first converted to corresponding $z_{[i]}$ values via equation (C.33) and the quantile function estimated via equation (C.35).
3. Compute the sample correlation coefficient, r_{X,F^*} , between the $x_{[i]}$ values and the corresponding $F_X^{*-1}(x_{[i]})$ values via equation (CB6.1) (see disk).
4. If r_{X,F^*} exceeds a critical value, r_{PPCC}^* , that depends on the distribution F_X^* , the chosen significance level, α , and the sample size, N , the null hypothesis is not rejected. Table C.5 (see disk) gives r_{PPCC}^* for the normal distribution for $\alpha = 0.05$ and 0.10 as a function of N .

An example application of the PPCC test is given in box C.10 (see disk).

C.9.2 Regional L-Moment Approach

Here we outline the regional L-moment approach that is fully described in the book by Hosking and Wallis (1997). The objective of this approach is to identify a single “robust” probability distribution that characterizes a particular variable (e.g., annual floods) in a hydrologic “region.” The “region” need not be geographically defined—it may be based wholly or in part on other characteristics such as drainage basin size, elevation, slope, etc.

Figure C.10a is an **L-moment diagram**, a plot showing values of L-skewness (*LSK*) and L-kurtosis (*LKU*) (section C.3.6) that characterize various probability distributions. Two-parameter distributions plot as a single point and three-parameter distributions as a line on an L-moment diagram.

The regional L-moment approach is a variant of the **index-flood approach**, which postulates that flood frequencies at a particular site in a region can be estimated as

$$X_j(F) = \mu_{X_j} \cdot {}_R F_X^*, \quad (\text{C.47})$$

where $X_j(F)$ is the flood discharge with nonexceedence probability F at site j , μ_{X_j} is the mean annual flood at site j (the **index flood**), and ${}_R F_X^* = F$ is the nonexceedence probability given by a **regional frequency distribution (RFD)** with mean = 1 that applies to all sites in region R (the **regional growth curve**). L-moment analysis (section C.3.6) (box C.3; see disk) is used to identify the appropriate RFD. The test is done via the following steps:

1. Identify sites where observations of the variable of interest have been made in the region of interest.
2. Compute the *LSK* and *LKU* (section C.3.6, box C.3) at each site.
3. Plot the *LSK* and *LKU* values as points on an L-moment diagram (figure C.10b).
4. A candidate RFD is selected based on the pattern of points on the L-moment diagram. Hosking and Wallis (1997) describe quantitative tests that can help identify sites that are outliers to the regional pattern, and further tests that can confirm that the distribution is appropriate. Figure C.11 shows

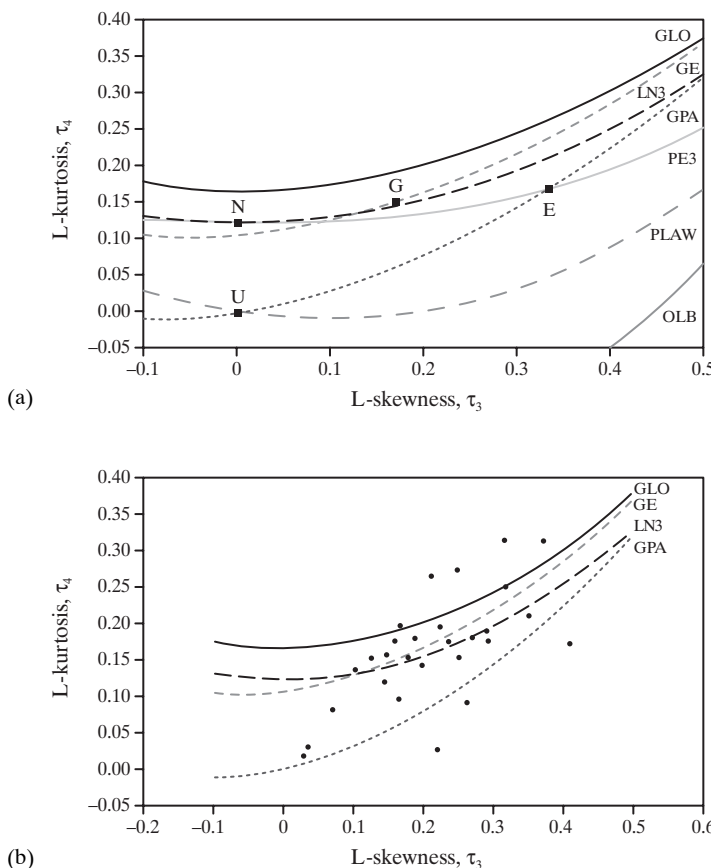


Figure C.10 (a) L-moment diagram showing values of L-skewness (*LSK*) and L-kurtosis (*LKU*) characterizing the normal (N), uniform (U), Gumbel (G), exponential (E), generalized logistic (GLO), generalized extreme value (GE), three-parameter log-normal (LN3), generalized Pareto (GPA), Pearson type 3 (PE3), and power-law (PLAW) distributions. OLB is the lower bound of possible (*LSK*, *LKU*) values [adapted from Hosking and Wallis (1997)]. (b) Sample (*LSK*, *LKU*) values for 29 New Hampshire gauging stations plotted on L-moment diagram (box C.11; see disk).

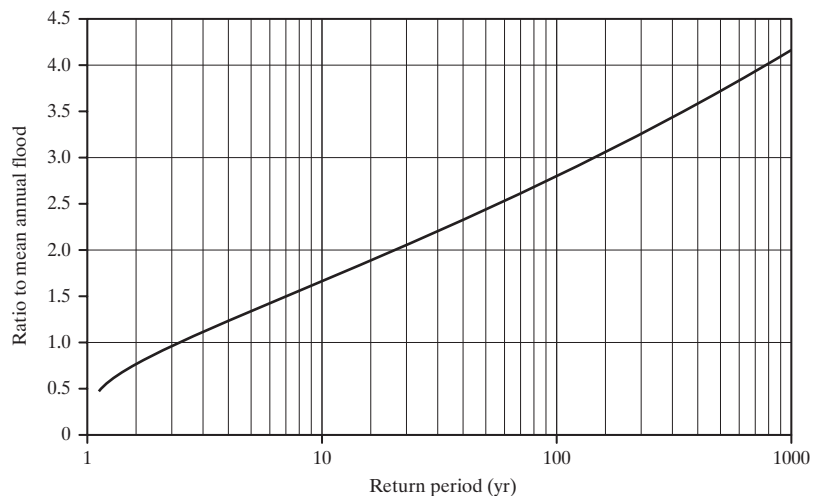


Figure C.11 Regional frequency distribution (growth curve) for the example of box C.11 (see disk).

the RFD developed for the example in box C.11 (see disk).

5. Using the relations between parameters and L-moments for the selected distribution, the parameters of the RFD are determined from the weighted-mean values of the sample L-moment ratios, where the weights are proportional to record length at each station. Relations between parameters and L-moments for some distributions are given in column 4 of table C.1.
6. Usually, the mean annual flood in the region can be related to watershed characteristics such as area, slope, etc. If so, the mean annual flood can be estimated for any watershed in the region, and the value of a flood of any exceedence probability estimated by multiplying the estimated mean annual flood by the value given by the RFD for that probability.

Box C.11 (see disk) describes an example application of this approach.

C.10 Data Analysis: Estimating Parameters of Probability Distributions

As noted earlier, probability distributions are usually expressed as equations giving the pdf or cdf as a function of the variable value, x , and one or more parameters, θ_i [equation (C.13)]. In order to use the equations to compute probabilities for a given variable, values of the parameters must be estimated from sample values of the variable.

There are three general approaches to estimating parameter values from samples: (1) the method of moments; (2) the method of maximum likelihood; and (3) the method of L-moments. A brief description of each is given here; more detailed discussions of their statistical properties can be found in Yevjevich (1972), Stedinger et al. (1992), Haan (2002), and general statistics texts.

C.10.1 Method of (Product) Moments

As indicated in table C.1, product moments can be mathematically related to parameters. In the method of moments, the sample product moments are calculated as in box C.2 (see disk) and substituted in those relations. The relations are then solved to give the parameter values. Generally the number of moments needed equals the number of parameters in the distribution.

C.10.2 Method of Maximum Likelihood

Maximum-likelihood (ML) estimators are derived by finding the parameter values that maximize the probability of obtaining the sample at hand. In some cases, ML estimators are identical to product-moment estimators. When they differ, the ML estimators generally have better statistical properties. However, in some cases the formulas for computing ML estimators are complex; consult statistical texts (e.g., Stedinger et al. 1992) for more detailed discussion.

C.10.3 Method of L-Moments

The method of L-moments is analogous to the method of moments: the sample L-moments are com-

puted (box C.3; see disk) and substituted into equations relating L-moments and parameters (table C.1; see also Hosking and Wallis 1997). Again, the number of L-moments that must be calculated generally equals the number of parameters. Although not widely used in conventional statistics, “In a wide range of hydrologic applications, L-moments provide simple and reasonably efficient estimators . . . of a distribution’s parameters” (Stedinger et al. 1992, p. 18.6).

C.11 Data Analysis: Sampling Error

In general, the population values of statistics such as quantiles, moments and L-moments, and correlation coefficients are unknowable. We can only estimate these values by taking samples calculating sample statistics, as in boxes C.1–C.3, C6, and C.7 (see disk).

Sampling error is the uncertainty inherent in sample estimates of population statistics.

Here we consider approaches to quantifying that uncertainty.

Imagine that we could take an infinite number of samples of size N from a population and calculate the statistics of interest for each sample.¹ The underlying (unknown) population from which the sample values were taken is called the **parent distribution**. The values of each statistic so calculated are functions of random variables (the measured values in the sample), and thus can also be considered random variables. These sample statistics each have a theoretical probability distribution, with its own quantiles and moment statistics; these distributions are known as **sampling distributions**. If the parent distribution is normal, the sampling distribution of various statistics can be derived theoretically.

The standard deviations of sampling distributions are called **standard errors** of the sample estimates that provide measures of the sampling error. Standard errors can be calculated, at least approximately, for all the statistics discussed here; these are discussed in section C.11.2. If the sampling distribution is known, this information along with the standard error can be used to compute absolute measures of the uncertainty in the form of **confidence intervals**; these are discussed in section C.11.3.

C.11.1 Sampling Distributions

The sampling distributions of product-moment and quantile statistics are “asymptotically normal” (Yevjevich 1972). This means that as the sample size, N , gets larger, the sampling distribution approaches the normal distribution. However, at small and medium values of N the sampling distribution may differ significantly from the normal. The value of N for which the sampling distribution can usefully be approximated by the normal distribution is larger: (1) the higher the moment or the farther the quantile from the mean and (2) the higher the skew of the parent distribution.

We examine two sampling distributions that have application to quantifying the uncertainty of sample estimates of the moment statistics μ_X and σ_X for the sample sizes and distributions commonly found in hydrology.

C.11.1.1 The t-Distribution

The mathematical definition of the *t*-distribution can be found in most statistics books (e.g., Haan 2002). For our purposes, it is important to note that the exact form of the distribution is determined by a quantity called the **degrees of freedom**, DF , which can be calculated directly from the sample size, N . In the situations encountered in this appendix,

$$DF = N - 1. \quad (\text{C.48})$$

The *t*-distribution is useful because it can be shown that, if the parent distribution of X is normal, the quantity

$$T = \frac{N^{1/2} \cdot [m_X - \mu_X]}{s_X} \quad (\text{C.49})$$

has a *t*-distribution with $DF = N - 1$. T is thus analogous to the standard normal variate, Z [equation (C.33)].

The *t*-distribution is symmetrical about its mean value $\mu_T = 0$, and has a variance $\sigma_T^2 = DF/(DF - 2)$. The quantiles of the distribution can be readily calculated if DF (i.e., N) is given, and these quantiles are tabulated in statistics books. Table C.6 (see disk) gives the quantiles $t_{0.025}$ and $t_{0.975}$ for selected values of DF . As DF gets large the *t*-distribution approaches the standard normal distribution, and for $DF > 120$, $t_q = z_q$ to close approximation.

Even though T follows the *t*-distribution only when the parent distribution is normal, it is a good approximation, even for skewed parent distributions

and N in the range of 30 or more (Barrett and Goldsmith 1976).

C.11.1.2 The Chi-Squared (χ^2) Distribution

Like the t -distribution, the form of the χ^2 -distribution depends on the degrees of freedom as given by equation (C.48). The χ^2 -distribution is important because, if the parent distribution of X is normal, the quantity

$$\chi^2 = \frac{(N-1) \cdot s_X^2}{\sigma_X^2} \quad (\text{C.50})$$

has a χ^2 -distribution with $DF = N - 1$.

The mean of the distribution $\mu_{\chi^2} = DF$ and its variance $\sigma_{\chi^2}^2 = 2 \cdot DF$. However, this distribution is asymmetrical; values of the quantiles $\chi^2_{0.025}$ and $\chi^2_{0.975}$ are tabulated in table C.6 (see disk).

As N gets large, the χ^2 -distribution approaches the normal distribution (Yevjevich 1972), but the approximation is not very close for the sample sizes usually available in hydrology.

C.11.2 Standard Errors

If the parent distribution is normal, formulas for computing standard errors can be developed from statistical theory. In all cases the theoretical standard errors are functions of the population moments and are inversely related to the sample size. Sample estimates of standard errors are thus estimated from the sample size and various sample statistics (Yevjevich 1972; Haan 2002). Note that the uncertainty in these sample statistics decreases with the square root of the sample size. The use of standard errors in estimating confidence intervals for sample statistics is given in section C.11.3.

Even though sampling from time series seems quite different from sampling from objects distributed in space, the same concepts apply for stationary time series. In general, however, we do not have the option of reducing uncertainty (i.e., the standard error) by increasing the sample size: We must use the measurements that have been made to date. Special considerations that apply to estimating sampling error for time series with significant autocorrelation are discussed in section C.11.4.

C.11.2.1 Mean

If the parent distribution is approximately normal, the **standard error of the mean**, σ_{mX} , is given by

$$\sigma_{mX} = \frac{\sigma_X}{N^{1/2}}; \quad (\text{C.51})$$

It is estimated by substituting s_X for σ_X in equation (C.51).

C.11.2.2 Standard Deviation

If the parent distribution is approximately normal, the **standard error of the standard deviation**, σ_{sX} , is given by

$$\sigma_{sX} = \frac{\sigma_X}{(2 \cdot N)^{1/2}}. \quad (\text{C.52})$$

The sample estimate of σ_{sX} , s_{sX} , is found by substituting s_X for σ_X in equation (C.52).

C.11.2.3 Skewness

If X is normally distributed, the **standard error of the skewness coefficient** g_X , σ_{gX} , is given by

$$\sigma_{gX} = \left(\frac{6}{N} \right)^{1/2}. \quad (\text{C.53})$$

C.11.2.4 Quantiles

If the pdf of the parent distribution, $f_X(x)$, is known or assumed, the **standard error of a quantile**, σ_{qX} , is given by

$$\sigma_{qX} = \frac{1}{f_X(x_q)} \cdot \left[\frac{q \cdot (1-q)}{N} \right]^{1/2}. \quad (\text{C.54})$$

C.11.2.5 Correlation Coefficient

For $\rho_{X,Y}$ near zero and $N > 25$, the **standard error of the correlation coefficient** $r_{X,Y}$, $\sigma_{rX,Y}$, is estimated as

$$\sigma_{rX,Y} = \frac{1 - r_{X,Y}}{N^{1/2}}. \quad (\text{C.55})$$

C.11.3 Confidence Intervals

A general expression for the uncertainty of a statistic Θ computed from sample values is expressed as

$$Pr\{L_{\alpha\Theta} \leq \Theta^* \leq U_{\alpha\Theta}\} = 1 - \alpha, \quad (\text{C.56a})$$

where Θ^* is the true value of the population statistic of interest, $L_{\alpha\Theta}$ and $U_{\alpha\Theta}$ are respectively the lower and upper **confidence limits** that define the **confidence interval**, and $1 - \alpha$ is the **confidence level**. In words, this is stated as

“I am $100 \cdot (1 - \alpha)\%$ confident that the interval $L_{\alpha\Theta}$ to $U_{\alpha\Theta}$ contains Θ^* .” (C.56b)

If the distribution of the estimator of Θ is known, $L_{\alpha\Theta}$ and $U_{\alpha\Theta}$ can be determined for any selected value of α as functions of the sample values x_1, x_2, \dots, x_N ; i.e.,

$$L_{\alpha\Theta}, U_{\alpha\Theta} = f_{\Theta}(\alpha; x_1, x_2, \dots, x_N) \quad (\text{C.57})$$

The following sections describe how confidence intervals are determined for commonly used statistics; examples are given in box C.12 (see disk).

C.11.3.1 Mean

Since T in equation (C.49) follows the t -distribution, we can write

$$\Pr \left\{ t_{N-1,\alpha/2} \leq \frac{N^{1/2} \cdot [m_X - \mu_X]}{s_X} \leq t_{N-1,1-\alpha/2} \right\} = 1 - \alpha. \quad (\text{C.58a})$$

Because of the symmetry of the t -distribution, $t_{N-1,\alpha/2} = -t_{N-1,1-\alpha/2}$, and the expression in brackets in equation (C.58a) can be rearranged to give

$$\Pr \left\{ m_X - \frac{t_{N-1,1-\alpha/2} \cdot s_X}{N^{1/2}} \leq \mu_X \leq m_X + \frac{t_{N-1,1-\alpha/2} \cdot s_X}{N^{1/2}} \right\} = 1 - \alpha. \quad (\text{C.58b})$$

Example CB12.1 shows how equation (C.58b) is applied to compute the confidence interval for the mean.

C.11.3.2 Standard Deviation

Since χ^2 in equation (C.50) has a χ^2 -distribution, we can write

$$\Pr \left\{ \chi^2_{N-1,\alpha/2} \leq \frac{(N-1) \cdot s_X^2}{\sigma_X^2} \leq \chi^2_{N-1,1-\alpha/2} \right\} = 1 - \alpha. \quad (\text{C.59a})$$

Rearranging the quantities inside the brackets,

$$\Pr \left\{ \frac{(N-1) \cdot s_X^2}{\chi^2_{N-1,1-\alpha/2}} \leq \sigma_X^2 \leq \frac{(N-1) \cdot s_X^2}{\chi^2_{N-1,\alpha/2}} \right\} = 1 - \alpha. \quad (\text{C.59b})$$

Example CB12.2 shows how equation (C.59b) is used to estimate the confidence intervals for the standard deviation.

C.11.3.3 Skewness and Kurtosis

The sampling distributions for the skewness, γ_X , and kurtosis, κ_X , are not known for the sample sizes usually available in hydrology. Monte Carlo experi-

ments have shown that estimates of these quantities are highly unreliable even for very large N . Furthermore, it has been shown that sample estimates of skewness and kurtosis have upper bounds that depend on sample size and are independent of the actual population values (Kirby 1974; Stedinger et al. 1992) (see box C.2 on the disk).

C.11.3.4 Quantiles

As explained in box C.1 (see disk), sample estimates of quantiles are based on the ranks of the sample values. Precise calculation of confidence intervals for these estimates is not possible. However, Loucks et al. (1981) show that the probability that the q th quantile of X , x_q , lies between the j th-ranked sample value, $x_{(j)}$, and the k th-ranked sample value, $x_{(k)}$, with $j < k$, is given by

$$\Pr \left\{ x_{(j)} \leq x_q \leq x_{(k)} \right\} = \sum_{i=j}^{k-1} \frac{N!}{i! \cdot (N-i)!} \cdot q^i \cdot (1-q)^{N-i}. \quad (\text{C.60})$$

Table C.7 (see disk) shows the at-least-90% confidence intervals for the median ($x_{0.50}$) as calculated via equation (C.60). Note that (1) the confidence intervals are symmetric in terms of ranks, but not necessarily in terms of x values and (2) the spread is wide: For $N = 25$, we would estimate the median as the 13th-ranked value, but the 95.7% confidence interval is between the 8th-ranked and 18th-ranked values (inclusive). As q gets further from the median, the confidence intervals get wider.

C.11.3.5 Correlation Coefficient

Following Haan (2002), confidence intervals for correlation coefficients are computed using the transformed variable $W_{X,Y}$, defined as

$$W_{X,Y} \equiv 0.5 \cdot \ln \left[\frac{1 + r_{X,Y}}{1 - r_{X,Y}} \right] = \operatorname{arctanh}(r_{X,Y}). \quad (\text{C.61})$$

If $N > 25$, $W_{X,Y}$ has a normal distribution with mean

$$\mu_W = 0.5 \cdot \ln \left[\frac{1 + \rho_{X,Y}}{1 - \rho_{X,Y}} \right] = \operatorname{arctanh}(\rho_{X,Y}) \quad (\text{C.62})$$

and standard deviation

$$\sigma_W = \frac{1}{(N-3)^{1/2}}. \quad (\text{C.63})$$

Thus Z_W is a standard normal variate, where

$$Z_W \equiv \frac{W_{X,Y} - \mu_W}{\sigma_W}, \quad (\text{C.64})$$

and confidence intervals for Z_W are

$$\Pr\{z_{\alpha/2} \leq Z_W \leq z_{1-\alpha/2}\} = 1 - \alpha. \quad (\text{C.65})$$

Substituting equation (C.64) into (C.65), rearranging, and using sample estimates then gives the $1 - \alpha$ confidence limits for $W_{X,Y}$:

$$L_{\alpha W} = \hat{W}_{X,Y} - z_{1-\alpha/2} \cdot s_W, \quad (\text{C.66a})$$

$$U_{\alpha W} = \hat{W}_{X,Y} + z_{1-\alpha/2} \cdot s_W. \quad (\text{C.66b})$$

These are converted to confidence limits for $\rho_{X,Y}$ via the inverse of equation (C.61):

$$L_{\alpha\rho} = \tanh(L_{\alpha W}), \quad (\text{C.67a})$$

$$U_{\alpha\rho} = \tanh(U_{\alpha W}). \quad (\text{C.67b})$$

Example CB12.3 shows how equations (C.66) and (C.67) are applied.

C.11.4 Effects of Autocorrelation on Sampling Error

As noted in section C.6.2, some hydrologic variables, particularly time-series variables, may be persistent, as reflected in a lag-1 autocorrelation coefficient $\rho_{1X} > 0$. When this is true, statistics calculated from a sample of a given size are more uncer-

tain than those calculated from a nonautocorrelated sample of the same size.

Here we present an approach to account for this loss of sample information for variables in which the value of ρ_{1X} completely characterizes the persistence. For all the statistics discussed, this involves calculating an **effective sample size** that is less than the actual sample size by an amount that depends on the estimate of ρ_{1X} . The effective sample size is then used in place of N in calculating standard errors (Yevjevich 1972).

C.11.4.1 Mean and Standard Deviation

The standard error of the mean for a nonautocorrelated variable is calculated via equation (C.51). If $\rho_{1X} > 0$, the effective sample size is estimated as

$$N_{e\mu} = N \cdot \left(\frac{1 - \rho_{1X}}{1 + \rho_{1X}} \right). \quad (\text{C.68})$$

The standard error of the standard deviation for a non-autocorrelated variable is calculated via equation (C.52). If $\rho_{1X} > 0$, the effective sample size is estimated as

$$N_{e\sigma} = N \cdot \left(\frac{1 - \rho_{1X}^2}{1 + \rho_{1X}^2} \right). \quad (\text{C.69})$$

In practice, the estimate r_{1X} is used in place of ρ_{1X} in equations (C.68) and (C.69).

Figure C.12 shows how these effective record lengths vary with ρ_{1X} , and example CB12.4 shows

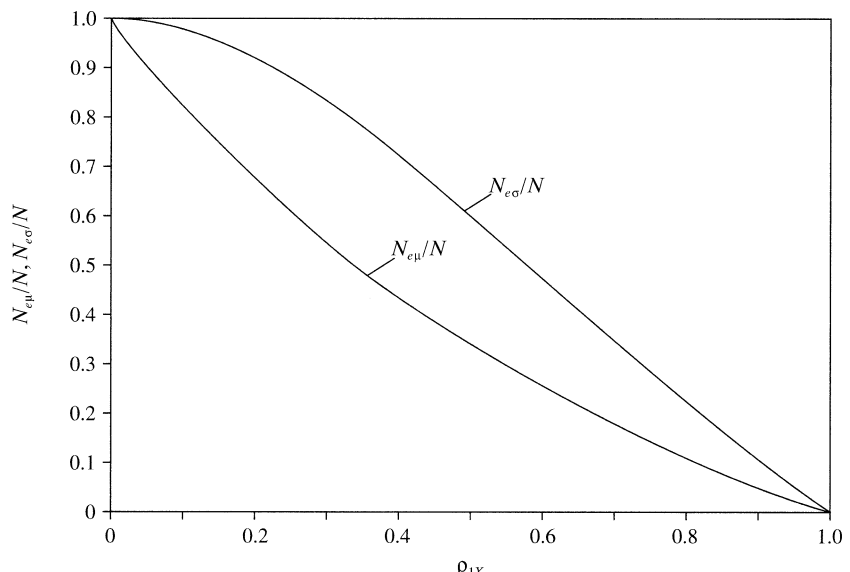


Figure C.12 Effects of autocorrelation (ρ_{1X}) on effective sample size for calculating standard errors of the mean [$N_{e\mu}/N$; equation (C.68)] and standard deviation [$N_{e\sigma}/N$; equation (C.69)].

how these relations are applied in the estimation of uncertainty.

C.11.4.2 Correlation Coefficient

If two variables X and Y have autocorrelation (i.e., $\rho_{1X} > 0$ and $\rho_{1Y} > 0$), they will tend to appear to be more highly linearly correlated than they actually are. This “inflation” in the value of $r_{X,Y}$ can be accounted for by computing an effective sample size, N_{ep} , for the significance test of $r_{X,Y}$ [equation (CB6.2)]. From Yevjevich (1972), N_{ep} is approximately

$$N_{ep} = \frac{N}{1 + 2 \cdot r_{1X} \cdot r_{1Y}}, \quad (\text{C.70})$$

and we define r^* by analogy with equation (CB6.2) as

$$r^* = \frac{1.96}{(N_{ep} - 3)^{1/2}}. \quad (\text{C.71})$$

C.11.4.3 Other Statistics

Adjustment for the effect of autocorrelation on skewness is given by Stedinger et al. (1992).

The effect of autocorrelation on quantile or L-moment estimates has not been well documented. However, it is intuitively clear that such estimates made by the methods described in box C.1 (see disk) could be highly inaccurate when ρ_{1X} is significant.

▼ NOTE

¹ It is not possible to do this with actual hydrologic data, but repeated sampling from a known distribution can readily be simulated using computer-generated data available in most spreadsheets. This method of empirical statistical analysis is called **Monte-Carlo simulation**.

Appendix

D

Estimation of Daily Clear-Sky Incident Solar Radiation

The flux of solar energy, K , contributing to the surface energy balance over a time period is

$$K \equiv K_{in} - K_{out} = K_{in} \cdot (1 - a), \quad (\text{D.1})$$

where K_{in} [$\text{E L}^{-2} \text{T}^{-1}$] is the flux of solar energy incident on the surface (**incident solar radiation** or **insolation**), K_{out} [$\text{E L}^{-2} \text{T}^{-1}$] is the flux of reflected solar energy, and a [1] is the shortwave reflectance of the surface, or **albedo** [equation (2.7), table 2.4, table 6.4]. Solar radiation is usually an important contributor to the energy balance at the earth's surface, and hence is an important quantity in models of snowmelt (section 5.5.2.1) and evapotranspiration (section 6.3.3).

Continuous measurements of solar radiation can be obtained with **pyranometers** facing upward to measure K_{in} and downward to measure K_{out} (Iqbal 1983; Delany and Semmer 1998). However, pyranometers are installed at only a few permanent locations and research stations. The 1991–2010 National Solar Radiation Data Base (NSRDB) was completed by the National Renewable Energy Laboratory (NREL) (Wilcox 2012). It includes modeled hourly solar radiation data for 1,454 sites, 40 of which have measured data (figure D.1). Solar-radiation data were modeled using a meteorological-statistical (METSTAT) solar-radiation model that attempts to provide average hourly values over a “typical” year.

Suckling (1997) studied the spatial coherence of solar radiation, i.e., the degree to which measurements at a single location are representative of a wider area, in five regions of the United States. His results are summarized in figure D.2 on p. 573; they show that measured values differ by more than 15% at locations over 100 km apart. Hourly, daily, and monthly insolation values for large areas ($\sim 0.5^\circ$ latitude $\times 0.5^\circ$ longitude) can be obtained from GOES observations (Justus et al. 1986), but the data are subject to error over areas with significant snow cover (Lindsey and Farnsworth 1997).

Because of the difficulty in obtaining reliable measurements for specific locations and times, it is often necessary to estimate insolation for hydrological analysis. Badescu (2008) provided a detailed exploration of recent advances in modeling and measuring solar radiation. This appendix develops a simple model for estimating daily average clear-sky solar radiation flux incident on an unvegetated sloping surface. This model has been programmed in Excel format on the disk accompanying this text as file SolarRad.xls. Empirical adjustments for the effects of cloud cover and vegetation on K_{in} can be made as indicated in equations (5.34)–(5.40).

D.1 Extraterrestrial Solar Radiation

The sun's energy arrives at the outer edge of the atmosphere at an average rate of 1.74×10^{17} W. This

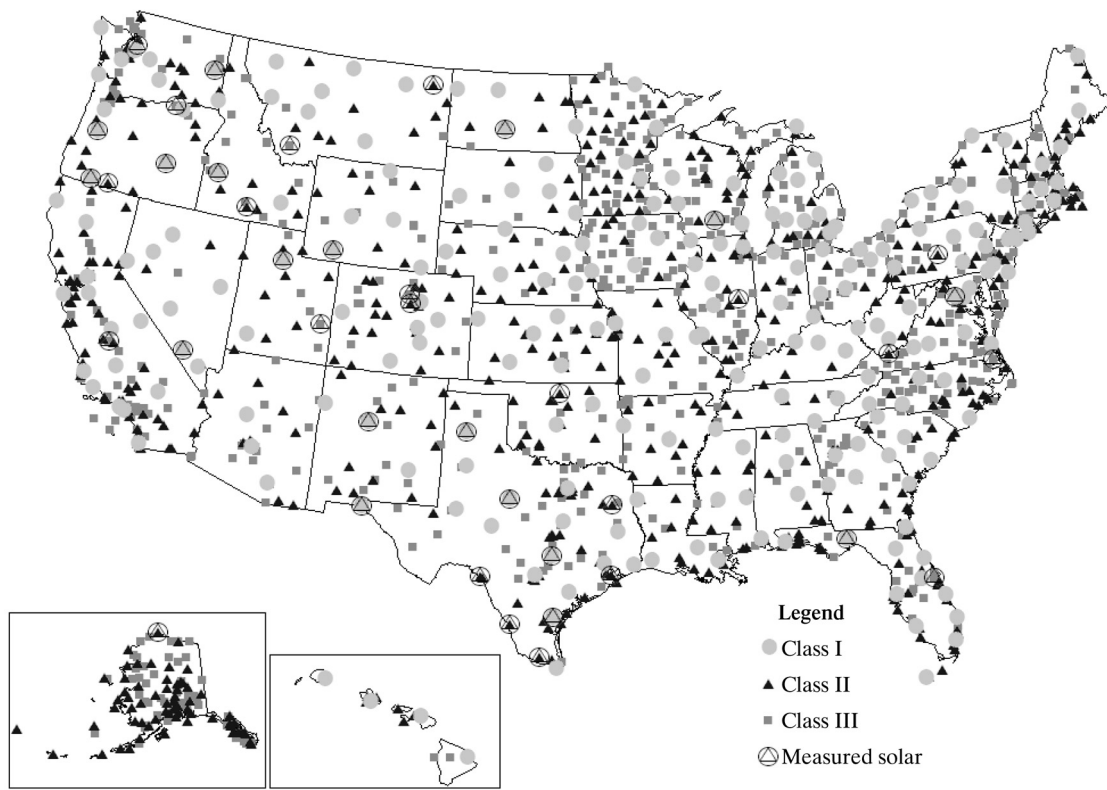


Figure D.1 Locations of primary and secondary stations in the 1991–2010 National Solar Radiation Data Base (NSRDB). Class I sites are those with the lowest uncertainty data, Class II sites have higher uncertainty data, and Class III sites have an incomplete period of record (Wilcox 2012).

quantity divided by the area of the planar projection of the earth, $1.28 \times 10^{14} \text{ m}^2$, is called the **solar constant**, S ; thus

$$S = 1,364 \text{ W/m}^2 = 117.8 \text{ MJ/m}^2 \cdot \text{day} = 4.910 \text{ MJ/m}^2 \cdot \text{hr.}$$

This energy is at wavelengths from 0.2 to 3 μm (**shortwave radiation**), with most in the **visible range** (0.4 to 0.7 μm) (figure 2.4).

The flux of solar radiation at the top of the atmosphere on a plane parallel to a tangent plane at a given surface point is the **extraterrestrial radiation flux** at that point. The instantaneous extraterrestrial flux, k_{ET} , is given by

$$k_{ET} = S \cdot E_0 \cdot \cos[\theta(\Lambda, \delta, t)], \quad (\text{D.2})$$

where E_0 is the **orbital eccentricity**, θ is the **zenith angle**, Λ is the latitude of the surface point, δ is the **declina-**

tion of the sun, and t is the time of day. E_0 and δ vary with the earth's position in its orbit around the sun (figure D.3 on p. 574), which is given by the **day angle**, Γ , where

$$\Gamma = \frac{2 \cdot \pi \cdot (J - 1)}{365}, \quad (\text{D.3})$$

Γ is in radians, and J is the **day number** (sometimes called **Julian date**); $J = 1$ on 1 January and 365 on 31 December.

D.1.1 Orbital Eccentricity

The earth-sun distance affects the extraterrestrial energy flux according to the inverse-square law. This distance is expressed in relative terms as the **orbital eccentricity**, E_0 , which is the square of the ratio of the average distance, r_0 , to the distance at any time, r . E_0 can be calculated as a function of day angle as

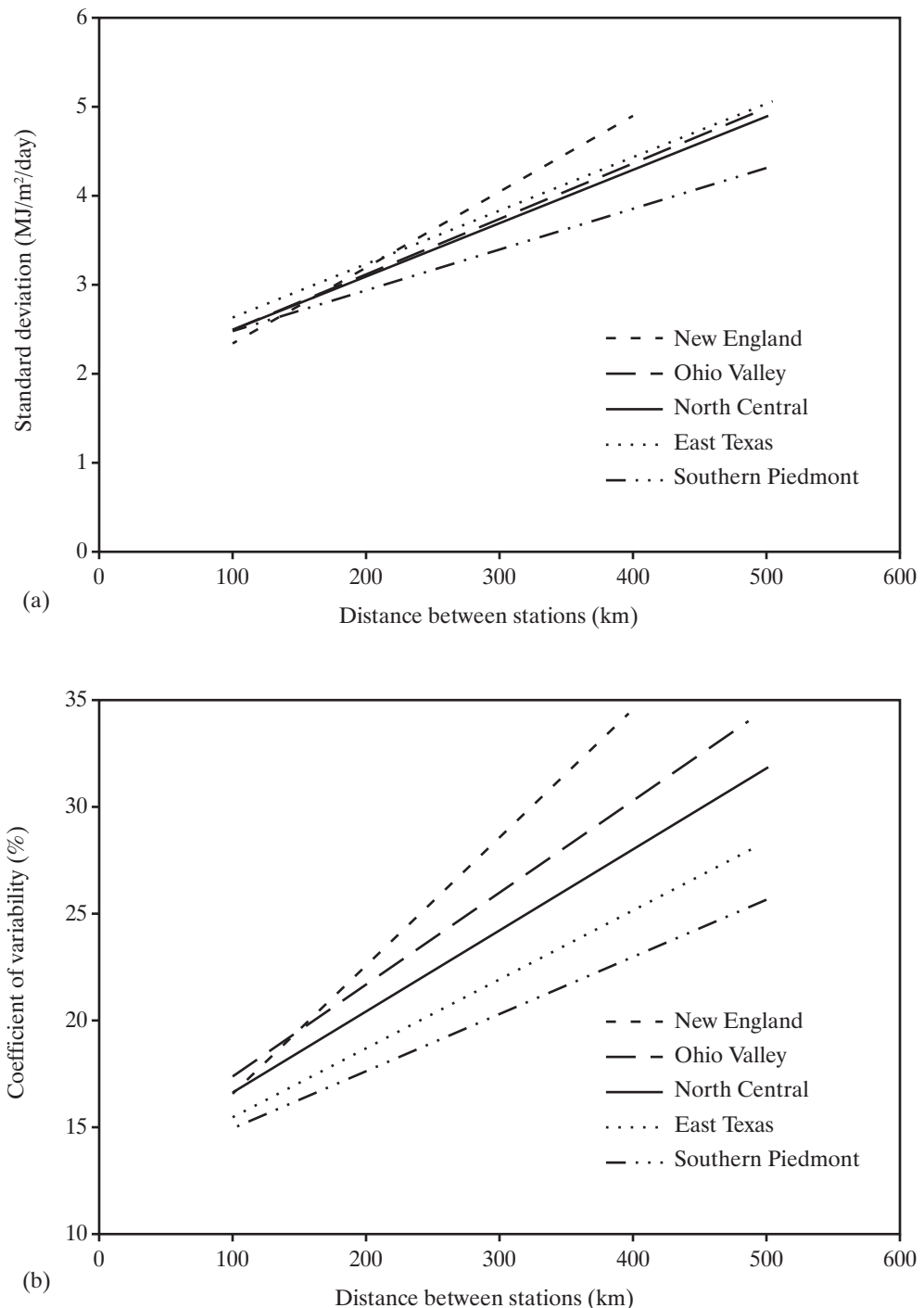


Figure D.2 Relations between (a) standard deviation (= square root of average squared difference) and (b) coefficient of variability (= square root of average squared difference/mean) of average daily solar radiation flux and distance for pairs of stations in five regions of the United States [Suckling (1997). *Physical Geography* 18(1):53–62. Reprinted by permission of the publisher (Taylor & Francis Ltd.)].

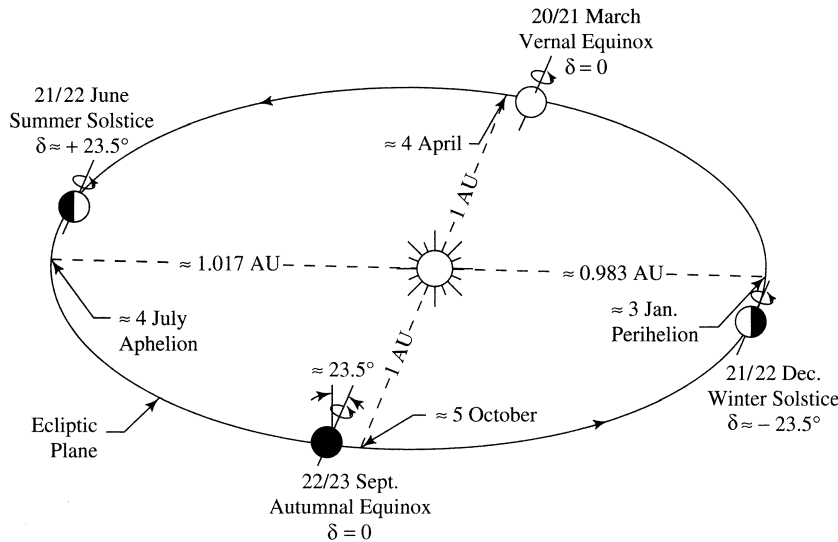


Figure D.3 Earth's orbit showing seasonal variation of eccentricity and rotational axis relative to the earth-sun direction. AU = astronomical unit (average earth-sun distance), δ is declination [Iqbal (1983). *An Introduction to Solar Radiation*. San Diego, CA: Academic Press, with permission of Elsevier].

$$E_0 \equiv (r_0/r)^2 = 1.000110 + 0.034221 \cdot \cos(\Gamma) + 0.001280 \cdot \sin(\Gamma) + 0.000719 \cdot \cos(2 \cdot \Gamma) + 0.000077 \cdot \sin(2 \cdot \Gamma). \quad (\text{D.4})$$

D.1.2 Declination

The **declination**, δ , is the angle between the plane of the equator and the rays of the sun; it is equal to the latitude at which the sun is directly overhead at noon. Due to the 23.5° tilt of the earth's rotational axis, declination varies sinusoidally between $+23.5^\circ$ (21 June) and -23.5° (21 December) as the earth revolves around the sun. It can be calculated as a function of day angle as

$$\delta = 0.006918 - 0.399912 \cdot \cos(\Gamma) + 0.070257 \cdot \sin(\Gamma) - 0.006758 \cdot \cos(2 \cdot \Gamma) + 0.000907 \cdot \sin(2 \cdot \Gamma) - 0.002697 \cdot \cos(3 \cdot \Gamma) + 0.00148 \cdot \sin(3 \cdot \Gamma), \quad (\text{D.5})$$

where δ is in radians.

D.1.3 Zenith Angle

The **zenith angle** θ is the angle between a line from an observer on the earth to the sun and a vertical line extending from the observer (figure D.4). It is a function of latitude and declination, and varies each day from 90° at sunrise, T_R , to a minimum at solar noon, to 90° at sunset, T_S :

$$\theta = \arccos[\sin(\Lambda) \cdot \sin(\delta) + \cos(\Lambda) \cdot \cos(\delta) \cdot \cos(\omega \cdot t)], \quad T_R \leq t \leq T_S, \quad (\text{D.6})$$

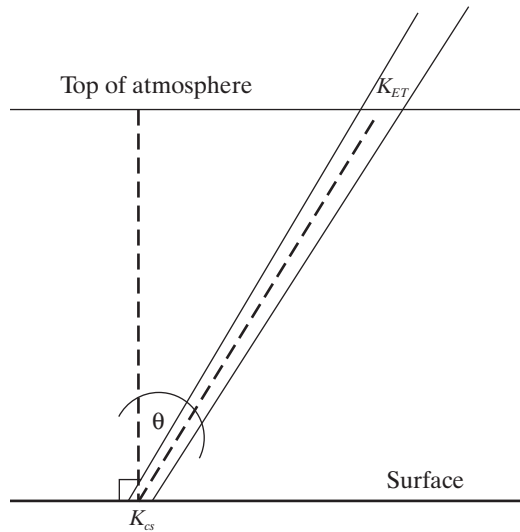


Figure D.4 Geometry of the solar beam. K_{ET} is the extraterrestrial solar flux, K_{CS} is the clear-sky incident solar flux. The angle between the dashed lines is the zenith angle, θ . The optical air mass, m , is the ratio of the hypotenuse to the vertical distance of θ [$\sec(\theta)$].

where θ is in radians, t is the number of hours before ($-$) or after ($+$) solar noon, ω is the angular velocity of the earth's rotation ($15^\circ/\text{hr} = 0.2618 \text{ rad/hr}$), and $\omega \cdot t$ is called the **hour angle**.

D.1.4 Solar Noon, Sunrise, and Sunset

Solar noon occurs when $t = 0$ hr, and the times of sunrise, T_R , and sunset, T_S , occur at equal times before and after solar noon, when $\cos(\theta) = 0$. These times can be calculated from equation (D.6) as

If $|\Lambda - \delta| < 90^\circ$ and $|\Lambda + \delta| < 90^\circ$,

$$\left. \begin{aligned} T_R &= -\frac{a \cos[-\tan(\delta) \cdot \tan(\Lambda)]}{\omega}, \\ T_S &= +\frac{a \cos[-\tan(\delta) \cdot \tan(\Lambda)]}{\omega}; \end{aligned} \right\} \quad (\text{D.7a})$$

If $|\Lambda - \delta| \geq 90^\circ$,

$$T_R = T_S = 0 \text{ hr}; \quad (\text{D.7b})$$

If $|\Lambda - \delta| < 90^\circ$ and $|\Lambda + \delta| \geq 90^\circ$,

$$|T_R| = |T_S| = 12 \text{ hr}. \quad (\text{D.7c})$$

D.1.5 Daily Total Extraterrestrial Solar Radiation

Daily total extraterrestrial radiation is given by integrating equation (D.2) between sunrise and sunset:

$$K_{ET} = \int_{T_R}^{T_S} k_{ET} \cdot dt. \quad (\text{D.8})$$

Eccentricity and declination do not change significantly during a day, so using equation (D.6),

$$\begin{aligned} K_{ET} &= S \cdot E_0 \cdot \int_{T_R}^{T_S} \cos[\theta(\Lambda, \delta, t)] \cdot dt \\ &= 2 \cdot S \cdot E_0 \cdot \int_0^{T_S} [\sin(\Lambda) \cdot \sin(\delta) + \cos(\Lambda) \cdot \\ &\quad \cos(\delta) \cdot \cos(\omega \cdot t)] \cdot dt \\ &= 2 \cdot S \cdot E_0 \cdot \left[\sin(\Lambda) \cdot \sin(\delta) \cdot T_S + \right. \\ &\quad \left. \frac{\cos(\Lambda) \cdot \cos(\delta) \cdot \sin(\omega \cdot T_S)}{\omega} \right]. \end{aligned} \quad (\text{D.9})$$

Note that the time units of S must be consistent with the time units of ω and T_S .

D.2 Clear-Sky Radiation on a Horizontal Surface

As it passes through the cloudless atmosphere, the energy in the solar beam is reduced due to absorption and reflection (scattering) by gaseous and

solid particles. The scattering produces two additional components of solar radiation in addition to the direct solar beam, **diffuse radiation** and **back-scattered radiation**. Total clear-sky insolation is the sum of these three components, which are evaluated separately as described below.

D.2.1 Direct (Beam) Radiation

D.2.1.1 Optical Air Mass

The scattering and absorption effects that reduce the energy in the direct solar beam are a function of the distance the beam travels through the atmosphere to the surface. In relative terms (i.e., as a multiple of atmospheric thickness), this distance is equal to the ratio of the hypotenuse to the vertical distance of the angle defining θ (figure D.4), i.e.,

$$\begin{aligned} m \approx \sec(\theta) &= \frac{1}{\cos(\theta)} \\ &= \frac{1}{\sin(\Lambda) \cdot \sin(\delta) + \cos(\Lambda) \cdot \cos(\delta) \cdot \cos(\omega \cdot t)}, \end{aligned} \quad (\text{D.10})$$

where m is called the **optical air mass**. However, the relation of (D.10) is only approximately true because of refraction effects, and is given more accurately by

$$m = 1.021 \cdot [0.008307 + \sin(\Lambda) \cdot \sin(\delta) + \cos(\Lambda) \cdot \cos(\delta) \cdot \cos(\omega \cdot t)]^{-1} - 0.01259 \quad (\text{D.11})$$

(Yin 1997).

Clearly m is a function of latitude, time of year, and time of day. For use in estimating daily insolation, Yin (1997) integrated equation (D.11) between T_R and T_S to give daily average optical air mass, M , as a function of latitude and declination. To write his results more compactly, we define $A \equiv 0.008307 + \sin(\Lambda) \cdot \sin(\delta)$; $B \equiv \cos(\Lambda) \cdot \cos(\delta)$; $C \equiv -0.01259$. Then

If $|\Lambda - \delta| \geq 90^\circ$ ($T_s = 0$ hr),

$$M = 39.7; \quad (\text{D.12a})$$

If $T_S \neq 0$ and $A > B$,

$$\begin{aligned} M &= \left(\frac{1}{T_S} \right) \cdot \left\{ \left(\frac{1}{\omega} \right) \cdot \left(\frac{1.021}{(A^2 - B^2)^{1/2}} \right) \cdot \right. \\ &\quad \left. a \cos \left[\frac{B + A \cdot \cos(\omega \cdot T_S)}{A + B \cdot \cos(\omega \cdot T_S)} \right] + C \cdot T_S \right\}; \end{aligned} \quad (\text{D.12b})$$

If $T_S \neq 0$ and $B > A$,

$$M = \left(\frac{1}{T_S} \right) \cdot \left\{ \left(\frac{1}{\omega} \right) \cdot \left(\frac{1.021}{\left(A^2 - B^2 \right)^{1/2}} \right) \cdot \ln \left[\frac{\left\{ [B + A] \cdot [1 + \cos(\omega \cdot T_S)] \right\}^{1/2} + \left\{ [B + A] \cdot [1 + \cos(\omega \cdot T_S)] \right\}^{1/2} - \left\{ [B - A] \cdot [1 - \cos(\omega \cdot T_S)] \right\}^{1/2}}{\left\{ [B - A] \cdot [1 - \cos(\omega \cdot T_S)] \right\}^{1/2}} \right] + C \cdot T_S \right\}; \quad (\text{D.12c})$$

If $T_S \neq 0$ and $B = A$,

$$M = \left(\frac{1}{T_S} \right) \left[\left(\frac{1}{\omega} \right) \cdot \left(\frac{1.021}{A} \right) \cdot \tan \left(\frac{\omega \cdot T_S}{2} \right) + C \right]. \quad (\text{D.12d})$$

The optical air mass values given by equation (D.12) are sea-level values. Values at higher elevations are reduced because of the smaller atmospheric thickness, which can be accounted for by calculating $M(z)$, where

$$M(z) = M \cdot \exp \left(-\frac{z}{7,000} \right), \quad (\text{D.13})$$

where z is elevation in m.

Figure D.5 shows sea-level M as a function of latitude and declination as given by these relations, and figure D.6 shows daily incident direct solar radiation, K_{dirh} , as a function of latitude and declination. The daily average optical air mass is used to compute the effects of scattering and absorption on the direct solar beam as described in the following sections.

D.2.1.2 Transmissivities

Following Suckling and Hay (1976), the clear-sky **direct-beam insolation** on a horizontal surface, K_{dirh} , is

$$K_{dirh} = K_{ET} \cdot \tau_{wa} \cdot \tau_{da} \cdot \tau_{ws} \cdot \tau_{rs} \cdot \tau_{ds}, \quad (\text{D.14})$$

where the τ quantities are **transmissivities** (section 2.1.1):

- $\tau_{wa} \equiv (1 - \alpha_w)$, where α_w is the fraction of solar radiation absorbed by water vapor;
- $\tau_{da} \equiv (1 - \alpha_d)$, where α_d is the fraction of solar radiation absorbed by dust and other solid aerosols;

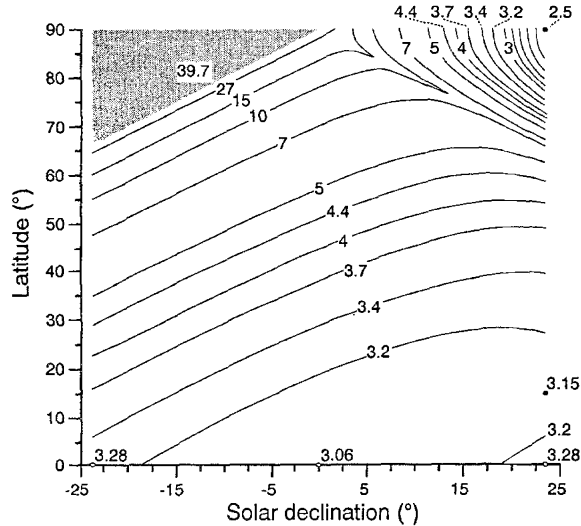


Figure D.5 Contours of mean daily sea-level optical air mass M in the Northern Hemisphere as given by equation (D.12) [Yin (1997)]. Optical air mass: Daily integration and its applications. *Meteorology and Atmospheric Physics* 63:227–233. With kind permission from Springer Science and Business Media].

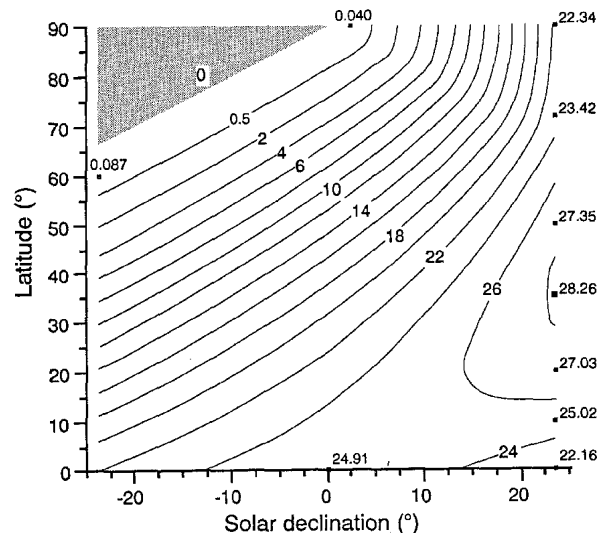


Figure D.6 Daily average clear-sky direct-beam incident solar radiation, K_{dirh} ($\text{MJ}/\text{m}^2 \cdot \text{day}$) as a function of latitude and declination as given by equation (D.9) and (D.12) with total transmissivity = 0.75 [Yin (1997)]. Optical air mass: Daily integration and its applications. *Meteorology and Atmospheric Physics* 63:227–233. With kind permission from Springer Science and Business Media].

- $\tau_{ws} \equiv (1 - \rho_w)$, where ρ_w is the fraction of solar radiation scattered by water vapor;
- $\tau_{rs} \equiv (1 - \rho_{rs})$, where ρ_{rs} is the fraction of solar radiation scattered by air molecules (**Rayleigh scattering**, which is responsible for the blue of the sky);
- $\tau_{ds} \equiv (1 - \rho_d)$, where ρ_d is the fraction of solar radiation scattered by dust and solid aerosols.

These transmissivities are empirically related to optical air mass, humidity, and air temperature as:

$$\tau_{wa} = 1 - 0.077 \cdot (M \cdot W)^{0.3}; \quad (\text{D.15})$$

$$\tau_{da} = 0.965^M; \quad (\text{D.16})$$

$$\tau_{ws} = 1 - 0.0225 \cdot M \cdot W; \quad (\text{D.17})$$

$$\begin{aligned} \tau_{rs} &= 0.972 - 0.08262 \cdot M + 0.00933 \cdot \\ &M^2 - 0.00095 \cdot M^3 + 0.0000437 \cdot M^4; \end{aligned} \quad (\text{D.18})$$

$$\tau_{ds} = 0.965^M; \quad (\text{D.19})$$

W is precipitable water content in cm (section 3.2.6), estimated as

$$W = 0.00493 \cdot \left(\frac{RH}{T_a} \right) \cdot \exp \left(26.23 - \frac{5,416}{T_a} \right); \quad (\text{D.20})$$

RH is relative humidity (%); and T_a is air temperature (K).

D.2.2 Diffuse Radiation

About one-half the energy scattered from the solar beam reaches the surface as **diffuse radiation**, K_{dif} . This quantity can be calculated as

$$\begin{aligned} K_{dif} &= 0.5 \cdot K_{ET} \cdot \tau_{wa} \cdot \tau_{da} \cdot \\ &(1 - \tau_{ws} \cdot \tau_{rs} \cdot \tau_{ds}). \end{aligned} \quad (\text{D.21})$$

D.2.3 Backscattered Radiation

Of the solar radiation striking the surface, a portion given by the albedo, α , is reflected back to the atmosphere. Of this, about one-half is re-reflected from the atmosphere to the surface to increase the total radiation flux. This backscattered radiation, K_{BS} , can be estimated as

$$\begin{aligned} K_{BS} &= \alpha \cdot (K_{dirh} + K_{dif}) \cdot \\ &[0.5 \cdot \tau_{wa} \cdot \tau_{da} \cdot (1 - \tau_{ws} \cdot \tau_{rs} \cdot \tau_{ds})]. \end{aligned} \quad (\text{D.22})$$

D.2.4 Total Incident Radiation

Total daily clear-sky incident radiation (**global radiation**) on a horizontal plane, K_{CSH} , is the sum of the direct beam, diffuse, and backscattered components:

$$K_{CSH} = K_{dirh} + K_{dif} + K_{BS}. \quad (\text{D.23})$$

D.3 Radiation on a Sloping Surface

D.3.1 Equivalent Slope

A hillslope is defined by its slope angle, β (positive downward), and its orientation angle, α (measured clockwise from north). Any given slope is parallel to a horizontal plane at a different latitude and longitude, and the direct-beam clear-sky radiation on the slope is equal to that on the horizontal plane. This is the concept of the **equivalent slope** (Lee 1964):

The angle of incidence of the solar beam on a sloping plane at latitude Λ and longitude Ω is the same as the angle of incidence on a horizontal plane at a point on a great circle passing through the slope at right angles to it and as many degrees removed from it as the angle of the slope.

The latitude of the parallel horizontal plane is the **equivalent latitude**, Λ_{eq} , given by

$$\Lambda_{eq} = \arcsin[\sin(\beta) \cdot \cos(\alpha) \cdot \cos(\Lambda) + \cos(\beta) \cdot \sin(\Lambda)] \quad (\text{D.24})$$

(see figure 5.20). The *difference* in longitude between the original slope and the parallel horizontal plane, $\Delta\Omega$, is given by

$$\Delta\Omega = \arctan \left[\frac{\sin(\beta) \cdot \sin(\alpha)}{\cos(\Lambda) \cdot \cos(\beta) - \sin(\Lambda) \cdot \sin(\beta) \cdot \cos(\alpha)} \right]. \quad (\text{D.25})$$

D.3.2 Solar Noon, Sunrise, and Sunset

The concept of equivalent slope permits computation of the times of solar noon, sunrise, and sunset on any slope using relations analogous to those for a horizontal plane. Solar noon occurs at $-\Delta\Omega/\omega$, and the times of sunrise, T_{Rs} , and sunset, T_{Ss} , are

$$T_{Rs} = -\frac{a \cos[-\tan(\Lambda_{eq}) \cdot \tan(\delta)] - \Delta\Omega}{\omega} \quad (\text{D.26a})$$

and

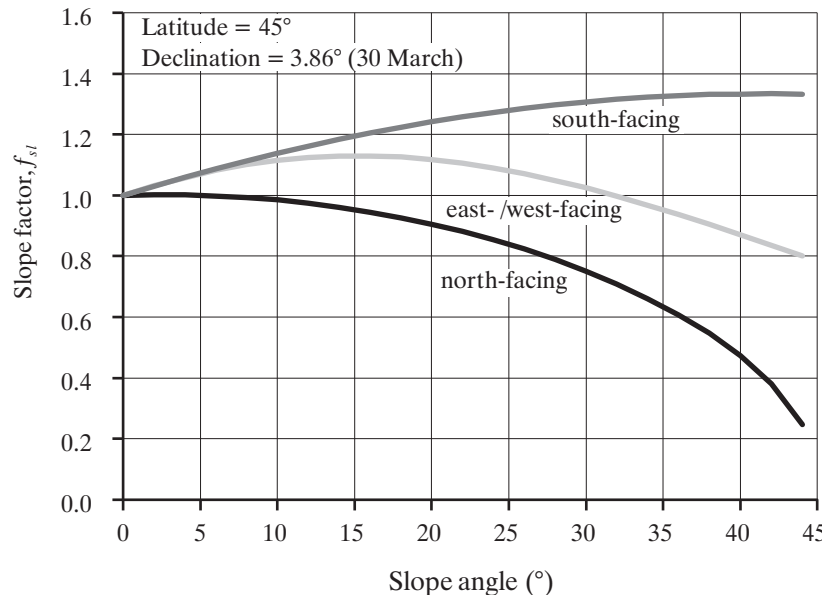
$$T_{Ss} = + \frac{a \cos[-\tan(\Lambda_{eq}) \cdot \tan(\delta)] - \Delta\Omega}{\omega}. \quad (\text{D.26b})$$

Note that neither sunrise nor sunset on a slope can have an absolute value greater than that for a horizontal surface at the same latitude. There are situations for slopes at high latitudes and where $\beta + \Lambda_{eq} > 90^\circ$ for north-facing slopes, when there are two sunrises and two sunsets in a single calendar day. In these cases the times of first sunrise and last sunset are the same as those for a horizontal surface at the same latitude (Lee 1964).

D.3.3 Total Incident Radiation at the Surface

By direct analogy with equation (D.9), the average daily extraterrestrial radiation flux on a sloping plane, K_{ETs} , is given by

$$K_{ETs} = 2 \cdot S \cdot E_0 \cdot \left[\sin(\Lambda_{eq}) \cdot \sin(\delta) \cdot T_S + \frac{\cos(\Lambda_{eq}) \cdot \cos(\delta) \cdot \sin(\omega \cdot T_S)}{\omega} \right]. \quad (\text{D.27})$$



Since only the direct-beam radiation is dependent on slope and aspect, the total daily clear-sky solar radiation incident on a sloping plane, K_{CSs} , is given by analogy to equations (D.14) and (D.23) as

$$K_{CSs} = \tau_{wa} \cdot \tau_{da} \cdot \tau_{ws} \cdot \tau_{rs} \cdot \tau_{ds} \cdot K_{ETs} + K_{dif} + K_{BS}, \quad (\text{D.28})$$

where transmissivities are found via equations (D.15)–(D.19), K_{ETs} is from equation (D.27), K_{dif} is from equation (D.21), and K_{BS} is from equation (D.22).

The relative radiation received on a slope can be expressed as a **slope factor**, f_{sl} , where

$$f_{sl} \equiv \frac{K_{CSs}}{K_{CSh}}. \quad (\text{D.29})$$

Figure D.7 compares slope factors for north-, east-/west-, and south-facing slopes as a function of inclination for a particular latitude and day of year (see also figure 5.21).

Figure D.7 Slope factors for north-, east-/west-, and south-facing slopes as a function of inclination for latitude $\Lambda = 45^\circ$ on 30 Mar ($\delta = 3.86^\circ$).

Appendix

E

Stream-Gauging Methods for Short-Term Studies

As discussed in chapter 1, streamflow is the residual of precipitation minus evapotranspiration over a region (typically a watershed) and represents the water available for instream and withdrawal uses. Its measurement is thus of critical scientific and practical value. Streamflow is measured as stream **discharge**, Q , the volume rate of flow [$L^3 T^{-1}$] through a stream cross section at right angles to the flow direction:

$$Q = U \cdot A = U \cdot W \cdot Y, \quad (\text{E.1})$$

where U is average velocity through the cross section [$L T^{-1}$], A is the area of the cross section [L^2], W is the water-surface width at the cross section [L], and Y is the average depth at the cross section [L].

The process of measuring discharge is called **stream gauging**. Methods for determining the discharge occurring at the time of observation can be classified as shown in table E.1: It can be measured directly by several methods, or determined indirectly by (1) observing the **stage**, Z_s , defined as

$$Z_s \equiv Z_w - Z_0, \quad (\text{E.2})$$

where Z_w is the elevation of the water surface and Z_0 is the elevation of an arbitrary datum, and (2) using a previously established relation between stage and discharge. The stage-discharge relation is called a **rating curve** (or **rating table**); its form is determined by the configuration of the stream channel in the measurement reach. This configuration may be that of the natural channel (**natural control**) or it may be

Table E.1 Classification of Stream-Gauging Methods.

- I. Direct measurement
 - A. Volumetric gauging
 - B. Velocity-area gauging
 - C. Dilution gauging
 - II. Indirect measurement via stage-discharge relation
 - A. Empirical rating curve (natural control)
 - B. Theoretical rating curve (artificial control)
 - 1. Weirs
 - 2. Flumes
-

that of an artificial structure such as a weir or flume (**artificial control**).

This appendix describes stream-gauging methods that are suitable for short-term and special-purpose studies: (1) direct measurement via volumetric, velocity-area, and dilution gauging; (2) indirect measurement via portable weirs and flumes; and (3) the measurement of stage. The details of constructing permanent stream-gauging installations for long-term measurement stations were described by Shaw (1988), Herschy (1999), and Sauer and Turnipseed (2010). Herschy (1999) and Sauer and Meyer (1992) discuss measurement errors using various techniques. Increasingly, water-resource agencies such as the USGS measure discharge with acoustic Doppler current profilers (ADCPs) that provide simultaneous depth and vertically integrated velocity (Simpson

2001; Mueller and Wagner 2009; Sauer and Turnipseed 2010); these instruments and techniques are not discussed here.

E.1 Selection of Measurement Location

The general location of a stream-gauging location is determined by the overall purpose of a study. For studies of watershed response to rainfall, the gauge is sited near the watershed outlet; for studies of lake water balance, gauges are sited near the mouths of major streams entering and draining the lake; when discharge data are to be used in the design of structures or land-use plans, the gauge should be located near the site of the structure or plan. Gauges used as part of a general-purpose hydrologic network may be variously placed to provide information on a range of watershed types and sizes.

The specific location of a stream-gauging site depends on: (1) physical accessibility; (2) legal accessibility (e.g., landowner permission); (3) presence of conditions suitable for the selected measurement (e.g., wadeability of stream or presence of bridge, compatibility of stream size and portable weir or flume); (4) ability to measure total flow at all stages (e.g., minimization of flow bypassing the measurement site as ground water beneath the channel or in flood channels at high flows); and (5) absence of conditions in which water levels and/or discharge are affected by conditions that cause spurious rela-

tions between discharge and stage (e.g., backwater from lakes, tributaries, dams, storm-sewer discharges, or tidal fluctuations).

E.2 Volumetric Gauging

Volumetric gauging involves diverting streamflow into a container with a known volume and measuring the time it takes for the volume to fill. Obviously this is feasible only for very low discharges, but in small streams at low flows it may be the only way to get accurate measurements. Usually it will be necessary to use a flexible liner to collect and divert the flow, as shown in figure E.1.

E.3 Velocity-Area Method

The velocity-area method involves: (1) direct measurement of the components of discharge [equation (E.1)] at successive locations (called **verticals**) along a stream cross section and (2) numerical integration of the measured values to give the total discharge.

Figure E.2 defines the quantities involved. The more verticals used in a measurement (N), the more accurate it will be; $N \geq 25$ is usually recommended, with the spacing of verticals adjusted such that < 5% of the total discharge occurs in each subsection. Thus, in general, spacings between verticals will vary, being closer together where the flow is deeper and faster and farther apart where the flow is slower and shallower.



Figure E.1 Volumetric gauging at low flows on a small Alaskan stream. Plastic sheets collect the flow and divert it into a trough. Flow from the trough is collected in a bucket of known volume and the time it takes to fill is recorded (photo by author).

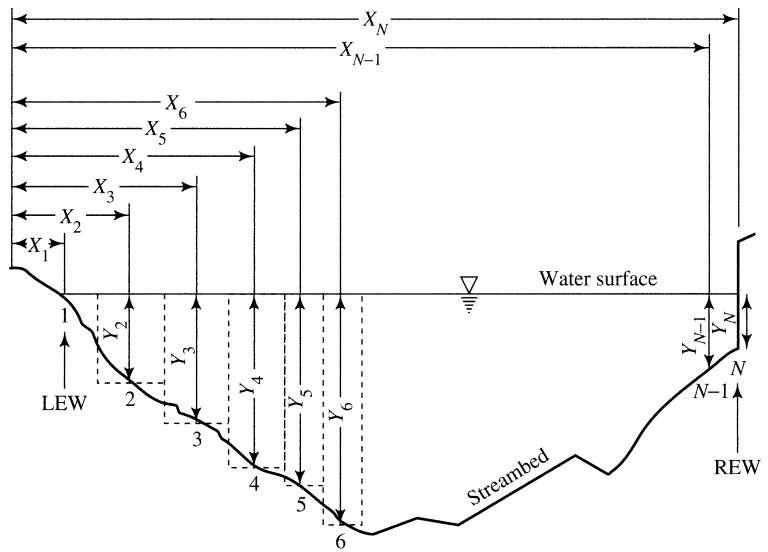


Figure E.2 Definitions of terms for stream gauging by the velocity-area method [equation (E.3) and (E.4)]. Left and right edges of water (LEW and REW, respectively) are defined for an observer facing downstream. Dashed lines delineate individual subsections numbered consecutively $i = 1, 2, \dots, N$, in this case from the left bank. X_i are distances from the horizontal datum, which can be on either bank; Y_i are depths.

Cross sections may be negotiated by wading, by boat, or from bridges or specially constructed cableways (Buchanan and Somers 1969; Herschy 1999). In wading measurements (figure E.3), velocity (U_i) is measured by a current meter fixed to a handheld vertical rod (called a **wading rod**) that is also used to gauge the depth (Y_i). In measurements from bridges, cableways, and boats, the current meter is suspended on a weighted cable and depth is measured by sounding the bottom with the weight. Cross-section location (X_i) is measured by tape or range finder.

E.3.1 Selection of Measurement Section

The quality of a velocity-area measurement is strongly influenced by the nature of the measurement cross section. Accuracy and precision are enhanced in sections with the following characteristics:

1. Converging flow (i.e., cross-sectional area decreasing downstream) without areas of near-zero velocity or eddies.

2. Absence of backwater conditions (due, for example, to high water levels in a stream or lake to which the gauged stream is tributary) or tidal influence.
3. Smooth cross section with minimal flow obstructions upstream or downstream.
4. Velocities and depths not exceeding the range for which the velocity- and depth-measuring devices give accurate results and for which one can safely negotiate the section by wading or boat if a bridge is not present.

The accuracy of measurements at natural sections can be improved by removing obstructions in and above and below the section, since this will not affect discharge. If this is done, however, the measured velocities and depths will not be representative of the natural values.

For small streams, the accuracy of repeated measurements can be improved by making them from a specially constructed temporary wooden bridge on which cross-stream distances are permanently marked (figure E.4).

Cross sections should be perpendicular to the dominant velocity vector and all velocities used in the computation should be perpendicular to the section. Where the vector is not perpendicular to the section at a particular vertical, the velocity used in the computations must be corrected by multiplying by the cosine of the angle between the perpendicular and the actual velocity vector.

E.3.2 Method of Integration

Referring to figure E.2, discharge through the cross section is given by

$$Q = \sum_{i=1}^N U_i \cdot A_i, \quad (\text{E.3})$$

where the area of each subsection, A_i , is computed as

$$A_i = Y_i \cdot \frac{|X_{i+1} - X_{i-1}|}{2}, \quad (\text{E.4})$$



Figure E.3 Velocity-area stream gauging using a wading rod. The tape marking the cross section is visible just in front of the observer (photo by J. V. Z. Dingman).

where X_i are cross-stream distances to successive verticals measured from an arbitrary horizontal datum, the U_i are the vertically averaged velocities at each vertical, and the Y_i are the depths at each vertical. X_1 and X_N are located at the ends of the section (**left and right edges of water**, defined relative to an observer facing *downstream*), and X_{N-1} and X_{N+1} are taken as zero. The velocities at the ends of the section (U_1 and U_N) will always equal zero and, unless the bank is vertical, Y_1 and Y_N will also equal zero. Equation (E.4) is called the **mid-section method**, which has been shown to give the most precise measurements (Hipolito and Loureiro 1988).

E.3.3 Measurement of Velocity

E.3.3.1 Vertical Velocity Profile

The vertically averaged velocity is usually estimated by assuming that the velocity is logarithmically related to distance above the bottom, as for wind flow over the ground surface [equation (3.27)] with zero-plane displacement height = 0:

$$u(y_i) = \frac{1}{\kappa} \cdot u_* \cdot \ln\left(\frac{y_i}{y_{0i}}\right), \quad (\text{E.5})$$

where $\kappa = 0.4$, $u(y_i)$ is velocity at a distance y_i above the bottom at vertical i , u_{*i} is the friction velocity at vertical i , and y_{0i} is the roughness height at vertical i .

The local friction velocity for water flow can be directly calculated as

$$u_{*i} = (g \cdot Y_i \cdot S_c)^{1/2}, \quad (\text{E.6})$$

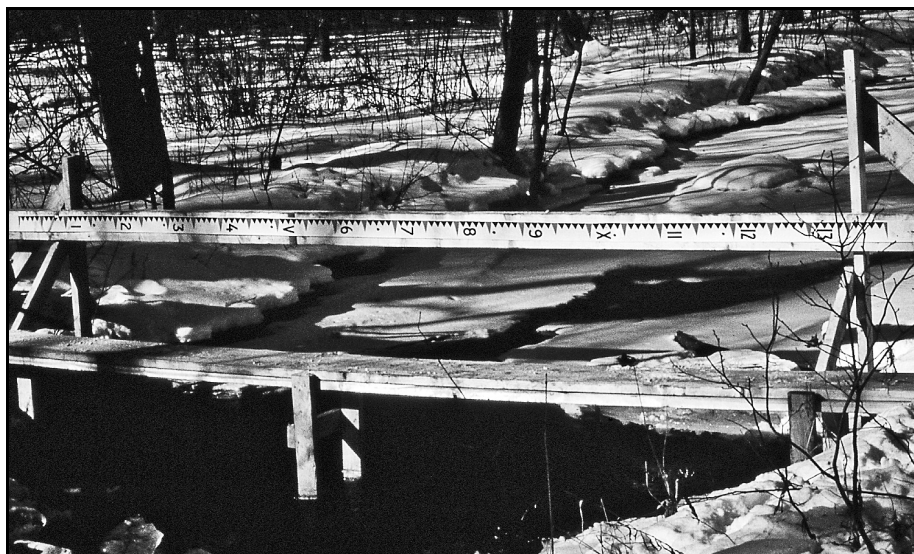


Figure E.4 Temporary bridge structure used in velocity-area gauging with a wading rod. Note the cross-section distances permanently fixed to the structure.

where g is gravitational acceleration, Y_i is local flow depth, and S_c is channel slope.

The value of y_{0i} is determined as:

$$\begin{aligned} \text{If } d_{50} < \frac{4 \cdot \mu}{\rho_w \cdot u_{*i}}, \\ y_{0i} &= \frac{0.11 \cdot \mu}{\rho \cdot u_{*i}}; \end{aligned} \quad (\text{E.7a})$$

otherwise,

$$y_{0i} = 0.033 \cdot d_{50}, \quad (\text{E.7b})$$

where μ is viscosity, ρ is mass density, and d_{50} is the median diameter of the bed particles.

E.3.3.2 Estimating Average Velocity in a Vertical

E.3.3.2.1 Six-Tenths-Depth Method

If equation (E.5) applies and y_{0i} is very small relative to the flow depth, it can be shown that the average velocity occurs at a distance of $0.368 \cdot Y_i$ above the bottom (Dingman 2009). Based on this, the **six-tenths-depth method** assumes that the velocity measured at a distance of $0.6 \cdot Y_i$ below the surface ($0.4 \cdot Y_i$ above the bottom) is the average velocity at that point in the cross section. Standard USGS practice is to use the six-tenths-depth method where $Y_i < 2.5$ ft (0.75 m).

E.3.3.2.2 Two-Tenths-and-Eight-Tenths-Depth Method

If the velocity is given by equation (E.5), it can be shown that

$$u(0.4 \cdot Y_i) = \frac{u(0.2 \cdot Y_i) + u(0.8 \cdot Y_i)}{2}. \quad (\text{E.8})$$

Thus average vertical velocity can be estimated as the average of the velocities at $0.2 \cdot Y_i$ and $0.8 \cdot Y_i$. The **two-tenths-and-eight-tenths-depth method** gives more accurate estimates of average velocity than does the six-tenths-depth method (Carter and Anderson 1963), and standard USGS practice is to use the two-tenths-and-eight-tenths-depth method where $Y_i > 2.5$ ft (0.75 m).

E.3.3.2.3 General Two-Point Method

If velocity is measured at two points, each at an arbitrary fixed distance above the bottom, the relative depths of those sensors will change as the discharge changes. In this case [again assuming that equation (E.5) applies], the average vertical velocity is

$$U_i = \frac{[1 + \ln(y_{i2})] \cdot u(y_{i1}) + [1 + \ln(y_{i1})] \cdot u(y_{i2})}{\ln(y_{i2}/y_{i1})}, \quad (\text{E.9})$$

where y_{i1} and y_{i2} are the depths of the velocity sensors and $y_{i2} > y_{i1}$ (Walker 1988).

E.3.3.2.4 Multi-Point Method

As noted, the standard formulas for calculating average vertical velocity assume a logarithmic vertical velocity distribution with $y_{0i} \ll Y_i$. These assumptions may not be appropriate for channels with roughness elements (boulders, weeds) whose heights are a significant fraction of depth or that have significant obstructions upstream and downstream of the measurement section. In these cases, the best strategy is to measure velocity at several heights at each vertical, with averages found by numerical integration over each vertical or over the entire cross section. Alternatively, a statistical sampling approach may be appropriate (Dingman 1989).

E.3.3.2.5 Surface-Velocity (Float) Method

If it is not possible to accurately measure velocities at various depths, the average velocity can be estimated by observing the time it takes floats inserted at representative locations across the stream to travel a given distance. The measurement distance should be at least 10 times the stream width. The average velocity for each path can be estimated as

$$U_i = f \left(\frac{d_{50}}{Y_i} \right) \cdot u(Y_i), \quad (\text{E.10})$$

where $u(Y_i)$ is the velocity of the i th float and $f(d_{50}/Y_i)$ is a proportion that depends on the ratio of the average height of channel roughness elements, d_{50} , to the flow depth. Figure E.5 shows this relation, again assuming a logarithmic velocity profile. A reasonable general value is $f(d_{50}/Y_i) = 0.85$.

Tauro et al. (2012) described a stream-gauging method that uses ultraviolet lamps and a digital camera to record the arrival of buoyant fluorescent microspheres that can be used to measure velocities in small streams.

E.3.3.3 Current Meters

Several types of current meters are available that measure single-direction velocity at a point, including horizontal axis (propeller or screw type), vertical axis (Price-type; this is standard for the USGS), and electromagnetic instruments. Accurate measurements require carefully calibrated and maintained current meters (Smoot and Novak 1968) and, at each measurement point, averaging the velocity over time (usually 30 to 60 s) to eliminate fluctuations due to turbulence.

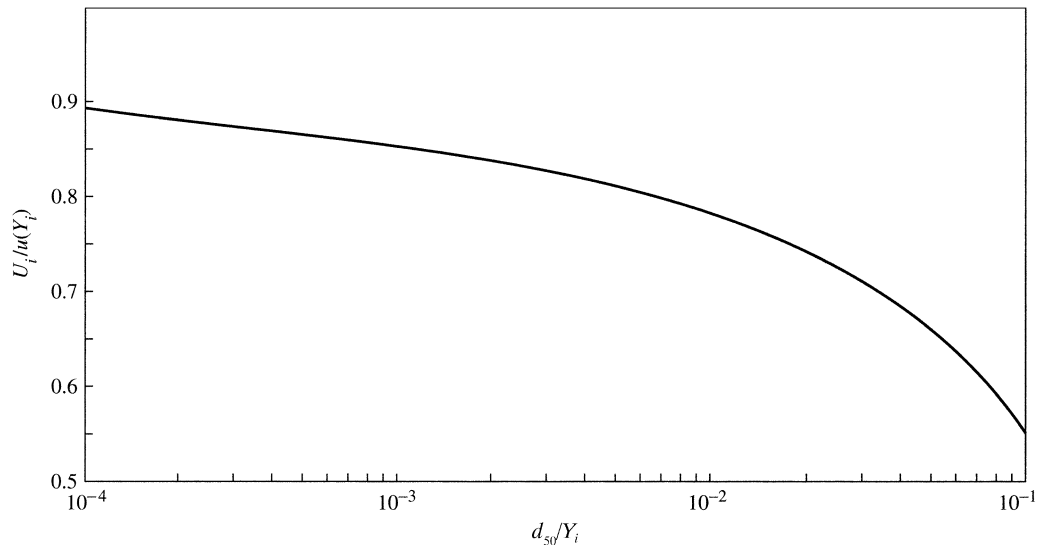


Figure E.5 Ratio of average velocity, U_i , to surface velocity, $u(Y_i)$, as a function of the ratio of median bed-particle diameter, d_{50} , to depth, Y_i , assuming a logarithmic (Prandtl–von Kármán) velocity distribution.

E.3.4 Accuracy

Traditional methods of estimating uncertainty in velocity-area discharge measurements use error-propagation techniques (section 1.11.2), in which the relative uncertainty in discharge, ε_Q , is a function of the uncertainties in the individual measurements of width, w ; depth, y ; and velocity, u :

$$\varepsilon_Q = \pm \left\{ \varepsilon_I^2 + \varepsilon_c^2 + \frac{\sum_{i=1}^N \left[(w_i \cdot y_i \cdot u_i)^2 \cdot (\varepsilon_{wi}^2 + \varepsilon_{yi}^2 + \varepsilon_{ui}^2) \right]}{\left(\sum_{i=1}^N w_i \cdot y_i \cdot u_i \right)^2} \right\}^{1/2}, \quad (\text{E.11})$$

where ε_I is the relative uncertainty due to approximation of the integral using a finite number of verticals, ε_c is relative uncertainty due to calibration errors in the current meter and other measurement devices, and ε_w , ε_y , and ε_u are the relative errors in the individual measurements of width, depth, and average velocity, respectively. Estimates of the various components of the total uncertainty are derived from empirical and laboratory studies and are generally insensitive to the site-specific measurement and flow

conditions (Pelletier 1988). Cohn et al. (2013) have developed and tested an “interpolated variance estimator” that estimates uncertainty based on the data collected during the streamflow measurement and therefore reflects local conditions and includes all sources of random uncertainty in the velocity and depth measurements.

Carter and Anderson (1963) evaluated the accuracy of velocity-area measurements using standard USGS techniques. They determined discharge from measurements of velocity and depth at over 100 verticals in 127 cross sections in different streams, then recomputed the discharge using smaller numbers of observations at each site. Carefully calibrated current meters were used in these observations. The results are summarized in figure E.6: they show the standard deviation of the error as a function of number of verticals (N) for the six-tenths and two-tenths-and-eight-tenths methods. About two-thirds of discharge measurements should have percentage errors less than the values given by the curves, and about 95% of measurements should have errors less than twice the values given by the curves. Although Carter and Anderson (1963) gave no information about the nature of the streams they measured, it is likely that errors for highly irregular channels would be larger than indicated by figure E.6.

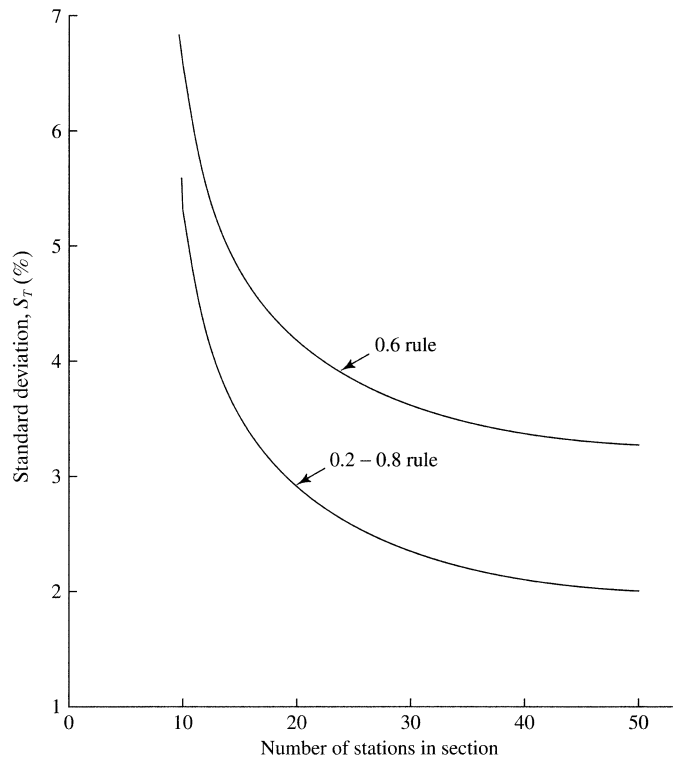


Figure E.6 Standard deviation of error as a function of number of verticals used in velocity-area measurements using the six-tenths- and two-and-eight-tenths-depth methods [Carter and Anderson (1963). Accuracy of current meter measurements. American Society of Civil Engineers Proceedings, *Journal of the Hydraulics Division* 89:105–115, with permission from ASCE].

Cohn et al. (2013) evaluated the uncertainty in velocity-area discharge measurements in natural streams as the standard deviation of repeated measurements made when discharge was constant. Using 4 to 21 measurements at 11 sites, they found values of ε_Q ranging from less than 1% to about 10%.

E.4 Dilution Gauging

Dilution gauging involves introducing a tracer into the flow at an upstream location and measuring the rate of arrival of the tracer at a downstream location. It is usually a more accurate method than velocity-area gauging in small, highly turbulent streams with rough, irregular channels. As with velocity-area measurements, the method is most accurate when there is no change in discharge during the measurement. Kilpatrick and Cobb (1985) and Herschy (1999) gave a complete discussion of the method.

E.4.1 Mixing Length

The distance between the two measurement locations must be long enough to allow complete mixing of the tracer with the flow, but short enough so

that the downstream change in discharge is insignificant. It is best to determine the distance required for complete mixing empirically, by observing the mixing of a visible dye such as fluorescein in the reach of interest. Alternatively, this length, X_{mix} , may be estimated as

$$X_{mix} = K_{mix} \cdot \frac{C \cdot W^2}{g^{1/2} \cdot Y}, \quad (\text{E.12})$$

where W is average reach width (m), Y is average reach depth (m), g is gravitational acceleration (9.81 m/s^2), and K_{mix} is found from table E.2 (Kilpatrick and Cobb 1985). C is a factor (called Chézy's C) that characterizes the channel conductance: An average

Table E.2 Mixing Coefficients for Dilution Gauging.

Number and Location of Injection Points	K_{mix}
1 point at center of flow	0.500
2 points, 1 at center of each half of flow	0.125
3 points, 1 at center of each third of flow	0.055
1 point at edge of flow	2.00

Source: Kilpatrick and Wilson (1989).

value is $C = 30 \text{ m}^{1/2}/\text{s}$; very rough turbulent streams may have $C \approx 15 \text{ m}^{1/2}/\text{s}$ or less; very smoothly flowing streams may have $C \approx 45 \text{ m}^{1/2}/\text{s}$ or more (Dingman 2009).

E.4.2 Tracer Properties

The tracer used in dilution gauging should (1) be readily soluble; (2) have zero or very low natural concentration in the stream; (3) not be chemically reactive with or physically absorbed by substances in the stream; (4) be easily detectable at low concentrations; (5) be harmless to the observer and to stream life; and (6) be of reasonable cost (Gregory and Walling 1973). Sodium chloride (NaCl) is probably the best choice in most situations; its concentration can usually be readily detected by measuring the electrical conductivity of the water and comparing the results with a previously developed calibration curve between conductivity and concentration. Rhodamine WT, a fluorescent dye, is also used. It has low toxicity, low background concentrations, high diffusivity, and absorbs only slightly on sediments. Its concentration can be measured by a submersible fluorometer (e.g., Clow and Fleming 2008).

E.4.3 Measurement Techniques

There are two techniques for dilution gauging: (1) **constant-rate injection** and (2) **slug, or gulp, injection** (figure E.7).

In constant-rate injection, the tracer solution is injected at a constant rate Q_T for a period of time sufficient for the downstream concentration to reach a steady equilibrium value, C_{eq} . Then the discharge, Q , is calculated as

$$Q = Q_T \cdot \frac{C_T - C_{eq}}{C_{eq} - C_b}, \quad (\text{E.13})$$

where C_T is the concentration of the tracer solution and C_b is the natural background concentration of the tracer in the stream.

Slug injection involves dumping a volume, V_T , of tracer solution with concentration C_T into the stream at the upstream site. Concentration at the downstream site, $C_d(t)$, is then recorded as a function of time until it recedes to its background value C_b . Stream discharge is then given by

$$Q = \frac{(C_T - C_b) \cdot V_T}{\int_0^{\infty} [C_d(t) - C_b] \cdot dt}, \quad (\text{E.14})$$

where the integral is evaluated by graphically measuring the area under the $C_d(t)$ versus t curve.

Figure E.8 on p. 588 shows dilution gauging in a highly turbulent glacial stream in the Himalayas.

E.5 Gauging with Portable Weirs and Flumes

E.5.1 Sharp-Crested V-Notch Weirs

Accurate discharge measurements in small streams can be made using portable V-notch weirs in temporary installations. The weir plate can be constructed of plywood, plastic, or metal. The notch should be sharp-edged so that the water “springs free” even at low discharges; thus if plywood is used, the notch itself should be formed of metal strips (figure E.9 on p. 588).

The weir should be installed in the stream such that all the flow is diverted through it, which may require altering the channel and use of plastic liners. A virtually horizontal pool should extend some distance upstream of the weir, and the weir plate must be carefully leveled so that the V-notch is symmetric about a vertical line.

Discharge through a V-notch weir is given by

$$Q = C_w \cdot g^{1/2} \cdot \tan\left(\frac{\theta_w}{2}\right) \cdot H_w^{5/2}, \quad (\text{E.15})$$

where C_w is a dimensionless **weir coefficient**, g is gravitational acceleration, and θ_w is the angle of the V-notch. H_w is the **weir head**, defined as

$$H_w \equiv (Z_w - Z_v), \quad (\text{E.16})$$

where Z_w is the elevation of the water surface *where it is essentially horizontal in the weir pool* above the point of the V-notch, and Z_v is the elevation of the point of the V-notch. A constant weir coefficient $C_w = 0.43$ can be used when $(Z_w - Z_v) > 0.3 \cdot (Z_v - Z_b)$, where Z_b is the streambed elevation at the downstream face. If $(Z_w - Z_v) < 0.3 \cdot (Z_v - Z_b)$, C_w should be determined by calibration (see Herschy 1999; Dingman 2009).

Because of the 5/2-power relationship in equation (E.15), precise measurement of H_w is essential. Z_w should be measured where the water surface is virtually horizontal in the pool formed by the weir; this should ideally be at an upstream distance at least twice the vertical dimension of the weir opening. However, acceptably approximate Z_w measurements may be obtained by observing the water level on a

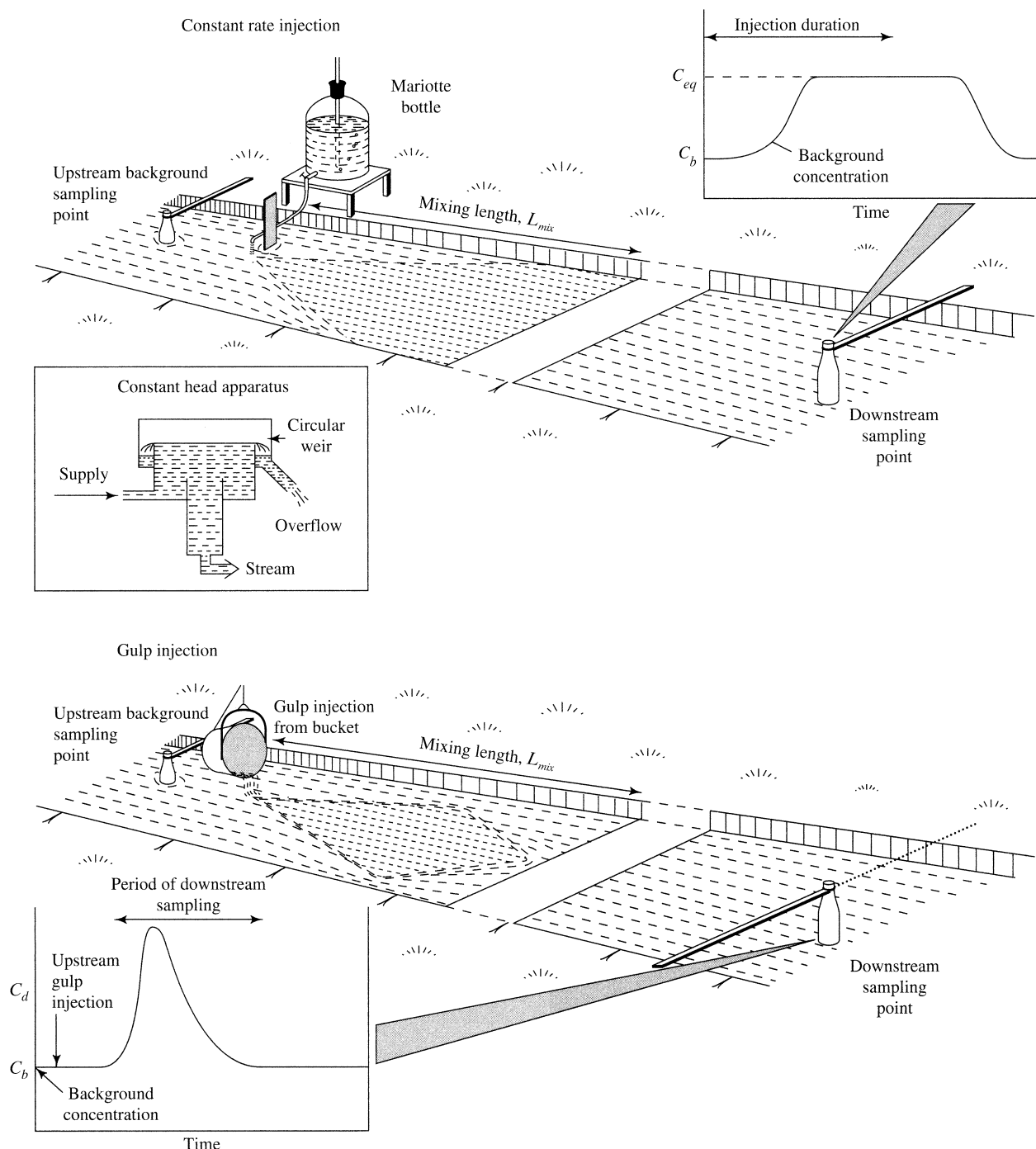


Figure E.7 Dilution-gauging techniques [republished with permission from Wiley, from Gregory and Walling (1973). *Drainage Basin Form and Process: A Geomorphological Approach*].



Figure E.8 Injection of dye for dilution gauging in a highly turbulent Himalayan stream, where velocity-area gauging is not feasible (photo courtesy of Richard Pendleton).

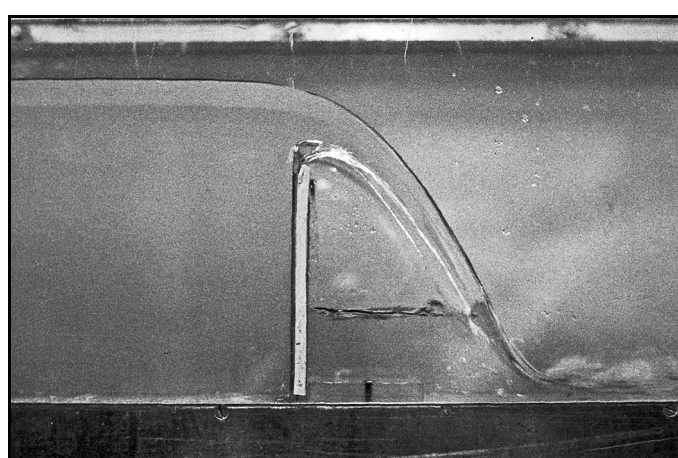
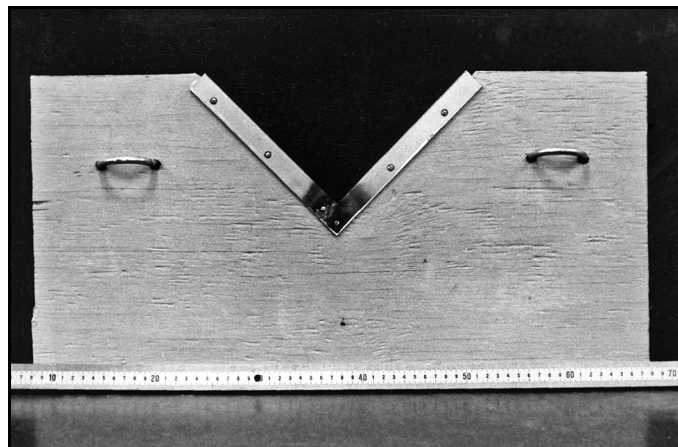


Figure E.9 (a) Construction of a small, portable 90° V-notch weir. The notch is metal; the weir plate is plywood. Plate is 60 cm wide. (b) Side view of weir showing water springing free, as required for proper measurement.

scale fixed to the upstream face of the weir plate far enough from the notch to avoid the effects of drawdown (figure E.10). This latter arrangement eliminates the need for precise leveling to establish the relation between elevations observed upstream and the elevation of the point of the V-notch.

The maximum vertical opening and angle of a V-notch weir are dictated by the anticipated range of flows and the required measurement precision. Narrower angles give greater precision at low flows, but reduce the overall range of measurement for a given size of opening. Table E.3 gives the capacity of 90° and 60° V-notch weirs with various maximum dimensions. Weirs with compound angles can be constructed to give more optimal combinations of low-flow sensitivity and range; these must be calibrated to obtain the stage-discharge relation.

E.5.2 Flumes

Flumes are devices that conduct the streamflow through a short reach with a constricted cross section that accelerates the flow and provides a fixed stage-discharge relation. Large flumes are used in permanent gauging stations, and portable flumes can be used for short-term measurements in small streams. Both flumes and weirs give stable rating curves, but flumes are advantageous where one wishes to avoid inducing sediment deposition or inundating upstream areas.

There are many flume designs, each with its own rating curve (Herschy 1999). Some types may be commercially purchased. Figure E.11 and tables E.4 (p. 591) and E.5 (p. 592) show the design and ranges of one of the most commonly used portable designs, the **Parshall flume**; and figure E.12 on p. 593 gives the design of the **modified Parshall flume** used by the USGS for temporary gauging of small streams.

Table E.3 Maximum Discharges Measurable by 60° and 90° V-Notch Weirs.

90° Notch		
Maximum Weir Head, H_w (m)	Discharge (m^3/s)	Discharge (L/s)
0.15	0.0117	11.7
0.25	0.0421	42.1
0.30	0.0664	66.4
0.50	0.238	238
60° Notch		
0.15	0.00677	6.77
0.25	0.0243	24.3
0.30	0.0383	38.3
0.50	0.137	137

As with weirs, flumes must be properly leveled, and are usually installed in temporary dams that assure that all the flow passes through the measuring device.

E.6 Stage Measurement

Direct measurement of discharge is difficult and time-consuming, and recording it is impossible; however, observing and recording water-surface elevation, or stage [equation (E.2)], is relatively simple. Thus the stage-discharge relation (rating curve) is an essential component of discharge measurement where repeated or continuous records are required. A complete discussion of the measurement of stage is given by Sauer and Turnipseed (2010).

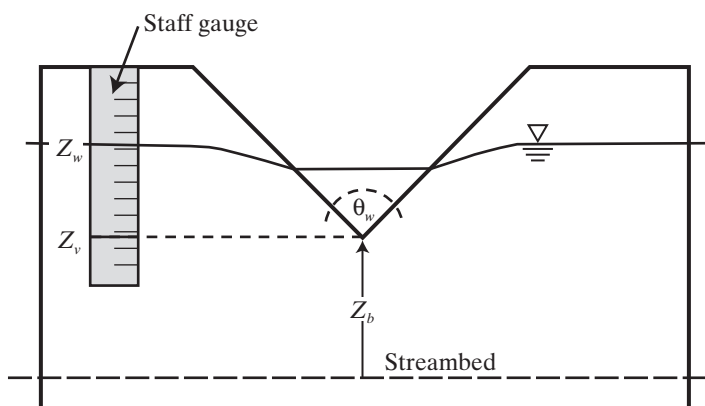


Figure E.10 Diagram of a portable weir plate showing measurement of Z_w on a scale fixed to the upstream face far enough from the notch to avoid drawdown. This arrangement eliminates the need for precise leveling to establish the relation between water-level elevations observed upstream and the elevation of the point of the V-notch, Z_v .

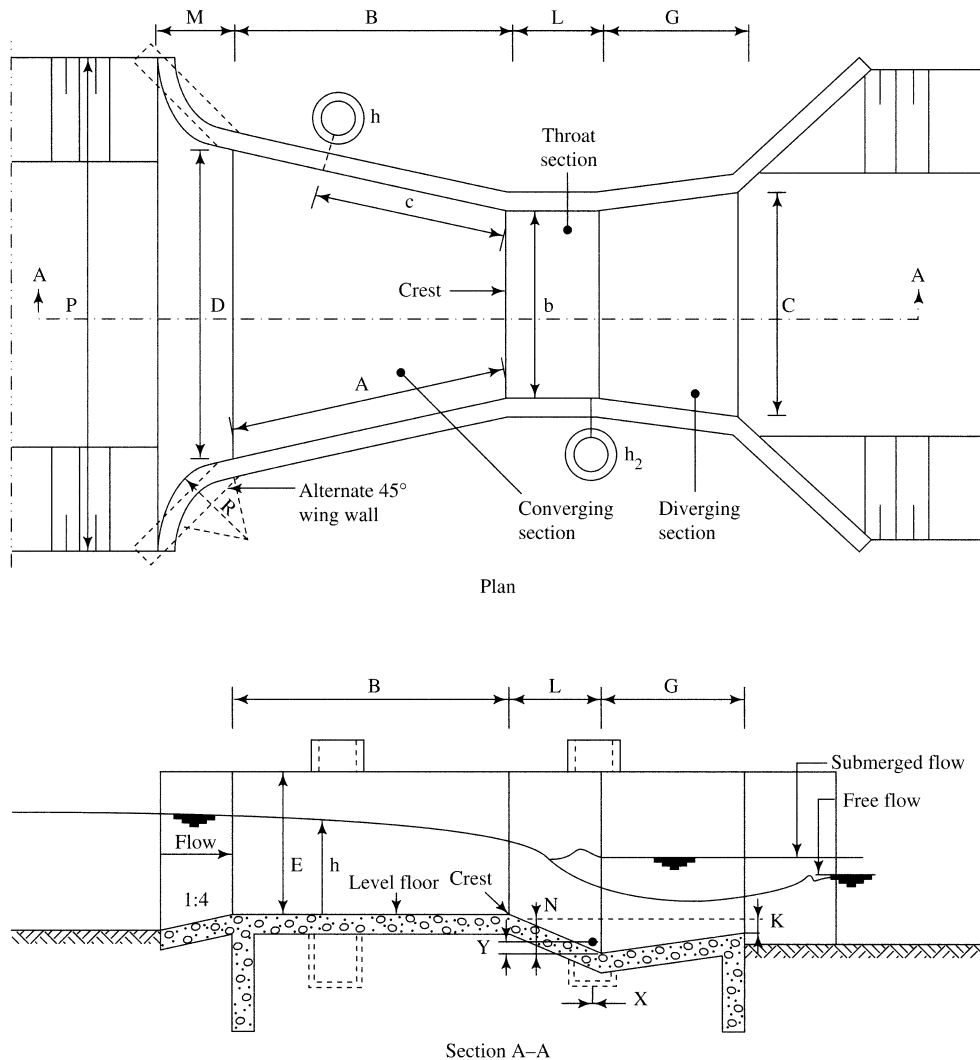


Figure E.11
Configuration of the Parshall flume.
Actual dimensions corresponding to letters for flumes of various sizes are given in table E.4, and discharge ranges in table E.5 [Herschy (1985)].

E.6.1 Methods of Measurement

Stage is most simply determined by observing the position of the water surface on a ruler-like **staff gauge** (figure E.13 on p. 593). Stage can also be determined via a float-counterweight system (figure E.14 on p. 594), and with instruments that directly measure water pressure (pressure transducers). The staff-gauge datum, Z_0 [equation (E.2)], must be below, but ideally close to, the level of zero discharge. The elevation of the datum relative to a point whose elevation will not change should be established by survey and periodically checked to avoid errors due to disturbance of the staff gauge.

Continuous records of stage are obtained by recording stage by means of a float or pressure sensor attached to an analog or digital recorder. Buchanan and Somers (1968), Herschy (1999), and Sauer and Turnipseed (2010) describe many approaches to measuring and recording stage.

E.6.2 Measurement Location

To establish a useful stage-discharge relation, stage must be measured where it is sensitive to discharge variations (i.e., where dZ_s/dQ is relatively large) and where it can be accurately measured, usually to within 0.003 m (0.01 ft). These conditions are

Table E.4 Dimensions of Standard Parshall Flumes.^a

b	D	C	B	L	G	E	N	K	A	c	h₂	
											X	Y
0.025	0.167	0.093	0.357	0.076	0.204	0.153– 0.229	0.029	0.019	0.363	0.241	0.008	0.013
0.051	0.213	0.135	0.405	0.114	0.253	0.153– 0.253	0.043	0.022	0.415	0.277	0.016	0.025
0.076	0.259	0.178	0.457	0.152	0.30	0.305– 0.610	0.057	0.025	0.466	0.311	0.025	0.038
0.152	0.396	0.393	0.610	0.30	0.61	0.61	0.114	0.076	0.719	0.415	0.051	0.076
0.229	0.573	0.381	0.862	0.30	0.46	0.76	0.114	0.076	0.878	0.588	0.051	0.076
0.305	0.844	0.610	1.34	0.61	0.91	0.91	0.228	0.076	1.37	0.914	0.051	0.076
0.457	1.02	0.762	1.42	0.61	0.91	0.91	0.228	0.076	1.45	0.966	0.051	0.076
0.610	1.21	0.914	1.50	0.61	0.91	0.91	0.228	0.076	1.52	1.01	0.051	0.076
0.914	1.57	1.22	1.64	0.61	0.91	0.91	0.228	0.076	1.68	1.12	0.051	0.076
1.22	1.93	1.52	1.79	0.61	0.91	0.91	0.228	0.076	1.83	1.22	0.051	0.076
1.52	2.30	1.83	1.94	0.61	0.91	0.91	0.228	0.076	1.98	1.32	0.051	0.076
1.83	2.67	2.13	2.09	0.61	0.91	0.91	0.228	0.076	2.13	1.42	0.051	0.076
2.13	3.03	2.44	2.24	0.61	0.91	0.91	0.228	0.076	2.29	1.52	0.051	0.076
2.44	3.40	2.74	2.39	0.61	0.91	0.91	0.228	0.076	2.44	1.62	0.051	0.076
3.05	4.75	3.66	4.27	0.91	1.83	1.22	0.34	0.152	2.74	1.83		
3.66	5.61	4.47	4.88	0.91	2.44	1.52	0.34	0.152	3.05	2.03		
4.57	7.62	5.59	7.62	1.22	3.05	1.83	0.46	0.229	3.50	2.34		
6.10	9.14	7.31	7.62	1.83	3.66	2.13	0.68	0.31	4.27	2.84		
7.62	10.67	8.94	7.62	1.83	3.96	2.13	0.68	0.31	5.03	3.35		
9.14	12.31	10.57	7.92	1.83	4.27	2.13	0.68	0.31	5.79	3.86		
12.19	15.48	13.82	8.23	1.83	4.88	2.13	0.68	0.31	7.31	4.88		
15.24	18.53	17.27	8.23	1.83	6.10	2.13	0.68	0.31	8.84	5.89		

^aLetters refer to dimensions in figure E.11. All values in meters.

Source: Herschy (1985).

usually met in an area of quiet water not far upstream of a reach of accelerating flow and near the bank, where wave action is minimal.

If necessary, wave action can be virtually eliminated by measuring stage in a **stilling well**. Such a device can be constructed by surrounding the staff gauge with a section of metal or plastic barrel into which holes have been punched, or simply with piled rocks. Construction of more elaborate stilling wells dug into stream banks and communicating to the stream via pipes is discussed by Buchanan and Somers (1968) and Herschy (1999).

E.6.3 Stage-Discharge Relations at Natural Controls

The rating curve has a theoretical form when artificial controls are used [e.g., equation (E.15)], although calibration of the relation by direct measurements may be required over at least some flow ranges. For natural controls, the rating curve is established empirically by concurrent direct measurement of discharge and observation of stage over a range of discharges. Typically it will take several months to experience the range of flows required to

Table E.5 Ranges of Measurable Discharges and Rating-Curve Equations for Parshall Flumes of Various Dimensions.

Throat Width, b (m)	Discharge Range			Equation $Q = K \cdot h^a$ (m^3/s)
	Minimum	Maximum	Units	
0.025	0.09	5.5	L/s	$0.0604 \cdot h^{1.55}$
0.051	0.18	13.2	L/s	$0.1207 \cdot h^{1.55}$
0.076	0.77	32.1	L/s	$0.1771 \cdot h^{1.55}$
0.152	1.50	111	L/s	$0.3812 \cdot h^{1.58}$
0.229	2.50	251	L/s	$0.5354 \cdot h^{1.53}$
0.305	3.32	457	L/s	$0.6909 \cdot h^{1.52}$
0.457	4.80	697	L/s	$1.056 \cdot h^{1.54}$
0.610	12.1	937	L/s	$1.428 \cdot h^{1.55}$
0.914	17.6	1,427	L/s	$2.184 \cdot h^{1.57}$
1.219	35.8	1,923	L/s	$2.953 \cdot h^{1.58}$
1.524	44.1	2,424	L/s	$3.732 \cdot h^{1.59}$
1.829	74.1	2,929	L/s	$4.519 \cdot h^{1.60}$
2.134	85.8	3,438	L/s	$5.312 \cdot h^{1.60}$
2.438	97.2	3,949	L/s	$6.112 \cdot h^{1.61}$
3.048	0.16	8.28	m^3/s	$7.463 \cdot h^{1.60}$
3.658	0.19	14.68	m^3/s	$8.859 \cdot h^{1.60}$
4.572	0.23	25.04	m^3/s	$10.96 \cdot h^{1.60}$
6.096	0.31	37.97	m^3/s	$14.45 \cdot h^{1.60}$
7.620	0.38	47.14	m^3/s	$17.94 \cdot h^{1.60}$
9.144	0.46	56.33	m^3/s	$21.44 \cdot h^{1.60}$
12.192	0.60	74.70	m^3/s	$28.43 \cdot h^{1.60}$
15.240	0.75	93.04	m^3/s	$35.41 \cdot h^{1.60}$

b = throat width in m (see figure E.11)

Q = discharge in m^3/s

h = water-surface elevation measured at upstream stilling well (m) (see figure E.11)

Source: Herschy (1985).

establish a satisfactory curve. Birgand et al. (2013) found that a minimum of 22 measurements were necessary to construct acceptable ratings in stable channels. However, channel configurations often change over time due to erosion and sedimentation (figure E.15 on p. 594), and one must regularly check the rating curve by making discharge measurements. Jalbert et al. (2011) developed an approach for estimating temporal uncertainty in rating curves due to channel changes.

Although not necessary for establishing a useful rating, the rating curve can often be approximated by a power law,

$$Q = a_1 \cdot Z_s^b, \quad (\text{E.17})$$

or a second-order polynomial,

$$Q = a_2 \cdot Z_s^2 + a_3 \cdot Z_s, \quad (\text{E.18})$$

where the constants are determined by regression analysis (Birgand et al. 2013).

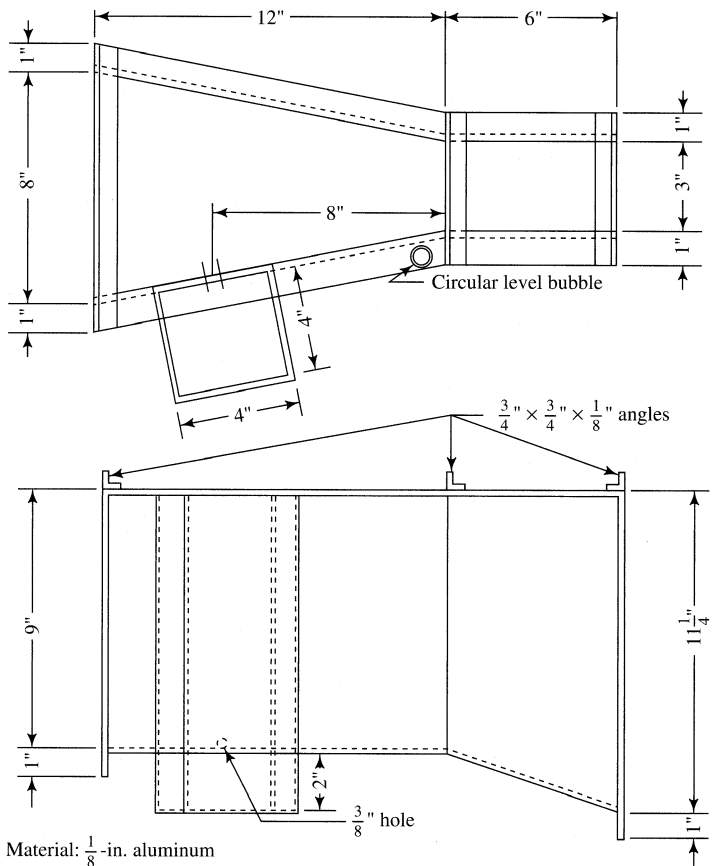


Figure E.12 Configuration of a 3-in (7.5-cm) modified Parshall flume, with a discharge capacity of about $0.014 \text{ m}^3/\text{s}$. This design can be made in larger sizes [Buchanan and Somers (1968)].

Material: $\frac{1}{8}$ -in. aluminum
Welded construction
Note: This stilling well can accommodate a 3-in. float and be used with a recorder if continuous measurement is desired for a period.



Figure E.13 Staff gauge installed on a small stream (photo by author).



Figure E.14 Simple float-counterweight system for measuring and recording stage. The pulley can be attached to an analog or digital recorder to obtain a continuous stage record [Buchanan and Somers (1968)].

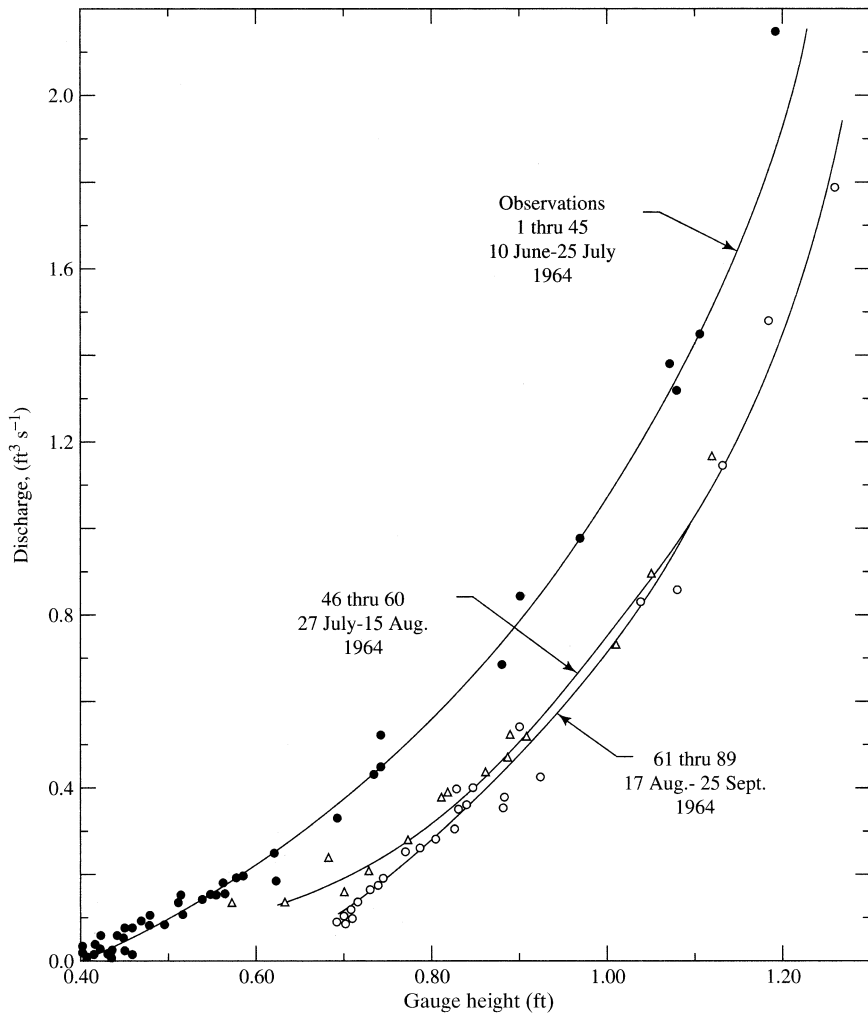


Figure E.15 Rating curves for a natural cross section in a small Alaskan stream. Note that the relation has shifted over time due to siltation [Dingman (1970)].

Appendix

F

Hydrologic Simulation Modeling

The development of hydrologic simulation models has been a consequence of the complexity and spatial and temporal variability of hydrologic processes and the limited availability of spatially and temporally distributed hydrologic, climatologic, geologic, pedologic, vegetative, and land-use data. This text explicitly discusses the modeling of many portions of the land phase of the hydrologic cycle, including snowmelt (section 5.7), free-water evaporation (section 6.3), evaporation from soil (section 6.4), transpiration (section 6.5.3), interception (section 6.6.3), total evapotranspiration (section 6.8), infiltration (section 8.4), aspects of ground-water flow (section 8.1.6), open-channel flow (section 10.5.2), and runoff to streams (section 10.6). Section 1.12 and box 6.8 describe watershed models that combine several processes to simulate the storages and outputs in response to precipitation inputs.

As computing power and the ability to extract extensive land-surface and meteorological data via satellites have increased, many models that attempt to simulate the land phase of the hydrologic cycle have been developed for scientific and practical purposes. The centrality of modeling to the science and application of hydrology requires that we define modeling terms and explore approaches to and issues in modeling more broadly. We begin with a consideration of what a hydrologic model is; then we consider how and why models are used in hydrologic science and engineering, the various types of models, the modeling process, and model evaluation.

F.1 What Is a Simulation Model?

As stated by Dooge (1986, p. 46S), a simulation model is “a system which is simpler than the prototype system and which can reproduce some but not all of the characteristics thereof.” More specifically,

A **hydrologic simulation model** is a physical system or mathematical algorithm that is intended to reproduce actually or symbolically the essential aspects of the operation of a portion of the hydrologic cycle.

Perhaps the best metaphor for a hydrologic simulation model is that of a map:

A model is to hydrologic reality as a map is to the actual landscape.

A mental comparison of a map of a region you’re familiar with to the actual region gives a good sense of how a model approximates reality. The map metaphor also makes clear two essential characteristics of models:

1. *A model, like a map, is designed for a specific purpose.*

A model emphasizes features appropriate to its purpose while omitting other features: a road map shows road types, route numbers, and locations of

cities and towns, but usually does not show topography, land cover, or other features that might be extremely important for purposes other than finding your way by car from point A to point B.

2. *A model, like a map, is constructed at a particular scale.*

Neither represents features that are not visible at that scale—and some of the omitted features could be important in many contexts. The issue of scale—time as well as space—in modeling is an active area of research and discussion in the hydrological literature (e.g., Giorgi and Avissar 1997; Bergstrom and Graham 1998; Kirchner 2006, 2009).

F.2 Purposes of Simulation Models

F.2.1 Models as Scientific Tools

The goal of hydrologic science is to understand the operation of the hydrologic cycle. Because of the complexity of hydrologic processes that operate over a range of temporal and spatial scales (figure 1.4), simulation models are widely used to increase that understanding. In this context, models are used along with observational data to test hypotheses about the processes operating in some portion of the hydrologic cycle (Beven 1989). This is done by repetition of the following sequence:

1. Construct a model that incorporates current understanding of and hypotheses about the operation of a portion of the hydrologic cycle at spatial and temporal scales of interest;
2. Obtain relevant observational data;
3. Compare model output to observations; and
4. Refine the understanding and hypotheses based on those comparisons.

Wigmosta and Burges (1997) reported an excellent example of the interactive use of models and field measurement in understanding runoff processes. They used a combination of soil and topographic mapping, simple hydrologic monitoring, and hydrologic modeling to understand runoff processes in two small watersheds, one undeveloped forest, the other suburban. Monitoring included continuous measurement of streamflow, precipitation, and ground-water levels. A hydrologic model was developed in conjunction with the measurement program to assure that the level of model detail was consistent with the level of field measurements used for model input and testing. The authors initially anticipated that saturation

overland flow (section 10.4.2.2) would be the major component of peak discharge in the forested watershed and Hortonian overland flow (section 10.4.2.1) from impervious surfaces would dominate storm runoff in the suburban catchment. Instead, they found that subsurface flow (section 10.4.3) dominated both total and peak discharge in the forested site, and discharge from lawns and other pervious areas accounted for roughly 60% of total and storm runoff from the suburban watershed. The adaptive combination of modeling and measurements was essential to elucidate the various components of flow production and flow paths in these watersheds. The Thornthwaite Continuous Model exercise on the disk accompanying this text provides an exploration of the application of models to scientific understanding of hydrologic processes.

F.2.2 Water-Resource Management Models

Hydrologic simulation models are widely used to guide the formulation of water-resource management strategies (including the design of structures). These applications require either *predictions* or *forecasts*.

Predictions are estimates of the magnitude of some hydrologic quantity (e.g., the peak flow) that is either (1) associated with a particular exceedence probability (section C.5) or other statistic of the quantity or (2) produced by a hypothetical rainfall or snowmelt event, often called the *design storm* (section 4.4.3). Predictions are the basis for the design of civil engineering works such as reservoirs and reservoir spillways and land-use plans (e.g., floodplain zoning), and for the assessment of the hydrologic impacts of land-use and climate changes.

Forecasts are estimates of the response to an actual anticipated event; e.g., the peak flow rate that will result from the rain that is expected in the next 24 hr on a given watershed. Forecasts are used to guide the operation of reservoir systems and to provide flood warnings. Forecasting models are also commonly used for **hindcasts** (or **backcasts**), in which the objective is to estimate an unmeasured hydrologic response to a past event, or to test a model by comparing a past measured response with model output.

Much current research in hydrology is directed at improving our ability to predict or forecast the effects of land-use and climate changes on the water balance, ground-water levels, streamflow, and water quality of regions ranging from hillslopes or landfills to river basins to entire continents. These and most other applications of hydrology to practical problems

of design and forecasting require the use of hydrologic models, and a principal motivation for understanding the physics of hydrologic processes as developed in this text is to provide a sound basis for development and application of such models. The heuristic rainfall-runoff models described in section 10.6 are widely used for prediction and forecasting.

F.3 Types of Simulation Models

F.3.1 Model Forms

F.3.1.1 Physical Models

A **physical model** is a tangible, constructed representation of a portion of the natural world. If it is constructed at a larger or smaller scale than the natural system, formal rules of scaling based on dimensional analysis (see King et al. 1960; Dingman 2009) are used to relate observations on the model to the real world. Physical models have been important means to understanding problems of hydraulics and fluid mechanics, and they are often used to help design complex engineering structures, particularly those involving open-channel flow. Ground-water hydrologists use physical models, called **Hele-Shaw models** (see Fetter 2001), to simulate two-dimensional ground-water flow under various boundary conditions. One-to-one-scale physical models in the form of sprinkler-plot studies have been used to understand the process of infiltration (e.g., Nassif and Wilson 1975; see figure 8.10), and small-scale physical models of watersheds have been used to elucidate some basic characteristics of watershed response to rainfall (Amorochio and Hart 1965; Grace and Eagleson 1966; Chery 1967, 1968; Dickinson et al. 1967; Black 1970).

F.3.1.2 Analog Models

Analog models use observations of one process to simulate a physically analogous natural process. For example, Darcy's law of ground-water flow [equation (7.9)] is exactly analogous to the flow of electricity as given by Ohm's law,

$$I = \frac{1}{R} \cdot E, \quad (\text{F.1})$$

where I is current flow (equivalent to water flow), R is electrical resistance ($1/R$ is equivalent to hydraulic conductivity), and E is voltage drop (equivalent to hydraulic-head gradient). Thus the distribution of electrical potentials (voltage) on specially designed

conductive paper can be used to determine the patterns of ground-water potentials and hence of ground-water flow under various boundary conditions.

F.3.1.3 Mathematical Models

Mathematical simulation models are algorithms consisting of logical steps and equations that calculate the values of flows and storages of water and/or energy at specified physical locations. Most hydrologic simulation models can be represented as box-and-arrow diagrams like figure 1.3. The quantities of water or energy present in specific compartments (i.e., the boxes) at specific times are **state variables**. The “guts” of a mathematical model are **transfer functions** (i.e., the arrows), which are equations that calculate the rates of flows between compartments. Transfer functions may be based on fundamental scientific principles, heuristic concepts, or empirical (statistical) relations.

In most cases, transfer-function equations contain **parameters**, which are a priori specified values:

- **Fixed parameters** are physical constants such as mass density, the Stefan–Boltzmann constant, or viscosity.
- **Adjustable parameters** are quantities that are intended to characterize the region being simulated but whose values are not known with certainty, such as hydraulic conductivity, roughness height, or leaf-area index. Initial values of these parameters are selected by the modeler, and one of the main issues in model development and implementation is determining their “best” values, as discussed below.

Mathematical models are operated by specifying **inputs** (e.g., rainfall, incident solar radiation), which may be single values or sequences. The model calculates the resulting values of state variables and **outputs** (e.g., evapotranspiration, streamflows, snowmelt), which are the results used for the scientific or water-resource management purposes described above. In models that generate sequences of outputs, the **initial conditions**, which are the initial values of state variables, must be specified.

As the availability of more powerful digital computers, modeling techniques, and software has rapidly increased, the use of both physical and analog models in hydrology has been largely replaced by computer-implemented mathematical models, which are usually cheaper and much more flexible. Thus subsequent discussion here will focus on mathematical simulation models.

F.3.2 Types of Mathematical Models

Any given mathematical simulation model can usually be described by one or more terms from each of the six categories in table F.1. The terms denoting physical domain and process should be self-explanatory; those in the other categories are defined in the following sections.

F.3.2.1 Simulation Basis

Physically based models use transfer functions derived from basic physics, such as conservation of mass, energy, or momentum; force-balance; and/or diffusion laws (table 1.1) to simulate flows and storages. These equations are generally derived at “infinitesimal” time and space scales and discretized at much larger scales when implemented in models. Examples are the regional ground-water-flow models based on the Laplace equation [equation (9.15b)] shown in figures 9.5–9.7 and 9.10–9.12. Although physically based transfer functions might seem to be the “gold standard” for modeling, they usually describe processes at scales much smaller than those at which hydrological observations are made. Thus, as noted by Kirchner (2009, p. 1),

[A]lthough it seems obvious that catchment [i.e., watershed] models should be “physically based,” it seems less obvious how those models should be based on physics. Many hydrologic models are based on an implicit premise that the microphysics

in the subsurface will “scale up” such that the behavior at larger scales will be described by the same governing equations (e.g., Darcy’s law, Richards equation), with “effective” parameters that somehow subsume the heterogeneity of the subsurface. . . . It is currently unclear whether this upscaling premise is correct, or whether the effective large-scale governing equations for these heterogeneous systems are different in form, not just different in the parameters, from the equations that describe the small-scale physics.

Conceptual (heuristic) models use transfer functions that are relatively simple, “reasonable” relationships with few adjustable parameters. Such models are often characterized as “parsimonious” because they minimize the number of parameters that must be estimated. Although such models may seem to be highly idealized versions of physical reality, they are often surprisingly effective. For example, the Thornthwaite monthly water-balance model of box 6.8, the SCS-CN event-flow prediction model of section 10.6.4, and the convex streamflow-routing model of section 10.5.2 are conceptual models that have proved practically useful. A study by Clark et al. (2009) found that a model with parallel linear reservoirs provided the most plausible explanation of hillslope and watershed response to rainfall for an intensely studied watershed, and was consistent with flow paths identified by water chemistry (section

Table F.1 Terms Used to Characterize Hydrologic Process Models (see section F.3 for definitions of terms).

Physical Domain	Process	Simulation Basis
Vegetative canopy	Interception	Physically based
Snowpack	Snowmelt	Conceptual/heuristic
Unsaturated zone	Infiltration	Statistical (regression)
Aquifer	Overland flow	Stochastic (time series)
Hillslope	Unsaturated flow	
Stream reach	Transpiration	
Lake or reservoir	Ground-water flow/head	
Watershed	Evaporation	
Region/continent	Open-channel flow	
	Stream hydrograph	
	Integrated watershed/region	
Spatial Representation	Temporal Representation	Method of Solution
Lumped	Steady state	Ad hoc
Distributed	Steady state–seasonal	Formal-analytical
Coordinate system	Single event	Formal-numerical
two-dimensional	Continuous	Finite difference
three-dimensional		Finite element
circular		Other
		Hybrid

10.3) and with water-balance estimates of bedrock recharge (section 9.5.1).

Statistically based models use transfer functions developed by fitting plausible equation forms to observational data using regression techniques. The relation between snowmelt and air temperature shown in figure 5.31 and the determination of constants in the Philip infiltration equation described in box 8.3 are examples of this approach. A more sophisticated statistical approach described by Bulygina and Gupta (2009) uses Bayesian probability analysis to estimate the uncertain (probabilistic) mathematical structure of the transfer equations that are valid at the scale of available observations and conditioned on conceptual understanding of the physical processes.

Stochastic time-series models use transfer functions developed using statistical time-series-analysis techniques. These functions estimate a given rate from preceding values of that rate, and perhaps other observations. An example is the impulse-response model of ground-water recharge given in equation (9.35).

F.3.2.2 Spatial Representation

In **lumped models**, the region or watershed being modeled is treated as a single entity characterized by a single set of parameters such as slope, aspect, vegetation, soils, precipitation, temperature, etc. that are meant to be representative. Examples are (1) the Thornthwaite monthly water-balance model of box 6.8, where the watershed is characterized by a single parameter, the soil-water storage capacity $SOIL_{max}$; and (2) the linear-reservoir model of a watershed of section 10.2.5, where all the spatially varying properties that control the time of travel to the watershed outlet are characterized by the watershed response time, T^* .

By contrast, **distributed models** provide some representation of the spatial variability in the region being modeled. Distributed watershed models are often developed by linking lumped models of subwatersheds, or by dividing a watershed into a small number of subregions (e.g., upland and lowland) with differing parameters. More elaborate representations of spatial variability, such as subdividing the region by a grid system with model parameters that vary from cell to cell, are increasingly used to model hydrologic response of subcontinental to continental regions based on satellite observations of inputs and surface characteristics.

Where formal mathematical relations are the basis for a model, spatial variability can be captured by

use of **formal coordinate systems** of one, two, or three dimensions. This is most commonly done in ground-water flow models, as in the two-dimensional regional-flow models of section 9.2. As in those models, the coordinate system is usually orthogonal (Cartesian), but radial coordinates are used for ground-water models involving flows to or from wells (section 9.6.1.1).

Martina et al. (2011) explored how the essential features of the rainfall-runoff process at the “point” scale can be preserved at larger scales by integrating the point-scale differential equations over a grid cell, and from the grid cell to the watershed scale. An essential aspect of their approach was a relationship between the fraction of rainfall that infiltrates and the fraction of watershed area that is saturated (the same relation modeled by the TOPMODEL approach described in section 10.4.2.2). Their method can generate scale-independent models that preserve the physical meanings of physical parameters, which increases confidence in model predictions and forecasts.

F.3.2.3 Temporal Representation

In **steady-state models**, outputs represent a long-term-average, ultimate, or equilibrium magnitude of a quantity. The evaporation models described in sections 6.3 and 6.8, the regional ground-water flow models of section 9.2, and the Dupuit model of ground-water flow to streams of section 9.3.1.5 are examples. The outputs of **steady state–seasonal models**, such as the Thornthwaite water-balance model of box 6.8, are long-term average seasonal (monthly) values of one or more quantities.

Single-event models simulate response of a system to an isolated input, as in all the rainfall-runoff models discussed in section 10.6.4; inputs may be specified as a single value representing the total input over a time period (as in the unit-hydrograph model), or a sequence of input values. The outputs of **continuous models** are a sequence of responses to a sequence of inputs over a specific period; the time step of the sequence may be seconds to years. The Thornthwaite Continuous Model exercise found on the disk accompanying this text is a continuous model with a monthly time step (see *ThornContx.xls*).

F.3.2.4 Method of Solution

In most lumped models, computations follow a series of **ad hoc** algorithmic steps, as in the Thornthwaite monthly water-balance model of box 6.8. Other models implement **analytical solutions** to the basic differential equations that describe the process,

as in the Philip solution of the Richards equation of infiltration (section 8.4.2). Analytical solutions may be discretized and implemented in successive time steps, as in the Kirchner (2009) watershed described in section 1.12 [equation (1.51b)].

Where discretization of differential equations are the model basis (as in the regional ground-water flow models of section 9.2), **formal numerical methods** are used to solve the equations in a Cartesian or radial coordinate system using “finite difference” or “finite element” spatial-discretization schemes (Wang and Anderson 1982; Bear and Verruijt 1987). In formal continuous models, the spatial discretization is implemented in a sequence of discrete time steps. As pointed out by Clark and Kavetski (2010) and Kavetski and Clark (2010), numerical models with fixed time steps, which are very commonly used, can introduce errors that are much greater than errors arising from model conceptualization. These numerical artifacts can substantially degrade model predictions and lead to inconsistent and biased estimates of model parameters, but can also fortuitously compensate for model structural errors, giving “the right result for the wrong reason.”

Many hydrologic models use different solution methods for different processes within a model; these are called **hybrid models**. A common example in watershed models is the use of formal numerical solutions for soil-water movement and ad hoc methods for other processes.

F.4 The Modeling Process

An idealization of the modeling process is diagrammed in figure F.1; its major elements are (1) specification of the purposes of the model, (2) conceptualization of the problem, (3) **selection** or development of the appropriate model (“identification”), (4) **parameter estimation** (“calibration”), and (5) **acceptance testing** (“validation”). The terms indicated in bold type are preferable to the more commonly used terms in quotes, because they “remind us that a model is an abstraction of the physical process and not the physical process per se” (Matalas and Maddock 1976, p. 123).

F.4.1 Conceptualization of the Problem

Once the purposes of a model are established, the most important step in the modeling process is the determination of the overall form and essential

components of the model. These decisions must be based on a clear idea of the scientific or engineering purpose of the model, and this idea must be translated into an explicit formulation of the nature and form of the model output that is required, specifically

- the type of information required (e.g., peak flows, flow volumes, ground-water heads, soil-water contents, evapotranspiration rates);
- the required accuracy and precision of the output;
- the locations for which the output is required; and
- the time intervals for which the output is required.

Model conceptualization is dictated also by the nature and form of the information that is available about the available input data and the system being modeled, and by the resources and time available to collect needed additional information.

F.4.2 Model Selection or Development

Descriptions of or references to many widely used hydrologic models were given by DeVries and Hromadka (1992) and Kavetski and Clark (2010) for watershed models and by Anderson et al. (1992) for subsurface-flow models. New models are continually being developed, and many are readily available as computer software designed to be easily modified to apply to a particular situation. This state of affairs would seem to make the task of creating a model for a new situation easier. However, as noted by Clark et al. (2011b, p. 1),

The current overabundance of models is symptomatic of an insufficient scientific understanding of environmental dynamics at the catchment scale, which can be attributed to difficulties in measuring and representing the heterogeneity encountered in natural systems.

They recommend an approach to the development of realistic catchment-scale models that is embedded in a framework that rigorously scrutinizes hypotheses against observed data.

F.4.3 Parameter Estimation and Acceptance Testing

Both adjustable-parameter estimation and acceptance testing require measured values of input and output quantities for the prototype system of interest and involve numerical and/or graphical comparison of measured outputs to modeled outputs. This requires splitting the input data into a parameter-estimation

mation set (“calibration data”) and an acceptance-testing set (“validation data”). There are no firm rules for the proportion of the total data allocated to each set, but usually no more than half the data is allocated for acceptance testing. For some types of data the allocation can be done randomly, but for data representing a time sequence it is usually necessary to select a continuous period for parameter estimation and a prior or subsequent period for acceptance testing.

Although the canonical approach to model development (figure F.1) proceeds by first estimating parameters and then “validating” model results with new data, Vogel and Sankarasubramanian (2003) pointed out that once a watershed model is calibrated, the unavoidable model error can distort the validation process. Thus they recommend that validation be performed using covariance (section C.6.1) procedures before, and independent of, parameter estimation.

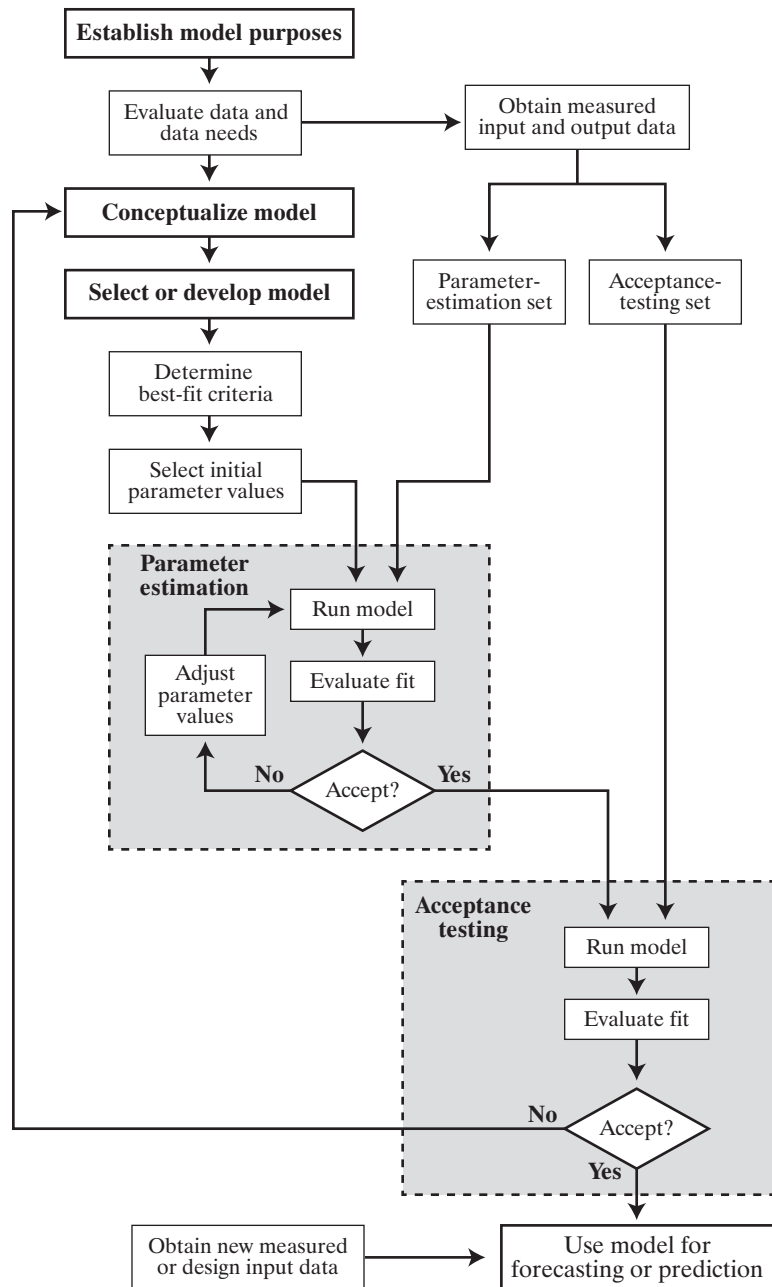


Figure F.1 Flow chart for the modeling process.

In both parameter estimation and acceptance testing it is important to focus on the purposes of the model. For example, the following aspects of model output might be more or less important in different contexts:

- the ability to reproduce the long-term or spatial mean value of a quantity;
- the ability to reproduce overall variability (e.g., the standard deviation or range of the quantity);
- the ability to minimize *absolute errors* (errors as measured in the units in which the quantity is measured; e.g., streamflows in m³/s, see section F.5);
- the ability to minimize *relative errors* (errors expressed as a percentage or fraction of the mean, see section F.5);
- the ability to reproduce high values of a quantity (e.g., peak streamflows);
- the ability to reproduce low values of a quantity (e.g., drought streamflows); and
- the ability to reproduce patterns of seasonal or spatial variability.

It is also important to remember that measured values of model inputs and outputs are themselves more or less in error (section 1.11.2) due to instrumental limitations and/or the inherent inability of observational networks like rain gauges or wells to capture the temporal and/or spatial variability of input or output quantities. To the extent that such errors exist, they will be propagated in the modeling computations and parameter selection and evaluation of model performance will be subject to error.

F.4.3.1 Parameter Estimation (“Calibration”)

The objective of parameter estimation is to determine appropriate values for adjustable model parameters. To do this, the input data of the parameter-estimation set are entered into the model and the values of parameters are systematically adjusted (“tuned”) to determine which values give the “best” fit between the modeled and the measured outputs according to predetermined criteria (section F.5).

Although conceptually straightforward, the parameter-estimation process is often fraught with difficulty and ambiguity, especially in multiparameter models, because:

- Very different sets of parameter values may give nearly equivalent fits; this is the problem of **equifinality** (Beven and Freer 2001; Beven 2006).

- Model outputs may be insensitive to the values of one or more parameters.
- One or more “best-fit” parameter values may differ greatly from what seems intuitively reasonable.
- “Best-fit” parameter values may differ in different time periods or at different scales (Merz et al. 2011).

When these situations occur, confidence in a model’s ability to simulate the situation of interest is diminished.

F.4.3.2 Acceptance Testing (“Validation”)

Once the parameter values are selected, performance testing leading to acceptance or rejection of the model for a particular application should be evaluated by graphical and/or numerical comparison of modeled and measured outputs *for situations not used in parameter estimation*. Goodness-of-fit can be judged qualitatively by visual comparison of measured and simulated hydrographs or flow-duration curves or of scatter plots of simulated versus actual output quantities. Numerical measures of goodness-of-fit are discussed in section F.5. If a model does not satisfactorily simulate the measured values, a new model, perhaps based on a revised conceptualization of the situation, should be developed.

F.5 Model Evaluation

Klemeš (1986b) and Clark et al. (2011b) provided excellent discussions of the philosophy and process of testing simulation models. Numerical measures of model goodness-of-fit are reviewed by Nash and Sutcliffe (1970), Garrick et al. (1978), World Meteorological Organization (1986a), and Martinec and Rango (1989), and many are described in box F.1. However, a recent study by Ritter and Muñoz-Carpena (2013) noted that all numerical criteria have limitations and are often subjective and ambiguous, leading to incorrect model verification. The papers by Vogel and Sankarasubramanian (2003), Blöschl (2006), McDonnell et al. (2007), Bullygina and Gupta (2009), Clark et al. (2009, 2011b), and Kumar (2011) also explore the topic of model development and selection in depth.

Studies comparing models have been published by the World Meteorological Organization (1986b, 1992), Perrin et al. (2001), and Vansteenkiste et al. (2014), among others.

Box F.1 Some Numerical Criteria for Model “Calibration” and “Validation”

Here we introduce some numerical criteria that may be used to evaluate the degree to which modeled output reproduces measured output in the parameter-estimation (“calibration”) and acceptance-testing (“validation”) phases of model development, and for comparing performance among models. Note that (1) it is often useful to apply these criteria separately for different flow ranges, different seasons, and different years and (2) no combination of numerical criteria can truly validate a model (section F.6, box F.2).

In the following, we consider that we have a time series of $i = 1, 2, \dots, N$ measured values x_i (the “calibration” or “validation” data) and corresponding model-simulated values ξ_i .

Actual Error

Actual error, e_i , is defined as

$$e_i \equiv \xi_i - x_i. \quad (\text{FB1.1})$$

- Minimize average absolute error, $\mu_{|e|}$

$$\mu_{|e|} = \frac{1}{N} \cdot \sum_{i=1}^N |e_i|. \quad (\text{FB1.2})$$

- Minimize estimation **bias**, represented as **average error**, μ_e

$$\mu_e = \frac{1}{N} \cdot \sum_{i=1}^N e_i. \quad (\text{FB1.3})$$

- Assess model fit by regressing model estimates ξ_i against measured values x_i , resulting in

$$\xi_i = a_1 + b_1 \cdot x_i + \varepsilon_i, \quad (\text{FB1.4})$$

where a_1 is the regression constant, b_1 the regression slope, and ε_i the regression-model error. Better fit is represented by smaller values of $|a_1|$, $|b_1 - 1|$, and average $|\varepsilon_i|$; the latter is equivalent to larger values of the coefficient of determination for the regression, R^2 .

- Assess model **precision** by smaller values of the **standard deviation of error**, σ_e ,

$$\sigma_e = \left[\frac{1}{N-1} \cdot \sum_{i=1}^N (e_i - \mu_e)^2 \right]^{1/2}. \quad (\text{FB1.5})$$

- Assess the combination of accuracy and precision as smaller values of the **root-mean-square error**, **RMSE**,

$$RMSE = \left[\frac{1}{N} \cdot \sum_{i=1}^N e_i^2 \right]^{1/2} = \left(\mu_e^2 + \sigma_e^2 \right)^{1/2}. \quad (\text{FB1.6})$$

Relative Error

Relative error, r_i , is

$$r_i \equiv \frac{\xi_i - x_i}{x_i} = \frac{e_i}{x_i}. \quad (\text{FB1.7})$$

Many hydrologic variables cannot take on negative values. For these, the minimum possible value for r_i is -1 , whereas the maximum is unbounded. To avoid this asymmetry when comparing relative values, we can compare the statistics of the logarithmic error, Le_i , where

$$\begin{aligned} Le_i &\equiv \log(\xi_i) - \log(x_i) \\ &= \log\left(\frac{\xi_i}{x_i}\right) = \log(r_i + 1). \end{aligned} \quad (\text{FB1.8})$$

- Bias in relative error is proportional to the value of μ_{Le} , where

$$\mu_{Le} = \frac{1}{N} \cdot \sum_{i=1}^N Le_i. \quad (\text{FB1.9})$$

- Relative model fit can be assessed by regressing model estimates $\log(\xi_i)$ against measured values $\log(x_i)$, resulting in

$$\log(\xi_i) = a_2 + b_2 \cdot \log(x_i) + L\varepsilon_i, \quad (\text{FB1.10})$$

where a_2 is the regression constant, b_2 the regression slope, and $L\varepsilon_i$ the regression-model error. Better fit is represented by smaller values of $|a_2|$, $|b_2 - 1|$, and average $|L\varepsilon_i|$; the latter is equivalent to larger values of the coefficient of determination for the regression, R^2 .

- Assess relative model precision by smaller values of the **standard deviation of relative error**, σ_{Le} ,

$$\sigma_{Le} = \left[\frac{1}{N-1} \cdot \sum_{i=1}^N (Le_i - \mu_{Le})^2 \right]^{1/2}. \quad (\text{FB1.11})$$

(continued)

9. Assess the combination of relative accuracy and precision as smaller values of the **root-mean-square relative error, RMSLE**,

$$RMSLE = \left[\frac{1}{N} \cdot \sum_{i=1}^N Le_i^2 \right]^{1/2} = (\mu_{Le}^2 + \sigma_{Le}^2)^{1/2}. \quad (\text{FB1.12})$$

10. A widely used measure of model relative error is the **Nash–Sutcliffe coefficient, R_{NS}** , where

$$R_{NS}^2 = 1 - \frac{\sum_{i=1}^N (x_i - \xi_i)^2}{\sum_{i=1}^N (x_i - \mu_x)^2} \quad (\text{FB1.13})$$

(Nash and Sutcliffe 1970). R_{NS} increases in proportion to the extent to which model output improves estimation above that achieved by simply assuming the mean value of the observed values.

F.6 Final Words of Caution

Developing and working with computer-simulation models is challenging and fun, and it can be done in a comfortable room with a coffee cup at hand. Collection of data in the field is also challenging and sometimes fun, but often uncomfortable, tedious, frustrating, and expensive. Thus, although computer models have greatly facilitated the science of hydrology and its application, and will play an increasing role in the future, we must continually remind ourselves that the goal is to understand and predict nature, not to demonstrate our cleverness.

Models are essential tools for almost all practical applications of hydrology and can be powerful aids in scientific analysis. However, anyone seeking to use a model to provide predictions or forecasts that will be used for critical design, operational applications, or

scientific decisions should first review the discussions by Matalas and Maddock (1976), Dooge (1986), Klemeš (1986b), Beven (1993), Oreskes et al. (1994), and Perrin et al. (2001). Some of their insights are summarized in box F.2; the collective wisdom of these discussions can be summarized as follows:

Although acceptable parameter values can be determined for almost any model, in most cases the parameters are not unique and may not be transferable to new situations. And, because of the inevitable errors in measured data and the impossibility of representing the space-time continuum of nature as a finite array of space-time points, no model can be validated as a true simulation of nature.

Box F.2 Some Insights on Simulation Modeling in Hydrology**Dooge (1986, p. 49S)**

Many . . . modelers seem to follow . . . the example of Pygmalion, the sculptor of Cyprus, who carved a statue so beautiful that he fell deeply in love with his own creation. It is to be feared that a number of hydrologists fall in love with the models they create. In hydrology, . . . the proliferation of models has not been matched by the development of criteria for the evaluation of their effectiveness in reproducing the relevant properties of the prototype.

Oreskes et al. (1994, p. 641)

Verification and validation of numerical models of natural systems is impossible. This is because natural systems are never closed and because model results are always non-unique. Models can be confirmed by the demonstration of agreement between observation and prediction, but confirmation is inherently partial. Complete confirmation is logically precluded by the fallacy of affirming the consequent and by incomplete access to natural phenomena. Models can only be evaluated in relative terms, and their predictive value is always open to question. The primary value of models is heuristic: Models are representations, useful for guiding further study but not susceptible to proof.

Kirchner (2006, p. 1)

[S]cientific progress will mostly be achieved through the collision of theory and data, rather than through

increasingly elaborate and parameter-rich models that may succeed as mathematical marionettes, dancing to match the calibration data even if their underlying premises are unrealistic. Thus advancing the science of hydrology will require not only developing theories that get the right answers but also testing whether they get the right answers for the right reasons.

McDonnell et al. (2007, p. 1)

In spite of their apparent physical basis and complexity, the current generation of detailed models is process weak. . . . In order to make continued progress in watershed hydrology and to bring greater coherence to the science, we need to move beyond the status quo of having to explicitly characterize or prescribe landscape heterogeneity in our (highly calibrated) models and in this way reproduce process complexity and instead explore the set of organizing principles that might underlie the heterogeneity and complexity.

Doherty (2011, p. 455)

Modeling should constitute a scientific expression of our ignorance rather than a claim to knowledge that we do not possess. . . . Learning how to define and locate the optimal compromise between simplicity and complexity is one of the biggest problems facing current modeling practice.

Development of Scientific Hydrology

This brief overview is based on the books by Adams (1938), Rouse and Ince (1957), Biswas (1970), Nace (1974), and Eagleson et al. (1991), as well as Brutsaert's (1992) detailed examination of the evolution of theories on the origins of springs and rivers.

Humans have been concerned with managing water as a necessity of life and as a potential hazard at least since the first civilizations developed along the banks of rivers. Hydraulic engineers built functioning canals, levees, dams, subterranean water conduits, and wells along the Indus in Pakistan, the Tigris and Euphrates in Mesopotamia, the Hwang Ho in China, and the Nile in Egypt as early as 5,000–6,000 years ago (BP). Hydroclimatologic information was vital to these civilizations; monitoring of river flows was begun by the Egyptians about 3800 BP, and the first known rainfall measurements were taken by the Kautilya of India by 2400 BP. The concept of a global hydrologic cycle dates from at least 2400 BP, when it was written by Ecclesiastes (1:7) that

All the rivers run into the sea; yet the sea is not full; unto the place from whence the rivers come, thither they return again.

Other, even earlier, texts in the Hebrew, Chinese, and Indian traditions seem also to refer to the global hydrologic cycle, and the concept appears in the writings of early Greek philosophers such as Thales, Anaxagoras, Herodotus, Hippocrates, Plato, and Aristotle.

However, the question of the origin of rivers and springs, i.e., the mechanism by which sea water returned to land as fresh water to complete the cycle, was disputed and continued to be a subject of specu-

lation and debate into the eighteenth century. Over these years, various writers espoused one or more of the following theories, which were first articulated by Greek writers:

- Ocean water extends under the land, loses its salt by filtration as it rises through the earth, and condenses to form rivers and springs [theory of Hippo (fifth century BCE)].
- Rivers and springs receive water from percolating rain, but this is insufficient to maintain river flows and the main source is condensation of water vapor from air rising within the earth [theory of Aristotle (384–322 BCE)].
- Rivers and springs originate only from rain [theory of Anaxagoras (500–428 BCE) and others].

The Romans had extensive practical knowledge of hydrology, especially hydraulics, and developed extensive aqueduct systems (many of which are still standing), but did little to advance scientific ideas beyond those of the Greeks. An exception was Vitruvius (first century BCE), a Roman architect and civil engineer who concluded in his well-known treatise *De Architectura* that rain and snowmelt were the sole source of springs.

The above theories on the origin of rivers and springs continued to be debated into the Middle Ages, the Renaissance, and beyond; even Leonardo da Vinci (1452–1519) and René Descartes (1596–1650) espoused the sea-water filtration theory. However, the Frenchman Bernard Palissy (1510–1589) concluded on the basis of field observations that the water in rivers comes from precipitation, and he and

countryman Guillaume de Salluste du Bartas (1544–1590) gave descriptions of the origins of springs and rivers that are “close to the rainfall percolation mechanism as it is known today” (Brutsaert 1992, p. 571).

By 1674 Pierre Perrault (French, 1608–1680), in his book *On the Origin of Springs*, characterized the percolation theory as the “common opinion.” However, he himself thought that the main cause of springs was vapor rising within the earth, even though he had made calculations showing that the annual flow of the upper Seine River was only one-sixth of the precipitation on its watershed. Interestingly, his rejection of the percolation theory was based on his own experiments that seemed to indicate that infiltrated precipitation could not flow laterally to rivers.

Even though Perrault came to the incorrect conclusion about the origin of rivers, his work initiated the modern measurement-based approach to the hydrologic cycle. The other major contemporary contributor was Edmé Mariotte (French, 1620–1684). His book *Treatise on the Movement of the Waters and of the Other Fluid Bodies* (1686) affirmed the percolation theory based on (1) his observations of water in soils and (2) his measurements and calculations of the flow of the Seine at Paris and the precipitation on its watershed, which showed, like Perrault, that the flow was less than one-sixth the rainfall. As noted by Brutsaert (1992, p. 579),

Mariotte’s work is without question one of the highlights in the history of hydrology. His treatment is clear and sound enough that it would not be out of place in present-day descriptions . . . His determination of the river discharge rate is based on solid reasoning, and therefore his comparison between precipitation and river flow is a marked improvement over Perrault’s calculation a decade earlier. In addition, he shows cogently by different examples that rain does penetrate the soil in sufficiently large quantities and to sufficiently large depths to be the only possible cause of springs.

However, the question was not settled, due in part to the work of P. LaHire (French, 1640–1718), whose experiments on water flow in soils (1703) seemed to support Perrault’s conclusion and refute the percolation theory. The well-known British astronomer Edmund Halley (1656–1741) also concluded, based on his studies of evaporation (1691), that one source of rivers is water vapor that enters directly into the earth, collects in caverns, and then breaks out through the hillsides as springs. In spite of

this error, Halley contributed to the development of hydrologic science by being the first to conduct a quantitative water-balance study (1687): He estimated the amounts of water involved in the ocean-atmosphere-rivers-ocean cycle of the Mediterranean Sea and its watershed, concluding that river inflow was about one-third of evaporation loss, with the rest of the inflow from precipitation.

The percolation theory continued to gain strength into the eighteenth century, in part through the works of the English naturalist John Ray (1627–1705) and the Dutch physicist Pieter Van Musschenbroek (1692–1761). However, it is clear from the writings of the famous English scientist John Dalton (1766–1844) that various theories were still being discussed in 1799. Part of the problem was the persistent erroneous perception that rainfall was generally insufficient to supply river flow (in spite of the calculations by Perrault and Mariotte) and the difficulty in gathering areal rainfall data and streamflow measurements. However, Dalton did estimate precipitation, evaporation, and streamflow for England and Wales and concluded in 1802 that

[W]e may fairly conclude that the rain and dew of this country are equivalent to the quantity of water carried off by evaporation and by the rivers. And, as nature acts upon general laws, we ought to infer, that it must be the case in every other country, till the contrary is proved. (as quoted in Brutsaert 1992, p. 584)

The eighteenth century saw major advances in applications of mathematics to fluid mechanics and hydraulics by Henri de Pitot (1695–1771), Daniel Bernoulli (1700–1782), Leonhard Euler (1707–1783), Antoine de Chézy (1718–1798), Joseph Lagrange (1736–1813), Pierre Laplace (1749–1827), and others in Europe. Use of the term “hydrology” in approximately its current meaning began about 1750. By about 1800 Dalton had firmly established the nature of evaporation and the present concepts of the global hydrologic cycle, and James Hutton (1726–1797) and John Playfair (1748–1819) had published scientific work on the fluvial erosion of valleys. Routine network measurements of precipitation began before 1800 in Europe and the United States, and were well established there and in India by 1820.

A major reason for the persistence of erroneous ideas about the origin of rivers and the nature of the global hydrologic cycle was ignorance of the process

of ground-water flow. This ignorance lasted until 1856, when the French engineer Henry Darcy (1803–1858) established the basic phenomenological law of flow through porous material. The nineteenth century also saw many advances in fluid mechanics, open-channel hydraulics, and sediment transport by J.-C. B. de Saint-Venant (1797–1886), Jean Poiseuille (1799–1869), A. J. E. J. Dupuit (1804–1866), Robert Manning (1816–1897), George Stokes (1819–1903), Osborne Reynolds (1842–1912), P. F. D. DuBoys (1847–1924), and others whose names have become associated with basic laws or principles underlying hydrologic science.

The first major book devoted to hydrology was the *Manual of Hydrology* (1862) by the Englishman Nathaniel Beardmore (1816–1872), which contained sections on hydraulic and other tables; rivers, flow of water, springs, wells, and percolation; tides, estuaries, and tidal rivers; and rainfall and evaporation. Treatises on other aspects of hydrology appeared with increasing frequency in the last half of the nineteenth century. Many of these works examined relations between rainfall amounts and streamflow rates due to the need to estimate flood flows for the design of bridges and other structures. This was the beginning of a close association between hydrology and civil engineering; the first English-language texts in hydrology were those of Daniel Mead in 1904 and Adolf Meyer in 1919, which were written for civil engineers. This association has in some respects enhanced, and in other respects may have inhibited, the development of hydrology as a science.

The first half of the twentieth century saw great progress in many aspects of hydrology and, with the formation of the Section of Scientific Hydrology in the International Union of Geodesy and Geophysics (1922) and the Hydrology Section of the American Geophysical Union (1930), the formal recognition of hydrology as a major branch of earth sciences. Among those contributing notably to advances in particular areas in the early and middle decades of the century were: A. Hazen, E. J. Gumbel, H. E.

Hurst, and W. B. Langbein in the application of statistics to hydrologic data; O. E. Meinzer, C. V. Theis, C. S. Slichter, and M. K. Hubbert in the development of the theoretical and practical aspects of ground-water hydraulics; L. Prandtl, T. von Kármán, H. Rouse, V. T. Chow, G. K. Gilbert, and H. A. Einstein in stream hydraulics and sediment transport; R. E. Horton, L. B. Leopold, M. G. Wolman, and T. E. Dunne in understanding runoff processes and quantitative geomorphology; and W. Thornthwaite, H. E. Penman, J. L. Monteith, and W. Brutsaert in understanding and modeling evapotranspiration.

Although the long-standing dispute about the source of streamflow has been resolved for two centuries, it is interesting that detailed field studies to understand the exact mechanisms of runoff production began only with R. E. Horton in the 1930s and T. E. Dunne in the 1960s. Study of these processes remains a very active area of research, now enhanced by new methods for identifying and tracing runoff components (section 10.3). The search for appropriate approaches to modeling runoff processes at different scales remains a significant challenge (appendix F).

The need for hydrologic understanding is as essential for sustaining human society today as it was for the first civilizations. Advances in this understanding are accelerating in the early twenty-first century, and new scientific questions are emerging. Developments in instrumentation, satellite observation, computing power, and availability of large regional and global data sets are making possible new progress on formerly intractable questions, including the determination of regional storage changes, assessment of regional precipitation and snowpack properties, the movement of ground water in rock fractures, the relation between ground water and surface water, the relations between hydrologic behavior at different scales, the relation of hydrologic regimes to past and future climates, and the interaction of hydrologic processes and landform development. We can look forward to steady progress in scientific hydrology.

References

- Abdul, A. S., and R. W. Gillham (1984). Laboratory studies of the effects of the capillary fringe on streamflow generation. *Water Resources Research* 20:691–698.
- Abdul, A. S., and R. W. Gillham (1989). Field studies of the effects of the capillary fringe on streamflow generation. *Journal of Hydrology* 112:1–18.
- Abrahams, A. D., A. J. Parsons, and S.-H. Luk (1986). Resistance to overland flow on desert hillslopes. *Journal of Hydrology* 88:343–363.
- Abramowitz, G., L. Pouyanné, and H. Ajami (2012). On the information content of surface meteorology for downward atmospheric long-wave radiation. *Geophysical Research Letters* 39(5), doi:10.1029/2011GL050726.
- Adam, J. C., and D. P. Lettenmaier (2003). Adjustment of global gridded precipitation for systematic bias. *Journal of Geophysical Research: Atmospheres* 108(D9):4257, doi:10.1029/2002JD002499.
- Adams, F. D. (1938). *The Birth and Development of the Geological Sciences*. Baltimore, MD: Williams and Wilkins.
- Adams, W. P. (1976). Areal differentiation of snow cover in east central Ontario. *Water Resources Research* 12:1226–1234.
- AghaKouchak, A., A. Behrangi, S. Sorooshian, K. Hsu, and E. Amitai (2011). Evaluation of satellite-retrieved extreme precipitation rates across the central United States. *Journal of Geophysical Research: Atmospheres* 116(D02115), doi:10.1029/2010JD014741.
- Akinbile, C. (2010). Comparative analysis of infiltration measurements of two irrigated soils in Akure, Nigeria. *Advances in Applied Science Research* 1:49–57.
- Aksoy, H., I. Kurt, and E. Eris (2009). Filtered smoothed minima baseflow separation method. *Journal of Hydrology* 372:94–101.
- Alam, M., and T. P. Trooien (2001). Estimating reference evapotranspiration with an atmometer. *Applied Engineering in Agriculture* 17(2):153–158.
- Allaire, S. A., S. Roulier, A. J. Cessna (2009). Quantifying preferential flow in soils: A review of different techniques. *Journal of Hydrology* 378:179–204.
- Allen, M. R., and W. J. Ingram (2002). Constraints on future changes in climate and the hydrologic cycle. *Nature* 419:224–232.
- Allen, R. G., M. E. Jensen, J. L. Wright, and R. D. Burman (1989). Operational estimates of reference evapotranspiration. *Agronomy Journal* 81:650–662.
- Allen, R. G., L. S. Pereira, D. Raes, and M. Smith (1998). *Crop Evapotranspiration—Guidelines for Computing Crop Water Requirements*. Irrigation and Drainage Paper 56. Rome: United Nations Food and Agriculture Organization.
- Alley, W. M. (1984). On the treatment of evapotranspiration, soil moisture accounting, and aquifer recharge in monthly water balance models. *Water Resources Research* 20:1137–1149.
- Allison, G. B., and C. J. Barnes (1983). Estimation of evaporation from non-vegetated surfaces using natural deuterium. *Nature* 301:143–145.
- Allison, G. B., W. J. Stone, and M. W. Hughes (1984). Recharge in karst and dune elements of a semi-arid landscape as indicated by natural isotopes and chloride. *Journal of Hydrology* 76:1–25.
- Amarasekera, K. N., R. F. Lee, E. R. Williams, and E. A. B. Eltahir (1997). ENSO and the natural variability in the flow of tropical rivers. *Journal of Hydrology* 200:24–39.
- Ambroise, B., K. Beven, and J. Freer (1996). Toward a generalization of the TOP-MODEL concepts: Topographic indices of hydrological similarity. *Water Resources Research* 32:2135–2145.
- American Meteorological Society (1992). Policy statement: Planned and inadvertent weather modification. *Bulletin of the American Meteorological Society* 73:331–337.
- Amorochio, J., and W. E. Hart (1965). The use of laboratory catchments in the study of hydrologic systems. *Journal of Hydrology* 3:106–123.
- Anagnostou, M. N., J. Kalogiros, E. N. Anagnostou, M. Tarolli, A. Papadopoulos, and M. Borga (2010). Performance evaluation of high-resolution rainfall estimation by X-band dual-polarization radar for flash-flood applications in mountainous basins. *Journal of Hydrology* 394(1–2):4–16.
- Anderson, E. A. (1968). Development and testing of snow pack energy balance equations. *Water Resources Research* 4:19–37.
- Anderson, E. A. (1973). *National Weather Service River Forecast System—Snow Accumulation and Ablation Model*. NWS Technical Memorandum HYDRO-17. Silver Spring, MD: US National Oceanic and Atmospheric Administration.
- Anderson, E. A. (1976). *A Point Energy and Mass Balance Model of a Snow Cover*. NOAA Technical Report NWS-19. Silver Spring, MD: US National Oceanic and Atmospheric Administration.
- Anderson, E. A., H. J. Greenan, R. Z. Whipple, and C. T. Machell (1977). *NOAA-ARS Cooperative Snow Research Project Watershed Hydro-Climatology and Data for Water Years 1960–1974*. US National Oceanic and Atmospheric Administration and US Agricultural Research Service.
- Anderson, M. G., and T. P. Burt (1977). A laboratory model to investigate the soil moisture conditions on a draining slope. *Journal of Hydrology* 33:383–390.
- Anderson, M. G., and T. P. Burt (1980). Interpretation of recession flow. *Journal of Hydrology* 46:89–101.
- Anderson, M. P., and X. Cheng (1993). Long- and short-term transience in a groundwater/lake system in Wisconsin, USA. *Journal of Hydrology* 145:1–18.
- Anderson, M. P., D. S. Ward, E. G. Lappala, and T. A. Prickett (1992). Computer models for subsurface water. In D. R. Maidment, ed., *Handbook of Hydrology* (chapter 22). New York: McGraw-Hill.
- Andreadis, K. M., P. Storck, and D. P. Lettenmaier (2009). Modeling snow accumulation and ablation processes in forested environments. *Water Resources Research* 45:W05429, doi:10.1029/2008WR007042.
- Arkin, P., and P. Ardanuy (1989). Estimating climatic-scale precipitation from space: A review. *Journal of Climate* 2:1229–1238.

- Arndt, D. S., M. O. Baringer, and M. R. Johnson, eds. (2010). State of the Climate in 2009. Special Supplement, *Bulletin of the American Meteorological Society* 91(7):S1–S224.
- Arnold, J. G., and P. M. Allen (1999). Automated methods for estimating baseflow and ground water recharge from streamflow records. *Journal of the American Water Resources Association* 35:411–424.
- Askew, A. J. (1970). Derivation of formulae for variable lag time. *Journal of Hydrology* 10:225–242.
- Assouline, S., and Y. Mualem (1997). Modeling the dynamics of seal formation and its effect on infiltration as related to soil and rainfall characteristics. *Water Resources Research* 33:1527–1536.
- Auer, A. H., Jr. (1974). The rain versus snow threshold temperature. *Weatherwise* 27:67.
- Badescu, V. (2008). *Modeling Solar Radiation at the Earth's Surface: Recent Advances*. Berlin/Heidelberg: Springer.
- Barlow, M. (2011). Influence of hurricane-related activity on North American extreme precipitation. *Geophysical Research Letters* 38:L04705, doi:10.1029/2010GL046258.
- Barnes, H. B. (1967). *Roughness Characteristics of Natural Channels*. Water-Supply Paper 1849. Washington, DC: US Geological Survey.
- Barnett, T. P., L. Dumenil, U. Schleser, and E. Roeckner (1988). The effect of Eurasian snow cover on global climate. *Science* 239:504–507.
- Barrett, J. P., and L. Goldsmith (1976). When is n large enough? *The American Statistician* 30:67–71.
- Barros, A. P., and D. P. Lettenmaier (1994). Dynamic modeling of orographically induced precipitation. *Reviews of Geophysics* 32:265–284.
- Barry, D. A., J.-Y. Parlange, and L. Li (2000). Approximation for the exponential integral (Theis well function). *Journal of Hydrology* 227:287–291.
- Barry, R. G., and R. J. Chorley (1982). *Atmosphere, Weather, and Climate*. New York: Methuen & Co.
- Barry, R. G., and R. J. Chorley (1987). *Atmosphere, Weather, and Climate* (5th ed.). New York: Methuen & Co.
- Barthold, F. K., C. Tyralla, K. Schneider, K. B. Vaché, H.-G. Frede, and L. Breuer (2011). How many tracers do we need for end member mixing analysis (EMMA)? A sensitivity analysis. *Water Resources Research* 47:W08519, doi:10.1029/2011WR010604.
- Barton, M. (1974). New concepts in snow surveying to meet expanding needs. *Advanced Concepts Technical Study on Snow and Ice Resources*. Washington, DC: National Academy of Sciences.
- Bazemore, D. E., K. N. Eshleman, and K. J. Hollenbeck (1994). The role of soil water in stormflow generation in a forested headwater catchment: Synthesis of natural tracer and hydrometric evidence. *Journal of Hydrology* 162:47–75.
- Bear, J. (1979). *Hydraulics of Groundwater*. New York: McGraw-Hill.
- Bear, J., and A. Verruijt (1987). *Modeling Groundwater Flow and Pollution*. Dordrecht, Netherlands: D. Reidel.
- Beckers, J., and Y. Alila (2004). A model of rapid preferential hillslope run-off contributions to peak flow generation in a temperate rain forest watershed. *Water Resources Research* 40:W03501, doi:10.1029/2003WR002582.
- Behrangi, A., B. Khakbaz, T. C. Jaw, A. Agha-Kouchak, K. Hsu, and S. Sorooshian (2011). Hydrologic evaluation of satellite precipitation products over a mid-size basin. *Journal of Hydrology* 397(3–4):225–237.
- Bell, J. P., T. J. Dean, and M. G. Hodnett (1987). Soil moisture measurement by an improved capacitance technique, part II. Field techniques, evaluation, and calibration. *Journal of Hydrology* 93:79–90.
- Ben-Asher, J., P. Alpert, and A. Ben-Zvi (2010). Dew is a major factor affecting vegetation water use efficiency rather than a source of water in the eastern Mediterranean area. *Water Resources Research* 46:W10532, doi:10.1029/2008WR007484.
- Bengtsson, L. (1982). Percolation of meltwater through snowpack. *Cold Regions Science and Technology* 6: 73–81.
- Bengtsson, L. (1988). Movement of meltwater in small basins. *Nordic Hydrology* 19:237–244.
- Benton, G. S., R. T. Blackburn, and V. O. Snead (1950). The role of the atmosphere in the hydrologic cycle. *American Geophysical Union Transactions* 31:61–73.
- Beran, M. A., and J. V. Sutcliffe (1972). An index of flood-producing rainfall based on rainfall and soil-moisture deficit. *Journal of Hydrology* 17:229–236.
- Bergstrom, S., and M. Brandt (1985). Measurement of areal water equivalent of snow by natural gamma radiation—experiences from northern Sweden. *Hydrological Sciences Journal* 30:465.
- Bergstrom, S., and L. P. Graham (1998). On the scale problem in hydrologic modeling. *Journal of Hydrology* 211:253–265.
- Berkowicz, R., and L. P. Prahm (1982). Sensible heat flux estimated from routine meteorological data by the resistance method. *Journal of Applied Meteorology* 21:1845–1864.
- Berndt, H. W., and W. B. Fowler (1969). Rime and hoarfrost in upper-slope forests of eastern Washington. *Journal of Forestry* 67:92–95.
- Berndtsson, R. (1987). Application of infiltration equations to a catchment with large spatial variability in infiltration. *Hydrological Sciences Journal* 32:399–413.
- Berndtsson, R., and M. Larson (1987). Spatial variability of infiltration in a semi-arid environment. *Journal of Hydrology* 90:117–133.
- Berner, E. K., and R. A. Berner (1987). *The Global Water Cycle*. Englewood Cliffs, NJ: Prentice-Hall.
- Berry, M. O. (1981). Snow and climate. Chap. 2 in Gray and Male (1981).
- Bethlahmy, N. (1976). The two-axis method: A new method to calculate average precipitation over a basin. *Hydrological Sciences Bulletin* 21:379–385.
- Betson, R. P. (1964). What is watershed runoff? *Journal of Geophysical Research* 69:1541–1552.
- Beven, K. (1981). Kinematic subsurface stormflow. *Water Resources Research* 17:1419–1424.
- Beven, K. (1982a). On subsurface stormflow: Predictions with simple kinematic theory for saturated and unsaturated flows. *Water Resources Research* 18:1627–1633.
- Beven, K. (1982b). On subsurface stormflow: An analysis of response times. *Hydrological Sciences Journal* 4:505–521.
- Beven, K. (1984). Infiltration into a class of vertically non-uniform soils. *Hydrological Sciences Journal* 29:425–434.
- Beven, K. (1989). Changing ideas in hydrology—the case of physically-based models. *Journal of Hydrology* 105:157–172.
- Beven, K. (1993). Prophesy, reality and uncertainty in distributed hydrological modeling. *Advances in Water Resources* 16(1):41–51.
- Beven, K. (1997). TOPMODEL: A critique. *Hydrological Processes* 11:1069–1085.
- Beven, K. (2006). Searching for the Holy Grail of scientific hydrology: $Q_t = (S, R, ?)A$ as closure. *Hydrology and Earth System Sciences* 10:609–618.
- Beven, K. J., and J. E. Freer (2001). Equifinality, data assimilation, and uncertainty estimation in mechanistic modeling of complex environmental systems using the GLUE methodology. *Journal of Hydrology* 249:11–29.
- Beven, K., and P. Germann (1982). Macropores and water flow in soils. *Water Resources Research* 18:1311–1325.
- Beven, K., and P. Germann (2013). Macropores and water flow in soils revisited. *Water Resources Research* 49, doi:10.1002/wrcr.20156.
- Beven, K., and M. J. Kirkby (1979). A physically-based variable contributing-area model of catchment hydrology. *Hydrological Science Bulletin* 24(1):43–69.
- Beven, K., and E. F. Wood (1993). Flow routing and the hydrological response of channel networks. In K. Beven and M. J. Kirkby, eds. *Channel Network Hydrology* (chapter 5). New York: John Wiley.
- Birgand, F., G. Lellouche, and T. W. Appelboom (2013). Measuring flow in non-ideal conditions for short-term projects: Uncertainties associated with the use of stage-discharge rating curves. *Journal of Hydrology* 503:186–195.
- Bissell, V. C., and E. L. Peck (1973). Monitoring snow water equivalent by using natural soil radioactivity. *Water Resources Research* 9:885–890.
- Biswas, A. K. (1970). *History of Hydrology*. Amsterdam: North-Holland Publishing Co.
- Biswas, T. D., D. R. Nielsen, and J. W. Biggar (1966). Redistribution of soil water after infiltration. *Water Resources Research* 2:513–524.
- Bjerkie, D. M. (2007). Estimating the bankfull velocity and discharge for rivers using remotely sensed river morphology information. *Journal of Hydrology* 341:144–155.
- Bjerkie, D. M., S. L. Dingman, C. J. Vörösmarty, C. H. Bolster, and R. G. Congalton (2003). Evaluating the potential for measuring river discharge from space. *Journal of Hydrology* 278:17–38.

- Bjerklie, D. M., D. Moller, L. C. Smith, and S. L. Dingman (2005). Estimating discharge in rivers using remotely sensed hydraulic information. *Journal of Hydrology* 309:191–209.
- Black, P. E. (1970). Runoff from watershed models. *Water Resources Research* 6(2):465–477.
- Black, P. E. (1975). Runoff from watershed models. *Water Resources Research* 6:465–477.
- Black, T. A., W. R. Gardner, and C. B. Tanner (1970). Water storage and drainage under a row crop on a sandy soil. *Agronomy Journal* 62:46–51.
- Bland, W. L., P. A. Helmke, and J. M. Baker. (1997). High-resolution snow-water equivalent measurement by gamma-ray spectroscopy. *Agricultural and Forest Meteorology* 83:27–36.
- Blazkova, S., K. Beven, P. Tacheci, and A. Kulsova (2002). Testing the distributed water table predictions of TOPMODEL (allowing for uncertainty in model calibration): The death of TOPMODEL? *Water Resources Research* 38(11), doi:10.1029/2001WR000912.
- Bloomfield, J. P., D. J. Allen, and K. J. Griffiths (2009). Examining geological controls on baseflow index (BFI) using regression analysis: An illustration from the Thames Basin, UK. *Journal of Hydrology* 373:164–176.
- Blöschl, G. (2006). Hydrologic synthesis: Across processes, places, and scales. *Water Resources Research* 42:W03S02, doi:10.1029/2005WR004319.
- Blöschl, G., D. Gutknecht, and R. Kirnbauer (1991a). Distributed snowmelt simulations in an Alpine catchment: 2. Parameter study and model predictions. *Water Resources Research* 27:3181–3188.
- Blöschl, G., R. Kirnbauer, and D. Gutknecht (1991b). Distributed snowmelt simulations in an Alpine catchment: 1. Model evaluation on the basis of snow cover patterns. *Water Resources Research* 27:3171–3179.
- Bocchieri, J. R. (1980). The objective use of upper air soundings to specify precipitation type. *Monthly Weather Review* 98:596–603.
- Bolin, B., and H. Rodhe (1973). A note on the concepts of age distribution and transit time in natural reservoirs. *Tellus* 25:58–62.
- Boltzmann, L. (1894). Zur Integration der Diffusionsgleichung bei variablen Diffusionskoeffizienten. *Annalen Physiks* (Leipzig) 53:959–964.
- Bonan, G. R., K. W. Oleson, M. Vertenstein, S. Levis, X. Zeng, Y. Dai, R. E. Dickinson, and Z.-L. Yang (2002). The land surface climatology of the Community Land Model coupled to the NCAR Community Climate Model. *Journal of Climate* 15:3123–3149.
- Bonell, M. (1993). Progress in the understanding of runoff generation dynamics in forests. *Journal of Hydrology* 150:217–275.
- Bookhagen, B., and D. W. Burbank (2010). Toward a complete Himalayan hydrological budget: Spatiotemporal distribution of snowmelt and rainfall and their impact on river discharge. *Journal of Geophysical Research* 115:F03019, doi:10.1029/2009JF001426.
- Boonstra, J., and M. N. Bhutta (1996). Groundwater recharge in irrigated agriculture: The theory and practice of inverse modeling. *Journal of Hydrology* 174:357–374.
- Bosch, J. M., and J. D. Hewlett (1982). A review of catchment experiments to determine the effect of vegetation changes on water yield and evapotranspiration. *Journal of Hydrology* 55:3–23.
- Bouchet, R. B. (1963). Evapotranspiration réelle et potentielle, signification climatique. Gentbrugge, Belgium: International Association of Scientific Hydrology Publication 62:134–142.
- Boughton, W. C. (1989). A review of the USDA SCS curve number method. *Australian Journal of Soil Research* 27:511–523.
- Boughton, W. C. (1994). An error in the SCS curve number method. Unpublished Technical Note, Griffith University, Brisbane, Australia.
- Bouwer, H. (1986). Intake rate: Cylinder infiltrometer. In A. Klute, ed., *Methods of Soil Analysis*. Part 1: Physical and Mineralogical Methods. Madison, WI: Soil Science Society of America.
- Bowen, G. J., C. D. Kennedy, Z. Lin, and J. Stalker (2011). Water balance model for mean annual hydrogen and oxygen isotope distributions in surface waters of the contiguous United States. *Journal of Geophysical Research* 116:G04011, doi:10.1029/2011JG001581.
- Bowen, I. S. (1926). The ratio of heat losses by conduction and by evaporation from any water surface. *Physical Review* 27:777–787.
- Bradbury, J. A., S. L. Dingman, and B. D. Keim (2002). New England drought and relations with large scale atmospheric circulation patterns. *Journal of the American Water Resources Association* 38:1287–1299.
- Brakensiek, D. L., H. B. Osborn, and W. J. Rawls, eds. (1979). *Field Manual for Research in Agricultural Hydrology*. Science and Education Administration, US Department of Agriculture.
- Branson, F. A., G. F. Gifford, K. G. Renard, and R. F. Hadley (1981). *Rangeland Hydrology*. Dubuque, IA: Kendall/Hunt Publishing Co.
- Bras, R. L. (1990). *Hydrology*. Reading, MA: Addison-Wesley Publishing Co.
- Bras, R. L., and I. Rodriguez-Iturbe (1984). *Random Functions in Hydrology*. Reading, MA: Addison-Wesley Publishing Co.
- Bredehoeft, J. D. (1997). Safe yield and the water budget myth. *Ground Water* 35(6):929.
- Bredehoeft, J. D. (2002). The water budget myth revisited: Why hydrogeologists model. *Ground Water* 40(4):340–345.
- Bredehoeft, J. D., S. S. Papadopoulos, and H. H. Cooper, Jr. (1982). Groundwater: The water-budget myth. In *The Scientific Basis of Water-Resource Management*. Washington, DC: National Academy Press.
- Bristow, K. L. (1992). Prediction of daily mean vapor density from daily minimum air temperature. *Agricultural and Forest Meteorology* 59:309–317.
- Bromley, J., W. M. Edmunds, E. Fellman, J. Brouwer, S. R. Gaze, J. Sudlow, and J.-D. Taupin (1997). Estimation of rainfall inputs and direct recharge to the deep unsaturated zone of southern Niger using the chloride profile method. *Journal of Hydrology* 188/189:139–154.
- Brooks, C. F. (1940). Hurricanes into New England: Meteorology of the storm of September 21, 1938. *Report for 1939*:241–251. Washington, DC: Smithsonian Institution.
- Brooks, R. H., and A. T. Corey (1964). *Hydraulic Properties of Porous Media*. Hydrology Paper 3. Colorado State University.
- Brown, J., S. L. Dingman, and R. J. Lewellen (1968). *Hydrology of a Drainage Basin on the Alaskan Coastal Plain*. Research Report 240. Hanover, NH: US Army Cold Regions Research and Engineering Lab.
- Brown, R. J. E., and T. L. Péwé (1973). Distribution of permafrost in North America and its relationship to the environment: A review, 1963–1973. In *Permafrost: North American Contribution to the Second International Conference*. Washington, DC: National Academy of Sciences.
- Brubaker, K. L., A. Rango, and W. Kustas (1996). Incorporating radiation inputs into the Snowmelt Runoff Model. *Hydrological Processes* 10:1329–1343.
- Brubaker, K. L., D. Entekhabi, and P. S. Eagleson (1993). Estimation of continental precipitation recycling. *Journal of Climate* 6:1077–1089.
- Bruce, J. P., and R. H. Clark (1966). *Introduction to Hydrometeorology*. Long Island City, NY: Pergamon Press.
- Brutsaert, W. (1982). *Evaporation into the Atmosphere*. Dordrecht, Holland: D. Reidel Publishing Company.
- Brutsaert, W. (1988). The parameterization of regional evaporation—some directions and strategies. *Journal of Hydrology* 102:407–426.
- Brutsaert, W. (1992). *Hydrology: An Introduction*. Cambridge, UK: Cambridge University Press.
- Brutsaert, W. (1994). The unit response of groundwater outflow from a hillslope. *Water Resources Research* 30:2759–2763.
- Brutsaert, W., and J. P. Lopez (1998). Basin-scale geohydrologic drought flow features of riparian aquifers in the southern Great Plains. *Water Resources Research* 34:233–240.
- Brutsaert, W., and J. L. Nieber (1977). Regionalized drought flow hydro graphs from a mature glaciated plateau. *Water Resources Research* 13:637–643.
- Brutsaert, W., and H. Stricker (1979). An advection-aridity approach to estimate actual regional evapotranspiration. *Water Resources Research* 15:443–450.
- Buchanan, T. J., and W. P. Somers (1968). Stage measurement at gaging stations. In *Techniques of Water-Resources Investigations* (book 3, chapter A7). Washington, DC: US Geological Survey.
- Buchanan, T. J., and W. P. Somers (1969). Discharge measurement at gaging stations. In *Techniques of Water-Resources Investigations* (book 3, chapter A8). Washington, DC: US Geological Survey.
- Budyko, M. I. (1958). The heat balance of the Earth's surface (pp. 144–155). Washington, DC: US Department of Commerce, National Weather Service.

- Budyko, M. I. (1974). Climate and life. Vol. 18, *International Geophysics Series*. San Diego, CA: Academic Press.
- Bulygina, N., and H. Gupta (2009). Estimating the uncertain mathematical structure of a water balance model via Bayesian data assimilation. *Water Resources Research* 45:W00B13, doi:10.1029/2007WR006749.
- Burgy, R. H., and J. N. Luthin (1956). A test of the single- and double-ring types of infiltrometers. *American Geophysical Union Transactions* 37:189–191.
- Burt, R., ed. (2004). *Soil Survey Laboratory Methods Manual*. Soil Survey Investigations Report 42, Version 4.0. Washington, DC: US Natural Resources Conservation Service.
- Busenberg, E., and L. N. Plummer (1992). Use of chlorofluorocarbons (CCl_3F and CCl_2F_2) as hydrologic tracers and age-dating tools: The alluvium and terrace system of central Oklahoma. *Water Resources Research* 28:2257–2283.
- Butler, J. H., and S. A. Montzka (2014). The NOAA Annual Greenhouse Gas Index (AGGI) (<http://www.esrl.noaa.gov/gmd/aggi/aggi.html>).
- Buttle, J. M., and A. G. Farnsworth (2012). Measurement and modeling of canopy water partitioning in a reforested landscape: The Ganaraska Forest, southern Ontario, Canada. *Journal of Hydrology* 466–467:103–114.
- Buttle, J. M., and D. A. House (1997). Spatial variability of saturated hydraulic conductivity in shallow macroporous soils in a forested basin. *Journal of Hydrology* 203:127–142.
- Buttle, J. M., and D. J. McDonald (2002). Coupled vertical and lateral preferential flow on a forested slope. *Water Resources Research* 38(5):1060, doi:10.1029/2001WR000773.
- Buttle, J. M., and J. J. McDonnell (1987). Modeling the areal depletion of snow cover in a forested catchment. *Journal of Hydrology* 90:43–60.
- Caine, N. (1975). An elevational control of peak snowpack variability. *Water Resources Research* 11:613–621.
- Caissie, D., T. L. Pollock, and R. A. Cunjak (1996). Variation in stream water chemistry and hydrograph separation in a small drainage basin. *Journal of Hydrology* 178:137–157.
- Calder, I. R. (1977). A model of transpiration and interception loss from a spruce forest in Plynlimon, central Wales. *Journal of Hydrology* 33:247–265.
- Calder, I. R. (1978). Transpiration observations from a spruce forest and comparisons with predictions from an evaporation model. *Journal of Hydrology* 38:33–47.
- Calder, I. R., and P. T. W. Rosier (1976). The design of large plastic-sheet net-rainfall gauges. *Journal of Hydrology* 30:403–405.
- Caldwell, R. J., and J. M. Palmer (2009). *LOUZIE: An Operational Quality Control Procedure at the Lower Mississippi River Forecast Center*. NOAA/NWS/Lower Mississippi River Forecast Center (<http://www.srh.noaa.gov/images/lmfc/tech/louzie.pdf>).
- Callis, L. B., and M. Natarajan (1986). Ozone and nitrogen dioxide changes in the stratosphere during 1979–84. *Nature* 323:772–775.
- Calvo, J. C. (1986). An evaluation of Thornthwaite's water balance technique in predicting stream runoff in Costa Rica. *Hydrological Sciences Journal* 31:51–60.
- Campbell, G. S. (1974). A simple method for determining unsaturated conductivity from moisture retention data. *Soil Science* 117:311–314.
- Carlson, R. E., J. W. Enz, and D. G. Baker (1994). Quality and variability of long term climate data relative to agriculture. *Agricultural and Forest Meteorology* 69:61–74.
- Carlson, T. (1991). Modeling stomatal resistance: An overview of the 1989 workshop at the Pennsylvania State University. *Agricultural and Forest Meteorology* 54:103–106.
- Carroll, S. S., and T. R. Carroll (1989). Effect of uneven snow cover on airborne snow water equivalent estimates obtained by measuring terrestrial gamma radiation. *Water Resources Research* 25:1505–1510.
- Carroll, S. S., and N. Cressie (1996). A comparison of geostatistical methodologies used to estimate snow water equivalent. *Water Resources Bulletin* 32:267–278.
- Carroll, T., and G. D. Voss (1984). Airborne snow-water equivalent over a forested environment using terrestrial gamma radiation. Proceedings of the 41st Annual Meeting of the Eastern Snow Conference.
- Carter, R. W., and I. E. Anderson (1963). Accuracy of current meter measurements. American Society of Civil Engineers Proceedings, *Journal of the Hydraulics Division* 89:105–115.
- Casas, M. C., R. Rodríguez, R. Nieto, and A. Redaño (2008). The estimation of probable maximum precipitation. *Annals of the New York Academy of Sciences* 1146:291–302.
- Casas, M. C., R. Rodríguez, M. Prohon, A. Gázquez, and A. Redaño (2010). Estimation of the probable maximum precipitation in Barcelona (Spain). *International Journal of Climatology*, doi:10.1002/joc.449.
- Castellarin, A., R. Merz, and G. Blöschl (2009). Probabilistic envelope curves for extreme rainfall events. *Journal of Hydrology* 378(3–4):263–271.
- Cedergren, H. (1989). *Seepage, Drainage, and Flow Nets*. New York: John Wiley.
- Ceresetti, D., G. Molinié, and J.-D. Creutin (2010). Scaling properties of heavy rainfall at short duration: A regional analysis. *Water Resources Research* 46:W09531, doi:10.1029/2009WR008603.
- Cey, E. E., D. L. Rudolph, G. W. Parkin, and R. Aravena (1998). Quantifying groundwater discharge to a small perennial stream in southern Ontario, Canada. *Journal of Hydrology* 210:21–37.
- Chang, M., and R. Lee (1974). Objective double-mass analysis. *Water Resources Research* 10:1123–1126.
- Changnon, S. A., ed. (1981). METROMEX: A review and summary. *Meteorological Monographs* 18:(40).
- Chapman, D. S., and M. G. Davis (2010). Climate change: Past, present, and future. *Eos* 91:325–326.
- Chapman, P. J., B. Reynolds, and H. S. Wheater (1993). Hydrochemical changes along stormflow pathways in a small moorland headwater catchment in Mid-Wales, UK. *Journal of Hydrology* 151:241–265.
- Chapman, T. (1999). A comparison of algorithms for stream flow recession and baseflow separation. *Hydrological Processes* 13:701–714.
- Chappell, N. A. (2010). Soil pipe distribution and hydrological forecasting within the humid tropics: A synthesis. *Hydrological Processes* 24:1567–1581, doi:10.1002/hyp.7579.
- Chatfield, C. (1984). *Time Series Analysis: An Introduction* (3rd ed.). New York: Chapman and Hall.
- Chen, C.-L. (1982). Infiltration formulas by curve number procedure. American Society of Civil Engineers Proceedings, *Journal of the Hydraulics Division* 108:823–829.
- Cheng, Q., Xi Chen, X. Chen, Z. Zhang, and M. Ling (2011). Water infiltration underneath single-ring permeameters and hydraulic conductivity determination. *Journal of Hydrology* 398:135–143.
- Cheng, X., and M. P. Anderson (1994). Simulating the influence of lake position on groundwater fluxes. *Water Resources Research* 30:2041–2049.
- Cherkauer, D. S., and D. C. Nader (1989). Distribution of groundwater seepage to large surface-water bodies: The effect of hydraulic heterogeneities. *Journal of Hydrology* 109:151–165.
- Cherkauer, D. S., and J. P. Zager (1989). Groundwater interaction with a kettlehole lake: Relation of observations to digital simulations. *Journal of Hydrology* 109:167–184.
- Chery, D. L., Jr. (1967). A review of rainfall-runoff physical models as developed by dimensional analysis and other methods. *Water Resources Research* 3:881–889.
- Chery, D. L., Jr. (1968). *Output Response to Pulse Inputs of a Scaled Laboratory Watershed System*. Tucson, AZ: US Department of Agriculture Southeast Watershed Research Center.
- Chiew, F. H. S., and T. A. McMahon (1990). Estimating groundwater recharge using a surface watershed modeling approach. *Journal of Hydrology* 114:285–304.
- Chiew, F. H. S., T. A. McMahon, and I. C. O'Neill. (1992). Estimating groundwater recharge using an integrated surface and groundwater modeling approach. *Journal of Hydrology* 131:151–186.
- Chow, T. L. (1992). Performance of an ultrasonic level sensing system for automated monitoring of snowcover depth. *Agricultural and Forest Meteorology* 62:75–85.
- Chu, C.-R., M.-H. Li, Y.-Y. Chen, and Y.-H. Kuo (2010). A wind tunnel experiment on the evaporation rate of class A evaporation pan. *Journal of Hydrology* 381:221–224.
- Chu, S. T. (1978). Infiltration during an unsteady rain. *Water Resources Research* 14:461–466.
- Chu, X., J. Yang, Y. Chi, and J. Zhang (2013). Dynamic puddle delineation and modeling of puddle-to-puddle filling-spilling-merging-splitting overland flow processes. *Water Resources Research* 49, doi:10.1002/wrcr.20286.

- Church, J. A., N. J. White, L. F. Konikow, C. M. Domingues, J. G. Cogley, E. Rignot, J. M. Gregory, M. R. van den Broeke, A. J. Monaghan, and I. Velicogna (2011). Revisiting the Earth's sea-level and energy budgets from 1961 to 2008. *Geophysical Research Letters* 38:L18601, doi:10.1029/2011GL048794.
- Cifelli, R., and V. Chandrasekar (2010). Dual-polarization radar rainfall estimation. In F. Y. Testi and M. Gebremichael, eds., *Rainfall: State of the Science* (pp. 105–126). Washington, DC: American Geophysical Union.
- Claassen, H. C., and D. R. Halm (1996). Estimates of evapotranspiration or effective moisture in Rocky Mountain watersheds from chloride ion concentrations in stream baseflow. *Water Resources Research* 32:363–372.
- Claassen, H. C., M. M. Reddy, and D. R. Halm (1986). Use of the chloride ion in determining hydrologic-basin water budgets—a 3-year case study in the San Juan Mountains, Colorado, USA. *Journal of Hydrology* 85:49–71.
- Clapp, R. B., and G. M. Hornberger (1978). Empirical equations for some soil hydraulic properties. *Water Resources Research* 14:601–604.
- Clark, M. P., J. Hendrikx, A. G. Slater, D. Kavetski, B. Anderson, N. J. Cullen, T. Kerr, E. Ö. Hreinsson, and R. A. Woods (2011a). Representing spatial variability of snow water equivalent in hydrologic and land-surface models: A review. *Water Resources Research* 47:W07539, doi:10.1029/2011WR010745.
- Clark, M. P., D. Kavetski, and F. Fenicia (2011b). Pursuing the method of multiple working hypotheses for hydrological modeling. *Water Resources Research* 47:W09301, doi:10.1029/2010WR009827.
- Clark, M. P., and D. Kavetski (2010). Ancient numerical daemons of conceptual hydrological modeling. Part 1: Fidelity and efficiency of time stepping schemes. *Water Resources Research* 46:W10510, doi:10.1029/2009WR008894.
- Clark, M. P., D. E. Rupp, R. A. Woods, H. J. Tromp-van Meerveld, N. E. Peters, and J. E. Freer (2009). Consistency between hydrological models and field observations: Linking processes at the hillslope scale to hydrological responses at the watershed scale. *Hydrological Processes* 23:311–319.
- Cline, D. W. (1997). Snow surface energy exchanges and snowmelt at a continental midlatitude Alpine site. *Water Resources Research* 33:689–701.
- Clow, D. W., and A. C. Fleming (2008). Tracer gauge: An automated dye dilution gauging system for ice-affected streams. *Water Resources Research* 44:W12441, doi:10.1029/2008WR007090.
- Cohen, P., O. L. Franke, and B. L. Foxworthy (1968). An atlas of Long Island's water resources. *Bulletin* 62. Albany: New York Water Resources Commission.
- Cohn, T. A., J. E. Kiang, and R. R. Mason, Jr. (2013). Discharge measurement uncertainty using the Interpolated Variance Estimator. *Journal of Hydraulic Engineering* 139(5):502–510.
- Colbeck, S. C. (1971). *One-Dimensional Water Flow through Snow*. Research Report 296. Hanover, NH: US Army Cold Regions Research and Engineering Laboratory.
- Colbeck, S. C. (1974). Water flow through snow overlying an impermeable boundary. *Water Resources Research* 10:119–123.
- Colbeck, S. C. (1978). The physical aspects of water flow through snow. *Advances in Hydroscience* 11:165–206.
- Colbeck, S. C., E. Akitaya, R. Armstrong, H. Gubler, J. Lafeuille, K. Lied, D. McClung, and E. Morris (1990). *The International Classification for Seasonal Snow on the Ground*. International Commission on Snow and Ice of the International Association of Scientific Hydrology.
- Colonell, J. M., and G. R. Higgins (1973). Hydrologic response of Massachusetts watersheds. *Water Resources Bulletin* 9:793–800.
- Comiso, J. C., and C. L. Parkinson (2004, August). Satellite-observed changes in the Arctic. *Physics Today*, pp. 38–44.
- Conover, W. J. (1980). *Practical Nonparametric Statistics*. New York: John Wiley.
- Conway, H., and R. Benedict (1994). Infiltration of water into snow. *Water Resources Research* 30:641–649.
- Cooper, J. D. (1980). *Measurement of Moisture Fluxes in Unsaturated Soil in Thetford Forest*. Report 66. Wallingford, Oxford, UK: Natural Environment Research Council Institute of Hydrology.
- Cosby, B. J., G. M. Hornberger, R. B. Clapp, and T. R. Ginn (1984). A statistical exploration of the relationships of soil moisture characteristics to the physical properties of soils. *Water Resources Research* 20:682–690.
- Court, A., and M. T. Bare (1984). Basin precipitation estimates by Bethlhamy's two-axis method. *Journal of Hydrology* 68:149–158.
- Cox, L. M. (1971). Field performance of the universal surface precipitation gage. Proceedings, 39th Annual Meeting of the Western Snow Conference.
- Cox, L. M. et al. (1978). The care and feeding of snow pillows. Proceedings, 46th Annual Meeting of the Western Snow Conference.
- Crayosky, T. W., D. R. De Walle, T. A. Seybert, and T. E. Johnson (1999). Channel precipitation dynamics in a forested Pennsylvania headwater catchment (USA). *Hydrological Processes* 13:1303–1314.
- Creutin, J. D., and C. Obled (1982). Objective analyses and mapping techniques for rainfall fields: An objective comparison. *Water Resources Research* 18:413–431.
- Croley, T. E., II (1989). Verifiable evaporation modeling on the Laurentian Great Lakes. *Water Resources Research* 25:781–792.
- Croley, T. E., II (1992). Long-term heat storage in the Great Lakes. *Water Resources Research* 28:69–81.
- Croley, T. E., II, and H. C. Hartmann (1985). Resolving Thiessen polygons. *Journal of Hydrology* 76:363–379.
- Crowe, A. S., and F. W. Schwartz (1985). Application of a lake-watershed model for the determination of water balance. *Journal of Hydrology* 81:1–26.
- Currie, D. J., and V. Paquin (1987). Large-scale biogeographical patterns of species richness of trees. *Nature* 329:326–327.
- Custer, S. G., P. Fames, J. P. Wilson, and R. D. Snyder (1996). A comparison of hand- and spline-drawn precipitation maps for mountainous Montana. *Water Resources Bulletin* 32:393–405.
- Dai, A., A. D. Del Genio, and I. T. Fung (1997). Clouds, precipitation, and temperature range. *Nature* 386:665–666.
- Dai, A., and K. E. Trenberth (2002). Estimates of freshwater discharge from continents: latitudinal and seasonal variations. *Journal of Hydrometeorology* 3:660–687.
- Dai, A., K. E. Trenberth, and T. Qian (2004). A global dataset of Palmer drought severity index for 1870–2002: Relationship with soil moisture and effects of surface warming. *Journal of Hydrometeorology* 5:1117–1130.
- Daly, C., R. P. Neilson, and D. L. Phillips (1994). A statistical-topographic model for mapping climatological precipitation over mountainous terrain. *Journal of Applied Meteorology* 33:140–158.
- Daniel, J. F. (1976). Estimating groundwater evapotranspiration from streamflow records. *Water Resources Research* 12:360–364.
- Darling, W. G., and A. H. Bath (1988). A stable isotope study of recharge processes in the English Chalk. *Journal of Hydrology* 101:31–46.
- Das Gupta, A., and G. N. Paudyal (1988). Estimating aquifer recharge and parameters from water level observations. *Journal of Hydrology* 99:103–116.
- Davies, J. A., and C. D. Allen (1973). Equilibrium, potential, and actual evaporation from cropped surfaces in southern Ontario. *Journal of Applied Meteorology* 12:647–657.
- Davis, K. S., and J. A. Day (1961). *Water: The Mirror of Science*. New York: Doubleday-Anchor.
- Davis, R. T. (1973). Operational snow sensors. Proceedings, 30th Annual Meeting of the Eastern Snow Conference.
- Davis, S. N., and E. Murphy, eds. (1987). Dating ground water and the evaluation of repositories for radioactive waste. US Nuclear Regulatory Commission NUREG/CR-4912.
- Davis, W. M. (1899). The geographic cycle. *The Geographical Journal* 14(5):481–504.
- Day, J. A., and G. L. Sternes (1970). *Climate and Weather*. Reading, MA: Addison-Wesley.
- de Lima, J. L. M. P. (1990). The effect of oblique rain on inclined surfaces: A nomograph for the rain-gauge correction factor. *Journal of Hydrology* 115:407–412.
- De Michele, C., N. T. Kottekoda, and R. Rosso (2001). The derivation of areal reduction factor of storm rainfall from its scaling properties. *Water Resources Research* 37(12):3247–3252.
- Dean, T. J., J. P. Bell, and A. J. B. Baty (1987). Soil moisture measurement by an improved capacitance technique. Part I. Sensor design and performance. *Journal of Hydrology* 93:67–78.
- DeAngelis, A., F. Dominguez, Y. Fan, A. Robock, M. D. Kustu, and D. Robinson

- (2010). Evidence of enhanced precipitation due to irrigation over the Great Plains of the United States. *Journal of Geophysical Research* 115:D15115, doi:10.1029/2010JD013892.
- Deevey, E. E., Jr. (1970). Mineral cycles. In *The Biosphere*. San Francisco, CA: W.H. Freeman and Co.
- Degu, A. M., F. Hossain, D. Niyogi, R. Pielke, Sr., J. M. Shepherd, N. Voisin, and T. Chronis (2011). The influence of large dams on surrounding climate and precipitation patterns. *Geophysical Research Letters* 38:L04405, doi:10.1029/2010GL046482.
- Delany, A. C., and S. R. Semmer (1998). An integrated surface radiation measurement system. *Journal of Atmospheric and Oceanic Technology* 15:46–53.
- Derecki, J. A. (1976). Multiple estimates of Lake Erie evaporation. *Journal of Great Lakes Research* 2:124–149.
- Derecki, J. A. (1981). Operational estimates of Lake Superior evaporation based on IFYGL findings. *Water Resources Research* 17:1453–1462.
- Derksen, C., R. Brown, and L. Wang (2010). Terrestrial snow. In Special Supplement, “State of the Climate in 2009.” *Bulletin of the American Meteorological Society* 91(7):S117–S118.
- Déry, S. J., M. A. Hernández-Henríquez, J. E. Burford, and E. F. Wood (2009). Observational evidence of an intensifying hydrological cycle in northern Canada. *Geophysical Research Letters* 36:L13402, doi:10.1029/2009GL038852.
- Dettinger, M. D., and H. F. Diaz (2000). Global characteristics of stream flow seasonality and variability. *Journal of Hydroclimatology* 1:289–310.
- DeVries, J. J., and T. V. Hromadka (1992). Computer models for surface water. In D. R. Maidment, ed., *Handbook of Hydrology* (chapter 21). New York: McGraw-Hill.
- Dey, B., and O. S. R. U. Bhanu Kumar (1983). Himalayan winter snow cover area and summer monsoon rainfall over India. *Journal of Geophysical Research* 88:5471–5474.
- Dickinson, W. T., M. E. Holland, and G. L. Smith (1967). *An Experimental Rainfall-Runoff Facility*. Hydrology Paper 25. Colorado State University.
- Dickson, R. R. (1984). Eurasian snow cover versus Indian monsoon rainfall—an extension of the Hahn-Shukla results. *Journal of Climatology and Applied Meteorology* 23:171–173.
- Diggle, P. J. (1983). *Statistical Analysis of Spatial Point Patterns*. London, UK: Academic Press.
- Ding, B., K. Yang, J. Qin, L. Wang, Y. Chen, and X. He (2014). The dependence of precipitation types on surface elevation and meteorological conditions and its parameterization. *Journal of Hydrology* 513:154–163.
- Dingman, S. L. (1970). *Hydrology of the Glenn Creek Watershed, Tanana River Drainage, Central Alaska*. Research Report 297. Hanover, NH: US Army Cold Regions Research and Engineering Laboratory.
- Dingman, S. L. (1973). Effects of permafrost on streamflow characteristics in the discontinuous permafrost zone of central Alaska. In *Permafrost: North American Contribution to the Second International Conference*. Washington, DC: National Academy of Sciences.
- Dingman, S. L. (1975). *Hydrologic Effects of Frozen Ground*. Special Report 218. Hanover, NH: US Army Cold Regions Research and Engineering Laboratory.
- Dingman, S. L. (1978). Drainage density and streamflow: A closer look. *Water Resources Research* 14:1183–1187.
- Dingman, S. L. (1981). Elevation: A major influence on the hydrology of New Hampshire and Vermont, USA. *Hydrological Sciences Bulletin* 26:399–413.
- Dingman, S. L. (1984). *Fluvial Hydrology*. New York: W.H. Freeman and Co.
- Dingman, S. L. (1989). Probability distribution of velocity in natural channel cross sections. *Water Resources Research* 25(3):509–518.
- Dingman, S. L. (2003). Preliminary regional frequency analysis of floods on unregulated streams in New Hampshire. Unpublished manuscript, Earth Sciences Department, University of New Hampshire.
- Dingman, S. L. (2009). *Fluvial Hydraulics*. New York: Oxford University Press.
- Dingman, S. L., D. Seely-Reynolds, and R. C. Reynolds III (1988). Application of kriging to estimating mean annual precipitation in a region of orographic influence. *Water Resources Bulletin* 24:329–339.
- Dingman, S. L. et al. (1971). *Hydrologic Reconnaissance of the Delta River and Its Drainage Basin, Alaska*. Research Report 262. Hanover, NH: US Army Cold Regions Research and Engineering Laboratory.
- Dingman, S. L., R. G. Barry, G. Weller, et al. (1980). Climate, snow cover, microclimate, and hydrology. In J. Brown, P. C. Miller, L. L. Tieszen, and F. L. Bunnell, eds., *An Arctic Ecosystem: The Coastal Tundra at Barrow, Alaska*. Stroudsburg, PA: Dowden, Hutchinson, and Ross.
- Dingman, S. L., W. F. Weeks, and Y. C. Yen (1968). The effects of thermal pollution on river ice conditions. *Water Resources Research* 4(2):349–362.
- Dirmeyer, P. A. (2011). The terrestrial segment of soil moisture-climate coupling. *Geophysical Research Letters* 38:L16702, doi:10.1029/2011GL048268.
- Diskin, M. H. (1970). On the computer evaluation of Thiessen weights. *Journal of Hydrology* 11:69–78.
- DiTomaso, E., F. Romano, and V. Cuomo (2009). Rainfall estimation from satellite passive microwave observations in the range 89 GHz to 190 GHz. *Journal of Geophysical Research* 114:D18203.
- DOBRIYAL, P. A., QURESHI, R., BADOLA, S. A., and HUSSAIN, (2012). A review of the methods available for estimating soil moisture and its implications for water resource management. *Journal of Hydrology* 458–459:110–117.
- Doherty, J. (2011). Modeling: Picture perfect or abstract art? *Ground Water* 49(4):455.
- Dolman, A. J., J. B. Stewart, and J. D. Cooper (1988). Predicting forest transpiration from climatological data. *Agricultural and Forest Meteorology* 42:337–353.
- Donahue, R. L., R. W. Miller, and J. C. Shikloman (1983). *Soils: An Introduction to Soils and Plant Growth* (5th ed.). Englewood Cliffs, NJ: Prentice-Hall.
- Donald, J. R., E. D. Soulis, N. Kouwen, and A. Pietrino (1995). A land cover-based snow cover representation for distributed hydrologic models. *Water Resources Research* 31:995–1009.
- Dooge, J. (1975). The water balance of bogs and fens. In *Hydrology of Marsh-Ridden Areas*. Proceedings of Minsk Symposium 1972. Paris, France: UNESCO Press.
- Dooge, J. (1986). Looking for hydrologic laws. *Water Resources Research* 22:46S–58S.
- Dorsey, N. E. (1940). *Properties of Ordinary Water Substance in All Its Phases: Water, Water-Vapor and All the Ices*. New York: Reinhold.
- Doss, P. K. (1993). The nature of a dynamic water table in a system of non-tidal, freshwater coastal wetlands. *Journal of Hydrology* 141:107–126.
- Dowdeswell, J. A. et al. (1998). The mass balance of circum-Arctic glaciers and recent climate change. *Quaternary Research* 48:1–14.
- Dozier, J. (2011). Mountain hydrology, snow color, and the Fourth Paradigm. *Eos* 92(43):373–374.
- Dracup, J. A., and E. Kahya (1994). The relationships between U.S. streamflow and La Niña events. *Water Resources Research* 30:2133–2141.
- Dreibelbis, F. R. (1962). Some aspects of watershed hydrology as determined from soil moisture data. *Journal of Geophysical Research* 67:3425–3435.
- Drever, J. I. (1982). *The Geochemistry of Natural Waters*. Englewood Cliffs, NJ: Prentice-Hall.
- Duffy, P. B., B. D. Santer, and T. M. L. Wigley (2009, January). Solar variability does not explain late-20th-century warming. *Physics Today*, pp. 48–49.
- Dunkle, S. A., L. N. Plummer, E. Busenberg, P. J. Phillips, J. M. Denver, P. A. Hamilton, R. L. Michel, and T. B. Coplen (1993). Chlorofluorocarbons (CCl_3F and CCl_2F_2) as dating tools and hydrologic tracers in shallow groundwater of the Dehnarva Peninsula, Atlantic Coastal Plain, United States. *Water Resources Research* 29:3837–3860.
- Dunne, T. (1970). *Runoff production in a humid area*. ARS-41-160. Washington, DC: USDA, Agricultural Research Service.
- Dunne, T. (1978). Field studies of hillslope flow processes. In M. J. Kirkby, ed., *Hillslope Hydrology* (pp. 227–293). New York: John Wiley.
- Dunne, T., and R. D. Black (1970). Partial area contributions to storm runoff in a small New England watershed. *Water Resources Research* 6:1296–1311.
- Dunne, T., and L. B. Leopold (1978). *Water in Environmental Planning*. San Francisco, CA: W. H. Freeman and Co.
- Dunne, T., T. R. Moore, and C. H. Taylor (1975). Recognition and prediction of runoff-producing zones in humid regions. *Hydrological Sciences Bulletin* 20:305–327.
- Dunne, T., A. G. Price, and S. C. Colbeck (1976). The generation of runoff from subarctic snowpacks. *Water Resources Research* 12:675–694.

- Durack, P. J., S. E. Wijffels, and R. J. Matear (2012). Ocean salinities reveal strong global water cycle intensification during 1950 to 2000. *Science* 336:455–458.
- Durand, M., J. Neal, E. Rodríguez, K. M. Andreadis, L. C. Smith, and Y. Yoon (2014). Estimating reach-averaged discharge for the River Severn from measurements of river water surface elevation and slope. *Journal of Hydrology* 511:92–101.
- Durrans, S. R. (2010). Intensity-duration-frequency curves. In F. Y. Testik and M. Gebremichael, eds., *Rainfall: State of the Science* (pp. 159–169). Washington, DC: American Geophysical Union.
- Dye, D. G. (2002). Variability and trends in the annual snow-cover cycle in Northern Hemisphere land areas, 1972–2000. *Hydrological Processes* 16:3065–3077.
- Eagleson, P. S. (1970). *Dynamic Hydrology*. New York: McGraw-Hill.
- Eagleson, P. S. (1972). Dynamics of flood frequency. *Water Resources Research* 8:878–898.
- Eagleson, P. S. (1982). Ecological optimality in water-limited soil-vegetation systems: 1. Theory and hypothesis. *Water Resources Research* 18:323–340.
- Eagleson, P. S. (1986). The emergence of global-scale hydrology. *Water Resources Research* 22:6S–14S.
- Eagleson, P. S. (2004). *Ecohydrology: Darwinian Expression of Vegetation Form and Function*. New York: Cambridge University Press.
- Eagleson, P. S., et al. (1991). *Opportunities in the Hydrologic Sciences*. Washington, DC: National Academy Press.
- Eichinger, W. E., M. B. Parlange, and H. Stricker (1996). On the concept of equilibrium evaporation and the value of the Priestley–Taylor coefficient. *Water Resources Research* 32:161–164.
- Eller, H., and A. Denoth (1996). A capacitive soil moisture sensor. *Journal of Hydrology* 185:137–146.
- Ellins, K. K., A. Roman-Mas, and R. Lee (1990). Using ^{222}Rn to examine groundwater/surface discharge interaction in the Rio Grande de Manati, Puerto Rico. *Journal of Hydrology* 115:319–341.
- Elrick, D. E., W. D. Reynolds, H. R. Geering, and K.-A. Tan (1990). Estimating steady infiltration rate times for infiltrometers and permeameters. *Water Resources Research* 26:759–769.
- Elsenbeer, H., D. Lorieri, and N. Bonell (1995). Mixing model approaches to estimate storm flow sources in an overland flow-dominated tropical rain forest catchment. *Water Resources Research* 3:2267–2278.
- Eltahir, E. A. B. (1996). El Niño and the natural variability in the flow of the Nile River. *Water Resources Research* 32:131–137.
- Eltahir, E. A. B., and R. L. Bras (1994). Precipitation recycling in the Amazon basin. *Quarterly Journal of the Royal Meteorological Society* 120:861–880.
- Emmett, W. W. (1978). Overland flow. In M. J. Kirkby, ed., *Hillslope Hydrology* (pp. 145–176). New York: John Wiley.
- Enfield, D. B. (1989). El Niño, past and present. *Reviews of Geophysics* 27:159–187.
- Engman, E. T., and D. M. Hershfield (1969). *Precipitation Climatology of the Sleepers River Watershed Near Danville, Vermont*. Paper ARS 41-148. Washington, DC: US Agricultural Research Service.
- Erskine, A. D., and A. Papaioannou (1997). The use of aquifer response rate in the assessment of groundwater resources. *Journal of Hydrology* 202:373–391.
- Eshleman, K. N., J. S. Pollard, and A. K. O'Brien (1993). Determination of contributing areas for saturation overland flow from chemical hydrograph separation. *Water Resources Research* 19:3577–3587.
- Evans, C., T. D. Davies, and P. S. Murdoch (1998). Component flow processes at four streams in the Catskill Mountains, New York, analyzed using episodic concentration/discharge relationships. *Hydrological Processes* 13:563–575.
- Farnsworth, R. K., and E. S. Thompson (1982). *Mean Monthly, Seasonal, and Annual Pan Evaporation for the United States*. Technical Report NWS 34. Washington, DC: US National Atmospheric and Oceanic Administration.
- Farnsworth, R. K., E. S. Thompson, and E. L. Peck (1982). *Evaporation Atlas for the Contiguous 48 United States*. Technical Report NWS 33. Washington, DC: US National Atmospheric and Oceanic Administration.
- Federer, C. A. (1979). A soil-plant-atmosphere model for transpiration and availability of soil water. *Water Resources Research* 15:555–562.
- Federer, C. A. (1982). Transpirational supply and demand: Plant, soil, and atmospheric effects evaluated by simulation. *Water Resources Research* 18:355–362.
- Federer, C. A. (1995). BROOK90: A simulation model for evaporation, soil water, and streamflow, Version 3.1. Computer software and documentation. Durham, NH: US Forest Service.
- Federer, C. A., and D. Lash (1978a). *BROOK: A Hydrologic Simulation Model for Eastern Forests*. Research Report No. 19. Durham, NH: University of New Hampshire Water Resources Research Center.
- Federer, C. A., and D. Lash (1978b). Simulated streamflow response to possible differences in transpiration among species of hardwood trees. *Water Resources Research* 14:1089–1097.
- Federer, C. A., C. Vörösmarty, and B. Fekete (1996). Intercomparison of methods for calculating evaporation in regional and global water balance models. *Water Resources Research* 32:2315–2321.
- Federer, C. A. et al. (1990). *Thirty Years of Hydrometeorologic Data at the Hubbard Brook Experimental Forest, New Hampshire*. General Technical Report NE-141. Radnor, PA: US Forest Service, Northeastern Forest Experiment Station.
- Fekete, B. M., J. J. Gibson, P. Aggarwal, and C. J. Vörösmarty (2006). Application of isotope tracers in continental scale hydrological modeling. *Journal of Hydrology* 330:444–456.
- Fekete, B. M., R. B. Lammers, A. MacDonald, L. C. Bowling, and R. Lawford (2010). River discharge. In Special Supplement, “State of the Climate in 2009.” *Bulletin of the American Meteorological Society* 91(7):S35, S38.
- Fekete, B. M., C. J. Vörösmarty, and W. Grabs (2002). High-resolution fields of global runoff combining observed river discharge and simulated water balances. *Global Biogeochemical Cycles* 16(3), doi:10.1029/1999GB001254.
- Fekete, B. M., C. J. Vörösmarty, J. O. Roads, and C. J. Willmott (2004). Uncertainties in precipitation and their impacts on runoff estimates. *Journal of Climate* 17:294–304.
- Fekete, B. M., J. J. Gibson, P. Aggarwal, and C. J. Vörösmarty (2006). Application of isotope tracers in continental scale hydrological modeling. *Journal of Hydrology* 330:444–456.
- Fetter, C. W. (2001). *Applied Hydrogeology* (4th ed.). Upper Saddle River, NJ: Prentice-Hall.
- Ficke, J. F. (1972). *Comparison of Evaporation Computation Methods, Pretty Lake, Lagrange County, Northeastern Indiana*. Professional Paper 686-A. Washington, DC: US Geological Survey.
- Finch, J. W. (1998). Estimating direct groundwater recharge using a simple water balance model—sensitivity to land surface parameters. *Journal of Hydrology* 211:112–125.
- Fisher, N. I. (1993). *Statistical Analysis of Circular Data*. New York: Cambridge University Press.
- Flerchinger, G. N., W. Xaio, D. Marks, T. J. Sauer, and Q. Yu (2009). Comparison of algorithms for incoming atmospheric long-wave radiation. *Water Resources Research* 45:W03423, doi:10.1029/2008WR007394.
- Fontaine, T. A., and D. E. Todd, Jr. (1993). Measuring evaporation with ceramic Bel-lani plate atmometers. *Water Resources Bulletin* 29:785–795.
- Foster, J. L., D. K. Hall, and A. T. C. Chang (1987). Remote sensing of snow. *Eos* 11 Aug 1987:681–684.
- Frederick, R. H., V. A. Myers, and E. P. Auciello (1977). *Five to 60-minute Precipitation Frequency for Eastern and Central United States*. Technical Memo NWS HYDRO-35. Silver Spring, MD: US National Oceanic and Atmospheric Administration.
- Freeze, R. A. (1968). *Quantitative Interpretation of Regional Groundwater Flow Patterns as an Aid to Water Balance Studies*. Publication 77. Gentbrugge, Belgium: International Association of Scientific Hydrology.
- Freeze, R. A. (1971). Three-dimensional, transient, saturated-unsaturated flow in a groundwater basin. *Water Resources Research* 7:929–941.
- Freeze, R. A. (1972a). Role of subsurface flow in generating surface runoff: 1. Baseflow contributions to channel flow. *Water Resources Research* 8:609–623.
- Freeze, R. A. (1972b). Role of subsurface flow in generating surface runoff: 2. Upstream source areas. *Water Resources Research* 8:1272–1283.
- Freeze, R. A. (1974). Streamflow generation. *Reviews of Geophysics and Space Physics* 12:627–647.
- Freeze, R. A., and J. A. Cherry (1979). *Groundwater*. Englewood Cliffs, NJ: Prentice-Hall.
- Freeze, R. A., and P. A. Witherspoon (1967). Theoretical analysis of regional groundwater flow: 2. Effect of water-table configura-

- tion and subsurface permeability variation. *Water Resources Research* 3:623–634.
- Freeze, R. A., and P. A. Witherspoon (1968). Theoretical analysis of regional groundwater flow: 3. Quantitative interpretations. *Water Resources Research* 4:581–590.
- Frei, A., M. Tedesco, S. Lee, J. Foster, D. K. Hall, R. Kelly, and D. A. Robinson (2012). A review of global satellite-derived snow products. *Advances in Space Research* 50:1007–1029.
- Freyberg, D. L., J. W. Reeder, J. B. Franzini, and I. Remson (1980). Application of the Green-Ampt model to infiltration under time-dependent surface water depths. *Water Resources Research* 16:517–528.
- Frisbee, M. D., F. M. Phillips, A. R. Campbell, F. Liu, and S. A. Sanchez (2011). Streamflow generation in a large, alpine watershed in the southern Rocky Mountains of Colorado: Is streamflow generation simply the aggregation of hillslope runoff responses? *Water Resources Research* 47:W06512, doi:10.1029/2010WR009391.
- Fritz, P., and J. C. Fontes, eds. (1980). *Handbook of Environmental Isotope Geochemistry*. New York: Elsevier.
- Gardner, A. S., and M. J. Sharp (2010). A review of snow and ice albedo and the development of new physically based broadband albedo parameterization. *Journal of Geophysical Research* 115:F01009, doi:10.1029/JF001444.
- Gardner, L. R. (2009). Assessing the effect of climate change on mean annual runoff. *Journal of Hydrology* 379:351–359.
- Garrick, M., C. Cunnane, and J. E. Nash (1978). A criterion of efficiency for rainfall-runoff models. *Journal of Hydrology* 36:375–381.
- Garstka, W. U. (1964). Snow and snow survey. In Y. T. Chow, ed., *Handbook of Applied Hydrology* (Section 10). New York: McGraw-Hill.
- Gary, H. L. (1972). Rime contributes to water balance in high-elevation aspen forests. *Journal of Forestry* 70:93–97.
- Gash, J. H. C. (1979). An analytical model of rainfall interception in forests. *Quarterly Journal of the Royal Meteorological Society* 105:43–55.
- Gash, J. H. C., and A. J. Morton (1978). An application of the Rutter model to the estimation of the interception loss from Thetford forest. *Journal of Hydrology* 38:47–58.
- Gash, J. H. C., I. R. Wright, and C. R. Lloyd (1980). Comparative estimates of interception loss from three coniferous forests in Great Britain. *Journal of Hydrology* 48:87–105.
- Gat, J. R. (1996). Oxygen and hydrogen isotopes in the hydrologic cycle. *Annual Reviews of Earth and Planetary Science* 24:225–262.
- Gavilán, P., and F. Castillo-Llanque (2009). Estimating reference evapotranspiration with atmometers in a semiarid environment. *Agricultural Water Management* 96(3):465–472.
- Gburek, W. J. (1990). Initial contributing area of a small watershed. *Journal of Hydrology* 118:387–403.
- Gentilli, J. (1955). Estimating dew point from minimum temperature. *Bulletin of the American Meteorological Society* 36:128–131.
- Giambelluca, T. W., D. L. McKenna, and P. C. Ekern (1992). An automated recording atmometer: 1. Calibration and testing. *Agricultural and Forest Meteorology* 62:109–125.
- Gibbs, R. J. (1970). Mechanisms controlling world water chemistry. *Science* 170:1088–1090.
- Gillet, N. P., V. K. Arora, G. M. Flato, J. F. Scinocca, and K. von Salzen (2012). Improved constraints on 21st-century warming derived using 160 years of temperature observations. *Geophysical Research Letters* 39:L01704, doi:10.1029/2011GL050226.
- Gillham, R. W. (1984). The capillary fringe and its effect on water-table response. *Journal of Hydrology* 67:307–324.
- Gilman, C. S. (1964). Rainfall. In Y. T. Chow, ed., *Handbook of Applied Hydrology* (Section 9). New York: McGraw-Hill.
- Gilroy, K. L., and R. H. McCuen (2012). A nonstationary flood-frequency analysis method to adjust for future climate change and urbanization. *Journal of Hydrology* 414–415:40–48.
- Giorgi, F., and R. Avissar (1997). Representation of heterogeneity effects in earth system modeling: Experience from land surface modeling. *Reviews of Geophysics* 35:413–437.
- Giusti, L., and C. Neal (1993). Hydrological pathways and solute chemistry of storm runoff at Dargall Lane, southwest Scotland. *Journal of Hydrology* 142:1–27.
- Gleeson, T., L. Marklund, L. Smith, and A. H. Manning (2011). Classifying the water table at regional to continental scales. *Geophysical Research Letters* 38:L05401, doi:10.1029/2010GL046427.
- Gleick, P. H., ed. (1993). *Water in Crisis*. New York: Oxford University Press.
- Glover, R. E. (1964). *The Pattern of Freshwater Flow in a Coastal Aquifer*. Water-Supply Paper 1613-C. Washington, DC: US Geological Survey.
- Golding, D. L., and R. H. Swanson (1986). Snow distribution patterns in clearings and adjacent forest. *Water Resources Research* 22:1931–1940.
- Goodison, B. E., P. Y. T. Louie, and D. Yang (1998). *WMO Solid Precipitation Measurement Intercomparison Final Report*. WMO/TD No. 872. Geneva: World Meteorological Organization.
- Goodison, R. E. (1981). Compatibility of Canadian snowfall and snowcover data. *Water Resources Research* 17:893–900.
- Goodison, R. E., H. L. Ferguson, and G. A. McKay (1981). Measurement and data analysis. In Gray and Male (1981).
- Goovaerts, P. (2000). Geostatistical approaches for incorporating elevation into the spatial interpolation of rainfall. *Journal of Hydrology* 228:113–129.
- Goss, M. J., and W. Ehlers (2009). The role of lysimeters in the development of our understanding of soil water and nutrient dynamics in ecosystems. *Soil Use and Management* 25(3):213–223.
- Goto, H., K. Kikuchi, and M. Kajikawa (2012). Influence of different surface soils on snow-water content and snow type of the snow cover. *Japanese Journal of Snow and Ice* 74:145–158.
- Grace, R. A., and P. S. Eagleson (1966). The modeling of overland flow. *Water Resources Research* 2(3):393–403.
- Graf, W. L. (1999). Dam nation: A geographic census of American dams and their large-scale hydrologic impacts. *Water Resources Research* 35:1305–1311.
- Grasty, R. L. (1979). One flight snow-water equivalent measurement by airborne gamma-ray spectrometry. Paper presented at World Meteorological Organization Workshop on Remote Sensing of Snow and Soil Moisture by Nuclear Techniques, Voss, Norway, April 1979.
- Gray, D. M., and T. D. Prowse (1992). Snow and floating ice. In D. R. Maidment, ed., *Handbook of Hydrology* (chapter 7). New York: McGraw-Hill.
- Gray, D. M., and J. M. Wigham (1970). Peak flow-rainfall events. In D. M. Gray, ed., *Handbook on the Principles of Hydrology* (section VIII). Port Washington, NY: Water Information Center.
- Gray, W. G., and S. M. Hassanzadeh (1991). Paradoxes and realities in unsaturated flow theory. *Water Resources Research* 27:1847–1854.
- Green, W. H., and G. A. Ampt (1911). Studies on soil physics, 1: The flow of air and water through soils. *Journal of Agricultural Science* 4:1–24.
- Gregory, K. J., and D. E. Walling (1973). *Drainage Basin Form and Process: A Geomorphological Approach*. New York: John Wiley.
- Grimmond, C. S. B., S. A. Isard, and M. J. Belding (1992). Development and evaluation of continuously weighing mini-lysimeters. *Agricultural and Forest Meteorology* 62:205–218.
- Groisman, P. Ya., and D. R. Easterling (1994). Variability and trends of total precipitation and snowfall over the United States and Canada. *Journal of Climate* 7:184–205.
- Groisman, P. Ya., T. R. Karl, and R. W. Knight (1994). Observed impact of snow cover on the heat balance and the rise of continental spring temperatures. *Science* 263:198–200.
- Groisman, P. Ya., R. W. Knight, D. R. Easterling, T. R. Karl, G. C. Hegerl, and V. N. Razuvaev (2005). Trends in intense precipitation in the climate record. *Journal of Climate* 18:1326–1350.
- Groisman, P. Ya., and D. R. Legates (1994). The accuracy of United States precipitation data. *Bulletin of the American Meteorological Society* 75:215–227.
- Grove, M., J. Harbor, and B. Engel (1998). Composite vs. distributed curve numbers: Effects on estimates of storm runoff depths. *Journal of the American Water Resources Association* 34:1015–1023.
- Groves, J. R. (1989). A practical soil-moisture profile model. *Water Resources Bulletin* 25:875–880.
- Grundy, W. D. (1988). Using the USGS STATPAC Programs: A Hands-On Course. Denver, CO: The Computer-Oriented Geological Society.
- Güntner, A. (2008). Improvement of global hydrological models using GRACE data.

- Survey of Geophysics* 29:375–397, doi:10.1007/s10712-008-9038-y.
- Gupta, V. L., S. M. Afad, J. W. Fordham, and J. M. Federici (1979). Unsteady streamflow modeling guidelines. *Journal of Hydrology* 43:79–97.
- Gupta, V. K., E. Waymire, and C. T. Wang (1980). Representation of an instantaneous unit hydrograph from geomorphology. *Water Resources Research* 16:855–862.
- Haan, C. T. (2002). *Statistical Methods in Hydrology*, 2nd ed. Ames: Iowa State University Press.
- Habib, E., G. Lee, D. Kim, and G. J. Ciach (2010). Ground-based direct measurement. In F. Y. Testik and M. Gebremichael, eds., *Rainfall: State of the Science* (pp. 61–77). Washington, DC: American Geophysical Union.
- Haerter, J. O., P. Berg, and S. Hagemann (2010). Heavy rain intensity distributions on varying time scales and at different temperatures. *Journal of Geophysical Research* 115, doi:10.1029/2009JD013384.
- Haitjema, H. M. (1995). On the residence time distribution in idealized groundwater sheds. *Journal of Hydrology* 172:127–146.
- Hakenkamp, C. C., H. M. Valett, and A. J. Boulton (1993). Perspectives on the hyporheic zone: Integrating hydrology and biology—concluding remarks. *Journal of the North American Benthological Society* 12:94–99.
- Hall, F. R. (1968). Base-flow recessions—a review. *Water Resources Research* 4:973–983.
- Halpert, M. S., and C. F. Ropelewski (1992). Surface temperature patterns associated with the Southern Oscillation. *Journal of Climate* 5:577–593.
- Hamon, R. W. (1963). *Computation of Direct Runoff Amounts from Storm Rainfall*. Publication 63. Wallingford, Oxon., UK: International Association of Scientific Hydrology.
- Hamon, R. W., L. L. Weiss, and W. T. Wilson (1954). Insolation as an empirical function of daily sunshine duration. *Monthly Weather Review* 82(6):141–146.
- Hansen, E. M. (1987). Probable maximum precipitation for design floods in the United States. *Journal of Hydrology* 96:267–278.
- Hansen, E. M., L. C. Schreiner, and J. F. Miller (1982). *Application of Probable Maximum Precipitation Estimates—United States East of the 105th Meridian*. Hydrometeorological Report 52. Washington, DC: US National Oceanographic and Atmospheric Administration.
- Hansen, J., R. Ruedy, M. Sato, and K. Lo (2010). Global surface temperature change. *Reviews of Geophysics* 48:RG4004, doi:10.1029/2010RG000345.
- Hansen, J., M. Sato, P. Kharecha, D. Beerling, R. Berner, V. Masson-Delmotte, M. Pagani, M. Raymo, D. L. Royer, and J. C. Zachos (2008). Target atmospheric CO₂: Where should humanity aim? *The Open Atmospheric Science Journal* 2:217–231.
- Harbeck, G. E. (1962). *A Practical Field Technique for Measuring Reservoir Evaporation Utilizing Mass-Transfer Theory*. Professional Paper 272-E. Washington, DC: US Geological Survey.
- Harbeck, G. E. et al. (1954). *Water-Loss Investigations: Lake Hefner Studies*, Technical Report. Professional Paper 269. Washington, DC: US Geological Survey.
- Hardy, J. P., R. Melloch, G. Koenig, D. Marks, A. Winstral, J. W. Pomeroy, and T. Link (2004). Solar radiation transmission through conifer canopies. *Agricultural and Forest Meteorology* 126:257–270.
- Harlin, J. M. (1984). Watershed morphometry and time to hydro graph peak. *Journal of Hydrology* 67:141–154.
- Harman, C. J., M. Sivapalan, and P. Kumar (2009). Power law catchment-scale recessions rising from heterogeneous linear small-scale dynamics. *Water Resources Research* 45:W09404, doi:10.1029/2008WR007392.
- Harr, R. D. (1982). Fog drip in the Bull Run Municipal Watershed, Oregon. *Water Resources Bulletin* 18:785–789.
- Harte, J. (1985). *Consider A Spherical Cow*. Los Altos, CA: William Kaufmann.
- Haupt, H. F. (1969). A simple snowmelt lysimeter. *Water Resources Research* 5(3):714–718.
- Heath, R. C. (1982). *Basic Ground-Water Hydrology*. Water-Supply Paper 2220. Washington, DC: US Geological Survey.
- Heggen, R. J. (1983). Thermal dependent physical properties of water. *Journal of Hydraulic Engineering* 109:298–302.
- Helm, K. P., N. L. Bindoff, and J. A. Church (2010). Changes in the global hydrological cycle inferred from ocean salinity. *Geophysical Research Letters* 37:L18701, doi:10.1029/2010GL044222.
- Helsel, D. R., and R. M. Hirsch (1992). Statistical methods in water resources. In *Techniques of Water-Resources Investigations* (book 4, chapter A3). Washington, DC: US Geological Survey.
- Helvey, J. D. (1971). A summary of rainfall interception by certain conifers of North America. In *Biological Effects in the Hydrological Cycle*, Proceedings of Third International Seminar for Hydrology Professors. West Lafayette, IN: Purdue University Agricultural Experiment Station: 103–113.
- Helvey, J. D., and J. H. Patric (1965a). Design criteria for interception studies. Wallingford, Oxon., UK: International Association of Hydrologic Sciences Publication 67:131–137.
- Helvey, J. D., and J. H. Patric (1965b). Canopy and litter interception of rainfall by hardwoods of eastern United States. *Water Resources Research* 1:193–206.
- Helvey, J. D., and J. H. Patric (1983). Sampling accuracy of pit vs. standard rain gages on the Fernow Experimental Forest. *Water Resources Bulletin* 19:87–89.
- Henderson, F. M., and R. A. Wooding (1964). Overland flow and groundwater flow from a steady rainfall of finite duration. *Journal of Geophysical Research* 69(8):1531–1540.
- Henderson-Sellers, A. (1992). Continental cloudiness changes this century. *GeoJournal* 27:255–262.
- Hendrick, R. L., and R. J. DeAngelis (1976). Seasonal snow accumulation, melt and water input—a New England model. *Journal of Applied Meteorology* 15:715–727.
- Hendrick, R. L., R. J. DeAngelis, and S. L. Dingman (1978). The role of elevation in determining spatial distributions of precipitation, snow, and water input at Mt. Mansfield, Vermont. Proceedings of a Workshop on Modelling of Snow-Cover Runoff. Hanover, NH: US Army Cold Regions Research and Engineering Laboratory.
- Hengl, T., A. AghaKouchak, and M. Perćec Tadić (2010). Methods and data sources for spatial prediction of rainfall. In F. Y. Testik and M. Gebremichael, eds., *Rainfall: State of the Science* (pp. 189–214). Washington, DC: American Geophysical Union.
- Herschy, R. W. (1985). *Streamflow Measurement*. New York: Elsevier.
- Herschy, R. W. (1999). Flow measurement. In R. W. Herschy (ed.), *Hydrometry: Principles and Practices* (2nd ed., pp. 9–83). Chichester, UK: John Wiley & Sons.
- Hershfield, D. M. (1961). *Rainfall Frequency Atlas of the United States for Durations from 30 Minutes to 24 Hours and Return Periods from 1 to 100 Years*. Technical Paper 40. US Weather Bureau.
- Hewlett, J. D. (1982). *Principles of Forest Hydrology* (2nd ed.). Athens: University of Georgia Press.
- Hewlett, J. D., and A. R. Hibbert (1961). Increases in water yield after several types of forest cutting. *International Association of Scientific Hydrology Bulletin* 6:5–17.
- Hewlett, J. D., and A. R. Hibbert (1963). Moisture and energy conditions within a sloping soil mass during drainage. *Journal of Geophysical Research* 68:1081–1087.
- Hewlett, J. D., and A. R. Hibbert (1967). Factors affecting the response of small watersheds to precipitation in humid areas. In W. E. Sopper and H. W. Lull, eds., *International Symposium on Forest Hydrology* (pp. 275–290). New York: Pergamon.
- Hicks, D. M., and P. J. Mason (1991). *Roughness Characteristics of New Zealand Rivers*. Wellington: New Zealand Water Resources Survey.
- Hillel, D. (1971). *Soil and Water*. San Diego, CA: Academic Press.
- Hillel, D. (1980a). *Fundamentals of Soil Physics*. San Diego, CA: Academic Press.
- Hillel, D. (1980b). *Applications of Soil Physics*. San Diego, CA: Academic Press.
- Hillel, D. (1998). Evaporation from bare-surface soils and wind erosion. In *Environmental Soil Physics* (pp. 508–522). San Diego, CA: Academic Press.
- Hills, R. C. (1971). Lateral flow under cylinder infiltrometers: A graphical correction procedure. *Journal of Hydrology* 13:153–162.
- Hinkleman, L. M., P. W. Stackhouse, Jr., B. A. Wielicki, T. Zhang, and S. R. Wilson (2009). Surface insolation trends from satellite and ground measurements: Comparisons and challenges. *Journal of Geophysical Research: Atmospheres* 114:D00D20, doi:10.1029/2008JD011004.
- Hino, M., K. Fujita, and H. Shutto (1987). A laboratory experiment on the role of grass for infiltration and runoff processes. *Journal of Hydrology* 90:303–325.
- Hinzman, L., N. D. Bettez, W. R. Bolton, F. S. Chapin, et al. (2005). Evidence and implications of recent climate change in northern Alaska and other Arctic regions. *Climatic Change* 72:251–298.

- Hipolito, J. N., and J. M. Loureiro (1988). Analysis of some velocity-area methods for calculating open-channel flow. *Hydrological Sciences Journal* 33:311–320.
- Hirashima, H., S. Yamaguchi, A. Sato, and M. Lehning (2010). Numerical modeling of liquid water movement through layered snow based on new measurements of the water retention curve. *Cold Regions Science and Technology* 64:94–103.
- Hirsch, R. M., D. R. Helsel, T. A. Cohn, and E. J. Gilroy (1992). Statistical treatment of hydrologic data. In D. R. Maidment, ed., *Handbook of Hydrology* (chapter 17). New York: McGraw-Hill.
- Holtan, H. N., and D. E. Overton (1963). Analyses and application of simple hydro graphs. *Journal of Hydrology* 1:250–264.
- Holtan, H. N., and D. E. Overton (1964). Storage-flow hysteresis in hydrograph synthesis. *Journal of Hydrology* 2:309–323.
- Hooper, R. P. (2003). Diagnostic tools for mixing models of stream water chemistry. *Water Resources Research* 39(3):1055, doi:10.1029/2002WR001528.
- Hooper, R. P., N. Christopherson, and N. E. Peters (1990). Modeling streamwater chemistry as a mixture of soil-water end-members—an application to the Panola Mountain catchment, Georgia, U.S.A. *Journal of Hydrology* 116:321–343.
- Hoover, M. D. (1971). Snow interception and redistribution in the forest. In *Biological Effects in the Hydrological Cycle*. Proceedings of Third International Seminar for Hydrology Professors. West Lafayette, IN: Purdue University Agricultural Experiment Station:114–122.
- Hopkins, C. D., Jr. (1973). Estimates of precipitation, flood stages, and frequency. In *What If Agnes Had Hit the Connecticut River Basin?* Boston: New England River Basins Commission.
- Hornberger, G. M., K. J. Beven, B. J. Cosby, and D. E. Sappington (1985). Shenandoah Watershed Study: Calibration of a topography-based, variable contributing area hydrological model to a small forested catchment. *Water Resources Research* 21:1841–1850.
- Horne, F. E., and M. L. Kavvas (1997). Physics of the spatially averaged snowmelt process. *Journal of Hydrology* 191:179–207.
- Horton, R. E. (1931). The field, scope, and status of the science of hydrology. American Geophysical Union, Transactions, Reports and Papers, Hydrology:189–202.
- Horton, R. E. (1933). The role of infiltration in the hydrologic cycle. *American Geophysical Union Transactions* 14:446–460.
- Horton, R. E. (1945). Erosional development of streams and their drainage basins: Hydrophysical approach to quantitative morphology. *Geological Society of America Bulletin* 56:275–370.
- Hosking, J. R. M., and J. R. Wallis (1997). *Regional Frequency Analysis*. New York: Cambridge University Press.
- Hostetler, S. W., and P. J. Bartlein (1990). Simulation of lake evaporation with application to modeling lake level variations of Harney-Malheur Lake, Oregon. *Water Resources Research* 26:2603–2612.
- Howell, D. G., and R. W. Murray (1986). A budget for continental growth and denudation. *Science* 233:446–449.
- Hoyos, C. D., P. A. Agudela, P. J. Webster, and J. A. Curry (2005). Deconvolution of the factors contributing to the increase in global hurricane intensity. *Science* 312:94–97.
- Hubbert, M. K. (1940). The theory of groundwater motion. *Journal of Geology* 48:785–944.
- Huff, F. A. (1955). Comparison between standard and small orifice rain gages. *American Geophysical Union Transactions* 36:689–694.
- Huff, F. A. (1970). Sampling errors in measurement of mean precipitation. *Journal of Applied Meteorology* 9:35–44.
- Huff, F. A. (1977). Effects of the urban environment on heavy rainfall distribution. *Water Resources Bulletin* 13:807–816.
- Huff, F. A. (1995). Characteristics and contributing causes of an abnormal frequency of flood-producing rainstorms at Chicago. *Water Resources Bulletin* 31:703–714.
- Huff, F. A., and S. A. Changnon (1973). Precipitation modification by major urban areas. *Bulletin of the American Meteorological Society* 54:1220–1232.
- Hunt, B. (1990). An approximation of the bank storage effect. *Water Resources Research* 26:2769–2775.
- Hunt, L. A., L. Kuchar, and C. J. Swanton (1998). Estimation of solar radiation for use in crop modeling. *Agricultural and Forest Meteorology* 91:293–300.
- Hunt, R. J., D. P. Krabbenhoft, and M. P. Anderson (1996). Groundwater inflow measurements in wetland systems. *Water Resources Research* 32:495–507.
- Huntington, T. G. (2006). Evidence for intensification of the global water cycle: Review and synthesis. *Journal of Hydrology* 380:83–95.
- Hurrell, J. W. (1995). Decadal trends in the North Atlantic oscillation regional temperatures and precipitation. *Science* 269:676–679.
- Inamdar, S., G. Dhillon, S. Singh, S. Dutta, D. Levia, D. Scott, M. Mitchell, J. Van Stan, and P. McHale (2013). Temporal variation in end-member chemistry and its influence on runoff mixing patterns in a forested, Piedmont catchment. *Water Resources Research* 49, doi:10.1002/wrcr.20158.
- Intergovernmental Panel on Climate Change (2007). *Climate Change 2007: Synthesis Report*. Contribution of Working Groups I, II and III to the Fourth Assessment Report of the Intergovernmental Panel on Climate Change. Core Writing Team, R. K. Pachauri and A. Reisinger, eds. Geneva, Switzerland: Author.
- International Association of Hydrological Sciences, The Ad Hoc Group on Global Water Data Sets (2001). Global water data: A newly endangered species. *Eos* 82(5):54, 56, 58.
- Institute of Hydrology (1980). *Low-Flow Studies Report*. Wallingford, UK: Institute of Hydrology.
- Iqbal, M. (1983). *An Introduction to Solar Radiation*. San Diego, CA: Academic Press.
- Jackson, C. R. (1992). Hillslope infiltration and lateral downslope unsaturated flow. *Water Resources Research* 28:2533–2539.
- Jacobsen, O. H., and P. Schjønning (1993). Field evaluation of time domain reflectometry for soil water measurements. *Journal of Hydrology* 152:159–172.
- Jalbert, J., T. Mathevot, and A.-C. Favre (2011). Temporal uncertainty estimation of discharges from rating curves using a variographic analysis. *Journal of Hydrology* 397:83–92.
- Jana, R. B., and B. P. Mohanty (2012). A comparative study of multiple approaches to soil hydraulic parameter scaling applied at the hillslope scale. *Water Resources Research* 48:W02520, doi:10.1029/2010WR010185.
- Jarvis, P. G. (1976). The interpretations of the variations in leaf water potential and stomatal conductance found in canopies in the field. Royal Society of London *Philosophical Transactions Series B* 273:593–610.
- Jayatilaka, C. J., R. W. Gillham, D. W. Blowes, and R. J. Nathan (1996). A deterministic-empirical model of the effect of the capillary fringe on near-stream area runoff. 2. Testing and application. *Journal of Hydrology* 184:317–336.
- Jellinek, H. H. G. (1972). The ice interface. In R. A. Horne (ed.), *Water and Aqueous Solutions*. New York: Wiley-Interscience.
- Jenkins, C. T. (1968). Techniques for computing rate and volume of stream depletion by wells. *Groundwater* 6(2):37–46.
- Jensen, M. E., R. D. Burman, and R. G. Allen, eds. (1990). *Evapotranspiration and Irrigation Water Requirements*. Manuals and Reports of Engineering Practice No. 70. New York: American Society of Civil Engineering.
- Jobson, H. E. (1972). Effect of using averaged data on the computed evaporation. *Water Resources Research* 8:513–518.
- Johansson, P.-O. (1986). Diurnal groundwater level fluctuations in sandy till—a model analysis. *Journal of Hydrology* 87:125–134.
- Johansson, P.-O. (1987). Estimation of groundwater recharge in sandy till with two different methods using groundwater level fluctuations. *Journal of Hydrology* 90:183–198.
- Johnson, A. I. (1963). *A Field Method for Measurement of Infiltration*. Water-Supply Paper 1544-F. Washington, DC: US Geological Survey.
- Johnson, D., M. Smith, V. Koren, and B. Finnerty (1999). Comparing mean areal precipitation estimates from NEXRAD and rain gauge networks. *Journal of Hydrologic Engineering* 4(2):117–124.
- Johnson, G. C., J. M. Lyman, J. K. Willis, S. Levitus, T. Boyer, J. Antonov, M. D. Palmer, and S. A. Good (2010). Ocean heat content. In Special Supplement, “State of the Climate in 2009.” *Bulletin of the American Meteorological Society* 91(7):S56–S59.
- Jonas, T., C. Marty, and J. Magnusson (2009). Estimating the snow water equivalent from snow depth measurements in the Swiss Alps. *Journal of Hydrology* 378:161–167.
- Jones, J. A., and L. J. Connolly (2002). A semi-distributed simulation model for natural pipeflow. *Journal of Hydrology* 262(1–4):28–49.
- Jones, J. A., and R. M. Perkins (2010). Extreme flood sensitivity to snow and forest harvest, western Cascades, Oregon, United States.

- Water Resources Research* 46:W12512, doi:10.1029/2009WR008632.
- Jones, J. A. A. (2010). Soil piping and catchment response. *Hydrological Processes* 24:1548–1566.
- Jones, K. L., G. C. Poole, W. W. Woessner, M. V. Vitale, B. R. Boer, S. J. O'Daniel, S. A. Thomas, and B. A. Geffen (2007). Geomorphology, hydrology, and aquatic vegetation drive seasonal hyporheic flow patterns across a gravel-dominated floodplain. *Hydrologic Processes* 22:2105–2113.
- Jordan, J. P. (1994). Spatial and temporal variability of stormflow generation processes on a Swiss catchment. *Journal of Hydrology* 153:357–382.
- Jorgenson, M. T., Y. L. Shur, and E. R. Pullman (2006). Abrupt increase in permafrost degradation in Arctic Alaska. *Geophysical Research Letters* 33:L02503, doi:10.1029/2005GL024960.
- Justus, C. G., M. V. Paris, and J. D. Tarpley (1986). Satellite-measured insolation in the United States, Mexico, and South America. *Remote Sensing of Environment* 20:57–83.
- Kabat, P., R. W. A. Hutjes, and R. A. Feddes (1997). The scaling characteristics of soil parameters: From plot scale heterogeneity to subgrid parameterization. *Journal of Hydrology* 190:363–396.
- Kahler, D. M., and W. Brutsaert (2006). Complementary relationship between daily evaporation in the environment and pan evaporation. *Water Resources Research* 42:W05413, doi:10.1029/2005WR004541.
- Kampf, S. K., and S. J. Burges (2010). Quantifying the water balance in a planar hillslope plot: Effects of measurement errors on flow prediction. *Journal of Hydrology* 380:191–202.
- Karl, T. R., P. Ya. Croisman, R. W. Knight, and R. R. Heim, Jr. (1993). Recent variations in snow cover and snowfall in North America and their relation to precipitation and temperature variations. *Journal of Climate* 6:1327–1344.
- Karl, T. R., R. W. Knight, K. P. Gallo, T. C. Peterson, et al. (1993). Asymmetric trends of daily maximum and minimum temperature. *Bulletin of the American Meteorological Society* 74:1007–1023.
- Karl, T. R., R. W. Knight, and N. Plummer. 1995. Trends in high-frequency climate variability in the twentieth century. *Nature* 377:217–220.
- Karl, T. R., and R. G. Quayle (1988). Climate change in fact and theory: Are we collecting the facts? *Climatic Change* 13:5–17.
- Karl, T. R., and W. E. Riebsame (1989). The impact of decadal fluctuations in mean precipitation and temperature on runoff: A sensitivity study over the United States. *Climatic Change* 15:423–447.
- Karl, T. R., and K. E. Trenberth (2003). Modern global climate change. *Science* 302:1719–1723.
- Kasahara, T., and S. M. Wondzell (2003). Geomorphic controls on hyporheic exchange flow in mountain streams. *Water Resources Research* 39:1005, doi:10.1029/2002WR001386.
- Kavetski, D., and M. P. Clark (2010). Ancient numerical daemons of conceptual hydrological modeling. Part 2: Impact of time stepping schemes on model analysis and prediction. *Water Resources Research* 46:W10511, doi:10.1029/2009WR008896.
- Kavetski, D., G. Kuczera, and S. W. Franks (2003). Semidistributed hydrological modeling: A “saturation path” perspective on TOPMODEL and VIC. *Water Resources Research* 39(9), doi:10.1029/2003WR002122.
- Keim, B. D., A. M. Wilson, C. P. Wake, and T. G. Huntington (2003). Are there spurious temperature trends in the United States Climate Division database? *Geophysical Research Letters* 30(7), doi:10.1029/2002GL016295.
- Kendall, C., M. G. Sklash, and T. D. Bullen (1995). Isotope tracers of water and solute sources in catchments. In S. T. Trudgill, ed., *Solute Modelling in Catchment Systems* (pp. 261–303). New York: John Wiley.
- Khan, A., K. S. Richards, G. Parker, A. McRobie, and B. Mukhopadhyay (2013). How large is the Upper Indus Basin? The pitfalls of auto-delimitation using DEMs. *Journal of Hydrology* 509:442–453.
- Khosla, B. K. (1980). Comparison of calculated and in situ measured unsaturated hydraulic conductivity. *Journal of Hydrology* 47:325–332.
- Kidd, C., V. Levizzani, and S. Laviola (2010). Quantitative precipitation estimates from earth observation satellites. In F. Y. Testik and M. Gebremichael, eds., *Rainfall: State of the Science* (pp. 127–158). Washington, DC: American Geophysical Union.
- Kiehl, J. (2011). Lessons from Earth's past. *Science* 331:158–159.
- Kilpatrick, F. A., and E. D. Cobb (1985). Measurement of discharge using tracers. In *Techniques of Water-Resources Investigations* (book 3, chapter A16). Washington, DC: US Geological Survey.
- Kilpatrick, F. A., and J. F. Wilson, Jr. (1989). Measurement of time of travel in streams by dye tracing. In *Techniques of Water-Resources Investigations* (book 3, chapter A9). Washington, DC: US Geological Survey.
- King, H. W., C. O. Whisler, and G. Woodburn (1960). Hydraulic similitude and dimensional analysis. In *Hydraulics* (5th ed., pp. 318–330). New York: John Wiley.
- Kirby, W. (1974). Algebraic boundedness of sample statistics. *Water Resources Research* 10:220–222.
- Kirchner, J. W. (2006). Getting the right answers for the right reasons: Linking measurements, analyses, and models to advance the science of hydrology. *Water Resources Research* 42:W03S04, doi:10.1029/2005WR004362.
- Kirchner, J. W. (2009). Catchments as simple dynamical systems: Catchment characterization, rainfall-runoff modeling, and doing hydrology backward. *Water Resources Research* 45:W02429, doi:10.1029/2008WR006912.
- Kirkby, M. J. (1976). Tests of the random network model and its application to basin hydrology. *Earth Surface Processes* 1:197–212.
- Kirkby, M. J. (1988). Hillslope runoff processes and models. *Journal of Hydrology* 100:315–339.
- Kirkby, M. J. (1993). Network hydrology and geomorphology. In K. Beven and M. J. Kirkby, eds., *Channel Network Hydrology* (chapter 1). New York: John Wiley.
- Kirkby, M. J. (1997). TOPMODEL: A personal view. *Hydrological Processes* 11:1087–1097.
- Kitanidis, P. K. (1992). Geostatistics. In D. R. Maidment, ed., *Handbook of Hydrology* (chapter 20). New York: McGraw-Hill.
- Klemeš, V. (1986a). Dilettantism in hydrology: Transition or destiny? *Water Resources Research* 22:177S–188S.
- Klemeš, V. (1986b). Operational testing of hydrological simulation models. *Hydrological Sciences Journal* 31:13–24.
- Kling, H., and H. P. Nachtnebel (2009). A method for the regional estimation of runoff separation parameters for hydrological modeling. *Journal of Hydrology* 364:163–174.
- Klock, G. O. (1972). Snowmelt temperature influence on infiltration and soil water retention. *Journal of Soil and Water Conservation* 27:12–14.
- Knight, D. B., and R. E. Davis (2009). Contribution of tropical cyclones to extreme rainfall events in the southeastern United States. *Journal of Geophysical Research: Atmospheres* 114:D23102, doi:10.1029/2009JD012511.
- Knighton, D. (1998). *Fluvial Forms and Processes: A New Perspective*. London, UK: Hodder Arnold.
- Koberg, G. E. (1964). *Methods to Compute Long-Wave Radiation from the Atmosphere and Reflected Solar Radiation from a Water Surface* (Professional Paper 272-F). Washington, DC: US Geological Survey.
- Kohler, M. A., and L. H. Parmele (1967). Generalized estimates of free-water evaporation. *Water Resources Research* 3:997–1005.
- Kohler, M. A., T. J. Nordenson, and W. E. Fox (1955). *Evaporation from Pans and Lakes*. Research Paper 38. US Weather Bureau.
- Kuhl, S. C., and J. R. Miller (1992). Seasonal river runoff calculated from a global atmospheric model. *Water Resources Research* 28(8):2029–2039.
- Kuligowski, R. J. (1997). *An Overview of National Weather Service Quantitative Precipitation Estimates*. TDL Office Note 97-4. NOAA, NWS, Office of Systems Development, Techniques Development Laboratory.
- Kumar, P. (2011). Typology of hydrologic predictability. *Water Resources Research* 47:W00H05, doi:10.1029/2010WR009769.
- Kumar, S., and S. C. Jain (1982). Application of SCS infiltration model. *Water Resources Bulletin* 18:503–507.
- Kunkel, K. E., D. R. Easterling, D. A. R. Krstovich, B. Gleason, L. Stoecker, and R. Smith (2010). Recent increases in U.S. heavy precipitation associated with tropical cyclones. *Geophysical Research Letters* 37:L24706, doi:10.1029/2010GL045164.
- Kustas, W. P., A. Rango, and R. Uijlenhoet (1994). A simple energy budget algorithm for the snowmelt runoff model. *Water Resources Research* 30:1515–1527.

- Kuusisto, E. (1986). The energy balance of a melting snow cover in different environments. In E. M. Morris (ed.), *Modeling Snowmelt-Induced Processes* (IAHS Publication 155). Wallingford, Oxford, UK: International Association of Hydrological Sciences.
- Kuznetsova, L. P. (1990). Use of data on atmospheric moisture transport over continents and large river basins for the estimation of water balances and other purposes. International Hydrological Programme. IHP-III Project 1.1. Paris: UNESCO.
- Labat, D., Y. Goddérus, J. L. Probst, and J. L. Guyot (2004). Evidence for global runoff increase related to climate warming. *Advances in Water Resources* 27:631–642.
- LaBaugh, J. W. (1985). Uncertainty in phosphorus retention, Williams Fork Reservoir, Colorado. *Water Resources Research* 21:1684–1692.
- LaBaugh, J. W. (1986). Wetland ecosystem studies from a hydrologic perspective. *Water Resources Bulletin* 22:1–10.
- Lacis, A. A., G. A. Schmidt, D. Rind, and R. A. Ruedy (2010). Atmospheric CO₂: Principal control knob governing earth's temperature. *Science* 330:356–359.
- Lamb, H. H. (1982). *Climate, History and the Modern World*. New York: Methuen.
- Langhans, C., G. Govers, J. Diels, A. Leys, W. Clymans, A. Van den Putte, and J. Valckx (2011). Experimental rainfall-runoff data: Reconsidering the concept of infiltration capacity. *Journal of Hydrology* 399:255–262.
- Larson, G. J., M. R. Delcore, and S. Offer (1987). Application of the tritium interface method for determining recharge rates to unconfined drift aquifers, I. Homogeneous case. *Journal of Hydrology* 91:59–72.
- Larson, K. M., E. D. Gutmann, V. U. Zavorotny, J. J. Braun, M. W. Williams, and F. G. Nieviniski (2009). Can we measure snow depth with GPS receivers? *Geophysical Research Letters* 36:L17502, doi:10.1029/2009GL039430.
- Larson, L. L., and E. L. Peck (1974). Accuracy of precipitation measurements for hydrologic modeling. *Water Resources Research* 10:857–863.
- Lean, J., and D. A. Warrilow (1989). Simulation of the regional climatic impact of Amazon deforestation. *Nature* 342:411–413.
- Lean, J. L., and D. H. Rind (2008). How natural and anthropogenic influences alter global and regional surface temperatures: 1889 to 2006. *Geophysical Research Letters* 35:L18701, doi:10.1029/2008GL034864.
- Lean, J. L., and D. H. Rind (2009). How will Earth's surface temperature change in future decades? *Geophysical Research Letters* 36:L15708, doi:10.1029/2009GL038932.
- Leaney, F. W., K. R. J. Smettem, and D. J. Chittleborough (1993). Estimating the contribution of preferential flow to subsurface runoff from a hillslope using deuterium and chloride. *Journal of Hydrology* 147:83–103.
- Leathers, D. J., and D. A. Robinson (1993). The association between extremes in North American snow cover extent and United States temperatures. *Journal of Climate* 6:1345–1355.
- Leathers, D. J., B. Yarnal, and M. A. Palecki (1991). The Pacific/North American teleconnection pattern and United States climate. Part 1: Regional temperature and precipitation associations. *Journal of Climate* 4:517–528.
- Lebel, T., G. Bastin, C. Obled, and J. D. Creutin (1987). On the accuracy of areal rainfall estimation: A case study. *Water Resources Research* 23:2123–2134.
- Lee, D. R. (1977). A device for measuring seepage flux in lakes and estuaries. *Limnology and Oceanography* 22:140–147.
- Lee, D. R., and H. B. N. Hynes (1978). Identification of groundwater discharge zones in a reach of Hillman Creek in southern Ontario. *Water Pollution Research Canada* 13:121–133.
- Lee, J.-E., and K. Boyce (2010). Impact of the hydraulic capacity of plants on water and carbon fluxes in tropical South America. *Journal of Geophysical Research: Atmospheres* 115:D23123, doi:10.1029/2010JD014568.
- Lee, R. (1964). Potential insolation as a topoclimatic characteristic of drainage basins. *International Association of Scientific Hydrology Bulletin* 9:27–41.
- Lee, R. (1980). *Forest Hydrology*. New York: Columbia University Press.
- Legates, D. R., and T. L. DeLiberty (1993). Precipitation measurement biases in the United States. *Water Resources Bulletin* 29:855–861.
- Lehner, B., and P. Döll (2004). Development and validation of a new database of lakes, reservoirs and wetlands. *Journal of Hydrology* 296:1–22.
- Lehner, B., K. Verdin, and A. Jarvis (2008). New global hydrography derived from spaceborne elevation data. *Eos* 89(10):93–104.
- Lemeur, R., and L. Zhang (1990). Evaluation of three evapotranspiration models in terms of their applicability for an arid region. *Journal of Hydrology* 114:395–411.
- Lemon, E. R., ed. (1983). *CO₂ and Plants: The Response of Plants to Rising Levels of Carbon Dioxide*. American Association for the Advancement of Science Symposium No. 84. Boulder, CO: Westview.
- Leonard, R. E., and A. R. Eschner (1968). Albedo of intercepted snow. *Water Resources Research* 4:931–935.
- Leopold, L. B. (1994). *A View of the River*. Cambridge: Harvard University Press.
- Leopold, L. B., M. G. Wolman, and J. P. Miller (1964). *Fluvial Processes in Geomorphology*. San Francisco, CA: W.H. Freeman.
- Lettenmaier, D. P., and J. S. Famiglietti (2006). Hydrology: Water from on high. *Nature* 444(7119):562–563.
- Lettenmaier, D. P., and E. F. Wood (1992). Hydrologic forecasting. In D. R. Maidment, ed., *Handbook of Hydrology* (chapter 26). New York: McGraw-Hill.
- Lettenmaier, D. P., E. F. Wood, and J. R. Wallis (1994). Hydro-climatological trends in the continental United States, 1948–88. *Journal of Climate* 7:588–607.
- Levine, J. B., and G. D. Salvucci (1999). Equilibrium analysis of groundwater-vadose zone interactions and the resulting spatial distribution of hydrologic fluxes across a Canadian prairie. *Water Resources Research* 35:1369–1383.
- Levinson, D. H., K. A. Hilburn, J. H. Lawrimore, and M. C. Kruk (2010). Global precipitation. In Special Supplement, "State of the Climate in 2009." *Bulletin of the American Meteorological Society* 91(7):S31–32.
- Li, M., and Q. Shao (2010). An improved statistical approach to merge satellite rainfall estimates and rain gauge data. *Journal of Hydrology* 385(1–4):51–64.
- Lin, A., and X. L. Wang (2011). An algorithm for blending multiple satellite precipitation measurements with in situ precipitation measurements in Canada. *Journal of Geophysical Research: Atmospheres* 116:D21111, doi:10.1029/2011JD016359.
- Lin, H. (2010). Earth's Critical Zone and hydropedology: Concepts, characteristics, and advances. *Hydrology and Earth System Sciences* 14:25–45.
- Linacre, E. T. (1993). Data-sparse estimation of lake evaporation, using a simplified Penman equation. *Agricultural and Forest Meteorology* 64:237–256.
- Linderholm, H. W. (2006). Growing season changes in the last century. *Agricultural and Forest Meteorology* 137:1–14.
- Lindroth, A. (1985). Canopy conductance of coniferous forests related to climate. *Water Resources Research* 21:297–304.
- Lindsey, S. D., and R. K. Farnsworth (1997). Sources of solar radiation estimates and their effect on daily potential evaporation for use in streamflow modeling. *Journal of Hydrology* 201:348–366.
- Linkin, M. E., and S. Nigam (2008). The North Pacific Oscillation–West Pacific teleconnection pattern: Mature-phase structure and winter impacts. *Journal of Climate* 21:1979–1997.
- Lins, H. F., and P. J. Michaels (1994). Increasing U.S. streamflow linked to greenhouse forcing. *EOS* 75:281, 284, 285.
- Linsley, R. K., M. A. Kohler, and J. L. H. Paulhus (1982). *Hydrology for Engineers* (3rd ed.). New York: McGraw-Hill.
- List, R. J. (1971). *Smithsonian Meteorological Tables* (6th ed.). Washington, DC: Smithsonian Institution Press.
- Liu, S. (1997). A new model for the prediction of rainfall interception in forest canopies. *Ecological Modelling* 99:151–159.
- Liu, S. (2001). Evaluation of the Liu model for predicting rainfall interception in forests worldwide. *Hydrological Processes* 15:2341–2360.
- Liu, S. M., Z. W. Xu, Z. L. Zhu, Z. Z. Jia, and M. J. Zhu (2013). Measurements of evapotranspiration from eddy-covariance systems and large aperture scintillometers in the Hai River Basin, China. *Journal of Hydrology* 487:24–38.
- Liu, X., Y. Luo, D. Zhang, M. Zhang, and C. Liu (2011). Recent changes in pan?evaporation dynamics in China. *Geophysical Research Letters* 38:L13404, doi:10.1029/2011GL047929.
- Lloyd, C. R., J. H. C. Gash, W. J. Shuttleworth, and F. A. de O. Marques (1988). The measurement and modeling of rainfall interception by Amazonian rain forest.

- Agricultural and Forest Meteorology* 43:277–294.
- Loague, K. (1990). Simple design for simultaneous steady-state infiltration experiments with ring infiltrometers. *Water Resources Bulletin* 26:935–938.
- Loague, K., and G. A. Gander (1990). R-5 revisited: 1. Spatial variability of infiltration on a small rangeland catchment. *Water Resources Research* 28:957–971.
- Loague, K. M., and R. A. Freeze (1985). A comparison of rainfall-runoff modeling techniques on small upland catchments. *Water Resources Research* 21:229–248.
- Loaiciga, H. A., et al. (1996). Global warming and the hydrologic cycle. *Journal of Hydrology* 174:83–127.
- Lohman, S. W. (1979). *Ground-Water Hydraulics*. Professional Paper 708. Washington, DC: US Geological Survey.
- Loijens, H. S., and R. L. Grasty (1973). *Airborne Measurement of Snow-Water Equivalent Using Natural Gamma Radiation over Southern Ontario, 1972–1973*. Science Series No. 34. Ottawa, Ontario: Inland Waters Directorate, Environment Canada.
- Longuevergne, L., B. R. Scanlon, and C. R. Wilson (2010). GRACE hydrological estimates for small basins: Evaluating processing approaches on the High Plains Aquifer, USA. *Water Resources Research* 46:W11517, doi:10.1029/2009WR008564.
- Loosvelt, L., V. R. N. Pauwels, W. M. Cornelis, G. J. M. De Lannoy, and N. E. C. Verhoest (2011). Impact of soil hydraulic parameter uncertainty on soil moisture modeling. *Water Resources Research* 47:W03505, doi:10.1029/2010WR009204.
- Lottes, A. L., and A. M. Ziegler (1994). World peat occurrence and the seasonality of climate and vegetation. *Paleogeography, Paleoclimatology, Paleoecology* 106:23–37.
- Loucks, D. P., J. R. Stedinger, and D. A. Haith (1981). *Water Resource Systems Planning and Analysis*. Englewood Cliffs, NJ: Prentice-Hall.
- Loukas, A., and M. C. Quick (1996). Physically based estimation of lag time for forested mountainous watersheds. *Hydrological Sciences Journal* 41:1–19.
- Lovett, G. M., W. A. Reiners, and R. K. Olson (1982). Cloud droplet deposition in subalpine balsam fir forests: Hydrological and chemical inputs. *Science* 218:1303–1304.
- Lubchenco, J., and T. R. Karl (2012). Predicting and managing extreme weather events. *Physics Today* 65(3):31–37.
- Ludwig, W., and J.-L. Probst (1998). River sediment discharge to the oceans: Present-day controls and global budgets. *American Journal of Science* 298:265–295.
- Luk'yanovich, M. A. (2011). The genetic and seasonal structures of river runoff of the continents. *Geography and Natural Resources* 32(3):267–274. Original Russian text published in *Geography and Natural Resources* 32(3):125–133.
- Lull, H. W. (1964). Ecological and silvicultural aspects. In V. T. Chow (ed.), *Handbook of Applied Hydrology* (section 6). New York: McGraw-Hill.
- Lundberg, A., and S. Halldin (1994). Evaporation of intercepted snow: Analysis of gov-
- erning factors. *Water Resources Research* 30:2587–2598.
- Lundberg, A., I. Calder, and R. Harding (1998). Evaporation of intercepted snow: Measurement and modeling. *Journal of Hydrology* 206:151–163.
- Lundquist, J. D., and F. Lott (2008). Using inexpensive temperature sensors to monitor the duration and heterogeneity of snow-covered areas. *Water Resources Research* 44:W00D16, doi:10.1029/2008WR007035.
- Lv, M., Z. Hao, Z. Liu, and Z. Yu (2013). Conditions for lateral downslope unsaturated flow and effects of slope angle on soil moisture movement. *Journal of Hydrology* 486:321–333.
- L'vovich, M. I. (1974). *World Water Resources and Their Future*. Trans. by R. L. Nace. Washington DC: American Geophysical Union.
- Lyford, F. P., and H. K. Qashu (1969). Infiltration rates as affected by desert vegetation. *Water Resources Research* 5:1373–1376.
- Macek-Rowland, K. M. (1997). *1997 Floods in the Red River of the North and Missouri River Basins in North Dakota and Western Minnesota*. Open-File Report 97-575. Washington, DC: US Geological Survey.
- MacMillan, H., B. Jackson, M. Clark, D. Kavetski, and R. Woods (2011). Rainfall uncertainty in hydrologic modeling: An evaluation of multiplicative error models. *Journal of Hydrology* 400(1–2):83–94.
- Mahat, V., and D. G. Tarboton (2012). Canopy radiation transmission for an energy balance snowmelt model. *Water Resources Research* 48:W01534, doi:10.1029/2011WR010438.
- Male, D. H., and D. M. Gray (1981). Snow-cover ablation and runoff. In D. M. Gray and D. H. Male, eds., *Handbook of Snow*. Elmsford, NY: Pergamon Press.
- Maller, R. A., and M. L. Sharma (1981). An analysis of areal infiltration considering spatial variability. *Journal of Hydrology* 52:25–37.
- Manley, R. E. (1977). The soil moisture component of mathematical catchment simulation models. *Journal of Hydrology* 35:341–356.
- Marengo, J. A., J. Tomasella, L. M. Alves, W. R. Soares, and D. A. Rodriguez (2011). The drought of 2010 in the context of historical droughts in the Amazon region. *Geophysical Research Letters* 38:L12703, doi:10.1029/2011GL047436.
- Margaritz, M., A. Kaufman, M. Paul, E. Boaretto, and G. Hollos (1990). A new method to determine regional evapotranspiration. *Water Resources Research* 26:1757–1762.
- Markham, C. G. (1970). Seasonality of precipitation in the United States. *Annals of the Association of American Geographers* 60:593–597.
- Marsh, P., and M. K. Woo (1985). Meltwater movement in natural heterogeneous snow covers. *Water Resources Research* 21:1710–1716.
- Martina, M. L. V., E. Todini, and Z. Liu (2011). Preserving the dominant physical processes in a lumped hydrological model. *Journal of Hydrology* 399:121–131.
- Martinec, J., and A. Rango (1989). Merits of statistical criteria for the performance of hydrological models. *Water Resources Bulletin* 25:421–432.
- Martz, L. W., and J. Garbrecht (1992). Numerical definition of drainage network and subcatchment areas from digital elevation models. *Computers in Geoscience* 18:747–761.
- Matalas, N., and M. A. Benson (1961). Effect of interstation correlation on regression analysis. *Journal of Geophysical Research* 66:3285–3293.
- Matalas, N. C., and T. Maddock III (1976). Hydrologic semantics. *Water Resources Research* 12:123.
- Mather, J. R. (1984). *Water Resources*. New York: John Wiley and Sons.
- McBride, M. S., and H. O. Pfannkuch (1975). The distribution of seepage within lakes. US Geological Survey, *Journal of Research* 3:505–512.
- McCabe, G. J., M. P. Clark, and L. E. Hay (2007). Rain-on-snow events in the western United States. *Bulletin of the American Meteorological Society* 88(3):319–328.
- McCabe, G. J., and D. M. Wolock (2011). Independent effects of temperature and precipitation on modeled runoff in the conterminous United States. *Water Resources Research* 47:W11522, doi:10.1029/2011WR010630.
- McCallum, A. M., M. S. Andersen, G. C. Rau, and R. I. Acworth (2012). A 1-D analytical method for estimating surface water-groundwater interactions and effective thermal diffusivity using temperature time series. *Water Resources Research* 48:W11532, doi:10.1029/2012WR012007.
- McCuen, R. (1989). *Hydrologic Analysis and Design*. Englewood Cliffs, NJ: Prentice-Hall.
- McCuen, R. H. (1998). *Hydrologic Analysis and Design* (2nd ed.). Upper Saddle River, NJ: Prentice-Hall.
- McDonnell, J. J. (1990). A rationale for old water discharge through macropores in a steep, humid catchment. *Water Resources Research* 26:2821–2832.
- McDonnell, J. J., M. Sivapalan, K. Vaché, S. Dunn, G. Grant, R. Haggerty, C. Hinz, R. Hooper, J. Kirchner, M. L. Roderrick, J. Selker, and M. Weiler (2007). Moving beyond heterogeneity and process complexity: A new vision for watershed hydrology. *Water Resources Research* 43:W07301, doi:10.1029/2006WR005467.
- McGuinness, C. L. (1963). *The Role of Ground Water in the National Water Situation*. Water-Supply Paper 1800. Washington, DC: US Geological Survey.
- McGurk, B. J., and D. L. Azuma (1992). *Correlation and Prediction of Snow Water Equivalent from Snow Sensors*. Report PSW-RP-211. Washington, DC: USDA Forest Service, Pacific Southwest Research Station.
- McGurk, B. J., T. J. Edens, and D. L. Azuma (1993). Predicting wilderness snow water equivalent with nonwilderness snow sensors. *Water Resources Bulletin* 29:85–94.
- McKay, G. A. (1970). Precipitation. In D. M. Gray, ed., *Handbook on the Principles of Hydrology*. Port Washington, NY: Water Information Center.

- McMillan, W. D., and R. H. Burgy (1960). Interception loss from grass. *Journal of Geophysical Research* 65:2387–2394.
- McNamara, J. P., D. L. Kane, and L. D. Hinzman (1997). Hydrograph separations in an Arctic watershed using mixing model and graphical techniques. *Water Resources Research* 33:1701–1719.
- McQueen, I. S. (1963). *Development of a Hand-Portable Rainfall-Simulator Infiltrometer*. Circular 482. Washington, DC: US Geological Survey.
- McVicar, T. R., M. L. Rodger, R. J. Donohue, L. T. Li, T. G. Van Niel, A. Thomas, J. Grieser, D. Jhajharia, Y. Himri, N. M. Mahowald, A. V. Mescherskayai, A. C. Kruger, S. Rehman, and Y. Dinpanash (2012). Global review and synthesis of trends in observed terrestrial near-surface wind speeds: Implications for evaporation. *Journal of Hydrology* 416–417:182–205.
- Mears, C., J. Wang, S. Ho, L. Zhang, and X. Zhou (2010). Total column water vapor. In Special Supplement, “State of the Climate in 2009.” *Bulletin of the American Meteorological Society* 91(7):S29–S30.
- Meiman, J. R. (1968). Snow accumulation related to elevation, aspect and forest canopy. In Fredericton, Proceedings, Workshop Seminar on Snow Hydrology. New Brunswick, Canada: University of New Brunswick.
- Mein, R. G., and C. L. Larson (1973). Modeling infiltration during a steady rain. *Water Resources Research* 9:384–394.
- Meinzer, O. E. (1932). *Outline of Methods for Estimating Ground-Water Supplies*. Water-Supply Paper 638-C. Washington, DC: US Geological Survey.
- Melloh, R. A. (1999). *A Synopsis and Comparison of Selected Snowmelt Algorithms*. CRREL Report 99-8. Hanover, NH: US Army Corps of Engineers, Cold Regions Research and Engineering Laboratory.
- Melloh, R. A., J. P. Hardy, R. N. Bailey, and T. J. Hall (2002). An efficient snow albedo model for the open and sub-canopy. *Hydrological Processes* 16:3571–3584.
- Mellor, M. (1964). *Snow and Ice at the Earth's Surface*. Monograph II-C1. Hanover, NH: US Army Cold Regions Research and Engineering Laboratory Cold Regions Science and Engineering.
- Menne, M. J., C. N. Williams, Jr., and R. S. Vose (2009). The U.S. Historical Climatology Network monthly temperature data, Version 2. *Bulletin of the American Meteorological Society* 90(7):993–1007.
- Merriam, R. A. (1961). Surface water storage on annual ryegrass. *Journal of Geophysical Research* 66:1833–1838.
- Merz, R., J. Parajka, and G. Blöschl (2011). Time stability of catchment model parameters: Implications for climate impact analyses. *Water Resources Research* 47:W02531, doi:10.1029/2010WR009505.
- Meybeck, M., L. Laroche, H. H. Dürr, and J. P. M. Syvitski (2003). Global variability of daily total suspended solids and their fluxes in rivers. *Global and Planetary Change* 39:65–93.
- Meyboom, P. (1966). Unsteady groundwater flow near a willow ring in hummocky terrain. *Journal of Hydrology* 4:38–62.
- Michel, B. (1971). *Winter Regime of Rivers and Lakes*. Cold Regions Science and Engineering Monograph III-B1a. Hanover, NH: US Army Cold Regions Research and Engineering Laboratory.
- Michel, C., V. Andréassian, and C. Perrin (2005). Soil Conservation Service curve number method: How to mend a wrong soil moisture accounting procedure? *Water Resources Research* 41:W02011, doi:10.1029/2004WR003191.
- Miller, A., J. C. Thompson, R. E. Peterson, and D. R. Haragan (1983). *Elements of Meteorology*. Columbus, OH: C.E. Merrill Publishing Co.
- Miller, J. F., R. H. Frederick, and R. J. Tracey (1973). *Precipitation Frequency Atlas of the Contiguous Western United States (by States)*. NOAA Atlas 2 (11 volumes). Silver Spring, MD: US National Weather Service.
- Miller, N., and R. Cronshay (1989). Runoff curve numbers—the next step. In B. C. Yen, ed., *Channel Flow and Catchment Runoff* (pp. 910–916). Department of Civil Engineering, University of Virginia.
- Milliman, J. D., and J. P. M. Syvitski (1992). Geomorphic/tectonic control of sediment discharge to the ocean: The importance of small mountain rivers. *Journal of Geology* 100:525–544.
- Milly, P. C. D. (1988). Advances in modeling of water in the unsaturated zone. *Transport in Porous Media* 3:491–514.
- Milly, P. C. D., J. Betancourt, M. Falkenmark, R. M. Hirsch, Z. W. Kundzewicz, D. P. Lettenmaier, and R. J. Stouffer (2008). Stationarity is dead: Whither water management? *Science* 319:573–574.
- Milly, P. C. D., and K. A. Dunne (2002). Macroscale water fluxes: 1. Quantifying errors in the estimation of basin mean precipitation. *Water Resources Research* 38(10):1205, doi:10.1029/2001WR000759.
- Milly, P. C. D., and A. B. Shmakin (2002). Global modeling of land water and energy balances. Part I: The Land Dynamics (LaD) model. *Journal of Hydro-meteorology* 3:283–299.
- Min, S.-K., X. Zhang, F. W. Zwiers, and G. C. Hegerl (2011). Human contribution to more-intense precipitation extremes. *Nature* 470:378–381.
- Minnich, R. A. (1986). Snow levels and amounts in the mountains of southern California. *Journal of Hydrology* 89:37–58.
- Miralles, D. G., J. H. Gash, T. R. H. Holmes, R. A. M. de Jeu, and A. J. Dolman (2010). Global canopy interception from satellite observations. *Journal of Geophysical Research* 115:D16122, doi:10.1029/2009JD013530.
- Mirus, B. B., and K. Loague (2013). How runoff begins (and ends): Characterizing hydrologic response at the catchment scale. *Water Resources Research* 49, doi:10.1002/wrcr.20218.
- Mishra, A. K., and P. Coulibaly (2009). Hydrometric network evaluation for Canadian watersheds. *Journal of Hydrology* 380:420–437.
- Mishra, S., J. C. Parker, and N. Singhal (1989). Estimation of soil hydraulic properties and their uncertainty from particle size distribution data. *Journal of Hydrology* 108:1–18.
- Mizukami, N., S. Perica, and D. Hatch (2011). Regional approach for mapping climatological snow water equivalent over the mountainous regions of the western United States. *Journal of Hydrology* 400(1–2):72–82.
- Mockus, V. (1957). *Use of Storm and Watershed Characteristics in Synthetic Hydrograph Analysis*. Washington, DC: US Soil Conservation Service.
- Moench, A. F., V. B. Sauer, and E. M. Jennings (1974). Modification of routed streamflow by channel loss and base flow. *Water Resources Research* 10:963–968.
- Moene, A. F., F. Beyrich, and O. K. Hartogenis (2009). Developments in scintillometry. *Bulletin of the American Meteorological Society* 90(5):689–693.
- Molinari, A., G. G. Katul, and A. Porporato (2011). Maximum discharge from snowmelt in a changing climate. *Geophysical Research Letters* 38:L05402, doi:10.1029/2010GL046477.
- Montanari, A., C. A. Shoemaker, and N. van de Giesen (2009). Introduction to special section on uncertainty assessment in surface and subsurface hydrology: An overview of issues and challenges. *Water Resources Research* 45:W00B00, doi:10.1029/2009WR008471.
- Monteith, J. L. (1957). Dew. *Quarterly Journal of the Royal Meteorological Society* 83:322–341.
- Monteith, J. L. (1965). Evaporation and environment. In Proceedings of the 19th Symposium of the Society for Experimental Biology (pp. 205–233). New York: Cambridge University Press.
- Montzka, S. A. (2010). The combined influence of long-lived trace gases on the radiative balance of the atmosphere. In Special Supplement, “State of the Climate in 2009.” *Bulletin of the American Meteorological Society* 91(7):S44.
- Moret, D., M. V. López, and J. L. Arrué (2004). TDR application for automated water level measurement from Mariotte reservoirs in tension disc infiltrometers. *Journal of Hydrology* 297:229–235.
- Moret-Fernández, D., and C. González-Cebollada (2009). New method for monitoring soil water infiltration rates applied to a disc infiltrometer. *Journal of Hydrology* 379:315–322.
- Morris, D. A., and A. I. Johnson (1967). *Summary of Hydrologic and Physical Properties of Rock and Soil Materials, as Analyzed by the Hydrologic Laboratory of the US Geological Survey 1948–1960*. Water-Supply Paper 1839-D. Washington, DC: US Geological Survey.
- Morrissey, D. J. (1987). *Estimation of the Recharge Area Contributing Water to a Pumped Well in a Glacial-Drift, River-Valley Aquifer*. Open-File Report 86-543. Washington, DC: US Geological Survey.
- Morrissey, M. L., J. A. Malick, J. S. Greene, and J. Wang (1995). The uncertainty of simple spatial averages using rain gauge networks. *Water Resources Research* 31:2011–2017.

- Mosley, M. P. (1979). Streamflow generation in a forested watershed, New Zealand. *Water Resources Research* 15:795–806.
- Mosley, M. P. (1982). Subsurface flow velocities through selected forest soils, South Island, New Zealand. *Journal of Hydrology* 55:65–92.
- Mostaghimi, S., and J. K. Mitchell (1982). Peak runoff model comparison on central Illinois watersheds. *Water Resources Bulletin* 18:9–18.
- Motoyama, H. (1990). Simulation of seasonal snowcover based on air temperature and precipitation. *Bulletin of the American Meteorological Society* 29:1104–1110.
- Mualem, Y. (1976). A new model for predicting the hydraulic conductivity of unsaturated porous media. *Water Resources Research* 12:513–522.
- Mueller, D. S., and C. R. Wagner (2009). Measuring discharge with acoustic Doppler profilers from a moving boat. In *Techniques of Water-Resources Investigations* (book 3, chapter 22, section A). Washington, DC: US Geological Survey.
- Mukammal, E. I., and H. H. Neumann (1977). Application of the Priestly–Taylor evaporation model to assess the influence of soil moisture on the evaporation from a large weighing lysimeter and Class A pan. *Boundary-Layer Meteorology* 12:243–256.
- Mulholland, P. J. (1993). Hydrometric and stream chemistry evidence of three storm flowpaths in Walker Branch Watershed. *Journal of Hydrology* 151:291–316.
- Munley, W. G., Jr., and L. E. Hippis (1991). Estimation of regional evaporation for a tall-grass prairie from measurements of properties of the atmospheric boundary layer. *Water Resources Research* 27:225–230.
- Murphy, D. M., S. Solomon, R. W. Portmann, K. H. Rosenlof, P. M. Forster, and T. Wong (2009). An observationally based energy balance for the Earth since 1950. *Journal of Geophysical Research* 114:D17107, doi:10.1029/2009JD012105.
- Musiake, K., Y. Oka, and M. Koike (1988). Unsaturated zone soil moisture behavior under temperate humid conditions—tensiometric observations and numerical simulations. *Journal of Hydrology* 102:179–200.
- Myinen, R. B., et al. (1997). Increased plant growth in the northern high latitudes from 1981 to 1991. *Nature* 386:698–702.
- Nace, R. L. (1974). General evolution of the concept of the hydrological cycle. In *Three Centuries of Scientific Hydrology* (pp. 40–48). UNESCO, World Meteorological Organization, International Association of Hydrological Sciences.
- Nash, J. E., and J. V. Sutcliffe (1970). River flow forecasting through conceptual models, part I: A discussion of principles. *Journal of Hydrology* 10:282–290.
- Nassif, S. H., and E. M. Wilson (1975). The influence of slope and rain intensity on runoff and infiltration. *Hydrological Sciences Bulletin* 20:539–553.
- Nathan, R. J., and T. A. McMahon (1990). Evaluation of automated techniques for baseflow and recession analyses. *Water Resources Research* 26(7):1465–1473.
- National Academy of Sciences (1983). *Safety of Existing Dams: Evaluation and Improvement*. Washington, DC: National Academy Press.
- Neff, E. L. (1977). How much rain does a rain gage gage? *Journal of Hydrology* 35:213–220.
- Newbury, R. W., J. A. Cherry, and R. A. Cox (1969). Groundwater-streamflow systems in Wilson Creek Experimental Watershed, Manitoba. *Canadian Journal of Earth Sciences* 6:613–623.
- Newman, B. D., A. R. Campbell, and B. P. Wilcox (1998). Lateral subsurface flow pathways in a semiarid ponderosa pine hillslope. *Water Resources Research* 34(12):3485–3496.
- Nichols, W. D. (1993). Estimating discharge of shallow groundwater by transpiration from greasewood in the northern Great Basin. *Water Resources Research* 29:2771–2778.
- Nichols, W. D. (1994). Groundwater discharge by phreatophyte shrubs in the Great Basin as related to depth to groundwater. *Water Resources Research* 30:3265–3274.
- Nielsen, D. R., D. Kirkham, and W. R. Van Wijk (1961). Diffusion equation calculations of field soil water infiltration profiles. *Soil Science Society of America Proceedings* 25:165–168.
- Nielsen, D. R., M. T. van Genuchten, and J. W. Biggar (1986). Water flow and solute transport processes in the unsaturated zone. *Water Resources Research* 22:89S–108S.
- Norbiato, D., M. Borga, R. Merz, G. Blöschl, and A. Carton (2009). Controls on event runoff coefficients in the eastern Italian Alps. *Journal of Hydrology* 375:312–325.
- Novakowski, K. S., and R. W. Gillham (1988). Field investigations of the nature of water-table response to precipitation in shallow water-table environments. *Journal of Hydrology* 97:23–32.
- Nutter, W. L. (1975). *Moisture and Energy Conditions in a Draining Soil Mass*. ERC 0875. Atlanta: Georgia Institute of Technology Environmental Resources Center.
- Nwaozagie, F. I. L., and A. K. Tyagi (1984). Unified streamflow routing by finite elements. American Society of Civil Engineers Proceedings, *Journal of the Hydraulics Division* 110:1595–1611.
- Nystuen, J. A., J. R. Pronin, P. G. Black, and J. C. Wilkerson (1996). A comparison of automatic rain gauges. *Journal of Atmospheric and Oceanic Technology* 13:62–73.
- Olin, M. H. E., and C. Svensson (1992). Evaluation of geological and recharge parameters for an aquifer in southern Sweden. *Nordic Hydrology* 23:305–314.
- Oliver, J. E., and J. J. Hidore (1984). *Climatology: An Introduction*. Columbus, OH: C.E. Merrill.
- O'Loughlin, E. M. (1981). Saturation regions in catchments and their relations to soil and topographic properties. *Journal of Hydrology* 53:229–246.
- Olson, D. M., E. Dinerstein, E. D. Wikramanayake, et al. (2001). Terrestrial ecoregions of the world: A new map of life on earth. *BioScience* 51:933–938.
- Omolayo, A. S. (1993). On the transposition of areal reduction factors for rainfall frequency estimation. *Journal of Hydrology* 145:191–205.
- Ophori, D., and J. Tóth (1990). Relationships in regional groundwater discharge to streams: An analysis by numerical simulation. *Journal of Hydrology* 119:215–244.
- Oreskes, N., K. Shader-Frechette, and K. Belitz (1994). Verification, validation and confirmation of numerical models in the earth sciences. *Science* 263:641–646.
- Ormsbee, L. E., and A. Q. Khan (1989). A parametric model for steeply sloping forested watersheds. *Water Resources Research* 25:2053–2065.
- Orville, H. D. (1995). Report on the Sixth WMO Scientific Conference on Weather Modification. *Bulletin of the American Meteorological Society* 76:372–373.
- Osterkamp, T. E. (2007). Characteristics of recent warming of permafrost in Alaska. *Journal of Geophysical Research* 112:F02S02, doi:10.1029/2006JF000578.
- Osterkamp, W. R., L. J. Lane, and C. S. Savard (1994). Recharge estimates using a geomorphic/distributed-parameter simulation approach, Amargosa River Basin. *Water Resources Bulletin* 30:493–507.
- Paetzold, R. F., G. A. Matzkanin, and A. De Los Santos (1985). Surface soil water content measurement using pulsed nuclear magnetic resonance techniques. *Soil Science Society of America Journal* 49:537–540.
- Pan, F., M. Stieglitz, and R. B. McKane (2012). An algorithm for treating flat areas and depressions in digital elevation models using linear interpolation. *Water Resources Research* 48:W00L10, doi:10.1029/2011WR010735.
- Pan, H., H. Li, and E. Wood (2010). Assessing the skill of satellite-based precipitation estimates in hydrologic applications. *Water Resources Research* 46:W09535.
- Papalexiou, S. M., and D. Koutsoyiannis (2006). A probabilistic approach to the concept of probable maximum precipitation. *Advances in Geosciences* 7:51–54.
- Parajka, J., S. Dadson, T. Lafon, and R. Essery (2010a). Evaluation of snow cover and depth simulated by a land surface model using detailed regional snow observations from Austria. *Journal of Geophysical Research* 115:D24117, doi:10.1029/2010JD014086.
- Parajka, J., M. Pepe, A. Rampini, S. Rossi, and G. Blöschl (2010b). A regional snow-line method for estimating snow cover from MODIS during cloud cover. *Journal of Hydrology* 381: 203–212.
- Parlange, M. B., and G. G. Katul (1992a). Estimation of diurnal variation of potential evaporation from a wet bare soil surface. *Journal of Hydrology* 132:71–89.
- Parlange, M. B., and G. G. Katul (1992b). An advection-aridity evaporation model. *Water Resources Research* 28:127–132.
- Patric, J. H. (1974). River flow increases in central New England after the hurricane of 1938. *Journal of Forestry* 72:21–25.
- Paulhus, J. L. H. (1965). Indian Ocean and Taiwan rainfalls set new records. *Monthly Weather Review* 93:331–335.
- Peck, A. J., and R. M. Rabbidge (1966). Soil water potential: Direct measurement by a new technique. *Science* 151:1385–1386.

- Peck, E. L. (1997). Quality of hydrometeorological data in cold regions. *Journal of the American Water Resources Association* 33:125–134.
- Pederson, G. T., S. T. Gray, C. A. Woodhouse, J. L. Betancourt, D. B. Fagre, J. S. Littell, E. Watson, B. H. Luckman, and L. J. Graumlich (2011). The unusual nature of recent snowpack declines in the North American Cordillera. *Science* 333:332–335.
- Peel, M. C., T. A. McMahon, and B. L. Finlayson (2010). Vegetation impact on mean annual evapotranspiration at a global catchment scale. *Water Resources Research* 46:W09508, doi:10.1029/2009WR008233.
- Peixoto, J. P., and Oort, A. H. (1992). *Physics of Climate*. New York: American Institute of Physics.
- Pekárová, P., P. Miklánek, and J. Pekár (2003). Spatial and temporal runoff oscillation analysis of the main rivers of the world during the 19th–20th centuries. *Journal of Hydrology* 274:62–79.
- Pelletier, P. M. (1988). Uncertainties in the single determination of river discharge: A literature review. *Canadian Journal of Civil Engineering* 15:834–850.
- Pelto, M. S. (2010). Alpine glaciers and ice sheets. In Special Supplement, “State of the Climate in 2009.” *Bulletin of the American Meteorological Society* 91(7):S49–S50.
- Penman, H. L. (1948). Natural evaporation from open water, bare soil, and grass. *Royal Society of London Proceedings, Series A*, 193:120–145.
- Penman, H. L. (1956). Evaporation: An introductory survey. *Netherlands Journal of Agricultural Science* 4:7–29.
- Perrens, S. J., and K. K. Watson (1977). Numerical analysis of two-dimensional infiltration and redistribution. *Water Resources Research* 13:781–790.
- Perrin, C., C. Michel, and V. Andréassian (2001). Does a large number of parameters enhance model performance? Comparative assessment of common catchment model structures on 429 catchments. *Journal of Hydrology* 242:275–301.
- Perroux, K. M., and I. White (1988). Designs for disc permeameters. *Soil Science Society of America Journal* 52:1205–1215.
- Perry, E. C., Jr., and C. W. Montgomery, eds. (1982). *Isotope Studies of Hydrologic Processes*. DeKalb, IL: Northern Illinois University Press.
- Peters, D. L., J. M. Buttle, C. H. Taylor, and B. D. Lazerte (1995). Runoff production in a forested, shallow soil, Canadian Shield basin. *Water Resources Research* 31:1291–1304.
- Peterson, T. C., V. S. Golubev, and P. Ya. Groisman (1995). Evaporation losing its strength. *Nature* 377:687–688.
- Philip, J. R. (1957). The theory of infiltration: 4. Sorptivity and algebraic infiltration equations. *Soil Science* 84:257–264.
- Philip, J. R. (1969). Theory of infiltration. *Advances in Hydroscience* 5:215–290.
- Pickard, W. F., and P. J. Melcher (2005). Perspectives on the biophysics of xylem transport. In N. M. Holbrook and M. A. Zwieniecki, eds., *Vascular Transport in Plants* (chapter 1). New York: Elsevier.
- Piechota, T. C., J. A. Dracup, and R. G. Fovell (1997). Western US streamflow and atmospheric circulation patterns during El Niño-Southern Oscillation. *Journal of Hydrology* 201:249–271.
- Pielke, R. A., Sr., G. E. Liston, W. L. Chapman, and D. A. Robinson (2004). Actual and insolation-weighted Northern Hemisphere snow cover and sea-ice between 1973–2002. *Climate Dynamics* 22:591–595.
- Pike, J. (1964). The estimation of annual runoff from meteorological data in a tropical climate. *Journal of Hydrology* 2:116–123.
- Piles, M., A. Camps, M. Vall-llossera, A. Monneris, M. Talone, and J. M. Sabater (2010). Performance of soil moisture retrieval algorithms using multiangular L band brightness temperatures. *Water Resources Research* 46:W06506, doi:10.1029/2009WR008554.
- Pilgrim, D. H. (1976). Travel times and nonlinearity of flood runoff from tracer measurements on small watersheds. *Water Resources Research* 12:487–496.
- Pilgrim, D. H., and I. Cordery (1992). Flood runoff. In D. R. Maidment, ed., *Handbook of Hydrology* (chapter 9). New York: McGraw-Hill.
- Pilgrim, D. H., D. D. Huff, and T. D. Steele (1979). Use of specific conductance and contact time relations for separating flow components in storm runoff. *Water Resources Research* 15:329–339.
- Pinder, G. F., and J. F. Jones (1969). Determination of the ground-water component of peak discharge from the chemistry of total runoff. *Water Resources Research* 5(2):438–445.
- Pinder, G. F., and S. P. Sauer (1971). Numerical simulation of flood-wave modification due to bank storage. *Water Resources Research* 7:63–70.
- Pitman, J. I. (1989). Rainfall interception by bracken litter—relationship between biomass, storage, and drainage rate. *Journal of Hydrology* 111:281–291.
- Ponce, V. M. (1989). *Engineering Hydrology*. Englewood Cliffs, NJ: Prentice-Hall.
- Ponce, V. M., and R. H. Hawkins (1996). Runoff curve number: Has it reached maturity? *Journal of Hydrologic Engineering* 1:11–19.
- Priestley, C. H. B., and R. J. Taylor (1972). On the assessment of surface heat flux and evaporation using large-scale parameters. *Monthly Weather Review* 100:81–92.
- Prince, K. R., T. E. Reilly, and O. L. Franke (1989). Analysis of the shallow groundwater flow system near Connetquot Brook, Long Island, New York. *Journal of Hydrology* 107:223–250.
- Putkonen, J., T. C. Grenfell, K. Rennert, C. Bitz, P. Jacobson, and D. Russell (2009). Rain on snow: Little understood killer in the north. *Eos* 90(26):221–222.
- Putuhena, W. M., and I. Cordery (1996). Estimation of interception capacity of the forest floor. *Journal of Hydrology* 180:283–299.
- Qian, Y., D. Gong, J. Fan, L. R. Yeung, R. Bennartz, D. Chen, and W. Wang (2009). Heavy pollution suppresses light rain in China: Observations and modeling. *Journal of Geophysical Research: Atmospheres* 114:D00K02, doi:10.1029/2008JD011575.
- Quinn, P. F., K. J. Beven, and R. Lamb (1995). The $\ln(a/\tan \beta)$ index: How to calculate it and to use it within the TOPMODEL framework. *Hydrological Processes* 9:161–182.
- Radke, L. F., and P. V. Hobbs (1976). Cloud condensation nuclei on the Atlantic seaboard of the United States. *Science* 193:999–1002.
- Ragab, R., J. Finch, and R. Harding (1997). Estimation of groundwater recharge to chalk and sandstone aquifers using simple soil models. *Journal of Hydrology* 190:19–41.
- Ragan, R. M. (1966). An experimental investigation of partial area contributions. *International Association of Scientific Hydrology Publication* 76:241–249.
- Ralph, F. M., and M. D. Dettinger (2011). Storms, floods, and the science of atmospheric rivers. *Eos* 92(32):265–266.
- Ramanathan, V. (1988). The greenhouse theory of climatic change: A test by an inadvertent global experiment. *Science* 240:293–299.
- Ramillien, G., J. S. Famiglietti, and J. Wahr (2008). Detection of continental hydrology and glaciology signals from GRACE: A review. *Survey of Geophysics* 29:361–374, doi:10.1007/s10712-008-9048-9.
- Rango, A., and J. Martinez (1994). Model accuracy in snowmelt-runoff forecasts. *Water Resources Bulletin* 30:463–470.
- Rasmussen, A. H., M. Hondzo, and H. G. Stefan (1995). A test of several evaporation equations for water temperature simulations in lakes. *Journal of the American Water Resources Association* 31:1023–1028.
- Rasmussen, E. M. (1985). El Niño and variations in climate. *American Scientist* 73:168–177.
- Rasmussen, W. C., and G. E. Andreasen (1959). *Hydrologic budget of the Beaverdam Creek basin, Maryland*. Water-Supply Paper 1472. Washington, DC: US Geological Survey.
- Raven, P. H., R. F. Evert, and H. Curtis (1976). *The Biology of Plants* (2nd ed.). New York: Worth Publishers.
- Rawls, W. J., L. R. Ahuja, D. L. Brakensiek, and A. Shirmohammadi (1992). Infiltration and soil water movement. In D. R. Maidment, ed., *Handbook of Hydrology* (chapter 5). New York: McGraw-Hill.
- Rawls, W. J., and D. L. Brakensiek (1983). A procedure to predict Green Ampt infiltration parameters. In *Advances in Infiltration* (pp. 102–112). St. Joseph, MI: American Society of Agricultural Engineering.
- Reichle, R. H., R. D. Koster, G. J. M. De Lannoy, B. A. Forman, Q. L., S. P. P. Mahanama, and A. Touré (2011). Assessment and enhancement of MERRA land surface hydrology estimates. *Journal of Climate* 24:6322–6338.
- Rice, K., and G. M. Hornberger (1998). Comparison of hydrochemical tracers to estimate source contributions to peak flow in a small, forested, headwater catchment. *Water Resources Research* 34:1755–1766.
- Rice, R., and R. C. Bales (2010). Embedded sensor network design for snow cover measurements around snow pillow and snow course sites in the Sierra Nevada of California. *Water Resources Research* 46:W03537, doi:10.1029/2008WR007318.
- Richards, A. L. (1931). Capillary conduction of liquids through porous media. *Physics* 1:316–333.

- Rignot, E., I. Velicogna, M. R. van den Broeke, A. Monaghan, and J. Lenaerts (2011). Acceleration of the contribution of the Greenland and Antarctic ice sheets to sea level rise. *Geophysical Research Letters* 38:L05503, doi:10.1029/2011GL046583.
- Rikhter, G. D. (1954). *Snowcover, Its Formation and Properties*. Moskva, USSR: Izdatel'stvo Akademii Nauk SSSR Translation No. 6. US Army Snow, Ice, and Permafrost Research Establishment.
- Risley, J. C., and N. W. Gannett (2006). *An Evaluation and Review of Water-Use Estimates and Flow Data for the Lower Klamath and Tule Lake National Wildlife Refuges, Oregon and California*. Scientific Investigations Report 5036. Washington, DC: US Geological Survey.
- Ritter, A., and R. Muñoz-Carpena (2013). Performance evaluation of hydrological models: Statistical significance for reducing subjectivity in goodness-of-fit assessments. *Journal of Hydrology* 480:33–45.
- Roberge, J., and A. P. Plamondon (1987). Snowmelt runoff pathways in a boreal forest hillslope: The role of pipe throughflow. *Journal of Hydrology* 95:39–54.
- Robinson, D. A. (2010). Northern Hemisphere continental snow cover extent. In Special Supplement, "State of the Climate in 2009." *Bulletin of the American Meteorological Society* 91(7):S32–S34.
- Robinson, D. A., C. S. Campbell, J. W. Hopmans, B. K. Hornbuckle, S. B. Jones, R. Knight, F. Ogden, J. Selker, and O. Wendorff (2008). Soil moisture measurement for ecological and hydrological watershed-scale observatories: A review. *Vadose Zone Journal* 7:358–389.
- Robinson, D. A., K. F. Dewey, and R. R. Heim, Jr. (1993). Global snow cover monitoring: An update. *Bulletin of the American Meteorological Society* 74:1689–1696.
- Robock, A., Y. V. Konstantin, J. K. Srinivasan, J. K. Entin, N. A. Hollinger, S. L. Speranskaya, and A. Nampakai (2000). The global soil moisture data bank. *Bulletin of the American Meteorological Society* 81:1281–1299.
- Rodda, J. C. (1985, January). Precipitation research. *Eos*, p. 10.
- Rodriguez-Iturbe, I. (1993). The geomorphological unit hydrograph. In K. Beven and M. J. Kirkby, eds., *Channel Network Hydrology* (chapter 3). New York: John Wiley.
- Rodriguez-Iturbe, I., G. Devoto, and J. B. Valdes (1979). Discharge response analysis and hydrologic similarity: The interrelation between the geomorphologic IUH and the storm characteristics. *Water Resources Research* 15:1435–1444.
- Rodriguez-Iturbe, I., and J. M. Mejia (1974). Design of rainfall networks in time and space. *Water Resources Research* 10:713–728.
- Rodriguez-Iturbe, I., and J. B. Valdes (1979). The geomorphologic structure of hydrologic response. *Water Resources Research* 15:1409–1420.
- Roesch, A. (2006). Evaluation of surface albedo and snow cover in AR4 coupled climate models. *Journal of Geophysical Research: Atmospheres* 111:D15111, doi:10.1029/2005JD006473.
- Romanovsky, V., N. Oberman, D. Drozdov, G. Malkova, A. Kholodov, and S. Marchenko (2010). Permafrost. In Special Supplement, "State of the Climate in 2009." *Bulletin of the American Meteorological Society* 91(7):S116.
- Rorabaugh, M. I. (1964). Estimating changes in bank storage and ground-water contribution to streamflow. *International Association of Scientific Hydrology Publication* 63:432–441.
- Rosenbaum, U., R. Bogena, M. Herbst, J. A. Huisman, T. J. Peterson, A. Weuthen, A. W. Western, and H. Vereecken (2012). Seasonal and event dynamics of spatial soil moisture patterns at the small catchment scale. *Water Resources Research* 48:W10544, doi:10.1029/2011WR011518.
- Rosenberg, N. J. (1987, spring). *Climate Change: A Primer, Part II* (pp. 8–14). Washington, DC: Resources for the Future.
- Rosenberg, N. J., M. S. McKenney, and P. Martin (1989). Evapotranspiration in a greenhouse-warmed world: A review and a simulation. *Agricultural and Forest Meteorology* 47:303–320.
- Rosenberry, D. O., A. M. Sturrock, and T. C. Winter (1993). Evaluation of the energy budget method of determining evaporation at Williams Lake, Minnesota, using alternative instrumentation and study approaches. *Water Resources Research* 29:2473–2483.
- Rosenberry, D. O., and T. C. Winter (1997). Dynamics of water-table fluctuations in an upland between two prairie-pothole wetlands in North Dakota. *Journal of Hydrology* 191:266–289.
- Rosenberry, D. O., T. C. Winter, D. C. Buso, and G. E. Likens (2007). Comparison of 15 evaporation methods applied to a small mountain lake in the northeastern USA. *Journal of Hydrology* 340:149–166.
- Roth, K., R. Schulin, H. Fluhler, and W. Attinger (1990). Calibration of time domain reflectometry for water content measurement using a composite dielectric approach. *Water Resources Research* 26:2267–2273.
- Rouse, H., and S. Ince (1957). *History of Hydraulics*. Iowa City: Iowa Institute of Hydraulic Research.
- Rouse, W. R., and R. G. Wilson (1972). A test of the potential accuracy of the water-budget approach to estimating evapotranspiration. *Agricultural Meteorology* 9:421–446.
- Rubin, J. (1967). Numerical method for analyzing hysteresis-affected post-infiltration redistribution of soil moisture. *Soil Science Society of America Proceedings* 31:13–20.
- Rushton, K. R., and C. Ward (1979). The estimation of groundwater recharge. *Journal of Hydrology* 41:345–361.
- Rutter, A. J., K. A. Kershaw, P. C. Robins, and A. J. Morton (1971). A predictive model of rainfall interception in forests; 1. Derivation of the model from observations in a plantation of Corsican pine. *Agricultural Meteorology* 9:367–384.
- Rutter, N., R. Essery, J. Pomeroy, et al. (2009). Evaluation of forest snow processes models (SnowMIP2). *Journal of Geophysical Research: Atmospheres* 114:D06111, doi:10.1029/2008JD011063.
- Ryan, W. A., N. J. Doesken, and S. R. Fassnacht (2008). Preliminary results of ultrasonic snow depth sensor testing for National Weather Service (NWS). Snow measurements in the US. *Hydrological Processes*, doi:10.1002/hyp.7065.
- Sabol, G. V., and T. J. Ward (1983). Discussion of Cheng (1982). American Society of Civil Engineers Proceedings, *Journal of the Hydraulics Division* 109:344–346.
- Sacks, L. A., J. S. Herman, L. F. Konikow, and A. L. Vela (1992). Seasonal dynamics of groundwater-lake interactions at Doñana National Park, Spain. *Journal of Hydrology* 130:123–134.
- Sadeghi, M., N. Shokri, and S. B. Jones (2012). A novel analytical solution to steady-state evaporation from porous media. *Water Resources Research* 48:W09516, doi:10.1029/2012WR012060.
- Salama, R. B., I. Tapley, T. Ishii, and G. Hawkes (1994). Identification of areas of recharge and discharge using Landsat-TM satellite imagery and aerial photography mapping techniques. *Journal of Hydrology* 162:119–141.
- Salas, J. D. (1992). Analysis and modeling of hydrologic time series. In D. R. Maidment, ed., *Handbook of Hydrology* (chapter 19). New York: McGraw-Hill.
- Salvucci, G. D. (1993). An approximate solution for steady vertical flux of moisture through an unsaturated homogeneous soil. *Water Resources Research* 29:3749–3753.
- Salvucci, G. D. (1996). Series solution for Richards equation under concentration boundary conditions and uniform initial conditions. *Water Resources Research* 32:2401–2407.
- Salvucci, G. D. (1997). Soil and moisture independent estimation of stage-two evaporation from potential evaporation and albedo or surface temperature. *Water Resources Research* 33:111–122.
- Salvucci, G. D., and D. Entekhabi (1994a). Explicit expressions for Green-Ampt (delta function diffusivity) infiltration rate and cumulative storage. *Water Resources Research* 30:2661–2661.
- Salvucci, G. D., and D. Entekhabi (1994b). Equivalent steady soil moisture profile and the time compression approximation in water balance modeling. *Water Resources Research* 30:2737–2749.
- Salvucci, G. D., and D. Entekhabi (1995). Pended infiltration into soils bounded by a water table. *Water Resources Research* 31:2751–2759.
- Sanderson, E. W., M. Jaiteh, M. A. Levy, K. H. Redford, A. V. Wannebo, and G. Wollmer (2002). The human footprint and the last of the wild. *BioScience* 52:891–904.
- Sankarasubramanian, A., and R. M. Vogel (2003). Hydroclimatology of the continental United States. *Geophysical Research Letters* 30(7):1363, doi:10.1029/2002GL015937.
- Sankarasubramanian, A., R. M. Vogel, and J. F. Limbrunner (2001). Climate elasticity of streamflow in the United States. *Water Resources Research* 37(6):1771–1781.
- Santhi, C., P. M. Allen, R. S. Mutiah, J. G. Arnold, and P. Tuppad (2008). Regional estimation of base flow for the conterminous United States by hydrologic landscape regions. *Journal of Hydrology* 351:139–153.

- Sauer, V. B., and R. W. Meyer (1992). *Determination of Error in Individual Discharge Measurements*. Open-File Report 92-144. Washington, DC: US Geological Survey.
- Sauer, V. B., and D. P. Turnipseed (2010). Stage measurement at gaging stations. In *Techniques and Methods* (book 3, chapter A7). Washington, DC: US Geological Survey.
- Savenije, H. H. G. (1995). New definitions for moisture recycling and the relationship with land-use changes in the Sahel. *Journal of Hydrology* 167:57–78.
- Sayde, C., C. Gregory, M. Gil-Rodriguez, N. Tufillaro, S. Tyler, N. van de Giesen, M. English, R. Cuenca, and J. S. Selker (2010). Feasibility of soil moisture monitoring with heated fiber optics. *Water Resources Research* 46:W06201, doi:10.1029/2009WR007846.
- Schaefer, G. L., and J. G. Werner (1996). SNOTEL into the year 2000. Paper presented at American Meteorological Society 12th Conference on Biometeorology and Aerobiology, Atlanta, GA, 28 Jan–2 Feb 1996.
- Schaller, M. F., and Y. Fan (2009). River basins as groundwater exporters and importers: Implications for water cycle and climate modeling. *Journal of Geophysical Research* 114:D04103, doi:10.1029/2008JD010636.
- Schmidt, G. A., R. A. Ruedy, R. L. Miller, and A. A. Lacis (2010). Attribution of the present-day total greenhouse effect. *Journal of Geophysical Research* 115:D20106, doi:10.1029/2010JD014287.
- Schmidt, R. A., and D. R. Gluns (1991). Snowfall interception on branches of three conifer species. *Canadian Journal of Forest Research* 21:1262–1269.
- Schmidt, R. A., and C. A. Troendle (1989). Snowfall into a forest clearing. *Journal of Hydrology* 110:335–348.
- Schneider, P., and S. J. Hook (2010). Space observations of inland water bodies show rapid surface warming since 1985. *Geophysical Research Letters* 37:L22405, doi:10.1029/2010GL045059.
- Schreiner, L. C., and J. T. Reidel (1978). *Probable Maximum Precipitation Estimates, United States East of 105th Meridian* (Hydrometeorological Report 51). Washington, DC: US National Weather Service.
- Schumm, S. A. (1956). The evolution of drainage systems and slopes in badlands at Perth Amboy, New Jersey. *Geological Society of America Bulletin* 67:597–646.
- Schumm, S. A., and G. C. Lusby (1963). Seasonal variation of infiltration capacity and runoff on hillslopes in western Colorado. *Journal of Geophysical Research* 68:3655–3666.
- Scotter, D. R., B. E. Clothier, and E. R. Harper (1982). Measuring saturated hydraulic conductivity and sorptivity using twin rings. *Australian Journal of Soil Research* 20:295–304.
- Searcy, J. K., and C. H. Hardison (1960). *Double-Mass Curves*. Water-Supply Paper 1541-B. Washington, DC: US Geological Survey.
- Seidel, D. J., V. Zhang, A. Beljaars, J.-C. Golaz, A. R. Jacobson, and B. Medeiros (2012). Climatology of the planetary boundary layer over the continental United States and Europe. *Journal of Geophysical Research* 117:D17106, doi:10.1029/2012JD018143.
- Sellmann, P. V., and S. L. Dingman (1970). Prediction of stream frequency from maps. *Journal of Teramechanics* 7:101–115.
- Sene, K. J., J. H. C. Gash, and D. D. McNeil (1991). Evaporation from a tropical lake: Comparison of theory with direct measurements. *Journal of Hydrology* 127:193–217.
- Seo, D.-J., A. Seed, and G. Delrieu (2010). Radar and multisensor rainfall estimation for hydrologic applications. In F. Y. Teslik and M. Gebremichael, eds., *Rainfall: State of the Science* (pp. 79–104). Washington, DC: American Geophysical Union.
- Seo, K.-W., D. Ryu, B.?M. Kim, D. E. Waliser, B. Tian, and J. Eom (2010). GRACE and AMSR2-based estimates of winter season solid precipitation accumulation in the Arctic drainage region. *Journal of Geophysical Research* 115:D20117, doi:10.1029/2009JD013504.
- Shafer, B. A., and L. E. Dezman (1982). Development of a surface water supply index (SWSI) to assess the severity of drought conditions in snowpack runoff areas. In 50th Annual Western Snow Conference (Reno, NV) Proceedings.
- Sharma, M. L., G. A. Gander, and G. C. Hunt (1980). Spatial variability of infiltration in a watershed. *Journal of Hydrology* 45:101–122.
- Sharp, M., D. O. Burgess, J. G. Cogley, M. Ecclestone, C. Labine, and G. J. Wolken (2011). Extreme melt on Canada's Arctic ice caps in the 21st century. *Geophysical Research Letters* 38:L11501, doi:10.1029/2011GL047381.
- Shaw, E. M., and P. P. Lynn (1972). Areal rainfall evaluation using two surface fitting techniques. *Hydrological Sciences Bulletin* 17:419–433.
- Shaw, E. M. (1988). *Hydrology in Practice* (2nd ed.). London, UK.: Van Nostrand-Reinhold.
- Shaw, R. E., and E. E. Prepas (1990). Groundwater-lake interactions: I. Accuracy of seepage meter estimates of lake seepage. *Journal of Hydrology* 119:105–120.
- Shiklomanov, I. A. (2010). River discharge. In “Arctic: State of the Climate in 2009” (chapter 5). *Bulletin of the American Meteorological Society* 91(7):116–117.
- Shiklomanov, I. A., and A. A. Sokolov (1983). Methodological basis of world water balance investigation and computation. In *New Approaches in Water Balance Computations*. International Association for Hydrological Sciences Publ. No. 148. (Proceedings of the Hamburg Symposium).
- Shimizu, H. (1970). Air permeability of deposited snow. *Contributions of the Institute of Low Temperature Science*, Ser. A, 22:1–32.
- Shiu, C.-J., S. C. Liu, C. Fu, A. Dai, and Y. Sun (2012). How much do precipitation extremes change in a warming climate? *Geophysical Research Letters* 39:L17707, doi:10.1029/2012GL052762.
- Shokri, N., and D. Or (2011). What determines drying rates at the onset of diffusion controlled stage-2 evaporation from porous media? *Water Resources Research* 47:W09513, doi:10.1029/2010WR010284.
- Shukla, J., and Y. Mintz (1982). Influence of land-surface evapotranspiration on the earth's climate. *Science* 215:1498–1500.
- Shuttleworth, W. J. (1988). Macrohydrology—the new challenge for process hydrology. *Journal of Hydrology* 100:31–56.
- Shuttleworth, W. J. (1992). Evaporation. In D. R. Maidment, ed., *Handbook of Hydrology* (chapter 4). New York: McGraw-Hill.
- Shuttleworth, W. J., and J. S. Wallace (1985). Evaporation from sparse crops—an energy combination theory. *Quarterly Journal of the Royal Meteorological Society* 111:838–855.
- Silliman, S. E., J. Ramirez, and R. L. McCabe (1995). Quantifying downflow through creek sediments using temperature time series: One-dimensional solution incorporating measured surface temperature. *Journal of Hydrology* 167:99–119.
- Simpson, M. R. (2001). *Discharge Measurements Using a Broad-Band Acoustic Doppler Current Profiler*. Open-File Report 01-1. Washington, DC: US Geological Survey.
- Šimůnek, J., and M. T. van Genuchten (2009). Modeling nonequilibrium flow and transport processes using HYDRUS. *Vadose Zone Journal* 7:782–797.
- Singh, P., G. Spitzbart, H. Hübl, and H. W. Weinmeister (1997). Hydrological response of snowpack under rain-on-snow events: A field study. *Journal of Hydrology* 202:1–20.
- Singh, P. K., S. K. Mishra, and M. K. Jain (2013). A review of the synthetic unit hydrograph: From the empirical UH to advanced geomorphological methods. *Hydrological Sciences Journal* 59(2):1–23.
- Singh, V. P., and P. K. Chowdhury (1986). Comparing some methods of estimating mean areal rainfall. *Water Resources Bulletin* 22:275–282.
- Singh, V. P., L. Bengtsson, and G. Westerstrom (1997). Kinematic wave modeling of saturated basal flow in a snowpack. *Hydrological Processes* 11:177–187.
- Sivapalan, M., and G. Blöschl (1998). Transformation of point rainfall to areal rainfall: Intensity-duration-frequency curves. *Journal of Hydrology* 204:150–167.
- Sklash, M. G., and R. N. Farvolden (1979). The role of groundwater in storm runoff. *Journal of Hydrology* 43:45–65.
- Slatyer, R. O., and I. C. McIlroy (1961). *Practical Microclimatology*. Melbourne, Australia: CSIRO.
- Slaughter, C. W. (1966). *Evaporation from Snow and Evaporation Retardation by Monomolecular Films*. Colorado Springs: Watershed Management Unit, Colorado State University.
- Sloan, P. G., and I. D. Moore (1984). Modeling subsurface stormflow on steeply sloping forested watersheds. *Water Resources Research* 20:1815–1822.
- Smerdon, B. D., D. M. Allen, S. E. Grasby, and M. A. Berg (2009). An approach for predicting groundwater recharge in mountainous watersheds. *Journal of Hydrology* 365:156–172.
- Smith, J. A. (1992). Precipitation. In D. R. Maidment, ed., *Handbook of Hydrology* (chapter 3). New York: McGraw-Hill.
- Smith, J. A., M. L. Baeck, A. A. Ntelekos, G. Villarini, and M. Steiner (2011). Extreme rainfall and flooding from orographic thunderstorms in the central Appalachians. *Water Resources Research* 47:W04514, doi:10.1029/2010WR010190.

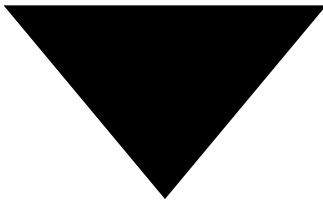
- Smith, L., and S. W. Wheatcraft (1992). Groundwater flow. In D. R. Maidment, ed., *Handbook of Hydrology* (chapter 6). New York: McGraw-Hill.
- Smith, L. C., Y. Sheng, G. M. MacDonald, and L. D. Hinzman (2005). Disappearing arctic lakes. *Science* 308:1429.
- Smith, L. C., and T. M. Pavelsky (2008). Estimation of river discharge, propagation speed, and hydraulic geometry from space: Lena River, Siberia. *Water Resources Research* 44:W03427, doi:10.1029/2007WR006133.
- Smith, P. J., and R. S. Wikramaratna (1981). A method for estimating recharge and boundary flux from groundwater level observations. *Hydrological Sciences Bulletin* 26:113–136.
- Smits, K. M., V. V. Ngo, A. Cihan, T. Sakaki, and T. H. Illangasekare (2012). An evaluation of models of bare soil evaporation formulated with different land surface boundary conditions and assumptions. *Water Resources Research* 48:W12526, doi:10.1029/2012WR012113.
- Smoot, G. F., and C. E. Novak (1968). Calibration and maintenance of vertical-axis type current meters. In *Techniques of Water-Resources Investigations* (book 8, chapter B2). Washington, DC: US Geological Survey.
- Sophocleous, M. (1985). The role of specific yield in ground-water recharge estimations. *Ground Water* 23:52–58.
- Sophocleous, M., and C. A. Perry (1984). Experimental studies in natural ground-water-recharge dynamics: Assessment of recent advances in instrumentation. *Journal of Hydrology* 70:369–382.
- Sophocleous, M., and C. A. Perry (1985). Experimental studies in natural ground-water-recharge dynamics: The analysis of observed recharge events. *Journal of Hydrology* 81:297–332.
- Souch, C., C. P. Wolfe, and C. S. B. Grimmond (1996). Wetland evaporation and energy partitioning: Indiana Dunes National Lakeshore. *Journal of Hydrology* 184:189–208.
- Space, M. L., N. L. Ingraham, and J. W. Hess (1991). The use of stable isotopes in quantifying groundwater discharge to a partially diverted creek. *Journal of Hydrology* 129:175–193.
- Spangler, W. M. L., and R. L. Jenne (1988). *World Monthly Surface Station Climatology*. Boulder, CO: National Center for Atmospheric Research, Scientific Computing Division.
- Spittlehouse, D. L., and T. A. Black (1981). A growing season water balance model applied to two Douglas fir stands. *Water Resources Research* 17:1651–1656.
- Springer, E. P., and G. F. Gifford (1980). Spatial variability of rangeland infiltration rates. *Water Resources Bulletin* 16:550–552.
- Stannard, D. I., and D. O. Rosenberry (1991). A comparison of short-term measurements of lake evaporation using eddy correlation and energy budget methods. *Journal of Hydrology* 122:15–22.
- Stedinger, J. R., R. M. Vogel, and E. Foufoula-Georgiou (1992). Frequency analysis of extreme events. In D. R. Maidment, ed., *Handbook of Hydrology* (chapter 18). New York: McGraw-Hill.
- Steenhuis, T. S., and W. H. Van Der Molen (1986). The Thornthwaite-Mather procedure as a simple engineering method to predict recharge. *Journal of Hydrology* 84:221–229.
- Steenhuis, T. S., C. D. Jackson, S. K. J. Kung, and W. Brutsaert (1985). Measurement of groundwater recharge on eastern Long Island, New York, USA. *Journal of Hydrology* 79:145–169.
- Stephens, D. B. (1995). *Vadose Zone Hydrology*. Boca Raton, FL: CRC Press.
- Stephens, D. B., and R. Knowlton, Jr. (1986). Soil water movement and recharge through sand at a semiarid site in New Mexico. *Water Resources Research* 22:881–889.
- Stephenson, D., and M. E. Meadows (1986). *Kinematic Hydrology and Modeling*. Developments in Water Science 26. New York: Elsevier.
- Stewart, J. B. (1977). Evaporation from the wet canopy of a pine forest. *Water Resources Research* 13:915–921.
- Stewart, J. B. (1988). Modeling surface conductance of pine forest. *Agricultural and Forest Meteorology* 43:17–35.
- Stewart, J. B. (1989). On the use of the Penman-Monteith equation for determining areal evapotranspiration. In T. A. Black et al., eds., *Estimation of Areal Evapotranspiration*. Wallingford, Oxon, UK: International Association of Hydrological Sciences Publication 177:3–12.
- Stewart, J. B., and L. W. Gay (1989). Preliminary modelling of transpiration from the FIFE site in Kansas. *Agricultural and Forest Meteorology* 48:305–315.
- Stillinger, F. H. (1980). Water revisited. *Science* 209:451–455.
- Strahler, A. N. (1952). Hypsometric (area-altitude) analysis of erosional topography. *Geological Society of America Bulletin* 63:1117–1142.
- Strangeways, I. (2007). *Precipitation: Theory, Measurement, and Distribution*. New York: Cambridge University Press.
- Stresky, S. J. (1991). Morphology and Flow Characteristics of Pipes in a Forested New England Hillslope. Durham, NH: Thesis, M.Sc. in Hydrology, University of New Hampshire.
- Sturm, M., and A. M. Wagner (2010). Using repeated patterns in snow distribution modeling: An Arctic example. *Water Resources Research* 46:W12549, doi:10.1029/2010WR009434.
- Su, H., Z.-L. Yang, R. E. Dickinson, C. R. Wilson, and G.-Y. Niu (2010). Multisensor snow data assimilation at the continental scale: The value of Gravity Recovery and Climate Experiment terrestrial water storage information. *Journal of Geophysical Research* 115:D10104, doi:10.1029/2009JD013035.
- Suckling, P. W. (1997). Spatial coherence of solar radiation for regions in the central and eastern United States. *Physical Geography* 18(1):53–62.
- Suckling, P. W., and J. E. Hay (1976). Modeling direct, diffuse, and total solar radiation for cloudless days. *Atmosphere* 14:298–308.
- Sugiura, K., T. Ohata, and D. Yang (2006). Catch characteristics of precipitation gauges in high-latitude regions with high winds. *Journal of Hydrometeorology* 7:984–994.
- Sui, J., and G. Kochler (2001). Rain-on-snow-induced floods in southern Germany. *Journal of Hydrology* 252:205–220.
- Sun, D.-Z., and F. Bryan (2010). *Climate Dynamics: Why Does Climate Vary?* Geophysical Monograph 189. Washington, DC: American Geophysical Union.
- Svensson, C., and D. A. Jones (2010). Review of rainfall frequency estimation methods. *Journal of Flood Risk Management* 3(4):296–313.
- Swamee, P. K., P. N. Rathie, and L. C. de S. M. Ozelim (2012). Explicit equations for infiltration. *Journal of Hydrology* 426:427:151–153.
- Swan, A. R. H., and M. Sandilands (1995). *Introduction to Geological Data Analysis*. Oxford, UK: Blackwell Scientific.
- Swartzendruber, D. (1997). Exact mathematical derivation of a two-term infiltration equation. *Water Resources Research* 33:491–496.
- Swartzendruber, D., and F. R. Clague (1989). An inclusive infiltration equation for downward water entry into soil. *Water Resources Research*: 25:619–626.
- Swartzendruber, D., and T. C. Olson (1961a). Sand-model study of buffer effects in the double-ring infiltrometer. *Soil Science Society of America Proceedings* 25:5–8.
- Swartzendruber, D., and T. C. Olson (1961b). Model study of the double-ring infiltrometer as affected by depth of wetting and particle size. *Soil Science* 92:219–225.
- Swistock, B. R., D. R. DeWalle, and W. E. Sharpe (1989). Sources of acidic storm flow in an Appalachian headwater stream. *Water Resources Research* 25:2139–2147.
- Svitiski, J. P. M. (2003). Supply and flux of sediment along hydrological pathways: Research for the 21st century. *Global and Planetary Change* 39:1–11.
- Tabios, G. Q., and J. D. Salas (1985). A comparative analysis of techniques for spatial interpolation of precipitation. *Water Resources Bulletin* 21:365–380.
- Tallaksen, L. M. (1995). A review of baseflow recession analysis. *Journal of Hydrology* 165:349–370.
- Tang, Q., and D. P. Lettenmaier (2012). 21st century runoff sensitivities of major global river basins. *Geophysical Research Letters* 39:L06403, doi:10.1029/2011GL050834.
- Tani, M. (1997). Runoff generation processes estimated from hydrological observations on a steep forested hillslope with a thin soil layer. *Journal of Hydrology* 200:84–109.
- Taniguchi, M., and M. L. Sharma (1990). Solute and heat transport experiments for estimating recharge rate. *Journal of Hydrology* 119:57–69.
- Tanny, J., S. Cohen, S. Assouline, F. Lange, A. Grava, D. Berger, B. Teltsch, and M. B. Parlange (2008). Evaporation from a small water reservoir: Direct measurements and estimates. *Journal of Hydrology* 351:218–229.
- Tapley, B. D., S. Bettadpur, J. C. Ries, P. F. Thompson, and M. M. Watkins (2004).

- GRACE measurements of mass variability in the Earth system. *Science* 305(5683):593–505.
- Tarboton, D. G. (1997). A new method for the determination of flow directions and upslope areas in grid digital elevation models. *Water Resources Research* 33:309–319.
- Tarboton, D. G., R. J. Bras, and I. Rodriguez-Iturbe (1991). On the extraction of channel networks from digital elevation data. *Hydrologic Processes* 5(1):81–100.
- Tauro, F., S. Grimaldi, A. Petroselli, and M. Porfiri (2012). Fluorescent particle tracers for surface flow measurements: A proof of concept in a natural stream. *Water Resources Research* 48:W06528, doi:10.1029/2011WR011610.
- Taylor, G. H., C. Daly, and W. P. Gibson (1993). Development of a new Oregon annual precipitation map using the PRISM model. *The State Climatologist* 17(2):1–4.
- Taylor, J. R. (1997). *An Introduction to Error Analysis* (2nd ed.). Sausalito, CA: University Science Books.
- Techel, F., and C. Piehlmeier (2011). Point observations of liquid water content in wet snow—investigating methodical, spatial and temporal aspects. *The Cryosphere* 5:405–418.
- Tennyson, L. C., P. F. Ffolliott, and D. B. Thorrud (1974) Use of time-lapse photography to assess potential interception in Arizona ponderosa pine. *Water Resources Bulletin* 10:1246–1254.
- Theis, C. V. (1935). The relation between the lowering of the piezometric surface and the rate and duration of discharge of a well using groundwater storage. *American Geophysical Union Transactions* 2:519–524.
- Thierry, D. (1988). Forecast of changes in piezometric levels by a lumped hydrological model. *Journal of Hydrology* 97:129–148.
- Thiessen, A. H. (1911). Precipitation for large areas. *Monthly Weather Review* 39:1082–1084.
- Thorburn, P. J., B. A. Cowie, and P. A. Lawrence (1991). Effect of land development on groundwater recharge determined from non-steady chloride profiles. *Journal of Hydrology* 124:43–58.
- Thornthwaite, C. W. (1948). An approach toward a rational classification of climate. *Geographical Review* 38:55–94.
- Thornthwaite, C. W., and J. R. Mather (1955). *The Water Balance*. Climatological Laboratory Publication 8. Philadelphia, PA: Drexel Institute of Technology.
- Tian, Y., C. Peters-Lidard, J. B. Eylander, et al. (2009). Component analysis of errors in satellite-based precipitation estimates. *Journal of Geophysical Research* 114:D24101.
- Tian, Y., and C. Peters-Lidard (2010). A global map of uncertainties in satellite-based precipitation measurements. *Geophysical Research Letters* 37:L24407.
- Todd, D. K. (1953). Sea water intrusion in coastal aquifers. *American Geophysical Union Transactions* 34:749–754.
- Todd, D. K. (1959). *Ground Water Hydrology*. New York: John Wiley and Sons.
- Todd, D. K., ed. (1970). *The Water Encyclopedia*. Port Washington, NY: Water Information Center.
- Todd, D. K., and L. W. Mays (2014). *Groundwater Hydrology*. New York: Wiley.
- Tonina, D., and J. M. Buffington (2011). Effects of stream discharge, alluvial depth and bar amplitude on hyporheic flow in pool-riffle channels. *Water Resources Research* 47:W08508, doi:10.1029/2010WR009140.
- Topp, G. C., J. L. Davis, and A. P. Annan (1980). Electromagnetic determination of soil water content: Measurements in coaxial transmission lines. *Water Resources Research* 16:574–582.
- Tóth, J. (1962). A theory of groundwater motion in small drainage basins in central Alberta, Canada. *Journal of Geophysical Research* 67:4375–4387.
- Tóth, J. (1963). A theoretical analysis of groundwater flow in small drainage basins. *Journal of Geophysical Research* 68:4795–4812.
- Trenberth, K. E., G. W. Branstator, and P. A. Arkin (1988). Origins of the 1988 North American drought. *Science* 242:1640–1645.
- Trenberth, K. E., and J. M. Caron (2001). Estimates of meridional atmosphere and ocean heat transports. *Journal of Climate* 14:3433–3443.
- Trenberth, K. E., J. T. Fasullo, and J. Kiehl (2009). Earth's global energy budget. *Bulletin of the American Meteorological Society* 90:311–323.
- Trenberth, K. E., J. T. Fasullo, and J. Mackaro (2011). Atmospheric moisture transports from ocean to land and global energy flows in reanalyses. *Journal of Climate* 24:4907–4924.
- Trenberth, K. E., L. Smith, T. Qian, A. Dal, and J. Fasullo (2007). Estimates of the global water budget and its annual cycle using observational and model data. *Journal of Hydrometeorology* 8:758–769.
- Trenberth, K. E., and D. P. Stepaniak (2003). Covariability of components of poleward atmospheric energy transports on seasonal and interannual time scales. *Journal of Climate* 16:3691–3705.
- Tricker, A. S. (1978). The infiltration cylinder: Some comments on its use. *Journal of Hydrology* 36:383–391.
- Tricker, A. S. (1979). The design of a portable rainfall simulator infiltrometer. *Journal of Hydrology* 41:143–147.
- Tricker, A. S. (1981). Spatial and temporal patterns of infiltration. *Journal of Hydrology* 49:261–277.
- Troch, P. A., F. P. De Troch, and W. Brutsaert (1993). Effective water table depth to describe initial conditions prior to storm rainfall in humid regions. *Water Resources Research* 29:427–434.
- Troxell, H. C., et al. (1942). *Characteristic Spatial Variation of Orographic Precipitation*. Water-Supply Paper 844. Washington, DC: US Geological Survey.
- Tseng, P.-H., T. H. Illangasekare, and M. F. Meier (1994). Modeling of snow melting and uniform wetting front migration in a layered subfreezing snowpack. *Water Resources Research* 30:2363–2376.
- Tsonis, A. A. (1996). Widespread increases in low-frequency variability of precipitation over the past century. *Nature* 382:700–702.
- Turk, J. T. (1983). *An Evaluation of Trends in the Acidity of Precipitation and the Related Acidification of Surface Water in North America* (Water-Supply Paper 2249). Washington, DC: US Geological Survey.
- Twarakavi, N. K. C., M. Sakai, and J. Šimůnek (2009). An objective analysis of the dynamic nature of field capacity. *Water Resources Research* 45:W10410, doi:10.1029/2009WR007944.
- Twarakavi, N. K. C., J. Šimůnek, and M. G. Schaap (2010). Can texture-based classification optimally classify soils with respect to soil hydraulics? *Water Resources Research* 46:W01501, doi:10.1029/2009WR007939.
- US Army Corps of Engineers (1956). *Snow Hydrology: Summary Report of the Snow Investigations*. Portland, OR: North Pacific Division, US Army Corps of Engineers.
- US Department of Agriculture (1982). *Computer program for project formulation—hydrology* (TR-20). Washington, DC: US Department of Agriculture.
- US Geological Survey (1954). *Water-Loss Investigations: Lake Hefner Studies, Base Data Report*. Professional Paper 270. Washington, DC: US Geological Survey.
- US Geological Survey (1984). *National Water Summary 1983—Hydrologic Events and Issues*. Water-Supply Paper 2250. Washington, DC: US Geological Survey.
- US Geological Survey (1985). *National Water Summary 1984—Hydrologic Events, Selected Water-Quality Trends, and Ground-Water Resources*. Water-Supply Paper 2275. Washington, DC: US Geological Survey.
- US National Imagery and Mapping Agency (2002). *The American Practical Navigator*. Washington, DC: US National Geospatial-Intelligence Agency.
- US National Research Council (2001). *Basic Research Opportunities in Earth Science*. Washington DC: National Academy Press.
- US National Research Council (2003). *Critical Issues in Weather Modification Research*. Washington DC: National Academy Press.
- US Soil Conservation Service (1964). Hydrology. In *SCS National Engineering Handbook* (section 4). Washington, DC: US Soil Conservation Service.
- US Soil Conservation Service (1984). *Snow Survey Sampling Guide*. Agricultural Handbook Number 169. Washington, DC: Author.
- Valdes, J. B., M. Diaz-Granados, and R. L. Bras (1990). A derived PDF for the initial soil moisture in a catchment. *Journal of Hydrology* 113:163–176.
- Valdes, J. B., Y. Fiallo, and I. Rodriguez-Iturbe (1979). A rainfall-runoff analysis of the geomorphologic IUH. *Water Resources Research* 15:1421–1434.
- Valente, F., J. S. David, and J. H. C. Gash (1997). Modelling interception loss for two sparse eucalypt and pine forests in central Portugal using reformulated Rutter and Gash analytical models. *Journal of Hydrology* 190:141–162.
- Van Bavel, C. H. M. (1966). Potential evaporation: The combination concept and its experimental verification. *Water Resources Research* 2:455–467.

- Van de Greind, A. A., and E. T. Engman (1985). Partial area hydrology and remote sensing. *Journal of Hydrology* 81:211–251.
- van der Ent, R. J., H. H. G. Savenije, B. Schaeffli, and S. C. Steele-Dunne (2010). Origin and fate of atmospheric moisture over continents. *Water Resources Research* 46:W09525, doi:10.1029/2010WR009127.
- Van Dyke, M. (1982). *An Album of Fluid Motion*. Stanford, CA: The Parabolic Press.
- Van Genuchten, M. T. (1980). A closed-form equation for predicting the hydraulic conductivity of unsaturated soils. *Soil Science Society of America Journal* 44:892–898.
- van Hyckama, T. E. A. (1979). Water, something peculiar. *Hydrological Sciences Bulletin* 24:499–507.
- Van Tonder, G. J., and J. Kirchner (1990). Estimation of natural groundwater recharge in the Karroo aquifers of South Africa. *Journal of Hydrology* 121:395–419.
- Vansteenkiste, T., M. Tavakoli, N. Van Steenbergen, F. De Smedt, O. Batelaan, F. Pereira, and P. Willems (2014). Intercomparison of five lumped and distributed models for catchment runoff and extreme flow simulation. *Journal of Hydrology* 511:335–349.
- Varhola, A., N. C. Coops, M. Weiler, and R. D. Moore (2010). Forest canopy effects on snow accumulation and ablation: An integrative review of empirical results. *Journal of Hydrology* 392:219–233.
- Veatch, W., P. D. Brooks, J. R. Gustafson, and N. P. Molotch (2009). Quantifying the effects of forest canopy cover on net snow accumulation at a continental, mid-latitude site. *Ecohydrology* 2(2):115–128.
- Verdin, K. L., and J. P. Verdin (1999). A topological system for delineation and codification of the Earth's river basins. *Journal of Hydrology* 218(1–2):1–12.
- Viessman, W., Jr., G. L. Lewis, and J. W. Knapp (1989). *Introduction to Hydrology* (3rd ed.). New York: Harper & Row.
- Villarini, G., J. A. Smith, M. L. Baech, R. Vitolo, D. B. Stephenson, and W. F. Krajewski (2011). On the frequency of heavy rainfall for the Midwest of the United States. *Journal of Hydrology* 400:103–120.
- Villholth, K. G., K. H. Jensen, and J. Fredericia (1998). Flow and transport processes in a macroporous subsurface-drained glacial till soil. I. Field investigations. *Journal of Hydrology* 207:98–120.
- Visbeck, M. H., J. W. Hurrell, L. Polvani, and H. M. Cullen (2000). The North Atlantic Oscillation: Past, present, and future. Paper presented at US National Academy of Science 12th Symposium on Frontiers of Science, Irvine, CA.
- Viswanathan, M. N. (1984). Recharge characteristics of an unconfined aquifer from the rainfall-water table relationship. *Journal of Hydrology* 70:233–250.
- Vogel, R. M. (1986). The probability plot correlation coefficient test for normal, lognormal, and Gumbel distributions. *Water Resources Research* 22:587–590.
- Vogel, R. M., and A. Sankarasubramanian (2003). Validation of a watershed model without calibration. *Water Resources Research* 39(10):1292, doi:10.1029/2002WR001940.
- Vörösmarty, C. J., C. Birkett, L. Dingman, D. P. Lettenmaier, Y. Kim, E. Rodriguez, G. D. Emmitt, W. Plant, and E. Wood (1999). NASA Post-2002 Land Surface Hydrology Mission Component for Surface Water Monitoring, HYDRA_SAT, A Report from the NASA Post 2002 Land Surface Hydrology Planning Workshop, Irvine CA, April 12–14, p. 53.
- Vörösmarty, C. J., C. A. Federer, and A. L. Schloss (1998). Potential evaporation functions compared on US watersheds: Possible implications for global-scale water balance and terrestrial ecosystem modeling. *Journal of Hydrology* 207:147–169.
- Vörösmarty, C. J., B. M. Fekete, M. Meybeck, and R. B. Lammers (2000a). Geomorphic attributes of the global system of rivers at 30-minute spatial resolution. *Journal of Hydrology* 237:17–39.
- Vörösmarty, C. J., P. Green, J. Salisbury, and R. B. Lammers (2000). Global water resources: Vulnerability from climate change and population growth. *Science* 289:284–288.
- Vörösmarty, C. J., M. Meybeck, B. Fekete, and K. Sharma (1997b). The potential impact of neo-Castorization on sediment transport by the global network of rivers. In *Human Impact on Erosion and Sedimentation*, International Association of Hydrologic Sciences Publication 245.
- Vörösmarty, C. J., K. P. Sharma, B. M. Fekete, A. H. Copeland, J. Holden, J. Marble, and J. A. Lough (1997). The storage and aging of continental runoff in large reservoir systems of the world. *Ambio* 26(4):210–219.
- Waddington, J. M., N. T. Roulet, and A. R. Hill (1993). Runoff mechanisms in a forested groundwater discharge wetland. *Journal of Hydrology* 147:37–60.
- Wagener, T., M. Sivapalan, P. A. Troch, et al. (2010). The future of hydrology: An evolving science for a changing world. *Water Resources Research* 46:W05301, doi:10.1029/2009WR008906.
- Wagenet, R. J., and P. F. Germann (1989). Concepts and models of water flow in macropore soils. In C. R. Frink (ed.), *Ground Water in the Northeast* (Bulletin 876). New Haven: Connecticut Agricultural Experiment Station.
- Waggoner, P. E. (1989). Anticipating the frequency distribution of precipitation if climate change alters its mean. *Agricultural and Forest Meteorology* 47:321–337.
- Wagner, A. (2009). *Literature Study on the Correction of Precipitation Measurements*. Fumon C1-Met-29 (BY). Freising, Germany: Bavarian State Institute of Forestry.
- Walker, C. D., and J.-P. Brunel (1990). Examining evapotranspiration in a semi-arid region using stable isotopes of hydrogen and oxygen. *Journal of Hydrology* 118:55–75.
- Walker, G. R., I. D. Jolly, and P. G. Cook (1991). A new chloride leaching approach to the estimation of diffuse recharge following a change in land use. *Journal of Hydrology* 128:49–67.
- Walker, J. F. (1988). General two-point method for determining velocity in open channel.
- American Society of Civil Engineers Proceedings, *Journal of Hydraulic Engineering* 114:801–805.
- Walkotten, W. J. (1972). *A Recording Soil Moisture Tensiometer*. Research Note PNW-180. Portland, OR: US Forest Service Pacific Northwest Forest and Range Experiment Station.
- Wallace, J. M., and D. S. Gutzler (1981). Teleconnections in the geopotential height field during the Northern Hemisphere winter. *Monthly Weather Review* 109:784–812.
- Wallace, J. M., and P. V. Hobbs (1977). *Atmospheric Science: An Introductory Survey*. New York: Academic Press.
- Walling, D. E., and D. Fang (2003). Recent trends in the suspended sediment loads of the world's rivers. *Global and Planetary Change* 39:111–126.
- Walling, D. E., and B. W. Webb (1987). Material transport by the world's rivers: Evolving perspectives. In *Water for the Future: Hydrology in Perspective*. International Association for Hydrological Sciences Publ. No. 164. (Proceedings of the Rome Symposium).
- Wallis, J. R., and P. E. O'Connell (1972). Small sample estimation of ρ_1 . *Water Resources Research* 8:707–712.
- Walsh, J. E. (1984). Snow cover and atmospheric variability. *American Scientist* 72:50–57.
- Wang, H. F., and M. P. Anderson (1982). *Introduction to Groundwater Flow Modeling*. San Francisco, CA: W.H. Freeman and Co.
- Wang, K., and R. E. Dickinson (2012). A review of global terrestrial evapotranspiration: Observation, modeling, climatology, and climatic variability. *Reviews of Geophysics* 50:RG2005, doi:10.1029/2011RG000373.
- Wang, Q. J., and J. C. Dooge (1994). Limiting cases of water flux at the land surface. *Journal of Hydrology* 155:429–440.
- Wang, Z., X. Zeng, and M. Decker (2010). Improving snow processes in the Noah land model. *Journal of Geophysical Research: Atmospheres* 115:D20108, doi:10.1029/2009JD013761.
- Ward, R. C. (1984). On the response to precipitation of headwater streams in humid areas. *Journal of Hydrology* 74:171–189.
- Waring, E. A., and J. A. A. Jones (1980). A snowmelt and water equivalent gauge for British conditions. *Hydrological Sciences Bulletin* 25:129–134.
- Webb, R. W., C. E. Rosenzweig, and E. R. Levine (2000). Global Soil Texture and Derived Water-Holding Capacities. Data set from Oak Ridge National Lab Distributed Archive Center, doi:10.3334/ORN-LDAAC/548.
- Weill, S., E. Mouche, and J. Patin (2009). A generalized Richards equation for surface/subsurface flow modeling. *Journal of Hydrology* 366:9–20.
- Weinman, P. E., and E. M. Laurenson (1979). Approximate flood routing methods: A review. American Society of Civil Engineers Proceedings, *Journal of the Hydraulics Division* 105(HY-12):1521–1536.
- Wellings, S. R. (1984). Recharge of a chalk aquifer at a site in Hampshire, England—1. Water Balance and Unsaturated Flow. *Journal of Hydrology* 69:259–273.

- Wentz, F. J., L. Ricciardelli, K. Hillburn, and C. Mears (2007). How much more rain will global warming bring? *Science* 317:233–235.
- Wenzel, H. G., Jr. (1982). Rainfall for urban storm water design. In D. F. Kibler, ed., *Urban Stormwater Hydrology*. American Geophysical Union Water Resources Monograph 7.
- Wenzel, L. K. (1942). *Methods of Determining Permeability of Water-Bearing Materials* (Water-Supply Paper 887). Washington, DC: US Geological Survey.
- Weyman, D. R. (1970). Throughflow on hillslopes and its relation to the stream hydrograph. *International Association of Scientific Hydrology Bulletin* 15(2):25–32.
- Whipkey, R. Z., and M. J. Kirkby (1978). Flow within the soil. In M. J. Kirkby, ed., *Hillslope Hydrology* (pp. 121–144). New York: John Wiley.
- Whisler, F. D., and H. Bouwer (1970). Comparison of methods for calculating vertical drainage and infiltration in soils. *Journal of Hydrology* 10:1–19.
- White, W. N. (1932). *A Method of Estimating Groundwater Supplies Based on Discharge by Plants and Evaporation from Soil*. Water-Supply Paper 659-A. Washington, DC: US Geological Survey.
- Whiting, P. J., and M. Pomeranets (1997). A numerical study of bank storage and its contribution to streamflow. *Journal of Hydrology* 202:121–136.
- Whittaker, R. H. (1975). *Communities and Ecosystems* (2nd ed.). New York: Macmillan.
- Wigmsta, M. S., and S. J. Burges (1997). An adaptive modeling and monitoring approach to describe the hydrologic behavior of small catchments. *Journal of Hydrology* 202:48–77.
- Wikramaratne, R. S., and C. E. Reeve (1984). A modeling approach to estimating aquifer recharge on a regional scale. *Hydrological Sciences Journal* 29:327–337.
- Wilcock, D. N., and C. I. Essery (1984). Infiltration measurements in a small lowland catchment. *Journal of Hydrology* 74:191–204.
- Wilcox, S. (2012). *National Solar Radiation Database, 1991–2010 Update: User's Manual*. Technical Report NREL/TP-5500-54824. Washington, DC: US Department of Energy.
- Wilding, L. P., and H. Lin (2006). Advancing the frontiers of soil science towards a geosciences. *Geoderma* 131:257–274.
- Wilf, P., S. L. Wing, D. R. Greenwood, and C. L. Greenwood (1998). Using fossil leaves as paleoprecipitation indicators: An Eocene example. *Geology* 26:203–206.
- Wilkinson, B. H. (2005). Humans as geological agents: A deep-time perspective. *Geology* 33(3):161–164.
- Williams, J. R., and R. O. van Everdingen (1973). Groundwater investigations in permafrost regions of North America: A review. In *Permafrost: North American Contributions to the Second International Conference*. Washington, DC: National Academy of Sciences.
- Williams, T. H. L. (1978). An automatic scanning and recording tensiometer system. *Journal of Hydrology* 39:175–183.
- Willmott, C. J., S. M. Robeson, and J. J. Fedema (1994). Estimating continental and terrestrial precipitation averages from rain-gauge networks. *International Journal of Climatology* 14:403–414.
- Winter, T. C. (1976). *Numerical Simulation Analysis of the Interaction of Lakes and Ground Water*. Professional Paper 1001. Washington, DC: US Geological Survey.
- Winter, T. C. (1978). Numerical simulation of steady state three dimensional groundwater flow near lakes. *Water Resources Research* 14:245–254.
- Winter, T. C. (1981). Uncertainties in estimating the water balance of lakes. *Water Resources Bulletin* 17:82–115.
- Winter, T. C. (1983). The interaction of lakes with variably saturated porous media. *Water Resources Research* 19:1203–1218.
- Winter, T. C. (1999). Relation of streams, lakes, and wetlands to groundwater flow systems. *Hydrogeology Journal* 7:28–45.
- Winter, T. C. (2001). The concept of hydrologic landscapes. *Journal of the American Water Resources Association* 37(2):335–349.
- Winter, T. C., J. S. Eaton, and G. E. Likens (1989). Evaluation of inflow to Mirror Lake, New Hampshire. *Water Resources Bulletin* 25:991–1008.
- Winter, T. C., J. W. LaBaugh, and D. O. Rosenberry (1988). The design and use of a hydraulic potentiometer for direct measurement of difference in hydraulic head between groundwater and surface water. *Limnology and Oceanography* 33:1209–1214.
- Winter, T. C., D. O. Rosenberry, and J. W. LaBaugh (2003). Where does the ground water in small watersheds come from? *Ground Water* 41(7):989–1000.
- Winter, T. C., D. O. Rosenberry, and A. M. Sturrock (1995). Evaluation of 11 equations for determining evaporation for a small lake in the north central United States. *Water Resources Research* 31:983–993.
- Wolfe, B. B., T. W. D. Edwards, R. I. Hall, and J. W. Johnston (2011). A 5200-year record of freshwater availability for regions in western North America fed by high-elevation runoff. *Geophysical Research Letters* 38:L11404, doi:10.1029/2011GL047599.
- Wolock, D. M. (2003). *Base-Flow Index Grid for the Contiguous United States*. Open-File Report 03-263. Washington, DC: US Geological Survey.
- Woo, M.-K., and P. Steer (1979). Measurement of trace rainfall at a high arctic site. *Arctic* 32:80–84.
- Woo, M.-K., and P. Steer (1986). Monte Carlo simulation of snow depth in a forest. *Water Resources Research* 22:864–868.
- Wood, E. F., M. Sivapalan, and K. Beven (1990). Similarity and scale in catchment storm response. *Reviews of Geophysics* 28:1–18.
- Wood, M. K., and W. H. Blackburn (1984). An evaluation of the hydrologic soil groups as used in the SCS runoff method on rangelands. *Water Resources Bulletin* 20:379–389.
- Woodruff, J. F., and J. D. Hewlett (1970). Predicting and mapping the average hydrologic response for the eastern United States. *Water Resources Research* 6:1312–1326.
- Woods, R., and M. Sivapalan (1999). A synthesis of space-time variability in storm response: Rainfall, runoff generation, and routing. *Water Resources Research* 35:2469–2485.
- Woodward, F. I. (1987). *Climate and Plant Distribution*. Cambridge, UK.: Cambridge University Press.
- Woolhiser, D. A., and J. A. Liggett (1967). Unsteady one-dimensional flow over a plane—The rising hydrograph. *Water Resources Research* 3:753–771.
- Work, R. A., H. J. Stockwell, T. G. Freeman, and R. T. Beaumont (1965). *Accuracy of Field Snow Surveys*. Technical Report 163. Hanover, NH: US Army Cold Regions Research and Engineering Laboratory.
- Workman, S. R., and S. E. Serrano (1999). Recharge to alluvial valley aquifers from overbank flow and excess infiltration. *Journal of the American Water Resources Association* 35:425–432.
- World Meteorological Organization (1986a). *Intercomparison of Models of Snowmelt Runoff*. Operational Hydrology Report 23. Geneva, Switzerland: Author.
- World Meteorological Organization (1986b). *Manual for Estimation of Probable Maximum Precipitation*. Operational Hydrology Report 1, 2nd ed., Publication 332. Geneva, Switzerland: Author.
- World Meteorological Organization (1992). *Simulated Real Time Intercomparison of Hydrological Models*. Operational Hydrology Report 38. Geneva, Switzerland: Author.
- World Meteorological Organization (2008). *Guide to Meteorological Instruments and Methods of Observation*. Geneva, Switzerland: Author.
- Wösten, J. H. M., Y. A. Pachepsky, and W. J. Rawls (2001). Pedotransfer functions: Bridging the gap between available basic soil data and missing soil hydraulic characteristics. *Journal of Hydrology* 251:123–150.
- Wu, J., R. Zhang, and J. Yang (1996). Analysis of rainfall-recharge relationships. *Journal of Hydrology* 177:143–160.
- Xiao, H., R. Meissner, J. Seeger, H. Rupp, and H. Borg (2009). Effect of vegetation type and growth stage on dewfall, determined with high precision weighing lysimeters at a site in northern Germany. *Journal of Hydrology* 377:43–49.
- Xie, P., and A.-Y. Xiong (2011). A conceptual model for constructing high-resolution gauge-satellite merged precipitation analysis. *Journal of Geophysical Research: Atmospheres* 116:D21106, doi:10.1029/2011JD016118.
- Yamaguchi, S., K. Watanabe, T. Katsushima, A. Sato, and T. Kumakura (2012). Dependence of the water retention curve of snow on snow characteristics. *Annals of Glaciology* 53(61):1–7.
- Yang, D., B. E. Goodison, S. Ishida, and C. S. Benson (1998a). Adjustment of daily precipitation data at 10 climate stations in Alaska: Application of World Meteorological Organization intercomparison results. *Water Resources Research* 34:241–256.
- Yang, D., B. E. Goodison, J. R. Metcalfe, V. S. Golubev, R. Bates, T. Pangburn, and C.

- L. Hanson (1998b). Accuracy of NWS 8? standard nonrecording precipitation gauge: Results and application of WMO intercomparison. *Journal of Atmospheric and Oceanic Technology* 15:54–68.
- Yang, D., D. Kane, and Z. Zhang (2005). Bias correction of long-term (1973–2004) daily precipitation data over the northern regions. *Geophysical Research Letters* 32:19501–19506.
- Yang, D., F. Sun, Z. Liu, Z. Cong, G. Li, and Z. Lei (2007). Analyzing spatial and temporal variability of annual water-energy balance in non-humid regions of China using the Budyko hypothesis. *Water Resources Research* 43:W04426, doi:10.1029/2003WR005224.
- Yang, H., and D. Yang (2011). Derivation of climate elasticity of runoff to assess the effects of climate change on annual runoff. *Water Resources Research* 47:W07526, doi:10.1029/2010WR009287.
- Yang, H., D. Yang, Z. Lei, and F. Sun (2008). New analytical derivation of the mean annual water-energy balance equation. *Water Resources Research* 44:W03410, doi:10.1029/2007WR006135.
- Yang, K., and T. Koike (2005). A general model to estimate hourly and daily solar radiation for hydrological studies. *Water Resources Research* 41:W10403, doi:10.1029/2005WR003976.
- Yasunari, T. J., R. D. Koster, K. M. Lau, T. Aoki, Y. C. Sud, T. Yamazaki, H. Motyoshi, and Y. Kodama (2011). Influence of dust and black carbon on the snow albedo in the NASA Goddard Earth Observing System version 5 land surface model. *Journal of Geophysical Research* 116:D02210, doi:10.1029/2010JD014861.
- Yevjevich, V. (1972). *Probability and Statistics in Hydrology*. Fort Collins, CO: Water Resources Publications.
- Yin, X. (1997). Optical air mass: Daily integration and its applications. *Meteorology and Atmospheric Physics* 63:227–233.
- Yong, B., L.-L. Ren, Y. Hong, et al. (2010). Hydrologic evaluation of Multisatellite Precipitation Analysis standard precipitation products in basins beyond its inclined latitude band: A case study in Laohehe Basin, China. *Water Resources Research* 46:W07542.
- Young, I. R., S. Zieger, and A. V. Babanin (2011). Global trends in wind speed and wave height. *Science* 332:451–435.
- Youngs, E. G. (1988). Soil physics and hydrology. *Journal of Hydrology* 100:411–431.
- Youngs, E. G., and A. Poulovassilis (1976). The different forms of moisture profile development during the redistribution of soil water after infiltration. *Water Resources Research* 12:1007–1012.
- Yu, C., A. W. Warrick, M. H. Conklin, M. H. Young, and M. Zreda (1997). Two- and three-parameter calibrations of time domain reflectometry for soil moisture measurement. *Water Resources Research* 33:2417–2421.
- Zangvil, A. (1996). Six years of dew observations in the Negev Desert, Israel. *Journal of Arid Environments* 32:361–371.
- Zazueta, F. S., and J. Xin (1994). Soil moisture sensors. University of Florida, Florida Cooperative Extension Science Institute of Food and Agricultural Sciences *Bulletin* 292.
- Zegelin, S. J., I. White, and D. R. Jenkins (1989). Improved field probes for soil water content and electrical conductivity measurement using time domain reflectometry. *Water Resources Research* 25:2367–2376.
- Zhang, T., J. A. Heginbottom, R. G. Barry, and J. Brown (2000). Further statistics on the distribution of permafrost and ground ice in the Northern Hemisphere. *Polar Geography* 24(2):126–131.
- Zhang, Z., X. Chen, C.-Y. Xu, L. Yuan, B. Yong, and S. Yan (2011). Evaluating the non-stationary relationship between precipitation and streamflow in nine major basins of China during the past 50 years. *Journal of Hydrology* 409(1–2):81–93.
- Zhou, Y. (2009). A critical review of groundwater budget myth, safe yield and sustainability. *Journal of Hydrology* 370:207–213.
- Zobler, L. (1986). *A World Soil File for Global Climate Modeling*. NASA Technical Memo 87802. New York: NASA/GISS.
- Zolina, O., C. Simmer, S. K. Gulev, and S. Kollet (2010). Changing structure of European precipitation: Longer wet periods leading to more abundant rainfalls. *Geophysical Research Letters* 37:L06704, doi:10.1029/2010GL042468.



Index

Ablation, 210
Absolute error, 30
Absolute humidity, 113
Absolute precision, 531
Absorption
 of radiation, 218, 227–228, 575–576
 of soil water by root plants, 275–276
Absorptivity, 49
Adiabatic process, 112
 cooling, 112, 117
 warming, 112
Air
 density of, 112
 mass, definition, and types of, 134
 near-surface values of physical properties
 of, 112
 supersaturated, 114
Air-entry pressure/tension, 332
Albedo, 52, 54, 226, 229–230, 571
 planetary, 52
Alfisols, 103
Alternate hypothesis/null hypothesis, 559–560
Andisols, 103
Anisotropy, 395–396
Anticyclonic circulation, 59
Aquiclude, 390
Aquifer(s)
 coastal, fresh/salt ground-water interface
 in, 418
 coastal, salt-water intrusion in, 450
 of the coterminous United States, 402
 definition of, 390
 response time/residence time, 396–397
 storage properties of, 392–393
 and stream relations, 409
 transmission properties of, 395–396
 unconfined/confined, 390–393
Aquitards, 390, 392
Areal reduction factors (ARFs), 196, 198
Aridisols, 103
Aridity index, 91, 105
Atmometers, 295
Atmosphere
 composition of, 49–50
 general circulation of, 55, 58–59
 size ranges of nongaseous constituents, 118
 vertical structure and dynamics, 50
 water-vapor capacity of, 86

Atmospheric constant, 278
Atmospheric resistance, 279
Atmospheric rivers, 70–71
Atmospheric stability
 correction factors, 131
 effects of, 128–130
Autocorrelation
 assessment, 561–562
 coefficient, 558
 effects on effective sample size, 569
 effects on sampling error, 569–570
 persistence and, 178, 556–559, 569
Baguios, 137
Bank storage, 410–411
Base flow
 definition of, 433, 463
 index (BFI), 436
 separation, 435, 462
Biomes, 104–106
Blackbody(ies), 48, 53, 232
Boltzmann transform, 362–364
Bond number, 11
Bouchet's complementary relationship equation, 303
Bowen ratio, 256
Boxplots, 560–561
British/common system of measurement, 8
Brooks–Corey equations/models, 336–338
Brubaker's snowmelt runoff model, 247, 249
Bubble pressure, 332
Bulk Richardson number, 130–131
Calibration, 510
Campbell parameters for soil textures, 338
Canopy conductance, 281
Canopy interception, annual loss as fraction of
 gross precipitation, 291
Capacitance probes, 321
Capillarity, 11, 328–330, 340
Capillary fringe, 329, 352, 428, 438, 495
Capillary rise, 329, 352, 436–438
Centimeter-gram-second (cgs) system, 8
Centroid lag, 471, 474
Centroid lag-to-peak, 465, 471, 475–476
Centroid/center of mass, 471, 474

Channel(s)
 flow, event-response processes/residence times, 508
 precipitation/channel interception, 479–480
processes
 hydraulic relations, 503–505
 simple streamflow routing, 505
Chemical tracers, 429
Chlorofluorocarbons (CFCs), 429
Circular statistics, 182
Clausius–Clapeyron (C–C) relation, 86
Clear-sky radiation, 575–577
 backscattered radiation, 577
 daily estimation of, 571–578
 diffuse radiation, 577
 direct-beam radiation, 575–577
 longwave radiation as, 231
 shortwave radiation as, 227
 solar flux, 574
 total incident radiation, 577
Climate
 biome formation and, 104
 elasticity, 92
 feedback factor, 84
 global. *See Global climate*
 soil development and, 103–104
Climate change
 evidence for recent climate-related hydrologic changes, 87–91
 greenhouse effect/greenhouse gases, 52–55
 moisture recycling and, 96–100
 overview of changes in hydrologic cycle, 84–86
 runoff sensitivity to, 91–96
Cloud
 condensation nuclei, 117–119
 cover
 effect on longwave radiation exchange, 231–232
 large-scale changes in, 88
 formation, 135
 seeding, 199
Coefficient of variation, 182
Cold fronts, 135
Concentration
 of particulate/dissolved material constituent, 79
 time of, 471, 476, 513

- Condensation, 113, 117–118
 Confidence intervals, 566–569
 Conservation of fluid mass, law of, 325
 Conservative substances, 13
 Constituent load, 81
 Continuous random variables, 550–551
 Continuous time traces, 24
 Control volumes, 13–14
 Convection
 free, 254, 258
 free/thermal, 119
 Convex routing method, 505
 Correlation coefficient, 556–567, 570
 Covalent bonding, 539–540
 Covariance and correlation, 556
 Critical Zone, 47, 100–107
 Curve numbers, 518, 520
 Cyclogenesis, process of, 134–135
 Cyclonic storms
 cloud seeding to increase precipitation from, 199
 cyclonic circulation, 59
 extratropical cyclones, 134–136
 tropical cyclones, 137–141
- Dalton's law, 112
 Darcy velocity, 324, 391
 Darcy's law
 Green-and-Ampt model application of, 366
 recharge and, 353, 428
 of saturated surface flow, 323–324, 327
 for unsaturated flow, 240, 330
 for vertical downward unsaturated flow, 345
- Data analysis
 display with preliminary assessment, 560–562
 estimating parameters of probability distributions, 565–566
 hypotheses tests, 559–560
 identifying candidate probability distributions, 562–565
 preliminary assessment of
 autocorrelation assessment, 561–562
 boxplots, 560
 empirical distribution function, 560–561
 histograms, 560
 stationarity assessment, 562
 sampling error, 566–570
- Deep seepage, 438–441
- Density
 bulk, 315
 water, 10–11
 weight, 10, 544
- Depression storage/surface detention, 486–487
- Depth hoar, 209
- Depth of ponding and water infiltration rate, 355, 357
- Dew, 146
- Dew point, 114
- Diffusion, 122–124
 equation for an isotropic/homogenous medium, 328
 general diffusion process, 125
 of momentum, 125–126
 of sensible heat, 127–128
 of water vapor, 126–127
- Diffusivity, 123–125, 254, 362–363
- Digital elevation models (DEMs), 17
- Dilution gauging, 585–586
 Dimensional homogeneity, 8
 Dimensionally inhomogeneous equations, conversion of, 537–538
 Dimensionless quantities, 8
 Dimensions, 7
 dynamic, 8
 geometric, 8
 kinematic, 8
- Direct weighted averages, 162–166
 arithmetic average, 163
 hypsometric method, 165–166
 Thiessen polygons, 163–164
 two-axis method, 164–165
- Direct-beam radiation, 575–577
- Direct-current resistivity, 321
- Discharge areas, 398
- Discrete random variables, 550
- Discrete time-series variables, 24
- Disdrometers, 150
- Dissolved load, 79
- Dissolved-solids concentrations, 307
- Double-mass curves, 157–159
- Drainage basin. *See* Watershed
- Drainage density, 458
- Drainage-network composition, laws of, 456–457
- Droplet growth, 118–119
- Dry adiabatic lapse rate, 112, 128
- Dunne overland flow, 484
- Dupuit approximation
 equations, 410, 412, 414
 and ground-water contribution to streamflow, 431
 for steady-state unconfined aquifer drainage to streams, 413
 for unconfined flow, 412
- Dupuit–Forchheimer equations, 496
- Duration curves, 25–26
- Dynamic/geometric scaling, 380
- Ecoregions, 104
- Eddy
 correlation, 129–132, 258, 306
 viscosity, 547–548
- Effective sample size, effects of autocorrelation on, 569
- Effective stress, and compressibility of water, 395
- El Niño–Southern Oscillation (ENSO), 62–63
- Electrical resistance blocks, 320
- Electromagnetic induction (EMI) instruments, 321
- Electromagnetic spectrum, 48
- Emissivity, 48
- Empirical distribution function, 560–562
- Empirical orthogonal functions, 169
- End-member chemical composition, 478–479
- End-member mixing analysis (EMMA), 477–478
- Energy, conservative substance of, 13
- Energy-balance components
 case study of snowmelt at Danville, VT, 234, 236–237
 comparison of energy balances in different environments, 237–239
 effects of forest cover and weather, 234
- Energy-balance equation(s), 15
 for evaporating water body, 260–263
- Energy-exchange processes
 conductive exchange of sensible heat with the ground, 234
 heat input by rain, 233
 longwave radiation exchange, 231–232
 relative importance of energy-balance terms, 234–239
 shortwave (solar) radiation, 226–230
 turbulent exchange of latent/sensible heat, 232–234
- Entisols, 101
- Equation(s)
 conservation, 14–15, 326
 conversion, 537–538
 dimensional properties of, 8–9
 empirical, 8
 homogeneous, 8
 inhomogeneous, 8–9
- Equifinality, problem of, 510
- Equilibrium
 potential evapotranspiration, 294
 runoff, 471, 497
 soil-water profiles, 352–353
 water-content profile, 353–354
- Equipotentials, 328
- Equivalent latitude/longitude, 229
- Error(s)
 absolute and relative, 30
 Gaussian theory, 30–31
 in precipitation measurement, 20
 propagation, 31
 random, statistical characterization, 30–31
 sampling error, 566–570
 standard deviation, 31
 systematic and random, 30
- Evaporation
 Bowen ratio, 256
 diffusive process of, 254–255
 energy balance, 256–257
 evaporative fraction, 256
 heat-exchange processes and, 254–257
 latent-heat exchange, 255
 mass-transfer equation for evaporation rate, 254
 oceanic, 74
 psychrometric constant, 256
 sensible-heat exchange, 255–256
- Evaporation process
 latent heat of vaporization, 115–116
 vapor exchange, 114–115
- Evaporimeters, 295
- Evapotranspiration, 18–19, 88, 253–309
 actual, 298–307
 methods based on water quality, 307
 potential-evapotranspiration approaches, 298–304
 turbulent-exchange and energy-balance approaches, 306–307
 water-balance approaches, 304–306
- bare-soil evaporation, 274–283
- capillary rise and, 436–438
- classification of processes, 257
- classification of types, 257
- continental water balances, 77
- continental, average recycling ratio, 99
- energy-limited/water-limited, 91, 74
- evapotranspiration-recycling ratio, 98
- free-water and lake evaporation, 257–272

- eddy correlation, 258
 energy balance, 260–263
 mass transfer, 258–260
 pan evaporation, 267–270
 Penman/combination method, 263–267
 summary and example calculations, 271–272
 water-balance approach, 270–271
 global distribution of, 71–75
 interception and interception loss, 283–292
 mass-transfer approach, 115, 126
 Penman-Monteith model, 282–283
 potential and reference-crop, 74, 292–298
 comparison of PET/RET estimation methods, 296–298
 direct measurement, 295–296
 operational definitions, 293–295
 redistribution of soil water and, 381, 384–385
 reference-crop evapotranspiration (RET), 292–294
 transpiration process, 275–283
 as water-balance component, 21–22
- Event flow, as direct response to a given water-input event, 463
- Event-flow-generation processes, 478–503
 channel precipitation/channel interception, 479–480
 overland flow, 480–487
 overview of hillslope processes, 499–503
 subsurface flow, 487–499
- Exceedence probability, 556
- Exfiltration, 274, 313
- Expected value, 168, 551
- Experimental variogram, 169
- Extraterrestrial solar radiation
 daily total, 575
 day number/Julian date, 572
 declination, 574
 modeling/measuring, 571–575
 orbital eccentricity, 572, 574
 solar noon, sunrise, and sunset, 575
 zenith angle, 574
- Fick's law, 123, 125
- Field capacity, 345–348, 350
- Float gauges, 150
- Flood(s)
 design rainfalls and, 185
 designed vs. floods from actual storms, 510–511
 flood wave, 459–460, 462
 flood-wave velocity, 504–505
 predictions/forecasts, 455
- Flow
 boundary-layer, resistance in, 546
 bypass, 490
 laminar, 324, 546–547
 mechanisms, classification of event responses, 479
 meridional, 63
 nets, 398–400, 403, 431, 438
 open-channel, 548
 potential, 546
 preferential, 361, 489–492
 quick, 463
 systems, local/intermediate/regional, 399, 401
- uniform, 504
 zonal, 63
- Flow-duration curves (FDCs), 26
- Fluid potential, 323
- Flumes, stream gauging with, 589
- Fluxes, 63–69, 123
- Fog drip, 146
- Forced convection, 119, 254
- Fractionation, 543–544
- Fragipan/hardpan, 355
- Free-water evaporation, Penman/combination equation for, 263–267
- Free-water/potential evaporation, 257–258
- Frequency-domain reflectometry (FDR), 320
- Friction velocity, 122
- Fronts, 134–136
- Fundamental hydrologic landscape unit (FHLU), 404, 406
- Gamma-ray instruments, 320
- Gas constant, 111
- Gash Interception Model, 290
- Gauge(s)
 acoustical, 150
 capacitance, 150
 hook, 267
 networks, uncertainty analysis of, 172–178
 optical, 150
 pressure, 323
 recording, 150
 reference, 154
 tipping-bucket, 150
 weighing, 149
- Gaussian theory of errors, 30–31
- Gelisols, 103
- Geology, effects on regional ground-water flow, 400–404
- Geometric/dynamic scaling, 379–380
- Geomorphologic instantaneous unit hydrograph (GIUH), 527–528
- Geostatistics, 168–171
- Ghyben–Herzberg relation, 416, 418
- Glaciers, large-scale changes in, 89
- Gleying, 355
- Global climate
 atmosphere's impact, 49–50
 energy budget of the earth, 51–54
 general circulation of the atmosphere, 58
 general circulation/distribution, pressure and temperature, 55–59
 large-scale internal climatic variability and teleconnections, 59–63
 latitudinal energy transfer, 54–58
 laws of radiant energy exchange, 47–49
- Global hydrologic cycle, 68–100
 climate change and, 84–100
 continental water balances, 77
 distribution of evapotranspiration, 71–75
 distribution of precipitation, 67–71
 global-warming-related changes, 87–91
 land phase of, 3–5
 major storage components and flows of, 4
 recent large-scale changes in, 88–89
 rivers, lakes, and reservoirs, 77–79
 role of individuals in, 69
 runoff distribution, 74–77
 stocks and fluxes, 63–69
- Goodness-of-fit analysis, 563
- Graphical flow separation, 463–464, 466
- Gravity Recovery and Climate Experiment (GRACE) satellite mission, 21–22
- Green-and-Ampt model, 366–369, 374–375, 379
- comparison, 376, 378
 explicit method, 371–372, 377–378
 implicit method, 376–378
 time of ponding, 370
- Greenhouse effect/greenhouse gases, 52–55
- Ground water
 aquifers and aquitards, 390–397
 balance equations, 421
 contributions to streamflow, 431–436
 definition/significance of, 389–390
 development, impacts on areal hydrology, 441–451
 effects of ground-water extraction, 446–450
 hydraulics of ground-water development, 441–446
 sustainable extraction rate/safe yield, 450–451
- evaluation of ground-water balance components, 422–441
 capillary rise, 436–438
 contribution to streamflow, 431–436
 deep seepage, 438–441
 recharge from infiltration, 422–430
 recharge from surface water, 430–431
 flow. *See* Ground-water flow
 fresh/salt interface in coastal aquifers, 418
 mounds, 493–495
 recharge, 313
 regional flow of, 397–408
 effects of geology on, 400–404
 effects of topography on, 399–400
 equation for steady ground-water flow, 397, 428
 general features, 397–398
 hydrologic landscapes synthesizing effects of, 404–407
 water-table ratio analysis of, 406–408
 in the regional water balance, 416–421
 safe-yield, 450–451
 storage/specific, and storage coefficients, 392
 surface water and, 408–416
 zone, 350–352
- Groundmelt, 234
- Ground-penetrating radar (GPR), 321
- Ground-water flow
 continuity equation for, 327
 effects of geology on, 400–404
 general equation of, 391
 inflow and outflow, 20–21
 inverse application of equation for, 428
 stratigraphy and ground-water movement, 400
- Ground-water/surface-water relations
 lakes/wetlands and oceans, 414–416
 streams, 408–414
- Growing season, large-scale changes in, 89
- Hardpan/fragipan, 355
- Head
 gravitational, 323
 hydraulic, 323, 391

- pressure, 323, 331
 suction, 330
 tension, 330
 total, 331
 total hydraulic, 323
- Heat capacity/specific heat, 12, 548
 Heat pulse probes, 323
 Heat storage/advection effects, 264
 Heterogeneity, 395–396
 Hillslope processes
 overview of, 499–503
 residence times, 508
 response mechanisms, 460–461, 502
- Hingeline, 398
 Histograms, 560–561
 Histosols, 103
 Hortonian overland flow, 14, 481–482
 Humidity
 absolute (vapor density), 113
 large-scale changes in, 88
 relative, 113–114
 specific (mixing ratio), 113
- Hurricanes, 137–139. *See also* Cyclones
- Hydraulic conductivity of soil surfaces
 conceptual basis of Green-and-Ampt model, 367
 degree of saturation vs., 335
 human modification of soil surface, 358
 inwashing of fine sediment, 358
 minimum value of the infiltrability of a soil, 357
 organic surface layers, 357–358
 permeability and, 391
 rain compaction, 358
 ranges, 325
 saturated, 323–325, 337, 396, 401
 swelling-drying of soils, 358
 unsaturated, 333–334
 water-content relations, 335–339
 water-input rate and, 367–371
- Hydraulic diffusivity, 362
 Hydraulic relations
 basic equations, 503–504
 flood-wave activity, 504–505
 typical forms of, 332
 uniform flow, 504
- Hydroclimatic variables, summary of trends in, 87
- Hydrogen bonding, 9–10, 539, 541
- Hydrograph(s)
 exploration, effects of input/basin characteristics on, 471–477
 geomorphologic instantaneous unit hydrograph (GIUH), 527–528
 heuristic, separation of, 462–464
 lateral-inflow, 505
 linear-watershed instantaneous unit, 525–527
 outflow, 505
 response, 469–471
 basic terms, 470
 definition of terms describing, 470
 dependence of characteristics on watershed/input characteristics, 476
 heuristic hydrograph separation and, 463
 quantitative description of, 469, 471
 rise/peak/recession, 433, 435, 459, 469
 S-hydrograph, 528
- schematic for equilibrium runoff, 471
 SCS generalized dimensionless synthetic hydrograph, 519
 snowmelt runoff, 249
 storm, 460, 463, 469
 streamflow, 433, 459
 synthetic unit, 526
 unit, 521–529
- Hydrologic cycle
 global, 63–100
 ground water in, 313–343, 389–453
- Hydrologic horizons, 355
- Hydrologic landscapes, 404, 406–407
- Hydrologic science, 3, 6
 key elements of paradigm shift in, 39–40
 range of time and space scales in, 3, 6
- Hydrologic simulation modeling
 caveats, 604
 definition of, 595
 model evaluation, 602
 process of, 600–602
 purposes of, 596–597
 types of, 597–600
- Hydrologic soil horizons, 350–353
 ground-water zone, 350–352
 hydrologic soil-profile horizons, 351
 intermediate zone, 352
 root zone, 352
 tension-saturated zone, 352
- Hydrologic storage
 definition, 27
 residence time, 28
 storage effects, 27–28
 watershed storage function, 37
- Hydrologic systems, 13–14
- Hydrologic variables
 spatial variability, 23–24
 special characteristics, 23–27
 temporal variability, 24–27
- Hydrology
 Critical Zone, 100–107
 definition and scope of, 3
 future of, 39
 physical quantities and laws, 7
 scientific development of, 607–609
 soils and, 100
 uncertainty in, 28–36
- Hydrometeors, 159
- HydroSHEDS, 17–18
- Hydrostatic relation, 111
- Hyetographs, 459, 461, 463, 466, 469–470
- Hygroscopic soil water, 350
- Hyporheic flow, 409–410
- Hypothesis testing, 559–560
- Hypsometric curve, 165
- Hypsometric method, 165–166
- Hysteresis, 333–334, 339
- Ice, crystal lattice of, 540, 542
- Ice-crystal formation/growth, 119, 146
- Ideal gas law, 111
- Impulse-response analysis, 429
- Inceptisols, 101
- Incident solar radiation, 52, 571
- Index-flood approach, 564
- Infiltrability/infiltration capacity, 355
- Infiltration, 313
 definition of, 345
 with depth-varying water content, 373
- horizontal, 362, 364
 over areas, 375–381
 heuristic approaches, 380–381
 theoretical scaling approaches, 375–381
- profile-controlled, 355
- redistribution of soil water, 381–384
 with evapotranspiration, 383–384
 without evapotranspiration, 381–383
- spatial/temporal variability of, 375
- Infiltration process, 355–359
 basic definitions, 355–356
 comparison of Green-and-Ampt model and Richards equation, 374
 factors affecting infiltration rate, 357–359
 chemical characteristics of soil surface, 359
 hydraulic conductivity of soil surface, 357–358
 physical/chemical properties of water, 359
 surface slope and roughness, 358–359
 water content of soil surface pores, 358
 water-input rate/depth of ponding, 357
- general features, 356
- measurement of infiltration, 359–361
 observation of soil-water changes, 361
 preferential flow, 361
- ring infiltrometers, 359–360
- sprinkler-plot studies, 360
- tension/disc infiltrometers, 360
- quantitative modeling at a point, 361–375
 comparison of Green-and-Ampt and Philip models, 375, 379
- Green-and-Ampt model, 366–375
- idealized conditions, 361
- solutions to the Richards equation, 361–364
- unsaturated porous-media flow and, 345–387
- Infiltrometers, 360
 double-ring, 360
 tension/disc, 360
- Insolation
 effect of cloud cover on, 226–228
 effect of forest canopy on, 228
 effect of slope and aspect on, 229–230
 incident solar radiation, 52, 571
- Instantaneous unit hydrographs, 525
- Interception loss, 253
- Interception process, definition of terms, 285
- Interception/interception loss, 283–292
 definitions used in describing/measuring interception, 285–286
 evaporation of intercepted water, 290
 field measurement of interception, 286
 hydrologic importance of interception loss, 290–292
 modeling, 286–290
 Liu model, 287
 sparse Rutter model, 286
- Interfacial sublayer, 120
- Interflow, 313, 487
- Intermediate zone, 352
- Interpolation function, 166
 optimal, 169
- Interpolation surface-fitting methods, 166
- Intertropical convergence zone, 67, 136–137
- Inverse-distance weighting, 166–167

- Inversion, 128
 Isobars, 59, 134
 Isohyets, 166
 Isotopes
 fractionated, 543–544
 isotopic composition, 307
 radioactive, 429–430, 543–544
 stable, 429, 543–544
 tritium, 543
- Kinematic-wave approximation, 493, 496
 Kirchoff's law, 49
 Kriging, 169
 Kurtosis, 564, 568
- Lag- k autocorrelation coefficient, 558
 Lag-1 autocorrelation coefficient, 178
 Lag-to-peak, 469–470, 475–476, 509
 Lakes
 evaporation, 258
 Kohler/Parmele expression, 262, 264
 interaction with ground water, 414–416
 large-scale changes in number and size of, 89
 main hydrologic functions of, 77
 water-balance computation, 270
 world's 25 largest, 79
- Laplace equation, 328, 397
 Lapse rate
 definition, 50
 dry adiabatic, 112, 128
 environmental, 128
 saturated adiabatic, 117
- Latent heat, 12
 definition of, 111
 diffusion of, 127
 exchange, 116, 255
 of fusion, 12
 of sublimation, 116
 of vaporization, 12, 115–116
- Lateral inflow, 461
 hydrograph, 505
- Latitudinal energy transfer, 54–58
 Leaf-area index, 228, 281–283
 Least-squares method, 365–366
 Linear-watershed instantaneous unit hydrograph, 526–527
 Liu model, 287
 L-moments, 553, 555, 564
 Local recycling ratio, 146
 Log-normal distribution, 555–556
 Longwave radiation
 greenhouse effect, 52, 54
 exchange, 231–232
 clear-sky. *See* Clear-sky radiation
 effect of cloud cover on, 231–232
 effect of forest canopy on, 232
- Lysimeters, 218, 248, 250, 295, 297
- Macropores, 355, 489–492
 Mass density, 10, 544
 Mass transfer, 258–260
 approach to evaporation, 126
 Mass, conservative substance of, 13
 Matric potential, 330
 Matrix (Darcian) flow, 487–489
 Mean, 551, 567
 and standard deviation, 569–570
- Measured quantities
 computations with, 532
 error/uncertainty in measurement, 531
 fundamental dimensional character of, 7–8
 precision and significant figures, 531–532
- Measurement, 148–162.
 active microwave (radar), 321
 See also Precipitation measurement
- Meniscus, 329–330
- Metamorphism
 constructive, 209
 destructive, 209
 melt, 209
 snowpack, 208–209
- Meteorology, 133
 convective precipitation, 141
 fronts and extratropical cyclones, 134–136
 intertropical convergence zone, 136–137
 moisture sources and precipitation recycling, 146–147
 occult precipitation and dew, 146
 orographic precipitation, 141–146
 tropical cyclones, 137–141
- Mixed layer/Prandtl layer, 119–120
 Mixing ratio, 113–114
 Model error, 36
 Model/theoretical variogram, 169
 Moisture recycling, 99
 climate change's impact on, 96–100
- Moisture-characteristic curve, 332
 Moisture-conductivity curve, 333
 Mollisols, 103
 Momentum
 conservative substance of, 13
 diffusion of, 125–126
- Monsoon, 71
 Motes, 320
 Multiquadric cone/interpolation, 167–168
- National Solar Radiation Data Base, 572
 Net recharge, 421
 Neutral stability, 254
 Neutron moisture meters, 320
 Newton's second law of motion, 7
 Nonparametric/parametric tests, 559
 Nonrecording storage gauges, 149–150
 Nonstationarity, 26–27
 Normal (Gaussian) distribution, 31–33
 log-normal distribution, 555–556
 normal pdf and cdf, 555
- North Atlantic Oscillation (NAO), 63
 North Pacific Oscillation (NPO), 63
 No-slip condition, 12, 546
 Notation, 462
 Nuclear magnetic resonance (NMR), 321
 Null hypothesis/alternate hypothesis, 559–560
- Occluded front, 136
 Oceans, ground-water outflow to/interactions with, 416–418
 Optical air mass, 575–576
 Orbital eccentricity of earth, 572, 574
 Ordered variables, 556
 Orographic effects, 20
 Orographic uplift, 141
 Outflow function, 27
 Outflow hydrograph, 505
- Overland flow, 480–487
 definition of, 345, 480
 Hortonian (saturation from above), 480–481
 saturation (Dunne) from below, 483–486
 surface detention (depression storage), 486–487
- Oxisols, 104
- Pacific–North America Oscillation (PNA), 63
 Pan coefficient, 268
 Pan evaporation, 267–270, 293, 297
 Parametric/nonparametric tests, 559
 Partial pressure, 112
 Partial-area concept, 481
 Particle density, 315
 Particulate load, 79
 Particulate sediment yields, global distribution of, 85
 Passive microwave measurements, 321
 Peak discharge, 459, 519
 Pedologic soil horizons, 353, 355
 Pedotransfer functions (PTFs), 335
 Penman/combination equation for free-water evaporation, 263–267
 Penman–Monteith equation/model of evapotranspiration, 282–283, 294–295, 297
 Percolation, 345
 Permafrost, 89, 101, 103
 Permanent wilting point, 347–348, 350
 Permeability, 324–325, 391
 intrinsic, 325, 391
 pH, definition of, 543
 Philip equation, 361
 apparent time of ponding, 364
 comparison with Green-and-Ampt model, 375–379
 compression time/effective time, 364
 least-squares method, 365–366
 with time adjustment, 378
- Phreatic zone, 350
 Phreatophytes, 453
 Piezometers, 323, 391, 438
 Pike equation, 298
 Planck's law, 48
 Planetary boundary layer, 50
 mixed/Prandtl, 119
- Planets, surface temperatures/pressures, 10
 Plot correlation-coefficient test, 563
 Point-precipitation measurement, 148–159
 areal estimation from, 162–178
 conventional recording gauges, 149–150
 errors in, 150–159
 distance to obstructions/splash, evaporation, and wetting losses, 153
 gauge-catch efficiency due to occult/low-intensity precipitation, 154
 instrument and recording errors, 155
 orifice size/orientation/wind shielding, 150–153
 factors affecting accuracy, 150–159
 unconventional recording gauges, 150
- Polynomial trend surfaces, 166
 Ponding, 355–356, 370
 apparent time of, 364
 depth of, and water-infiltration rate, 355–357
 effective time of, 364
 time of, 370, 481

- Population, target, 23
 Pore size, factors affecting, 357–358
 Porosity(ies)
 of geologic materials, 394
 primary/secondary, 453
 table of, 394
 Porous media
 conservation-of-mass equation, 326
 distribution of particle sizes/pores, 313–316
 particle density/porosity defined, 315
 ranges of porosity for soils of various textures, 319
 laminar flows, 548
 material properties, 313, 315–319
 bulk density, 315
 compressibility of, 395
 Potential evapotranspiration (PET), 74, 292–298
 Potentiometric surface, 391
 Prandtl layer/mixed layer, 119
 Prandtl–von Kármán universal velocity distribution, 122–123, 125, 254, 547
 Precipitation
 annual, coefficient of variation of, 182
 average annual, ratio of global distribution, 75
 average, latitudinal distribution of, 70
 climatology, 181–200
 anthropogenic effects on, 198–200
 extreme values of, 181
 long-term average, 181–183
 variability of, 182–185
 continental
 average recycling ratio of, 98
 water balances, 77
 convective, 141–142
 definition of, 133
 determining type of, 147–148
 estimates of annual recycling ratio, 147
 evapotranspiration of, 253
 generalized map of seasonal regimes, 72
 global
 average annual, 70
 distribution of, 67–71
 mean, variability of, 87
 large-scale changes in the hydrologic cycle, 88
 measurement. *See* Precipitation measurement
 meteorological situations conducive to, 133
 occult, 146, 154
 orographic, 141–146
 processes of, 116–119. *See also* Precipitation processes
 rain/snow partitioning of, 148
 recycling, and moisture sources, 146–147
 seasonal distribution of, 70
 variability
 interannual, 182
 intra-annual, 182–185
 normalized annual precipitation, 182
 as water-balance component, 20
 Precipitation measurement
 areal estimation from point measurements, 162–178
 comparison of methods, 171
 direct weighted averages, 162–166
 point measurement, 148–159
 spatial interpolation (surface fitting), 166–171
 error, sources of, 20
 gauges/gauge networks/wind shields, 151–153, 172–178, 180
 point measurement, 148–159. *See also* Point-precipitation measurement
 radar, 159–161, 211
 reference gauges, 150
 satellite-based precipitation estimates, 161–162
 of snow/snowmelt, 209–213
 standard gauges for snowfall/snowpack, 210–212
 universal surface gauge for snowfall/snowpack, 211
 Precipitation processes
 condensation, 117–118
 cooling, 117
 droplet growth, 118–119
 importation of water vapor, 119
 second-order stationary, 168
 Precipitation-recycling ratio, 98
 Precision
 correct treatment of, 533
 definition of, 531
 of measurement, random error inversely reflected in, 30
 Priestley–Taylor equilibrium equation, 297
 PRISM model, 171
 Probability, 549–550
 Probability distribution(s)
 common, 552
 continuous random variables, 550–551
 discrete random variables, 550
 estimating parameters of, 565–566
 identification of, 562–565
 method of L-moments, 565–566
 method of maximum likelihood, 565
 method of (product) moments, 565
 of potential measurement errors, 32
 regional L-moment approach, 564–565
 Probability-plot correlation-coefficient test, 563
 Probability-weighted moments, 553, 555
 Product moments, 551–553
 Psychrometric constant, 256
 Pyranometers, 226, 571
 Pyrgeometers, 231, 261
 Quantiles, 551
 Radiant energy exchange laws, 47–49
 Radiation
 absorption. *See* Absorption
 clear-sky. *See* Clear-sky radiation
 components, determining values of, 260–261
 on a sloping surface, 577–578
 equivalent slope, 577
 solar noon, sunrise, and sunset, 577. *See also* Solar radiation
 total incident radiation at the surface, 576, 578
 Radiometers, 231, 261
 Rain
 compaction, 358
 gauges/precipitation gauges, 148
 shadow, 142
 Rainfall
 effective/excess, 469
 extreme
 depth-duration-frequency analysis, 190–198
 design rainfalls/design floods, 185
 durations of, 185
 extreme-value analysis of rainfall, 185
 probable maximum precipitation, 186–190
 time distribution of, 198
 Rainfall-runoff models
 inputs to, 510–514
 rational method, 514–515
 runoff processes and, 505–510
 Soil Conservation Service curve-number method, 515–521
 unit hydrographs, 521–529
 Random error, statistical characterization, 30–31
 Random uncertainty, treatment in computations, 29–36
 Random variables, 549
 continuous, 550–551
 discrete, 550
 Range, 169
 Recharge
 areas, 398
 definition of, 389
 from infiltration
 direct application of Darcy's law, 428
 and ground-water balance and, 422–430
 impulse-response analysis, 429
 inverse application of ground-water flow equation, 428
 methods based on water quality, 429–430
 soil-water balance method, 423
 well hydrograph analysis, 423–428
 from surface water
 direct measurement of ground-water potential/flux, 430
 direct measurement of streamflow increments, 430–431
 and ground-water balance, 430–431
 water-temperature measurements, 431
 Reference-crop evapotranspiration (RET), 292, 294
 Reflectivity, 49
 Regional frequency distribution, 565
 Regression analysis, 8
 Relative error, 30
 Relative humidity, 113–114
 Representative elementary volume (REV), 324
 Reservoirs
 human-made, locations of, 80
 increased volume of fresh surface-water storage, 77, 79
 linear, 27, 29, 505
 residence time, 28–29
 storage effects, 27–28
 Response lag, 469, 474
 Return period/recurrence interval, 556
 Reynolds number, 12, 324, 548
 Richards equation, 340, 356, 361–364, 374
 Richardson number, 130
 Rime, 146
 Rivers
 function of, 77
 location of world's 16 largest, 78

- material transport by, 79–84
 sedimentation
 dissolved material, 81, 84
 particulate material, 84
 sediment loads, yields, and erosion rates, 83
 total material transport to oceans, 84
See also Streams
- Root zone
 depths by vegetation type, 352
 of soil, water balance for, 423
- Roughness height, 122–123, 254, 279
- Routing coefficient/time step, 505–506
- Runoff
 average annual global distribution of, 75
 climate elasticity of, 92
 coefficients, 519
 continental water balances, 77
 definition/equation for, 19
 direct (event flow), 463
 global distribution of, 74–77
 infiltration-excess, 480
 mechanisms, field studies of, 500
 processes and rainfall-runoff models, 506–510
 saturation-excess, 483–485
 seasonal regimes, 76
 sensitivity to climate change, 91–96
 snowmelt, 206, 239–244
 sources, identification of, 477–478
 storm runoff/storm flow, 463
 TOPMODEL approach, 486, 508
 twentieth-century increase in, 90
- Sample correlation coefficient, 556–557
- Samples from target populations, 23
- Sampling distributions, 566–567
 chi-squared (χ^2) distribution, 567
 t-distribution, 566–567
- Sampling error, 566–570
 effects of autocorrelation on, 569–570
- Satellite reanalysis, 171
- Saturated conductivity, 241
- Saturated flow
 ground-water, derivation of general equation for, 326–327
 porous-media flow, conservation-of-mass equation for, 326
 subsurface flow, basic principles, 323–328
 Darcy's law, 323–324
 general saturated-flow equation, 325–328
 permeability and hydraulic conductivity, 324–325
- Saturated zone, 313
- Saturation/wetness
 from below, 356, 358, 372–373
 defined, 323
 effective, 323
 overland flow/subsurface event flow, 483–485
 vapor pressure, 86, 113, 116
- Scatter plots, 557–558
- Scintillometry, 307
- SCS generalized dimensionless synthetic hydrograph, 519
- Seasonality index, 184–185, 187
- Sediment yield, 81
- Seepage, deep, 438–441
- Seepage face, 409
- Sensible heat
 definition of, 111
 diffusion of, 127–128
 exchange, 255–256
 exchange coefficient, 128
 transfer coefficient, 256
- Serial correlation coefficient, 558
- Shear stress, 125, 547
- Shelter factor, 281
- Shortwave (solar) radiation. *See Solar radiation*
- S-hydrograph, 528
- Significant figures, 531
- Simulation models. *See Hydrologic simulation modeling*
- Sintering, 209
- Skewness, 552, 564, 567–568
- Sloping-slab flow, hydraulics of, 496
- Sloping-slab runoff, 493–499
- Smoothing surface-fitting methods, 166
- Snow
 cover
 definition of, 209
 global, seasonal distribution/duration of, 71, 73
 measurement, 213–218
 satellite observation of, 216
 distribution of, 218–221
 effects of elevation and aspect on, 219
 effects of vegetation on, 219–221
 hydrologic importance of, 203–205
 material characteristics of, 205–209
 snow properties, 205–208
 snowpack metamorphism, 208–209
 measurement of snow/snowmelt, 209–218
 depth sensors, ultrasonic, 213
 precipitation, 210–213
 snowfall, 213–218
 snowmelt, ablation, and water output, 218
 snowpack/snow cover, 213–218
 properties of, 207
 radar detection of, 211, 213
- Snow pillows, 214–215, 218
- Snowfall
 definition, 209
 measurement of, 213
 precipitation measurement with universal gauges, 211
- Snowmelt
 definition, 210
 measurement, 211
 case study at Danville, VT, 234, 236–237
 modeling, 244–250
 approaches to, 245–246
 comparison of, 247–248
 energy-balance approach, 245
 evaluation of snowmelt models, 246–250
 hybrid approach, 245–246, 250
 importance of, 244–245
 temperature-index approach, 245, 250
- processes, 221–239
 energy-exchange process, 226–234
 relative importance of energy-balance terms, 234–239
 snowpack energy balance, 221, 224–226
- runoff generation, 206
 flow in the basal saturated zone, 244
 flow in the unsaturated zone, 240–244
- runoff hydrographs, 249
- runoff processes
 definition diagram for, 241
 water input from, 203
- Snowpack
 accumulation period/melt period, 223
 definition/defining properties of, 208–209
 density, field estimation of, 207
 energy balance, phases of, 221, 224–226
 large-scale changes in, 88
 liquid-water-holding capacity of, 225
 measurement, 211, 213–218
 metamorphism, 208–209
 seasonal variation in, 210
 water output from, 210
- Snow-water equivalent (SWE), 208
- Soil(s)
 formation and classification of, 101–102
 horizons
 Critical Zone, 100–101
 hydrologic/pedologic, 353, 355
- hydraulic behavior
 modeling parameters, 340
 pedotransfer functions for modeling, 337
- hydraulic classes, 335, 338–341
- hydraulic curves, 341
- hydraulic properties, estimation of, 371
- hydraulic relations, 338, 340
- hydraulic triangle, 337, 340
- hydrologic horizons, 350–352
- hydrophobic, 359
- moisture content, 320
- orders, global distribution of, 101–104
- pipes, 490
- profile, 353
- properties, example calculations, 318
- surface, hydraulic conductivity of, 357
- texture
 Brooks–Corey parameters for soil textures, 338
 determination, 318
 soil-texture triangle, 317, 335, 338
- water-repellent, 359
- Soil-water
 balance, 305
 conditions, 345–355
 content, annual range of, 385
 content, measurement of, 320–321
 pressure, 330–333
 status, 349
 storage, 320
- Solar beam, geometry of, 574
- Solar constant, 51, 572
- Solar radiation
 clear-sky. *See Clear-sky radiation*
 effect of forest canopy on insolation, 228
 effect of slope and aspect, 229–230
 extraterrestrial, 571–575
 on a horizontal surface, 575–577
 incident, 52, 231, 571
 longwave. *See Longwave radiation*
 near-ultraviolet/near-infrared wavelengths, 51
 shortwave, 226–234
 on a sloping surface, 577–578
 snow-surface albedo, 229–230
 spatial coherence of, 571, 573
 spectrum, 51, 53

- Solvent power, 12–13
 Sorptivity, 361–363
 “Sparse” Rutter conceptual model of interception, 286, 289
 Spatial correlation
 of annual precipitation, 180
 concept/coefficient of, 168–169
 Spatial interpolation (surface fitting)
 geostatistical methods, 168–171
 inverse-distance weighting, 166
 multiquadric interpolation, 167–168
 polynomial trend surfaces, 166
 PRISM model, 171
 satellite reanalysis, 171
 spline functions, 167
 Spatial variability, 23–24
 Spatial variance-reduction function, 178
 Specific discharge, 323
 Specific gravity, 545
 Specific heat/heat capacity, 12
 Specific humidity, 113
 Specific retention, 393
 Specific storage, 391
 Specific weight/weight density, 10
 Specific yield
 difficulty in determining areal value of, 427–428
 and specific retention of geologic materials, 393–394
 Spline functions, 167
 Spodosols, 104
 Sprinkler-plot studies, 360
 Stability conditions, summary of, 130
 Stage-measurement stream gauging, 589–592
 Standard deviation, 552, 567
 and mean deviation, 569–570
 standard error of a quantile, 567
 standard error of estimate, 175
 Stationarity, 27, 562
 Statistical inference, goal of, 549
 Statistical/stochastic surface-fitting methods, 166
 Stefan–Boltzmann constant, 47–48
 Stewart Model of Leaf Conductance, 281, 302
 Stiff diagram, 478–479
 Stocks and fluxes, 68–69
 Storage
 coefficient, 392
 gauges, nonrecording, 149
 hydrologic, 27–28. *See also* Hydrologic storage
 as water-balance component, 21
 Storativity, 392–393
 Stored-energy use, 257
 Storm(s)
 duration, 469
 hydrograph, 460, 463, 469
 runoff/storm flow, 463
 Stratigraphy and ground-water movement, 400
 Streamflow
 base-flow analysis, 433–436
 characteristics, quantitative description of response hydrographs, 469, 471
 ground-water contributions to, 431–436
 hydrographs, 433, 459
 identification of runoff sources, 477–478
 increments, direct measurement of, 430–433
 as indicator of climate change, 89
 Kirchner’s model of streamflow prediction, 38–39
 large-scale changes in, 88–89
 measurement methods based on water quality, 433
 routing, 505
 runoff generation and, 455–529. *See also* Runoff
 temporal variability of, 25–26
 in water-balance component evaluation, 20
 Stream-gauging methods, 579–592
 dilution gauging, 585–588
 portable weirs and flumes, 586–589
 selection of measurement location, 580
 stage measurement, 589–592
 velocity-area method, 580, 582–585
 volumetric gauging, 580
 Streamlines, 328
 Stream(s), 409–410
 bank storage, 410–411
 depletion/drawdown calculation, 444–446, 449
 depletion function/calculation, 445–446, 450
 Dupuit approximation, 410–414
 effects of ground-water extraction on, 449–450
 effluent (gaining), 409
 event flow/base flow, 408
 first-/second-/third-order, 456
 flow-through, 409
 hyporheic flow of, 409–410
 influent (losing), 409
 networks, 456–458
 drainage density and, 458
 links, nodes, and network magnitude, 458
 relations between stream response and properties of, 458–459
 stream orders and laws of network composition, 456–458
 width of, 458
 perennial/intermittent/ephemeral reaches, 409
 response characteristics, 459–477
 basic features, 459–462
 effects of input and basin characteristics on hydrograph exploration, 471–477
 event-flow volume, 465–469
 heuristic hydrograph separation, 462–464
 quantitative description of response hydrographs, 469–471
 volumetric flow rate (discharge/streamflow), 408
 watershed order of, 456
 water-temperature measurements of, 431
 See also Rivers
 Subsurface flow, 487–499
 convergence in the topographic index concept, 486
 event flow/storm flow, 493
 in the saturated zone, 493–499
 in the unsaturated zone, 487–492
 Subsystems, 14
 Surface detention/depression storage, 486–487
 Surface runoff. *See* Overland flow
 Surface tension, 10–11, 328–330, 340
 Surface-fitting methods, 166
 Systematic error/bias, 30
 Système International, 8
 Systems approach, 510–511
 Systems model, 509–510
 Tectonic cycle, 79
 Teleconnections, 62
 El Niño–Southern Oscillation (ENSO), 62–63
 North Atlantic Oscillation (NAO), 63
 North Pacific Oscillation (NPO), 63
 Pacific–North America Oscillation (PNA), 63
 Temperature
 base/index, 245
 conversion, 533, 536–537
 global distribution of mean temperature, 59
 increase due to greenhouse gases, 54–55
 lapse rate and inversion, 50
 monthly, observed global mean, 86
 potential, 130
 wet-bulb, 147–148
 Temporal variability, 24–27
 nonstationarity, 26
 streamflow, 25–26
 time series, 24–25
 variance-reduction function, 178
 Tensiometers, 321, 330–331
 Tension-saturated zone, 329, 352
 Thermal convection, 119, 141
 Thermal dimensions, 8
 Thiessen polygons, 163–164
 Time of concentration, 471, 476, 513
 Time of rise/time to peak, 469
 Time series, 24–25, 27, 556, 563
 Time to equilibrium, 471
 Time-domain reflectometry (TDR), 320
 TOPMODEL, 486, 508
 Topographic index, 486
 distribution of, 487
 Topography, effects on regional ground-water flow, 399–400
 Transfer functions, formulations of, 510
 Transmissivity, 49
 Transpiration, 18, 114, 253
 measuring, 277–278
 sap-flow measurement, 278
 stable-isotope techniques, 278
 modeling, 278–283
 atmospheric conductance/resistance, 278–280
 canopy conductance, 281–282
 leaf-conductance/resistance, 280–281
 Tropical Rainfall Measuring Mission (NASA), 161
 Turbulence, 12, 120–122
 turbulent flow, 547–548
 Turbulent diffusion, 120–121
 atmospheric stability, effects of, 128–129
 diffusion of latent heat, 127
 diffusion of momentum, 125–126
 diffusion of sensible heat, 127–128
 diffusion of water vapor, 126–127
 diffusion process, 122–124
 diffusivity, 124–125
 Two-axis method, 164
 Type I/Type II errors, 559
 Typhoons, 137

- Ultisols, 104
- Uncertainty
- analysis of gauge networks, 172–178
 - causes of, 28–29
 - random, treatment in computations, 29–36
 - absolute and relative error, 30
 - statistical characterization of random error, 30–31
 - systematic and random error, 30
- Unit conversion, 535–536
- temperature conversion, 533, 536–537
 - units with common zero, 532, 534–536
- Unitary homogeneity, 8–9
- Units, 8
- Unsaturated flow
- analytic approximation of $\psi(\theta)$ and $K_h(\theta)$ relations, 334–336
 - Darcy's law for, 330
 - general unsaturated-flow equation, 339
 - porous-media, infiltration processes and, 345–387
 - soil-water pressure, 330–333
 - subsurface, basic principles of, 328–340
 - surface tension and capillarity, 328–330, 340
 - unsaturated hydraulic conductivity, 333–334
- Unsaturated hydraulic conductivity, 241
- Unsaturated zone, 313–314, 352
- Vadose zone, 313–314, 352
- Validation, 510
- van Genuchten model, 334–337
- Vapor
- density, 113
 - exchange, 114–115
 - pressure, 112
- Variable source area concept, 484
- Variograms, 169–170
- Vegetation
- biomes, 104–105
 - effects on snow distribution, 219–221
 - impact on hydrologic response, 104–107
 - large-scale changes in plant growth, 89
- Vertisols, 104
- Virtual surface, 120
- Viscosity, 11–12, 546–547
- dynamic, 546
 - kinematic, 547
 - molecular, 547–548
- Voids, 314
- Warm fronts, 135–136
- Water
- availability
 - for evaporation, 257
 - strategies for increasing, 26
 - balance
 - analysis, 438–441
 - components, 19–22
 - continental, 77
 - equations, 14, 18–19
 - regional, 416–421
 - basin elevation, 439, 441
 - conditions in soils
 - field capacity, 345–348
 - hydrologic soil horizons, 350–352
 - permanent wilting point, 347–348
 - soil-water status, 348–350
 - content measurement, comparison of methods, 322
 - gravimetric measurement, 320
 - effective stress and compressibility of, 393, 395
 - output from snowpack, 210
 - paths in porous subsurface materials, 314
 - physical/chemical properties impacting infiltration, 359
 - physics of storage/movement in porous media, 313–341
 - saturation, 323
 - water storage, 320–323
 - precipitable, 114
 - properties of, 9–13
 - density, 10, 544–545
 - freezing and melting temperatures, 10
 - heat capacity (specific heat), 548
 - latent heat, 12
 - solvent power, 12–13
 - surface tension, 10–11, 545
 - viscosity and turbulence, 11–12, 546–548
 - stocks and fluxes of, 63, 67
 - storage
 - in porous media, physics of, 313–341
 - saturation, 323
 - specific, 326
 - volumetric water content, 320–323
 - as water-balance component, 20–21
 - structure
 - dissociation, 543
 - isotopes, 543–544
 - latent heat of freezing/melting, 540, 542–543
 - latent heat of vaporization/condensation, 543
 - molecular/intermolecular structure of, 539–540
 - Water table(s), 313, 406–408
 - perched, 493
 - ratio, 406
 - Water vapor
 - absolute humidity/vapor density, 113
 - atmospheric conductance for, 278
 - composition of, 112
 - dew point, 114
 - diffusion of, 126–127
 - humidity, relative/specific, 113–114
 - precipitable water, 114
 - transfer coefficient, 255
 - vapor pressure, 113
- Water-advedted energy, 256–257
- Water-input rate/depth of ponding, 355–357, 369
- Watershed(s)
- definition of, 15, 455
 - delineation, 15–17
 - digital elevation models (DEMs), 17
 - divide and drainage area of, 15
 - effective vs. total precipitation for, 468
 - event flow/effective rainfall of, 466
 - functioning, Kirchner's predictive model, 36–39
 - as impulse-response systems, 510
 - manual, 15, 17
 - order of streams, 456
 - outlet, 456
 - response, liner-reservoir model of, 472–477
 - basic hydrograph shape, 473–474
 - lag-to-peak/centroid lag-to-peak, 475–476
 - peak discharge, 476
 - prediction of watershed/input characteristics, 476
 - response time and centroid lag, 474
 - time base and recession/time of concentration, 476
 - time of rise, 475
 - schematic three-dimensional diagram of, 19
 - spatial distribution of average annual event-flow volume for, 467
 - storage function, 37
 - streamflow network and, 455–459
- Weather modification, intentional, 199–200
- Weirs, stream gauging with, 586–589
- Wells
- contributing area of, 444, 446–448
 - hydrograph analysis, 423–428
 - radial flow to, 441–444
 - salt-water intrusion in, 450
 - stilling, 267
 - well function values, tabulation of, 444
- Wetlands, interaction with ground water, 414–416
- Wetting front, 356–357, 360, 367, 374
- Wien's displacement law, 48
- Wind
- profiles, example calculations, 124
 - speed, large-scale changes in, 88
 - velocity, 122–124
- Zero-plane displacement height, 122–123, 254, 279

PHYSICAL HYDROLOGY

Third Edition

For twenty years, Lawrence Dingman's well-written, comprehensive *Physical Hydrology* has set standards for balancing theoretical depth and breadth of applications. Rich in substance and written to meet the needs of future researchers and experts in the field, Dingman treats hydrology as a distinct geoscience that is continually expanding to deal with large-scale changes in land use and climate. The third edition provides a solid conceptual basis of the subject and introduces the quantitative relations involved in answering scientific and management questions about water resources. The text is organized around three principal themes: the basic concepts underlying the science of hydrology; the exchange of water and energy between the atmosphere and the earth's surface; and the land phase of the hydrologic cycle. Dingman supplies the basic physical principles necessary for developing a sound, instructive sense of the way in which water moves on and through the land; in addition, he describes the assumptions behind each analytical approach and identifies the limitations of each.

Outstanding features include:

- An examination of documented trends in global change of climatic and hydrologic quantities
- Statistical and measurement methods for the development and management of hydrologic simulation modeling
- Additional exercises that emphasize analyses using data sets obtained via the Internet
- Excel spreadsheets on the accompanying CD

Waveland Press, Inc.

www.waveland.com

ISBN 13: 978-1-4786-1118-9
ISBN 10: 1-4786-1118-9



9 781478 611189